U.S. DEPARTMENT OF ENERGY | Energy Efficiency & Renewable Energy

DOE/EE-1038

Energy Storage R&D

2013

VEHICLE TECHNOLOGIES OFFICE

U.S. Department of Energy
1000 Independence Avenue, S.W.
Washington, D.C. 20585-0121

Fiscal Year 2013 Annual Progress Report for Energy Storage R&D

February 2014

Approved by

David Howell, Hybrid Electric Systems Program Manager

Vehicle Technologies Office, Energy Efficiency and Renewable Energy

Table of Contents

LIST OF FIGURES

LIST OF TABLES

I

Introduction

Vehicle Technologies Office Overview

Automotive Battery R&D Overview

I. INTRODUCTION

I.A Vehicle Technologies Office Overview

The Department of Energy's (DOE's) Vehicle Technologies Office (VTO) develops advanced transportation technologies that would reduce the nation's use of imported oil. Technologies supported by VTO include electric drive components such as advanced energy storage devices (batteries and ultracapacitors), power electronics and drive motors, advanced structural materials, advanced combustion engines, and fuels.[1] VTO is focused on funding high-reward/high-risk research by national laboratories, universities, and industry partners promising improvements in critical components needed for more fuel efficient (and cleaner) vehicles.

VTO works with U.S. automakers through the United States Council for Automotive Research (USCAR)—an umbrella organization for collaborative research consisting of Chrysler LLC, the Ford Motor Company, and the General Motors Company.[2] Collaboration with automakers through the US DRIVE (Driving Research and Innovation for Vehicle Efficiency and Energy Sustainability) Partnership enhances the relevance and the success potential of such programs.

During the past year, the U.S. government continued its strong R&D support of plug-in electric vehicles (PEVs) such as plug-in hybrids, extended range electric vehicles and all-electric vehicles. Earlier, in March 2012, President Obama announced the *EV Everywhere* Grand Challenge. One of its primary objectives is to enable U.S. innovators rapidly develop/commercialize the next generation of technologies achieving the cost, range, and charging infrastructure necessary for widespread adoption of PEVs. Their significant penetration into the transportation sector would reduce our dependence on foreign oil and any negative economic impacts associated with crude oil price fluctuations, as well as our greenhouse gas emissions.

An important step for the electrification of the nation's light duty transportation sector is the development of more cost-effective, longer lasting, and more abuse-tolerant PEV batteries. In fiscal year 2013 the DOE VTO battery R&D funding totaled nearly $88 million. R&D continued to focus on the development of high-energy batteries for PEVs and very high power devices for hybrid vehicles. This document summarizes the progress of VTO battery R&D projects supported in FY 2013. An electronic version of this report can be accessed at http://www1.eere.energy.gov/vehiclesandfuels/resources/fcvt_reports.html.

I.B Vehicle Technologies Battery R&D Overview

I.B.1 DOE Battery R&D Goals and Technical Targets

The *EV Everywhere* Grand Challenge[3] establishes a vehicle-level framework in which the technological progress toward achieving the Grand Challenge objectives can be evaluated. To meet those objectives, batteries, power electronics, motors, lightweight materials and vehicle structures must see dramatic advances. Performance and cost targets have been established for all the key technical areas associated with a PEV. Achieving those targets will meet the needs for a range of vehicle types including plug-in hybrids as well as short and long range all-electric vehicles. Some of the technology

[1] See http://www1.eere.energy.gov/vehiclesandfuels/ for more information.

[2] For more information, please see http://www.uscar.org/guest/view_partnership.php?partnership_id=1.

[3] For more information, please see http://www1.eere.energy.gov/vehiclesandfuels/about/partnerships/ev_everywhere.html.

targets, derived from modeling and hardware-in-the-loop simulations of batteries operating in PEVs under multiple drive cycles, are shown in Figure I - 1.

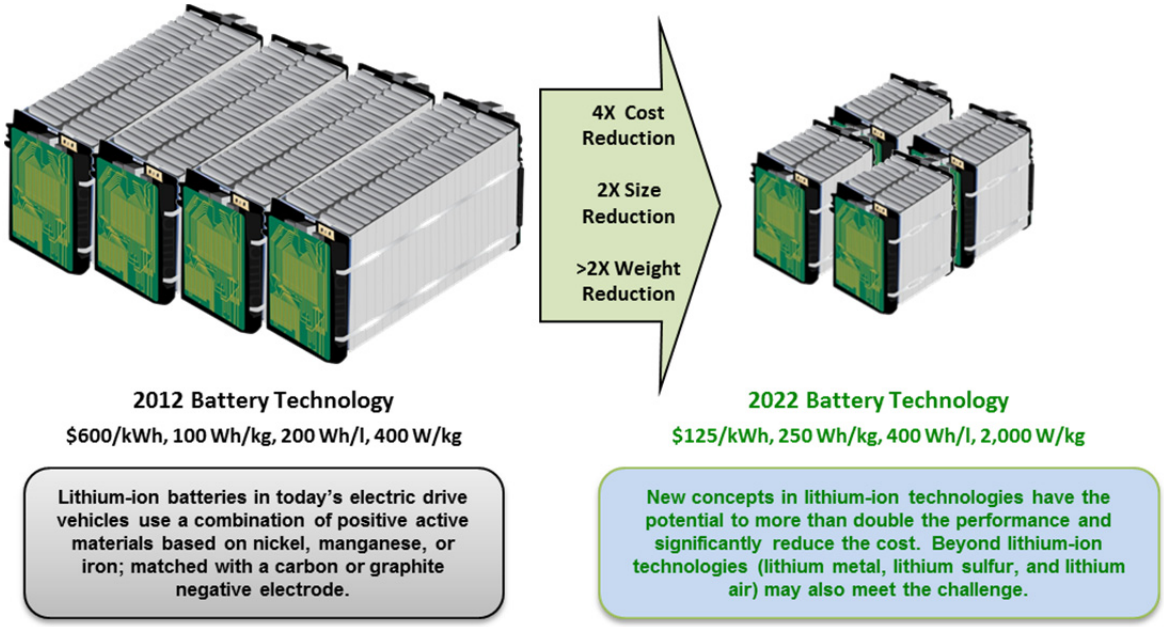

Figure I - 1: Battery advancements needed to enable a large market penetration of PEVs

I.B.2 DOE Battery R&D Plans

The objective of the VTO battery R&D effort is to advance the development of batteries to enable a large market penetration of hybrid and electric vehicles. Program targets focus on overcoming technical barriers to enable market success and they include: (1) significantly reducing battery cost, (2) increasing battery performance (power, energy, durability), (3) reducing battery weight & volume, and (4) increasing battery tolerance to abusive conditions such as short circuit, overcharge, and crush.

Current battery technology performs far below its theoretical limits. For example, in the near-term (2012-2017), with existing lithium-ion technology, there is an opportunity to more than double the battery pack energy density (from 100 Wh/kg to 250 Wh/kg) by using new high-capacity cathode materials, higher voltage electrolytes, and high capacity silicon or tin-based intermetallic alloys to replace graphite anodes. Despite recent promising advances, much more R&D is needed to achieve the performance and lifetime requirements for deploying those advanced technologies in PEVs.

In the longer term (2017-2027), battery chemistries "beyond Li-ion", such as lithium-sulfur, magnesium-ion, zinc-air, lithium-air, and certain other advanced chemistries; offer the possibility of specific energy levels significantly greater than those for current lithium-ion batteries and they also have the potential of greatly reducing battery cost. However, major shortcomings in cycle life, power density, energy efficiency, and/or other critical performance parameters, including cost, currently hinder commercial introduction of state-of-the-art "beyond Li-ion" battery systems. Therefore, some kind of innovative breakthroughs would be needed for those new battery technologies to enter the market.

The energy density increases described above are critical to achieving the *EV Everywhere* cost and performance targets. Additional R&D efforts, including those related to pack design optimization and simplification, manufacturing improvements at cell/pack levels, production cost reduction for battery materials, and novel thermal management technologies will also help reduce battery cost. The major associated technical challenges and potential solutions to those challenges are listed in Table I - 1.

Table I - 1: Major Li-ion technology technical challenges and potential pathways to address them

Barrier/Challenge	Potential Solutions
• Reduce the cost and improve the performance of lithium-ion battery technology	• Improved material and cell durability • Improved energy density of active materials • Reduction of inactive material • Improved design tools/design optimization • Improved manufacturing processes
• Develop higher energy battery technology such as next generation lithium ion, lithium-sulfur and lithium-air ○ Issues with these materials include poor cycle life, low power, low efficiencies, and safety	• Improved electrolyte/separator combinations to reduce dendrite growth for Li metal anodes • Advanced material coatings • New ceramic, polymer, and hybrid structures with high conductivity, low impedance, and structural stability
• Improve abuse tolerance performance of battery technology	• Non-flammable electrolytes • High-temperature melt integrity separators • Advanced materials and coatings • Improved understanding of reactions • Battery cell and pack level innovations such as improved sensing, monitoring, and thermal management systems

I.B.3 Energy Storage R&D Programmatic Structure

The energy storage effort includes multiple activities, ranging from focused fundamental materials research to battery cell and pack development and testing. The R&D activities can involve either short-term directed research by commercial developers and national laboratories or exploratory materials research generally spearheaded by the national laboratories and universities. These consist of four major program elements which are inter-related and complementary, namely:

- Advanced Battery Development.
- Battery Testing, Analysis, and Design.
- Applied Battery Research (ABR).
- Focused Fundamental Materials Research, or Batteries for Advanced Transportation Technologies (BATT).

The *Advanced Battery Development program*'s goal is to support the development of a domestic advanced battery industry whose products can meet electric drive vehicle performance targets. Such R&D activity focuses, for example, on the development of robust battery cells and modules to significantly reduce battery cost, increase life, and improve performance. It takes place in close partnership with the automotive industry, through our cooperative agreement with the United States Advanced Battery Consortium (USABC). DOE works in close collaboration with USABC to develop battery and ultracapacitor requirements for various vehicle types[4] and test procedures.[5] In FY 2013, the USABC supported

[4] See http://www.uscar.org/guest/article_view.php?articles_id=85

[5] See http://www.uscar.org/guest/article_view.php?articles_id=86

9 cost-shared contracts with developers to further the development of batteries for PEVs and HEVs. Also, DOE often works directly with battery and material suppliers via National Energy Technology Laboratory (NETL) contracts. In FY 2013, NETL managed 14 battery R&D contracts. Chapter III focuses on the battery development program.

The Battery Testing, Analysis, and Design activity supports certain complementary aspects of the battery development program. The high-level projects pursued in this area include cost modeling; secondary and other energy storage use and life studies; analysis of the recycling of core materials; requirements analysis for PEVs and HEVs; performance, life and abuse testing of contract deliverables, those of laboratory and university developed cells, and also those of benchmark systems from industry; thermal analysis, thermal testing and modeling; development of new test procedures and maintenance of current test procedures; and finally the development of tools for computer aided engineering of batteries. Battery technologies are evaluated according to USABC Battery Test Procedures. The manuals for the relevant PEV and HEV applications are available online.[6,7,8] A benchmark testing of an emerging technology would be performed to remain abreast of the latest industry developments. Within this report, Chapter IV focuses on the *Battery Testing, Analysis, and TestingDesign* activity.

The *Applied Battery Research* (ABR) activity is focused on the optimization of next generation, high-energy lithium-ion electrochemistries that incorporate new battery materials. Its emphasis is on identifying, diagnosing, and mitigating issues that impact the performance and life of cells containing advanced materials. It investigates interaction between all cell components (including the cathode, anode, electrolyte, binders, conductive additives, and separator) which impact performance and life. Typical issues associated with incorporating new material developments into working PEV cells can include: (1) inadequate power capability needed to meet the requirements of PEVs, (2) insufficient cycle life stability to achieve the 1,000 to 5,000 "charge-depleting" deep discharge cycles, and (3) poor performance at lower temperatures. It is conducted by a team which is headed by the Argonne National Laboratory (ANL) and includes five other national labs and several universities. Chapter V lists all the projects under the Applied Battery Research activity.

The *Focused Fundamental Materials Research* activity, also called the Batteries for Advanced Transportation Technologies (BATT) activity, addresses fundamental issues of materials and electrochemical interactions associated with lithium batteries. It attempts to develop new and promising materials, to use advanced material models to discover new materials and predict failure modes, and scientific diagnostic tools and techniques to gain insight into why material and systems fail. Battery chemistries are monitored continuously with periodic substitution of more promising components based on advice from within this activity, from outside experts, and from the assessments of world-wide battery R&D. The work is carried out by a team headed by the Lawrence Berkeley National Laboratory (LBNL) and involves several other national labs, universities, and commercial entities. The program is also studying issues critical to the realization of beyond Li-ion technologies. Two of the most promising such technologies are Lithium/Sulfur and Lithium/Air. Some of the main areas of focus are to devise new methods to understand and stabilize lithium metal anodes; to contain Li polysulfides to enable the use of sulfur cathodes; and to develop electrolytes that support Li air and Li/sulfur cells. Chapter VI lists all the projects which are part of the Focused Fundamental Research activity.

Several *Small Business Innovation Research* (SBIR) contracts are also supported by VTO, in addition to the R&D described above. SBIR projects have been the source of new ideas and concepts. These SBIR projects are focused on the development of new battery materials and components.

---

[6] United States Advanced Batteries Consortium, USABC Electric Vehicle Battery Test Procedure Manual, Rev. 2, U.S. Department of Energy, DOE/ID 10479, January 1996.

[7] U.S. Department of Energy, PNGV Battery Test Procedures Manual, Rev. 2, August 1999, DOE/ID-10597.

[8] United States Council for Automotive Research, RFP and Goals for Advanced Battery Development for Plug-in Electric Vehicles, http://www.uscar.org/.

Dramatic improvements in battery performance and cost will require a well-coordinated effort across all of the DOE complex and with America's most innovative researchers and companies. Coordination within DOE and with other government agencies is a key attribute of the VTO energy storage R&D effort. VTO coordinates efforts on energy storage R&D with the DOE Office of Science, the DOE Office of Electricity, and the Advanced Research Projects Agency – Energy (ARPA-E). Innovations in battery technology occur as a result of fundamental investigations carried out at national labs and universities supported by the DOE Office of Science, through translational research sponsored by ARPA-E, and through applied research and development at labs, universities and industry supported by VTO. Innovations coming from R&D on pre-competitive technologies will be transferred to and implemented by industry partners as a business case develops for these technologies through the US DRIVE public/private partnership. The USABC makes cost-shared, competitively awarded projects to industry to facilitate commercialization of pre-competitive technologies and introduce them into the marketplace.

VTO also has established extensive and comprehensive ongoing coordination efforts in energy storage R&D with other government agencies. Such efforts include membership and participation in the Chemical Working Group of the Interagency Advanced Power Group (IAPG), active participation in program reviews and technical meetings sponsored by other government agencies, and coordinating the participation of representatives from other government agencies in the contract and program reviews of DOE-sponsored efforts. DOE also coordinates with the Department of Transportation/National Highway Traffic Safety Administration (DOT/NHTSA), the Environmental Protection Agency (EPA), and with the United Nations Working Group on Battery Shipment Requirements. Additional international collaboration occurs through a variety of programs and initiatives. These include: the International Energy Agency's (IEA's) Implementing Agreement on Hybrid Electric Vehicles (IA-HEV), the eight-nation Electric Vehicle Initiative (EVI), and the Clean Energy Research Center (CERC) bilateral agreement between the U.S. and China.

I.B.4 Recent Highlights

Chapter II of this report contains brief summaries of some key accomplishments resulting from the VTO Energy Storage R&D and associated efforts in support of the *EV Everywhere* Grand Challenge – each one selected from many active projects and representing a significant technical breakthrough. In addition, the following highlights specifically pertain to the U.S. electric drive vehicle market during FY 2013.

U.S. sales of electric drive vehicles nearly doubled in 2013. The *EV Everywhere* Grand Challenge remains focused on overcoming barriers to widespread market acceptance of PEVs, with cost reduction being a primary component. Despite obstacles, the electric-drive vehicle market is growing. Evidence of this can be seen in vehicle sales and increased investment by auto makers (see Figure I - 2).

- Total U.S. PEV sales in model year 2013 nearly doubled those of 2012, approaching 100,000 sold for the year alone.
- Additionally, PEVs reached nearly 160,000 cumulative sales in November 2013.

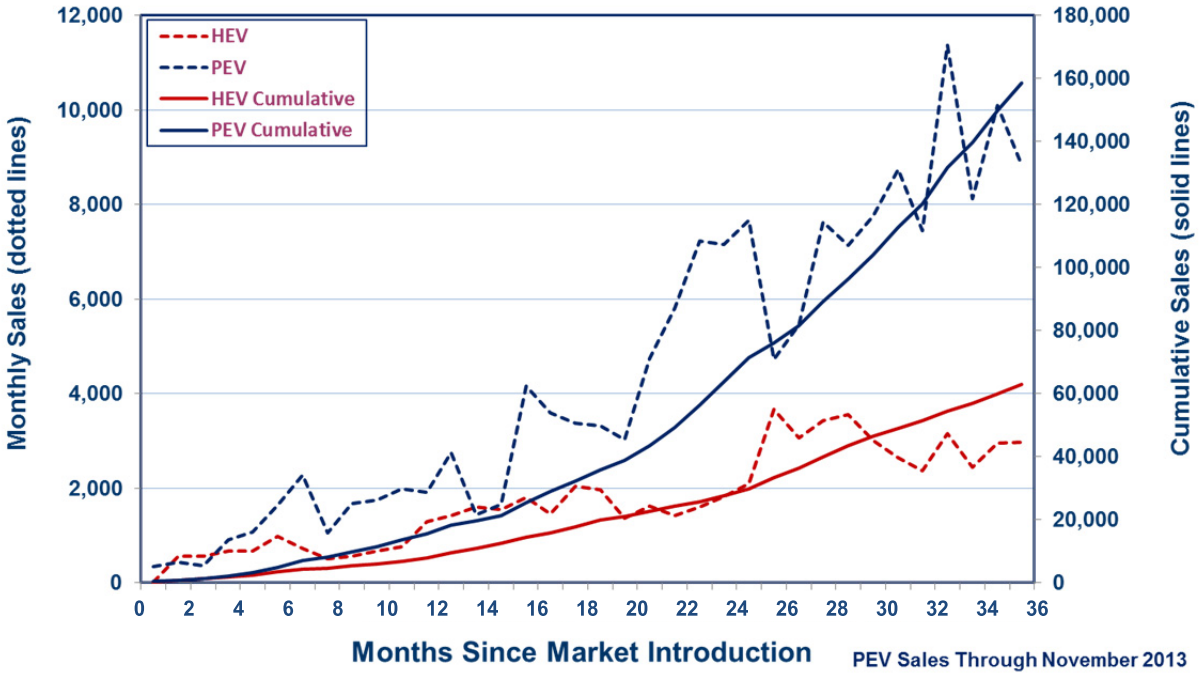

(Source: HybridCars.com)

Figure I - 2: New PEV sales compared to hybrid electric vehicle (HEV) sales over their respective 36 month introductory periods

Commercial applications of DOE-supported technologies. Several technologies, developed partially under VTO-sponsored projects, have moved into commercial applications. Hybrid electric vehicles on the market from BMW and Mercedes are using lithium-ion technology developed under projects with Johnson Controls Inc. (JCI). Lithium-ion battery technology developed partially with DOE funding of a USABC project at LG Chem is being used in GM's Chevrolet Volt extended-range electric vehicle and also in the Ford Focus EV battery. LG Chem will also supply Li-ion batteries to Eaton for hybrid drive heavy vehicles. A123Systems is producing lithium-ion battery systems for the GM Spark EV.

PEV battery cost reduction. DOE-funded research has helped bring down lithium-ion battery costs from $1,000/kWh in 2008 to less than $325/kWh today. DOE's goals are to continue to drive down battery cost to $300/kWh by 2014 and to $125/kWh by 2022.

I.B.5 Organization of this Report

This report covers all the projects currently ongoing or starting up as part of the energy storage R&D effort in VTO. Chapter II contains the *EV Everywhere* Grand Challenge R&D Progress highlights, and chapters III through VI contain descriptions and progress of various R&D projects supported through VTO funding. A list of individuals who contributed to this annual progress report (or who are otherwise collaborating with the energy storage R&D effort) appears in Appendix A. A list of acronyms is provided in Appendix B.

We are pleased with the progress made during the year and look forward to continued work with our industrial, government, and scientific partners to overcome the remaining challenges to delivering advanced energy storage systems for vehicle applications.

David Howell

Program Manager, Hybrid and Electric Systems

Vehicle Technologies Program

Tien Q. Duong

Manager, Exploratory Technology Research

Vehicle Technologies Program

Peter W. Faguy

Manager, Applied Battery Research

Vehicle Technologies Program

Brian Cunningham

Lead, Battery Testing, Analysis and Design

Vehicle Technologies Program

II

The *EV Everywhere* Challenge

Background

FY 13 Highlights

Planned Activities

II. The *EV Everywhere* Challenge

II.A Background

In March 2012, President Obama announced the *EV Everywhere* Grand Challenge—to produce plug-in electric vehicles (PEVs) as affordable and convenient for the American family as gasoline-powered vehicles by 2022. Realizing the promise of PEVs is one of the grand challenges of this era. Today, our transportation system is still dependent on internal combustion engines and oil. In fact, 93% of our transportation fuel is derived from petroleum and much of this is imported. PEVs can decouple personal mobility from oil, cut pollution and help build a 21st Century American automotive industry that will lead the world.

America is the world's leading market for electric vehicles and is producing some of the most advanced PEVs available today. Consumer excitement and interest in PEVs is growing — in 2012, PEV sales in the U.S. tripled, with more than 50,000 cars sold, and a plug-in electric vehicle (the Chevrolet Volt) beat all other vehicle models in Consumer Reports' owner satisfaction survey for the second time. In 2013, PEV sales are on pace to nearly double prior year sales, with nearly 100,000 annual sales of PEVs projected.

PEVs have won critical acclaim with awards such as 2011 World Car of the Year (Nissan Leaf), 2013 Motor Trend Car of the Year (Tesla Model S) and 2012 Green Car Vision Award Winner (Ford C-MAX Energi). To maintain this leadership, strong growth in the U.S. PEV sector will need to continue.

The Department of Energy (DOE) developed an *EV Everywhere* "Blueprint" document that provides an outline for technical and deployment goals for PEVs over the next five years. DOE will pursue these targets in cooperation with a host of public and private partners. The technical targets for the DOE PEV program fall into four areas: battery R&D; electric drive system R&D; vehicle lightweighting; and advanced climate control technologies. Some specific goals include:

- Cutting battery costs from their current $500/kWh to $125/kWh
- Reducing the cost of electric drive systems from $30/kW to $8/kW
- Eliminating almost 30% of vehicle weight through lightweighting

These numbers represent difficult to reach "stretch goals" established in consultation with stakeholders across the industry—including the *EV Everywhere* workshops held during the summer and fall of 2012. When these goals are met, the levelized cost of an all-electric vehicle with a 280-mile range will be comparable to that of an ICE vehicle of similar size. Even before these ambitious goals are met, the levelized cost of most plug-in electric vehicles — and of all-electric vehicles with shorter ranges (such as 100 miles) — will be comparable to the levelized cost of ICE vehicles of similar size. Meeting these targets will help to reduce the purchase price for plug-in electric vehicles

The *EV Everywhere* "Blueprint" document also describes the deployment programs related to charging infrastructure and consumer education. Efforts to promote home, workplace, and public charging can also help speed PEV deployment.

II.B *EV Everywhere* Technical Targets

DOE defined *EV Everywhere* technology targets using an analytical framework that evaluated the performance of component technologies as well as vehicle cost and performance. We synthesized data about future vehicle potential by using expert projections of component technology to create virtual vehicles of the future via computer modeling and simulation. The range of vehicle costs and efficiencies made possible a comparison of the degree to which the portfolio of these technologies must progress, in both performance and cost terms, to yield PEVs that are cost-competitive, as measured by the initial vehicle purchase price and the fuel expenditure accrued over a 5-year ownership period. Ultimately, an analysis of this balance yielded technical targets at the technology progress frontier: *EV Everywhere* targets are consistent with what experts see as very aggressive but still possible within the *EV Everywhere* timeframe.

The complete set of *EV Everywhere* technical targets are presented in the Blueprint document. The specific technical targets that pertain to batteries are listed in Table II - 1.

Table II - 1: *EV Everywhere* energy storage targets for 2022

		Current Status	Target
Battery Cost	$/kWh (usable)	500	125
Pack Specific Energy	Wh/kg	80-100	250
Pack Energy Density	Wh/L	200	400
Pack Specific Power	W/kg	500	2000

II.C *EV Everywhere* FY2013 Highlights

1. Progress in Lithium-Ion Battery Technology

DOE has reduced the cost of lithium-ion batteries by nearly 70% and improved their energy density by 60% during the last five years.

DOE-sponsored R&D has reduced the cost of PEV batteries by nearly 70% over the last five years. As shown in Figure II - 1, the modeled cost of PHEV batteries under development has been reduced from $1,000 per kilowatt-hour of useable energy in 2008, to a current cost of $325 per kilowatt-hour. Three USABC battery developers have made significant advances in cost reduction using improved cathodes. These battery development projects focus on advanced cathodes, processing improvements, cell design, and pack optimization. Standard electrolytes and graphite anodes were used by each developer. These battery cost projections are derived by the manufacturer using USABC's battery manufacturing cost model based on a production volume of 100,000 batteries per year for specific battery cell and module designs that meet DOE/USABC requirements for power, energy, and cycle life as well as calendar life.

Concurrently, the size and weight of PEV batteries have also been reduced by over 60%. As shown in Figure II - 1, battery energy density has increased from 60 Wh/liter in 2008, to 150 Wh/liter in 2013.

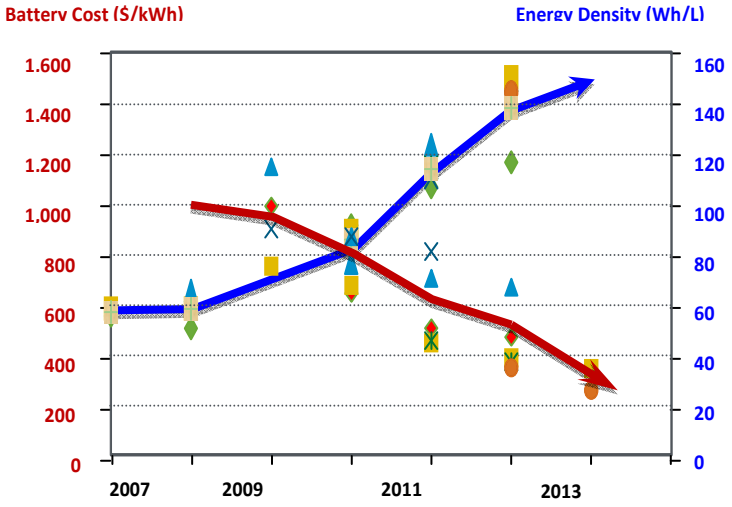

Figure II - 1: Modeled cost and energy density of PHEV batteries developed and tested

2. Estimating Battery Pack-Level Energy Density, Specific Energy and Cost for *EV Everywhere* Goals

A free BatPaC model is a tool for estimating Li-ion battery costs for vehicles. The model estimates that an advanced Li-ion cathode paired with a silicon-alloy or a lithium-metal anode can reach EV Everywhere's cost and performance goals for a 100 kWh (~300 mile) battery. **(Argonne National Laboratory)**

The ability to predict the cost of batteries made using advanced materials is critical to correctly focusing research efforts. The battery performance and cost (BatPaC) model developed at ANL represents the only public model that captures the interplay between design and cost of Li-ion batteries for transportation (available free-of-charge from the ANL BatPac site). This model has been subject to peer-reviews by experts in academia and industry. The first version of BatPaC was distributed on November 1st, 2011, since then, more than 1,000 independent downloads have occurred worldwide.

The *EV Everywhere* initiative has challenging battery goals (i.e. $125/kWh, 400 Wh/l, 250 Wh/kg). The potential of battery chemistries to reach these goals have been quantified using BatPaC. The systems-level energy density, specific energy, and cost for select lithium batteries are illustrated in Figure II - 2.

The representative Li-ion cell chemistry graphite/$LiNi_{1/3}Mn_{1/3}Co_{1/3}O_2$ (Gr/NMC333) is commercially available today and likely to see incremental improvements, several percent per year, over the next decade through achieving long life with thicker electrodes, larger capacity cells, and more efficient peak power designs. Also considered is the lithium- and manganese-rich high capacity cathode (LMRNMC). Finally, a composite silicon-alloy anode is considered.

Both the Li/LMRNMC and Si/LMRNMC couples meet the goals for a 100 kWh battery. These estimations show both the promise of future battery chemistries and the challenges that remain.

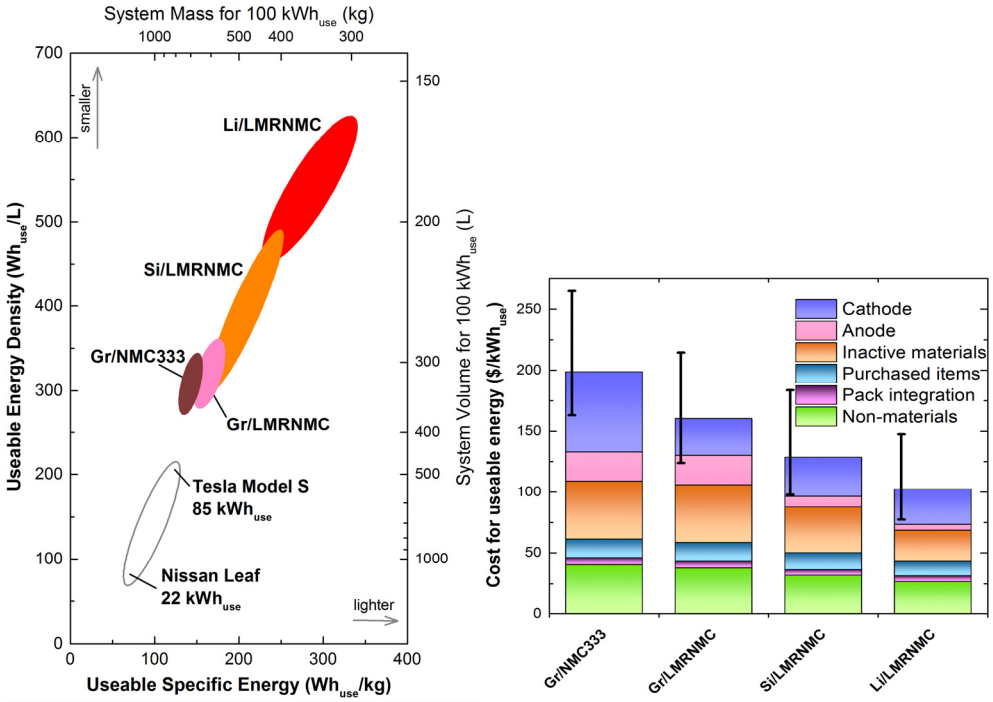

Figure II - 2: Estimated useable specific energy, energy density, and cost for a 100 kWh$_{use}$, 80kW$_{net}$ 360V battery produced at 100k/year

3. Johnson Controls Inc. Increases Cell Energy Density by 25%

JCI has increased prismatic PHEV-20 cell energy density from 275 Wh/L to 345 Wh/L through a concerted multi-disciplinary effort involving material stabilization, novel processing, and cell design innovations.
(Johnson Controls Inc.)

JCI's $4.1 million, 2 year program is focused on reducing the cost to capacity ratio of a standard format prismatic cell through a multidisciplinary pursuit of volumetric energy improvement. Building on JCI's Gen-1 prismatic NMC-graphite cell developed in the preceding USABC program, the work targets a medium-range PHEV20 application.

Cost to capacity ratio reduction is being achieved directly through increased energy density of the cell (increased mAh/g) which drives down battery size and cost. Indirectly, contributing improvements in the critical enablers of abuse tolerance and cold temperature performance are needed to be able to fully harness the opportunity of energy density gains. Development efforts focus not only on inherently low-risk materials, seeking to exploit their full, unrealized potential, but also on process development and mechanical design innovations.

The following highlights from each major work stream illustrate progress made during this contract.

- Multiple cathode materials representing a broad spectrum of stabilization approaches and stoichiometries were evaluated. Two candidates remain after exhaustive down selection trials
- Paste mix processing was evaluated as a potential enabler of solvent reduction goals, and increased active material loadings. Promising results were obtained, attaining the high electrode densities needed for the cell energy density targets. Further testing will assess high solids processing potential.
- Upper voltage limits of 4.2V and 4.3V were evaluated in parallel with extensive electrolyte development to enhance stability. Excellent results have allowed increasing the upper voltage from 4.1V to 4.2V, and expanding the state of charge window usage from 70% to 80%. The latest build's capacity retention at 4.2V compares to the baseline chemistry at 4.1V, showing only 7% fade after 135 days at 60˚C, a remarkable achievement.
- Mechanical design efforts yielded mandrel elimination, current collector optimization, coated area increase, and fill-hole closure method down-selection, each of which increases the cell capacity.
- Abuse tolerance work focused on a Thermal Protective Barrier anodic coating, ceramic separators, electrolytes and cathodes with functional overcharge additives, all leading to enhanced over-charge results and understanding.
- Mid-program cells demonstrate a 25% increase in capacity, while the projected final cell design translates to a 30% cost reduction at the system level. Both of these achievements showcase the meaningful progress made to JCI's technology (see Figure II - 3).

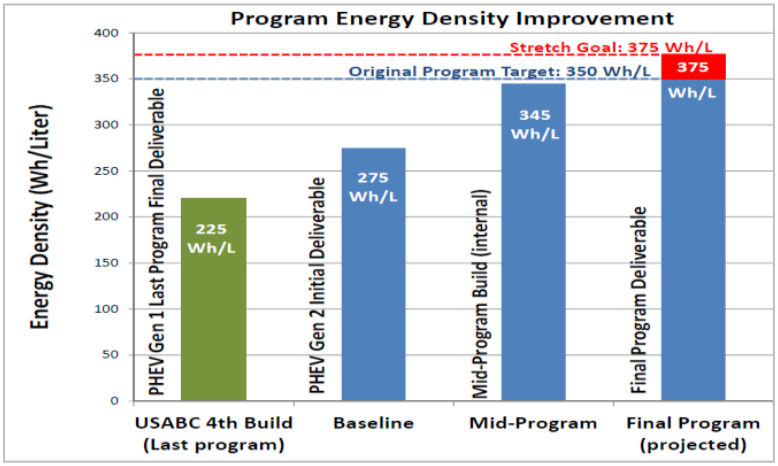

Figure II - 3: Progression of achieved cell-level energy density increases

4. High Energy NMC Cathode/Si Alloy Automotive Cell

3M demonstrates a 50% increase in energy over NMC/graphite cells using synergistically matched Core-Shell NMC cathode and Silicon alloy anode. **(3M)**

Electrification of the vehicle is fast becoming a reality around the world. Reducing the cost of the battery is one of the keys to success. In order to reduce the cost of the battery ($/Wh), new active materials (anodes and cathodes) are needed to increase battery energy. These new active materials need to be carefully matched to enable the highest energy density. With DOE support, 3M has integrated new cathode materials, anode materials and electrolytes that can increase cell energy by 50% over the industry standard $Li(Ni_{1/3}Mn_{1/3}Co_{1/3})O_2$ (NMC)/Graphite cell.

3M™ Core-Shell NMC Cathode: 3M's cathode materials are mixed nickel, manganese, and cobalt oxides with a high Ni core (for high energy) and high Mn shell (for high voltage stability). These materials have high capacity, high voltage, and good cycle stability.

3M™ Silicon (Si) Alloy Anode: 3M's Si alloy anode materials enable high energy density and have proper structure (amorphous active phase), particle morphology, and surface chemistry leading to controlled volume expansion upon lithiation and good cycling.

The Importance of the System: New cathode materials that have a Cathode Energy Factor (CEF) beyond the traditional NMC materials invariably require charging to higher cell voltage. To maximize the energy of the system, the cathode irreversible capacity should also "match" the irreversible capacity of the alloy anode. In addition, for cell balance and control of lower cut-off cell voltage, it is desirable if the irreversible capacity of the composite cathode be slightly larger than that of the anode. The electrolyte and separator must be designed to be stable against the two electrodes, across the complete cell voltage range, to mitigate any parasitic reactions. The 3M™ Core Shell (C/S) high-energy cathode material has a CEF 45% higher than NMC as shown in Table II - 2. When this cathode is combined with 3M™ Si anode in an 18650 cell a 50% improvement in energy (Wh/L) is demonstrated, as shown in Figure II - 4.

Next Steps: Cycle life optimization is underway and will be reported in the future. 3M™ Silicon Si alloy anode materials have been scaled into production. Cathode materials have been scaled to the kg level.

Table II - 2: CEFs for different cathodes—irreversible factor accounts for the irreversible loss of the matched active materials

	Oxide	X Capacity (Ah/g)	X Density (g/cc)	X Voltage (V)	X Irreversible Factor	= CEF
Automotive	NMC	0.16	3.3	3.90	0.98	2.02
	NMC	0.16	3.3	3.90	0.95	1.96
Core Shell	126M	0.23	3.4	3.84	0.95	2.85
	126T	0.22	3.4	3.88	1.00	2.90

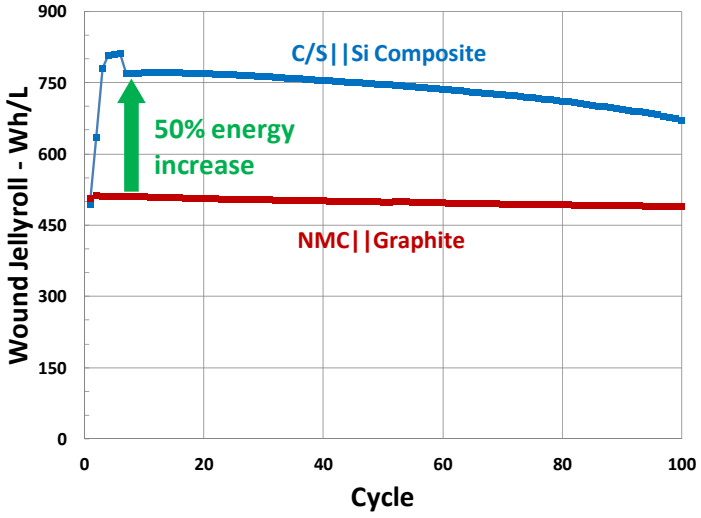

Figure II - 4: 18650 data demonstrating a 50% energy improvement for the C/S||Si composite over the NMC||Graphite design

5. Process Development and Scale-up of Advanced Cathode Materials

Scale-up process development is a key missing link between basic research and commercialization and provides kilogram quantities of advanced cathode materials for R&D purpose and industrial evaluation.
(Argonne National Laboratory)

Process development and scale-up of advanced cathode materials is a critical step between discovery of advanced battery materials, market evaluation, and high-volume manufacturing. This project produces large quantities of the target lab-scale candidate materials with equal or better quality. The performance of cathode material such as capacity, tap density and life is strongly affected by the synthesis process and its optimization even though it has the same composition. Additionally, development of cathode synthesis processes that are economically feasible is important to reduce the cost of the full battery pack.

A high capacity/voltage cathode development project through JPL/NASA had produced a cathode ($Li_{1.5}Ni_{0.16}Mn_{0.68}Co_{0.16}O_{2.5}$) with high capacity (~230 mAh/g) and high tap density (>1.7 g/cc) at the bench scale, but JPL had difficulties scaling the material in kilogram scales for commercial evaluation. Toda America has produced this composition (HE-5050) at high capacity (~250 mAh/g) but at a much lower tap density (~1.0 g/cc). In FY2013, Argonne's cathode scale-up program was tasked to scale this composition and produce high capacity, high tap density material for evaluation. The target properties are:

- Composition:$Li_{1.5}Ni_{0.16}Mn_{0.68}Co_{0.16}O_{2.5}$
- Tap density: >1.5 g/cc
- Capacity: ~240 mAh/g (1st discharge)
- Cycle life: ~200 cycles

The first approach was to optimize a hydroxide based process to synthesize the material. ANL was able to achieve a higher tap density than the Toda hydroxide based material but with a tradeoff of lower capacity - not meeting the JPL specifications. ANL then focused on a carbonate based approach and were able to exceed capacity and tap density specifications, producing kilogram quantities of material for evaluation (see Table II - 3 and Figure II - 5).

Table II - 3: Comparison of 6 cathode materials with the same composition: ① SEM (8000x), ② D10/D50/D90 (μm), ③ tap density (g/cc), ④ initial discharge capacity at C/20 (mAh/g)

	Toda-HE5050 B#1 5-P767	Toda-HE5050 B#2 P1407	Toda-HE5050 B#3 P2564	JPL pristine	ANL scale-up JPL hydroxide ES-20131004	ANL scale-up JPL carbonate ES-20130924
	Commercial	Commercial	Commercial	Bench scale	Pre-pilot	Pre-pilot
①	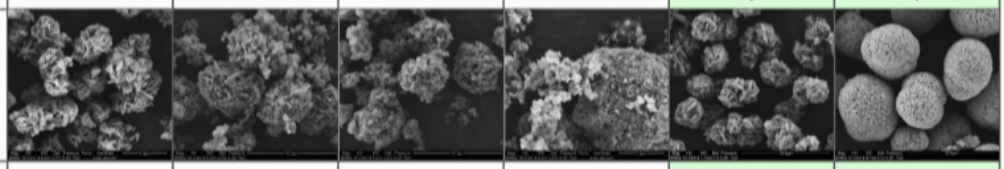					
②	3.1/5.3/9.2	1.1/5.2/11.3	2.0/4.9/10.4	1.2/11.1/29.3	3.0/5.1/9.0	4.0/6.7/11.4
③	1.03	1.16	1.07	1.70	1.23	1.82
④	255.3	261.8	254.5	228.2	237.7 *	292.0 *

** Under optimization*

The precursor and cathode materials were produced by a reproducible, scalable process and were delivered to Argonne's Materials Screening team and to JPL for evaluation.

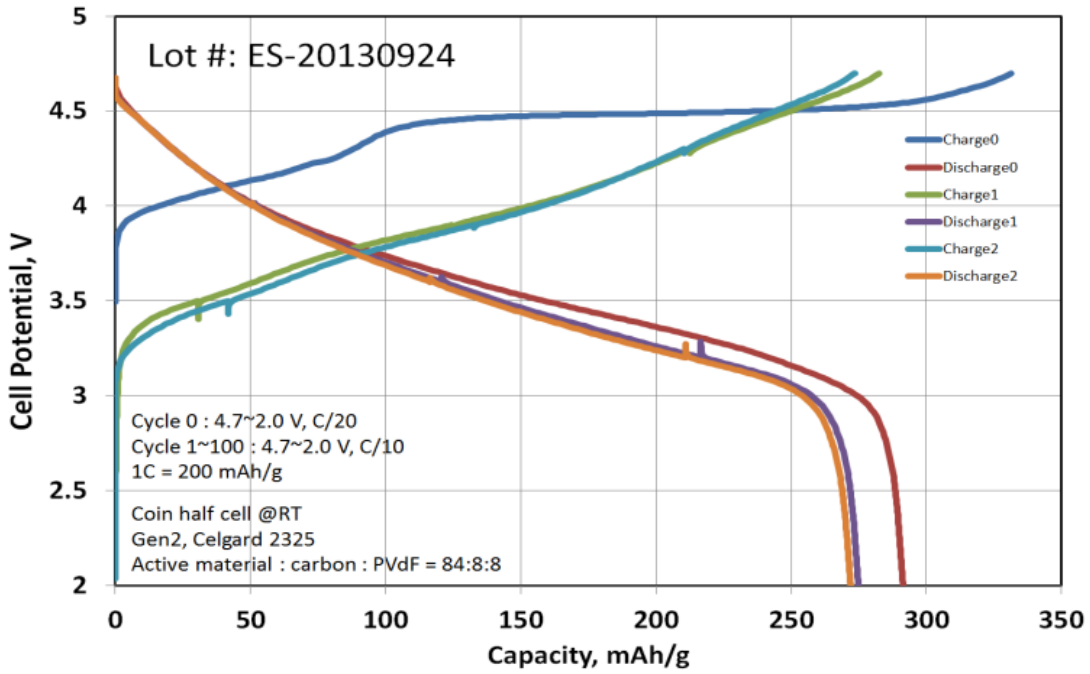

Figure II - 5: Voltage profile of the Argonne scale-up JPL carbonate material

6. Scale up and Production of Low Cost Nickel/Manganese/Cobalt Cathode Material

BASF has developed and scaled up the production process for three nickel/manganese/cobalt cathode materials. Two such materials are currently in production in BASF's plant in Elyria Ohio, and the final material is to be produced in its production plant. ***(BASF)***

According to multiple cost models from DOE National Laboratories and from battery developers, the cathode material dominates high-energy battery cost. The production of low cost cathode materials depends on the proper selection of raw materials and a cost effective production process. There are also many requirements for chemical purity, physical characteristics, and electrochemical performance that must be met.

This project aimed to scale up and reduce the production cost of nickel/manganese/cobalt (NMC) cathode materials. As a result of this project, BASF has developed and scaled up the production process for NCM 111, 523 and 424 (numbers represent the relative ratios of the three components). The first two materials are in production in BASF's plant in Elyria, Ohio, and the final material will be produced there. BASF has been able to qualify both NCM 111 and NCM 424 for use in EV and PHEV applications through independent testing by SKC PowerTech.

BASF has recently shifted much of the research and development work to the production of NCM 424. Results from the initial lab work have been used to identify the major production elements that are critical for the end product performance. Work with NCM 424 has progressed through the pilot plant stage. BASF has demonstrated that with its existing pilot plant equipment it can produce NCM 424 consistently with minimal lot variation. Figure II - 6 shows 2C (5 ampere) charge discharge cycle life results from cells made with blends of BASF's NMC111 and LMO, where LMO is $LiMn_2O_4$ spinel, and another cell using a blend of NMC424 and LMO. BASF will continue to focus on precursor improvements and modifications in order to improve the quality of the NCM 424.

BASF has also worked on the production of the high energy NCM (HE-NCM). Although there is still ongoing research to improve the material, BASF has made progress improving its performance as well as understanding the critical production parameters. BASF has produced enough HE-NCM to sample to customers and research partners during the past year.

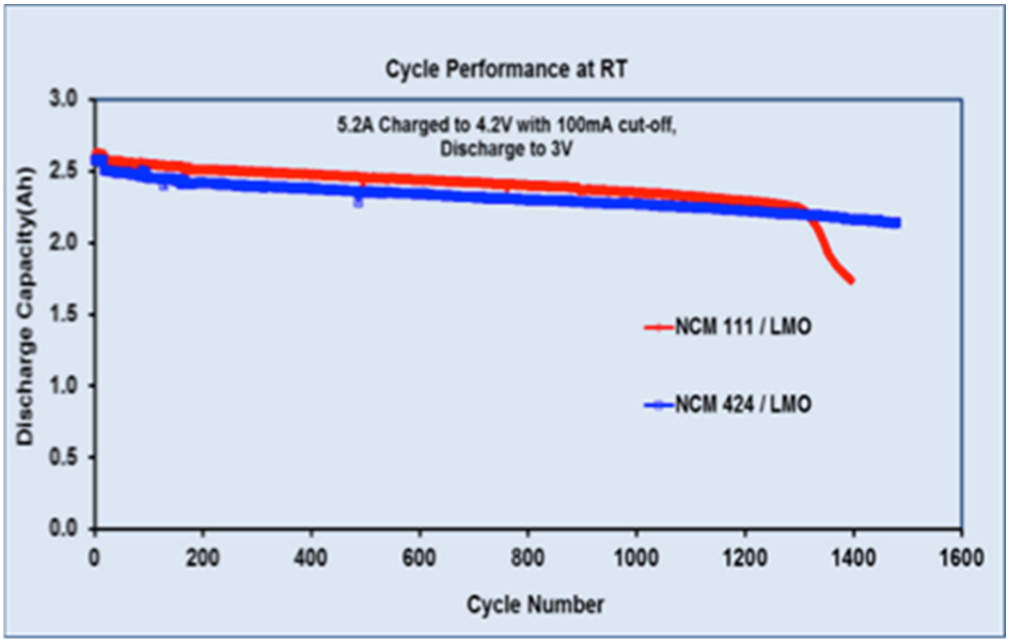

Figure II - 6: Cycle life data of NMC111/LMO blend and NMC424/LMO blend at room temperature (RT), appropriate for long-range PHEV and EV applications

7. Progress in Silicon Anodes

Many developers in the battery industry, supporting by the modeling results of BatPaC, have concluded that abundant and inexpensive Silicon-based anodes are needed to meet the DOE *EV Everywhere* battery performance and cost goals. Si offers 4,200mAh/g vs. 350mAh/g for currently used graphite. However, numerous technical hurdles remain, including the large volume change during cycling, which leads to loss of contact between particles, and electrolyte consumption leading to rapid capacity fade and cell failure. Several institutions are exploring approaches to mitigating the volume change problem. These approaches, and some of their progress, are listed in Table II - 4.

Table II - 4: Progress in Si Anodes

Institution	Technical Approach	Loading mg/cm2	Specific Capacity mAh/g	Initial Areal Capacity mAh/cm2	Final Areal Capacity mAh/cm2	Number of Cycles
U. of Pittsburgh	Hollow Si nanotubes	0.8	775	0.62	0.56	150
SUNY Binghampton	Spherical nano Si	2.5	1500	3.7	3	60
Penn. State U.	Si-C nanocomposites	1.7	975	1.6	1.45	160
PNNL	Porous silicon	2.0	750	1.5	1.2	300
Stanford	Conducting hydrogel on Si nanoparticles	0.4	1900	0.75	0.70	1,000
NREL	Si nanoparticles/coating	0.8	1500	1.2	0.9	150

8. Technologies for Improved Safety of Li-ion Batteries

TIAX has developed a non-invasive, chemistry-agnostic technology for detecting incipient internal short circuits in Li-ion batteries even before they pose a thermal runaway threat. **(TIAX, LLC)**

Li-ion batteries are a key to enabling widespread deployment of plug-in electric vehicles (PEV). However, concerns regarding safety of Li-ion batteries could hinder their rapid adoption in PEVs. Essentially, under various triggers, Li-ion batteries can undergo violent thermal runaway accompanied by smoke and flames. Many of the potential triggers have been studied over the years and solutions for preventing the possibility of thermal runaway from these triggers have been developed and incorporated into battery packs.

However, one particular trigger, the internal short circuit, has not received much attention, and new technologies are needed to manage the outcome from this trigger. Internal shorts are particularly insidious because they can promote thermal runaway under otherwise normal operating conditions. At TIAX, using a combination of experiments and numerical simulations, we have investigated the mechanism of short initiation and growth, as well as the conditions needed to promote thermal runaway. Based on insights gained from these investigations we are developing solutions to manage internal short circuits in Li-ion. Here, we report on an exciting new technology to detect incipient internal shorts before they pose a thermal runaway threat. Once detected, several approaches are available to intervene and prevent thermal runaway.

The TIAX internal short detection technology includes a combination of proprietary non-invasive sensors and signal processing algorithms to enable real-time detection of incipient internal shorts in Li-ion cells. Figure II - 7 shows an example of internal short detection in a Li-ion cell in a pack subjected to a FTP75 automotive duty cycle (that has been accelerated by 8x). A 100 Ω internal short (which is 25 times weaker than that needed to induce thermal runaway) was introduced in one of the cells at ~ 43 s and removed at ~ 170 s. As seen in the top figure, voltage traces that a conventional battery management unit (BMU) would record show no indication of the internal short, illustrating the inability of conventional BMUs to detect such low-level shorts. The bottom figure shows the output from TIAX's sensor system, clearly indicating successful detection of the internal short even amidst wildly fluctuating automotive duty cycles. This patent-pending technology has been demonstrated at the breadboard level for a wide range of chemistries, cell designs, and automotive temperatures. We are now in discussions to commercialize the technology.

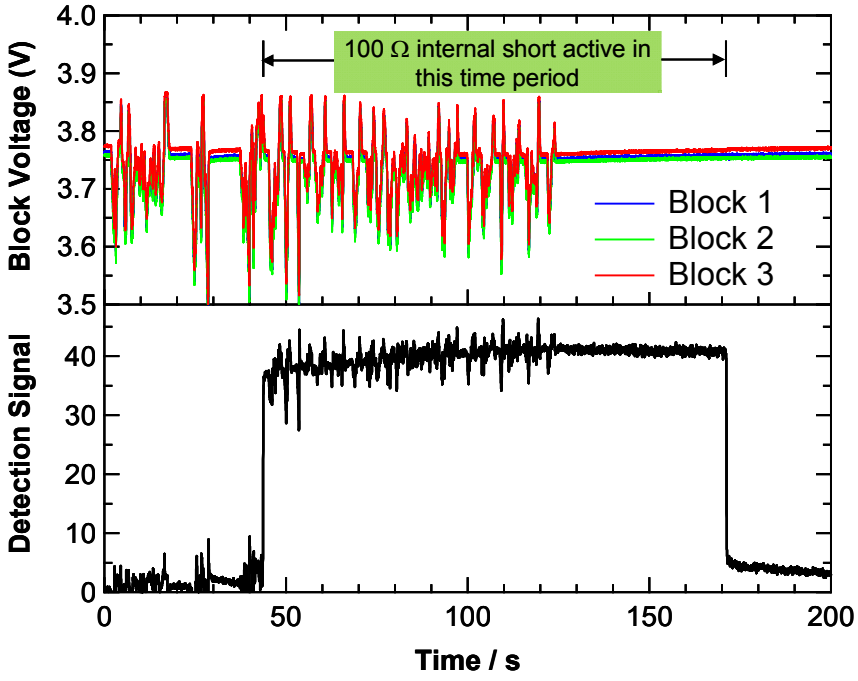

Figure II - 7: Experimental demonstration of TIAX's real-time internal short detection technology in a battery pack under an automotive duty cycle

9. Safe Electrolytes Based on Imide Salt Solutions in Fluorinated Solvents

Leyden Energy developed electrolytes that are up to 85% by weight non-flammable components. NFi ™ electrolytes demonstrate great safety, long cycle life, good rate and low temperature performance. ***(Leyden Energy)***

Regular Li-ion cells use highly flammable electrolyte solutions of $LiPF_6$ in organic solvents. Under abuse conditions, the electrolyte may ignite, often resulting in a battery fire or explosion. Previous attempts to formulate non-flammable electrolytes included ionic liquids formulations or addition of a flame retardant to regular solvents. Both approaches failed to combine in one formulation good safety and fast lithium transport that allows quick charge and discharge over a wide temperature range.

Leyden Energy's approach was to use lithium imid salts solutions in non-flammable solvents. Imide salts have significantly higher solubility in fluorinated solvents compared to regular salts such as $LiPF_6$, $LiBF_4$ and LiBOB. This approach allowed Leyden's R&D to formulate electrolytes with up to 85% non-flammable components by weight. Small amounts of carbonates are preserved in the electrolyte for efficient SEI formation; limited amounts of esters or linear carbonates assist rate and low temperature performance.

Electrolytes were extensively tested in 18650 and pouch cells and demonstrated long cycle life at up to 60°C (see Figure II - 8), discharge capability at as low as -30°C, rate up to 5C and vastly improved safety under abuse conditions. Electrolytes did not ignite when the cells vented; cell safety improvements were seen in overcharge, hot box, nail and impact tests. Leyden findings and results of the development were independently verified by Mobile Power Solutions test lab and Exponent Failure Analysis. Additional tests included a cone calorimetry measurement test (see Figure II - 9), when a fully charged battery is burned and the amount of heat generated by this process is recorded. Remarkably, total heat release is about half of the heat compared to the same cell with a regular electrolyte such as 1M $LiPF_6$/EC:DEC1:2.

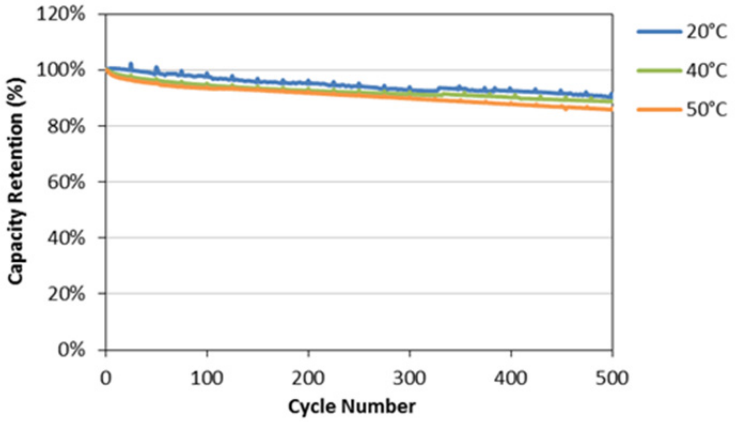

Figure II - 8: Cycle life of the 2.0Ah NCM pouch cell with NFi™ electrolyte

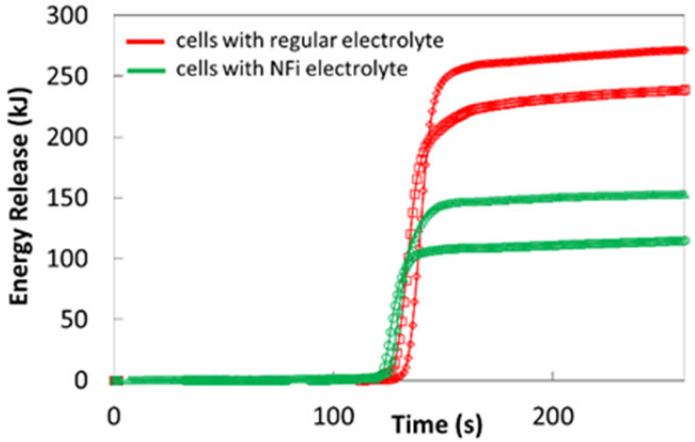

Figure II - 9: Heat release measured by using cone calorimetry in 2.0Ah NCM cells

10. Lowering the Cost and Improving the Performance of Separators for Lithium-ion Batteries

Development and installation of advanced manufacturing processes and research into new material formulations have resulted in improved separator quality and lower cost. ***(ENTEK Membranes LLC)***

In 2009, ARRA provided $1.5 billion in funding to support the establishment of Li-ion battery manufacturing facilities in the United States. One goal of this investment was to reduce the cost of the battery for plug-in electric vehicle (PEV) applications. It was recognized that an important step for the electrification of the nation's light duty transportation sector is the development of more cost-effective, long lasting, and abuse-tolerant PEV batteries.

The separator is a critical component of the battery that impacts both performance and safety. The thin (≤25 microns), microporous membrane provides an electrically non-conductive barrier between the positive and negative electrodes and also a network of pores that can be filled with electrolyte to allow ionic flow between those electrodes. In addition to preventing contact between the electrodes, it enhances safety by collapsing its pores and shutting down ion flow when the battery temperature rises to a hazardous level.

The cost of the separator membrane can be a significant fraction of the material cost of the Li-ion battery, particularly in high-power designs such as for HEVs. Depending on the battery design, the separator may be 25% or more of the materials cost of a cell. Thus a reduction in separator cost is necessary to help meet the battery cost goal of $125/kWh by 2022.

With the assistance of ARRA funding, ENTEK has made improvements to one of its existing production lines and constructed an entirely new line with advanced process capabilities and higher throughput. The ENTEK production facility has state-of-the-art online characterization equipment and a clean room for slitting master rolls. These improvements have contributed greatly toward meeting the aggressive cost targets of less than $1/m² for high volume purchases.

ENTEK has also received funding through the United States Advanced Battery Consortium (USABC) for the development of an inorganic-filled separator. The material produced from this work has a new formulation that has demonstrated improved high-voltage stability, improved power capability, and improved thermal stability compared to standard microporous polyethylene separators. The higher power capability can contribute to lower battery costs by reducing the size of batteries needed to meet low temperature performance requirements.

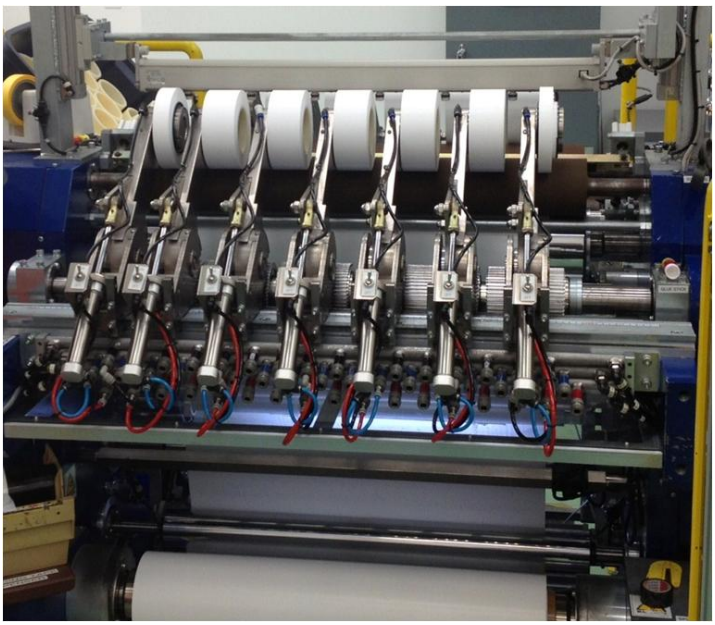

Figure II-10: Nishimura slitter installed in ENTEK's new separator production facility, utilizing ARRA funding

II.D *EV Everywhere* Planned Activities

An important step for the electrification of the nation's light duty transportation sector is the development of more cost-effective, long lasting, and abuse-tolerant PEV batteries. The cost of today's batteries is over four times too high. In addition, PEV design optimization and performance is often hindered by the size and weight of the battery.

Current battery technology is very far from its theoretical energy density limit. In the near-term (2012–2017), with advances in lithium-ion technology, there is an opportunity to more than double the battery pack energy density from 100 Wh/kg to 250 Wh/kg through the use of new high-capacity cathode materials, higher voltage electrolytes, and the use of high capacity silicon or tin-based intermetallic alloys to replace graphite anodes. Despite current promising advances, much more R&D will be needed to achieve the performance and lifetime requirements for deployment of these advanced technologies in PEVs.

In the longer term (2017–2027), "beyond Li-ion" battery chemistries, such as lithium-sulfur, magnesium ion, zinc-air, and lithium-air, offer the possibility of energy densities that are significantly greater than current lithium-ion batteries as well as the potential for greatly reducing battery cost. However, major shortcomings in cycle life, power density, energy efficiency, and/or other critical performance parameters currently stand in the way of commercial introduction of state-of-the-art "beyond Li-ion" battery systems. Breakthrough innovation will be required for these new battery technologies to enter the PEV market.

The energy density increases described above will be critical to achieving the *EV Everywhere* cost and performance targets. Additional R&D efforts including pack design optimization and simplification, manufacturing improvements at the cell and pack level, materials production cost reduction, and novel thermal management technologies will also contribute to battery cost reduction. Also, achieving the *EV Everywhere* battery power density target (2000 W/kg) is important to assure that technology breakthroughs meet the discharge power requirements for a wide range of PEV architectures and to enable the battery to be rapidly charged. Fast-charging may be important for consumer adoption of certain PEVs.

In 2013, U.S. DRIVE updated its Electrochemical Energy Storage Roadmap which describes ongoing and planned efforts to develop electrochemical energy storage technologies for plug-in electric vehicles (PEVs) and can be found at the EERE roadmap page.

In support of the *EV Everywhere* Grand Challenge, DOE released a Funding Opportunity Announcement (FOA) in March 2013, soliciting proposals in the areas of energy storage, electric drive systems, lightweight materials, and auxiliary load reductions. DOE announced the selection of 38 awards from the FOA in September 2013.

In the area of advanced batteries, 13 projects totaling $22.5 million were awarded. The projects will help improve cell chemistry and composition, develop advanced electrolytes and create new battery design tools – helping to further reduce costs. Broadly, the projects aim to cut battery size and weight in half, while improving efficiency and performance. These projects, which were initiated in September 2013, fund R&D in pursuit of the *EV Everywhere* goals and will be described in more detail in next year's annual report.

Advanced Battery Development

USABC Battery Development Projects

Advanced Lithium Battery Cell Technology

Low-cost Processing Research

Advanced Materials and Processing (FY 2008 DOE FOA)

Small Business Innovative Research Projects (SBIR)

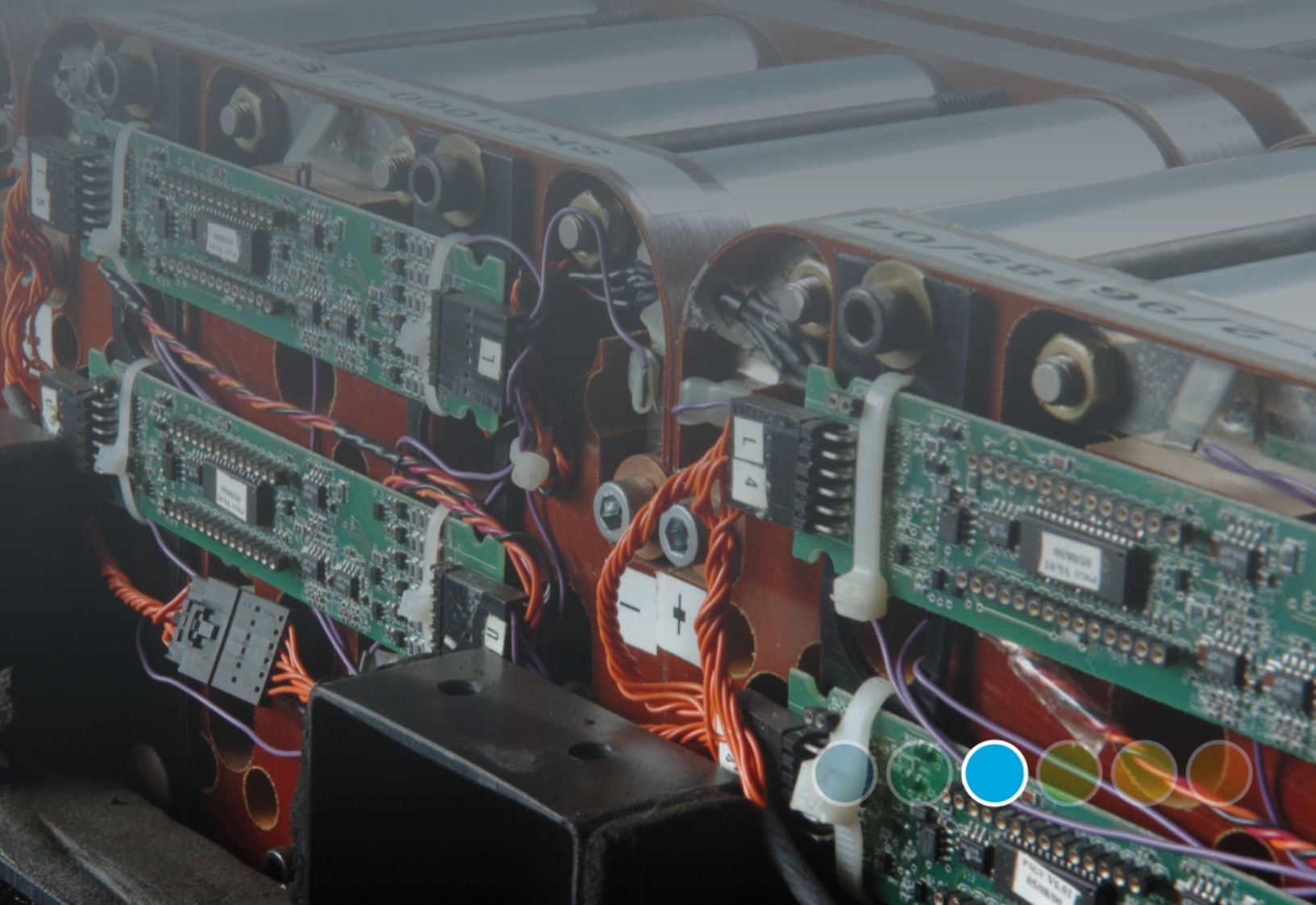

III. Advanced Battery Development

One of the primary objectives of the Energy Storage effort is the development of durable and affordable advanced batteries and ultracapacitors for use in advanced vehicles, from start/stop to full-power HEVs, PHEVs, and EVs. The battery technology development activity supports this objective through projects in several areas:

- Full-scale battery R&D under multiple battery development contracts—conducted through the United States Advanced Battery Consortium (USABC),
- Numerous advanced cell, materials and components contracts—administered through the National Energy and Technology Laboratory (NETL), and
- Small Business Innovative Research (SBIR)—to fund early-stage R&D for small businesses/entrepreneurs.

All battery development projects are conducted with a set of technical goals in mind and in order to overcome specific technical barriers which prevent the large-scale commercialization of advanced automotive batteries.

Technical Goals

- By 2014, develop a PHEV battery that enables a 40 mile all-electric range and costs $3,400.
- By 2022, reduce PEV battery cost to $125/kWh.

Technical Barriers

- **Cost** – The current cost of Li-based batteries is approximately a factor of four too high on a kWh basis for PEVs and approximately a factor of 50% too high on a kW basis for HEVs. The main cost drivers being addressed are the high costs of raw materials and materials processing, cell and module packaging, and manufacturing.
- **Performance** – The performance advancements required include the need for much higher energy densities to meet the volume and weight requirements, especially for the 40 mile PHEV system and longer range EVs, and to reduce the number of cells in the battery (thus reducing system cost).
- **Abuse Tolerance** – Many Li batteries are not intrinsically tolerant to abusive conditions such as a short circuit (including an internal short circuit), overcharge, over-discharge, crush, or exposure to fire and/or other high temperature environments. The use of Li chemistry in the larger (PEV) batteries increases the urgency to address these issues.
- **Life** – A 15-year life with 5,000 HEV cycles or 1,000 EV cycles is unproven.

Technical Targets

- Focus on the small-scale manufacture of cells, batteries, and advanced materials for high-power applications (HEVs) and high-energy applications (e.g., PEVs).
- Attempt to meet the summary requirements for EVs, PHEVs, HEVs, and Lower-energy energy storage systems (LEESS) developed with industry – as shown in Table III - 1, Table III - 2, and Table III - 3.

Accomplishments

- The R&D activity remains fully underway with multiple battery development contracts being conducted through the USABC.
- Numerous advanced cell, materials, and components contracts are ongoing – administered through the National Energy and Technology Laboratory (NETL).

Table III - 1: Summary of USABC performance targets for EV batteries[9]

USABC Goals for Advanced Batteries for EVs - CY 2020 Commercialization

End of Life Characteristics at 30°C	Units	System Level	Cell Level
Peak Discharge Power Density, 30 s Pulse	W/L	1000	1500
Peak Specific Discharge Power, 30 s Pulse	W/kg	470	700
Peak Specific Regen Power, 10 s Pulse	W/kg	200	300
Useable Energy Density @ C/3 Discharge Rate	Wh/L	500	750
Useable Specific Energy @ C/3 Discharge Rate	Wh/kg	235	350
Useable Energy @ C/3 Discharge Rate	kWh	45	N/A
Calendar Life	Years	15	15
DST Cycle Life	Cycles	1000	1000
Selling Price @ 100K units	$/kWh	125	100
Operating Environment	°C	-30 to +52	-30 to +52
Normal Recharge Time	Hours	< 7 Hours, J1772	< 7 Hours, J1772
High Rate Charge	Minutes	80% ΔSOC in 15 min	80% ΔSOC in 15 min
Maximum Operating Voltage	V	420	N/A
Minimum Operating Voltage	V	220	N/A
Peak Current, 30 s	A	400	400
Unassisted Operating at Low Temperature	%	> 70% Useable Energy @ C/3 Discharge rate at -20 °C	> 70% Useable Energy @ C/3 Discharge rate at -20 °C
Survival Temperature Range, 24 Hr	°C	-40 to+ 66	-40 to+ 66
Maximum Self-discharge	%/month	< 1	< 1

[9] For more details and for additional goals, see http://www.uscar.org/guest/article_view.php?articles_id=87 .

Table III - 2: Summary of USABC performance targets for PHEV batteries

Characteristics at End of Life (EOL)		High Power/ Energy Ratio Battery	Moderate Energy/Power Ratio Battery	High Energy/ Power Ratio Battery
Reference Equivalent Electric Range	miles	10	20	40
Peak Pulse Discharge Power (2 sec/10 sec)	kW	50/45	45/37	46/38
Peak Regen Pulse Power (10 sec)	kW	30	25	25
Available Energy for CD (Charge Depleting) Mode, 10 kW Rate	kWh	3.4	5.8	11.6
Available Energy in CS (Charge Sustaining) Mode	kWh	0.5	0.3	0.3
Cold cranking power at -30°C, 2 sec – 3 pulses	kW	7	7	7
CD Life / Discharge Throughput	Cycles/MWh	5,000/17	5,000/29	5,000/58
CS HEV Cycle Life, 50 Wh Profile	Cycles	300,000	300,000	300,000
Calendar Life, 35°C	year	15	15	15
Maximum System Weight	kg	60	70	120
Maximum System Volume	Liter	40	46	80
Maximum Operating Voltage	Vdc	400	400	400
Minimum Operating Voltage	Vdc	$>0.55*V_{max}$	$>0.55*V_{max}$	$>0.55*V_{max}$
Maximum self-discharge	Wh/day	50	50	50
System Recharge Rate at 30°C	kW	1.4 (120V/15A)	1.4 (120V/15A)	1.4 (120V/15A)
Unassisted Operating & Charging Temperature	°C	-30 to +52	-30 to +52	-30 to +52
Survival Temperature Range	°C	-46 to +66	-46 to +66	-46 to +66
Maximum current (10 sec pulse)	Amp	300	300	300
Maximum System Production Price @ 100k units/year	$	$1,700	$2,200	$3,400

Table III - 3: Summary of USABC performance targets for power assist hybrid electric vehicles

Characteristics	Lower Energy Energy Storage System (LEESS)	Power Assist (Minimum)	Power Assist (Maximum)
Pulse discharge power (kW)	20 (10 sec)	25 (10 sec)	40 (10 sec)
	55 (2 sec)		
Peak Regenerating Pulse Power (kW)	30 (10 sec; 83 Wh)	20 (10 sec; 55 Wh pulse)	35 (10 sec; 97 Wh pulse)
	40 (2 sec; 22 Wh)		
Total Available Energy (kWh)	0.056 (Discharge)	0.3	0.5
	0.083(Regenerative)		
	0.026 (Both)		
	0.165 (Total vehicle window)		
Cycle Life (cycles)	300k	300k; 25-Wh cycle (7.5 MWh)	300k; 50-Wh cycle (15 MWh)
Cold-cranking Power at −30ºC (kW)	5 (after 30 day stand at 30ºC)	5 (three 2-sec pulses, 10-sec rests between)	7(three 2-sec pulses, 10-sec rests between)
Calendar Life (years)	15	15	15
Maximum System Weight (kg)	20	40	60
Maximum System Volume (liters)	16	32	45
Production Price @ 100k units/year ($)	$400 (Selling price per system)	$500	$800
Unassisted Operating temperature Range (ºC)	−30 to +52	−30 to +52	−30 to +52
Survival Temperature Range (ºC)	−46 to +66	−46 to +66	−46 to +66

III.A USABC Battery Development Projects

III.A.1 EV Battery Development (Envia Systems)

Harshad Tataria, USABC Program Manager
Subcontractor: Envia Systems

Herman A. Lopez, Program Manager,
7979 Gateway Boulevard
Newark, CA 94560
Phone: (510) 962-3687; Fax: (510) 372-0318
E-mail: hlopez@enviasystems.com

Start Date: December 2010
Projected End Date: July 2013

Objectives

- Develop and evaluate high capacity manganese rich (HCMR^{TM}) cathode materials and screen various electrolyte formulations that meet the material target specifications.
- Design, build and test large capacity pouch cells integrating Envia's HCMR^{TM} cathode and optimized electrolyte formulations that meet the USABC minimum goals for long term commercialization.

Technical Barriers

One challenge is to develop a cathode material with very specific electrochemical performance and incorporate it into a cell expected to meet numerous USABC cell targets. Many of the cell target specifications as with the material specifications will require optimization and balance in order to meet the various targets. In the cell, a balance between energy and power will exist and in the material, a compromise between specific capacity and cycle and calendar life will exist. This project consists of developing the best materials and integrating them in an optimal cell design to meet the USABC targets.

Another challenge is that the HCMR^{TM} cathode is a relatively new material. Unlike other more established cathode chemistries where there is an abundance of data and performance trends, HCMR^{TM} cathode data in many occasions (specially for large cell data) is being reported for the first time.

Envia's HCMRTM/graphite cells potentially operate at higher voltages than commercially available cells. In order to meet the USABC targets, this will require an electrolyte that operates at high voltages, low and high temperatures and supports long cycle and calendar life. Some specific barriers that have been addressed throughout this project are:

- High irreversible capacity loss (IRCL)
- Oxygen loss during cycling ($Li_2MnO_3 \rightarrow MnO_2 + 2\ Li^+ + 1/2O_2$), which leads to gassing in the pouch cell
- High DC-Resistance
- Fade in average voltage upon cycling
- High Manganese dissolution leading to poor cycle life and calendar life

Technical Targets

- Develop a high specific capacity cathode (>200mAh/g at C/3) able to meet the energy, power, cycle life, calendar life and cost targets.
- Develop and utilize a high voltage, stable electrolyte formulation that can operate in the temperature range of -40°C to 55°C and be able to support high energy and power, a cycle life of 1,000 cycles and a calendar life of 10 years.
- Design, develop, build and test ≥20Ah cells, which meet the USABC minimum goals for long term commercialization of EVs.

Accomplishments

- Envia down-selected an HCMR^{TM} cathode after extensive material development with respect to composition, dopants and surface coatings. The material development consisted of optimizing the chemical and physical properties of the cathode to improve the specific discharge capacity, rate capability, cycle life, transition metal (TM) dissolution, and DC-resistance of the material.
- The down selected cathode materials were scaled up to kilogram levels and integrated in large capacity cells to support a total of nine project cell builds.
- A new baseline electrolyte was selected based on improved low temperature performance while maintaining similar room temperature cycling stability, power and energy characteristics compared to Envia's high voltage baseline electrolyte.

- Envia has met a majority of the stringent requirements for electric vehicle (EV) batteries. Envia demonstrated meeting the gravimetric and volumetric power and energy targets from 20Ah capacity pouch cells.

✧ ✧ ✧ ✧ ✧

Introduction

Envia Systems proposed to develop large capacity (20Ah-40Ah) pouch cells based on a novel high-voltage lithium rich cathode chemistry containing a layered-layered structure. The layer-layer composition is made up of interconnected Li_2MnO_3 and $LiMO_2$ domains. Upon initial charging to high potentials (>4.5V vs Li^0), the material gets activated resulting in lithium extraction from the Li_2MnO_3 component along with the loss of oxygen. This lithium removal gives rise to a first cycle irreversible capacity loss.

The new cathode chemistry can also be written in the form of $Li_{1+x}Ni_\alpha Co_\beta Mn_\gamma O_2$ where the major TM component is Manganese, which reduces the amount of the costlier Nickel and Cobalt components. Having a high amount of manganese in the structure translates to high capacity, increased safety, and low cost.

Approach

Our approach is very cathode centric, as we believe that the cathode is the biggest driver of overall performance and cost. New lithium-rich cathode compositions have been created with the layered-layered structure $xLi_2MnO_3 \cdot (1-x)LiMO_2$ where M= Ni, Co, Mn. In general, when the cathode chemical composition, surface nanocoating and morphology are changed, the cathode specific capacity, IRCL, average voltage, cycle life, and tap density of the material change. We will also explore dopants that are able to reversibly intercalate greater amounts of lithium, while controlling the oxidation state of the transition metal components (Ni^{+2}, Co^{+3} and Mn^{+4}) and retaining the crystal structure of the cathode.

Another way to engineer and control the cathode specific capacity, IRCL and average voltage is by having a nanocoating covering the surface of the cathode. The nanocoating has been shown to stabilize the cathode structure by preventing unwanted side reactions with the electrolyte and reducing the amount of cathode TM dissolution. As part of the project, various nanocoating compositions, as well as coating thicknesses will be explored and optimized. The thickness and uniformity of the nanocoating are dependent on the particle morphology (particle size, surface area and porosity) and reaction conditions.

Initial testing is performed using coin cells or 1Ah pouch cells and will be scaled up to larger pouch cells. Electrochemical and battery testing are being performed, along with material characterization using various analytical techniques.

Results

In this first USABC project, Envia has met a majority of the stringent requirements for EV batteries. Envia demonstrated meeting the gravimetric and volumetric power and energy targets from 20Ah capacity pouch cells. Low temperature energy retention was shown to meet the specifications from room temperature to -30°C. DST cycle life testing is still ongoing with the latest data showing greater than 800 DST cycles (9 RPTs) while both energy and discharge power continue to stay above the 80% beginning of life (BOL) target (see Figure III - 1).

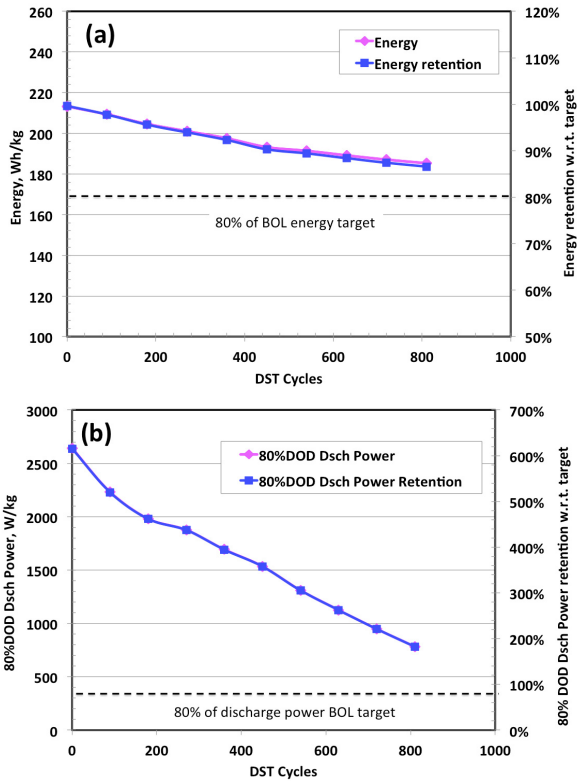

Figure III - 1: DST cycle life test results in terms of energy (a) and discharge power (b) for 20Ah capacity pouch cells

Calendar life testing is also ongoing with promising results being shown after seven months of testing. The models to properly predict the calendar life continue to be developed as more data continues to be collected. During the course of the project, the cell-to-pack conversion factors and pack-related costs were calculated by working with a system integration

company. The pack related costs for a 40kWh pack were determined to be $2,626 and volumetric and gravimetric energy and power cell-to-pack multiplication factors found to be 58% and 70%, respectively. Cell cost analysis was also performed determining the cell related selling price to be $258/kWh.

Envia has been successful in meeting most of the USABC goals for EV batteries. With respect to calendar life, it is debatable as to whether our cells will meet the 10 year mark. Ideally we would be able to test the cells for 10 full years to determine this qualification, but that is not practical. Preliminary calendar life results at 30°C from our latest cells, suggest promising calendar life results. Envia continues testing and more data will be available to validate the calendar life models and life predictions.

Conclusions and Future Directions

In its first USABC project, Envia has been able to meet all of the energy and power goals without maximizing the energy of the cathode by operating between 2.2V and 4.35V. As a continuation of the work, Envia continues to be committed to meeting the aggressive USABC cell targets to enable widespread adoption of EVs. Recently, new more aggressive USABC targets for EVs were made public together with a request for proposal information (RFPI). In order to have a better chance to meet the targets, Envia will propose to integrate high capacity lithium-rich cathodes with high capacity silicon-based anodes. Only in this combination can the new aggressive cost and energy targets be met. During this proposal, Envia will also partner with leading silicon chemical companies, as well as with leading electrolyte, separator and pre-lithiation companies. Having the right partners during the development will increase the probability of meeting the technical targets and ensuring that the developed technology can be mass-produced and commercialized.

III.A.2 EV Battery Technology Assessment Program (Farasis Energy, Inc.)

Harshad Tataria, USABC Program Manager
Subcontractor: Farasis Energy, Inc.

Keith Kepler, Program Manager
21363 Cabot Boulevard
Hayward, CA 94545
Phone: (510) 732-6600; Fax: (510) 887-1211
E-mail: kkepler@farasis.com

Start Date: July 2012
End Date: August 2013

Objectives

- Manufacture pouch cells based on BASF produced HENCM high capacity cathode material and Farasis cell technology.
- Conduct performance, life and safety testing of cells in parallel with DOE National Laboratories.

Technical Barriers

New high capacity and high voltage cathode materials offer great promise in meeting the battery performance and cost goals required for the commercial acceptance of electric vehicles (EVs). However, Li-ion cells using these new materials can experience a range of challenges that can limit the full realization of their potential and must be addressed at both the material and cell level. These challenges include minimizing impedance and achieving acceptable cycle life at elevated voltages and temperatures, maximizing cathode material long term stability and ensuring the safety of large energy dense cells.

Technical Targets

- Manufacture large, 30Ah Li-ion pouch cells suitable for EV applications based on BASF produced HENCM cathode material.
- Demonstrate the potential to meet DOE EV performance and safety goals through evaluation at Farasis and DOE National Laboratories.

Accomplishments

- Demonstration of over 1,000 cycles in prototype small pouch cells cycling at a C/3 rate at 25 C.
- Manufacture and delivery of 50, 30 Ah Li-ion pouch cells to DOE for evaluation at Idaho National Laboratory (INL), Sandia National Laboratory (SNL) and the National Renewable Energy Laboratory (NREL).

✧ ✧ ✧ ✧ ✧

Introduction

Farasis Energy, Inc proposed to produce and supply prototype high energy density Li-ion cells to USABC based on their current commercial 25Ah Li-ion pouch cell for detailed testing and evaluation. The cells were developed using the new transition metal layered-layered type cathode material originally developed at Argonne National Laboratory. BASF, a fully licensed supplier for this class of material is one of the few companies capable of producing these developmental materials on a large scale with commercial quality and consistency. Farasis has developed material processing and cell design methods to address some of the inherent issues associated with the performance and utilization of these cathode materials that have been major barriers to their commercialization, despite the major increase in gravimetric energy density they offer over current commercial cathode material alternatives. Beginning with cathode material supplied by BASF, Farasis proposed to process, build and supply Li-ion cells to USABC in a similar form factor to our current 25 Ah cells but with an almost 20-30% greater energy density.

Approach

Farasis Energy, Inc currently produces a range of Li-ion cell and battery products including a 25 Ah, NCM cathode based pouch cell (Figure III - 2). The form factor and performance make it ideal for use in a range of automotive EV systems (Figure III - 3). We proposed to use this commercial form factor as the basis for the deliverable prototype cells.

Figure III - 2: Commercial 25 Ah Li-ion pouch cell

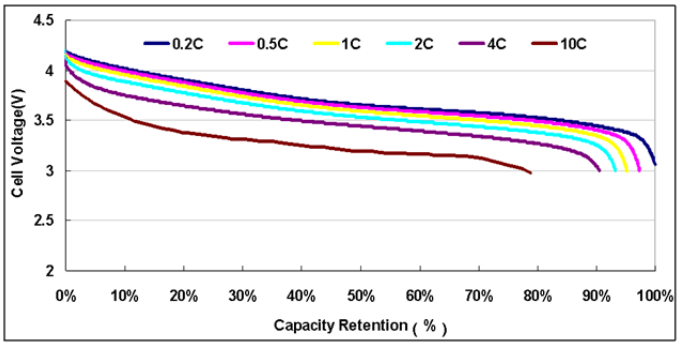

Figure III - 3: Rate capability of 25 Ah Li-ion pouch cell

To ensure the greatest performance and to enable us to optimize the cell design and material utilization, Farasis started with BASF's HENCM "Layered-layered" cathode material produced from their pilot manufacturing plant to make the cells. Additional processing of the materials prior to building the cells was conducted at Farasis. Initial batches of small prototype pouch cells were planned to deliver to DOE for initial evaluation.

Results

Farasis manufactured both small pouch cells and large pouch cells as deliverables for this program. Cathode material from BASF was processed at Farasis Hayward and then used at its manufacturing facility to make pouch cells on its pre-production line. Figure III - 4 shows cycling data from prototype small pouch cells cycled at C/3 discharge rate.

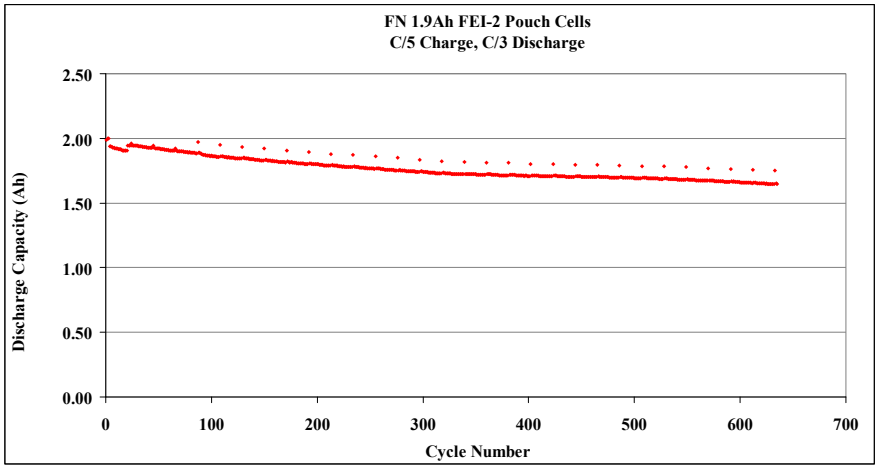

Figure III - 4: 2.0 Ah Li-ion pouch cell cycling data: C/5 charge, C/3 discharge

Figure III - 5 shows cycling data for several early prototypes of the 30 Ah cell design tested at Farasis before the final production build. These cells were cycled with a C/3 charge and discharge rate.

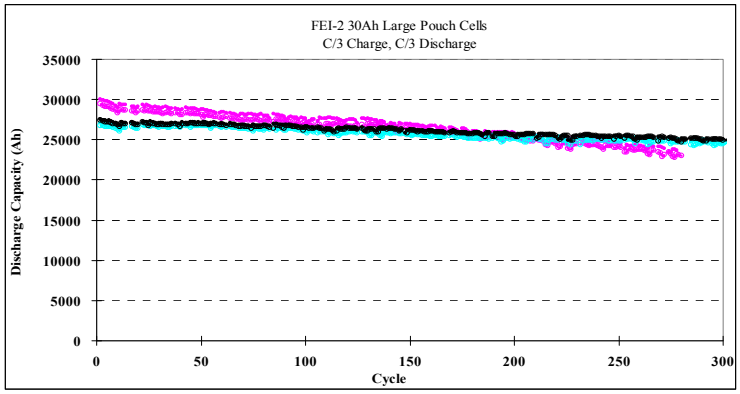

Figure III - 5: 30 Ah Li-ion pouch cell cycling data: C/3 charge, C/3 discharge

Farasis shipped a large quantity of processed cathode material to its factory in March 2013 for the final deliverable cell build. Approximately 80 30 Ah cells were built at the factory using a design based on the 25 Ah production pouch cell form factor. Seventy cells were shipped to Farasis in Hayward, CA and 46 of these cells were shipped to Idaho National Laboratory for performance testing, Sandia National Laboratory for safety testing, and the National Renewable Energy Laboratory for thermal evaluation. The cells will be tested at these facilities and at Farasis over the next 6 months.

Conclusions and Future Directions

Farasis has successfully delivered large high energy density Li-ion pouch cells for evaluation by USABC and DOE aimed at meeting the USABC PHEV battery performance targets. These cells will be evaluated both at Farasis and at the National Laboratories over the coming months. Farasis will continue its development of this high capacity Li-ion cathode chemistry to further improve the performance of this system. This technology has the potential to meet the long term USABC goals for PHEV and EV battery systems.

III.A.3 EV Battery Technology Assessment (SK Innovation)

Chulheung Bae, USABC Program Manager
Subcontractor: SK Innovation

Kyungjin Park, Program Manager
325 Expo Road, Wonchondong, Yuseongku,
Daejeon, Korea
Phone: (82) 42-609-8133; Fax: (82) 42-609-8740
E-mail: kj.park@sk.com

Start Date: November 2012
Projected End Date: January 2014

Objectives

- Develop and validate a pure NCM battery system
  - High energy density
  - Long life performance
  - High abuse tolerance

Technical Barriers

One of the concerns about pure NCM system is safety. Therefore, improved ceramic coated separator and a new electrolyte system are required.

SK applied ceramic coated separator with superior strength and heat stability based on SK's own technology and also adjusted the electrolyte system.

Technical Targets

The USABC minimum electric vehicle (EV) battery technical targets for the system are listed inTable III - 4.

Accomplishments

- Validation of power density with over 600W/L and specific discharge and charge powers of over 460W/kg and 480W/kg
- Development of 40Ah cell with 230Wh/L and specific energy 150Wh/kg
- Successful life performance with over 2,000 cycles (expected)

Table III - 4: Summary of USABC targets for the system being developed

Parameter(Units) of fully burdened system	USABC minimum goals
Power density (W/L)	460
Specific power Dis. 80%DOD/30s (W/kg)	300
Specific power Regen, 20%DOD/10s (W/kg)	150
Energy density C/3 Discharge rate (Wh/L)	230
Specific energy C/3 Discharge rate (Wh/kg)	150
Specific power/Specific energy ratio	2 : 1
Total pack size (kWh)	40
Life (Years)	10
Cycle life - 80% DOD (Cycles)	1,000
Power & Capacity degradation (% of rated spec)	20
Operating environment (℃)	-40 to +50 20% performance loss (10% desired)
Normal recharge time	6 hours (4 hours desired)
High rate charge	20-70% SOC < 30minutes @150 W/kg (<20min @ 270W/kg Desired)
Continuous discharge in 1hour – No failure (% of rated energy capacity)	75

✧ ✧ ✧ ✧ ✧

Introduction

As the requirements for the EV market are getting more demanding in energy density and life including driving distance, SKI has developed and introduced high energy 40Ah (LMO-free) cells for this USABC EV technology assessment program. SKI set a goal of higher energy density and improved calendar life maintaining good cycle life and stability, and also developed 40Ah cell with Mn-spinel free and named it LMO-free E400. The LMO-free cell can avoid Mn-dissolution which brings crucial deterioration at high temperatures, so this program's cell is expected to have an improved calendar life.

SKI also applied a thermally superior ceramic coated separator and developed electrolyte formulation with adjusted electrolyte additives for LMO-free system. From performance validation tests, LMO-free

E400 could maintain other electrical performance as in previous systems.

Approach

SKI applied pure NCM as cathode material to get high energy density and to avoid crucial deterioration at high temperature. However, high Ni-content NCM has a detrimental effect on the abuse tolerance and cycle life. In order to obtain structural stability, SKI has researched surface-coated NMC with stable materials. The surface-treated particles have shell-core morphology, that is, SC-NMC.

In addition, we enhanced the separator properties to minimize shrinkage of the separator at high temperatures, and developed the new electrolyte system which is an optimized formulation for the new cathode.

Cycle life and calendar life are expected to improve significantly after eliminating the Mn-spinel.

Results

Core Test. SKI tested 18 cells in total (6 cells for cycle life and 12 cells for calendar life) and measured that the average capacity is over 40 Ah at current condition of C/3, C/2 and C/1 (Figure III - 6).

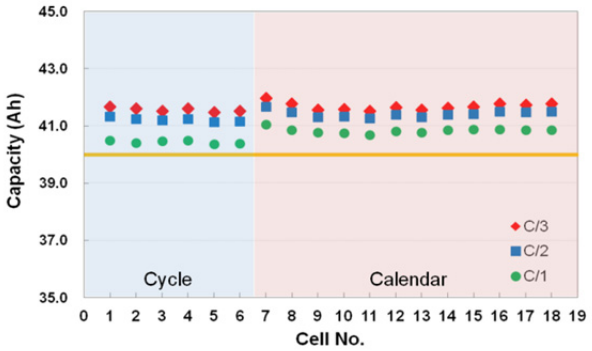

Figure III - 6: Constant current discharge test for LMO-free E400

100% DST Discharge capacity at the DST power of 400W/kg is 40.8Ah on average.

Peak power capability was calculated as shown below and showed a result of over 670W/kg.

$$\text{Peak power} = I_{max} \cdot (V_{IRFree} + R \cdot I_{max})$$

48h stand test showed very stable capacity retention with 0.95% capacity loss.

Life Performance. After successfully completing the core tests, six batteries have been in testing for cycle life. Cycle life tests will be conducted until End of Life (EOL).

Approximately, 4 cycles are accumulated per day and RPTs are being conducted every 100 cycles (~1/month). Figure III - 7 shows C/3 capacity retention and results show 91.3% of retention at 800 cycles. Similar tendency is seen in DST capacity retention (92.7%) and peak power retention (94.7%).

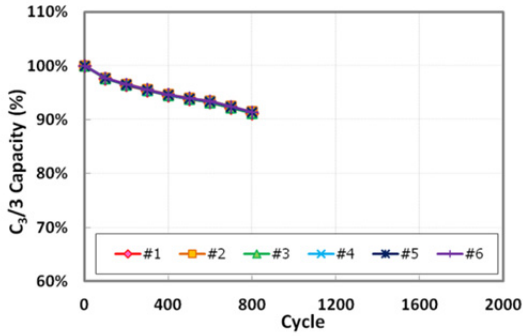

Figure III - 7: C/3 capacity retention of LMO-free E400 in cycle life

Calendar life tests are ongoing at four different temperatures of 25, 35, 45, and 55°C. Each battery is charged to SOC 100% at the C/3 rate and allowed to rest in an open circuit condition at the desired temperature for 4 weeks. At the end of 4 weeks, the batteries undergo RPTs at 30°C. Figure III - 8 shows C/3 capacity retention at four temperatures after 24 weeks and the results show 94.4%, 91.5% 87.4% and 81.0%, respectively.

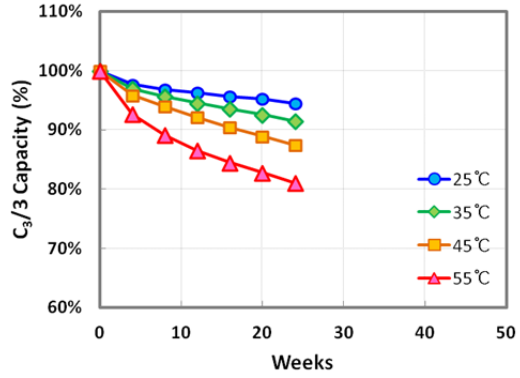

Figure III - 8: C/3 capacity retention of LMO-free E400 in calendar life

There is no significant degradation to 45°C and similar tendency is shown in DST capacity retention (96.1%, 92.4%, 89.0% and 82.2% at 25°C, 35°C, 45°C and 55°C, respectively; after 24weeks).

However, comparatively high degradation is observed at 55°C and this appears clearly in peak power retention (98.4%, 95.8%, 92.9% and 76.8% at 25°C, 35°C, 45°C and 55°C, respectively; after 24 weeks). We can presume that unstable SEI forms on anode surface

from electrolyte decomposition between 45°C and 55°C, and it brings comparatively high capacity irreversibility.

Abuse tests were carried out and LMO-free E400 showed stable behavior after abuse tests as shown in Table III - 5. SKI followed SAND 2005-3123 abuse tests manual which was distributed by SNL, and some specific test conditions (e.g., resistance for short circuit; 1mΩ and 10mΩ) were given by SNL for this program. Abuse tests were performed and the tested cells met most of the established goals, with the exception of the thermal ramp test. In the case of thermal ramp test, the objective of the test is monitoring thermal onset through temperature increase. The LMO-free cell turned out to be stable up to 180°C.

Table III - 5: Summary of abuse test results for LMO-free E400

Items		Conditions	LMO free 400
Thermal Stability	Thermal Stability	SAND 2005-3123; Increasing temp. up to 200°C (hold 30min every 20°C from 110°C to 200°C, with 5°C/min) @ SOC90%	L4 (mainly leakage, no smoke)
	Thermal ramp	SAND 2005-3123; Increasing temp. up to thermal runaway with 5°C/min @ SOC90%	Stable up to 180°C
Nail Penetration	Face	SAND 2005-3123; Pin dia=3㎜, Speed 80㎜/s @ SOC100%	L3
	Edge		L3
Short Circuit	Resistance 1mΩ	SAND 2005-3123; @ SOC100%	L3
	Resistance 10mΩ		L3
Overdischarge		SAND 2005-3123;1C, 1.5h @SOC100%	L2

Conclusions and Future Directions

SKI has evaluated LMO-free E400 and cycle life and calendar life will be continuously conducted until RPT10. Currently, based on capacity retention of 80%, cycle life is expected to exceed 2,000 cycles and calendar life of over 70weeks at 45℃ and 100% SOC – SKI will estimate battery life with RPT10 data at the end of the program. SKI would like to continuously develop and modify cell design including electrolyte optimization and adjustment of cathode formulation in order to improve safety further.

III.A.4 Advanced High-Performance Batteries for Plug-In Hybrid Electric Vehicle Applications (JCI)

Renata Arsenault, USABC Project Manager
Subcontractor: Johnson Controls Inc.

Avie Judes, JCI Program Manager
5757 N. Green Bay Road
Glendale, WI 53209
Phone: (414) 524-6173
E-mail: avie.judes@jci.com

Start Date: April 1, 2012
End Date: March 31, 2014

Objectives

- Build on the prismatic cell platform developed in the previous program and achieve a step-change in energy density from 275 Wh/L to a 375 Wh/L. stretch goal.
- Achieve cost target of $250/kWh for the prismatic cell.
- Target EUCAR 4 abuse tolerance rating or better.
- Deliver two generations of prismatic cells.

Technical Barriers

- Higher specific capacity cathode materials of interest have reduced thermal stability (reduced life).
- Novel electrode material processing techniques may have a negative impact on performance and life.
- Lowering the power to energy ratio must not result in an unacceptable reduction in low temperature power.
- Higher upper voltages adversely affect life and require countermeasures to stabilize the chemistry.
- Abuse tolerance improvements require material and process innovation to overcome impact on life and cost.

Technical Targets

- Available Energy (Charge Depleting mode): 5.8 kWh for 20-mile system at End of Life (EOL).
- Energy Density: 375 Wh/L (stretch goal).
- Packaged Energy Cost: $250/kWh for cell.
- EUCAR 4 abuse tolerance rating or better.

Accomplishments

- Evaluated multiple cathode materials from six suppliers. Two materials remain as candidates after exhaustive down selection trials.
- Mid-program cells demonstrated a 25% capacity increase.
- Projected final cell design translates to 40% cost reduction at the system level.
- Dry compounding trials achieved desired reduction of solvent and binder. High resistance growth and cost have eliminated this process technique going forward.
- Paste mix processing was evaluated using an in-line compound mixer as a potential enabler of solvent reduction goals. Promising results were obtained, attaining the high electrode densities needed for the cell energy density targets. Testing through December 2013 will assess potential for anode and cathode high solids processing.
- Evaluated 4.2V and 4.3V upper voltage limits in parallel with electrolyte development (base solvents and additives) for enhanced stability. Demonstrated results at 4.2V have allowed V_{max} increase from 4.1V.
- Mechanical improvement activity resulted in mandrel elimination as well as current collector and coating area optimization, plus alternate fill hole closure method down-selection. Results inform final build choices.
- Abuse tolerance improvements focused on Thermal Protective Barrier (TPB), ceramic coating on anode, ceramic separators, electrolytes and cathodes with functional overcharge additives, all leading to improved over-charge protection and enhanced understanding.

✧ ✧ ✧ ✧ ✧

Introduction

In 2011, JCI completed a three-year program which developed a first generation NMC-graphite, rigid prismatic cell technology headed for commercialization

in late 2013. This $4.1 million, 2 year follow-on program builds on the first generation platform. The theme of this program is to achieve a major energy density improvement of the cell.

Between the conclusion of the previous program and the kick-off of this program, the upward march in energy density continued, through continuous improvements made in process, materials and mechanical design. This improvement is seen in Figure III - 9.

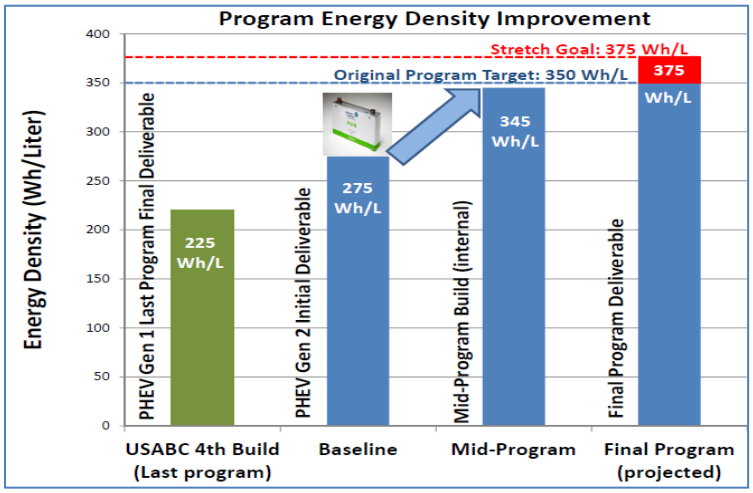

Figure III - 9: Energy density roadmap

Approach

The objective of the program is to increase the energy density of the cell technology and drive down the cost to capacity ratio, either directly (with increased mAh/g, reduced BSF and cost) or indirectly (with improved critical enablers: life and abuse tolerance). The focus is on active materials that fall midway on the 'state-of-the-art' to 'high-risk' continuum, striving to exploit their full, unrealized potential through concerted material, process, and mechanical design innovation. Specifically, the family of $LiNi_xCo_yMn_zO_2$ (where $x>1/3$) is targeted for the positive electrode coupled with a graphitic negative material. Module and system development have been excluded from the program to focus resources on closing the gap in cell technology. If achieved, derivative system-level benefits of cost, volume and mass reduction will be realized and gap chart targets will be met.

Increased energy density is being pursued on four discrete levels: 1) active material specific capacity increase, 2) electrode composition (increased active material to inactive constituents ratio, 3) electrode densification, and 4) maximizing space occupied by the electrode coil in the cell envelope and increasing coated electrode width.

The following five improvement areas form the framework of the program, and all converge toward the central program goal of reducing the $/kWh metric.

Higher Energy Density Materials. JCI is focusing on high-nickel NMC cathode materials. Compared to the baseline NMC111, high-nickel materials exhibit reduced structural and thermal stability, manifested by accelerated aging and lower abuse tolerance. To address this, stabilized active materials (doped, coated, and / or surface treated) from six global suppliers were evaluated.

Lithium-rich layered-layered cathode materials are also being evaluated to identify the main barriers that need to be overcome prior to commercialization.

Electrode Processing Optimization. Novel slurry processing techniques are being studied with two objectives: 1) reducing the quantity of N-Methyl Pyrrolidinone (NMP) solvent used in the positive electrode manufacturing process by 18-22% (result: cost reduction) and 2) improving the electrode handling through calendaring and winding to support electrode densification (result: increase in cell energy density).

Drivers for the amount of solvent, conductive agent and binder used in the current process are intimately linked to the type of mixing applied. JCI's process uses the classic industry approach for solids dispersion. Alternative methods of first compounding or pre-mixing active material with the conductive agent are being explored as paths to solvent reduction and associated increase in active to inactive material ratios and energy density.

Electrode Design Optimization. Electrode optimization focuses on reducing the power to energy

ratio (P:E) to the practical boundary where acceptable performance and life characteristics are maintained. This is being achieved by the aforementioned campaigns to increase specific capacity of the active material, increase energy density of the coated electrodes, and increase the loading level itself.

Increased Upper V Limit and Increased SOC Window. Increasing the upper voltage limit beyond its current value of 4.1 V offers increased energy density and reduced $/kWh, but may adversely impact life and abuse tolerance. To surmount these issues, stabilized active materials and electrode and interface stabilization will be evaluated.

Stabilization of the negative electrode/electrolyte interface would in turn allow expansion of the SOC window beyond 70% thus offering an opportunity to reduce the Battery Size Factor (BSF) and hence cost. Test efforts seek the lowest operating voltage limit where the inevitable trade-offs in life remain acceptable in magnitude. Expansion efforts would focus on moving from 25 to 95% SOC to a stretch goal of 15 to 95% SOC.

Mechanical Design and Advanced Manufacturing. Significant effort is directed at advancing the cell design and manufacturing processes, striving to minimize the void volume in the cell and achieve a step-change reduction in component and assembly costs. Some of the concepts being investigated are: thin wall cans with special features, mandrel elimination, current collector design optimization, reduced foil margin (wider electrode coated width), electrolyte fill hole closure using torsional ultrasonic welding, and low pressure vent development.

WBS 5.0 Abuse Tolerance. Abuse tolerance improvement is a *critical enabler* to all other work aimed at increasing energy content of the cell, and is being pursued on multiple parallel fronts:

- *High temperature separator.* JCI is working closely with separator developer Entek to optimize their ceramic filled separator technology and solve several manufacturing related issues.
- *JCI's Thermal Protective Barrier (TPB) technology.* JCI applied TPB on the anode in the last program and are now optimizing TPB coating, including thickness, coverage, and uniformity.
- *Overcharge protection additives.* These are being tested both in the electrolyte and in the electrode itself.

Results

For discussion purposes, the key design versions from the previous program are defined in Table III - 6.

Table III - 6: Version parameters and base & mid-program performance

Cell Type	Size	1C_Rate Capacity (Ah)	Energy Density (Wh/L)	Discharge Power (10s, 50%SOC) (W)	Discharge R (10s, 50%SOC) (mOhm)	P/E Ratio
USABC 4th Build (Last Program)	141x124x22.6	23.7	245	1510	1.99	17
Baseline New Program	148x91x26.5	27.0	275	1540	1.92	16
Mid-Program	148x91x26.5	33.3	345	1880	1.60	16
Final	148x91x26.5	36	375	TBD	TBD	TBD

The new electrolyte additive developed in the last program and anode active material implemented in the baseline cell have remarkably low cell resistance growth during storage at elevated temperatures. This can be seen in Figure III - 10, which shows cell resistance increasing only 13% and 34% after one year calendar life at 45°C and 60°C respectively.

The prismatic cell representing mid-program results has an increased energy density of 26%. It shows good discharge and regeneration power capability, with similar power/energy ratio as baseline. With increased upper voltage at 4.2V, the resistance growth in calendar life at 60˚C is higher than baseline at 4.1V after 100 days. However, their capacity fade remains the same as the baseline at 4.1V, as seen in Figure III - 11.

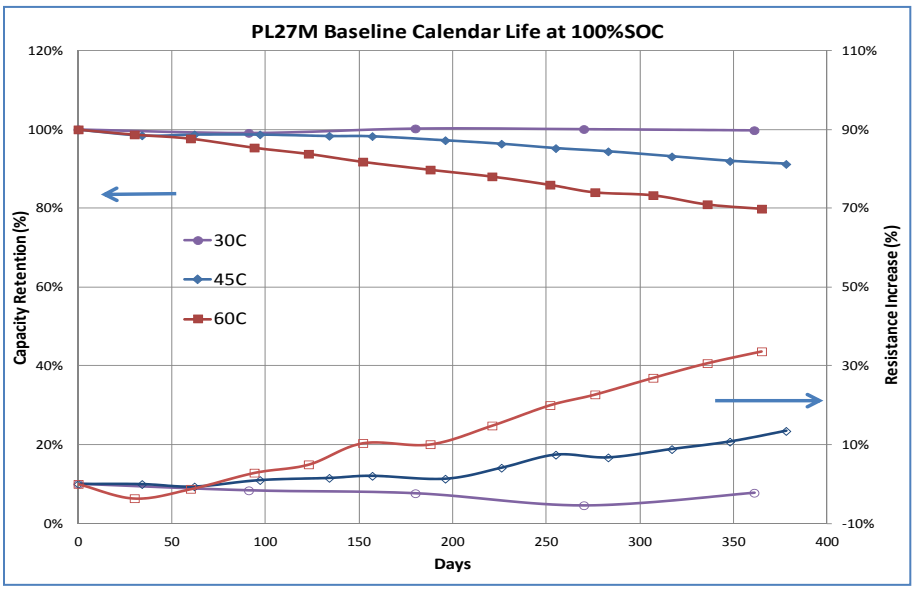

Figure III - 10: Baseline prismatic cell calendar life

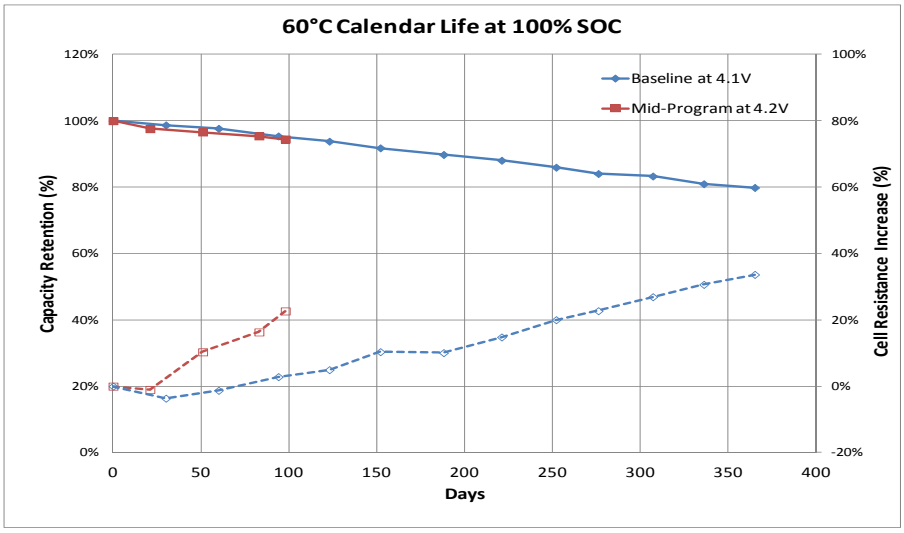

Figure III - 11: Mid-program cell calendar life at 60°C

Results by development area at month 18 (of 24) are presented below:

Higher Energy Density Materials. Six suppliers of candidate nickel-rich NMC have been engaged and the materials (designated Cat_1 through Cat_6) are at various stages of testing. Different NMC stoichiometries have been evaluated to identify high energy materials with good power and life. The tests have shown that the high nickel NMC has low thermal stability. Despite high initial capacity, high nickel NMC suffers high capacity degradation and poor life at high temperatures. Several suppliers provided high nickel NMC with surface treatment, but this significantly increased cell resistance. Development activities have improved its capacity fade over initial versions, but end of life (EOL) capacity is lower than baseline (111) at EOL.

Three NMC materials have been down-selected as candidates for the final design, the baseline material (Cat_1), Cat_2 NMC (442) and Cat_4 (improved 111).

Lithium-rich layered-layered oxide cathode material was evaluated paired with a high voltage electrolyte in 1-3 Ah pouch cells. It has very poor capacity fade, and a large voltage fade during cycle life. Further work with it is not planned.

Electrode Processing Optimization. The two approaches studied for solvent reduction through improved electrode processing methods are shown in Figure III - 12. Dry compound mixing yielded material which met solvent reduction targets, but cell testing has shown high resistance and poor calendar life behavior. This is attributed to the excessive shear undergone by the material during compounding. This process is no longer being considered for high solids mixing.

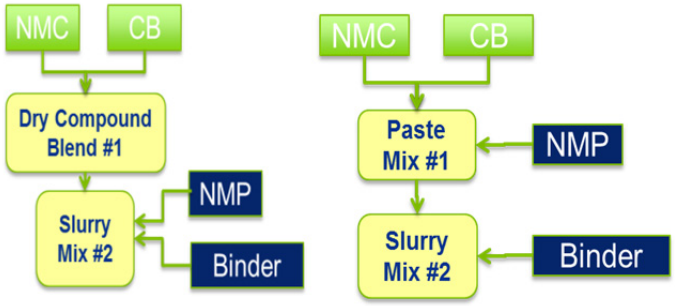

Figure III - 12: High solids mixing approaches using dry compounding (left) and paste mix (right) methods

A second method being tested to achieve the high solids targets is paste mixing. With this method, materials are combined with a portion of the solvent in an in-line compound mixer to achieve the work needed for the initial combination of materials to contribute to reduced solvent demand. The internal workings of this pre-blending equipment are shown in Figure III - 13. Following initial trials, equipment was rented and installed in the JCI Pilot line for further testing of electrode processing and resulting cell evaluation. Initial electrodes produced, shown in Figure III - 13, appear promising for achieving good uniformity with calendaring to the high density targets for improved energy density. Electrode quality after calendaring is a significant accomplishment not realized with previous trials. A solvent reduction of 13% was achieved, still below the 18% target. However, optimization work continues.

Figure III - 13: Paste mixing equipment and electrodes

An alternate (higher risk/higher reward) process incorporating aqueous binder (allowing total solvent elimination) was pursued for the positive. This offers a significant cost reduction opportunity by avoiding the need to capture the evaporated NMP solvent from the electrode process. The application of water-based binder for the cathode has shown minimal adverse impact in cell testing. Primary efforts have focused on quantifying the potential corrosion effects of the water-based cathode slurries as this corrosion can have detrimental effects on life and cell resistance. Evaluations indicate no impact on stability of the water-based slurry with 30 minutes of contact with aluminum foil, well beyond the normal processing time before electrode drying. Scaled up mixing and electrode processing is scheduled for February 2014.

Electrode Design Optimization. Different approaches were tested to optimize electrode design. Higher electrode loading was proven not to be efficient. Electrode densification delivered more capacity, and better power and life. A new conductive carbon has improved electrode processing and cell performance. The anode optimization has been applied in the mid-program cells.

Increased Voltage Limit. Accelerated testing began with prismatic cells at upper voltages of 4.1, 4.2 and 4.3V. The 4.2 V group showed acceptable power and energy fade. The first generation (baseline) 4.3 V tests were stopped due to poor results. Chemistry stabilization improvements have demonstrated life at 4.2V that meets EOL targets. 4.2V has been selected as the standard upper voltage limit.

A few electrolyte additives tested at 4.3V imparted some stability improvement. Overall, however, capacity saw a crossover with cells at 4.2V.

To maximize cell energy utilization, the usable SOC window was widened from 95%-25% to 95%-15% SOC. The cycle life of baseline cells has shown excellent performance, even with the expanded SOC window (see Figure III - 14).

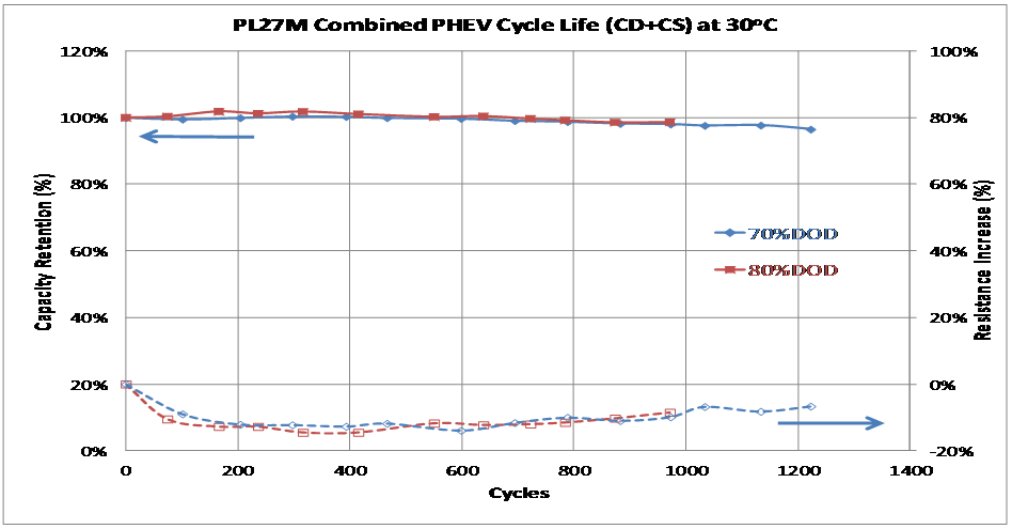

Figure III - 14: PHEV cycle life: 95%-25% vs 95%-15%SOC

Mechanical Design and Advanced Manufacturing. Numerous concepts were studied that have the potential to dramatically drive down component cost and assembly complexity, increasing cell energy density and performance.

- Torsional ultrasonic welding was selected as the lead alternative fill hole closure method after extensive evaluation of competing methods. The novel sealing process was successfully developed in a production-like environment (Figure III - 15). The approach shows great potential to reduce cell void volume and replace baseline rivet insertion.
- The design of a thin wall can with inwardly embossed features was completed. It has the potential to reduce the complexity of tolerance management and clamping forces needed in future module designs.

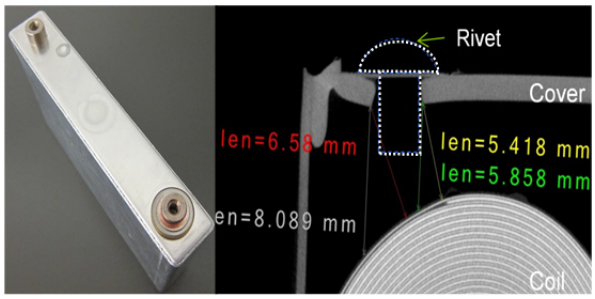

Figure III - 15: Cell sealed by torsional ultrasonic welding

- Mandrel-less cells produced in the mid-term build are on test with promising results and are planned for incorporation into the final build.
- Current collector width was optimized using results of component level high current pulse tests. This, along with foil margin reduction and electrode layout redesign, increased cell capacity by 4.5%.
- A low pressure vent is being developed to investigate whether earlier activation and associated release of thermal energy and fuel might avoid or mitigate thermal runaway. Abuse testing with prototypes is planned.

Abuse Tolerance: Joint trials were conducted with Entek to address manufacturing and performance issues of the ceramic filled separator. These separators provided remarkable improvement in cell resistance, power capability, and life. At 25°C, cell power improved by 30%, and 20% at -25°C. In calendar life at 60°C, no resistance increase was measured after 262 days at 4.1V.

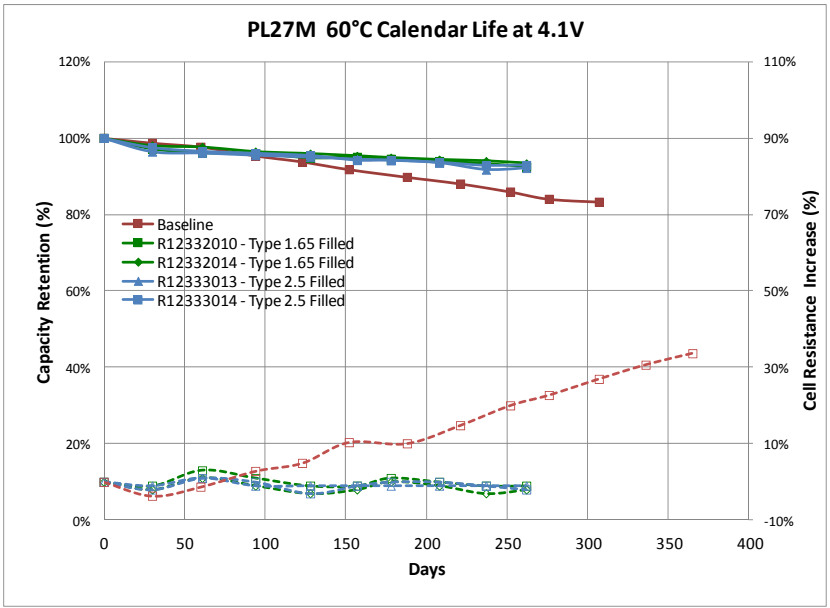

Figure III - 16: Ceramic separators calendar life at 60°C

Excellent performance was also found when cells with ceramic filled separators were tested at 4.2V at 70°C. After one year storage, cell resistance only increased 34%.

Ceramic filled separators lack the shutdown function which is considered to be an essential safety attribute for high energy cells. Efforts with Entek to adjust the ceramic/ polyolefin ratio to achieve full or partial shutdown and retain the life-enhancing properties were not successful.

Thermal Protective Barrier (TPB) technology was optimized on thickness, coverage and uniformity, resulting in tangible improvements in abuse tolerance results.

Two cathode additives were found to delay the onset of thermal runaway during overcharge with no adverse impact on life detected thus far. A formulation of electrolyte additives for overcharge control showed very promising results with more work required.

Next Steps

Convergence of design choices based on this work has started. From this, final cells will be produced and delivered in CY Q1 2014.

FY 2013 Publications/Presentations

1. Presentation to the 2013 DOE Annual Peer Merit Review Meeting (May 13, 2013).

III.A.5 Development of a High-Performance PHEV Battery Pack (LG Chem)

Paul Groshek, USABC Project Manager
Contractor: LG Chem Power, Inc.

Mohamed Alamgir, Program Manager
E-mail: alamgir@lgcpi.com
1857 Technology Drive
Troy, MI 48083
Phone: (248) 291-2375; Fax: (248) 597-0900

Subcontractor:
LG Chem, Seoul, South Korea

Start Date: January 1, 2008
Projected End Date: March 31, 2010

Objectives

- This is a 24 month program focused on developing a Li-ion pack technology that meets the energy, power and life requirements of the 40-Mile PHEV program of the USABC. A key part of the work is aimed at developing a cell that will significantly reduce cost to meet the USABC pack cost target by utilizing high specific energy cathode materials.
- An important objective of the program is also to develop an automotive-grade, self-contained battery pack using a refrigerant-based cooling system. The goal is to increase the efficiency of the thermal management system to increase life, lower cell count and more importantly, lower pack cost. The system is expected to be much more efficient and robust than its liquid-cooled counterpart commonly used in PHEV packs.

Technical Barriers

The project is addressing the following technical barriers.

(1) Validation of the high capacity of new generation of Mn-rich cathode materials.
(2) Demonstration of cycle-life of > 5,000 cycles
(3) Demonstration of calendar-life of 15 years
(4) Make considerable progress towards achieving the USABC pack cost target of $3,400.

Technical Targets

- Establish the high specific energy of new generation of Mn-rich cathode materials.
- Demonstrate both cycle- and calendar-life under USABC test conditions.
- Develop a cooling system that is electrically and mechanically robust and efficient.
- Develop a pack design that is modular, easy to manufacture and close to the USABC cost target.

Accomplishments

- Extensive studies of the material and electrode properties such as morphology, surface area and porosities were carried out to identify electrode formulations optimal from performance as well as from life points of view.
- Process variables such as formation conditions which affect the amounts of gas generated as well as life have been examined and optimized.
- Since this high capacity cathode material necessitates the use of high-voltage electrolyte additives to prolong life at high voltage have been studied.
- Cyclability of the cathode has been found to be strongly dependent on the charge voltage as well as the SOC window of operation. Key among the root causes for cell degradation is the dissolution of Mn from the cathode particles and subsequent passivation of the anode.
- Stabilization of the cathode particle surface leads to significantly improved life characteristics.
- Material we have developed in-house demonstrates state-of-the-art cathode capacity as well as life. Current estimates show that this material when fully developed will lead to a cell cost target of below $200/kWh.
- The thermal system and pack volumetric efficiency have been significantly improved by optimizing compressor and evaporator designs, as well as by improving the contact between the thermal fins and the cold plate.
- Modules and packs have been designed, built and delivered to the National Labs for testing.

✧ ✧ ✧ ✧ ✧

Introduction

Development of a cost-effective, high performance battery is a prerequisite for the successful introduction of PHEVs and EVs. The advent of new high specific energy cathode materials has opened up significant opportunities to achieve this objective. Low-cost, high capacity cathode materials using a large operational SOC window will result in the use of less of active materials, thus lowering the pack cost. In addition, development of a thermal management system that is more robust and simpler to implement than conventional, liquid cooled system is also important for advanced, next generation battery pack technologies.

Approach

To achieve the proposed objectives for a 40-Mile PHEV program, we have been studying cell chemistries based on next-generation Mn-rich layered-layered compounds, our patented Safety Reinforcing Separator (SRS) and a laminated packaging cell design. The goal is to understand, develop and optimize this cathode chemistry, corresponding anode and electrolyte compositions in order to meet the USABC targets for performance, life and cost. Evaluation of critical factors such as cathode and anode compositions, effect of binders and electrolyte compositions as well as the identification of conditions optimum for cycle- and calendar-life are the important tasks of the program.

Another important aspect of the work is to develop a pack that has superior thermal management using indirect cooling entailing a refrigerant-cold plate system. This work is aimed at developing a thermal system that will be thermally and mechanically robust with optimized volumetric and gravimetric efficiencies as well as cost.

Results

Characterization of the Mn-rich cathode. The layered-layered compound $xLi_2MnO_3(1-x)LiMO_2$ with reported capacities > 250 mAh/g. has one of the highest specific energies of any high voltage cathode material currently being studied. To obtain such high capacity, however, the material needs to be charged to voltages around 4.6V. Additionally, it is characterized by high surface area and low conductivity at low SOCs. There is also the phenomenon of voltage sagging throughout life that lowers cell energy and is also undesirable from battery control point of view. To improve upon these drawbacks, we carried out systematic studies to optimize electrode formulations, evaluated cell performance as a function of charge voltages, modified cathode particle surfaces using a variety of approaches, studied a range of electrolytes and optimized cell process parameters such as formation conditions, etc. These studies led to the following key observations.

Durability of the cell is critically dependent on the charge voltage. Operation above ~4.35V leads to significant reduction in cycle-life. Cathode surface modification and electrolyte composition appear to mitigate these drawbacks to some extent (Figure III - 17, Figure III - 18).

a. Considerable amount of gas generation takes place during activation and high voltage operation. This causes significant cell swelling and premature cell failure. Surface treatments of the cathode particle show good improvement.

b. Voltage sagging appears to stem from the continuous structural evolution of the cathode material. Surface coatings do not appear to be effective in alleviating this phenomenon.

c. Dissolution of Mn from the cathode and its migration to and subsequent passivation of the anode remains the key mechanism that appears to control the life of this Mn-rich high capacity cathode. Modification of the particle surface using coatings appears to significantly improve the life of the cell.

Pack Development. As mentioned above, we have developed a compact and self-contained battery pack system utilizing a refrigerant-to-coldplate cooling concept, (Figure III - 19). The essential components for this cooling system are solid fins, a cold plate, compressor and evaporator. Studies were carried out to optimize these components with respect to cooling and volumetric efficiency, manufacturability and cost. For example, we studied compressors of different ratings (e.g., 12V, dual 12V or a single 24V) to determine their efficacy in thermally managing the cells during cycling. Two iterations of module and pack builds have been carried out in course of the program.

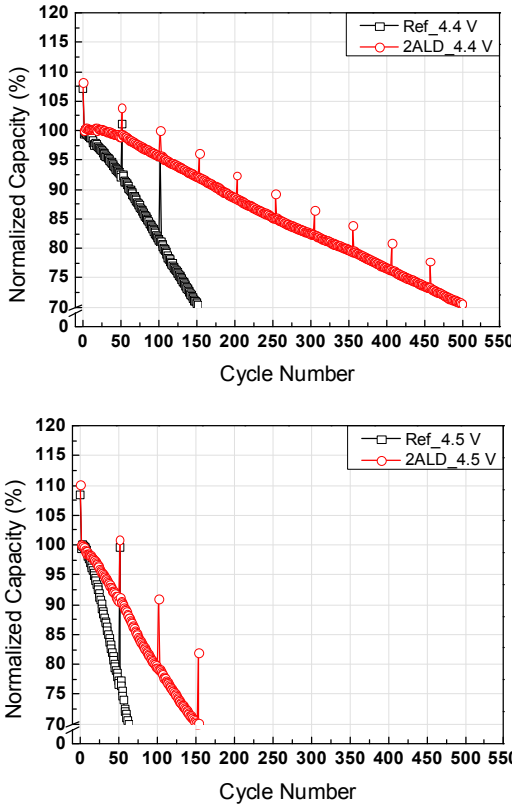

Figure III - 17: Effect of charge voltage and surface coatings on cycle-life. Top: Data showing the beneficial effect of ALD surface coating on the cycle-life at 45°C. The cell was charged at 0.5C and discharged at 1C. Bottom: When the charge voltage was raised to 4.5V, instead of 4.4V as in Top figure, there is a substantial decline in cycle-life

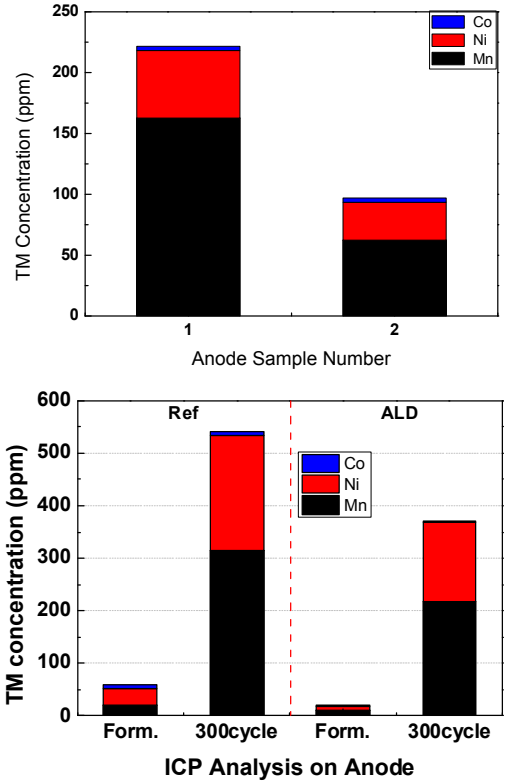

Figure III - 18: Top) Effect of formation voltage on the amount of transition metal deposited on carbon anode. Sample 1 was formed at 4.6V. Sample 2 was formed at 4.4V. Note the significantly large quantity of Mn deposited at 4.6V. Bottom) Effect of surface coating on Mn dissolution. ALD coating reduces Mn dissolution both during formation as well as cycling

The packs were subjected to automotive drive-cycles to assess their capability in thermally managing the cells during cycling. Figure III - 20 shows the data for a pack using a dual 12V compressor system and cycled at an ambient temperature of 40°C and US06 drive pattern. The data show that the cooling system was effective in maintaining the cell temperatures at around 32°C. It took ~30 mins to reach the steady-state. The bottom picture compares the efficiencies of packs using different compressors. The dual 12V system showed the best efficiency in cooling the packs. The steady-state, however, for all three packs were reached within ~30 mins. The cold-plate temperatures for the three systems are also plotted. A key observation from all our pack data is that the thermal system was efficient in cooling the cells and maintaining the modules within a narrow range of temperature.

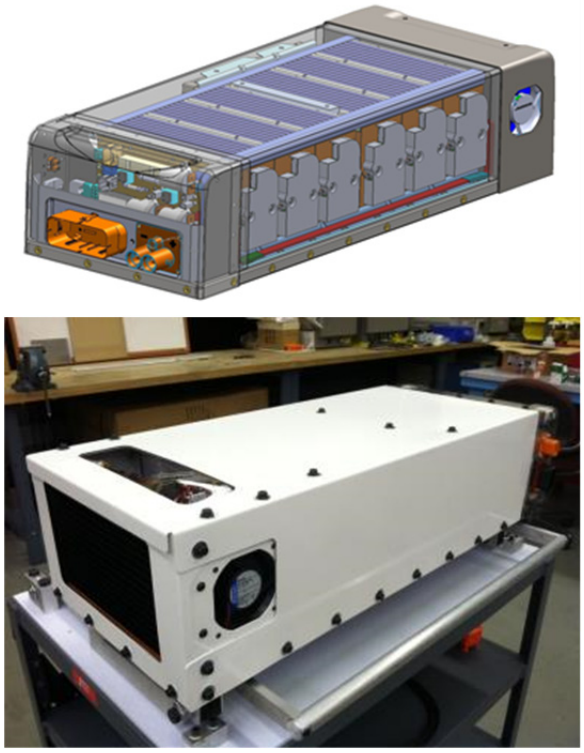

Figure III - 19: Top: Schematic of the PHEV-40 mile pack we have developed. The thermal chamber containing elements such as the compressor, the cold-plate and the evaporator is on the right while the electrical chamber is on the left; Bottom: picture of the finished pack as delivered to the National Labs

Conclusions and Future Directions

While the Mn-rich cathode has the potential of delivering very high specific energy, several key drawbacks need to be mitigated to make it a long-life, low-cost cathode. Various approaches we have studied show that there are considerable opportunities to improve the cathode material properties. Extensive test data involving analytical studies have clearly established the usefulness of our approaches toward improving the performance and life of the cells. However, none of the methods we have investigated thus far was able to fully alleviate the key challenges of Mn dissolution, gassing and voltage sagging, which leads to poor life.

Multiple design iterations have led to the development of a pack using an indirect cooling method comprising a refrigerant-to-cold plate system. These packs have been built and delivered to the USABC for testing by the National Labs.

FY 2013 Publications/Presentations

1. Presentation at the 2013 DOE Annual Peer Review Meeting, Washington, DC, May 2013.

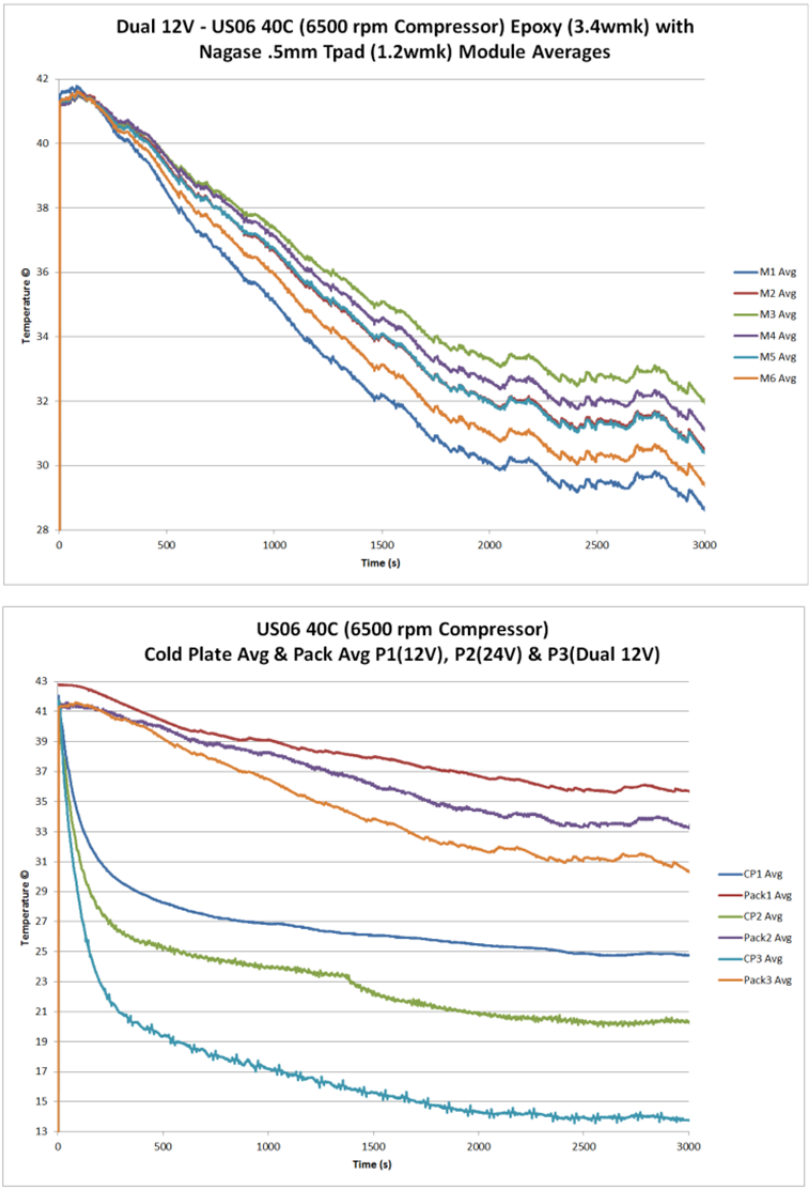

Figure III - 20: Examples of the thermal performance of the pack using the cooling system we have developed. Top figure shows the average temperature of the modules during US06 cycling at 40°C. The data show that the modules are within 4°C of each other, indicating uniform and efficient cooling. Bottom figure compares three different packs using different compressor ratings (single 12V, dual 12V and a 24V. The associated cold-plate temperatures are also shown in the graph. The cold plate temperature is the bottom curve

III.A.6 Energy Storage System for High Power HEV Applications (Maxwell)

Scott Jorgensen, USABC Program Manager
Subcontractor: Maxwell Technologies, Inc.

Allen Stoneberg, Program Manager
3912 Calle Fortunada
San Diego, CA, 92123
Phone: (858) 503-3582
E-mail: astoneberg@maxwell.com

Collaborators:
University of Rhode Island

Start Date: January 2011
Projected End Date: March 2014

Objectives

- Design, build, and test hybrid ultracapacitor cells and packs capable of meeting USABC goals for LEESS HEV applications.
- Extend device upper voltage range above 4.0 V with good life and low temperature performance.
- Develop and demonstrate a new design architecture for cell and system which is cost effective, small and light.

Technical Barriers

- Low temperature performance (operation at -30ºC).
- Energy density (increased stable operating voltage window).
- Cell and system cost decreases.

Technical Targets

- Develop a hybrid capacitor cell and associated module to meet LEESS HEV power and energy goals.
- Develop and utilize a stable electrolyte system that has a voltage window of 4.0 V or higher and can operate in the temperature range of -30 to 55 ºC.
- Identify optimal electrode materials for higher energy, lower impedance, and stability at increased potential over lifetime, and lower cost relative to existing commercial capacitive technologies.
- Identify a separator that represents a significant cost reduction while maintaining or exceeding existing performance and safety metrics.

Accomplishments

- Completed the development and fabrication of third generation 3.8 Wh hybrid ultracapacitor cells. Representative cells have been sent to Idaho National Laboratory for testing.
- Produced over 1,000 third generation cells in support of module build utilizing Maxwell's low cost dry electrode fabrication process.
- Finalized the design of the Maxwell LEESS Module incorporating key features to optimize cost, weight and volume.
- Completed production of LEESS modules and packs in support of internal and testing at national labs per the FreedomCAR Battery Test Manual.
- Demonstrated over 390,000 HEV cycles with first generation cells. These cells are still exceeding performance requirements.
- 15% reduction of EOP Projected Cost matching SOW requirement.

✧ ✧ ✧ ✧ ✧

Introduction

Maxwell Technologies is developing a new energy storage system based on a novel hybrid ultracapacitor to meet LEESS HEV requirements while maintaining long life, excellent safety, and low cost. While conventional ultracapacitors generally lack the energy density required for automotive traction applications, Maxwell's hybrid technology almost triples the energy density of state of the art conventional ultracapacitors. New approaches to packaging and manufacturing are focused on significantly reducing the system cost. Key improvements to be demonstrated over existing capacitive technologies are increased energy density and low temperature performance at a size, weight, and cost that is practical for consumer vehicle use.

Approach

Leveraging its capabilities in low cost ultracapacitor manufacturing, Maxwell has developed a new large format hybrid ultracapacitor cell capable of cycling to at least 4.0 V. The compact and economical design of this

large cell is being leveraged to produce the lowest cost and smallest/lightest system possible while meeting LEESS power and energy requirements. Cell performance has been improved by:

- Identifying and selecting the highest performing anode and cathode carbons leveraging over a decade of previous carbon screening work.
- Identifying and selecting a stable electrolyte in conjunction with the University of Rhode Island.
- Identifying and characterizing separator materials with good performance but significant cost reduction.
- Use of a completely dry electrode fabrication process (solvent-free, reduced processing) to decrease cell manufacturing cost and increase cell lifetime.
- Quantifying performance/weight/size reduction of new cell architecture via cell-level electrochemical and physical testing.

Cells and systems will be tested for performance and life at Idaho National Laboratory, for abuse tolerance at Sandia National Laboratories, and for thermal performance at the National Renewable Energy Laboratory.

Results

Electrode Development. The electrode material and processing method for third generation cells was finalized at the end of 2012. Focus in 2013 was on the scale-up of electrode for larger quantity cell production. Ongoing optimization of the Maxwell electrode dry process for improved electrode physical and performance characteristics have yielded opportunities for overall improved cell performance.

Electrolyte Development. The current Maxwell control electrolyte was selected for the third generation cell and has proven to be stable in a temperature window of -20 to 55ºC. Ongoing electrolyte screening has identified a stable candidate that meets the -30°C operational requirement that will undergo further evaluation beyond the program.

Cell Development. 3.8 Wh third generation cells have been designed, produced and shipped to Idaho National Laboratory for testing per the USABC Battery Test Manual. Internal HPPC BOL data indicates that the cell chemistry meets LEESS EOL performance targets (Figure III - 21).

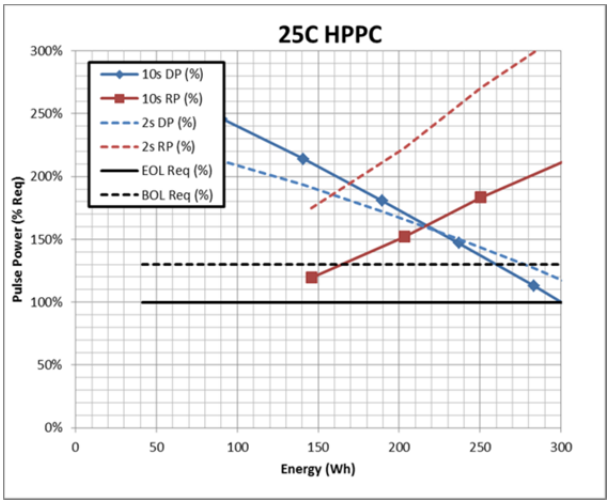

Figure III - 21: 3.8 Wh third generation HPPC BOL pulse power capability

LEESS Module Development. The LEESS Module (Figure III - 22) has been designed and tested and high-level prototypes have been completed. Full modules and sub-modules have been shipped to Idaho National Laboratory (performance), National Renewable Energy Laboratory (thermal) and Sandia National Laboratories (safety) for evaluation.

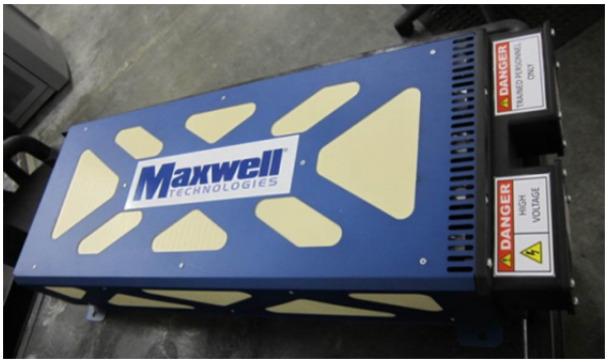

Figure III - 22:- Maxwell LEESS module

Cost Modeling. System cost is a critical program element and all decisions from cell component selection to system design have been driven by the cost model in order to deliver the lowest cost, highest value system possible. Projected end of program cost is $920 – matching the program target of $920.

Conclusions and Future Directions

In 2013, the third generation cell chemistry and configuration was finalized and scalable production processes validated. Maxwell testing has confirmed that cell safety, stability and performance meet program requirements with the exception of low temperature operation related to electrolyte selection. Over 1,000

cells have been produced and screened. The full scale LEESS Module deliverables have been designed, assembled and shipped for USABC evaluation.

Gap analysis as of Q3 2013 (Table III - 7) indicates that, with the exception of low temperature performance and size/weight, the system is on track to meet power and energy performance targets.

Current attention will be focused on the internal and USABC testing of the Maxwell LEESS Module and cells. Although the cell architecture has been frozen since mid-year for module production and USABC testing, Maxwell has made key electrolyte and electrode performance improvements that will enable the -30ºC operational requirement and increase power density by the end of the program but beyond available time for USABC testing. These cell material improvements in turn will enable both size and weight reductions at the system level.

FY 2013 Publications/Presentations

1. 2013 DOE Annual Peer Review Meeting Presentation.

Table III - 7: 2013 Q3 gap analysis

USABC LEESS PAHEV		USABC REQUIREMENTS at EOL		PROMISED – EOL (PER SOW)		PROJECTED Deliverable End of Program - EOL	
End of Life Characteristics	Unit	PA (Lower Energy)		PA (Lower Energy)		PA (Lower Energy)	
2s / 10s Discharge Pulse Power	kW	55	20	55	20	55	20
2s / 10s Regen Pulse Power	kW	40	30	40	30	40	30
Maximum current	A	300		300		250	
Energy over which both requirements are met	Wh	26		26			
Energy Efficiency	%	95		95		96.1	
Cycle-life	Cycles	300,000 (HEV)		300,000 (HEV)		300,000 (HEV)	
Cold-Cranking Power at -30ºC	kW	5		5		3	
Calendar Life	Years	15		15		15	
Maximum System Weight	kg	20		22		35	
Maximum System Volume	Liter	16		25		33	
Maximum Operating Voltage	V_{dc}	<=400		<=400		320	
Minimum Operating Voltage	V_{dc}	>=0.55 V_{max}		>=0.55 V_{max}		0.56	
Unassisted Operating Temperature Range	°C	-30^{o} - 52^{o}		-30^{o} - 52^{o}		-20^{o} - 52^{o}	
30º - 52º	%	100		100		67	
0º	%	50		50		37	
-10º	%	30		30		21	
-20º	%	15		15		9	
-30º	%	10		10		6	
Survival Temperature Range	°C	-46 to +66		-46 to +66		-46 to +66	
Selling Price/System @ 100k/yr)	$	$400		$920		$920	
Hardware Level		System		System		System	
Capacity	Wh					310	
Battery Size Factor (BSF)						**80**	

III.A.7 12 Volt Start/Stop Battery Development (Saft)

Harshad Tataria, USABC Program Manager
Subcontractor: Saft

Michael Duffield, Program Manager
13575 Waterworks Street
Jacksonville, FL 32221-2215
Phone: (904) 861-1521; Fax: (904) 772-1463
E-mail: michael.duffield@saftbatteries.com

Subcontractors:
Wildcat Discovery Technologies
Virginia Commonwealth University

Start Date: April 2013
Projected End Date: March 2014

Objectives

- To develop an advanced, high-performance battery for 12V Start-Stop (12VSS) vehicle applications based on Saft's advanced NMC-LTO lithium-ion battery technology.

Technical Barriers

The cost of automotive battery is the single most critical challenging requirement and a generally acknowledged critical path to widespread deployment of the Li-ion battery in the automotive industry. About 20% of the cost of a robust cell design in volume-production today is in the cell hardware. Cell hardware is anything other than electrodes including the foils, separator, and electrolyte. Another 50% cost burden is added as cells are integrated into a turnkey battery pack. Thus, the hardware in a Li-ion battery pack is responsible for a combined 80% of the cost add-on before indirect costs (G&A, O/H, and Profit), and is the single most significant part of the total unit cost.

A dramatically different approach to the way Li-ion cells are fabricated and assembled into a battery is needed for a significant reduction in the hardware cost.

Technical Targets

- Develop a novel cell assembly process which reduces the overall battery cost.
- Reduce elevated temperature impedance growth in order to meet cycle life requirements.
- Identify polymer materials that can hermetically seal the stack from external moisture and prevent electrolyte egress.
- Optimization of LTO and electrolytes for -30°C performance, while maintaining calendar life and cycle life up to 75°C

Accomplishments

- Saft has successfully supplied NMC based Li-ion cells for high power, high temperature automotive application.
- Saft is producing the NMC line of products in two formats, cylindrical and prismatic.
- Saft LTO technology has excellent power capability with a 15s pulse-discharge impedance of around 1.6 mΩ in small cells.

✧ ✧ ✧ ✧ ✧

Introduction

Saft's NMC-LTO technology will meet or exceed the USABC requirements for this application. Saft can meet all of the performance requirements for power, cycle life, cold cranking power, etc. using the LTO technology already demonstrated. Integration of Saft's high temperature stable NMC technology will allow for additional improvements to cell calendar life. Accordingly, this development program will scale up the Saft LTO technology from small cells to a 10-20Ah PHEV-2 VDA size prismatic cell as a demonstration of the ability to meet cost and size requirements.

Approach

A key innovation in the effort, primarily focused on cost reduction, is combining the cell and module packaging in a single injection-molded thermoplastic polymer (IMTP) monoblock. Further proposed cost reductions include optimization of the electrolyte and NMC cathode to meet the cold-cranking requirements. LTO is a chemistry particularly well suited to this optimization, as the lack of solid-electrolyte interphase (SEI) allows for the use of very low cost, low temperature electrolytes.

In order to reduce the electrode material costs, the LTO manufacturing process is being addressed by large volume manufacturers of TiO_2 for the paint industry. This could result in extremely low cost LTO, giving a significant cost advantage over graphite-based Li-ion.

With the cost reduction advantages offered by LTO chemistry and the monoblock module design, the proposed NMC-LTO monoblock battery system will meet the USABC cost target.

Results

Polymer Material Study. Saft is currently working with Virginia Commonwealth University (VCU) Department of Chemical and Life Science Engineering to conduct polymer material studies. A paper study of potential polymer candidates for the battery case has been completed. Based on Saft's polymer requirements, VCU has identified a number of polymer candidates.

VCU will now begin lab studies of the polymer candidates. Lab studies will include moisture absorption, chemical degradation, mechanical properties, and thermal degradation.

Electrolyte Development. Initially cells have been built using our low temperature electrolytes which were previously developed for our graphite anode Li-ion cells. The study of novel electrolytes is limited with LTO based Li-ion cells. Saft is investigating numerous typical and atypical solvents. In addition, we are studying different salts and molarities. The testing of the electrolytes (using SAFT-provided electrodes) is sub-contracted to Wildcat Discovery Technologies (WDT). These tests of coin cells will screen for low temperature performance, and gas generation at 70°C.

We are focusing our work to a select set of electrolyte formulations for optimal low temperature performance while maintaining stable high temperature impedance growth. After we have narrowed the electrolyte studies using Wildcat Discovery Technology's rapid prototyping and testing, we will examine these select electrolytes for gas generation. An example of the components to be studied is given in Table III - 8. The investigation will focus on component formulations 1 to 8.

Table III - 8: Electrolyte formulation test matrix

	Solvent - Dissolve Salts			Solvent - Mobility	Solvent - Low Temp		Salts	
Formulation No.	A	B	C	D	E	F	$LiBF_4$	$LiPF_6$
Baseline 1 (1 M salt)	X			X		X		X
Baseline 2 (1.3M salt)	X			X		X		X
9	X	X		X			X	
10		X		X			X	
1		X	X	X	X		X	
2		X	X		X		X	
3		X	X	X		X	X	
4		X	X			X	X	
5		X			X		X	
6		X		X	X		X	
7		X				X	X	
8		X		X		X	X	

Cell Development. There are three cell deliverables within the program. The first occurred after three months in the program and consisted of 5 LP10 Ah cells for early review and testing by USABC. The second is a set of 15 LTO-NMC prismatic cells. These will be delivered to USABC after approximately nine months in the program for independent testing & evaluation (reference cell). The final capacity of these cells will vary due to a fixed hardware size. It is currently estimated that the cells will have a capacity of 10-15Ah. The third and final deliverable is a set of 20 optimized LTO-NMC cells in PHEV-2 VDA size housings at the end of the program. These prismatic cells will also be built in a stacked electrode configuration and have a capacity of 10-15Ah.

The first deliverable of five LP10 Ah sized cells has been built and shipped to Idaho National Laboratory for testing according to the USABC 12V Start-Stop manual.

Internal Saft testing reveal the deliverable cells meet cold cranking spec at 75% SOC at the end of the 4.0 second pulse and ~65% at the end of the 0.5 second pulse (Figure III - 23). However, the cells are not aged, thus the data reflects beginning of life performance.

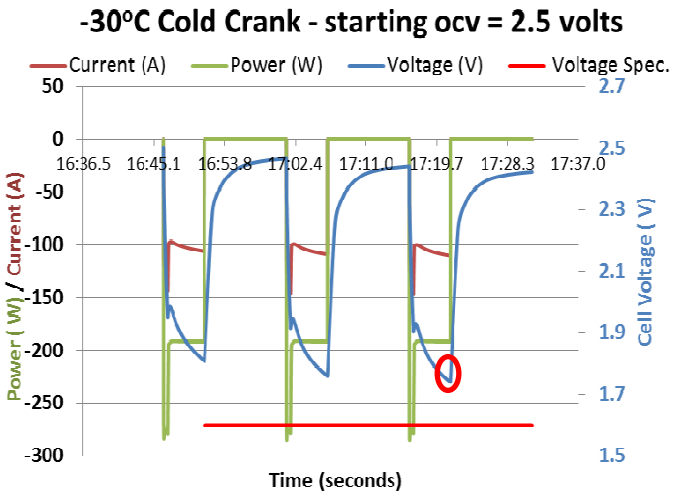

Figure III - 23: Cold crank results of 1st deliverable cells

Cycling at 30°C on one cell from the deliverable cell lot is given below (Figure III - 24). The impedance growth is presently 3-4% impedance growth at 800 cycles and stabilizing.

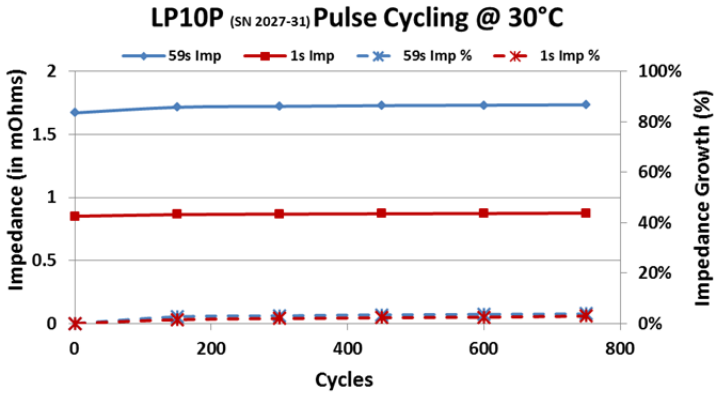

Figure III - 24: Impedance growth results

Conclusions and Future Directions

Saft is currently seven months into the one year development program. Saft internal testing of 1st deliverable cells has shown that the cells could meet or exceed most USABC Start-Stop performance targets.

The areas of concern for the LTO-NMC cell development continue to be cold crank power at lower states of charge, high temperature impedance growth, and the current high cost of the LTO material. During the remaining months of this program, Saft will continue to evaluate and test ways to reduce or eliminate these concerns. A Design of Experiment is underway to identify the key contributors to high temperature impedance growth and the electrolyte studies currently being conducted at Wildcat Discovery Technologies will lead to an optimized low temperature electrolyte for use in the final deliverable cells.

Saft is interested in continuing its development of the LTO/NMC cell for wide scale use in 12V start-stop automotive applications.

FY 2013 Publications/Presentations

None.

III.A.8 Development of an Advanced, Lithium Ion, 12V Start-Stop Battery (Leyden Energy, Inc)

Chulheung Bae USABC Program Manager
Subcontractor: Leyden Energy, Inc.

Marc Juzkow, Program Manager
46840 Lakeview Boulevard
Fremont, CA 94538
Phone: (510) 938-3815; Fax: (510) 445-1032
E-mail: mjuzkow@leydenenergy.com
mailto:cashtiani@ENERDEL.com
Start Date: February 2013
Projected End Date: March 2014

Objectives

The program objective is to design, develop, and assemble 12V Start-Stop cell and battery "A" sample prototypes that meet and exceed the USABC targets using the LTO-LMO system and Leyden Li-imide™ electrolyte.

Technical Barriers

The main challenge of developing a 12V Li-ion Start-Stop battery is to combine superior low temperature performance enabling cold-cranking and long elevated temperature cycle life in a competitively priced system. Leyden is basing its development on commercially available LTO and LMO materials, which are surface-treated in-house and then assembled and tested in pouch cell prototypes. Electrolyte development under this program requires formulation of the solvent system and additive package. Dow Kokam, our cell manufacturing partner, will assemble the electrodes coated at Leyden into 20Ah cells at no cost to USABC. Flextronics, our pack manufacturing partner, will develop and assemble 12V battery "A" prototypes with balancing circuitry.

Technical Targets

- Develop an LTO-LMO cell that meets USABC 12V Start-Stop performance targets. Most important targets are -30°C cold-cranking and 30°C 450k cycle life.
- Scale up the coating capability at Leyden and produce anodes and cathodes for the deliverables. Design and assemble 20Ah cells at Dow Kokam facility for USABC deliverables.
- Develop pack design and balancing circuitry for 12V "A" prototype pack at Flextronics.
- Deliver up to 50 20Ah cells and three 12V packs to USABC at the end of the program

Accomplishments

- Met USABC -30°C cold-cracking targets at 100% and 50% SOC in 2.2Ah prototypes and 20Ah cells.
- Projecting >450k USABC shallow cycles at 30°C with the latest 2.2Ah prototype cells.
- Developed and evaluated 15+ surface treatments to improve high temperature calendar and cycle life of LTO-LMO cells.
- Delivered requested total of 28 prototypes cells for evaluation to ANL and NREL.
- Designed and built first 20Ah cells at Dow Kokam
- Designed a balancing circuitry and assembled first 40Ah 12V prototype packs at Flextronics.

✧ ✧ ✧ ✧ ✧

Introduction

Leyden Energy is developing an affordable, advanced lithium-ion 12 V Start-Stop battery to meet performance, life and cost targets of the USABC's RFP for "Development Of Advanced High-Performance Batteries For 12V Start-Stop Vehicle Applications". Leyden is engaging with a high volume cell manufacturer (Dow Kokam) and a capable pack manufacturer (Flextronics) to leverage their respective expertise and resources to address technical challenges and advance low cost, domestic manufacturing. The key elements of our program include:

- Use of an LTO/LMO couple with Leyden's Li-imide^{tm} electrolyte to enable a system that meets target capacity, cold cranking power, cycle life, calendar life and price targets.
- Advancement of Leyden's technical foundation and leveraging of Dow Kokam's investment in large volume, domestic lithium-ion manufacturing.
- Utilization of an innovative cell and battery design to result in a lower weight and lower volume system, approximately 7.2 kg and 6 liters.

- A rapid program timeline with development running 14 months until 3/31/14, including "A" sample prototype delivery in 14 months to designated National Labs enabling production "C" samples in 30 months.

Approach

Two major technical challenges of the program are the cold-cranking power at -30°C and high temperature cycle and calendar life.

For the cold-cranking power, Leyden Energy's approach is to optimize electrode thicknesses and press densities and formulate a low temperature electrolyte solvent base that allows for superior low temperature operation. The LTO system is unique compared to graphite anode batteries as it does not require high melting point ethylene carbonate (EC) as a solvent. EC is the biggest impediment to good low temperature performance. Electrolyte solvent base development approach is focused on a combination of propylene carbonate and butyrolactone with linear carbonates, low melting point esters and nitriles.

Long cycle life and calendar life targets are addressed by employing Li-imide™ electrolyte with the additive packages designed to improve cycle life of LTO-LMO cells and, most importantly, surface treatments of LTO material. The reduction of electrolyte on the catalytically active surface of LTO is understood to be the main reason of high temperature power fade and gassing.

Cell design, pack design, manufacturability and cost targets are addressed by close cooperation with our manufacturing partners. Leyden is leveraging Dow Kokam's expertise in automated high volume cell manufacturing and Flextronics knowledge and experience in circuitry and pack development and manufacturing.

Results

Cold cranking and power capability. Leyden Energy has made significant progress since the beginning of this program in improving low temperature performance of the LTO-LMO cells as shown on Figure III - 25. We are meeting stringent USABC cold-cranking requirements in 2.2Ah cell prototypes at 100% and 50% SOC and are close to the target and maximum DOD as presented on Figure III - 26.

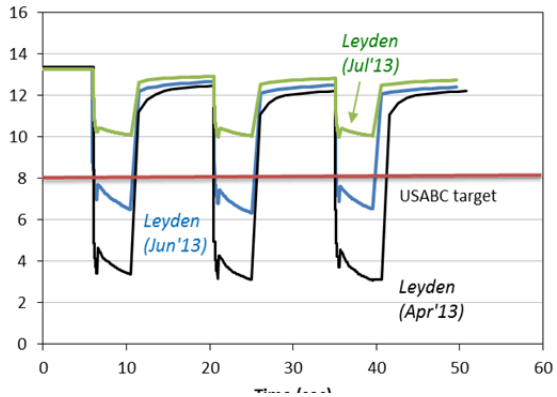

Figure III - 25: Improvements in 100% SOC -30°C cold-cranking performance over the course of the program; recalculated to pack level

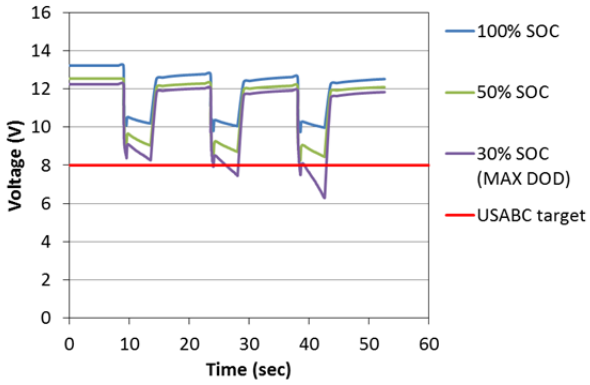

Figure III - 26: Cold-cranking performance of 2.2Ah LTO-LMO prototype cells at various SOC; recalculated to pack level

Improvements in cold-cranking performance were accompanied by an overall increase in rate capability that resulted in the ability of the cells to handle continuous 40C discharge (Figure III - 27) and superior power for auto-start function, *i.e.*, ability of the system to deliver 1 sec 6kW pulses over a wide range of temperatures and SOC (Figure III - 28).

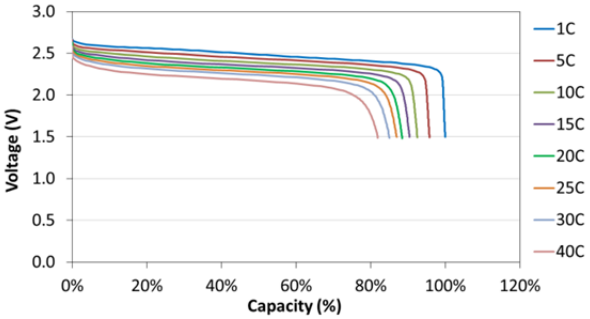

Figure III - 27: Rate performance of 2.2Ah prototype cells

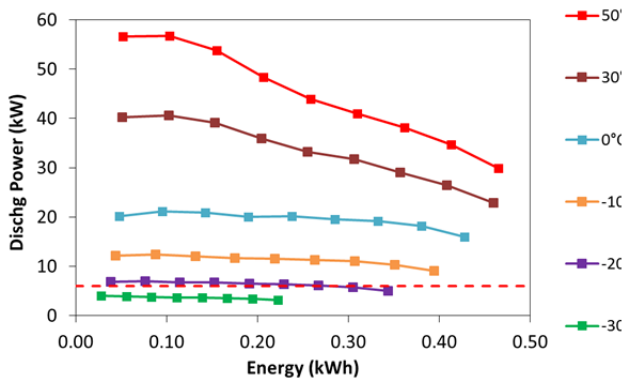

Figure III - 28: Thermal performance test on 2.2Ah prototype cells

Superior charge acceptance, even at low temperatures, is distinguishing feature of the LTO chemistry. It remains high and significantly above 2.2kW target to enable regenerative braking across a wide range of SOC as USABC L-HPPC pulse data demonstrates in Figure III - 29.

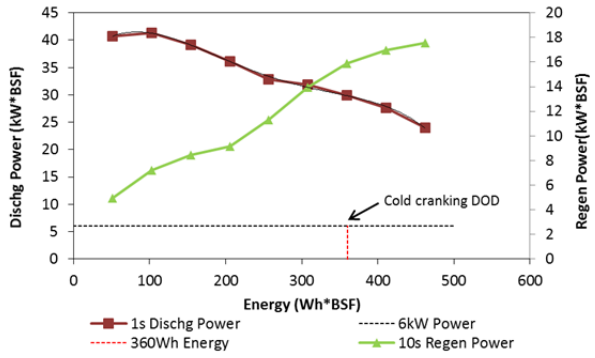

Figure III - 29: USABC L-HPPC test on 2.2Ah prototype cells

Cycle life. Cycle life at 30°C and higher temperatures remains the focus of Leyden development. Over the past few months, Leyden has finalized the choice of LMO and LTO materials in terms of high temperature cycle life; developed and optimized electrode formulations, completed process development for prototype cell assembly and initiated work on formation thermal treatments that improve high temperature performance. This allowed us to meet the USABC cycle life requirements: as shown on Figure III - 30; we project to reach >450k shallow cycles at 30°C.

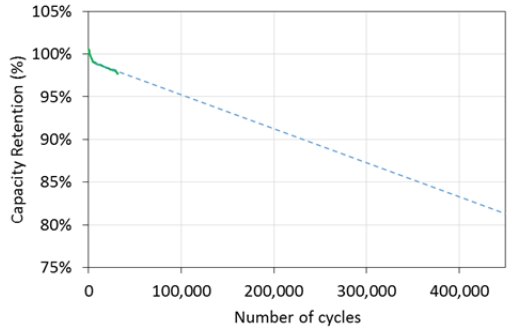

Figure III - 30: USABC shallow cycling at 30°C on 2.2Ah cells

Leyden has also demonstrated stable shallow cycling at 50°C (shown in Figure III - 31) for the cells delivered to ANL and NREL.

Further improvements in cycle life at high temperature are expected to emerge from our development work on an electrolyte additive package and surface treatments. To date, Leyden has evaluated >15 surface treatment techniques. The test results comparison of the most promising surface treatments are shown on Figure III - 32.

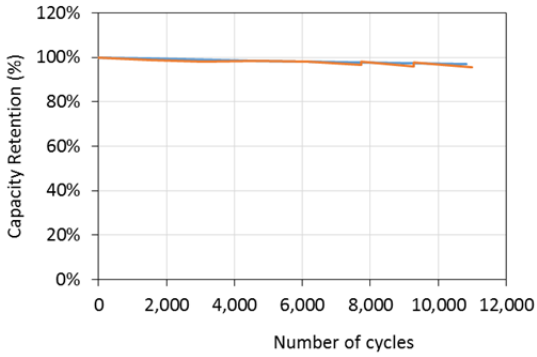

Figure III - 31: USABC shallow cycling at 50°C on 2.2Ah cells

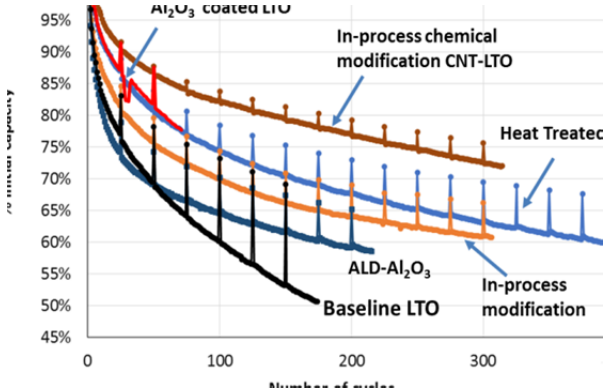

Figure III - 32: Comparison of most promising surface treatments in 0.8Ah prototype cells in 60°C unconstrained cycling; 1C/1C 1.5-2.7V

Cell development. Over the course of this program Leyden transitioned from 0.8Ah prototypes to 2.2Ah prototypes. The new cell design incorporates thicker (300µm) and wider (20mm) aluminum tabs resulting in low 1.5mΩ impedance and the ability to support up to continuous 50C discharges and 100C pulses. Process development included qualification of a new automated stacker, new top and side sealer as well as improved ultrasonic welder horn design.

During the month of October, we assembled the first 20Ah cell prototypes (see Figure III - 33). Electrodes were coated at Leyden and shipped to Dow Kokam where they were punched, dried, stacked and packaged. Ready-to-fill cells were shipped to Leyden for filling and formation.

Figure III - 33: 2.2Ah and 20Ah cell prototype

We confirmed capability of the cells to support cold-cranking requirements and initiated limited cycle life testing. After aging and binning, a number of cells were shipped to Flextronics to assemble the first 12V 40Ah packs.

Pack and electronics. Balancing circuitry (see Figure III - 34) for the prototype packs was developed independently by both Leyden and Flextronics. The circuitry decreases the charging current to a cell if its voltage exceeds a set threshold. The parasitic currents of the circuitry were confirmed to be in double digits of microamps.

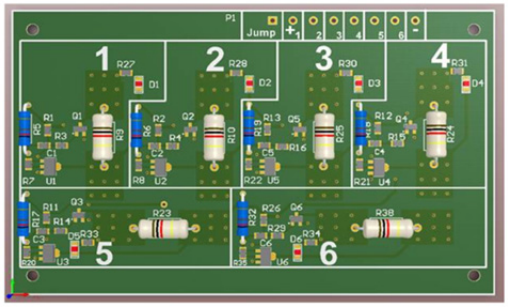

Figure III - 34: Leyden pack balancing circuitry

Pack concept drawings were completed and prototypes were assembled during the month of November.

The pack consists of 2p cell modules with thermal barrier/expansion pads between the cells constrained by aluminum plates with a molded retention frame positioned around the cell. Modules are connected to each other with two sets of aluminum bus bars; cell tabs protrude through the bottom bus bars and are clamped with a top bus bar. The module and pack drawing are shown in Figure III - 35 and Figure III - 36 below.

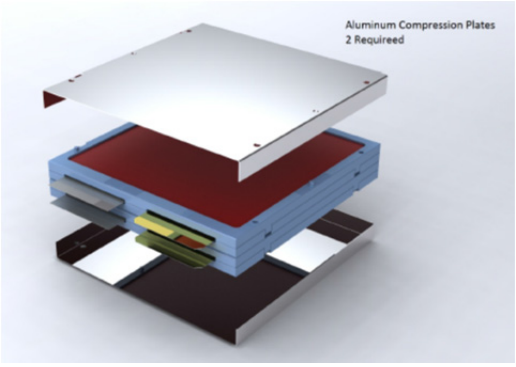

Figure III - 35: Cell module assembly drawing

Figure III - 36: 12V 40Ah LTO-LMO pack drawing

Cost targets. Leyden Energy has prepared a cost model for the cells and packs based on the template provided by USABC. Based on the data stemming from Leyden's manufacturing experience in Asia, Dow Kokam's expertise in domestic manufacturing and Flextronics pack assembly experience, we have formulated three cost scenarios and presented our findings to USABC. We remain optimistic in achieving the cost targets making LTO-LMO system a competitive solution for 12V Start-Stop systems.

Conclusions and Future Directions

Leyden Energy is proud to present significant progress towards meeting the goals of USABC for a 12V Start-Stop battery. Over the duration of this program, Leyden Energy has significantly improved the power and cold-cranking of the LTO-LMO system and demonstrated the ability to meet USABC long cycle life and calendar life requirements. Samples to validate these results were delivered to ANL and NREL per the contract schedule.

Leyden Energy would like to continue its development of the LMO-LTO cells and packs to further improve the performance of this system. Specifically, over the next several months, Leyden will focus on surface coatings and electrolyte development to improve the high temperature cycle life and survival test results. We will continue the internal testing of the prototype cells from the first deliverables build.

Leyden is committed to proceed with the second, optimized 20Ah cell build at Dow Kokam to fulfill cell and pack deliverables to USABC at the end of the program.

FY 2013 Publications/Presentations

1. Florida Battery Seminar, March 2013, Ft. Lauderdale, FL: Start-Stop Lithium-ion Battery Enabled by Li Imide™ Electrolyte System
2. The Battery Show, September 2013, Novi, MI: Battery Trends for Micro-Hybrid Applications (Expanding Start / Stop and Increasing Electrification)

III.A.9 Multifunctional, Inorganic-Filled Separator Development for Large Format Li-ion Batteries (ENTEK)

Ion Halalay, USABC Program Manager
Subcontractor: ENTEK Membranes LLC

Richard W. Pekala, Project Manager
ENTEK Membranes LLC
250 N. Hansard Avenue
Lebanon, OR 97355
Phone: (541) 259-3901, Fax: (541) 259-8016
E-mail: rpekala@entek-membranes.com

Start Date: August 22, 2011
Projected End Date: December 31, 2013

Objectives

- Deliver a quantity of 18650 cells with silica filled separator and control cells with unfilled polyolefin separators to USABC.
- Continue data collection and analysis for cells still one test.

Technical Barriers

The project addresses conflicting separator requirements, technical barriers and material cost issues.

(A) Thermal stability and minimum puncture requirements trend in opposite directions with filler contents: high thermal stability requires high inorganic phase contents (> 50 wt %), while high puncture strength requires high polymeric phase contents.

(B) Production of defect free precursor films for biaxial stretching with good thickness uniformity in machine and cross machine direction as well as low polymer crystallinity.

Technical Targets

- Thickness: less than 25 µm
- Permeability: MacMullin Number less than 11
- Wettability: Rapid wet out in electrolytes
- Pore Size: less than 1 µm
- Puncture Strength: greater than 300 gf / 25.4 µm
- Thermal Stability at 200°C: less than 5% shrinkage
- Tensile Strength: Less than 2% offset at 1000 psi
- No adverse effects on cell performance due to presence of fillers in the separator

Accomplishments

- All technical targets have been met except puncture, 285 gf @ 25.4 µm versus target of 300 gf @ 25.4 µm.
- Cell test results for 18650 cells with silica-filled separator are reproducible and when compared to controls built with unfilled polyolefin separator:
  - Cycle life is 80% longer.
  - Self-discharge is lower.
  - Low temperature performance is better.

✧ ✧ ✧ ✧ ✧

Introduction

For small commercial lithium-ion cells under abuse conditions, such as external short circuit or overcharging, the separator is required to shutdown at temperatures well below where thermal runaway can occur. Shutdown results from collapse of the pores in the separator due to softening or melting of the polymer, thus slowing down or stopping ion flow between the electrodes. Nearly all Li-ion battery separators contain polyethylene as part of a single or multi-layer construction so that shutdown begins at ~130°C, the melting point of polyethylene. After shutting down, residual stress and reduced mechanical properties above the polymer melting point can lead to shrinkage, tearing, or pinhole formation in the separator.

For larger cells such as those used in hybrid, plug-in hybrid and electric vehicles (HEV, PHEV, EV), shutdown may or may not be required depending on the specific application and system design. In HEV applications, failure modes in which separator shutdown might play a role are handled at a system level. For this reason high temperature melt integrity may be more important than shutdown.

In Phase II of this project, ENTEK produced silica-filled, UHMWPE gel process separators with low impedance and excellent high temperature, mechanical and dimensional stability at pilot and production scale. Extrusion, biaxial orientation, extraction and annealing have been performed step wise to date. The goal of Phase III of this project is to optimize processing and separator performance and to supply samples to battery

makers who will test silica filled separators in large format batteries in order to determine the commercial viability of this technology.

Approach

ENTEK will:

- Deliver a quantity of 18650 cells with silica filled separator and control cells with unfilled polyolefin separator to USABC for testing by DOE labs.
- Extrude and biaxially orient additional films filled with the preferred spray dried and jet milled silica to improve dispersion. An ample quantity of separator will be prepared to serve as inventory for samples needs.

Results

Deliverables. In October 2013, a set of 18650 cells were shipped to INL and Sandia for abuse testing, as shown in Table III - 9.

Table III - 9: A summary of 18650 cells shipped for abuse testing

	Control cells	SFS cells
INL	23	20
Sandia	12	10
Total	35	30

Cell Testing. 60°C Calendar Life Test. Figure III - 37 shows OCV vs. days on storage for 18650 cells made with densified silica filled separator. The control cells are off test after 28 weeks at 60°C. Three cells with densified SFS are still on test at 60°C after 69 weeks.

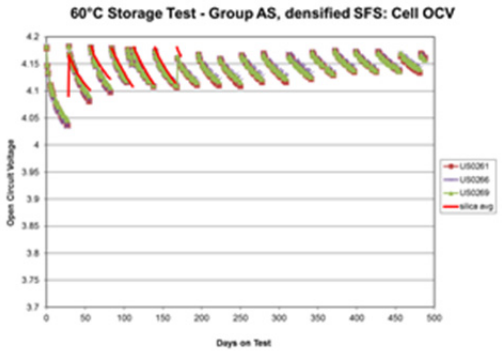

Figure III - 37: 18650 cells with silica-filled separators

Figure III - 38 below compares standard capacity (30°C) fade for 18650 cells made with silica filled separator and a tri-layer polyolefin separator both stored at 60°C.

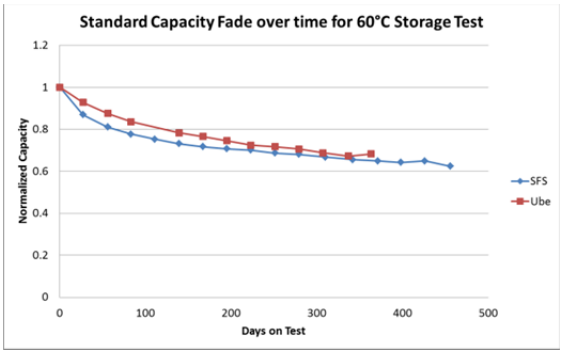

Figure III - 38: Standard capacity fade 60°C storage test

Conclusions and Future Directions

Based on a limited amount of testing, abuse tolerance of cells made with silica filled separators is as good as cells made with an unfilled polyolefin separator; while cycle life, self-discharge and low temperature performance of silica filled cells is significantly better than unfilled controls

The improvement in cell performance for cells with silica- filled separators was unexpected and has potential advantages for new cell designs and applications.

III.B Advanced Lithium Battery Cell Technology

III.B.1 Silicon-Nanowire Based Lithium Ion Batteries for Vehicles with Higher Energy Density (Amprius)

Bruce Mixer, NETL Program Manager
Grant Recipient: Amprius

Ionel Stefan, PhD, Principal Investigator
225 Humboldt Court
Sunnyvale, CA 94089
Phone: (800) 425-8803
E-mail: ionel@amprius.com

Subcontractors:
Nissan, BASF, Yardney Technical Products

Start Date: October 2011
Projected End Date: January 2015

Objectives

- Extend the cycle life and increase the capacity of Amprius' silicon nanowire anodes.
- Identify electrolyte formulations that improve the performance of Amprius' silicon nanowire.
- Design, build and test large format cells integrating Amprius' silicon nanowire anodes with BASF's NCM cathodes.
- Deliver large format cells that meet DOE goals for energy density, power density, cycle life and calendar life.

Technical Barriers

- Development of silicon anodes capable of the long cycle life required for electric vehicles (EVs).
- Development of silicon anodes capable of the high loading as necessary for high energy density.
- Matching of silicon anodes with NCM cathodes capable of long cycle life and high energy density.
- Optimization of electrolyte formulations for long cycle life, high energy, and high conductivity over a wide temperature range.
- Production of silicon anodes and full cells in large vehicle form factors.

Technical Targets

Amprius will match its next generation silicon nanowire anode with BASF's high-energy NCM cathode to demonstrate large format cells capable with:

- Energy density of at least 500 Wh/l.
- Power density of at least 500 W/l.
- Cycle life of 300-1,000 cycles at 80% depth of discharge.
- Calendar life of at least 5-10 years.
- A durable design for affordable mass production.

Accomplishments

- Set anode, electrolyte and cathode performance targets.
- Confirmed the compatibility of Amprius' silicon nanowire anodes with NCM cathodes.
- Improved anode design to enable longer silicon cycle life.
- Increased the cycle life of full cells matching silicon nanowire anodes with NCA and NCM cathodes.
- Identified additives that extend silicon cycle life.
- Improved the stability of the solid electrolyte interphase (SEI) that forms on the surface of the silicon electrode.
- Purchased and installed equipment to increase silicon nanowire anode production capabilities and enable the production of silicon nanowire anodes in larger form factors.
- Qualified the NCM cathode to be integrated into the baseline cells.
- Designed, built and delivered 18 baseline cells matching graphite anodes with NCM cathodes.

✧ ✧ ✧ ✧ ✧

Introduction

Today's lithium-ion batteries have very limited room to improve energy density or specific energy. Their active materials are used at energy capacities close to their theoretical limits and their packaging has been

largely optimized. New active materials are needed to boost performance and extend EV driving range.

Amprius has proven silicon's potential as a new anode material. Silicon offers nearly 10 times the theoretical energy of graphite, the traditional anode for lithium-ion batteries. However, when charged with lithium ions, silicon swells to up to four times its volume, causing capacity fade and mechanical failure. Because of swelling, conventional approaches to silicon anodes have not produced cells with the cycle life required for EV applications.

Amprius' anode replaces graphite with silicon nanowires. Amprius' unique nanowire structure addresses swelling by enabling silicon to expand and contract internally (see Figure III - 39). Amprius does not rely on particle-to-particle contact and is able to maintain high electrical conductivity.

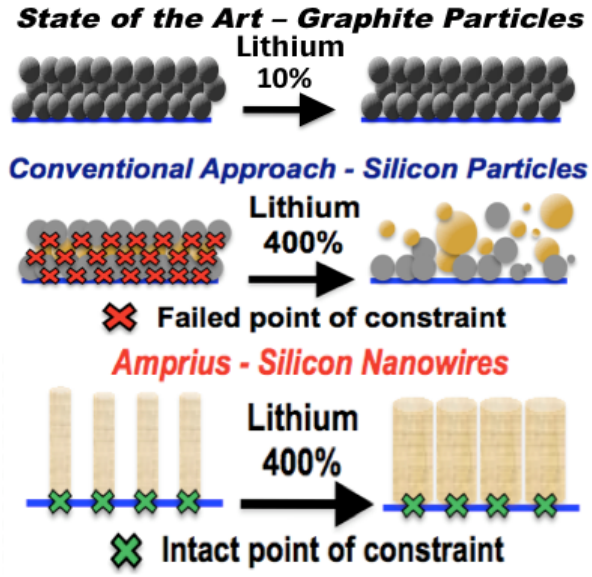

Figure III - 39: Silicon swelling causes capacity fade and mechanical failure. Amprius' nanowires address swelling by allowing silicon to swell successfully

Approach

Amprius is coordinating the three-year project and leading the anode development effort. BASF is supplying cathode materials and supporting development and integration. Yardney Technical Products is contributing to cell design and integration, including cathode development with BASF, cell physical design, separator selection, and ensuring the compatibility of cell additives. Nissan North America is providing guidance regarding customer requirements.

During Phase I, Amprius conducted experiments to increase the cycle life of its first generation anode material. Amprius' work included both material and electrochemical efforts. Yardney procured and qualified baseline cathodes. To minimize manufacturing risk later in the project, baseline cells matching graphite anodes with BASF's NCM 1:1:1 cathodes were designed, built and delivered.

During Phase II, Amprius will increase the capacity of its silicon nanowire anode material through internal structure modification. Amprius will also pair its silicon anode with BASF's NCM 5:2:3 and high-energy NCM cathodes. Before pairing, Yardney will quantify BASF's cathode against commercial competition, then optimize cathode composition. Amprius will then deliver interim cells matching Amprius' silicon anodes with NCM 1:1:1 cathodes.

During Phase III, Amprius will focus on optimizing cells matching Amprius' silicon nanowire anode and BASF's high-energy NCM cathode. Amprius will also confirm secondary performance criteria including safety. Yardney will help integrate Amprius' anode and BASF's cathode into large 20 Ah cells and conduct safety testing. Amprius will then deliver final cells matching Amprius' silicon anodes with high-energy NCM cathodes.

Results

Anode Development. Amprius improved the performance of its next generation silicon nanowire anode. Amprius adjusted the porosity, crystallinity, length, height and diameter of its nanowires, reviewing SEM images of electrodes built from different recipes and studying the volume expansion at different lithiation stages. By tuning these process parameters, Amprius increased the cycle life of its silicon anode in full silicon/NCA and silicon/NCM cells. Figure III - 40 details the cycle life of laboratory cells matching silicon anodes with NCA cathodes.

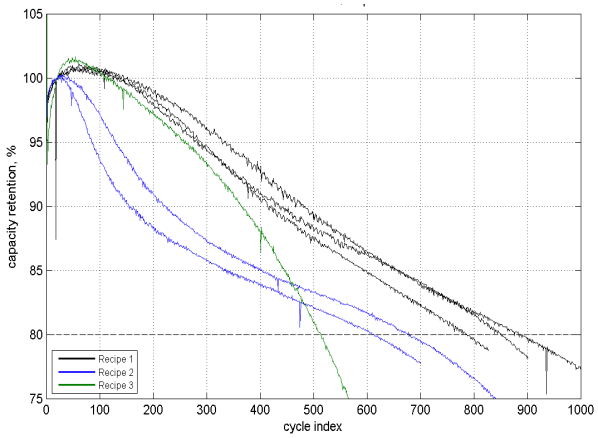

Figure III - 40: Amprius improved the cycle life of laboratory cells matching silicon anodes and NCA cathodes

Electrolyte Development. By studying the specific conditions on silicon's surface that result in the formation of the SEI, Amprius was able to develop a better understanding of SEI formation and manage the configuration of silicon and the composition of the electrolyte to enable a more stable SEI.

Amprius also tested various electrolyte formulations and identified additives that extend cycle life and enable silicon cells to maintain high conductivity over a wider temperature range. Figure III - 41 reviewed the boost various additives provided to the median cycle life of early-stage laboratory cells built from silicon nanowire anodes.

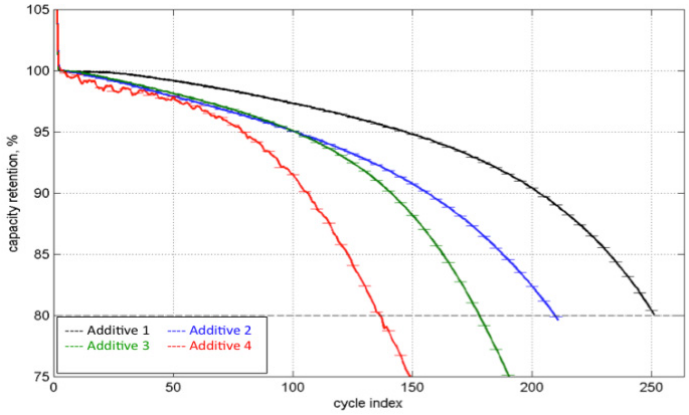

Figure III - 41: Amprius identified additives that extended the cycle life of early-stage, silicon-based lab cells

Cell Design and Baseline Cell Delivery. Eighteen (18) baseline cells were designed, built and delivered to Idaho National Laboratory. These large vehicle form factor cells matched graphite anodes with NCM cathodes. Their production during Phase 1 will minimize manufacturing risk later in the project. Figure III - 42 shows the cells in fixtures during cell acceptance testing.

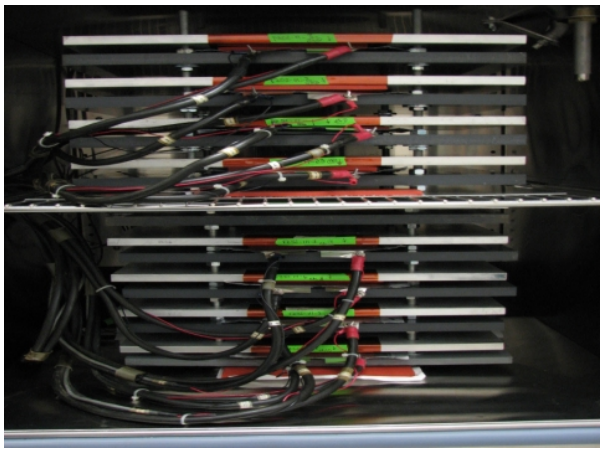

Figure III - 42: Amprius delivered to the DOE 18 baseline cells matching graphite anodes and NCM cathodes

Conclusions and Future Directions

During the project's first phase, Amprius improved the cycle life of its silicon nanowire anode and advanced silicon electrochemistry. Yardney designed and built baseline cells.

During the project's second phase, by further tuning nanowire structure, Amprius will continue to extend the cycle life of its silicon nanowire anode and increase the capacity of its anode. Amprius will also deliver 18 vehicle form factor cells matching Amprius' silicon nanowire anodes with BASF's NCM 1:1:1 cathodes. These interim cells will have a specific energy of at least 250 Wh/kg.

Next year, in preparation for Phase III deliverables, Amprius will also pair its silicon anode with BASF's NCM 5:2:3 and high-energy NCM cathodes. Yardney will also qualify BASF's high-energy cathode.

III.B.2 Development of Large Format Lithium-Ion Cells with Higher Energy Density (Dow Kokam)

Ralph Nine, U.S. DOE NETL Program Administrator
Dow Kokam, LLC, Contractor

Erin O'Driscoll, Ph.D., Principal Investigator
2901 NE Hagan Road
Lee's Summit, MO 64064
Phone (816) 525 1153; Fax (816) 525 5388
E-mail: eodriscoll@dowkokam.com

Subcontractors:
Wildcat Discovery Technologies, Inc.
Oak Ridge National Laboratory

Start Date: October, 2011
Projected End Date: March 2015

Objectives

The objective of this project is to research, develop, and demonstrate Li-ion battery cells that are capable of achieving an energy density of at least 500 Wh/l while maintaining comparable performance standards in terms of cycle life, calendar life, and durable cell construction and design capable of being affordably mass produced.

Technical Barriers

The energy density needed to both effectively and efficiently power electric vehicles (EV) is not available with current lithium ion cell technology. Today's solution falls significantly short of meeting the general consumer's cost and life expectations. In order for the EV industry to be successful, battery cell with twice the energy density must be developed.

Technical Targets

- Develop and optimize new materials and design of lithium ion cells which will double the energy density of commercially available cells from 260 – 340 Wh/L to 500 – 750 Wh/L.
- Implement these improvements to mass production system exceeding 500 W/L, superior overall performance and cost compared to currently available PHEV and EV cells, and safety comparable to today's commercial Li-ion cells.
- Improve EV battery affordability by reducing cell cost to $0.20 – 0.25/Wh.

Major Accomplishments

- Samples of 2 Ah baseline cells with NMC and graphite as the active materials were delivered to Argonne National Laboratory for evaluation.
- Both of the high capacity anode (HCA) materials tested by Dow Kokam have demonstrated >2,500 mAh/g. However, satisfactory performance can be obtained only when the utilization is controlled below 1,250 mAh/g. Dow Kokam is testing full cells with HCA and high voltage cathode (HVC) materials.
- In addition to the cobalt phosphate-based HVC materials, Dow Kokam added NMC-class HVC materials to the list of evaluations. Leveraging the experiences learned from another program, funded by the Department of Defense (DoD), Dow Kokam has demonstrated energy densities of >500 Wh/L with the HVC/graphite chemistry.
- One high capacity cathode (HCC) material has demonstrated >260 mAh/g. However, it has been difficult to produce this material in a cost effective way. Dow Kokam decided to stop the synthesis of this material; however, we will evaluate other established HCC materials from commercial suppliers.

✧ ✧ ✧ ✧ ✧

Introduction

Dow Kokam proposed to develop a large format battery cell design that could double the energy density of current lithium-ion cells.

According to our calculations, this can be done by either increasing the operating voltage of the cell or increasing the capacity of the active materials. Therefore, a parallel approach has been taken. A high voltage phosphate-based cathode material and a lithium-rich based high capacity cathode (HCC) material, both developed by Wildcat Discovery Technologies (WDT), will be evaluated using silicon-based high capacity

materials or conventional graphite as the anode. 2 Ah format sample cells will be used as a common platform during the evaluation of the materials. 40 Ah production size cells will be produced and delivered to demonstrate that the materials can be scaled up to a production scale manufacturing environment.

Approach

The following approach will be taken to achieve the goals:

- Design and fabricate baseline cells in 2 Ah format. The cell design is a direct reduction of the 40 Ah production cell produced by DK.
- Develop a cell performance model to represent the behavior of the cell. This model will be used to predict the performance of cells when the novel materials described above are used.
- Evaluate those novel materials in half-cell format to understand their performance. The data will be used to design full cells with these materials as the electrodes.
- Design and construct a small-volume slot die coating system that can produce electrodes with very little material and have the same quality as production scale electrodes.
- Design and fabricate samples cells, of the 2 Ah format, using HVC and HCC materials as the cathode and HCA or conventional graphite as the anode.
- Design and fabricate a full size, 40 Ah cell that can be produced in DK's cell manufacturing facility.
- Collaborate with WDT to develop the cathode materials and with Oak Ridge National Laboratory (ORNL) to characterize these materials.

Results

Baseline cell. Cells were designed, built, and tested. Test results show that these 2 Ah cells behave very similar to the 40 Ah, large format, cells Dow Kokam manufactures. Eighteen cells have been delivered to Argonne National Laboratory for testing.

High Capacity Anode Material. Two silicon-based anodes were selected. The maximum specific capacities of these materials were both above 2,500 mAh/g. However, if utilized above 1,250 mAh/g the materials showed fast decay. It was found that matching the electrode designs between the HCA and the cathode is extremely important to the performance of the cell. Sample cells made with HVC and HCA were fabricated and tested at Dow Kokam. To date, cells with 570 mAh/L energy densities has been demonstrated, Figure III - 43. Optimization of cell design is in progress.

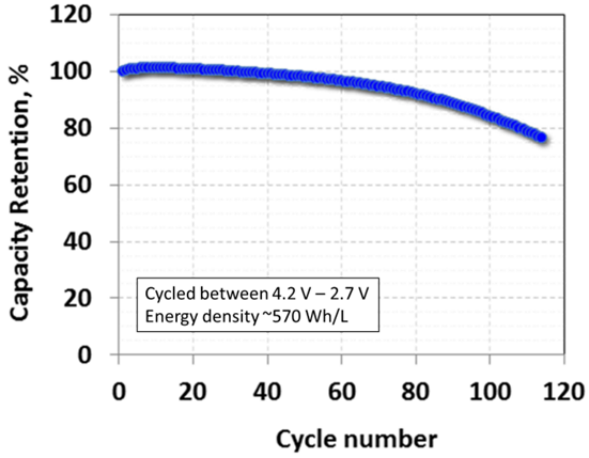

Figure III - 43: Cycle performance of an HVC/Si-based anode cell

High Voltage Cathode Material. In addition to the CM1 material developed by WDT, Dow Kokam has also been testing NMC-class materials operating at higher voltages under a research program funded by the Department of Defense. Applying the knowledge gathered, Dow Kokam has demonstrated 500 Wh/L energy density using HVC with graphite in a 2 Ah cell format. The energy density of these cells using HVC and HCA is expected to be >600 Wh/L. When charged to 4.4 V, the energy density of an HVC/graphite cell at various discharge rates is shown in Figure III - 44.

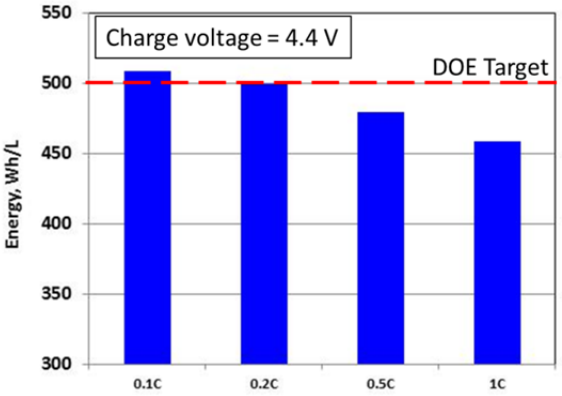

Figure III - 44: Energy density of an HVC/graphite sample cell

The stability of this material as a function of the charge voltage was investigated by differential scanning calorimetry (DSC) at ORNL. It was concluded that the behavior of this NMC material, when charged to 4.4 V is similar to when it is charged to 4.2 V below ~600°C, as shown in Figure III - 45.

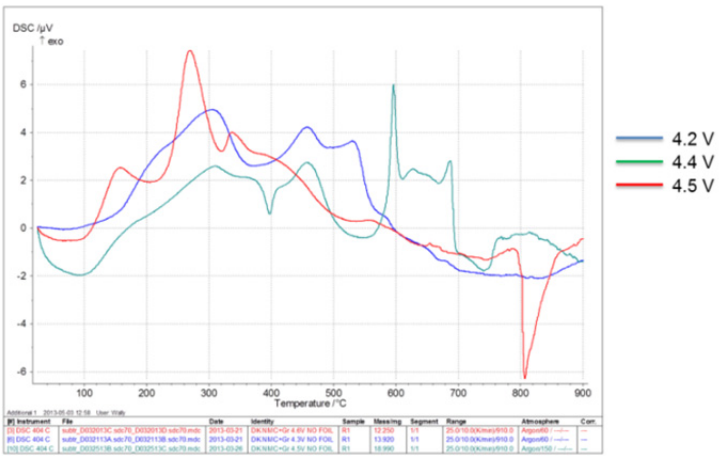

Figure III - 45: Thermal behavior of a high voltage NMC material when charged to various voltages

High Capacity Cathode Material. A lithium-rich oxide material has been selected by WDT as the HCC material. The capacity of the material synthesized using lab-scale equipment has achieved >260 mAh/g of capacity. However, the usable capacity decreased when synthesized using an affordable technique, Table III - 10.

Table III - 10: Characteristics of HCC by various synthesis methods.

	Target	Solution	Solid State	
		Best	Control	Best
Capacity (mAh/g)	260	266	233	275
Usable Capacity (mAh/g)	260	266	153	180
Energy (Wh/kg)	1000	972	825	975
Rate (%, 1h)	80	77	74	81

Given the limited resources available for this effort, Dow Kokam decided to stop the development of affordable synthesis techniques. Instead, we will acquire other HCC materials from commercial suppliers.

Conclusions and Future Directions

- Baseline cell test results show that the design and fabrication are suitable to produce cells with the same performance as commercial, large format, cells manufactured by Dow Kokam. Cells have been delivered to Argonne National Laboratory for testing.
- Dow Kokam evaluated the cell performance of HCA materials and demonstrated >2,500 mAh/g of specific capacity. However, the performance is sensitive to the electrode design and matching between the HCA and the cathode. Dow Kokam will optimize the electrode design to improve cell performance.
- Dow Kokam has satisfied the goal of >500 Wh/L in energy density using HVC and graphite anode. It will continue to improve the energy density of cells using HVC and silicon-based HCA.
- Due to the difficulties to synthesis the HCC affordably within limited resources, Dow Kokam will stop the work at WDT and source HCC material from commercial suppliers.
- DK believes, from the results obtained so far, it is moving in the right direction and will continue with the development of cells with HVC and HCC.

FY 2013 Publications/Presentations

1. 2013 DOE Annual Peer Review Meeting Presentation
2. 2013 Technical Review Meeting

III.B.3 Innovative Cell Materials and Designs for 300 Mile Range EVs (Nanosys)

John Tabacchi, NETL Program Manager
Award Recipient - Nanosys, Inc.

Yimin Zhu, Nanosys, Inc. – PD/PI
2625 Hanover Street
Palo Alto, CA 94304
Phone: 650-331-2232; Fax: 408-240-6900
E-mail: yzhu@nanosysinc.com

Subcontractor:
A123 Systems
200 West Street
Waltham, MA

Start Date: October 2011
Projected End Date: September 2014

Objectives

- We propose to develop a 700~1,000 mAh/g Si anode (SiNANOde™) with a target cycle-life of >800, and an eventual goal of achieving an energy density of 1,600 mAh/g at the end of the program. An ideal target will be a cell with 350 Wh/kg and 800 Wh/L, which is capable of driving 300 miles on a single charge and achieving a cell level cost target of <$150/kWh.

Technical Barriers

In order for EVs to achieve mass adoption and make a significant dent in U.S and global CO_2 production, the key problems of driving range per charge and cost per kWh must be addressed.

Barriers addressed:

- Performance: Low Wh/kg & Wh/l.
- Life: Poor deep discharge cycle life.
- Cost: High $/kWh.

Technical Targets

- Anode Targets: 700-1,000 mAh/g and > 800 cycle; 1,600 mAh/g as needed at end of the project.
- Cathode Targets: 255 mAh/g and >800 cycles; other well-performed cathode and >800 cycles at end of the project.
- Cell Targets: 350 Wh/kg, 800 Wh/L, <$150/kWh at end of the project.

Accomplishments

- We have achieved the full cell cycling performance of >1,000 cycles using baseline SiNANOde and have been continuously improving it.
- We have demonstrated SiNANOde specific capacity as high as 1,678mAh/g with >92% first cycle coulombic efficiency.
- A 700 ~1,000 mAh/g SiNANOde has exhibited a cycle life of >700 cycles.
- We have produced SiNANOde on different graphite substrate using low cost precursors and improved material production uniformity.
- Pouch cells have showed an energy density of 250Wh/kg using 550mAh/g baseline SiNANOde and LCO baseline cathode. The pouch cells have showed acceptable cell thickness increase of < 14% over 300 cycles. SiNANOde cell's self discharge and subsequent recharge is comparable to commercial graphite cells.
- The hysteresis effect is less pronounced for 8%SiNANOde full cell in comparison with 8%Si powder-graphite full cell.
- We have demonstrated the feasibility of using the SiNANOde and the improved cathode materials to make full cell with 300~400Wh/kg.
- We are optimizing SiNANOde electrode and other well-performed cathode to achieve higher electrode loading (3~5mAh/cm^2 one side).
- We have developed a new electrolyte C1.1 that enables higher coulombic efficiency and hence improved cycling performance.

✧ ✧ ✧ ✧ ✧

Introduction

Consumers have been frightened by high gasoline price at the pump reaching $4 or even $5/gallon. In the future, the biggest opportunities will be in fuel efficiency technologies for cars and light trucks. More and more people believe that batteries based on Li-ion technologies are the optimal solution for transportation.

The cell that we proposed with a novel SiNANOde™ and composite cathode will significantly advance the current state-of-the-art in Li-ion technologies.

Approach

Innovative Approach. The objectives outlined above, will be accomplished by combining a high energy cathode technology with, SiNANOde™, a Si graphite composite. Cathode materials currently being used in PHEVs and EVs have a maximum capacity of ~150 mAh/g or less. We will use the well-performed cathode or the composite cathode containing a layered component with high specific capacity. The major technology innovations will be undertaken to accomplish the objectives of this effort are:

1. Improve SiNANOde™ capacity from 650 mAh/g to 700~1,000 mAh/g in Phase I and to 1,600 mAh/g later. Graphite particle size and morphology will be further optimized to achieve this goal.
2. Achieve increased cycle-life from 220 to >800. To achieve this, innovative surface modification of the Si nanowire anode is required for improved stability and SEI formation. The electrolyte and binder chemistry will be optimized.
3. Achieve cell specific energy of 350 Wh/kg and energy density of 800 Wh/L by combining the above high energy anode and cathode materials. The baseline performance of the full cell at the onset of the effort is 210 Wh/kg and 400 Wh/L
4. Achieve cost reduction resulting in <$150/kWh (cell level). This will be achieved by moving from synthetic graphite ($35/kg) to natural graphite which is projected to be $5-$10/kg. Cost reduction will also be supported through increased efficiency in manufacturing processes and scale-up of both anode and cathode.

Results

Cycle Life Enhancement for 700~1000 mAh/g Anode. We have been continuously working on producing pilot-scale manufacturing quantities of SiNANOde. The specific capacity of ~650mAh/g has been achieved and SiNANOde half cells can be cycled more than 1,200 times with a capacity retention of > 85%. Using an LCO cathode, the SiNANOde was integrated in the full cells and exhibited ~350 cycles at ~76% capacity retention (see Figure III - 46), which still showed much higher anode-specific capacity over graphite anode. After 200 cycles SiNANOde full cell showed a capacity fade rate comparable to graphite full cell.

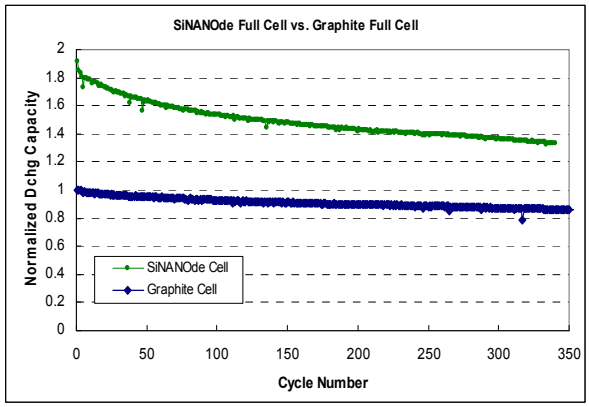

Figure III - 46: Baseline SiNANOde/LCO full cell

It is well known that OCV and SOC have a relationship based on the Nernst equation. As a peculiar problem for HEV battery, there is the voltage hysteresis phenomenon, in which measured OCV after charge (discharge) is higher (lower) than the estimated OCV by Nernst equation. This voltage hysteresis has been modeled by adding simple voltage modification term to the Nernst equation, by using a SOC-dependent voltage source including hysteresis. These method needs history information whether battery has been charged or discharged. And SOC and OCV no longer has a one-to-one relationship. Minimizing the voltage hysteresis is certainly critical. With the full cell SiNANOde/LCO this cell voltage hysteresis has been evaluated. Our SiNANOde cell voltage hysteresis effect is much less pronounced (<0.1V). The hysteresis effect is less pronounced for 8%SiNANOde/LCO full cell in comparison with 8%Si powder-graphite/LCO full cell (see Figure III - 47).

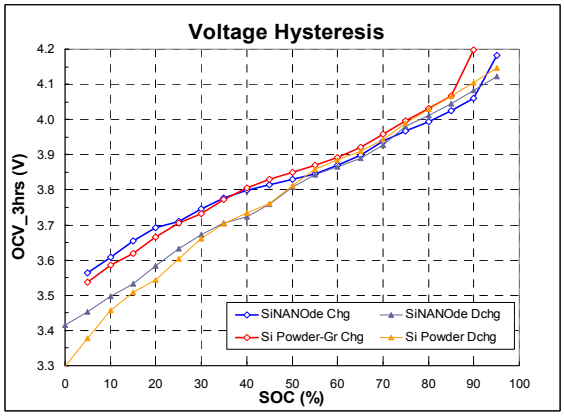

Figure III - 47: Voltage hysteresis of SiNANOde and Si powder-graphite full cells

We have made improvement in the specific capacity of SiNANOde of up to 850mAh/g of reversible capacity. We further improved the conductivity of SiNANOde to optimize the SiNANOde material, which has showed longer cycling life of ~700 cycles at 81%

capacity retention at 0.3C cycling in half cells (see Figure III - 48). It should be noted that at beginning the cell has been used for various C-rate testings.

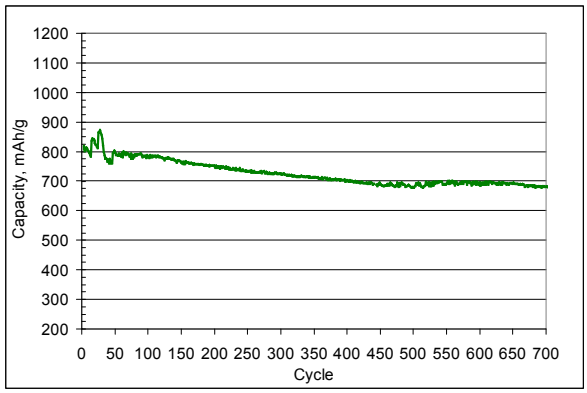

Figure III - 48: SiNANOde half cell with 700~1000mAh/g

Enhanced Si Capacity 1,600 mAh/g Anode. We are improving the high specific capacity of SiNANOde and obtained ca. 1,678mAh/g. The first coulombic efficiency is still more than 92%, shown in Figure III - 49. Various binders have been used to achieve better cycling performance (ongoing). Even though the specific capacity has been increased up to >1,600mAh/g the Si nanowires can also be uniformly distributed on the graphite powders, shown in Figure III - 50. This proves that the SiNANOde production approach allows Si-content to be tuned in a wide range to meet various application requirements.

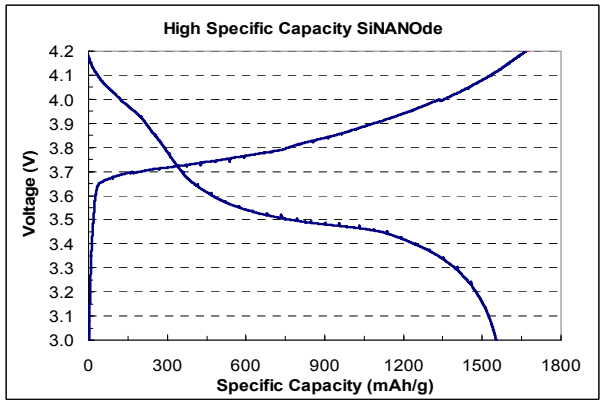

Figure III - 49: >1600mAh/g SiNANOde's voltage profile

Optimization of Cathode Composition. We have tested Mn-rich cathode materials in coin half cells to confirm their electrochemical performance, so that the optimal cathode will be combined with Si anode, SiNANOde.

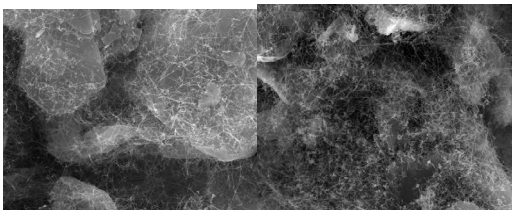

Figure III - 50: Uniform Si nanowire distribution on graphite powders for 700mAh/g (Left) and >1600mAh/g (Right)

To improve the cathode materials, its surface has been modified in various ways to enhance capacity, see Figure III - 51 (Top). The ICE of the cathode electrode can be improved by optimizing its electrode composition in Figure III - 51 (Middle). Those improvements result in enhancement of its C-rate performance (Figure III - 51, Bottom).

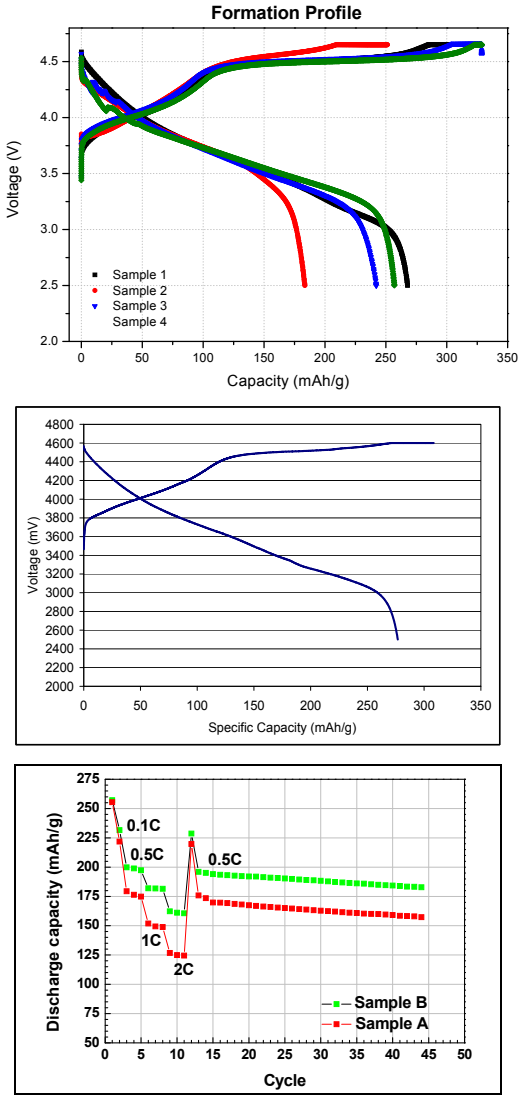

Figure III - 51: Voltage profiles and rate capabilities of cathode candidates

It is critical to identify an appropriate high voltage electrolyte to enhance the cathode cyclability. The electrolyte composition has significant impact on the cycling performance of the cathodes. Cell #2 uses an electrolyte tailored to have high voltage stability, which shows much better cycling performance over the cell#1 that uses the regular electrolyte (Figure III - 52).

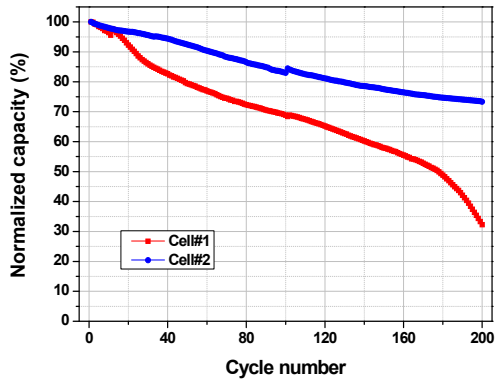

Figure III - 52: Cathode cyclability vs. different electrolyte

Feasibility Test of High Energy Cells with Mn-rich Cathode and SiNANOde. In order to demonstrate very high energy density in the cells using Mn-rich cathode and ~1,300 mAh/g SiNANOde, various cells were designed to achieve 250, 300, 350, and 400 Wh/kg. One key finding from this work is that the rate capability needs to be improved.

The cycle life test of each cell is carried out at 0.3C rate under 80% DOD. In the case of 400 Wh/kg-target cell, its initial capacity distinguishedly decreases, compared with other cells. The 400Wh/kg cell showed ~55% capacity retention at 150th cycle (Figure III - 53).

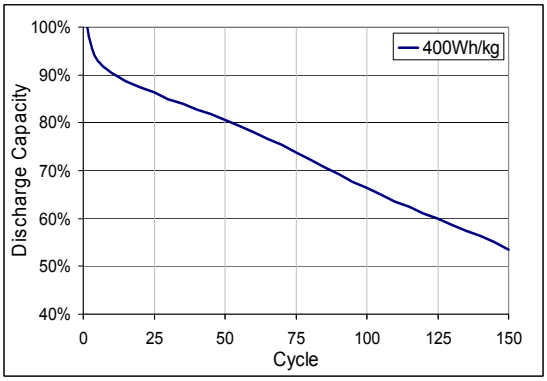

Figure III - 53: Cycle life at 0.3C rate (80% DOD)

The specific capacity of SiNANOde has been increased up to 1,300~1,400mAh/g by controlling Si nanowire content, shown in Figure III - 54. At beginning, the cell formation has been done at 0.05C. The high capacity SiNANOde material shows better cycle life at 0.5C (>88% retention so far). After 100 cycles, the cycle life will be typically more stable (see Figure III - 54). This implies that the high capacity cathode also has negative impact on the cycle life of the high energy full cell (Figure III - 53), which suggests that in order to evaluate SiNANOde cyclability we should select other well-performing cathode (e.g., NCA or LCO or NCM).

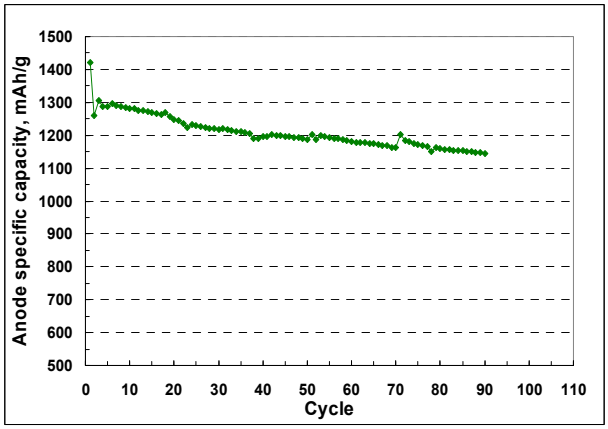

Figure III - 54: ~1300 mAh/g SiNANOde cyclability

Cell Design Study for High Energy Cells with Mn-rich Cathode and SiNANOde. It is found that the electrode loading is a dominant factor in demonstrating the high energy cell with Mn-rich cathode and SiNANOde. The electrodes with the desired high loadings are difficult to be coated on larger coater and result in the substantial increase in resistance. We have tried to prepare the electrode with higher loading through formulation work so that the pouch cells can be made in plant.

In addition, cell design study has been carried out using three different grades of Si anode with specific capacity of 600, 800 and 1200 mAh/g, respectively. Only processable electrodes with high loading are used for the cell design study. The cell operation voltage is up to 4.4 V or 4.5 V (Table III - 11).

Table III - 11: In plant – processable high loading electrode study for high energy cell design

Loading	600 mAh/g	800 mAh/g	1200 mAh/g
Processable (in plant), 4.4 V	225 Wh/kg	240 Wh/kg	255 Wh/kg
Not processable (in plant), 4.4 V (~1300 mg/25 cm^2)	255 Wh/kg	275 Wh/kg	300 Wh/kg

Cycle Life of 1.3 Ah Cell with 500~600 mAh/g Anode. The 1.3 Ah pouch cells are built using the baseline 550 mAh/g SiNANOde and LCO cathode (Figure III - 55). An energy density of 250 Wh/kg can be achieved in the cells. As the electrode has been heavily calendered the capacity retention is about 55% at 200th cycle.

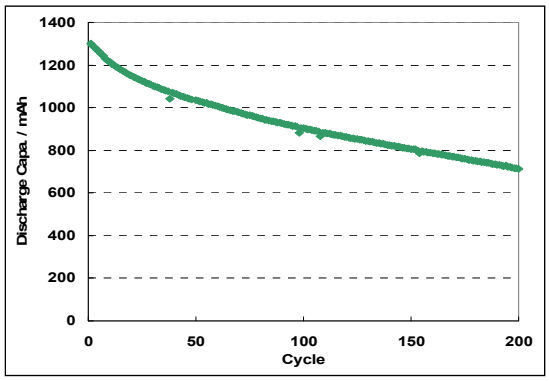

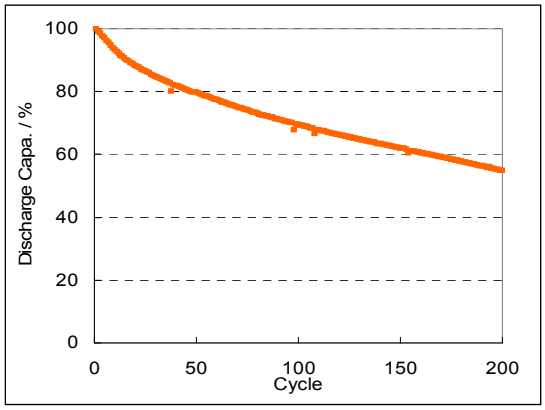

Figure III - 55: Cycle life of 250 Wh/kg pouch cell using 550 mAh/g SiNANOde at 0.5C rate (DOD 100)

The pouch cells have showed acceptable cell thickness change of < 14% cell swelling over 300 cycles (Figure III - 56).

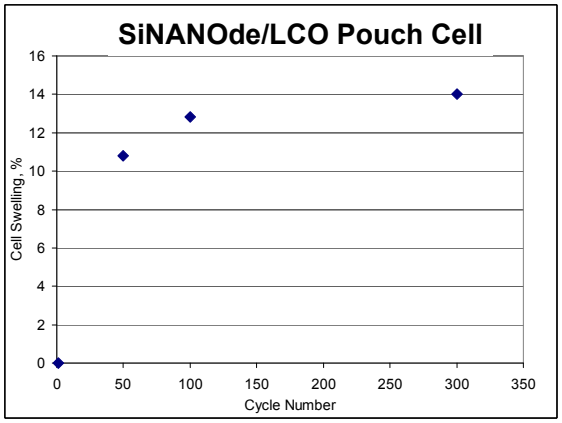

Figure III - 56: Thickness change of High Energy Density Pouch Cells: SiNANOde/LCO

Combining with the well-performed NCA cathode the SiNANOde full cell shows 80% retention after 1,000 cycles at +0.3C/-0.5C cycling. Relatively faster capacity fading was observed in the first 100 cycles (see Figure III - 57). Then the cell approached a more stable zone and last >1,000 cycles at a 80% retention. It demonstrates that the SiNANOde can be very stable over cycles and also can be further improved by forming more stable SEI in the first 100 cycles.

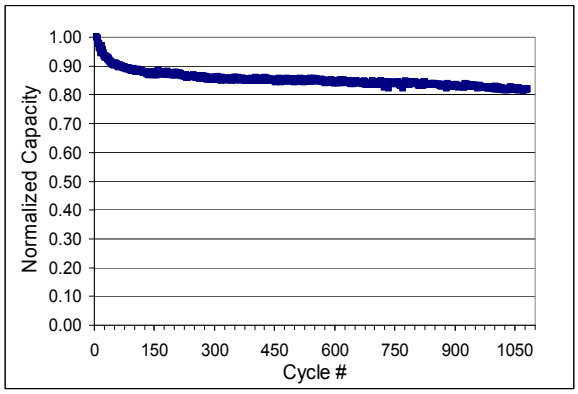

Figure III - 57: SiNANOde full cell cyclability

SiNANOde cells' self-discharge properties have been investigated at 20°C for one month or at 60°C for one week. SiNANOde cell's self discharge and subsequent recharge is comparable to commercial graphite cells (Table III - 12).

Table III - 12: SiNANOde Cell Self discharge

Condition	8% SiNANOde/LCO Normalized to Graphite/LCO Control
Retention % @20°C at end of 1 month	99.6%
Realized capacity upon recharge after discharging at 20°C for 1 month	98.7%
Retention % @60°C at end of 1 week	98.7%
Realized capacity upon recharge after discharging at 60°C for 1 week	99.3%

We have developed a new electrolyte C1.1 that enables higher coulombic efficiency and hence cycling performance compard to a cell with the baseline electrolyte C1 over 250 cycles (Figure III - 58).

SiNANOde development on different graphite substrates has been extensively explored, which results in a wide range of tunable Si nanowire density on the graphite substrate (Figure III - 59). Smaller graphite powders have higher surface area that can host more Si nanowires. It allows us to grow Si nanowires with >50%Si in the SiNANOde composite.

The 500~700mAh/g -SiNANOde pouch cells have already showed >620Wh/L in conventional 4.2 ~3.0V range. The SiNANOde electrode density can be as high as 1.5g/cm^3 (Figure III - 60) without breaking Si nanowires.

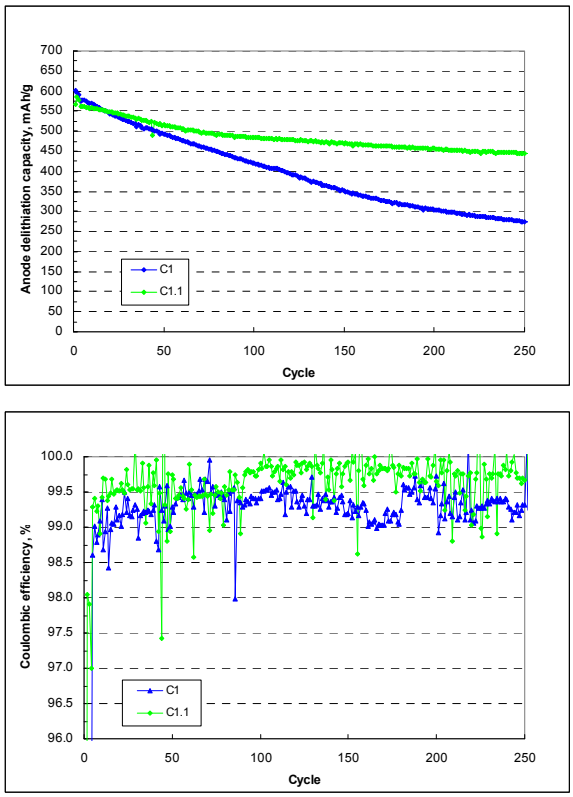

Figure III - 58: New electrolyte enables better cycling performance

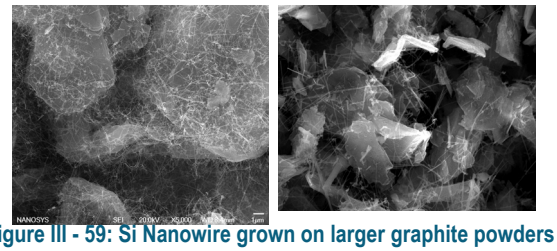

Figure III - 59: Si Nanowire grown on larger graphite powders (Left) and smaller graphite powders (Right) for 700mAh/g

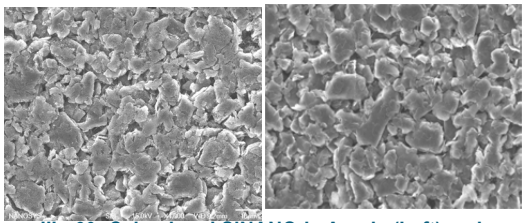

Figure III - 60: Calendered SiNANOde Anode (Left) and Graphite Anode (Right) with 1.5g/cm^3

Conclusions and Future Directions

We have made dramatic progress in Si composite anode (SiNANOde^{TM}), Mn-rich cathode and cell performance improvement. The specific capacity of SiNANOde can be controlled in a range of 500 to 1,800mAh/g by tuning amounts of engineered silicon nanowires, as needed. Initial coloumbic efficiency has been improved to more than 92% for all the SiNANOde products. Almost 100% utilization of Si capacity has been realized in the cells. By optimizing Si nanowire coverage and distribution on the desired graphite surface as well as by optimizing electrolyte and binder chemistry, cycle life has been greatly improved. We have demonstrated a cycle life of more than 700 cycles at a capacity retention of 81% for the SiNANOde with 700~1,000 mAh/g in half cell. We have also demonstrated good cycling performance of >1,000 cycles in the full cells combined with well-performed NCA cathodes.

Further cathode development has achieved a reversible capacity of >255 mAh/g and has improved its C-rate performance from 0.2C to >0.5C even at high loading. Therefore, we are able to make full cells with high specific energies of 300~400Wh/kg using the SiNANOde of 1,200mAh/g and the improved cathode materials of 255mAh/g.

We are determining the optimal Si percentage, electrode density and thickness so that we are able to achieve high energy density in the cells with good C-rate performance and cycling performance.

Pouch cell have attained an energy density of 250Wh/kg using 550mAh/g SiNANOde and LCO cathode. The pouch cells have showed acceptable cell thickness increase of < 14% over 300 cycles. SiNANOde cell's self discharge and subsequent recharge is comparable to commercial graphite cells.

The hysteresis effect is less pronounced for 8%SiNANOde full cell in comparison with 8%Si powder-graphite full cell.

We have developed a new electrolyte C1.1 that enables higher coulombic efficiency and hence cycling performance.

In addition, SiNANOde development on different graphite substrate has been extensively explored, which results in a wide range of tunable Si nanowire density on the graphite substrate.

The above results prove that the proposed technical approach is viable.

FY 2013 Publications/Presentations

1. "Innovative Cell Materials and Design for 300 Mile Range EVs," ES130_Zhu_2013_p, U.S. DOE Vehicle Technologies AMR, 2013

III.B.4 High Energy Novel Cathode/Alloy Automotive Cell (3M)

John Tabacchi, DOE Program Manager
Award Recipient - 3M Company

Jagat D. Singh, Program Manager
3M Center, Building 209-2C-26
St Paul, MN 55144
Phone: (651) 575-1230; Fax: (651) 736-7478
E-mail: jdsingh@mmm.com

Start Date: October 2011
Projected End Date: January 2015

Objectives

- Develop a >2 Ah cylindrical wound or stacked pouch cell with high energy density at low cost for automotive application.
- Integrate advanced chemistries including an advanced high-voltage cathode, high capacity alloy anode and advanced electrolyte materials as well as enabling technologies related to electrode preparation and cell build such as binder, conductive agent, and processing aids.

Technical Barriers

This project addresses the following technical barriers associated with the combination of high energy cathode and advanced alloy anode material:

- Low Cycle Life.
- Low Rate Capability.
- High irreversible capacity leading to low overall cell energy density.
- Large volume expansion of alloy anode.

Technical Targets

- Establish a baseline cell with similar energy density to USABC EV targets with commercial $LiMn_{1/3}Ni_{1/3}Co_{1/3}O_2$ (NMC 111) cathode and graphite anode.
- Provide an advanced cell with at least 40% (1.4 x baseWh/L) increase in energy density compared to the baseline cell.
- Demonstrate as good or superior thermal stability, long-term cycling, and rate capability, of the advanced cell compared to baseline test cell.
- Demonstrate by calculation at least 25% lower cost per unit energy at the cell level for comparative integrated advanced materials cell to a baseline materials cell.

Accomplishments

- Downselected high energy core shell cathode and Si alloy anode materials for 18650 performance optimization.
- Demonstrated material scale up to multi kg levels.
- Optimized pilot process parameters to improve process robustness.
- Demonstrated advanced materials stability large scale dispersion preparation, electrode coating and 18650 assembly with advanced materials.
- Demonstrated >40% energy increase, with intermediate design (C/S||Si) in 18650 cells over baseline (NMC || Graphite).
- Improved cycle life using electrolyte formulations including novel high voltage (>4.5V) additives.
- Sampled 18650 format cells to ANL for testing; 18 cells with baseline materials and 6 cells with intermediate materials.

✧ ✧ ✧ ✧ ✧

Introduction

In order to design a lithium-ion cell with a stepfunction increase in energy, it is necessary to start from scratch with new well designed and matched active materials. First, the cathode needs to have a Cathode Energy Factor (CEF) beyond the traditional LCO and NMC materials. This invariably requires charging to higher cell voltage. Second, the cathode irreversible capacity has to "match" the irreversible capacity of the composite alloy anode. In fact, for cell balance and control of the lower cut of cell voltage, it is convenient if the irreversible capacity of the composite cathode is slightly larger than that of the anode. For the Active alloy it is critical to have the proper morphology (amorphous active phase), the proper particle size (microns), and the proper activity leading to a volume expansion of 110 to 120% upon lithiation. Next, the composite electrode has to be formulated with graphite for highest density and best inter particle contact, while still providing the required volumetric energy when fully lithiated. Finally, the electrolyte and separator must be stable against the two active composite

electrodes, across the complete cell voltage range, to eliminate any parasitic reactions.

Approach

The 3M team has been leveraging its expertise in R&D of lithium-ion batteries to develop a high energy cell using synergistically matched anode and cathode electrodes. To achieve the goal, a three phase approach has been taken. The phases are:

- Phase 1 - Verify baseline materials performance, and select advanced cell material candidates for further evaluation and optimization.
- Phase II - Integrate individual optimized materials into full cells and optimization of EV test cell.
- Phase III – Perform final optimization of integrated advanced materials in EV test cells, complete cell evaluation, fabrication of final cells and submission of final cells to National Labs.

Results

Cathode Material Development. The team has successfully developed a core shell (C/S) based high energy cathode material. Table III - 13 compares the two developed cathode material with baseline NMC material. 126T shows >35% CEF increase over the baseline. The capacity of the core shell cathode along with its flat cycling performance is shown in Figure III - 61.

Table III - 13: Cathode Energy Factor comparison of different cathodes when matched to graphite or a Si composite

	Oxide	Capacity X	Density X	Voltage X	Irrev Factor =	Cathode Energy Factor
Electronics	LCO	0.179	3.75	3.99	0.95	2.54 (graphite)
	LCO	0.179	3.75	3.99	0.88	2.36 (alloy)
	NCA	0.196	3.5	3.78	0.97	2.51 (graphite)
Automotive	NMC	0.160	3.3	3.90	0.98	2.01 (graphite)
	NMC	0.160	3.3	3.90	0.95	1.96 (alloy)
Core-Shell	126M	0.230	3.4	3.84	0.95	2.85 (alloy)
	126T	0.220	3.4	3.88	1.00	2.90 (alloy)

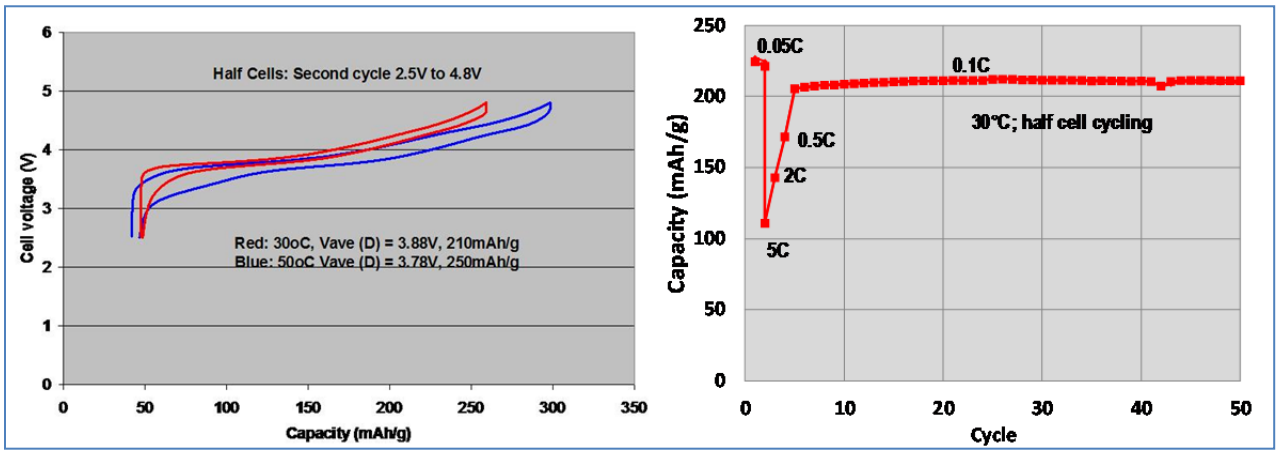

Figure III - 61: Material Validation in coin cells vs. Li

The material shows a stable voltage profile and less average discharge voltage fade during cycle life testing than the oxygen loss cathode materials. Figure III - 62 shows the data.

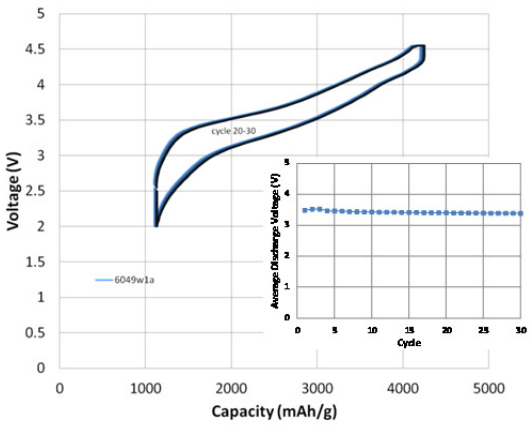

Figure III - 62: Stable voltage curve than pure O_2 loss cathode

Anode Material Development. The team successfully developed a new Si anode composition, studied parameters for process optimization and scaled up material production. L20772 was down selected and is being tested for performance optimization. Key parameters to improve the performance of Si anode composite were also studied. One of key findings was the effect of particle size on the electrode expansion, as shown in Figure III - 63. Small particle (micron level) size and optimum electrode composite formulation are key for lower electrode expansion, at same mAh/cc. Nano Si electrode composite shows significantly high expansion compared to small particle size.

High precision measurements using *in situ* isothemal calorimetry were also performed on Si composite electrodes. Figure III - 64 shows the significance of flake graphite to overcome electrical network failure.

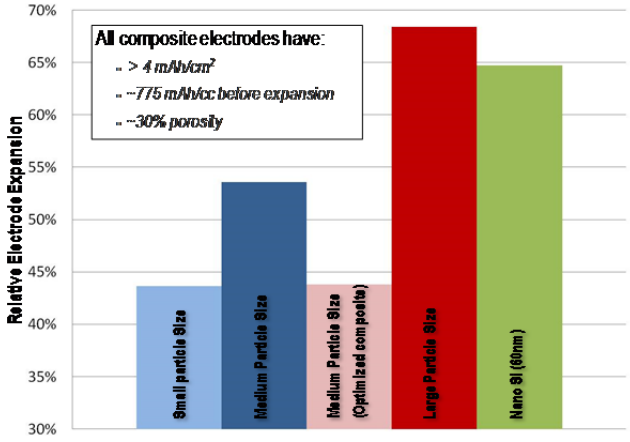

Figure III - 63: Si composite electrode expansion vs. particle size

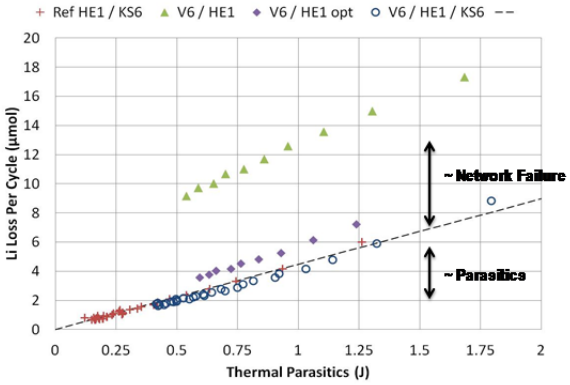

Figure III - 64: Calorimetry to characterize electrical network failure mechanisms

Electrolyte Development. A new electrolyte with significant improvement in cycle life of NMC||Si cell design was discovered (see Figure III - 65).

Cell Development. The advantage of the core shell cathode and Si anode is shown in Figure III - 66. The matched irreversible capacity helps to prevent the anode from going to a high potential during the bottom of full cell discharge.

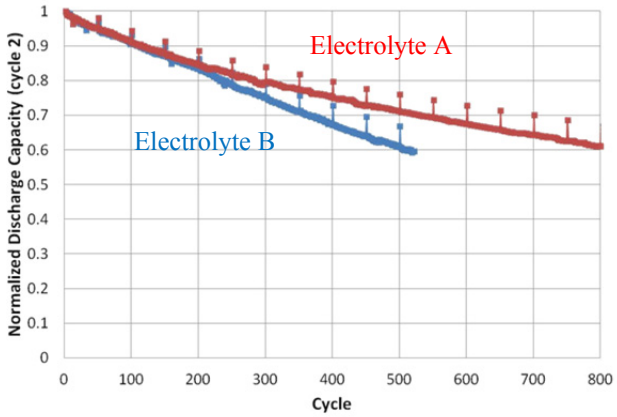

Figure III - 65: 18650 cell data comparing electrolyte A to B

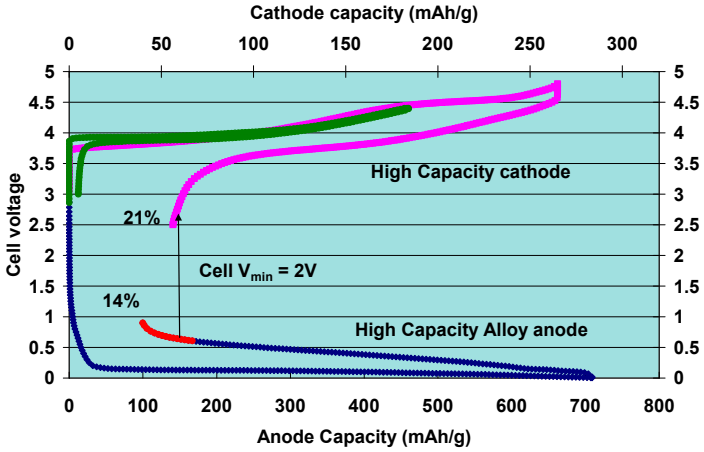

Figure III - 66: Matching 1st cycle efficiencies maximizes benefit of both materials

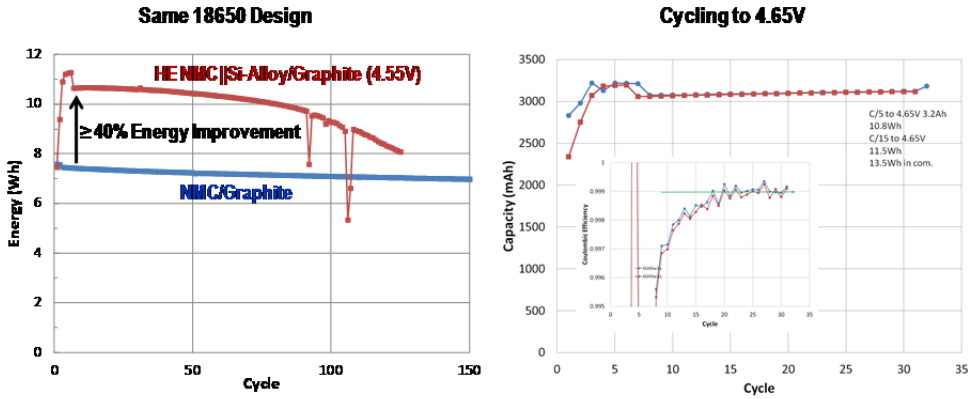

Figure III - 67: Energy increase and cycle life of C/S||Si design

Activities such as large scale dispersion, roll to roll electrode coating and drying were done to validate the energy improvement and characterize cycle life. 18650 format cells (C/S||Si) showed >40% energy increase over the NMC||Graphite cells (Figure III - 67).

However the cells start to fade after 100 cycles. Optimization of cycle life is in progress.

Conclusions and Future Directions

The anode and cathode materials were down selected for future cycle life optimization. The team successfully demonstrated capability to scale up and make multi kg levels of these materials. Multiple roll to roll electrode coating and 18650 format cells were assembled. Over 40% improvement in energy was shown over the baseline design. The baseline data package was completed and 18650 cells with baseline and intermediate materials were shipped to ANL for energy validation.

Going forward, the team will focus on next level of scale up and optimize the performance of C/S||Si design in 18650 cell format.

FY 2013 Publications/Presentations

1. 2013 DOE Annual Peer Review Meeting Presentation
2. 2013 Progress review at 3M

III.B.5 Solid Polymer Batteries for Electric Drive Vehicles (SEEO)

Bruce Mixer, NETL Project Manager
Grant Recipient: Seeo, Inc.

Hany Eitouni
3906 Trust Way
Hayward, CA 94545
Phone: (510) 782-7336; Fax: (510) 782-7337
E-mail: heitouni@seeo.com

Start Date: October 2011
Projected End Date: September 2014

Objectives

- Develop, build, and test high-voltage solid polymer electrolyte cells with an energy density ≥ 500 Wh/l that meet USABC performance, lifetime and safety standards.
- Develop a robust commercialization plan that evaluates key risks associated with high-volume manufacturing and estimates cell production costs.

Technical Barriers

This project addresses the following technical barriers:

- Cycling of Li metal anodes.
- Electrolyte stability at >4V cathode potentials.
- Mechanical performance of high-voltage cathode materials within solid polymer architecture.
- Interfacial performance of layered polymer electrolyte system.

Technical Targets

- Evaluation of high-voltage cathode materials within polymer electrolyte system, including electrochemical stability and mechanical properties.
- Development of polymer materials stable to potentials of high voltage cathode materials.
- Scalable, repeatable synthetic method for polymers
- Robust, prismatic pouch cell design.
- Test and evaluation to USABC performance and abuse tolerance requirements.

Accomplishments

In 2013, the project focused on:

- Development of polymeric materials to achieve target voltage stability, conductivity and mechanical properties, including evaluation of conductive salts for high-voltage stability in solid-state cells.
- Investigation of coating techniques to stabilize high-voltage cathode materials.
- Development and analysis of treated Li foil anodes using commercially-scalable production processes.

✧ ✧ ✧ ✧ ✧

Introduction

Achieving DOE performance targets for high energy cells requires new materials and approaches to electrochemical energy storage devices. Seeo proposes to meet these targets using high-capacity Li anodes and high-voltage cathode materials contained within a solid polymer electrolyte system which, in turn, enhances the lifetime, efficiency and safety of vehicle batteries.

Approach

The project will be executed in three consecutive phases:

Phase I: Baseline Evaluation and Material Synthesis – Deliver 2Ah baseline cells to establish stability and performance of solid polymer electrolyte cells and perform initial synthesis and characterization of high-voltage materials

Phase II: Material Formulation and Scale-Up – Iterate on design of high-voltage materials, cycle laboratory-scale cells to isolate polymer-cathode couples and deliver interim design cells for technical review

Phase III: Cell Fabrication and Testing – Monitor stability and performance of large-area cells, execute internal performance and abuse tests and deliver final design cells for independent verification

Results

High-voltage stable polymer materials and conductive salts demonstrated the requisite

electrochemical stability; improving conductivity and demonstrating long-term stability over cycle testing will be a focus of Phase III.

Treated Li foil samples provided by Seeo's project partner Hydro-Québec demonstrated a similar order of low impedance as that of the best performing commercial supplier tested. Replicating/improving this using thinner foils on the same production process is an ongoing activity; foils will be used as the anode for the project's final deliverable cells.

Conclusions and Future Directions

In Phase I, Seeo's baseline cells established the stability of Seeo's solid polymer electrolyte system with high capacity Li anodes at a performance suitable for electric drive applications. In Phase II, Seeo focused on improving this baseline performance through incorporation of high-energy active materials and compatible solid electrolyte systems comprised of novel polymeric materials and conductive salts. In addition, Seeo investigated alternate techniques to stabilize high-voltage materials within a solid-state cell architecture. In Phase III, Seeo will isolate the most promising approach and deliver high-energy cells for testing to USABC protocol.

It is challenging to achieve high energy densities alongside safety and long-term reliability using conventional, Li-ion cells that utilize liquid electrolytes. Seeo's novel approach incorporates the inherent safety, speed of manufacturing and robust supply chain associated with solid polymer materials, thus offering a distinct opportunity to breakthrough traditional cost barriers associated with electric drive vehicle batteries.

FY 2013 Publications/Presentation

None.

III.B.6 Development of High-Energy Lithium Sulfur Cells (PSU)

Christopher Johnson, DOE Program Manager
Subcontractor: Pennsylvania State University

Donghai Wang, Program Manager
328 Reber Building
University Park, PA 16802
Phone: (814) 863-1287; Fax: (814) 863-4848
E-mail: dwang@psu.edu

Subcontractors:
EC Power, Subcontractor: Johnson Controls,
Argonne National Lab

Start Date: September 30, 2011
Projected End Date: January 15, 2015

Objectives

- Develop a novel nanocomposite sulfur cathode for lithium-sulfur batteries with high energy density, efficiency, and cycle life.
- Develop a novel Li-rich composite anode for Li-S batteries to improve cell cycle life.
- Develop novel electrolyte and electrolyte additives for Li-S batteries to improve cell efficiency, stability, and safety.
- Design, fabricate, test, and optimize the design of Li-S batteries using the above new technologies to maximize energy, power, abuse tolerance, and other favorable traits.
- Perform thermal testing of the developed Li-S cells and materials.

Technical Barriers

- Polysulfide dissolution and shuttling, combined with degradation of the lithium metal anode and formation of an unstable SEI layer, can severely limit cell lifespan.
- High sulfur loading in the cathode is required for achieving a high energy density; however, high loading often leads to parts of the electrode becoming inaccessible to electrolyte, thereby decreasing energy density and cycle life.
- Cathodes must have high active material loading – however, the low density of sulfur and common composite materials (porous carbon, etc) make thin, crack-free, high-loading electrodes difficult to achieve.
- Electrolyte modifications that decrease polysulfide solubility or improve SEI layer stability often come at the cost of increased impedance and other issues.

Technical Targets

- Scale up active material production to the 1 kg level.
- Design pouch cells with energy density > 400 Wh/l, 80% capacity retention after 200 cycles at C/2.
- Nail penetration testing at USABC EUCAR Level 3.

Accomplishments

- Scaled up production of PSU-3 cathode material to the 0.5 kg level.
- Optimized coating techniques for high-loading, double-sided electrodes.
- Characterized and tested several new electrolytes for high-loading sulfur cathodes, along with additives for those electrolytes, enabling lower stable cycling, high capacity, high efficiency, and decreased self-discharge.
- Thoroughly characterized and optimized different Li powder based anodes.
- Optimized and tested design parameters for Li-S pouch cells.
- Fabricated and tested pouch cells with PSU-3 cathodes, Li foil and Li powder based anodes, different electrolytes, demonstrating above-design-capacity performance with LiP anodes, and identified possible failure mechanisms.

✧ ✧ ✧ ✧ ✧

Introduction

DOE goals require the development of a high-energy, high-power, high-efficiency, long-lasting, low-cost, and safe battery. This project aims to meet these goals by using the extremely promising lithium-sulfur battery chemistry. The S cathode has a theoretical capacity of 1,672 mAh/g with a nominal voltage of 2V. In addition, sulfur does not experience any significant size change during lithium insertion/extraction, making it very stable in principle.

The price of lithium-sulfur's great promise is the major challenges with which it is replete. Lithium

polysulfides – intermediate charge/discharge states of the cathode – are highly soluble in traditional electrolytes and can move throughout the battery, experiencing redox reactions and thus causing poor efficiency and loss of active material. Additionally, the lithium metal commonly used as the anode is vulnerable to mossy lithium and dendrite growth and cannot generally form a stable SEI layer, causing further capacity loss and safety concerns. These, combined with optimization and thermal safety considerations, necessitate a significant body of work to bring the Li-S to the commercialization stage.

Approach

To design a superior lithium-sulfur battery, we will focus on several aspects of cathode, anode, electrolyte, and whole-cell study and design. On the cathode side, we aim to increase the sulfur loading, optimize the carbon framework's geometry and ability to adsorb lithium polysulfides, and enhance its practical usability and each-of-production. On the anode side, our work focuses on designing and optimizing lithium powder- and silicon-based composite anodes and determining the mechanisms behind their function. Electrolyte-wise, we are working to design new systems that improve SEI stability, decrease active material loss, increase active material utilization, and ensure battery safety. Additionally, we also seek to optimize battery fabrication parameters, ensure compatibility between all battery elements, and characterize the thermal safety and abuse tolerance of our Li-S system.

Results

Cathode. PSU-3 cathode material production has been scaled up to the 0.5 kg level, thanks to the development of a specially-designed large-capacity reactor system, with 100 g of materials shown in Figure III - 68 for scale. This has created a constant flow of material for use in full cell testing and pouch cell development. Material properties have been standardized and performance is consistent from batch to batch. Scale-up of PSU-4 and PSU-6 high-rate, high-loading cathode materials is still being investigated for the final phase of the project. PSU-3 cathode fabrication has also been optimized so as to allow for making high-loading, double-sided electrodes, thereby increasing cell level energy density by decreasing the mass of the current collector in the cell.

In addition, rate and cycling performance of the PSU-3 and PSU-4 cathode materials have been investigated. PSU-3 cathodes with an active material loading of 5 mg S/cm^2 can maintain a capacity of over 500 mAh/g even at 1C rate, and cycling performance was also tested and found to be excellent within 50 cycles. PSU-4 cathodes showed a stable capacity of over 700 mAh/g at a C/3 rate.

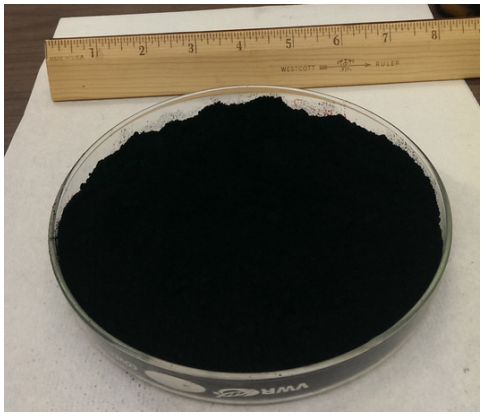

Figure III - 68: 100 g of PSU-3 sulfur cathode material, synthesized via a new large-scale reactor approach

Anode. Lithium powder/graphite (LiG) anodes have been tested in both full and half cells with various electrolytes. It was found that these anodes provided excellent half-cell stability (little capacity loss for 200 cycles at 0.5C rate) and a true capacity of over 1,000 mAh/g of electrode. However, full cell tests showed only modest performance (up to 400 mAh/g S, depending on choice of electrolyte).

Another novel lithium-powder-based anode material, dubbed LiP, was also tested and showed much stronger full-cell performance. Coin cell full-cell tests showed capacities of around 600 mAh/g S after 100 cycles. The N/P ratio and pressing of these anodes were also studied. It was found that pressed electrodes had superior performance to unpressed electrodes, possibly because excess porosity in the unpressed electrodes enabling easier polysulfide diffusion and a stronger shuttle effect. In addition, scanning electron microscopy (SEM) imaging of LiP anodes after cycling shows that they maintain their overall structure better than lithium foil anodes, which is good for long term cell stability.

Electrolyte. Several electrolyte systems have been tested this past year. Both PSU-E-1 and ANL-E-3 electrolytes showed promising performance, allowing for high-capacity stable cycling of sulfur cathodes. However, cells with PSU-E-1 electrolyte and high-loading cathodes were found to be quite sensitive to minor temperature fluctuations, while ANL-E-3 electrolyte was found to not perform well with high sulfur contents.

To overcome these limitations, new electrolytes were developed. The new PSU-E-5 electrolyte was aimed specifically at high-sulfur-loading cathodes. This electrolyte was found to allow for stable cycling of cathodes with ~5 mg S/cm^2 with a capacity of around

1000 mAh/g, as shown in Figure III - 69a. Its low viscosity also leads to low cell polarization.

ANL-E-4 fluorinated ether based electrolyte was shown to give high initial capacity and a decreased polysulfide shuttle effect. Several additives for this electrolyte were tested. Addition of 0.2M LiBr was found to help stabilize the capacity of cells with PSU-3 sulfur cathodes, Li foil anodes, and the new fluorinated electrolyte at around 800 mAh/g for 50 cycles, but did not improve the efficiency above ~95%; this is shown in Figure III - 69b. With an eye toward better utilizing Li2S formed at the end of the discharge process, anion receptors – organic molecules which can form a strong coordination bond between the S2- anion and the electron deficient atom such as B and Al – were also tested as electrolyte additives. Triethyl borate was found to increase coulombic efficiency, albeit with relatively low capacity retention. Finally, LiNO3 was also tested in combination with the fluorinated electrolyte and was found to significantly improve efficiency, but not capacity retention, as it is not believed to prevent polysulfide dissolution.

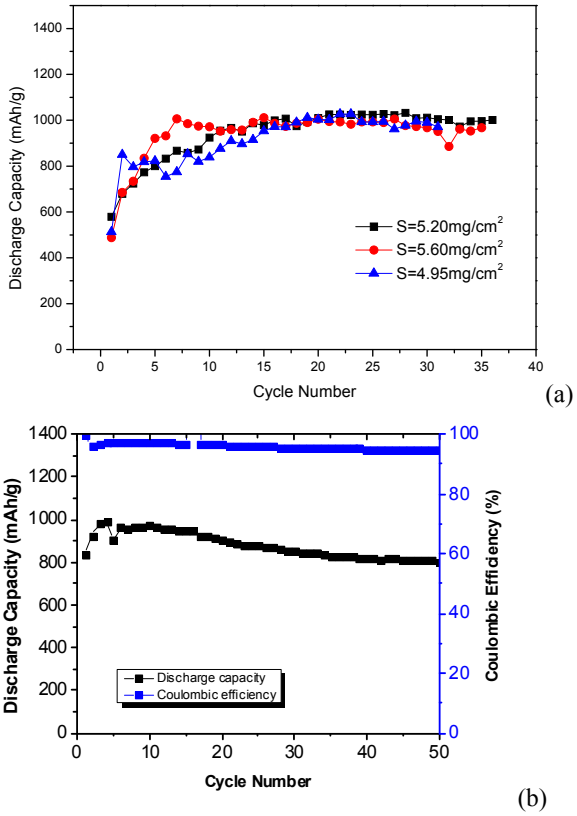

Figure III - 69: Cycling of cells with PSU-3 cathodes and a) PSU-E-5 electrolyte or b) ANL-E-4 fluorinated ether electrolyte with 0.2M LiBr

Several tests were also conducted to better understand the mechanism by which $LiNO_3$ improves battery performance. By testing cells with varying electrolytes having $LiNO_3$ concentrations, it was determined that $LiNO_3$ is used up during cycling and thus cannot provide long-term efficiency improvement, and furthermore, that it cannot prevent long-term loss of capacity. It was also found, by moving Li anodes from cells cycled in $LiNO_3$-containing electrolyte to cells with $LiNO_3$-free electrolyte, that $LiNO_3$ does not appear to form a very stable protective layer on the anode.

Pouch Cell. Initially, pouch cell designs were planned and optimized, particularly with regard to the N/P ratio of cells. It was found that in order to achieve a cell-level capacity of 200 Wh/kg, the specific capacity must be 800 mAh/g S with an N/P ratio of 5.2, or over 900 mAh/g S with an N/P ratio of 2.0. This and other design factors were taken into account during pouch cell design.

Numerous pouch cells were fabricated and tested. Cells with Li foil anodes, PSU-3 cathodes, and baseline electrolyte with 0.4M $LiNO_3$ proved to have poor capacity, stability, and efficiency. Cells with 0.34 Ah designed capacities showed only a 0.2 Ah after 50 cycles, with an efficiency of only 40% by that point. Cells with 1.5 Ah designed capacity had at most a 1.19

Ah discharge capacity after 5 cycles, dropping to 0.95 Ah after 16 cycles, corresponding to an energy density of just 110 Wh/kg. In contrast, cells with LiP anodes and the same cathode and electrolyte showed more promising performance. The 0.34 Ah designed capacity pouch cell maintained a capacity of 0.32 Ah after 36 cycles, although efficiency was relatively low. 1.5 Ah design capacity pouch cells showed a discharge capacity of ~1.7 Ah – higher than the designed capacity – after 5 cycles, although the capacity decreased to ~1.2-1.3 Ah after 12 cycles. This fading and relatively low efficiency may be due to consumption of $LiNO_3$ in the cells. Performance of example cells with Li foil and LiP anodes is shown in Figure III - 70.

Conclusions and Future Directions

Moving into the next year of this project, continued work will focus most heavily on pouch cell development and optimization. Further work on improving reliability and compatibility of the newest electrolytes and scaling up high-performance material production will continue, as will their testing in pouch cells. In addition, we will proceed to work on 4 Ah pouch cells and continue to optimize design parameters such as N/P ratio and electrode pressing. Concurrently, material development will continue in an effort to further improve cell performance. Safety evaluations, such as nail penetration and oven tests, will also be conducted.

FY 2013 Publications/Presentations

Journal Publications

1. Xu, T., Song, J. X., Gordin, M. L., Sohn, H. S., Yu, Z. X., Chen, S. R., Wang, D. H. Mesoporous Carbon-Carbon Nanotube-Sulfur Composite Microspheres for High-Areal-Capacity Lithium-Sulfur Battery Cathodes, *ACS Applied Materials & Interface*, **2013**, DOI: 10.1021/am4035784.
2. Song, J. X., Xu, T., Gordin, M. L., Zhu, P. Y., Lv, D. P., Jiang, Y-B, Chen, Y. S., Duan Y. H., Wang, D. H. Nitrogen-Doped Mesoporous Carbon Promoted Chemical Adsorption of Sulfur and Fabrication of High-Areal-Capacity Sulfur Cathode with Exceptional Cycling Stability for Lithium-Sulfur Batteries, *Advanced Functional Materials*, **2013**, DOI: 10.1002/adfm.20130263.
3. Chen, S. R., Dai F., Gordin, M. L., Wang, D. H. Exceptional electrochemical performance of rechargeable Li-S batteries with polysulfide-containing electrolyte, *RSC Advances* **2013**, *3*, 3540.

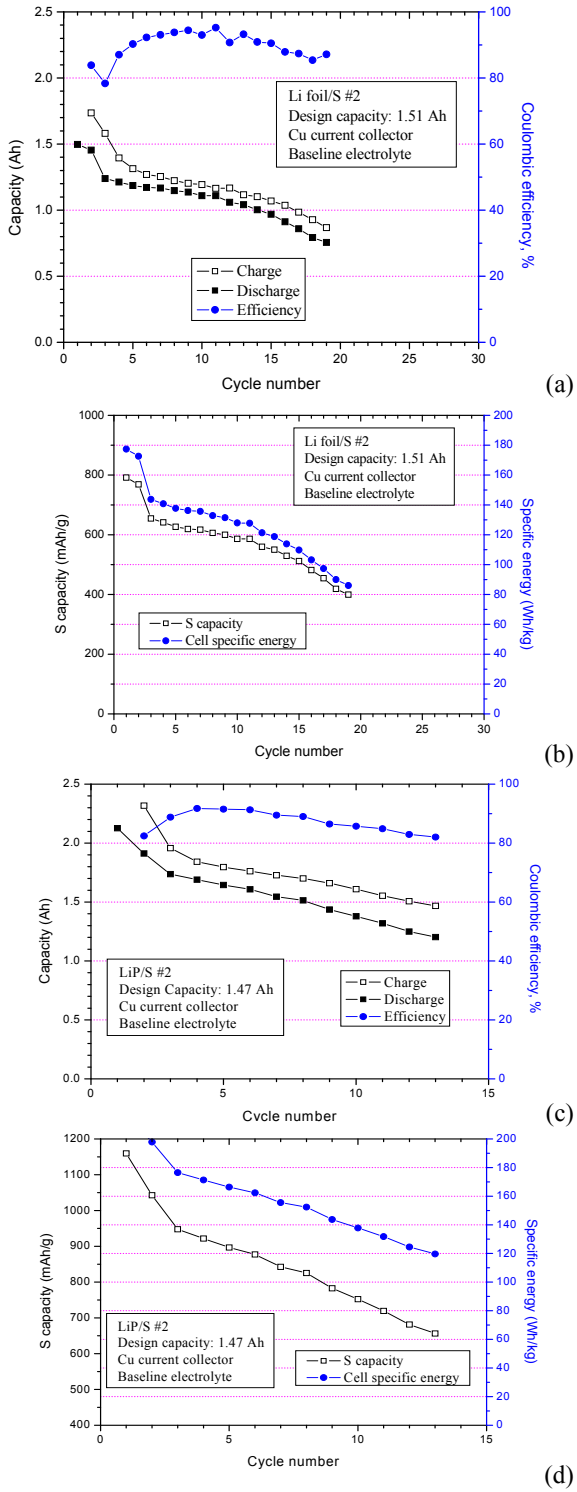

Figure III - 70: Cycling performance, efficiency, sulfur-specific capacity, and energy density of 1.5 Ah design capacity pouch cells with a), b) Li foil and c), d) LiP anodes, using PSU-3 cathodes and 1M LiTFSI and 0.4M LiNO3 in DOL/DME (1:1, v/v) electrolyte

Presentation

1. 2013 DOE Annual Peer Review Meeting Presentation.
2. Wang, D. H. Development of Lithium-Sulfur Batteries, In Beyond Li-ion Symposium VI, Boulder, Colorado, June 2013.
3. Chen, S. Performance Booster: A Different Role of Polysulfide in Rechargeable Lithium-Sulfur Batteries, In the 224th ECS Meeting, San Francisco, CA, October 2013.

III.B.7 Stand Alone Battery Thermal Management System (DENSO)

Christopher Johnson, NETL Program Manager
Subcontractor: DENSO International America, Inc.

Brad Brodie, Project Manager
DENSO International America, Inc.
24777 Denso Drive
Southfield, MI 48086
www.densocorp-na.com
Phone: (248) 350-8851; Fax: (248) 350-7774
E-mail: bradley_brodie@denso-diam.com

Start Date: October 2011
Projected End Date: September 2014

Objective

Reduce the vehicle battery pack size by 20% (or increase driving range by 30%) through an optimized battery thermal management system.

Technical Barriers

Cost – This project's first priority is to develop a thermal system that would allow battery pack size reduction of 20%. This is possible because current battery packs are oversized to guarantee they have acceptable performance for the advertised life of the battery pack. One major reason for the oversize of the battery pack is from cell degradation due to exposure to high temperatures. This project will attempt to address the exposure to high temperatures, and thus enable size reduction of the battery pack.

Performance – It is also known in the industry that cell performance is reduced at low temperatures. This project will also attempt to improve battery pack performance by efficiently warming the batteries in cold ambient temperatures.

Technical Targets

- Develop a simulation program that will duplicate the battery thermal behavior in the vehicle.
- Develop a detailed thermal system design based on the information from the simulation program.
- Produce a prototype thermal system and bench test to prove the system is able to achieve the goals of the project.

Accomplishments

- Established set test conditions to which the battery pack will be evaluated.
- Basic cell characteristics have been identified and used for the simulation model.
- Developed a battery pack simulation model using AMEsim software which can duplicate the conditions from vehicle testing.
- Developed initial thermal system models in AMEsim software.
- Evaluated scenarios based on input from Chrysler. Includes a mix of ambient temperatures and driving profiles.
- Battery model from Phase I was combined with thermal system, BMS, and battery life calculations into one simulation model.

✧ ✧ ✧ ✧ ✧

Introduction

The objective of this project is to design a thermal system that will enable a PHEV/EV battery pack size reduction by 20%. The project is broken into three phases. Phase I will involve understanding the thermal requirements for the battery pack. A simulation program will be established to duplicate the battery thermal behavior in the vehicle. Phase II is the design of the thermal system, using the battery pack model created in Phase I, that can both cool and heat the battery pack to allow the size reduction and performance improvement. In Phase III, prototype thermal system is made based on the design in Phase II. Phase III also includes bench testing to prove the system is able to achieve the goals of the project.

Approach

The intent of the program is to demonstrate that a thermal system could enable the reduction of the battery pack size through optimal thermal management. The key points are considering performance at cold temperatures and battery life when exposed to high temperatures.

A battery pack model will be created in AMEsim to simulate the battery pack. This will be done using equivalent circuit models (empirical), a physics-based model would be too complicated for the purpose of this

study. The type of Equivalent Circuit model is DC Resistance-Capacitor (RC).

After the battery model is created in Phase I, Phase II will involve incorporating the battery model with a thermal system model. This may not be easy because this needs to include a battery management system and influence of temperature from the vehicle cabin and the ambient to the battery pack. The conditions used for the evaluation are provided by Chrysler based on its experience with specifying the battery packs for electric vehicles. Each concept for the thermal system will be run, using the simulation program, through each driving and ambient temperature scenario. After that, the battery life will be determined using the NREL battery life model. Then, a comparison can be made between various thermal system concepts and the effect on battery life. If battery life is increased, the battery pack size can be reduced and still achieve the target life span for the battery packs.

Results

Evaluation conditions were established among all members of the project, with strong input from Chrysler. This includes warming the battery pack from cold soak, cooling the battery from a hot soak, three drive profiles, and two battery charging conditions. These conditions will be used next year when the thermal system is developed in the simulation program. Basic thermal characteristics of the battery cells were determined and used to establish the battery pack simulation model in AMEsim.

An image of the battery simulation model is shown in Figure III - 71. There are five key parts of the model; inputs, electrical controls, battery pack model, thermal controls and thermal model. The inputs include the drive profile conditions. (Charge and discharge rate of the battery pack.) The electrical controls simulate a battery management system and monitor items like state of charge. The battery pack model simulates the battery cells based on equivalent circuits model. Thermal controls monitor thermal characteristics and make decisions on whether heating or cooling is needed. Finally, the thermal model processes the ambient conditions of the battery pack which includes ambient temperature, cabin temperature and solar load plus other inputs.

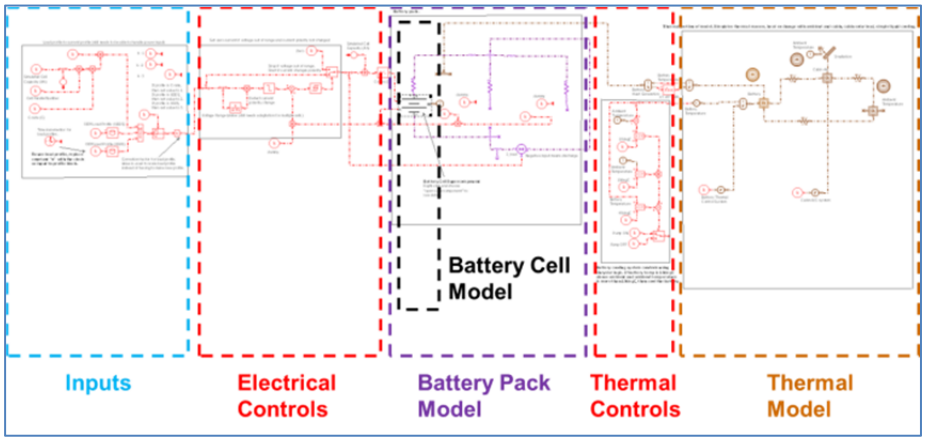

Figure III - 71: Battery model using AMEsim

Using the battery model in Figure III - 71, one roadblock that was encountered was the time to run the simulation. There are about 25 scenarios that will be run on each thermal system technology to find the best option. However, simulation time was almost 80 hrs for just one scenario. After optimizing the simulation model for speed, and using a faster PC, the simulation time was reduced to 10 hrs. Further work will be done to further optimize the model and increase the speed.

Conclusions and Future Directions

Because of the roadblock encountered with simulation speed, the project is delayed approximately 1.5 months. However, there is a recovery plan to get the project on schedule by the middle of 2014.

Because of the delay, there are currently no results to show how well the new system will reduce the battery pack compared to the base system. These works will occur in November and December of 2013. The final results of the simulations and thermal system performance should be ready to publish at the 2014 Annual Merit Review.

III.C Low-Cost Processing Research

III.C.1 Low-Cost Manufacturing Project (JCI)

Christopher Johnson, NETL Program Manager
Subcontractor: Johnson Controls, Inc.

YK Son, Principal Investigator
Johnson Controls, Inc.
5757 N Green Bay Avenue
Milwaukee, WI 53201
Phone: (414) 374-3709
E-mail: yk.son@jci.com

Subrecipients:
Maxwell Technologies, ENTEK Membranes

Start Date: October 2011
Projected End Date: January 2015

Objectives

- Research, develop and demonstrate the advanced Li-ion cell manufacturing processes and techniques such as non-N-methyl-2-pyrrolidone (NMP) electrode, direct coating separator, and fast formation to reduce the existing Li-ion manufacturing costs by 50%.
- Maintain or exceed existing battery performance and requirements.

Technical Barriers

- Dry processed electrode fabrication: A key challenge related to the preparation of solvent-free processed anode and cathode is achieving proper electrode thickness while producing desired active loading, porosity, pore size, and electrode structure. To overcome this challenge, new binders, powder mixing techniques, and new formulation are being developed to optimize active layer properties.
- Direct separator coating: There are multiple challenges for direct separator coating technology, such as producing a uniform microporous polymer film on the electrode surface and maintaining the rigidity of the microporous separator coating. Therefore, it requires investigating various polymers, solvents, inorganic materials including process conditions. Self discharge and calendar life studies will be used to evaluate performance against these risks.

Technical Targets

- Develop dry processed cathode and anode electrodes to meet the existing wet coated electrode performance.
- Develop direct coated separator to meet the existing poly-olefin separator performance.
- Develop the fast formation process to meet the existing baseline formation process performance while improving cell uniformity and maintaining detectability.
- Develop a 15Ah Li-ion cell that integrates all three advanced technologies to meet a baseline NMC/Graphite cell performance, durability and safety.

Accomplishments

- Developed and proved out 15Ah NMC/Graphite baseline cell design with 155Wh/kg and 300Wh/l energy density.
- Developed lab scale pilot lines for dry electrode production and separator lamination for 3Ah integrated cell delivery.
- Developed 3Ah integrated cell design and process to incorporate dry processed electrodes and separator lamination technologies.
- Developed the activation process for fast formation.
- Developed interim cost model.

✧ ✧ ✧ ✧ ✧

Introduction

Johnson Controls proposes to develop a portfolio of advanced manufacturing technologies to reduce the manufacturing cost of large format Li-ion cells by 50%. Three key technologies to be developed are: Non-NMP electrode, direct separator coating, and fast cell formation. The integration of these three advanced manufacturing technologies will achieve the targeted cost savings through the elimination of material, lower capital equipment expenses, and reduced energy and manufacturing costs.

Approach

During the second phase of the program, we have developed and evaluated all targeted technologies – Non-NMP electrodes, direct coating separators – in coin cells and 3Ah pouch cells. The technologies that are under investigation for the 3 Ah pouch cell delivery are:

- Dry processed cathode, direct coated separator on dry processed anode.
- Aqueous cathode, direct coated separator on standard anode.

Results

Cell Development. Johnson Controls has developed two designs for this project to serve as the baseline to support developing and evaluating new advanced technologies as shown in Table III - 14 and Figure III - 72.

Table III - 14: 3Ah / 15Ah baseline cell design

Items		3Ah	15Ah	Reference
Chemistry	Cathode	NMC	NMC	* AG: Artificial Graphite ** PE: Poly Ethylene
	Anode	*AG	*AG	
	Separator	**PE	**PE	
Capacity (Ah)		3.18	15.3	@30°C * Tested at 25°C
Energy Density	Specific (Wh/kg)	145	155	
	Volumetric (Wh/l)	251	300	
HPPC Power	Gen (W/kg)	2,307	*2,864	
	Regen (W/kg)	2,101	*2,541	
Cell Weight (g)		78	360	

Figure III - 72: 3Ah / 15Ah baseline cell

The design of the baseline cells is intended for PHEV applications between high energy and high power performance. The test results are in line with the parameters of the design: The HPPC in Figure III - 73 shows a rate performance of 2,300W/kg for 3Ah cell, and 2,800W/kg for 15Ah cell, and it shows good capacity retention after 1,000 full cycles as shown in Figure III - 74.

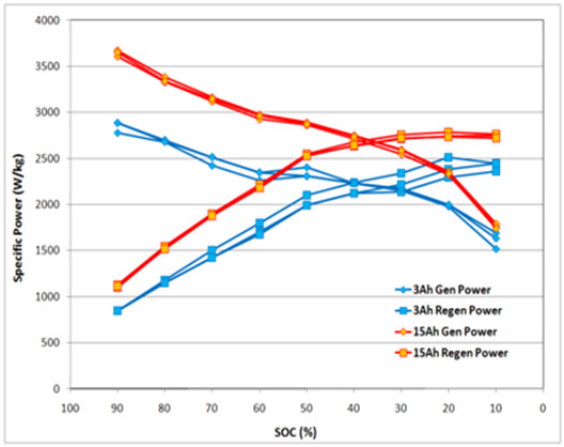

Figure III - 73: Baseline cell HPPC test: red: 15Ah baseline cell, blue: 3Ah baseline cell

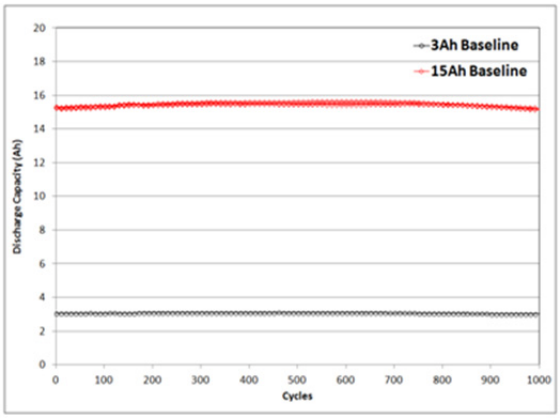

Figure III - 74: Baseline cell full cycle life test: red: 15Ah baseline cell, blue: 3Ah baseline cell

Overall, the baseline 3Ah and 15Ah cells have shown good and consistent results for most test items, and these will be used as the baseline data to compare the characteristics of the advanced technologies integrated cells.

Dry Coated Electrodes. Leveraging from previous experience in dry processed electrode production, critical mixing processes and binder candidates have been identified for the production of Li-ion battery anodes and cathodes. Overall, dry processed electrodes have improved significantly in both cycle life and power performance in 2013. However, their high current rate

performance to 100% DOD is lower than that of baseline electrodes as shown in Figure III - 75.

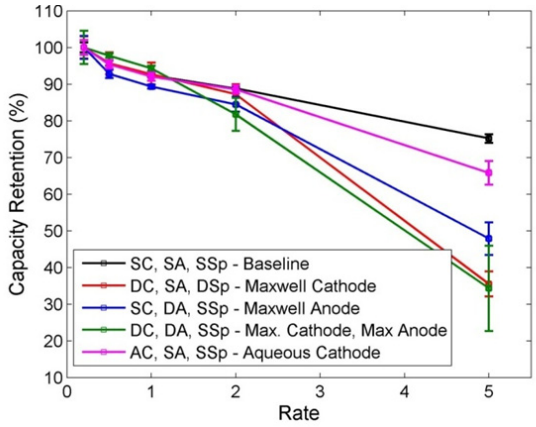

Figure III - 75: Non-NMP electrodes evaluation: black: baseline, red: dry cathode electrode and baseline anode, blue: baseline cathode and dry anode electrode, green: dry cathode and dry anode, purple: aqueous cathode and baseline anode

We believe that the major contributors to the low performance of the dry processed electrodes are the higher loading weight and lower porosity, specifically smaller pore size diameter. Bound by program schedule and customized equipment limitation, we have optimized the current dry electrode designs to match that of the baseline cells under HPPC test protocol 3Ah dry electrode cells from Build 1 Set 2 electrode design produced a 15.2 mohm DC impedance using a 10 sec generation pulse. This performance is better than the baseline cells (16.1 mohm) as shown in Figure III - 76.

These results demonstrate the attractiveness of dry electrode process technology and its potential to match wet electrode coating technology once process and formulation optimization is achieved.

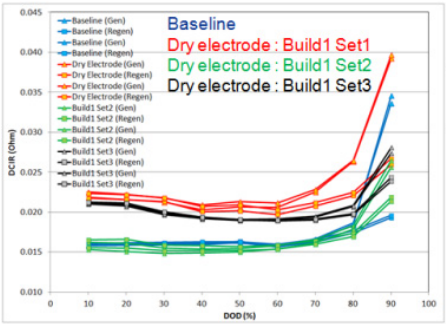

DCR (ohm)		Gen	Regen
Baseline		0.0161	0.0163
Dry electrode	Build1 Set1	0.0209	0.0205
	Build1 Set2	0.0152	0.0154
	Build1 Set3	0.0190	0.0190

Figure III - 76: HPPC test result: blue: baseline, red: build 1 set 1 dry electrode, green: build 1 set 2 dry electrode, black: build 1 set 3 dry electrode

Direct Coated Separator. Three technologies (A, B, and C) were developed to incorporate the separator as a component of the electrodes. The implementation of the separator on the electrodes has positive implications on production speed and cost within the production process. The three technologies are currently investigated with lab scale electrodes. Technology A displayed better performance compared to baseline and other technologies as shown in Figure III - 77.

The results of technology A for integration have shown better performance at high current rate capability test as shown in Figure III - 78.

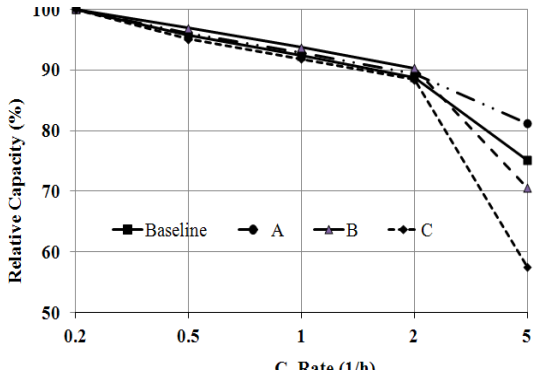

Figure III - 77: Rate capability of separator technologies

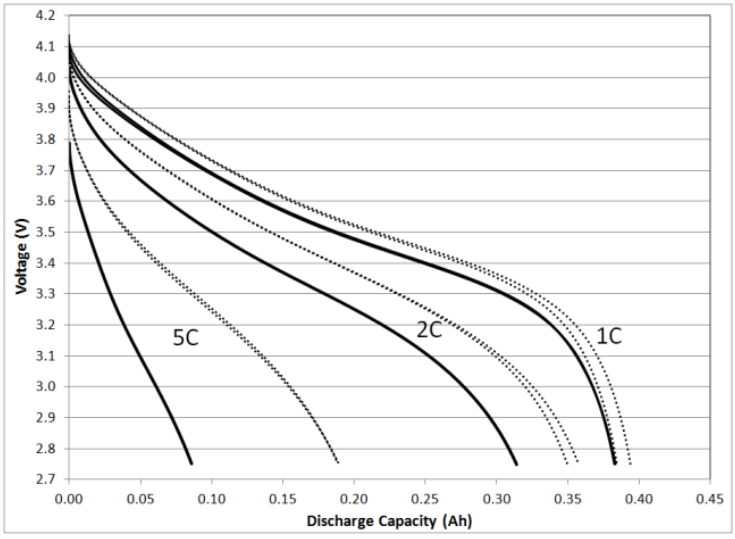

Figure III - 78: Single layer pouch cell rate capability, solid line: dry electrodes with baseline separator, dotted line: dry electrodes with A technology

Technology A is very promising. We are concentrating to reduce variations and to improve the self-discharge rate.

Conclusions and Future Directions

In summary, the team has evaluated the technologies in the area of non-NMP coating, direct coated separator, and fast formation and developed technology integrated cell design and processes. The 15Ah baseline cells performed according to expectations.

During the second phase of this program, the integration of these advanced manufacturing technologies was achieved for 3Ah cells. We have identified and are working to solve the technical barriers for performance and process improvement.

The key future directions are listed as following:

- 3Ah interim integrated cell development and delivery for evaluation.
- Final cost model including advanced technologies.
- Process development for pilot scale production of dry electrode and direct coated separator.
- Process development for integration.
- Fast formation for integrated cells.
- 15Ah final integrated cell development and delivery.

FY 2013 Publications/Presentations

1. Merit award poster presentation (5/13/2013)

III.C.2 Ultraviolet Curable Binder Lithium Ion Battery Project (Miltec UV)

John Tabacchi, NETL Manager
Contractor: Miltec UV International, LLC

Primary Contact:
Gary E. Voelker, Project Director
Dr. John Arnold, Principal Investigator
146 Log Canoe Circle
Stevensville, MD 21666
Phone: (410) 604-2900; Fax: (410) 604-2906
E-mail: gvoelker@miltec.com,jarnold@miltec.com

Start Date: October 1, 2011
Projected End Date: October 1, 2014

✧ ✧ ✧ ✧ ✧

Introduction

The objective of this project is to reduce lithium ion battery electrode manufacturing costs by 50% by replacing thermal drying of solvent-based binders with ultraviolet (UV) or electron beam (EB) curable binders. The project goal is to demonstrate that battery cells made from UV or EB cured electrode coatings perform equal to or greater than equivalent cells made from solvent based binders.

Previously identified UV and EB curable binders and associated curing technology will be shown to reduce the time required to cure electrode coatings from tens of minutes to less than one second. This revolutionary approach can result in dramatic increases in process speeds and significantly reduced capital costs (a factor of 10 to 20) and operating costs, reduced energy requirements and reduced environmental concerns and costs due to the virtual elimination of volatile organic solvents and associated solvent dryers and recovery systems. Multiple lithium ion battery cells will be fabricated using various approaches to UV and EB curing technology; performance of the cells will be evaluated; and analytical testing will be used to further improve the performance of the cells. Eventual cells made with UV/EB curable binders will be submitted to the DOE for independent testing and performance verification. Commercialization of UV/EB technology will lead to greater market penetration of HEVs, PHEVs and EVs as well as significantly reducing the environmental intrusion associated with the manufacturing processes.

Progress and Current Status

During FY 2013, Miltec UV researchers formulated UV curable binders (patents pending) and used them to successfully make lithium ion battery anode and cathode coatings. These coatings have been applied at thicknesses up to 100 microns and successfully cured at speeds up to 200 feet per minute (FPM). Electrode coatings have been made which retained physical integrity after being immersed in pure electrolyte at elevated temperatures for extended periods. Coin cells have been made using UV curable binder anodes and cathodes and tested. The initial charge/discharge and first 50 cycles for two such coin cells are shown later in this section. The long term cycling performance of full cells made with a conventional anode and UV curable binder cathodes are shown below. Anodes have also been fabricated using UV curable binder and tested in half cells. The initial charge/discharge results for one such test is shown below. These efforts culminated in the delivery of 18 Interim cells made with UV curable binder anodes and cathodes with the goal of having performance equal to or greater than conventional cells.

A slot die coater and reel to reel conveyor have been installed on a Miltec UV multiple lamp UV curing system. The system is capable of accommodating a 10” current collector foil and an 8” coating width and is capable of coating and curing at speeds up to 200 fpm.

Interim Cell Evaluation and Test. The major part of the efforts during FY2013 has focused on research and development to improve and verify the adhesion, chemical stability, and other qualities of selected UV and EB curable binders leading to the delivery of 18 Interim cells for independent evaluation. These efforts are described below.

Figure III - 79 shows the initial charge discharge performance for a baseline cell. Figure III - 80 shows the initial charge/discharge performance of a half cell made with a cathode using UV curable binder and Figure III - 81 the cycling performance to 50 cycles. The active material is NMC and the coating is 87% NMC, 5% Carbon, 8% Binder (by weight); cured at 100 FPM; and 50 microns coating thickness. Full cells using these same UV curable binder coatings have completed long term cycling and the results of one full coin cell are shown in Figure III - 82. The initial charge and discharge tests for a UV cured anode are shown in Figure III - 83.

The Interim cells are 500 mAh pouch cells prepared by ANL. The cells coatings were comprised of 87% active material, 5% carbon and 8% binder. Cell test plans which include the testing limits and specifications for the interim cell validation tests such as voltage and current limits, state of charge, charging, and temperature recommendations, number of test sequences, and other appropriate test conditions were be delivered simultaneously with the 18 Interim cells. These tests are based upon full cell configuration using PHEV test procedure based on the USABC test profile

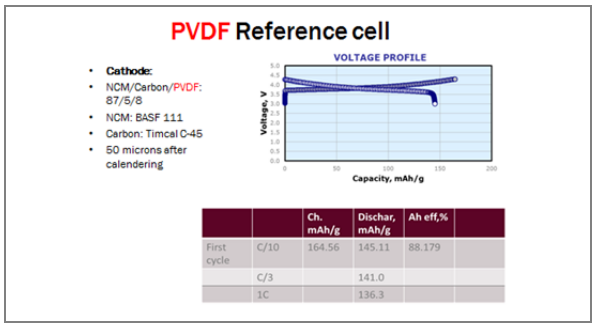

Figure III - 79: Reference cell

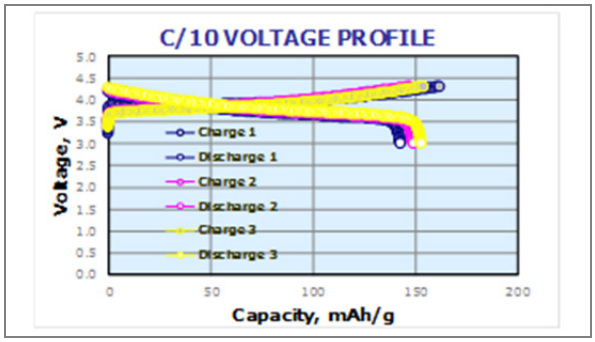

Figure III - 80: Initial charge and discharge

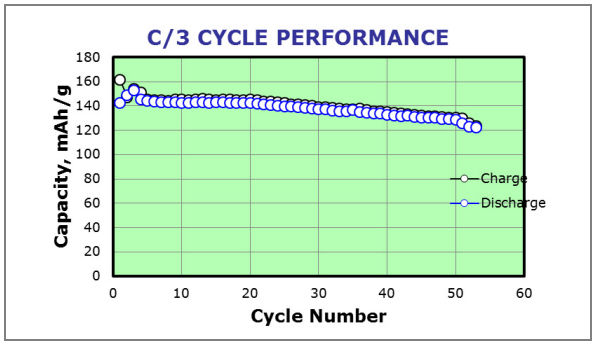

Figure III - 81: 50 cycle performance

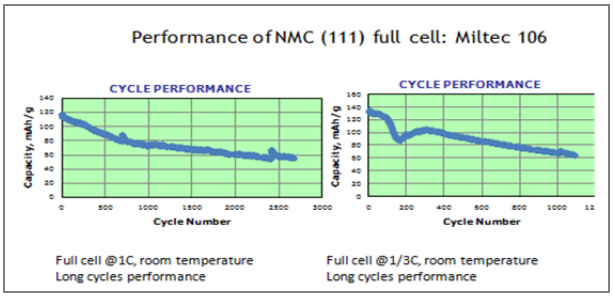

Figure III - 82: Full cell 1000+ cycle 1C and 1/3C data demonstrate UV cathode binder is durable and electrochemically stable

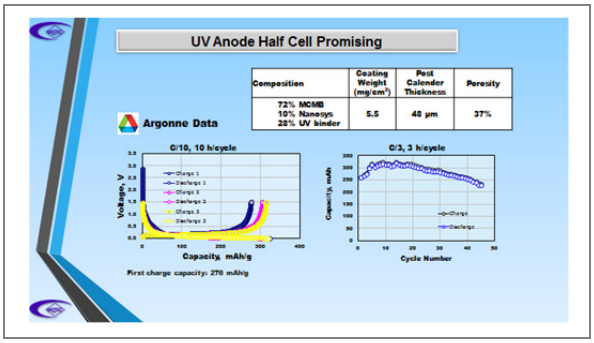

Figure III - 83: Half cell 1/3C data for anode with UV cured binder

Planned Work for FY2014

During FY2014, research and development efforts will continue on the application of UV/EB cured binders in the fabrication of lithium ion battery anodes and cathodes. Optimum binder/anode and cathode material combinations will be subjected to testing in half coin cells, full coin cells, and full pouch cells during FY2014. Miltec UV will prepare and deliver 18 final design pouch cells to DOE for independent validation testing. The Miltec UV curing system and slot die coater will be operated and performance evaluated for both anode and cathode fabrication with a desired goal of demonstrating 150-200 feet per minute successful coating and UV curing of electrodes.

III.C.3 High Capacity Alloy Anodes (Applied Materials)

John Tabacchi, NETL Project Manager
Grant Recipient: Applied Materials, Inc.

Sergey Lopatin, Project Director/Principal Investigator
3100 Bowers Avenue, M/S 202
Santa Clara, CA 95052
Phone: (408) 235-4742; Fax: (408) 235-6863
E-mail: sergey_lopatin@amat.com

Subcontractors:
Lawrence Berkeley National Laboratory
Oak Ridge National Laboratory
FMC Lithium Division
Navitas Systems
Nissan Technical Center North America

Start Date: October 1, 2011
Projected End Date: September 30, 2014

Objectives

- Develop and demonstrate the feasibility of depositing alloy anode materials at high deposition rates.
- Characterize, evaluate, and optimize the resulting electrodes using pouch cells and demonstrate the low cost potential of the new manufacturing methodology.

Technical Barriers

Cycle life of alloy based anodes is one of the main issues that limit their viability. We are working closely with our partners (subcontractors) to understand the underlying issues leading to the low cycle life of these anodes and then make necessary process changes to meet requirements.

Technical Targets

- Demonstrate high capacity Li-ion battery cell anodes that are capable of achieving an energy density of at least 500 Wh/l and a power density of at least 500 W/l.
- Demonstrate cycle life (300-1,000 cycles at 80% depth of discharge), calendar life (5-10 years), and durable cell construction and design capable of being affordably mass produced.

Accomplishments

- Development of electro-deposition module which allows for 3D-porous structure formation in a single prototype tool for both 3D Cu collector and 3D CuSnFe alloy anode.
- Development of modular technological steps for forming 3-3.5 mAh/cm^2 cells including process methodology for Graphite coating by water soluble process to achieve adhesion to the 3D-porous structures. Testing rate performance in half-cell assembly *vs*. Li demonstrated capacity retention advantages up to 25-27% at 2C and 3C-rates.
- Testing baseline pouch cell assembly. Porous 3D electrodes were assembled in single layer pouch cells with $Li_{1-x}[Ni_{1/3}Mn_{1/3}Co_{1/3}]O_2$ (NMC) cathodes. The retention capacity for 3DCu/Graphite vs. NMC was measured 81.8% at 1310 cycles. Projection from these data is that the baseline cell is capable of over 1,400 cycles at capacity retention of 80% at C/3 rate.
- Eighteen cells comprised the program's 1st deliverable sent to Idaho National Laboratory (INL) for further evaluation.
- Development of 3DCuSnFe nano-structure alloy anode. Coulombic efficiency (CE) is improved by grain size reduction, pre-lithiation, and mitigation with combining alloy with Graphite.
- Extending 3D electrode concept to the high loading 3DCuSnFe/Graphite alloy electrodes and testing interim pouch cell. Capacity retention of 76.2% at 1280 cycles was demonstrated. These data show that the interim cell is capable of 985 cycles at 80% capacity retention at C/3 rate.

✧ ✧ ✧ ✧ ✧

Introduction

Applied Materials is working on a new class of Li battery anodes with high capacity based on an innovative micro-cell porous 3DCu-Li alloy structure. Micro-cell 3DCu-Li alloy architecture of controlled thickness forms continuous highly conductive Cu pathways for electrons through the full electrode. The technology holds great potential for electric vehicle lithium-ion batteries. The electrode structure also has a very large surface to volume ratio to contact with Li-ion

electrolyte. The porous 3DCu can accommodate the volumetric expansion during electrochemical cycling and contributes to long cycle life. The improved electrodes are assembled into prismatic battery cells and tested to demonstrate the feasibility of producing Li-ion batteries with the target energy density.

Approach

Experimental development focused on initial electro-deposition module which allows for 3D-porous structure formation. Baseline processes have been developed for (a) 3DCu current collector and (b) for graphite coating using a water soluble process. Extending the baseline electrode concept to the high loading 3DCuSnFe/graphite alloy electrodes should allow a) low resistivity at the electrode/current collector interface, b) fast charge transfer at the electrode/ electrolyte interface, and c) alloy expansion and contraction mitigated by reduced alloy grain size with Fe addition.

Modular technological steps were developed for forming 3-3.5 mAh/cm^2 cells (Figure III - 84).

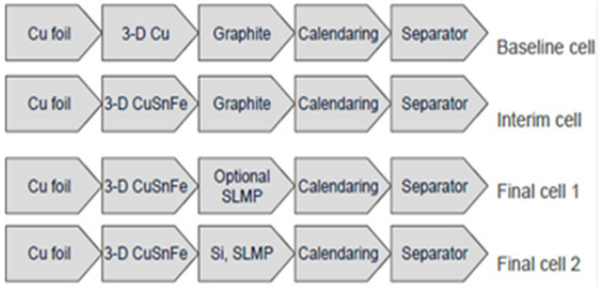

Figure III - 84: Schematic diagram of process flows for manufacturing baseline cells, interim cells and final cells with 3D current collector and alloy anodes

Results

3D Cu Current Collector Material. Baseline processes have been developed for (a) 3DCu current collector and (b) for graphite coating using a water soluble process. Scanning Electron Microscopy (SEM) images of 3DCu/graphite structures showed crack-free coating. 3DCu/graphite baseline cell material was studied before and after calendaring. 3DCu remained unchanged with no mechanical damage as result of calendaring. Testing rate performance in half-cell assembly *vs.* Li demonstrated capacity retention advantages up to 25-27% at 2C and 3C-rates.

Baseline Cell Testing. 30-38 mAh single layer baseline full cells using 3DCu/graphite *vs.* NMC (Figure III - 85), have been assembled and shipped to INL for testing according to the USABC PHEV manual.

Figure III - 85: Single layer pouch cells (SLP) made with 3D structure electrode. Eighteen cells have been shipped to INL for testing

For the pre-tested cell, the capacity retention was 81.8% at 1310 cycles. Projection from these data is that the baseline cell is capable of over 1400 cycles at 80% capacity retention at C/3 rate (Figure III - 86).

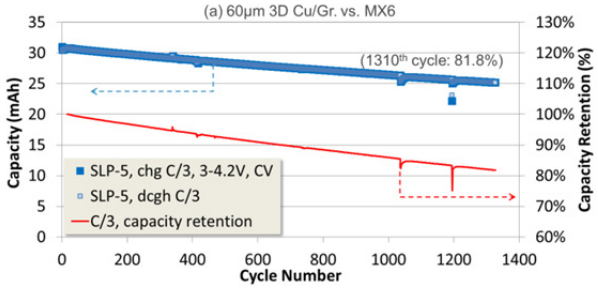

Figure III - 86: Cycling test results for baseline cell: 3DCu/Graphite *vs.* NMC. Projection for capacity retention over 80% is >1400 cycles

3D CuSnFe Nano-Size Grain Material. Electro-chemical deposition has been developed for forming ~50 nm grains (Figure III - 87a) of alloy anode from Cu_6Sn_5(Fe). Connected nano-size grains form a conductive network of porous active material on Cu foil (Figure III - 87b).

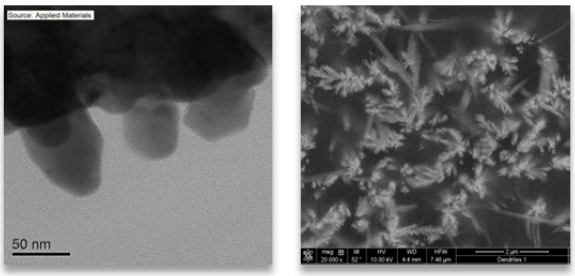

a) ~50 nm grain size b) conductive network

Figure III - 87: a) TEM and b) high resolution SEM images of the 3DCuSnFe Material

Coulombic efficiency (CE) of the alloy electrodes has been improved (Figure III - 88) by following techniques: grain size reduction, pre-lithiation, and combining alloy with graphite. Dense and porous versions of CuSnFe alloy depositions with thickness between 25-50 microns were developed. These 3D CuSn(Fe) electrodes were fabricated by using electroplating from acidic solutions. The mass loading, chemical composition, porosity, and thickness were controlled to obtain ~1.5 mAh/cm^2. These alloy electrodes were then coated with graphite to obtain 3-3.5 mAh/cm^2. Samples were evaluated at ORNL, LBNL and Nissan TCNA in cell assemblies with different electrolytes (Figure III - 88). Improving CE was observed in electrolytes containing fluoroethylene carbonate (FEC) in the composition.

Interim Cell Development. Full cells including 3DCuSnFe/graphite *vs.* NMC have been assembled and tested. Modular technological steps were developed for forming 3-3.5 mAh/cm^2 cells including a methodology for graphite coating via a water soluble process to achieve adhesion to the 3DCuSnFe structures. Graphite was coated on 3D alloy of different loadings: 1, 1.5, 2 and 3 mAh/cm^2 for the 3DCuSnFe alloy. Assembly and testing of graphite coated 3D alloy electrodes showed results of 1280 cycles having high CE (Figure III - 89 and Figure III - 90). Capacity retention of 76.2% at 1280 cycles was demonstrated.

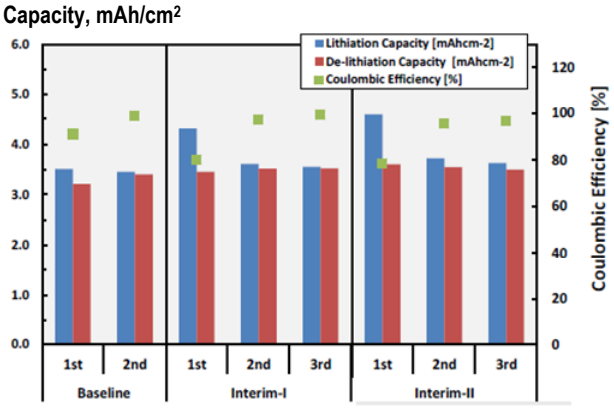

Figure III - 88: Half-cell capacity and CE *vs.* cycle number; for 3-3.5 mAh/cm^2 cells; baseline with 3DCu/graphite and interim I, interim II including the 3DCuSnFe/graphite material with 30% thickness reduction

Applied Materials and project partners continue to develop these cells in order to improve the cycling capability and energy density of the system. The second deliverable, eighteen interim cells, will be delivered to INL for further testing at the completion of formation protocol development including anode-cathode matching.

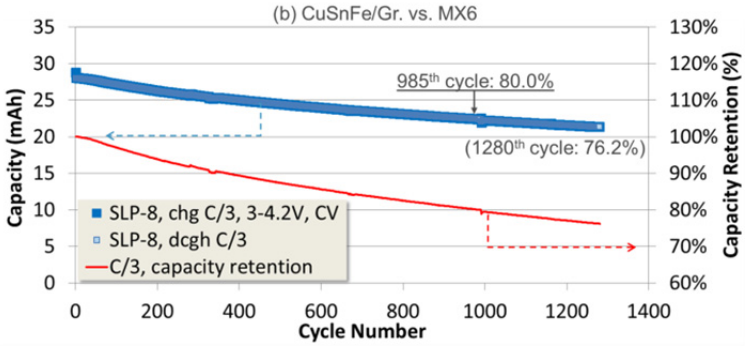

Figure III - 89: Cycling test results for interim cell: 3DCuSnFe/Graphite *vs.* NMC. Measured capacity retention over 80% is ~1000 cycles

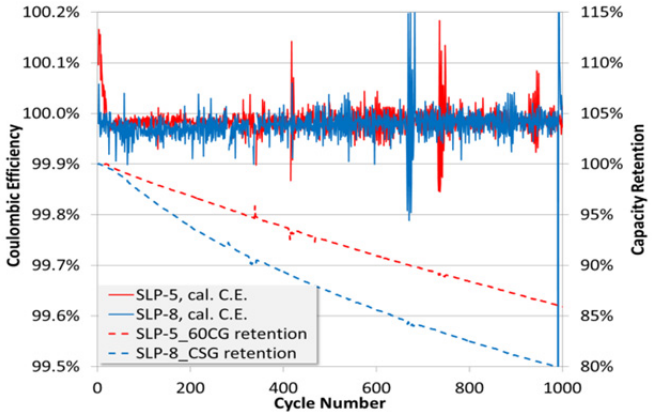

Figure III - 90: Comparative analysis of CE and capacity retention of cycling test results for baseline and interim cells: SLP-5 3DCu/Graphite *vs.* NMC and SLP-8 3DCuSnFe/Graphite *vs.* NMC

Experimental cells including coatings of 3DCuSnFe with Si were assembled and are being tested. Results will be included in the next technical progress report. The third deliverable, twenty four final cells, will be delivered after further cell optimization at the completion of the program.

Current results show that more optimizations for the cell formation protocol, ratio of alloy anode to graphite and for alloy pre-lithiation are necessary.

Conclusions and Future Directions

Assembling and testing full prismatic cells with 3D current collectors resulted in CE over 99.96% at cycles 1000-1400. Projection from the data is that the baseline cell with 3DCu/graphite anode is capable of >1,400 cycles at capacity retention of 80% at C/3 rate, and that the interim cell with 3DCuSnFe/Graphite anode is capable of 985 cycles at the same conditions.

Development of 3DCuSnFe nano-structure alloy anode resulted in half-cell and full cell electrode thickness reduction. CE was improved by grain size reduction, pre-lithiation, and combining the alloy with graphite.

Equipment design concept and laboratory scale chamber prototype were developed. Plating module concept incorporated capability to form 3D structure on both sides of the Cu foil. The individual module designs as well as module integration concepts will be fine-tuned. This will allow Applied Materials and project partners to produce the interim and final sets of cell deliverables for the program. These cells will incorporate the most optimal alloy anode composition.

Applied Materials and project partners would like to continue development of the alloy anode to further improve the cycling performance. This development allows the benefits of the 3D CuSnFe alloy to be utilized in a higher energy density system.

FY 2013 Publications/Presentations

1. Presentation at the 2012 DOE Annual Peer Review Meeting, Arlington, VA.
2. Presentation at the 2013 Applied Materials Annual Engineering Technology (ET) Conference, Santa Clara, CA.

III.C.4 Innovative Manufacturing and Materials for Low Cost Lithium Ion Batteries (Optodot)

John G. Tabacchi, NETL Project Manager
Subcontractor: Optodot Corporation

Steven A. Carlson, Program Manager
100 TradeCenter, Suite G-700
Woburn, MA 01801
Phone: (617) 513-6313; Fax: (781) 569-5201
E-mail: scarlson@optodot.com
mailto:cashtiani@ENERDEL.com

Subcontractors:
Madico Inc., Woburn, MA
Dow Kokam, LLC, Lee's Summit, MO
University of Rhode Island (URI), Kingston, RI
Ashland Inc., Wayne, NJ

Start Date: October 1, 2011
Projected End Date: September 30, 2014

Objectives

- Demonstrate technology that reduces the cell or battery inactive component weight, volume, and/or cost by at least 20% (goal of at least 40%), while maintaining overall cell or battery performance.
- Design, develop, optimize and improve the separator, current collectors, electrolyte, termination materials, and cell casing used for manufacturing lithium ion batteries.
- Develop a simpler and faster battery coating and assembly process.

Technical Barriers

At least a two-fold reduction in the cost of manufacturing lithium-ion batteries is needed for widespread adoption of electric vehicles. Even though improvements in the battery anode and cathode materials will provide significant cost reduction, it is difficult to achieve this overall two-fold level of cost reduction from incremental improvements of the current generation of battery inactive components and of battery coating and assembly processes.

Technical Targets

- Develop a high performance cell that reduces the combined cost of the battery inactive components of separator, current collectors, electrolyte, termination materials, and casing by at least 20%.
- Demonstrate a manufacturing process based on new inactive components that provides high performance cells while reducing the coating and assembly cost by at least 20%.

Accomplishments

- Developed new versions of 8 micron thick ceramic separator layers with an all-nanoporous design and a very narrow pore size distribution with a 30 nm average pore diameter.
- Using the Argonne National Lab(ANL) battery cost model, cost savings from the 8 micron ceramic separator component including the reduced usage of electrolyte were estimated to be greater than 20% for the inactive components of the cell. This estimated saving meets the cost reduction objectives of this project from the thinner ceramic separator alone.
- 3 micron thick copper and aluminum current collector layers were coated onto anode/separator and cathode/separator coated stacks, respectively, and showed good cycling and conductivity. A low cost proprietary process was developed for coating the 3 micron thick copper current collection layer.

✧ ✧ ✧ ✧ ✧

Introduction

Optodot has proposed to develop a new set of battery inactive components and a new battery coating and assembly process. These innovative materials and manufacturing process are based on the use of a thinner, safer, and lower cost ceramic separator. The proposed work comprises development of advanced ceramic separator, current collector, and electrolyte materials and of advanced battery stack coating and current collection methods. A new system of edge termination and cell casing will be developed for use with these coated anode and cathode stacks. The thinner ceramic separator enables the use of lower cost and more thermally stable electrolytes. Wider and higher speed industrial coaters will be utilized to make the coated battery electrode stacks to obtain the cost benefits of at least a five-fold increase in coating output. The new battery manufacturing process eliminates the expensive

conventional assembly equipment to precisely interleave the electrodes with free standing separators.

Approach

Optodot will characterize the performance and cost of the inactive components and assembly process of current baseline cells. Starting with a thinner ceramic separator layer for this project, Optodot and its subcontractors will overcoat this separator with conventional anode and cathode layers. Optodot will design and develop thinner and lower cost current collector layers for the anode and cathode electrodes before coating a second anode or cathode layer. Optodot is also developing a cell termination and casing system for use in making and demonstrating high performance 2 Ah cells. With its subcontractors, Optodot is working to develop a lower cost and more thermally stable electrolyte that functions well with the much thinner ceramic separator and coated battery stack. Optodot and its subcontractors will demonstrate and document the acceptable performance and overall cost reduction of these improved inactive components for lithium ion batteries and of the simpler and faster coating and assembly processes. A cost analysis report will document the cell cost reduction achieved compared to the cost of current baseline cells.

Results

The capability of overcoating the electrodes onto an 8 micron thick ceramic separator layer without penetration of the pigments of the electrode into the separator and without damage to the electrode/separator coated stack during calendering was demonstrated in FY2012. This 8 micron ceramic separator is 40% porous with a narrow pore size distribution centered at 30 nm.

The use of an 8 micron nanoporous ceramic separator as the layer on which the electrodes and current collector layers are coated to form anode and cathode coated stacks provides significant cell cost savings of 20-25% of the inactive components of the cell, using the ANL battery cost model. The cost savings are derived from the use of the much thinner separator, a reduction in the usage of the electrolyte due to the thinner separator, and cell cost reduction in $/kWh from the much thinner separator that allows more active material to be used in the cell.

The ceramic separator layers and the release substrates of this project have excellent stability to the heat and stress of the electrode coating process, as demonstrated during the machine coating of the electrodes and subsequent calendering of the electrode/separator stacks. Safety- and cell performance-related features of the ceramic separator layer include dimensional stability of less than 0.5% shrinkage at 220°C, much greater compression strength than plastic separators, excellent thermal conductivity and heat dissipation, excellent cycling rate capability and low resistance from the much thinner ceramic separator, and non-flammability.

Metal current collector layers and edge connections are being incorporated into the electrode/separator coated stacks to produce the full anode and cathode coated stacks. Considerable progress was made in developing a low cost proprietary process for coating 3 micron copper metal layers as the anode current collector layer with an electrical conductivity of about 0.5 ohms/square. The estimated cost savings for this copper current collector layer is about 40% with a large weight savings compared to the existing copper foils used as the substrate for coating the anodes.

Figure III - 91 shows cross-sections of anode and cathode coated stacks of this project. Small cells made with these coated stacks showed good cycling and high and low temperature performance.

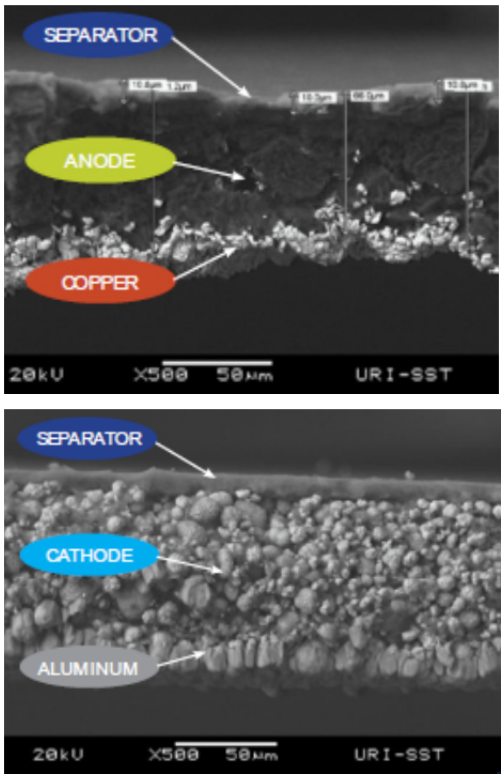

Figure III - 91: Anode electrode stack and cathode electrode stack

The new separator and current collector layers of this project are generic and compatible for use with various anode, cathode, and electrolyte materials as improved cell materials become available.

Since the much thinner ceramic separator provides more flexibility and latitude in the selection of

electrolytes that provide a suitable conductivity, URI is working on more stable and flame retardant electrolytes to use in the cells of this project.

Work was done in FY2013 to eliminate coating-related defects in the coated electrode stacks, and to scale up the machine coating of the ceramic separator layer to a full production width using slot die coating application. This project is ready to make the anode and cathode coated stacks on machine coaters and to assemble them into 2 Ah cells. From this, the estimated cell cost savings from coating at wider widths and higher line speeds and with a simpler cell assembly process will be determined.

Conclusions and Future Directions

- Meeting the performance requirements of at least 20% improved cost, volume and weight for the key inactive components of Li-ion cells and developing a low cost next generation manufacturing process will help meet the DOE goals of cost reduction to $270/kWh by 2017 for PHEVs and to $125/kWh by 2022 for EVs.
- The use of the 8 micron thick ceramic separator alone meets the project's > 20% cost improvement objective for the inactive components, while providing 10% lighter batteries and the safety of a ceramic separator with very high dimensional stability at 220°C.

FY 2013 Publications/Presentations

1. 2013 DOE Annual Peer Review Meeting Presentation

III.D Advanced Materials and Processing (Funded by FY 2008 DOE FOA)

III.D.1 Protection of Lithium (Li) Anodes Using Dual Phase Electrolytes (Sion Power)

John Tabacchi, NETL Project Manager
Grant Recipient: Sion Power Corporation

Yuriy Mikhaylik, Principal Investigator
Sion Power Corporation
2900 East Elvira Road
Tucson, AZ 85756
Phone: (520) 799-7609
E-mail: ymikhaylik@sionpower.com

Start Date: October 1, 2009
Projected End Date: September 30, 2014

Objectives

The objective of this project is to develop a unique electrolyte providing two liquid phases having good Li conductivity, self-partitioning and immiscibility, serving separately the cathode and anode electrodes. Introduce dual-phase electrolyte into Li-S cells and demonstrate improved cycling and thermal stability.

Technical Barriers

Barriers addressed for EV application

- Specific Energy >250 Wh/kg
- Thermal stability, safety
- Cycle Life

Technical Targets

Introduce dual-phase electrolyte into 250 mAh cell format. Perform full scale USABC test evaluation and abuse tolerance test and demonstrate improvement of specific energy > 250 Wh/kg, cycle life >100 cycles and cells thermal stability – increasing the runaway temperature to >165°C.

Accomplishments

Phases 1 and 2 of the Project were successfully completed.

Phase 3 of the Dual-Phase project was synchronized with Sion's ARPA-E project to develop Protected Lithium Anode (PLA) for the Li-S system which ended on September 30, 2013.

The ARPA-E project resulted in development of an advanced PLA structure including ceramic/polymer protective layer and gel-electrolyte layer. The main function of the gel-electrolyte polymer was immobilizing the anode part of the dual-phase electrolyte. Newly introduced PLA structure developed under ARPA-E added two new functions for gel-polymer:

- Surface for coating of advanced protective ceramic/polymer layer
- Carrier and substrate for finished PLA

The dual phase gel-electrolyte polymer was modified to meet the new requirements and to be fully integrated into the new PLA structure.

The first step of integration of Dual-Phase gel-electrolyte into PLA was a combination of gel-polymer layer and polymer layer developed for ceramic/polymer structure. These two layers were combined with vacuum deposited lithium and tested in the laboratory in 0.25Ah cells. A new structure test confirmed improved thermal stability (no runaway) at temperatures exceeding metallic lithium's melting point.

✧ ✧ ✧ ✧ ✧

Introduction

Achieving the DOE cell performance targets for electric vehicle application will require improved Li anode chemical stability (safety), cycle-ability and capacity. It also requires higher cell-level specific energy and the ability to be manufactured at high volume. To meet the DOE targets Sion Power is developing a unique electrolyte providing lithium protection and cell thermal stability.

Approach

Sion Power's approach is to develop an electrolyte consisting of two liquid phases having good Li conductivity, self-partitioning and immiscibility, serving separately the cathode and anode electrodes. This self-

partitioning dual-phase electrolyte will enable us to tailor electrolyte composition at each electrode to provide the optimum chemical stability. This innovative approach was applied to stabilize a high energy metallic lithium anode. While this approach could be generally applied to any Li metal or Li-ion rechargeable cell, SION Power uses a Lithium-Sulfur rechargeable battery system to apply two liquid phases concept.

Results

Li-S cells were produced with vacuum deposited Li anodes coated with two polymer layers: gel-electrolyte polymer and another polymer designed to support the ceramic/polymer protective layer. The cells were discharged and charged at C/5 and C/8 respectively. The cells generated specific energy in the range 260 -310 Wh/kg. Cycling behavior is shown in Figure III - 92.

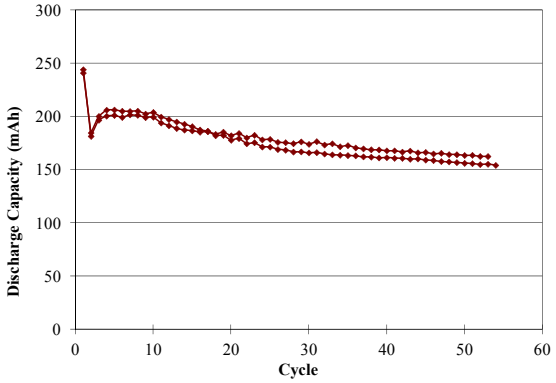

Figure III - 92: Discharge capacity vs cycle for Li-S cells with two polymer layers on the vacuum deposited lithium anode

A subset of cells were stopped after the 10th charge and were subjected to thermal ramp test shown in Figure III - 93. The cells did not show signs of thermal runaway at temperatures exceeding lithium metal's melting point (+181°C). In fact, cell thermal stability at temperatures over 200°C was limited by the packaging material showing loss of mechanical integrity and noisy signal in Figure III - 93.

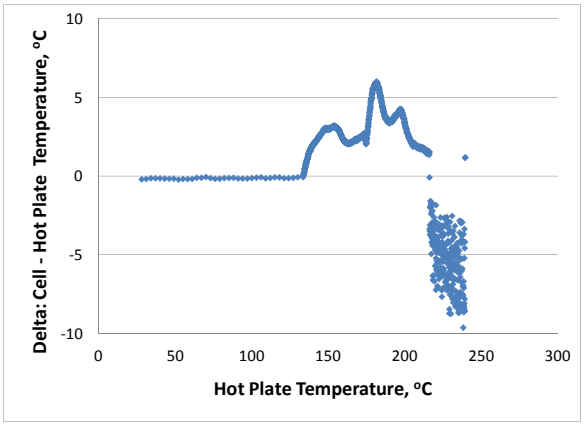

Figure III - 93: Cell thermal ramp test at 5°C/min. Fully charged cell after 10 cycles

Conclusions and Future Directions

The next step is integration of this dual-phase electrolyte into the newly introduced advanced protected lithium anode ceramic/polymer structure and completion of Phase 3 goals: 250 mAh format production cells manufacturing, full scale USABC test performance evaluation and abuse tolerance test and improvement demonstration by making the cell more thermally stable – specifically increasing the runaway temperature to >165°C.

III.D.2 New High-Energy Nanofiber Anode Materials (NCSU)

Bruce Mixer, NETL Project Manager
Grant Recipient: North Carolina State University

Xiangwu Zhang, Primary Contact
North Carolina State University
2401 Research Drive
Raleigh, NC 27695-8301
Phone: (919) 515-6547; Fax: (919) 515-6532
E-mail: xiangwu_zhang@ncsu.edu

Start Date: September 15th, 2009
Projected End Date: November 15th, 2013

Introduction

- **Objective:** Use electrospinning technology to integrate dissimilar materials (silicon and carbon) into novel composite nanofiber anodes, which simultaneously have large energy density, high powder capability, reduced cost, and improved abuse tolerance.

✧ ✧ ✧ ✧ ✧

Progress and Current Status

Achieving the DOE anode targets for advanced lithium-ion batteries will require novel material manufacturing technologies that can produce anodes with large energy density, high power capability, reduced cost, and improved abuse tolerance. In previous project years, we have used electrospinning technology (combined with carbonization) to synthesize a novel type of Si/C composite nanofiber anode (Figure III - 94), combining the advantageous properties of silicon (high storage capacity) and carbon (long cycle life). The nanofiber structure allowed the anode to withstand repeated cycles of expansion and contraction. Si/C composite nanofibers were electronically conductive and provided effective conductive pathways in electrodes. In addition, composite nanofibers formed a desirable porous electrode structure, thereby leading to fast Li-ion transport. Results demonstrated that anodes made of Si/C composite nanofibers were able to deliver high capacity and long cycle life.

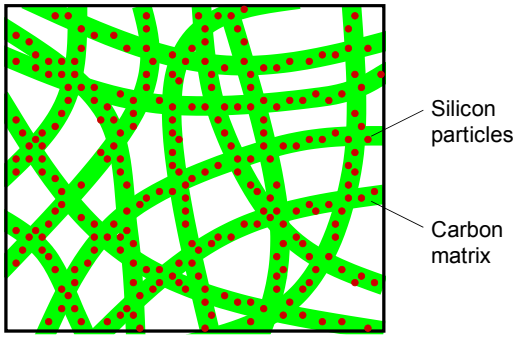

Figure III - 94: Schematic of composite nanofiber anode

In this project year, we utilized several novel approaches to further improve the overall performance of Si/C composite nanofiber anodes. The following are two examples:

Improvement of C-rate Performance by Employing Carbon Nano Tube (CNT). In order to obtain Si/C composite nanofiber anodes with improved C-rate performance, we employed CNTs to increase the electrode conductivity. Si/CNT/C composite nanofibers were prepared by electrospinning 15 wt% Si/0.75 wt% CNT/PAN precursor. These electrospun nanofibers were firstly stabilized in air environment at 280°C for 5 h (heating rate: 5°C/min) and then carbonized at 800°C for 2 h in argon atmosphere (heating rate: 2°C/min) to form Si/CNT/C composite nanofibers. In the previous project year, we studied the charge-discharge profiles of Si/CNT/C composite nanofiber anodes.

Figure III - 95 displays the impedance spectra of Si/C and Si/CNT/C composite nanofiber anodes. Both spectra show one depressed semicircle in the high and intermediate frequency range and a straight line in the low frequency range, corresponding to the migration within the surface layer, interfacial charge transfer process, and lithium diffusion in the electrode, respectively. With the addition of CNTs, the diameter of the depressed semicircle decreases, which indicates a decrease in charge transfer resistance. Figure III - 96 shows the corresponding equivalent circuit. Here, R_e is the electrolyte resistance of the cell, R_{sl} the resistance of ions transferring through the surface layer in the high frequency range, R_{ct} the charge transfer resistance in intermediate frequency region. Warburg impedance (W) corresponds to the diffusion process of lithium ions within the electrode in the low frequency range. Constant phase element (CPE) other than ideal capacitor is introduced due to the porous nature of the composite nanofiber anodes. The results of impedance analysis are listed in Table III - 15. The addition of CNTs does not

have significant influence on the R_e and R_{sl} values. However, the R_{ct} value decreases from 167 to 90 Ω·cm^2 after the introduction of CNTs, indicating that Si/CNT/C composite nanofiber anodes might have better reaction kinetics during electrochemical cycling than Si/C composite nanofiber anodes.

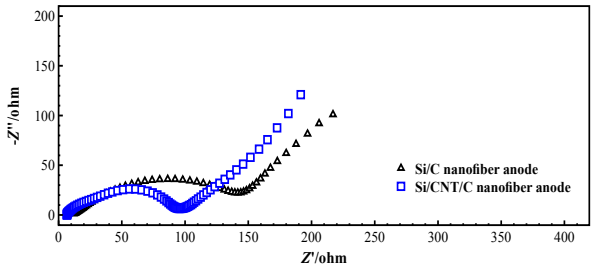

Figure III - 95: Nyquist plots of Si/C and Si/CNT/C composite nanofiber anodes

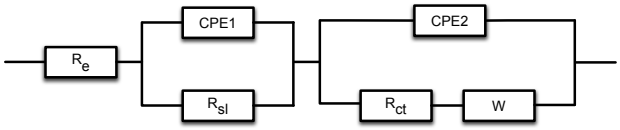

Figure III - 96: Equivalent circuit of Si/C and Si/CNT/C composite nanofiber anodes

Table III - 15: AC impedance analysis results of Si/C and Si/CNT/C nanofiber anodes

Electrodes	R_e (ohm.cm^2)	R_{sl} (ohm.cm^2)	R_{ct} (ohm.cm^2)
Si/C	9.00	15.29	167.72
Si/CNT/C	8.15	19.47	90.68

Galvanostatic charge-discharge experiments were carried out to evaluate the electrochemical performance of Si/C and Si/CNT/C composite nanofiber anodes. Figure III - 97 shows galvanostatic charge-discharge curves of Si/C nanofiber anodes under current densities of 50 and 300 mA/g. At the first cycle, when the current density is 50 mA/g, the Si/C nanofibers show a specific charge capacity of approximately 1363 mAh/g and discharge capacity of 947 mAh/g, respectively, corresponding to a Coulombic efficiency of 69.4%. When the current density is 300 mA/g, the Si/C nanofibers show a specific charge capacity of 1,123 mAh/g and discharge capacity of 736 mAh/g, respectively, corresponding to a Coulombic efficiency of 65.5%. The galvanostatic charge-discharge curves of Si/CNT/C nanofiber anodes under two different current densities are shown in Figure III - 98. At the first cycle, when the current density is 50 mA/g, the Si/CNT/C nanofibers show a specific charge capacity of 1,410 mAh/g and discharge capacity of 976 mAh/g, respectively, corresponding to a Coulombic efficiency of 69.2% (Figure III - 98a). It is seen in Figure III - 98b that at the first cycle, the specific charge and discharge capacities of the Si/CNT/C nanofibers under 300 mA/g are 1,248 and 852 mA/g, respectively, corresponding to a Coulombic efficiency of 68.3%. The results indicate there is the relatively small degradation of capacity with the increase of current density. Here, the capacities were calculated based on the total weight of Si, CNFs and carbon nanofiber matrix.

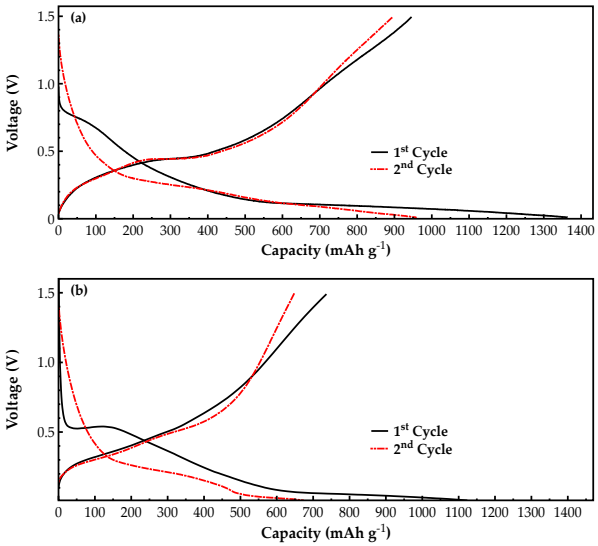

Figure III - 97: Galvanostatic charge-discharge curves of Si/C nanofiber anodes under different current densities: (a) 50 mA g^{-1}, and (b) 300 mA g^{-1}

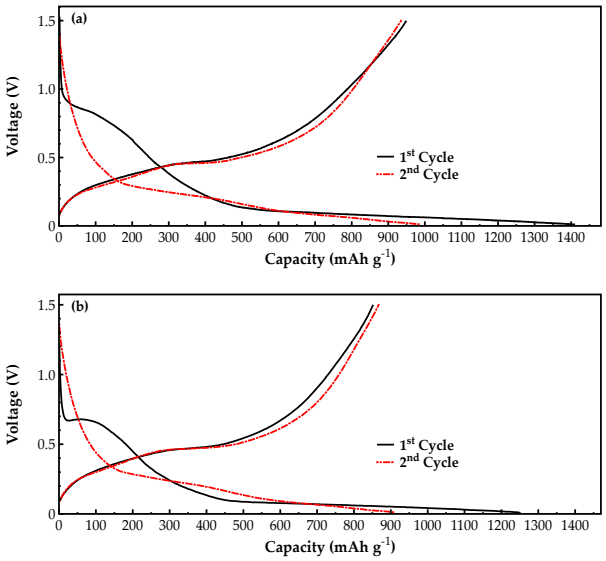

Figure III - 98: Galvanostatic charge-discharge curves of Si/CNT/C composite nanofiber anodes under different current densities: (a) 50 mA g^{-1}, and (b) 300 mA g^{-1}

Figure III - 99 compares the cycling performance of Si/C and Si/CNT/C composite nanofiber anodes under two different current densities. It is seen that under 50 mA/g and at the 30th cycle, the discharge capacities are 775 and 837 mA/g, respectively, for Si/C and Si/CNT/C nanofiber anodes. The corresponding capacity retentions are 81.6 and 84.5%, respectively. At a current density of 300 mA/g, after 30 cycles, the discharge capacities are 492 and 710 mA/g, respectively, for Si/C and Si/CNT/C nanofiber anodes. The corresponding capacity retentions are 64.9 and 83.3%, respectively. Results indicate that at both current densities, the Si/CNT/C nanofiber anode have greater capacity retention than the Si/C nanofiber anode.

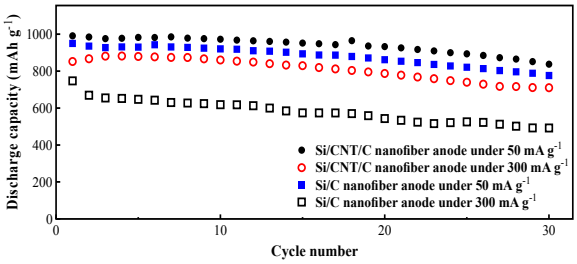

Figure III - 99: Cycling performance comparison of Si/C and Si/CNT/C composite nanofiber anodes under different current densities

The comparison of rate capacities of Si/C and Si/CNT/C nanofiber anodes is shown in Figure III - 100. The discharge capacity of the Si/C nanofiber anode decreases rapidly with increase in current density. However, the capacity decrease of the Si/CNT/C nanofiber anode is much slower. Even at a high current density of 300 mA g^{-1}, a relatively high capacity value of 602 mA/g is still achieved with the Si/CNT/C nanofiber anode. The capacity of Si/CNT/C nanofiber anode almost rebounds back to the original value when a low current density of 50 mA/g was applied again after 20 cycles. This demonstrates the excellent stability of the Si/CNT/C nanofiber anode under various charge/discharge conditions. The enhanced C-rate performance is mainly due to the use of well-dispersed CNTs. Because of their high aspect ratio and high conductivity, the dispersed CNTs can effectively form a conducting pathway throughout the composite nanofibers even at low concentrations.

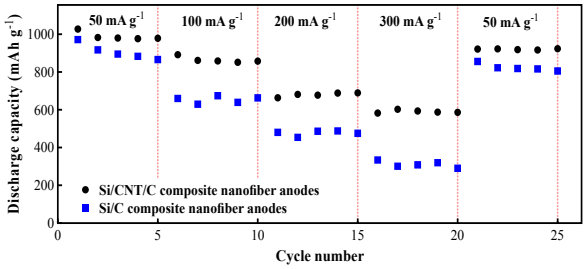

Figure III - 100: Rate capabilities of Si/C and Si/CNT/C composite nanofiber anodes

The results demonstrated that the electrochemical performance of Si/CNT/C nanofibers, especially the capacity retention and rate capability, has been improved significantly, which can be ascribed to the enhanced electrical conductivity of composite nanofibers. The unique morphology and structure of the one-dimensional conductive nanofibrous composite are beneficial to improve the electrochemical behavior of Si/CNT/C composite nanofibers. The incorporation of CNTs further enhances the electrochemical efficiency. These factors lead to Si/CNT/C composite nanofiber anode with high reversible capacity, good cycling performance, and excellent rate capability.

Improvement of Cycling Performance by Employing ALD Alumina Coating. In order to improve the cycling performance of Si/C composite nanofiber anodes, atomic layer deposition (ALD) was employed to coat the fiber surface. ALD is a unique technique for the deposition of conformal and homogenous thin films. In this study, we coated Si/C composite nanofibers with Al_2O_3 by the ALD method. The purpose was to control the stability of the solid electrolyte interphase (SEI) by employing the Al_2O_3 coating layer to prevent side reactions between the electrode and the electrolyte. The ALD process of alumina was performed on the surface of Si/C nanofiber electrodes using tri-methyl aluminum (TMA) and H_2O as precursors at 120°C.

Figure III - 101 displays the impedance spectra of Si/C and ALD Al_2O_3-coated Si/C composite nanofiber anodes prepared with an ALD cycle number of 28. Both spectra show one depressed semicircle in the high and intermediate frequency range and a straight line in the low frequency range, corresponding to the migration within the surface layer, interfacial charge transfer process, and lithium diffusion in the electrode, respectively. The ionic conduction of the SEI film is a result of the migration of solvated Li ions through the micro-pores of SEI since the dried SEI itself is neither electronically nor ionically conductive. Hence, higher interfacial resistance corresponds to a more compact and more stable SEI. As shown in Figure III - 101, the addition of ALD Al_2O_3 coating results in an increased semicircle diameter, *i.e.*, increased charge

transfer resistance. This means the SEI structure has become more compact and less conductive by the introduction of ALD Al_2O_3 coating.

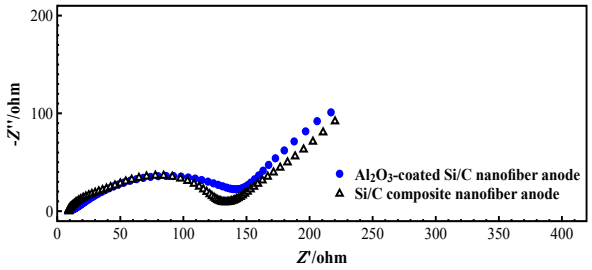

Figure III - 101: Nyquist plots of Si/C and Al_2O_3-coated Si/C nanofiber anodes (ALD cycle number = 28)

Galvanostatic charge-discharge tests were carried out within a voltage window of 0.02 – 1.5 V to evaluate the electrochemical performance of Si/C and Al_2O_3-coated Si/C composite nanofiber anodes. Figure III - 102 shows galvanostatic charge-discharge curves of Si/C and Al_2O_3-coated Si/C composite nanofibers under 50 mA g^{-1}. When the ALD coating cycle number is 35, the resultant Al_2O_3-coated Si/C composite nanofibers exhibit no useful capacity. This means that an Al_2O_3 coating layer of 35 ALD cycles is too thick and blocks lithium diffusion. As shown in Figure III - 102, all other uncoated and Al_2O_3-coated Si/C composite nanofibers show reversible capacities of greater than 900 mA/g in the first cycle.

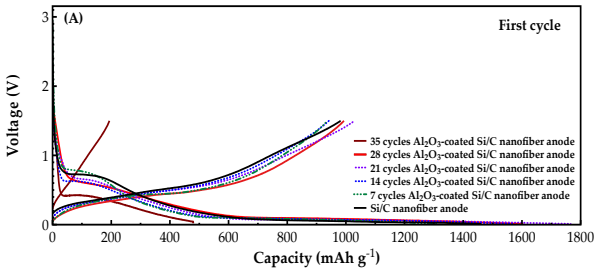

Figure III - 102: Galvanostatic charge-discharge curves of Si/C composite nanofiber anodes and Al_2O_3-coated Si/C composite nanofiber anodes

Figure III - 103 shows the cycling performance of uncoated and Al_2O_3-coated Si/C composite nanofibers. It is seen that at the 100th cycle, the discharge capacities are 338.8, 378.8, 473.5, 685.1 and 827.3 mA/g, respectively, for composite nanofibers with 0, 7, 14, 21, and 28 ALD cycles. The corresponding capacity retentions are 36.1, 39.8, 47.4, 66.5 and 82.3%, respectively. When the ALD coating cycle number is 7 or 14, the cycling performance of Al_2O_3-coated Si/C nanofibers is comparable to that of the uncoated Si/C nanofibers. When the ALD coating cycle number is 21, the capacity fades slower than that of uncoated Si/C nanofibers and shows an increased capacity retention of 66.5% at the 100th cycle. When the ALD coating cycle number is 28, the capacity exhibits the highest stability and the capacity retention at the 100th cycle increases significantly from 36.1% to 82.3%, compared to that of uncoated Si/C nanofibers. However, when the ALD coating cycle number further increases to 35, the capacity is lower than 200 mA/g and fades very quickly. These results demonstrate that Al_2O_3-coated Si/C composite nanofibers prepared with an ALD cycle number of 28 have the most stable cycling performance. The enhanced cycling performance is mainly due to the protective effect of conformal ALD alumina coating which could improve the mechanical integrity and prevent the side reactions between the electrode and the electrolyte. To achieve the enhanced cycling performance, it is important to select an appropriate ALD Al_2O_3 coating thickness, which is a critical parameter for determining the electrochemical performance of the Al_2O_3-coated composite nanofibers.

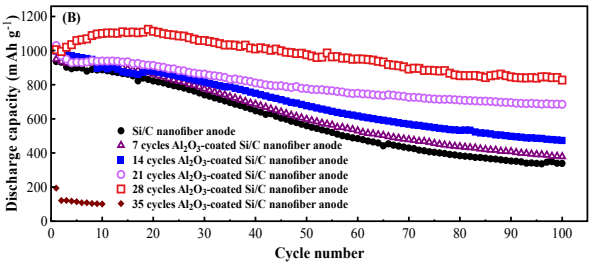

Figure III - 103: Cycling performance of Si/C composite nanofiber anodes and Al_2O_3-coated Si/C composite nanofiber anodes

Figure III - 104 compares the Columbic efficiencies of Si/C and Al_2O_3-coated Si/C composite nanofiber anodes during cycling. It is seen that Al_2O_3-coated Si/C composite nanofibers prepared with 28 ALD cycles deliver the highest Columbic efficiency of 99.9% at the 100th cycle, corresponding to a 1.5% point improvement compared to that of uncoated Si/C composite nanofibers. Similar to the enhanced cycling performance, the improved Columbic efficient can be mainly attributed to the ultrathin conformal ALD Al_2O_3 coating, which minimizes the side reactions between the electrode and the electrolyte.

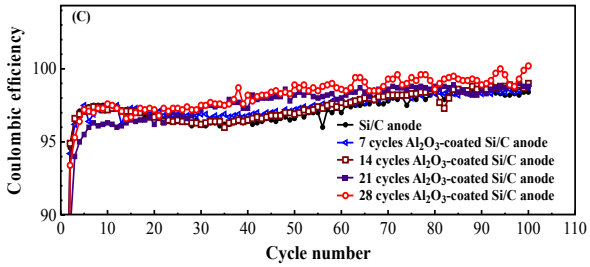

Figure III - 104: Columbic efficiencies of Si/C composite nanofiber anodes and Al_2O_3-coated Si/C composite nanofiber anodes

ALD Al_2O_3 coating tunes the electrochemical performance of Si-based anode materials from both physical and chemical aspects, as shown in Figure III - 105. Firstly, the ALD Al_2O_3 coating has strong physical/mechanical restrain effects on the Si/C composite nanofibers since the coating might transfer the stress of Si nanoparticle expansion from radial direction to in-plane restrain when the Si nanoparticle is partly exposed on the surface. As a result, due to the presence of disordered carbon structure or voids, the buffer effect of carbon matrix could be well realized by restricting the expansion of silicon to the carbon nanofiber (Figure III - 105A). Secondly, the ALD Al_2O_3 coating may act as a barrier for further side reactions between the electrode and the electrolyte (Figure III - 105B). The role of a chemical barrier combined with the reasonable mechanical properties makes the Al_2O_3 coating an artificial but strong and stable SEI-like structure to improve the cycling performance and Columbic efficiency of Si-based anode.

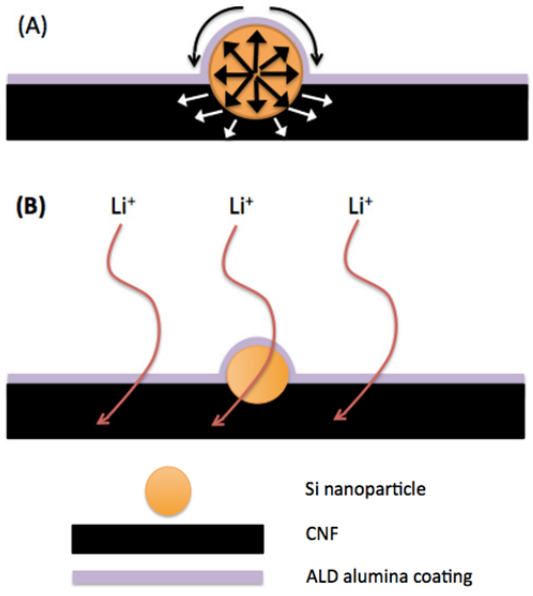

Figure III - 105: Schematic of (A) Physical/Mechanical, (B) Chemical protective effect of the ALD Al_2O_3 coating

The above are just two examples of the approaches that we used in the project year to improve the overall performance of Si/C composite nanofiber anodes. This year's results demonstrate that we have achieved the project objective of using electrospinning technology to integrate dissimilar materials (silicon and carbon) into novel composite nanofiber anodes, which simultaneously have large energy density, high powder capability, reduced cost, and improved abuse tolerance.

FY 2013 Publications/Presentations

1. Kun Fu, Leigang Xue, Ozkan Yildiz, Shuli Li, Hun Lee, Ying Li, Guanjie Xu, Lan Zhou, Philip D. Bradford, and Xiangwu Zhang, "Effect of CVD Carbon Coatings on Si@CNF Composite as Anode for Lithium-ion Batteries," Nano Energy, 2, 976-986, 2013.
2. Shuli Li, Leigang Xue, Kun Fu, Xin Xia, Chengxin Zhao, and Xiangwu Zhang, "High-performance Sn/Carbon Composite Anodes Derived from Sn(II) Acetate/Polyacrylonitrile Precursors by Electrospinning Technology," Current Organic Chemistry, 17, 1448-1454 (2013).
3. Leigang Xue, Kun Fu, Ying Li, Guanjie Xu, Yao Lu, Shu Zhang, Ozan Toprakci, and Xiangwu Zhang, "Si/C Composite Nanofibers with Stable Electric Conductive Network for Use as Durable Lithium-Ion Battery Anode," Nano Energy, 2, 361-367 (2013).
4. Ying Li, Guanjie Xu, Yingfang Yao, Leigang Xue, Shu Zhang, Yao Lu, Ozan Toprakci, and Xiangwu Zhang, "Improvement of Cyclability of Silicon-Containing Carbon Nanofiber Anodes for Lithium-Ion Batteries by Employing Succinic Anhydride as an Electrolyte Additive," Journal of Solid State Electrochemistry, 17, 1393-1399 (2013).
5. Leigang Xue, Guanjie Xu, Ying Li, Shuli Li, Kun Fu, Quan Shi, and Xiangwu Zhang, "Carbon-Coated Si Nanoparticles Dispersed in Carbon Nanotube Networks as Anode Material for Lithium-Ion Batteries," ACS Applied Materials & Interfaces, 5, 21-25 (2013).
6. Ying Li, Guanjie Xu, Leigang Xue, Shu Zhang, Yingfang Yao, Yao Lu, Ozan Topracki, and Xiangwu Zhang, "Enhanced Rate Capability by Employing Carbon Nanotube-Loaded Electrospun Si/C Composite Nanofibers as Binder-Free Anodes," Journal of Electrochemical Society, 160, A528-A534 (2013).
7. Xiangwu Zhang, "A Nanofiber Approach to Advanced Energy Storage," Department of Fiber Science and Apparel Design at Cornell University, Ithaca, New York, March 2013.

8. Kun Fu, and Xiangwu Zhang, "Flexible and Binder-Free Design: Nonwoven Structure Based Si Materials as Anodes for Lithium-Ion Batteries," The 8th Annual NC State University Graduate Student Research Symposium, Raleigh, NC, March 2013.
9. Xiangwu Zhang, "Advanced Nanofibrous Energy-Storage Materials," 2nd Annual World Congress of Advanced Materials-2013 (WCAM-2013), Suzhou, China, June 2013.
10. Xiangwu Zhang, "A Nanofiber Approach to Advanced Energy Storage," The 5th International R&D Brokerage Event in Textiles and Clothing, Bursa, Turkey, April 2013.

III.D.3 Internal Short Circuits in Lithium-Ion Cells for PHEVs (TIAX)

Christopher Johnson, NETL Project Manager
Subcontractor: TIAX LLC

Suresh Sriramulu
Richard Stringfellow
TIAX LLC
35 Hartwell Avenue
Lexington, MA 02421
Phone: (781) 879-1240; Fax: (781) 879-1209
E-mail: sriramulu.suresh@TIAXLLC.com

Start Date: May 2010
Projected End Date: May 2013

Objectives

- Develop an improved understanding of the conditions under which a thermal runaway will occur in a Li-ion cell.
- Use modeling to determine the threshold conditions for thermal runaway following an internal short circuit.
- Identify design factors for cells that can reduce propensity for thermal runaway.
- Identify and analyze opportunities for prevention of internal short circuits, or intervention/mitigation before they can cause thermal runaway.

Technical Barriers

On rare occasions, Li-ion cells experience thermal runaway during normal charge/discharge cycles because of internal short-circuits; we term such incidents "field-failures." Even though such incidents are rare, the potential consequences can be very serious. Safety technologies currently employed in Li-ion cells, such as positive thermal coefficient current limiting devices (PTC), current interrupt devices (CID), shut-down separators, etc., have not prevented thermal runaway due to internal shorts in commercial Li-ion cells. Development of new safety technologies is hindered by the rarity of field-failures in Li-ion cells, and the current incomplete understanding of field-failures. In this program, we fabricate Li-ion cells with various means to stimulate or develop appropriate internal shorts in order to study the effect of cell design variables, and cell-level materials choices. This improved understanding will help identify and evaluate technologies that enhance the safety of PHEV Li-ion batteries.

Technical Targets

- Develop guidelines that will enable the development of technologies for a safe battery.
- Establish a facility for fabricating Li-ion cells to (1) study the effect of cell materials and cell design parameters on thermal runaway, (2) compare to TIAX's Li-ion cell finite element analysis (FEA) model predictions, and (3) validate FEA model.
- Establish an experimental facility that permits testing the efficacy of technologies developed to mitigate safety incidents that occur in the field.
- Select and test approaches to enhance Li-ion battery safety using validated model and experimental data.

Accomplishments

- Set-up fully functional cell prototyping facility with capability to fabricate high-quality multi-Ah cells.
- Adapted method for stimulating thermal runaway to cells fabricated on our prototyping line.
- Conducted experiments to induce thermal runaway of custom-built Li-ion cells under a range of external heat transfer conditions.
- Validated FEA model for simulating thermal runaway of Li-ion cells by fitting experimental thermal runaway data.
- Demonstrated ability to stop the progression to thermal runaway by adjusting the rate of heat transfer out of the cell.

✧ ✧ ✧ ✧ ✧

Introduction

Concerns regarding the safety of Li-ion batteries could severely limit their use in PHEVs, and undermine the prospects for realizing the appealing benefits of PHEVs. Recent highly-publicized safety incidents and the ensuing widespread recalls of Li-ion batteries used in laptops and cell phones have elevated such concerns. In these safety incidents, called field-failures, Li-ion batteries operating under otherwise normal conditions undergo what appear to be spontaneous thermal runaway events, with violent flaming and extremely high temperatures. These field-failures cause significant damage to cells, packs and devices, and sometimes to

their surroundings. Because a typical PHEV pack would be significantly larger than a typical laptop pack, the consequences of a field-failure in a PHEV pack could be far more severe than would be the case for a laptop pack, and may occur far more frequently.

Although it is well-recognized that the commercial viability of Li-ion technology in PHEVs is dependent on avoiding spontaneous occurrence of such incidents on board vehicles, it is clear but less well-recognized that the safety technologies currently employed in commercial Li-ion batteries for portable electronic applications are inadequate with respect to such incidents. Furthermore, there are currently a variety of standard safety-related technologies to guard against abuse of the Li-ion battery. However, field-failures have occurred despite the presence of these technologies in cells and packs. There is also no adequate test for the type of field-failure that presents the basic safety issue for Li-ion.

Given that field-failures occur in a manner that is not effectively addressed by any of the standard safety measures currently used in Li-ion batteries, and that there is no test currently available that can identify these cells before they undergo field-failure, it is clear that a fundamentally new approach is required to develop technologies that will prevent these rare but profoundly destructive safety incidents caused by internal short circuits in PHEV cells.

Approach

Our approach to developing guidelines for safe PHEV pack design is to employ an FEA model to determine the conditions under which thermal runaway of PHEV-size cells occurs and can be suppressed. The FEA model is first validated using thermal runaway data on 18650 cells. Thermal runaway was induced in an 18650 cell by introducing a miniature heater into the center of the cell through a hole drilled at the bottom of the can. This approach allowed us to simulate local, spot heating of the cell, akin to an internal short. These cells were custom-built on our cell prototyping line with a range of design variations (including active materials) and were tested under a range of external heat transfer conditions in a custom-built wind tunnel. Here we describe our work in validating the FEA model, as well as initial experimental data in suppressing thermal runaway.

Results

Cell thermal parameters. The heater method employed for estimating the thermal parameters for the 18650 cells is described in Figure III - 106. Temperature measurements inside the cell and at the cell surface were made for different heater powers (Figure III - 107). By fitting the model to these time-dependent data, we were able to estimate/verify the thermal parameters for the cell (Figure III - 107).

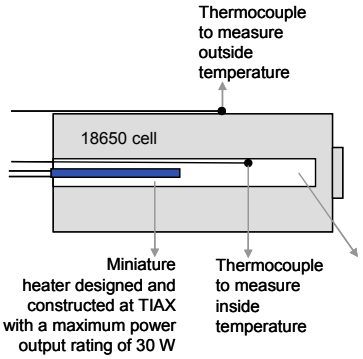

Figure III - 106: Schematic of experimental set-up to simulate internal short heat release in a cylindrical cell by using a miniature heater inserted in cell core. The heater power and external rate of heat transfer can be independently controlled

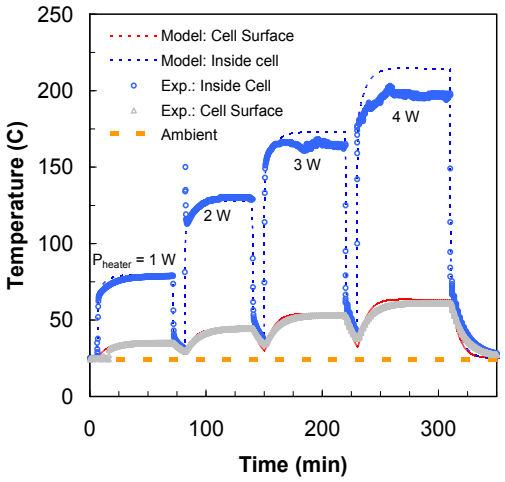

Figure III - 107: Cell thermal properties, including specific heat and thermal conductivity were estimated/verified through heater experiments. Figure shows measured internal and cell surface temperatures for different heater power levels. Model fits are also shown. The cell was completely discharged prior to the experiment

Heat release kinetics from active materials. Kinetics of heat release from the anode and cathode active materials are key inputs for any thermal runaway model of Li-ion cells. We developed representative models for heat release kinetics by fitting *ex situ* Differential Scanning Calorimeter (DSC) data for charged anode and cathode active materials used in our 18650 cells (Figure III - 108). These kinetic sub-models were then used in our FEA model for thermal runaway simulations.

Thermal runaway of Li-ion cells. We induced thermal runaway by internally heating fully charged (4.2

V) 18650 cells using the heater method. Representative thermal runaway data are shown in Figure III - 109. In this test, the cell surface temperature initially rises slowly due to the internal heating. At ~680 s (cell surface temperature of 110 ºC), there is a sharp drop in the cell voltage and thermal runaway ensues as indicated by the rapid rise in cell surface temperature. The measured cell temperature in this experiment exceeded 700ºC. Separate experiments have confirmed that the sharp drop in cell voltage is due to an internal hard short. This phenomenon will be discussed in detail in a future publication.

Model fit to the thermal runaway data. Figure III - 110 shows a comparison of the model fit to the experimental data from Figure III - 109. The only parameter adjusted was the power dissipated in the hard short. The model is able to determine the time and cell surface temperature at which thermal runaway occurs. We attribute the slight disagreement in the peak temperature between the model and the experiment to the experimental observation that the cell vents during thermal runaway, expelling electrolyte and active material mass, which is not yet taken into account in our model.

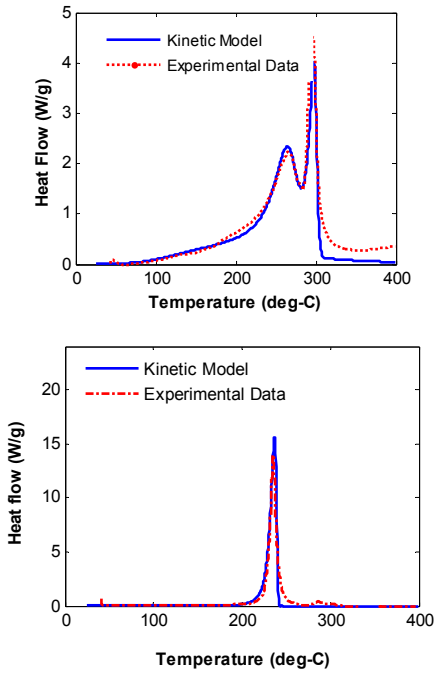

Figure III - 108: Kinetic models for heat generation were developed by fitting experimental DSC data for the materials used in our cells. Top plot shows fit to charged anode (graphite) data and bottom plot the fit to the charged cathode (NCA) data. The scan rate for the DSC measurement was 5ºC/min

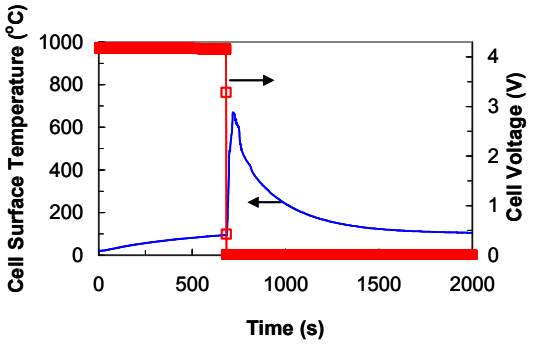

Figure III - 109: Experimental thermal runaway data from the heater experiment. The heater power was ~10 W and the external heat transfer coefficient was ~15 W/m²-K (low-level air flow past the cell)

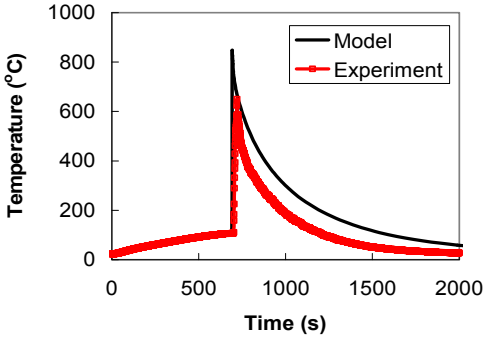

Figure III - 110: Experimental thermal runaway data from the heater experiment. The heater power was ~10 W and the external heat transfer coefficient was ~15 W/m²-K

Effect of ambient conditions on thermal runaway. Previous *model* calculations had shown that increasing the heat transfer coefficient would prevent progression to thermal runaway. As shown in Figure III - 111, *experimental data show that* increasing the heat transfer coefficient from 12 W/m^2-K (no air flow past the cell) to 50 W/m^2-K (substantial air flow past the cell) when the cell surface temperature exceeded 130ºC suppressed thermal runaway as predicted by the model.

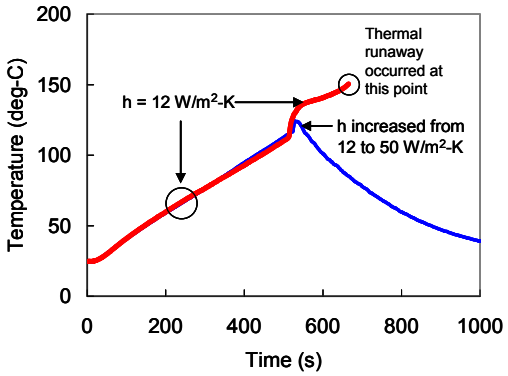

Figure III - 111: Experimental data demonstrating the benefit of increased heat transfer coefficient (h) in suppressing thermal runaway. When h was maintained at ~12 W/m²-K, thermal runaway occurred at ~700 s (cell surface temperature ~150ºC). Temperatures higher than 150ºC are not reported because the thermocouple was dislodged when the cell experienced thermal runaway, but we visually observed flames and a red-hot cell surface. In a subsequent experiment, h was increased from ~12 W/m²-K to ~50 W/m²-K when the surface temperature exceeded 130°C, resulting in cell cool down and suppression of thermal runaway. Identical cells were used in the two experiments

Conclusions and Future Directions

Collection and analysis of thermal runaway data under controlled conditions on custom-built 18650 cells have allowed us to validate an FEA model. Using the validated model, we are simulating thermal runaway in a large PHEV Li-ion cell following an internal short. Sensitivity analyses will help further elucidate the conditions that influence thermal runaway following an internal short circuit. We will derive some general guidelines for safe cells and packs from these simulations.

FY 2013 Publications/Presentations

Portions of this work were presented at:

1. 30th International Battery Seminar and Exhibit, Ft. Lauderdale, FL, March 2013.
2. 224th Electrochemical Society Meeting, San Francisco, CA, October 2013

III.E Small Business Innovative Research Projects

Brian Cunningham
U.S. Department of Energy
1000 Independence Avenue, SW
Washington, DC 20585
Phone: (202) 287-5686; Fax: (202) 586-7409
E-mail: brian.cunningham@ee.doe.gov

Start Date: Ongoing
Projected End Date: Ongoing

Objectives

Use the resources available through the Small Business Innovation Research (SBIR) and Small Business Technology Transfer (STTR) programs to conduct research and development of benefit to the Energy Storage effort within the Vehicle Technologies Program Office.

Introduction and Approach

The Energy Storage effort of the Vehicle Technologies Program Office supports small businesses through two focused programs: Small Business Innovation Research (SBIR) and Small Business Technology Transfer (STTR). Both of these programs are established by law and administered by the Small Business Administration. Grants under these programs are funded by set aside resources from all Extramural R&D budgets; 2.7% of these budgets are allocated for SBIR programs while 0.35% for STTR grants. These programs are administered for all of DOE by the SBIR Office within the Office of Science. Grants under these programs are awarded in two phases: a 6-9 month Phase I with a maximum award of $150K and a 2 year Phase II with a maximum award of $1M. Both Phase I and Phase II awards are made through a competitive solicitation and review process.

The Energy Storage team participates in this process by writing a topic which is released as part of the general DOE solicitation. In FY12, the Energy Storage team decided to broaden its applicant pool by removing specific subtopics and allowing businesses to apply if their technology could help advance the state of the art by improving specific electric drive vehicle platform goals developed by the DOE with close collaboration with the United States Advanced Battery Consortium.

Phase II Awards Made in FY 2013. Under the SBIR/STTR process, companies with Phase I awards that were made in FY 2012 are eligible to apply for a Phase II award in FY 2013.

Two Phase II grants were awarded in FY 2013 from ten Phase I grants that were conducted in FY 2012.

Applied Spectra, Inc., (Fremont, CA 94538-6410). This project will develop a bench top optical sensor for direct real-time measurements of the chemical composition of battery materials and electrode/electrolyte interfaces with depth resolution down to the nanometer range. This development will enable capabilities to improve domestic manufacturing of Li-ion batteries with higher yield and improved performance.

XG Sciences, Inc., (Lansing, MI 48911-4224). This project will develop a low cost high energy silicon/graphene anode for use in extended range electric vehicle applications.

Phase I Awards Made in FY 2013. Three Phase I grants were awarded in the Summer of FY 2013.

Navitas Systems, LLC, (Woodridge, IL 60517-4795). This project will develop a low cost and high capacity silicon based anode for lithium-ion batteries. This will result in new battery technology capable of reducing the cost and extending the range of electric vehicles. This addresses the two key barriers that are limiting electric vehicle adoption.

Pneumaticoat Technologies, LLC, (Westminster, CO 80021-3523). This project will implement a low-cost, lean-manufacturing approach to providing safety and stability to lithium-ion battery materials using a nanotechnology-enabling coating solution. Expected outcomes are higher retained performance under extreme conditions using statistical experimental designs, and a roadmap toward rapid commercialization and domestic production of next generation Li-ion battery materials.

TIAX, LLC, (Lexington, MA 02421-3102). This project will develop a high voltage cathode material that improves the energy efficiency and mileage of HEVs and PHEVs, while also making it possible to charge PHEVs more quickly.

IV

Battery Testing, Analysis and Design

Cost Assessments and Requirements Anlysis

Battery Testing Activities

Computer Aided Engineering of Batteries

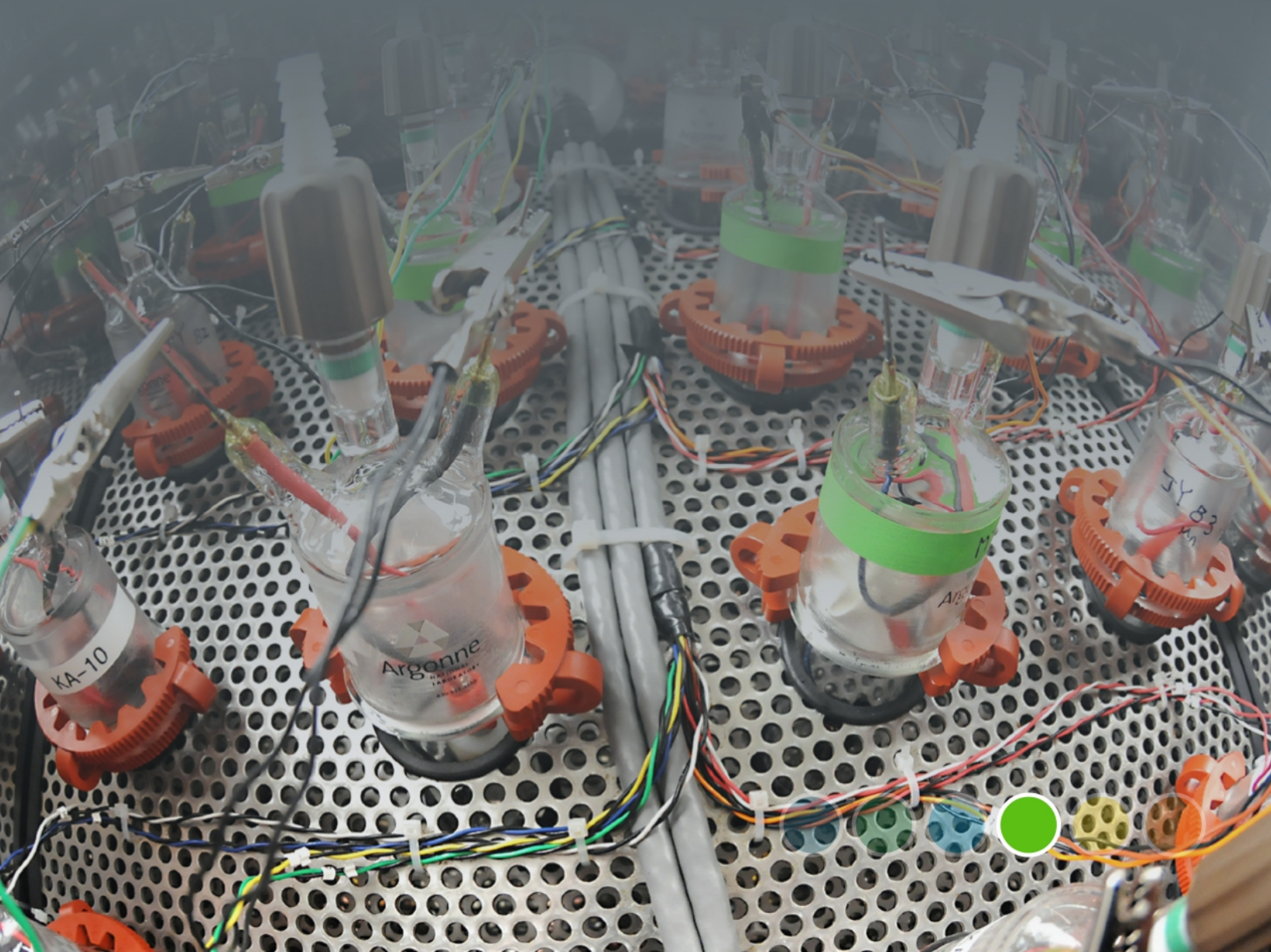

IV. Battery Testing, Analysis, and Design

The Battery Testing, Analysis, and Design activity supports several complementary but crucial aspects of the battery development program. The activity's goal is to support the development of a U.S. domestic advanced battery industry whose products can meet electric drive vehicle performance targets. Within this activity, battery technologies are also evaluated according to USABC Battery Test Procedures. The manuals for the relevant PEV and HEV applications are available online. A benchmark testing of an emerging technology can be performed to remain abreast of the latest industry developments. High-level projects pursued in this area include the following topics:

- Cost Assessments and Requirements Analysis.
  - Cost modeling.
  - Secondary and other energy storage use and life studies.
  - Analysis of the recycling of core materials.
  - Requirements analysis for PEVs and HEVs.
- Battery Testing Activities.
  - Performance, life and abuse testing of contract deliverables.
  - Performance, life and abuse testing of laboratory and university developed cells.
  - Performance, life and abuse testing of benchmark systems from industry.
  - Thermal analysis, thermal testing and modeling.
  - Development of new test procedures.
  - Maintenance of current test procedures.
- Computer Aided Engineering of Batteries.
  - development of tools for computer aided engineering of batteries.

The rest of this section lists the projects which were active for the above three key areas during FY 2013.

IV.A Cost Assessments and Requirements Analysis

IV.A.1 Core BatPac Development and Implementation (ANL)

Kevin G. Gallagher, Paul A. Nelson, Shabbir Ahmed & Dennis W. Dees

Argonne National Laboratory
9700 South Cass Avenue
Argonne, IL 60439-4837
Phone: (630) 252-4473; Fax: (630) 972-4520
E-mail: kevin.gallagher@anl.gov

Collaborators:
Ira Bloom, Argonne National Laboratory
Wenquan Lu, Argonne National Laboratory
Dan Santini, Argonne National Laboratory
Fritz Kalhammer, Electric Power Research Institute
Satish Rajagopalan, Electric Power Research Institute
Joe McDonald, U.S. Environmental Protection Agency
Aymeric Rousseau, Argonne National Laboratory
Ram Vijayagopal, Argonne National Laboratory

Start Date: October 2012
Projected End Date: September 2016

Objectives

The objective of this task is to develop and utilize efficient simulation and design tools for advanced lithium-ion batteries capable of predicting precise overall and component weights and dimensions, as well as cost and performance characteristics.

Technical Barriers

The primary technical barrier to commercialization is the development of a safe cost-effective PHEV battery with a 40 mile all electric range that meets or exceeds all performance goals. The major challenge specific to this project is accurately predicting the impact of promising new battery materials on the performance and cost of advanced full-size lithium-ion batteries for transportation applications.

Technical Targets

- Develop model for calculating total battery mass, volume, & cost from individual components.
- Predict methods & materials that enable manufacturers to reach the necessary goals.
- Evaluate the interplay between performance and cost for advanced materials, such as anodes and cathodes, on total battery pack cost.
- Support policy making process of U.S. Government.
- Document and publicly distribute the model.

Accomplishments

- Distribution of BatPaC v2.1 and revised supporting 100+ page report began on November 15, 2012 from the website www.cse.anl.gov/batpac. Over 600 independent downloads have occurred in FY2013 including those by major commercial entities, universities, and laboratories. This is more than double the number of downloads in the FY2012 for the previous version BatPaC v1.1.
- Continued to support the EPA and DOT in refining BatPaC to enable use in the 2017-2025 rule making process for CAFE and GHG regulations. Identified and initiated critical BatPaC development pathway to support mid-term review of rule.
- Continually interacted with EERE-VTO program participants to quantify the effect of materials development on cost. Particular focus was to support the ABR Voltage Fade program.
- Validated critical design parameter target voltage efficiency at rated power by combing a two-time constant performance model into the Autonomie vehicle simulation tool. Heat generation under drive cycle conditions and net-present value of battery was determined for a number of cases.
- Supported the U.S. Competitiveness program, PAINT learning curve initiative, IEA activities, and life cycle analysis for transportation batteries.

✧ ✧ ✧ ✧ ✧

Introduction

The penetration of lithium-ion (Li-ion) batteries into the vehicle market has prompted interest in projecting and understanding the costs of this family of chemistries being used to electrify the automotive powertrain. Additionally, research laboratories throughout the DOE complex and various academic institutions are developing new materials for Li-ion batteries regularly. The performance of the materials within the battery directly affects the end energy density and cost of the integrated battery pack. The development of a publicly available model that can project bench-scale results to real world battery pack values would be of great use. The battery performance and cost (BatPaC) model, represents the only public-domain, peer-reviewed model that captures the interplay between design and cost of Li-ion batteries for transportation applications. Moreover, BatPaC is the basis for the quantification of battery costs in U.S. EPA and NHTSA 2017-2025 Light-Duty Vehicle Technical Assessment. This assessment is then used to determine what mileage (i.e., for CAFE) and CO_2 emission standards are optimal from a cost-benefit analysis.

Approach

BatPaC is the product of long-term research and development at Argonne through sponsorship by the U.S. Department of Energy. Over a decade, Argonne has developed methods to design Li-ion batteries for electric-drive vehicles based on modeling with Microsoft® Office Excel spreadsheets. These design models provided all the data needed to estimate the annual materials requirements for manufacturing the batteries being designed. This facilitated the next step, which was to extend the effort to include modeling of the manufacturing costs of the batteries. The battery pack design and cost calculated in BatPaC represent projections of a 2020 production year and a specified level of annual battery production, 10,000-500,000. As the goal is to predict the future cost of manufacturing batteries, a mature manufacturing process is assumed. The model designs a manufacturing plant with the sole purpose of producing the battery being modeled. The assumed battery design and manufacturing facility are based on common practice today but also assume some problems have been solved to result in a more efficient production process and a more energy dense battery. Our proposed solutions do not have to be the same methods used in the future by industry. We assume the leading battery manufacturers, those having successful operations in the year 2020, will reach these ends by some means.

Establishing the validity of the model calculation is important in justifying the conclusions drawn from exercising the model. The design assumptions and methodologies have been documented and reported in a number of formats. The most notable of those is the 100+ page public report that accompanies the model at the BatPaC webpage. The report and model have been subjected to a public peer-review by battery experts assembled by the U.S. Environmental Protection Agency as well as many private reviews by vehicle original equipment manufacturers (OEMs) and cell suppliers. Changes have been made in response to the comments received during the peer-reviews. The peer-review comments are publicly available. The battery pack price to the OEM calculated by the model inherently assumes the existence of mature, high-volume manufacturing of Li-ion batteries for transportation applications. Therefore, the increased costs that current manufacturers face due to low scale of production, higher than expected cell failures in the field, and product launch issues are not accounted for in the calculation. BatPaC is the only model that has all of the following attributes: freely available, transparent in methodology and assumptions, links performance and cost, and uses a bottom-up approach.

Results

Distribution of BatPaC v2.1. The first version of BatPaC with supporting documentation was distributed on November 1st, 2011. The updated BatPaC v2.1 with improved documentation was released on November 15th, 2012. Since the 2011 release date, more than 1,075 independent downloads have occurred worldwide. The breakdown of these downloads is shown in Figure IV - 1. The majority of downloads took place within the United States. Industrial users, from high profile start-ups to world leading large cap companies, make up the largest percentage of downloads. The registered users in FY2013 were dispersed geographically and organizationally similar to that in FY2012 even though the number of downloads have more than doubled in FY2013. We note that no software lock is placed on the model meaning that once it is downloaded, it may be shared freely. Therefore, the likely number of owners of the model is higher than the number of downloads.

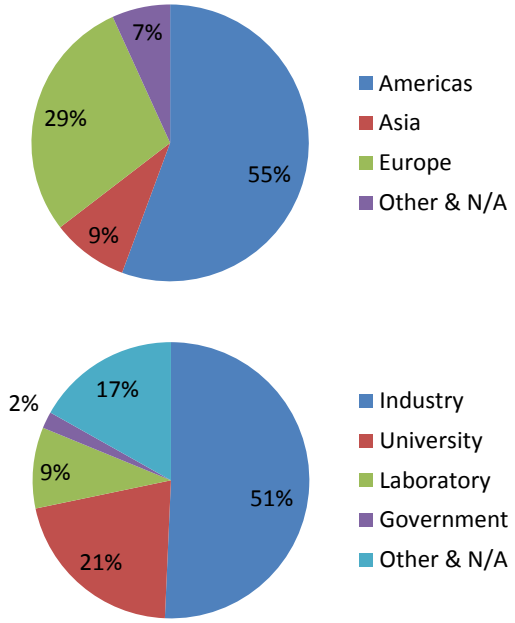

Figure IV - 1: Breakdown of the more than 1075 independent downloads of BatPaC during FY2012-2013

BatPaC v2.1 includes the following improvements over the BatPaC v1.1 model: the addition of air thermal management options, automatic uncertainty calculation, updated heat generation calculation, new parallel connection options, and certain other changes.

Voltage at Rated Power. The appropriate sizing and utilization of the battery is key to making an efficient and cost effective PHEV. Over-sizing results in an increased cost and weight of the vehicle, whereas under-sizing might result in higher fuel consumption and diminished value to the consumer. The difference between the open-circuit voltage (OCV) and the voltage at which a cell achieves the rated power is one of the most important factors in the design of a battery (i.e., the target voltage efficiency at rated power). The designed voltage at rated power has a direct effect on round-trip battery efficiency, heat removal requirements, cold-cranking power, and allowable power fade. To preserve battery power to the end of life, BatPaC designs the battery to produce the initial rated power at 80% of OCV (e.g., [V/U] = 0.8). This provides for meeting the full rated power after a considerable increase in the battery impedance, although at higher current and higher internal heat generation values.

For this study, we considered setting the voltage for full power at 70%, 80%, and 90% of OCV (Figure IV - 2). For the 70%-OCV battery pack, the cost saving of about $100 compared to the battery producing full power at 80% OCV does not appear to warrant the likely reduction in battery life that would result from the increase in the initial battery impedance. At 90% of OCV, the additional cost for the battery for almost doubling the cell area over that required for reaching full power at 80% of OCV is considerable and sets a strong incentive to develop batteries with relatively stable impedance with battery aging.

Heat generation for these batteries was calculated using a two-time constant equivalent circuit model that accounted for changes in state-of-charge and electrode thickness. This model was implemented into Autonomie and used to accurately estimate the heat generation rate during a drive cycle (e.g., US06). The use of a two-time constant model was critical to capture the increase in battery impedance that occurs during a continuous discharge or charge condition due to the concentration gradients that form within the cell. Additionally, we found in preliminary calculations with the Autonomie model that driving at a constant speed of about 65 mph generated as much battery heating as driving on the US06 driving cycle. The high rate of heat generation at constant speed is caused by the increase in the battery impedance with steady discharge. With the results obtained on Autonomie, a method of calculating the battery power required at constant speed was developed for BatPaC v2.1. This method uses the energy requirement for the vehicle on the UDDS cycle (Wh/mile) to estimate the coefficients for rolling friction and aerodynamic drag.

Figure IV - 3 demonstrates that a target voltage efficiency for rated power at beginning of life of [V/U] = 0.8 is a good compromise between the price of the battery and the heat generation within the cell. Higher cell temperatures lead to accelerated degradation mechanisms within the cell and thus a shortened battery life. A [V/U] = 0.8 is the default value of this parameter within BatPaC v2.1.

Towards an understanding of the Li-ion learning curves. Increased production volume is one of most obvious pathways to reduce the cost of batteries for transportation applications. The savings from increased production come from many different areas. First, economies of scale dictate the manufacturing cost does not change in a linear fashion for large changes in production volume. BatPaC accounts for this behavior in each step of the manufacturing process. The capital cost, plant area, and labor requirements are all scaled using a power law equation. The value of the power factor determines the sensitivity of the cost to the change in production volume from the initial baseline manufacturing plant. Additional savings from increased volume come through optimization of the process steps. This optimization results in higher yields as well as higher throughput. These advances are all part of the gains achieved through “sweat and tears” that drive the continuous improvements in a manufacturing environment.

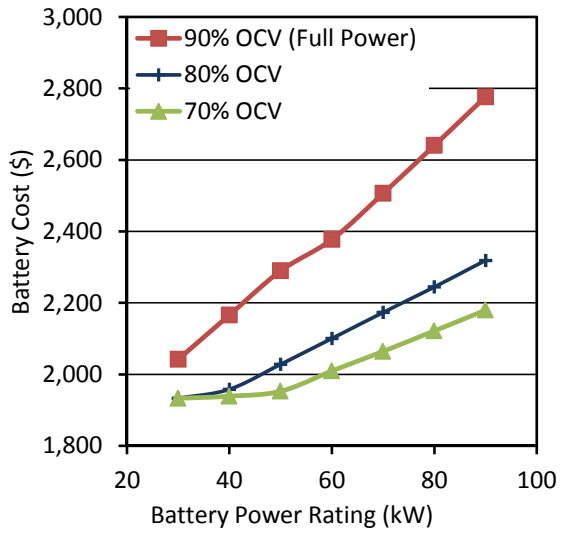

Figure IV - 2: Effects of target voltage efficiency (% OCV) at rated power on total cost to OEM for PHEV10 batteries with LMO-G electrodes and energy requirement of 200 Wh/mile

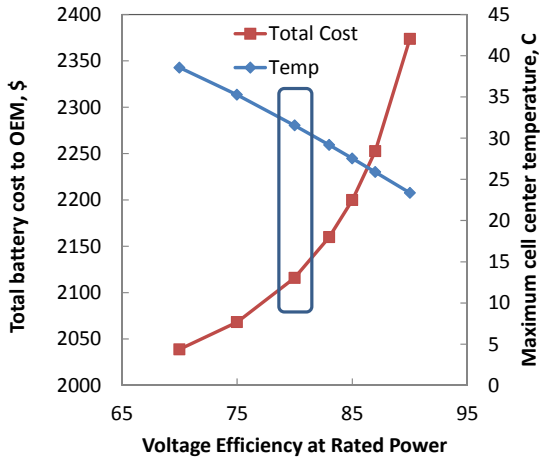

Figure IV - 3: Effects of target voltage efficiency (% OCV) at rated power on total cost to OEM for PHEV10 batteries with LMO-G electrodes and energy requirement of 200 Wh/mile. The secondary axis shows estimated maximum cell center temperature while driving the US06 drive cycle or continuous discharge at 65 mph

A potential learning curve resulting from increased volume and yield improvements is shown in Figure IV - 4. This simplified curve neglects the cost of underutilized equipment and improvements in yield at the individual process step. It only shows the effects of a plant designed to produce the number of batteries in question and the role of cell yield through the formation cycling step. Nevertheless, it is clear how increased production volume and yields lead to significantly lower battery prices to the OEM.

BatPaC assumes that the manufacturing facility produces only the type of battery being studied with the model. In practice, a battery plant will likely produce multiple battery sizes to gain economies of scale and meet customer needs for different vehicle powertrains (i.e., HEV, PHEV, EV). We estimate in Figure IV - 5, an approximation of the savings that may be realized by a plant that combines a mix of batteries into their production line. The key design constraint is to maintain the same geometry of the individual layers that make up the cell. The capacity of the cell can simply be increased by increasing electrode loading (i.e., thickness) and/or stacking additional layers increasing the cell thickness. Utilizing the same coaters, slitters, and stackers will result in significant savings compared to producing these four different batteries on their own equipment. We will build on this estimation to gain a better understanding of flexible manufacturing facilities in FY2014.

As production volumes increase and manufacturers gain more experience, increased rates at the individual process steps will be realized through engineering efforts to improve process center throughput. These increased rates will likely be obtained through design-of-experiments studies that identify optimal operating conditions to maintain yield and reliability even at increased processing rates. In the creation of the BatPaC baseline plant, we have assumed these advances have removed the largest bottlenecks found in contemporary battery production facilities (e.g., improved electrode stacking speed and coater throughput).

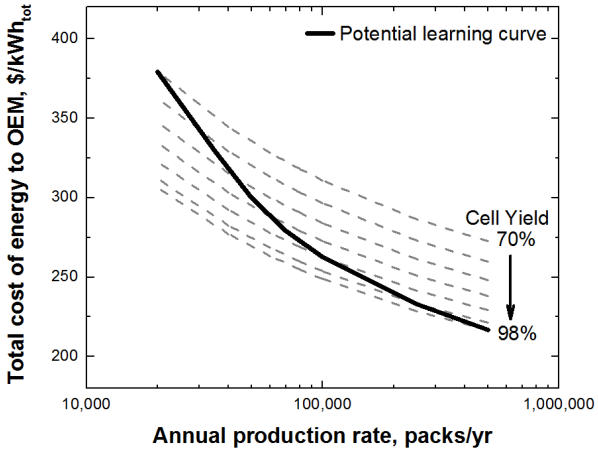

Figure IV - 4: Potential learning curve considering yield improvements in the cell formation cycling step and increased benefits of scale from going to larger production volumes

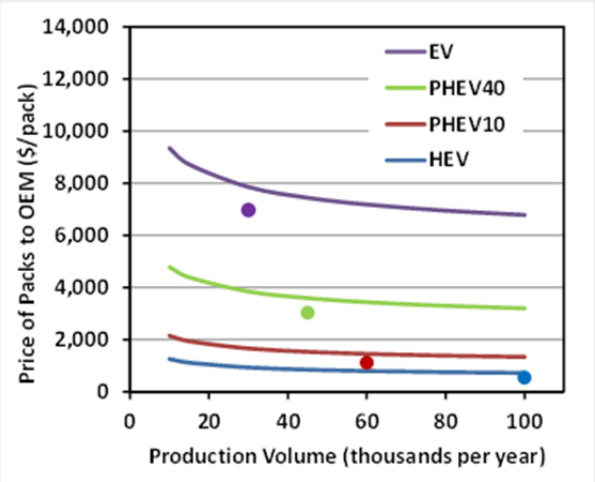

Figure IV - 5: Price to OEMs for battery packs of different types produced in dedicated plants (shown as lines) and in a combined plant with a total production of 235,000 batteries (shown as dots)

Conclusions and Future Directions

The first public distribution of BatPaC began in November 2011 and has since resulted in over 1,075 unique downloads from leading companies, universities and research laboratories around the world. We have successfully supported the 2017-2025 EPA/DOT GHG and CAFE rule making process. An updated version of BatPaC was publically released in mid-November 2012 and includes many value added features.

The target voltage efficiency at rated power, a key design constraint in BatPaC, was validated through a combined BatPaC, electrochemical model, and vehicle simulation to compare heat generation and the net present value of plug-in hybrid electric vehicles. Next year, we look forward to examining the effect of designed electrode thickness and tradeoffs between cost and cycle life. This work will be completed in collaboration with the CAMP group at ANL (formally the Cell Fabrication Facility). The focus of future BatPaC development will continue to be based on meeting the needs of the EPA and DOE-EERE.

FY 2013 Publications/Presentations

1. P. A. Nelson, K. G. Gallagher, I. Bloom, and D. W. Dees “Modeling the Performance and Cost of Lithium-Ion Batteries for Electric Vehicles, Second Edition” Chemical Sciences and Engineering Division, Argonne National Laboratory, ANL-12/55, Argonne, IL USA (2012).
2. K. G. Gallagher and P. A. Nelson “Battery Performance and Cost (BatPaC): Modeling the energy density and cost of Li-ion batteries for use in transportation applications” National Research Council Workshop on Issues in Estimating Costs on Fuel Economy Improvements under Future CAFE regulations, Washington, DC USA, March 27, (2013).
3. K. G. Gallagher and P. A. Nelson “Battery Performance and Cost Modeling” Advanced Automotive Battery Conference, Pasadena, CA USA, February 4 – February 8, (2013).
4. D. J. Santini, Y. Zhou, N. Kim, K. G. Gallagher, and A. Vyas, “Deploying Plug-in Electric Cars Which are Used for Work: Compatibility of Varying Daily Patterns of Use with Four Electric Powertrain Architectures”, Transportation Research Record, 13-4925 (2013).
5. P. A. Nelson, R.Vijayagopal, K. G. Gallagher, and A. Rousseau “Sizing the Battery Power for PHEVs Based on Battery Efficiency, Cost and Operational Cost Savings” Electric Vehicle Systems 27, Barcelona, Spain, Nov. 17-20, (2013).
6. D. J. Santini, T.S. Stephens, N. Kim, Y. Zhou, and K. G. Gallagher “Cost Effective Annual Use and Charging Frequency for Four Different Plug-in Powertrains” SAE 2013 World Congress, 2013-01-0494 Detroit, MI USA, Apr. 16-18, (2013).
7. D. J. Santini, Y. Zhou, N. Kim, K. G. Gallagher, and A. Vyas, “Deploying Plug-in Electric Cars Which are Used for Work: Compatibility of Varying Daily Patterns of Use with Four Electric Powertrain Architectures” 92nd Annual Meeting of the Transportation Research Board, TRB13-4925, Washington, DC USA Jan. 13-17, (2013).
8. K. G. Gallagher “Promises and Challenges of Lithium- and Manganese-Rich Transition-Metal Layered-Oxide Cathodes” DOE Merit Review, Washington D.C. USA, May 13 – May 17, (2013).

IV.A.2 Battery Ownership Model: A Tool for Evaluating the Economics of Electrified Vehicles and Related Infrastructure (NREL)

Jeremy Neubauer

National Renewable Energy Laboratory
15013 Denver West Parkway
Golden, Colorado 80401-3393
Phone: (303) 275-3084
E-mail: Jeremy.Neubauer@nrel.gov

Collaborators:
Eric Wood, Kandler Smith, Aaron Brooker, and Ahmad Pesaran
National Renewable Energy Laboratory

Start Date: FY2009
Projected End Date: FY2014

Objectives

- Identify cost-optimal electric vehicle (EV) use strategies and pathways capable of achieving national oil displacement goals in support of the DOE's EV Everywhere Grand Challenge.
- Evaluate various business models and impact of other factors such as driving patterns, geography, battery wear, and charge profiles using the National Renewable Energy Laboratory (NREL)-developed Battery Ownership Model (BOM).

Technical Barriers

- The economics of plug-in electric vehicles (PEVs) are highly sensitive not only to vehicle hardware and fuel costs, but also to infrastructure costs, driving patterns, all-electric range, battery wear, charging strategies, third-party involvement, and other factors. Proper analysis requires a detailed, comprehensive, systems-level approach.
- The broad range of complex EV usage strategies proposed, including battery leasing, battery swapping, fast charging, opportunity charging, vehicle-to-grid service, battery second use, etc., presents a large number of scenarios to assess.
- Battery life is typically a major factor in the total cost of ownership of EVs, but accurate modeling of battery degradation under the complex and varied conditions of potential automotive use is challenging.
- Economics are highly sensitive to vehicle drive patterns; thus, different drive patterns require different use strategies to minimize cost. Drive pattern data sufficient for economic analysis is also in short supply.

Technical Targets

- Quantify the total cost of ownership of EVs when complex usage scenarios and business models are employed.
- Understand how battery performance, life, and usage affect cost and other engineering parameters.
- Design use strategies that achieve cost parity between EVs and gasoline-powered conventional vehicles (CVs).

Accomplishments

- Analyzed the economics of service providers offering fast charge infrastructure access; found that the total cost to the consumer is similar to that of battery swapping service plans.
- Quantified variations in driver aggression and developed a drive cycle that can be employed to project median aggression vehicle efficiency across multiple powertrains.
- Assessed the impact of climate, cabin heating, ventilating and air conditioning (HVAC), and battery thermal management on EV utility. Identified cabin heating loads as the primary source of utility reduction in cold climates, and saw that the added electrical load of battery cooling systems can offset their reductions in battery degradation.
- Simulated multiple charging infrastructure deployments to investigate their impact on EV utility. Found that level 1 home chargers are nearly as good as level 2 home chargers; work chargers add little to overall utility on average; and when widely available, level 2 public chargers provide nearly as much added utility as DC fast chargers.

✧ ✧ ✧ ✧ ✧

Introduction

The eventual goal of the DOE's *EV Everywhere* Grand Challenge is to have 5-passenger EVs that are on par with convential vehicles based on performance and cost by 2022. Battery cost reduction; widespread charging infrastructure, etc. are essential to meet this goal. Until that happens, the EV market needs to become acceptable to various consumers through differenet business strategies. Wide-scale consumer acceptance of alternatives to CVs such as hybrid electric vehicles (HEVs), plug-in hybrid electric vehicle (PHEVs), and EVs will depend at least in part on their cost effectiveness and their functionality, including driving range and ease of refueling. The present state of technology presents challenges in each of these areas when traditional ownership and usage models are employed. However, a number of advanced technical and business strategies have been proposed to enable the transition to these alternative powertrain technologies, including the electric utility utilization of the vehicle batteries as a distributed resource; battery leasing by a service provider who takes on the risk and upfront cost of battery ownership; public infrastructure development to recharge EVs while parked; fast-charge and/or battery swap stations that effectively extend EV range; and alternative car ownership models that allow users to own a EV but rent other vehicles for long-distance excursions. Each strategy has unique implications to the vehicle design, operating characteristics, and battery life. Accordingly, it can be challenging to compare different system options on a consistent basis to assess their ability to support the consumer adoption of such advanced vehicles.

To address this issue in search of cost-optimal EV use strategies, NREL has developed a computer tool called the Battery Ownership Model (BOM).

Approach

The purpose of the BOM is to calculate the utility and total cost of vehicle ownership under various scenarios of vehicle and component cost, battery and fuel price forecasts, driving characteristics, charging infrastructure cost, financing, and other criteria—including advanced business and ownership models. The vehicle economics that are considered include vehicle purchase, financing, fuel, non-fuel operating and maintenance costs, battery replacement, salvage value, and any costs passed on by a third-party such as a service provider to account for the installation, use, and availability of infrastructure.

Through FY 2012 the BOM was developed to account for real-world daily driving distance distributions, the sensitivity of battery degradation to variances in usage and vehicle design, the cost of an EV's limited range, and the inclusion of service providers providing battery swapping and fast charging services. Studies were completed on the sensitivity of PHEV and EV economics to drive patterns, charge strategies, electric range, and other operational considerations under traditional ownership schemes and when battery swapping service providers were available.

In FY 2013, we applied this version of the BOM to the analysis of a service provider that offered fast charge services. This study closely mirrored the battery swapping study of FY 2012; the results are described briefly below. Subsequently, the BOM received a major overhaul that included addition of the following features:

- Increased resolution of daily travel histories to the individual trip level, including identification of destination type.
- Developed an upgraded EV infrastructure model that considers location of the vehicle and time of day and enables consideration of level 1, level 2, and fast charging, as well as electric roadways.
- Added range estimation algorithms and driver decision criteria to model travel decision choices for EVs.
- Developed models for variable driver aggression to correlate energy consumption rates with trip speed and driver type.
- Upgraded the battery model to account for current, voltage, and thermal response to improve accuracy of driving and charging simulations.
- Added vehicle cabin thermal model, including cabin HVAC systems, and external climate data to better simulate the impact of cabin thermal response on battery temperature and auxiliary loads.

These new capabilities were used to study the sensitivity of vehicle efficiency to driver aggression, develop a drive cycle that consistently represents vehicle efficiency observed in real-world driving across varying degrees of vehicle electrification, and study the impact of climate, vehicle auxiliary loads, battery thermal management, and charging strategies on EV utility.

Results

Fast Charging Study. Using the FY 2012-developed BOM, we assessed the economics of a service provider offering access to fast chargers. This study paralleled the FY 2012 battery swapping study, beginning with identification of likely subscribers and their driving patterns, calculating their service usage

statistics when under a service plan, quantifying infrastructure requirements and service fees for multiple deployment scenarios, and then comparing individual driver economics to traditional ownership scenarios of EVs and CVs.

Our ultimate findings on driver economics are shown in Figure IV - 6. Interestingly, they are nearly identical to those of the battery swapping study, indicating that while an EV operated under such a service plan in a single-vehicle household may likely be more cost effective than direct ownership of an EV, it is unlikely to be more cost-effective than direct ownership of a CV. Although it was expected that the fast charge scenario would improve driver economics due to reduced infrastructure costs relative to the battery swapping case, we found that the longer duration of a range extension event under the fast charge scenario (~30 minutes vs. ~3 minutes) required the service provider to deploy a much larger number of fast charge stations than battery swap stations to provide the same level of range extension availability to its customers. This counteracted the decreased cost of range extension hardware at the per-site level and resulted in nearly identical total infrastructure costs.

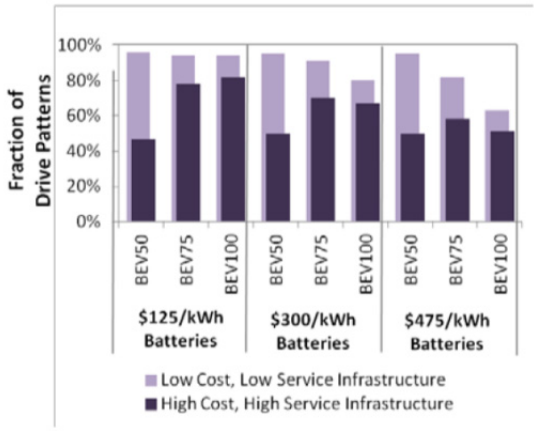

Figure IV - 6: Fraction of driver patterns where a fast charge service plan EV is more cost effective than direct ownership of an EV without fast charger access

Given the similarity in cost, but increased driver convenience of battery swapping, we hypothesize that a battery swapping service plan would be more successful than a fast charge service plan. However, it is unlikely that either option could compete well on a strictly economic basis with direct ownership of a CV.

Driver Aggression. Assessing the potential benefits of HEVs, PHEVs, and EVs is complicated by the driving habits of the operator, as vehicle efficiency is sensitive to driver aggression. Quantifying the impact of driver aggression first requires an understanding of the variation of aggression within large, real-world drive datasets. For this we collected and analyzed 2,154 unique 1- to 2-day-long vehicle records and assessed speed, acceleration, and kinetic intensity statistics.

Next, we applied high-fidelity vehicle simulation to each of these vehicle records and four standard drive cycles of four different light-duty vehicles: a CV, an HEV, a PHEV, and a EV. We found that normalized energy consumption rates can vary substantially around the mean in response to aggression, from -20% to +50%.

We also found that commonly used drive cycles (UDDS, HWFET, LA92, and US06) inconsistently represent various levels of aggression across all four powertrains. For example, in a CV, the fuel consumption predicted by US06 only slightly overestimates the median aggression fuel consumption. However, in an EV, US06 very significantly overestimates the median aggression electricity assumption value. To rectify this issue, we developed the drive cycle shown in Figure IV - 7 that closely predicts median aggression fuel consumption regardless of powertrain type.

Climate, Cabin HVAC, and Battery Thermal Management. Following completion of the FY 2013 updated BOM, we studied the effects of climate, cabin HVAC, and battery thermal management on EV utility. We modeled 10 years of vehicle operation under numerous scenarios as described in Table IV - 1.

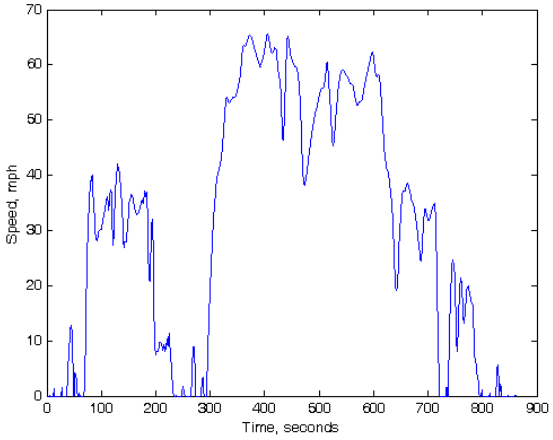

Figure IV - 7: Representative drive cycle produced from 2,154 vehicles using DRIVE

Table IV - 1: Design of experiments for thermal analyses

Parameter	Values Simulated
Aggression	Low, Normal, and High
Climates	Phoenix, AZ; Los Angeles, CA; Minneapolis, MN
Cabin HVAC	No HVAC; A/C + positive temperature coefficient (PTC) heater; A/C + heat pump
Cabin Preconditioning	With and without
Battery Thermal Management	Passive; stand-by electrical heater; key-on refrigerant cooling; key-on and stand-by refrigerant cooling; stand-by refrigerant cooling

Our findings suggest that, in the absence of cabin HVAC loads, variations in climate have little effect on EV utility in year one. However, warm climates can significantly increase battery degradation rates, thereby impacting vehicle utility later in life. Once HVAC loads are considered, we find that the additional demand on the battery from air conditioning and heating systems can notably reduce both year one and year ten utility. PTC heater loads in cold climates have the largest impact; upgrading to a more efficient heat pump based system appears worthwhile.

As we did not see significant decreases in vehicle utility in cold climates due to increased battery resistance, the addition of a stand-by electrical heater to keep the battery warm showed no ability to improve vehicle utility. And while there was room for a battery cooling system to decrease degradation and improve year ten utility, we generally found that the increased load of key-on battery cooling systems had the opposite effect, resulting in slightly decreased utility.

Cumulatively, accurate accounting of trip distributions, driver aggression, climate, and cabin and battery thermal management yielded average utility factors that varied from 83% in the best case to 55% in the worst case (across a sampling of likely EV driver trip histories). The latter value implies that estimates of EV utility that do not account for these effects could be overestimating utility by nearly a factor of 2, thereby stressing their importance in continued analyses.

Charging Infrastructure. We also investigated the impacts of home, work, public, and on-road power transfer on the utility of a 75-mile EV. Our simulations included consideration of level 1 (120V, 15A AC) and level 2 (240V, 32A AC) at-home charging, level 1 and 2 at-work charging, level 1, 2, and 3 (50 kW DC) public charging, and electrified roadway options (see Figure IV - 8). At-home charging considered cases with and without timing restrictions; all other charging scenarios assumed chargers available 24/7. The electric roadway power value was set such that battery state of charge remained constant when on an electrified roadway due to limitations with our available dataset.

Comparisons of at-home charging revealed that level 1 charging, when unencumbered by time-based use limits, yields nearly as much utility as level 2. This implies that level 2 chargers are not a prerequisite for EV ownership and can thereby reduce the total cost to consumers.

Somewhat surprisingly, we also found that the addition of at-work chargers had only a small impact on utility for drivers classified as “commuters,” who were most likely to benefit from the added infrastructure. We hypothesize that this is due to the fact that most long travel days that can benefit from additional charging infrastructure are either not workdays, or that the additional travel is longer than the increase in range provided by a work charger alone.

When we explored pairing level 1 home charging with ubiquitous public charging (but no charging at work), we found that the year 10 achievable VMT could be increased by 1,200 miles, resulting in an average utility factor of 93%. This corresponded to a decrease in average annual tours not taken from approximately 20 to less than five. Interestingly, when public chargers are always available to the EV driver, the additional benefit of access to 50-kW fast chargers over level 2 chargers is marginal.

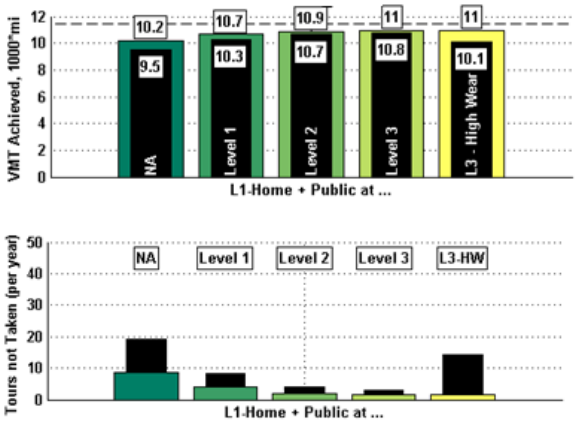

Figure IV - 8: Effect of ubiquitous public charging on achievable VMT and tours not taken

Conclusion and Future Directions

In FY 2013, we made significant upgrades to the BOM to expand our consideration of driver habits, battery thermal response, and auxiliary loads. We applied these new capabilities to study the impacts of driver aggression, climate, cabin HVAC, battery thermal management, and charging infrastructure on EV utility.

These investigations have highlighted the need to improve standard drive cycles and have pointed towards vehicle configurations and charge infrastructure deployments that can optimize EV utility.

In future work, we plan to upgrade our battery model to a multi-cell model, which will enable investigations of the impact of thermal gradients and electrical imbalance within a pack. We will also upgrade our handling of fast charge and battery swapping events, such that we can consider the impacts where such infrastructure is installed. We may consider impact of car-sharing and rentals if resources and times permit.

FY2013 Publications/Presentations

1. Neubauer, Jeremy, and Ahmad Pesaran, "A Techno-Economic Analysis of BEVs with Fast Charging Infrastructure," EVS27, November 2013 (pending).
2. Neubauer, Jeremy, Eric Wood, and Ahmad Pesaran, "Analysis of Range Extension Techniques for Battery Electric Vehicles," DOE milestone report, July 2013.
3. Neubauer, Jeremy, and Eric Wood, "Accounting for the Variation of Driver Aggression in the Simulation of Conventional and Advanced Vehicles," SAE 2013 World Congress and Exhibit, April 2013.
4. Neubauer, Jeremy, and Ahmad Pesaran, "A Techno-Economic Analysis of BEV Service Providers Offering Battery Swapping Services," SAE 2013 World Congress and Exhibit, April 2013.
5. Neubauer, Jeremy, and Ahmad Pesaran, "Analysis on Kinetic Intensity, Climate, Vehicle Ancillary Loads, and Battery Thermal Management," DOE Milestone Report, March 2013.

IV.A.3 PEV Battery Second Use (NREL)

Jeremy Neubauer

National Renewable Energy Laboratory (NREL)
1617 Cole Boulevard
Golden, CO 80401
Phone: (720) 989-1919
E-mail: Jeremy.neubauer@nrel.gov

Collaborators:
Andy Burke, University of California, Davis
Mike Ferry, California Center for Sustainable Energy
John Holmes, San Diego Gas & Electric
Omo Velev, Aerovironment
Byron Washom, University of California, San Diego
Brett Williams, University of California, Berkeley

Start Date: February 2009
Projected End Date: Projected September 2014

Objectives

- Identify, assess, and verify sustainable applications for the second use of plug-in electric vehicle (PEV) lithium-ion (Li-ion) traction batteries after their end of useful life in a vehicle.
- Collaborate with industry through cost-share subcontracts to demonstrate and evaluate the potential of battery second use in real applications.

Technical Barriers

- PEV end-of-service burdens (battery recycling, disposal) could impede PEV deployment. Re-using PEV batteries in secondary applications and delaying recycling can shift these burdens away from the automotive industry.
- Finding suitable second-use applications for the large quantity of used PEV batteries that could become available from automotive markets.
- Assessing the value of post-automotive applications for PEV batteries is challenged by uncertain electrical demands, complex and difficult-to-assess revenue streams, and prohibitive regulatory structures.
- The processes of repurposing PEV batteries are yet to be identified and could have a major impact on the viability of second use strategies.
- Battery degradation in both automotive and post-automotive use is notoriously difficult to ascertain, yet has a strong impact on the potential profitability of secondary use strategies.

Technical Targets

- Identify and demonstrate sustainable second use applications for PEV Li-ion traction batteries.
- Devise optimized use strategies for automotive traction batteries to facilitate their second use, maximizing their value and reducing cost to the automotive consumer and also preventing premature recycling of otherwise useable batteries.

Accomplishments

- Subcontract with California Center for Sustainable Energy (CCSE) and partners has resulted in an in-field test-bed for second-use batteries and has begun testing used batteries in our identified second-use applications to demonstrate viability and quantify long term degradation.
- Constructed an analysis framework for analyzing the second use of advanced automotive batteries, addressing repurposing costs, sale price, automotive discounts, and second use applications.
- Applied the framework to a Li-ion PEV battery second use analysis that has highlighted the need for efficient repurposing strategies, identified a promising market for repurposed batteries, and began to quantify the potential of second use strategies to affect the cost of energy storage to both automotive and secondary markets.
- Discussed partnership with BMW to support and assess deployment of a large pre-commercial stage second-use energy storage system.

✧ ✧ ✧ ✧ ✧

Introduction

Accelerated market penetration of PEVs as targeted by the DOE's *EV Everywhere* Grand Challenge is

presently limited by the high cost of Li-ion batteries. It has been estimated that more than a 50% reduction in battery costs is necessary to equalize the current economics of owning PEVs and conventionally fueled vehicles. Further, both vehicle manufacturers and consumers are concerned about end-of-service costs associated with proper handling of the battery.

One strategy that can positively affect both topics is battery second use – allocating a retired automotive battery to other applications where it may still have sufficient performance to be valuable. By extracting additional services and revenue from the battery in a post-vehicle application, the total lifetime value of the battery is increased. This increase could be credited back to the automotive consumer, effectively decreasing automotive battery costs. Further, it transfers the cost of battery recycling or disposal from the automotive community to the second use industry.

There are several current and emerging applications where PEV battery technology may be beneficial. For example, the use of renewable solar and wind technologies to produce electricity is growing, and their increased market penetration can benefit from energy storage, mitigating the intermittency of wind and solar energy. New trends in utility peak load reduction, energy efficiency, and load management can also benefit from the addition of energy storage, as will smart grid, grid stabilization, low-energy buildings, and utility reliability. The prospect of extremely low-cost energy storage via second use batteries is attractive to these industries.

Approach

This effort investigates the application of used Li-ion PEV batteries to utility and other applications. The major technical barriers to success are second-use application selection, long-term battery degradation, and cost of certifying and repurposing automotive batteries.

To address these barriers, NREL has partnered with a team of hardware providers, utilities, and academic institutions led by the CCSE. This team is a testimony to the interest of industry in second use as it has brought a 50% cost share (amounting to more than $600,000) to the effort with support from the California Energy Commission. Our team has worked collaboratively to perform techno-economic analyses, acquire aged batteries, and set up in-field and laboratory experiments to evaluate the performance and longevity of second use batteries as discussed below. Success of the project is measured by the completion of long-term testing and the determination of used battery value.

Results

Second-Use Battery Availability. To guide subsequent investigation of relevant second-use battery applications and value, it is worthwhile to project the availability and state of health of used automotive batteries. From a detailed Battery Ownership Model analysis, we found that it is generally not economically advantageous for PEV owners to replace their batteries prior to the end of life of the vehicle. Assuming an average vehicle life of 15 years and total battery lifetime of 20 years leaves a conservative 5-year second-use lifetime estimate. Using these values along with a spectrum of PEV deployment scenarios yields the projection of functional second-use batteries in Figure IV - 9. Note that the mean scenario predicts more than 20 GWh of second-use energy storage could be available by 2030.

Stationary Applications Analysis. The preceding projection of used battery availability suggests that an extremely large market must be found to absorb such a large quantity of energy storage capacity. This, along with expected performance capabilities, price levels, and industry trends, motivates investigating stationary storage applications. An assessment of grid-based secondary use applications accounting for the value of service, the expected limitations of repurposed automotive batteries, and the costs of the balance of system necessary to provide said service, suggests that area regulation, electric service power quality and reliability, and transmission and distribution upgrade deferral offer considerable value, as seen in Figure IV - 10.

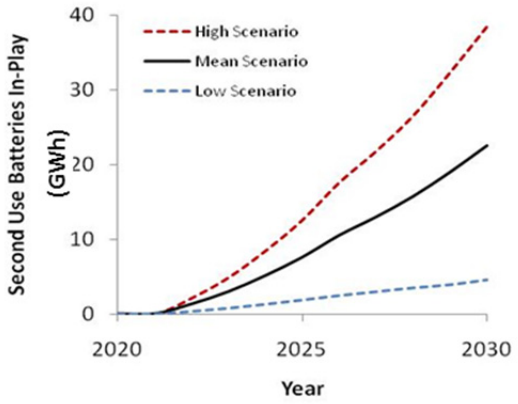

Figure IV - 9: Projected amount of functional second-use battery energy storage available. High, mean, and low scenarios correspond to different PEV deployment rates

Figure IV - 10: Preliminary analysis results show multiple applications that could profitably employ second-use batteries

However, market potential may be an issue for these applications. Area regulation—a service intended to balance the supply of and demand for energy on a relatively fast time scale—is an inherently small market. While the regulation market is expected to change in response to the increased penetration of renewables on the grid, as well as changing consumer load profiles, it is not expected by itself to fully support the supply of used PEV batteries. Power quality and reliability is a high-value end-user market that is well established today (e.g., uninterruptible power supplies) and is growing. While the market is larger than that of area regulation (in terms of GWh) and there are synergies with other behind-the-meter applications, by itself this application cannot absorb the full quantity of second-use batteries expected. Similarly, the projected need for transmission upgrade deferral—using energy storage to reduce peak loads on transmission assets with projected overloads, enabling the upgrade or replacement of such assets to be deferred—is small in comparison to anticipated battery supplies.

While our analysis predicts that these markets are insufficiently deep to support the expected quantity of used PEV batteries available in the long run, they are nonetheless important to study as they may be the first applications targeted by the earliest available second-use batteries. Further, they will potentially play a role in the long run as secondary applications aggregated with some primary application to increase the value that individual storage systems will capture.

Our current expectation is that second-use batteries should be deployed in a distributed fashion with peak-shaving as their primary service, reaping their value from reducing peak power loads on grid assets. Peak-shaving can take place in many forms, be it behind the meter as demand charge reduction, by a utility to reduce generation capacity requirements, etc. Value is generated primarily by reducing or eliminating the need for other, more expensive hardware investments. While this created value is often significantly less than that achievable with the three high value applications discussed previously, this market is much larger and more likely capable of absorbing the quantities of second-use batteries expected.

Repurposed Battery Costs. To assess if second-use batteries can be deployed as peak-shaving assets cost-effectively, it is important to estimate the cost at which a battery can be repurposed and sold. Using a bottom-up approach that considers all labor, capital equipment, facility needs, required rate of return by the operating entity, and many other factors, we calculate the cost of repurposing used PEV batteries as a function of the size of the module being processed and the frequency of occurrence of irreparable cells (cell fault rate). Some example results of this process are shown in Figure IV - 11.

Our results imply that the technician labor and costs of capitol are the most significant cost elements of repurposing activities. These sensitivities have two considerable implications: first, the effect of technician labor rules out the possibility of labor-intensive repurposing operations (such as addressing individual instances of faulty cells). This requires that facilities repurpose modules or packs and creates large variations in repurposing costs due to the interplay of module size and cell fault rate. Efficiencies of scale encourage repurposing larger modules, but larger modules also mean more waste when a faulty cell is identified.

The sensitivity to cost of capital (e.g., return on investment requirements, cost of debt) makes repurposing costs a strong function of the price at which a repurposing facility can sell the repurposed batteries. To address this, we evaluate both high- and low-price approaches.

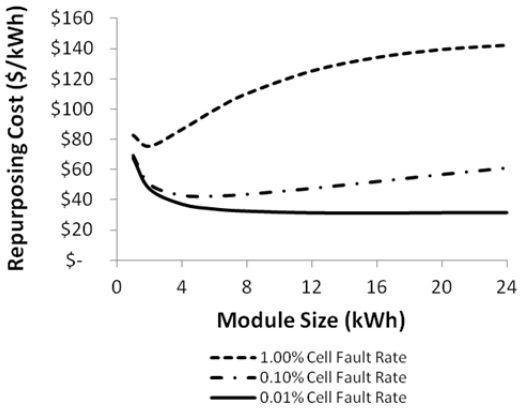

Figure IV - 11: Projected second-use battery repurposing cost for a repurposed battery selling price of $132/kWh

In the high-price approach, we assume that repurposed PEV batteries are priced competitively with newly manufactured Li-ion batteries. Accounting for the anticipated future decline in new battery prices,

degraded battery health at automotive retirement, and a repurposed product discount factor, we can then forecast anticipated repurposed battery sale prices (Figure IV - 12). The possible variations in the aforementioned inputs—particularly for future battery prices—lead to significant uncertainty in the results, but in all cases the expected cost of repurposed batteries to grid or other applications is low.

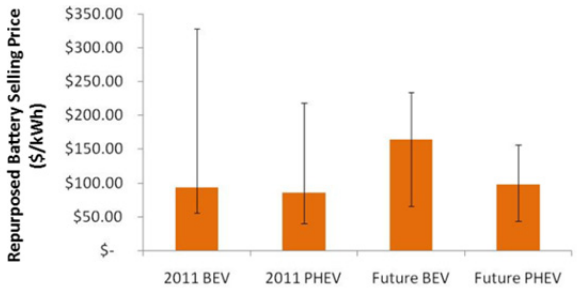

Figure IV - 12: Projected repurposed battery selling price, competitive pricing scenario

Note that the high-cost approach results in a small but not insignificant salvage value for the automotive battery owner in most cases. However, with repurposed battery prices mostly above $100/kWh, it may be difficult to cost-effectively provide peak-shaving services at a large enough scale to consume the number of available used PEV batteries. If a market that values repurposed PEV batteries greater than our calculated selling price, then the use of a competition-based price model is in error.

Alternatively, in the low cost approach, we assume that an overabundance of used PEV batteries is present and seek to calculate the lowest economically feasible repurposed battery selling price (see Figure IV - 13). To do so, we set the used battery buying price equal to the assumed cost of removing the batteries from the vehicle, such that the net cost (value) of second use to the automotive owner is zero. This removes economic disincentives for the automotive owner, minimizes the price paid for batteries by the repurposing facility, and thereby minimizes the repurposing cost and selling price of repurposed batteries.

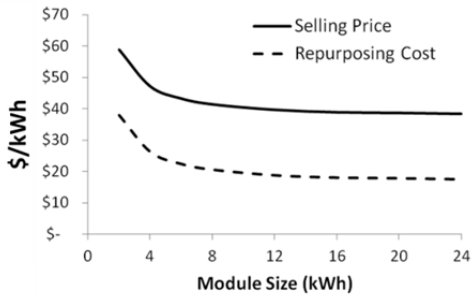

Figure IV - 13: Repurposing cost and repurposed battery selling price for the low cost scenario

We find that the minimum repurposed battery selling price in this scenario is approximately $40/kWh. This is highly encouraging, as it is probable that peak-shaving applications could be performed cost effectively at a large scale when batteries are available at this price point.

Validating Second Use Viability. Based on these findings, it is our anticipation that large supplies of second-use batteries will suppress repurposed battery selling prices until a suitably large market is found that adequately values this resource. We believe this market will be peak-shaving services on the grid. Secondary services, such as area regulation, power quality, power reliability, and asset deferral will likely be paired with this service to increase value (and may serve as primary applications in early second-use battery deployments).

To enable this market for second-use batteries, it is necessary to demonstrate the capability of such batteries to adequately provide these services. In particular, quantifying system response in real-world scenarios and validating the longevity of these batteries in these applications are critical.

To this end, we have acquired numerous aged automotive battery packs spanning multiple Li-ion chemistries, including iron phosphate, nickel manganese cobalt, and manganese oxide cathodes, and graphite, hard carbon, and lithium titanate anodes. Acceptance testing to quantify basic battery performance and state of health has been completed, as have short-term application tests for peak shaving, area regulation, and power reliability services. Furthermore, a long-term field test site on the University of California – San Diego microgrid has also been completed. Control strategies to provide real-time peak shaving services for select sites on campus have been completed, and real-time testing has been initiated. As testing continues, we will begin to assess the degradation characteristics of second-use batteries, and learn more about optimizing deployment strategies for this resource.

In parallel, NREL has initiated laboratory life tests to further characterize second-use battery degradation. Included is a 10-kW pack that has been substantially cycled to an automotive use duty cycle and that has been

disassembled to the cell level. Cells from this pack are being tested individually to provide insight into the variation in degradation across a single battery pack, as well as the response of cells to different duty cycles. Four ~4-kWh modules have also been acquired following extensive automotive cycling to the same state of health, albeit via different conditions (temperatures and number of cycles). A life test has been designed and initiated for these modules to answer the question of whether simple state data or full pack history data are necessary at the point of repurposing to quantify a battery's value.

Conclusions and Future Directions

NREL has created a detailed framework for analyzing the second use of advanced automotive batteries, addressing repurposing costs, sale price, automotive discounts, and second use applications. The applications of this framework to Li-ion PEV batteries has highlighted the need for efficient repurposing strategies, and identified a promising market for repurposed batteries.

The major uncertainty that remains is the longevity of repurposed batteries in post-automotive applications. To address this matter, NREL has acquired aged batteries, developed a long-term field test site and strategy, and initiated long-term testing via a subcontract with CCSE through a 50-50 cost share partnership with industry. NREL has also acquired additional aged batteries for on-site laboratory testing. These efforts will be the focus of continued project work in FY 2014. Additionally, we will be working with Southern California Edison to evaluate the potential of second use batteries in community energy storage applications, and with BMW to demonstrate a pre-commercial second-use battery system.

FY 2013 Publications/Presentations

1. Ferry, Mike, William Torre, Jeremy Neubauer, and Peter Dempster, "Second-Life Applications for PEV Battery Systems: Early Testing to Early – Commercialization," EESAT, October 2013.
2. Neubauer, Jeremy, et al., "Analyzing the Effects of Climate and Thermal Configuration on Community Energy Storage Systems," EESAT, October 2013.
3. Neubauer, Jeremy, and Mike Simpson, "Optimal Sizing of Energy Storage and Photovoltaic Power Systems for Demand Charge Mitigation," EESAT, October 2013.
4. Neubauer, Jeremy, and Ahmad Pesaran, "Uncertainties and Challenges for Battery 2nd Use Strategies," The Battery Show, September 2013.
5. Neubauer, Jeremy, and Ahmad Pesaran, "Analysis of Community Energy Storage as a BEV Battery Second Use Application," 2013 DOE Milestone Report.
6. Neubauer, Jeremy and Ahmad Pesaran, "Analysis and Testing of Plug-In Electric Vehicle Batteries in Second Life Applications," The 30th International Battery Seminar and Exhibit, March, 2013.

IV.A.4 Battery Life Trade-Off Studies (NREL)

Kandler Smith

National Renewable Energy Laboratory
1617 Cole Boulevard
Golden, CO 80401
Phone: (303) 275-4423
E-mail: kandler.smith@nrel.gov

Start Date: FY08
End Date: FY13

Objectives

- Develop physics based battery life prediction models that quantify battery longevity over a range of real-world temperature and duty-cycle conditions.
- Extend cell life models to pack-level, capturing impacts of temperature non-uniformity, cell performance and aging variability on system lifetime.
- Perform trade-off studies to quantify potential battery lifetime extension and cost reduction achievable via advanced systems, controls and operating strategies for electric-drive-vehicle (EDV) battery packs.

Technical Barriers

- Multiplicity of degradation modes (10+) faced by Li-ion battery cells in automotive environment.
- Lack of models and methods to accurately quantify battery lifetime.
- Lifetime uncertainty leading to conservative, oversized batteries in order to reduce warranty risk.

Technical Targets

- 10-15 years battery life for EDVs in disparate geographic environments and duty-cycles.
- Battery lifetime predictive models validated against real-world data with less than 10% error.
- Thermal and other control systems that reduce cell energy content while still meeting 10-15 year lifetime.

Accomplishments

- Developed new life model for the Li-ion graphite/nickel-manganese-cobalt (NMC) chemisty, complementing previous models for graphite/nickel-cobalt-aluminum (NCA) and graphite/iron-phosphate (FeP) chemistries.
- Quantified electrochemical-thermal-mechanical fade mechanisms that accelerate capacity loss and lead to sudden end-of-life.
- Integrated cell-level life model with multi-cell pack electrical-thermal model, creating pack-level life prediction models that reduce the need for expensive pack aging experiments.
- Validated NMC cell- and pack-level aging models under Cooperative Research & Development Agreement (CRADA) with General Motors.

✧ ✧ ✧ ✧ ✧

Introduction

Battery aging behavior directly impacts the degree of EDV battery oversizing needed to achieve desired service life across applications and environments. Eliminating extra cost associated with oversizing would positively benefit market acceptance of EDVs. Automotive batteries face large variability in thermal environment and duty-cycle, with 10+ degradation factors that must be considered to predict lifetime. Worst-case cell aging conditions within a multi-cell battery pack drives the need to oversize battery cell energy content.

Physics-based models describing cell- and pack-level aging processes are needed to support engineering optimization of next generation batteries. Cell life models must capture a multiplicity of degradation modes experienced by Li-ion cells, such as interfacial film growth, loss of cycleable lithium, loss of active material, degradation of electronic and ionic pathways, with dependence on temperature, state-of-charge, depth-of-discharge, C-rate and other duty-cycle factors. Pack-level life models must capture effects leading to non-uniform cell aging, including temperature imbalance, cell performance and aging variability, and interaction with balance of plant systems such as cell balancing.

Approach

In FY13, NREL's exising life model framework developed for NCA and FeP chemistries was extended to the NMC chemisty. End-of-life effects were further studied for the FeP chemistry. Cell-level aging models were coupled to pack multi-cell electrical-thermal models to capture limiting mechanisms inherent in complete battery systems including balance of plant effects.

Cell-level life models were based on the life modeling and regression framework previously developed at NREL. The physics based models capture changes in resistance and capacity with lifetime due to factors such as:

- Side reactions forming electrode impedance films and consuming Li.
- Impedance film fracture and regrowth.
- Lithium plating at low temperatures.
- Binder decomposition at high temperatures.
- Electrolyte decomposition at high temperatures and voltages.
- SEI fracture & reformation.
- Particle & electrode fracture/fatigue/isolation due to electrochemical-thermal-mechanical cycling.
- Separator pore closure due to viscoelestic creep caused by cycling.
- Gas pressure build-up.
- Break-in processes releasing excess Li and enhancing reaction/transport initially at beginning of life.

Surrogate models for above degradation mechanisms are implemented in NREL's software framework to be statistically regressed to cell aging data. The rate of each process is coupled to calendar and charge/discharge duty-cycle in an appropriate manner to properly extrapolate lifetime from accelerated aging experiments. During model development, multiple degradation hypotheses can be proposed, guided by knowledge of cell chemistry and cell teardown experiments when available. Mechanism hypotheses are confirmed/refuted based on regression statistics of model versus data.

Results

Accelerating fade leading to sudden end-of-life. Accurate prediction of end-of-life is the most critical factor for analyses of EDV battery lifetime. Mature Li-ion chemistries typically fade in a graceful manner from beginning through the middle of their lifetime. Nearing end-of-life however, performance can sometimes rapidly degrade depending on the aging duty-cycle. From a database of more than 50 aging tests for a 2.3 Ah FeP cell, Figure IV - 14 highlights 13 such conditions where capacity fade accelerates.

A hypothesized model was developed that attributes the acceleration of fade to a change in mechanism. Early in life, capacity is controlled by available-Li. Late in life, capacity is controlled by remaining electrode-active-sites. Rate laws for loss of electrode-active-sites were developed with dependence on:

- C-rate (intercalation gradient strains).
- Depth-of-discharge (bulk intercalation strains).
- Low temperature (exacerbates Li intercalation-gradients).
- High temperature (exacerbates binder degradation in the composite electrode).
- Temperature swings with cycling (causing stress due to differential thermal expansion of components).

Figure IV - 15 shows good agreement of the life model compared to experimental data. Further details are given in [1,2]. At room temperature 1C cycling, the model predicts

- 83% of capacity fade is caused by cycle depth-of-discharge (bulk intercalation strains).
- 13% of capacity fade is caused by particle fracture due to C-rate (intercalation gradient strain).
- 4% of capacity fade is caused by temperature swings encountered by the cell.

These conclusions, to be further investigated in future studies, provide guidance as to the relative importance of different mechanical-coupled fade mechanisms in Li-ion cells.

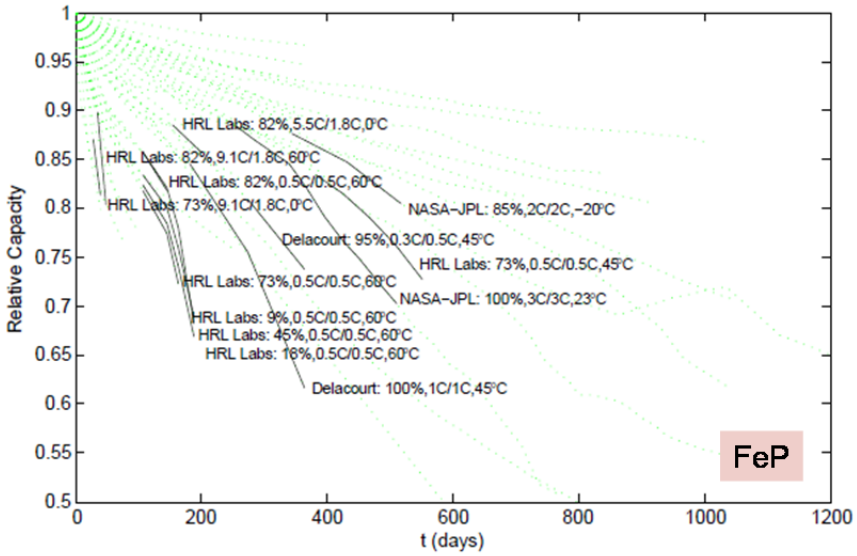

Figure IV - 14: Aging test conditions with apparent sudden acceleration in fade rate nearing end-of-life. Labels indicate the data source, percent depth-of-discharge, discharge & charge C-rate, and temperature

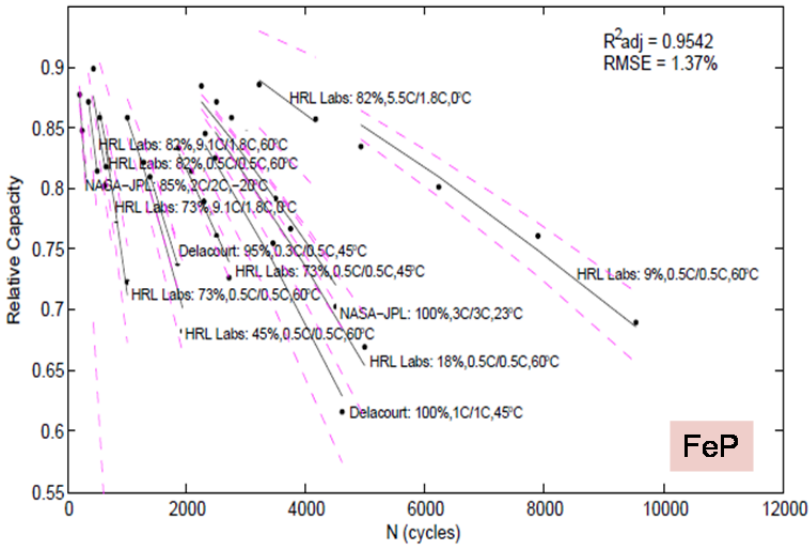

Figure IV - 15: Comparison of experimental data (symbols) with life model predictions (solid black lines) and 95% confidence intervals (dashed purple lines)

Pack-level NMC life prediction. In addition to cell-level aging effects, lifetime of EDV batteries is also impacted by pack-level effects. For accurate life prediction, it is important to capture factors that contribute to non-uniform aging of cells in a multi-cell pack. These include the effect of temperature gradients within the pack and cell non-uniform aging processes.

In FY13, NREL combined previously developed cell and pack models to create a pack-level life prediction tool. The tool was validated using proprietary data shared by GM under a CRADA. First, a cell-level life model was regressed to aging data for a NMC chemistry Li-ion cell. Next, a cell electrical circuit model was regressed to HPPC data for the same cell and linked to the life model to describe cell performance changes with aging. A pack thermal model was regressed to pack thermal characterization experiments, capturing cell heat generation with drive cycle and heat dissipation through passive and active cooling paths.

Shown in Figure IV - 16, the cell life and electrical models were linked with the pack-level thermal/electrical model to create a predictive tool for

pack-level lifetime. The model-based process greatly reduces the need to run pack-level aging experiments, saving substantial cost from the battery engineering development process. The proprietary NMC pack life models are being implemented in NREL's Battery Ownership model to enhance the fidelity of future technoeconomic analysis of EDV batteries.

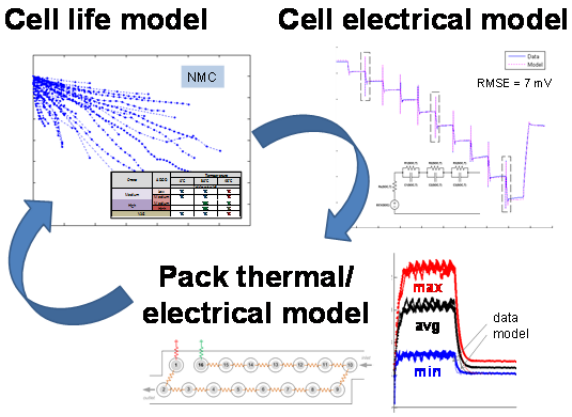

Figure IV - 16: Integrated models for battery pack-level life prediction

Conclusions and Future Directions

In FY13, previously developed life models and framework were enhanced to capture

- End-of-life effects, namely accelerating fade driven by electrochemical-thermal-mechanical coupled processes.
- NMC chemistry cell lifetime, complementing previously developed models for NCA and FeP chemistries.
- Pack-level degradation processes including temperature non-uniformity and cell performance and aging variability.

These life models directly support NREL analysis on cost-of-ownership for EDV consumers and fleets, battery 2nd use technoeconomic analysis, thermal management and balance of plant design. The life models are also being applied in ARPA-E AMPED projects developing battery prognostic controls (with Eaton Corporation) and an active balancing system that seeks to eliminate non-uniform cell aging and life extension for multi-cell battery packs (with Utah State and Ford). Versions of the NREL life models have been licensed to external industry and academic partners.

Pending opportunities, future work may enhance the models' descriptions of cell electrochemical-thermal-mechanical degradation processes and integrate the life models with commercial battery computer-aided engineering software.

FY2013 Publications/Presentations

1. K. Smith, J. Neubauer, E. Wood, M. Jun, A. Pesaran, Models for Battery Reliability and Lifetime: Applications in Design and Health Management, Battery Congress 2013, Ann Arbor, MI; April 15-16, 2013. NREL Report No. PR-5400-58550.
2. K. Smith, J. Neubauer, E. Wood, M. Jun, A. Pesaran, SAE World Congress, Detroit, MI; April, 2013.

IV.A.5 PHEV Cost Effectiveness and Life-Cycle Analysis (ANL)

Danilo J. Santini, J. Dunn, and A. Rousseau

Argonne National Laboratory
9700 South Cass Avenue
Argonne, IL 60439
Phone: (703) 678-7656; Fax: (630) 252-3443
E-mail: dsantini@anl.gov

Subcontractor:
Electric Power Research Institute (2006)

Project Lead: Argonne

Partner: IEA HEV Implementing Agreement

Start Dates: 2001 IEA HEV
October 2006-09 (EPRI)
Projected End Date: ongoing

Objectives

- Examine Li-ion electric drive battery chemistries.
- Evaluate Li-ion options for AEVs, ER-EVs, PHEVs, & HEVs with parallel, split & series powertrains.
- Determine cell power and energy cost trade-offs, by chemistry (for 6 chemistries).
- Determine best electric drive system attributes to maximize U.S. electricity-for-gasoline substitution, and fuel use reduction, including HEVs.
- Estimate representative real world fuel & electricity use by electric drive vehicles.
- Determine likely early U.S. market for plug-in electric drive vehicles.
- Estimate WTW emissions and energy use by electric drive vehicle type and pattern of use.
- Work with the IEA HEV& EV Implementing Agreement to disseminate, reevaluate, and revise study results in an international context.

Technical Barriers

This project addresses the following technical barriers in the choice of battery chemistry and battery pack configuration in support of maximum market success of electric drive.

A. Initial costs of providing various mixes of power and energy in plug-in hybrid (PHEV) and electric vehicle (EV) batteries.

B. Establishing a cost effective balance/mix of mechanical and electric drive in PHEVs.

C. Achieving battery life cycle net benefits, given probable U.S. gasoline prices, considering trade-offs among:
   - Initial cost.
   - Cycle life.
   - Calendar life.
   - Energy and power densities.

Technical Targets

- Maximization of net present value benefits per kWh of grid electricity used. Evaluate chemistries, powertrains, pack kW and kWh, by target market niche.
- Determination of cost effectiveness of battery power and kWh energy storage relative to other powertrain costs and charging infrastructure costs
- Determination of fuel saved per kWh used during charge depletion, by chemistry and powertrain type.

Accomplishments

- Hosted the 38th Executive Committee (ExCO) meeting of the IEA-HEV-IA and meetings of Task 1, 17 and 19 (April 2013).
- Participated in three workshops (in Braunschweig, Germany, at ANL, and at Davos, Switzerland) and co-authored presentations/publications with other task members for Task 15 on plug-in hybrids and Task 19 on life cycle assessment of EVs (initiated in March of 2012).
- Contributed to the compilation of a database of EV LCA studies containing more than 60 studies.
- On October 22, a joint Task 10 and Task 15 Workshop on Batteries at Extreme Temperatures was held in Montreal Canada, arranged primarily by the Task 10 Operating Agent Jim Barnes. D. Santini attended the workshop on behalf of Task 15.
- Task 15 on Plug-in Hybrids was nearly completed.
- Two additional SAE World Congress Papers were prepared.
- A paper using annual vehicle use data for the metro Atlanta area was submitted for consideration for publication in the Annual

Transportation Research Board Meeting in January 2013.

✧ ✧ ✧ ✧ ✧

Introduction

The market into which the various kinds of battery packs will "fit" (powertrain type, charge depletion strategy, vehicle size and function, driving behavior of probable purchasers, charging costs and availability) have been thoroughly investigated. Reasons for reconsidering and/or adjusting multiple existing technical targets have been discovered. In earlier years, this project focused on accurate estimation of battery pack costs by chemistry. In 2012, the focus was on simulation of a large number alternative plug-in electric hybrid powertrains of various types (parallel, input-split, output split, series) using battery packs with differing peak kW and kWh. Last year's progress report discussed cost effectiveness results obtained in the January 2013 Transportation Research Board (TRB) paper, which had been originally prepared and submitted in August of 2012.

Approach

This year's progress report presents an altered perspective, based on total cost of ownership (TCO) estimates obtained in two additional papers prepared subsequent to the TRB paper. TCO is a different methodology than cost effectiveness. Last year's TRB paper focused only on everyday intra-urban driving, and particularly on vehicles commuting to work, which are about a third of the vehicle population. The TRB paper ignored use of vehicles in intercity travel. The SAE TCO paper considered consumer preferences for intercity travel. It was assumed that the pure AEV would not be used on intercity trips, due to very short range in Interstate highway driving. Costs of use of a substitute gasoline car were considered. Also, though no paper was produced, TCO analyses of prior EPRI vehicle simulations were also internally examined using an approach consistent with the SAE paper.

This year results for incremental costs of powertrain components were separated into battery cost effects and "other" effects (electric machines, inverters, cables, engine size changes, etc.) (see Figure IV - 17). This separation showed that for PHEVs and ER-EVs, powertrain costs other than the battery pack are relatively more important than they are for EVs. ER-EV cost penalties, which were significant, are driven by the cost increase of other components, due to higher kW. Cost of adding kW for the ER-EV battery pack was relatively small.

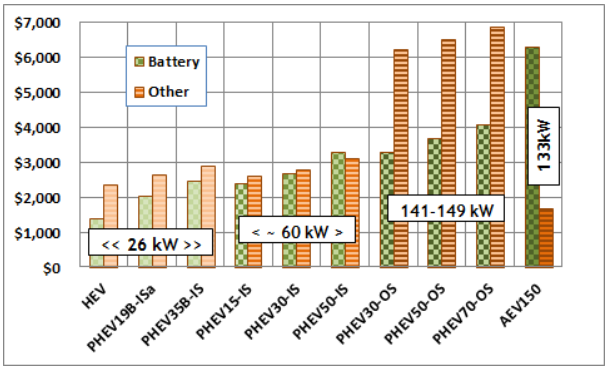

Figure IV - 17: Contributions to increment in PEV price over CV: battery vs. other powertrain changes

Results

International Energy Agency (IEA) activities. [Note: In this progress report and the final report, the term E-REV or EREV will be changed to ER-EV. This term applies to any vehicle that can operate all-electrically in all conditions when charge depleting, then use a gasoline engine to extend range, however accomplished. It is an "Extended Range Electric Vehicle". In the Task 15 study the umbrella of this term covers both the input-split powertrain cases and the series powertrain cases. Inconsistencies with prior labels are noted, as necessary. The term AEV (all electric vehicle) is used in Task 15 discussion instead of EV or BEV. IEA Hybrid and Electric Vehicle Implementing Agreement (IEA-HEV-IA) Task 17 & 19 continue to use EV.]

In April of 2013 Argonne hosted the 38th Executive Committee (ExCO) meeting of the IEA-HEV-IA and also hosted meetings of Task 1, 17 and 19 of this Agreement.

During FY 2013, in addition to its continued participation in Task 15 on PHEVs, this project continued its new responsibility for participation in Task 19 on life cycle assessment of EVs (initiated in March of 2012). Jennifer Dunn was the lead Argonne participant. In FY 2013 ANL staff participated in three workshops and co-authored presentations/publications with other task members.

The first workshop, "LCA Methodology and Case Studies of Electric Vehicles" (20 attendees) was in Braunschweig, Germany on December 7, 2012. Key methodological issues in electric vehicle LCA were addressed by reviewing both theory and case studies. Methodology discussion focused on electricity generation mix and pros and cons of using attributional vs. consequential LCA approaches. Proper treatment of co-products was discussed. Recommendations of the ISO 14040 and 14044 standards for LCA were judged rigid and deficient. Other topics were market and

charging technological uncertainty, policy impacts, and baseline reference points. ANL's A. Elgowainy gave two presentations, one on LCA at ANL and another on ANL evaluations of PHEVs.

The April workshop at Argonne, titled "Vehicle and Battery Production in LCA of Electric Vehicles," had 28 attendees from four countries (United States, Germany, Austria, and Switzerland). Industry, academic, and government researchers participated. State of knowledge, best practices, available data, and data gaps for key steps in EV LCA were discussed. J. Dunn and K. Gallagher gave presentations, and Gallagher hosted a group tour of Argonne's battery R&D facilities. It was agreed that battery assembly and cathode material preparation remain key areas for more in-depth research, but steel, copper and aluminum do not. Dunn was invited to be the Vice Operating Agent for Task 19.

The workshop "Recovery of Critical Metals from Vehicles with an Electric Drivetrain," was held in Davos, Switzerland on October 9-10, 2013. Though travel restrictions prevented Linda Gaines from attending, her presentation "Can Automotive Battery Recycling Help Meet Critical Material Demand?" was delivered by the Task 19 Operating Agent Gerfried Jungmeier.

Fulfilling an objective of Task 19, Argonne has contributed to the compilation of a database of EV LCA studies containing more than 60 studies.

On October 22, a joint Task 10 and Task 15 Workshop on Batteries at Extreme Temperatures was held in Montreal Canada, arranged primarily by the Task 10 Operating Agent Jim Barnes. D. Santini attended the workshop on behalf of Task 15.

During FY 2013 Task 15 on Plug-in Hybrids was nearly completed. In Nov. 2012 a joint paper by German, French and U.S. Task Experts was presented at the European Electric Vehicle Congress in Brussels. Two U.S. focused spin-off papers making use of Task 15 vehicle simulations and powertrain cost estimates were written and presented, one at the Transportation Research Board Meeting in January and one at the SAE World Congress in April. Since it was close to completion, Task 15 contributed the longest project description among all active Tasks in the 2013 IEA-HEV-IA Report. A draft Task 15 summary report was delivered by Operating Agent D. Santini at the 38th Meeting of the IEA-HEV-IA ExCO, also in April. This purely text write-up was similar to the extended discussion of Task 15 findings published in the IEA-HEV-IA Annual Report. A discussion of selected findings from the SAE World Congress paper on Total Cost of Ownership of various plug-in vehicles was written for a later IEA-HEV-IA website report on recent Task 15 activities. Toward the end of FY13, in preparation for the November 2013 39th Meeting of the IEA HEV ExCO in Barcelona, D. Santini worked on a final edit of the Task 15 report, incorporating several figures.

Two additional SAE World Congress Papers were prepared. One made use of data on commercially available U.S. PHEVs and EVs, as well as a diesel, a dedicated natural gas vehicle, and a fuel cell vehicle. This paper examined fuel savings and GHG emissions reductions of plug-in vehicles as a function of average speed driven, finding that savings tended to be relatively constant when expressed on the basis of hours of operation. This paper also illustrated that all electric operation of plug-in vehicles, when powered via renewable electricity, would result in about twice the miles of service that would otherwise be obtained if that electricity were instead used to produce hydrogen via electrolysis for use in a fuel cell vehicle. The third SAE Congress paper addressed the value of battery pack power for capture of regenerative braking energy. Using Argonne's Advanced Powertrain Test Facility data it demonstrated that regenerative braking-energy-capture benefits exist for battery pack power levels up to about 60 kW, but there was essentially no regenerative braking energy benefit of higher battery pack kW.

Finally, a paper using annual vehicle use data for the metro Atlanta area was prepared and submitted for consideration for publication in the Annual Transportation Research Board Meeting in January 2013. This paper provided evidence that the daily distance market segment from the SAE TCO paper where AEVs could be the least cost solution is a very small market niche. In other words, even though the SAE TCO paper found a market niche at $5.00/gallon gasoline where a future unsubsidized EV used only within a metro area would be least cost (high daily driving distances, frequent daily use), the investigation of one metro area (Atlanta) implied that the niche was far smaller than implied by the single day National Household Travel Survey data, which had been used in the prior SAE TCO paper.

Examine Li-ion electric drive battery chemistries. Prior years of analysis had indicated that the LMO-G chemistry was least cost, but that NMC-G was next lowest for battery packs with high energy to power ratios, while also having superiority to LMO-G in Wh/l and Wh/kg. When estimating costs of plug-in vehicles for IEA-HEV-IA Task 15, German country experts chose to use NMC-G, while U.S. country experts used LMO-G. It is understood that a blend of these two chemistries is often being used in practice.

Evaluate Li-ion options for EVs, ER-EVs, PHEVs, & HEVs with parallel, split & series powertrains. The collective implications from the Task 15 papers is that plug-in hybrids with about 60 kW of peak battery pack power and 5-10 kWh of energy storage capacity will be long-term least TCO

alternatives should gasoline prices rise by about 40% ($5.00/gallon) (see Figure IV - 18). A shortcoming of the analysis is that no 60 kW HEV has been evaluated, but the cost trend in the SAE TCO paper implied increasing TCO as evaluated PHEV pack kWh dropped toward that found in HEVs. Nevertheless, an HEV with 60 peak battery pack kW should be examined to confirm this trend. The cost trends when adding power in HEVs should be determined. Although several powertrain architectures have been investigated, there is not a basis for choosing among them, since there has been no evaluation of the four candidate powertrains for PHEVs holding peak pack power constant at 60 kW, each with energy storage capability from 5-10 kWh.

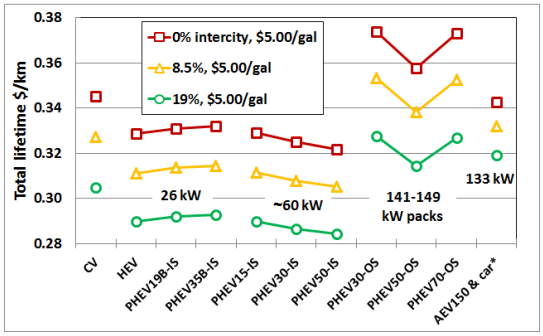

Figure IV - 18: TCO for one assessed market niche, considering intercity driving at 8.5% and 19% of annual miles. IS = input split, OS = output split. B = blended charge depletion. AEV = all electric vehicle. Range predictions are miles

Determine cell power and energy cost trade-offs, by chemistry. Prior papers on this topic imply important nonlinearities in properties of battery packs, largely having to do with the transition from high power to high energy packs. For high power packs, electrodes are typically thinner than present manufacturing tolerances will allow. Adding energy involves only adding electrode thickness, while copper, aluminum and steel content remain relatively constant. This allows a rapid drop in costs for a transition from HEV power packs to PHEV energy packs (see Figure IV - 19). However, this is limited by allowable electrode thickness, and there are also nonlinear diminishing returns in benefits from added electrode thickness. Once the electrode thickness limits are reached, adding more energy storage capability to the pack involves adding more aluminum, copper and steel. Consequently, the rate of decline of $/kWh cost is much less as one moves from PHEV to AEV.

Determine best electric drive system attributes to maximize U.S. electricity-for-gasoline substitution, and fuel use reduction, including HEVs. Considering the role of international investigations in this study, the question is whether U.S. results discussed under objective 2 are robust across nations. Despite much lower gasoline prices in the U.S., the collaborative study concluded that the only market niche where an input-split plug-in hybrid with 30 km of range was the best solution (longer annual driving distances) was in the U.S. (See Figure IV - 20.)

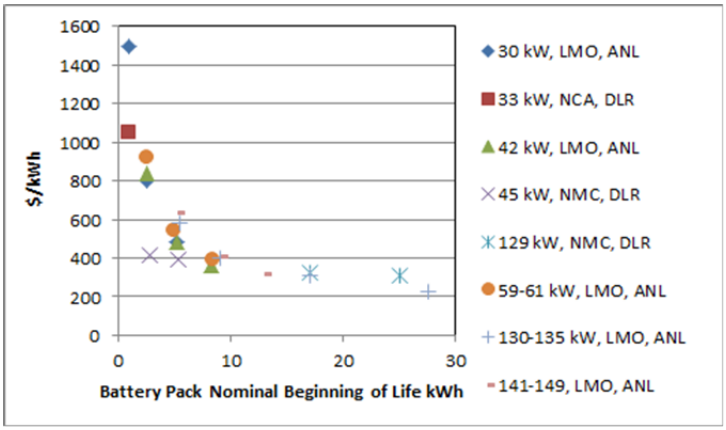

Figure IV - 19: ANL and DLR Estimates of beginning of life battery pack cost per kWh, by peak pack kW and chemistry

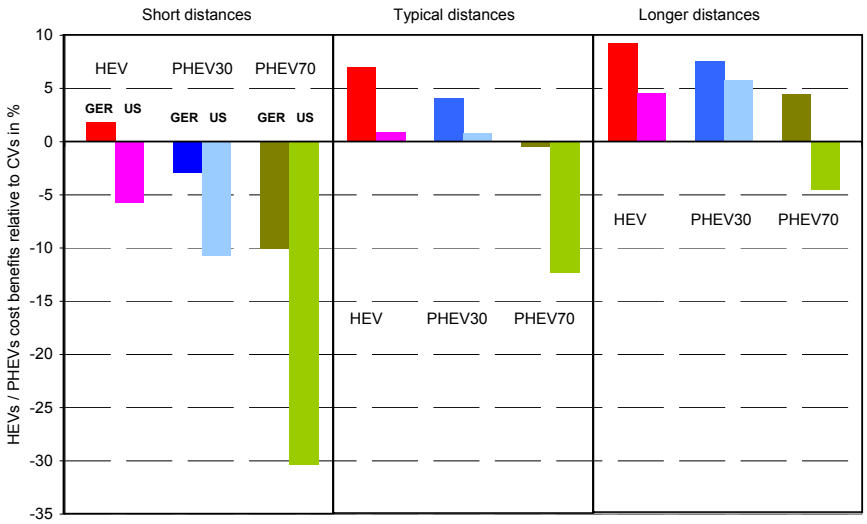

Figure IV - 20: Percent improvement of PHEV ownership cost (TCO) vs. conventional vehicle, by drivetrain and distance (range predictions are km). Vehicle labeled PHEV70 is a series ER-EV; PHEV30 is an input split PHEV

The differences in the U.S. and European results call into question the robustness of the U.S. results discussed for objective 2. This result suggests further collaborative investigation is desirable to better understand reasons for differences. The European cost estimates also were considerably more optimistic for the series powertrain. Ideally, a more comprehensive cross comparison will be done if a new phase of Task 15 can be agreed to. As in the multiple annual distances evaluated above, details in the SAE TCO paper also indicate that HEVs with 26 kW peak battery pack power are often the least cost solution when daily driving is not adequate to make effective use of PHEV battery pack capabilities. Above average vehicle use is necessary for financial viability of early PHEVs, given present gasoline prices and projected battery costs.

Estimate representative real world fuel & electricity use by electric drive vehicles. One of the interesting attributes of the study was its investigation of PHEVs with different levels of power. The PHEVs simulated by IFP Energies Nouvelles used a parallel powertrain and had a low battery pack power of 30 kW and high of 42 kW. PHEVs simulated by Argonne with the input split powertrain used power levels of 26 kW and 60 kW. Inspection of the fuel consumption estimates on limited access highways implies that the charge depleting gasoline fuel consumption increased by an order of magnitude with a drop from peak battery pack power of 40 kW down to 26 kW (see Figure IV - 21). At 60 kW U.S. highway gasoline consumption for the input split was zero, but for the European case (higher top speeds) it was about the same as for the 40 kW parallel PHEV. Clearly, if all electric highway operations capability is desired, adequate battery pack power must be provided. A drawback of the 26 kW input split case was very long distances to charge depletion, which can reduce the amount of times per 100 miles that such a vehicle can be depleted and recharged. To illustrate that highway energy consumption is much different than urban and suburban/rural driving, two figures were constructed showing the distance to depletion in the three different driving conditions. The U.S. figure is provided here.

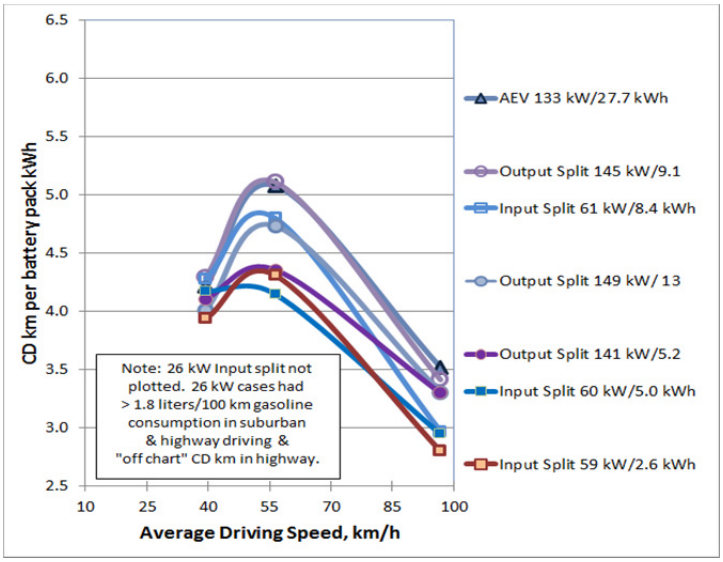

Figure IV - 21: Estimates of charge depleting km achieved per kWh of battery pack on three U.S. "on-road" driving cycles, for 7 powertrain simulations

The plots suggested that suburban/rural driving might be the most efficient, allowing longer all electric operations range for PHEVs with adequate battery pack power. The plots also illustrate that the range of an EV drops sharply in highway driving, helping analysts understand the reasonableness of assuming that gasoline vehicles would tend to be chosen instead of EVs for long distance intercity trips.

Determine likely early U.S. market for plug-in electric drive vehicles. Last year's report highlighted the fact that the least cost implementation of PHEVs is in the suburbs, where dwelling units with garages with existing electrical service are commonly found. The Workshop on Batteries at Extreme Temperatures included reporting on field tests that have demonstrated that climate controlled garages lead to more efficient real world operation of HEVs, which is likely to translate to PHEVs, ER-EVs and EVs as well. In this year's report we highlight that the driving patterns of the suburbs *may* also represent the most efficient all-electric operations in terms of kWh/mile consumed. While the zero tailpipe emissions and quiet operations attributes of plug-in vehicles makes them intuitively attractive for use in core cities, more limited days and miles of use and fewer garages or dedicated overnight parking spots with electrical service significantly damages their financial viability.

Estimate WTW emissions and energy use by electric drive vehicle type and pattern of use. The papers completed by participating country experts and institutions used multiple methods of estimating net emissions and energy use. This was consistent with the interim findings of Task 19 that it is important for issues in estimating electric generation mix for LCA analyses to be addressed. In light of the variety of methods chosen by participating experts, Task 15 guidance for Task 19 is that it may be desirable to consider the "consequential" LCA approach, allowing for uncertainty and considering alternative scenarios and perspectives. One perspective investigated by Santini and Burnham in an SAE Congress paper was to start with the fuel resource and compare alternative technological pathways to vehicle miles of service creatable by the original feedstock.

From this perspective, for natural gas, it was estimated that the two plug-in vehicle options evaluated had the lowest full fuel cycle GHG emissions and annual energy use. The most dramatic illustration is that conversion of a given amount of natural gas to diesel fuel to support operations of diesels would result in far less vehicle miles of service provided. Alternatively, as Figure IV - 22 illustrates, for the same amount of annual miles of service, far more GHGs and energy use would result. Another illustration (not shown) was that a given amount of (renewable) electricity would provide about double the miles of service if used via batteries to provide all electric operation, than if it were used via electrolysis to produce hydrogen used by a fuel cell vehicle.

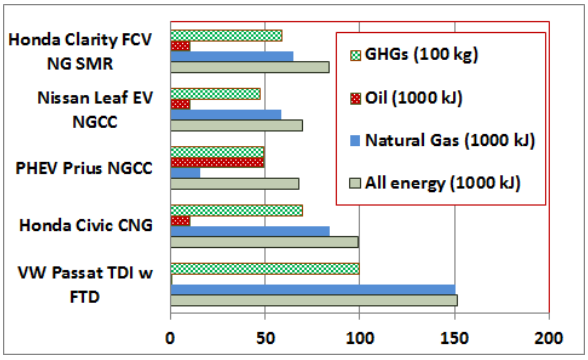

Figure IV - 22: Natural gas to vehicle distance pathways – annual energy use and GHG emissions

Work with the IEA-HEV-IA to disseminate, reevaluate, and revise study results in an international context. The IEA-HEV-IA collaboration has been very valuable. Consensus findings of the study participants carry more weight than would any single paper alone. The Task 15 findings have begun to be disseminated, with an extensive write up in the 2012 IEA-HEV-IA annual report. By adding figures (several shown here) to the Task 15 report text, a more informative report will be created for future dissemination on the IEA-HEV-IA website. At the close of FY 2013, the Task 15 Operating Agent D. Santini and Vice Operating Agent A. Rousseau were arranging to disseminate Task 15 results at Electric Vehicle Symposium 27, to be held in Nov. 2013 in Barcelona Spain. A proposal for a second phase of Task 15 was made at the IEA-HEV-IA ExCO meeting at Argonne in April and was to be repeated, along with a presentation of the final report's figures, at the Nov. 2013 IEA-HEV-IA ExCO meeting in Barcelona, Spain. The final report will include a list of topics meriting reevaluation and/or revision (some discussed herein), should a new phase of Task 15 begin.

Conclusions

Appropriate evaluation of the financial merits of electric drive requires prediction of the driving and charging behavior of most probable owners. The near-term target market for personal light duty HEVs, PHEVs, ER-EVs and EVs is the suburbs, for consumers who drive more than average. The last two years of R&D indicates that the near term, Li-ion based plug-in electric drive "sweet spot" is for PHEVs designed to reliably deplete all electrically in nearly all driving conditions, using engine power only for unusual atypical bursts of acceleration. PHEVs with a combination of 60 kW of peak battery electric power and energy storage of 5-10 kWh should represent the best mass market PHEV design strategy. This finding implies that any alteration of U.S. battery pack subsidies adopt a 5-10 kWh window, and include a minimum battery pack peak power level of about 60 kW. PHEVs with these pack attributes will have superior charge sustaining (CS) fuel efficiency in comparison to ER-EVs (due to excessive ER-EV pack mass), and also superior to blended mode PHEVs (due to inadequate pack power) enabling lower cost of operation than either in such CS driving.

Due to shrinkage of range when on limited access highways, the EV market (for EVs with 20-24 kWh packs designed for the mass market) is limited by its inability to serve vacation travel at high speed on Interstate highways, even with fast charging. For consumers who have no desire or need to use EVs in this fashion, a very intensively driven EV could be a more financially desirable option than a PHEV, but only if pack life equivalent to vehicle life can be assured. Last year, it was stated that in the event of significant gasoline price increases, the EV can begin to find a small niche where it should have lowest TCO/m (50-100 miles/day of daily driving, infrequent, short distance vacation travel). This year, an examination of Atlanta data on annual vehicle use suggests that this market niche is vanishingly small. Very few vehicles are consistently driven this far each day.

For HEVs and PHEVs, selected Li-ion chemistries evaluated are already very promising, as much due to increases in power density as energy density.

Where FY 2012 R&D using cost effectiveness found a candidate market niche for ER-EVs, FY 2013 TCO analysis did not. There was no case in the TCO investigation where an ER-EV was estimated to be the least cost option.

In addition to battery cost issues, costs of charging equipment installation limit the extent of the market for plug-in electric vehicles. Unless gasoline prices rise significantly, PHEVs will only be financially desirable when used very intensively near existing charge circuits, allowing no-cost or low-cost charging infrastructure investment.

More than in FY 2012, it appears that battery pack costs lower than used in this study's projections will be necessary for ER-EVs or EVs to become superior plug-in options to PHEVs. The ER-EV has an additional hurdle to overcome. Powertrain costs other than for the battery pack appear to be an impediment to this technology.

If a portfolio of plug-in vehicles facing $5/gallon gasoline in 2020 becomes necessary, then if costs of both batteries and electric drive equipment drop significantly, the development of ER-EVs and EVs from 2012-2020 *might* prove to have been a wise strategic addition to HEV and PHEV options. However, additional cost comparisons including consideration of the possibility for lower battery pack and electric drive component costs should be conducted to determine whether the relative ranking of PHEVs, ER-EVs and

EVs changes, or PHEVs continue to be estimated to be the least cost option.

Another possibility is that a version of the series ER-EV could be attractive to a U.S. mass market, given its ability to operate all electrically in all charge depleting conditions, yet maintain an option to travel between cities (inefficiently) if necessary. There was a significant divergence in estimated financial viability of this option estimated by European country experts compared to U.S. country experts (Figure IV - 20 – the vehicle labeled PHEV70 is actually a series ER-EV). This difference should be resolved.

FY 2013 Publications/Presentations

Publications

1. *Life Cycle Assessment of Electric Vehicles – Key Issues of Task 19 of the International Energy Agency (IEA) on Hybrid and Electric Vehicles (HEV),* G. Jungmeier, J.B. Dunn, A. Elgowainy, L. Gaines, S. Ehrenberger, E. D. Özdemir, H.J. Althaus, R. Widmer, Transport Research Arena 2014, Paris.
2. *Comparison of Energy consumption and costs of different HEVs and PHEVs in European and American context.* A. Rousseau, F. Badin, M. Redelbach, N. Kim, A. Da Costa, D. Santini, A. Vyas, F. Le Berr, H. Friedrich. Presented at the European Electric Vehicle Congress Brussels. Nov. 19-22 2012.
3. *Deploying Plug-in Electric Cars Which are Used for Work: Compatibility of Varying Daily Patterns of Use with Four Electric Powertrain Architectures.* D. Santini, Y. Zhou, N. Kim, K. Gallagher, and A. Vyas Paper TRB13-4925. Presented at the Transportation Research Board Meeting Jan. 2013 Washington DC. (forthcoming in Transportation Research Record volume 2385, Alternative Fuels and Technologies 2013, pp. 53-60).
4. *Reducing Light Duty Vehicle Fuel Consumption and Greenhouse Gas Emissions: The Combined Potential of Hybrid Technology and Behavioral Adaptation.* D. J. Santini, and A. J. Burnham (2013). SAE 2013-01-1282 SAE World Congress, Detroit. April 16-18, 2013.
5. *Cost Effective Annual Use and Charging Frequency for Four Different Plug-in Powertrains.* Santini, D.J. et al SAE 2013-01-0494 SAE World Congress, Detroit. April 16-18, 2013.
6. *Analysis of Input Power, Energy Availability, and Efficiency during Deceleration for X-EV Vehicles*. E.M. Rask, Henning Lohse-Busch and D.J. Santini SAE 2013-01-1064 SAE World Congress, Detroit. April 16-18, 2013. Also *SAE Int. J. Alt. Power.* 2(2):350-361, 2013.
7. *Plug-in Hybrid Electric Vehicles (PHEVs) (Task 15).* Chapter 5 of Hybrid and Electric Vehicles: The Electric Drive Gains Traction. IEA-HEV Implementing Agreement Report, May 2013. Pp. 33-45.
8. *Task 15, PHEVs, writing up report, studying financial viability of PHEVs*. D. Santini, IEA-HEV IA website report, Oct. 2013.

Submitted Paper

1. *Daytime charging – what is the hierarchy of opportunities and customer needs? ─ A Case Study based on Atlanta Commute Data.* D. J. Santini, Y. Zhou, V. V. Elango, Y. Xu, and R. Guensler. Submitted Aug. 4 to be considered for presentation at Jan. 2014 Transportation Research Board Meeting.

Presentations

1. *IA-HEV Task 15. Plug-in Hybrid Electric Vehicles. Conclusions, Report Status, and Next Steps.* A. Rousseau 37th Executive Committee meeting of the IEA Hybrid and Electric Vehicle Implementing Agreement, Stuttgart Germany Oct. 15-16, 2012.
2. *Well-to-wheels Analysis of PHEVs*, A. Elgowainy, IEA Task 19 Workshop 1, Braunschweig, Germany (December 7, 2012).
3. *Life-Cycle Analysis Methodology for Electric Vehicles*, A. Elgowainy, IEA Task 19 Worskshop 1, Braunschweig, Germany, (December 7, 2012).
4. *Energy Consumption and Greenhouse Gas Emissions During Automotive Lithium-Ion Battery Production and Assembly.* J. Dunn, IEA Task 19 Workshop 2 Argonne National Laboratory, Argonne, IL (April 25, 2013).
5. *Can Automotive Battery Recycling Help Meet Critical Material Demand?* L. Gaines, IEA Task 19 Workshop 3 Davos, Switzerland (October 9-10, 2013).
6. (being scheduled at end of FY 2013) *IA-HEV Task 15. Plug-in Hybrid Electric Vehicles. Phase 1 Findings & Phase 2 Recommendations.* D. Santini, 39th Executive Committee meeting of the IEA Hybrid and Electric Vehicle Implementing Agreement, Barcelona Spain, Nov. 14-15, 2013 and A. Rousseau, Electric Vehicle Symposium 27, Barcelona, Spain, Nov. 17-20.

IV.A.6 Battery Production and Recycling Materials Issues (ANL)

Linda Gaines and Jennifer Dunn

Center for Transportation Research
Argonne National Laboratory
9700 S. Cass Avenue
Argonne, IL 60439
Phone: (630) 252-4919, Fax: (630) 252-3443
E-mail: lgaines@anl.gov

Start: Spring 2008
Projected Completion: Ongoing

Objectives

- Examine emissions to air, water, and land from acquisition of current and future battery materials.
- Analyze active materials production from metals and other precursors.
- Identify barriers in development of active material supply chain.
- Identify precursors of greatest concern in the supply chain.
- Estimate material demands for Li-ion batteries.
  - Identify any potential scarcities.
- Calculate theoretical potential for material recovery.
- Evaluate real potential for recovery using current recycling processes.
- Determine potential for recovery via process development.
- Characterize ideal recycling process.
- Develop improved process to maximize material recovery.
- Determine how each of these factors changes with battery chemistry (or mixtures of chemistries).
- Determine how reuse of batteries will impact recycling processes and economics.
- Identify economic and regulatory factors impacting battery recycling.
- Formulate actions to make recycling happen.

Barriers

- Nickel and cobalt are energy intensive to produce and have significant environmental impacts, but the need to access virgin supplies could be reduced by recycling.
- Scarcity could increase costs for battery materials
  - Recycling could increase effective material supply and keep costs down.
  - Current processes recover cobalt, use of which will decline.
  - Recycling economics in doubt because of low prices for lithium and other materials.
- Material recovered after use may be obsolete.
- Producers may be reluctant to use recovered materials.
- Mixed streams may be difficult to recycle.
- Process data are not published and may in fact not be known yet.
- Future battery chemistry is not determined.

Technical Goals

- Estimate energy use/emissions for current material processes.
- Estimate energy use/emissions for current battery assembly processes.
- Characterize current battery recycling processes.
- Estimate impacts of current recycling processes.
- Evaluate alternative strategies for additional material recovery.
- Develop improved recycling processes.
- Screen new battery materials for potential negative impacts from production or problems in recycling.

Accomplishments

- Compared critical material demand to supply out to 2050 for maximum penetration of EVs.
- Compiled information on environmental burdens of metal production.
- Analyzed cradle-to-gate impacts of producing four new cathode materials.
- Determined and characterized current production and recycling methods for lithium-ion batteries.
- Performed battery production and recycling lifecycle analysis to compare impacts and identify ideal recycling processes.
- Determined roles battery chemistry plays in both environmental and economic benefits of recycling.

- Identified institutional factors that can enable or hinder battery recycling.
- Presented and published analyses and recycling process comparison.
- Established collaboration with Chinese scientists on battery recycling.
- Participated in IEA HEV Task 19, SAE, USCAR, and NRC working groups

✧ ✧ ✧ ✧ ✧

Introduction

Examination of the production of batteries from raw material acquisition to assembly illuminates the stages of this supply chain that incur the greatest energy and environmental burdens. Recycling of material from spent batteries will be a key factor in alleviating potential environmental and material supply problems. We are examining battery material production, battery assembly, and battery recycling processes that are available commercially now or have been proposed. Battery materials, assembly and recycling processes are being compared on the basis of energy consumed and emissions, suitability for different types of feedstock, and potential advantages relating to economics and scale. We are comparing the potential of several recycling processes to displace virgin materials at different process stages, thereby reducing energy and scarce resource use, as well as potentially harmful emissions from battery production. Although few automotive batteries have been produced to date, work is under way to develop the best processes to recycle these batteries when they are no longer usable in vehicles. Secondary use of the batteries could delay return of material for recycling.

Approach

In our initial work, we developed cradle-to-gate energy consumption and air emissions for electric vehicle batteries with an $LiMn_2O_4$ cathode. These data were incorporated into Argonne's Greenhouse gases, Regulated Emissions, and Energy use in Transportation (GREET) model. We also estimated the maximum reasonable demand for battery materials, based on extremely aggressive scenarios for penetration of electric-drive vehicles. We combined vehicle demand growth with detailed battery designs and looked at how lithium demand might grow world-wide. We also estimated how much material could be recovered by recycling, thus reducing demand for virgin materials. We determined that cumulative world demand for lithium to 2050 would not strain known reserves. Although cobalt supplies, and possibly those of nickel as well, could be significant constraints by 2050, the envisioned move away from chemistries containing these elements would obviate potential problems.

Now, life cycle analysis (LCA) of batteries with other cathode materials based on detailed process data is being used to further identify potential environmental roadblocks to battery production, and to compare energy savings and emissions reductions enabled by different types of recycling processes. The cathode materials that are the focus of current work are lithium cobalt oxide ($LiCoO_2$), lithium iron phosphate ($LiFePO_4$), nickel manganese cobalt ($LiNi_{0.4}Co_{0.2}Mn_{0.4}O_2$), and an advanced cathode that has been the subject of research at Argonne, $0.5Li_2MnO{\cdot}0.5LiNi_{0.44}Co_{0.25}Mn_{0.31}O_2$. The anode paired with each of these cathode materials is typically graphite, although we have also developed a preliminary analysis for silicon.

Results

Battery Production. Roughly half of battery mass consists of materials (Cu, steel, plastics, Al) that have been extensively documented in previous analyses. Therefore, our focus was on the active battery materials that are not as well-characterized, and their fabrication into finished cells. Our earliest work emphasized production of the raw materials and their conversion to active materials. In order to understand the impact of our dependence on imported raw materials, we compared energy use and emissions from lithium carbonate production in Chile to domestic production in Nevada. Domestic production was determined to have somewhat greater impacts, but not enough to cause concern. Our focus then shifted to component manufacture and battery assembly, which must be repeated even if recycled materials are used. Previous work on Ni-MH batteries had suggested that these steps could be energy intensive.

Argonne's LCA of lithium-ion batteries is based upon a model of lithium-ion battery assembly that Nelson et al. developed[1]. This peer-reviewed model provides an inventory of battery components and describes the equipment and steps involved in assembling these components into a battery at a manufacturing facility. The dry room was found to consume 1.3 MJ/kg battery or 60% of the total manufacturing energy, in the forms of electricity and natural gas. Total energy for the manufacturing stage is estimated to be only 2.2 MJ/kg, compared to over 130 MJ/kg for the material production for a battery with an $LiMn_2O_4$ cathode. Therefore, recycling has the potential to save a very large fraction of the total battery production energy. Recycling is even more beneficial when cathode materials contain nickel or cobalt. Cathode materials with these metals have higher cradle-to-gate energy consumption and greenhouse gas (GHG) emissions than $LiMn_2O_4$ (30 MJ/kg). The greater energy

intensity of cobalt and nickel-containing cathode materials is evident when the cradle-to-gate energy consumption for batteries with different cathode materials are compared side-by-side as in Figure IV - 23. In the case of batteries made with $LiCoO_2$, the cathode material dominates the overall energy consumption of battery production and assembly.

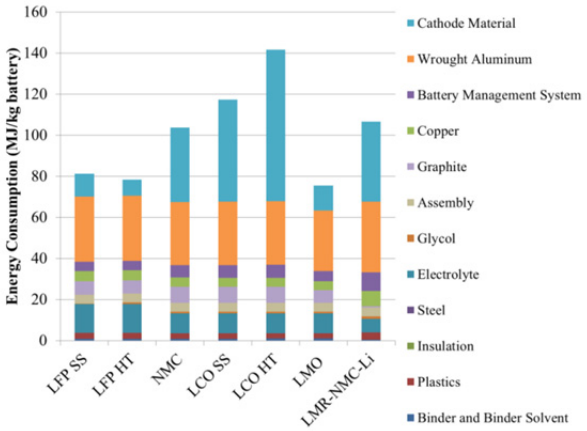

Figure IV - 23: Cradle-to-gate energy consumption for batteries with different cathode materials (NMC= $LiNi_{.4}Co_{.2}Mn_{.4}O_2$, LMR-NMC=.$5Li_2MnO_3$..$5LiNi_{.44}Co_{.25}Mn_{.31}O_2$, LCO=$LiCoO_2$, LFP=$LiFePO_4$, HT=hydrothermal preparation, SS=solid state)

Recycling Processes. Recycling can recover materials at different production stages, from elements to battery-grade materials. Figure IV - 24 shows how some battery production processes can be avoided by the use of materials recovered by different recycling processes.

Figure IV - 24: The battery material life cycle can be closed to reduce impacts

At one extreme are pyrometallurgical (smelting) processes that recover basic elements or salts. These are represented by the red area. Smelting is operational now on a large scale in Europe, processing both Li-ion and Ni-MH batteries. At high temperature, all organics, including the electrolyte and carbon anodes, are burned as fuel or reductant. The valuable metals (Co and Ni) are recovered and sent to refining so that the product is suitable for any use. If these are not contained in the batteries, the economic driver for smelting disappears. The other materials, including aluminum and lithium are contained in the slag, which is now used as an additive in concrete. The lithium could be recovered, if justified by price or regulations, but the impacts of lithium recovery from slag could be greater than those from primary production. Smelting chemistry could be changed to keep the lithium out of the slag or make the slag easier to handle. Note that the rare-earths from Ni-MH smelting slag are now being recovered.

At the other extreme, direct recovery of battery-grade material by a physical process has been demonstrated. This process requires as uniform feed as possible, because impurities jeopardize product quality. The valuable active materials and metals can be recovered. It may be necessary to purify or reactivate some components to make them suitable for reuse in new batteries. If cathode material can be recovered, a high-value product can be produced, even if the elemental value of the constituent elements is low. This is a big potential economic advantage for direct recycling (see Table IV - 2). Only the separator is unlikely to be usable, because its form cannot be retained. This is a low-temperature process with a minimal energy requirement. Almost all of the original energy and processing required to produce battery-grade material from raw materials is saved. The quality of the recovered material must be demonstrated, and there must be a market for it in 10 or more years, when cathode materials may be different. Direct recovery, which is economical on a small scale, could be used for prompt scrap from battery production now without these concerns.

Table IV - 2: Comparison of element values to cathode price

Cathode	Price of Constituents ($/lb)	Price of Cathode ($/lb)
$LiCoO_2$	8.30	12–16
$LiNi_{1/3}Co_{1/3}Mn_{1/3}O_2$	4.90	10–13
$LiMnO_2$	1.70	4.50
$LiFePO_4$	0.70	9

Intermediate or hydrometallurgical processes, such as the one funded by DOE under the Recovery Act (Toxco, now Retriev Technologies), are between the

two extremes. These do not require as uniform a feed as direct recovery, but recover materials further along the process chain than does smelting. If battery materials are treated hydrometallurgically, the lithium is easy to get out, in comparison to pyrometallurgical processing, which traps it in the slag, making it very difficult and expensive to recover. Although the lithium can be recovered (as the carbonate), the high value of the cathode material is not preserved.

Argonne performed a six-month analysis of a hydrometallurgical process developed in Beijing, in collaboration with a visiting Chinese scientist. This process, in contrast to many others, uses no mineral acids, and so produces no toxic wastes. However, production of the organic acids used instead is somewhat energy-intensive, reducing the benefits of recycling compared to virgin material production. Figure IV - 25 compares estimated energies to produce recycled $LiMn_2O_4$ by the intermediate process (Toxco), hydrometallurgically by the Chinese process, and by direct recycling to the energy needed for virgin production from Chile or Nevada. It can be seen that direct recycling has by far the lowest energy requirement. Figure IV - 26 illustrates how production energy for the entire battery can be minimized by the use of recycled metals as well as recycled cathode material.

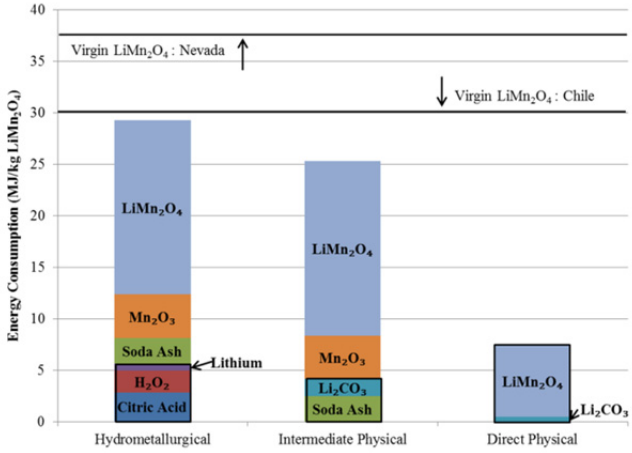

Figure IV - 25: Energy required to produce cathode material

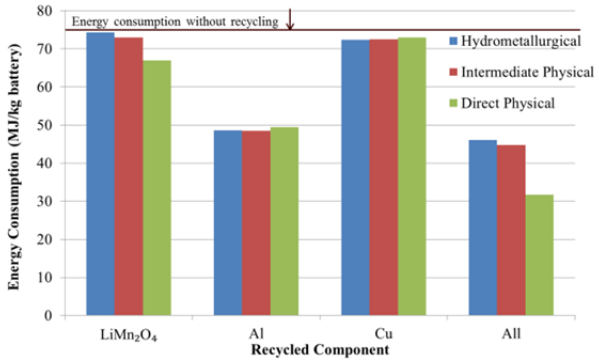

Figure IV - 26: Energy required to produce battery

Sulfur Emission Reductions by Recycling. Several of the metals used in batteries are smelted from sulfide ores, leading to significant emissions of SO_x. These constitute a significant fraction of the vehicle's life-cycle emissions (see Figure IV - 27). Recycling produces no such emissions, and thus cathode materials made from recycled materials would have lower production emissions, as can be seen in Figure IV - 28.

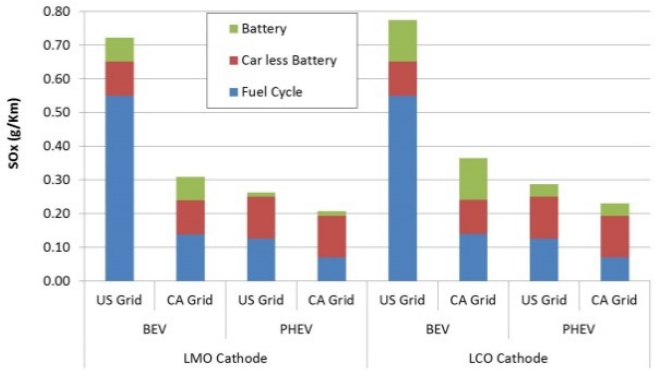

Figure IV - 27: Batteries contribute a significant fraction of life-cycle sulfur emissions

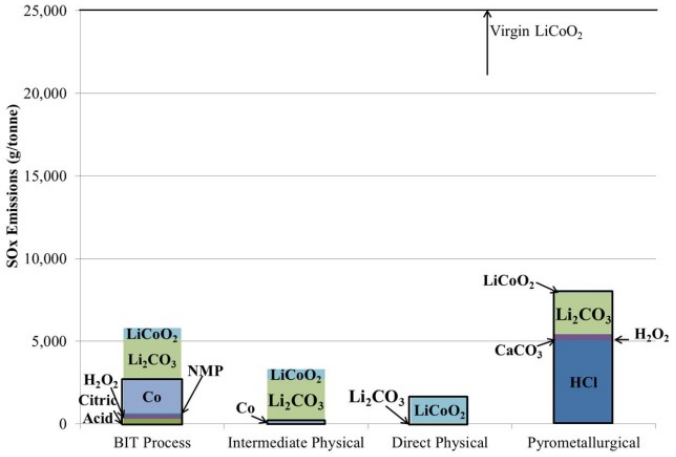

Figure IV - 28: Cathodes made from recycled materials minimize sulfur emissions

Enablers of Recycling and Reuse. Material separation is often a stumbling block for recovery of high-value materials. Therefore, design for disassembly or recycling would be beneficial. Similarly, standardization of materials would reduce the need for separation. In the absence of material standardization, labeling of cells would enable recyclers to sort before recycling. Argonne staff contributed heavily to the draft labeling standards being proposed by SAE. They also participated in several U.S. and international working groups to help enable recycling. Standardization of cell design, at least in size and shape, would foster design of automated recycling equipment. Standardization would also be beneficial to reuse schemes, where cells from various sources would be tested and repackaged in compatible groups for use by utilities or remote locations. It and proper labeling also help mitigate the emerging problem of Li-ion batteries disrupting secondary lead smelter operation.

FY2013 Presentations and Publications

Presentations

1. *Can Automotive Battery Recycling Help Meet Critical Material Demand*? , IEA HEV Task 19 Workshop, (October 9-10, 2013) (during shutdown—script written for surrogate presenter).
2. *Recycling of Lithium-Ion Batteries*, Plug-In 2013 (Sept. 30-October 2, 2013).
3. *Electric Vehicle Battery Recycling: Not for Dummies (for students)* (July 17, 2013).
4. *To recycle, or not to recycle, that is the question: Insights from life-cycle analysis,* Walter Payton College Prep HS (June 6, 2013).
5. *Energy Consumption and Greenhouse Gas Emissions During Automotive Lithium-Ion Battery Production and Assembly.* IEA Task 19 Workshop 2 (April 25, 2013).
6. *Cathode Material Identity's Influence on the Environmental Impact of Automotive Lithium-Ion Batteries,* SAE World Congress (April 18, 2013).
7. *Can Automotive Battery Recycling Help Meet Lithium Demand?*, invited for American Chemical Society (April 8-11, 2013).
8. *Energy and Environmental Impacts of Lithium Production for Automotive Batteries,* invited for American Chemical Society (April 8-11, 2013).
9. *Cathode Material as the Key to Battery Lifecycle Impacts,* U.S. China Battery Working Group, (April 4-5, 2013).
10. *Cathode Material Is Key to Evaluating EV Battery Life-Cycle Impacts,* 30th International Battery Seminar and Exhibit (March 14, 2013).
11. *Well-to-wheels Analysis of PHEVs*, IEA Task 19 Workshop 1, (December 7, 2012).
12. *Life-Cycle Analysis Methodology for Electric Vehicles,* IEA Task 19 Worskshop 1, (December 7, 2012).
13. *To recycle, or not to recycle, that is the question: Insights from life-cycle analysis,* invited for 2012 Materials Research Society Fall Meeting & Exhibit, Symposium G: Materials as Tools for Sustainability (November 25-30, 2012).

Book Chapter, Papers, Posters, and Fact Sheets

1. *Lithium-Ion Battery Environmental Impacts*, in Lithium-Ion Batteries: Advances and Applications, Elsevier (to be published 2014)(book chapter).
2. *Recovery of Metals from Spent Lithium-ion Batteries with Organic Acids as Leaching Reagents and Environmental Assessment,* Journal of Power Sources (February 2013)(paper).
3. *Life Cycle Assessment of Electric Vehicles – Key Issues of Task 19 of the International Energy Agency (IEA) on Hybrid and Electric Vehicles (HEV),* G. Jungmeier, J.B. Dunn, A. Elgowainy, L. Gaines, S. Ehrenberger, E. D. Özdemir, H.J. Althaus, R. Widmer, Transport Research Arena 2014, Paris (paper).
4. *Closing the Lithium-Ion Battery Life Cycle*, 6th International Conference on Advanced Lithium Batteries for Automotive Applications (September 9-11, 2013) (poster).
5. *Energy and Materials Issues That Affect Electric Vehicle Batteries* (May 2013) (fact sheet).
6. *How Green is Battery Recycling* (October 2012) (fact sheet).

Reference

1. Nelson, P., Gallagher, K., & Bloom, I. (2011). *Modeling the performance and cost of lithium-ion batteries for electric-drive vehicles.*Argonne National Laboratory.

IV.A.7 Updating USABC Battery Technology Targets for Battery Electric Vehicles (NREL)

Jeremy Neubauer

National Renewable Energy Laboratory
15013 Denver West Parkway
Golden, CO 80401
Phone: (303) 275-3084
E-mail: jeremy.neubauer@nrel.gov

Collaborators:
E. Wood, A. Brooker, and A. Pesaran, NREL
C. Bae, Ford
R. Elder, Chrysler
H. Tataria, General Motors
B. Cunningham, U.S. Department of Energy

Start Date: FY2012
Projected End Date: FY2013

Objective

- Provide analysis to support the *EV Everywhere* Grand Challenge and the DOE/United States Advanced Battery Consortium (USABC) identification of battery available energy, mass, volume, cost, discharge power, and charge power requirements that will enable broad commercial success of battery electric vehicles (EVs).

Technical Barriers

- Current USABC EV battery targets were developed more than 20 years ago. Documentation on their development is scarce, and the necessary vehicle performance for market success has changed since their creation.

Accomplishments

- Developed a simulation-based approach to calculate EV battery technology requirements necessary to deliver the vehicle level performance required for commercial success of EVs.
- Implemented the process across a range of inputs and provided results to the USABC and to DOE for finalizing inputs and assumptions.

✧ ✧ ✧ ✧ ✧

Introduction

EVs offer significant potential to reduce the nation's consumption of gasoline and production of greenhouse gases as identified in the DOE *EV Everywhere* Grand Challenge. However, one large impediment to the commercial success and proliferation of these vehicles is limited battery technology. EVs on the market today come with a significant cost premium relative to their conventionally powered counterparts, even after significant federal and state purchase incentives. In addition, the range of the vehicle is typically restricted by limited battery energy to less than 100 miles. Furthermore, when an EV is based upon a platform designed for a conventional powertrain, the size of the battery necessary to achieve this limited range often subtracts from available passenger or cargo volume.

Improvements in battery technology have the capacity to resolve all of these issues. Accordingly, in support of Administration's *EV Everywhere* Grand Challenge, DOE's Vehicle Technology Office, working with USABC and others are directing significant resources towards the development of batteries for EVs. Historically, these developments have been focused towards a set of DOE/USABC EV battery targets developed more than 20 years ago. Documentation providing insight into the development of these targets is exceptionally scarce; thus, the justification for these values is unclear. For this reason, and on the basis that the necessary vehicle performance for market success has changed since the creation of the original targets, there is motivation to develop an updated set of EV battery technology targets.

In 2012, the USABC and DOE began the process of creating a new set of battery technology targets for EVs. It was desired that the requirements be designed to deliver an EV capable of broad market success in support of the *EV Everywhere* Grand Challenge. To this end, the resources provided by DOE VTO to the National Renewable Energy Laboratory (NREL) were leveraged to supply detailed technical analysis, guided by the insight of the USABC's vehicle original equipment manufacturers (OEM) on consumer requirements and future technology trends.

Approach

The objective of this analysis is to support USABC and DOE identification of battery available energy, mass, volume, cost, discharge power, and charge power requirements that will enable broad commercial success of EVs. Working closely with USABC and DOE, NREL has developed a simulation-based approach to achieving this objective.

It begins by first specifying the relevant vehicle-level performance requirements necessary for commercial success; most relevant to this analysis are acceleration and range. Next, we select a vehicle platform with broad market appeal and define its mass and aerodynamic properties using forecasted values for our timeframe of interest. At this point, we calculate the required energy and power to meet our range and acceleration targets, then analyze the charge and discharge power requirements of varying durations across multiple drive cycles using vehicle simulation software. Finally, we calculate available battery mass and volume, followed by allowable battery cost to provide cost-parity with a comparable conventionally powered vehicle. We leverage OEM input via the USABC throughout to ensure that all assumptions are relevant to the anticipated level of future vehicle technology and market expectations.

Results

At the request of the DOE and USABC, we applied this approach to multiple vehicle platforms (compact car, midsize sedan, and small SUV) and vehicle ranges (150 and 300 miles). For each vehicle platform we defined the total vehicle mass using a vehicle mass factor parameter (the ratio of total EV mass to total conventional vehicle mass) and varied this as well. Some high level results are shown in Figure IV - 29.

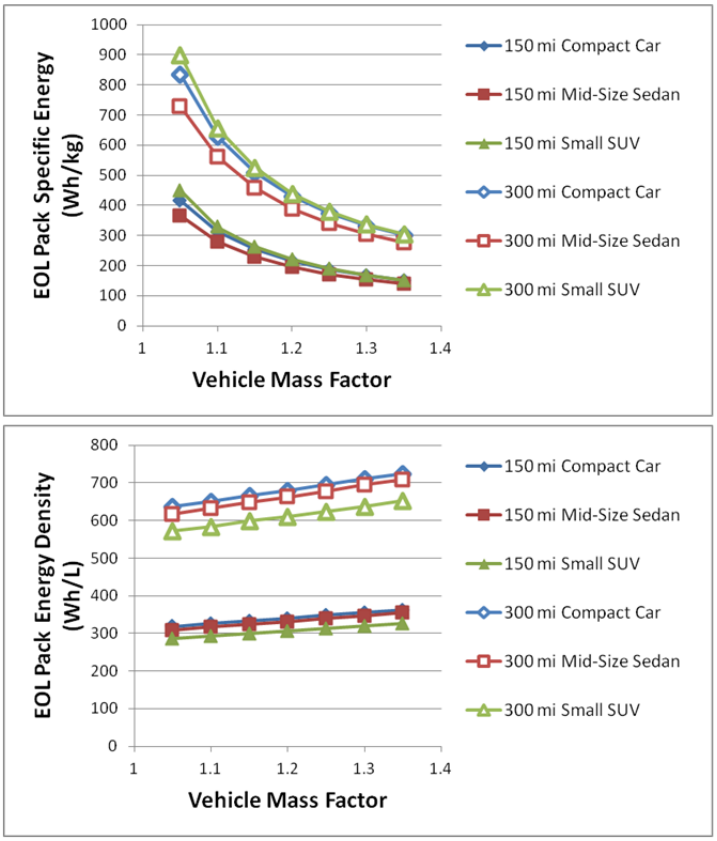

Figure IV - 29: Required end-of-life (EOL) pack specific energy and energy density as a function of vehicle range, platform, and mass factor

We have also simulated these configurations to multiple drive cycles to calculate discharge and charge power requirements. Results for a mid-size sedan with a 1.2 vehicle mass factor are shown in Figure IV - 30.

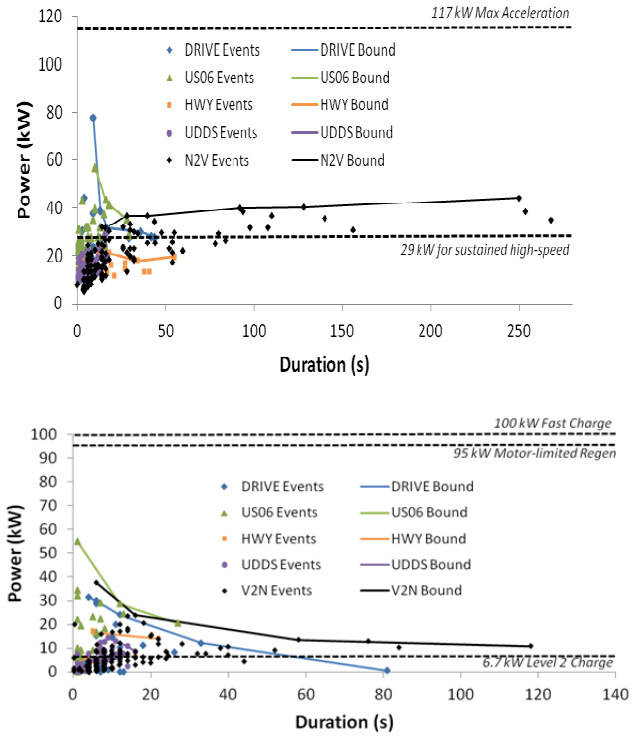

Figure IV - 30: Discharge (top) and charge (bottom) power requirements for a mid-size sedan with a vehicle mass factor of 1.2.

In addition, cost requirements were calculated and implications for beginning-of-life cell-level targets were extrapolated. All of this data was presented to USABC to support their target setting process.

Conclusions and Future Directions

This project successfully analyzed EV battery targets and the findings were provided to DOE and USABC. USABC subsequently selected new targets for its EV battery technology development programs using this input, which have been published[10]. To conclude this work, NREL plans to publish on its target analysis process to guide future target-setting efforts.

[10] Please see the EV requirements listed in Chapter II of this report and those listed at the USCAR website (http://www.uscar.org/guest/article_view.php?articles_id=87).

IV.B Battery Testing Activities

IV.B.1 Battery Performance and Life Testing (ANL)

Ira Bloom, Primary Contact
John Basco, Panos Prezas,
David Robertson, Lee Walker

Argonne National Laboratory
9700 South Cass Avenue
Argonne, IL 60439
Phone: (630) 252-4516; Fax: (630) 252-4176
E-mail: ira.bloom@anl.gov

Start Date: September 1976
Projected End Date: Open

Objectives

- Provide DOE, USABC, and battery developers with reliable, independent and unbiased performance evaluations of cells, modules and battery packs.
- Benchmark battery technologies which were not developed with DOE/USABC funding to ascertain their level of maturity.

Technical Barriers

This project addresses the following technical barriers as described in the USABC goals [1, 2, and 3]:

(A) Performance at ambient and sub-ambient temperatures.
(B) Calendar and cycle life.

Technical Targets

PHEV Technical Targets

- 15-year calendar life.
- 5,000 CD cycles.

Other technical targets exist for EV, HEV and LEESS applications

Accomplishments

Tested battery deliverables from many developers:

- HEV and LEESS batteries: Test contract deliverables from A123 Systems (in progress) and Leyden Energy (in progress).
- PHEV batteries: Test contract deliverables from Johnson Controls, Incorporated (in progress) and A123 (in progress).
- EV batteries: Seeo (complete), Optodot (in progress), 3M (in progress) and DowKokam (in progress).
- Benchmark battery technologies for vehicle applications. Test deliverables from Cobasys (in progress), SK Energy (in progress), ActaCell (in progress) and DowKokam (EV; complete).
- Compare EV battery test protocols used in the U.S. and in China (Argonne lead; in progress).

✧ ✧ ✧ ✧ ✧

Introduction

Batteries are evaluated using standard tests and protocols which are transparent to technology. Two protocol sets are used: one that was developed by the USABC [1, 2], and another which provides a rapid screening of the technology. The discussion below focuses on results obtained using these standard protocols.

Approach

The batteries are evaluated using standardized and unbiased protocols, allowing a direct comparison of performance within a technology and across technologies. For those tested using the USABC methods, the performance of small cells can be compared to that of larger cells and full-sized pack by means of a battery scaling factor [1, 2].

Results

Independently, organizations in the U.S. and China have developed battery testing protocols. Even though these protocols started from the same basic understanding of electrochemistry, the protocols that each country uses reflect differences in philosophy and approach.

In the U.S., ANL and INL and in China, CATARC are collaborating to compare battery testing procedures and methods. The collaboration may establish

standardized, accelerated test procedures and will allow battery testing organizations to cooperate in the analysis of the resulting data. In turn, the collaboration may accelerate electric vehicle development and deployment. The three steps and progress in this collaborative effort are shown in Table IV - 3.

Table IV - 3. Steps and progress in the collaborative testing effort

Step	Status
Collect and discuss battery test protocols from various organizations/countries	Complete
Conduct side-by-side tests using all protocols for a given application, such as an EV	In progress
Compare the results, noting similarities and differences between protocols and test sites	In progress

Initially, the approach to testing was different. The USABC tests focus on pre-competitive experiments using an ideal, family-sized car. In contrast, those from China were centered on how the battery performed in a given automobile.

The tests focused on the EV application. Here, the USABC protocol consisted of a dynamic, constant-power discharge and constant-current charging. The Chinese protocol consisted of constant-current discharges (C/3 rate) and charges. USABC reference performance test (RPT) consisted of two C/3 capacity cycles, a peak power pulse test at 10% DOD increments and full DST cycle. The cells were characterized using these tests every 50 cycles. In contrast, the Chinese RPT consisted of one C/3 capacity cycle and 10 second discharge pulse at 50% DOD. The RPT is performed every 25 cycles. Both cycle-life protocols terminate discharge at 80% DOD.

The tests were performed using commercially-available cells containing $LiFePO_4$- and graphite-based chemistry. Figure IV - 31 shows the trend in specific power obtained using the Chinese test protocol and measured at ANL and INL. The figure shows that the specific power of the battery decreased with cycling and that the measurements and trends obtained at the two labs were very similar.

Figure IV - 32 shows the change in average, relative capacity using the two test protocols, USABC and Chinese. From the figure, the Chinese protocol produced more capacity fade than the USABC at ANL; there was no significant difference between the protocols at INL; and, at CATARC, the result indicate that the capacity faded more using the Chinese protocol than the USABC. Some of these differences may be due to lot and cell-to-cell variation. Investigation into these differences is still in progress.

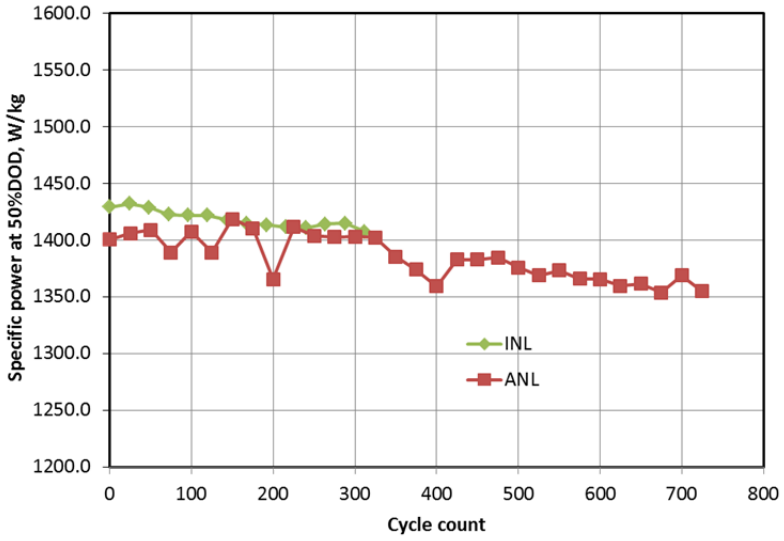

Figure IV - 31: Specific power vs. cycle count for cells cycled using the Chinese test protocol at ANL and INL

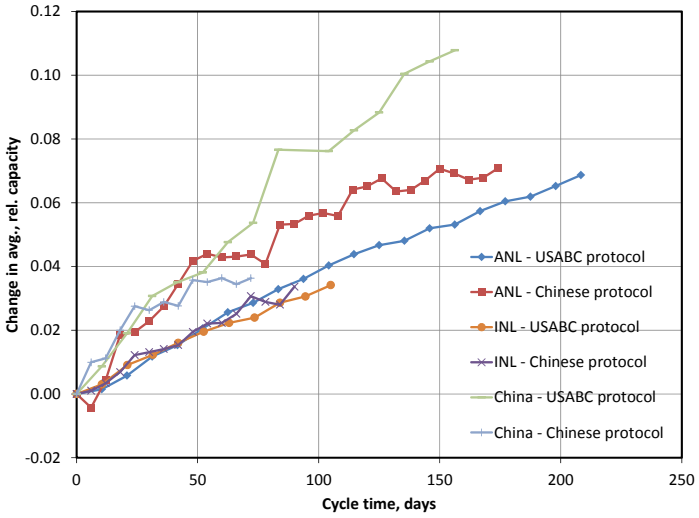

Figure IV - 32: Change in average, relative capacity measured using the two test protocols at the three test sites

Conclusions and Future Directions

Testing has been shown to be a useful way to gauge the state of a developer's technology and to estimate the life of a battery.

For the future, we plan to:

- Continue testing HEV contract deliverables.
- Continue testing PHEV contract deliverables.
- Continue testing EV contract deliverables.
- Begin testing LEESS contract deliverables.
- Continue acquiring and benchmarking batteries from non-DOE sources.
- Aid in refining standardized test protocols.
- Upgrade and expand test capabilities to handle increase in deliverables.
- Continue the protocol comparison.
- Explore other possibilities for test protocol comparison and, perhaps, standardization with Europe, Japan and China.

List of Abbreviations

HEV:	hybrid electric vehicle
PHEV:	plug-in hybrid electric vehicle
EV:	electric vehicle
LEESS:	Low-Energy Energy Storge System
USABC:	United States Advanced Battery Consortium (DOE, GM, Chrysler and Ford)
CATARC:	China Automotive Technology and Research Center
ANL:	Argonne National Laboratory
INL:	Idaho National Laboratory
RPT:	reference performance test
DST:	dynamic stress test, see reference 3.

FY 2013 Publications/Presentations

1. *A Comparison of U.S. and Chinese EV Battery Testing Protocols: Results*, I. Bloom, D. Robertson, F. Wang, S. Liu, and J. Christophersen, 8th U.S./China Electric Vehicle and Battery Technology Meeting, September 21-22, 2013, Chengdu, China.
2. *Effect Of Ultracapacitor-Modified PHEV Protocol On Performance Degradation In Lithium-Ion Cells*, Clark G. Hochgraf, John K. Basco, Theodore P. Bohn, And Ira Bloom, J. Power Sources, 246 (2014) 965-969.

References

1. FreedomCAR Battery Test Manual for Power-Assist Hybrid Electric Vehicles, DOE/ID-11069, October 2003.
2. FreedomCAR Battery Test Manual for Plug-In Hybrid Electric Vehicles, June 2010.
3. Electric Vehicle Battery Test Procedures Manual, Revision 2, January 1996.

IV.B.2 Advanced Energy Storage Life and Health Prognostics (INL)

Jon P. Christophersen, PhD (PI)

Idaho National Laboratory
P.O. Box 1625
Idaho Falls, ID 83415
Phone: (208) 526-4280; Fax: (208) 526-3150
E-mail: jon.christophersen@inl.gov

Ira Bloom (Argonne National Laboratory)
Ed Thomas (Sandia National Laboratories)
John L. Morrison, PhD (Montana Tech)
William H. Morrison (Montana Tech)
Christopher E. Hendricks (University of Maryland)
Sergiy V. Sazhin (INL)
Chinh D. Ho (INL)

Subcontractor:
Montana Tech of the University of Montana
Butte, MT

Start Date: October 2008
Projected End Date: September 2013 (extended into FY-14)

Objectives

- Develop techniques for accurate estimations of state-of-health (SOH) and remaining useful life (RUL) for electrochemical energy storage devices using both offline and online (i.e., *in situ*) techniques:
  - Design statistically robust accelerated aging protocols with identified stress factor interactions for improved offline battery life estimation.
  - Develop novel onboard sensor technology for improved online battery diagnostics, prognostics and control.

Technical Barriers

Developing relevant approaches for both offline and online battery life and health prognostics addresses four primary technical barriers: cost, performance, abuse tolerance, and accurate life estimation (i.e., reliability). Successful SOH and RUL estimation techniques enable smarter battery pack designs with reduced weight and cost in addition to optimized power management for enhanced reliability and performance. Battery safety could also be more thoroughly addressed with improved online sensor technology that rapidly identifies failure mechanisms and helps to prevent catastrophic events. Finally, enhanced SOH and RUL estimations enable smarter decisions about secondary use applications.

Technical Targets

- Update the Technology Life Verification Test Manual.
- Demonstrate cell-level rapid impedance measurements as a function of depth of discharge (DOD) and cell age.
- Enhance existing prototype rapid impedance measurement system (both hardware and software) for module-level testing.
- Demonstrate module-level measurements using rapid impedance techniques using combinations of cell strings.

Accomplishments

- Published Revision 1 of the *Technology Life Verification Testing* (TLVT) Manual.
- Completed validation study using rapid impedance measurements at various DOD conditions.
- Completed design of 50-V hardware and upgraded control software for string-level rapid impedance measurements.
- Developed test plan for string-level measurements of cells to determine SOH (cell testing to be performed in FY-14).

✧ ✧ ✧ ✧ ✧

Introduction

Improving the accuracy of offline and online battery life estimation is critical for the successful and widespread implementation of battery technologies for various applications including automotive, military, utilities, etc. Offline battery life estimation is important for establishing a technology's readiness for transition into mass production or to serve as a useful adjunct for warranty determinations. Once a battery technology is deployed, online monitoring is required for advanced management and control to ensure extended performance capability and reduced range anxiety.

Approach

Idaho National Laboratory (INL) has extensive experience with battery performance testing and is uniquely positioned to address advanced energy storage life and health prognostics. INL collaborated with Argonne National Laboratory (ANL) and Sandia National Laboratories (SNL) to develop statistically robust accelerated aging protocols under controlled (i.e., offline) conditions to assess the expected calendar life for automotive applications within one or two years of testing. The automotive battery life targets for the U.S. Advanced Battery Consortium (USABC) are generally 15 years of calendar life with at least 150,000 miles of cycle-life operations.

For Revision 1 of the TLVT Manual, the aging protocols were designed to be more compatible with standardized USABC testing as well as the updated *Battery Life Estimator* software tool that was completed in FY-12. The software tool uses the TLVT test matrices and default (semi-empirical) life models with Monte Carlo simulations to predict overall life capability at a designated reference condition (e.g., 30°C) within a statistical confidence interval.

INL also collaborated with Montana Tech of the University of Montana to develop a rapid impedance measurement technique for module-level systems up to 50V. The upgraded hardware and control software enable the acquisition of a broad-spectrum impedance measurement within approximately ten seconds or less depending on the frequency range (the excitation signal generally requires at least one period of the lowest frequency, so the measurement duration will increase for lower frequencies if a better definition of the Warburg tail is desired). Although the prototype hardware is a rack-mount system, it could also be re-designed as an onboard sensor for embedded systems.

In addition to completing the prototype hardware and control software, a test plan was developed for string-level testing of commercially-available lithium-ion cells. Due to some unanticipated losses in personnel at INL, testing under this plan was delayed and is expected to start in FY-14. However, the validation study with the 5-V prototype system hardware was completed in FY-13 using Sanyo SA cells. The purpose of this study was to explore the differences in impedance spectra as a function of DOD and aging. Nine cells were calendar-life aged at 50°C with reference performance tests (RPT) every 32.5 days. One group of three cells was subjected to a standard pulse-per-day test followed by a voltage clamp at 60% state of charge (SOC); a second group of three cells was also voltage clamped at 60% SOC with a rapid impedance measurement once per day; the third group was simply clamped at 60% SOC without any daily measurements. RPTs consisted of a standard low-current Hybrid Pulse Power Characterization (L-HPPC) with a ten-second rapid impedance measurement immediately prior to the pulse profile at each 10% DOD increment. The frequency range for the impedance measurements in all cases was 1638.4 to 0.1 Hz with octave harmonic separation (i.e., 10-second measurements).

Results

Offline Battery Life Estimation. Revision 1 of the *Technology Life Verification Test Manual* was published in December 2012. It is primarily meant to verify / demonstrate a battery's readiness for transition to production and is generally expected to be implemented at the cell-level, though module and pack-level technologies could be used as well. In Revision 1, the accelerated aging methodology and test matrices are more synergistic with standardized protocols developed for USABC testing to ensure a smoother transition between prototype cell testing for USABC and pre-production testing.

The TLVT methodology requires both a core- and supplemental-life test matrix. The core-life test matrix design first requires the identification of all relevant wear out mechanisms and associated stress factors that affect battery life. Most of these can be identified from USABC testing and/or knowledge of the cell chemistry. Once identified, a battery life model is developed to account for individual stressors as well as stress factor interactions. An error model is also developed to address cell-to-cell variability. The core-life test matrix is then designed based on the anticipated level of stressor interactions and level of maturity of the life model. Three different levels of matrix designs are discussed in the manual, ranging from a minimal (verification) test matrix to a full-factorial design. Once the core matrix is completed, performance data are primarily simulated using the *Battery Life Estimator* software tool and then verified with actual cell testing. Due to resource limitations, only a subset of the full matrix may be used for actual cell testing to verify the accuracy of the life and error models. If the test data validate the anticipated results from the models and simulations, then the simulated data can be used to estimate offline battery life capability within a designated statistical confidence limit (e.g., 95% upper and lower confidence).

In addition to the core-life test matrix, a supplemental matrix design is also described in the manual where various assumptions about battery behavior can be verified. For example, a supplemental matrix may include a path dependence study that examines the memory effects of cells, a low-temperature cycling condition, or even periodic cold crank tests during life aging. If results from the supplemental matrix testing reveal weaknesses in the overall life

model, then the model will need to be modified and the core matrix simulation and testing will need to be repeated.

Online Battery Life Estimation. The 50-V rapid impedance measurement system is a significant advancement over previous generations. The hardware included a USB-driven data acquisition system to enable more portability. It also included a digitally isolated voltage feedback system to eliminate the high-voltage DC bias when capturing the sum-of-sines excitation signal. Protection features were added for higher voltages such that it will not excite a test article with a sum-of-sines signal if the terminals are connected backwards. The calibration system was also significantly improved to enable computer controlled automation and now accounts for both the magnitude and phase (previous hardware generations required manual shunt connections and calibrated only the magnitude). Calibration is now performed at each frequency within the sum-of-sines whereas previous techniques were based on an average for all frequencies. In addition to the hardware improvements, the control software was upgraded with significant speed improvement for capturing and processing the response signal and enabling higher frequency resolution in the excitation signals.

This 50-V prototype system will be used for the string-level cell study using commercially-available Sanyo SAX cells. A test plan was developed for this study and consists of the following research questions:

- Can the 50-V rapid impedance measurement system be used for string-level diagnostics and prognostics?
- How sensitive is the detection of anomalous cells in a string given string length and the cell aging intensity (e.g., temperature)?

The test matrix is shown in Table IV - 4. The cells will be calendar-life aged individually at the designated test temperature and SOC and then assembled into various string combinations for rapid impedance measurements as part of the RPTs.

Table IV - 4: Test group for cell string-level study

Group	# of Cells	Temperature	SOC
A	6	30ºC	60% SOC
B	2	40ºC	60% SOC
C	2	50ºC	60% SOC

Table IV - 5 shows the string combinations of cells for rapid impedance measurements at each RPT. All cells will be subjected to individual impedance measurements and then combined into various cell series and parallel combinations. The 2, 3, and 4-cell series connections will reach approximately 8, 12, and 16 V, respectively, for the impedance measurements. A total of 32 impedance spectrum measurements will be conducted at each RPT. Bolted Anderson connectors will be used in the test fixture design to facilitate series and parallel connections at each RPT without having to disturb the cells within the temperature chambers.

Table IV - 5: String combinations for rapid impedance measurements

Measurement Type	Cells
Single Cell	A1, A2, A3, A4, A5, A6, B1, B2, C1, C2
2 Cell Series (same group condition)	A5 in series with A6 B1 in series with B2 C1 in series with C2
2 Cell Parallel (same group condition)	A5 in parallel with A6 B1 in parallel with B2 C1 in parallel with C2
2 Cell Series (different group condition)	A6 in series with B1 A6 in series with C1
2 Cell Parallel (different group condition)	A6 in parallel with B1 A6 in parallel with C1
3 Cell Series (same group condition)	A4, A5, A6 in series
3 Cell Parallel (same group condition)	A4, A5, A6 in parallel
3 Cells Series (different group condition)	A4, A5, B2 in series A4, A5, C2 in series
3 Cells Parallel (different group condition)	A4, A5, B2 in parallel A4, A5, C2 in parallel
4 Cells Series (same group condition)	A1, A2, A3, A4 in series
4 Cells Parallel (same group condition)	A1, A2, A3, A4 in parallel
4 Cells Series (different group condition)	A1, A2, A3, B2 in series A1, A2, A3, C2 in series
4 Cells Parallel (different group condition)	A1, A2, A3, B2 in parallel A1, A2, A3, C2 in parallel

Cell-testing for this string study was delayed due to unanticipated losses in personnel, but is expected to start early in FY-14. However, the 5-V prototype system validation testing activities were concluded in FY-13 with the successful completion of the rapid impedance spectrum measurements as a function of DOD and cell age. The Sanyo cells were calendar-life aged at 50ºC for a total of eight months. Table IV - 6 shows the average capacity and available power at RPT 8 with the corresponding percent-fade for each calendar-life group.

The average results for each cell group are generally within a couple standard deviations of each other, which indicate that there is no significant difference in performance between a pulse per day, a rapid impedance measurement per day, or clamping the OCV at the target SOC condition.

Table IV - 6: Sanyo SA performance summary from DOD study

RPT8	Capacity Ah (%-Fade)	Power kW (%-Fade)
Pulse-per-Day	0.878 (31.23%)	39.75 (32.65%)
Clamp-Voltage	0.887 (30.42%)	40.80 (31.01%)
Impedance-per-Day	0.897 (29.64%)	41.17 (30.11%)

Figure IV - 33 shows the ten-second impedance spectra measurement captured at each 10% DOD increment for a representative cell at beginning of life (RPT0) and RPT8; where the RPT8 data were artificially shifted to the right by 10 mΩ for better qualitative comparisons. Note that fewer impedance spectra are available at RPT8 since several of the data were corrupted by noisy measurements caused by the mechanical relays wearing out in the 5-V prototype system or software glitches. The relays wore out due to the significant amount of cumulative measurements during validation testing over the previous several years. The upgraded software tool for the 50-V system includes various fixes for storing and processing captured test data. Nevertheless, these data clearly show that the impedance spectra for this lithium-ion cell change as a function of increasing DOD condition. The ohmic resistance (i.e., where the spectra cross the real axis) remains relatively constant at each RPT, but the mid-frequency charge transfer resistance (i.e., the semicircle) increases in both height and width. There also appears to be a minor deviation in the low-frequency Warburg tail for the cells as a function of DOD (although not shown here, this was also observed for some aged cell results as well). The spectra also change as a function of cell age, as expected. The ohmic resistance shows only a minor increase over eight months of aging at 50ºC from approximately 28 mΩ at RPT0 to 35 mΩ at RPT8 (again, the data are artificially shifted in the figure by 10 mΩ). The charge transfer resistance, however, shows significant increase as a result of cell age.

Figure IV - 34 shows the average real impedance measured at the semicircle trough (i.e., the transition point between the charge transfer resistance and the low-frequency Warburg tail) at each 10% DOD increment plotted against the corresponding discharge pulse resistance calculated from the L-HPPC test. Aside from a few outliers due to the noisy measurements (not shown in this figure), the data generally show a linear trend line having a slope of approximately 1.3, so the discharge pulse resistance data is growing more quickly than the corresponding measured impedance. However, the results are highly correlated with an overall r^2 value of 0.994. Thus, these data indicate that rapid impedance measurements can be used to rapidly estimate changes in discharge pulse resistance as a function of DOD and age for onboard applications.

Conclusions and Future Directions

Accurate battery life and health prognostics are critical for the successful commercialization and implementation of advanced alternative transportation. Methodologies for both offline and online battery life estimation have been developed using accelerated aging techniques and novel sensor technology, respectively. The purpose of the newly released *Technology Life Verification Test Manual*, Revision 1 is to define a core and supplemental life testing regime that incorporates various stress-factors and their interactions for a technology that is transitioning into mass production. If the life and error models are sufficiently mature, test data from the full factorial matrix is primarily simulated for life estimation, followed by actual battery testing on a strategically-targeted subset of the matrix depending on available resources.

For online health estimation, a 50-V prototype hardware system has been successfully developed for rapid impedance measurements on module-level systems. String-level cell testing is expected to begin in FY-14 to validate and demonstrate the new hardware and upgraded control software. The DOD study at the cell-level was completed and the results indicate that impedance spectrum measurements can be used as an online sensor to rapidly estimate changes in discharge pulse resistance (as determined from an HPPC test).

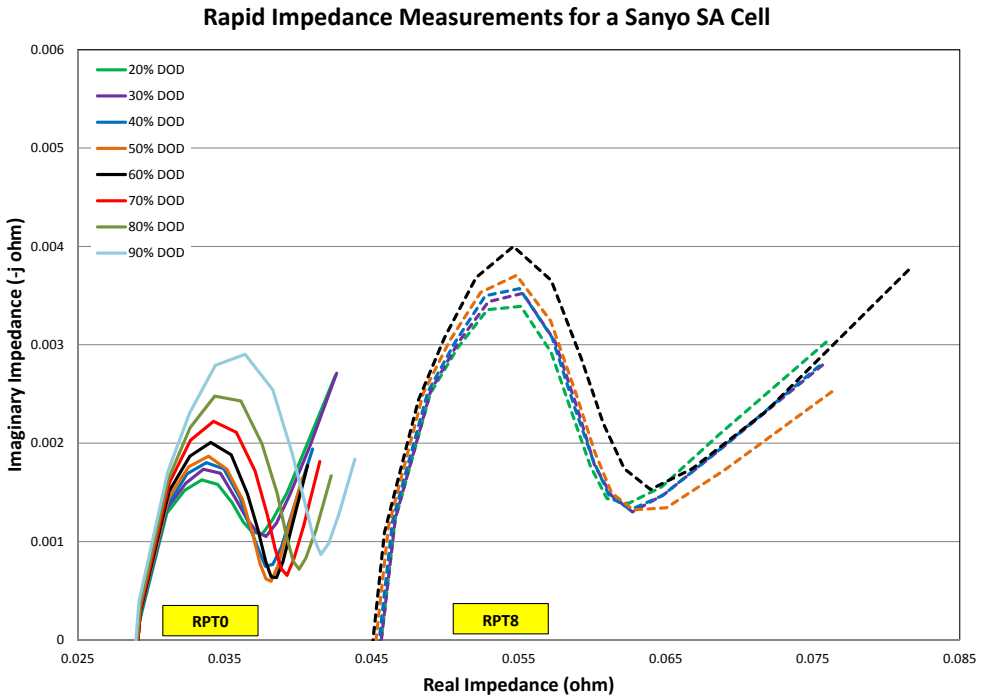

Figure IV - 33: Impedance spectra as a function of DOD for a representative Sanyo SA cell at RPT0 and RPT8

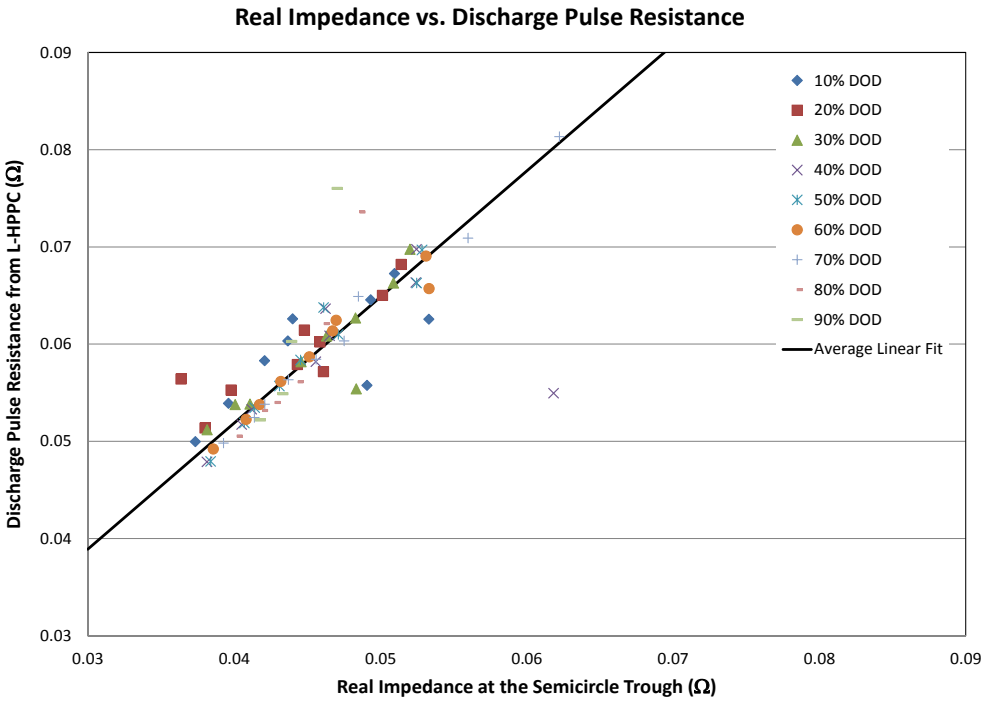

Figure IV - 34: Average real impedance as a function of the discharge pulse resistance for the Sanyo SA cells

FY 2013 Publications/Presentations

1. *Battery Technology Life Verification Test Manual, Revision 1,* INL/EXT-12-27920, December 2012.
2. Christophersen, J., Morrison, J., Motloch, C. and Morrison, W., "Long-Term Validation of Rapid Impedance Spectrum Measurements as a Battery State-of-Health Assessment Technique," *SAE Int. J. Alt. Power* 6(1):2013.
3. Christophersen, J. P., Morrison, J. L., and Morrison, W. H., "Acquiring Impedance Spectra from Diode Coupled Primary Batteries to Determine Health and State of Charge," Proceedings from the *IEEE Aerospace Conference*, March 2013.
4. Christophersen, J. P., "Battery Life Estimations for Offline ad Online Applications," invited presentation for the 2013 Advanced Automotive Battery Conference, Pasadena, CA, February 2013.

IV.B.3 Battery Performance and Life Testing (INL)

Jon P. Christophersen, PhD (PI)

Idaho National Laboratory
P.O. Box 1625
Idaho Falls, ID 83415
Phone: (208) 526-4280; Fax: (208) 526-3150
E-mail: jon.christophersen@inl.gov

Christopher J. Michelbacher
Matthew G. Shirk
Clair K. Ashton
Taylor L. Bennett
Randy L. Bewley
Michael C. Evans
Chinh D. Ho

INL Contract Number: DE-AC07-051D14517

Start Date: September 1983
Projected End Date: Open Contract

Objectives

- Provide high fidelity performance and life testing, analysis, modeling, reporting, and other support related to electrochemical energy storage devices under development funded by VTO.
- Develop test methodologies and analysis procedures for various alternative vehicle applications in conjunction with the U.S. Advanced Battery Consortium (USABC).

Technical Barriers

The successful adoption of cost-effective, safe, reliable and environmentally sustainable alternative vehicles remains a challenge. Performance and life testing of energy storage devices (e.g., batteries) in a controlled, laboratory environment is a critical component of DOE's mission to support the development of electric drive vehicle and component technology. Battery testing at the Idaho National Laboratory (INL) addresses all of the primary technical barriers: performance, life, cost, abuse tolerance and reliability. Accumulated test data are used to gauge battery capability relative to the DOE/USABC targets as a function of age as well as for developing battery life and cell-to-cell error models for advanced life and health prognostic tools. Performance and life testing are also useful for battery manufacturers as they develop lower-cost systems that can still meet the established targets. Finally, fresh and aged test articles are useful for abuse testing and thermal analysis in collaboration with other national laboratory efforts.

Technical Targets

- Battery performance and life testing in FY-13 at INL primarily focused on USABC technical targets for power-assist Hybrid Electric Vehicles (HEVs), Plug-in Hybrid Electric Vehicles (PHEV), Electric Vehicles (EV), Low-Energy Energy Storage Systems (LEESS) and 12 V Start/Stop.
- Technical targets for each of these automotive applications are available in the on-line manuals located at the USABC website.

Accomplishments

- Performance and life testing for USABC Programs:
  - 264 cells.
  - 9 modules.
- Performance and life testing for Benchmark Programs:
  - 46 cells.
  - 14 modules.
- Performance and life testing for FOA-2011 Programs:
  - 18 cells.
- Performance and life testing for FOA-ARRA (American Recovery and Reinvestment Act) Programs:
  - 31 modules.
- Published the LEESS Manual and 12V Start/Stop draft Manual.
- Completed setup of new 10,000 ft^2 battery testing facility with 165 new test channels, and walk-in environmental chambers.

✧ ✧ ✧ ✧ ✧

Introduction

Advancing alternative transportation is a top priority within the DOE given its potential to reduce U.S. dependency on oil. The INL Battery Testing Center is a world leader in performance testing and assessment of advanced electrochemical energy storage technologies, primarily for automotive applications, and has been

designated by DOE as the lead test facility for USABC activities. The development of batteries and other energy storage devices requires validation testing from an independent source to accurately characterize the performance and life capability against the established DOE/USABC technical targets for HEVs, PHEVs, EVs, and other electric drive system applications.

Approach

The INL Battery Testing Center (BTC) has over 20,000 square feet of laboratory space and is equipped with over 650 test channels for advanced energy storage testing at the cell-level (e.g., up to 7V, 300A), module-level (e.g., up to 65V, 250A), and pack-level (e.g., 500-1000V, 500A). The test equipment can be programmed to perform any test profile while simultaneously monitoring constraints such as voltage and temperature. Batteries and other energy storage devices are typically subjected to a test sequence while housed inside thermal chambers to ensure consistent and repeatable results. Two new walk-in environmental chambers were also installed in FY-13 for pack-level testing. All of the temperature chambers cover a broad range (e.g., -70 to 200°C) for enhanced testing and modeling capability.

Successful performance testing and accurate life modeling are highly dependent on the accuracy of the acquired test data. The INL BTC has developed advanced calibration verification and uncertainty analysis methodologies to ensure that the voltage, current, and temperature measurements are within the tolerance specified by the manufacturer (e.g., 0.02% of the full scale). These measured parameters are subsequently used in various mathematical combinations to determine performance capability (e.g., resistance, energy, power, etc.). INL has also quantified the error associated with these derived parameters using the accuracy and precision of the relevant measured parameter (e.g., voltage) to ensure high-quality and repeatable results.

The INL BTC capability has also been enhanced with additional equipment for advanced characterization of battery technologies. For example, in FY-13, a Ling Dynamic Systems V8-640 SPA56k shaker table was installed for vertical, longitudinal, and lateral spectrum vibrations of energy storage devices. The system is capable of displacements of 2.5 inches peak-to-peak, acceleragtions of 40 g's, and can accommodate large format test articles. Options for safety shielding and/or installation of a thermal chamber on the shaker table for controlled vibration testing are presently under investigation.

Results

INL Testing Activities. The INL BTC continues to test articles of various sizes and configurations using standardized test protocols. Table IV - 7 and Table IV - 8 summarize the testing activities under the USABC and Benchmarking Programs, respectively, for FY-13. The purpose of the USABC testing activities is to evaluate a candidate technology against the specified targets (EV, PHEV, etc.) and, where applicable, against previous generations of test articles from the same manufacturer. The purpose of the Benchmark Program is to evaluate devices that do not have existing contracts in place, but have technologies that are of interest to DOE/USABC. In some cases, a Benchmark Program is also used to validate newly developed test procedures and analysis methodologies (e.g., the 12V Start/Stop Manual).

Table IV - 7: Testing activities under the USABC Program

Manufacturer	Type	# of Articles	Application
LG/CPI	Cells	20	HEV
	Cells	40	PHEV
Envia	Cells	57	EV
K2	Cells	40	EV
Saft	Cells	12	HEV
Quallion	Cells	20	EV
	Modules	9	EV
Maxwell	Cells	15	LEESS
Entek	Cells	40	PHEV
Leyden	Cells	20	EV

Table IV - 8: Testing activities under the Benchmark Program

Manufacturer	Type	# of Articles	Application
Lishen	Cells	10	EV
Axion	Modules	12	HEV
Hydroquebec	Cells	16	HEV
Smart Battery	Modules	2	12 Volt Start/Stop
Sanyo	Cells	20	PHEV

Table IV - 9 and Table IV - 10 summarize the testing activities under the FOA-2011 and FOA-ARRA Programs, respectively, for FY-13. The FOA-2011 (i.e., 2011 Advanced Cells and Design Technology For Electric Drive Batteries awards) focuses on developing high performance cells for electric drive vehicles that significantly exceed existing technology, in regards to

both cost and performance. Technologies addressed include EV, PHEV, and HEV applications. The FOA-ARRA (i.e., 2009 Electric Drive Vehicle Battery and Component Manufacturing Initiative) focuses on battery and battery material manufacturing plants and equipment for advanced batteries for advanced vehicles. INL test results from both of these programs are presented to DOE to verify the performance of the articles delivered as part of the programs.

Table IV - 9: Testing activities under the FOA-2011 Program

Manufacturer	Type	# of Articles	Application
Miltec	Cells	18	PHEV

Table IV - 10: Testing activities under the FOA-ARRA Program

Manufacturer	Type	# of Articles	Application
East Penn Deka	Modules	25	Start/Lighting Ignition
East Penn Ultra Battery	Modules	3	HEV
Exide Columbus	Modules	3	Idle/Stop Start/Lighting Ignition

The INL BTC tested 382 devices in FY-13, including 325 cells and 57 modules. Table IV - 11 summarizes the anticipated INL testing activities for FY-14. USABC and Benchmark Program testing on existing deliverables are expected to continue and new deliverables will be added as well, including Farasis (USBAC), Angstrom, and EIG (both Benchmark). Note, also, that pack-level testing for USABC Programs is expected to begin as well.

Under the FOA-ARRA Program, non-disclosure agreements and test plans were established with three additional awardees in preparation of testing three 12V Starting-Lighting-Ignition (SLI) modules, five ultra-capacitors, and ten cells. Typical tests in this program consist of capacity and cycle life tests.

Under the FOA-2011 Program, non disclosure agreements and test plans have been established with four manufacturers in preparation of testing 55 additional cells with advanced materials. INL expects to test three generations of deliverables from each awardee. Typical reference performance tests include static capacity tests and cycle life testing, along with high and low temperature capacity testing. Some deliverables will be pulse tested, while others will not, depending on the maturity of the technology.

Table IV - 11: Anticipated testing activities for FY14

Program	Type	Manufacturer
USABC	Cells	LG/CPI, Maxwell, Envia, K2, Leyden, Entek, Farasis, Saft
	Modules	Quallion
	Packs	LG/CPI, Maxwell
Benchmark	Cells	Lishen, Hydroquebec, Sanyo, EIG, Angstrom
	Modules	Axion, Smart Battery
FOA-2011	Cells	Amprius, Applied Materials, Nanosys, PSU/JCI
FOA-ARRA	Cells	Enerdel, EnerG2 (ultracapacitor), LG Chem, Saft
	Modules	Exide Bristol

12 V Start/Stop Testing and Analysis. Both the LEESS and 12V Start/Stop manuals were published in FY-13. The test procedures for the LEESS Manual (INL/EXT-12-27620) are similar to the existing HEV manual but the analysis is based on a different set of targets. This section provides a brief overview of some testing and analysis procedures for the 12V Start.Stop Manual (INL/EXT-12-26503). The manual was published to evaluate test articles against a specific set of targets for "Under Hood" and "Not Under Hood" application. The targets include a 15-year calendar life capability (at 45ºC for "Under Hood" and at 30ºC for "Not Under Hood") and a cycle-life of 450,000 engine starts. The cycle-life test profile is shown in Figure IV - 35; this 240-s profile is repeated continuously during life aging. The profile was designed to be near 100% coulombically efficient with each cycle.

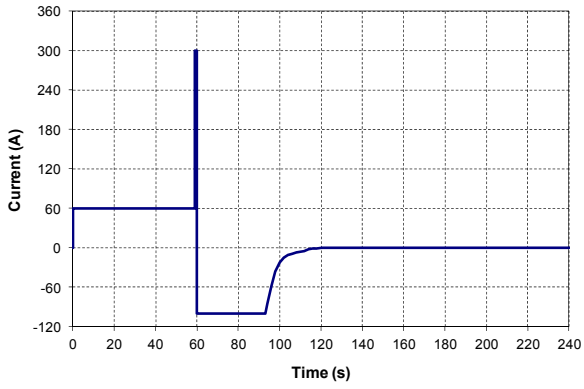

Figure IV - 35: Cycle-life profile for the 12V Start/Stop application

Cycle- or calendar-life aging is periodically interrupted (i.e., approximately once a month) for RPTs to gauge overall degradation in the device under test. RPTs include a constant power discharge test and a Hybrid Pulse Power Characterization (HPPC) test. Every fourth reference test, a cold crank test at -30ºC is also included. The HPPC profile for the 12V Start/Stop application is shown in Figure IV - 36 and consists of a 1-second discharge, a 40-second rest, and a 10-s regen step having 33% of the discharge current level. The discharge current is established based on the target engine-off accessory load (i.e., 750 W) divided by the average voltage and the cell scaling factor. This HPPC profile is repeated at each 10% DOD increment. Note, however, that in this HPPC profile, the regen step restores more capacity than is removed during the discharge step and the extra capacity restored needs to be accounted for when discharging to the next 10% depth-of-discharge increment. The HPPC test is conducted at the reference temperature, which is 30°C for "Not Under Hood" and 45°C for "Under Hood" applications.

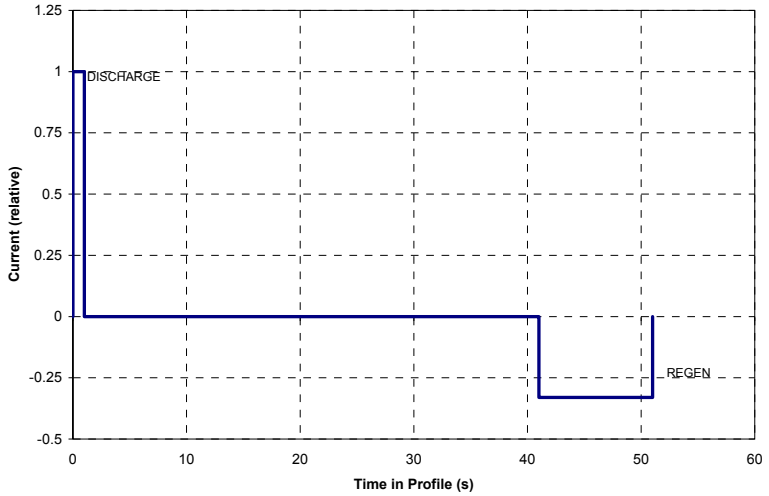

Figure IV - 36: HPPC profile for the 12V Start/Stop application

Results from the HPPC are used to directly compare the test article performance with the established targets (e.g., 6 kW discharge pulse power capability and 360 Wh of available energy at the 750W constant power rate). Figure IV - 37 shows the HPPC pulse power capability as a function of energy removed for an example test article scaled by a battery size factor (BSF) of 2.44 (note that this BSF exactly provides a 30% power margin at beginning of life and is for calculation purposes only; the actual BSF should be an integer value). The 10-second regen power capability (shown in the right-hand *y*-axis) has been scaled such that the 6 kW discharge and 2.2 kW regen power targets would align in this figure. Unlike a typical HPPC plot for HEV or PHEV applications, the discharge and regen curves do not cross over each other in the 12V Start/Stop application. This means that useable energy must be determined from the discharge pulse power capability curve.

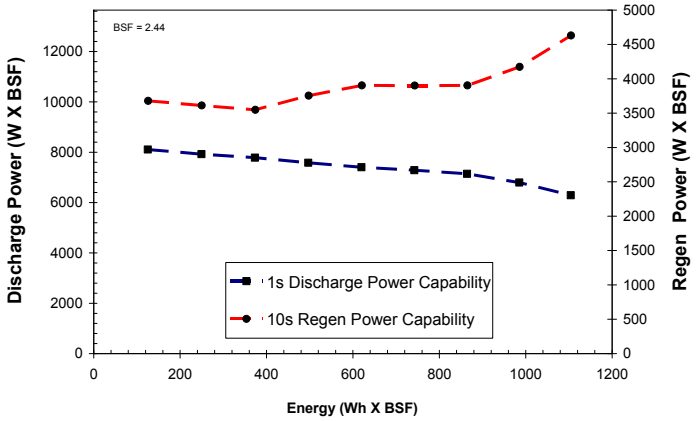

Figure IV - 37: HPPC scaled power vs. energy for the 12V Start/Stop application

Figure IV - 38 shows the resulting useable energy curve for the example test article using a BSF of 2.44. The 6 kW discharge pulse power capability and 360 Wh available energy targets are also identified in the figure with solid lines. For this example device, the beginning of life available power is 7.8 kW (i.e., 6 kW with a 30% margin) and the available energy is 1104 Wh. As this device ages, the useable energy curve should shift to the left. Once it crosses the intersection of the solid lines, it is no longer capable of meeting the targets and has reached end of life. This useable energy curve is generated at each RPT (i.e., once a month) to evaluate degradation rates as a function of aging.

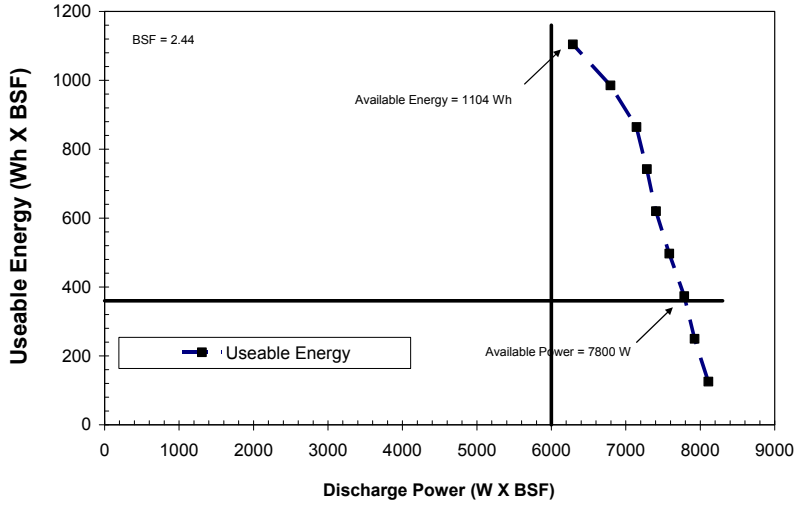

Figure IV - 38: HPPC scaled useable energy curve for the 12V Start/Stop application

Conclusions and Future Directions

Battery performance and life testing is critical for the successful adoption and implementation of advanced alternative vehicles. The INL is well equipped to conduct accelerated aging protocols on battery technologies of various sizes and shapes while ensuring high quality, repeatable results as an independent source of information for DOE, the automotive industry, and the battery manufacturers. In FY-14, INL plans to continue accelerated aging protocols for existing and new devices designated for the DOE/USABC, Benchmarking, FOA-2011, and FOA-ARRA Programs. In addition to testing and life modeling, INL will also continue developing and refining standard test protocols and analysis procedures in collaboration with USABC.

FY 2013 Publications/Presentations

1. Battery Test Manual for Low-Energy Energy Storage System for Power-Assist Hybrid Electric Vehicles, Revision 0, INL/EXT-12-27620, April 2013.
2. *Battery Test Manual for 12 Volt Start/Stop Vehicles*, Draft Temporary Manual, INL/EXT-12-26503, April 2013.

IV.B.4 Battery Abuse Testing (SNL)

Christopher J. Orendorff, Josh Lamb, Leigh Anna M. Steele, and William A. Averill

Sandia National Laboratories
P. O. Box 5800, Mail Stop 0614
Albuquerque, NM 87185-0614
Phone: (505) 844-5879; FAX: (505) 844-6972
E-mail: corendo@sandia.gov

Collaborators:
USABC Contractors/TAC
Ahmad Pesearan, NREL
Jon Christophersen, INL
Ira Bloom, ANL

Start Date: October 2012
Projected End Date: Ongoing

Objectives

- Serve as an independent abuse test laboratory for DOE and USABC.
- Abuse test in accordance with the USABC abuse testing manual.
- Sucessful testing of all deliverables from developers under USABC contracts.
- Test the propensity towards propagation of cell failure through multiple cell batteries.
- Evaluate the effect of cell age on abuse response.

Technical Barriers

- Abuse tolerance of energy storage devices is identified as a barrier in USABC and DOE battery development programs.
- The failure modes for lithium-ion batteries are complex and need to be evaluated for all types of chemistry, design, packaging and systems for PHEV/EV applications.
- Lack of understanding of how single cell or cell group failures propagate and what the primary drivers are for different battery designs.
- Limited knowledge on how cell level abuse tolerance changes over the age of a cell or battery.

Technical Targets

- Perform abuse testing and evaluation of cells and modules delivered from contractors to USABC.
- Perform failure propagation testing and evaluation.
- Characterize aged cells.
- Report results to DOE, the USABC, and contractors to USABC.

Accomplishments

- Successful tesing of cell and module deliverables through USABC contracts including:
  - K2 Energy.
  - SKI.
  - Cobasys.
  - Envia Systems.
  - Maxwell Technology.
- Performed multi-cell pack propagation testing to explore the susceptibility of different battery designs and series/parallel configurations to failure propagation.
- Completed the characterization of calendar aged cells to 20% power fade.

✧ ✧ ✧ ✧ ✧

Introduction

Abuse tests are designed to determine the safe operating limits of HEV/PHEV energy storage devices. The tests are performed to yield quantitative data on cell/module/pack response to allow determination of failure modes and help guide developers toward improved materials and designs. Standard abuse tests are performed on all devices to allow comparison of different cell chemistries and designs. New tests and protocols are developed and evaluated to more closely simulate real-world failure conditions.

In scaling from the cell to the battery level, it is important to understand safety performance which includes a detailed understanding of cell interactions. Single point failures from a single cell or group of cells can be initiated by a number of triggers including an internal short circuit, misuse or abuse, or a component failure at the battery or system level. Propagation of that single failure event (regardless of the initiation trigger)

through an entire battery, system or vehicle is an unacceptable outcome. Our work focuses on evaluating the propagation of a single cell thermal runaway event through a battery using a variety of design considerations.

Many development efforts directed toward improving safety performance are designed and evaluated using fresh cells. However, it is important to understand how reliable a materials or design improvement will be over time or if there is a "tipping point" somewhere along the age of a battery. Our work is directed toward understanding the effects of cell age on safety performance, themal stability and abuse tolerance.

Approach

Abuse tolerance tests are performed which evaluate the response to expected abuse conditions.

- Test to failure of energy storage device.
- Document conditions that cause failure.
- Evaluate failure modes and abuse conditions using destructive physical analysis (DPA).
- Provide quantitative measurements of cell/module response.
- Document improvements in abuse tolerance.
- Develop new abuse test procedures that more accurately determine cell performance under most likely abuse conditions.

Possible tests that can be performed cover three main categories of abuse conditions:

- Mechanical Abuse
  - Controlled crush, penetration, blunt rod, drop, water immersion, mechanical shock and vibration.
- Thermal Abuse
  - Thermal stability, simulated fuel fire, elevated temperature storage, rapid charge/discharge, thermal shock cycling.
- Electrical Abuse
  - Overcharge/overvoltage, short circuit, overdischarge/voltage reversal, partial short circuit.

Batteries for failure propagation evaluation are based on both pouch cell and cylindrical cell designs. Pouch cell batteries are built using 3 Ah cells in either a 5-cell series (5S1P) or 5-cell parallel (1S5P) configuration. Cylindrical cell batteries are built using 2.2 Ah 18650 cells in both 10S1P and 1S10P close-packed configuration. Cell failure and thermal runaway are initiated by a mechanical nail penetration into a single cell.

Results

Battery Abuse Testing. The actual USABC testing results are Battery Protected Information and are prohibited from public release. However, representative data is shown below for an overcharge abuse test of a commercial-off-the-shelf (COTS) cell purchased on the open market.

One type of mechanical abuse test that is performed on cell deliverables is the blunt rod test, where a 3 mm diameter steel rod with a rounded tip is pressed into a cell. Figure IV - 39 shows a representative force/displacement curve for a COTS pouch cell subjected to a blunt rod test. At ~4 mm deflection, the cell package was ruptured at ~100 lbf (~450 N). Figure IV - 39 also shows a photograph of the test where the blunt rod is penetrated into the face of the pouch cell. This particular test resulted in a hard short circuit and cell thermal runaway, but did not self ignite.

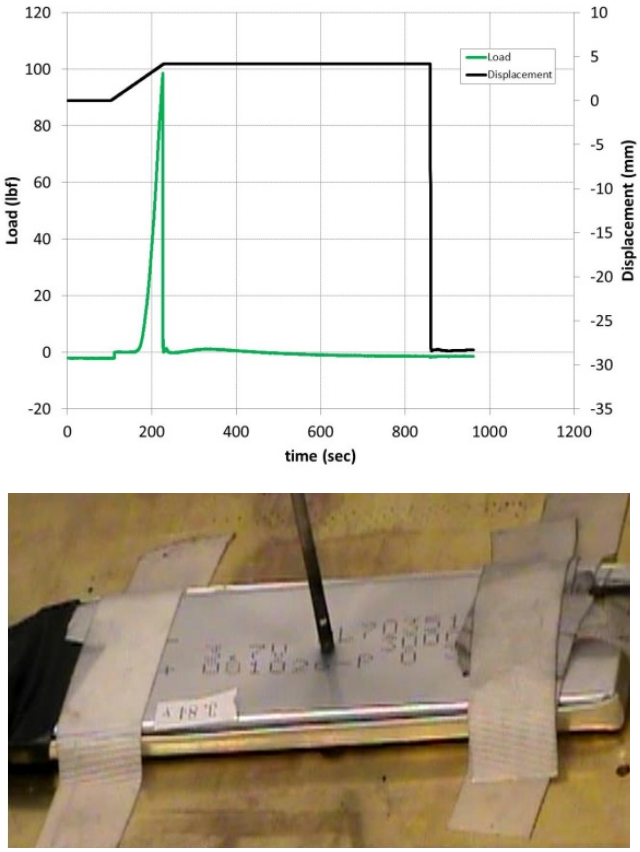

Figure IV - 39: (top) Force/displacement curve for the blunt rod test of a COTS cell and (bottom) a still photograph of that test showing the orientation fo the blunt rod into the face of the cell

Propagation. There has been significant study of the response of single cells to field and abusive failures, however less attention has been paid to how a battery system responds to the energetic failure of a constituent cell. A single cell failure may be a relatively rare occurance, but the consequence can increase exponentially if these failures routinely propagate through the entire battery. To study this further, we have tested a series of small batteries constructed with COTS cells using 18650 as well as prismatic pouch cells.

Batteries consisting of 3 Ah pouch cells were constructed in fully parallel (1S5P) and fully series (5S1P) configurations. These were stacked together such that the largest area faces of the cells were in contact with each other and the battery tabs were all located on the same side of the pack. Failure initiation was performed on the central cell as well as the outside edge cell. In all cases the failure propagated through the entire battery within roughly the same time frame (50-60 s) and with similar runaway temperatures (600-700°C).

Batteries consisting of 2.2 Ah 18650 cells were constructed in fully parallel (1S10P) and fully series (10S1P) orientation. The cells were placed in a close-packed configuration and the central cell failed (see Figure IV - 40). The temperature data can be seen in the figure above. The 1S10P pack showed initial propagation to cells near the failed cell soon after the initial failure, ~5 minutes after the initial failure propagation of thermal runaway surges through the remainder of the pack. The 10s1p pack showed some cells near the initial failure joining in thermal runaway; however thermal runaway did not propagate through all cells in the pack. The maximum observed temperatures were also significantly lower than in the parallel pack.

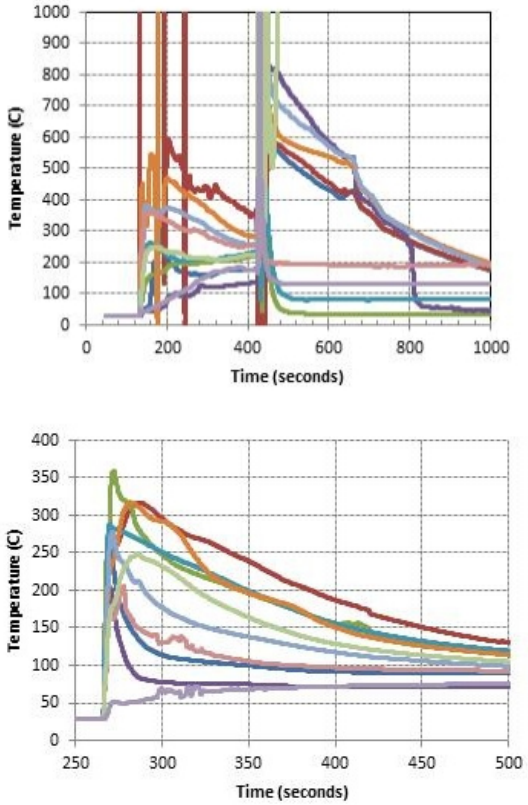

Figure IV - 40: Failure propagation in 1S10P (top) and 10S1P (bottom) 18650 cell batteries

An initial finding of this work shows that the impact of the electrical configuration is minimized when the cells are in strong thermal contact with one another. The prismatic pouch cells have a large area of contact with neighboring cells, allowing for efficient heat transfer during thermal runaway. The cylindrical 18650 cells, even in a close packed configuration, have a relatively limited area of contact with neighboring cells, limiting heat transfer between cells and allowing for impacts from the electrical configuration to become more pronounced.We have also partnered in this work with the battery team at NREL for modeling of cell behavior during runaway. The temperature contour profile they have developed for the 1S5P pouch cell battery during propagation of thermal runaway can be seen in the Figure IV - 41.

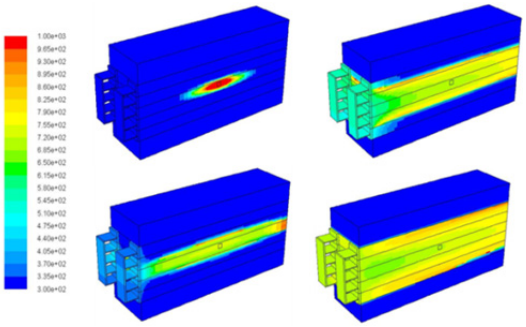

Figure IV - 41: NREL model showing temperature contour of 1S5P pouch cell battery during propagation of thermal runaway

Aged Cells. While significant attention has been paid to cell performance over time (capacity fade, available power, etc.) very little is known about how a cell failure, in particular thermal runaway profiles, may change over time. Moreover, with the measurable progress that has been made in cell safety and advanced materials, there is surpisingly very little data on whether or not the improvements observed at the beginning of cell life will continue to have the same positive benefit as these cells age. This is important not only in understanding cell behavior, but also in designing thermal management controls for battery systems. Since these are designed for new or fresh cells in a battery, we must understand how the runaway response may change over cell lifetime and how cell-to-cell variations in thermal response may change over time and also impact the system response.

We have previously studied COTS NMC cells aged to 20% power fade (60°C storage for approx. 60 days). Accelerating rate calorimetry (ARC) results from this work show increased variability in the thermal runaway kinetics and measureably lower onset temperatures for aged cells compared to the control population (Table IV - 12). However, results are widely variable. Fresh cells at 80% SOC were also evaluated by ARC to determine if the runaway response is controlled primarily by stored capacity. Figure IV - 42 shows representative ARC profiles for fresh cells at 100% and 80% SOC and aged cells that show 20% power and capacity fade. The higher rate runaway reaction > 225°C kinetics and total enthalpy of the aged cell and fresh cell at 80% SOC are very similar. This suggests that the higher rate reactions are less impacted by an aging mechanism (at 20% fade) and more governed by capacity. This is consistent with the fact that much of the cell age impacts the negative electrode and its interface with the electrolyte.

Table IV - 12: ARC Results for the COTS NMC Cells

Condition	Fresh Cells	Aged Cells
SEI breakdown (°C)	**93 ± 8**	**104 ± 7**
Cathode onset (°C)	**240 ± 3**	**230 ± 6**
Peak rate (°C/min)	**221 ± 17**	**148 ± 37**

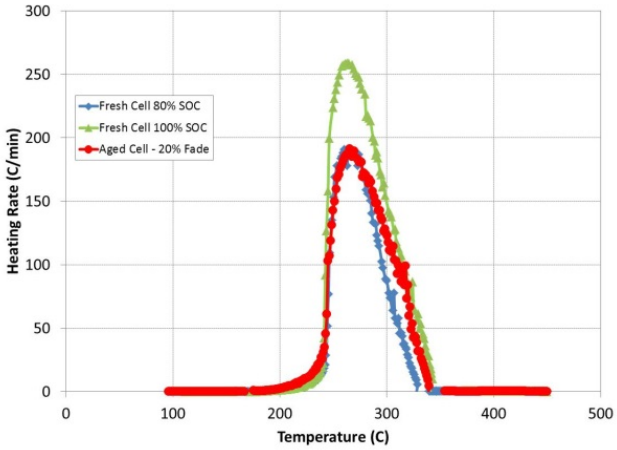

Figure IV - 42: ARC profiles for a fresh cells at 100% and 80% SOC and a calendar aged cell to 20% fade (80% power retention)

Cells were also subjected to thermal abuse tests to determine if the subtle differences in the ARC response have any notable impact on abuse tolerance. Figure IV - 43 shows the heating rate of representative fresh and 20% aged cells during a thermal abuse test. While there are some stuble differences in the onset heating rates the response of the fresh and 20% aged cells to thermal abuse are very similar.

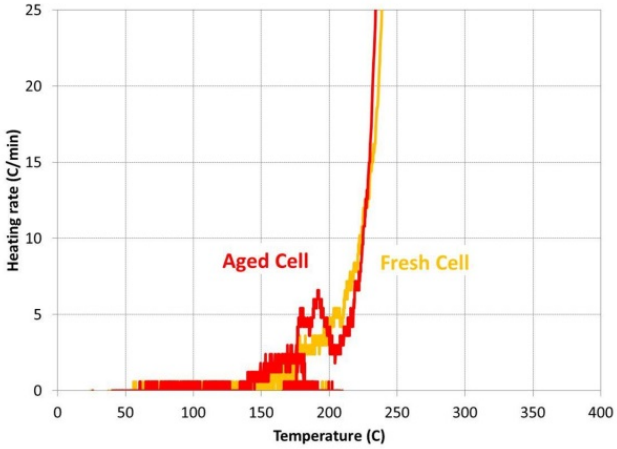

Figure IV - 43: Cell heating rates during a thermal ramp abuse test for a fresh cell at 100% SOC and a calendar aged cell to 20% power fade

Conclusions and Future Directions

Testing has continued on larger format cells, modules, and packs for USABC cell developers. This has required careful control and monitoring of tests with the potential of high energy release. This has provided critical information to cell developers to aid in the development of increasingly abuse tolerant cell chemistries and module designs. This independent testing is also necessary to perform objective evaluations of these various designs and chemistries by the DOE and U.S. automobile manufacturers. Testing

will continue in FY 14 on new module and cell designs from USABC contractors.

Initial work on failure propagation highlights the contributions of battery design, cell format, and configuration to the ability of a single point failure to propagate through a battery. Future work on this project includes evaluating different cell chemistries, passive design changes, and active temperature management. We will also continue to work with our colleagues to model this failure propagation behavior in order to develop a predictive design capability.

Cells calendar-aged to 20% power fade show some measureable changes abuse response kinetics, but very little impact on total runaway enthalpy or any significant performance changes to thermal insult. Future directions for the aged cell abuse response work includes evaluating cells at 20% cycle life fade and comparing cell performance to the fresh cell control population and the calendar aged cells to 20%. In addition, we will study cells that were aged for longer periods of time (>30% fade) and study different cell chemistries to determine the chemistry effect on aging mechanisms.

FY 2013 Publications/Presentations

1. USABC TAC, November 2012.
2. C. J. Orendorff, J. Lamb, K. R. Fenton, and L. A. M. Steele, “Approaches to Evaluating and Improving Lithium-Ion Battery Safety” AABC February 2013.
3. C. J. Orendorff, “Approaches to Evaluating and Improving Lithium-Ion Battery Safety” CU-Boulder, February 2013.
4. USABC TAC, Februrary 2013.
5. USABC TAC, May 2013.
6. USABC TAC, August 2013.
7. J. Lamb, C. J. Orendorff, J. Power Sources 247 (2014) 189-196. “Evaluation of mechanical abuse techniques in lithium ion batteries.”

IV.B.5 Battery Thermal Analysis and Characterization Activities (NREL)

Matt Keyser

National Renewable Energy Laboratory
15013 Denver West Parkway
Golden, CO 80401
Phone: (303) 275-3876; Fax: (303) 275-4415
E-mail: matthew.keyser@nrel.gov

Collaborators:
Dirk Long, John Ireland, Shriram Santhanagopalan, GM, Ford, Chrysler, USABC

Start Date: October 1, 2009
Projected End Date: Ongoing

Objectives

- Thermally characterize battery cells and evaluate thermal performance of battery packs provided by USABC developers.
- Provide technical assistance and modeling support to USDRIVE/USABC and developers to improve thermal design and performance of energy storage systems.
- Quantify the impact of temperature and duty-cycle on energy storage system life and cost.

Technical Targets

- Battery operating temperature from -30°C to 52°C.
- Develop a high-power battery technology exceeding 300,000 shallow HEV cycles.
- 15-year calendar life at 30°C.

Accomplishments

- Obtained cells from various USABC battery partners including Actacell, Cobasys, Johnson Controls Incorporated (JCI), Quallion, LGCPI, and SK Innovation.
- Obtained infrared thermal images of cells provided by USABC battery developers and identified any areas of thermal concern.
- Used NREL's unique calorimeters to measure heat generation from cells and modules under various charge/discharge profiles.
- Obtained thermal and electrical performance data of cells under HEV, PHEV, and EV power profiles.
- Evaluated thermal performance of a PHEV pack.
- Presented results of cell thermal characterization and pack thermal evaluation at USABC/battery developer review meetings.

✧ ✧ ✧ ✧ ✧

Introduction

Operating temperature is critical in achieving the right balance between performance, cost, and life for both Li-ion batteries and ultracapacitors. At NREL, we have developed unique capabilities to measure the thermal properties of cells and evaluate thermal performance of battery packs (air- or liquid-cooled). We also use our electro-thermal finite element models to analyze the thermal performance of battery systems in order to aid battery developers with improved thermal designs.

Approach

Using NREL's unique calorimeters and infrared thermal imaging equipment, we obtain thermal characteristics (heat generation, heat capacity, and thermal images) of batteries and ultracapacitors developed by USABC battery developers and other industry partners. NREL supports the Energy Storage Technical Team by participating in various work groups such as the Actacell, Cobasys, JCI, LGCPI, Quallion, and SK Innovations Work Groups.

Results

NREL's Calorimeter Development leads to R&D 100 Award. Advanced energy storage devices, such as lithium-based batteries, are very sensitive to operating temperatures. High temperatures degrade batteries faster and pose safety hazards, while low temperatures decrease power and capacity. The Isothermal Battery Calorimeters (IBCs) developed by NREL are the only calorimeters in the world capable of performing the precise thermal measurements needed to make safer, longer-lasting, and more cost-effective batteries for the next generation of electric-drive vehicles (EDVs).

Recently recognized with an R&D 100 Award, the IBCs are the most accurate devices of their kind—able to determine heat levels and battery energy efficiency with 98% accuracy. The IBCs make it possible to precisely measure the heat generated by EDV batteries,

analyze the effects of temperature on battery systems, and pinpoint ways to manage temperatures for the best performance and maximum life.

Capable of testing a wide size range of samples, the calorimeters can determine the heat generated by battery cells, modules, sub-packs, and even some full-size packs. The IBCs also evaluate system heat generation, from the individual cells within a module, the inter-connects between the cells, and the entire battery system.

The cell/module version of the IBC has the capacity to test more than 95% of EDV energy storage cells and small modules. The IBCs can also be used to test a variety of cell formats (i.e., pouch, cylindrical, and prismatic), while most other calorimeters on the market are limited to a single format.

The incredible precision of the IBCs can be attributed to patent-pending features that deliver total thermal isolation and highly sensitive temperature readings across a wide range of conditions. NREL has licensed the IBC technology to NETZSCH Instruments North America, LLC., a leading provider of thermal analysis instruments, for commercial production and distribution. The commercially-available IBC-284 being developed by NETZSCH and NREL is shown in Figure IV - 44.

Figure IV - 44: NETZSCH IBC-284

Calorimeter Testing. Figure IV - 45 shows the efficiency of cells tested in FY12/FY13 at NREL. The lithium-ion cells were fully discharged from 100% to 0% SOC under C/2, C/1, and 2C currents. It should be noted that the cells in the figure represent both power and energy cells, and have been developed for the HEV, PHEV, EV, or Low Energy Energy Storage System (LEESS) programs with USABC. The figure shows that most of the lithium-ion cells, A-J, are very efficient over this cycling regime—typically greater than 93%. The range of efficiencies at a 2C discharge rate is between 93% and 97%. A 4% difference in efficiency may not appear to be of concern; however, if one considers a 50 kW pulse from the battery in an electrified advanced vehicle, then a 1% difference in efficiency results in an additional 500 Watts of heat for the pulse duration—taking the example farther, a 4% difference results in 2,000 Watts of additional heat. The efficiency differences between the cells will require the thermal management system to be tailored to the cell thermal characteristics so as not to affect cell cycle life.

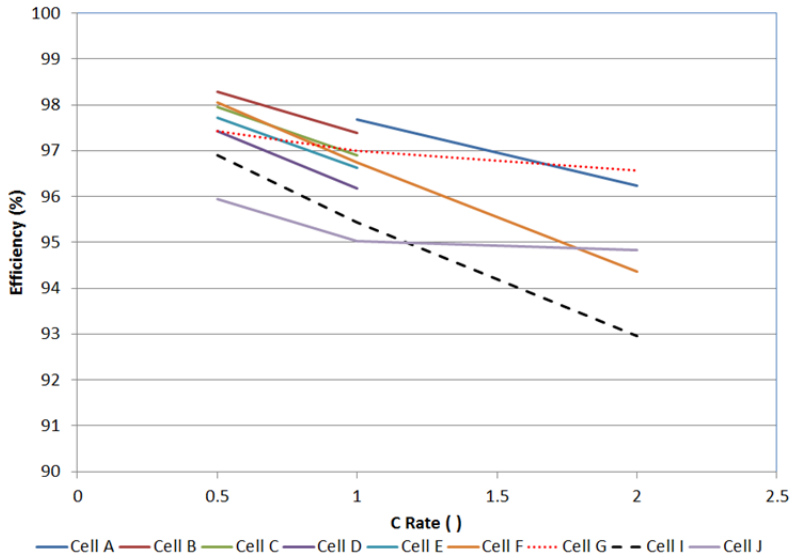

Figure IV - 45: Efficiency of cells tested at 30°C in NREL's calorimeter during FY12/FY13

Figure IV - 46 compares the efficiency of a Gen 2 and a Gen 3 cell from the same manufacturer. The cells were discharged under a constant current from 100% to 0% SOC. The efficiency of the Gen 3 cell is slightly below the efficiency its predecessor, the Gen 2 cell, indicating that from an efficiency perspective, the cell design has not improved. However, cells are not typically used over their full capacity range due to life cycle limitations of the cell. In this particular case, the cells will be used from approximately 70% to 30% SOC. Figure IV - 47 compares the efficiency of the Gen 2 and Gen 3 cells over this usage range. As can be seen from the figure, the efficiencies of the two cells are fairly well matched. Battery manufacturers use the data from the calorimeter to ensure that the cell has the desired efficiency over the usage range while making trade-offs on other aspects of the cell design such as low temperature operation, safety, cost, and ease of manufacturing.

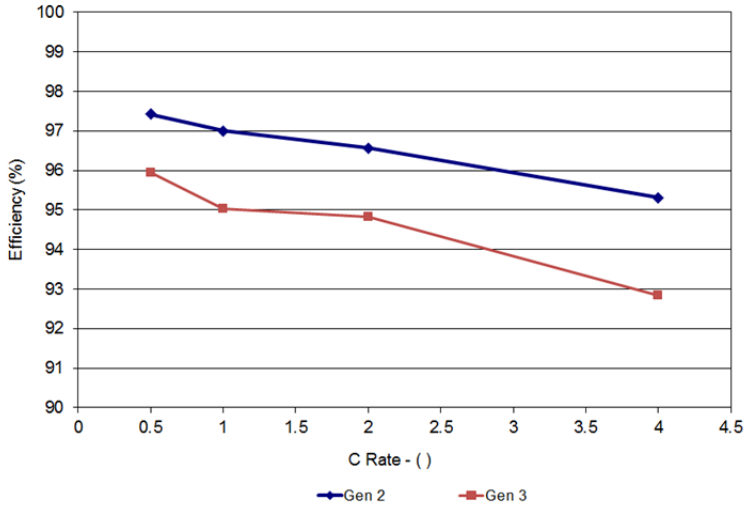

Figure IV - 46: Efficiency of two generations of cells tested at 30°C from 100% to 0% SOC

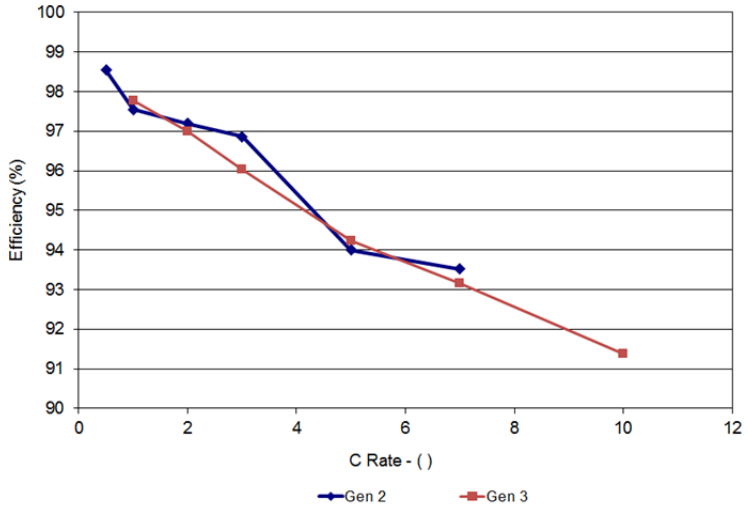

Figure IV - 47: Efficiency of two generations of cells tested at 30°C from 70% to 30% SOC

Figure IV - 48 shows the entropic heat signature of the cell with regards to temperature. The battery in this figure was cycled from 0% to 100% SOC at a very low current. A low current is used to limit the ohmic heating within the cell. As shown in the figure, the battery undergoes endothermic and exothermic heat generation over the cycling range. The figure also shows how temperature affects the entropic signature of the battery during operation—the battery is endothermic at the beginning of the charge for all temperatures above 15°C. Furthermore, the data indicates that the ohmic losses in the cell dominate at temperatures below 0°C. A closer look at the graph indicates inflection points that correspond to phase changes occurring within the cathode or anode during cycling. Knowing where these phase transitions occur allows the manufacturers and OEMs to cycle their battery outside of these areas so as to increase the cycle life of the battery. Measuring the phase transition requires an extremely accurate calorimeter with a very stable baseline that only NREL's calorimeters can provide for these large format cells.

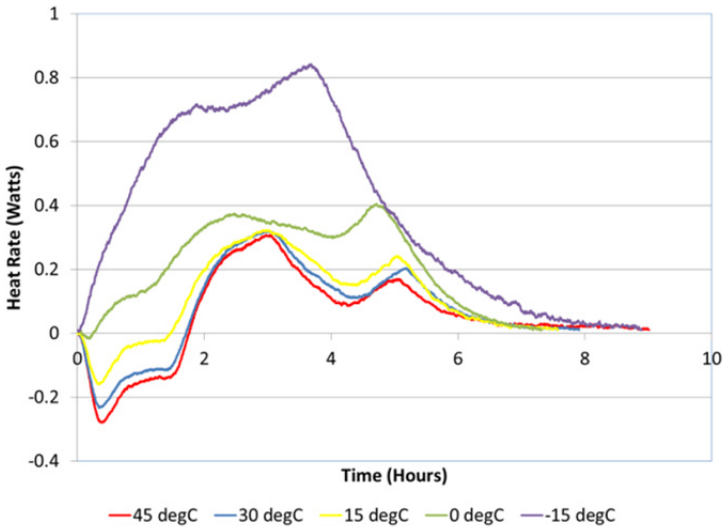

Figure IV - 48: Efficiency of two generations of cells tested at 30°C from 70% to 30% SOC

Infrared Imaging. NREL performs infrared (IR) imaging of battery manufacturers' cells to determine areas of thermal concern. NREL combines the IR imaging equipment with a battery cycler to place the cells under various drive cycles, such as the US06 charge-depletion cycle for a PHEV, to understand the temperature differences within the cell. We then make recommendations to the battery manufacturers and

USABC on how to improve the thermal design of the cell to increase its cycle life and safety.

Figure IV - 49 and Figure IV - 50 show the thermal images of two PHEV cells from different manufacturers at the end of a constant current discharge—the Ah capacities of the cells are within 5% of one another. Each figure contains a thermal image of the cell at the end of the constant current discharge, as well as a plot indicating the horizontal contour lines across the face of the cell—L01, L02, L03, and L04. Figure IV - 49 shows a hot spot in the upper right corner of the cell as well as a wide spread in temperature across the face of the cell from top to bottom and left to right. Figure IV - 50, on the other hand, shows a very uniform temperature distribution across the face of the cell at the end of discharge. When the cell temperature is uniform and consistent, all areas within the cell age at the same rate, leading to better cycle life. NREL is working with battery developers to understand how these temperature non-uniformities affect the efficiency and cost of the cell over its life.

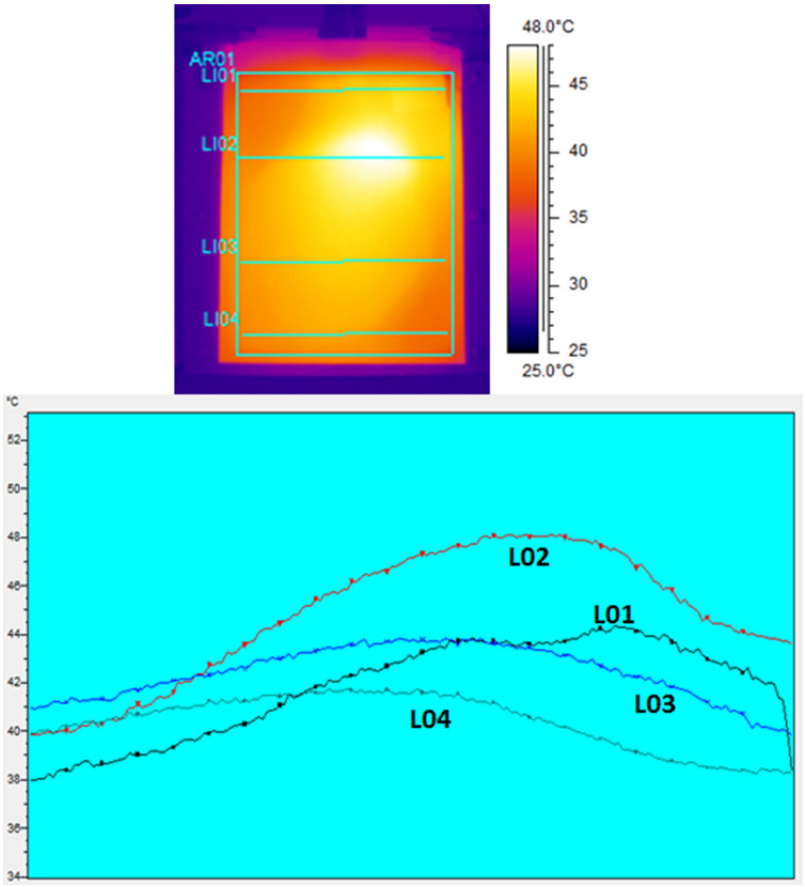

Figure IV - 49: Thermal image of a cell from manufacturer A under constant current discharge from 100% to 0% SOC

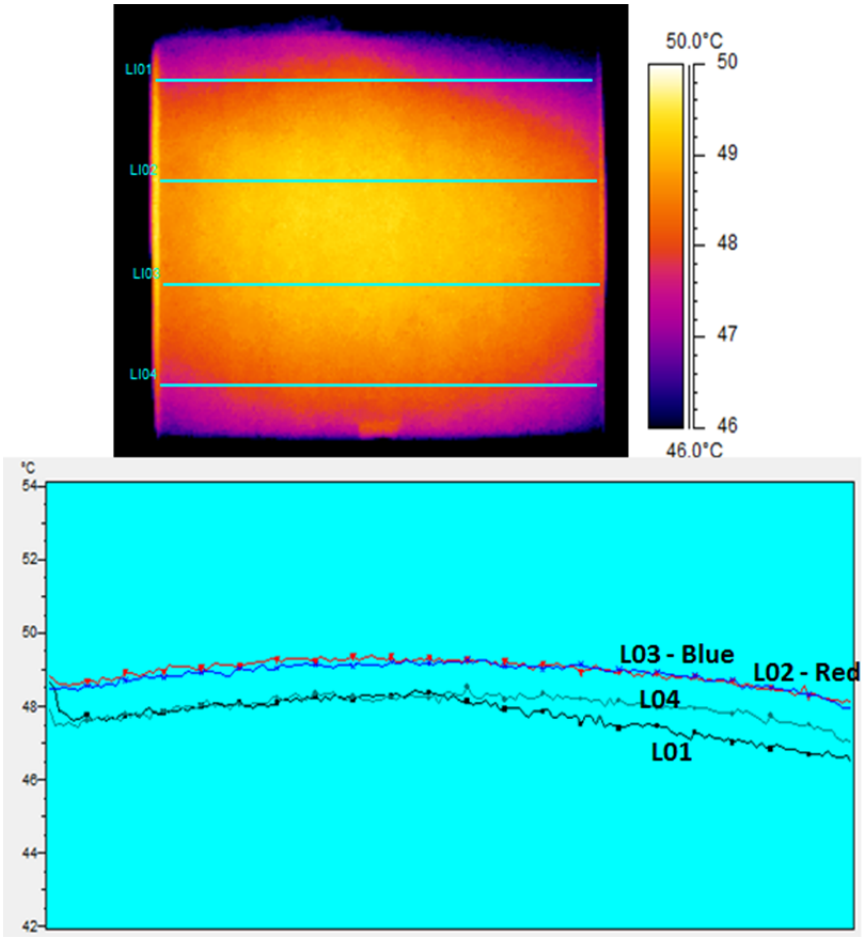

Figure IV - 50: Thermal image of a cell from manufacturer B under constant current discharge from 100% to 0% SOC

Pack Thermal Studies. In FY13, NREL evaluated air-, liquid-, and vapor compression-cooled packs for USABC battery developers. We measured the temperature rise and difference between corresponding cells, as well as the voltage of each cell within the pack. Testing is performed at temperatures between -20°C and 30°C with drive cycles pertinent for the battery under test—PHEV or EV. It has been shown that a 2-3% difference in cell temperature can have a 2-3% effect on fuel economy. The higher temperature cells within a pack are also typically more efficient and, therefore, work harder than the cells at lower temperatures—higher temperature cells typically provide more power. If different cells within the pack provide different amounts of energy over time, then the cells age differently and may cause imbalances within the pack, resulting in possible warranty issues.

Figure IV - 51 shows the average cell temperature in a pack with the cooling system on and off. The pack underwent a US06 charge-depletion cycle followed by a US06 charge-sustaining cycle. The difference in temperature at the end of the charge-depletion cycle between the cooling and no-cooling case is about 1°C. The negligible change in temperature is due to the high thermal impedances between the cooling system and where the heat in the cell is generated. The coefficient of performance (COP) of the cooling system is on the order of 0.10. We are working with the battery manufacturers and OEMs to improve the temperature uniformity of the cells within a pack and the effectiveness of the thermal management system.

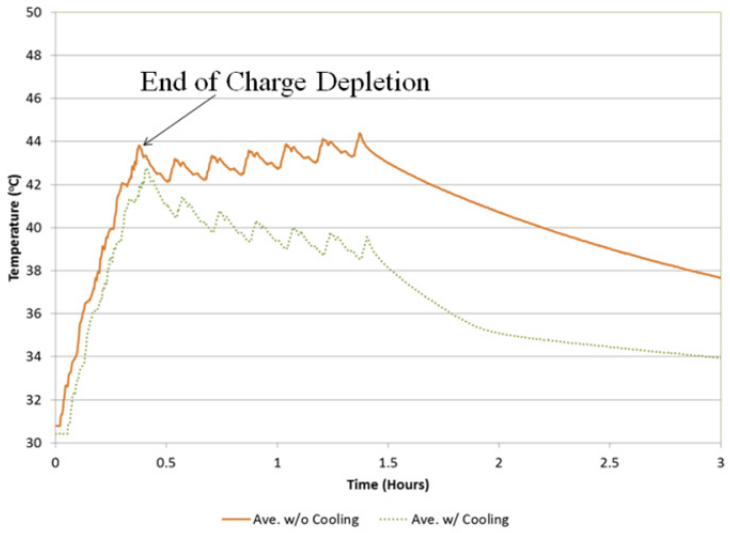

Figure IV - 51: Average cell temperature in a pack with and without cooling; the pack underwent a US06 CD cycle followed by a US06 CS cycle.

Conclusions and Future Directions

NREL has thermally tested cells, modules, and/or packs from Actacell, Cobasys, LGCPI, Johnson Controls, Quallion, K2, and SK Innovation. We've provided critical data to the battery manufacturers and automotive OEMs that can be used to improve the design of cells, modules, and packs, and their respective thermal management systems. The data included heat generation of cells under typical profiles for HEV, PHEV, and EV applications. We found that the majority of the cells tested had a thermal efficiency greater than 93% when cycled under a 2C constant current discharge. During thermal imaging of the cells, we identified areas of thermal concern and helped the battery manufacturers with the electrical design of their cells. Finally, we evaluated multiple packs during FY13 and determined that all aspects of the design need to be evaluated for the best thermal performance of the pack and the longest life.

In FY14, NREL will continue to thermally characterize cells, modules, and packs for USABC and DOE.

FY 2013 Publications/Presentations

1. Thermal data was shared with the Energy Storage Tech Team and each of the individual battery manufacturers' work groups.
2. March 2013 DOE Milestone Report, "Thermal Analysis and Characterization of Advanced Lithium-Ion Batteries."
3. September 2013 DOE Milestone Report, "Thermal Analysis and Characterization of Advanced Lithium-Ion Batteries and Packs."

IV.B.6 Development of an On-Demand Internal Short Circuit (NREL)

Matt Keyser

National Renewable Energy Laboratory
15013 Denver West Parkway
Golden, CO 80401
Phone: (303) 275-3876; Fax: (303) 275-4415
E-mail: matthew.keyser@nrel.gov

Collaborators:
Dirk Long, John Ireland, NASA, Dow Kokam,
E-One Moli, Leyden

Start Date: October 2009
Projected End Date: September 2014

Objectives

The objective of this effort is to establish an improved internal short circuit (ISC) cell-level test method that:

1. Replicates a catastrophic field failure due to latent flaws that are introduced during manufacturing.
2. Demonstrates the capability to trigger all four types of cell internal shorts.
3. Produces consistent and reproducible results.
4. Allows the cell to behave normally until the short is activated—the cell can be aged before activation.
5. Establishes test conditions for the cell—SOC, temperature, power, etc.
6. Provides relevant data to validate ISC models.

Technical Targets

It is critical for any new vehicle technology (including advanced energy storage systems) to operate safely under both routine and abuse conditions, which can include conditions of high temperature, overcharge, or crush. Lithium-ion cells need to be tolerant of internal short circuits.

Accomplishments

- USABC/NREL continues to make progress towards the development of an on-demand internal short circuit for lithium-ion batteries.
- Our internal short circuit emulator does not affect the performance of the battery under test and can be activated without puncturing or deforming the battery.
- The NREL ISC emulator was improved and successfully tested in cylindrical 18650 cells and a large format pouch cell.

✧ ✧ ✧ ✧ ✧

Introduction

Battery safety is the key to widespread acceptance and market penetration of electrified vehicles into the marketplace. NREL has developed a device to test one of the most challenging failure mechanisms of lithium-ion (Li-ion) batteries—a battery internal short circuit.

When battery internal shorts occur, they tend to surface without warning and usually after the cell has been in use for several months. While some failures simply result in the cells getting very hot, in extreme cases cells go into thermal runaway, igniting the device in which they are installed. The most publicized failures involved burning laptop batteries, and resulted in millions of recalls, as well as consumer injuries and lawsuits.

Many members of the technical community believe that this type of failure is caused by a latent flaw that results in a short circuit between electrodes during use. As electric car manufacturers turn to Li-ion batteries for energy storage, solving these safety issues becomes significantly more urgent.

Due to the dormant nature of this flaw, battery manufacturers have found it difficult to precisely identify and study it. NREL's device introduces a latent flaw into a battery that may be activated to produce an internal short circuit. NREL uses the internal short circuit device to better understand the failure modes of Li-ion cells and to validate NREL's abuse models.

The device can be placed anywhere within the battery, and can be used with both spirally-wound and flat-plate cells containing any of the common Li-ion electrochemistries. Producing a true internal short, the device is small compared to other shorting tools being developed by the industry, and does not rely on mechanically deforming the battery to activate the short, as do most other test methodologies. With the internal short in place, the battery can be used and cycled within normal operating conditions without activating the internal short device. This allows the battery to be aged prior to activation.

The internal short produced by NREL's device is consistent and is being developed as an analysis tool for

battery manufacturers and other national laboratories as well as OEMs. This has broad-reaching applications as automakers bring electrified vehicles to market in larger numbers.

Approach

NREL conceptualized and initiated laboratory testing of an internal short that has an insulating wax layer that is wicked away by the battery separator once the melting point of the wax is reached. A graphical representation of the ISC concept is shown in Figure IV - 52.

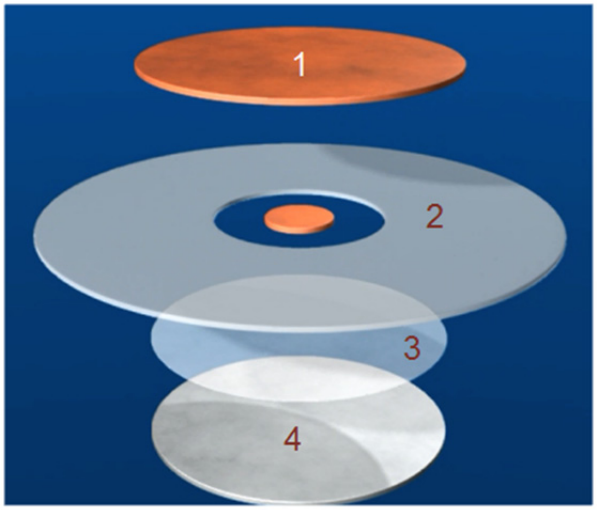

Figure IV - 52: ISC schematic (not to scale)

A unique feature of NREL's internal short device is that it has the ability to simulate all four types of shorts within a battery: 1) cathode active material to anode active material, as shown in Figure IV - 53; 2) cathode active material to anode current collector; 3) cathode current collector to anode active material; and 4) cathode current collector material to anode current collector, as shown in Figure IV - 53. Furthermore, the resistance of the short can be tuned to simulate a hard (more energetic) or soft (less energetic) short. Once the short is activated, the positive and negative components of the battery are internally connected within the cell and an internal short circuit begins.

Results

In FY12, NREL developed a spin coating apparatus to evenly distribute a thin layer of wax across the aluminum disc of the ISC. We performed design experiments on wax type, wax mixture, spin temperature, spin coating speed, amount of wax, and duration of spin coating. After several months of testing and modifying the various input parameters, we were able to attain a uniform coating of wax, approximately 15 µm thick, where the copper puck contacts the wax surface. The thin coating was then tested to determine how much pressure could be applied to the wax without such activation. The pressure tests showed that the ISC could withstand pressures exceeding 780 psi without premature activation, and, using this data, we developed a go/no-go gauge for the ISCs to be placed in cells. Finally, we reduced the burrs on the metal components of the ISC through manufacturing improvements—we did not want to accidently introduce a flaw into the battery that would generate an unwanted internal short.

During FY13, NREL took the improved ISC and incorporated all four types of shorts in an 8 Ah Dow Kokam cell (prismatic stacked pouch). Figure IV - 54 shows the device implanted in the DK 8 Ah pouch cell.

Figure IV - 55 shows the voltage response to all four types of activated ISCs within the DK cell at 10% SOC. NREL's previous modeling indicated that different types of shorts should exhibit different voltage and temperature responses within the cell. In particular, the cathode and anode materials for most lithium cells have high impedances as compared to the aluminum or copper electrode/collector material. Thus, if the active material is part of the ISC circuit, then the voltage should decay slowly or act as a "soft" short. If there is an aluminum collector to copper collector internal short, then the voltage should drop precipitously, or act as a "hard" short. Figure IV - 55 confirms NREL modeling data, showing that the collector to collector (Al-Cu) short is the most severe.

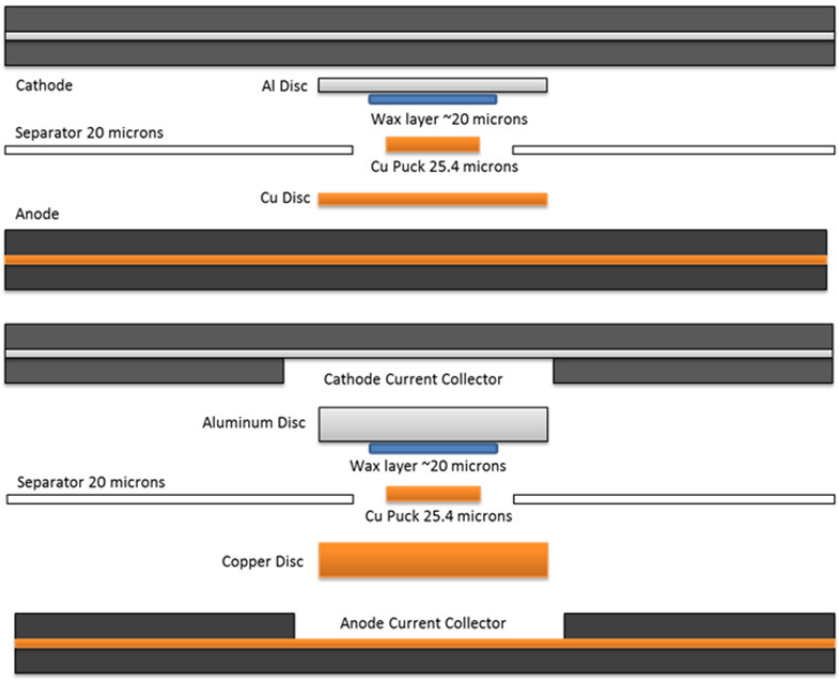

Figure IV - 53: Cathode-to-anode ISC (top) and collector-to-collector ISC (bottom) (not to scale)

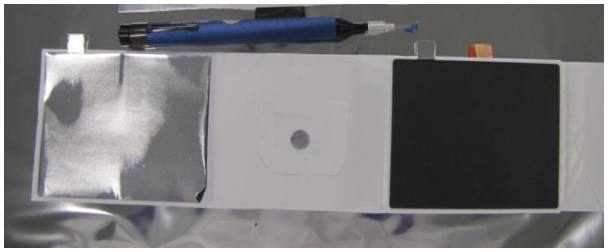

Figure IV - 54: ISC placed in DK 8 Ah cell; note the actual diameter of the short (Cu puck) is 0.125

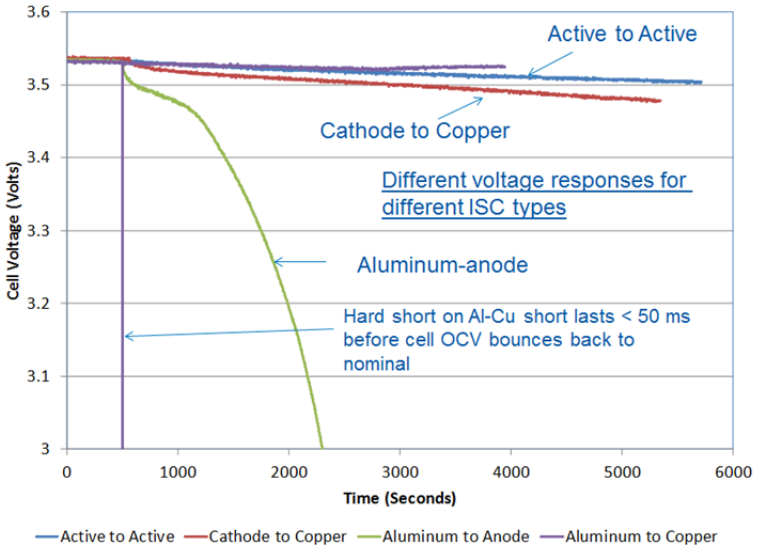

Figure IV - 55: Voltage response to various ISC activations in DK 8 Ah pouch cell at 10% SOC

The collector to collector short, however, only lasted about 50 ms. In order to understand why the voltage recovered after activation, NREL performed a destructive physical analysis (DPA) of the cell. The DK 8 Ah cell has multiple cathode and anode plates stacked in parallel. The ISC is in contact with only one set of these anode/cathode plates. When the ISC is activated, the remaining anode and cathode plates supply current through the aluminum (cathode) and copper (anode) tabs on the plates in contact with the ISC. The individual tabs are not meant for these high currents. In particular, the aluminum tab has a higher electrical resistance than the copper tab and acts as a fuse. Figure IV - 56 shows a macro image of the melted aluminum tab in question. Once the tab experienced a higher than normal current, the aluminum melted and prevented the current from flowing from the adjacent cathode plates to the ISC, effectively isolating the short circuit.

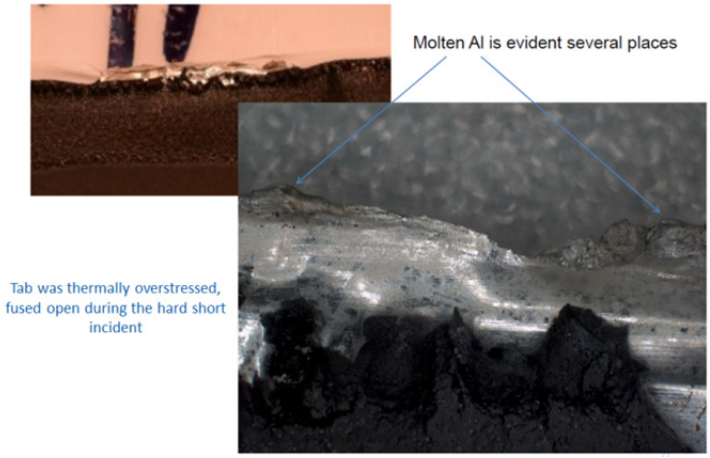

Figure IV - 56: Melted aluminum tab in DK 8 Ah cell upon activation of collector-to-collector ISC

NREL also performed a number of tests with the 8 Ah DK cells at 100% SOC with variable success. When an ISC is activated, gas generation quickly results. The underlying problem is that the pouch material acts as a balloon when pressurized and prevents the electrical components within the ISC from continuing to make contact. In order to maintain contact with the ISC, we experimented with placing the pouch cell between two rigid aluminum plates, as typically occurs within a battery pack. Initial tests of this type of setup (and others) were positive, and NREL is presently assessing how these new tests work with a larger sample set.

In FY12, NREL showed good progress when combining the ISC with an E-One Moli 18650 cell. In FY13, NREL used these cells to assess if the ISC affected the performance of the cell during cycling and how safety features incorporated into the cell were affected by the type of short. NREL placed a collector-to-collector (Type 4) short and aluminum-to-anode (Type 2) short into the E-One Moli 18650 cell with the standard shutdown separator (PP/PE/PP). The tests on both types of shorts were performed at 100% SOC. Twenty cells were fabricated for the test—10 cells with a Type 4 ISC and 10 cells with a Type 2 ISC. All 20 cells successfully went through formation and were put through 20 full discharge cycles consisting of a C/2 discharge cycle, a C/10 discharge cycle, and eighteen C/1 discharge cycles. We achieved nominal cycle stability for all 20 cells.

Table IV - 13 shows the Type 4 ISC activation results—7 out of 10 of the ISCs activated when the cell's temperature was brought to the melting point of the wax at 57°C. Of the seven ISCs that activated, one of the cells went into thermal runaway. Figure IV - 57 shows a plot of the cell temperature after activation of the Type 4 ISC. Cell #2 was the only cell to go into thermal runaway and achieved a maximum temperature of about 710°C. In the remaining six cells, the shutdown separator activated and prevented the cells from going into thermal runaway. The maximum temperature that each of these cells attained was around 120°C, which is the melting point of the polyethylene component of the shutdown separator.

Table IV - 13: Results from Type 4 ISC implantation in 10 E-One Moli 18650 cells

Cell	Successful Activation?	Thermal Runaway?
1	Yes	No
2	Yes	Yes
3	Yes	No
4	No	-
5	No	-
6	Yes	No
7	No	-
8	Yes	No
9	Yes	No
10	Yes	No

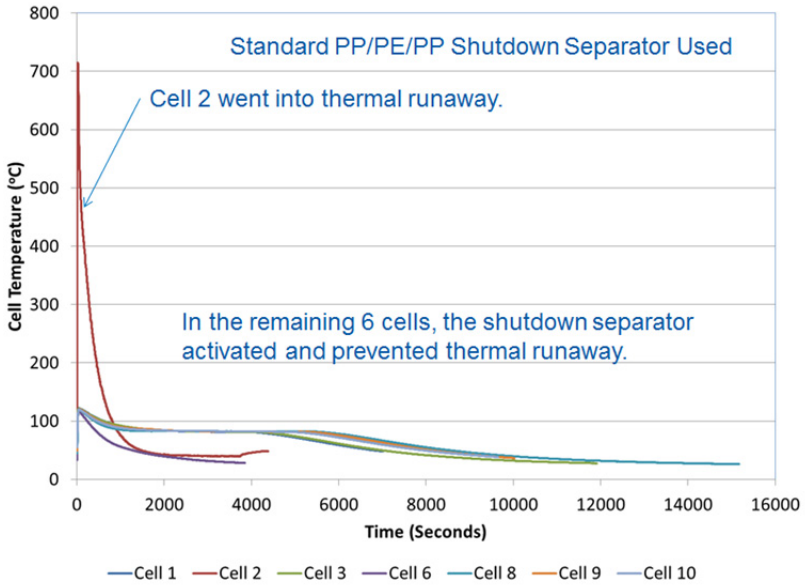

Figure IV - 57: Temperature response to Type 4 ISC (aluminum-to-copper) implantation in E-One Moli 18650 cells

Table IV - 14 shows the Type 2 ISC activation results—8 out of 10 of the ISCs activated when the cell's temperature was brought to the melting point of the wax at 57°C. Of the eight ISCs that successfully activated, six of the cells went into thermal runaway. Figure IV - 58 shows a plot of the cell temperature after activation of the Type 2 ISC. The maximum temperature attained by the six cells that went into thermal runaway was between 675°C and 775°C. In the remaining two cells, the shutdown separator activated and prevented the cells from going into thermal runaway.

Table IV - 14: Results from Type 2 ISC implantation in 10 E-One Moli 18650 cells

Cell	Successful Activation?	Thermal Runaway?
1	Yes	Yes
2	Yes	Yes
3	Yes	No
4	Yes	Yes
5	Yes	No
6	Yes	Yes
7	No	-
8	Yes	Yes
9	Yes	Yes
10	No	-

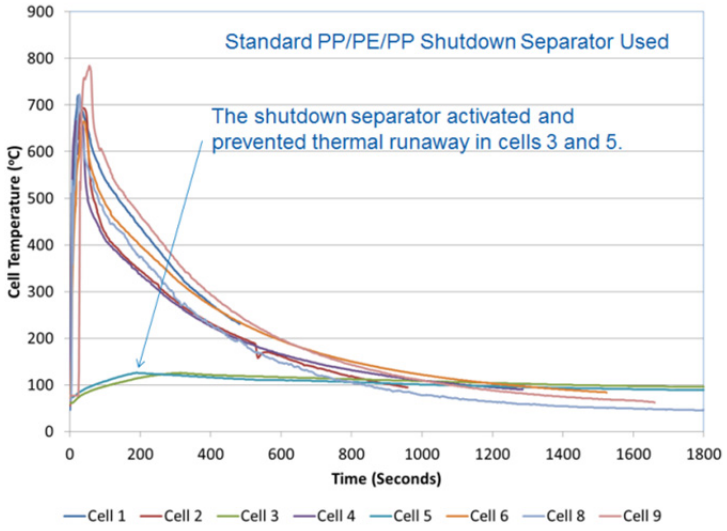

Figure IV - 58: Temperature response to Type 2 ISC (aluminum-to-anode) implantation in E-One Moli 18650 cells

From previous test results at lower SOCs, NREL determined that the Type 4 ISC was the most severe, but this appears to be a benefit when a shutdown separator is incorporated into the cell. The Type 4 ISC results in the quickest temperature rise within the cell and causes more of the separator to shutdown faster. In contrast, a Type 2 ISC is more resistive than a Type 4 ISC due to the electrical resistance of the anode. The higher resistance initially delays the temperature rise within the cell and allows for more of the cell's energy to be dissipated through the ISC—the higher energy eventually overwhelms the separator and allows the cell to go into thermal runaway.

Conclusions and Future Directions

In summary, our goal was to develop an ISC that:

1. Is small, with a low profile, which can be implanted into a Li-ion cell, preferably during assembly.
2. Is triggered by heating the cell above the melting temperature of the phase change material (wax).
3. Can handle currents in excess of 200 amps; this has already been proven in laboratory testing.
4. Has impedance that is consistent and can be selected to simulate a hard or soft short.
5. Can short between any of the battery components within a cell.

NREL's ISC is the only ISC in development that can be used selectively to connect different components (anode, cathode, aluminum current collector, and copper current collector) within a cell. When different components within a cell are connected, there should

and will be different outcomes. For instance, directly connecting the anode and cathode within a cell is much less likely to lead to thermal runaway than connecting the aluminum and copper current collectors. The end goal is not to send the cell into thermal runaway when activating the ISC, but to accurately simulate an emergent short.

The internal short device can be used to determine how changes to the battery affect the safety of the battery, either positively or negatively. Furthermore, the internal short can be used as a test methodology to evaluate how a battery would react to a latent defect.

NREL hopes to have the opportunity to continue researching how the type of internal short affects the performance of safety devices incorporated into lithium-ion cells. In the future, NREL hopes to use the ISC to verify the abuse models being developed by battery manufacturers and other national laboratories.

FY 2013 Publications/Presentations

1. 2013 NASA Aerospace Battery Workshop, Alabama.
2. 2013 DOE Milestone Report titled, “Evaluate NREL Improved Version of Internal Short-Circuit Instigator in Large Cells.
3. Presented concept to Underwriter’s Laboratory and USABC ISC working groups.
4. Battery Safety Conference 2013, San Diego, CA.

IV.C Computer Aided Engineering for Batteries

IV.C.1 Computer Aided Engineering for Batteries (NREL)

Ahmad Pesaran

National Renewable Energy Laboratory
15013 Denver West Parkway
Golden, CO 80401
Phone: (303) 275-4441; Fax: (303) 275-4415
E-mail: ahmad.pesaran@nrel.gov

Collaborators:
G.H. Kim, K. Smith, S. Santhanagopalan, NREL
S. Pannala, J. Turner, ORNL

Subcontract Teams:
GM, ANSYS, and ESim
EC Power, Ford, JCI, and PSU
CD-adapco, Battery Design, JCI, and A123

Start Date: April 2010
Projected End Date: September 2015

Objectives

The overall objective of the Computer Aided Engineering of Batteries (CAEBAT) project is to develop electrochemical-thermal software tools for design and simulation of performance, life, and safety of electric drive vehicle (EDV) batteries. As part of this effort, the NREL objectives are:

- Coordinate the activities of CAEBAT for DOE.
- Develop battery modeling tools to enhance understanding of battery performance, life, and safety, to enable development of cost-effective batteries for electric drive vehicles.
- Collaborate with Oak Ridge National Laboratory (ORNL) in the development of an Open Architecture Software (OAS) platform to link material and battery models developed under DOE Energy Storage R&D.
- Disseminate project results to the public and promote collaboration on modeling and software tools within the automotive battery community.

Technical Barriers

- Cost, life (calendar and cycle), high performance at all temperatures, and safety are barriers for widespread adoption of lithium-ion batteries in EDVs.
- Large investment and long lead time in cell and pack research, design, prototyping, and test cycle—and repeating the design-build-test-break cycle many times over several iterations—increases production costs.
- Lack of advanced computer-aided engineering tools to quickly design and simulate battery packs for EDVs impedes the optimization of cost-effective solutions.

Technical Targets

- Develop suites of software tools that enable automobile manufacturers, battery developers, pack integrators, and other end users to design and simulate cells and battery packs in order to accelerate the development of energy storage systems that meet EDV requirements.

Accomplishments

- In mid FY11, after a competitive procurement process, NREL entered into subcontract agreements with three industry-led teams to develop CAEBAT tools with 50-50 cost sharing.
- Three subcontract teams started the technical work in July 2011:
  - **CD-adapco** (teamed with Battery Design LLC, Johnson Controls-Saft and A123 Systems); NREL technical monitor: Kandler Smith.
  - **EC Power** (teamed with Pennsylvania State University, Johnson Controls Inc., and Ford Motor Company); NREL technical monitor: Shriram Santhanagopalan.
  - **General Motors** (teamed with ANSYS and ESim); NREL technical monitor: Gi-Heon Kim.
- In FY13, NREL continued to monitor the technical performance of the three subcontract teams through monthly conference calls, quarterly review meetings, and annual reports with DOE/HQ; quarterly review meetings took place at subcontractor sites, NREL, and DOE/HQ.

- The three subcontractors have already delivered the first version of their software tools to end users, and are on track to deliver software tools to the industry by the end of their period of performance (specific progress for each subcontract is provided in Sections IV.C.3 – IV.C.5 of this report).
- The following are major accomplishments from each team in FY13:
  - **CD-adapco** delivered the overall modeling framework, both electrochemical and thermal, for spirally-wound cells in the computer-aided engineering tool STAR-CCM+; JCI validated the model.
  - **EC Power** developed and delivered improved versions of ECT3D software to Ford, JCI, and NREL for evaluation, and performed localized current distribution measurement in large-format cells for model validation.
  - **GM and ANSYS** delivered the first battery pack-level software tool to team members for evaluation; the team also completed validation of the tool with electrochemical-thermal testing of a 24-cell module.
- NREL collaborated closely with ORNL on evaluation of elements of the OAS, such as Battery Input and Battery State (specific progress for ORNL's work is provided in Section IV.C.2 of this report).
- NREL continued its electrochemical-thermal modeling of cells through the multi-physics, multi-scale, multi-domain (MSMD) platform for CAEBAT (this activity is further discussed in Section IV.C.6 of this report); particularly, NREL:
  - Developed the Discrete Particle Diffusion Model (DPDM) as an advanced option for the MSMD particle domain model
  - Solved solid-phase lithium diffusion dynamics and transfer kinetics in a discrete diffusion particle system with the DPDM

✧ ✧ ✧ ✧ ✧

Introduction

In April of 2010, DOE announced a new program activity called Computer-Aided Engineering of Electric Drive Vehicle Batteries (CAEBAT) to develop software tools for battery design, R&D, and manufacturing. The objective of CAEBAT was to incorporate existing and new models into battery design suites/tools with the goal of shortening design cycles and optimizing batteries (cells and packs) for improved performance, safety, life, and cost. The work would address the existing practices under which battery and pack developers operated—tediously experimenting with many different cell chemistries and geometries in an attempt to produce greater cell capacity, power, life, thermal performance and safety, and lower cost. Introducing battery simulations and design automation at an early stage in the battery design life cycle, would make it possible to significantly reduce product cycle time and cost, thus significantly reducing the cost of the battery. Despite extensive modeling efforts at national laboratories, universities, private companies, and other institutions to capture the electrochemical performance, life, thermal profile, and cost of batteries, including NREL's development of an electrochemical-thermal model of lithium-ion cells with three-dimentional geometries, these tools were not integrated with a 3-D computer-aided engineering approach, which automotive engineers routinely use for other components. In many industries, including those involved in automotive and combustion engine development, CAE tools have been proven pathways to:

- Improve performance by resolving relevant physics in complex systems;
- Shorten product development design cycles, thus reducing cost; and
- Provide an efficient manner for evaluating parameters for robust design.

DOE initiated the CAEBAT project to extend these improvement pathways to battery CAE tools to the benefit of the entire industry. The CAEBAT project is broken down into four elements, as shown in Figure IV - 59:

- Material- and component-level models (developed under the BATT and ABR program elements of DOE Energy Storage R&D).
- Cell-level models.
- Pack-level models.
- Open architecture software to interface and link all models, particularly those from national labs

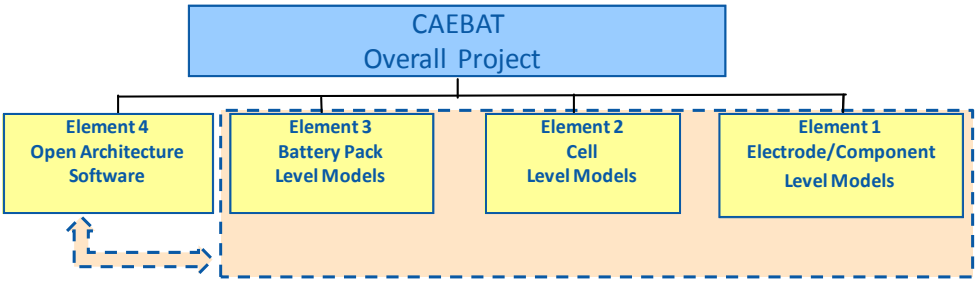

Figure IV - 59: Four Elements of the Computer-Aided Engineering for Batteries (CAEBAT) Activity

Since the goal of CAEBAT is to develop suites of software tools for automobile manufacturers, battery developers, pack integrators, and other end users, involvement of the industry (car makers, battery developers, and pack integrators) in the CAEBAT activity, particularly for Elements 2 and 3 (development of cell and pack models), is essential. DOE's major strategy to address this was to solicit active participation of industry partners in the development of cell and pack software tools from the beginning of the project.

To oversee the successful execution of the CAEBAT program, DOE designated NREL as the overall project coordinator, with the project tasks divided as follows:

- *Cell-Level Modeling* and *Pack-Level Modeling:* performed by industry, national laboratories, and academia; coordinated by NREL
- *Open Architecture Software:* performed by national laboratories; coordinated by ORNL

In order to engage serious involvement of the industry, NREL, with guidance from DOE, issued a Request for Proposals (RFP) in FY10 for the development of cell and pack battery design tools over a period of three years with 50-50% cost sharing. Teams led by CD-adapco, GM, and EC Power were awarded subcontracts, and the technical work began in July 2011. Additionally, NREL continued development and improvement of 3D electrochemical-thermal models, and collaborated with ORNL on development of open architecture software.

Results

Subcontracts with Industry. Significant progress has been reported by each subcontractor, according to each team's statement of work, and initial versions of their software tools have been released. More details on GM's progress may be found in Section IV.C.3 of this report. CD-adapco's progress is described in Section IV.C.4. Finally, Section IV.C.5 provides details on the progress made by EC Power. A summary of major accomplishments for each subcontractor is provided below.

CD-adapco.

- The project has now delivered the overall modeling framework, both electrochemical and thermal, in the computer-aided engineering tool STAR-CCM+, produced by CD-adapco, Figure IV - 60.
- An enhanced electrochemistry model has now been created; this model has been significantly extended to include the effect of concentration dependence of the solid-phase diffusion coefficient and also multiple active materials, as often found in contemporary lithium-ion cell design.
- Electrochemical and thermal datasets have been created and validated within the project for spiral cells; these have been created after the provision of cell-specific data from Johnson Controls, Saft; a process to extract unknown electrochemical properties from specific test work has been developed.
- The electrochemistry model and resultant datasets have been implemented in STAR-CCM+; this implementation allows the use of parallel computations within the electrochemistry model.
- A dataset of contemporary electrolytes modeled by Idaho National Labarotory (INL) has been added to the simulation environment; the dataset contains molarity, conductivity, diffusion coefficient, transport number, activity coefficient, density, and viscosity for twelve electrolyes.
- An approach to simulate aging within lithium-ion cells has been formulated, which considers SEI layer growth and associated capacity reduction driven by lithium loss.

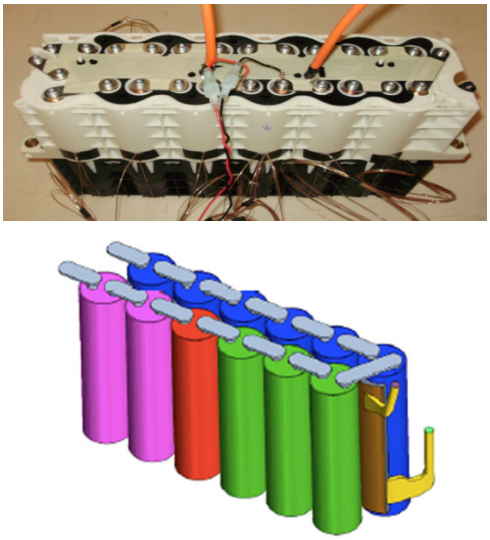

Figure IV - 60: Validation of electrochemical-thermal STAR-CCM+ model with 12-cell lithium-ion module

EC Power.

- Released two new and improved versions of ECT3D software to Ford, JCI, and NREL
- Performed localized current distribution measurement in large-format cell for model validation (Figure IV - 61)
- Demonstrated compatibility with ORNL's Open Architecture Software
- Conducted software validation with JCI pack
- Delivered final safety report
- Began life testing and data acquisition

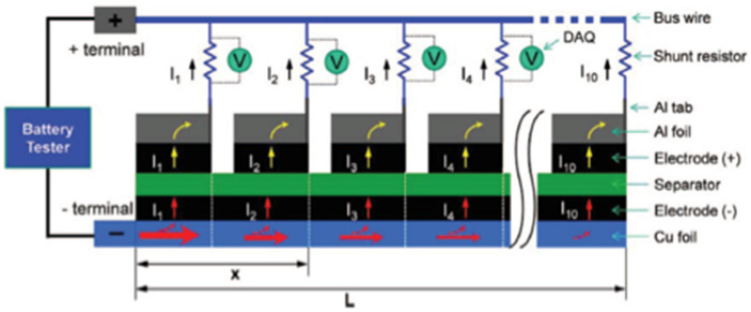

Figure IV - 61: Current distribution measurement in large-format cell

GM.

- Delivered several cell-level software tools
  - NREL's MSMD framework implemented in FLUENT with three electrochemistry sub-models.
  - Cell-level validation completed for ECM and NTGK models, and validation of P2D model in progress.
  - Developed user-defined electrochemistry capability allowing users to apply their own models while utilizing FLUENT's battery framework.
- Delivered first pack-level software tool to GM, NREL, and ESim
  - Auto electrical connection by detecting cell configurations in the pack.
  - Built in internal electric circuit model to speed up potential field convergence in the pack.
- Completed cycle life test at room temperature with 30% capacity fade
  - Cycle life test at elevated temperature in progress.
  - Physics-based cycle life model has been developed.
- Completed pack-level validation for 24-cell module (Figure IV - 62)
  - Full field simulation validated, and satisfactory comparison with test data obtained.
  - System-level model completed and validated compared to full field simulation, and test data and comparisons are satisfactory.
- Linear time invariant (LTI) system-level reduced-order model (ROM) approach validated and compared to full field simulation results.

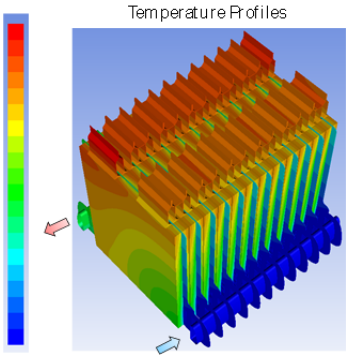

Figure IV - 62: Simulated temperature distribution for the 24-cell module

Collaboration with ORNL on Open Architecture Software. NREL and ORNL held regular meetings to discuss the best approach and strategy for the Open Architecture Software (OAS). This included collaboration on the Battery Input, Battery State, wrappers, and translators. CAEBAT subcontractors were engaged with ORNL to understand the standard battery input. Further details on ORNL's progress may be found in Section IV.C.2 of this report.

Development of Multi-Physics Battery Models at NREL. NREL continued its electrochemical-thermal cell modeling through the multi-physics, multi-scale, multi-domain (MSMD) platform for CAEBAT. The GM team is working with NREL to incorporate the MSMD lithium-ion battery modeling framework in their CAEBAT tools. We expect this approach to lead to more efficient computational time, reducing the time required to run different battery design scenarios. This activity is discussed in Section IV.C.6 of this report.

Conclusions and Future Directions

- The CAEBAT subcontract teams continued their progress toward the objectives of their respective programs; monthly technical meetings and quarterly program review meetings were held to monitor technical progress; experimental data are being collected by each team to validate the models, and first versions of cell software tools by each team have been released for partner and NREL evaluation.
- Each subcontractor released first (or subsequent) versions of their CAEBAT software tools to selected industry end users for evaluation.
- NREL continued electrochemical-thermal modeling of cells through the MSMD and collaborated with ORNL on development of the OAS to link developed and existing models.
- In FY14, we will continue to monitor the technical progress of each team through monthly and quarterly meetings to ensure success; we anticipate that software tools will be released to the pubic for purchase and evaluation; we will also continue to collaborate with ORNL on OAS development and example problem performance.

FY 2013 Publications/Presentations

1. A. A. Pesaran, Taeyoung Han, Steve Hartridge, Christian Shaffer, "Annual Progress Report on CAEBAT Subcontracts," NREL Milestone Report, September 2013.
2. A.A. Pesaran, G.-H. Kim, K. Smith, and S. Santhanagopalan, "Progrss of Computer-Aided Engineering of Electric Drive Batteries," presented at VTO Annual Merit Review (AMR), May 14-17 2013, Washington, DC. NREL Report No. PR-5400-58202.
3. A.A. Pesaran, Matt Keyser, Gi-Heon Kim, Shriram Santhanagopalan, and Kandler Smith. "Tools for Designing Thermal Management of Batteries in Electric Drive Vehicles." Presented at the Large Lithium Ion Battery Technology & Application Symposia Advanced Automotive Battery Conference; Pasadena, CA. February 4–8, 2013. NREL Report No. PR-5400-57747.
4. A.A. Pesaran, G-H. Kim, S. Santhanagopalan, and K. Smith, "Update on Computer-Aided Engineering of Batteries for Designing Better Li-Ion Batteries," presented at the USABC Technical Advisory Comitte Meeting, USCAR, Southfield, MI, August 2013.

IV.C.2 Computer Aided Engineering for Batteries (ORNL)

Brian Cunningham, VTO Program Manager
Subcontractor: ORNL

John A. Turner, Program Manager
Computational Engineering and Energy Sciences Group
Oak Ridge National Laboratory
Phone: (865) 241-3943; Fax: (865) 241-4811
E-mail: turnerja@ornl.gov

Collaborators:
S. Pannala, S. Allu, W. Elwasif, S. Simunovic, J. Billings, and S. Kalnaus

Start Date: July 2010
Projected End Date: September 2014

Objectives

- Develop a flexible and scalable computational framework that can integrate multiple physics models at various scales (battery pack, cell, electrodes, etc.), and provide a predictive modeling tool under the auspices of the CAEBAT program.
- Coordinate with partners across the program on requirements and design of the framework so as to preserve the investment in existing models.
- Ultimately, the detailed simulation capability will model coupled physical phenomena (charge and thermal transport; electrochemical reactions; mechanical stresses) across the porous 3D structure of the electrodes (cathodes and anodes) and the solid or liquid electrolyte system while including nanoscale effects through closures based on resolved quantities.
- The simulation tool will be validated both at the full-cell level and at the battery-pack level, providing an unprecedented capability to design next-generation batteries with the desired performance and safety needs for transportation.

Technical Barriers

Given the complex requirements for development of electrical energy storage devices for future transportation needs, a predictive simulation capability which can guide rapid design by considering performance and safety implications of different chemistry and materials choices is required. This capability must leverage existing investments and integrate multiple physics models across scales in order to (1) provide feedback to experiments by exploring the design space effectively, (2) optimize material components and geometry, and (3) address safety and durability in an integrated fashion. Such models do not currently exist.

Technical Targets

Develop the computational framework that will integrate existing models and new models developed by different CAEBAT subcontractor teams that span across the battery pack, modules, cells, etc. to provide an integrated design tool to battery manufacturers to optimize performance and safety in an accelerated fashion.

Accomplishments

- Released Beta V1a of the CAEBAT-OAS framework together with VIBE (Virtual Integrated Battery Environment), Battery ML (BatML) Schema specifications, battery state, and few examples.
- Completed porting of OAS (Open Architecture Software) to Windows.
- Revisions to the BatML standard and translators to/from: ANSYS, EC-Power, and AMPERES.
- Integrated workflow environment through NiCE: job launch, postprocessing of the results, XML files editing.

✧ ✧ ✧ ✧ ✧

Introduction

Computational tools for the analysis of performance and safety of battery systems are not currently predictive, in that they rely heavily on fitted parameters. While there is ongoing experimental research at various length scales around the world, computational models are primarily developed for the lower-length scales (atomistic and mesoscopic), which do not scale to the system-level. Existing models at the macroscopic or system-level are based on electrical circuit models or simple 1D models. The 1D models are limited in their ability to capture spatial variations in temperature, potential in the electrical circuits of the battery cells and

packs. Currently there is no design tool for batteries that can leverage the significant investments in modeling efforts across DOE and academia. An open and flexible computational framework that can incorporate the diverse existing capabilities and new capabilities coming through CAEBAT partners, can provide a foundation for a predictive tool for the rapid design and prototyping of batteries.

Approach

We are developing a flexible, robust, and computationally scalable open-architecture framework that integrates multi-physics and multi-scale battery models. The physics phenomena of interest include charge and thermal transport, electrochemical reactions, and mechanical stresses. They operate and interact across the porous 3D structure of the electrodes (cathodes and anodes), the solid or liquid electrolyte system and the other battery components. The underlying lower-length processes are accounted for through closure equations and sub-models that are based on resolved quantities. The schematic of this framework is given in Figure IV - 63.

The end result will be a verified, computationally scalable, portable, and flexible (extensible and easily-modified) framework that can integrate models from the other CAEBAT tasks and industrial partners. The framework will be used to validate models and modeling approaches against experiments and to support rapid prototyping of advanced battery concepts. Figure IV - 64 provides the roadmap for initial loosely-coupled model integration framework with a fully-implicit coupled capability in the later years.

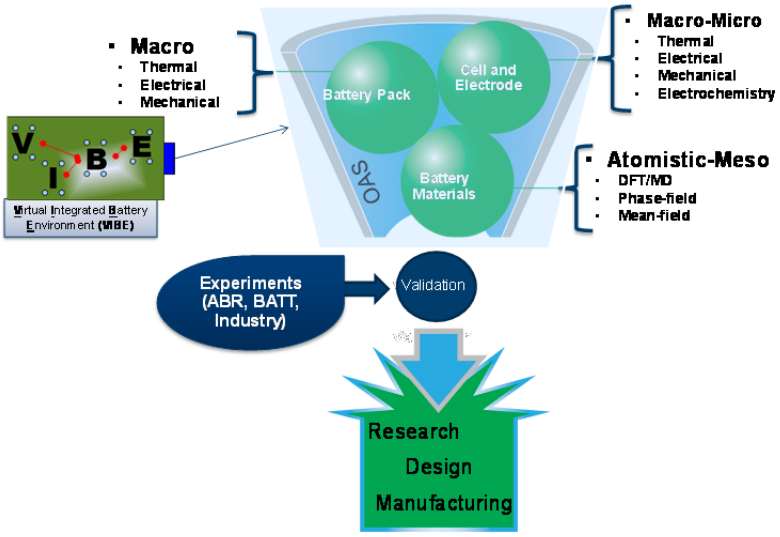

Figure IV - 63: Schematic of the OAS modeling framework and interactions with other tasks within the CAEBAT program and external activities.

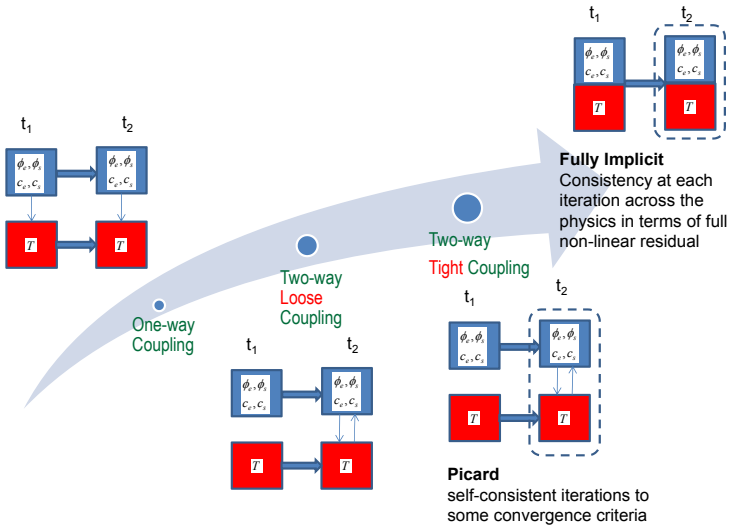

Figure IV - 64: Coupling scenarios in battery modeling. We started with one-way and two-way loose coupling. In later years, as needed, we will move towards two-way tight coupling with Picard and Full-implicit methodologies

Results

Virtual Integrated Battery Environment (VIBE). Integration of several components (pseudo-2D DualFoil, NTG, AMPERES, NREL's MSMD) has been completed. Initial linking to the ANL cost model has been done. In this current scenario the electrochemical component in VIBE supplies the area specific impedance (ASI) to the cost model to be further used in battery parameters calculations. The results of the modeling of a pouch cell (Farasis Energy, Inc.) were validated by experimental measurements of the cell surface temperature during discharge (Figure IV - 65). Excellent correlation can be observed that provides confidence in the modeling approach and integration of components in OAS.

Flexibility of the OAS was tested by substitution of one of the components in VIBE (DualFoil) with another (NTG) for electrochemical modeling. It was determined that with finer discretization of the electrodes in DualFoil the results from the two models are nearly identical. This provides users with a choice of the model most suitable for particular simulation scenario. DualFoil can be used when the details of concentration across the cell sandwich are needed, while NTG can be used when the thermal analysis is the primary goal in addition to significant savings of compute time.

Module level coupling allowed performing simulations of modules consisting of four pouch cells connected either in parallel or in series. Simulations of uneven cooling conditions on the module surface show that the potential difference in the cells on two sides can be as high as 2.5 mV. The battery state was expanded in order to include depth of discharge as an additional variable passed between the components. Figure IV - 66 shows the temperature distribution in a module with four cells in parallel. Initial integration of the mechanical component in VIBE has been performed. Coupling with mechanical modeling including elastic and elastic-plastic response of the material allows simulating scenarios involving battery abuse (Figure IV - 67) and provides guidance for battery safety testing.

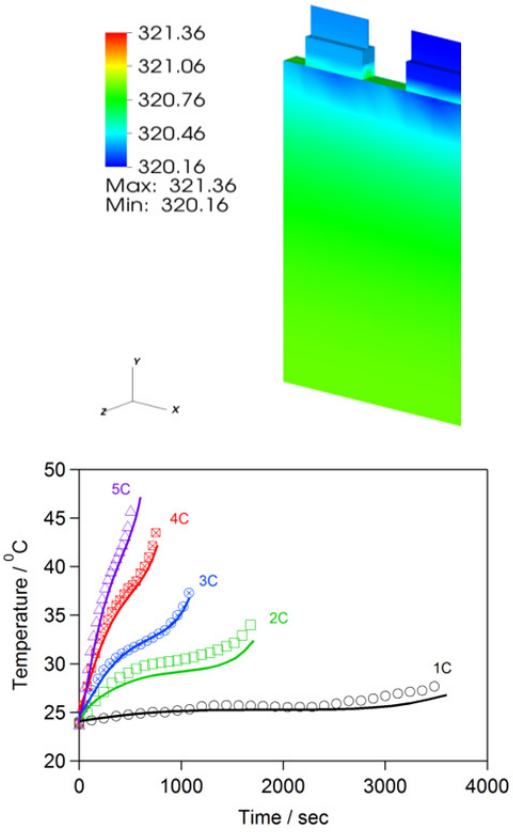

Figure IV - 65: Validation of 4.3 Ah pouch cell modeling (solid lines) with experimental temperature measurements (markers)

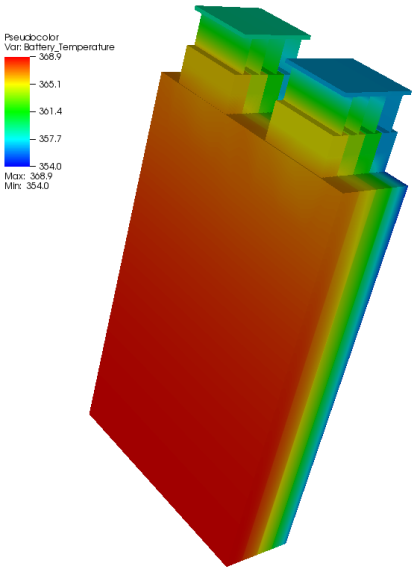

Figure IV - 66: Temperature distribution in a module with assymetric cooling

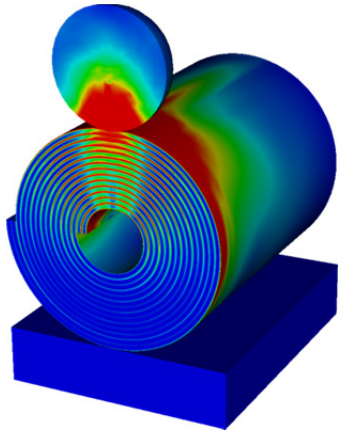

Figure IV - 67: Mechanical abuse of cylindrical cell (electrochemical-electrical-thermal-mechanical components)

OAS Capabilities of DAKOTA optimization toolkit were explored by running a numerical study of the effect of tab placement on cell temperature. 2000 configurations were run within the simulation with geometry parametrization and automated mesh generation. The lowest temperature was determined in the cell configuration where the tabs were placed on the opposite edges; the effect was more pronounced with an increase of the width of the cooled tabs. Example of

mesh generation and the temperature distribution corresponding to one of the arrangements is shown in Figure IV - 68.

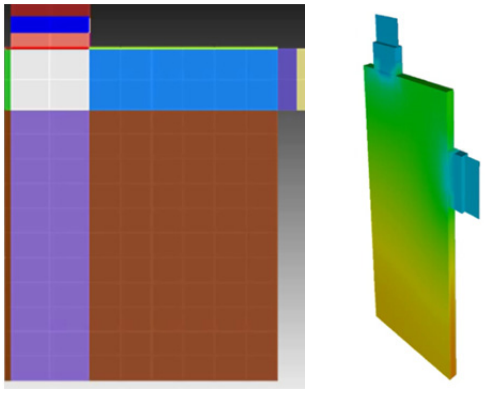

Figure IV - 68: Tab placement study using DAKOTA

Graphical User Interface and Integrated Workflow Environment. The development of a tool for simulation launch and post-processing of the results was based on NiCE project for workflow and data management. In 2013 we have deployed:

- Input editing for OAS setup files.
- Editing for BatML files.
- Local and remote OAS job launch.
- Multi-file upload and download of OAS VIBE data
- 3D static visualization of output.

A screen shot of CAEBAT-NiCE environment is shown in Figure IV - 69. The tool provides easy model setup with drop-down menus for model (component) selection, simulation control parameters and input of the material properties.

Bat ML. The Battery Markup Language (BatML) supports the CAEBAT OAS and enables standardized generation of simulation input files. As an essential part of the development, translation back and forth to various other native formats should be enabled. In 2013, we completed translators to/from EC Power, ANSYS, and AMPERES. The XML validating tool against BatML schema has been completed and can be used to validate the user supplied XML files. As an example, Figure IV - 70 shows the input file for thermal component in battery simulation translated to BatML format.

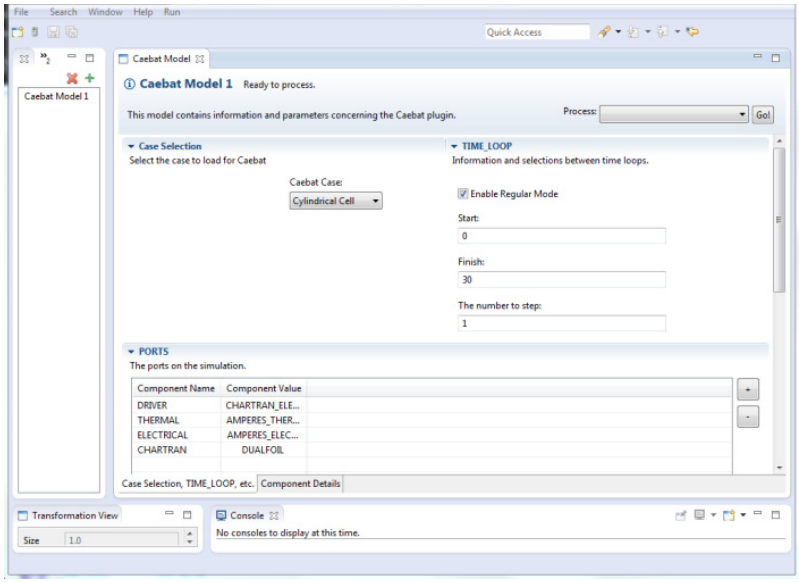

Figure IV - 69: CAEBAT-NiCE workflow environment for simulation setup, job launch and data post-processing.

Figure IV - 70: Input file for thermal component (AMPERES) translated to BatML

Conclusions and Future Directions

CAEBAT OAS framework core is stable and has been ported to Windows. Components for electrochemical, electrical, and thermal modeling have been successfully integrated and initial coupling to a mechanics model has been done. The framework possesses the ability for exchange of the components and integration of DAKOTA optimization toolkit provides a unique set of instruments to perform parametric sweeps and optimization study. Job launch and results post-processing through NiCE gives users an organized and easy to use workflow environment for battery simulations.

In the following year, we will:

- Complete integration of the mechanical component in VIBE.
- Extend battery state definition to include battery pack simulations.
- Implement additional BatML translators as necessary.
- BatML revisions based on community feedback.
- Release another version of the standard and associated tools.
- Implement two-way coupling in OAS.
- Finalize post-processing and real-time manipulation in NiCE.
- Develop a refined and user-friendly BatML editing in NiCE.

FY 2013 Publications/Presentations

1. Allu, S., Kalnaus, S., Elwasif, W., Simunovic, S., Turner, J.A., and Pannala, S., 2014, "A New Open Computational Framework for Highly-Resolved Coupled Three-Dimensional Multiphysics Simulations of Li-ion Cells," *Journal of Power Sources*, **246**, pp. 876-886.
2. Pannala, S., Allu, S., Elwasif, W., Kalnaus, S., Simunovic, S., and Turner, J.A., "Understanding the Effect of Temperature Gradients in Modules on Cell Balance Using Coupled Multi-Physics Modeling Approach With OAS Framework", *ECS 224th Meeting*, San Francisco, CA, Oct. 27 – Nov. 1, 2013.
3. Kalnaus, S., Allu, S., Pannala, S., Elwasif, W., Simunovic, S., and Turner, J.A., "Three-dimensional Thermal, Electrical, and Electrochemical Modeling of Li-ion Batteries," *ECS 224th Meeting*, San Francisco, CA, Oct. 27 – Nov. 1, 2013.
4. Allu, S., Elwasif, W., Pannala, S., Kalnaus, S., Simunovic, S., and Turner, J.A., "Optimization of tab Placement in Li-ion Battery Using Multi-Physics Simulations," *ECS 224th Meeting*, San Francisco, CA, Oct. 27 – Nov. 1, 2013.
5. Simunovic, S., Allu, S., Pannala, S., Kalnaus, S., Elwasif, W., and Turner, J.A., Coupled Multi-Physics Model for Li-ion Battery Cells During Impact," *EUROMAT 2013* – European Congress and Exhibition on Advanced Materials and Processes, Seville, Spain, Sept. 08 – 13, 2013.

IV.C.3 Development of Computer Aided Design Tools for Automotive Batteries (GM)

Dr. Gi-Heon Kim, NREL Technical Monitor
Subcontractor: General Motors LLC

Dr. Taeyoung Han, Principal Investigator
30500 Mound Road
Warren, MI 48090
Phone: (586) 986-1651; Fax: (586) 986-0446
E-mail: taeyoung.han@gm.com

Subcontractors:
ANSYS Inc. and ESIM LLC

Start Date: June 2011
Projected End Date: Dec 2014

Objectives

- As one of the subcontract teams, support the DOE/NREL Computer Aided Engineering for Batteries (CAEBAT) activity to shorten the product development cycle for EDVs and to reduce the cost associated with the current hardware build and test design iterations.
- Provide simulation tools that expand the inclusion of advanced lithium-ion battery systems into ground transportation. Validate advanced lithium-ion battery systems using GM's six-step model verification and validation approach.
- Participate in the Open Architecture Software program led by Oak Ridge National Lab to develop a flexible and scalable computational framework to integrate multiple battery physics sub-models produced by different teams.

Technical Barriers

- Existing design tools are not practical for realistic battery pack design and optimization.
- Various cell physics sub-models exist, but they have not been integrated in a single framework in commercial code.
- Current engineering workstations do not have the computational power required to simulate pack-level thermal response coupled with electrochemistry. System-level analysis or Reduced Order Modeling (ROM) is required to simulate integrated pack-level physics. However, ROM approaches for battery packs are not well understood.
- Collaboration to date has been difficult to achieve since software developer's commercial code, automaker's electrification strategies, and battery developer's cell designs and chemistry represent well-guarded intellectual property.

Technical Targets

Project goals for the GM team are summarized schematically in Figure IV - 71. To be useful to automotive engineers, battery cell and pack design tools should have the following analytical capabilities:

1. Predict optimum cell energy capacity in terms of electrical performance, cooling requirements, life, safety, and cost.
2. Predict battery pack life for various vehicle operating conditions.
3. Predict optimum state-of-charge (SOC) range for maximum life and safety.
4. Evaluate battery pack thermal management by predicting max intra/inter cell temperature difference under various drive-cycles.
5. Ability to provide system simulations with ROM that allows for trade off studies between the cooling cost and the battery pack warrenty cost in the early stage of vehicle development.
6. Ability for a real time system simulations that can lead to BMS deveopement and enhancement.

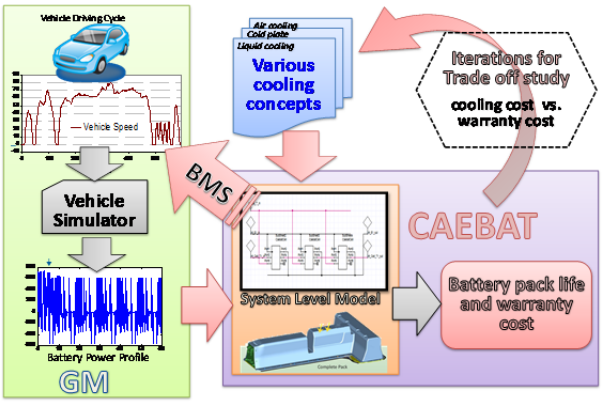

Figure IV - 71: Project goals for the CAEBAT battery design tool development

Accomplishments

- Several software deliverables for the cell level tools.
  - NREL's MSMD framework is implemented in FLUENT with three electrochemistry sub-models.
  - Cell level validation was completed for ECM and NTGK models and validation of P2D model is in progress.
  - Developed user defined electrochemistry capability that allows users to apply their own models while utilizing FLUENT's battery framework.
  - A detailed release note/tutorial has been provided. Official public release of these tools is scheduled for December 2013 (version 15).
- First pack level software tool was delivered to GM, NREL, and ESim
  - Auto electrical connection by detecting the cell configurations in the pack.
  - Built in internal electric circuit model to speed up the potential field convergence in the pack.
  - Code is completely parallelized.
- Cycle life test at the room temperature completed with 30% capacity fade.
  - Cycle life test at an elevated temperature is in progress.
  - Physics based cycle life model has been developed.
- Pack level validation is completed for a 24-cell module.
  - Full field simulation has been validated and satisfactory comparison with the test data has been obtained.
  - System level model was completed and validated compared to the full field simulation and the test data and comparisons are satisfactory.
  - Linear Time Invariant (LTI) system level ROM model approach has been validated in comparison with the full field simulation results.
  - Demonstration for various driving cycles is in progress

✧ ✧ ✧ ✧ ✧

Introduction

DOE established the Computer Aided Engineering for Electric Drive Vehicle Batteries (CAEBAT) activity to develop multi-physic design tools. NREL, with guidance from DOE, funded three subcontractors including the GM team, to develop software tools for CAEBAT. The principal objective of the GM team is to produce an efficient and flexible simulation tool that predicts multi-physics battery responses for bettery pack thermal management and predicts an optimum cell energy capacity in terms of electrical performance, cooling requirements, life, safety, and cost. GM has assembled a CAEBAT Project Team composed of GM researchers and engineers, ANSYS software developers, and Prof. White of the University of South Carolina and his ESim staff. In partnership with DOE/NREL, the Project Team will interact with the CAEBAT working groups to integrate and enhance existing sub-models, develop cell- and pack-level design tools, and perform experimental testing to validate the tools. The GM team will also create interfaces to enable these new tools to interact and interface with current and future battery models developed by others. NREL has been providing the technical consultations and monitored the overall progress. ORNL has provided the standard for Open Architecture Software (OAS). With a rapid deployment to industry, these project results will contribute to accelerating the pace of battery innovation and development for future electric-drive vehicles.

Approach

The objective of this project is to develop an open, flexible, efficient software tool for multi-scale, multi-physics battery simulation based on the ANSYS Workbench framework. ANSYS is leveraging and enhancing its existing commercial products to provide both field-level (FLUENT) and system-level (Simplorer) capabilities, including novel reduced-order modeling (ROM) methods and with other battery tools through the OAS interface.

ANSYS Battery Design Tool (ABDT) is part of the CAEBAT project funded during 2011-2014 by DOE through NREL, in which ANSYS is teaming with GM and ESim. ABDT is a graphical user interface layer that automates and customizes battery simulation workflow using ANSYS software products.

The essential role of the ABDT is to automate and integrate the ANSYS tools to make the various components emulate battery applications for cell and pack capabilities. ABDT is the newly-developed customization layer that ties the ANSYS building-blocks together to provide a unified, intuitive simulation workflow (Figure IV - 72).

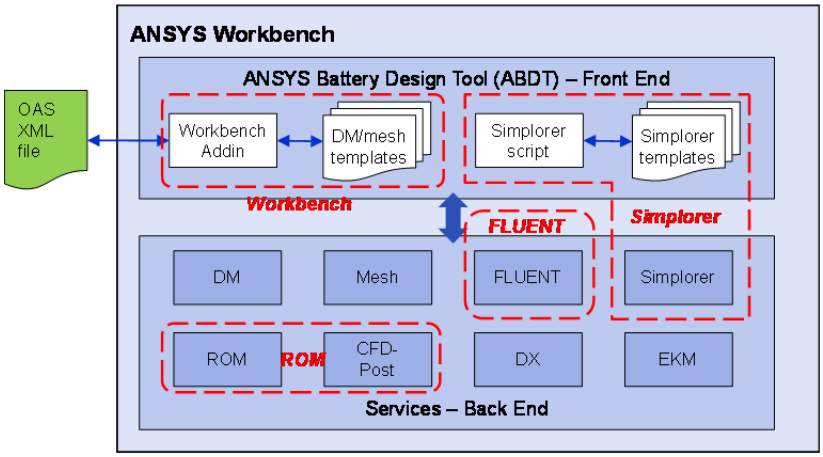

Figure IV - 72: Proposed software architecture for the combined the cell-level, pack-level, and OAS-interface capability

GM engineers and ESim tested the sub-models, cell- and pack-level design tools and evaluated the ABDT tools and provided furhter enhancements. The GM team also built prototypes for a battery module and a pack and performed experimental tests to validate these tools. At the pack level, the tools will be significantly advanced by the development of innovative reduced-order models, derived and calibrated from the cell-level models and carefully validated through experiments.

Results

In 2013, ANSYS delivered several versions of the cell- and pack-level battery simulation tools. First, the ECM model was enhanced to allow using different functions in the charging and discharging processes. Secondly, the electrochemistry model options were expanded and so the user has the capability to customize or develop a new electrochemistry model. The user has the option to specify system voltage, current, power, or C-rate and the battery module is fully coupled with all other ANSYS Fluent models and physics. The validation for the cell level models with ECM and NTGK for LG Chem pouch cell (P1.4 chemistry) was completed. The comparison with the test data for the cell temperatures are satisfactory as shown in Figure IV - 73. Cycle life tests were completed at room temperature and the cycle life test data has been delivered to ESim for cycle life modeling.

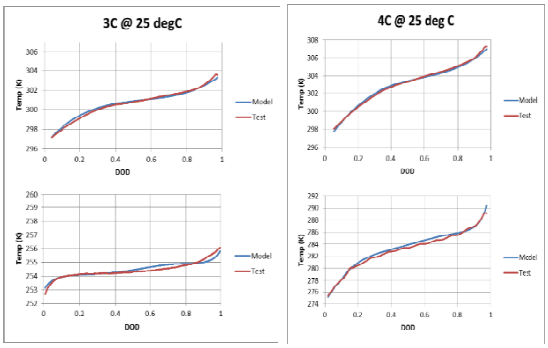

Figure IV - 73: Comparison of cell level models with the test data at various C-rates and operating temperatures

The wound cells with continuous tabs can be handled with the capability developed previously for the stacked cell configurations. The wound cell with discrete tabs requires further development. The GM team has developed two approaches to handle the wound cell configurations with discrete tabs. The first approach is based on the MSMD approach and has been extended and demonstrated for the wound cylindrical cell battery design as shown in Figure IV - 74. In this geometry, the electric current cannot conduct radially through layers while thermal temperature can. The second approach introduces the coordinate transform and variable extrusion developed by Esim (Figure IV - 75). This approach significantly reduces the mesh requirements and simulation time.

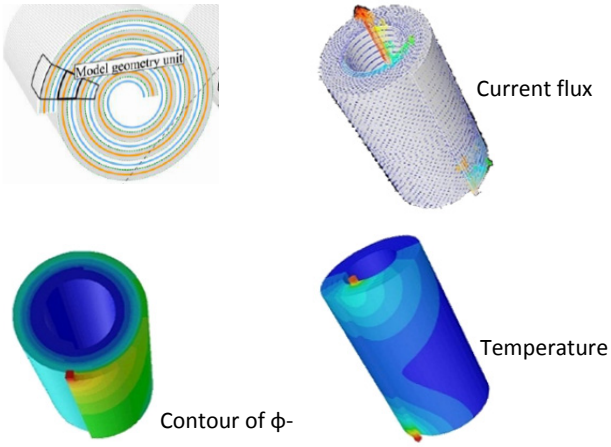

Figure IV - 74: Simulation results based on MSMD approach

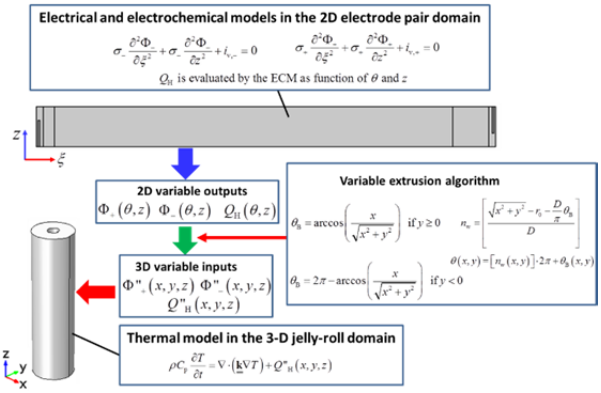

Figure IV - 75: Flowchart for the solution procedure using coordinate transformation

ANSYS has developed and delivered the first version of the ABDT, the Workbench (WB) graphical user interface layer that automates and customizes battery simulations using ANSYS software products. Within WB, the ABDT adds a new Toolbox section named Battery Design Tools. In addition, in the Custom Systems section two entries appear as the top-level templates for battery workflow. These entries, named Battery Cell Multiphysics and Battery Pack Multiphysics, follow the cell and pack organization of the CAEBAT project. Each template can also be further customized as needed, for example by manually adding links for data flow, or including ANSYS DesignXplorer (DX) for parametric exploration, and then store back to the Toolbox under Custom Systems for future use. The user can also display results based on standard visualization capabilities augmented with built-in menu for electrochemistry results.

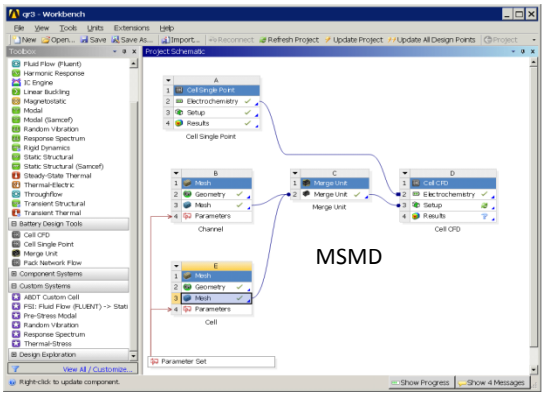

Figure IV - 76: ABDT Cell Level Design in Workbench

Customized ABDT components typically present one or more tabbed dialogs with data-entry fields with default values already entered (see Figure IV - 76, Figure IV - 77, and Figure IV - 78). In addition, fly-out menus available from a right-click on components in the Project Schematic can be used to access WB-standard utility functions.

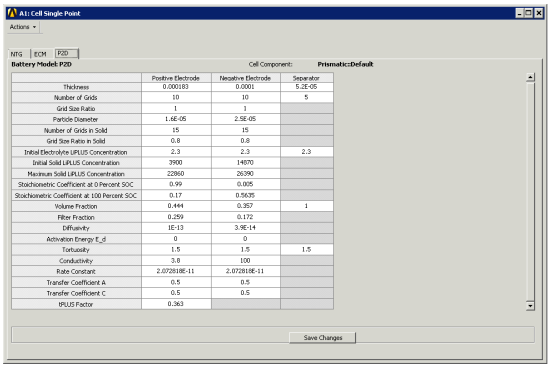

Figure IV - 77: Tabbed panel for the P2D sub model

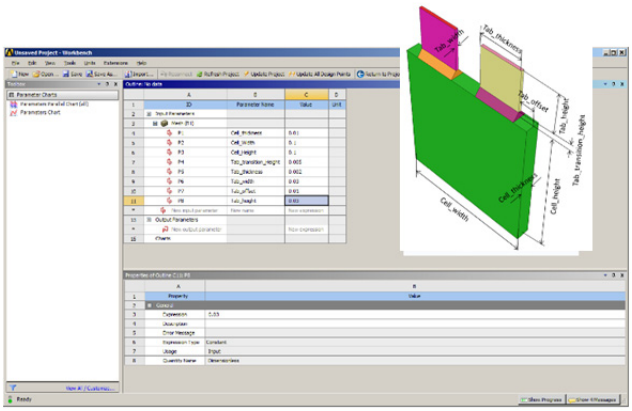

Figure IV - 78: Set cell geometry based on parameterized templates

GM has built a 24-cell module with a liquid-fin cooling system (Figure IV - 79). Thermocouples were located at various places in the module to compare the

full field computational fluid dynamics (CFD) simulations for the 24-cell module (Figure IV - 80). Full CFD model for the 24-cell module was constructed by GM engineers and has been simulated to compare the simulation results with the test data. GM engineers verified the 24-cell module simulations and confirmed that most temperature comparisons are very successful and predictions are within 1°C accuracy (Figure IV - 81 and Figure IV - 82). For the final validation of the pack level tools, activity also has been initiated to leverage the existing battery pack CAE models and test data sets.

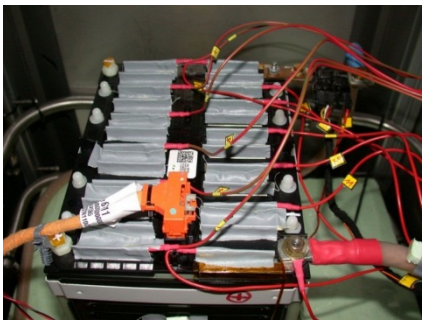

Figure IV - 79: A 24 cell module validation test set up for full field simulation against test data for high-frequency pulse charge-discharge

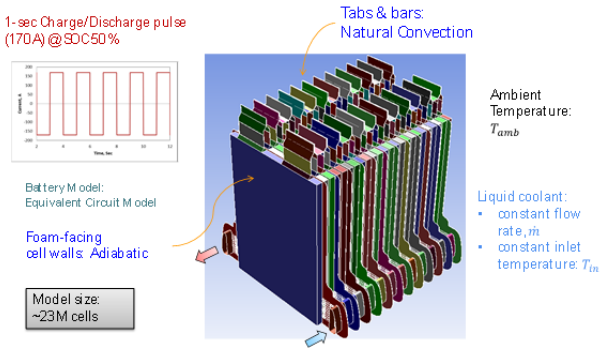

Figure IV - 80: A 24 cell module CFD full field simulation

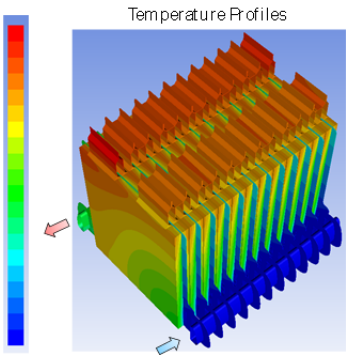

Figure IV - 81: Simulated temperature distribution for 24 cell module

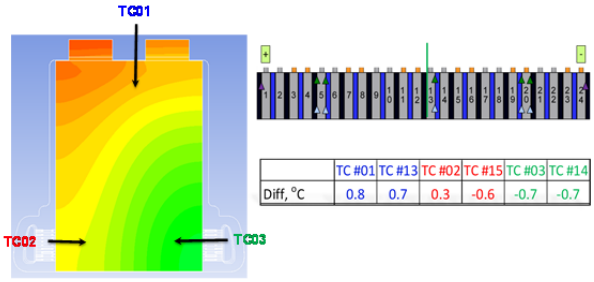

Figure IV - 82: Comparison of temperatures between the full field simulation and the test data

In System Simulation, ANSYS has developed a layered software approach to balance automation and flexibility. This approach is analogous to the cell-level approach with mesh templates and ABDT. The user has a highly-automated, intuitive interface for building and solving a system-level model of a battery pack using ANSYS system-simulation tool Simplorer, with the option to represent selected items in the pack using CFD models and/or reduced-order models (ROM) derived from CFD. This tool captures the effects of manifold geometry, coolant properties, and flow distribution through the microchannels and produces a look-up-table for mass flow rate distribution among cells to be used in Simplorer system simulations.

In 2013, GM team continued making progress on simulating full battery packs and developing linear and nonlinear ROM. Research and development work has continued on the algorithms for a LTI ROM. In order to validate the LTI ROM with respect to the test data, GM-team engineers constructed the ROM data by building LTI ROMs from a set of pre-generated Fluent step-responses. GM engineers validated the LTI ROM approach for realistic USO6 driving cycles as shown in Figure IV - 83-Figure IV - 86. A highly accurate CFD/thermal model of a 24 cell module was employeed to generate the training data for creating ROMs. The validation of the linear ROM system simulations for the 24 cell module was completed and the predicted temperatures were within 1°C compared to the test data at various cell locations as shown in Figure IV - 87. The GM team has also developed a procedure to obtain empirical parameters from the HPPC test data that performs and predicts accurately the load voltage, and hence the heat generation in cells under various drive-cycles. Heat generation in the tabs and inter-connects are included in the LTI ROM simulations.

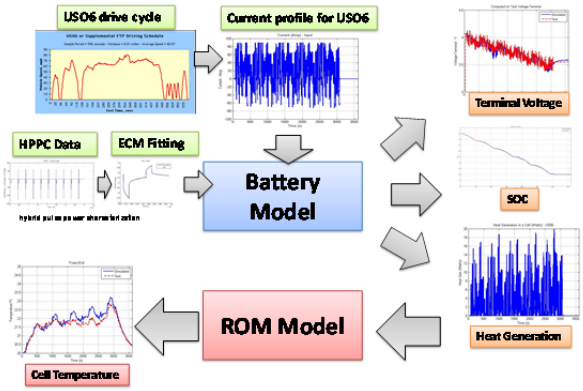

Figure IV - 83: LTI ROM System-Modeling approach for Battery Thermal Modeling

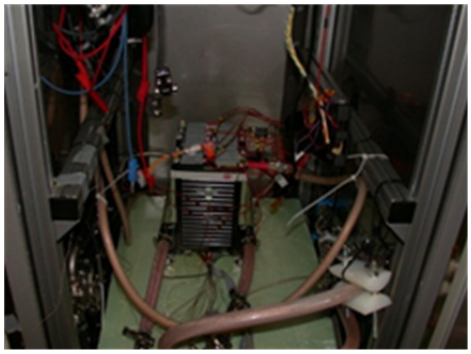

Figure IV - 84: Cell module validation test set up for LTI ROM validation against test data for US06 drive-cycle

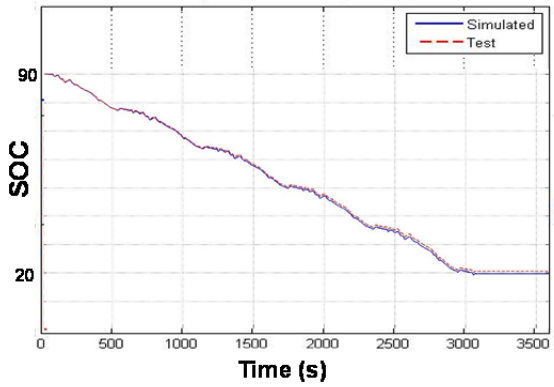

Figure IV - 85: Comparison of SOC between the model and the test data during US06 Drive-Cycle

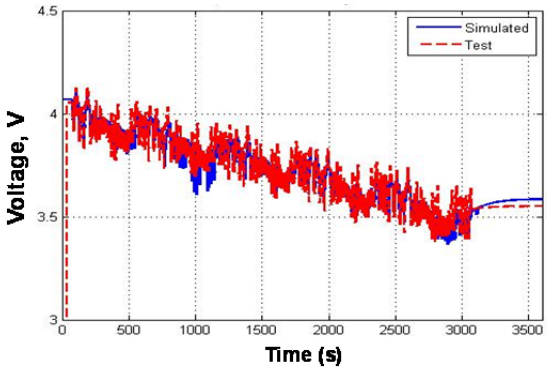

Figure IV - 86: Comparison of Voltage during US06 Drive-Cycle

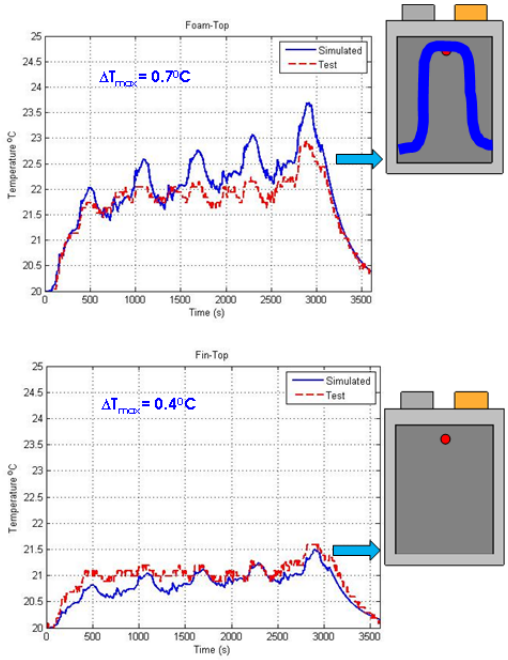

Figure IV - 87: Comparison of cell temperatures during US06 Drive-Cycle

Simulation of the five back-to-back US06 drive cycles for a total of 30 minutes driving cycle simulation took less than a few seconds in computational time with LTI ROM. Generating training data for LTI ROM using CFD model of a 2-cell/1-fin unit took roughly 7 hours for 2 million cells on an HPC using 64 CPUs. The agreement for the cell total heat generation is satisfactory compared with the measured total heat rejection by the coolant mass flow rate and the coolant temperature difference between the inlet and the outlet. We demonstrated that the LTI ROM accurately characterizes the thermal behavior of the cells in the 24 cell module.

Conclusions and Future Directions

Overall the project is on-track to meet all the objectives and its year two technical progress is consistent with the project plan.

1. Develop non-linear model order reduction methods for the pack level.
2. Extend cell-level models for aging and abuse, multiple active materials.
3. Define pack-level validation requirements for the production battery packs to meet the future capability matrix for pack-level CAE.
4. Build a standard data-exchange interface based on specifications from the OAS Workgroup.
5. Apply battery design tools to future vehicle programs and justify the value of the CAEBAT project.

An updated and validated version of the software will be available from in FLUENT/SIMPLORER ANSYS in July 2014.

Acknowledgement

Supported by Department of Energy, specifically Dave Howell and Brian Cunningham.

FY 2013 Publications/Presentations

1. Xiao Hu, Scott Stanton, Long Cai, Ralph E. White, “Model order reduction for solid-phase diffusion in physics-based lithium ion cell models,” Journal of Power Sources 218 (2012) 212-220.
2. Meng Guo, Ralph E. White, Gi-Heon Kim “A distributed thermal model for a Li-ion electrode plate pair,” Journal of Power Sources 221 (2013) 334-344.
3. Meng Guo, Gi-Heon Kim, Ralph E White, “A three-dimensional multi-physics model for a Li-ion battery,” Journal of Power Source, 240 (2013) 80-94.
4. Saeed Asgari, Xiao Hu, Michael Tsuk, Shailendra Kaushik, “Application of POD plus LTI ROM to Battery Thermal Modeling: SISO Case,” to be presented in 2014 SAE World Congress.
5. Ramesh Rebba, Justin McDade, Shailendra Kaushik, Jasmine Wang, Taeyoung Han, ”Verification and Validation of Semi-Empirical Thermal Models for Lithium Ion Batteries,” to be presented in 2014 SAE World Congress.

IV.C.4 Development of Computer Aided Design Tools for Automotive Batteries (CD-adapco)

Kandler Smith, NREL Technical Monitor
Subcontractor: CD-adapco

Steve Hartridge
CD-adapco, New York
60 Broadhollow Road
Melville, NY 11747
Phone: (631) 549-2300; Fax: (631) 549-2654
E-mail: steve.hartridge@cd-adapco.com

Subcontractor:
Battery Design LLC
2277 DeLucchi Drive
Pleasanton, CA 94588
E-mail: rspotnitz@batdesign.com

Start Date: August 2011
Projected End Date: July 2014

Objectives

- As one of the subcontract teams, support the DOE/NREL Computer Aided Engineering for Batteries (CAEBAT) activity.
- Provide simulation tools that expand the inclusion of advanced lithium-ion battery systems into ground transporation.
- Specifically develop a numerical simulation model which can resolve the appropriate phenomena required to create a coupled thermal and electrochemical response model.
- Apply advanced numerical techniques to expedite the solution of the governing fundamental equations within lithium-ion battery cells to enable advanced electrochemical models to be used in module and pack simulations.

Technical Barriers

One of the major challenges of this project is to include the important aspects of the rapidly maturing lithium ion battery simulation field in to an easy to use, widely accepted computer aided engineering tool. This implementation should be flexible and extensible to ensure the methods can move forward as the level of understanding in the fundamental physics evolves.

Another significant challenge is the creation of a modeling concept for spirally wound cells and their underlying architectures. Spiral cells can be grouped into several categories and hence flexible templates were created, the user then provides appropriate data to populate such templates creating a complete electrochemical and thermal cell model. The creation of such electrochemical and thermal templates and overall method is a significant part of this project.

It should also be stated that obtaining some of the modeling parameters used within such electrochemical models has proved a challenge. Part of enhancing the use of such a coupled thermal-electrochemical tool is to present a process to obtain such parameters to users so there is confidence in results obtained from such models.

Technical Targets

- Create a spiral cell analysis framework which includes the two electrodes, one positive and one negative, which are wound together to create the spiral jellyroll. This method should resolve the planar electrical/thermal gradients along the length and height of the electrodes as well as the overall performance of the electrode pair.
- Validate the created cell simulation models against test work provided by sub-contractors including both cylindrical and prismatic forms of spiral cells as well as power and energy focused chemistry.
- Use the validated methods within a larger framework to create simulations of battery modules which include such cells. These methods will be validated against electrical and thermal results from appropriate battery modules.

Accomplishments

- The project has now delivered the overall modeling framework, both electrochemical and thermal, as described above in the computer aided engineering tool STAR-CCM+, produced by CD-adapco.
- An enhanced electrochemistry model has now been created. The original model is based on the work of Newman et al[1]. This model has been significantly extended to include the effect of concentration dependence of the solid

phase diffusion coefficient[2] and also multiple active materials as often found in contemporary lithium ion cell design.

- Electrochemical and thermal datasets have been created and validated within the project for the spiral cells listed below. These have been created after the provision of cell specific data from Johnson Controls Inc. A process to extract the unknown electrochemical properties from specific test work has been developed
- The above listed electrochemistry model and datasets have also been implemented in STAR-CCM+. The implementation allows the use of parallel processing. This development addresses one of the major drawbacks often repeated regarding Newman type models which is the runtime of the calculation.
- A dataset of contemporary electrolytes has been added to the simulation environment. The dataset contains molarity, conductivity, diffusion coefficient, transport number, activity coefficient, density, and viscosity for 12 electrolyes. All values are concentration and temperature dependent within appropriate ranges.
- An approach to simulating aging within lithium-ion cells has been formulated which considers SEI layer growth and associated capacity reduction driven by lithium loss. This model is based on the work of H. Ploehn[3].

✧ ✧ ✧ ✧ ✧

Introduction

DOE established the Computer Aided Engineering for Electric Drive Vehicle Batteries (CAEBAT) activity to develop multi-physics design tools. NREL, with guidance from DOE, funded three subcontractors including CD-adapco, to develop software tools for CAEBAT. CD-adapco has extended its computer aided engineering code, STAR-CCM+, to analyze the flow, thermal and electrochemical phenomena occurring within spirally wound lithium ion battery modules and packs. This development created additional coding and methods which focus on the electrochemistry analysis of the spirally wound electrodes. This coding has been developed in collaboration with Battery Design LLC who is a sub-contractor to CD-adapco and has considerable experience in the field of electrochemistry modeling. As well as resolving the electrochemistry active regions in a spiral cell the model accounts for the tabbing of the electrode in the overall performance.

The created model has now been applied to the lithium ion cells listed below (see Table IV - 15), excluding the pouch cell where an empirical model has been used. The inclusion of a pouch cell to this project is to provide a control through which one can validate the results for analysis methods on components around the cell itself. The A123 test work includes considerable measurements from the conducting components around the cells to ensure their thermal and electrical effects are also represented correctly.

Table IV - 15: A list of lithium-ion cells used in testing the CD-adapco model

Manufacturer	Format	Capacity
JCI	Cylindrical	7Ah (HP)
JCI	Cylindrical	40Ah (HE)
JCI	Prismatic	6Ah (HP)
JCI	Prismatic	27Ah (HE)
A123	Pouch	20Ah

Approach

Detailed design information was obtained from the cell supplier to describe the dimensions of the electrode, the details of the can and finally, details of the electrode chemistry used in each of the designs. These cell models also used the appropriate electrolyte formulation from the newly integrated dataset provided by K.Gering at INL (also part of this project). Tightly controlled cell level test work was specified to enable the remaining modeling parameters to be extracted. This has now been done for all four spiral cells. The project now has a high level of confidence in the overall process, including cell test work specification and parameter extraction. This is borne out by the validation results presented below.

Results

Electrochemistry results. Once the electrochemistry models were fully defined and confirmed using the controlled cell test work, a validation of the voltage response from the created models was completed. This validation used either a charge-sustaining or charge-depleting load as appropriate for the cell in question and compared with experimentally obtained voltage curves. Validation results are shown below:

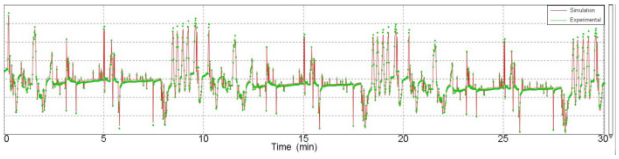

Figure IV - 88: Voltage response from the created electrochemical model for the JCI VL6P cell over a 30min drive cycle compared to test work (Voltage scale removed)

The mean error for the VL6P simulation model (Figure IV - 88) over the 30 minutes drive cycle is 9 mv. Similar error levels are seen in the other models (Figure IV - 89, Figure IV - 90)

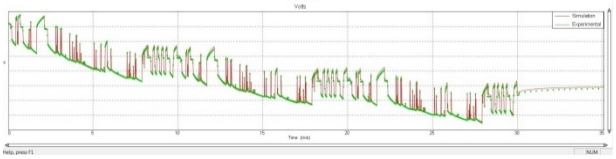

Figure IV - 89: Voltage response using the electrochemistry model for the JCI VL41M cell over a 30min drive cycle compared to test work (Voltage scale removed)

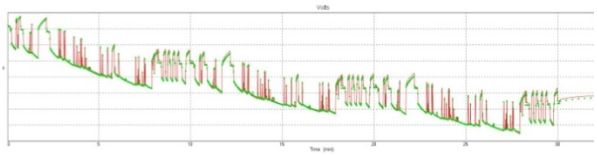

Figure IV - 90: Voltage response using the electrochemistry model for the PL27M cell over a 30min drive cycle compared to test work (Voltage scale removed)

The above validation work was completed using a 'lumped' electrochemistry model. This essentially means a single temperature for the whole cell is assumed. The cell representations were then transferred in to STAR-CCM+ and complex three dimensional models of the cell were created. This model now accounts for the internal anisotropic thermal conductivity of the jelly roll as well as the jelly roll's thermal interfaces with neightbour components such as mandrels and external cans. The electric conductivity of the current collectors is also included in the model. Figure IV - 91 compares the simulation results for the VL6P electrochemistry model using the lumped model and the 3D model. The mean difference is 8 mV over the 30 minutes drive cycle. Differences are expected within the results due to the 3D model having a distribution of temperature within the jelly roll, hence a differing response. Overall we can conclude that the voltage response of the cell is well captured within both lumped and 3D modelling domains hence engineers can use the same cell data within either modeling framework, lumped or detailed 3D.

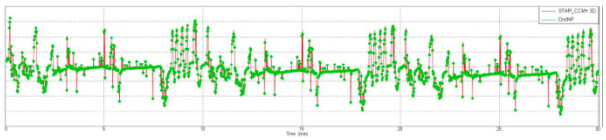

Figure IV - 91: Comparison of lumped electrochemistry model vs three dimensional electrochemistry model over a 30min drive cycle (Voltage scale removed)

Thermal results. The thermal validation was completed using the 3D model within STAR-CCM+. Module test work for the VL6P, PL6P & PL27M has now been complete. Figure IV - 92 shows the VL6P 12 module that is used within the module tests. This arrangement is liquid cooled.

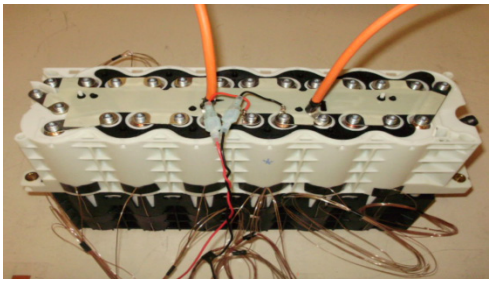

Figure IV - 92: VL6P 12 module used for thermal valication of the 3D model within STAR-CCM+

The main thermal validation test used the same drive cycle input condition as used in the lumped model and cell can surface temperatures were monitored.

A high fidelity finite volume model was created within STAR-CCM+ (see Figure IV - 93) including all cell components (jelly rolls, current collection designs, outer cans) as well as current carrying straps and coolant system.

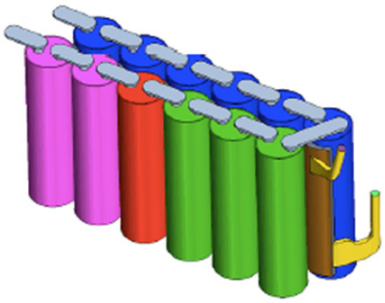

Figure IV - 93: High-fidelity volume model created within STAR-CCM+

A number of thermacouples were located on the cell of interest and the graph below shows one result compared to the appropriate test result. These thermocouples were located on the outer surface of the cell can. The scales have been removed as this is sensitive data.

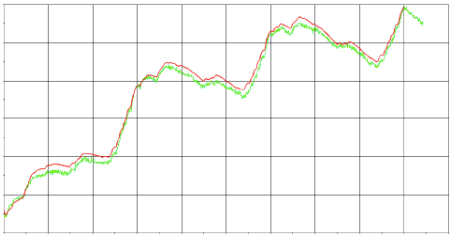

Figure IV - 94: Thermal result for a cell within the VL6P module (Red line is simulation, Green experiment)

The spatial distribution around the cell is considered by having a number of thermocouples and this was used to validate the simulation model. Due to the confidential nature of the commercial cells and modules used for validation more extensive plots cannot be shown within this report.

Electrolyte results. Complimentary to the core simulation technology, a suite of comtemporary electrolytes have been added to the database to enable users to rapidly select appropriate properties. These are used within the overall electrochemical models which represent the cells. As a sample of the data, the graph below shows the conductivity of EC31_PC10_DMC59_$LiPF_6$ compared to published data by Valoen et. Al[4].

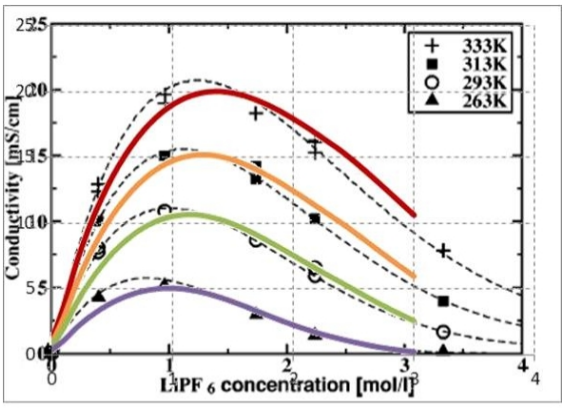

Figure IV - 95: Conductivity of $LiPF_6$ in PC/EC/DMC as a function of $LiPF_6$ concentration for 333, 313, 293, and 263 K

The electrolyte properties were used in a physics-based model to correlate discharge energy as a function of rate and temperature to electrolyte properties[5,6].

Conclusions and Future Directions

The project is about two-thirds complete. The described flow, thermal & electrochemistry simulation architecture is now established and differing modeling domains, lumped and three-dimensional, are available. Cell level and module level test work is now complete and validation of the lumped electrochemical models is presented. A comparison of the modeling domains has been presented and the differences between results are as expected and explainable. Finally the complex three-dimensional domains for the module level validation are constructed and a thermal result is presented. The technology developed in this project is now contained within the three-dimensional computer aided engineering code STAR-CCM+, which is commercially available from CD-adapco. An updated and validated version of the software will be available from CD-adapco in July 2014.

Acknowledgements

The subcontractors would like to acknowledge the contribution and input that the National Renewable Energy Laboratory has made, particularly Kandler Smith and the support of the Department of Energy, specifically Dave Howell and Brian Cunningham. The authors would like to acknowledge the subcontractors', namely JCI. Inc and A123 Systems, support in sharing some of the results from this work.

References

1. Simulation and Optimization of the Dual Lithium Ion Insertion Cell, T. Fuller, M. Doyle, J. Newman, *J. Electrochem. Soc.* 141 (1994) 1-10.
2. Concentration dependence of lithium diffusion coefficient in LiCoO2, Young-Il Jang, Bernd J. Neudecker, and Nancy J. Dudney, *Electrochemical and Solid-State Letters*, 4 (6) A74-A77 (2001).
3. Solvent diffusion model for aging of lithium-Ion battery cells, Ploehn, P Ramadass & R. White *J. Ele Soc* A456-A462(2004).
4. Transport Properties of LiPF6-Based Li-Ion Battery Electrolyte, L. Valoen & J. Reimers, *J. Electrochem Soc.*, 152 (5) A882-A891 (2005).
5. Design and Simulation of Spirally-Wound, Lithium-Ion Cells Lithium-Ion Batteries: Modeling, R. Spotnitz, S. Hartridge, G. Damblanc, G. Yeduvaka, D. Schad, V. Gudimetla, J. Votteler, G. Poole, C. Lueth, C. Walchshofer, and E. Oxenham, *ECS Trans.* 2013 50(26): 209-218; doi:10.1149/05026.0209ecst.
6. Simulation of Electrolyte Composition Effects on High Energy Lithium-Ion Cells, R. Spotnitz, K. Gering, S. Hartridge, G. Damblanc, 224th ECS Meeting San Francisco, Oct 30, 2013.

IV.C.5 Development of Computer Aided Design Tools for Automotive Batteries (EC Power)

S. Santhanagopalan, NREL Technical Monitor
Subcontractor: EC Power

Chrisitan E. Shaffer, Project Manager
200 Innovation Boulevard
State College, PA 16803
Phone: (814) 861-6233; Fax: (814) 861-6234
E-mail: ceshaffer@ecpowergroup.com

Subcontractor:
Ford Motor Company
Johnson Controls, Inc.
Penn State University

Start Date: May 2011
Projected End Date: May 2014

Objectives

- Develop an electrochemical-thermal coupled model and associated computer code for large-format, automotive Li-ion cells and packs.
- Create a novel computational framework that allows for rapid and accurate performance/safety simulations. Algorithms will span across several length scales, ranging from particle size, to an electrochemical unit cell, to a 3D battery, and finally to an entire battery pack. This computational framework will be able to model both wound and stacked cell geometries.
- Develop a comprehensive materials database that is critical for accurate modeling and simulation of large-format Li-ion batteries.
- Test and validate the developed cell and pack models against a wide range of operating conditions relevant to automotive use, such as extreme temperature operation, complex power profiles, etc.

Technical Barriers

The large format nature of automotive Li-ion batteries presents a unique set of challenges that set them apart from the batteries used in cell phones, laptops, and other consumer goods. For example, high rates of charge and discharge, in combination with the large surface area of the cell, lead to widely varied temperature distributions on the cell and throughout the packs. This non-uniformity causes a number of serious issues, including poor battery performance, increased degradation effects, potential safety concerns, and the inability to fully utilize the active material inside the battery. Creating actual cells and packs is time consuming and extremely expensive, which makes an efficient, high fidelity simulation tool very desirable.

However, the strongly coupled nature of electrochemical and thermal physics, the relevant scales of a battery cell or pack (ranging from sub-microns to meters), and the need for a comprehensive materials database, makes the creation and development of a Li-ion battery model a unique and challenging task.

Technical Targets

- Development of an extensive database of material properties for accurate model input.
- Creation of a multi-dimensional, electrochemical-thermal coupled model, complete with an easy to use, intuitive graphical user interface (GUI).
- Development of fast, scalable numerical algorithms enabling near real-time simulation of batteries on a single PC, and packs with thermal management systems on a small computer cluster.
- Experimental validation of the model and corresponding software.

Accomplishments

- Delivered new versions of the large-format software tool, “Electrochemical-Thermal Coupled 3-Dimensional Li-ion Battery Model” (ECT3D) to partners during FY2013. Updates to software include additional safety features/capabilities, enhanced user interfaces, and upgrades based on Ford, JCI, and NREL user feedback.
- Property characterization for materials database ~ 80% complete.
- Cell *in situ* current distribution measurements at varying C-rates and temperatures complete; data used for initial validation, additional validation to be performed in final year of project.
- Initial life models complete.

- Demonstrated compatibility of ECT3D with Open Architecture Standard being developed by Oak Ridge National Laboratory.
- Nine high-impact publications and presentations from the team in FY2013.

✧ ✧ ✧ ✧ ✧

Introduction

In order to reduce greenhouse gas emissions and reduce U.S. dependence on foreign oil, the development of hybrid electric, electric, and plug-in electric (HEV, EV, PHEV) vehicles is extremely important. The Li-ion chemistry used in automotive batteries can store large amounts of energy, while maintaining a low weight (relative to other battery chemistries).

The design, build, and testing process for batteries and packs is extremely time consuming and expensive. EC Power's code, ECT3D, directly addresses the issues related to the design and engineering of these cells. Many technical characteristics of batteries and packs that are critical to battery performance and safety are impossible to measure experimentally.

However, these same characteristics are easily analyzed using ECT3D in a virtual environment. The use of advanced software such as ECT3D allows the design engineer to gain unique insights into the performance of his/her system that would be inaccessible via experimental measurements. Furthermore, the analysis is done completely in a virtual environment, eliminating the need for any physical production of test cells.

Approach

EC Power is developing the large-format, Li-ion battery simulation software, ECT3D to analyze battery cells and packs for electrified vehicles (EV, PHEV, HEV). Team member Penn State University is primarily responsible for performing materials characterization experiments and diagnostic experiments for multi-dimensional validation. The materials characterization experiments will supply data for the extensive materials database being incorporated into ECT3D. Significant progress has been made, and is ongoing in this area.

Industrial partners Ford Motor Company and Johnson Controls, Inc. are currently testing and validating ECT3D to ensure its utility for industrial use. The overarching goal of the project is to produce a world-class, large-format lithium-ion cell and pack design tool that drives innovation and accelerates the design process for electric vehicles and their power systems.

Results

Figure IV - 98 and Figure IV - 97 illustrate a pack simulation investigating the effects of thermal management on cell balancing for a 2.8 kWh battery pack, consisting of a serially connected string of 12 "cell groups"; each cell group contains two cells in parallel. The pack is initially at -10°C and undergoes a 1C discharge, along with heating by warm air pre-heated to 50°C. Figure IV - 97 highlights a current imbalance, as a result of cell 1 remaining substantially colder than its parallel-connected partner, cell 2, during pack heat-up. Such current imbalance will have substantial impact on pack life, safety, and performance.

This pack simulation of 1-hr discharge took only 15 min on an 8-CPU workstation. Only a thermally coupled battery pack model is capable of capturing this type of thermally-driven cell imbalance.

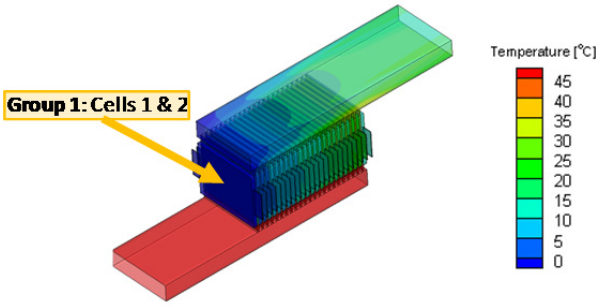

Figure IV - 96: Thermal contours at t=500 sec under cold-start discharge scenario

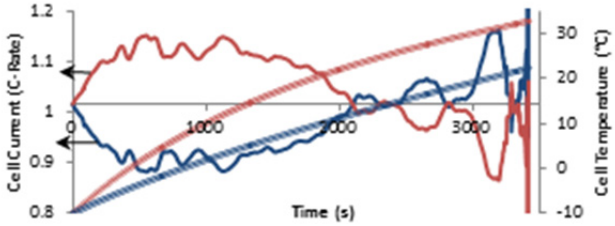

Figure IV - 97: Current and temperature of cells #1 and #2 (group 1); cell 1: blue, cell 2: red

Figure IV - 98 illustrates some of the ongoing work on intra-cell current measurement and model validation. Specifically, Figure IV - 98 shows the measured normalized current distribution ($I_{local}/I_{average}$) over the length of an electrode sheet (x/L), vs. depth of discharge (DOD) for a 1C discharge current at 21°C. The results are for a cell with one positive tab and one negative tab with the tabs co-located at x/L = 0. Data for additional temperatures, C-rates, etc., have been gathered, and validation with the model is ongoing. Further details of the cell for which results are shown in Figure IV - 98 can be found in reference [9].

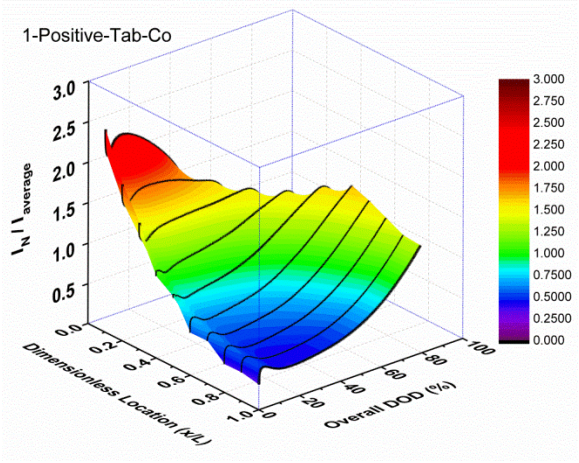

Figure IV - 98: Normalized current distribution ($I_N/I_{average}$) over the length of an electrode sheet (x/L); shown over cell DOD at a 1C discharge current at 21°C. One positive tab, one negative tab; tabs co-located at x/L = 0

Conclusions and Future Directions

Working hand-in-hand with our industrial partners Ford and Johnson Controls, the EC Power-led team has continued to make strides in the development of our ECT3D software. In the past year, using feedback from our industrial partners and NREL, EC Power has added extra safety features/capabilities and greatly enhanced user interfaces. We have also begun detailed model validation, on both the cell- and pack level, an activity which will continue through the end of the project.

Future work will include the following:

- Complete materials characterization and acquisition of database properties.
- Final testing and validation for spatio-temporal data testing and acquisition.
- Life/degradation modeling.
- Additional work with Ford/JCI
  - Complete software validation.
  - Continued application of software to their technical challenges.

FY 2013 Publications/Presentations

1. Yang, Xiao Guang , Miller, Ted and Yu, Paul, Ford Motor Company, "Li-Ion Electrochemical Model," 2012 Automotive Simulation World Congress, October 30-31, 2012, Detroit, MI.
2. Shaffer, C.E., Wang, C.Y., Luo, G. and Zhao, W., "Safety Analysis Design of Lithium-ion Battery EV Pack through Computer Simulation," Battery Safety 2012, Knowledge Foundation Conference, December 6-7, 2012, Las Vegas, NV.
3. Shaffer, C.E. and Wang, C.Y., "Thermal Management for Start-up of Li-Ion Batteries," 222nd Meeting of The Electrochemical Society (PRiME 2012), Honolulu, HI, October 7-12, 2012.
4. Luo, Gang, Shaffer, C.E. and Wang C.Y., "Electrochemical-thermal Coupled Modeling for Battery Pack Design," 222nd Meeting of The Electrochemical Society (PRiME 2012), Honolulu, HI, October 7-12, 2012.
5. Kalupson, J., Luo, G. and Shaffer, C., "AutoLion™: A Thermally Coupled Simulation Tool for Automotive Li-ion Batteries," SAE Technical Paper 2013-01-1522, 2013, doi: 10.4271/2013-01-1522. SAE International World Congress and Exhibition, April 16, 2013, Detroit, MI.
6. Ji, Y., Zhang, Y., and Wang, C.Y. (2013). "Li-Ion operation at low temperatures," Journal of the Electrochemical Society, 160(4), A636-A649.
7. Zhang, G., Shaffer, C. E., Wang, C. Y., & Rahn, C. D. (2013). "*In situ* measurement of current distribution in a li-ion cell," Journal of the Electrochemical Society, 160(4), A610-A615.
8. Ji, Y., Wang, C.Y. (2013). "Heating strategies for Li-ion batteries operated from subzero temperatures," Electrochimica Acta, 107, 664-674.
9. Zhang, G., Shaffer, C.E., Wang, C.Y., and Rahn, C.D. (2013), "Effects of Non-uniform Current Distribution on Energy Density of Li-ion Cells," Journal of the Electrochemical Society 160(11), A2299-A2305.

IV.C.6 Battery Multiscale Multidomain Framework & Modeling (NREL)

Gi-Heon Kim
Senior Researcher

National Reneable Energy Laboratory
1617 Cole Boulevard
Golden, CO 80401
Phone: (303) 275-4437
E-mail: gi-heon.kim@nrel.gov

Start Date: May 2011
Projected End Date: September 2014

Objectives

- Continue to develop models, methods, and codes in context of the Multiscale Multidomain Framework and Modeling (MSMD), and perform multiphysics battery simulations to enhance knowledge and to help fast adoption of electric drive vehciles.
- Develop an advanced option for MSMD particle domain model to address the effects of precisely contolled particulate shapes and sizes.

Technical Barriers

Significant efforts continue to be invested to improve energy-power capability and reliability of batteries by controlling particulate morphology and size, modifying particle surface, or redesigning thermodynamics. However, due to the complex nonlinear interactions across wide ranging scales, it is not straight forward to quantify such improvements for the benefits in device level response.

In conventional macro homogeneous porous electrode model approach, first suggested by Doyle et al., the active material was often assumed to be made up of spherical particles, with diffusion being the mechanism of transport of the lithium. Thanks to the self-balancing nature of LIBs, these macro-homogeneous model approaches have been successfully adopted to represent lithium-ion battery behaviors. However, this approach often suffers difficulties in properly representing complex kinetic/dynamic behavior of many practical systems.

In many practical battery systems, electrode particles are prepared in irregular shapes. However, capturing the diffusion dynamics by directly resolving the three dimensional irregular geometry of particles is too costly to apply in device level multiscale modeling.

Technical Targets

- Provide a methodology quantifying improvements from controlling particulate morphology and size, enhancing particle surface characteristics, and modifying thermodynamics as benefits in battery device level responses.
- Provide an advanced particle domain model to effectively represent diffusion dynamics and transfer kinetics in complex transport and kinetics systems.

Accomplishments

- Develop Discrete Particle Diffusion Model (DPDM) as an advanced option for MSMD particle domain model.
- This model solves solid phase lithium diffusion dynamics and transfer kinetics in a discrete diffusion particle system.
- The particles are considered electronically continuous, but ionically discrete.
- An arbitrary number of quantized discrete particles can be given as a user input.
- Kinetic, transport, and thermodynamic model parameters of each discrete particle can be independently determined.

✧ ✧ ✧ ✧ ✧

Introduction

NREL has developed the MSMD model framework, which is an expandable development platform providing a pre-defined but expandable protocol and a generic and modularized flexible architecture resolving interactions among multiple physics occurring in varied length and time scales with various fidelity and complexity. NREL researchers continue to develop models (governing equations and geometries), methods (numerical/analytical solution strategies), and codes (implementation into computer program) in the context of the MSMD, and perform computer simulations to answer scientific and engineering questions to help fast market adoption of electric drive vehicles. In FY12, we focused on development of cell domain models and solution methods applicable to all major cell formats such as stack pouch and wound cylindrical/prismatic

cells. The objective of the FY13 task was to develop an enhanced particle domain model, the Discrete Diffusion Particle Model.

Approach

Well-accepted porous electrode model suggested by Doyle et al. typically treats composite electrode as a homogeneous porous medium without regard to details of its particulate geometry, thus greatly simplifying numerical complexity. The active material was often assumed to be made up of spherical particles, with diffusion being the mechanism of transport of the lithium. Thanks to the self-balancing nature of lithium ion batteries (LIBs), the macro-homogeneous model approaches have been successfully adopted to represent LIB behaviors with only a few characteristic diffusion lengths. However, for better representation of complex kinetic/dynamic interactions critical in certain systems, a more advanced particle model is desired addressing kinetic, transport, and geometric particulate attributes including morphology, size distribution, surface modification, and the use of a composite of active materials. NREL has developed the DPDM for an advanced particle kinetics model as an particle-domain model option of the MSMD. The model solves solid phase lithium diffusion dynamics and transfer kinetics in a discrete diffusion particle system. The particles are considered electronically continuous, but ionically discrete. An arbitrary number of quantized discrete particles can be defined. Kinetic, transport, and thermodynamic model parameters of each discrete particle are independently determined.

The model governing equations are shown below at Eqs [1-6].

Butler-Volmer equation for charge transfer kinetics:

$$i''_{\xi,k}(\vec{\xi}_s) = i''_{o,k}(\vec{\xi}_s)\left\{\exp\left[\frac{\alpha_a F}{RT}\eta(\vec{\xi}_s)\right] - \exp\left[-\frac{\alpha_c F}{RT}\eta(\vec{\xi}_s)\right]\right\} \quad [1]$$

$$\eta(\vec{\xi}_s) = \phi_s - \phi_e - i''_{\xi,k}(\vec{\xi}_s)R_{film} - U(\vec{\xi}_s) \quad [2]$$

$$i''_{o,k}(\vec{\xi}_s) = k_i(c_e)^{\alpha_a}\left(c_{s,\max} - c_{s,k}(\vec{\xi}_s)\right)^{\alpha_a}\left(c_{s,k}(\vec{\xi}_s)\right)^{\alpha_c} \quad [3]$$

The Fick's law of diffusion for solid diffusion in k-th particle:

$$\frac{\partial c_{s,k}}{\partial t} = \nabla_\xi \cdot \left(D_s \nabla_\xi c_{s,k}\right) \quad [4]$$

$$\nabla_\xi c_{s,k}\big|_{A_\xi} \cdot \mathrm{n}_\xi = \frac{-i''_{\xi,k}}{D_s F} \quad [5]$$

The Kirchhoff's current law for charge conservation:

$$\vec{i}''_\xi = \sum_k \frac{\int_{A_\xi} i''_{\xi,k}(\vec{\xi}_s)dA_\xi}{A_\xi} a^\xi_{s,k} f_{v,k} \Big/ \sum_k a^\xi_{s,k} f_{v,k} \quad [6]$$

Results

Significant efforts are being invested to improve performance and life of batteries by controlling electrode particulate characteristics. Once certain electrode materials are produced by suppliers, various battery cells can be made in combination with other components for different cell design targets. After that, the cells become building blocks integrated into larger battery packs operated with different control and management strategies for varied types of electrified vehicles. Therefore, it is important to understand how the changes in physical and chemical characteristics of materials impact on system level performance and life through the complex nonlinear interactions across multiple layers of design and physics. In the present study, solid diffusion length, x_s, is selected to investigate distributed particulate characteristics: $0.5 \le x_s \le 5.0$ [μm]; number of discrete diffusion particle: N=100; uniform weight (volume) fraction for each bin: $f_{v,k}$=0.01; electrode chemistry: $Li_x(NCA)O_2$; particle geometry: 1D sphere. Other model parameters commonly used for all discrete particles are summarized in the Table IV - 16.

Table IV - 16: Particle-domain model parameters

Domain	Parameter	Value/Model
Particle		$Li_y(NCA)O_2$
	Maximum Li capacity, $c_{s,max}$ [mol m^{-3}]	4.90×10^4
	Characteristic diffusion length, R_s [m]	
	Stoichiometry at 0% SOC, $x_{0\%}$, $y_{0\%}$	0.9802
	Stoichiometry at 100% SOC, $x_{100\%}$, $y_{100\%}$	0.3171
	Reference exchange current density at 100% SOC, $i_o^{'ref}$ [A m^{-2}]	4.0
	- activation energy, $E_{act}^{i_o}$ [J/mol]	3.0×10^4
	Charge-transfer coefficients, α_a, α_c	0.5, 0.5
	Film resistance, R_{film} [Ω m^2]	0.015
	Solid diffusion coefficient, D_s [m^2 s^{-1}]	$3x10^{-15}$
	- activation energy, $E_{act}^{D_s}$ [J/mol]	2.0×10^4
	Positive electrode, U_+ [V]	$U_+(x) = 1.638\,x^{10} - 2.222\,x^9 + 15.056\,x^8 - 23.488\,x^7 + 81.246\,x^6 - 344.566\,x^5 + 621.3475\,x^4 - 554.774\,x^3 + 264.427\,x^2 - 66.3691\,x + 11.8058 - 0.61386\,\exp(5.8201\,x^{136.4})$

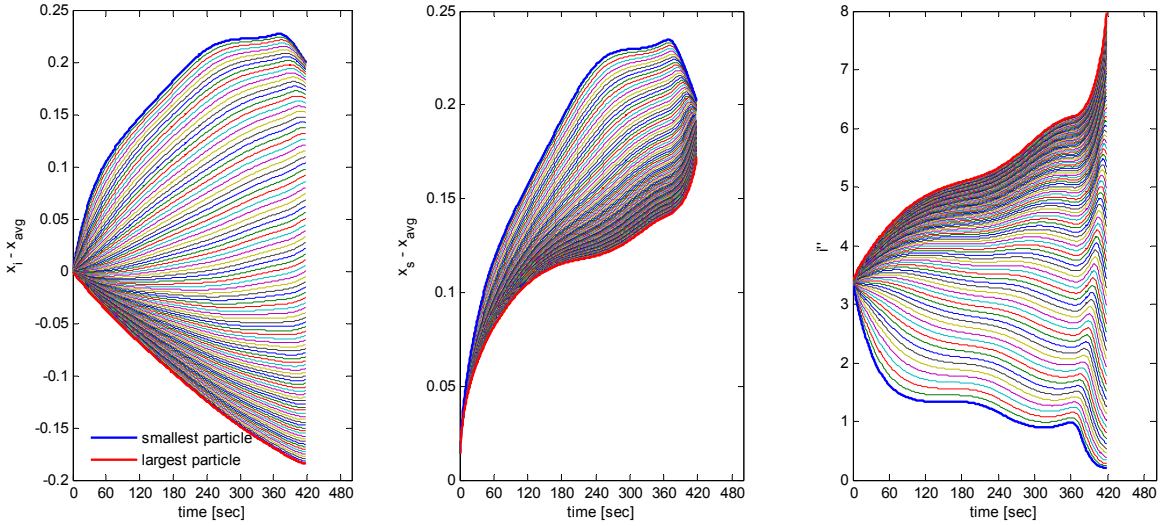

Figure IV - 99: Particle transfer current density and stoichiometry number evolution during 6-C constant current discharge (N=100)

Figure IV - 99 presents evolutions of particle bulk stoichiometry deviation (left), particle bulk stoichiometry deviation (center), from system average stoichiometry and charge transfer current density (right). During discharge, smaller particles discharge faster than larger ones. As a result, the bulk stoichiometry numbers in small particles grows higher than the system average, while large particle stoichiometry numbers lag behind the system average. Increase rate of surface stoichiometry number of large particles (which is catching up the small particle's surface stoichiometry) slows down in the middle of discharge where equilibrium potential slope becomes flat. Particle surface stoichiometry tends to converge toward the end of discharge. As a result, small particles suffer larger depth of discharge and large particles experience larger concentration gradient. Transfer current densities are initially identical in all different size particles. However, the magnitudes start to diverge afterward; larger particles have larger surface current density and the magnitudes keep increasing during discharge.

Figure IV - 100, particle bulk stoiciometry evolution during US06 driving cycles, shows how the environmental and design factors affect the use of active materials in batteries. Batteries made of identically prepared NCA cathode particles (distributed in size between 0.5 µm and 5 µm) were cycled to power 20 minutes of a US06 profile driving of an HEV(left), and a PHEV with 10-mile electric range (right). In the HEV applicaton, particles are cycled near the predetermined SOC range. Small particles are cycled with wider SOC window than large particles. Small particles respond more sensitively to high frequency load variation.

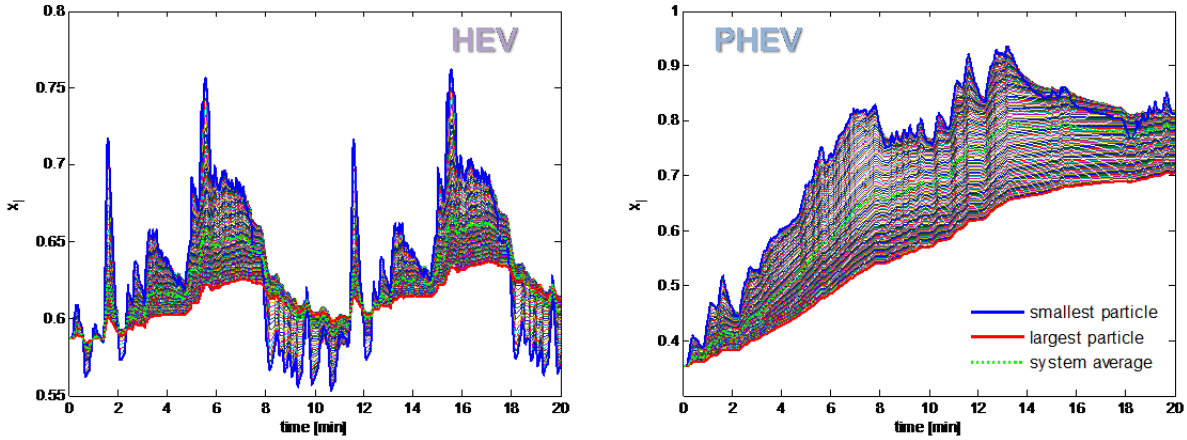

Figure IV - 100: Particle stoichiometry number evolution during mid-size sedan HEV (left) and PHEV10 (right) US06 driving (N=100)

Both amplitude and frequency of stoichiometry (lithium concentration) are larger in small particles than in large particles. In PHEV10 application, particle average stoichiometry increases in initial charge depleting stage and stay around predetermined SOC during the rest of charge sustaining mode. Difference in SOC among the particles tends to increase initially and to be reduced during charge sustaining mode. Change of SOC is nearly monotonous in large particles, while SOC in small particles fluctuates. This implies that large particles respond mostly to energy demand and small particles to both power and energy demand from the system. Identical particle sets are used in significantly different patterns for different EV applications. This result emphasizes the importance of capturing such "inhomogeneity" to properly predict a battery's long-term aging behaviors.

Conclusions and Future Directions

NREL developed the Discrete Particle Diffusion Model (DPDM) as an advanced option for an MSMD particle domain model. We demonstrated model applicability to a study quantifying the impacts of distributed characteristics of electrode particulate attributes. In many practical battery systems, electrode particles are prepared in irregular shapes and lithium transport in solid particulates and kinetics at surfaces of intricate geometry occur in complex relations. We will continue to enhance the model capability and apply it to a general procedure of identifying a reduced order representation of irregular particle electrode system.

FY 2013 Publications/Presentations

1. 2013DOE Annual Peer Review Meeting Presentation.
2. K.-J. Lee, K. Smith, A. Pesaran, G.-H. Kim, "Three dimensional thermal-, electrical-, and lectrochemical-coupled model for cylindrical wound large format lithium-ion batteries", *J. of Power Sources*, 241 (2013) 20-32.

IV.C.7 Lithium-Ion Abuse Model Development (NREL)

Shriram Santhanagopalan and Gi-Heon Kim

National Reneable Energy Laboratory
1617 Cole Boulevard
Golden, CO 80401
Phone: (303) 275-3944
E-mail: Shriram.Santhanagopalan@nrel.gov

Start Date: October 2008
Projected End Date: September 2013

Objectives

- Build theoretical tools to:
  - assess safety of large format lithium-ion batteries.
  - extend the temperature range for safe operation at higher rates of charge/discharge – especially at low temperatures – for batteries used in vehicles.

Technical Barriers

- Saftey concern for lithium-ion batteries in electric drive vehicles (EDV) is one of the major barriers to wide-spread adoption of EDVs.
- The number of design parameters for lithium batteries is large and the interaction among them is complicated, so it is not feasible to experimentally identify the weakest link by conducting tests on a case-by-case basis.
- Safety evaluation results for battery packs built with the same material by different manufacturers are very different. The cost associated with building and testing safety in large format cells, modules, and packs is quite high; whenever such data is collected, it is treated as proprietary, thus preventing the use of lessons learned by other battery developers.
- Scaling up a battery greatly changes the response of a system developing a defect and its consequent behaviors during fault evolution.
- Timely detection of fault signals in large capacity battery systems is extremely difficult.

Technical Targets

- Incorporate deformation of cell components and casing into the pressure build-up models developed in FY12.
- Develop electrochemical models that can reliably predict the origin of failure and the location of venting of a lithium-ion cell under pressure.

Accomplishments

- Built a model for venting of individual lithium-ion cells. This model was tested with parameters from cells of different form-factors.
- The model was used to analyze the safety implications for the cell choices made by the United States Army Tank Automotive Research, Development and Engineering Center (TARDEC).

✧ ✧ ✧ ✧ ✧

Introduction

In FY13, NREL's modeling activity to improve lithium-ion battery safety focused on correlating the failure mechanism within an individual cell (e.g., due to an internal short or decomposition of the electrolyte resulting in the formation of gaseous species) to the results observed externally when testing these cells. Testing a fully charged cell yields very different results from those of a discharged cell. For instance, when a cell is subjected to a crush test at low states of charge (SOC) (i.e., 30% or lower), the point of failure of the cell almost always coincides with the point where the external force is supplied. In a fully charged cell, however, the point of failure is typically farther from the location of crush. These differences imply that there is a difference between two cells of identical make, even when these are subjected to the same test procedure – depending on their energy content.

In order to capture such relationships between the energy content of the cells and their failure mechanism, a rigorous thermal-electrochemical model that includes the origin and distribution of pressure within the cell casing was developed. This model is an extension of the results shown in FY12 – the pressure generation due to gas generation during overcharge of a cell was previously shown as a case-study for this model. In the current effort, the mechanical strength of the casing and

cell components were used to determine the location of cell venting, which eventually follows the accumulation of pressure from the abuse reactions and phase-changes. These results are significant in making the transition from developing a mechanism for abuse of individual cells to analyzing the propagation of failure from one cell to the others within the module.

Approach

The interaction between the electrochemical-thermal response and the mechanical behavior of the cell components was captured using a rigorous jump momentum balance across the interface to calculate the pressure at any given point within the cell. The following expression is a modified form of the abuse-reaction models previously reported by us in FY12:

$$f^i = -\mathbf{n}.\left(P^i\mathbf{I} + \eta\left[\nabla\mathbf{u}^i + \left(\nabla\mathbf{u}^i\right)^T\right]\right)$$

The force, f^i, experienced at any point on the interface between two components (e.g., the electrode and the separator or the separator and the gaseous species produced by the reactions) is related to the pressure at that point Pi and to the extent of deformation tolerated by the corresponding components. The deformation is tracked using the interface velocity **u**.

The pressure is comprised of three terms (see Figure IV - 101):

$$P^i = P_1^i + P_2^i + P_3^i$$

P_1^i represents the pressure build-up due to the gas generation reactions, P_2^i the pressure due to expansion from evaporation of volatile components and P_3^i the restrictions imposed by the mechanical deformation of the individual cell components. The pressure generation models use the first one or two terms, depending on the nature of the problem studied. The interaction between the reactions, heat generation and mechanical deformation is introduced by the use of the P_3^i term, which is computed from stress-strain measurements of the individual components.

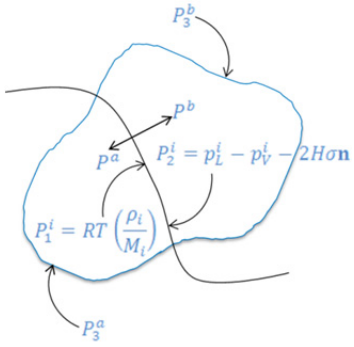

Figure IV - 101: Illustration of the interaction between thermal, electrochemical and mechanical components of pressure-generation within a lithium-ion cell

Results

Figure IV - 102 shows the contribution of the individual factors to the overall pressure within the cell, as a function of time, when the cell is subjected to mechanical deformation. As shown, the pressure due to external deformation increases instantaneously – and remains fairly constant through the entire duration of the test. The reaction and vaporization pressures are strong functions of the energy content and temperature of the cell. As the abuse test progresses in time, the relative magnitudes of the different components changes – the deformation term which dominates the pressure value at the beginning of the test, is eventually overcome by the reaction term – at which point the pressure exceeds the threshold for failure. Thus in this instance, when a fully-charged cell is subjected to an external load, or is subjected to a hot-box test, the point of failure is determined by the location within the cell at which the total pressure value – which, as described above, is dominated by the reaction term – exceeds the failure threshold.

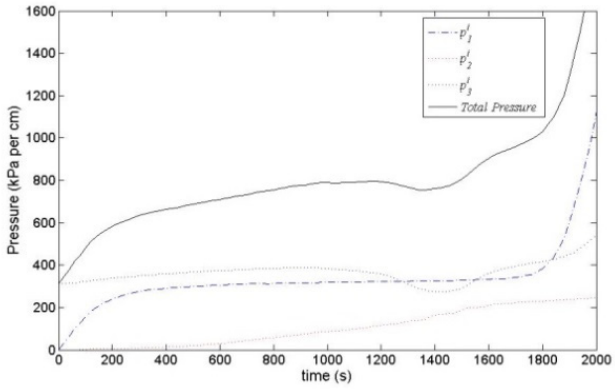

Figure IV - 102: Contribution of the gas-generating reactions, vaporization of volatile components and the mechanical constraint imposed by the casing to the overall pressure-build-up within a lithium-ion cell: the purely mechanical terms dominate the beginning of the test, while kinetic and thermal terms take over with the progression of the abuse reactions

Incorporating this insight into a cell-level model will help improve the predictive capability of the model to determine the location of failure of the cells. For instance, Figure IV - 103 shows results from a purely mechanical approach to simulating cell failure. In this case, literature values report the point of exertion of the force to be the point of failure as well – which is true in the case of cells with no significant contributions to the pressure term from the reaction heats (i.e., only the last term on our pressure-balance equation is significant).

Similar results for a prismatic cell subjected to venting, obtained using the model equations reported above are shown in Figure IV - 104.

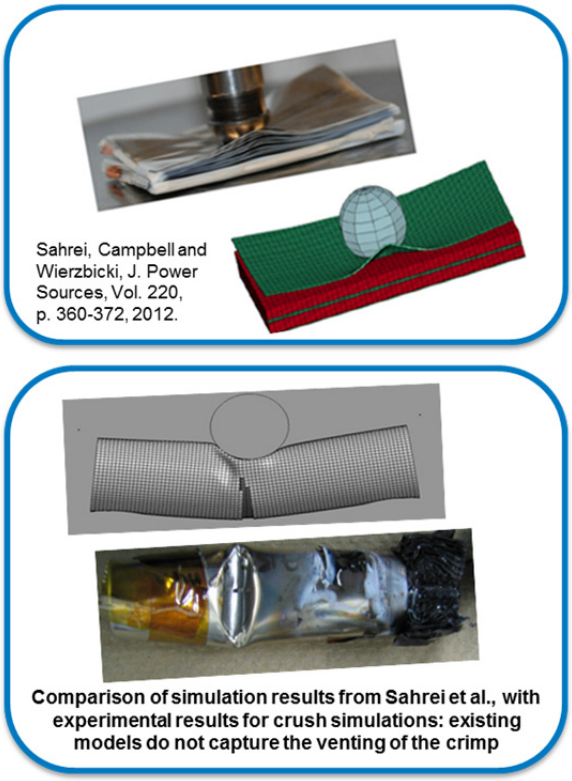

Figure IV - 103: Point of failure of a fully discharged cell coincides with the point of test, where as that for a fully charged cell is significantly different

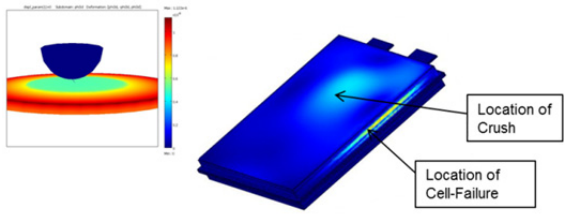

Figure IV - 104: NREL's cell venting simulation results show that for propagation purposes, the location of cell failure does not always coincide with the location of crush

Conclusions and Future Directions

Using a rigorous model that captures the contribution of kinetic, thermal and mechanical properties of the cell components is critical to identifying the failure mode of individual cells during abuse testing and the direction of propagation of failure within a module. Subsequent work will consider propagation mechanisms based on the understanding developed from these models.

Simultaneously, it is pertinent to develop a set of parameters from independent experiments to characterize the rate constants and transport coefficients for the abuse kinetics reactions, as well as the mechanical constants that are used in these models. Towards this end, we have started measurement of heat generation rates for the cell-components such as the cathode at different states of lithiation, the electrolyte, and combinations thereof. These results are currently being compared with similar measurements made at the cell level, to identify the most appropriate experimental technique to measure these parameters. These results will be documented in a future report.

FY 2013 Publications/Presentations

1. Ahmad Pesaran, Shriram Santhanagopalan, and Gi-Heon Kim; "Addressing the Impact of Temperature Extremes on Large Format Li-Ion Batteries for Vehicle Applications"; Presented at 30th International Battery Seminar, Ft. Lauderdale, FL; March 11-14, 2013. NREL Report No. PR-5400-58145.
2. Ahmad Pesaran, Matt Keyser, Gi-Heon Kim, Shriram Santhanagopalan, and Kandler Smith; "Tools for Designing Thermal Management of Batteries in Electric Drive Vehicles"; Presented at the Large Lithium Ion Battery Technology & Application Symposia Advanced Automotive Battery Conference; Pasadena, CA. February 4–8, 2013. NREL Report No. PR-5400-57747.
3. Ahmad Pesaran, Gi-Heon Kim, Kandler Smith, Shriram Santhanagopalan; "Accelerating Development of EV Batteries Through Computer-Aided Engineering"; Presented at the 2012 Automotive Simulation World Congress, Detroit, MI; October 30-31, 2012.

Applied Battery Research for Transportation

Introduction

Core Support Facilities

Critical Barrier Focus: Voltage Fade

Materials Optimization

Process Development

V. Applied Battery Research for Transportation

V.A Introduction

The critical technological component in plug-in electric vehicles (PEVs) that enables comparable convenience, affordability, and safety to those found in today's petroleum-powered vehicles continues to be energy storage. To promote the widespread adoption of electric vehicles and enable a strong U.S.-based battery manufacturing sector, the materials discovery and device innovation taking place in national laboratories and at universities must be translated into commercially viable products and processes. Such applied research activities are inherently high risk; coupling the frontier, cutting edge nature of materials discovery with the performance/cost needs of a market-changing new product. A significant portfolio of R&D projects funded through the VTO that meet these criteria are grouped together in the Applied Battery Research (ABR) for transportation program.

The ABR program is and will continue to be comprised of high risk projects investigating issues and advances at the cell level. Success in ABR projects means electric drive vehicle energy storage products that can be realized (manufactured) and that lead to cost reduction; thus, fulfilling the energy storage component of EERE's EV Everywhere Initiative. Such improvements will be accomplished through novel materials, particularly the active components of the cell, but also through innovative cell design and electrode composition. As well, materials production, electrode processing, and cell manufacture are also important thrusts within ABR.

The R&D projects in the 2013 ABR portfolio are divided into four distinct but complementary groups:

- Core Support Facilities,
- In-Depth Study—Voltage Fade in Li-ion Battery Cathode Materials,
- Materials & Diagnostic Studies, and
- Process Improvement Projects.

Core Support Facilities. Across several of the national laboratories, infrastructure has been created and resources grouped into facilities that support complex activities critical to applied battery research. This provides the U.S. energy storage research community a powerful tool to carry out scientific investigations using, for example, state-of-the-art fabricated Li-ion battery electrodes, commercially viable and high purity electrolyte additives, chemical and electrochemical analysis of cycled battery components, and component-level abuse response analysis. The services and products of these six facilities are fully funded through the ABR program and are available hierarchically, with VTO funded projects first, followed by other DOE funded projects (BES, ARPA-E), then other government agencies down the line through to U.S. small businesses. The majority of these facilities came on line with Recovery Act funding in 2009 and have now a significant track record in supporting applied research.

In-Depth Study—Voltage Fade in Li-ion Battery Cathode Materials. ABR programs always contain and can usually be defined by a major barrier, a set of structurally and functionally interrelated problems, that simultaneously appears unsolvable and that absolutely requires a solution in order to achieve a particular technical target. These are complex multi-component phenomena, multi-scale in space, time, and energy. The barrier is not going to be overcome by a single brilliant experiment or by a lone expert. Solutions, if possible, require understanding across the dimensions of the problem, and such understanding requires in-depth science practiced by a multi-disciplinary team—and a lot of data. This is the nature of a deep-dive investigation. Within the ABR program the first such deep-dive has been underway for over two years and has been focused on an issue common to a promising (high energy content) class of active cathode materials: Li-, Mn-rich layered, layered transition metal oxides. With these materials, a continuous decay of the average voltage with cycling is observed and this decrease in energy output with cycling is accompanied by an evolving energy inefficiency. For the FY2013 Annual Progress Report, six reports have been prepared detailing various aspects of this in-depth investigation, from the study of various mitigation strategies to the impact on voltage fade of surface coatings. The work was carried out by twenty-nine scientists and engineers and across three different national labs.

Materials and Diagnostic Studies. Eight projects predominately dealing with electrolyte component development and spectroscopic characterization are legacy projects from the first phase of applied research activities in Li-ion batteries. All of these projects have contributed towards the body of knowledge on Li-ion-related energy storage materials and all have been, or will be in 2014, terminated. All the work is of the highest caliber, but the direction of the overall program has changed to reflect the need for R&D efforts involving full cell chemistries as opposed to material-level investigations.

Process Improvement Projects. The second phase of ABR, initiated in FY2012, contained the first process-R&D projects. The work in 2013 continues some of these projects and expands to include more experimental work on electrode fabrication. Critical to establishing a U.S.-based battery manufacturing industry is the development of process-oriented

intellectual property. The four reports in this section detail work that not only has led to IP creation on its own, the research teams have also leveraged the EERE-funded work to partner with American companies developing their own proprietary processing technologies. As new processing resources are developed, they are also being made available to the U.S. energy storage research community in line with the Core Support Facilities described above.

Via FY2013 funding, a significant part of the ABR FY2014 portfolio is now composed of competitively awarded financial assistance grants made to several teams addressing the need for energy density improvement in electric drive vehicle batteries. These projects will be reported on in the next year's annual progress report. In coming years, there will be a reoccurring FOA soliciting proposals for team-based R&D efforts directed at "Applied Battery Research for Improvements in Cell Chemistry, Composition and Processing."

The remainder of this section provides technical highlights and progress on the Applied Battery Research program for FY 2013. The information provided is representative only and detailed information is available from publications cited in each project overview.

V.B Core Support Facilities

V.B.1 Process Development and Scale up of Advanced Cathode Materials (ANL)

Gregory K. Krumdick

Argonne National Laboratory
9700 South Cass Avenue
Argonne, IL 60439-4837
Phone: (630) 252-3952; Fax: (630) 252-1342
E-mail: gkrumdick@anl.gov

Collaborators:
YoungHo Shin, Argonne National Laboratory
Ozgenur K. Feridun, Argonne National Laboratory
Gerald Jeka, Argonne National Laboratory
Mike Kras, Argonne National Laboratory
Bryant Polzin, Argonne National Laboratory
Wenquan Lu, Argonne National Laboratory
Kumar Bugga, Jet Propulsion Laboratory

Start Date: June, 2010
Projected End Date: September, 2014

Objectives

- Process development, scale-up and producing kilogram quantities of the target bench-scale advanced cathode materials for basic research, market evaluation and high-volume manufacturing.
  - Develop scalable manufacturing process with economic feasibility and provide target materials with high quality and reproducibility.

Technical Barriers

Most advanced cathode materials like lithium and manganese-rich metal oxide (LMR-NMC) materials have been synthesized in small quantity at the bench-scale and lack commercial availability. Sufficient quantity of these high energy materials with high quality is hard to obtain for basic research and industrial evaluation. Each such material needs customized synthesis process and scale-up research and pilot-scale production facilities.

Technical Targets

- Develop a customized synthesis process for target bench-scale cathode material.
- Develop continuous carbonate and hydroxide co-precipitation methods (2-way synthesis approach) for precursor preparation.
- Identify and resolve constraints for the scale-up of target bench-scale material.
- Produce sufficient quantities of materials with equal or better quality than target bench-scale material.
- Evaluate and compare the performance of bench-scale and scaled-up material by coin cell test.

Accomplishments

For 1st candidate material - $Li_{1.14}Mn_{0.57}Ni_{0.29}O_2$

- Successful production of scaled-up carbonate cathode material with equal or better quality than target bench-scale carbonate cathode material by coin cell test.
- Achievement of 10% increased capacity, 20% increased tap density and better cycle life of scaled-up carbonate cathode material compared to target bench-scale carbonate cathode material.
- Preliminary synthesis of scaled-up cathode material via hydroxide process which shows equal or better quality than bench-scale hydroxide cathode material.
- Identification of cracking issue of scaled-up carbonate cathode material.
- Preparation and delivery of 200g pre-crushed scaled-up carbonate cathode material.
- Investigation of particle fracturing effect on rate performance and cycle life.
- Investigation of particle size effect on particle cracking during calendaring process.
- Investigation of relation between particle size, morphology and tap density.
- On-going research of particle cracking and mitigation by increased particle density and decreased particle size (using Nanoindenter analysis).

For 2nd candidate material - $Li_{1.2}Mn_{0.54}Ni_{0.13}Co_{0.13}O_2$

- Process development and scale-up via hydroxide co-precipitation for target material.
- Evaluation and comparison of three Toda HE-5050, JPL bench-scale and ANL scaled-up JPL hydroxide cathode materials.
- Synthesis of scaled cathode material via hydroxide process which shows an initial discharge capacity of 237 mAh/g and tap density of 1.23 g/cc. This did not meet JPL specifications.
- Preparation of ANL scaled-up JPL carbonate cathode material to meet specification.
- Successful achievement of 20% increased initial discharge capacity (292 mAh/g), 20% increased tap density (1.82 g/cc) of ANL scaled-up JPL carbonate cathode material compared to the specification.
- Delivery of ANL scaled-up JPL hydroxide precursor material to ANL CSE for domain size study.
- Delivery of ANL scaled-up JPL carbonate cathode material to ANL Cell Fabrication Facility to evaluate particle cracking strength by Nanoindenter.
- Delivery of ANL scaled-up JPL carbonate cathode material to JPL as an intermediate sample.

✧ ✧ ✧ ✧ ✧

Introduction

There is a strong need to produce advanced cathode materials like lithium and manganese rich metal oxide (LMR-NMC) materials with high quality in the kilogram and tens-of-kilograms quantities for basic R&D purposes and industrial needs. To achieve this goal, process development and scale-up of advanced cathode materials with high quality and reproducibility is a critical step between discovery of advanced battery materials, market evaluation and high-volume manufacturing. The performance measures of cathode material such as capacity, tap density and life are strongly affected by synthesis process and its optimization though it has the same composition. Additionally, development of cathode synthesis process with economic feasibility is important to reduce the cost of the full battery pack.

Until recently, there was no systematic engineering research capability or program across the DOE complex or in industry to identify and resolve constraints to the development of cost-effective process technology for the high-volume manufacture of these advanced cathode materials. Now, Argonne's Materials Engineering Research Facility (MERF) enables a systematic engineering approach to investigate customized synthesis processes and scale-up for each candidate material via carbonate and hydroxide co-precipitation and high energy ball mill synthesis methods. For co-precipitation process, MERF already set up two 4L continuous stirred tank reactor systems and a 20L continuous stirred tank reactor system in FY12. These do not represent a batch process or a semi-continuous process. Significant process improvement for these continuous co-precipitation systems was achieved including several inventions conceived, submitted or filed.

MERF's process engineering research will identify and resolve constraints for the scale-up of the target bench-scale candidate material, from the bench to pre-pilot scale, to complete qualified kilogram production corresponding to the specification of the target material.

MERF also carries out material characterization and electrochemical performance test in coin cell for the scaled-up materials. These results will be validated by ANL's Materials Screening Group to confirm a performance match to the original bench-scale materials.

Approach

The first step for the process development and scale-up of advanced cathode material is to identify candidate cathode materials of interest to the ABR program participants including materials produced by the carbonate, hydroxide or other processes. A database of materials to scale has been developed and maintained and is used to rate and prioritize candidates for scale-up. These candidates are ranked based on electrochemical performance, process complexity and interest level of the researcher and the lithium-ion battery industry.

In FY12, MERF successfully completed the process development, scale-up and kilogram production of the 1st candidate material ($Li_{1.14}Mn_{0.57}N_{i0.29}O_2$) with high quality. Carbonate process was fully developed and hydroxide process set-up was initiated. As a major constraint for the scale-up of the 1st candidate material, particle cracking issue was identified. Many approaches were made to mitigate particle cracking of carbonate cathode material and this work continued in FY13.

In FY13, we started the process development and scale-up of JPL hydroxide ($Li_{1.2}Ni_{0.13}Mn_{0.54}Co_{0.13}O_2$) cathode material as the 2nd candidate and will generate kilogram quantities of this material for evaluation and delivery. We plan to then select and begin the process development and scale-up of the next candidate in the materials queue.

Results

1st candidate material ($Li_{1.14}Mn_{0.57}N_{i0.29}O_2$): completion of process scale-up and kg production with equal or better quality.

The major technical targets for the 1st candidate material were as following:

- Scale-up process development via carbonate co-precipitation method.
- Production of kg quantities of uniform material.
- Achieving equal or better performance than bench-scale material.

We successfully developed the synthesis processes (both carbonate co-precipitation in FY12 and hydroxide co-precipitation in FY13) for this 1st candidate material. Production and delivery of kg quantities of this material was completed in FY12. In FY13, for this cobalt-free composition, the scaled-up carbonate and hydroxide materials were evaluated by coin cell test and compared to its bench-scale materials.

Table V - 1 shows that scaled-up carbonate (optimized) and hydroxide (preliminary) materials has equal or better tap density and initial discharge capacity than bench-scale materials. The morphology and secondary particle size of scaled-up materials are more uniform and spherical compared to bench-scale materials.

Table V - 1: Comparison of bench-scale and scaled-up carbonate and hydroxide cathode materials for 1st candidate

	Manufacturer Lot #	ANL CSE 101217B	ANL MERF ES-120905	ANL CSE 1108102	ANL MERF ES-130110
	Co-precipitation	Carbonate	Carbonate	Hydroxide	Hydroxide
	Scale Status	Bench-scale	Pre-pilot scale Optimized	Bench-scale	Pre-pilot scale Preliminary
Precursor	SEM 3000x	x	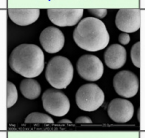	x	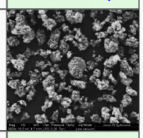
Precursor	ICP analysis	x	$Ni_{0.33}Mn_{0.67}(CO_3)_x$	x	$Ni_{0.33}Mn_{0.67}(OH)_x$
Precursor	$D_{10}/D_{50}/D_{90}$ [μm]	x	0.2/11.7/16.4	x	1.0/4.0/6.3
Precursor	Tap density [g/cc]	x	1.40	x	0.91
Cathode	SEM 8000x	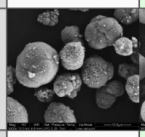	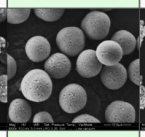	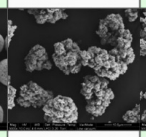	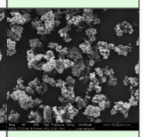
Cathode	ICP analysis	$Li_{1.35}Ni_{0.32}Mn_{0.68}O_y$	$Li_{1.37}Ni_{0.33}Mn_{0.67}O_y$	$Li_{1.31}Ni_{0.33}Mn_{0.67}O_y$	$Li_{1.35}Ni_{0.33}Mn_{0.67}O_y$
Cathode	$D_{10}/D_{50}/D_{90}$ [μm]	7.6/12.7/21.0	6.9/11.1/18.4	7.7/13.2/22.1	2.4/4.7/8.9
Cathode	Tap density [g/cc]	1.41	1.70	0.98	1.02
Cathode	Initial disch. [mAh/g]	221.7 *	251.0 *	172.4 *	184.2 *

** 4.75~2.4 V at 25 °C (25 mAh/g)*

As can be seen by the rate (Figure V - 1) and C/3 cycle life (Figure V - 2) comparisons, the optimized, pre-pilot scaled-up carbonate cathode material has the highest capacity at any C-rate and the lowest capacity loss during 160 cycles. The pre-pilot scaled-up hydroxide cathode material shows equal or better properties than bench-scale material. Improvement of hydroxide process was anticipated to get better material density and electrochemical performance.

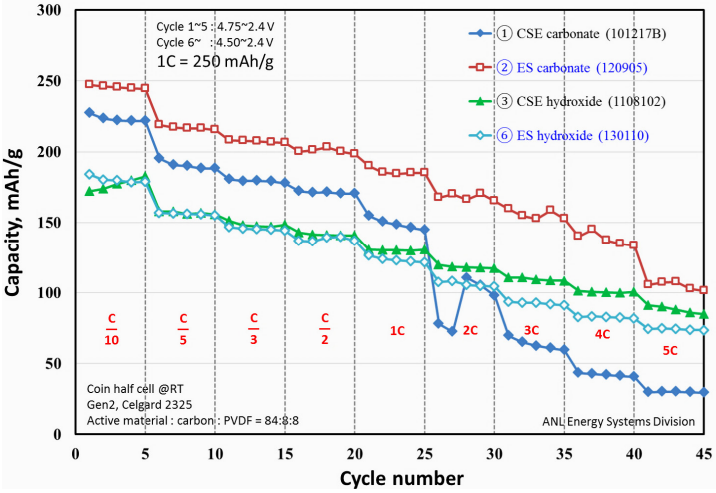

Figure V - 1: Rate performance comparison of scaled-up carbonate and hydroxide to bench-scale materials

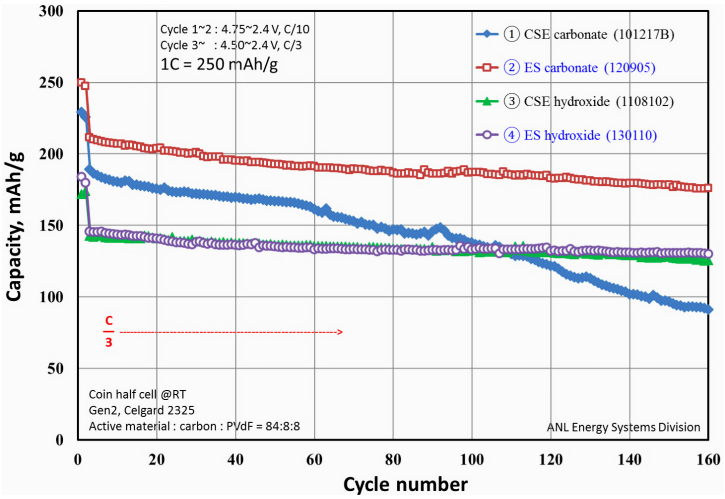

Figure V - 2: C/3 cycle life comparison of scaled-up carbonate and hydroxide to bench-scale materials

1st candidate material ($Li_{1.14}Mn_{0.57}N_{i0.29}O_2$): identify and mitigate particle cracking issue during process development and scale-up.

When the carbonate cathode material was calendared, it cracked, yielding unpredictable results. This particle fracturing issue seems to be an inherent problem with the carbonate process as it has also been reported from bench-scale researchers, which wasn't considered a critical problem at the initial stage. However, in FY12, the ANL Cell Fabrication Facility (CFF) noticed the particle fracture during calendaring process when they evaluated the scaled-up carbonate material (lot # ES-20120222, average secondary particle size of 15.6 µm). To mitigate particle cracking, the scaled-up carbonate product with precise particle-size control technology was evaluated by ANL Cell Fabrication Facility (lot # ES-20120709+11, average secondary particle size of 7.8 µm) in FY12, which also showed particle cracking problem.

In FY13, the second approach to mitigate particle cracking issue was the preparation of pre-crushed carbonate material. Using pulverizer, 200g pre-crushed carbonate material was prepared and delivered to ANL CFF at 02/20/2013, which showed increased surface area, low tap density (1.43 g/cc) and decreased electrochemical performance than un-crushed carbonate material as reported by ANL CFF.

The third approach was to synthesize the same material using the hydroxide process as one can see in Table V - 1. This scaled-up hydroxide material shows much lower tap density (around 1.0 g/cc) than the tap density of scaled-up carbonate material (around 1.7 g/cc) because of its leaf-like structure of primary

particle. The electrochemical performance of the hydroxide material is not good. These results have prompted us to revisit the carbonate process and to try to minimize the particle fracturing issue by improvement of calendaring process and carbonate co-precipitation. To evaluate the effect of particle cracking, we look at the calendaring process and at the relation between electrode porosity and electrochemical performance.

The effect of particle fracturing on electrode and its porosity on electrochemical performance was investigated. As one can see in Figure V - 3, we prepared four electrodes with different porosities and compared their electrochemical performances.

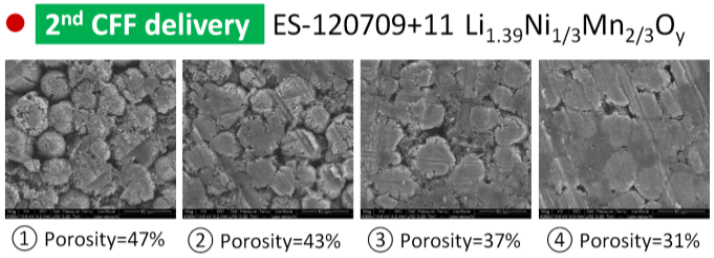

Figure V - 3: Preparation of electrode with different porosity for ES-20120709+11

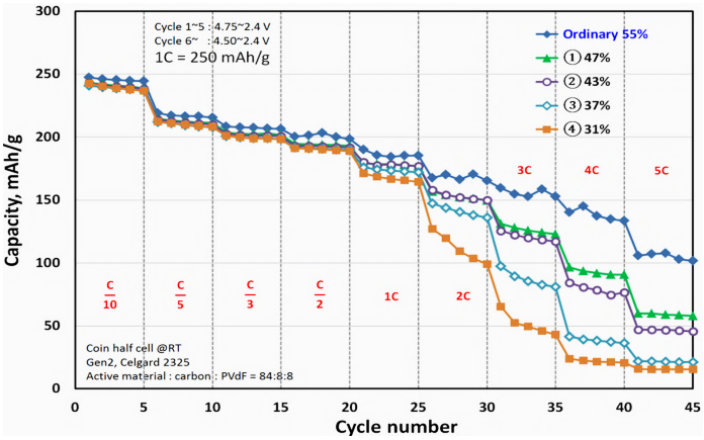

Figure V - 4: Rate performance comparison of electrode with different porosity for ES-20120709+11

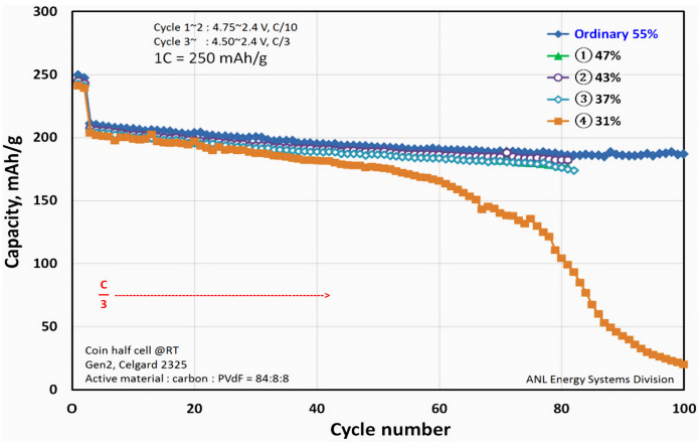

Figure V - 5: C/3 cycle life comparison of electrode with different porosity for ES-20120709+11

The rate performance and cycle life decrease as electrode porosity is reduced (Figure V - 4 and Figure V - 5). It is clear that particle cracking causes these undesirable behaviors.

We tried smaller particles (7.8 μm and 4.0 μm) for calendaring process to see the effect of particle size on cracking and there is a tendency that the smaller particles results in slightly less cracking (Figure V - 6). However, they also resulted in lower tap density.

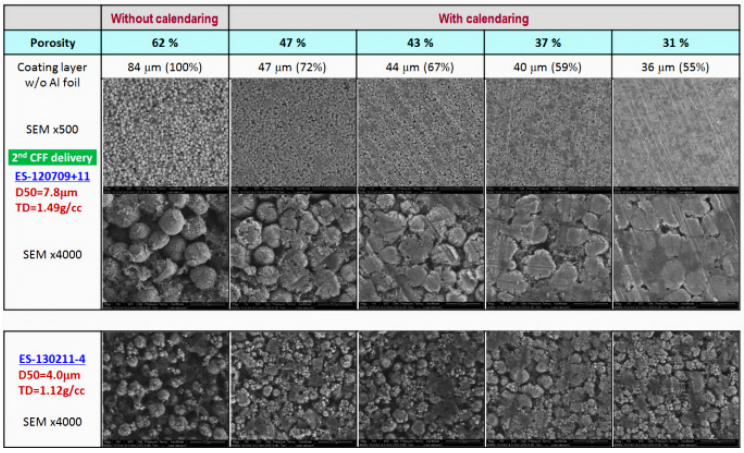

Figure V - 6: Effect of particle size on particle cracking during calendaring process

We then looked at the relation between secondary particle size, morphology and tap density. In Figure V - 7, the 1st, 2nd and 3rd carbonate cathode materials have similar tap densities even though their average secondary particle sizes are quite different because they are spherical. But the SEM images of 4 through 7 of Figure V - 7 clearly show that if the morphology becomes less spherical, the tap density decreases even though the average secondary particle sizes are similar. Therefore, we can say that particle morphology has a greater effect on tap density than secondary particle size. So, if the secondary particle is spherical, we can keep the same tap density of carbonate cathode material even though the secondary particle size is reduced for the purpose of mitigating particle cracking issue.

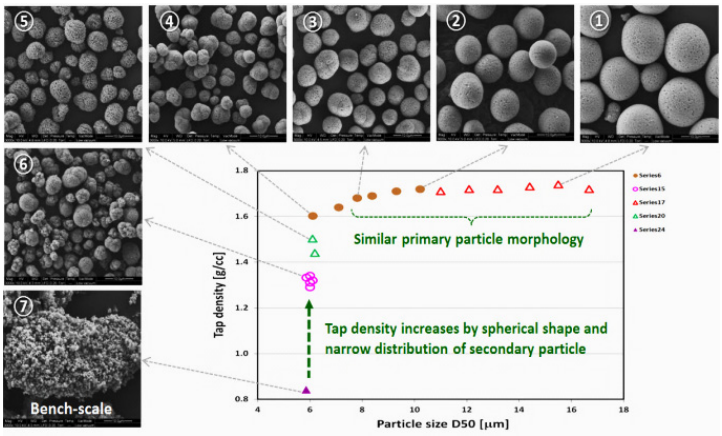

Figure V - 7: Comparison between secondary particle morphology, size and tap density of carbonate cathode material ($Li_{1.39}Ni_{0.33}Mn_{0.67}O_y$)

This relation between secondary particle size and tap density has encouraged us to improve the carbonate process to make small, spherical secondary particles with increased particle density to mitigate the particle fracturing. Also we plan to continue to work on the integrity of both carbonate and hydroxide co-precipitation processes in an attempt to control morphology and increase tap density.

Recently, we synthesized the 2nd candidate material ($Li_{1.2}Mn_{0.54}Ni_{0.13}Co_{0.13}O_2$) with increased tap density of 1.82 g/cc and decreased average secondary particle size of 6.7 μm via an improved carbonate process. For the

analysis of particle cracking for this material, we are collaborating with Bryant Polzin at Argonne who newly developed the Nanoindentor process which will be used to measure stresses required for particle cracking.

2nd candidate material (JPL, $Li_{1.2}Mn_{0.54}Ni_{0.13}Co_{0.13}O_2$): completion of process scale-up with equal or better cathode quality.

An existing high capacity/voltage cathode development project with JPL/NASA had produced a cathode composition ($Li_{1.2}Mn_{0.54}Ni_{0.13}Co_{0.13}O_2$) with high capacity (~230 mAh/g) and high tap density (>1.7 g/cc) at the bench scale, but JPL had difficulties scaling the material to kilogram scale for commercial evaluation. Toda America produced this composition (HE-5050) at high capacity (~250 mAh/g) but at a much lower tap density (~1.0 g/cc). In FY13, Argonne's cathode scale-up program was tasked to scale this composition and produce high capacity, high tap density material for evaluation. The target properties are:

- Composition: $Li_{1.2}Mn_{0.54}Ni_{0.13}Co_{0.13}O_2$
- Tap density: > 1.5 g/cc.
- Capacity: ~ 240 mAh/g (1st discharge)
- Cycle life: ~ 200 cycles

Our first approach was to optimize a hydroxide based process to synthesize the material. We evaluated and compared Toda HE-5050, JPL bench-scale and ANL scaled-up JPL hydroxide materials. The XRD analysis shows that these 3 materials have the same structure (Figure V - 8).

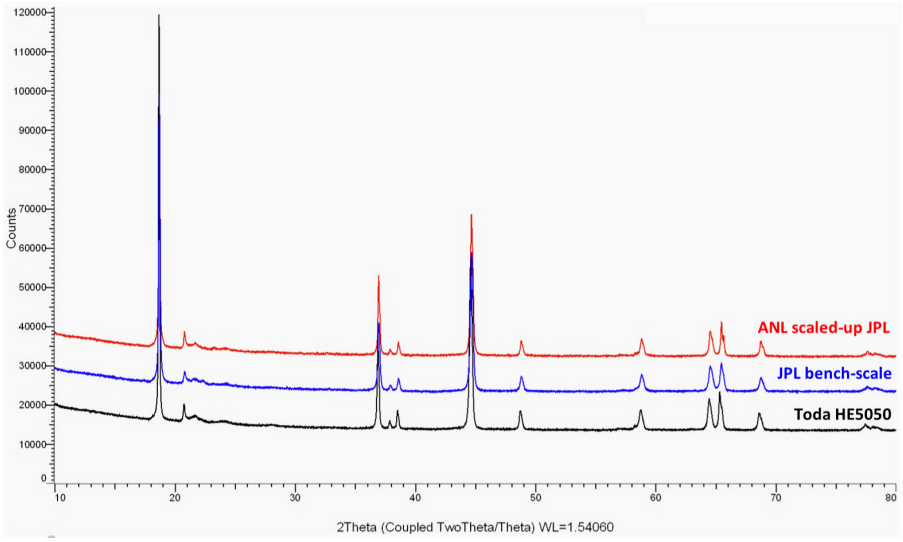

Figure V - 8: XRD comparison between Toda HE5050, JPL bench-scale and ANL scaled-up JPL hydroxide materials

The tap densities of synthesized ANL scaled-up JPL hydroxide materials were between 0.7 ~ 1.3 g/cc depending on the ratios of NaOH and NH_4OH to transition metals. It is difficult to achieve the target tap density (> 1.5 g/cc) via hydroxide process for this composition at the kilogram scale. We then focused on a carbonate based approach based on the scale-up experience of 1st candidate material. Successfully, ANL's scaled-up JPL carbonate material was synthesized and evaluated. Table V - 2 shows the comparison of three HE-5050 samples, JPL bench-scale, ANL scaled-up JPL hydroxide and carbonate materials.

Table V - 2: Comparison of 6 cathode materials with same composition: ① SEM (8000x), ② $D_{10}/D_{50}/D_{90}$ (µm), ③ tap density (g/cc), ④ initial discharge capacity at C/20 (mAh/g)

	Toda-HE5050 B#1 5-P767	Toda-HE5050 B#2 P1407	Toda-HE5050 B#3 P2564	JPL pristine	ANL scaled-up JPL hydroxide ES-20131004	ANL scaled-up JPL carbonate ES-20130924
	Hydroxide co-precipitation			Hydroxide	Hydroxide	Carbonate
	Commercial	Commercial	Commercial	Bench-scale	Pre-pilot	Pre-pilot
①	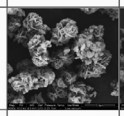	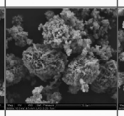	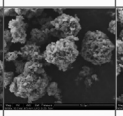	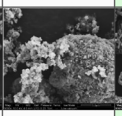	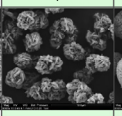	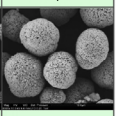
②	3.1/5.3/9.2	1.1/5.2/11.3	2.0/4.9/10.4	1.2/11.1/29.3	3.0/5.1/9.0	4.0/6.7/11.4
③	1.03	1.16	1.07	1.70	1.23	1.82
④	255.3	261.8	254.5	228.2	237.7 *	292.0 *

** Under optimization*

JPL bench-scale material shows the initial discharge capacity of 228 mAh/g and tap density of 1.7 g/cc. Toda America has produced this composition (HE-5050) at a high initial discharge capacity (~250 mAh/g) but at a much lower tap density (~1.0 g/cc). For ANL scaled-up JPL hydroxide material, the tap density is 1.23 g/cc and the initial discharge capacity is 238 mAh/g which is less than the target specification (Figure V - 9). However, as seen in Figure V - 10, ANL scaled-up JPL carbonate material shows a very high initial discharge capacity of 292 mAh/g with the highest tap density of 1.82 g/cc.

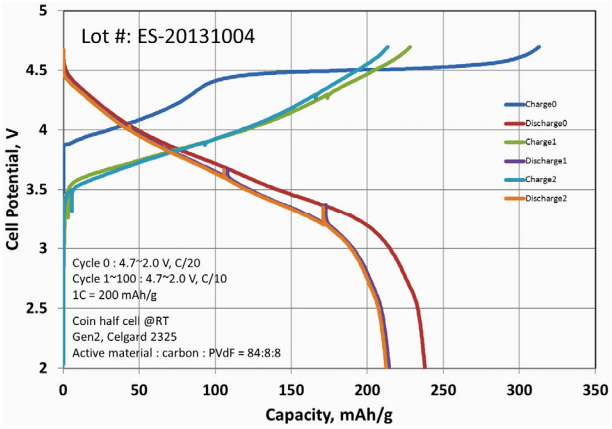

Figure V - 9: Voltage profile of Argonne scaled-up JPL hydroxide material (lot #: ES-20131004)

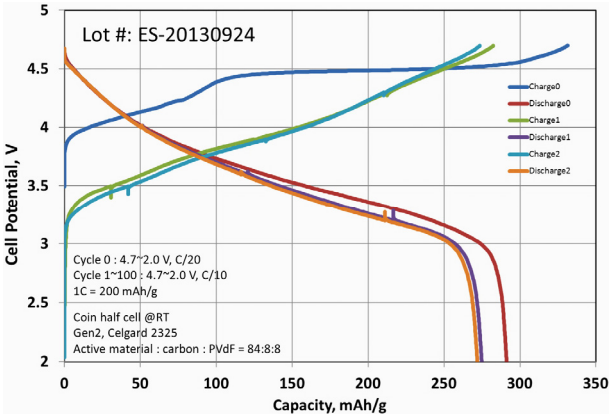

Figure V - 10: Voltage profile of Argonne scaled-up JPL carbonate material (lot #: ES-20130924)

2nd candidate material ($Li_{1.2}Mn_{0.54}Ni_{0.13}Co_{0.13}O_2$): production and delivery of precursor and cathode materials.

The precursor and cathode materials were produced by a reproducible, scalable process and were delivered to Argonne's Materials Screening Group and JPL for evaluation.

- 10/30/2013: 5g JPL hydroxide precursor to ANL CSE.
- 10/31/2013: 100g JPL carbonate cathode to JPL.
- 11/11/2013: 500g JPL hydroxide precursor to ANL CSE (scheduled).
- 12/20/2013: 2~3kg JPL carbonate cathode to JPL (scheduled).

Conclusions and Future Directions

ANL's MERF successfully completed the process development, scale-up and kilogram production of 1st candidate material with equal or better quality. This scaled-up cathode material shows 10% increased capacity, 20% increased tap density and a better cycle life compared to bench-scale material. To identify and mitigate the particle cracking issue of carbonate cathode material, many approaches were investigated. Hydroxide cathode material with same composition was synthesized. Pre-crushed carbonate cathode material was prepared and evaluated. Particle fracturing effect on electrochemical performance and particle size effect on

particle cracking during calendaring process were investigated. Also the relation between secondary particle size, morphology and tap density was studied. These kinds of efforts will open the possibility to mitigate particle cracking of carbonate cathode material. The increased particle density and decreased secondary particle size can be a direction to mitigate the particle cracking of carbonate cathode material which is under on-going investigation using Nanoindenter analysis.

For the 2nd candidate material (JPL, $Li_{1.2}Mn_{0.54}Ni_{0.13}Co_{0.13}O_2$), MERF successfully developed the synthesis processes (both carbonate and hydroxide co-precipitation). To compare the properties of scaled-up materials, three Toda HE-5050, JPL bench-scale and ANL scaled-up JPL hydroxide and carbonate cathode materials were evaluated which have the same composition. ANL scaled-up JPL carbonate cathode material shows excellent properties such as 20% increased initial discharge capacity (292 mAh/g) and 20% increased tap density (1.82 g/cc) compared to the specification.

In FY14, we plan to continue to develop synthesis routes and improve processes to mitigate particle cracking of lithium and manganese rich carbonate cathode material (LMR-NMC) without the trade-off between capacity and density. Kilogram quantities of the 2nd candidate material will be produced and delivered to JPL, ANL Cell Fabrication Facility and ANL Materials Screening Group. The 3rd candidate material will be selected and scaled to kilogram quantities. Additional cathode materials will be synthesized for research purposes as requested.

FY 2013 Publications/Presentations

1. 2013 DOE Annual Peer Review Meeting Presentation.
2. "METHOD FOR PRODUCING SIZE SELECTED PARTICLES," Provisional patent filed – May 14, 2013.

V.B.2 Process Development and Scale up of Advanced Electrolyte Materials (ANL)

Gregory K Krumdick, Program Manager

Argonne National Laboratory
9700 South Cass Avenue
Argonne, IL 60439-4837
Phone: (630) 252-3952; Fax: (630) 252-1342
E-mail: gkrumdick@anl.gov

Collaborators:
Krzysztof (Kris) Pupek, Argonne National Laboratory
Trevor Dzwiniel, Argonne National Laboratory
Daniel Abraham, Argonne National Laboratory
Zhengcheng (John) Zhang, Argonne National Laboratory
Wenquan Lu, Argonne National Laboratory
Gao Liu, Lawrence Berkeley National Laboratory
Dan Scherson, Case Western University
Wesley Henderson, North Carolina State University
Kang Xu, Army Research Laboratory

Start Date: June 2010
Projected End Date: September 2014

Objectives

The objective of this task is to conduct process engineering research for the scale-up of new electrolyte and additive materials. Advanced electrolytes and additives are being developed to stabilize the interface of lithium-ion batteries by forming a very stable passivation film at the carbon anode. Stabilizing the interface has proven to be key in significantly improving the cycle and calendar lives of lithium ion batteries for HEV and PHEV applications. Up to this point, these advanced electrolytes and additives have only been synthesized in small batches. Scaling up the process involves modification of the bench-scale process chemistry to allow for the semi–continuous production of materials, development of a process engineering flow diagram, design of a mini-scale system layout, construction of the experimental system and experimental validation of the optimized process. The mini system will be assembled utilizing an existing synthesis reactor system. Electrolyte materials so produced will be analyzed to confirm material properties and for quality assurance. The electrochemical properties of the material will be validated to confirm a performance match with the original materials.

Technical Barriers

Advanced electrolytes and additives have been synthesized in small batches using 1-5L vessels, which produce approximately 200 mL of the material. The bench-scale processes are labor-intensive and time-consuming. Sufficient quantity of material cannot be generated for prototype testing, which is required prior to scaling the process to the next level. Therefore, pilot-scale facilities are required for battery materials scale-up research and development.

Technical Targets

- Scale-up 4-6 electrolyte materials in FY13.

Accomplishments

- Scale-up work has been completed on the following electrolyte materials:
  - **ANL-RS21 (**6,7-dimethoxy-1,1,4,4-tetramethyl-1,2,3,4-tetrahydronaphthalene).
  - **ARL- LiPFTB (**Lithium perfluoro-tert-butoxide).
  - **ANL-RS5** [(2,5-dimethoxy-1,4-phenylene) bis(diisopropylphosphine oxide)].
  - **ANL-RS51** [(2,5-dimethoxy-1,4-phenylene) bis(diethylphosphine oxide].
- **CWU-FRION (**lithium [(2,5-bis(diethylphosphoryl) catecholato) oxalatoborate]).
- Work has begun on the following materials:
  - **Li-FSI** (electrolyte additive).
  - **Li-TDI** (electrolyte additive).
  - **LBNL-PEFM** (organic binder).
- We are in the process of developing protocol for electrochemical validation of scaled up materials:
  - Redox shuttle RS5 and RS51 are currently tested against baseline electrolyte.
  - Comparison study, RS5 vs. RS51 are in progress.
  - Electrochemical study of in-process materials will be used to develop material specification (minimum required purity and impurity profile).

✧ ✧ ✧ ✧ ✧

Introduction

Researchers in the battery materials programs across the DOE complex refer to scale up as synthesis of battery materials in gram quantities, and with time consuming, multiple small-scale runs. There is a need to develop scale-up processes for battery materials (primarily lithium-ion based batteries) to the kilogram and tens-of-kilograms quantities at DOE labs to support the transition of these technologies to industry. Currently, there is no systematic engineering research capability or program across the DOE complex or in industry to identify and resolve constraints to the development of cost-effective process technology for the high-volume manufacture of these advanced materials.

Approach

A formal approach for the scale-up of electrolyte materials has been defined (see Figure V - 11). This approach starts with the initial discovery of a new electrolyte material and an initial electrochemical evaluation. This determines if the material is to be added to the inventory spreadsheet, ranked and prioritized. At this point, the scale-up process begins with the initial feasibility study, proof of concept testing, 1st stage scale-up and 2nd scale scale-up. Go/No go decisions occur after feasibility determination and electrochemical validation testing.

For each material scaled, we will develop a scalable manufacturing process, analytical methods and quality control procedures. We will also prepare a "technology transfer package" which will include:

- Summary of the original process used by discovery researchers to synthesize the material.
- Summary of the scalable (revised) process suitable for large scale manufacturing.
- Detailed procedure of the revised process for material synthesis.
- Analytical data/Certificate of Analysis for the material (chemical identity and purity).
- The material impurity profile.
- Electrochemical performance test data.
- Preliminary estimates of production cost.
- MSDS for the material.
- Develop material specifications.

We will also make kilogram quantities of the material available for industrial evaluation, which would have been fully characterized chemically and electrochemically.

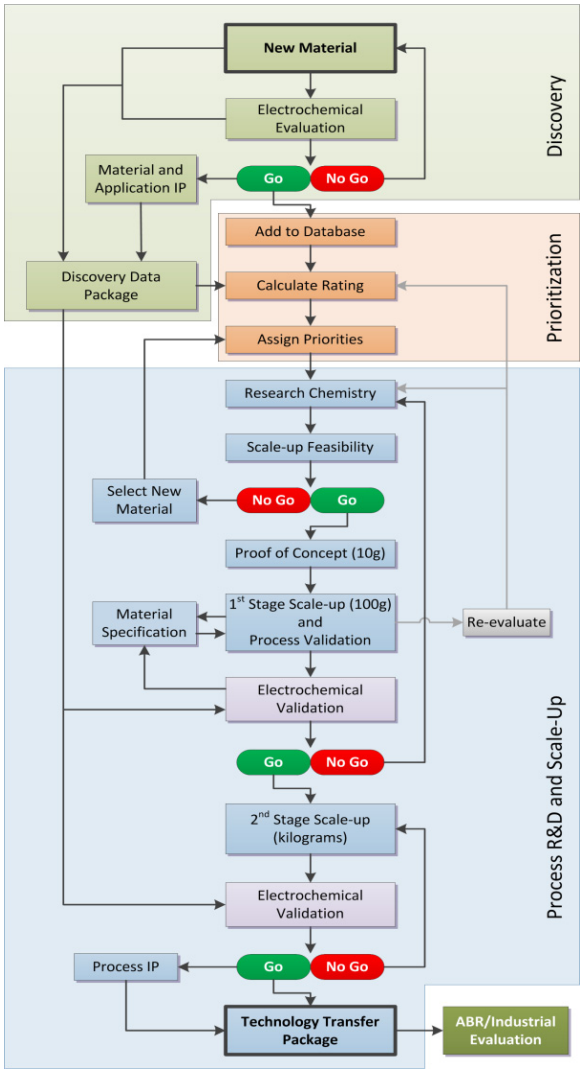

Figure V - 11: Electrolyte Materials Process R&D Workflow

Results

MILESTONE	DATE
ANL-RS21 – Complete	
Assess scalability of disclosed process	9/28/12
WP&C documentation approved	9/28/12
Develop and validate scalable process chemistry (10g scale)	10/30/12
First process scale-up (100g bench scale)	11/30/12
Second process scale-up (1000g pilot scale)	01/10/13
2,320g produced in a single batch, purity >99.5%	
ARL-LiPFTB – Complete	
Assess scalability of disclosed process	11/21/12
WP&C documentation approved	9/28/12
Develop and validate scalable process chemistry (10g scale)	12/21/12
First process scale-up (100g bench scale)	2/28/13
Second process scale-up (1000g pilot scale)	3/15/13
1,200g produced in a single batch, purity >99%	
ANL-RS5 – Complete	
Assess scalability of disclosed process	9/28/12
WP&C documentation approved	9/28/12
Develop and validate scalable process chemistry (10g scale)	7/31/13
First process scale-up (100g bench scale)	10/15/13
115g produced in a single batch, purity >99.9%	
ANL-RS51 – Complete	
Assess scalability of disclosed process	N/A
WP&C documentation approved	9/28/12
Develop and validate scalable process chemistry (10g scale)	7/31/13
First process scale-up (100g bench scale)	8/16/31
96g produced in a single batch, purity >99%	
CWU-FRION – Complete	
Assess scalability of disclosed process	5/21/13
WP&C documentation approved	9/28/12
Develop and validate scalable process chemistry (10g scale)	7/9/13
First process scale-up (100g bench scale)	9/24/13
118g produced in a single batch, purity >97%	

Wenquan Lu in the Materials Screening Group in the CSE division is conducting the electrochemical validation of the materials. RS21, RS5, RS51, and FRION are in the queue to be tested. Technology transfer packages have been prepared for all materials scaled. To date, we have provided 47 electrolyte material samples to interested companies and national labs. (NOTE: RS5, RS51 and FRION were synthesized on 100g scale to provide material for researchers and complete electrochemical evaluations.)

Conclusions and Future Directions

The technology transfer package for CWU-FRION is being written. Initially, scale-up work will continue on Li-FSI, Li-TDI and LBNL-PEFM. Additional materials to scale will be added after discussions with the project sponsor. The scale-up of 4-6 electrolyte materials are targeted for FY14.

Standardized protocols for validation of electrochemical performance for various classes of materials (electrolyte solvents, additives, redox shuttles) will be developed.

Over 24,000 g of battery grade materials have been produced, 47 samples have been provided to industry and various national labs for evaluation and experimentation (total 7,300 g, 4 samples in FY11, 25 samples in FY12 and 18 samples in FY13).

FY 2013 Publications/Presentations

1. 2013 DOE Annual Peer Review Meeting, May 13th-17th 2013, Arlington, VA.
2. T. Dzwiniel, K. Pupek and G. Krumdick: "*From Beaker to Bucket: The Safe Scale-up of Organic Electrolyte Materials,*" 246th ACS National Meeting, American Chemical Society, 2013.
3. Technology transfer packages were written for ANL-RS21, ANL-RS5, ANL-RS51, and ARL-LiPFTB.

V.B.3 Cell Analysis, Modeling, and Prototyping (CAMP) Facility Production and Research Activities (ANL)

Andrew N. Jansen
Argonne National Laboratory

Collaborators:
Daniel P. Abraham, Argonne National Laboratory
Dennis W. Dees, Argonne National Laboratory
Kevin G. Gallagher, Argonne National Laboratory
Wenquan Lu, Argonne National Laboratory
Bryant J. Polzin, Argonne National Laboratory
Stephen E. Trask, Argonne National Laboratory
Martin Bettge, Argonne National Laboratory
Joseph J. Kubal, Argonne National Laboratory
Yan Li, Argonne National Laboratory
Qingliu Wu, Argonne National Laboratory
Ye Zhu, Argonne National Laboratory

Start Date: October 2012
Projected End Date: September 2014

Objectives

- The objective of this core-funded effort is to design, fabricate, and characterize high-quality prototype cells that are based on the latest discoveries involving high-energy anode and cathode battery materials. Using this multi-discipline facility, analytical diagnostic results can be correlated with the electrochemical performance of advanced lithium-ion battery technologies for EV and PHEV applications.
  - Link experimental efforts through electrochemical modeling studies.
  - Identify performance limitations and aging mechanisms.

Technical Barriers

The primary technical barrier is the development of a high energy density battery for EV and PHEV applications that is safe, cost-effective, and has a long cycle life.

- Interpret complex cell electrochemical phenomena.
- Identify cell degradation mechanisms for a variety of novel high energy materials.

Technical Targets

- Obtain a viable supplier of battery grade silicon powder.
- Assess influence of LiDFOB, LiBOB, and HFiP electrolyte additives for HE5050 cathode.
- Evaluate MERF cathodes ($Li_{1.25}Ni_{0.3}Mn_{0.62}O_2$) based on hydroxide and carbonate precursors.
- Validate performance of advanced battery materials and add to Electrode Library as needed.
- Determine sources of impedance rise and capacity fade during extensive cycling of cells containing various electrochemical couples.
- Recommend solutions that can improve the life of high-energy lithium and manganese rich Ni/Mn (LMR-NMC) electrodes and cells.
- Enhance battery design and cost model concentrating on designs for advanced lithium-ion electrochemical couples.
- Advance development of electrochemical models focusing on the impedance of LMR-NMC positive electrodes.

Accomplishments

- The CAMP Facility was successfully organized into a streamlined effort with the task of assessing new battery materials in industrially relevant prototype formats.
- Over 14 cell builds were performed to date with combinations of baseline NCM523, 5V spinel, and high energy composite structure cathode materials (LMR-NMC) from Toda Kogyo, ABR researchers, and the Materials Engineering Research Facility (MERF). Over a thousand deep discharge cycles were achieved with many of these cells.
- Electrolyte additive studies for LMR-NMC suggest that the effect of additives is dependent on formation protocol and/or cell format.
- It was determined that the effective utilization of silicon in the anode will require a tailored silicon-carbon-binder system with limits on the silicon lithiation and use of electrolyte additives (FEC).

- Examined the LMR-NMC positive electrode SEI impedance using the EIS electrochemical model to study the impact of the voltage hysteresis during cycling.

✧ ✧ ✧ ✧ ✧

Introduction

The "valley of death" is a phrase that is often used to describe the path that a new discovery must traverse to become a commercial product. This is especially true for novel battery materials invented in research laboratories around the world. Often researchers are resource-limited and only able to make gram quantities of the new material. A few grams is enough for several coin cells to prove the concept, but never enough for a battery manufacturer to test in a realistic format. Consider that a typical coin cell has a capacity near 4 mAh, while a cell in a PHEV/EV battery has a capacity near 40 Ah – four orders of magnitude larger. An unwarranted amount of resources could be gambled to make the tens of kilograms needed for a full-sized cell for industrial demonstration. Many great materials may have been abandoned on the benchtop because the scale-up risks were deemed too excessive.

This is where the CAMP Facility contributes. The CAMP Facility is appropriately sized to enable the design, fabrication, and characterization of high-quality prototype cells using just a few hundred grams of the latest discoveries involving high-energy battery materials. Prototype cells made in the CAMP Facility generally have near 400-mAh capacity, which straddles the gap between coin cells and full cells nicely – two orders of magnitude from each end point. Thus, a realistic and consistent evaluation of candidate chemistries is enabled in a time-effective manner with practical quantities of novel materials.

The CAMP Facility is more than an arrangement of equipment, it is an integrated team effort designed to support the production of prototype electrodes and cells, and includes activities in materials validation, modeling, and diagnostics. It is not the aim of this facility to become a small battery manufacturer, but instead to be a laboratory research facility with cell production capabilities that adequately evaluate the merits and limitations of mid- to long-term lithium-ion chemistries in a close-to-realistic industrial format.

As new cell chemistries and systems progress, they reach the point where they are considered for further development in larger prototype cells. When this happens, a limited quantity of these materials, along with their preliminary data, are transferred from the lab to the CAMP Facility for materials validation to determine if they warrant further consideration. The source of these materials (anodes, cathodes, electrolytes, additives, separators, and binders) may originate from the ABR and BATT Programs, as well as from other domestic and foreign organizations such as universities, national labs, and industrial vendors. Electrochemical couples with high power and energy density are given extra priority. Lately efforts have focused on silicon-based anodes and LMR-NMC cathodes.

The CAMP Facility has the capability to make two prototype cell formats in a 45 m² dry room: pouch cells (xx3450 format, with capacity around 0.4 Ah) and 18650 cells. Pouch cells are anticipated to be easier to assemble, but they may suffer from bulging if gases are evolved during cell aging and cycling. 18650s, which are rigid containers, may be used if the pouch cell format is deemed unreliable due to gassing, or if higher capacity cells are needed (greater than 1 Ah). Central to this effort is a pilot-scale coating machine that operates with slurry sizes that range from 20 grams to a few kilograms. This is a key feature of the CAMP Facility that enables a professional evaluation of small quantities of novel materials. If needed, the MERF is available for scaling up materials for these prototype cell builds.

In general, two types of modeling are employed within this effort. First, battery design modeling is a spreadsheet based simulation that is used to determine the impedance behavior, available capacity, and thermal effects for general and specific cell, battery module, and battery pack designs. The model is also capable of performing simulations on multiple battery designs for comparison and optimization. In addition, the battery design model includes a module that calculates battery costs by combining materials and components costs with manufacturing expenses based on a plant design. A publicly available version of this work the battery performance and cost (BatPaC) model, is the only public domain model that captures the interplay between design and cost of lithium-ion batteries for transportation applications.

The other type of modeling is electrochemical modeling, which is aimed at associating electrochemical performance measurements with diagnostic studies conducted on lithium-ion cells. The methodology for the electrochemical model is described in detail in literature [1-3]. Essentially, continuum based transport equations are combined with kinetic and thermodynamic expressions to allow the potential, concentration, and current distributions to be determined throughout the cell. Two versions of the cell electrochemical model with the same basis are utilized to fully examine the broad range of electrochemical studies. One version of the electrochemical cell model is used to simulate the cell response from Electrochemical Impedance Spectroscopy (EIS) studies, and the other model version is utilized for examining DC studies, such as controlled

current or power cycling and diagnostic hybrid pulse power characterization (HPPC) tests.

Approach

The general approach used in this effort is to start small and grow large in terms of cell size and amount of resources devoted to each novel battery material. At various points in the development process, decisions are made to either advance, modify, or terminate studies to maximize utilization of available resources.

Coin cells (2032 size) are used for materials validation purposes with initial studies performed at room temperature or 30°C. After formation cycles, the coin cells go through HPPC testing, rate capability testing, and limited cycle life testing. Accelerated aging studies are also performed at 45°C to 55°C for promising materials to give a preliminary indication of life. Where appropriate, the thermal abuse response is studied using a differential scanning calorimeter.

Using the recommendations and results obtained by the materials validation of promising materials, single-sided electrodes are fabricated on the larger dry-room coater for diagnostic study. The new cell chemistries are studied in detail using advanced electrochemical and analytical techniques, including micro-reference electrode cells. Factors are identified that determine cell performance and performance degradation (capacity fade, impedance rise) on storage and on extensive deep-discharge cycling. The results of these tests are used to formulate data-driven recommendations to improve the electrochemical performance/life of materials and electrodes that will be incorporated in the prototype cells that are later fabricated in the dry room. This information also lays the foundation for electrochemical modeling focused on correlating the electrochemical and analytical studies, in order to identify performance limitations and aging mechanisms.

The approach for electrochemical modeling activities is to build on earlier successful characterization and modeling studies in extending efforts to new EV and PHEV technologies. The earlier studies involved developing a model based on the analytical diagnostic studies, establishing the model parameters, and conducting parametric studies with the model. The parametric studies were conducted to gain confidence with the model, examine degradation mechanisms, and analyze cell limitations. Efforts this year included expanding and improving the model's capabilities with the focus on LMR-NMC cathodes.

The approach for the battery design modeling studies is to continue to develop and improve methods to design lithium-ion batteries for electric-drive vehicles based on spreadsheet calculations. In addition, the battery design model is used to determine the impact of advanced materials on the current technology. The performance of the materials within the battery directly affects the energy density and cost of the battery pack. Both modeling efforts complement each other and are specifically aimed at supporting the CAMP facility goals.

If the results from diagnostics and modeling still look promising, full cell builds are conducted using double-sided electrodes. The electrodes are then either punched in the case of pouch cells, or slit in the case of 18650 cells and assembled into full cells in the dry room using the semi-automated cell assembly equipment. Formation procedures are conducted on the cells to encourage electrolyte wetting and solid-electrolyte-interface (SEI) formation. These cells undergo rigorous electrochemical evaluation and aging studies under the combined effort of the CAMP Facility team, and Argonne's Electrochemical Analysis and Diagnostic Laboratory (EADL) and Post-Test Facility. After testing, select cells are destructively examined by the Post-Test Facility to elucidate failure mechanisms. This information is then used to further improve the new chemistry, as well as future electrode and cell builds. The results of these tests are shared with other members of the ABR & BATT Programs and with those associated with the materials' origin, and with battery developers (if appropriate).

Results

Materials Validation.

Silicon-based Anodes. Three commercially available silicon materials have been obtained and are under various stages of testing. The first material is a 1-5 µm silicon powder from Alfa Aesar (Figure V - 12a); while the second is a silicon powder obtained from Nanostructured and Amorphous Materials Incorporated (NanoAmor). This material is a 130 nm silicon powder (spherical with some nanowires mixed in). A third source of silicon materials is from American Elements, which is available in several particle sizes in kg quantities. Particle sizes of 50, 150, and 1,000 microns were selected for validation and are now under test.

Lithium half cells have been made with laminates of various compositions. Currently in this study, the best electrode produced using Alfa Aesar silicon was a nearly pure silicon electrode with a lithiated PAA binder and a citric acid buffer (76 wt.% silicon, 10 wt.% C-45 carbon, and 14 wt.% LiPAA with citric acid buffer) (Figure V - 12b). This electrode was able to maintain high gravimetric capacities even at a 2C rate and has an average columbic efficiency of 99.4% during cycling.

While the morphology (and lack of surface treatment) of the readily available silicon powder from Alfa Aesar is not ideal, it is capable of being cycled and

was used as a temporary baseline for further binder development. Surprisingly, the cycle life was relatively good for initial electrode formulations that used high silicon to graphite content, which was attributed to competing binder functions, i.e., binders developed for silicon may not be ideal for graphite.

Studies were conducted with the silicon powder obtained from NanoAmor using lithiated polyacrylic acid (Li-PAA) as the binder, with graphite and a carbon additive in an aqueous slurry system. The electrode composition consisted of 9 wt% NanoAmor Silicon (130 nm), 80.5 wt% Timcal SFG-6 graphite, 5.5 wt% Li-PAA (450,000 m.w.) and 5 wt% Timcal C-45 carbon

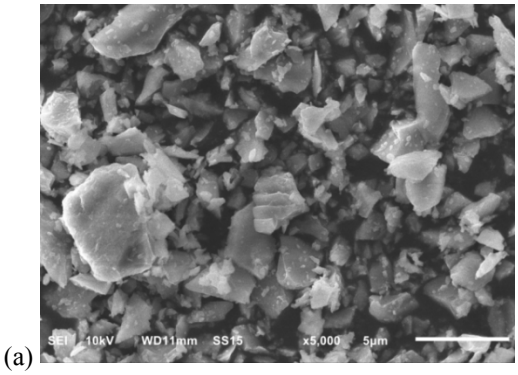

Figure V - 12: (a) SEM image of silicon powder from Alpha Aesar, and (b) capacity results for a silicon electrode (76 wt.% Alpha Aesar silicon, 10 wt.% C-45, and 14 wt.% LiPAA with citric acid buffer) vs. Li metal in 2032 coin cell (capacity limited cycles)

coated on 10 um copper foil. The slurry was prepared using sonication for the mixing process in de-ionized water. Half-cell coin cells were constructed using 97 wt.% 1.2 M $LiPF_6$ in EC:EMC (3:7 by wt) electrolyte with 3 wt.% fluoroethylene carbonate (FEC) additive. Electrochemical tests cycled the cells from 0.050V to 1.500V at a galvanostatic ~C/2.5 rate (Figure V - 13). It was encouraging to see a capacity that was higher than the graphite alone, but the capacity fade rate is still a problem that must be overcome. While additional validation needs to be performed, this appears to be a possible candidate to use for silicon-based anodes for prototype cell builds; it cycles better than most other silicon powders cycled thus far, and sizable quantities of this material can be obtained at reasonable prices without any limitations on its distribution and data reporting.

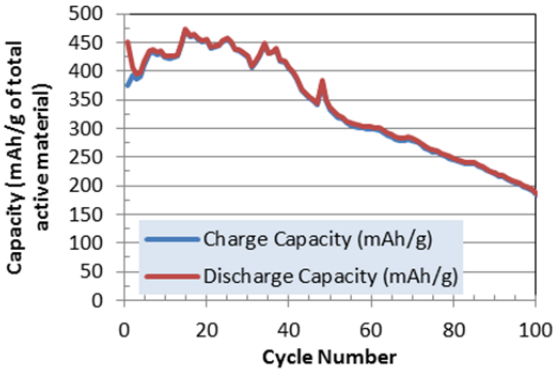

Figure V - 13: Silicon-graphite electrode using NanoAmor silicon powder vs. Li metal in coin cells. These cells were able to maintain capacities over 400 mAh/g for the first 40 cycles

An even more promising open source of silicon is the materials from American Elements, which has a range of particle sizes tailored to lithium-ion battery use. These silicon materials were received near the end of FY13 and are now under test.

In addition to testing commercial silicon materials obtained thus far, collaborations are ongoing with companies to make improved silicon/graphite composite electrodes. Samples of silicon were received from Electrochemical Materials (EM), with their proprietary organic coating on the silicon that allows it to cycle when using PVDF as a binder in a silicon/graphite composite electrode (Figure V - 14). Their improved coating also allows the particles to be coated in aqueous binder systems. A multitude of electrodes have been made with this new batch of powders, altering both the binder and the graphite. Currently, two different graphite powders are being used in conjunction with the EM powder. The first is the standard A12 (high power graphite) along with the less dense but more exfoliated SFG-6. A12 has been shown to underperform when mixed with silicon in aqueous systems, which is believed to be caused by improper binding to the graphite. However, since this silicon material can be made using PVDF (a binder which works well with the A12 graphite), this relationship needs to be further examined. In addition to testing PVDF, CMC (carboxyl methyl cellulose) is being tested as well per recommendation from EM.

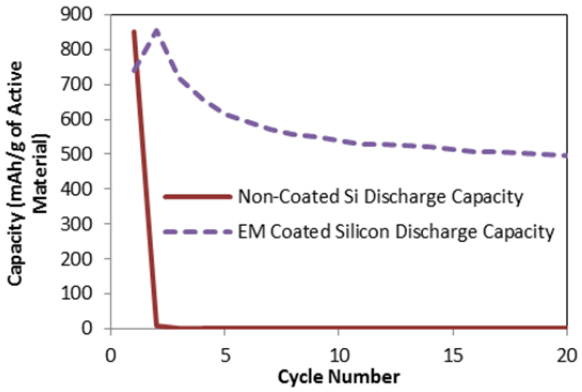

Figure V - 14: Comparison between Electrochemical Materials' (EM) surface-treated silicon against that of a silicon powder that has not been treated, both using PVDF as the binder. The EM electrode is 9 wt.% EM-treated silicon, 51 wt.% graphite, 10 wt.% carbon black, and 30 wt.% PVDF

A silicon-graphene electrode from XG Sciences was also received and tested. The electrode consisted of 70% Si/graphene active material, 20% graphene, and 10% PAA binder. The total loading, including grapheme and binder, is about 1.15 g/cm². 1.2 M $LiPF_6$ in EC/EMC with 10% FEC additive was used as the electrolyte. The Li/Si-C half cell was initially tested between 10mV and 1V at C/10 and 30°C. The test results of two formation cycles are shown in Figure V - 15. The reversible specific capacity was determined to be over 2,400 mAh/g based on the weight of silicon-graphene composite. The first cycle irreversible capacity loss was 17%. Rate performance tests were also conducted on the Li/Si-C half cell. The lithiation rate was fixed to C/5 rate and the delithiation rate varied from C/5 to 2C. Surprisingly, the silicon graphene composite electrode demonstrated excellent rate performance: no capacity drop was observed at even the 2C rate.

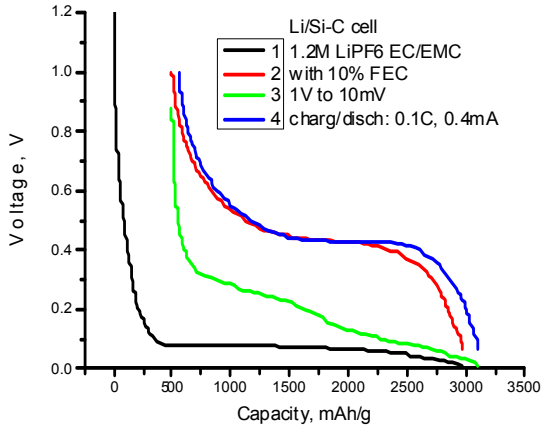

Figure V - 15: Voltage profile of Si-graphene from XG Sciences in a half cell during formation cycles

Since PVDF has been generally shown to be an inferior binder with uncoated silicon-based electrodes, other binders needed to be employed. Silicon undergoes major expansions and contractions during cycling, and when PVDF is used as the binder, electrical contacts between particles are difficult to be maintained. Repeated cycling of the electrode tends to fracture and isolate silicon particles from the conductive network, which diminishes the capacity. Using aqueous binders such as CMC, Alginic Acid or PAA increases cyclability by helping prevent the loss of contacts between particles, but these electrodes tend to be brittle.

The PAA aqueous binder system with graphite and silicon has shown positive performance in coin cell cycling, but there are challenging issues of physical properties during the slurry preparation process that need to be addressed. The PAA-based slurry has a shear thickening action and a time dependency for keeping the particles in suspension, which are not conducive to standard coating procedures. The dried electrodes are brittle as well. Typical PAA slurries have a pH between 2.6 and 3.0. An investigation to resolve these issues has included the use of a base, lithium hydroxide, to titrate the slurry to a higher pH. Several slurries were coated with varying pHs from a range below 3 to above 10. The study found that a slurry pH of 6 to 7 yielded slurries with reasonable fluid dynamics for coating, and dried calendered electrodes with the best cohesion and adhesion. Adjusting the pH to neutral has improved the fluidity of the slurry and electrode integrity, but the issue of particle separation in the slurry state is still prevalent. Future work will include considering thickening agents, such as xanthan gum, to minimize the particle settling issue. Also, supplementing or replacing lithium hydroxide with other bases, such as ammonium hydroxide, will be investigated.

In addition to the binders that have been tested, polyethylene-co-acrylic acid (PEAA) has been

considered a possible binder for silicon based electrodes. While electrodes made with only PEAA for a binder have shown poor electrochemical results, the electrode itself had better mechanical properties than electrodes made only with PAA or CMC, meaning that PEAA could be a useful additive. Electrodes made with xanthan gum have shown some promise as well. It is likely that a multi-component binder system will be needed to make an ideal silicon-composite anode.

Collaboration with binder manufacturer Zeon Chemical has produced useful insights into binder mechanisms. Zeon produces a polystyrene-butadiene rubber (SBR), which has been shown to improve the laminate's physical properties along with increased electrochemical performance. Zeon's binder has been tested in conjuction with mainly CMC upon their recommendations. In addition to supplying their binder, they loaned Argonne a Primix mixer, and with this mixer nine large scale slurries (all over 100 grams of solids) were made. Several graphite/SBR/CMC slurries were successfully coated on the large coater in the CAMP Facility dry room, with these being the first aqueous-based slurries to have been coated in the dry room environment. No adverse effect on the humidity in the dry room was noted. Future work involves creating a procedure that will maximize dispersion of the silicon particles with use of different mixers available along with trying a variety of additives to improve dispersion.

Silicon electrode provided by LBNL. Dr. Gao Liu (LBNL) invented a conductive binder designed to improve the cyclability of silicon electrodes by tailoring the polymer with dual functionality: conducting electricity and binding closely to silicon particles. This conductive binder is referred to as PFFOBM. A silicon electrode with 33% PFFOBM was prepared by Dr. Liu and shipped to Argonne. Upon receipt, the electrode was vacuum dried and then assembled in coin cells with 1.2 M $LiPF_6$ in EC/EMC (3:7 by wt.) electrolyte plus 10 wt.% FEC. Three formation cycles were conducted on these lithium half cells at a C/10 rate between 1 V and 10 mV. After three formation cycles, the half cells underwent various lower cut-off voltages during cycling: 10 mV, 40 mV, and 200 mV. For the cell with the 200 mV cut-off voltage cycling, a capacity rate test was conducted before life cycling. The delithiation capacity for each cell is shown in Figure V - 16.

All the cells showed relatively good cycling performance, regardless of the cut-off voltage, compared to non-conductive binders. It can also be seen from this plot that the cell with the lowest cut-off voltage (10 mV) experienced the fastest capacity fade rate, which is expected due to the excessive volume expansion upon lithiation. When the higher cut-off voltage is used, less lithiation of the silicon particle occurs, leading to less stress and volume expansion in the silicon particle. This will in turn improve the cycle life. In Figure V - 16 (bottom), the coulombic efficiency is plotted as a function of cycle number. Another interesting cut-off voltage effect was observed: the coulombic efficiency increased continuously with cycling when 10 mV and 40 mV were used as cut-off voltages. However, the coulombic efficiency jumped up to almost 100% when the cut-off voltage was changed to 200 mV. It is believed that the coulombic efficiency improvement is related to less stress of the SEI at 200 mV. When a low cut-off voltage is used, the high stress as discussed above will pulverize the particle and expose the new surface for new SEI formation, resulting in low coulombic efficiency.

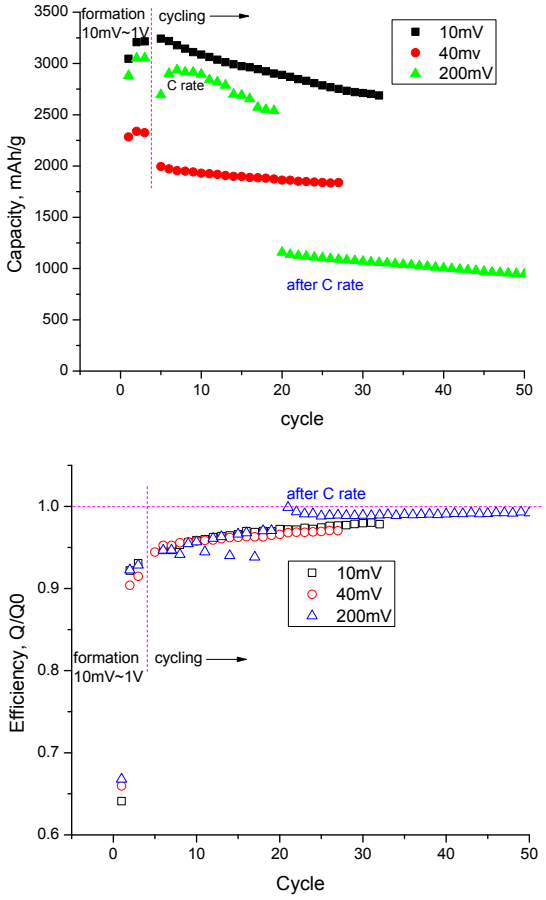

Figure V - 16: Cycling (top) and coulombic efficiency (bottom) of silicon electrode with PFFOBM conductive binder from LBNL. Note that, in the top curve, the lower cutoff was raised from 10 to 200mV at 20 cycles in the green data, resulting in a drop in capacity

Cathodes. Materials are constantly being sought that are of interest to the battery R&D community. If warranted, several of these materials are then added to the Electrode Library. The latest material that is ready to be made into electrodes is $LiCoO_2$. The materials

validation process has been completed on this material and an electrode has been designed for inclusion in the Electrode Library.

$LiCoO_2$ is one of the most used cathode materials in lithium-ion batteries and serves as a valuable baseline for material researchers. An electrode was made with $LiCoO_2$ from BTR (China), which was used as received. The electrode consisted of 94 wt.% $LiCoO_2$, 2 wt.% Super P-Li carbon black, and 4 wt.% PVDF binder. The punched electrode was fabricated into 2032 coin cells after calendaring with 1.2 M $LiPF_6$ in EC/EMC (3:7 by wt.) as the electrolyte. These lithium half cells were cycled between 4.1 V and 3.0 V at C/10 for three cycles. The voltage profile is shown in Figure V - 17. The reversible capacity after three cycles was 125 mAh/g with less than 10% initial irreversible capacity loss during the 1st cycle.

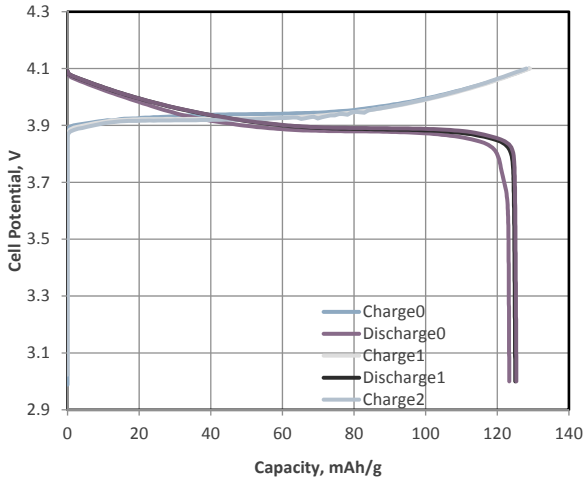

Figure V - 17: Voltage profile of Li/$LiCoO_2$ cell at C/10 rate

After three formation cycles, the cells were subjected to a capacity rate study. Those results are shown in Figure V - 18. It can be seen from the figure that this material can deliver over 110 mAh/g up to the 1C discharge rate. The cells were then cycled at a 0.3 C rate between 4.1 V and 3.0 V. More than 90% capacity retention was obtained after 50 cycles. More capacity can be expected if the voltage is increased to 4.2 V vs. lithium.

Additional materials that are currently going through the materials validation process are as follows: Hanwah $LiFePO_4$, Toda 4V Spinel, Toda NCM 424, and Toda HE5050 (5/13 10-kg batch). Kureha Hard Carbon (J and S(F) grades) and MCMB (G-15) graphite will also be added to the library. The electrochemical performance data on these materials will be used to design electrodes that will match those in the Electrode Library.

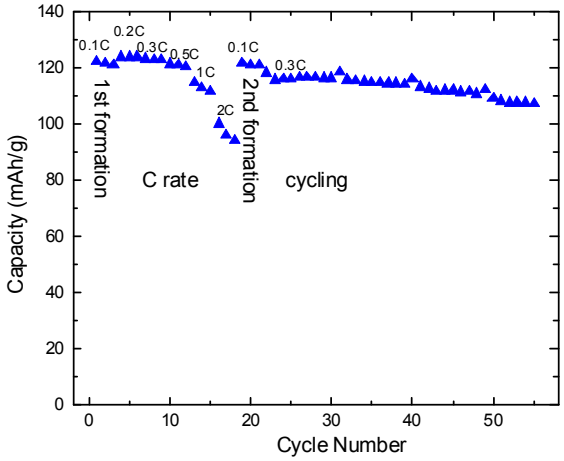

Figure V - 18: Rate study and cycling performance data for Li/$LiCoO_2$ half cell

The electrochemical validation of $LiFePO_4$ powder from Hanwha was completed using lithium metal half cells. The electrode consisted of 84% $LiFePO_4$, 4% SFG-6, 4% carbon black, and 8% PVDF binder. The loading was 9.3 mg/cm². The electrode porosity was calculated to be 30% after calendering. The electrolyte used was 1.2 M $LiPF_6$ in EC/EMC without any additive. According to the formation cycle at a C/10 rate between 2.9 V and 3.8 V, the specific capacity during the 3rd formation cycle was 150 mAh/g (Figure V - 19). The irreversible capacity loss was about 4% during the 1st cycle. The rate performance test was also conducted on the half cells. The capacity delivered at the 2C rate was still more than 82% of the C/10 capacity.

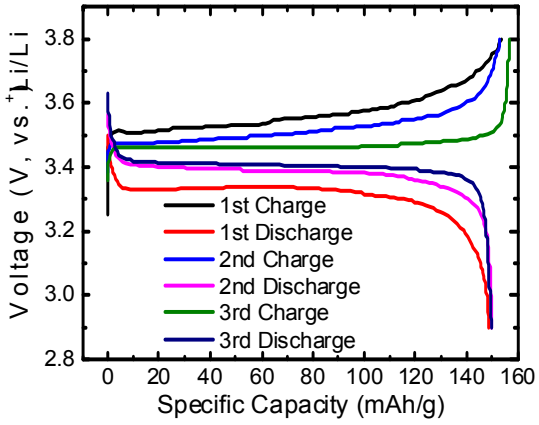

Figure V - 19: Voltage profile of Li/$LiFePO_4$ half cell during formation cycles

JPL Coated Cathode. Two cathode powders were received from Jet Propulsion Lab (JPL). One powder is $Li_{1.2}Mn_{0.54}Ni_{0.13}Co_{0.13}O_2$ and the other one is a similar powder with 1 wt.% $AlPO_4$ coating (Figure V - 20). The brightness of the coated particle is caused by the charge

during SEM measurement, which indicates the insulating feature of the coating.

These powders were made into electrodes using the same formulation: active materials/SFG-6/carbon black/PVDF = 86/4/2/8. Lithium half cells were used to characterize the electrochemical performance of these two active materials. The separator was Celgard 2325 and 1.2 M $LiPF_6$ in EC/EMC solvent was used as the electrolyte.

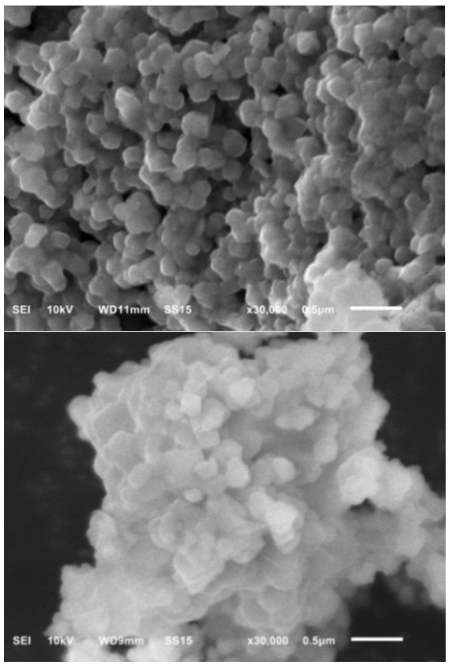

Figure V - 20: SEM images of $Li_{1.2}Mn_{0.54}Ni_{0.13}Co_{0.13}O_2$ (top) and similar material with 1 wt.% $AlPO_4$ coating (bottom). SEM from Argonne's Post Test Facility

It was noticed from the formation cycle that both materials showed a typical activation voltage plateau near 4.5 V, which is similar to other LMR-NMC materials. However, a difference between the two active materials was observed when the differential capacity profile was compared in Figure V - 21. For the coated sample, the reduction peak slightly above 3.0 V shifted to lower potentials. In addition, a new reduction peak was observed near 2.5 V, which suggests that the coating process has an impact on the electrochemical performance of LMR-NMC.

The voltage fade protocol was also applied to these two materials. Basically, a low current of 10 mA/g was used for the 1st formation cycle, followed by cycling at a current of 20 mA/g. The voltage profiles vs. normalized capacity are shown in Figure V - 22a. The black curves correspond to the uncoated sample and the red curves correspond to the coated sample. The lower operational voltage of the coated sample can be clearly seen near the end of discharge. This results in a lower average discharge voltage for the coated sample as shown in Figure V - 22b. It was also noticed that the discharge voltage fade rate of the coated sample is comparable, if not worse, to that of the uncoated sample.

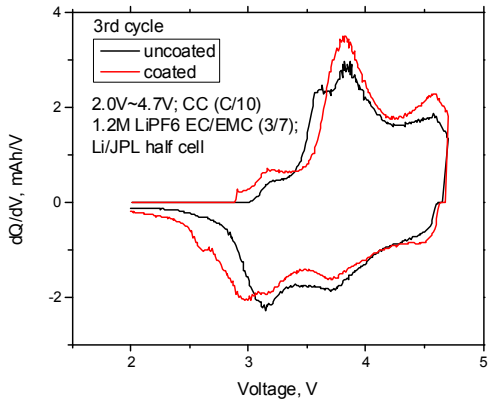

Figure V - 21: Different capacity plot of $Li_{1.2}Mn_{0.54}Ni_{0.13}Co_{0.13}O_2$ with and without $AlPO_4$ coating

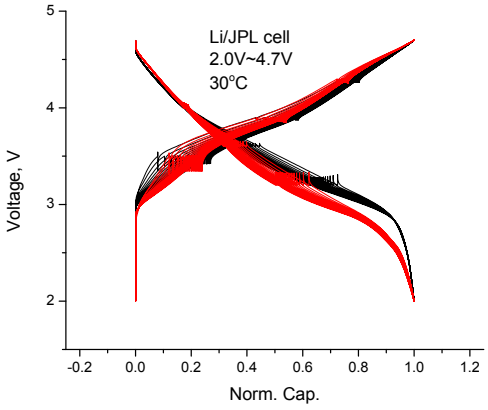

a)

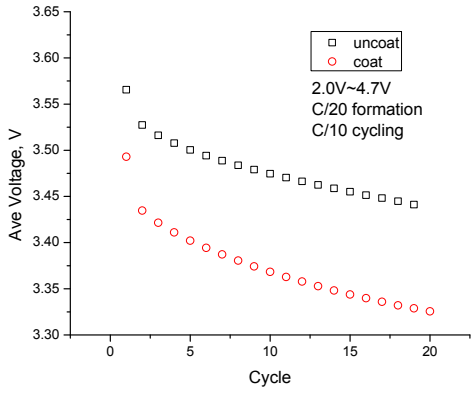

b)

Figure V - 22: a) Voltage profile and b) average voltage as a function of cycling for $Li_{1.2}Mn_{0.54}Ni_{0.13}Co_{0.13}O_2$ with and without $AlPO_4$ coating

Alumina-doped Cathode. It has been reported that addition of alumina powder to the positive electrode coating can improve cell capacity retention. To test this

claim, positive electrodes were prepared by blending 5 wt% Al_2O_3 nanosized powder with the other electrode constituents: $Li_{1.2}Mn_{0.55}Ni_{0.15}Co_{0.1}O_2$ (HE5050), SFG-6 graphite, Super P carbon and PVDF (Solvay 5130) binder. The Al_2O_3 powder had a particle size of ~50 nm and a high surface area (32–40 m^2/g). To ensure adequate dispersion, the Al_2O_3 powder was mixed into NMP at the beginning of the slurry making process.

Figure V - 23 shows cycling data and impedance spectra from full–cells containing the alumina-powder modified positive electrode and an A12 graphite negative electrode. The capacity fade after 50 cycles (~C/3 rate) is ~0.12% per cycle, significantly better than the ~0.48% per cycle for the baseline cell. The improved cell capacity retention probably results from HF- and water- scavenging by the alumina. On the other hand, the impedance rise of the alumina-powder modified cells is similar to that of baseline cells. The data suggest that cell capacity fade is largely independent of impedance rise for this cell couple.

Aqueous Binders. Due to its stronger adhesive ability and environmental friendliness, aqueous based binders have become very popular with graphite/carbon anode materials. Recently, Argonne has investigated the SBR based aqueous binders from JSR Micro for graphite electrodes. The electrochemical performance results obtained look promising.

JSR Micro is also working on an aqueous binder for cathode electrodes. Argonne used their fluorinated acrylic hybrid latex binder (FA) for a cathode using LMR-NMC (Toda HE5050). In this study, three different binder content, 1%, 2% and 4%, were used to make slurries. The carbon content in all the slurries was 5 wt.%. Lithium half cells were used as the test vehicle to investigate the binder impact on the electrochemical performance of LMR-NMC.

Figure V - 24 shows the resulting voltage profile of these Li/LMR-NMC half cells using 1 wt.% aqueous binder during three formation cycles. Compared to previous test results on HE5050 using PVDF-NMP binders, no difference was observed. The lithium half cells with 2% and 4% aqueous binders show similar results. HPPC, rate performance, and cycling tests were also conducted on the half cells. They all show comparable performance to that of cells with PVDF-NMP binders. The next step was to make a full cell that operated solely with aqueous binders.

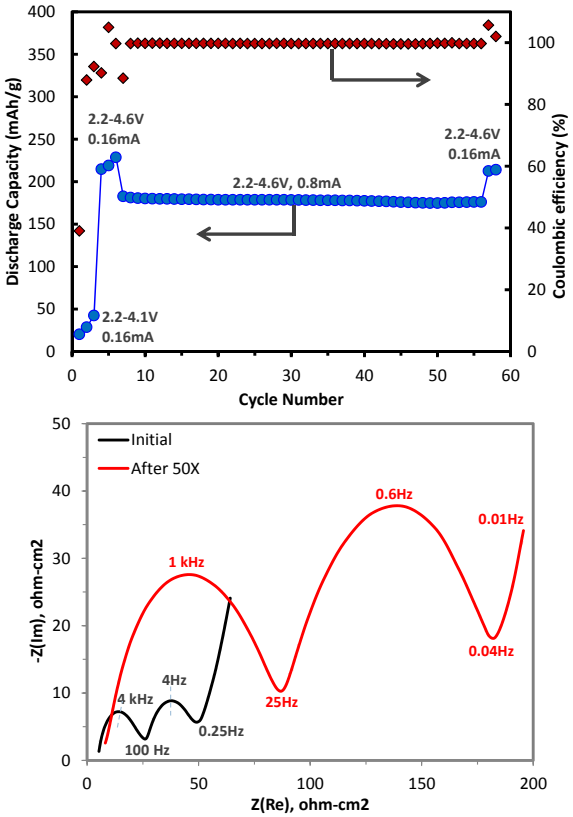

Figure V - 23: Plots for full cells containing the alumina-powder modified positive electrode showing (top) discharge capacity and columbic efficiency changes with cycle number, voltage range, and current, and (bottom) EIS data after initial cycles (black) and after fifty 2-4.6 V cycles (red)

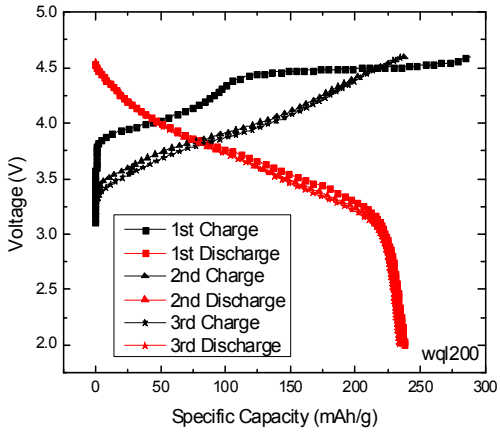

Figure V - 24: Formation cycles of LMR-NMC using aqueous binder from JSR Micro

Full cells were made and tested of graphite/HE5050 in coin cells using SBR and FA as binders, respectively. The electrode composition for the graphite anode was 98 wt.% graphite (A12, Phillips 66), 1 wt.% sodium carboxymethyl cellulose (CMC, MAC350, Nippon Paper Chemicals) and 1 wt.% SBR binder. The cathode

comprised 92 wt.% of HE5050, 5 wt.% of C-45 carbon black, 2 wt.% of CMC, and 1 wt.% of FA binder. The full cells were tested using established protocols from the Voltage Fade project: one cycle at 10 mA/g between 4.5 V and 2.0 V, followed by 20 mA/g with the same voltage window. The voltage profile is shown in Figure V - 25. There is roughly 85% capacity retention after 50 cycles, which is only slightly less than the full cell using PVDF binder. These results, combined with other favorable information from rate test and hybrid pulse power characterization tests (not shown here) highlight the possibility of designing novel battery systems with high energy, long cycle life, low cost, which are environmentally benign.

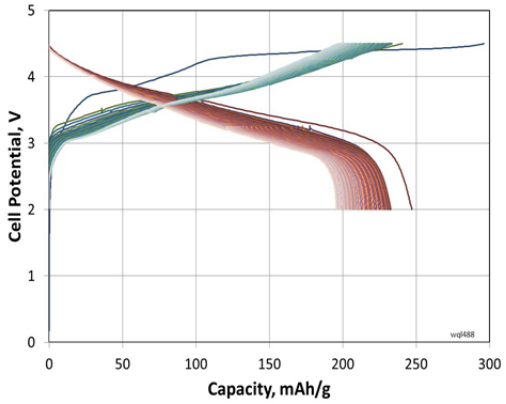

Figure V - 25: Voltage profile of graphite/LMR-NMC cell using aqueous binders from JSR Micro

Electrolyte Additives. Electrolyte additives are known to be an effective and economic approach to improving the stability of electrode surface films. In the past two decades, many organic and inorganic compounds have been identified as effective electrolyte additives: examples include vinylene carbonate (VC), ethylene sulfite (ES), vinyl ethylene carbonate (VEC), and FEC. In recent years, with the emergence of many high-voltage cathode materials, the anodic stability of common electrolytes is recognized as the main bottleneck limiting the calendar- and cycle- life of high-energy lithium-ion cells. Therefore, more attention has been devoted to improving stability of the cathode–electrolyte interface.

Ways are being examined to mitigate performance degradation of cells containing $Li_{1.2}Ni_{0.15}Mn_{0.55}Co_{0.1}O_2$-based positive electrodes that are cycled at voltages beyond 4.5 V versus Li. Studies indicate that common electrolyte additives such as VC, VEC, and FEC are not effective at enhancing long-term cycling performance of these cells, *i.e.,* stable electrode passivation is not achieved with traditional SEI-forming additives. This observation underscores the need for new electrolyte additives that effectively form stable electrode passivation films in high-energy and high-voltage lithium-ion cells.

The synergistic effects of $LiB(C_2O_4)_2$ (LiBOB), $LiF_2B(C_2O_4)$ (LiDFOB), triphenylamine (Ph_3N), and 1,4-benzodiozane-6,7-diol (BDOD) as functional electrolyte additives in cells was examined (see Figure V - 26). The influence of these additives, individually, and in different combinations, was evaluated using galvanostatic cycling of cells containing $Li_{1.2}Ni_{0.15}Mn_{0.55}Co_{0.1}O_2$-based positive electrodes, graphite–based negative electrodes, and a $LiPF_6$–based electrolyte. EIS, linear sweep voltammetry (LSV), and voltage-hold tests were also used. The data showed that cell performance can be significantly improved by choosing additives that separately affect the positive and negative electrodes, thus circumventing the difficulty of finding *one* good bifunctional additive. In addition, the synergistic effects of electrolyte additive combinations can be beneficial to cell performance.

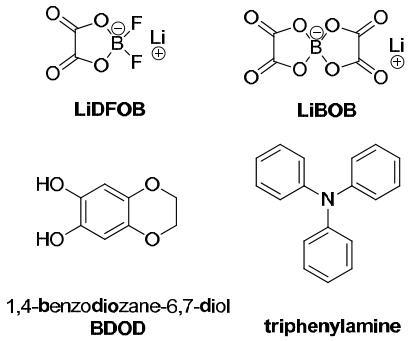

Figure V - 26: Chemical structures of additives used in this work

The following conclusions can be reached from these various tests:

1. All additive-bearing cells show certain performance improvements over cells containing the baseline electrolyte, both at 30° and 55°C.
2. Cells containing only the LiBOB additive show better capacity retention, but higher impedances, than those containing the structurally-similar LiDFOB additive.
3. The aromatic organic compounds Ph_3N and BDOD are oxidized at the positive electrode before the baseline electrolyte; these compounds are also effective at reducing electrolyte oxidation. However, when used individually, these additives do not reduce cell performance degradation on long-term cycling.
4. The addition of LiDFOB, Ph_3N, and BDOD to LiBOB-containing cells further improves capacity retention (see Figure V - 27) and lowers impedance rise on extended cycling. These additives may enhance the passivation characteristics of cathode surface films, reducing electrolyte oxidation and protecting the oxide surface.

5. The SEI films formed with additives examined in this study are not completely stable under the test conditions used. Even the best additive combination only slows down performance degradation and does not completely prevent it.

Polyfluoroalkyl (PFA) compounds are well known for their high chemical stabilities, and exhibit both hydrophobic and lipophobic behaviors. Upon dispersing in organic solvents, solvophobic PFAs tend to aggregate and form micelles in solution. These types of compounds have been extensively used as fluorosurfactants, and are especially valuable as additives in stain repellents. In light of these facts, it can be envisioned that compounds containing PFAs could serve as a new type of electrolyte additive, forming double-layered passivating layers that reduce both electrode surface degradation and electrolyte

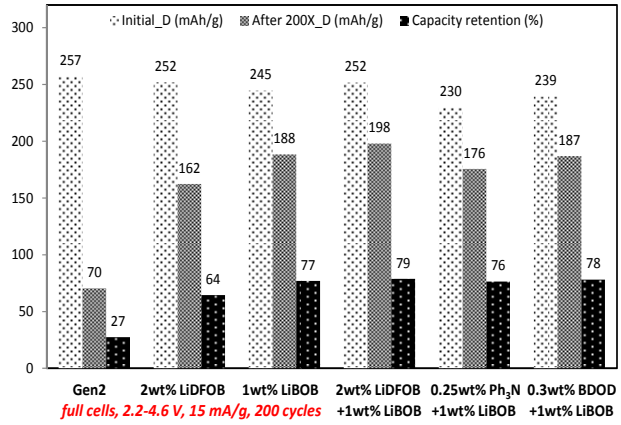

Figure V - 27: Capacity and capacity retention of full cells cycled at 30°C between 2.2 and 4.6 V at a 15 mA/g rate showing the effect of various additives in the Gen2 electrolyte. The capacity values (and cycling current) are based on the $Li_{1.2}Ni_{0.15}Mn_{0.55}Co_{0.1}O_2$ content in the positive electrode

decomposition. In our design, the PFA additive has two components: (i) a reactive headgroup for attachment onto electrode surfaces via either reductive or oxidative decomposition, so that it becomes an integral part of the surface layer (inner layer); (ii) a polyfluoroalkyl chain that self-assembles on this inner layer as a solvophobic layer (outer layer) that is highly stable and impermeable to the electrolyte solvent. To explore this novel idea, we synthesized a series of PFA-substituted ethylene carbonates (polyfluorooctyl-EC or PFO-EC) and studied them as electrolyte additives in our lithium-ion cells.

Figure V - 28 shows capacity-voltage data from $Li_{1.2}Ni_{0.15}Mn_{0.55}Co_{0.1}O_2$//graphite full cells containing the Gen2 electrolyte and Gen2+0.5wt% PFO-EC electrolyte. After 200 cycles, the discharge capacity of cells with 0.5 wt% PFO-EC is 172 mAh/g, which is 66% of its initial discharge capacity (260 mAh/g). In contrast, the discharge capacity of the baseline (Gen2 only) cells is 70 mAh/g, which is 27% of its initial discharge capacity (258 mAh/g). These data indicate that the 0.5 wt% PFO-EC additive enhances capacity retention.

The PFO-EC additive is also effective at inhibiting cell impedance rise during long-term cycling. Figure V - 29a shows that cells with 0.5 wt% PFO-EC have similar impedances as baseline cells after the initial cycling. However, after 200 cycles between 2.2 and 4.6 V (Figure V - 29b), the impedance of the PFO-EC bearing cell is much smaller than that of the Gen2 baseline cell. Previous studies have indicated that cell impedance rise in $Li_{1.2}Ni_{0.15}Mn_{0.55}Co_{0.1}O_2$//graphite full cells occurs primarily at the positive electrode. The reduced full cell impedance for the PFO-EC containing cells suggests that the additive forms effective surface films at this electrode.

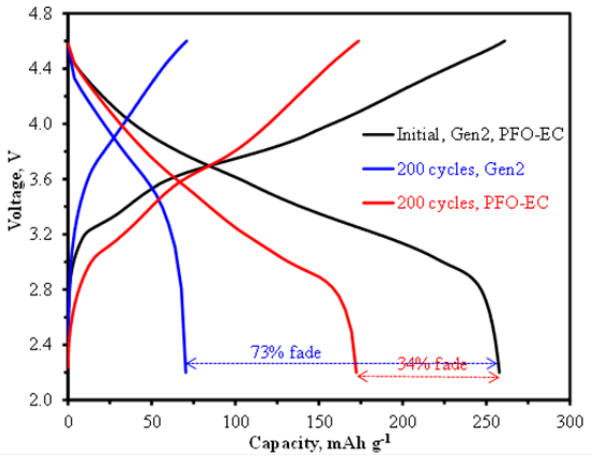

Figure V - 28: Capacity-voltage plots for full cells containing the Gen2 electrolyte and Gen2+0.5wt% PFO-EC electrolyte. The data were acquired with a 15 mA/g(oxide) current in the 2.2-4.6 V voltage window at 30˚C. The initial data are similar for cells with and without the additive

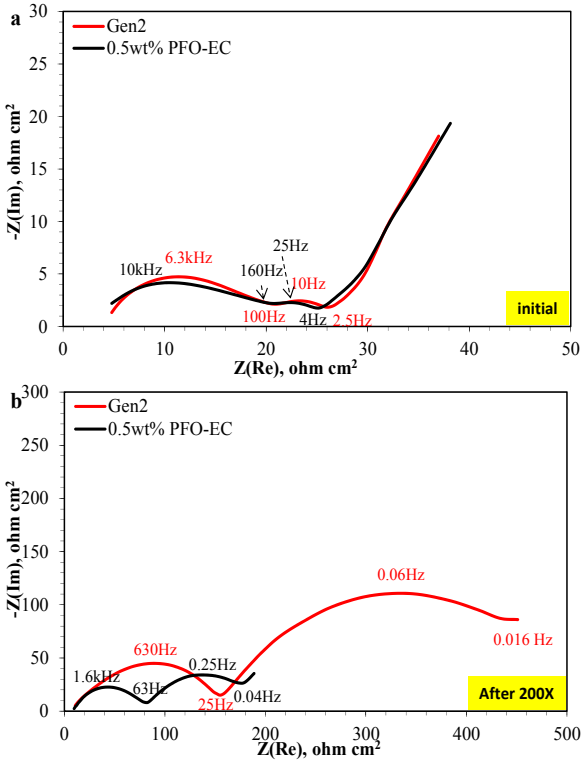

Figure V - 29: AC impedance spectra of $Li_{1.2}Ni_{0.15}Mn_{0.55}Co_{0.1}O_2$/ /graphite full cell after (a) formation cycles, (b) 200 cycles at 30°C with and without 0.5 wt% PFO-EC

Prototype Fabrication.

MERF Cathodes. The MERF has supplied the CAMP Facility with two separate batches of the $Li_{1.25}Ni_{0.3}Mn_{0.62}O_2$ cathode (LMR-NMC) material made via the carbonate process. This is a high-energy material that is of particular interest because it is cobalt free. The first batch (Lot# 2012-02-22) had a particle size distribution at D50 of 15µm, with a tap density of 1.36 g/cc (Figure V - 30). The second batch (Lot# 2012-07-09&11) has a particle size distribution at D50 of 7.8µm, with a tap density of 1.49 g/cc (Figure V - 31). The SEM images show the improved particle morphology from Lot# 2012-02-22 to Lot# 2012-07-09&11. The latter also has both a lower particle size distribution at D50 and higher tap density.

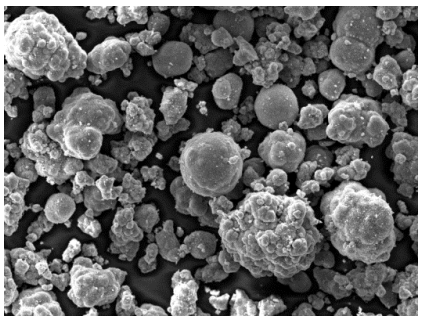

Figure V - 30: SEM images of MERF $Li_{1.25}Ni_{0.3}Mn_{0.62}O_2$ (Lot# 2012-02-22) powder at 1000x. SEM from Argonne's Post Test Facility

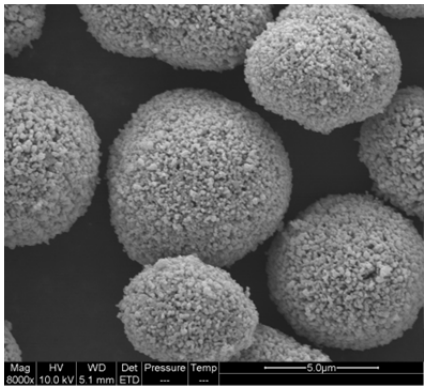

Figure V - 31: SEM images of MERF $Li_{1.25}Ni_{0.3}Mn_{0.62}O_2$ (Lot# 2012-07-09&11) powder. SEM from Argonne's Post Test Facility

Each cathode powder was used to fabricate electrodes for individual pouch cells builds. The Lot# 2012-02-22 was given the build name (CFF-B8), and the Lot# 2012-07-09&11 was given the build name (CFF-B13). Both cathode electrodes were fabricated using 90 wt.% LMR-NMC, 5 wt.% Timcal C-45 carbon black, and 5 wt.% Solvay 5130 PVDF. Both anode electrodes were fabricated using 91.8 wt.% Phillips 66 A12 graphite, 2 wt.% Timcal C-45 carbon black, 6 wt.% Kureha KF-9300 PVDF, and 0.17 wt.% oxalic acid. The coated and calendered cathode SEM images may be found in Figure V - 32 (CFF-B8) and Figure V - 33 (CFF-B13). Both cathode electrodes experienced particle fracturing during the calendering process, as seen in the SEM images, but the CFF-B13 cathode had less particle fracturing than CFF-B8.

a)
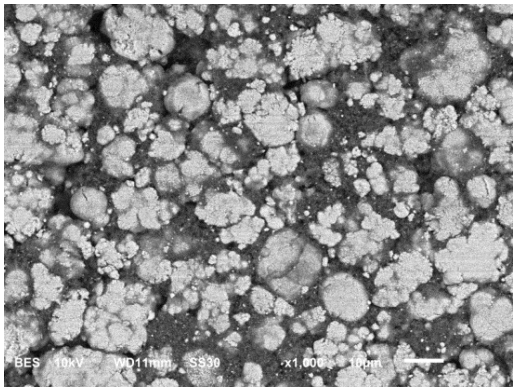

b)
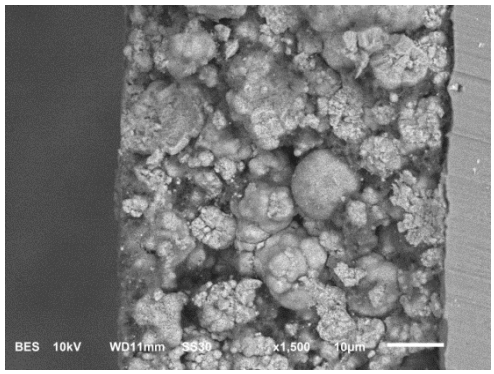

Figure V - 32: SEM images of CFF-B8 for a) Surface and b) Cross section. SEM from Argonne's Post Test Facility

a)
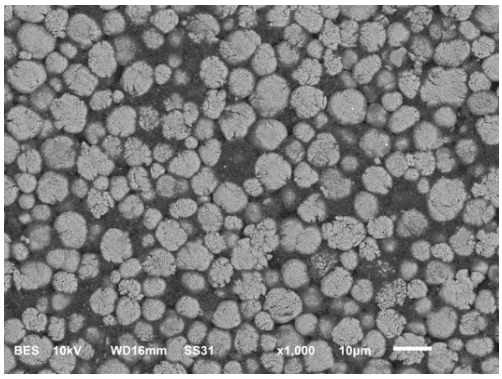

b)
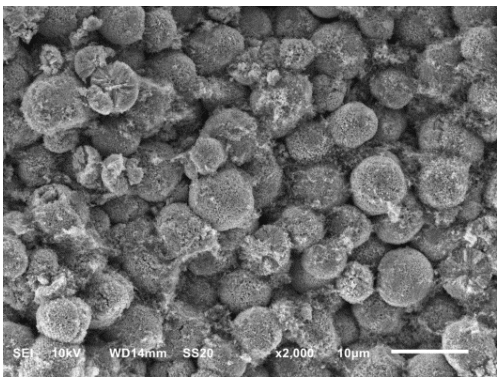

Figure V - 33: SEM images of CFF-B13 for a) surface and b) cross section. SEM from Argonne's Post Test Facility

The rate testing results of the CFF-B8 and CFF-B13 are shown in Figure V - 34a and Figure V - 34b, respectively. CFF-B13's rate performance surpassed that of CFF-B8's. The improved performance is likely due to the minimized particle cracking and fracturing during the calendering process, more uniform particle morphology, and lower particle size distribution. The CFF-B13 performance at lower rates (C/5) is reasonable, but the higher rates quickly degrade as can be observed in the data spread of the 8 cells plotted.

a)
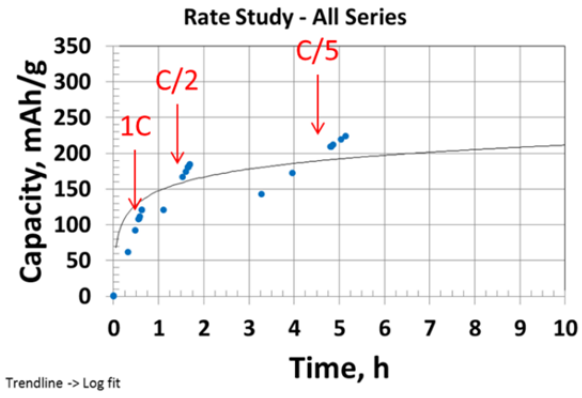

b)
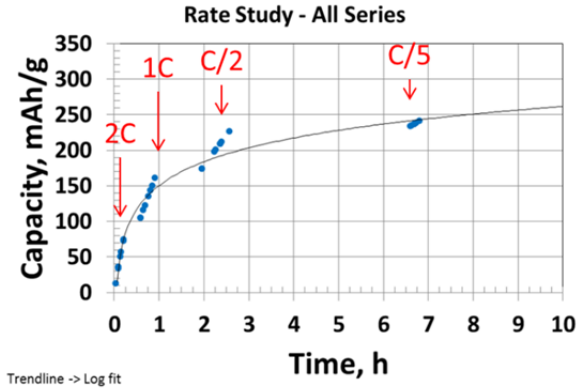

Figure V - 34: a) Rate performance results of 8 identical CFF-B8 cells. b) Rate performance results of 8 identical CFF-B13 cells. Note: testing was performed at 30°C using 1.2 M $LiPF_6$ in EC:EMC (3:7 by wt.). Trend line in both plots is the average log fit for the 8 cell data series

Similar trends were seen during the cycle life testing of CFF-B13 in Figure V - 35, where the cathode electrode is able to transfer charge at lower rates, but significant loss of charge transfer occurs during the C/2 rates. The pouch cell electrochemical results show improved performance of the MERF LMR-NMC Lot# 2012-07-09&11 over the MERF LMR-NMC Lot# 2012-02-22. These results coincide with the SEM and raw powder specification improvements in terms of particle size, morphology, and tap density. Continued efforts by the CAMP Facility will be performed to evaluate future

MERF cathode materials using pouch cells. These include LMR-NMC powders made via the carbonate and hydroxide processes.

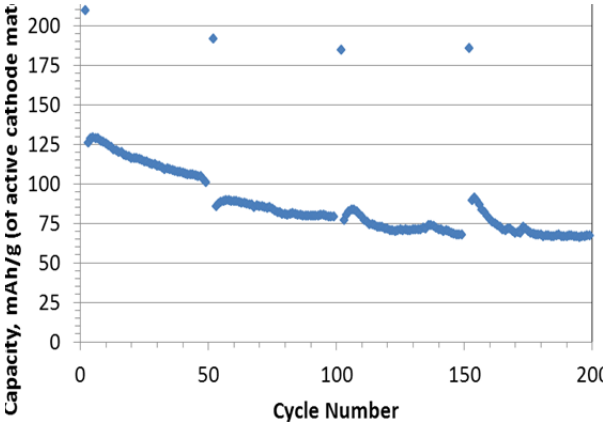

Figure V - 35: Cycle life plot of a CFF-B13 pouch cell with ~400 mAh C/1 capacity and 169 cm² cathode area, at 30°C, and C/2 rate. C/24 rate (data points included in plot) and HPPC (data points not reported in plot) performed every 50 cycles. 4.4 V to 2.5 V voltage window used

In an effort to understand and improve the performance of the MERF-made LMR-NMC ($Li_{1.25}Ni_{0.3}Mn_{0.62}O_2$) material, particle optimization and electrode composition was examined. Previous studies of the MERF-made LMR-NMC powder had shown that particle cracking occurred during the calendering process. The particle cracking has been hypothesized to be a significant factor in the poor performance at high current rates due to the particles having less of an electronic network because the particle fragments had been dislodged and isolated from the network. To troubleshoot the problem, staff at MERF milled the original LMR-NMC powder using the method of ball milling for 72 hours then dried the LMR-NMC material at 95°C for 48 hours. The dried material was then pulverized using a small-scale pulverizer for 3 minutes. The idea was to "pre-crack" the weaker particles before the calendering process to allow the binder and carbon black to coat the newly created particle during the slurry preparation for a thorough covering.

Electrodes were fabricated using both the original (un-milled) LMR-NMC powder and the milled LMR-NMC powder with 84/8/8 composition and 90/5/5 (LMR-NMC/Timcal C45/Solvay PVDF) composition. The results indicated that the milling of the LMR-NMC powder was detrimental to the overall electrochemical performance of the coin cell half-cells, especially at higher discharge rates in the rate study (Figure V - 36).

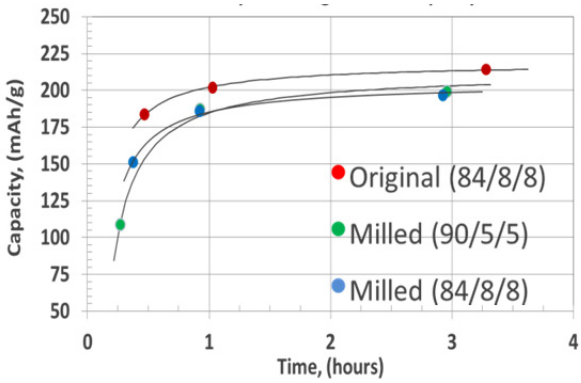

Figure V - 36: Discharge capacities for original (un-milled) and milled LMR-NMC powder from MERF versus lithium as a function of discharge time in 2032 coin cells. Voltage window (2.0 - 4.6 V), charged and discharged at C/3 (11 mA/mg), 1C (33 mA/mg), and 2C (66 mA/mg) rates; 5 cycles at each rate. All electrodes were calendered to ~35% porosity

Electrolyte Additives. Efforts by the CAMP team have shown improved capacity retention over time and cycles using LiDFOB and/or LiBOB additives in the standard 1.2 M $LiPF_6$ in EC:EMC 3:7 by wt (Gen2) in coin cells using graphite/LMR-NMC cells. (The additive validations for LiDFOB and another additive, HFiP, from MERF had been completed previously.) Based on these promising results, two combinations of the additives were chosen to be tested in the xx3450 pouch cell configuration, namely: 1) Gen2 + 2 wt.% LiDFOB and 2) Gen2 + 2 wt.% LiDFOB + 1 wt.% LiBOB. The electrode couple used for the pouch cell testing was Toda HE5050 ($Li_{1.2}Ni_{0.15}Mn_{0.55}Co_{0.1}O_2$) and A12 Graphite from Phillips 66.

The nomenclature shown in Table V - 3 depicts the Build 9 (Toda HE5050 vs. A12) electrode couple with varying suffixes (i.e., "A," "B," "C") for the electrolyte variables. 8 pouch cells were constructed and tested for B9A, 4 for B9B, and 4 for B9C.

Table V - 3: Pouch cell builds for electrolyte additive study using Gen2 electrolyte—1.2 M $LiPF_6$ in EC:EMC (3:7 by wt)

Build ID	Electrode Couple	Electrolyte
CFF-B9A	HE-5050 vs. A12	Gen2
CFF-B9B	HE-5050 vs. A12	Gen2 + 2wt.% LiDFOB
CFF-B9C	HE-5050 vs. A12	Gen2 + 2wt.% LiDFOB + 1wt.% LiBOB

The electrolyte additives were prepared for the B9B and B9C pouch cells on the same day the cells were filled with electrolyte and started formation procedure. Due to the nature of the pouch cell design and increased electrode area to electrolyte volume, the evacuated and sealed cells underwent a 24 h soak in the electrolyte to encourage wetting of the separator and electrodes. Immediately prior to the 24 h soak, a 5 minute C/10 tap

charge was performed on each cell to drive the anode potential down to mitigate corrosion of the anode copper foil. Following the 24 hour soak, formation cycling of the cells began (2.5 V to 4.1 V at C/10, then 4.55 V at C/10, then 4.5 V at C/3). There were slight differences seen in the voltage profile formation data when comparing the "Gen2 only" cells to the additive cells (Figure V - 37). It appears that the additives are being partially activated during the tap charge, and then fully activated during the first charge to 4.1 V (after the 24 hour hold).

Following the formation procedure, the cells were taken to the dry-room, cut open, evacuated, and resealed to remove any generated gas from formation (standard for typical pouch cell testing protocol). Cycling was then continued to determine the rate capability for each set of cells, which is shown in Figure V - 38.

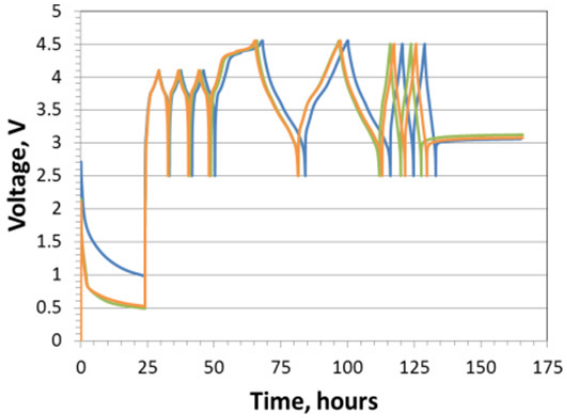

Figure V - 37: Formation profile used for B9A, B9B, and B9C consisting of sequential cycling with voltage window of 2.5 V to 4.1 V at C/10, then 4.55 V at C/10, then 4.5 V at C/3, performed at 30°C

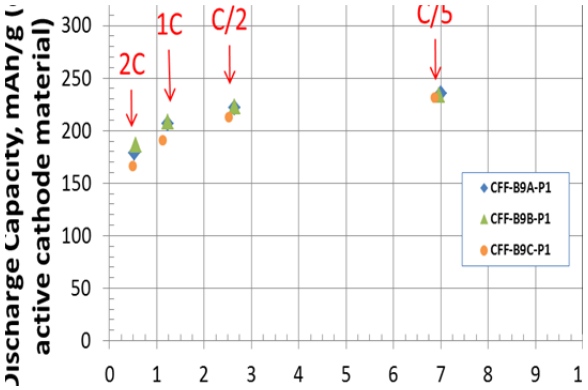

Figure V - 38: Rate Study of B9A, B9B, and B9C. Testing performed at 30°C. Voltage widow of 2.5 V to 4.5 V. Nominal rates of C/5, C/2, 1C and 2C at 3 cycles each were used. The 3rd cycle for each rate is plotted above

Cell builds B9A, B9B, and B9C all resulted in similar rate performance when compared with each other. The ~240 mAh/g for the C/7 rate and ~165 mAh/g for the 2C rate matched well to the coin half-cell data from the earlier materials validation results for HE5050 in Gen2 electrolyte. Following the rate study, HPPC testing was performed on these cell builds. The resulting ASI plots for both discharge and charge pulses are shown in Figure V - 39.

Similar to the rate study results, the initial HPPC results between the three cell builds show strong similarities to one another. Overall, a slight improvement in the discharge and charge ASI can be seen for the cell builds with additives. The coin cell studies also showed improvements in the impedance with the use of the LiDFOB/LiBOB additives.

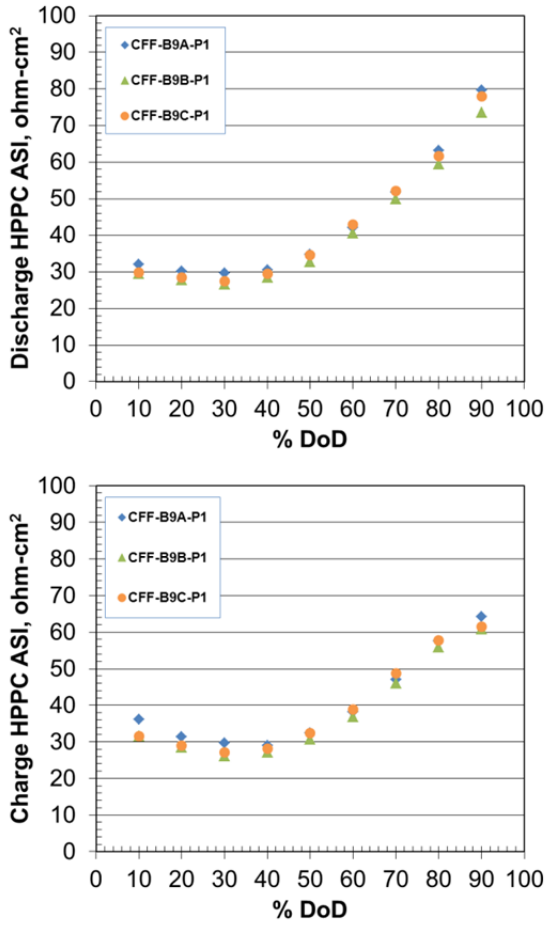

Figure V - 39: HPPC data for B9A, B9B, and B9C pouch cells. Testing performed at 30°C. Voltage window of 2.5 V to 4.4 V with 5C discharge pulse with 3.75 charge pulse at 10 s each

Cycle life testing began after the HPPC testing. General trends can be observed in Figure V - 40. Noticeable differences in cycle life performance are seen between B9A, B9B, and B9C. B9B shows a significant increase of capacity fade when compared to B9A. Whereas, B9C has similar capacity fade to B9A, but lower overall capacity in the cell. The initial cycle

capacities of B9B and B9C are also lower than B9A. It would be expected that all three builds would have the same starting capacity because they have all experienced the same testing conditions, but this was not the case here.

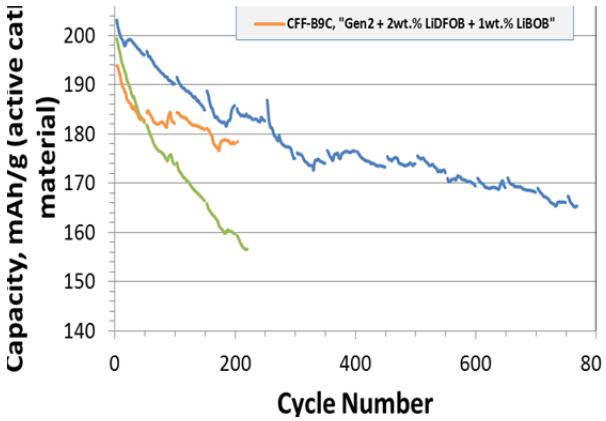

Figure V - 40: Cycle life study of B9A, B9B, B9C cell builds. Plot does not include cycle data from formation, rate study, or HPPC testing. All testing was performed at 30°C. Voltage window of 2.5 V to 4.4 V. Cells cycled at C/2 rate, with interruptions every 50 cycles for RPT/HPPC tests (data not shown in plot above)

In summary, the expected cycle life capacity retention improvements of the additives to the Gen2 electrolyte were not observed in the pouch cells as they were seen in the coin cell results. In these pouch cells, the additives actually poisoned the cells. There are several fundamental differences in cell design formats between coin cells and the larger pouch cells that could be the source of this discrepancy. First, the coin cell format is generally flooded with electrolyte which creates a high electrolyte to electrode area ratio. In a pouch cell format the design limits the amount of electrolyte that can be added. This lower ratio in the pouch cell format also correlates with there being less additive (mole basis) per area of electrode than there is in the coin cell format. The second factor is that in a coin cell, due to the larger electrolyte to electrode area ratio and the lower electrode thickness, the cells do not usually undergo a special formation procedure to ensure that the electrode has been wetted fully. Whereas, the larger format cells have thicker electrode coatings and multiple electrodes that are stacked, which take longer to wet fully.

The general procedure used in pouch cells to encourage proper wetting is to first perform a quick tap charge for five minutes to minimize copper corrosion, and then let the cell rest for 24 hours. This difference in cell formation could have significant implications for these additives and thus, were studied further.

The LiDFOB & LiBOB additives are bifunctional, in that they react on both the cathode and anode. In order to achieve improved cell performance, the additive should ideally form passivation layers that minimize cathode reactions with the electrolyte. The dQ/dV plots show that the additives (LiBOB & LiDFOB) are mainly consumed on the anode during both the tap charge and the 1st cycle charge of the formation procedure. The peak at ~1.8 to 2.0 V is due to the LiBOB additive reduction, and the peak at ~2.0 to 2.4 V is due to the LiDFOB additive reduction at the anode based on results found previously in diagnostic studies. Because of these reduction processes, there may be insufficient additive leftover to form effective passivation layers at the cathode later when the cell voltage is increased.

It is clear from the data shown in Figure V - 41 that the pouch cell formation protocol must be modified when using these additives. Suggested modifications include the following: (i) using elevated temperatures after the electrolyte fill to encourage electrode wetting; (ii) limiting the tap charge to less than 1.5 V before the 24-h hold; (iii) applying a higher C rate (greater than C/10) to pass through the 1.8 V to 2.4 V window more quickly to minimize consumption of additives on the anode; (iv) using a higher additive concentration (3-4 wt.%, instead of 1-2 wt.%) in the Gen2 electrolyte. These modifications and other formation cycling protocols are now being explored.

Initial tests are underway using the A12/HE5050 electrode couple in coin cells that are formed using the pouch cell formation process. A baseline set of data is being established that accounts for the effect of different electrode size configurations (matched 9/16" anode and cathode, or 14 mm cathode and 9/16" (14.3 mm) anode), as well as the ratio of electrolyte/additive to electrode area. Once it is established that the pouch cell conditions and performance can be replicated in coin cells, studies will begin with the targeted additives incorporated in the coin cell electrolyte. The formation process will then be adjusted to maximize the performance of the coin cells in a manner that will be later deployable in a pouch cell environment. After the formation and additive content is optimized, the process will be confirmed in a pouch cell build.

Aqueous Binders. Many of the silicon/graphite/binder systems that are being explored are aqueous based slurries. Initial coating trials of these systems were first performed using the standard bench top small scale coater. Several of the slurries and corresponding coatings that showed good adhesion, cohesion, and homogeneity were scaled up using the A-Pro coater in the dry room.

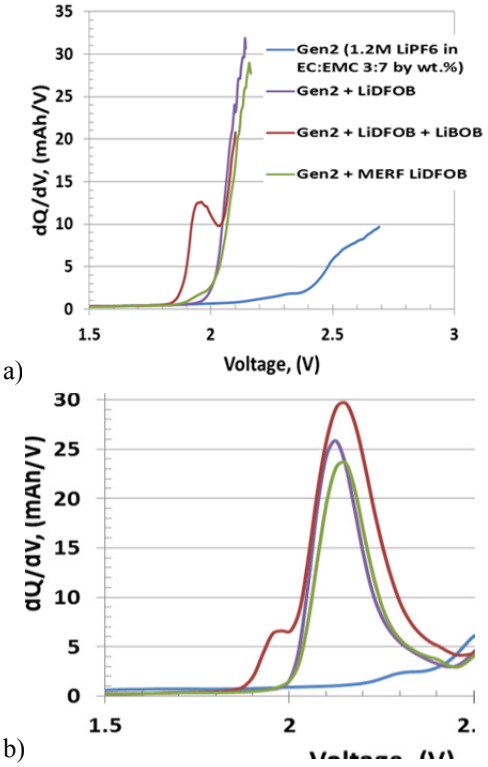

Figure V - 41: Pouch cell data of the initial 5 minute C/10 tap charge (a) and the subsequent C/10 charge of the 1st cycle dQ/dV that occurs after the 24 hour rest step (b) using various additives. (All data above is from CFF-B9 "HE-5050 vs. A12," except for the series "Gen2 + MERF LiDFOB" which is CFF-B12 "NHE5050 vs. A12." "Gen2" electrolyte is 1.2 M $LiPF_6$ in EC:EMC 3:7 by wt.%. "Gen2 + LiDFOB" is Gen2 + 2 wt.% LiDFOB. "Gen2 + LiDFOB + LiBOB" is Gen2 + 2 wt.% LiDFOB + 1wt.% LiBOB. "Gen2 + MERF LiDFOB" is Gen2 + 2 wt.% MERF-made LiDFOB)

There has been initial success in coating Phillips 66 A12 graphite in an aqueous-based binder slurry using the A-Pro coater. The aqueous system coated had the following components: 96 wt.% Phillips 66 A12 graphite, 2 wt.% Timcal C-45 carbon black, 1 wt.% CMC (MAC 350), and 1 wt.% SBR (Zeon X-3). A comparison of the aqueous CMC/SBR A12 electrode coin cell half-cell performance versus a PVDF/NMP-based A12 electrode (A-A002 from the CFF Electrode Library) coin cell half-cell performance is provided in Table V - 4. The CMC/SBR anode had a total coating loading of 4.6 mg/cm^2, coating thickness of 45 µm, and a porosity of 35.0%. The PVDF Electrode Library anode had a total coating loading of 6.0 mg/cm^2, coating thickness of 53 µm, and a porosity of 38.8%.

The data in Table V - 4 demonstrate the improved performance of the A12 graphite (no Si or SiO_x) when using the CMC-SBR aqueous binder system. In addition, a higher capacity was achieved with less total active material present in the CMC-SBR aqueous electrode compared to the PVDF/NMP electrode. As expected, the corresponding voltage plateaus were relatively unchanged. The results of using CMC/SBR for aqueous slurry making, its initial application in the dry room using the A-Pro coater, the homogeneous coating quality, and the good initial electrochemical performance are all a positive step forward. This newly gained information will greatly aid in incorporating Si/SiO_x powders in aqueous slurry systems for coating and ultimately be implemented into pouch cell fabrication.

Table V - 4: Electrochemical performance of CMC/SBR aqueous-based graphite anode compared to PVDF/NMP-based graphite anode in initial characterization cycling tests. Electrodes were made on large A-Pro coater in dry room

CMC/SBR A12 Graphite Electrode		PVDF A12 Graphite Electrode	
Formation		Formation	
1st Cycle Lithiation Capacity	363 mAh/g of A12	1st Cycle Lithiation Capacity	345 mAh/g of A12
1st Cycle Delithiation Capacity	342 mAh/g of A12	1st Cycle Delithiation Capacity	339 mAh/g of A12
1st Cycle Efficiency	94%*	1st Cycle Efficiency	97%
Rate Study		Rate Study	
C/5	358 mAh/g	C/5	330 mAh/g
C/2	355 mAh/g	C/2	326 mAh/g
1C	348 mAh/g	1C	318 mAh/g
2C	330 mAh/g	2C	310 mAh/g
HPPC		HPPC	
ASI at 50% DOD	47	ASI at 50% DOD	49

* A possible wetting issue may be present

Analysis.

Data Handling. Each pouch cell build has consisted of multiple cells, for each variable tested, to provide statistically relevant data. Providing the statistics of multiple cells being tested under the same variables is important. The data is simple to collect, but data processing can quickly become complex and time consuming. Effort has gone into utilizing Excel software to improve the data processing procedure. Excel macros and templates have been created in order to rapidly perform a significant number of consistently accurate automatic calculations for any size cell (i.e., coin cell, pouch cell, 18650, etc.), averaging of multiple data sets with sample standard deviation error bars, and creation of standard tables and plots for simplified data comparison. An Excel macro/template has been created for each of the main characterization tests used by the CAMP Facility, including: formation, rate study, HPPC, and cycle life testing. All the Excel macros/templates are accompanied with detailed instructions.

The formation macro/template automatically plots the voltage profiles, capacity curves, and dQ/dV plots for up to 8 cells, along with a table of the first cycle efficiency and reversible capacity values (Table V - 5). Both the individual cells and average processed data are available in the output.

Table V - 5: Capacity and efficiency values automatically calculated for formation testing (data provided from 8 pouch cells; CFF-B9A, "HE5050 LMR-NMC vs. A12 Graphite")

	Cell #									
mAh/g	1	2	3	4	5	6	7	8	Average	Standard Deviation
1st C cap (mAh/g)	299	298	297	297	297	303	294	297	298	2.5
1st D Cap (mAh/g)	268	267	266	266	267	265	263	267	266	1.4
1st Cycle Eff (%)	90	90	90	89	90	87	90	90	89	0.8
Reversible C Cap (mAh/g)	268	267	268	267	268	273	264	268	268	2.1
Reversible D Cap (mAh/g)	266	265	266	266	266	267	262	266	265	1.2
Irreversible Cap Loss (mAh/g)	33	32	31	31	32	36	31	31	32	1.7
Irreversible Cap Loss (%)	11	11	10	10	11	12	11	11	11	0.5

The rate study is an initial characterization test to determine a cell's rate capability. The rate study macro/template automatically plots the voltage profiles, capacity vs. current, capacity vs. cycle number, averaging plots with trend lines for reasonable forecasting, a table of C-rates based on trend lines, and tables of capacities each cell obtained for each cycle. The macro can process (and average) up to 12 cells at one time. Both the individual cells and average processed data are available in the output. (Table V - 6 and Figure V - 42).

Table V - 6: Expected discharge C-rates determined by the averaging of all the data with corresponding capacity values based on the rate study test results (data provided from 8 pouch cells; CFF-B9A, "HE5050 LMR-NMC vs. A12 Graphite")

C-rate	mAh	mAh/g	mAh/cm²
2C	409	196	2.42
1C	436	209	2.58
C/2	463	222	2.74
C/5	498	239	2.95
C/10	525	252	3.11

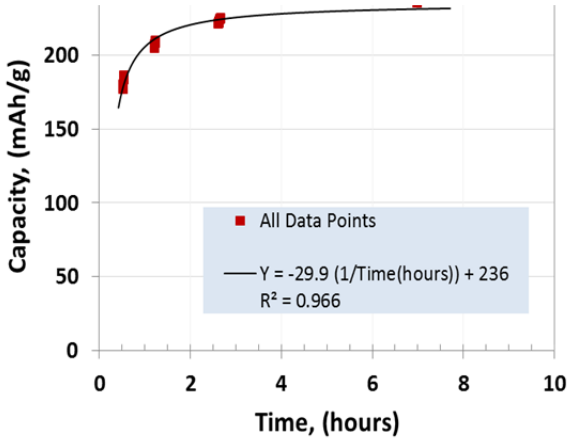

Figure V - 42: Typical discharge capacity plot of data from multiple cells showing an averaged trend line generated to predict an expected C-rate from the rate study test results (data provided from 8 pouch cells; CFF-B9A, "HE5050 LMR-NMC vs. A12 Graphite")

The HPPC test is intended to determine dynamic power capability over the device's usable voltage range using a test profile that incorporates both discharge and regen (charge) pulses. The HPPC macro/template automatically plots the voltage profiles, area specific impedance (ASI) vs. open circuit voltage (OCV), ASI vs. DoD or as a function of pulse number, and ASI vs. time during pulse. The macro can process up to 8 cells at one time. Both the individual cells and

average processed data are available in the output tab (Figure V - 43).

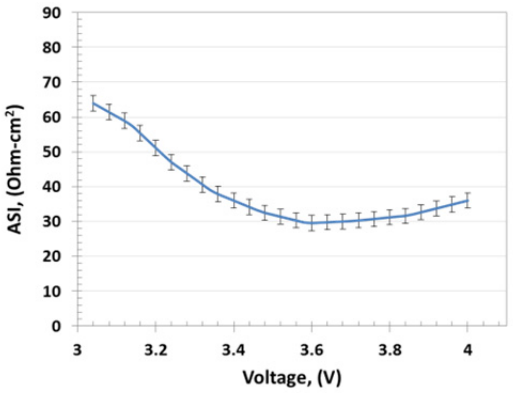

a)

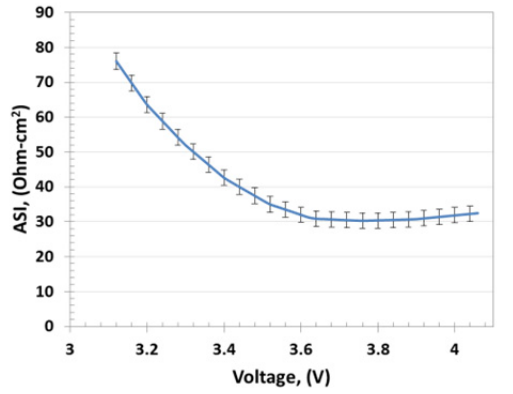

b)

Figure V - 43: Typical HPPC ASI vs. OCV plots of average data with sample standard deviation error bars from multiple cells (data provided from 8 pouch cells; CFF-B9A "HE5050 LMR-NMC vs. A12 Graphite") for a) charge and b) discharge

The cycle life test is used to accelerate the aging of cells by cycling at a C/2 capacity tests while monitoring the capacity fade and impedance rise via scheduled HPPCs and C/24 rates during cycling. The cycle life macro/template automatically creates multiple plots, including: capacity vs. cycle #, efficiency vs. cycle #, capacity retention vs. cycle #, energy and energy density vs. cycle #, energy retention vs. cycle #, ASI vs. DoD and voltage as a function of HPPC's performed throughout the cycle life, ASI vs. cycle # as a function of DoD, voltage vs. SOC as a function of cycle #, and dQ/dV vs. voltage as a function of cycle #. The macro processes only one cell at a time due to the large number of data points to be processed, and averaging of multiple cells takes place in a separate macro/template. The individual cell's processed data is available in the output tab (Figure V - 44 & Figure V - 45). The cycle life macro/template processes the data in a couple of minutes.

Diagnostic Investigations. In-depth investigations were conducted for positive electrodes that contain 86 wt% $Li_{1.2}Mn_{0.55}Ni_{0.15}Co_{0.1}O_2$ (HE5050), 4 wt.% SFG-6 graphite (Timcal), 2 wt.% Super P (Timcal) and 8 wt.% PVDF (Solvay 5130), and for negative electrodes that contain ~90 wt% graphite (Phillips 66 A12), 6 wt% PVDF (Kureha KF-9300) and 4 wt.% Super P (Timcal). In previous reports, we have shown that cell impedance rise is mainly governed by the positive electrode; impedance rise at the negative electrode is relatively small. In AC impedance data, the positive electrode impedance rise appears as an increase in the high-frequency arc width (electronic impedance) and in the mid-frequency arc width (ionic impedance).

XRD and Raman Spectroscopy results indicated structural changes in the positive electrode carbons during cell cycling. In particular, XRD data from a fresh positive electrode indicate a relatively sharp graphite (002) peak at $2\theta = 26.5°$. This peak arises from the SFG-6 graphite, present as an electron conduction additive, in the electrode coating. The peak becomes weak and broadens significantly after only a few 2–4.6V full-cell cycles; however, it does not disappear entirely and shows a small, but measurable, intensity even in electrodes harvested from cells after 300 and 1500 cycles.

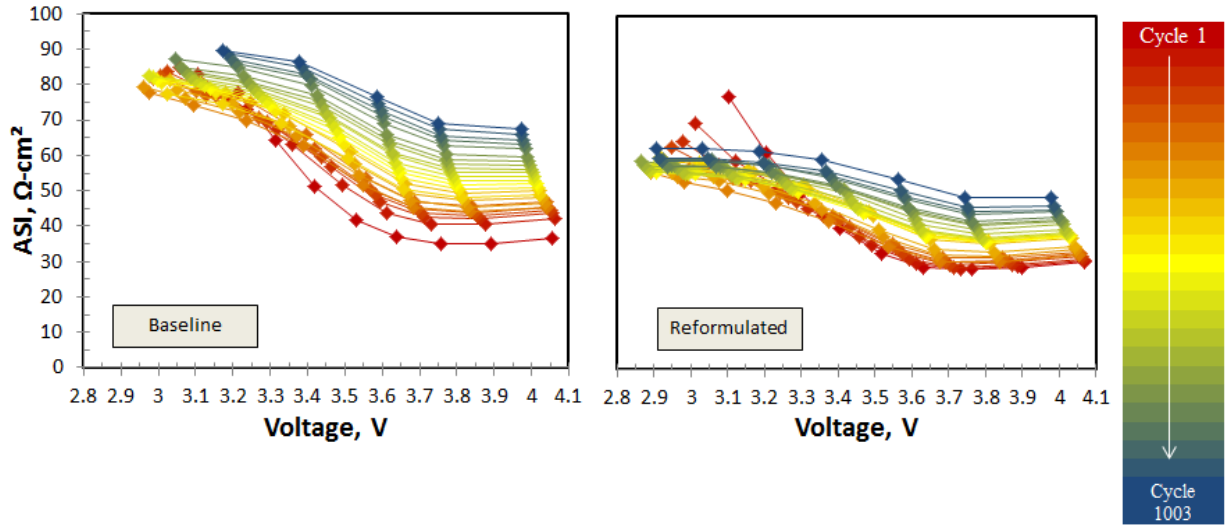

Figure V - 44: Example comparison plots exhibiting the powerful capabilities of the cycle life excel macro/template. The plots show the HPPC area specific impedance versus OCV, as a function of cycle life (color gradient) for "Baseline Cells" and "Reformulated Cells." Note that the impedance is higher at lower voltages for both sets of cells. The impedance rise for the Reformulated cells is lower than that of the Baseline cells for the entire life of the cell (data provided from 1 Baseline pouch cell; CFF-B4A, "HE5050 LMR-NMC vs. A12 Graphite" and from 1 Reformulated pouch cell; CFF-B9A, "HE5050 LMR-NMC vs. A12 Graphite")

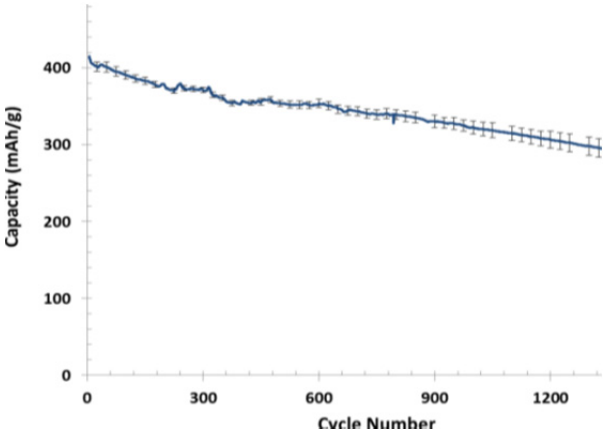

Figure V - 45: Typical discharge capacity vs. cycle number plot of average data with sample standard deviation error bars from multiple cells (data provided from 2 pouch cells; CFF-B9A, "HE5050 LMR-NMC vs. A12 Graphite")

Changes in the positive-electrode graphite behavior on cycling were also evident in data from Raman spectroscopy. Figure V - 46 shows representative Raman spectra from a fresh positive electrode and from electrodes harvested from cycled cells. The G-band observed at ~1,580 cm^{-1} corresponds to the E_{2g} vibrational mode and is commonly attributed to the in-plane stretching of all pairs of sp^2 carbon atoms in both rings and chains. The D-band observed at ~1,350 cm^{-1} and the D'-band observed at ~1,620 cm^{-1} are defect-induced Raman features. The D– to G– band intensity ratio (I_D/I_G) is commonly used to determine the extent of structure disorder in graphite.

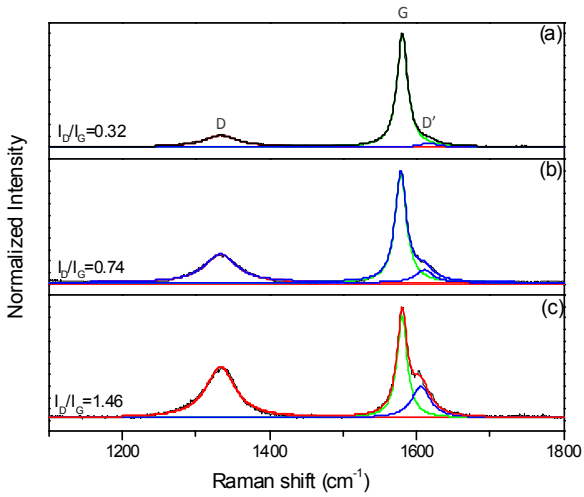

Figure V - 46: Raman spectra from (a) fresh positive electrode, (b), (c) positive electrodes harvested from cells after initial cycles, and after 1500 cycles, respectively. Band intensities are normalized to the G-band

From an analysis of Figure V - 46 the I_D/I_G ratio for the fresh electrode is 0.32. This value is higher than that expected for pure graphite because the electrode also contains Super P carbon, which is disordered and has an I_D/I_G ratio of 2.47. The I_D/I_G value increases to 0.74 for the initial–cycle sample, and to 1.46 for the 1,500–cycle sample. These data indicate that the positive electrode

carbons undergo severe structural disordering upon prolonged cycling. The structural disordering is related to the intercalation of PF_6^- anions into graphitic structures. Separate experiments have shown that significant PF_6^- intercalation into SFG-6 graphite occurs at voltages >4.45 V vs. Li. Anion intercalation into the Super P carbons also occurs, albeit in quantities that are ~2 orders of magnitude smaller than that for the graphite. These changes in the positive electrode carbons are partially responsible for the degradation of the electron conduction network that appears as the high-frequency arc in the AC impedance data. Based on the electrochemistry, diffraction, and spectroscopy data, it is recommended to not use graphite-based electron conductive additives in the preparation of LMR-NMC electrodes that are cycled at voltages >4.4 V vs. Li.

Secondary Ion Mass Spectrometry (SIMS) and Inductively Coupled Plasma–Mass Spectrometry (ICP-MS) were also performed to determine the accumulation of transition metal elements at the graphite electrode during cycling. Figure V - 47 shows SIMS sputter depth profiles for carbon, manganese, nickel, cobalt and lithium from negative electrodes harvested from cells that underwent the initial cycles (a), and the 1,500 aging cycles (b). In Figure V - 47a, the carbon signal increases for the first 200 seconds of sputtering, and then reaches a steady state value. The lower carbon signal near the surface is consistent with a SEI that contains a lower carbon concentration than the bulk electrode. In Figure V - 47b, however, the carbon signal reaches a steady state value indicative of the bulk electrode only after ~8,000 seconds of sputtering. The longer sputtering time indicates that the SEI is significantly thicker for the aged sample.

The Li signal during early sputtering mainly arises from lithium in the electrode's SEI layer near the top surface. At longer sputtering times the signal also includes contributions from lithium remnants deeper inside the electrode. Figure V - 47 shows that the Li count rate (counts per second, cps) of the aged sample is more than an order of magnitude greater than that of the sample after the initial characterization cycles. The data are consistent with lithium trapping in the negative electrode, especially in the SEI, and explain the significant deterioration of cell capacity that results from extended cycling.

In Figure V - 47a, the Mn, Ni and Co signals peak after ~50 s sputter time, then decrease relatively rapidly for Mn and more gradually for Ni and Co; the elements display quasi-steady state cps values after ~2,000 s sputter time. In Figure V - 47b also, the Mn, Ni and Co signals peak after short sputter times and then decrease. However, the cps values measured after ~2,000 s is more than an order of magnitude larger for Ni and more than two orders of magnitude larger for Mn. That is, the total Mn and Ni counts obtained by integration under the curves are significantly higher for the aged sample than for the sample after initial cycles.

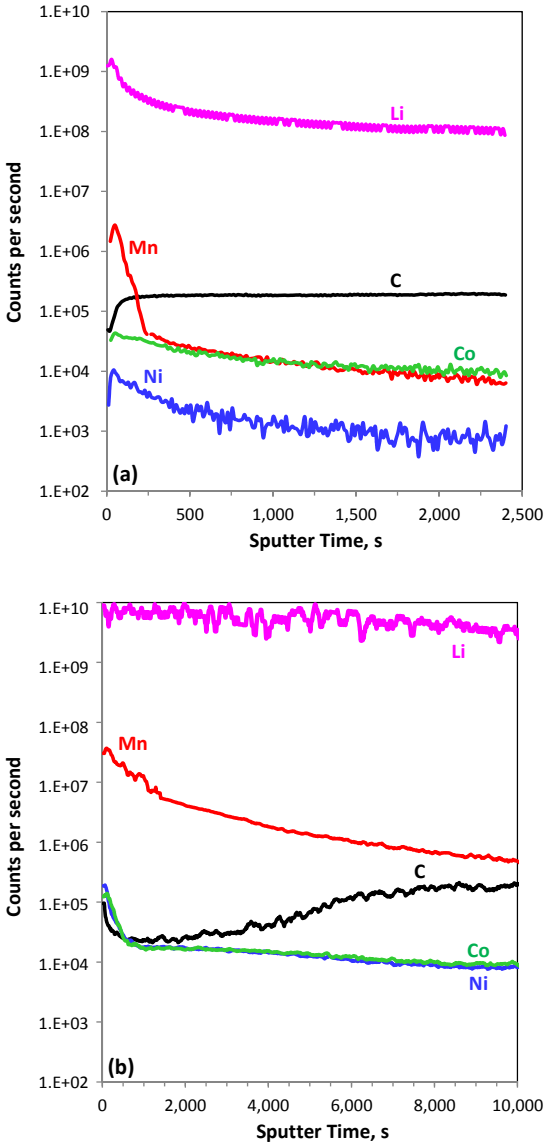

Figure V - 47: SIMS sputter depth profiles from negative electrodes after (a) Initial cycles, and (b) 1500 cycles. Data for carbon, manganese, nickel, cobalt and lithium are shown. The Y-axis scales are the same for (a) and (b), but the X-axis scales are different

The trends in the SIMS data were confirmed by ICP-MS data obtained on the negative electrode coatings, which were scraped off the current collector. The measured data are an average of the element concentrations contained in the samples, which comprises the graphite, SuperP, PVDF, electrolyte residue, and SEI components; the harvested electrodes were rinsed in DMC to minimize electrolyte residue while preserving the SEI. As expected, only trace

quantities of Li, Mn, Ni and Co data were measured in the fresh negative electrode, which serves as a control sample. For the initial–cycle sample, the average Li, Mn, Ni and Co concentrations are 9683, 617, 125 and 63 µg/g-sample, respectively, with a measurement uncertainty of ± 10%; the corresponding values for a 1500–cycle graphite electrode sample are 25936, 1446, 167 and 71 µg/g-sample, respectively. That is, the Li, Mn, Ni and Co content in the 1500–cycle graphite negative electrode are, on an average, 2.7, 2.3, 1.3 and 1.1 times greater than that in the initial–cycle electrode.

The transition metals at the negative electrode originate from the oxide in the positive electrode, and are an obvious example of metal-ion migration between the electrodes. A simple calculation shows that the Mn, Ni, and Co contents in the graphite electrode are 8.1, 0.9, and 0.4 µg/cm^2, respectively, which are several orders of magnitude smaller than the corresponding contents in the positive electrode. These data indicate that cell capacity loss arising from dissolution of these elements, from the positive electrode into the electrolyte, is negligibly small.

In order to elucidate the contribution of the negative electrode to full cell capacity loss, the cycling characteristics of cells containing $Li_{1.2}Ni_{0.15}Mn_{0.55}Co_{0.1}O_2$–based positive and $Li_4Ti_5O_{12}$–based negative electrodes (LTO) were investigated. SEI formation and Li trapping is not expected in the LTO electrodes because the material shows a flat voltage profile about 1.55V vs. Li, much higher than the voltage at which electrolyte reduction occurs (≤0.8V vs. Li/Li$^+$). These cells contained the same positive electrodes described above; the negative electrode comprised a coating of 87 wt% LTO, 5 wt% Timcal C45 carbon, and 8 wt% PVdF (Kureha 9300) binder on a 20 µm thick Al foil.

Representative data from a cell cycled in the 0.75–3.15V (2.3–4.7V for the positive vs. Li/Li$^+$) voltage window are shown in Figure V - 48. This cycling window is wider than a typical cycling window for graphite–based full cells and was selected to accelerate performance degradation. The cycling is mainly conducted at a ~C/2 rate, with periodic capacity measurements at a ~C/10 rate. It is apparent from Figure V - 48 that the cell shows negligible capacity loss even after 600 cycles. Moreover, the measured coulombic efficiency is greater than 99.9%, which also indicates negligible Li loss during cell cycling. These data confirm that capacity loss arises at the negative electrode in the graphite-based cells.

Electrochemical Modeling. The EIS electrochemical cell model was used to examine the impedance characteristics of the hysteresis between charge and discharge in LMR-NMC positive electrodes [4]. The EIS cell model was developed strictly for intercalation active materials. However, the hysteresis and other characteristics indicate that the LMR-NMC bulk material is much more complex. In contrast, the active material/electrolyte interface, commonly referred to as the solid electrolyte interphase or SEI, portion of the EIS electrochemical model should adequately capture the interfacial phenomena.

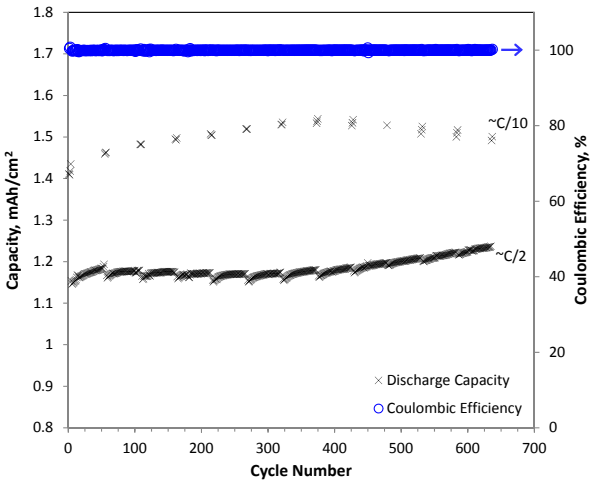

Figure V - 48: Capacity vs. cycle number plot for a full cell containing a $Li_4Ti_5O_{12}$–based negative electrode. The data were acquired at 30°C, with 0.1 mA/cm^2 (~C/10) and 0.5 mA/cm^2 (~C/2) currents, in the 0.75–3.15V cycling window; the corresponding positive electrode cycling window is ~2.3–4.7V vs. Li/Li$^+$. A 1 mAh/cm^2 full cell capacity value roughly equals 150 mAh/g-oxide in the positive electrode

The detailed theoretical description of the SEI is based on post-test analytical diagnostic studies. The SEI region is assumed to be a film on the active material. The film is taken to be an ill-defined mixture of organic and inorganic material through which Li-ions from the electrolyte must diffuse and/or migrate across to react electrochemically at the surface of the active material. The lithium is then assumed to diffuse through the surface layer and into the bulk active material in the particle. Capacitive effects are incorporated into the model at the electrochemical interfaces and a localized electronic resistance between the current carrying carbon and the oxide interface can also be included. The model can also accept multiple particle fractions with unique characteristics.

To accurately model the bulk transport characteristics of the LMR-NMC active materials the EIS electrochemical cell model will need to be modified. The bulk transport electrochemical model is being developed under the Voltage Fade effort (see Section V.C.1). Because this model development is lagging behind the EIS SEI modeling studies in this effort, work under this effort in the latter part of the year was directed towards advancing the electrochemical bulk transport model. As confidence in the bulk

transport model improves, it will be integrated into the EIS electrochemical model.

The EIS electrochemical cell model is applied here to obtain a "snapshot" of the electrode at each SOC. Diagnostic micro-reference electrode lab cell EIS studies were conducted on the baseline HE5050 LMR-NMC electrode at several states-of-charge (SOCs) during the charge and discharge half cycles. In general, over the voltage range where the EIS studies were conducted (between 3.3 and 4.0 volts vs. lithium) within the same half-cycle, either charge or discharge, impedance increases as the SOC and electrode potential decreases. The discussion here will be focused on three EIS sweeps: two taken at 3.74 and 3.36 volts (vs. lithium) during the discharge half cycle and one at 3.74 volts during the charge half cycle. Because of the hysteresis between charge and discharge, the two 3.74 volt sweeps are taken at the same electrode potential, but differing SOCs. While the 3.36 volt discharge sweep and 3.74 volt charge sweep are taken at about the same SOC (i.e., same lithium content).

The EIS data and electrochemical model fit for the LMR-NMC electrode at 3.74 volts is shown in Figure V - 49. The interfacial impedance for a lithium ion positive electrode typically consists of two circular arcs (i.e., a high-frequency arc and a mid-frequency arc) with a diffusional Warburg impedance tail at low frequencies.

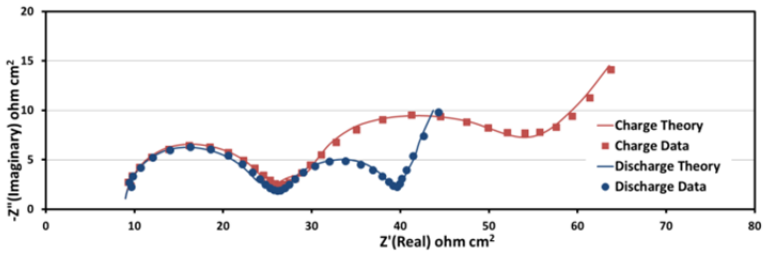

Figure V - 49: LMR-NMC electrode impedance (100kHz-10mHz) at 3.74 volts vs. lithium taken during the charge and discharge half cycles with a micro-reference electrode cell

The initial EIS electrochemical modeling studies on the LMR-NMC electrodes are discussed in the FY2012 annual report. The work focused on comparing the LMR-NMC electrode to earlier studies on other layered cathode materials and examining possible sources of aging effects. It highlighted the susceptibility of LMR-NMC cathodes to increases in the high frequency impedance owing to the lower overall bulk conductivity of the materials. This manifests in a high contact resistance between the particles and the conductive carbon additives that worsens with continued exposure to high potentials (i.e., electrolyte oxidation). Also included in the high frequency impedance arc are ion migration effects through the surface film on the active material. The lithium ion diffusion effects through the surface film can impact either or both the high and mid frequency arcs. These effects are generally less sensitive to SOC. The studies here focus on the changes in the mid-frequency arc and Warburg impedance. The mid frequency arc includes impedance effects from the electrochemical reaction (i.e., Butler Volmer kinetics) and lithium diffusion through active material surface layer. The Warburg impedance is dominated by solid-state diffusion in the oxide particles, but also includes electrolyte salt diffusion. Of all the parameters extracted from the EIS data, changes in the lithium diffusion coefficient (D_{sb}) of the bulk active material are most precisely followed. A general discussion of how the relative time constants for the various phenomena are determined was also discussed in the FY2012 annual report. The size of the impedance for the Butler Volmer kinetics is determined by the exchange current density (i_o). The impact of lithium diffusion through the surface layer is governed by its diffusion coefficient (D_{si}) and the partition coefficient (K_s) for lithium between the bulk material and the surface layer. These parameters are given in Table V - 7 for the indicated electrode potential and half-cycle.

Table V - 7: Selected electrochemical model parameters for LMR-NMC electrode at indicated electrode potential and half-cycle

Positive voltage vs. Li	Half-Cycle	D_{si}	D_{sb}	K_s	i_o
Volts		cm^2/s			mA/cm^2
3.36	Discharge	5.5E-13	2.0E-14	33.0	0.0055
3.74	Charge	6.0E-13	8.5E-14	10.0	0.015
3.74	Discharge	1.4E-12	1.7E-12	10.0	0.035

In general, as one goes down the columns in Table V - 7 the parameters change in the direction of lowering the electrode impedance. Therefore, for the constant SOC data (i.e., first and second lines) the discharge impedance is greater than the charge impedance and the opposite is true for the constant voltage data (i.e., second and third lines), as seen in Figure V - 49. How much of a trend this is over the full voltage range is yet to be determined. In Table V - 7 at an electrode potential of 3.74 volts, both i_o and D_{si} vary by about a factor of

two between the charge and discharge half-cycles. Since it is implicitly assumed that both phenomena contribute about equally to the impedance, the changes account for the doubling of the size of the mid-frequency interfacial arc, as seen in Figure V - 49. Less obvious from examining Figure V - 49 is the change in the bulk lithium diffusion coefficient (D_{sb}) of the active material by about a factor of twenty, suggesting that the bulk material is significantly different between the charge and discharge half-cycles. An even greater change in the discharge D_{sb} is observed between 3.74 and 3.36 volts. While more studies over a wider voltage range need to be conducted, it is clear that both the interface and bulk LMR-NMC material is changing significantly within and between each half-cycle.

Additional activities this year include modifying the open circuit voltage expressions for phase change active materials (i.e., in this case the graphite negative) in the DC electrochemical cell model. This corrects a nagging issue with the model that tended to occasionally drive one of the local lithium active material concentrations negative at high discharge rates. This model has been used extensively to examine performance changes with electrode thickness. Further electrode thickness studies are planned in support of the prototype cell fabrication effort and BatPaC development.

Conclusions and Future Directions

Significant effort this year was devoted to developing a silicon-based anode that could be used in future prototype cell builds and in the Electrode Library. Three sources for commercially available silicon powder were identified that could be used freely, without restrictions on data or material distribution. Traditional binders, which work well for graphite, do not function as well for silicon.

The value of the CAMP Facility was well demonstrated this year, particularly in the study of electrolyte additives. Ideas that work well in simple coin cell studies, may not always work in full size cell systems. Validation and studies using prototype cells can save valuable resources later on.

In FY14, efforts will continue on the analysis, modeling, and prototype cell fabrication of advanced electrochemical energy storage systems with an emphasis on high energy anode and cathode materials. The main goal will be to fabricate pouch cells using a silicon-based anode coupled with a high energy LMR-NMC cathode that is produced by the MERF at ANL.

Additional activities will be pursued to understand the mechanisms taking place in high energy cell systems. These include: determining the negative to positive (n:p) ratio effect on performance; role of the separator material; effect of formation process for prototype cells that use bifunctional electrolyte additives; and effect of electrode thickness.

Failure mechanisms of new energy storage chemistries will be determined, and remedies proposed, using diagnostic techniques within the CAMP Facility coupled with the support of the Post-Test Facility at Argonne.

The battery design modeling effort will continue to support the CAMP facility effort, but funding and reporting will be shifted to the core BatPaC studies. The development of advanced electrochemical models focusing on high energy lithium-ion electrochemical couples (e.g., LMR-NMC positive and silicon/graphite negative electrodes) will continue. As the interfacial impedance studies and bulk transport electrochemical model are developed further for the LMR-NMC positive electrode, they will be integrated into a single electrochemical model.

FY 2013 Publications/Presentations

1. Positive Electrode Passivation by LiDFOB Electrolyte Additive in High-capacity Lithium-ion Cells, by Ye Zhu, Yan Li, Martin Bettge, and Daniel P. Abraham, Journal of The Electrochemical Society 159, A2109-2117 (2012).
2. Overcharge Effect on Morphology and Structure of Carbon Electrodes for Lithium-ion Batteries, Wenquan Lu, Carmen M. Lopez, Nathan Liu, John T. Vaughey, Andrew Jansen, and Dennis W. Dees, Journal of The Electrochemical Society 159(5), A566-A570 (2012).
3. Electrolyte Additive Combinations that Enhance Performance of $Li_{1.2}Ni_{0.15}Mn_{0.55}Co_{0.1}O_2$-Graphite Lithium-ion Cells, by Y. Zhu, Y. Li, M. Bettge, and D.P. Abraham, Electrochimica Acta in press; 10.1016/j.electacta.2013.03.102 (2013).
4. Examining Hysteresis in Composite $xLi_2MnO_3\bullet(1-x)LiMO_2$ Cathode Structures, by J. R. Croy, K. G. Gallagher, M. Balasubramanian, Z. Chen, Y. Ren, D. Kim, S.-H. Kang, D. W. Dees, and M. M. Thackeray, Journal of Physical Chemistry C 117, 6525−6536 (2013).
5. Structure Evolution of $Li_{1-x}VPO_4F$ Studied by *In situ* Synchrotron Probes, by Ying Piao, Yan Qin, Chengjun Sun, Yang Ren, Steve M. Heald, Dehua Zhou, Bryant J. Polzin, Steve E. Trask, Khalil Amine, Yinjin Wei, Gang Chen, Ira Bloom, and Zonghai Chen, under review by Energy & Environmental Science.
6. Understanding Long-Term Cycling Performance of $Li_{1.2}Ni_{0.15}Mn_{0.55}Co_{0.1}O_2$ – Graphite Lithium-Ion Cells, by Y. Li, M. Bettge, B. Polzin, Y. Zhu, M. Balasubramanian and D.P. Abraham, Journal of

The Electrochemical Society 160(5), A3006-A3019 (2013).

7. Perfluoroalkyl-substituted ethylene carbonates: novel electrolyte additives for high-voltage lithium-ion batteries, by Y. Zhu, M.D. Casselman, Y. Li, A. Wei, D.P Abraham, J. Power Sources 246 (2013) 184 –191. 10.1016/j.jpowsour.2013.07.070.
8. Electrochemical Modeling the Impedance of a Lithium-Ion Positive Electrode Single Particle, by D. Dees, K. Gallagher, D. Abraham, *J. Electrochem. Soc.*, **160** (3), A478-A486 (2013).
9. A Volume Averaged Approach to the Numerical Modeling of Phase-Transition Intercalation Electrodes Presented for Li_xC_6, by K. Gallagher, D. Dees, A. Jansen, D. Abraham, and S.-H. Kang, *J. Electrochem. Soc.*, **159** (12), A2029-A2037 (2012).

References

1. D. Dees, E. Gunen, D. Abraham, A. Jansen, and J. Prakash, *J. Electrochem. Soc.*, **152** (7) (2005) A1409.
2. D. Abraham, S. Kawauchi, and D. Dees, *Electrochim. Acta*, **53** (2008) 2121.
3. D. Dees, E. Gunen, D. Abraham, A. Jansen, and J. Prakash, *J. Electrochem. Soc.*, **155** (8) (2008) A603.
4. J. R. Croy, K. G. Gallagher, M. Balasubramanian, Z. Chen, Y. Ren, D. Kim, S.-H. Kang, D. W. Dees, and M. M. Thackeray, *Journal of Physical Chemistry C*, **117**(13), 6525-6536 (2013).

V.B.4 Scale-up of BATT Program Materials for Cell Level Evaluation (LBNL)

Vincent Battaglia, Ph.D.

Lawrence Berkeley National Laboratory
Department of Energy Storage and Distributed Resources
1 Cyclotron Road
Berkeley, CA 94720
Phone: (510) 486-7172; Fax: (510) 486-4260
E-mail: vsbattaglia@lbl.gov

Start Date: October 2009
Projected End Date: September 2013

Objectives

- Identify baseline materials for a high-voltage system.
- Test materials developed in the BATT Program as a result of investigations of the High-voltage Focus Group.

Technical Barriers

With the advent of the *EV Everywhere* Grand Challenge, there is a renewed and heightened interest in high energy-density couples. The BATT Program is focused on finding materials with the capacity to improve cell energy density and the ABR Program is focused on verification and evaluation of these new materials in full cells.

Technical Targets

EV Performance Targets

- 200 Wh/kg at C/3, system level.
- 1000 full charge/discharge cycles.
- 2 to 1 Pulse-power to Energy.

Accomplishments

- Four carbon conductive additives tested in a cathode containing NMO.
- A compilation of data that allows for an explanation of the coulombic inefficiency during the formation cycles.
- Two materials from the BATT Program developed based on analysis performed by the High-voltage Focus Group.
- A new material from NEI evaluated at 30° and 55°C.

✧ ✧ ✧ ✧ ✧

Introduction

To meet the *EV Everywhere* Grand Challenge put forth by the DOE, it is important to find materials capable of functioning with higher capacity for lithium over a large voltage separation. Scientists throughout the world including some supported by the BATT Program are developing such materials. As they make progress it is important that these materials are tested in half- and full-cells in a like manner. Both Argonne and LBNL have materials testing facilities, but the production of new materials is difficult for any one group to stay ahead of. For this reason, the LBNL Group has focused its effort on BATT produced materials and NMO-based materials. In the previous year, one material from NEI was designated as the baseline material for the High-voltage Focus Group in the BATT Program. Materials from Ceder and Manthiram and from certain large suppliers were tested and all of them showed that the biggest problem with cells containing NMO is a large capacity loss in full cells during formation. This is a difficult challenge as it is highly dependent on interactions with the anode. This year, different carbon additives and separators, two new materials from Manthiram, and a new material from NEI were tested.

Approach

To assess materials, electrodes are cast according to our on-line manual. The electrodes loading is typically around 1 mAh/cm^2. This loading allows for the assessment of the material; loadings that are too much greater may result in electrodes that fail due to electrode breakdown as opposed to a chemistry issue. On the other hand, the electrode is thick enough so as to identify coulombic efficiency issues that may not be revealed at lower loadings. Investigators in the BATT Program and large material suppliers to Li-ion battery manufacturers are queried for their most current materials. Electrodes are made of the new materials where only the new material is swapped in. Materials are tested for irreversible capacity loss, reversible capacity, rate capability, and cycleability. Results are provided to the suppliers and reported in Quarterly Reports.

Results

Testing of Conductive Carbon Additives and Polypropylene Separators. Beyond the testing of materials developed in the BATT Program, it is our group's responsibility to test supplier materials for a $LiNi_{1/2}Mn_{3/2}O_4$ high-voltage baseline study for both the ABR and BATT Programs. Through this effort, an active material from NEI was identified last year. This year, three carbons from Timcal, Super C65, Super C45, and Super P-Li; and VCGF, were tested and compared to the present baseline carbon additive material Denka black (ATD Gen 2 baseline conductive additive).

Half-cells were fabricated with a fairly low active material loading of approximately 0.6 mAh/cm^2 with 4% binder and 3% conductive carbon. It has been shown by our lab that for half-cells with Denka black there is an extended amount of side reaction during the C/10 charge when a 4.95 V upper cut-off voltage is employed. Independent of the carbon used, the results shown below were identical except for the Super P-Li (Figure V - 50).

Close inspection of the data shows a highly variable voltage response during the constant-current charge and an extended charge time during the 5th charge cycle. Such an irregular voltage response is not only an indication of a side reaction but also of a side reaction that involves the production of a gas. And, not only is this most likely the result of a gas, but a gas that is reversibly oxidized or reduced to generate a benign shuttle between the two electrodes.

For a cell with a comparable loading but containing Super P-Li, the response is much more favorable, as seen in the lower figure (bottom, Figure V - 50). Consistent with this result, is that the Super P-Li consists of larger particles and a lower surface area. Also consistent with this result, is that at double the loading the half-cell response appears similar to that of the cells with the other carbons at half the loading. All of this data adds up to the conclusion that there is a reversible shuttle in the half cell that involves a gaseous reactant that is oxidized on the cathode and that this reaction is limited by reducing the surface area of the cathode and by the eventual formation of a protective film on one of the electrodes.

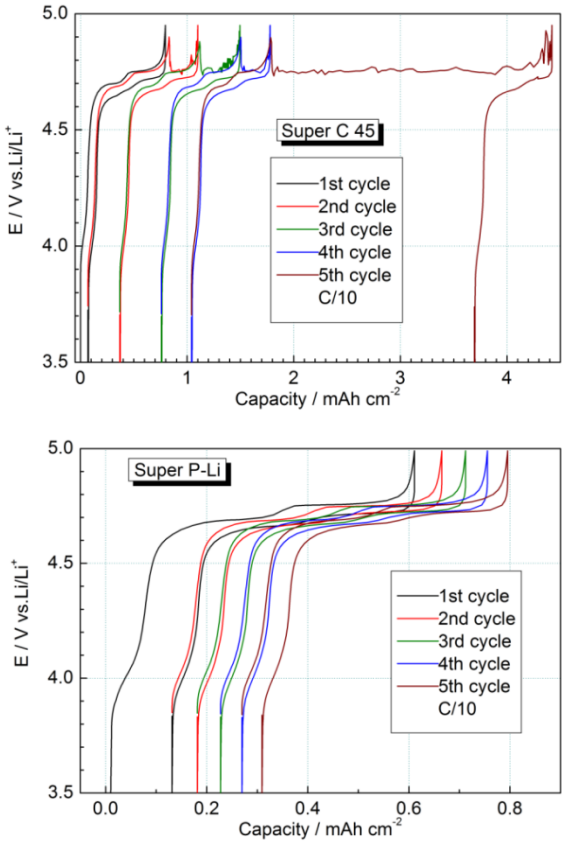

Figure V - 50: The first five cycles of half cells of NMO with, top, C45 conductive additive, and, bottom, Super PLi

Separators from Celgard were also tested: 2400, 2500, and 3501. They were all polypropylene based, however, the 2500 and 3501 are high-power separators with high porosity, and the 3501 also contains a wetting agent. Charging results, not provided here, indicated erratic voltage dependence for the more porous separators and favorable performance for the low-porosity separator. Based on these results, Super P-Li is recommended as the conductive additive and Celgard 2400 the separator for cells with high-voltage $LiNi_{1/2}Mn_{3/2}O_4$ cathodes.

Testing of Two BATT NMO Materials. Amongst the testing of baseline materials for the Ni-spinel high-voltage system and some salts from HQ, two NMO materials from the University of Texas produced by Prof. Manthiram's Group in the BATT Program were evaluated. From the BATT Focus Group on NMO, it was discovered that particle morphology and the level of transition metal disorder of the active material were critical parameters with regard to cathode performance. Specifically, Dr Guoying Chen showed that an octahedron shape demonstrated better performance than platelets, and Dr. Cabana showed that disordered material provides better rate performance than ordered materials. With this in mind, Dr. Manthiram synthesized

two NMO materials with the polyhedron shape and disordered configurations, one with and one without fluorine doping, referred to as NMFO and NMO, respectively. The fluorine is meant to improve cycling stability.

Figure V - 51 shows the SEMS of both materials. The images are nearly identical. The particles are between one half micron to 3 microns in size and polygonal in shape. Electrodes were made of the same active and inactive material fractions, thicknesses, and porosity. The laminates were punched to circular electrodes and tested in coin cells with a standard electrolyte of 1 M $LiPF_6$ in EC:DEC 1:2. The counter electrode was either lithium metal or graphite. As seen for NMO in our lab, cycling against Li is stable. Most of the capacity is available with very little fade over 100 cycles before Li dendrites short the cell. Cycling with a graphite anode is slightly different. In that case, only half of the capacity of the cathode is accessible after formation. However, once formation is completed, the loss of capacity for the next 200 cycles is minimal (see Figure V - 52). This is the same for the baseline chemistry as it is for the materials Prof. Manthiram produced,

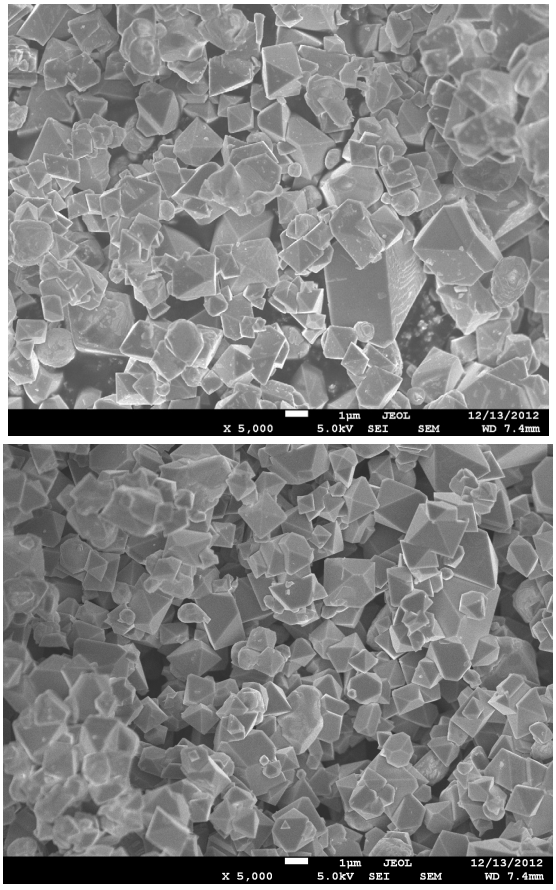

Figure V - 51: Top, SEM of NMO; bottom, SEM of NMFO. Materials appear nearly identical

see Figure V - 52. The source of capacity fade for the first five formation cycles is still under investigation. Half of the loss can be attributed to poor first cycle coulombic efficiency, seen for nearly all chemistries tested. Another 20% of the capacity loss occurs during the first five C/20 formation cycles, and another 15% of the capacity is lost when the cycling current is increased to C/3. Much of the loss can be attributed to SEI formation on the anode and a large impedance established in the first 3 cycles.

New NEI Material. At the 2013 DOE Annual Merit Review Meeting, discussions were held with representatives from NEI, the supplier of the baseline material used in the BATT, High-voltage, Ni-spinel Focus Group. They agreed to send LBNL their latest material. The results of the preliminary analysis of this latest material are reported here.

The physical characterization of this material included SEM, particle size analysis, and a measure of its surface area *via* the BET method. The SEM not only revealed that the particles are on the order of a few microns in diameter and consist of stacked crystal planes, but also provided no indication that these

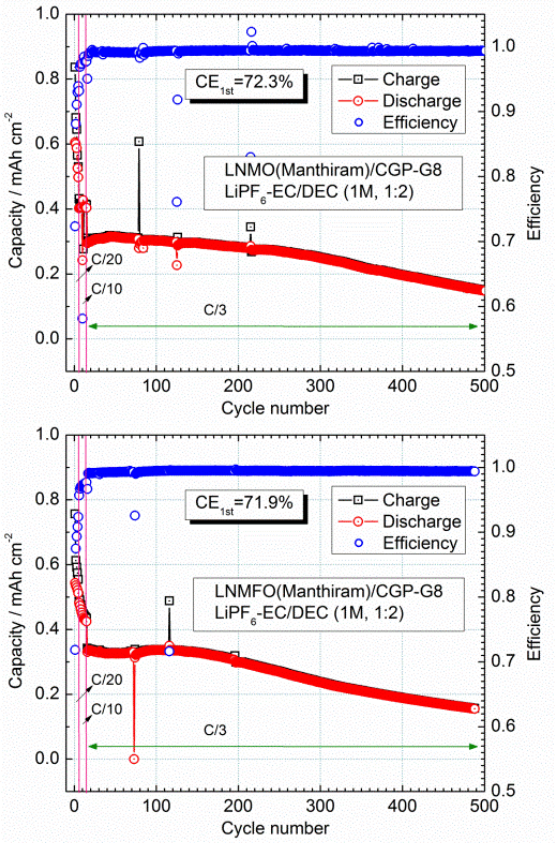

Figure V - 52: Top, capacity *versus* cycle number for a full cell of graphite/NMO; bottom, capacity *versus* cycle number for graphite/NMFO. Note the large capacity decline in the early cycles for both cells

particles consist of smaller primary particles. The particle size analysis indicated a fairly tight particle size distribution: d10 = 4. 2 microns and d90 = 11.8 microns. The mean particle size was measured at 6.6 microns with a standard deviation of 3.5 microns. The surface area was measured at 0.45 m^2/g, which is consistent with a particle diameter of 3.0 microns. It is typically found that the BET-derived diameter is approximately 1/3 the size as indicated by the PSA measurement, and this characteristic is attributed to a rough particle surface.

A cell of relatively low capacity, approximately 0.65 mAh/cm^2, was constructed for electrochemical characterization. The initial tests indicate that the material has a first-cycle coulombic efficiency of 94.1% and a discharge capacity of 133 mAh/g between 4.9 and 3.5 V. Of this capacity, 11.5% was accessible below 4.3 V.

This low specific-area capacity cell demonstrated high rate performance as expected. A modified Peukert plot of cell discharge capability for three different loadings is provided in Figure V - 53. It is clear that a C/2 discharge rate is within the capability of all three of these electrodes where mass transfer limitations are not a factor.

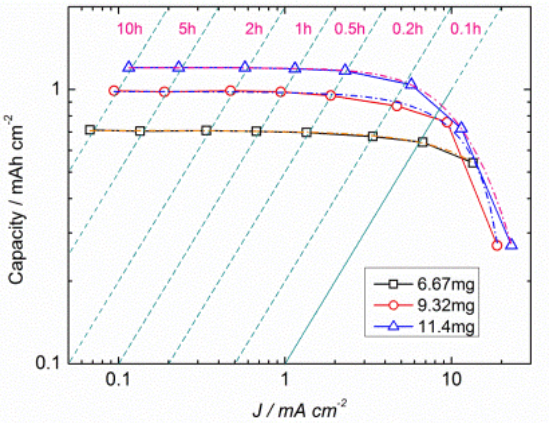

Figure V - 53: Capacity *versus* current density for three loadings

The half-cell capacity between 3.5 and 4.95 V *versus* cycle number is provided in Figure V - 54. With a large operational voltage range, one may not expect much capacity fade, and for this reason the energy of the cell *versus* cycle number is also provided (Figure V - 55.) These data include the impedance rise of both the cathode and lithium counter electrode. Since these data show very little energy decline, it is clear that there is very little impedance rise in this cell for over 150 cycles. All data were acquired from a cell with a standard electrolyte of 1 M $LiPF_6$ in EC:DEC, 1:2. As indicated previously, the problem with this chemistry is not its high-voltage instability but the effects this chemistry has on graphitic anodes.

Half cells of the latest NEI material were built and sealed to prevent leakage at elevated temperatures. The electrolyte was the baseline of 1 M $LiPF_6$ in EC:DEC 1:2. After 5 cycles at C/10 and 30°C, the temperature and cycling rate were both increased. The temperature was raised to 55°C and the C-rate to C/5 for 20 cycles and then increased again to C/2. One can see in Figure V - 56 that the capacity shows no loss after 120 cycles.

To test for impedance rise, the energy density was also tested. In Figure V - 57, the energy per gram of cathode *versus* cycle number is shown. One sees that the energy also does not decline with cycling, indicating that the cell's impedance does not rise with cycling.

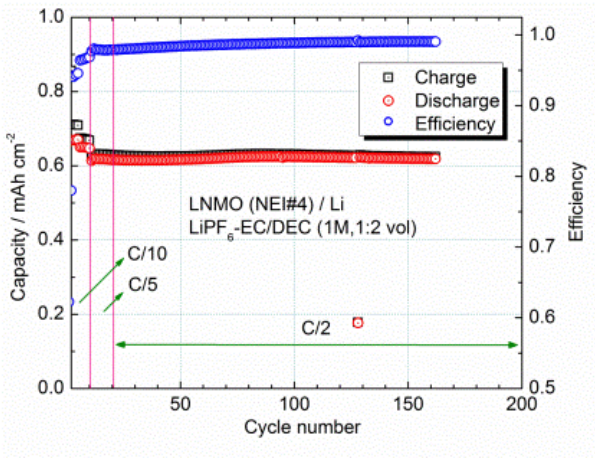

Figure V - 54: Capacity and efficiency *versus* cycle number

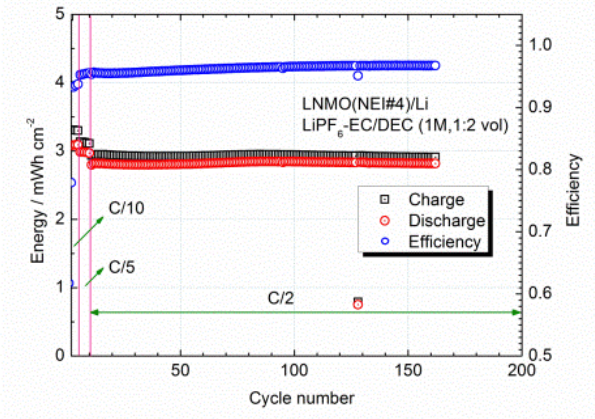

Figure V - 55. Energy and efficiency *versus* cycle number

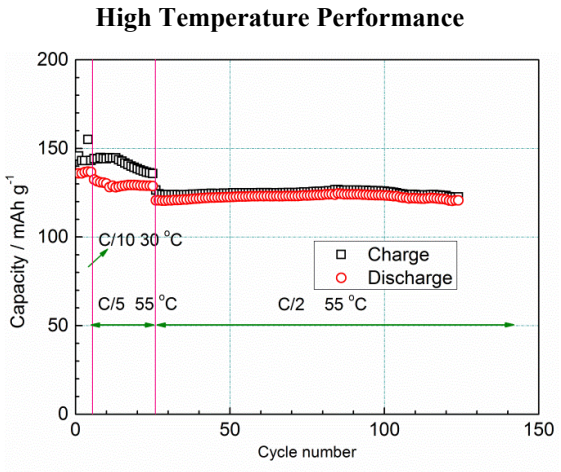

Figure V - 56: Capacity per gram of cathode active material *versus* cycle number at elevated temperature

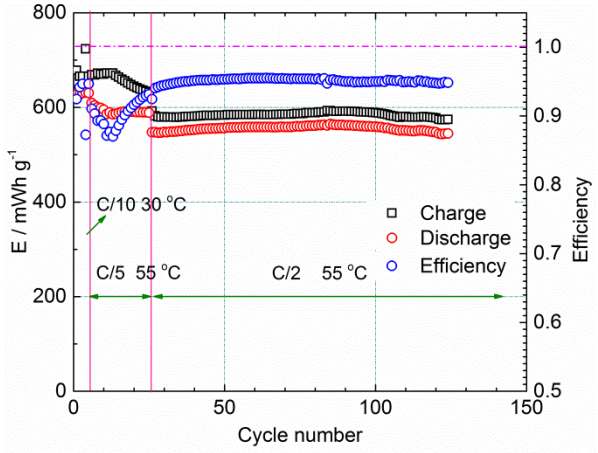

Figure V - 57: Energy per gram of cathode active material *versus* cycle number at elevated temperature

Conclusions and Future Directions

Investigations into the NMO material this year have revealed new information. The large, variable current seen in cells during the first few cycles can be abridged with a change in the conductive carbon and separator. This indicates that the carbon can be a catalyst to the oxidation reactions occurring in cells with this chemistry. It also provided further insight into the source of these reactions and methods on how to reduce them. It was also determined that materials designed based specifically on research that suggested better performance based on the level of disorder and particle morphology did not improve the biggest problem with this cell chemistry – a large capacity loss in full cells as a result of SEI formation. It was also found that the newest materials from NEI cycle very well, even at 55°C, indicating very good stability and no impedance rise up to 80 cycles.

The results obtained for the NMO material are much different than our experience with NMC material. For this reason, it is likely that a new study will soon begin to understand those differences. In particular, the NMC is known to show a great deal of instability and impedance rise when cycled above 4.4 V. It is not clear whether the instability is related to bulk properties of NMC or surface properties. To start, it will be important to identify a stable NMC that is well accepted in industry. We will work with our colleagues at ANL to identify this chemistry.

FY 2013 Publications/Presentations

1. 2013 DOE Annual Peer Review Meeting Presentation.

V.B.5 Impact of Materials on Abuse Response (SNL)

Christopher J. Orendorff, Kyle R. Fenton, Josh Lamb, and Ganesan Nagasubramanian

Sandia National Laboratories
P. O. Box 5800, Mail Stop 0614
Albuquerque, NM 87185-0614
Phone: (505) 844-5879; Fax: (505) 844-6972
E-mail: corendo@sandia.gov

Collaborators:
Prof. Steven George, CU-Boulder
Robert Tenent, NREL
Kevin Gering, INL
Rob Privette, XG Sciences

Start Date: October 2012
Projected End Date: September 2013

Objectives

- Elucidate degradation mechanisms in lithium-ion cells that lead to poor abuse tolerance (runaway thermodynamics, gas evolution, electrolyte combustion).
- Develop and evaluate advanced materials (or material combinations) that will lead to more abuse tolerant lithium-ion cell and battery systems.
- Build 18650 cells in the SNL fabrication facility for cell level evaluation of new materials in support of all ABR thrust areas.

Technical Barriers

There are several technical barriers to achieving the goals stated above including:

- Developing lithium-ion cells that are intrinsically abuse tolerant and do not lead to high order catastrophic failures.
- Mitigating the gas evolution and decomposition of the electrolyte.
- Passivation of cathode runaway reactions and interfacial reactions with electrolyte.
- Limited quantities of advanced materials (and numbers of cells with new materials) to evaluate abuse response.

Technical Targets

- Quantify the thermal runaway response of materials at the cell level (18650).
- Determine the effect of electrolyte salts, solvents and additives on the abuse response of lithium-ion cells.
- Evaluate the thermal response of candidate active materials.
- Identify materials that could be used to reduce gas evolution and the heat and kinetics of runaway reactions.

Accomplishments

- Continued evaluation of candidate electrolytes and salts that minimize the energetics of thermal runaway.
- Evaluated additives, electrode coatings, and new materials to improve abuse response and safety of lithium-ion systems.
- Fabricated electrodes to aid in standardization of ABR materials across national laboratories

✧ ✧ ✧ ✧ ✧

Introduction

As lithium-ion battery technologies mature, the size and energy of these systems continues to increase (> 50 kWh for EVs); making safety and reliability of these high energy systems increasingly important. While most material advances for lithium-ion chemistries are directed toward improving cell performance (capacity, energy, cycle life, etc.), there are a variety of material advancements that can be made to improve lithium-ion battery safety. Issues including energetic thermal runaway, electrolyte decomposition and flammability, anode SEI stability, and cell-level abuse tolerance continue to be critical safety concerns. This report highlights work with our collaborators to develop advanced materials to improve lithium-ion battery safety and abuse tolerance and to perform cell-level characterization of new materials.

Approach

The effect of materials (electrolytes, additives, anodes, and cathodes) on the thermal response of full cells is determined using several techniques. One of the

most useful and quantitative techniques is accelerating rate calorimetry (ARC). The ARCs at SNL are fitted with uniquely designed high pressure fixtures to not only measure quantitative heat flow but also gas generation under ideal adiabatic conditions during full cell runaway. Cells were fabricated using a variety of active materials, electrolytes, and additives in the SNL cell prototyping facility. The in-house prototyping capability gives us the versatility to target candidate materials, perform full cell evaluation, and correlate cell response to fundamental materials properties.

Abuse tolerance tests are performed which evaluate the response to expected abuse conditions and document and evaluate numerous outcomes including 1) failure point of energy storage device 2) conditions that cause failure 3) failure modes and abuse conditions using destructive physical analysis (DPA) 4) quantitate cell or module response to the abuse condition 5) provide feedback to develop new abuse test procedures that more accurately determines cell performance under the most likely abuse conditions.

Possible tests that can be performed cover three main categories of abuse conditions. Mechanical abuse tests include controlled crush, penetration, blunt rod, drop, water immersion, mechanical shock and vibration. Thermal abuse tests include thermal stability, simulated fuel fire, elevated temperature storage, rapid charge/discharge, and thermal shock cycling. Electrical Abuse tests include overcharge/overvoltage, short circuit, overdischarge/voltage reversal, and partial short circuit.

Results

Evaluation of High Energy Materials. One objective of this program is to determine baseline safety performance and thermal stability of the latest advanced high energy lithium-ion materials including lithium-rich layered metal oxide (LMO), Si-composites. The largest barrier to the success of this effort previously was the availability and access to these high energy materials. The first Si-composite anode evaluated at SNL as part of this program is a composite developed at XG Science. Electrodes were coated and cells prepared in the SNL prototyping facility. Performance of the Si-composite in a representative Li ½ cell (1.2 M $LiPF_6$ in EC:EMC (3:7) electrolyte) is shown in Figure V - 58. The specific capacities of all cells evaluated to date are on the order of 750 mAh/g.

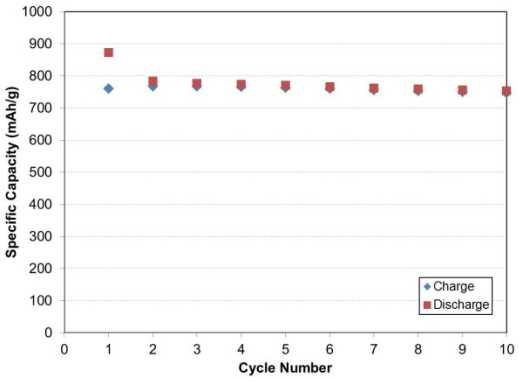

Figure V - 58: Specific capacity (mAh/g) of a representative Si-composite ½ cell vs. lithium

Differential scanning calorimetry (DSC) measurements of this material along with graphite and lithium titanate (LTO) samples for comparison are shown in Figure V - 59. The graphite anode shows the characteristic low heat flow onset at 100°C indicative of SEI decomposition followed by the higher rate decomposition > 200° C. The silicon composite shows a similar response but with an onset temperature of 150°C, but a comparable total specific heat to the graphite anode (3700J/g and 3360 J/g). LTO has a significantly more benign heat flow profile and a specific heat of 670 J/g.

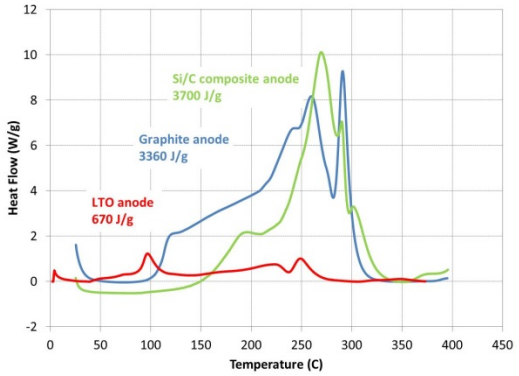

Figure V - 59: DSC profiles for graphite, LTO and Si-composite anodes

Evaluation of a LMR-NMC positive electrode material was also done recently. Initial work has focused on baseline materials characterization of HE5050 (Toda America). Figure V - 60 shows DSC data for HE5050 at 4.6 V and NMC 111 at 4.2 V for comparison. Results show a significantly higher specific heat for HE5050 (2,100 J/g) than NMC 111 (1,470 J/g) and a faster heat release rate. However, it is important to note that the LMR-NMC sample is evaluated at 400 mV higher voltage than NMC in this experiment. Work in FY14 will focus on cell fabrication and characterization of safety performance in 18650 cells.

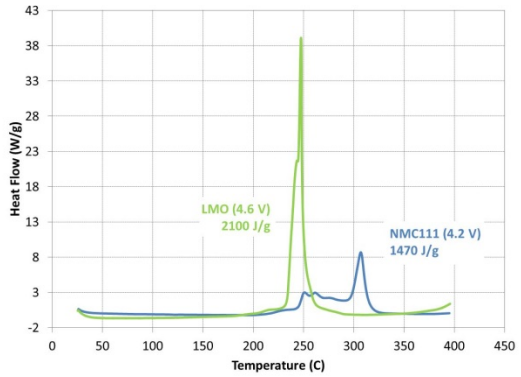

Figure V - 60: DSC profiles for LMR-NMC at 4.6 V and NMC 111 at 4.2 V

Coatings. For a number of years, the ABR program has focused on material coating strategies to improve cell performance and reliability. In earlier work, we have shown that AlF_3-coated NMC improves safety performance, as well. The NREL led coatings programs have focused on Al_2O_3 atomic layer deposition (ALD) coatings and the objective of our contribution is to evaluate the effect of these coatings on thermal stability and safety. NMC 111 (Toda) and graphite (CP A10) electrodes are coated with Al_2O_3 ALD to give ~0.3 nm and 0.8 nm thick coatings on each electrode, respectively. Figure V - 61 (top) shows DSC data for the coated and uncoated graphite electrode. Results show a significant reduction in the heat generation at the onset of SEI decomposition (~100°C). Figure V - 61 (bottom) shows ARC data for 18650 cells with Al_2O_3 ALD and uncoated electrodes. The coated cell shows an increase in the exotherm onset temperature by ~20°C, which is consistent with a stabilized SEI at the anode interface. The high rate cathode decomposition remains unchanged in the coated cell. This is likely due to the fact that the coating is not thick enough (nominally ~0.3 nm) to influence the decomposition of the positive electrode.

Ionic Liquid (IL) Development. Additional efforts to develop intrinsically non-flammable electrolytes with enhanced abuse tolerance performance have focused on ionic liquids as an alternative to the carbonate systems. Figure V - 62 (top) show cyclic voltammetry data of the candidate ILs prepared in FY12 and 13. The newest candidate, IL-3, shows the most promising voltage stability at both high and low potentials. IL-3 is stable to 5V which is comparable to carbonate solvent mixtures (no salt) and near the lithium potential without significant cation reduction. Electrolyte formulations of EC:EMC and IL-3 have been prepared to determine their performance in coin cells (NMC/graphite full cells). Figure V - 62 (bottom) shows specific capacity of for these coin cells with 0-60% IL. Results show that up to 40% IL the specific capacity during formation is identical to the EC:EMC control cell. At 60% IL, the performance begins to decay rapidly. Future work will focus on the optimization of the 40% IL-3 electrolyte formulations over longer cycle life and for safety performance (thermal stability and flammability).

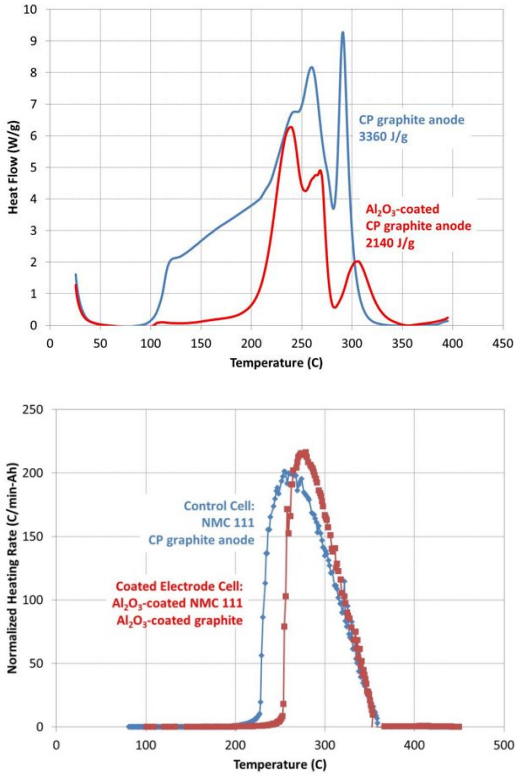

Figure V - 61: (Top) DSC profiles of Al_2O_3 ALD coated graphite and uncoated graphite and (bottom) ARC profiles for Al_2O_3 ALD coated electrodes and uncoated electrodes in an NMC/graphite 18650 cell

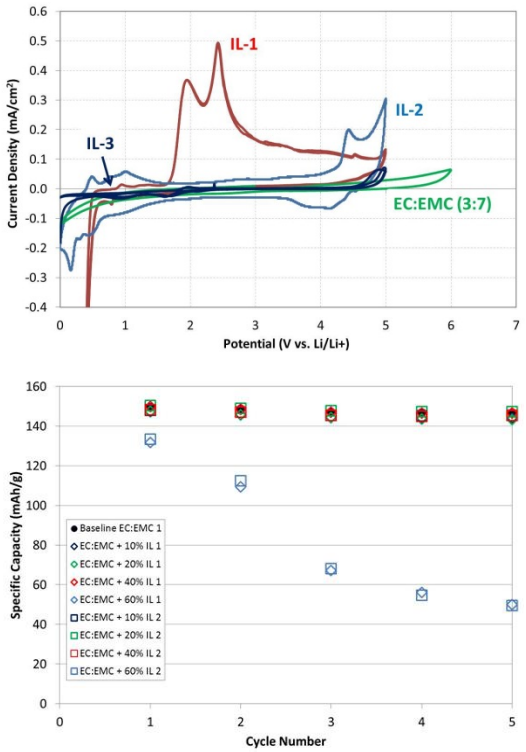

Figure V - 62: (Top) cyclic voltammetry of candidate ILs and (bottom) specific capacity at C/10 of NMC/graphite coin cells with different IL-3 fraction electrolyte formulations

Conclusions and Future Directions

This work demonstrates how specific advances in a variety of materials areas (anode, cathode, and electrolyte) can impact on cell-level safety and thermal characteristics. Work will continue in this area to evaluate cell-level abuse response using Al_2O_3 ALD coated cathodes electrodes to minimize thermal runaway reaction free energy, high energy materials including Si-composite anodes and LMR-NMC cathodes to determine baseline cell response, and IL-based electrolyte formulations for thermal performance and flammability. Future work will focus on the safety performance characterization of new coated materials (Physical Sciences, CU-Boulder, NREL), flame retardant additives (Case Western), and other advanced lithium-ion battery materials.

FY 2013 Publications/Presentations

1. C. J. Orendorff, J. Lamb, K. R. Fenton, and L. A. M. Steele, “Approaches to Evaluating and Improving Lithium-Ion Battery Safety” AABC February 2013.
2. C. J. Orendorff, “Approaches to Evaluating and Improving Lithium-Ion Battery Safety” CU-Boulder, February 2013.
3. 2013 DOE Annual Peer Review Meeting Presentation.
4. J. Lamb et al. J. Power Sources, 247 (2014) 1011-1017. “Thermal and overcharge abuse analysis of a redox shuttle for overcharge protection of $LiFePO_4$.”

V.B.6 Post-Test Diagnostic Activities (ANL)

Ira Bloom, Primary Contact,
Nancy Dietz-Rago, Javier Bareño

Argonne National Laboratory
9700 South Cass Avenue
Argonne, IL 60439
Phone: (630) 252-4516; Fax: 630 252 4176
E-mail: ira.bloom@anl.gov

Start Date: April 2010
Projected End Date: September 2010

Objectives

- To accelerate the R&D cycle of DOE and industrial collaborators by developing and conducting standard procedures for post-test characterization of batteries in order to provide insight into physicochemical causes of performance degradation.

Technical Barriers

This project addresses the following technical barriers as described in the USABC goals [1, 2, 3]:

(A) Performance at ambient and sub-ambient temperatures.

(B) Calendar and cycle life.

Technical Targets

- EV: 5-year calendar life; 1,000 80% DOD DST cycles.
- HEV: 15-year calendar life, 300,000 charge-sustaining cycles; EOL performance (min): 25 kW and 300 Wh.
- PHEV: 15-year calendar life, 300,000 charge-sustaining cycles, 5,000 charge-depleting cycles; EOL performance (min): 45 kW and 300 Wh.
- LEESS: 15-year calendar life, 300,000 charge-sustaining cycles; EOL performance (min): 20 kW and 56 Wh.

Accomplishments

- Provided SEM characterization support to CAMP facility to optimize electrode making procedures.
- Characterized structural and physicochemical changes due to cycling of LMR-NMC/graphite and high-energy spinel/graphite cells built at CAMP facility containing standard electrodes from the CAMP electrode library, available to ABR programs. These characterization results provide a baseline for future studies to correlate observed property, structural and physicochemical changes due to cell constitution; e.g., testing a new electrodes or electrolyte additive, while keeping all other cell components standard. (Further cell chemistries pending).
- Collaborations with industrial and academic partners:
  - Argonne CAMP.
  - JCI.
  - Maxwell.
  - Army Research Laboratory (initial discussions).
  - Jet Propulsion Laboratory (initial discussions).
  - University of Hawaii (initial discussions).
  - CIC Energunie (Spain).
  - Dalhoussie University, (Canada).

✧ ✧ ✧ ✧ ✧

Introduction

Post-test characterization of components harvested from aged batteries provides information about physicochemical changes at materials level that, previously, could only be inferred. This information can be correlated to device performance characterization to provide new insights into fundamental causes of device degradation and suggest new design routes to overcome performance limitations.

Approach

We apply a combination of physical, spectroscopic, metallographic, and electrochemical characterization techniques to examine aged cell constituent materials in a systematic fashion. Harvesting and analysis are performed under inert atmosphere conditions to avoid preparation artifacts.

Cells can come either from exploratory DOE programs, such as ABR and BATT, or from pre-competitive R&D programs managed by USABC and

USDRIVE. The Post-Test Facility uses the experience and techniques developed in DOE's ABR program in a standardized fashion.

Figure V - 63: Argonne Post-test facility. The inert-atmosphere glovebox used for sample harvesting and analysis is shown in the background

Results

Initial SEM characterization support was provided to the CAMP facility to assist in optimization of mixing procedures for different electrodes. Test electrodes were examined for homogeneity and structural changes due to slurry mixing and electrode calendering. Once optimized, the CAMP facility used these electrodes to produce several sets (cell builds) of ~ 400 mAh pouch cells of several cathode/graphite cehemistries, using Argonne's standard 1.2 M $LiPF_6$ in EC:EMC (3:7 by weight) electrolyte.

Two sets of cells containing LMR-NMC and high-energy NiMn spinel electrodes were received by the Post-test facility for examination. These cells had been previously cycled by CAMP at C/2 rates to 20-25% initial capacity loss.

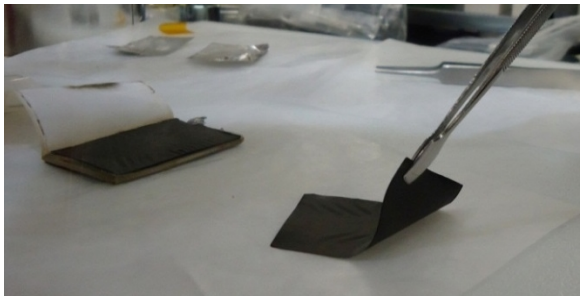

Figure V - 64: NiMn spinel / graphite pouch cell being disassembled from analysis. In this case, the cathode coating delaminated from the Al current-colletor due to adhesion failure

The cells were transferred to an inert-atmosphere glovebox for cell disassembly and sample harvesting, see Figure V - 64. Cells were disassembled by carefully cutting through the cell pouch material to avoid shorting the cell, while monitoring cell temperature in real time to alert the worker of a potential short-circuit or internal reaction. Visual examination of the disassembled cells revealed: (1) a "zebra pattern" of stains in electrodes and separator, probably related to differences in local current density and, hence, electrolyte decomposition rate; and (2) adhesion failure of spinel electrodes resulting in delamination from the current collector resulting in a self-supporting electrode coating layer (see Figure V - 64).

SEM (see Figure V - 65) examination of harvested electrode and separator samples did not reveal appreciable microstructural differences between lighter and darker regions (stripes) of the observed "zebra patters." However, EDS analysis showed F- and P-enrichment at lighter areas in the "zebra patterns," consistent with higher local concentrations of $LiPF_6$ salt decomposition products.

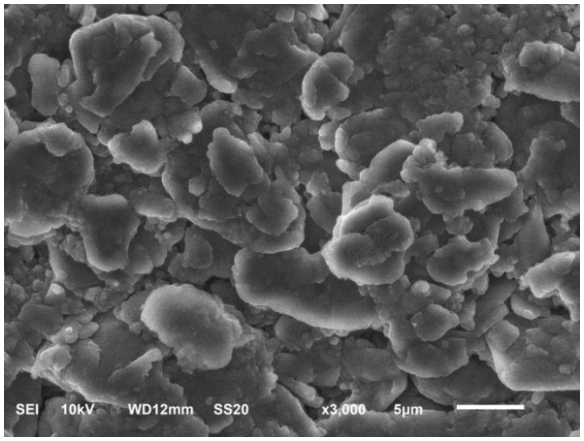

Figure V - 65: SEM micrograph of aged Li-Mn rich NMC electrode. EDS analysis indicates presence of fluorinated electrolyte reaction products

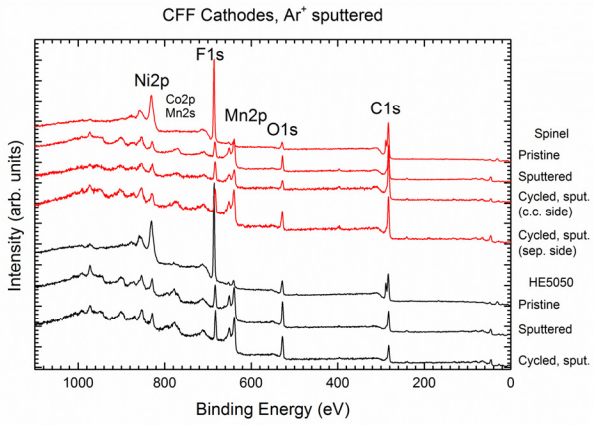

Figure V - 66: XPS comparison of pristine and aged LMR-NMC and NiMn spinel electrodes. Note that sputter cleaning of surface layers (binder, conductive additives) is needed to expose active oxides in pristine material

XPS characterization was used to track changes in surface chemistry of harvested components. Due to the extremely short information depth of XPS it is necessary to sputter away spurious surface films such as electrolyte residue. Figure V - 66 shows an example where oxygen and transition metal films from active oxide particles (LMR- NMC and Li-Ni-Mn-O spinel) are revealed only after Ar^+ sputtering of binder and conductive additives. Sputtering time required to reach underlying oxide can be used as a metric to determine relative thickness of evolved films in a series of samples. Furthermore, ion sputtering allows monitoring differences in chemical composition as a function of depth. Care must be taken to identify and avoid possible artifacts, such as loss of chemical resolution (peak broadening) due to the sputtering process. Well-defined pristine materials are subjected to the same cleaning/sputtering processes as samples of interest to gauge the extent of potential measurement artifacts.

Conclusions and Future Directions

Over FY 2013, Argonne's Post-test Facility has been collaborating with Argonne's CAMP facility and other ABR and USABC programs.

Argonne's CAMP facility is developing a standard library of balanced electrodes for DOE researchers to test new materials in standard cell configurations. Argonne's Post-test facility has started systematic characterization of CAMP's electrodes and physicochemical changes due to aging. In the near future, these tests will provide a characterization baseline to study the effect of new cell components (e.g., active materials, electrolytes, additives) on aging mechanisms of standard cells.

In the future, the Post-test Facility will continue to work with the CAMP facility to expand the library of standard electrodes available to ABR and BATT programs. In particular, we plan on expanding the range of negative electrodes to include Si-based systems.

Additionally, Argonne's Post-test Facility will continue to support ABR, BATT, and USABC development programs through planning, executing and interpreting state-of-the-art *in situ* characterization. Additionally, Post-test Facility workers will step up ongoing outreach efforts to increase our current portfolio of industrial and academic collaborations.

List of Abbreviations

ABR: Advanced Battery Research

BATT: Batteries for Advanced Transportation Technologies

CAMP: Cell Analysis Modeling and Prototyping

DOD: depth of discharge

DST: dynamic stress test (see ref. 3)

EC: ethylene carbonate ($C_3H_4O_3$)

EDS: energy dispersive spectroscopy

EMC: ethyl methyl carbonate ($C_4H_8O_3$)

EOL: end of life

EV: electric vehicle

HEV: hybrid electric vehicle

LEES: low-energy energy storage system

LMR-NMC: Li- and Mn-rich Ni-Mn-Co oxide

NMC: Li-Ni-Mn-Co oxide

PHEV: plug-in hybrid electric vehicle

R&D: research and development

SEI: solid-electrolyte interface

SEM: secondary electron microscopy/microscope

USABC: United States Advanced Battery Consortium (DOE, GM, Chrysler and Ford)

VC: vinylene-carbonate ($C_3H_2O_3$)

XPS: x-ray photoelectron spectroscopy

FY 2013 Publications/Presentations

1. "Compatibility of Lithium Salts with Solvent of the Non-Aqueous Electrolyte in Li-O_2 Batteries." P. Du, J. Lu, K.C. Lau, X. Luo, J. Bareño, X. Zhang, Y. Ren, Z. Zhang, L.A. Curtis, Y-K. Sun, and K. Amine. *Phys. Chem. Chem. Phys.,* 15 (2013) 5572. doi:10.1039/C3CP50500F
2. "Role of Polysulfides in Self-Healing Lithium-Sulfur Batteries." R. Xu, I. Bellharouak, J.C.M. Li, X. Zhang, I. Bloom, and J. Bareño. *Adv. Energy Mat.* 3 (2013) 833. doi:10.1002/aenm.201200990
3. "Improving high-capacity $Li_{1.2}Ni_{0.15}Mn_{0.55}Co_{0.1}O_2$-based lithium-ion cells by modifying the positive electrode with alumina." M. Bettge, Y. Li, B. Sankaran, N. Dietz Rago, T. Spila, R. T. Haasch , I. Petrov, and D.P. Abraham. *J. Power Sources,* 233 (2013) 346. doi:10.1016/j.jpowsour.2013.01.082
4. "A high performance separator with improved thermal stability for Li-ion batteries." J.-J. Woo, Z. Zhang, N. L. Dietz Rago, W. Lu and K. Amine. *J. Mater. Chem. A*, 1 (2013) 8538. doi:10.1039/c3ta12154b
5. (Invited talk) "Post-Test Analysis of Lithium-Ion Battery Materials at Argonne National Laboratory." J. Bareño, N. Dietz-Rago, and I. Bloom. International Battery Association Meeting. Barcelona, Spain. March 10-15, 2013.

6. (Poster) "Cell Fabrication and Post Test Facilities at Argonne National Laboratory ." B. Polzin, W. Lu, A. Janses, D. Dees, S. Trask, J. Bareño, N. Dietz-Rago, and I. Bloom. 30th International Battery Seminar and Exhibit. Fort Lauderdale, FL. March 11-13, 2013.
7. "Cell Fabrication Facility and Post Test Characterization Facility at Argonne National Laboratory." B. Polzin, Z. Chen, J. Bareño, S. Trask, N. Dietz-Rago, A. Jansen, and I. Bloom. 246th American Chemical Society National Meeting & Exposition. Indianapolis, IN. September 11-13, 2013.
8. (Poster) "Post-Test Analysis of Lithium-Ion Battery Materials at Argonne National Laboratory." J. Bareño, N. Dietz-Rago, and I. Bloom. 6th International Conference on Advanced Lithium Batteries for Automotive Applications. Argonne, IL. September 9-11, 2013.

References

1. FreedomCAR Battery Test Manual for Power-Assist Hybrid Electric Vehicles, DOE/ID-11069, October 2003.
2. FreedomCAR Battery Test Manual for Plug-In Hybrid Electric Vehicles, June 2010.

   Electric Vehicle Battery Test Procedures Manual, Revision 2, January 1996.

V.C Critical Barrier Focus: Voltage Fade

V.C.1 Voltage Fade in the LMR-NMC Materials: Background & Project Scope (ANL)

Anthony Burrell

Argonne National Laboratory
9700 South Cass Avenue
Argonne, IL 60439-4837.
Phone: (630) 252-2629
E-mail: Burrell@anl.gov

Collaborators:
Ali Abouimrane, Daniel Abraham, Khalil Amine, Mahalingam Balasubramanian, Javier Bareno Garcia-Ontiveros, Ilias Belharouak, Roy Benedek, Ira Bloom, Zonghai Chen, Dennis Dees, Kevin Gallagher, Hakim Iddir, Brian Ingram, Christopher Johnson, Wenquan Lu, Dean Miller, Yang Ren, Michael Thackeray, Lynn Trahey, and John Vaughey all from Argonne National Laboratory

Claus Daniel, Debasish Mohanty, David Wood III, Jianlin Li (ORNL)

Oak Ridge National Laboratory
One Bethel Valley Road
P.O. Box 2008, MS 6472
Oak Ridge, TN 37831
Phone : (865) 241-9521; Fax: (865) 241-5531
E-mail: danielc@ornl.gov

Start Date: October 2012
Projected End Date: September 2014

Objectives

Voltage fade is one of the major limitations to the commercialization of the LMR_NMC materials. The overarching goal of this project is to eliminate voltage fade in LMR-NMC. To do this in FY13 we proposed to:

- Map out performance and cost space for generic chemistries (complete).
- Make an initial techno economic assessment of LMR-NMC capacity and average voltage to outperform existing materials (complete).
- Finalize LMR-NMC material level properties required to meet DOE PHEV40 and EV goals (Complete).
- Document state-of-the-art performance and barriers still remaining to overcome for LMR-NMC (complete).
- Go-No/go for coatings (complete).

Technical Barriers

The primary technical barriers to the development of a safe cost-effective PHEV battery with a 40 mile all electric range that meets or exceeds all performance goals include:

- Interpreting complex cell electrochemical phenomena.
- Identification of cell degradation mechanisms.

Technical Targets

- Develop a cell to meet the 40-mile PHEV goal.
- Obtain a positive-electrode material that can operate in the high-potential range (4V - 5V vs. Li/Li+) while still achieving approximately 130 mAh/g of capacity.

Accomplishments

- **Go-NO-GO coatings and additives = NO-GO.** Within experimental error, there was little-to-no effect on voltage fade from the coatings and additives, pointing to voltage fade being tied to the intrinsic nature of the cathode material. All coatings work related to voltage fade was halted.
- Established a reliable sol-gel route to the syntheses of LMR-NMC and its variants.
- Evaluated dopants: Al , Fe, V, Ga, and Cr.
- Demonstrated that voltage fade is sensitive to Li-Ni-Mn-Co composition.
- Developed a statistical model relating composition to voltage fade to guide the selection of compositions.
- Developed and deployed a graphically-oriented database to collect and organize the information generated by team members.

- Demonstrated LMR-NMC electrodes display at stable hysteresis - gap exists even after 70 day hold.
- Linked hysteresis and voltage fade phenomena.
- Proposed mechanism for electrochemical behavior based on reversible and irreversible transition metal ion migration.
- Created a new hypothesis on why this class of materials is able to achieve significantly higher capacity than others (i.e., 250 vs 175 mAh/g).

✧ ✧ ✧ ✧ ✧

Introduction

$xLi_2MnO_3•LiMO_2$ (M = Ni, Co, Mn) or LMR-NMC composite cathode materials currently receive world-wide attention as promising candidates for the next generation of high-capacity lithium-ion batteries. This class of materials is capable of delivering 250 mAh/g or more over extended cycling. However, in order to access such capacities these materials must first be 'activated' to high voltages (>4.5 V) to access lithium associated with Li_2MnO_3-like domains. During the activation process oxygen loss and transition metal (TM) migration and rearrangement have both been reported; after which, a continuous decay of the average voltage with cycling is observed. In addition, a large hysteresis in voltage is observed when cycling over the extended windows (~4.6 – 2.0 V) needed to obtain the desired capacities. Therefore, the decrease in energy output with cycling is accompanied by an overall energy-inefficiency. To date, no work, to our knowledge, has been directly aimed at understanding hysteresis in lithium-excess materials. This work begins an initial investigation into the hysteresis phenomenon in order to better understand the structural and chemical properties of composite materials as a function of lithium content and to explore possible correlations, if any, related to voltage fade.

We propose an integrated approach to solving this critical issue which involves a coordinated set of characterization and synthesis experiments designed to both understand the causes of voltage fade and then eliminate the problem. To do this we have formed a team of researchers to maximize the project's abilities in theory, materials development, characterization, cell level modeling, testing, scale-up and characterization.

Approach

Bring together a diverse technical team that will share data and expertise to "fix" voltage fade in the LMR-NMC cathode materials. This will be a single team effort (i.e., not multiple PI's working independently on the same problem).

- Definition of the problem and limitations of the composite cathode materials.
- Data collection and review of compositional variety available using combinatorial methods.
- Modeling and theory.
- Fundamental characterization of the composite cathode materials.
- Understand the connections between electrochemistry and structure.
- Synthesis.
- Post treatment/system level fixes.

Results

We have utilized the team approach to understanding and correcting voltage fade. We have aggressively down-selected projects and different approaches to the research. The results of the research program are broken into different sections and the conclusions are described in the following chapters. One major accomplishment is the inclusion of other research groups in both the characterization of the LMR-NMC materials (BNL, ORNL) and in the down select process (ORNL, NREL, JPL, LBNL). The voltage fade project represents a large volume of research which is covered in the following chapters: IV.C.2- IV.C.6.

Conclusions and Future Directions

The enhanced capacity available in the lithium manganese rich materials us unique in the lithium ion materials. In FY14 we will continue to develop the solution to voltage fade. Specific tasks are:

- Determine effect of "break-in" cycling on voltage fade and the final average voltage.
- Determine the effect that elemental composition has on voltage fade and the final average voltage after "break-in".
- Determine the nature of the synthesis and the dopants that change the rate of voltage fade in the lithium magnesium rich materials.
- Determine the source of the enhanced capacity in the LMR-NMC materials.
- Determine voltage fade phenomenon mechanism.
- Provide a solution to the voltage fade phenomena in the LMR-NMC materials.

V.C.2 Electrochemical Characterization of Voltage Fade in LMR-NMC Cells (ANL)

Daniel Abraham
Argonne National Laboratory

Collaborators:
Martin Bettge, Argonne National Laboratory
Yan Li, Argonne National Laboratory
Ye Zhu, Argonne National Laboratory
Qingliu Wu, Argonne National Laboratory
Kevin Gallagher, Argonne National Laboratory
Wenquan Lu, Argonne National Laboratory
Dennis Dees, Argonne National Laboratory
Ira Bloom, Argonne National Laboratory

Start Date: October 2012
Projected End Date: September 2014

Objectives

- The primary objective of the work is to enable the Argonne high energy composite layered cathode $xLi_2MnO_3•(1-x)LiMO_2$ (M = Ni, Mn, Co), also referred to as lithium and manganese rich NMC material (LMR-NMC), for the 40-mile PHEV (PHEV-40) application.
- Increase understanding of electrochemical behavior of LMR-NMC electrode materials.

Technical Barriers

The primary technical barriers to the development of a high energy density battery for EV and PHEV applications that is safe, cost-effective, and has long cycle life include:

- Interpreting complex cell electrochemical phenomena.
- Identification of cell degradation mechanisms.

Technical Targets

- By 2014, a PHEV battery that can deliver a 40-mile all-electric range and costs $3,400.
- Enabling LMR-NMC materials to a state of commercial adoption.

Accomplishments

- A protocol to measure and quantify voltage fade throughout cycling has been developed and applied to a wide variety of oxide electrode materials.
- Cycling protocols have been shown to impact voltage fade in LMR-NMC electrode materials and their effect has been quantified.
- A probable mechanism for voltage fade has been proposed and examined.

✧ ✧ ✧ ✧ ✧

Introduction

Energy density is an important characteristic of Li-ion batteries. For a given volume or mass, it determines, among other factors, the duration and range of the battery's operational autonomy and the cost of the battery pack. Unfortunately, the deliverable energy of practical Li-ion cells fades when repeatedly charged and discharged. This energy loss can typically be traced back to three major causes: chemical trapping and loss of mobile lithium within the cell, loss of available lithium-hosting sites, and rising cell resistances. Under certain conditions, there exists yet another mechanism which causes the cell's energy output to decrease: a continuous cycle-to-cycle decrease of the cell voltage, during charge and discharge. This decrease is typically associated with the drop in equilibrium voltage of the positive electrode, as observed for many Li-intercalating oxides. This phenomenon, occasionally referred to as "voltage fade" or "voltage decay," reduces the usable energy because the voltage of the cell integrated over the capacity equals the cell's energy. It also complicates state-of-charge (SOC) determination which is crucial to effective battery management.

Although varying degrees of voltage fade have been observed in a range of materials over the past years, several issues remain unaddressed. First, the actual physical mechanisms leading to voltage decay are largely unknown, although theories exist [1, 6]. Second, no comprehensive studies exist which establish structural and experimental conditions for voltage fade to occur. In fact, it is not even clear whether the impact of voltage fade is technologically significant. And last, no formal description of voltage fade and its measurement exists. Especially, the latter one is critically important to successfully address the other issues and to evaluate effectiveness of proposed strategies to mitigate this voltage decay.

Approach

Basic methodology. To track voltage fade, we calculate the average voltage for each charge and discharge. This is possible because the composition-dependent cell voltage *U(q)*, which continuously decreases throughout cycling, affects the measured average voltage $\bar{U}_{meas}$ via $\bar{U}_{meas} = E/Q = (1/Q)\int U(q)dq$, with E and Q being the total energy and capacity of the cell. To correct for the many polarization losses that affect *U(q)* and cause a difference between measured and true (i.e., near equilibrium) average voltages, we use an average cell resistance to obtain a resistance-corrected average voltage, $\bar{U}_{corr} = \bar{U}_{meas} - i\bar{R}$. (Note that a rise in cell resistance forces *U(q)* to increase during charge and to decrease during discharge.) This way, we can compute an average open-circuit electrode potential for the compositional region of interest for each charge and discharge. This is henceforth referred to as "corrected average voltage."

Materials. The material of prime interest in this voltage fade study is a structurally-integrated, Li- and Mn-rich layered metal oxide expressed as $Li_{1.2}Ni_{0.15}Mn_{0.55}Co_{0.1}O_2$, and as $0.5Li_2MnO_3 \bullet 0.5LiMn_{0.375}Ni_{0.375}Co_{0.25}O_2$ in the two-component notation. This material is denoted as "LMR-NMC" throughout the text. The LMR-NMC exhibits high oxide-specific charge- and energy-densities exceeding 250 Ah-kg_{oxide}^{-1} and 900 Wh-kg_{oxide}^{-1} when charged beyond 4.5V vs. Li^+/Li. Details regarding cell chemistry, electrode formulation, and average cell resistances are given in Appendix A1 for a set of standard baseline cells and "modified" cells. The modifications of the latter cells yield improved capacity retention and lower impedance rise in graphite-containing full-cells, as shown elsewhere [2 - 4]. Voltage fade is also studied for other oxide chemistries, such as $LiNi_{0.8}Co_{0.15}Al_{0.05}O_2$ (also known as NCA), $Li_{1.05}(Ni_{1/3}Mn_{1/3}Co_{1/3})_{0.95}O_2$ (also known as NMC), $Li_{1.2}Ni_{0.4}Mn_{0.4}O_2$, $Li_{1.2}Ni_{0.2}Mn_{0.6}O_2$, $Li_{1.2}Co_{0.4}Mn_{0.4}O_2$, and $Li_{1.2}Cr_{0.4}Mn_{0.4}O_2$. The latter five compounds are also structurally-integrated composites and can be expressed in the two component notion as $xLi_2MnO_3 \bullet yLi(M_a,Mn_b)O_2$ with M being Ni, Co, or Cr. The LMR-NMC, NCA, and NMC are obtained from commercial sources. The $Li_{1.2}Ni_{0.2}Mn_{0.6}O_2$, $Li_{1.2}Ni_{0.4}Mn_{0.4}O_2$ and $Li_{1.2}Co_{0.4}Mn_{0.4}O_2$ compounds are prepared by a coprecipitation method. The $Li_{1.2}Cr_{0.4}Mn_{0.4}O_2$ compound is prepared by a chemical solution route. Electrodes for electrochemistry experiments are prepared by coating an Al foil with a mixture containing the oxide, SFG-6 graphite, acetylene black, and PVDF binder (84:4:4:8 by weight).

Experimentally measuring and tracking voltage fade. Galvanostatic cycling is conducted in 2032-type coin cells (1.6 cm^2 area electrodes) with Li-metal counter electrodes. All cells contain a 1.2 M $LiPF_6$ in EC:EMC (3:7 by wt.) electrolyte (referred to as "Gen2 electrolyte") and a Celgard 2325 (a polypropylene–polyethylene–polypropylene trilayer) separator. The cells are assembled in an Ar-atmosphere glove box (O_2 < 10 ppm, H_2O < 1 ppm) and cycled at 30°C in an environmental chamber according to a cycling protocol specifically developed to track voltage fade. This protocol uses moderate cycling currents of 10 mA-g_{oxide}^{-1} (0.1 mA, ~C/25 rate) between 2.0 and 4.7V vs. Li^+/Li for the first charge/discharge cycle and 20 mA-g_{oxide}^{-1} (0.2 mA, ~C/12 rate) for subsequent cycles in the same voltage range. The lower current during the first cycle promotes adequate wetting of the electrode and complete electrochemical activation of the active oxide. From the second cycle onwards, the protocol also implements current interrupts to estimate resistances at various cell voltages during charge and discharge. The current is stopped for 10 minutes and the voltages are recorded before and after the stopping period to estimate the cell resistance (i.e., dU/dI). For the LMR-NMC material specifically, resistances are recorded at a total of six different voltages during charge and discharge. The resistance-corrected average voltage is then calculated in three steps:

1. Average charge and discharge voltages are calculated by dividing the total cell's energy by the cell's capacity measured at 4.7V after charging and at 2.0V after discharging.
2. Average charge and discharge resistances are calculated from three interrupts for charge and discharge (at 3.5V, 3.9V, and 4.3V during charge, and at 4.0V, 3.6V, and 3.2V during discharge).
3. Resistance-corrected average voltages are then calculated by subtracting the averaged "$i\bar{R}$" polarization losses from the measured average voltages.

For the other layered oxides, minor adjustments are made to the position of the current interrupts based on their capacity-voltage profiles. Tracking voltage fade in such a manner is reasonably fast and can be carried out during normal cycling. Some limitations of this methodology are discussed later in this report.

Results

Voltage fade of the LMR-NMC baseline material. Figure V - 67 shows charge and discharge profiles for the LMR-NMC baseline material. In Figure V - 67A, a gradual cycle-to-cycle drop of the charge and discharge profiles, along with a relatively small capacity loss, is apparent. In Figure V - 67B, the capacities are normalized for each half-cycle, showing this gradual drop in electrode potential more clearly. Both figures

also show "electrochemical activation" of the material as a ~4.5 V plateau during 1st charge. The mechanistic origin of this plateau is still being debated, but it is typically associated with irreversible structural changes of, and partial oxygen loss from, the active oxide. After activation, charge and discharge profiles become gradually sloped, over nearly the entire compositional region, electrochemically revealing dramatic changes to the local Li environments. The drop in voltage from 1st to 2nd charge is especially striking. Upon continued cycling, the profiles continue to drop to lower voltages. Note that the voltage decay during charge occurs *despite* a rise in average cell resistance that is caused by a degrading positive electrode [2, 4]. Hence, irreversible structural changes of the oxide are the origin of this potential change, and not cell-level charge transport kinetics. The measured cell resistances as a function of the interrupt positions and the corresponding average voltages are shown in the Figure V - 67B (inset table). Although the average resistances increase during cycling, some voltage-specific resistances can decrease (e.g., at 3.2 and 3.5V) because of state-of-charge (oxide-lithium-content) changes with cycling.

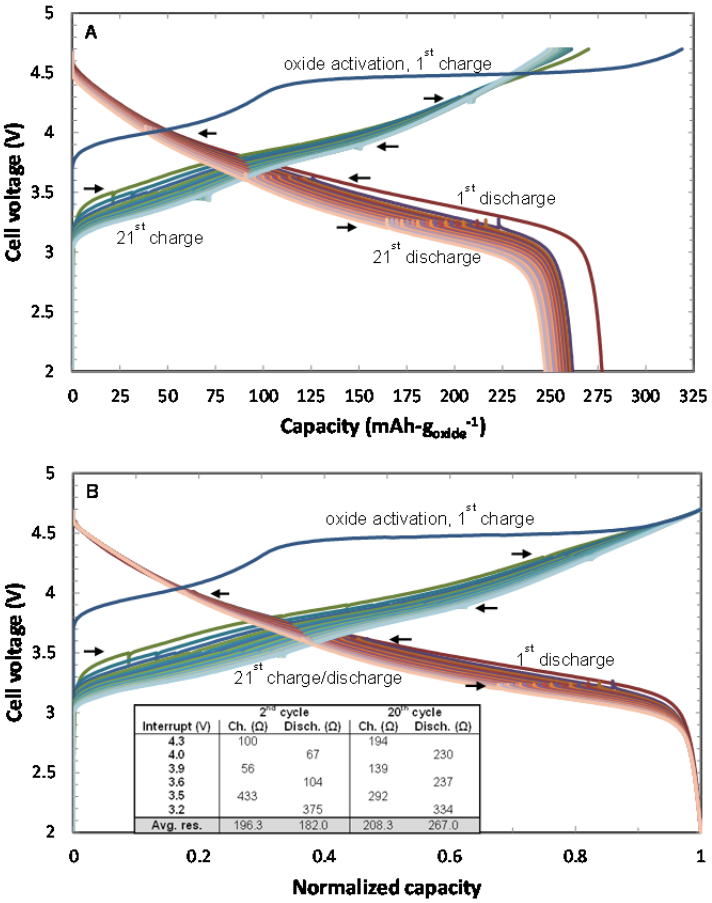

Figure V - 67: The first 21 galvanostatic charge/discharge cycles for LMR-NMC *vs.* Li in the 2.0-4.7V range at 30°C, as-measured (A) and capacity normalized (B). A depression of the voltage profiles is apparent for charge and discharge curves after capacity normalization. A capacity of unity refers to 319 mAh-g_{oxide}^{-1} (after 1st charge), 277 mAh-g_{oxide}^{-1} (after 1st discharge), and 248 mAh-g_{oxide}^{-1} (after 20th discharge). Black arrows indicate the positions of the six current interrupts used to calculate the average resistances. The inset table in the lower plot shows cell resistances as a function of the interrupt voltage for the 2nd and 20th cycle. fade

Figure V - 68 shows how voltage fade reveals itself in the differential capacity plots for charge and discharge. Here, the 1st cycle with its extensive activation plateau is removed to improve clarity. During the first 20 cycles after activation, the dQ/dV peaks between 3.0V and 3.5V shift down in charge voltage and grow at the expense of the higher voltage peak intensities (between ~3.8V and 4.7V) – a similar behavior is observed during discharge. As a result, the redox-active phase, initially located at ~3.5V (during charge), appears to simultaneously transform and grow into one or more redox-active phase(s). The differential capacity plots reveal also another characteristic of the material: a large hysteresis caused by a major

asymmetry between charge and discharge and by a relatively large voltage relaxation from 4.7V down to ~4.5V at the beginning of discharge. The voltage relaxation is partly caused by sluggish kinetics even at very low cycling currents.

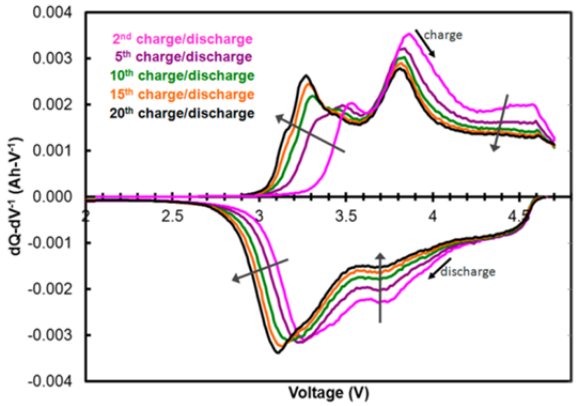

Figure V - 68: Differential capacity plots of the first 20 galvanostatic charge/discharge cycles after the initial activation cycle for LMR-NMC vs. Li over the 2.0-4.7V range at 30°C. The initial activation cycle is removed to highlight the changes that occur after activation. Increasing peak intensities and a shift to lower voltages at around 3.1V reveal voltage fade

Figure V - 69 depicts voltage fade as a drop in uncorrected and resistance-corrected average voltages. The average cell voltages are calculated for charge and discharge as described above. The nonzero average "$i\bar{R}$" polarization causes a difference of 30-70mV (at 0.2mA) between the uncorrected and corrected voltages; this polarization increases as cycling continues and cell resistance rises. A "voltage gap" between the corrected charge and discharge voltages of 240-300mV is the consequence of the material's intrinsic hysteresis. The corrected average voltages are not calculated during the 1st cycle because of uncertainties related to wetting of the electrode and structural changes of the oxide. Nevertheless, the abrupt drop in the uncorrected average voltage from 1st to 2nd charge, along with the difference between 1st charge and discharge, reflect the irreversible changes that occur within the material during its electrochemical activation. Upon continued cycling, a gradual decay in average voltage is clearly visible. For the first 20 cycles, the resistance-corrected average voltage drops by 185mV during charge and by 124mV during discharge which corresponds to a drop by ~3-5%, or, alternatively, to ~6-10mV per cycle. The difference in charge- and discharge-decay rates gradually reduces the initial voltage gap. The rate of decay is more rapid in the early cycles and continues nearly in a linear manner for at least 50 cycles under standard cycling conditions (not shown here).

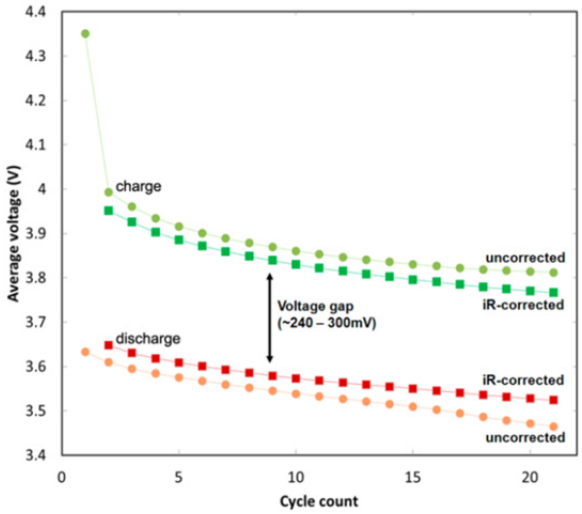

Figure V - 69: Average voltages, corrected and uncorrected, as a function of cycle number for the LMR-NMC *vs.* Li. Average voltages during charge are plotted in light/dark green, and those during discharge are plotted in orange/red. Voltage fade and voltage gap are apparent. Corrected average voltages drop by a total of 185mV during charge and by 124mV during discharge. Thin dotted lines are intended only as a guide to the eye, and are also shown in all subsequent figures

Additional measurements confirm the general voltage decay behavior and the overall effectiveness of the method. Figure V - 70 shows mean and standard deviation of the resistance-corrected average voltages for each cycle, for a total of five cells containing the LMR-NMC material. The standard deviation from the mean is always less than 7mV indicating very reproducible decay behavior with little cell-to-cell variability. On average, the voltage fade is 188mV (±11mV) during charge and 120mV (±1.6mV) during discharge between the 2nd and 20th cycle. Figure V - 70 also compares the corrected average voltages of a baseline cell (squares) to that of the modified baseline cell (diamonds). The modified cell contains the same active LMR-NMC material, but with 2.0 wt.% LiDFOB in the baseline electrolyte and a positive electrode with altered constituent ratios to mitigate the resistance increase of the positive electrode [2 - 4]. The average resistances of the two cell types during the 2nd and 20th cycle are given in Appendix A1; after 20 cycles the difference between the two types is large (~200Ω). Despite this large difference in average cell resistance, which would correspond to ~40mV at 0.2mA, the difference between the corrected average voltages remains small after 20 cycles (less than 14mV). Note also that the baseline cell shows voltage fade *during charge* despite a rise in average resistance; and that the modified cell shows voltage fade *during discharge* despite a decrease in average resistance. This shows that voltage fade and resistance effects can be effectively

decoupled using this approach of correcting the average voltage. Another important point here is that neither electrode formulation nor the addition of LiDFOB (which alters the surface films on the positive electrode) appear to affect the material's voltage fade in any significant manner. Another study, that used the same method to track voltage fade, confirms that surface modifications have no effect on the voltage fade [5].

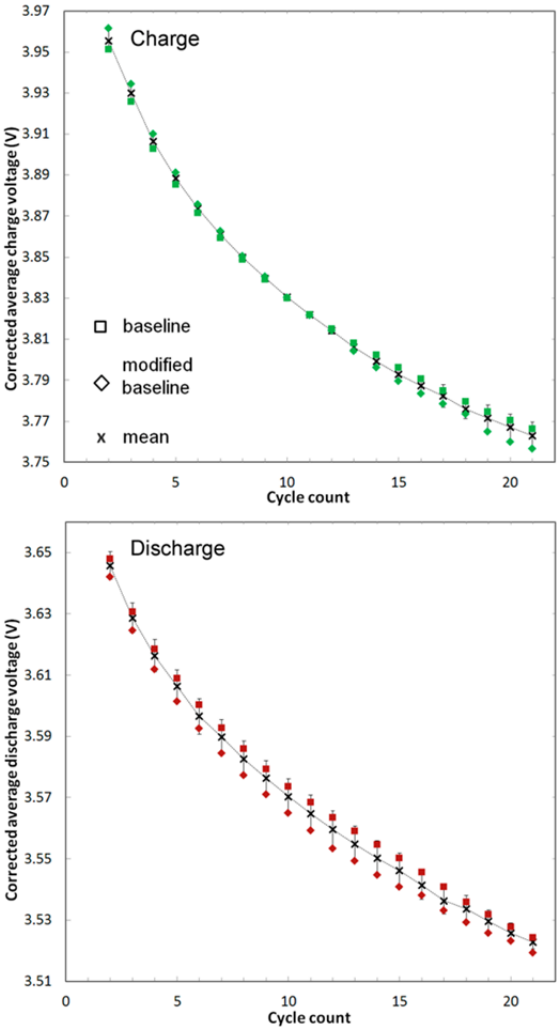

Figure V - 70: Mean and standard deviations, of the resistance-corrected average voltages during cycling, for five cells containing the same LMR-NMC oxide, top during chargem, bottom during discharge. The x-markers indicate the mean. The largest standard deviation from the mean, ±6.6 mV, is found after 21 cycles during charge. For comparison, square- and diamond markers indicate the average voltages for a baseline cell and for an improved baseline cell, respectively. The electrode formulation for the improved baseline cells is changed and LiDFOB is added to the electrolyte. As a result of these modifications, the cell resistance is much lower after 20 cycles

Figure V - 71 demonstrates the effect of voltage fade on energy density of the LMR-NMC cells. The measured discharge energies are shown as a function of cycle number for baseline and modified baseline cells. Assuming only a contribution from voltage fade (i.e., no capacity losses and no increase in cell resistance), the energy output continuously decays at a rate proportional to that in Figure V - 69 (as shown by the square red data points).

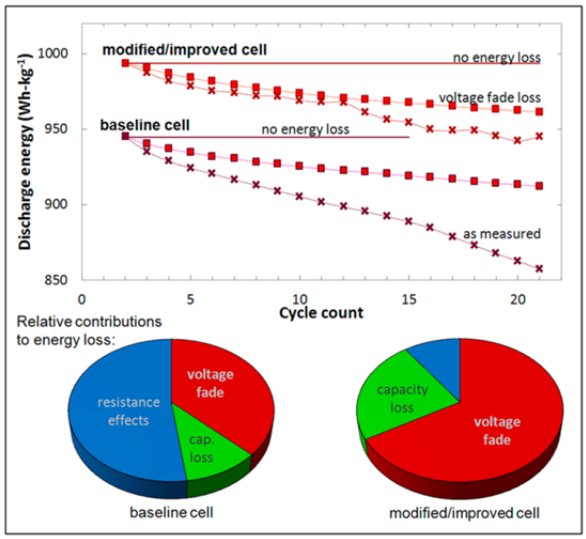

Figure V - 71: Discharge energies as a function of cycle number for the LMR-NMC-based baseline and modified cells. The cycling window is 2.0-4.7V. The measured energy densities for both cells are given by the x-shaped data points. Energy loss comprises contributions from capacity loss, resistance effects, and voltage fade. Energy loss only due to voltage fade is given by the squared data points. The relative contributions of capacity loss (green), resistance effects (blue), and voltage fade (red) after 20 cycles after activation are measured separately and plotted for each cell in the pie charts. Voltage fade is a significant contributor to the overall energy loss

In addition to voltage fade, capacity loss and resistance effects also cause the measured discharge energy to decrease; their physical origins have been identified and discussed elsewhere [2 - 4]. The relative contributions of these three factors leading to the difference between 2nd and 21st discharge energies are shown as pie charts in Figure V - 71. These charts are obtained by calculating the energy of the cell via $E(c) = \bar{U}(c)Q(c)$, with c being the cycle count and $E(c)$ the released energy upon discharge that decreases continuously throughout cycling. $\bar{U}(c)$ is the measured average cell voltage that decreases due to voltage fade and resistance effects; $Q(c)$ is the cell capacity that decreases due to resistance effects and *actual* loss in electrode capacity. This actual capacity loss is typically related to e.g., particle isolation and loss of active Li-hosting sites. The discharge energy after the 2nd

discharge is chosen to be the initial point of reference: it is 945 Wh-kg_{oxide}^{-1} for the baseline cell and 994 Wh-kg_{oxide}^{-1} for the modified baseline cell.

To obtain data for the pie charts, we first calculate the maximum contribution due to capacity loss by using the initial measured (i.e., uncorrected) average voltage, multiplied by the *actual capacity loss* after 21 cycles (i.e., resistance and voltage fade effects are excluded). This actual capacity loss is determined in a separate measurement in which a half-cell containing the oxide electrode is cycled under identical conditions and discharge capacities of the 2nd and 21st cycle are obtained. Here however, the 21st cycle discharge capacity is determined *after* Li counter electrode, separator, and electrolyte are replaced with fresh ones to minimize resistance effects from those components. Second, we calculate the minimum contribution due to voltage fade by using the above, separately determined, 21st cycle discharge capacity, multiplied by the *total drop* of the resistance-corrected average voltage after 21 cycles. Finally, cell resistance effects decrease both, the (uncorrected) average voltage and the measured capacity, and make up the remaining difference between initial and final energy densities.

Clearly, voltage fade is significant. In fact, once the increase in resistance is effectively mitigated through the improved cell design, voltage fade becomes the largest contributor (>65%) to the overall energy fade.

Factors influencing voltage fade of the LMR-NMC oxide. Experimental conditions affect voltage fade; some of these conditions are described below:

Cycling window: Upper and lower cut-off voltages affect the rate of fade. Figure V - 72 shows the corrected average discharge voltages for different upper cut-offs. Clearly, as the cut-off is raised, the voltage fades faster; at voltages less than 4.4V, fade is negligible. The impact of the lower cut-off was recently found to be more complex, as shown over a ~2-4V span by Gallagher et al. [1]. In that article, the largest degree of voltage fade is observed at a lower cut-off around 3.0-3.3V in combination with a 4.7V upper cut-off.

Temperature: Figure V - 73 shows that the corrected average voltages are also affected by temperature. They are ~40-70 mV lower at 55°C than at 30°C. The lower average voltages for charge *and* discharge at the elevated temperature exclude again any cell-level kinetics as a possible reason for this behavior. The cycling data also show that the rate of fade during charge is higher, and that the average voltage gap (between charge and discharge) is larger, at elevated temperatures.

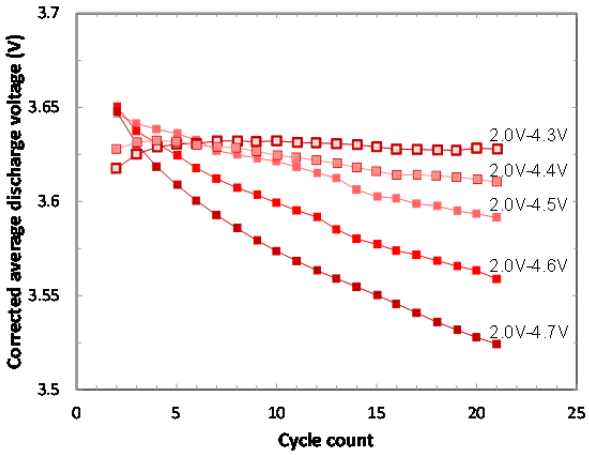

Figure V - 72: Effect of cycling window on the corrected average voltage and its fade during discharge for the LMR-NMC baseline material. For the first activation cycle, the cycling window is kept constant for all samples, i.e., 2.0V – 4.7V. During cycling, only the lower cut-off is kept constant at 2V. The degree of voltage fade increases as the upper cut-off increases. Voltage relaxation at the beginning of discharge down to ~4.5V forces the average voltage after the 2nd discharge to be nearly the same for the data sets with the three highest cut-off voltages

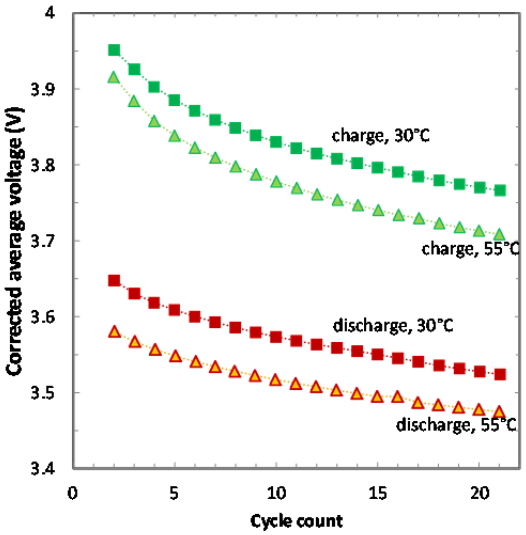

Figure V - 73: Effect of temperature on the corrected average voltages of the LMR-NMC baseline material under otherwise identical cycling conditions

Cycle life and calendar life: Figure V - 69 and Figure V - 70 show that the rate of fade is not constant throughout cycling; the highest rates occur during the initial cycles. Although the rate appears to slow down as cycling continues, ongoing studies have not yet identified a stable, or "final," voltage profile for the LMR-NMC oxide after 50+ cycles following the above protocol. Also, the rate of fade during extended galvanostatic cycling is larger than during potentiostatic

holds for identical time periods (for example, 4.7V *vs.* Li/Li^+) [1].

Voltage fade of selected layered oxides. Another factor influencing voltage fade is the oxide composition. Figure V - 74 and Figure V - 75 extend this study to other layered materials with varying lithium-to-metal ratios, including two which are currently being considered for commercial applications – $Li_{1.05}(Ni_{1/3}Mn_{1/3}Co_{1/3})_{0.95}O_2$ (NMC) and $LiNi_{0.8}Co_{0.15}Al_{0.05}O_2$ (NCA). Several Li-rich chemistries ($Li_{1.2}M_{0.8}O_2$, where "M" refers to any of the transition metals present) are also investigated. The exact cycling conditions for these materials follow the standard protocol given above, unless the material's potential window required adjustments of the current interrupts.

The left hand side of Figure V - 74 provides capacity-voltage profiles of the Li-rich chemistries over the 2.0-4.7V voltage range. The capacities are normalized to highlight the voltage decay. All materials show a 1st charge electrochemical activation near 4.5V, and display signs of voltage fade during subsequent cycles. Noteworthy is that the activation plateau for $Li_{1.2}Cr_{0.4}Mn_{0.4}O_2$ is slightly lower in voltage and more gradually sloped than that for the other materials, which probably results from irreversible structural changes. Note also the presence of a 2V plateau for $Li_{1.2}Ni_{0.4}Mn_{0.4}O_2$ upon 1st discharge, which indicates formation of a Li_2MO_2-like phase. This plateau disappears after the first three cycles, probably due to rising cell resistance on cycling that depress the feature below the lower (2.0V) cutoff voltage.

The right hand side of Figure V - 74 provides the corrected average voltages as a function of charge and discharge number. Again, all materials show voltage fade when cycled to 4.7V. The total drop in charge voltage after 20 cycles lies between 76mV and 191mV for $Ni_{0.4}Mn_{0.4}$ and $Co_{0.4}Mn_{0.4}$, respectively, showing that the rate of fade depends on the materials chemistry. It also depends on the stoichiometry, as seen for e.g., $Ni_{0.4}Mn_{0.4}$ and $Ni_{0.2}Mn_{0.6}$ which show a drop of 76mV and 144mV, respectively. Similar to LMR-NMC, the rate of fade for these materials is on the order of a few millivolts per cycles, ranging from approximately 4mV to 11mV per *charge* cycle. The rate of fade during *discharge* is slightly lower, approximately 1mV to 10mV per *discharge* cycle. Note that the initial average voltage of $Ni_{0.4}Mn_{0.4}$ rises during discharge because of the disappearance of its 2V plateau.

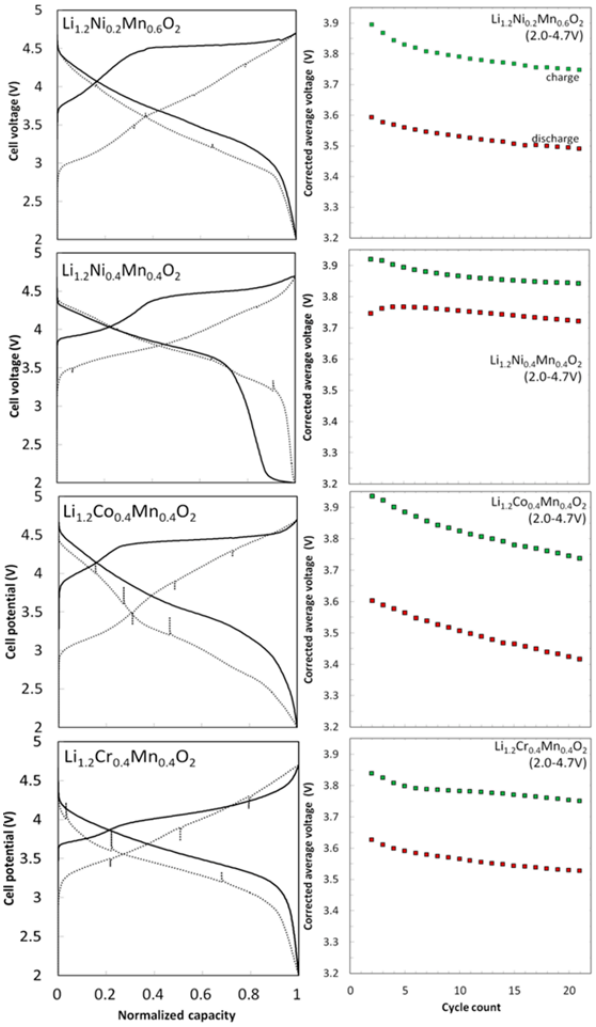

Figure V - 74: Voltage profiles and corrected average voltages as a function of cycle number for selected layered oxides. The cycling window ranges from 2.0V to 4.7V. On the left hand side, all capacities are normalized. The solid line shows the 1st ("activation") cycle; the dotted one the 20th cycle. On the right hand side, the top and bottom curves are the corrected average voltages during charge and discharge, respectively. All materials exhibit some degree of voltage fade if cycled to 4.7V *vs.* Li

Figure V - 75 provides normalized capacity-voltage profiles for NCA and NMC over two different cycling windows, 2.0-4.25V and 2.0-4.7V vs. Li/Li^+. The former range is depicted in the upper two panels of Figure V - 75, the latter one is depicted in the middle panels. To ensure comparable testing conditions, the first cycle is always from 2.0V to 4.7V. Practically, no voltage decay exists, for both materials during the lower voltage (4.25V) cycling, as the 2nd and 20th cycles are nearly identical. Some voltage fade is present at higher voltages (4.7V), although it is less than for the Li-rich chemistries described earlier.

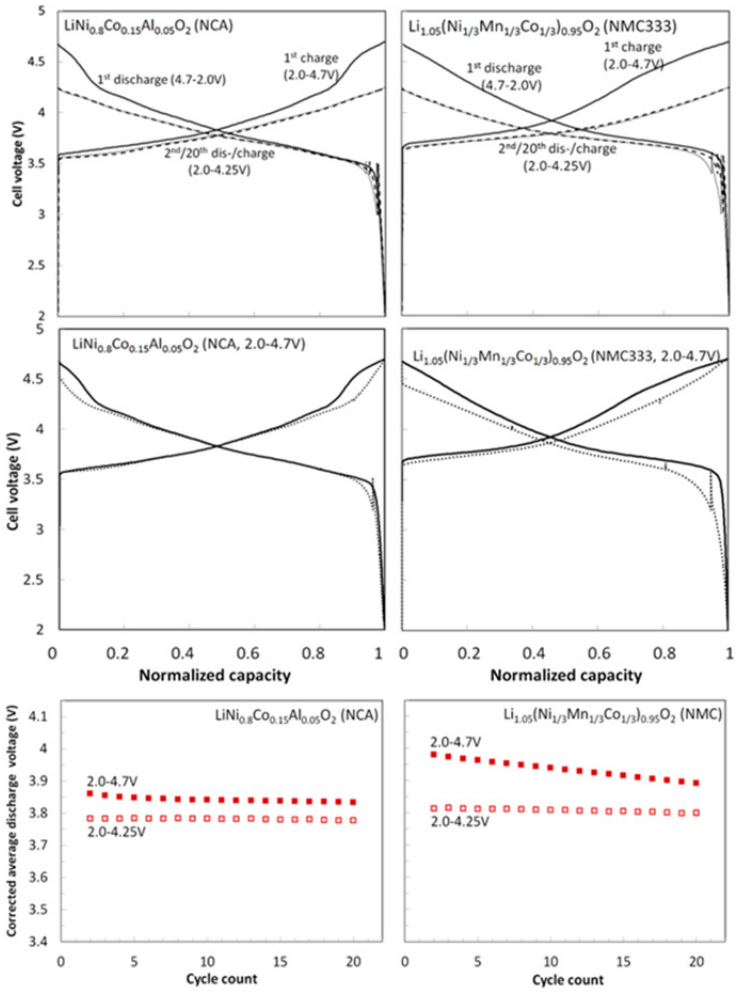

Figure V - 75: Voltage profiles and corrected average voltages as a function of cycle number for NCA and NMC. Both materials are cycled over two different voltage windows, 2.0-4.25V (top panels) and 2.0-4.7V (middle panels), with the first cycle *always* ranging from 2.0V to 4.7V. All capacities are normalized. The solid line shows the 1st cycle; the dashed one the 2nd (only shown for the 2.0-4.25V window); the dotted one the 20th cycle. The lower panels show the corrected average discharge voltages for the two voltage ranges. Both materials exhibit some degree of voltage fade only when cycled up to 4.7V *vs.* Li

The corrected average *discharge* voltages, depicted in the bottom panels, confirm that practically no change in average voltage occurs during the lower voltage (2-4.25V) cycling. When cycled to 4.7V, the *charge* voltage of NCA drops only by 8mV and that of NMC by 46mV; during *discharge* by 27mV and 88mV, respectively. Hence, the voltage gap widens for both materials.

Tracking voltage fade. As described above, a method to track (and quantify) voltage fade throughout cycling is to use a resistance-corrected average voltage. A standard testing protocol is proposed and demonstrated on several layered oxides under different cycling conditions. The advantages of our methodology are as follows: i) it facilitates data comparison through quantification, ii) it is reasonably fast (in comparison to e.g., lengthy galvanostatic intermittent titration technique, GITT, measurements), iii) it records the corrected average voltages for each cycle under the testing conditions of interest, and iv) it tracks simultaneously average and state-of-charge dependent cell resistances.

There are, however, some limitations with this methodology. For instance, voltage fade impacts different compositional regions in a different manner and mechanistic details are simply averaged out, as seen from Figure V - 68. Also, averaging effects, long relaxation times, and changes in the SOC cause a finite deviation from the "true" average resistance, and thus from the true equilibrium average voltage. The current interrupts implemented here are only 10 minutes, but relaxation and equilibration times on the order of hours can exist and have been observed for voltages >4.4V [2, 3]. And as the locations of the current interrupts are

voltage-controlled, state-of-charge changes are unavoidable because of decreasing electrode potentials (Figure V - 67B and table). Ultimately, all these effects can add up and induce a systematic error in the measurement of the corrected average voltage. This error propagates with $\delta\bar{U}_{corr} = i\delta\bar{R}$ and its upper bound can be estimated by taking $\delta\bar{R}$ to be on the order of $(1/2)(R_{max} - R_{min})$. For the LMR-NMC baseline cell, the biggest difference between R_{max} and R_{min} is measured during the first charge after activation, with 433Ω (at 3.5V) and 56Ω (at 3.9V). Such a difference would imply that the error is at most 40mV at 0.2mA. A more accurate prediction of the error is obtained through fitting the cell resistance as a function of capacity; integration and division by the total capacity leads to a capacity-weighted average resistance. Similar to the voltage-dependent resistance (e.g., reference [4]), the capacity-dependent resistance typically shows parabolic behavior for layered oxides. For the LMR-NMC oxide, the difference between this capacity-weighted and measured average resistance is around 50Ω or less, corresponding to an error of <10mV of the corrected average voltage. But regardless of the magnitude of this error, the rate of voltage fade is not, or at most only indirectly, affected by the experimental measurement of the average voltage.

Simply put, the combination of moderate cycling along with the resistance correction allows us to compute near-equilibrium values and voltage fade reproducibly (Figure V - 69 and Figure V - 70). Certainly, special attention to experimental parameters and cell conditions is warranted when data are compared. For instance, identical cells with varying internal resistances can show small differences in voltage fade, as cycling would occur over different SOC ranges, and structural transformations and cell-level kinetics can be very temperature sensitive. In addition, the number, location, and duration of the current interrupts may shift the computed average voltages, depending on material and actual cycling conditions. (Note: measurement accuracy can always be improved e.g., by lowering the current, and by increasing the number of current interrupts and their duration.)

Implications of voltage fade. For the LMR-NMC focused on here, voltage fade clearly worsens as upper cut-off voltages are raised to 4.7V *vs.* Li (Figure V - 72); and as the temperature is raised to 55°C, the initial fade rates and voltage gaps are more severe. Voltage fade will continue at a measureable rate of a few millivolts per cycle for quite some time before an expected stable voltage profile is achieved. And as the other materials share similar decay profiles, it is likely that the trends and behaviors observed for this oxide are in fact common to many other, if not all, layered materials.

Considering the above discussion, an obvious, yet complex, question arises – which oxide material yields the highest energy density during cycling? Among the materials we examined, LMR-NMC, NCA, and NMC exhibit the highest energy densities upon 1st discharge when cycled between 2.0-4.7V, justifying the technological interest in those materials. Of those materials, the LMR-NMC exhibits the highest energy density with more than 1,000 Wh-kg_{oxide}^{-1} on first discharge. Yet, finding the "winning material" is not as straight-forward. Voltage fade significantly lowers the energy density for the LMR-NMC (Figure V - 71), and is also measurably present for NMC at these high voltages. And at cycling voltages below 4.4V, voltage fade effects, along with increasing cell resistances, become negligible during early cycling.

Figure V - 76 provides some guidance in this regard. Here, the oxide-specific energy density of these three materials is examined over 20 cycles and two voltage windows (2.0-4.25V and 2.0-4.7V) after an initial, low current charge to 4.7V to ensure complete activation and comparable testing conditions. LMR-NMC is certainly a high voltage material with a oxide-specific energy density of around 950 Wh-kg_{oxide}^{-1} after 20 cycles for the wider cycling window; its energy drops to ~650 Wh-kg_{oxide}^{-1} when cycled to 4.25V. For NCA, this drop in energy is much less – its 20th cycle energy is lower and around 740 Wh-kg_{oxide}^{-1} when cycled to 4.7V, but it drops only to ~680 Wh-kg_{oxide}^{-1} when cut-off at 4.25V. At 4.7V, all three materials show energy fade; however, NCA and NMC show a more stable performance at 4.25V, with NCA having an energy output of more than 100 Wh-kg_{oxide}^{-1} higher than that of NMC. Therefore, based on an energy consideration alone, LMR-NMC is the material of choice for higher voltages. However, for lower voltage cycling, at which electrolyte oxidation and oxygen loss from the active material are less of an issue, NCA may provide higher energies and more stable performance.

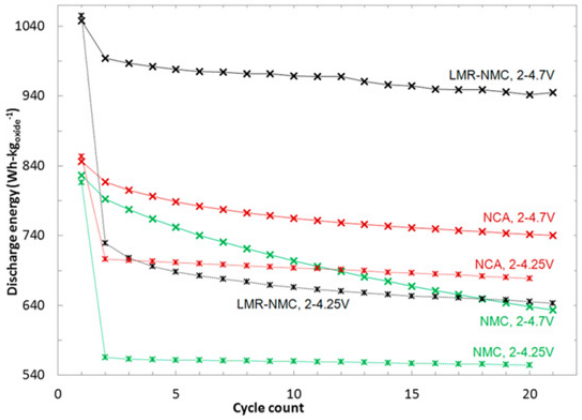

Figure V - 76: Discharge energies for LMR-NMC (embedded in the modified baseline cell), NCA, and NMC for two voltage windows (2.0-4.25V and 2.0-4.7V) as a function of cycle number. Note that all materials are charged to 4.7V *vs.* Li/Li$^+$ at 10 mA-g$_{oxide}^{-1}$ during the first cycle to ensure consistent testing among all materials and to ensure that the higher capacities of the LMR-NMC are accessed

Conclusions and Future Directions

It is clear that voltage fade reduces the energy density for a wide range of layered oxides as they are pushed to higher voltages to improve energy and power densities. A protocol to measure and quantify voltage fade throughout cycling is proposed, and applied to several materials demonstrating that this phenomenon is common for many layered oxides. Voltage fade can be effectively circumvented by choosing lower cut-off voltages and possibly reduced by choosing lower temperatures. Such cycling, however, is undesirable when higher energy and power densities are required. Voltage fade apparently results from irreversible changes that may involve the relocation of transition metals from the metal- into the Li-layer, ultimately leading to the formation of a spinel-like structural framework. To minimize such fade, irreversible transition metal migration needs to be inhibited and the layered structure needs to be stabilized to high voltages. Such stabilization is currently the subject of intense research at Argonne. To move forward, some unresolved questions will need to be addressed: What are the migrating species and what are their migration paths? What makes cation migration irreversible and could it be reversed (or accelerated)? Does the 1st charge cycle electrochemical activation of the oxides affect voltage fade and, if so, how? And, into what structure(s) do the layered oxides eventually transform into?

FY 2013 Publications/Presentations and References

1. K. G. Gallagher, J. R. Croy, M. Balasubramanian, M. Bettge, D. P. Abraham, A. K. Burrell, M. M. Thackeray, *Electrochem. Comm.* DOI: 10.1016/j.elecom.2013.04.022 (2013).
2. M. Bettge, Y. Li, B. Sankaran, N. Dietz Rago, T. Spila, R. T. Haasch, I. Petrov, D. P. Abraham, *J. Power Sources* **233**, 346 (2013).
3. Y. Zhu, Y. Li, M. Bettge, D. P. Abraham, *J. Electrochem. Soc.* **159**, A2109 (2012).
4. Y. Li, M. Bettge, B. Polzin, Y. Zhu, M. Balasubramanian, D. P. Abraham, *J. Electrochem. Soc.* **160**, A3006 (2013).
5. Bloom, L. Trahey, A. Abouimrane, I. Belharouak, H. Wu, Q. Wu, W. Lu, D. P. Abraham, M. Bettge, J. Elam, X. Meng, A. Burrell, C. Ban, R. Tenet, J. Nanda, N. Dudney, *submitted to J. Power Sources* (2013).
6. M. Bettge, Y. Li, K. Gallagher, Y. Zhu, Q.Wu, W. Lu, I. Bloom, D. P. Abraham, J. Electrochem. Soc., 160 (2013) A2046-A2055.

Appendix A1. Electrode chemistry and formulation for baseline cells and modified cells

	Baseline cells	Modified cells
Active positive material	86 wt.% $Li_{1.2}Ni_{0.15}Mn_{0.55}Co_{0.1}O_2$ (Toda HE5050)	92 wt.% $Li_{1.2}Ni_{0.15}Mn_{0.55}Co_{0.1}O_2$ (Toda HE5050)
Binder	8 wt.% PVdF (Solvay 5130)	4 wt.% PVdF (Solvay 5130)
Electrode additives	4 wt.% SFG-6 graphite (Timcal) 2 wt.% SuperP (Timcal)	4 wt.% C45 (Timcal)
Current collector	Al, 15 μm	Al, 20 μm
Active loading density of oxide	6.64 mg-cm^{-2}	5.89 mg-cm^{-2}
Electrode porosity	37%	36%
Laminate thickness	35 μm	26 μm
Negative electrode	Li metal	
Separator	25 μm thick (Celgard 2325)	
Electrolyte	1.2 M $LiPF_6$ in ethylene carbonate (EC) : ethyl methyl carbonate (EMC), 3:7 by wt.	
Electrolyte additive	none	2 wt.% LiDFOB
Avg. cell resistance for all cells; 2nd, 20th discharge cycle	184 Ω, 309 Ω	174 Ω, 120 Ω

V.C.3 Voltage Fade in the LMR-NMC Materials: Mitigation via Doping and Substitution (ANL)

Christopher Johnson

Argonne National Laboratory
9700 South Cass Avenue
Argonne, IL 60439
Phone: (630) 252-4787; Fax: (630) 252-4176
E-mail: cjohnson@anl.gov

VF Synthesis Team:
Abouimrane, Ali; Amine, Khalil; Belharouak, Ilias; Bloom, Ira D.; Chen, Zonghai; Croy, Jason R.; Lee, Eungje; Li, Yan; Lin, Chi-Kai; Long, Brandon R.; Slater, Michael D.; Thackeray, Michael M.; Vu, Anh D.

Collaborators:
ANL VF Characterization Team

Start Date: October 2012
Projected End Date: September 2014

Objectives

In this voltage fade (VF) synthesis project, our objective is to evaluate the structure-function property relationships in the 'layered-layered' composite LMR-NMC or Li-rich & Mn-rich NMC. The project involves conducting synthesis reactions to 1) help understand the mechanism of VF and 2) make new cathode materials that will mitigate VF. We take information from the VF project team and use it to help guide our synthesis efforts. We will also exchange knowledge with the VF team on the development of new materials or concepts that will counteract the VF. We will establish the chemistry occurring in the system which will help us address the mechanism of VF. The syntheses project effort is to make LMR-NMCs with modified compositions, dopants, substitutions and structures that promise low cost, good thermal stability and improved cycling stability.

There are a number of specific objectives of this study that include:

1) Use theory to guide the synthesis efforts.
2) Synthesize materials with variable Li, Ni, Mn, and Co compositions using a combinatorial approach.
3) Conduct doping study in order to evaluate its effect on VF.
4) Determine the effects of oxygen composition in LMR-NMC materials on VF.
5) Design and synthesize Li- and Mn-rich oxides with integrated structures, notably 'layered-spinel' materials, to counter the VF phenomenon.
6) Identify and overcome degradation issues.
7) Exchange information and collaborate closely with others in ABR's 'voltage fade' team.
8) Supply promising high-capacity cathode materials for PHEV cell build.

Technical Barriers

This project addresses the following technical barriers as described in the USABC goals [1, 2]:

- Cycle life
- Performance at ambient temperatures
- Low energy density
- Poor low temperature operation
- Abuse tolerance limitations

Technical Targets

The technical targets to meet at the end of the project are the following:

- PHEV specific energy targets (pack): 3.4 kWh (min) to 11.6 (max) [2].
- EV specific energy targets (pack): 80 (min) to 200 (max) Wh/kg [3].

To accomplish this we must develop a cell to meet the 40-mile PHEV goal (142 Wh/kg, 317 W/kg), a cycle life of 5,000 cycles, and a calendar life of 15 years.

Accomplishments

- Established a reliable sol-gel route to the syntheses of LMR-NMC and its variants.
- Evaluated the following dopants: Al , Fe, V, Ga, and Cr.
- Synthesized $Li_2M'O_3$ (M'=Mn, Sn) model compounds and studied their formation as a function of temperature from starting material compounds.
- Synthesized Li_2RuO_3 and variants to evaluate the electrochemical performance of materials that do not contain pure Mn.
- Determined the electrochemical properties of lithium-manganese-nickel-cobalt-oxide composite electrode structures in three component 'layered-layered-spinel' systems, prepared by lowering the lithium content of

'layered-layered' Li_2MnO_3●$LiMO_2$ materials (M=Mn,Ni,Co).

- Determined the effects of Co and Li_2MnO_3 content on 'layered-layered-spinel' electrode materials.
- Demonstrated that voltage fade is sensitive to Li-Ni-Mn-Co composition.
- Developed a statistical model relating composition to VF to guide the selection of compositions.
- Developed and deployed a graphically-oriented database to collect and organize the information generated by team members.

✧ ✧ ✧ ✧ ✧

Introduction

The LMR-NMC composite electrode structures offers the possibility of producing the highest capacity cathodes in the lithium-ion battery field today (~ 250 mAh/g). Argonne and the international lithium battery community have made considerable progress in understanding and optimizing these materials, their compositions and electrochemical properties. Argonne's deep experience and familiarity with a wide range of materials technologies will enable the team to explore the possibility of identifying and developing advanced cathode materials to meet the demanding performance requirements of transportation applications.

Present limitations of these cathode materials are 1) voltage fade on cycling, 2) a relatively poor rate capability, 3) high impedance, particularly at a low state of charge (SOC), and at low temperatures, and 4) poor cycling stability, notably at high temperatures, due to Mn dissolution. These performance limitations are attributed to poor electronic/ionic conductivity in the oxide bulk, and surface damage from repeated high-voltage cycling. It is now also established that these materials lose energy during cycling manifested by a drop in average discharge voltage. Coined 'voltage fade' or VF, this problem must be understood and corrected. It is likely (1) due to a slow change in phase during prolonged cycling, and (2) massive structural rearrangements on the Li_2MnO_3 component during the activation cycle on the first charge.

Approach

To address the limitations of xLi_2MnO_3•$(1-x)LiMO_2$ electrodes, several approaches were adopted:

1) Use compositional phase diagrams to design integrated 'layered-layered-spinel' structures and to stabilize the electrode to electrochemical cycling.
2) Use combinatorial synthetic methods to identify factors that contribute to voltage fade as part of a team effort. This part of the effort will investigate the effects of Li, Mn, Ni, Co and oxygen stoichiometries on the voltage fade phenomenon. One-hundred, forty-seven compositions (see Table V - 8), spanning the low-cobalt portion of the Li_2MnO_3-$LiCoO_2$-$LiNiO_2$-$LiMnO_2$ phase diagram, were identified for investigation. Selected compositions were made by sol-gel methods for characterization (XRD, elemental analysis and electrochemical performance).
3) Focused on the domain structure of $Li_2M'O_3$, where M' is a tetravalent transition metal & Sn model compound.
4) Developed a sufficient synthesis method to reliably dope the composite xLi_2MnO_3•$(1-x)LiMO_2$ with various ad-cations, and then evaluate the VF response.
5) Elucidated the causes of voltage decay by investigating both bulk and surface effects.

Table V - 8: Group numbers and compositions for the combinatioral type study

Group	Li	Ni	Co	Mn	Group	Li	Ni	Co	Mn
1	1~1.6	0.15	0	0.85	12	1~1.6	0.25	0.2	0.55
2	1~1.6	0.15	0.05	0.85	13	1~1.6	0.3	0	0.7
3	1~1.6	0.15	0.1	0.75	14	1~1.6	0.3	0.05	0.65
4	1~1.6	0.2	0	0.8	15	1~1.6	0.3	0.1	0.6
5	1~1.6	0.2	0.05	0.75	16	1~1.6	0.3	0.15	0.55
6	1~1.6	0.2	0.1	0.7	17	1~1.6	0.35	0	0.65
7	1~1.6	0.2	0.15	0.65	18	1~1.6	0.35	0.05	0.6
8	1~1.6	0.25	0	0.75	19	1~1.6	0.35	0.1	0.55
9	1~1.6	0.25	0.05	0.7	20	1~1.6	0.4	0	0.6
10	1~1.6	0.25	0.1	0.65	21	1~1.6	0.4	0.05	0.55
11	1~1.6	0.25	0.15	0.6					

Results

1. 'Layered-Layered-Spinel' Electrodes. Studies of 'layered-layered-spinel' materials were conducted by synthesizing twelve compositions of (1-z)[(x)Li_2MnO_3●(1-x)$LiMn_yNi_yCo_{1-2y}O_2$]●zLiM''_2O_4 system, where the portion of spinel is LiM''_2O_4. To promote good homogeneity of the transition metals, these samples were synthesized using the oxalate co-precipitation method. By exploring material compositions with a lower Li_2MnO_3 content, this will, in turn, promote growth of the spinel component (less Li/M ratio).

Experiments were done to evaluate the performance of these 'layered-layered-spinel' composite materials. Accordingly, one would expect less capacity on cycling and a lower voltage response due to the spinel character below 3 V in the cell, but the presence of spinel will improve the first-cycle coulombic efficiencies. Capacity versus cycle number from cycling the material between 4.45 and 2.0 V at 15 mA/g, following a formation cycle protocol are shown in Figure V - 77.

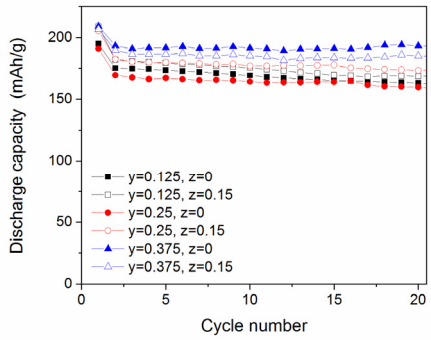

Figure V - 77: Specific capacity as a function of cycle number for the (1-z)[(x)Li_2MnO_3●(1-x)$LiMn_yNi_yCo_{1-2y}O_2$]●zLiM''_2O_4 system. The color markers and different shapes represent the different compositions studied

To follow-up this result, experiments were conducted to evaluate the electrochemical performance of higher xLi_2MnO_3 content compositions. Figure V - 78 shows the specific capacities upon discharge for such compositions studied (4.45 to 2.0 V, 15 mA/g). Increasing the Li_2MnO_3 content increases the capacity for all compositions, but with an apparent slight loss in stability.

Of particular interest are the dQ/dV plots of cells with different Li_2MnO_3 contents and associated spinel contents. Figure V - 79a shows the dQ/dV on the 2nd cycle and Figure V - 79b shows the dQ/dV on the 20th cycle. The dashed lines represent a larger content of Li_2MnO_3 and this result in a significantly larger amount of activity below 3.5 V when compared to the lower content Li_2MnO_3 samples. The tradeoff in capacity attained and average voltage is crucial to energy density and needs to be optimized with consideration of structural stability. Figure V - 79b shows the dQ/dV on the 20th cycle for all samples. The higher Li_2MnO_3 samples show a shift to lower voltages in the 2.5 – 3.5 V region, indicating voltage fade, and thus a loss in energy density. The lower content Li_2MnO_3 samples reach a more stable state with higher voltage activity, which results in a more stable energy density.

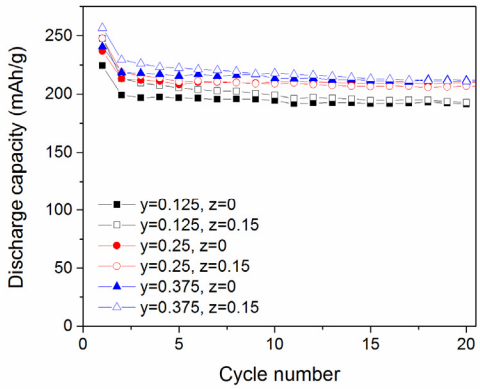

Figure V - 78: Specific capacity as a function of cycle number for the (1-z)[(x)Li_2MnO_3●(1-x)$LiMn_yNi_yCo_{1-2y}O_2$]●zLiM''_2O_4 system. The color markers and different shapes represent the different compositions studied

We can conclude that the addition of spinel into the composite improves the electrochemical performance for all samples, relative to the 'layered-layered' composition.

To obtain a deeper understanding of the composite structure, detailed structural analyses of 'layered-layered-spinel' composite electrodes have been undertaken at ANL's Advanced Photon Source (APS). Peaks that are representative of Li_2MnO_3 (C2/m), $LiMO_2$ (R-3m), and LiM''_2O_4 (Fd3m) structures are seen. The data suggests the formation of a complex structure with all three components integrated, but given the close similarity that can exist in the XRD patterns of cubic-close-packed layered and spinel lithium metal oxides, it is not surprising that low spinel content makes it difficult to distinguish layered and spinel components from one another with this technique. Detailed refinements of the data are underway.

2. Combinatorial Type Work.

Phase Relationships. The XRD patterns of oxides in the Li_2MnO_3-$LiCoO_2$-$LiNiO_2$-$LiMnO_2$ phase diagram are very similar and the phase relationships are complex. For example, Figure V - 80 shows the XRD patterns of $LiMO_2$ (R-3m space group), Li_2MnO_3 (C2/m), and spinel (Fd3m) phases. From the figure, these patterns are very similar, but can be distinguished using high-energy, synchrotron X-rays with their higher spatial resolution.

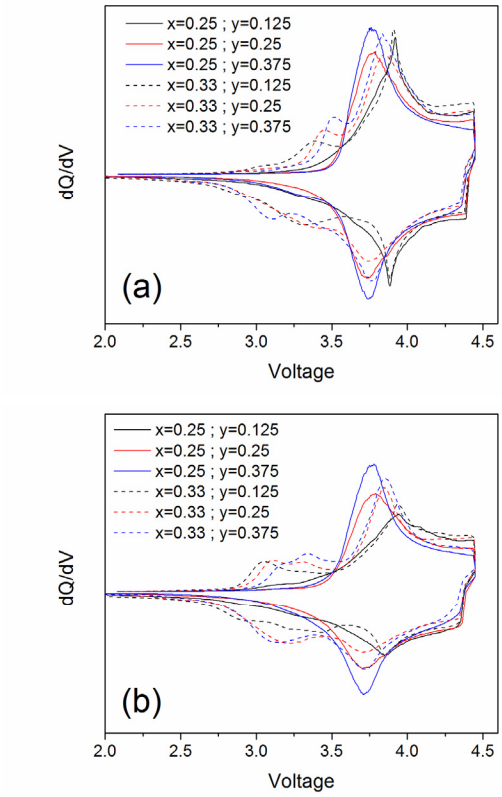

Figure V - 79: Specific capacity as a function of cycle number for the (1-z)[(x)Li_2MnO_3●(1-x)$LiMn_yNi_yCo_{1-2y}O_2$]●zLiM'_2O_4 system. The solid and dashed color lines represent the different compositions studied

The phase distribution was sensitive to lithium concentration. As shown in Figure V - 81, the intensities of the reflections associated with the spinel component were reduced with increasing lithium concentration. Additionally, the reflections due to Li_2MnO_3 (C2/m) and $LiMO_2$ (R-3m) were broadened, shifted, and, eventually, merged into each other. The data may indicate that interphase of domains of Li_2MnO_3 (C2/m) and $LiMO_2$ (R-3m) exist in the composite material as the domain sizes are reduced and become more integrated.

Voltage Fade. All cycling was performed at room temperature. All cells were cycled between 2 V and 4.7 V at 10 mA/g for the first cycle, and then between 2 V and 4.7 V (vs. Li^+/Li) at 20 mA/g for the following cycles. The cells were cycled between 2 and 4.7 V for a minimum of 20 and a maximum of 50 times. While cycling, current interrupt measurements were carried out at 3.5, 3.9, 4.3, and 4.7 V during charge and at 4.0, 3.6, 3.2, and 2.0 V during discharge. This is shown in Figure V - 82.

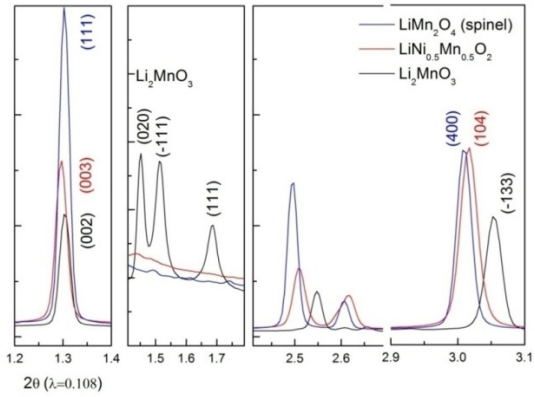

Figure V - 80: Example XRD patterns of the materials indicated in the legend

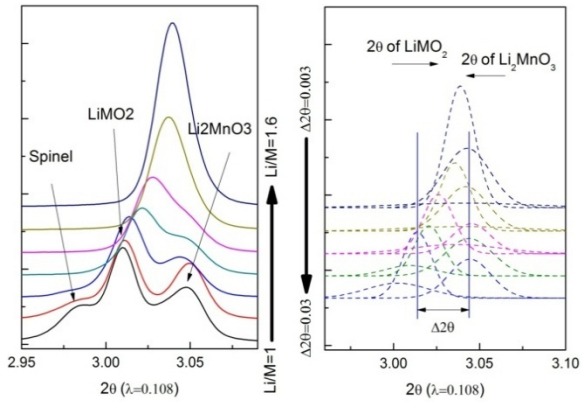

Figure V - 81: XRD patterns showing the effect of lithium:metal ratio. With more lithium, the difference between the peaks decreases

Estimates of cell resistance were calculated from the values of cell voltage and current at times t_0 and t_1 using Eq. 1.

$$R = \left|\frac{v_{t_1} - v_{t_0}}{i_{t_1} - i_{t_0}}\right|, R = \left|\frac{v_{t_1} - v_{t_0}}{i_{t_1} - i_{t_0}}\right|, \quad \text{Eq. 1.}$$

where v_{t_1} and v_{t_0} are the cell voltages at t_1 and t_0, respectively; i_{t_1} and i_{t_0} are the respective currents.

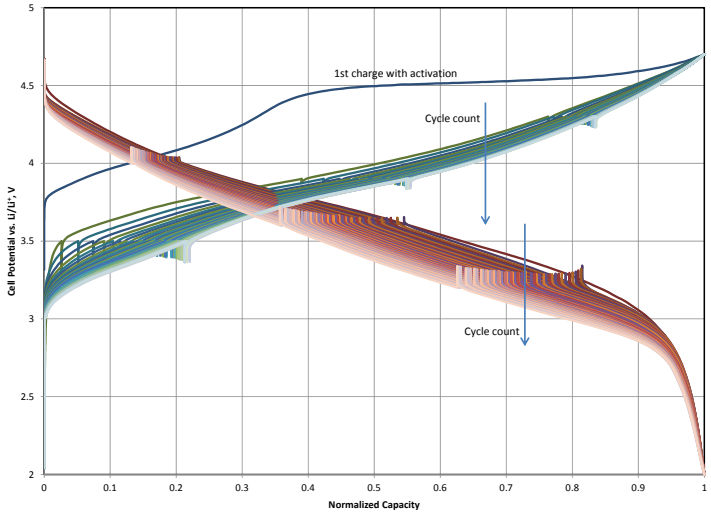

Figure V - 82: Cell potential vs. normalized capacity. The upward (discharge) and downward (charge) ticks in each curve represent the current interrupts

The activation charge subcycle and the discharge immediately following it were omitted from further analysis in this work. After that subcycle, the energy (Wh) and capacity (Ah) values were either extracted directly from the cycling data or were calculated from the raw data using Microsoft Excel®. The average voltage for a given charge or discharge subcycle was calculated as Wh/Ah. The resistance values at the first three voltages were averaged and used to correct the average voltage value for the average resistance of the cell during a given cycle. The relative change in the iR-corrected average voltage was calculated by comparing the value from the first discharge or charge subcycle to the respective value at the 20th discharge or charge subcycle, as shown in Eq. 2.

$$Rel.\,change\ in\ avg.voltage = \frac{Avg.voltage_0 - Avg.voltage_{20}}{Avg.voltage_0} \qquad \text{Eq. 2.}$$

These relative average voltage values (hereafter called ΔAvgV) then were used for plotting and subsequent analyses.

Figure V - 83 shows the effect of composition on ΔAvgV. From this figure, composition has a definite impact on the rate of change in ΔAvgV and to its final value. For example, compositions 5-G, 6-G, 7-G, and 8-G, have lower values of ΔAvgV than TODA HE5050. The ΔAvgV value for 5-G is about 85% of that of TODA HE5050.

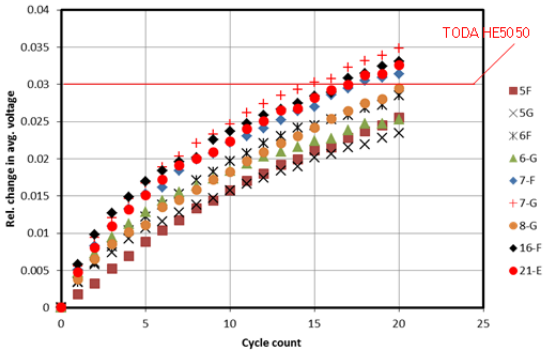

Figure V - 83: Relative change in average voltage vs. cycle count. The abbreviations in the legend reflect different Li, Mn, Ni, and Co stoichiometries. The composition of TODA HE5050 is $0.5Li_2MnO_3 \cdot 0.5LiNi_{0.375}Mn_{0.375}Co_{0.25}O_2$

Simplex Modeling of ΔAvgV. Modeling was limited to those compositions that crystallize in the R-3m space group (layered-layered materials). The ΔAvgV data were treated by multiple linear regression analysis using the cubic simplex equation for four-component mixtures, based on the work of Scheffé [3, 4]. The complete cubic equation is given below.

$Y=a_1x_1 + a_2x_2 + a_3x_3 + a_4x_4 + a_{12}x_1x_2 + a_{13}x_1x_3 + a_{14}x_1x_4 + a_{23}x_2x_3 + a_{24}x_2x_4 + a_{34}x_3x_4 + a_{123}x_1x_2x_3 + a_{124}x_1x_2x_4 + a_{134}x_1x_3x_4 + a_{234}x_2x_3x_4 + b_{12}(x_1 - x_2) + b_{13}(x_1 - x_3) + b_{14}(x_1 - x_4) + b_{23}(x_2 - x_3) + b_{24}(x_2 - x_4) + b_{34}(x_3 - x_4)$, where x_j is the mole fraction of the jth component and a_j are fitting constants.

Of the 26,333 possible solutions, candidate fits of the equation to the data must include the first four terms; use the fewest number of terms; have a high value of r^2, typically greater than 0.98; and have low RMS error. With the current data, a candidate fit was found using just the first four terms. Figure V - 84 shows some of

the result from fitting, plotted as a constant-concentration contour diagram.

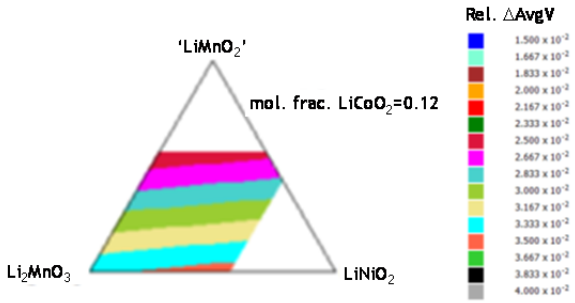

Figure V - 84: Example of some of the results from fitting a four-term polynomial to the ΔAvgV data

This model will be used to help select compositions for further study. As more data are generated, they will be used to refine the model.

3. Synthesis of $Li_2M'O_3$ Model compounds.

It is believed that the structural stability of delithiated Li_2MnO_3 has direct/indirect contribution to the voltage fade of LMR-NMC. In this portion of our work, we attempt to modulate the electrochemical properties of $Li_2M'O_3$ domain (M=transition metal) by doping Mn with Sn, which has more covalent bonding behavior. Figure V - 85(a) and Figure V - 85(b) shows a contour plot of *in situ* high-energy XRD patterns during solid state synthesis of Li_2MnO_3 and Li_2SnO_3, respectively, $Li_2M'O_3$ monoclinic-type structure can be formed for both Mn and Sn. In addition, the super-diffraction peaks for Li_2SnO_3 are much stronger than those for Li_2MnO_3, indicating less stack fault exists in Li_2SnO_3. The challenge for this work is that the *c* value of Li_2SnO_3 is much larger than that of Li_2MnO_3. Hence, we anticipate difficulty in incorporating Li_2SnO_3 directly into the composite materials to form $(1-x)Li_2SnO_3 \cdot xLiMO_2$. Alternatively, we will try to solve this issue by doping Sn into Li_2MnO_3 to (1) modulate the stacking fault in Li_2MO_3 component, and (2) obtain an optima *c* value for integration of Li_2MO_3 in LMR-NMC materials.

Moving forward on $Li_2M'O_3$ model compounds; in the previous annual report we focused on the domain structure of Li_2MnO_3 as the $Li_2M'O_3$ model compound. We used acid-treatment to convert the layer stacking from O3 to P3. It is possible to readily convert P3 to P2 then O2 and thus ultimately we want to synthesize an O2-$[xLi_2M'O_3 \bullet (1-x)LiMO_2]$ composite phase that won't convert to spinel. Recent theory work by Benedek and Iddir (2013) suggests that if the M' in $Li_2M'O_3$ can achieve an oxidation state above 4+, then it may be possible to eliminate the voltage plateau and avoid the massive structural rearrangement of $xLi_2M'O_3 \bullet (1-x)LiMO_2$ to a generic O3- $Li(M_{1-z}M'_z)O_2$ layered phase that is capable of converting to spinel during cycling .

As an electroactive compound, we chose Li_2RuO_3, that has the same crystal structure as Li_2MnO_3 and can achieve oxidation states above Ru(IV). Note that in these Li_2MnO_3 materials the oxidation of Mn(IV) is at a prohibitively high voltage and is not expected to occur. Li_2RuO_3, $Li_2Zr_{0.1}Ru_{0.9}O_3$ and $Li_2Mn_{0.5}Ru_{0.5}O_3$ were synthesized by a combustion method to ensure single phase products. The electrochemistry of these materials is shown in Figure V - 86, along with Li_2MnO_3 as a comparison. Briefly the Li_2RuO_3 compound shows no pronounced flat voltage plateau during Ru oxidation which supports the supposition that redox active M' elements will add capacity but not experience a phase change. It still remains to be seen from XRD analysis if this is the case. The mixed $Li_2Mn_{0.5}Ru_{0.5}O_3$ has a plateau that is shorter and a lower voltage than Li_2MnO_3. Thus, $Li_2Mn_{0.5}Ru_{0.5}O_3$ may be written as a composite: $0.5Li_2MnO_3 \bullet 0.5Li_2RuO_3$. The capacity expected from removal of two lithiums is approximately 340 $mAhg^{-1}$; nearly identical to what is experimentally observed. Finally, the voltage does fade (average discharge voltage change with cycle number; not shown) for $0.5Li_2MnO_3 \bullet 0.5Li_2RuO_3$ but the mechanism of fade appears different than conventional $xLi_2M'O_3 \bullet (1-x)LiMO_2$ (M'=Mn; M= Ni, Mn, and Co), that suggests that electroactive M' plays a role in altering VF. Theory has suggested other electroactive M' elements such as V, Cr, and Mo that have a similar ionic radii and coordination number as Mn, and energetically, prefer to form the monoclinic $Li_2M'O_3$ C2/c instead of $LiMO_2$ rhombohedral R-3m. To this end we have preferentially doped $xLi_2M'O_3 \bullet (1-x)LiMO_2$ (M'=Mn; M= Ni, Mn, and Co; TODAHE5050 based) with V, Cr. Fe, Ga, and Al.

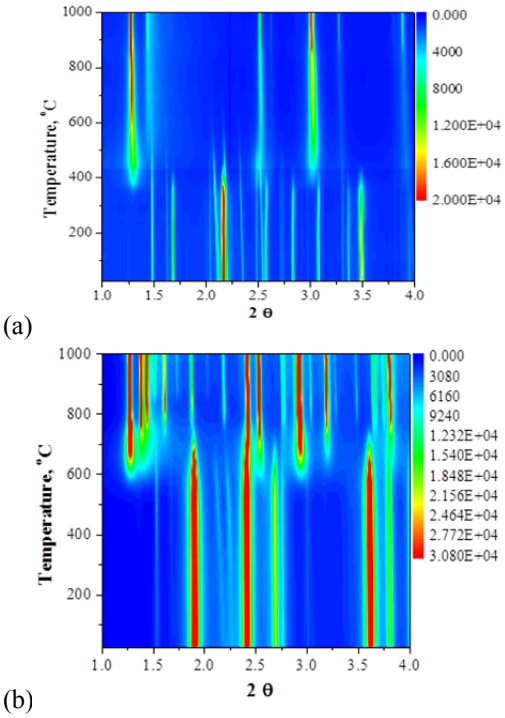

Figure V - 85: (a) Contour plot of *in situ* high-energy XRD patterns during solid state synthesis of Li_2MnO_3. (b): Contour plot of *in situ* high-energy XRD patterns during solid state synthesis of Li_2SnO_3

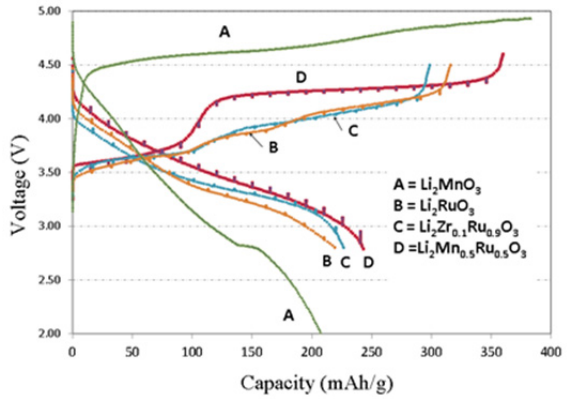

Figure V - 86: Li/$Li_2M'O_3$ cells

4. Doping into $xLi_2M'O_3 \bullet (1-x)LiMO_2$.

As this synthesis project is directed by theory, we are making materials that DFT calculations suggest are useful compositions that can possibly retard VF. Doping may be a way to retard VF if the dopant can alter the path of structural degradation during the first charge in the parent phase. Our hypotheses contain four criteria: (1) strong bonding with oxygen is required, (2) the oxidation state of the dopant can go higher than 4^+ and is stable (mitigate O_2 loss), (3) the dopant can preferentially substitute for Mn in the Li_2MnO_3 domain which will alter the structure or size of the domain, and (4), it should form reversible dumbbell configuration with Li_{tet} during deep charge in order to maintain structural stability. Each dopant tried can fit into one of those classifications. To this end, we have synthesized compositions that contain various dopants using sol-gel methods that create homogeneous distribution of all cations. The dopants evaluated this past year were Fe, Ga, Al, V, and Cr.

First to properly dope into the composite 'layered-layered' material, we need to firmly establish the synthetic method to use. To this end we decided to choose sol-gel methods. We developed a consistent sol-gel synthesis route to make TodaHE5050 composition: $(0.5Li_2MnO_3 \bullet 0.5Li[Ni_{0.375}Mn_{0.375}Co_{0.25}]O_2)$ and that which would facilitate the bulk incorporation of dopant or substitution.

We compared the VF in a carbonate co-precipitated precursor reactant with the target Toda HE5050 product composition to that of the aforementioned sol-gel derived product with the same composition, with the goal being to see if the synthesis route changes the VF. As is shown in Figure V - 87, the synthesis method used did not change the result – VF is about the same with the results similarly fitted to a paralinear function. So, moving forward, we will use the sol-gel method to incorporate dopants and/or substitutions.

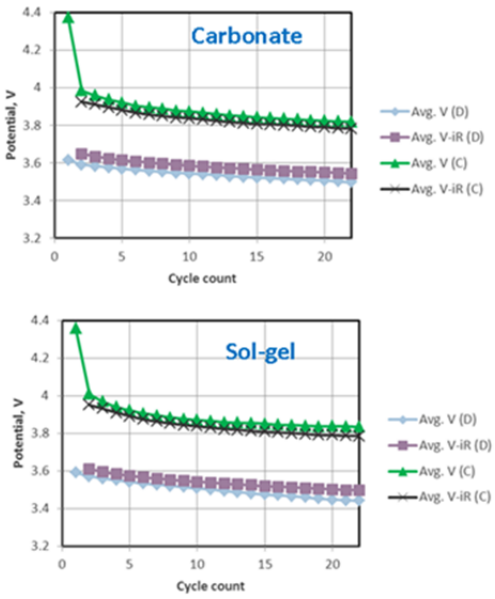

Figure V - 87: Voltage fade of $Li/0.5Li_2MnO_3 \bullet 0.5Li[Ni_{0.375}Mn_{0.375}Co_{0.25}]O_2$ (Toda HE5050 composition) cells

The Fe-doped $Li[(NMC)_{0.87}(Fe)_{0.013})]O_2$, was synthesized. The undoped and a Fe-doped (1.3%) materials show, by XRD, a pure layered phase, and the cycling resulted in approximately 265 mAh/g capacity.

However, the Fe-doping did not change the VF result (Figure V - 88).

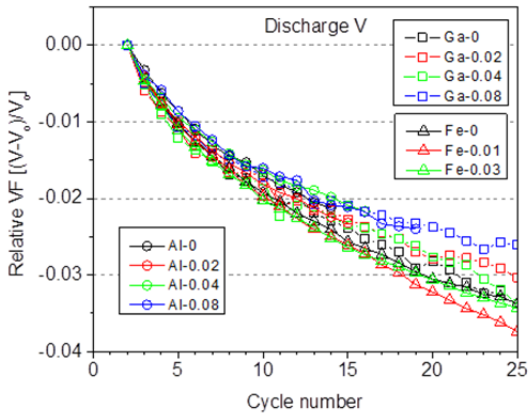

Figure V - 88: Al, Fe, and Ga-dopant VF curves

With increasing Al substitution, the Li-Mn ordering peak becomes broad thus indicating that the Al is doping into the structure, but at the high-end might be distorting or perturbing the Li_2MnO_3 domain. The lattice parameter of Al substituted samples showed almost no change. Also, the VF result as shown in Figure V - 88 is nominally the same as the Al-free sample, therefore indicating no beneficial effect of Al doping despite the chance that Al may sit in T_d sites in the structure.

Typically in the solid state, Gallium (Ga) is known to possess only one oxidation state of three and has been shown to move from O_h to T_d coordination in layered TM oxide phases during cycling. It may immobilize co-bonded cations in the surrounding second-shell T_d coordination sphere of the host phase, and can also act as a pillar effectively co-bonding the Li layer and keeping it intact at high states of charge. As a spectator ion, this could affect the Li_{tet} dumbbell reversibility. Figure V - 89 shows the data results from coin-cell cycling of the Ga-doped LMR-NMC. As is obvious, there is no beneficial effect having Ga in the structure. The VF still occurs. The capacity remains constant for low values of Ga, which is good sign of consistent electrochemical activity in the phase, however.

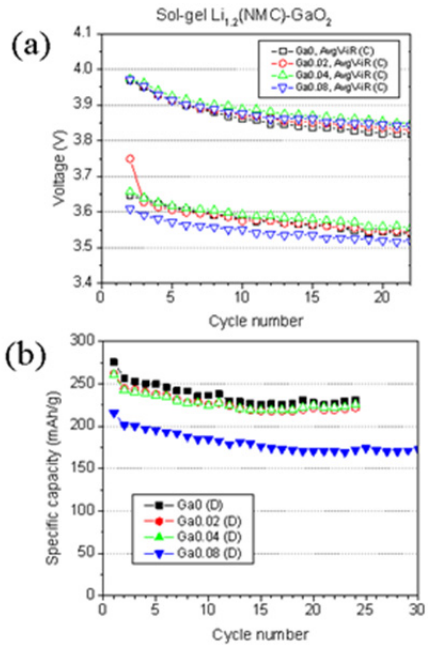

Figure V - 89: (a) Ga-dopant VF curves, and (b) capacity vs. cycle no

Vanadium (V) has a number of stable oxidation states from 2^+ to 5^+. It also can form a short apical bond with oxygen when it is in the 5^+ oxidation state that will actually distort the coordination sphere. Trivalent oxidation state is normally octahedral. Figure V - 90 shows the data from the syntheses of four different dopant levels for $Li_{1.2}Ni_{0.15}Mn_{0.55-x}V_xCo_{0.1}O_2$. As is evident, having V present causes a melting and sintering of the product. The melting is likely due to the formation of a stable lithium vanadium oxide such as LiV_3O_8 in air that creates a flux in the reaction. The product also has poor electrochemical cycling. Future work for doping of V will need to be conducted in inert atmosphere to stabilize the 3^+ V oxidation state. But this is problematic for the parent phase, as oxygen likely will be lost from the sample at high firing temperatures.

(a)

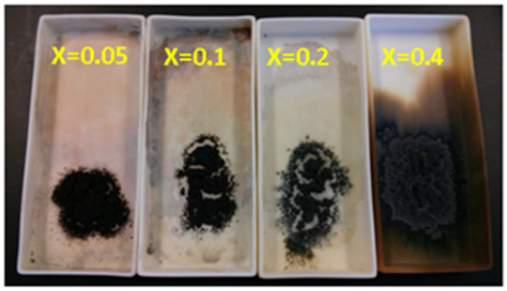

(b)

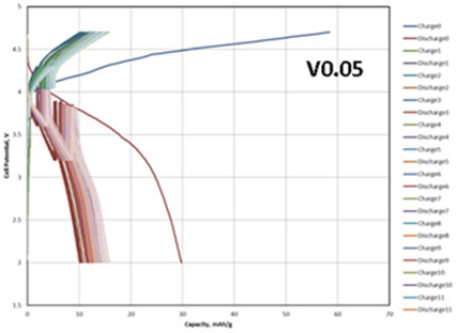

Figure V - 90: (a) Photo of V dopant fired samples. For composition value with x, see text. (b) Li/$Li_{1.2}Ni_{0.15}Mn_{0.50}V_{0.05}Co_{0.1}O_2$ coin cells

Chromium (Cr) doping is an interesting strategy to try since there is a possibility that Cr^{6+} may fill available T_d sites in the phase during first charge which in turn may change the mechanism of movement of other cations, like Mn. First, from the XRD patterns we find that single phases can be readily formed, likely with Cr^{3+}. The XRD peaks shift to lower angle with doping, indicating lattice expansion: the Cr cation radii is larger than the averaged sum of Ni^{2+} and Mn^{4+} radii (i.e., $R[Ni^{+2}_{1/4}Mn^{+4}_{3/4}]$=0.57Å, $R[Cr^{3+}]$=0.615Å). Li-Mn ordering peaks become stronger with a low degree of Cr doping (x = 0.05, 0.1). Figure V - 91 shows the result of cycling the Cr-doped cathodes in the first two cycles. What is interesting is that the first charge (activation) is dramatically altered. As Cr is increased, the plateau is shortened indicative of a change in the degree of oxygen loss in the resultant VF charged material. Cycling of this material continues and more work is needed to understand the role of Cr in the LMR-NMC and its mechanism.

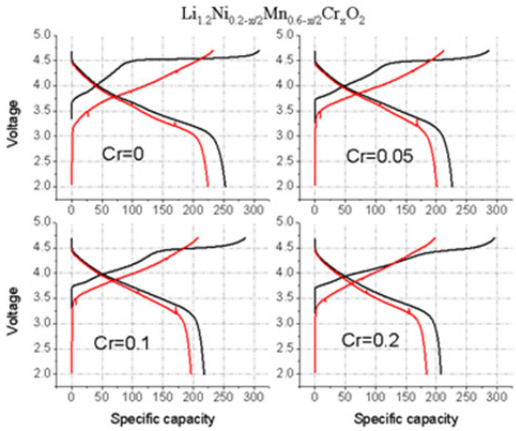

Figure V - 91: (a) Data result of cycling the Cr-doped cathodes. For composition value with x, see text. (b) Li/$Li_{1.2}Ni_{0.2-x/2}Mn_{0.6-x/2}V_{0.05}Cr_xO_2$ coin cells

Conclusions and Future Directions

1. 'Layered-Layered-Spinel' Electrodes.

- Lowering the Li_2MnO_3 content reduces low voltage activity (below 3.5 V) in composite structures, with a reduction in capacity.
- There is a tradeoff in capacity and voltage to optimize energy density that needs to be considered for high capacity lithium metal oxide cathodes.
- Structural analyses of 'layered-layered-spinel' composite electrodes are being conducted at the Advanced Photon Source to provide detailed structural insights before and after cycling.

The results obtained from this study are encouraging; they hold clues that may be used to advance the compositional and structural design of high capacity lithium metal oxide cathodes. This project will continue to further exploit, optimize, and characterize 'layered-layered-spinel' composite electrode structures.

2. Combinatorial Type Synthesis Study.

We have demonstrated that voltage fade, as quantified by ΔAvgV, is sensitive to composition. With a selected composition, we have decreased ΔAvgV to 85% of that of HE5050. A statistical model is being used to help guide the search for new compositions.

3. Synthesis of $Li_2M'O_3$ Model Compounds.

The use of $Li_2M'O_3$ model compounds (Mn, Sn, Ru, Mn-Ru, Zr-Ru) were synthesized with single phase. A comparison is made related to the *c* value axis and the potential ability to substitute into the lattice. An assessment of the electrochemistry of these materials was carried out and high capacities were recorded for Mn-Ru, Ru, and Zr-Ru. We intend to use these materials as a guide in understanding the synthesis of new phases

of 'layered-layered' composites, which ideally have little to no fade. Future work will focus on Zr-based materials, a much less expensive alternate to Ru.

4. Doping into $xLi_2M'O_3 \bullet (1-x)LiMO_2$

A sol-gel method for synthesis of doped and substituted composites was developed and refined. The electrochemical performance of the nominal composition that is the same as the Toda HE5050 formulation is equivalent to materials synthesized using a carbonate co-precipitated reactant.

Cationic dopants including, Fe, Al, Ga, Cr, and V all do not show an alteration in the VF response and have similar VF to the non-doped material. In future, we will terminate the cation doping study in favor of evaluation of anion dopants, such as fluoride or filling of possible oxygen vacancies (oxides O^{2-} anions) through synthesis of materials or annealing of materials strictly in an oxygen atmosphere.

List of Abbreviations

HEV: hybrid electric vehicle

PHEV: plug-in hybrid electric vehicle

EV: electric vehicle

USABC: United States Advanced Battery Consortium (DOE, GM, Chrysler and Ford)

XRD: x-ray diffraction

References

1. Battery Test Manual For Plug-In Hybrid Electric Vehicles, Rev. 1, June 2010, INL/EXT-07-12536.
2. Electric Vehicle Battery Test Procedures Manual, Rev. 2, June 1996.
3. H. Scheffé, J. Royal Statistical Soc. (B) 20 (1958) 344.
4. H. Scheffé, J. Royal Statistical Soc. (B) 25 (1963) 235.

FY 2013 Publications/Presentations

Publications

1. D. Kim, G. Sandi, J. R. Croy, K. G. Gallagher, S.-H. Kang, E. Lee, M. D. Slater, C. S. Johnson and M. M. Thackeray, *Composite 'Layered-Layered-Spinel' Cathode Structures for Lithium-Ion Batteries*. J. Electrochem. Soc. **160(1)**: A31-A38 (2013).
2. D. Kim, J. R. Croy and M. M. Thackeray, *Comments on Stabilizing Layered Manganese Oxide Electrodes for Li Batteries*. Electrochem. Comm. **36(0)**: 103-106 (2013).

Presentations

1. I. Bloom, et al., 2013 DOE Annual Peer Review Meeting Presentation.
2. C. Johnson, et al., 2013 DOE Annual Peer Review Meeting Presentation.
3. B. R. Long, J. R. Croy, D. Kim, K. Gallagher, Z. Chen, P. Chupas, K. Chapman, M. Suchomel, and M. M. Thackeray. *Development of High-Capacity Cathode Materials with Integrated Structures*. Annual Merit Review, Arlington, VA, May 13-17, 2013.
4. M. M. Thackeray, *Recent Developments in Lithium Battery Materials Research*, Presentations to Samsung SDI, LG Chem (Korea); Nissan Research Center, Toda Kogyo (Japan), 30 Aug-2 Sept (2013).
5. B. R. Long, J. R. Croy, and M. M. Thackeray. *'Layered*-Layered-*Spinel' Composite Electrodes for Advanced Lithium-ion Cathodes*. 6th International Conference on Advanced Lithium Batteries for Automobile Applications, Argonne, IL, September 9-11, 2013.

V.C.4 Structure-Activity Relationships for LMR-NMC Materials (ANL, ORNL)

Jack Vaughey, Jason R. Croy, Baris Key, Fulya Dogan, and Mahalingam Balasubramanian

Argonne National Laboratory
9700 South Cass Avenue
Argonne, IL 60439
Phone : (630) 252-9184 ; Fax : (630) 252-4176
E-mail: vaughey@anl.gov

Claus Daniel, Debasish Mohanty, David Wood III, Jianlin Li (ORNL)
Oak Ridge National Laboratory
One Bethel Valley Road
P.O. Box 2008, MS 6472
Oak Ridge, TN 37831
Phone : (865) 241-9521; Fax: (865) 241-5531
E-mail: danielc@ornl.gov

Collaborators:
Andrew Payzant, Ashfia Huq, Athena Sefa-Safat (ORNL)

Start Date: October, 2012
Projected End Date: September 2014

Objectives

- Characterize the local and long-range structure of pristine LMR-NMC materials.
- Understand cation ordering, how it changes with activation and cycling, and identify the associated structure-property relationships related to voltage fade (VF).
- Understand the critical role of lithium and manganese ordering in LMR-NMC with respect to electrochemical performance and voltage fade.
- Identify unknown electrochemical processes associated with the first-cycle activation, excess capacity, and irreversible capacity loss.

Technical Barriers

- Lack of a theoretical understanding of the voltage fade phenomena and its correlation with structural changes.
- Limited spectroscopic sensitivity to unidentified chemical and structural configurations which may occur in low concentrations and/or in disordered environments.
- Incomplete understanding of first-cycle charge compensation mechanisms and the associated structures.

Technical Targets

- Synthesis of LMR-NMC systems fully enriched with lithium-6 (enriched electrolyte, Li-metal and, cathode) for electrochemical characterization and quantitative, high-resolution ^{6}Li MAS NMR experiments.
- Design of novel experiments using synchrotron facilities such as the Advanced Photon Source (APS) at ANL and the spallation neutron source (SNS) at ORNL to gain new information on the atomic-level mechanisms of VF.
- Development of theory elucidating the spectroscopic signatures of defect configurations in LMR-NMC electrodes.

Accomplishments

- Electrochemical characterization of LMR-NMC cathode materials with fully lithium-6 enriched cells (enriched electrolyte, Li-metal and cathode) and quantitative high resolution ^{6}Li MAS NMR experiments on enriched, cycled materials.
- Study of cluster and domain sizes/morphologies with combination of ^{6}Li MAS NMR experimental data and theoretical calculations on paramagnetic NMR shifts and the effects on electrochemical performance
- Installation of a static probe to initiate additional *in situ* solid state NMR studies on related materials.
- Electrochemical characterization of electrochemically active, nano-Li_2MnO_3.
- X-ray absorption spectroscopy (XAS, XANES) of Li_2MnO_3 at various states of charge and discharge, complimentary to NMR studies, revealing the differences of the end-member Li_2MnO_3 relative to the "Li_2MnO_3 component" of LMR-NMC.
- SQUID and TEM investigation showing a direct correlation between cation-ordering and voltage fade in the TODA HE5050 LMR-NMC.

- Combined results from neutron diffraction (ND) and SQUID experiments reveal the structure of pristine TODA HE5050 as a composite between trigonal and monoclinic phase with ~3% inter-layer Li^{+}/Ni^{2+} exchange, providing complete crystallographic information needed to understand the structural changes related to voltage fade.

✧ ✧ ✧ ✧ ✧

Introduction

The ABR program has established a dedicated group to study the causes and propose solutions to the problem of voltage fade in composite lithium-rich cathode materials (LMR-NMC). While these high-capacity, high-energy materials offer attractive advantages over current, state of the art Li-ion chemistries, the issue of voltage fade has been identified as a potentially significant barrier to the success of this class of electrodes. The as-prepared composite materials undergo structural transformations on charge and discharge including changes in the Li-ion local structure and rearrangement of the coordinating cations. This rearrangement is believed to be directly related to the phenomenon of voltage fade. Within the ABR program, diagnostic, materials synthesis, and spectroscopy teams have worked to combine solid-state nuclear magnetic resonance spectroscopy (NMR) XAS, as well as X-ray (XRD), ND, and electron diffraction (SAED) to follow and understand these important and complex structural transitions.

Approach

Materials synthesis and spectroscopy will be combined to design and carry out experiments critical to the understanding of pristine structures, first-cycle processes and extended-cycling structural transformations.

- Characterize domain size in composite materials and how synthesis affects domain size and the subsequent voltage fade.
- Use theory to calculate NMR resonances assigned to domain boundaries.
- Study the critical role in VF of Li and Mn ordering (e.g., $LiMn_6$ units) in end-member Li_2MnO_3 and the integrated counterpart of LMR-NMC.
- Characterize and follow the evolution of cation ordering in pristine and cycled electrodes to gain further insight into structural transformations related to voltage fade.

Results

Characterization of Cathode Materials by Solid State NMR for High Capacity Li-ion Batteries (ANL). Solid state NMR techniques has been used for characterization of Li environments and local order present in Li-rich transition metal oxide cathode materials, correlating the lithium local environments observed with the electrochemical performance. With application of high resolution ^{6}Li MAS NMR spectroscopy we can study the local structural changes for different compositions of pristine and cycled baseline LMR-NMC materials and electrodes before and after activation.

Figure V - 92 highlights high resolution ^{6}Li MAS NMR data for the TODA HE5050 cathode material. Two groups of resonances were observed for the Li species present in the lattice; Li in Li layers around 500-800 ppm region and Li in transition metal layers around 1300-1500 ppm region. The deconvolution of the peaks observed for lithium in Li layers reveals at least five different lithium environments indicating different local ordering/domains and domain boundaries from Fermi-contact shifts of 1st and 2nd coordination shells of Ni, Co and Mn. For the octahedral lithium sites in transition metal layers, two main resonances at 1371 (Li coordinated to 5Mn) and 1475 (Li coordinated to 6Mn) ppm were observed. For the octahedral lithium sites in lithium layers, four ordered Lorentzian resonances and a disordered Gaussian resonance were observed. Apart from well characterized 735 ppm Li_2MnO_3-like domains, specific assignments of all these peaks are complicated. The peaks at 807 ppm, 594 ppm and 551ppm are tentatively assigned to various lithium 2nd coordination to a combination of transition metals and lithium cations. On the other hand, the significantly disordered Gaussian resonance(s) at approximately 600 ppm (green peak in deconvolution, 95 integral units, Figure V - 92) is assigned to domain boundary lithium that exist in the vicinity of two or more locally ordered domains. In order to study the effect of the domains and domain boundary resonances observed by ^{6}Li solid state NMR, a detailed NMR study was initiated on different composite materials synthesized under various reaction conditions.

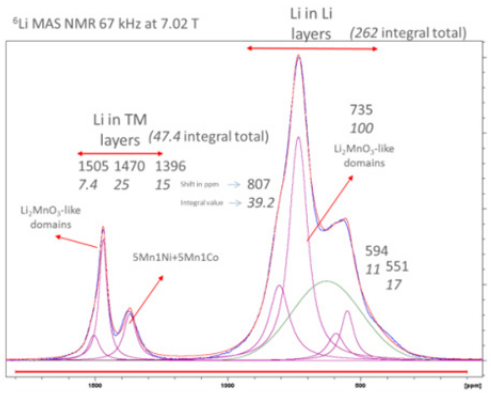

Figure V - 92: ^{6}Li MAS NMR of pristine TODA HE5050 composite $0.5Li_2MnO_3 \cdot 0.5LiMn_{0.375}Ni_{0.375}Co_{0.25}O_2$, or in layered notation, $Li_{1.2}[Ni_{0.15}Mn_{0.55}Co_{0.10}]O_2$

Figure V - 93 shows high resolution ^{6}Li MAS NMR data for the $Li_{1.5}[Mn_{0.5}Co_{0.5}]O_{2.5}$ composition. This composition is selected in order to utilize the calculation data from the theory group and to fundamentally study domain size effects on voltage fade. Two groups of resonances were observed for the Li species present in the lattice; Li in Li layers around 50-1100 ppm region and Li in transition metal layers around 1300-1500 ppm region. The deconvolution of the peaks observed for lithium in Li layers reveals many different lithium environments indicating different local ordering/domains and domain boundaries from Fermi-contact shifts of neighboring Co and Mn. The preliminary assignments for domain boundary lithium were confirmed in this study by varying the synthesis conditions (duration) from 1 hr to 84 hrs which is represented by a broad Gaussian resonance centered at 350 ppm. This resonance is gradually lost (intensity transferred to ordered Lorentzian peaks corresponding to specific Li-O-TM coordination) by increasing synthesis duration which presumably allows the small domains to coagulate, as dendritic branches of the composite structure to grow at high temperature. To be specific, the ratio of Li in domain boundaries to the total amount of Li in the sample is 0.68 for 1hr synthesis, 0.42 for 12hr synthesis and near to 0 for 84 hr synthesis. These deconvoluted Li intensities will be used by the theory group to estimate the average domain sizes/length-scales of the composite materials.

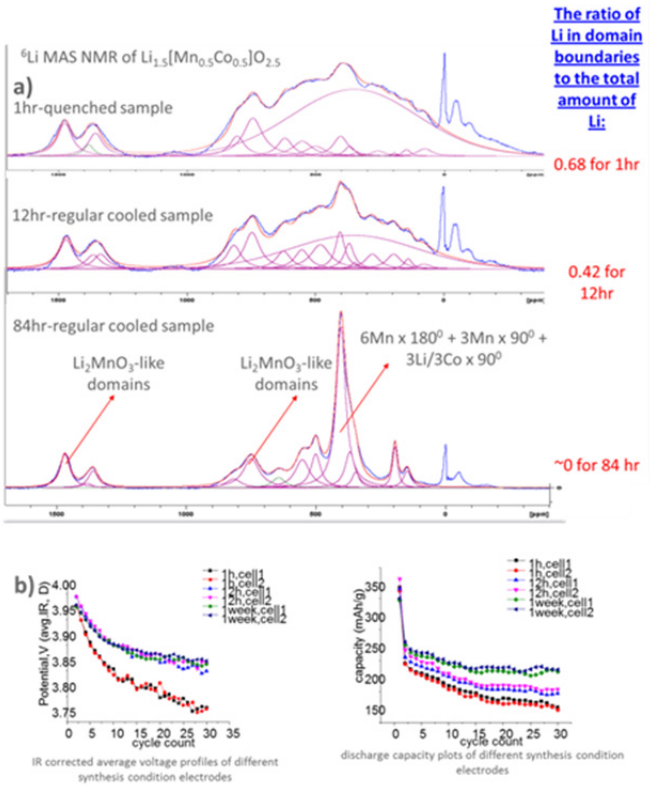

Figure V - 93: (a) Li MAS NMR of pristine $Li_{1.5}[Mn_{0.5}Co_{0.5}]O_{2.5}$ synthesized at 850°C for various annealing times. (b) Electrochemical performance of electrodes synthesized under the different conditions. NMR resonances at 0 ppm and at negative shifts are due to diamagnetic Li in $LiCoO_2$ and spinning sidebands, respectively

The effect of this synthesis parameter and Li occupancy is also correlated to electrochemical performance and voltage fade and can be seen in Figure V - 93b). The voltage fade rate is found to be a minimum but significantly present for the composites with larger domains/less disorder (1 week synthesis duration) and electrochemical discharge capacity and capacity retention values were maximum. The electrochemical performance drops and voltage fade rate increases as more domain boundary lithium are present in the structure and as the domain sizes get relatively smaller (1 and 12 hour synthesis duration).

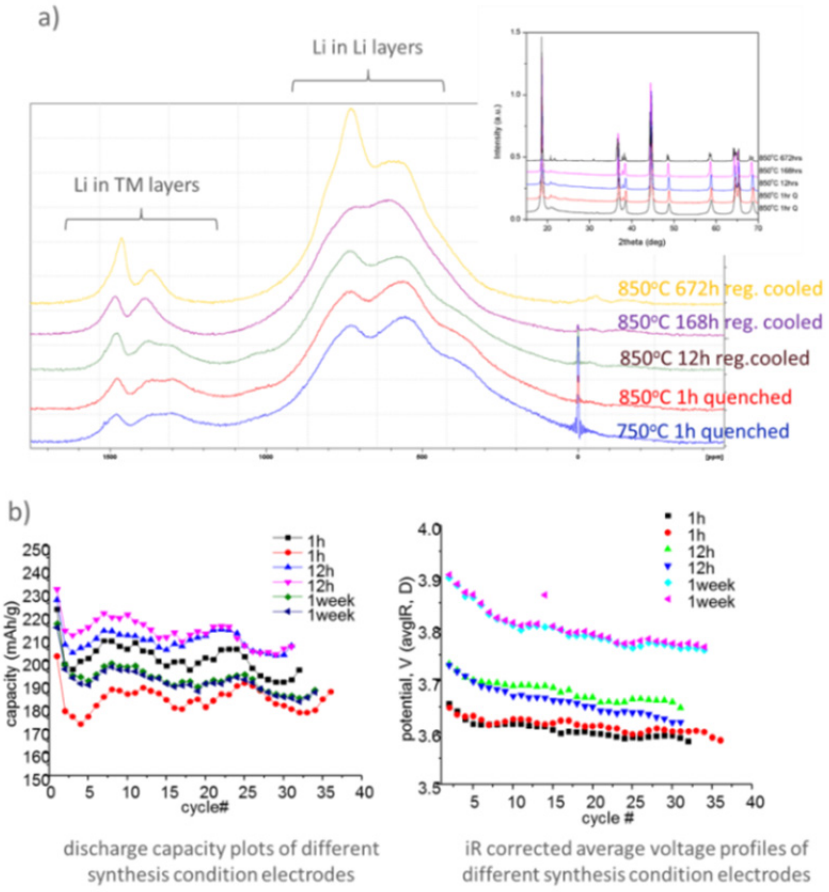

Figure V - 94: (a) Li MAS NMR of pristine $Li_{1.2}[Ni_{0.15}Mn_{0.55}Co_{0.10}]O_2$ compositions synthesized at 850°C for various annealing times, the inset shows X-ray diffraction data for the same samples. (b) Electrochemical performance electrodes synthesized under the different conditions

A new set of samples were synthesized, with ^{6}Li enriched precursors, for a targeted $Li_{1.2}[Ni_{0.15}Mn_{0.55}Co_{0.10}]O_2$ composition to study similar domain size effect with samples prepared at 850°C varying the synthesis duration. Figure V - 94a shows ^{6}Li MAS NMR of the prepared samples. Similar to the previous set of samples, two distinct lithium environments (lithium in lithium layers and lithium in transition metal layers) were observed with a similar, significantly disordered Gaussian resonance overlapping with the Lorentzian resonances. Again, a similar trend was observed with a decrease of the ratio of the intensity of the disordered resonance versus the overall intensity of the ordered resonances with increasing synthesis duration. In order to gain information on the evolution of mid- to long-range order of the composite material, synchrotron XRD patterns were collected for the same samples (Figure V - 94a inset). A typical evolution of increasing crystallinity was observed as samples synthesized at 750 and 850°C for 1 hr showed the lowest crystallinity. Interestingly, the highest crystallinity for a layered hexagonal composite lattice was reached at synthesis durations of 168 hours. Upon further annealing (672 hours) instead of an improvement in crystallinity, formation of a two phase mixture; a monoclinic lattice of Li_2MnO_3 structure and the hexagonal layered lattice of NMC material were observed. This result is consistent with the increase in local order and significant sharpening of the Li_2MnO_3-like resonance observed in ^{6}Li MAS NMR for the same samples. The most likely interpretation of these experimental results is: the well mixed, compatible lattices of the monoclinic Li_2MnO_3 structure and the hexagonal layered lattice of NMC materials, either in the well accepted dendridic domains or other nanodomain morphologies, begin to coagulate and form significant medium- to long-range order. This is the result of significant growth of the domain structure over the nano length-scale and therefore supports the Thackeray explanation (C.S.Johnson *et al.*, Electrochem. Com., 2004) of the composite nature of the Li rich NMC type electrode materials. It should also be noted that electrochemical performance of the sample annealed for 672 hours is very poor (below

150mAh/g discharge capacity, data not shown) which agrees well with the electrochemical inactivity of significant concentrations of crystalline Li_2MnO_3 in an electrode. As for samples which were annealed between 1hr-168hrs, preliminary electrochemical results (see Figure V - 94b) still show significant voltage fade but minimum fade behavior and optimum capacity and capacity retention values can be obtained by fine tuning annealing durations. At this point, it can be concluded that optimum overall electrochemical behavior can be realized for a given composition (for Li rich NMC type materials) not only by a standard 12 hour annealing step during synthesis. However, regardless of domain sizes, shapes, and morphologies of the composite particles, the voltage fade phenomenon persists and further, detailed spectroscopic understanding of the local structures associated with the fade mechanism is required.

In order to study the lithium local environment changes of the composite material upon cycling, we initiated a tedious and expensive preparation of LMR-NMC type cathode materials with fully lithium-6 enriched cells (electrolyte, metal and cathode) and performed a quantitative study with high resolution ^{6}Li MAS NMR spectroscopy on the enriched cycled materials. Figure V - 95a shows the NMR data after one cycle. Comparing with NMR data of the pristine sample (Figure V - 96) a profound loss of order or reordering in the material is observed post activation. It is clearly seen that only 7.1% of the lithium ions go back to the "formal" octahedral sites in the transition metal layers (see loss of Li in TM layers, Figure V - 96. see deconvoluted intensities in Figure V - 92 and Figure V - 95a). This is observed by deconvolution of the lithium resonances with shift values larger than 1,300 ppm (by using integral values in Figure V - 92 and Figure V - 95a). The deconvolution of the majority of the spectrum can be made by keeping a minimum amount of lithium peaks only by introducing a Gaussian and two Lorentzian components. After a dynamic fit of the deconvolution of the peaks the Lorentzian components observed match well with the fit for pristine material octahedral sites in lithium layers (714 and 525 ppm, Figure V - 96a). However a resonance(s) centered at 777 ppm was not observed in the pristine material. This resonance covers 34.5% of the lithium content of the cycled material whereas 58.4% of the lithium ions were found to be in the octahedral sites in the lithium layers. At this point a tentative assignment based on Grey *et al*.'s extensive NMR characterization works is made correlating this Li-occupancy to an extensive Li-Li dumbbell configuration composed of tetrahedral sites which are enabled after removal of octahedral Li from transition metal layers (M. Jiang, B. Key, Y.S. Meng, C. Grey., Chem. Mat., 2009/ Breger *et al.*, Chem. Mat., 2006). After 10 cycles (Figure V - 96b) the deconvoltion of the peaks reveals that the Lorentzian peak intensities and their shifts remain constant whereas there is shift of 122 ppm to lower frequency for the Gaussian component. In order to correlate the effect of the shift with electrochemistry, additional experiments are performed (5 cycles and 40 cycles). It is found that the shift gradually slows down as the voltage fade rate slows down (between cycle 1-10 being fastest, Figure V - 95c and Figure V - 95d red arrow) after 10 cycles the formation of a new lithium resonance at ~260 ppm is observed with solid state ^{6}Li NMR (Figure V - 95c and Figure V - 95d green arrows). The origin of the 122 ppm shift is currently unknown, however such significant and progressive behavior could be explained by significant transition metal migration (presumably Mn since both NM and MC type Li rich materials exhibit fade phenomenon), vacancy formation for both transition metals and/or oxygen.

Comparison of the electrochemical and structural characterization results show a direct correlation between the loss of lithium from the transition metal layers post activation and more importantly transformation/allocation of available lithium sites in lithium layers (presumably tetrahedral crystallographic positions) and electrochemical voltage fade. These changes correlate quantitatively with the amount of voltage fade and require further detailed analyses to narrow down the specific phenomena. In-depth analysis of the data is in progress to investigate the effect of lithium site formation in the lithium layers. Electrochemical performance and optimization of enriched cathode materials is in progress to obtain more reliable data and to reduce systematic errors in the analysis.

X-ray Absorption Spectroscopy of Li_2MnO_3 During First Cycle Charge and Discharge (ANL).

Li_2MnO_3 was prepared via solid state synthesis by mixing and firing the stoichiometrically required amounts of Li_2CO_3 and $MnCO_3$. A final firing temperature of 450°C was used to ensure electrochemically active, nanocrystalline particles (~200 nm). The powders were mixed with Super P carbon and assembled in coin cells with lithium metal anodes. XAS was carried out on the powders after electrochemical insertion/extraction to various states of charge on the first cycle. The element-specific nature of XAS as well as its ability to resolve local structures (~1 nm) allows us an opportunity to follow, at the atomic level, structural changes to specific environments.

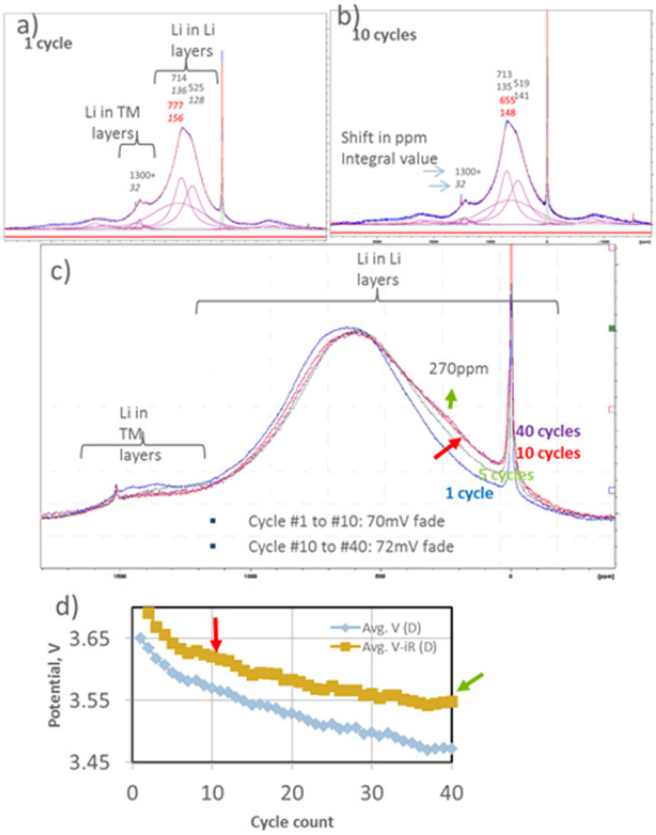

Figure V - 95: (a) and (b) are the deconvoluted 6Li MAS NMR $Li_{1.2}[Ni_{0.15}Mn_{0.55}Co_{0.10}]O_2$ after 1 and 10 cycles, respectively. (c) Comparison of ^{6}Li MAS NMR data for cycled $Li_{1.2}[Ni_{0.15}Mn_{0.55}Co_{0.10}]O_2$ and (d) electrochemical performance

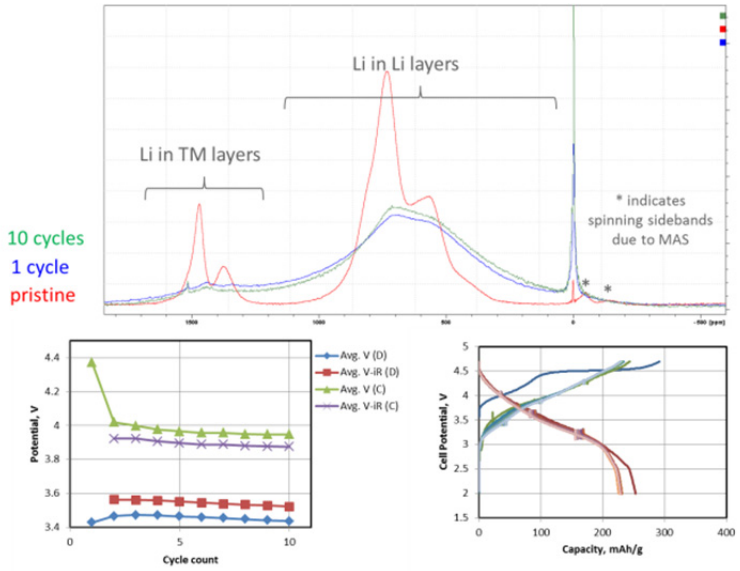

Figure V - 96: ^{6}Li MAS NMR (top) of pristine $Li_{1.2}[Ni_{0.15}Mn_{0.55}Co_{0.10}]O_2$ and after 1 and 10 cycles and plots of electrochemical performance (voltage fade data on the left, electrochemical plots on the right)

Figure V - 97 (a) shows the Mn K-edge data of the as-prepared Li_2MnO_3 powder as well as cells which had been charged to 5.1 V (red) giving ~280 mAh/g and subsequently discharged to obtain capacities of 100 mAh/g (blue), 200 mAh/g (green), and fully discharged to 2.0 V (purple) recovering ~265 mAh/g of the initial charge capacity. Quantitative NMR data (2012 report), however, showed that only ~50% of the lithium removed on charge was reinserted into the Li_2MnO_3 structure. Nevertheless, the overall shift of the NMR resonances toward higher frequency, post activation, revealed a reduction in the average manganese oxidation state below Mn^{4+}.

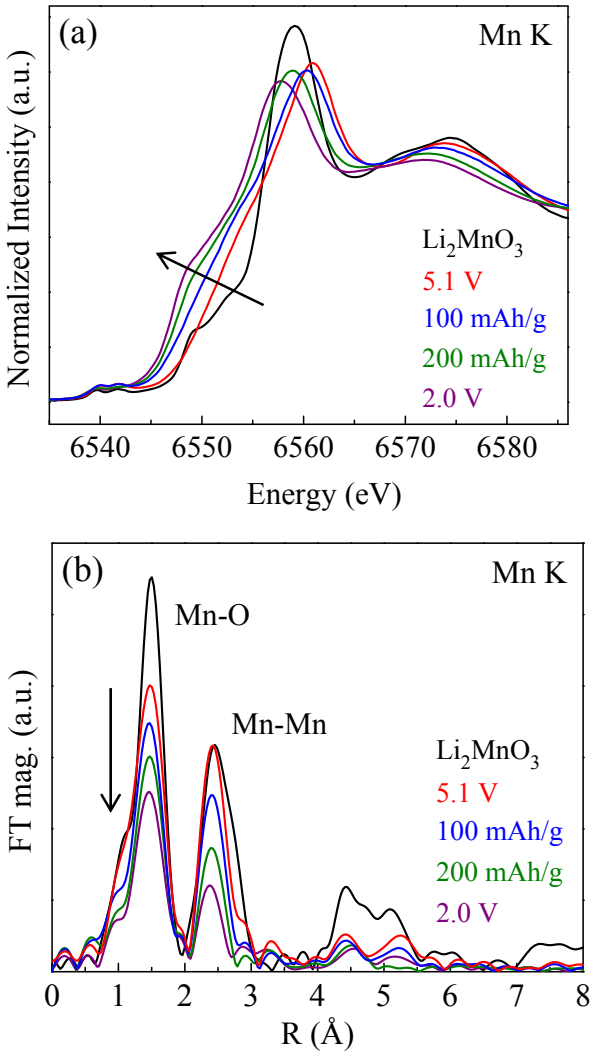

Figure V - 97: (a) Mn K-edge XANES of Li_2MnO_3 powders electrochemically charged and discharged between 5.1 – 2.0 V. (b) Mn K-edge EXAFS of Li_2MnO_3 powders electrochemically charged and discharged between 5.1 – 2.0 V

From Figure V - 97 (a) it can be seen that the charging process up to 5.1 V occurs with a change in shape of the Mn edge rather than any clear or rigid shift of the main edge to indicate oxidation of manganese. This situation is similar to what occurs in LMR-NMC on the first charge where it is generally assumed that manganese retains its 4+ oxidations state throughout the lithium extraction process. The evolution of the Mn K-edge on discharge to 100 mAh/g, 200 mAh/g, and finally to 2.0 V is indicated by the arrow in Figure V - 97(a). The large shift to lower energy and change of shape of the Mn K-edge during the discharge process clearly indicates a continuous reduction of manganese along with distortions in the manganese environment.

Figure V - 97 (b) shows the corresponding EXAF data of the samples in Figure V - 97(a). Upon charge to 5.1 V (red) obvious changes occur for the first shell Mn-O peak at ~1.5 Å (not corrected for photoelectron wave shift) similar to those observed for LMR-NMC materials. Unlike LMR-NMC, however, the Mn-O and Mn-Mn correlations in Li_2MnO_3 decrease continuously on discharge. This drastic decrease in the Mn K-edge EXAFS is in agreement with the continuous reduction of manganese shown in the Figure V - 97(a) XANES and is likely a result of Jahn-Teller distortions (due to Mn^{3+}) and is consistent with the conversion of a significant fraction of the layered structure to spinel. Detailed analysis of the EXAFS data is underway to confirm this hypothesis.

Figure V - 98(a) and Figure V - 98(b) show comparisons of the Mn K-edge XANES and EXAFS, respectively, of Li_2MnO_3 and LMR-NMC after one cycle as well as the as-prepared Li_2MnO_3 of this study; the LMR-NMC delivered ~310 mAh/g on the first cycle charge to 4.7 V and ~260 mAh/g on the subsequent discharge to 2.0 V. The most striking difference is the drastic reduction of manganese in the Li_2MnO_3 to an average oxidation state well below 4+ while the manganese in the LMR-NMC remains very much in line with the pristine Li_2MnO_3 (Mn^{4+}); even after ~75% activation of the "Li_2MnO_3 component" (assuming ~140 mAh/g from $LiMO_2$). According to the oxygen loss model for these materials the average oxidation state after the first cycle discharge should be ~$Mn^{3.5+}$ for the LMR-NMC sample, assuming routine charge compensation on Mn.

Figure V - 98 (b) shows the corresponding EXAFS for the samples in Figure V - 98(a). Again evident from the data is the striking differences between the Li_2MnO_3 and the LMR-NMC sample. The Mn K-edge EXAFS of the LMR-NMC revealed only small changes in the second-shell Mn-Metal correlations (pristine LMR-NMC not shown for clarity) while the first-shell, Mn-O correlations clearly decreased; the pristine material being similar to the Li_2MnO_3 (Mn-O coordination of 6).

In contrast, the pure Li_2MnO_3 sample shows a drastic reduction in the height of the Mn-metal correlation, consistent with the potential formation of a large component of spinel after the first cycle as mentioned earlier. Previous NMR results on these samples (see 2012 annual report) support the above conclusions for reduction of manganese in cycled Li_2MnO_3 as well as structural disorder that is clearly different from LMR-NMC materials.

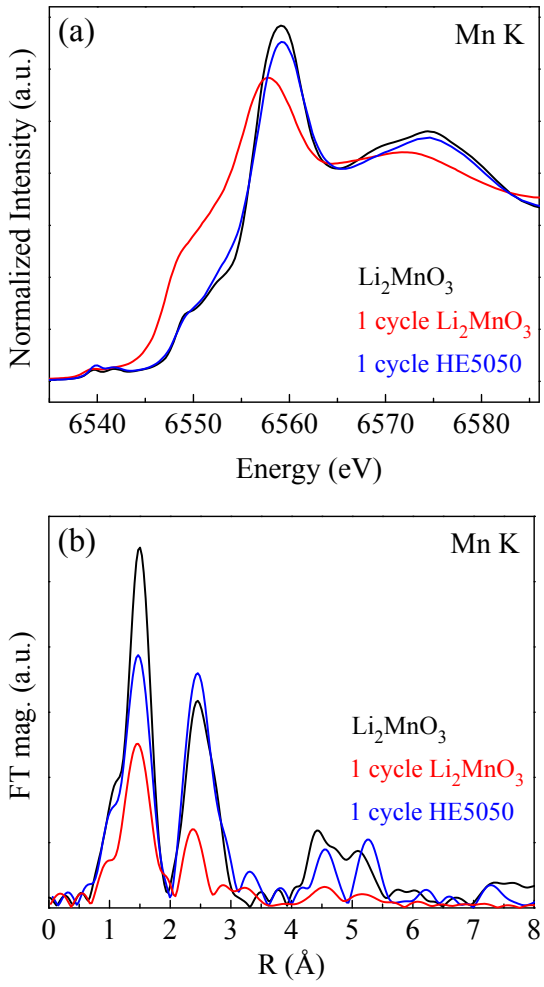

Figure V - 98: (a) Mn K-edge XANES after one cycle for Li_2MnO_3 (5.1 – 2.0 V) and LMR-NMC TODA HE5050 (4.7 – 2.0 V). The as-prepared Li_2MnO_3 is shown for reference. (b) Mn K-edge EXAFS after one cycle for Li_2MnO_3 (5.1 – 2.0 V) and LMR-NMC TODA HE5050 (4.7 – 2.0 V). The as-prepared Li_2MnO_3 is shown for reference

Correlating the voltage fade with the cation ordering in TODA HE5050 high-voltage cathode oxide (ORNL).

The task on determining microstructural changes in ABR developed cathodes during cycling by combined magnetic susceptibility, TEM, selected area electron diffraction (SAED), *in situ* XRD, and ND was carried out at Oak Ridge National Laboratory.

ORNL has implemented advanced diagnostic tools such as temperature dependant magnetic susceptibility and transmission electron microscopy (TEM) techniques to correlate the cation ordering and the voltage fade in the TODA HE5050 oxide cathode to obtain a deeper understanding of the mechanisms of voltage fade.

Two sets of electrochemical experiments were carried out; in one set, the upper-cut off voltage (UCV) was set to 4.2 V (2.4–4.2 V voltage window) and in the other set, the UCV was set to 4.8 V (2.4–4.8 V voltage window). The cells were cycled 125 times. The cycled HE5050 cathodes were harvested, washed with DMC and then dried. The electrochemical data revealed voltage fade from the cell which was cycled at a UCV of 4.8V; however, voltage fade was not observed when the UCV was 4.2V. The SAED, high-resolution TEM and magnetic susceptibility data from the pristine HE5050, after 125 cycles at a UCV of 4.2V and after 125 cycles at a UCV of 4.8V is presented in the Figure V - 99. The SAED collected from the pristine HE5050 material shows the fundamental O3 trigonal reflections (SG 166, $R\bar{3}m$) with faint extra reflections (indicated by arrows) which confirms the presence of cation-ordering arising from the monoclinic phase (SG 12, C2/m). The FFT calculated from the high-resolution TEM also shows the fundamental O3 along with the cation-ordering peaks. The high-resolution TEM shows the O3 phase. The magnetic susceptibility from the pristine HE5050 shows the divergence/splitting of field cooling (FC) and zero field cooling (ZFC) curves at T=50°C (see the highlighted arrow mark) which confirms the cation-ordering in the HE5050 pristine compound. The SAED collected from a particle which was cycled 125 times at a UCV of 4.2V retains the cation-ordering reflections and high-resolution TEM shows the O3 phase. In the magnetic susceptibility data, the divergence of FC and ZFC data is observed which provides further evidence that the cation-ordering is retained in the HE5050 oxides after 125 cycles when cycled at a UCV of 4.2V. After 125 cycles at a UCV of 4.8V, the SAED pattern showed the fundamental O3 reflections, however, it did not show cation-ordering reflections, instead, extra reflections in between two fundamental O3 spots are observed. These extra reflections indicate the presence of a spinel phase. The spinel phase in SAED is also in agreement with the high-resolution-TEM image where spinel-type atomic structure is observed. In the magnetic susceptibility

data, the splitting of FC and ZFC data at T=50°C (which indicates the cation-ordering) was not observed. These observations clearly demonstrate that the cation ordering has been supressed or lost for the HE5050 material which was cycled at a UCV of 4.8V for 125 cycles and the spinel phase has been introduced which lead to the voltage fade at higher UCV (4.8V in this study).

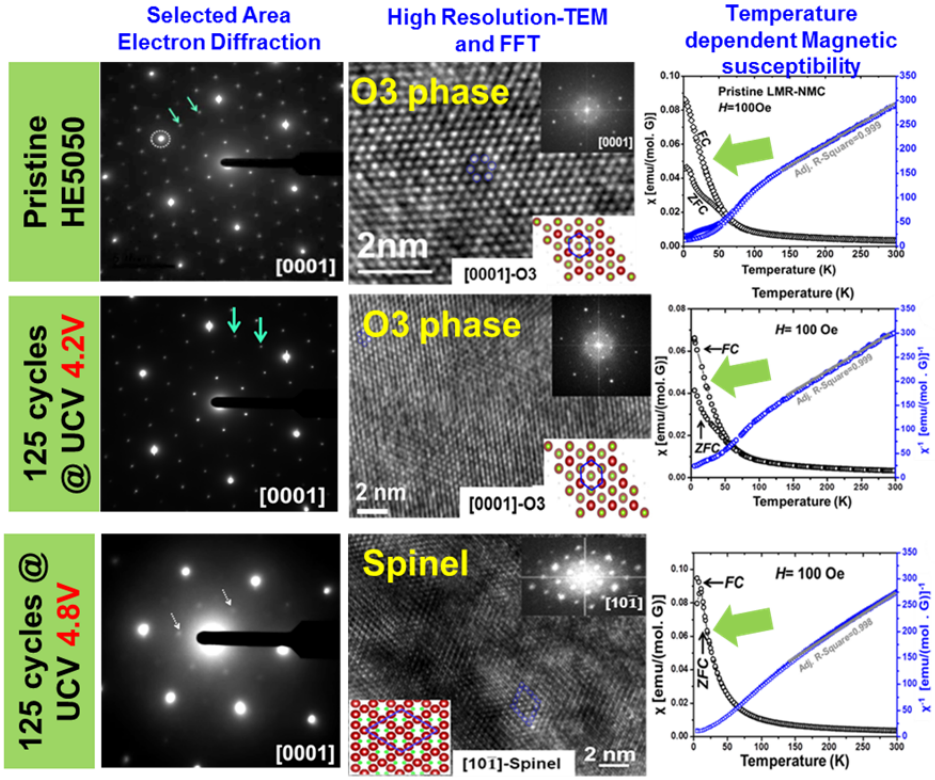

Figure V - 99: SAED, high-resolution TEM, and magnetic susceptibility data from pristine TODA HE5050 and after 125 cycles charged to a UCV of 4.2 V and 4.8 V [*Physical Chemistry Chemical Physics*, 15, 19496, (2013)]

The layered to spinel-type structural rearrangement in HE5050 is believed to occur via formation of an alkali atom in a tetrahedral site during early cycling. When a lithium ion is extracted from an octahedral site in the transition metal (TM) layer, cation-ordering is suppressed and two vacant tetrahedral sites, one in the lithium layer and another in the TM layer, are created. Li or TM ions can then migrate to the empty tetrahedral sites to create a "Li/TM dumbbell" cell, and this structure may be an intermediate between layered and spinel phases. After several cycles at a UCV of 4.8V, (~125 cycles in this study) the nucleation and growth of the spinel phase occurs and the structure may slowly transform to the spinel phase.

ND study to obtain the detailed crystallographic information on HE5050 (ORNL). Collaborating with ANL, ORNL is investigating the mechanisms of voltage fade in HE5050 oxide in order to propose routes to mitigate this adverse effect. ORNL is employing its unique capability of combined ND and magnetic susceptibility diagnostic tools to obtain insights into the atomic structural modifications, phase transformations, and modifications in electronic states of TM ions in the cycled HE5050 oxides to find the cause of voltage fade. Before presenting the data from the cycled materials, detailed crystallographic information of pristine HE5050 was obtained from the ND data. The ND experiment on pristine HE5050 materials was carried out on the POWGEN beam line at the Spallation Neutron Source at ORNL using a frame of neutrons with a centre wavelength of 1.066Å.

The experimental pattern was refined by the Rietveld method using GSAS and the EXPGUI interface. The experimental ND pattern could be refined by considering a composite structure of trigonal and monoclinic phases (Figure V - 100). The complete Crystallographic information is given in Table V - 9. It was observed that in a trigonal phase, a 3% interlayer Li/Ni exchange provided the best fit of the experimental ND pattern (see the inset of Figure V - 100). The crystallographic information along with the site occupancies obtained in the pristine HE5050 will be used to solve the crystal structure of cycled HE5050 in order to investigate the mechanisms of voltage fade.

Table V - 9: The refined crystallographic parameters for pristine HE5050 oxide by taking a composite structure of trigonal and monoclinic phases

Overall Composition: $Li_{1.20}Co_{0.1}Mn_{0.55}Ni_{0.15}O_2$

Agreement parameters: R_{WP}= 5.05% R_p= 8.09 χ^2 =1.50

Phase 2: Crystal System: Monoclinic SG: C2/m
Composition: Li_2MnO_3
Lattice constants: a=4.9464(27), b=8.5624 (5), c= 5.0332(21), β =109.3221 (32), V=201.186 (9), Z= 4, **Phase percentage**: 50% (δ=0.01)

Phase 1: Crystal System: Trigonal $R\bar{3}m$,
Composition: $LiCo_{0.25}Mn_{0.375}Ni_{0.375}O_2$
Lattice constants: a=b= 2.85525(12) 14.2483(10), V= 100.596(7), Z=3
Phase percentage : 5o% (δ=0.01)
Agreement parameters: R_{WP}= 5.05% Rp= 6.69 χ2 =1.50

Site	Atom	x	y	z	SOF	Uiso
3b	Li	0	0	0.5	0.9646(5)	0.0285 (4)
	Ni				0.0354 (5)	
3a	Co	0	0	0	0.25	0.03453 (8)
	Mn				0.375	
	Ni				0.3396	
	Li				0.0354	
6c	O	0	0	0.25941 (8)	1	0.00931 (4)

Site	Atom	X	y	Z	SOF	Uiso
2c	Li	0	0	0.5	1	0.0132(2)
4h	Li	0	0.6606	0.5	1	0.0132(2)
2b	Li	0	0.5	0	1	0.0132(4)
4g	Mn	0	0.1670	0	1	0.0101(4)
4i	O	0.2189 (10)	0	0.2283 (9)	1	0.0027(4)
8j	O	0.2548 (7)	0.3202 (20)	0.2243 (6)	1	0.0048(8)

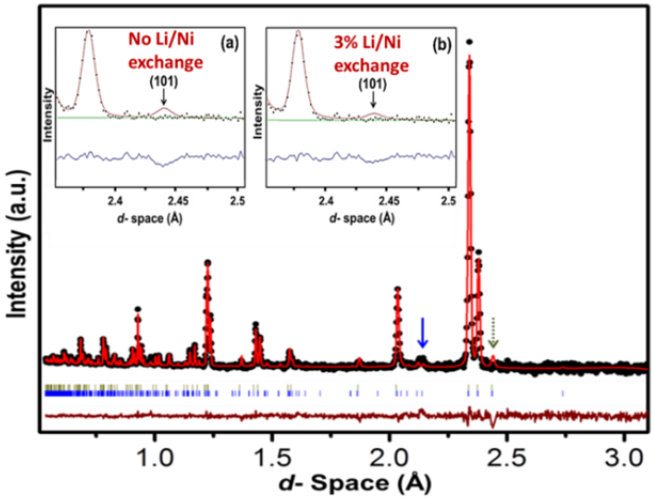

Figure V - 100: Refinement for HE5050 considering a composite monoclinic- Li_2MnO_3 and trigonal $LiMO_2$ (M=Co, Mn, Ni) unit cell. Solid arrow shows the cation-ordering peaks exclusively from monoclinic- Li_2MnO_3 and the dotted arrow marks the (101) reflection in the trigonal phase and (130)/$(20\bar{1})$ reflections in the monoclinic phase. The inset shows the trigonal (101) plane intensity (a) before Li/Ni exchange and (b) after 3% Li/Ni exchange

Conclusions

- Monitoring local structural changes via ^{6}Li MAS NMR has revealed that regardless of the domain sizes and/or morphologies, significant voltage fade is observed which indicates the mechanisms for the fade phenomenon must be linked to changes within the first few coordination shells of the cations.
- For the first time, with the application of solid state NMR, quantitative spectroscopic evidence of a specific lithium local structure change is directly correlated to the amount of voltage fade in a lithium rich NMC-type of composite cathode material.
- Future NMR studies will be focused on detailed analyses and assignments of new lithium environments and shift mechanism(s) observed, in collaboration with the theory group.
- Additional solid state NMR experiments are in progress to study the structural causes of electrochemical hysteresis in collaboration with the hysteresis phenomenon team.
- ^{6}Li static *in situ* and ^{6}Li MAS *ex situ* experiments are planned to quantitatively study the correlations of the formation of the new Li-order and understand the irreversible removal of the Li from transition metal octahedral Li sites.
- Obvious reduction of manganese to states well below 4+ occur for activated Li_2MnO_3 while no clear evidence of this for LMR-NMC exists. In addition, the formation of a spinel component can be inferred after just one cycle for Li_2MnO_3 while no such conclusions can be made for LMR-NMC, even on extended cycling for many cases.
- The XAS data indicate that unknown electrochemical processes are responsible for a considerable amount of the capacity obtained from LMR-NMC. Furthermore, structural transformations occurring in pristine Li_2MnO_3 with electrochemical cycling are likely different and much more facile than in the integrated counterpart of composite materials. As such, identifying these unknown electrochemical processes as well as the associated first-cycle structures will be necessary to the advancement of composite cathode technology. This will be a focused milestone in the coming year.
- Magnetic susceptibility and TEM studies on the TODA HE5050 oxide reveals a direct correlation between cation-ordering and voltage fade. Neutron diffraction studies on pristine HE5050 oxide provided detailed crystallographic information with site occupancy factors of lithium and oxygen atoms along with the TM atoms. Rietveld refinements revealed the structure is a composite between layered trigonal and layered monoclinic phases. The refinement showed a ~3% Li/Ni interlayer exchange in the pristine HE5050 oxides.
- Future studies will include the following:
  - Rietveld refinement on neutron diffraction data collected from cycled samples will be performed to propose the mechanism of voltage fade and low first-cycle efficiency.
  - The structure-electrochemical performance correlations leading to voltage fade will be pursued and new and/or modified materials compositions will be synthesized and examined for better electrochemical performance.

FY 2013 Publications/Presentations

1. D. Mohanty, J. Li, L.C. Maxey, R.B. Dinwiddie, C. Daniel, and D.L. Wood, "Improved QC of Slot-Die Coated Lithium Ion Battery Electrodes by IR Thermography and Laser Thickness Techniques," *Analytical Methods*, Revised, 2013.
2. D. Mohanty, A. Huq, E. Andrew Payzant, A. Safa-Sefat, J. Li, D. P Abraham, D.L. Wood, and C. Daniel, "Neutron Diffraction and Magnetic susceptibility studies on a High-voltage $Li_{1.2}Mn_{0.55}Ni_{0.15}Co_{0.10}O_2$ Lithium-ion Battery Cathode; In-sight into the Crystal Structure *Chemistry of Materials,* 25, 4064 (2013).
3. D. Mohanty, A. Sefat, J. Li, R.A. Meisner, R. A. Justine, E. A. Payzant, D.P. Abraham, D.L. Wood, and C. Daniel, "Correlating Cation Ordering and Voltage Fade in a Lithium- and Manganese-Rich Layered-Layered Lithium-ion Battery Cathode Oxide; a Joint Magnetic Susceptibility and TEM study," *Physical Chemistry Chemical Physics*, 15, 19496, (2013).
4. D. Mohanty, S. Kalnaus, R.A. Meisner, K.J. Rhodes, E.A. Payzant, D.L. Wood, and C. Daniel, "Structural Transformation of a Lithium-Rich $Li_{1.2}Co_{0.1}Mn_{0.55}Ni_{0.15}O_2$ Cathode During High Voltage Cycling Resolved by *In situ* X-Ray Diffraction," *Journal of Power Sources*, 229, 239–248 (2013).
5. D. Mohanty, S. Kalnaus, R.A. Meisner, A. Safa-Sefat, J. Li, K.J. Rhodes, E.A. Payzant, D.L. Wood, and C. Daniel "Structural Transformation in a $Li_{1.2}Co_{0.1}Mn_{0.55}Ni_{0.15}O_2$ Lithium-Ion Battery

Cathode During High-Voltage Hold," *RSC Advances*, 3, 7479–7485 (2013).

6. D. Mohanty, A. Safa-Sefat, S. Kalnaus, J. Li, R.A. Meisner, E.A. Payzant, D.P. Abraham, D.L. Wood, and C. Daniel, "Investigating Phase Transformation in $Li_{1.2}Co_{0.1}Mn_{0.55}Ni_{0.15}O_2$ Lithium-Ion Battery Cathode During High-Voltage Hold (4.5 V) via Magnetic, X-ray Diffraction and Electron Microscopy Studies," *Journal of Materials Chemistry A*, 1, 6249–6261 (2013).
7. L. Baggetto, D. Mohanty, R. A. Meisner, C. Daniel, D. L. Wood III, N. J. Dudney, G. M. Veith, "Fabrication and characterization of high capacity lithium rich nickel manganese cobalt oxide cathode thin films," *Journal of Power Sources,* Revised 2013.
8. D. Mohanty, A. Huq, A. Safa-Sefat, J. Li, D. P. Abraham, D.L. Wood, and C. Daniel, "Understanding voltage fade mechanism in a lithium and manganese rich layered-layered high-voltage lithium-ion battery cathode by neutron and magnetic susceptibility studies" In Preparation, 2013.
9. 2013 DOE Annual Peer Review Meeting Presentation.
10. D. Mohanty, J. Li, C. L. Maxey, R. B. Dinwiddie, C. Daniel and D. L. Wood, "In-Line Non-destructive testing of a lithium-ion Battery Electrode by Laser Caliper and Thermography" MRS Fall meeting Boston, Massachusetts, December 1-6, (2013) (accepted).
11. D. Mohanty, A. Huq, A. Safa-Sefat, J. Li, D. P. Abraham, D.L. Wood, and C. Daniel, "Investigating Voltage Fade Pathways in a Lithium and Manganese Rich Layered-Layered High-voltage Lithium-ion Battery Cathode by Neutron Diffraction studies" MRS Fall meeting Boston, Massachusetts, December 1-6, (2013) (accepted).
12. D. Mohanty, A. Safa-Sefat, J. Li, S. Kalnaus, R.A. Meisner, D.L. Wood, and C. Daniel, "Investigating the Cation-Ordering in $0.5Li_2MnO_3 \cdot 0.5LiNi_{0.375}Co_{0.25}Mn_{0.375}O_2$ Cathode by Magnetic and Transmission Electron Microscopy Studies," ACS Spring Meeting, New Orleans, Louisiana, April 7, 2013 (*Accepted as ACS Presentation On Demand)*.
13. D. Mohanty, S. Kalnaus, R. Meisner, A. Safa-Sefat, J. Li, D.L Wood, and C. Daniel, "Structural Evolution in Lithium-Rich $0.5Li_2MnO_3 \cdot 0.5LiNi_{0.375}Co_{0.25}Mn_{0.375}O_2$ Cathode During High Voltage Cycling; an *In situ* X-Ray Diffraction Investigation," MRS 2012, Boston, Massachusetts, November 25, 2012.
14. Croy et al. ECS, 2013.
15. Key et al. ECS, 2013.
16. Gallagher et al. ECS, 2013.
17. Dogan et al. ECS, 2013.
18. Croy et al. ABAA6.
19. Croy et al. USDRIVE.

V.C.5 Hysteresis in Li-ion Battery Active Cathode Materials (ANL)

Kevin Gallagher, Wenquan Lu, & Dennis Dees
Argonne National Laboratory

Collaborators:
Jason Croy, Argonne National Laboratory
Mali Balasubramanian, Argonne National Laboratory
Michael Thackeray, Argonne National Laboratory
Martin Bettge, Argonne National Laboratory
Daniel Abraham, Argonne National Laboratory

Start Date: October 2012
Projected End Date: September 2014

Objectives

- Increase understanding of electrochemical behavior of LMR-NMC electrode materials.
- Determine if hysteresis in LMR-NMC is related to the voltage fade phenomenon.
- Create a physics-based, numerical model of the LMR-NMC electrode materials to improve understanding and forecast long-term electrochemical behavior (e.g., aging of hysteresis and voltage fade phenomena).

Technical Barriers

The primary technical barrier to the development of a safe cost-effective PHEV battery with a 40 mile all electric range that meets or exceeds all performance goals:

- Interpreting complex cell electrochemical phenomena.
- Identification of cell degradation mechanisms.

Technical Targets

- By 2014, a PHEV battery that can deliver a 40-mile all-electric range and costs $3,400
  - Enabling LMR-NMC materials to a state of commercial adoption

Accomplishments

- Demonstrated LMR-NMC electrodes display at stable hysteresis – gap exists even after 70 day hold.
- Linked hysteresis and voltage fade phenomena.
- Proposed mechanism for electrochemical behavior based on reversible and irreversible transition metal ion migration.
- Created new hypothesis on why this class of materials is able to achieve significantly higher capacity than others (i.e., 250 vs 175 mAh/g).

✧ ✧ ✧ ✧ ✧

Introduction

The electrochemical behavior of lithium- and manganese-rich transition metal oxide (LMR-NMC) layered cathode electrode materials is poorly understood even though intense efforts exist attempting to commercialize this material. The hysteresis observed in the open-circuit voltage function between charge and discharge results in energy inefficiency and complicates state-of-charge (SOC) management. More importantly, we have shown this process is directly related to the voltage fade phenomenon that is the primary roadblock to commercialization of this class of materials.[1-5]

A broader implication of this work is the proposed hypothesis for the origin of hysteresis in LMR-NMC. Based on electrochemical and spectroscopic evidence, we propose that transition-metal ions migrate during charge and discharge and may be a key reason why LMR-NMC achieves significantly higher capacity than other materials. As this behavior was not previously widely accepted, our work is shedding light on how charge is stored in these materials and perhaps understand charge storage and decay mechanisms common to layered transition metal oxide materials.

Approach

Our approach combines electrochemical studies with local-structure spectroscopy and physics-based, numerical models. Both industrially provided and laboratory synthesized materials are used to enable a broader study of the LMR-NMC material space. This report examines first the observed electrochemistry and then our attempts to capture the physics responsible for the electrochemistry in a numerical electrochemical model.

Results

Electrochemical Analysis.

Hysteresis and Voltage Fade - Figure V - 101 displays critical electrochemical measurements on lithium half cells using electrodes of $0.5Li_2MnO_3•0.5LiMn_{0.375}Ni_{0.375}Co_{0.25}O_2$, or in standard notation $Li_{1.2}N_{i0.15}Mn_{0.55}Co_{0.10}O_2$ (Toda HE5050), that exhibit both the hysteresis and voltage fade phenomena. The galvanostatic cycling curves for the 3rd and 50th cycle show a clear change in both the charge and discharge voltage curves to lower values (i.e., voltage fade). The inset in Figure V - 101 displays the 3rd cycle dQ/dV with scanning curves measured between 2-4.1 V and 3.7-4.7 V. A significant amount of the lithium sites that are emptied above 4.1 V are not refilled until discharging to a potential of ~3.3 V (i.e., a 1 V hysteresis) as communicated by Croy et al.[1]

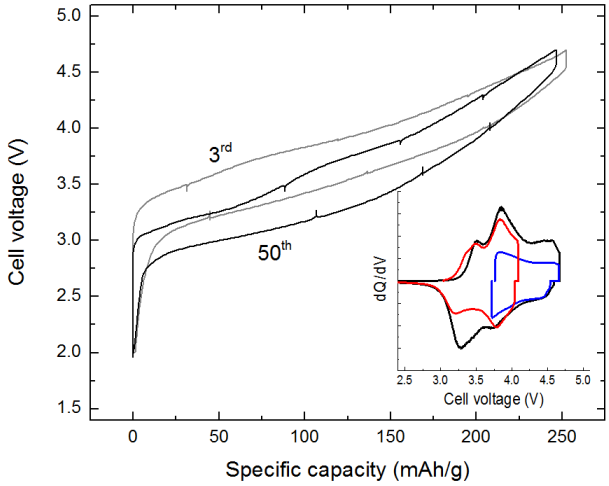

Figure V - 101: Voltage fade and (inset) hysteresis in the electrochemical profiles of a Li/Toda HE5050 half cell

The connection between voltage fade and hysteresis was elucidated in a cycling window study that was undertaken to tease out the accelerating factors related to voltage fade.[2] The testing protocol measured an IR corrected average voltage before and after cycling within a specified voltage window. The cycling windows chosen for the truncated voltage window cycling all included 4.7 V as the high voltage to utilize a large fraction of the total lithium content, thus accelerating voltage fade. The lower voltage window cutoff was varied among different samples to map out the mechanistic space. Figure V - 102 displays the drop in average OCV on discharge between the 2nd and 23rd cycles as a function of lower voltage cutoff during the truncated cycles. The greatest voltage fade occurs when cycling from a high voltage, such as 4.7 V, to a lower voltage, below ~3.4 V. To explore the calendar time dependence, the cycling data was transformed to a calendar time plot and additional data points were measured. The earlier test protocol was repeated on each of the same samples to put up to 65 cycles on the same coin cells. New coin cells were also made and tested with a potentiostatic hold at 4.7 V for 120, 240, 360, or 480 hours rather than continuous cycling in a truncated window.

Figure V - 102 (inset) presents the calendar time (total time on test) behavior of all of the different samples. Once again, it is shown that cycling between 4.7 V and 3.2 V accelerates voltage fade more than any other electrochemical exposure. The calendar time study shows a greater extent of voltage fade for the shortest hold of 120 hours relative to the equivalent 2-4.7 V cycling data; however, holding the electrode material at 4.7 V for longer periods of time only modestly increases the extent of voltage fade. From this observation, we may conclude that while calendar time is important, cycling to low potentials is necessary to significantly accelerate voltage fade. Moreover, the same critical potential, ~ 3.3 V, is observed for the hysteresis and voltage fade phenomena. Bettge et al. have also shown a correlation between the hysteresis in the second cycle and the rate of voltage fade after 20 cycles.[4]

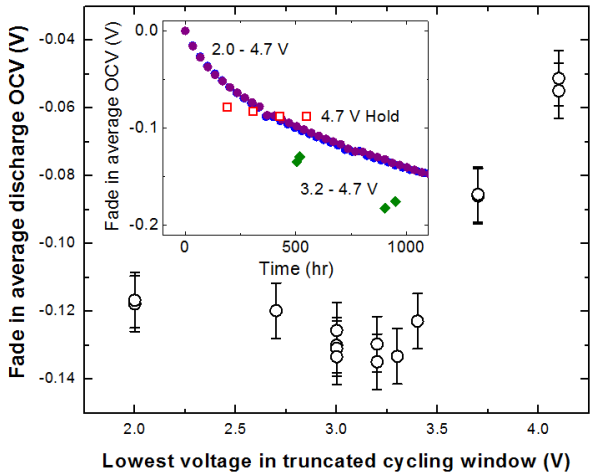

Figure V - 102: Fade in the average OCV on discharge as a function of the lower cut-off voltage between the 2nd and 23rd cycles. (inset) Fade data transformed to calendar time

Recently, Croy et al. further established the connection between voltage fade and hysteresis by carefully tracking the charge passed in different regions of the electrochemical activity.[3] This analysis used the path dependence of the different electrochemically active domains to determine how the capacity grew or shrank over cycling. The amount of capacity lost in the hysteresis region was exactly the same as that gained in the low voltage region, termed voltage fade configuration, around 3.1 V vs Li. This held true for the three stoichiometries analyzed, x=0.1, x=0.3 an d x=0.5, in $xLi_2MnO_3•(1-x)LiMn_{0.5}Ni_{0.5}O_2$. Based on the set of work analyzing the hysteresis and VF phenonmena, a mechanism was proposed, Figure V - 103.

The migration of transition metal ions, sometimes reversible, oftentimes irreversible, occurs in many layered intercalation compounds. This migration has been shown to involve tetrahedral sites in the lithium layer. The presence of a transition metal ion in the lithium layer tetrahedral site, perhaps as a TM--Li dumbbell defect straddling the TM-layer vacancy, directly affects the three nearest neighbor Li-layer octahedral site vacancies and could easily change the energy for lithium site occupancy, thus, resulting in the observed hysteresis. This dumbbell defect would be annihilated when a sufficient driving force for the reduction and migration of the transition metal ion was present, as seems to be the case near 3.3 V when a critical lithium concentration in the electrode structure is reached. With the critical driving force, the transition metal would return to the original octahedral site in the transition metal layer (i.e., hysteresis phenomenon) or it could migrate elsewhere to reside in a different local cubic environment (i.e., voltage fade).

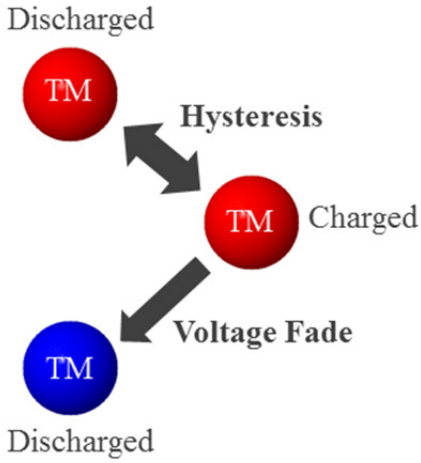

Figure V - 103: Proposed mechanism of transition-metal ion migration that when reversible is the source of hysteresis in LMR-NMC but may irreversibly lead to a lower energy, different cubic environment responsible for the growth of the voltage fade configuration (electrochemically active around 3.1 V)

From these studies we can show three distinct sources of capacity within the LMR-NMC electrode materials, Figure V - 104.[3] The first (white in Figure V - 104) behaves similar to standard intercalation material of layered oxides. The second region (red) is that associated with the hysteresis phenomenon and potentitally results from reversible transition-metal ion migration. Finally, the third region (blue) is the voltage fade configuration that shows electrochemically reversible behavior around 3.1 V. The voltage fade configuration grows at the expense of the hysteresis contribution and may result from irreversible transition metal migration.

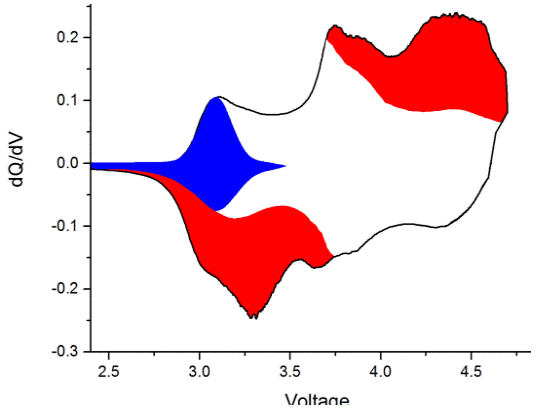

Figure V - 104: Illustration of the three distinct electrochemical contributions to the capacity of LMR-NMC electrode materials

Electrochemical Behavior of the Macro-Components Thought to Compose LMR-NMC on the Nano-Scale- The LMR-NMC electrode materials are often labeled in a composite notation to highlight the importance of the Li_2MnO_3-like structure found within these nano-composite materials. To investigate the relationship of the LMR-NMC materials to what might be considered their parent componds, we analyzed the electrochemistry of bulk (non composite) $LiNi_{1/3}Co_{1/3}Mn_{1/3}O_2$ (NCM) and Li_2MnO_3.[5] Figure V - 105 shows the differential capacity plot of NCM, Li_2MnO_3 and a 50/50 physical blend of powders during their first formation cycle. As expected, the differential capacity plot of the physically-blended electrode preserved the redox preaks of Li_2MnO_3 and NCM, respectively. At about 4.4V, both blend and Li_2MnO_3 start to be activated. Figure V - 106 compares the differential capacity plots of blend and LMR-NMC (HE5050, Toda) during the first cycle. The normalized dQ/dV (dQ/dV*Q) peaks of the Li/blend cell are in the similar potential regions with dQ/dV*Q peaks of Li/LMR-NMC cell. Both the blend and LMR-NMC start to be activated at almost same potential highlighting a signature of Li_2MnO_3; however, important differences exist. A shift was observed for the redox potential related to NCM between the blend and LMR-NMC, which could possibly be attributed the different stoichiometric ratio of Ni, Co, and Mn in NCM (1/1/1) and LMR-NMC (0.37/0.24/0.39). Another likely reason for the NCM redox peak shift is related to the small domain size (nm range) and local environment which is fundamentally different between the bulk NCM material and the nano-composite LMR-NMC material due to transition metal and lithium ordering. Another important distinction is the low voltage peak on discharge. The Li_2MnO_3 shows significant capacity below 3 V whereas the LMR-NMC material shows almost none. We conclude that the LMR-NMC material resembles, but is distinct from, the parent compounds often used to describe the stoichiometry in nano-composite notation.

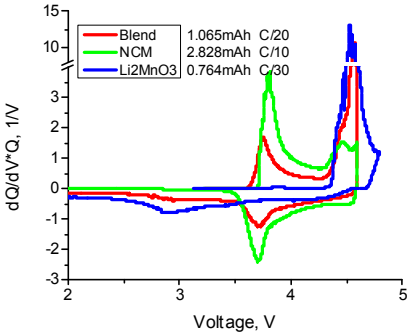

Figure V - 105: differential capacity plot of NCM, Li2MnO3 and their 50/50 blend

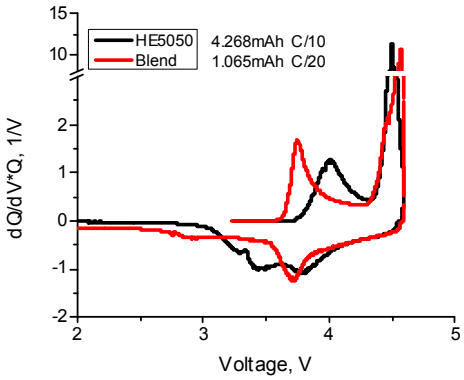

Figure V - 106: Comparision of differential capacity plots of blend and LMR-NMC

Electrochemical Modeling. The general methodology for the electrochemical model follows the work of Newman.[11] Essentially, continuum based transport equations are combined with kinetic and thermodynamic expressions to allow the potential, concentration, and current distributions to be determined throughout the cell. Volume-averaging of the transport equations accounts for the composite electrode geometry. Increasingly complex electrochemical models have been developed for lithium-ion cells that include a detailed model of the transport and reaction in the SEI and phase change active electrode materials [12-14]

The focus of this effort is on the hysteresis that LMR-NMC electrode materials are known to exhibit between their charge and discharge voltage curves, even at very slow cycling rates (e.g., C/200). A number of different models have been examined with varying degrees of success. The model development described below combines and extends some of the earlier work. As discussed below, this model exhibits characteristics that account qualitatively for many of the observed phenomena, but until the model is rigorously compared

and fitted to the experimental data, its true utility cannot be determined.

The activated LMR-NMC cathode material is obviously quite complex and suggested to be composed of nanometer scale sized domains. These domains are highly integrated, but appear to have unique electrochemical properties. The cathode material is assumed to be composed of two types of domains for the initial model development (as mentioned previously, three electrochemically distinct regions exist), where both domains can be electrochemically active. One domain (designated domain number 1) is considered to be relatively stable to changes in lithium concentration, while the other domain goes through a slow reversible structural transition during cycling. At low lithium concentrations, the unstable domain has one lattice structure (designated domain number 2) and at high concentrations, another (designated domain number 3). In other words, domains 2 and 3 are located in the same nanometer spatial regions within the material. Although, the model formulism does account for phase boundaries, domain 2 grows at the expense of the domain 3 in a reversible manner (thus 3 grows at the expense of 2). Each of these domains has an associated open circuit voltage (OCV) curve as a function of lithium concentration in that domain (c_{Si}, i = 1, 2, or 3). Figure V - 107 has the assumed OCV curve for each of the domains, where x_S is the ratio of the lithium concentration in the specific domain divided by its maximum concentration. The actual OCV curve is inevitably more complicated, but this should be adequate for an initial examination of the model. It is important here that the OCV curves are offset by a significant voltage.

Volume-averaged continuum-based diffusion equations are used to describe the transport of lithium through the material. The flux of lithium between two adjacent domains denoted *i* and *j* (N_{ij}) is described by an electrochemical potential (μ_{Li}) driven mass transport expression, Equation 1, where k_{ij} is the mass transfer coefficient. The electrochemical potential can be easily associated with the OCV of the domain.

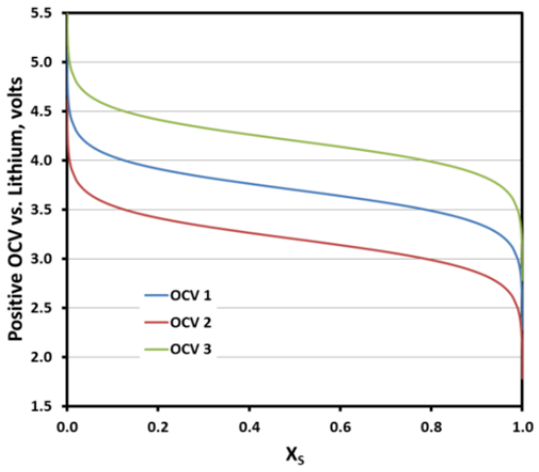

Figure V - 107: Assumed open circuit voltage curve as a function of relative lithium concentration in domain

$$N_{ij} = k_{ij}\left[\mu_{Li}(i) - \mu_{Li}(j)\right] \quad [1]$$

The transitions from domain 2 to 3 and from domain 3 to 2 are assumed to follow the Avrami phase change expression (see Equation 2), where *k* is a lithium concentration driven rate constant and ε_{Si} is the volume fraction of domain *i*.

$$\varepsilon_{Si} = 1 - \exp\left(-kt^n\right) \quad [2]$$

By offsetting the individual domain OCV curves and making the structural transitions and lithium transport between domains extremely slow (i.e., very small rate constant and mass transfer coefficient); the electrochemical model exhibits a hysteresis between charge and discharge, even at a C/200 rate, as seen in Figure V - 108. It should be noted that the model simulations presented here are only for the active material (i.e., single particle calculation), although at very slow rates there is little or no difference between the single particle and the full cell.

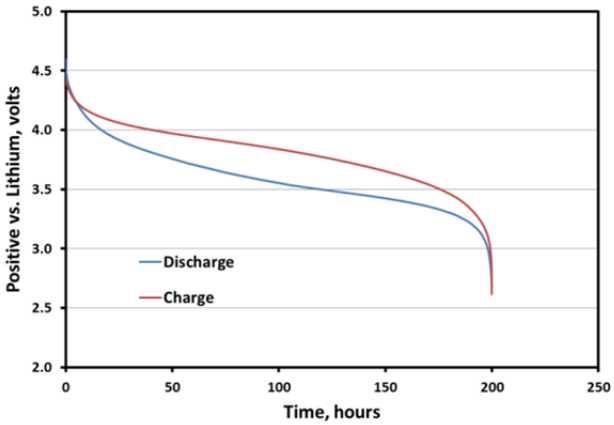

Figure V - 108: Electrochemical model simulation of active material charge and discharge curves at a C/200 rate

The electrochemical model described above will eventually come to equilibrium given enough time. At around a C/5000 rate the charge and discharge simulations collapse to a single curve, which indicates that the material takes months to come to a true equilibrium. This raises the question of whether a material with these poor transport characteristics could ever support high discharge/charge rates. To address this, a series of simulations were conducted over a range of C-rates from about C/5000 to C/1, as shown in Figure V - 109. One can see that there is a significant loss in total capacity over the range studied, but that the material can support these rates.

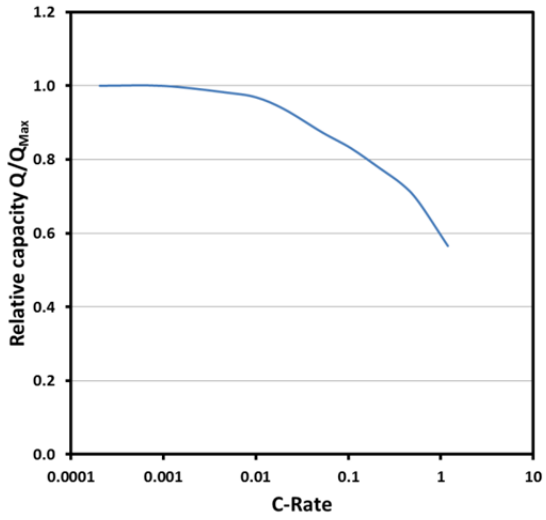

Figure V - 109: Electrochemical model simulation of active material rate behavior

To more rigorously examine the proposed electrochemical model, a specific LMR-NMC material and electrode has been adopted for study. The extensive database of the baseline Toda HE5050 LMR-NMC active material and electrode makes it the best option. While there are a wide variety of electrochemical studies on this material, two types of half-cell (i.e., lithium counter electrode) studies are being utilized for fitting the model parameters. The first type is constant current cycling (C/18) and the second type is relatively slow Galvanic Intermittent Titration Technique (GITT) study, both using the standard electrode. In the GITT study a C/18 current is applied for 10 minutes followed by a 100 minute rest, which is then repeated through a complete cycle. The approximately 30 model parameters associated with the LMR-NMC material makes the parameter fitting a challenge. It is anticipated that multiple fitting iterations of the data will be necessary to generate a full concentration dependent parameter set.

As a starting point, the constant current cycling data was utilized with the particle model described above to develop a working set of parameters. This data is not particularly sensitive to the transport parameters and was used mainly to fit the OCV curves of the three domains and establish average rate constants for the domain transitions, as well as their range of stability. It was clear from the exercise that a perfect fit of data was not possible without allowing the transition rate and transport parameters to be concentration dependent. However, a reasonably good fit of the data could be obtained with average parameters, as shown in Figure V - 110.

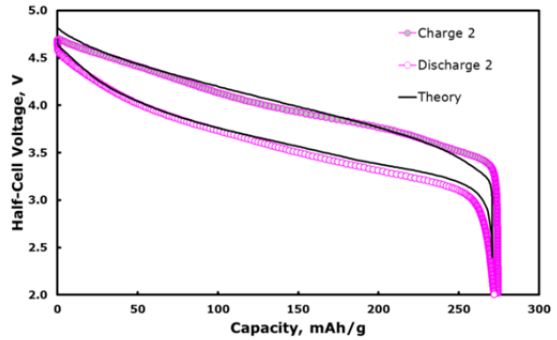

Figure V - 110: Electrochemical model simulation of HE5050 LMR-NMC standard electrode half-cell charge and discharge curves at a C/18 rate

The complex nature of this material that exhibits the hysteresis between charge and discharge curves can be seen by examining the relative amounts of domains 2 and 3 as the material is cycled (see Figure V - 111). As indicated above, domain 2 is stable when fully charged and domain 3 is stable when fully discharged. The data fit indicates that the crossover point for this material is around 3.5 volts. The sluggishness of the transition rates cause the material to never be at equilibrium at any reasonable cycling rate. Further, the slow transition rates result in the changes to appear to be out-of-phase with the cycling. Finally, the differences in the stability ranges and transition rates cause the asymmetry apparent in Figure V - 111.

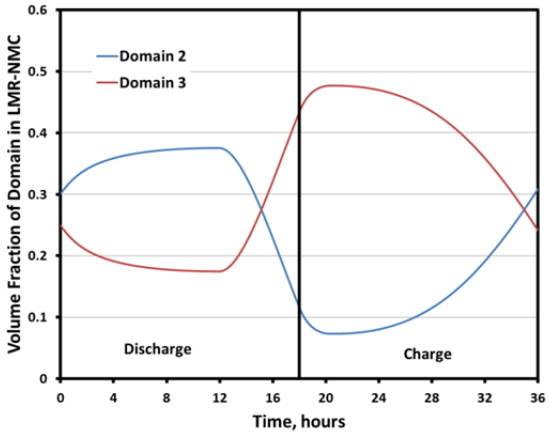

Figure V - 111: Volume fraction of domains 2 and 3 in HE5050 LMR-NMC active material from electrochemical model simulation of charge and discharge at a C/18 rate

The particle model was integrated into the half-cell electrochemical model to use in fitting the GITT half-cell data.[15] Since there is no actual reference electrode in the cell, an estimate of the lithium electrode interfacial area specific impedance (ASI) is important. This is complicated by the high probability that the lithium electrode impedance is likely not stable throughout the full experiment. Nevertheless, an average lithium electrode ASI was estimated by comparing impedance data on reference electrode cells to the approximately one second ASI of the half-cell. The more accurate the lithium ASI the better the LMR-NMC interfacial ASI can be determined. However, this information can best be determined using reference electrode impedance data on LMR-NMC electrodes (see annual report on electrochemical modeling studies in Cell Fabrication Facility Team Production and Research Activities section).

The fitting of GITT data has been initiated using the parameter set from the constant current cycling data. In the initial fitting, the OCV curves and the stability ranges of domains 2 and 3 are not varied. Also, the ratios of the transport parameters and transition rates for each domain are held constant. This reduces the fitted parameters to a reasonable number and these assumptions can be relaxed as the complete parameter set is developed. Even with these assumptions, there is sufficient flexibility to fit the data, as shown in Figure V - 112 for a single charge pulse and relaxation at about 3.8 volts.

Recent experimental studies, Figure V - 113, indicate that the stability range of domains 2 and 3 overlap (i.e., there is a voltage range where both domains are stable). This would create a “true voltage hysteresis” (i.e., a hysteresis that would exist at all cycling rates). Presently, the stability ranges in the model are being adjusted to take the recent observations into account.

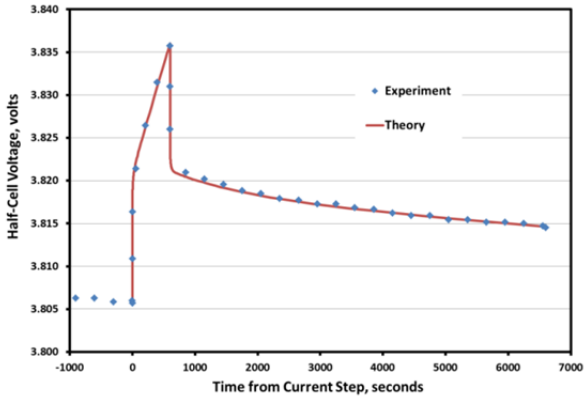

Figure V - 112: Electrochemical model simulation of HE5050 LMR-NMC standard electrode half-cell GITT experiment (600 second C/18 charge pulse and 6000 second relaxation at about 3.8 volts)

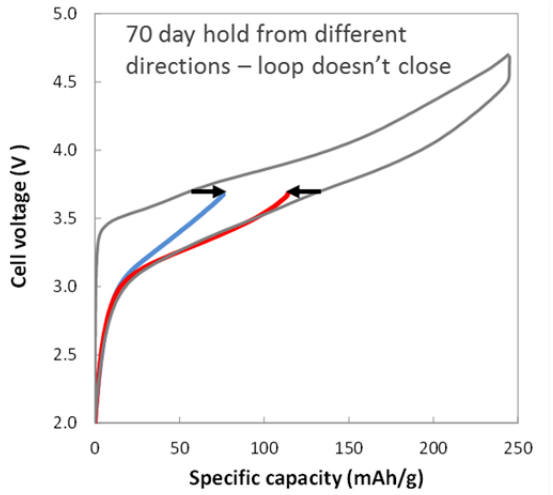

Figure V - 113: Hysteresis loop is not closed at a 70 day hold at 3.7 V from different directions (charge vs discharge). Here shown for the Toda HE5050 material in a lithium half cell

Conclusions and Future Directions

The LMR-NMC material is shown to be composed of three distinct electrochemical contributions: standard layered material intercalation, hysteresis, and voltage fade configuration. The voltage fade phase grows at the expense of the hysteresis contribution. The hysteresis is proposed to result from the migration of transition-metal ions during charge and then back on discharge. This process is postulated to be only semi-reversible. On some frequency, the transition-metal ion would migrate to a different cubic environment and initiate growth of the voltage fade configuration. A domain showing electrochemically reversible activity is found around 3.1 V. The growth of this lower voltage fade thus lowers the average voltage of the LMR-NMC electrode (i.e., Voltage Fade). Future work will support spectroscopic attempts to identify transition-metal ion migration.

An electrochemical model has been proposed that at least qualitatively explains much of the observed experimental behavior of the LMR-NMC electrode. The parameter fitting with the present model will continue. As confidence with the model improves, another domain will be added to the model to account for the voltage fade. Paralleling the voltage fade model modification, the bulk material electrochemical model will be integrated with the complex SEI electrochemical model.

FY 2013 Publications/Presentations

Publications

1. J. R. Croy, K. Gallagher, M. Balasubramanian, Z. Chen, Y. Ren, D. Kim, S.-H. Kang, D. Dees, and M. Thackeray, *Examining Hysteresis in Composite xLi_2MnO_3•(1-x)$LiMO_2$ Cathode Structures*, Phys. Chem. C 117, 6525 (2013).
2. K. Gallagher, J. R. Croy, M. Balasubramanian, M. Bettge, D. Abraham, A. Burrell, and M. Thackeray, *Correlating Hysteresis and Voltage Fade in Lithium- and Manganese-rich Layered Transition-Metal Oxide Electrodes*, Electrochem. Comm. 33, 96 (2013).
3. J. R. Croy, K. Gallagher, M. Balasubramanian, B. Long, and M. Thackeray, Quantifying Hysteresis and Voltage Fade in xLi_2MnO_3•(1-x)$LiMn_{0.5}Ni_{0.5}O_2$ Electrodes as a Function of Li_2MnO_3 Content (submitted).
4. Martin Bettge, Yan Li, Kevin Gallagher, Ye Zhu, Qingliu Wu, Wenquan Lu, Ira Bloom, Daniel P. Abraham, *Voltage fade of layered oxides: its measurement and impact on energy density*, J. Electrochem. Soc., 160 (11) A2046-A2055 (2013).
5. Wenquan Lu, Qingliu Wu, and Dennis W. Dees, Electrochemical Characterization of Lithium and Manganese Rich Composite Material for Lithium Ion Batteries, J. Electrochem. Soc., 160 (6) A950-A954 (2013).

Presentations

1. K. G. Gallagher, J. R. Croy, M. Balasubramanian, and M. M. Thackeray *Hysteresis and Voltage Fade in Lithium- and Manganese-Rich Transition Metal Oxide Electrodes* 224th Meeting of Electrochemical Society, San Francisco, CA USA, October 27-November 1st, 2013, #**958**.
2. K. G. Gallagher, Promises and Challenges of Lithium- and Manganese-Rich Transition-Metal Layered-Oxide Cathodes DOE Merit Review, Washington D.C. USA, May 13 – May 17, 2013.
3. K. G. Gallagher J. R. Croy, M. Balasubramanian, D. W. Dees and M. M. Thackeray, *Examining Hysteresis in Li- and Mn-Rich Composite Cathode Materials* DOE Merit Review, Washington D.C. USA, May 13 – May 17, 2013.
4. W. Lu, *Validation of Electrode Materials and Cell Chemistries* DOE Merit Review, Washington D.C. USA, May 13 – May 17, 2013.
5. K. G. Gallagher, J. Croy, M. Balasubramanian, D. W. Dees, and M. M. Thackeray, *Hysteresis in LMR-NMC Electrodes (xLi2MnO3 •(1-x)LiMO2, M = Ni, Co, Mn)* U.S. Drive Meeting on Cathode Material Development, Argonne National Laboratory, Lemont, IL USA, January 24, 2013.

References

1. J. Newman and K. Thomas-Alyea, *Electrochemical Systems*, John Wiley and Sons, New York (2004).
2. D. Dees, E. Gunen, D. Abraham, A. Jansen, and J. Prakash, *J. Electrochem. Soc.,* **152** (7) A1409 (2005).
3. D. Dees, E. Gunen, D. Abraham, A. Jansen, and J. Prakash, *J. Electrochem. Soc.,* **155** (8) A603 (2008).
4. K. Gallagher, D. Dees, A. Jansen, D. Abraham, and S.-H. Kang, *J. Electrochem. Soc.,* **159** (12), A2029-A2037 (2012).
5. D. W. Dees, S. Kawauchi, D. P. Abraham, and J. Prakash, *J. Power Sources,* **189** (1), 263-268 (2009).

V.C.6 Impact of Coatings on Voltage Fade in the LMR-NMC Materials (ANL, ORNL, NREL)

Coatings Team[11]

Argonne National Laboratory, Argonne, IL
Oak Ridge National Laboratory, Oak Ridge, TN
National Renewal Energy Laboratory, Golden, CO

Start Date: October 2012
Projected End Date: June 2013 (complete)

Objective

- Determine the efficacy of coatings and additives to slow or stop the voltage fade phenomenon

Technical Barriers

This project addresses the following technical barriers as described in the USABC goals [2, 3]:

(A) Performance at ambient temperatures
(B) Cycle life

Technical Targets

- PHEV specific energy targets (pack): 3.4 kWh (min) to 11.6 (max) [2]
- EV specific energy targets (pack): 80 (min) to 200 (max) Wh/kg [3]

[11] The Coatings Team (within the Voltage Fade project) members include: (from ANL) Ira Bloom, Lynn Trahey, Ali Abouimrane, Ilias Belharouak, Xiaofeng Zhang, Qingliu Wu, Wenquan Lu, Daniel P. Abraham, Martin Bettge, Jeffrey W. Elam, Xiangbo Meng, Anthony K. Burrell, (from NREL) Chunmei Ban, Robert Tenent, (from ORNL) Jagjit Nanda and Nancy Dudney.

Accomplishments

The effects of the coatings Al_2O_3, $LiAlO_x$, ZrO_2, TiO_2, $AlPO_4$, and LiPON and of the electrolyte additives 3-hexylthiophene and lithium difluoro (oxalato)borate (LiDFOB) on the voltage fade phenomenon in $0.5Li_2MnO_3 \bullet 0.5LiNi_{0.375}Mn_{0.375}Co_{0.25}O_2$ cathodes were investigated. Cells containing these materials or additives were cycled according to a standard protocol at room temperature between 2.0 and 4.7 V vs. Li^+/Li. As expected, the cells containing either an additive or a coated cathode displayed less capacity loss than cells containing an uncoated cathode and no additive. The voltage fade phenomenon was quantified in terms of changes in the average cell voltage (Wh/Ah). The results indicate that, within experimental error, all of the coatings and additives produced little-to-no effect on voltage fade.

✧ ✧ ✧ ✧ ✧

Introduction

Layered materials in the Li-Mn-rich portion of the Li-Ni-Mn-Co-O phase diagram (LMR-NMC), which are structurally integrated composites of Li_2MnO_3 and $Li(Ni,Mn,Co)O_2$ and are usually written as $aLi_2MnO_3 \bullet (1-a)Li(Ni,Mn,Co)O_2$, are promising cathodes for use in lithium-ion batteries. However, with cycling, the shape of the voltage vs. capacity curve changes. A similar decline is also observed on charging, strongly suggesting that changes to the equilibrium electrochemical potential of the active material cause the voltage fade. In the literature, the continuous change in the shape of the discharge (and charge) curves has been attributed to the formation of a spinel-like phase [4-8]. As a result of the loss in potential, there is a loss in energy, limiting the utility of these materials in energy-demanding applications, such as in electric vehicles.

Approach

Three national laboratories, Argonne National Laboratory, the National Renewable Energy Laboratory and Oak Ridge National Laboratory, are collaborating to devise methods to arrest this voltage fade. The work, described below, approaches this goal by investigating the effects of using cathode coatings and electrolyte

additives. In the literature, coatings, surface modifications, and additives of many descriptions have been used to stabilize the capacity of cathode materials and enhance cycling ability [4-46], enhance the rate capacity of cathode materials [17, 18, 20, 24, 25, 27, 35, 36, 47], lessen their thermal reactivity [16, 48-51], lessen their reactivity towards the organic electrolytes [52], and promote secondary electrolyte interface layer formation on the cathode [50]. The effects of the coatings Al_2O_3, $LiAlO_x$, ZrO_2, TiO_2, $AlPO_4$, and lithium phosphorus oxynitride (LiPON) and of the electrolyte additives 3-hexylthiophene and LiDFOB on voltage fade were investigated. It should be noted that both electrolyte additives are very effective in forming a protective layer on the surface of the positive electrode at high potentials [33, 45].

Results

Coatings. All positive electrodes contained the same commercially available LMR-NMC material, $0.5Li_2MnO_3 \bullet 0.5LiNi_{0.375}Mn_{0.375}Co_{0.25}O_2$ (Toda Kogyo, Japan; referred to as HE5050), which was used to fabricate coated and uncoated cathode laminates. Atomic-layer deposition (ALD) coatings of Al_2O_3 [54, 55-57], TiO_2, ZrO_2, and $LiAlO_x$ [58] were applied to HE5050 laminate sheets. $AlPO_4$ [40-43] and LIPON [18] were applied to HE5050 powders before casting into laminates. The compositions of the cathode materials are given in Table V - 10. All were assembled into coin cells with lithium metal anodes.

Cell cycling. All cycling was performed at room temperature. All cells were cycled between 2 V and 4.7 V at 10 mA/g for the first cycle, and then between 2 V and 4.7 V (vs. Li^+/Li) at 20 mA/g for the following cycles. The cells were cycled between 2 and 4.7 V for a minimum of 20 and a maximum of 50 times. While cycling, current interrupt measurements were carried out at 3.5, 3.9, 4.3, and 4.7 V during charge and at 4.0, 3.6, 3.2, and 2.0 V during discharge. Estimates of cell resistance were calculated from the values of cell voltage and current at times t_0 and t_1 using Eq. 1

$$R = \left|\frac{v_{t_1} - v_{t_0}}{i_{t_1} - i_{t_0}}\right|, R = \left|\frac{v_{t_1} - v_{t_0}}{i_{t_1} - i_{t_0}}\right|, \quad \text{Eq. 1.}$$

where v_{t_1} and v_{t_0} are the cell voltages at t_1 and t_0, respectively; i_{t_1} and i_{t_0} are the respective currents.

Table V - 10: Cathode compositions used in this work

Designation (deposition temperature or time)	Cathode
Baseline	86 wt% HE5050 4 wt% SFG-6 graphite 2 wt% SuperP carbon black 8 wt% PVDF
TiO_2 (100°C) TiO_2 (150°C)	92 wt% active material 4 wt% C45 conductive additive 4 wt% Solvey 5130 binder
ZrO_2 (100°C) ZrO_2 (150°C)	
$LiAlO_x$ (225°C)	
$AlPO_4$	86 wt% active material 4 wt% SFG-6 graphite 2 wt% SuperP carbon black 8 wt% PVDF
5 ALD cycles Al_2O_3 (120°C) 100 ALD cycles Al_2O_3 (120°C)	84 wt% active material 8 wt% PVDF binder 8 wt% Super P carbon black
LiPON (1 h) LiPON (2 h) LiPON (3 h)	85 wt% active material 7.5 wt% SuperP carbon black 7.5 wt% PVDF
LiDFOB, 2.0 wt%	92 wt% active material 4 wt% C45 conductive additive 4 wt% Solvey 5130 binder
3-hexylthiophene, 0.1 wt%	92 wt% active material 4 wt% C45 conductive additive 4 wt% Solvey 5130 binder

The activation charge subcycle and the discharge immediately following it were omitted from further analysis in this work. After that subcycle, the energy (Wh) and capacity (Ah) values were either extracted directly from the cycling data or were calculated from the raw data using Microsoft Excel®. The average voltage for a given charge or discharge subcycle was calculated as Wh/Ah. The resistance values at the first three voltages were averaged and used to correct the average voltage value for the average resistance of the cell during a given cycle. The relative change in the iR-corrected average voltage was calculated by comparing the value from the first discharge or charge subcycle to the respective value at the 20th discharge or charge subcycle, as shown in Eq. 2.

$$Rel.change\ in\ avg.voltage = \frac{Avg.voltage_{first\ cycle} - Avg.voltage_{last\ cycle}}{Avg.voltage_{first\ cycle}} \quad \text{Eq. 2.}$$

These relative average voltage values then were used for plotting and subsequent analyses.

Capacity fade. As expected, the cell discharge capacity faded with cycling for cells containing the electrolyte additives and the coated or uncoated cathode materials, as shown in Figure V - 114. The baseline showed the greatest amount of capacity fade, which was due to impedance rise and loss of active sites in the

positive electrode when cycled to 4.7 V. Figure V - 114 shows that the capacity fade rate of the coated materials is sensitive to the nature of the coating; some coated materials display greater capacity loss rates than others. It was interesting to note that the loss of capacity in cells containing an electrolyte additive were different, with the cell containing LiDFOB displaying about 25% of the capacity loss of the cell containing 3-hexylthiophene. Of more importance, the data in Figure V - 114 clearly show that the capacity of cells containing coated cathode materials or electrolyte additives fades slower than that of the cell containing either no additive or uncoated materials. This trend is consistent with reports in the literature [15-39, 44-46].

Voltage Fade. In these experiments, the cells containing either coated cathodes or an additive behaved similarly as those that were uncoated or contained no additive. Examples of the aging behavior of cells containing an uncoated cathode and coated cathode are shown in Figure V - 115 and Figure V - 116, respectively. The first charge cycle is believed to activate the Li_2MnO_3 portion of the composite cathode material, a process needed to achieve high capacity density. With continued cycling, the cathode material loses voltage, as indicated by the changes in the voltage vs. normalized capacity curves; this loss of voltage behavior is consistent with that seen by others [4, 9].

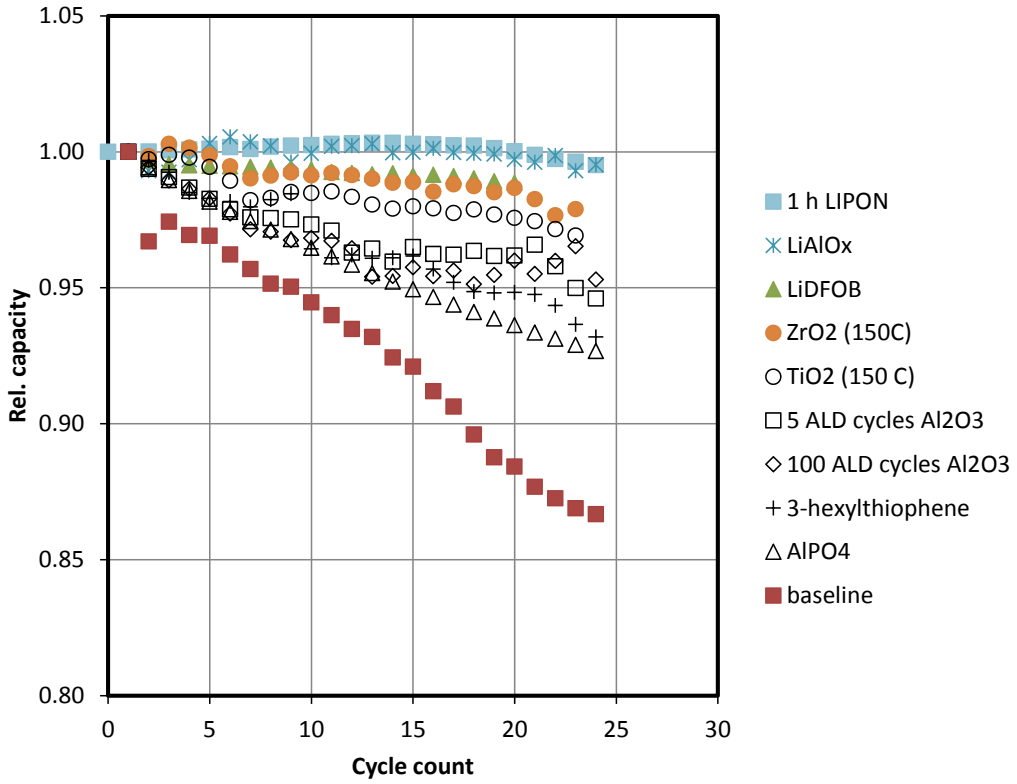

Figure V - 114: Rel. cell capacity vs. cycle count, showing capacity decline with cycle count. The capacity of coated materials tended to decline slower than that of uncoated materials. The relative cell capacity vs. cycle count for the 2- and 3-h LiPON coatings behaved similarly to that seen for the 1-h coating. These data were omitted for the sake of clarity

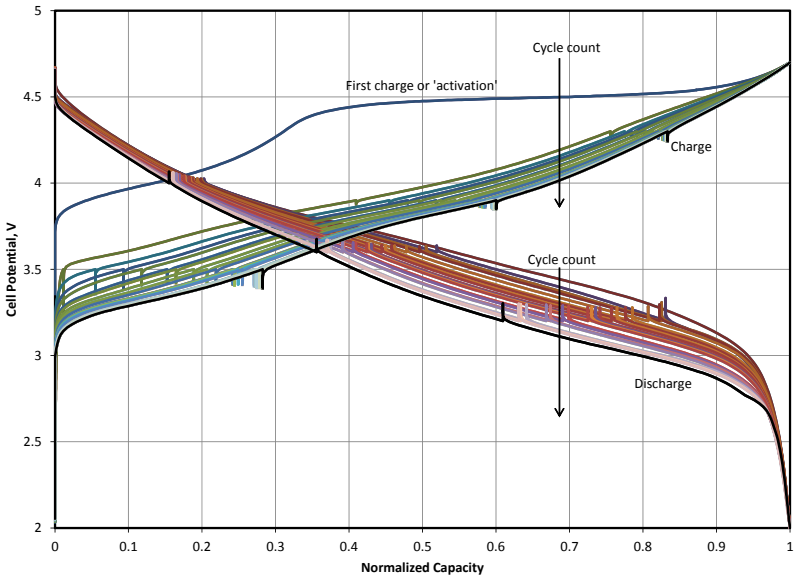

Figure V - 115: Cell potential vs. normalized capacity, representing the typical charge and discharge voltage response of a cell containing an uncoated cathode in these experiments. Selected curves were removed for the sake of clarity. During the first charge, the LMR NMC material was activated. With continued cycling, the voltage response for both the charge and discharge subcycles changed. The downward tick marks on the charge curves and upward tick marks on the discharge curves represent current interrupts

The iR-corrected, average voltage value for a given cycle was calculated using the data shown in Figure V - 116. A typical average voltage vs. cycle count plot is shown in Figure V - 117. The curves shown in Figure V - 117 closely follow the cell voltage behavior shown in Figure V - 116 for both charge and discharge. It should be noted that the shape of the average voltage curve was not sensitive to the presence of a coating or its nature, or to the presence of an electrolyte additive.

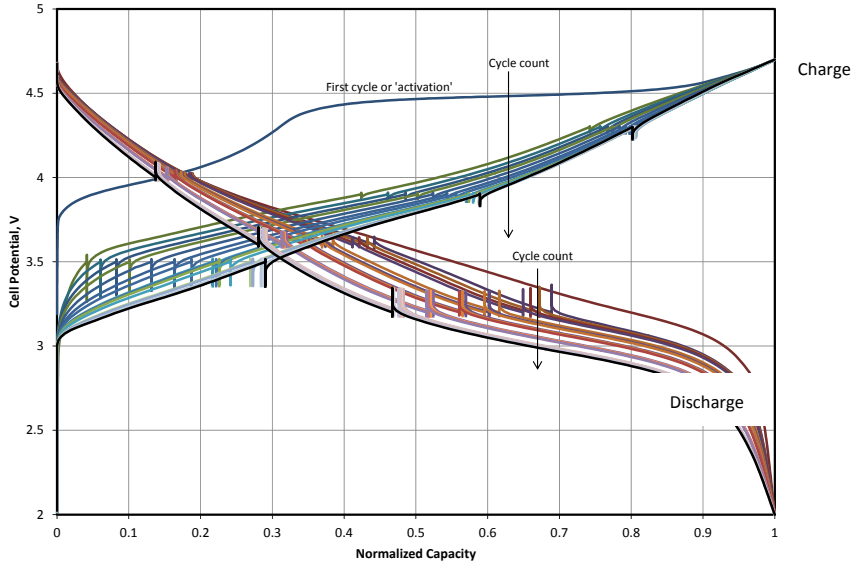

Figure V - 116: Cell potential vs. normalized capacity, representing the typical charge and discharge voltage response of a cell containing a coated cathode in these experiments. This particular cell contained a zirconia-coated cathode (150°C). Selected curves were removed for the sake of clarity. During the first charge, the LMR NMC material was activated. With continued cycling, the voltage response for both the charge and discharge subcycles changed. The downward tick marks on the charge curves and upward tick marks on the discharge curves represent current interrupts

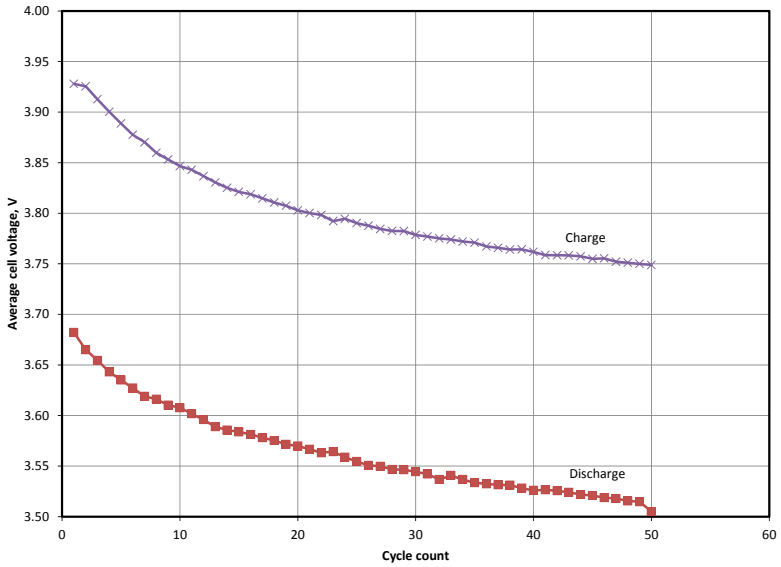

Figure V - 117: Typical plot of iR-corrected average cell voltage (Wh/Ah) vs. cycle count from a baseline cell, showing that, during both charge and discharge subcycles, the average cell voltage decreases with cycling. The first cycle was omitted from this plot

The relative change in average voltage for the cells is given in Table V - 11. In some cases, there was more than one cell for a given coating. This is indicated by the presence of a value for standard error (s.e.). Examining the values for the discharge subcycle shows that, after 20 cycles, most were within about 17% of the value given for the baseline material, and the value for LiPON (3 h) was almost twice that given for the baseline. The values given for the relative change in average voltage during the charge subcycle show a similar pattern after 20 cycles. Most values were within about 30% of the value given for the baseline, and that for LiPON(3 h) was twice that given for the baseline.

It is interesting to note that neither the thickness of the Al_2O_3 layer nor the deposition temperature of the TiO_2 and ZrO_2 layers had a significant effect on the relative change in the average voltage. The voltage loss from cathodes containing $LiAlO_x$ was approximately the same as those containing TiO_2 or ZrO_2 layers.

The data in Table V - 11 show that the values given for the 1-h and 2-h LiPON layers were outside the statistical range for the discharge subcycles and within the statistical range for the charge subcycles. The additional hour of sputtering time did not markedly change the voltage fade response characteristic. However, at 3 h, voltage fade increased by about a factor of 2 for both the charge and discharge subcycles, which was due to the increase in electronic resistance of the LiPON film surrounding the cathode particles [27, 28].

After 20 cycles, the values given for the $AlPO_4$ layer and the electrolyte additives are also outside the statistical range. The values for the electrolyte additives indicate that the average voltage decreased slightly less than the baseline. The value for $AlPO_4$ indicates that the average voltage decreased slightly more than the baseline. After 50 cycles, the values indicate a greater loss.

The central question underlying this work concerned the origin of voltage fade. That is, is the voltage fade phenomenon controlled by a reaction at the cathode-electrolyte interface? Theoretically, if voltage fade were caused by the loss of oxygen (e.g., during electrochemical activation [53]) or the loss of a soluble constituent, such as Mn^{2+}, changing the nature of the exposed cathode surface should change the rate at which the reaction proceeds by a significant amount.

In the literature [15-39, 44-46] and in this work, coatings and electrolyte additives were shown to be very effective in controlling capacity loss. The rates of these reactions displayed significant changes in the presence of an interface-modifying organic or inorganic material. However, the results in the present work indicate that using interface-modifying materials or additives had little-to-no effect on voltage fade. Under the cycling conditions used in these experiments, voltage fade appears to derive from an intrinsic property of the LMR-NMC materials, such as thermodynamic instability, and proceeds at a rate of a few millivolts per cycle [59]. Adjusting the cycling window was found to be one practical approach to reduce voltage fade [59, 60].

Table V - 11: Relative change in average voltage in baseline cells and in cells containing an electrolyte additive or a coated cathode

Coating/Additive	100 × Rel. Change in Average Voltage after 20 Cycles (100 × s.e.)	100 × Rel. Change in Average Voltage after 50 Cycles (100 × s.e.)
Discharge		
Baseline	3.14 (0.10)	4.81
3-hexylthiophene	2.88	4.52
LiDFOB	3.38	
Al_2O_3 (5 ALD cycles)	3.40	5.30
Al_2O_3 (100 ALD cycles)	3.22	5.47
$AlPO_4$	3.68	5.48
$LiAlO_x$	3.32 (0.07)	
TiO_2 (100°C)	3.14 (0.04)	
TiO_2 (150°C)	3.20 (0.07)	
ZrO_2 (100°C)	3.17 (0.01)	
ZrO_2 (150°C)	3.26 (0.03)	
LiPON (1 h)	2.69	
LiPON (2 h)	2.60	
LiPON (3 h)	5.20	
Charge		
Baseline	3.97 (0.49)	4.52
3-hexylthiophene	3.16	4.20
LiDFOB	4.89	
Al_2O_3 (5 ALD cycles)	3.52	5.15
Al_2O_3 (100 ALD cycles)	3.14	4.70
$AlPO_4$	3.66	5.03
$LiAlO_x$	5.21 (0.05)	
TiO_2 (100°C)	4.39 (0.01)	
TiO_2 (150°C)	4.60 (0.01)	
ZrO_2 (100°C)	4.62 (0.02)	
ZrO_2 (150°C)	4.85 (0.03)	
LiPON (1h)	3.67	
LiPON (2 h)	3.75	
LiPON (3 h)	7.97	

Conclusions and Future Directions

The effects of the coatings Al_2O_3, $LiAlO_x$, ZrO_2, TiO_2, $AlPO_4$, and LiPON and of the electrolyte additives 3-hexylthiophene and LiDFOB on the voltage fade phenomenon in $0.5Li_2MnO_3•0.5LiNi_{0.375}Mn_{0375}Co_{0.25}O_2$ cathodes were investigated. Cells containing these materials were cycled according to a standard protocol at room temperature. As expected, the cells containing either an additive or a coated cathode displayed less capacity loss than cells containing an uncoated cathode and no additive. The voltage fade phenomenon was quantified in terms of the change in a resistance-corrected average cell voltage. The results indicate that, within experimental error, there was little-to-no effect on voltage fade from the coatings and additives, pointing to voltage fade being tied to the intrinsic nature of the cathode material. Thus, methods, other than coatings and additives, to control voltage should be tried.

FY 2013 Publications/Presentations

1. Ira Bloom, Lynn Trahey, Ali Abouimrane, Ilias Belharouak, Xiaofeng Zhang, Qingliu Wu, Wenquan Lu, Daniel P. Abraham, Martin Bettge, Jeffrey W. Elam, Xiangbo Meng, Anthony K. Burrell, Chunmei Ban , Robert Tenent, Jagjit Nanda and Nancy Dudney, J. Power Sources, *in press.*

References

1. Coatings team members: Ira Bloom, Lynn Trahey, Ali Abouimrane, Ilias Belharouak, Xiaofeng Zhang, Qingliu Wu, Wenquan Lu, Daniel P. Abraham, Martin Bettge, Jeffrey W. Elam, Xiangbo Meng, Anthony K. Burrell, Chunmei Ban, Robert Tenent, Jagjit Nanda and Nancy Dudney.
2. Battery Test Manual For Plug-In Hybrid Electric Vehicles, Rev. 1, June 2010, INL/EXT-07-12536.
3. Electric Vehicle Battery Test Procedures Manual,Rev. 2, June 1996.
4. B. Xu, D. Qian, Z. Wang, and Y. S. Meng, Mater. Sci. Eng. R, 73 (2012) 51–65.
5. J. Croy, K. Gallagher, M. Balasubramanian, Z. Chen, Y. Ren, S.-H. Kang, D. W. Dees, and M. M. Thackeray, J. Phys. Chem. C, DOI: 10.1021/jp312658q.
6. M. M. Thackeray, S.-H. Kang, C. S. Johnson, J. T. Vaughey, R. Benedek, and S. A. Hackney, J. Mater. Chem., 17 (2007) 3112–3125.
7. B. Xu, C. R. Fell, M. Chic, and Y. S. Meng, Energy Environ. Sci., 4 (2011) 2223.

8. A. R. Armstrong, N. Dupre, A. J. Paterson, C. P. Grey, and P. G. Bruce, Chem. Mater., 16 (2004) 3106–3118.
9. D. Mohanty, S. Kalnaus, R. A. Meisner , K. J. Rhodes, J. Li, E. A. Payzant, D. L. Wood III, and C. Daniel, J. Power Sources, 229 (2013) 239–248.
10. M. Gu, I. Belharouak, J. Zheng, H. Wu, J. Xiao, A. Genc, K. Amine, and C. Wang, ACS Nano, 7 (2012) 760–767.
11. B. Xu, C. R. Fell, M. Chic, and Y. S. Meng, Energy Environ. Sci., 4 (2011) 2223.
12. A. R. Armstrong, N. Dupre, A. J. Paterson, C. P. Grey, and P. G. Bruce, Chem. Mater., 16 (2004) 3106–3118.
13. D. Mohanty, S. Kalnaus, R. A. Meisner , K. J. Rhodes, J. Li, E. A. Payzant, D. L. Wood III, and C. Daniel, J. Power Sources, 229 (2013) 239–248.
14. M. Gu, I. Belharouak, J. Zheng, H. Wu, J. Xiao, A. Genc, K. Amine, and C. Wang, ACS Nano, 7 (2012) 760–767.
15. J. Liu, Z. Chen, S. Busking, I. Belharouak, and K. Amine, J. Power Sources, 174 (2007) 852–855.
16. S. S. Zhang, J. Power Sources, 162 (2006) 1379–1394.
17. Y. Kim, N. J. Dudney, M. Chi, S. K. Martha, J. Nanda, G. M. Veith, and C. Liang, J. Electrochem. Soc., 160 (2013) A3113–A3125.
18. S. K. Martha, J. Nanda, Y. Kim, R. R. Unocic, S. Pannala, and N. J. Dudney, J. Mater. Chem. A, DOI: 10.1039/c3ta10586e.
19. D. Guan and Y. Wang, Ionics, 19 (2013) 1–8.
20. J.-H. Kim, M.-S. Park, J.-H. Song, D.-J. Byun, Y.-J. Kim, and J.-S. Kim, J. Alloys and Compounds, 517 (2012) 20–25.
21. H.-J. Kweon, S. J. Kim, and D. G. Park, J. Power Sources, 88 (2000) 255–261.
22. M. Mladenov, R. Stoyanova, E. Zhecheva, and S. Vassilev, Electrochem. Comm., 3 (2001) 410–416.
23. L. A. Riley, S. Van Atta, A. S. Cavanagh, Y. Yan, S. M. George, P. Liu, A. C. Dillon, and S.-H. Lee, J. Power Sources, 196 (2011) 3317–3324.
24. E.-G. Shim, T.-H. Nam, J.-G. Kim, H.-S. Kim, and S.-I. Moon, J. Power Sources, 172 (2007) 901–907.
25. W. C. West, J. Soler, M. C. Smart, B. V. Ratnakumar, S. Firdosy, V. Ravi, M. S. Anderson, J. Hrbacek, E. S. Lee, and A. Manthiram, J. Electrochem. Soc., 158 (2011) A883–A889.
26. F. Wu, M. Wang, Y. Su, S. Chen, and B. Xu, J. Power Sources, 191 (2009) 628–632.
27. R. Guo, P. Shi, X. Cheng, and L. Sun, Electrochimica Acta, 54 (2009) 5796–5803.
28. J. Liu and A. Manthiram, J. Mater. Chem., 20 (2010) 3961–3967.
29. J. Ni, L. Gao, and L. Lu, J. Power Sources, 221 (2013) 35–41.
30. F. Wu, M. Wang, Y. Su, L. Bao, and S. Chen, Electrochimica Acta, 54 (2009) 6803–6807.
31. L. Yang and B. L. Lucht, Electrochem. Sol. State Letters, 12 (2009) A229–A231.
32. H. Zhao, L. Gao,W. Qiu, and X. Zhang, J. Power Sources, 132 (2004) 195–200.
33. A. Abouimrane, S. A. Odom, H. Tavassol, M. V. Schulmerich, H. Wu, R. Bhargava, A. A. Gewirth, J. S. Moore, and K. Amine, J. Electrochem. Soc., 160 (2013) A268–A271.
34. J. C. Burns, N. N. Sinha, D. J. Coyle, G. Jain, C. M. VanElzen, W. M. Lamanna, A. Xiao, E. Scott, J. P. Gardner, and J. R. Dahn, J. Electrochem. Soc., 159 (2012) A85–A90.
35. Z. Chen and J. R. Dahn, Electrochem. Sol. State Letters, 5 (2002) A213–A216.
36. S.-K. Hu, G.-H. Cheng, M.-Y. Cheng, B.-J. Hwang, and R. Santhanam, J. Power Sources, 188 (2009) 564–569.
37. A. M. Kannan and A. Manthiram, Electrochem. Sol. State Letters, 5 (2002) A167–A169.
38. T. Liu, S.-X. Zhao, K. Wang, and C.-W. Nan, Electrochimica Acta, 85 (2012) 605–611.
39. Q. Wu, W. Lu, M. Miranda, T. K. Honaker-Schroeder, K. Y. Lakhsassi, and D. Dees, Electrochem. Comm., 24 (2012) 78–81.
40. J. Cho, T. G. Kim, C. Kim, J.-G. Lee, Y.-W. Kim, and B. Park, J. Power Sources, 146 (2004) 58–64.
41. Y. Wu, A.V. Murugan, and A. Manthiram, J. Electrochem Soc., 155 (2008) A635–A641.
42. E. Jung and Y.-J. Park, Nanoscale Research Letters, 7 (2012) 1–4.
43. J. Wang., Y. Wang, Y. Guo, Z. Ren, and C. Liu, J. Mater. Chem. A, 1 (2013) 4879–4884.
44. M. Bettge, Y. Li, B. Sankaran, N. Dietz Rago, T. Spila, R. T. Haasch, I. Petrov, and D. P. Abraham, J. Power Sources, 233 (2013) 346–357.
45. Y. Zhu, Y. Li, M. Bettge, and D. P. Abraham, J. Electrochem. Soc., 159 (2012) A2109–A2117.
46. Y. Zhu, Y. Li, M. Bettge, and D. P. Abraham, Electrochim. Acta – in press, http://dx.doi.org/10.1016/j.electacta.2013.03.102.
47. A. Abouimrane, O. C. Compton, H. Deng, I. Belharouak, D. A. Dikin, S-B. T. Nguyen, and K. Amine, Electrochemical and Solid-State Letters, 14(9) (2011) 126.

48. Y.-H. Cho, K. Kim, S. Ahn, H. K. Liu, J. Power Sources, 196 (2011) 1483–1487.
49. C.-C. Chang, K.-Y. Lee, H.-Y. Lee, Y.-H. Su, and L.-J. Her, J. Power Sources, 217 (2012) 524–529.
50. C. Li, H. P. Zhang, L. J. Fu, H. Liu, Y. P. Wu, E. Rahm, R. Holze, and H. Q. Wu, Electrochimica Acta, 51 (2006) 3872–3883.
51. S. Santee, A. Xiao, L. Yang, J. Gnanaraj, and B. L. Lucht, J. Power Sources, 194 (2009) 1053–1060.
52. Y. Iriyama, H. Kurita, I. Yamada, T. Abe, and Z. Ogumi, J. Power Sources, 137 (2004) 111–116.
53. C. Li, H. P. Zhang, L. J. Fu, H. Liu, Y. P. Wu, E. Rahm, R. Holze, and H. Q. Wu, Electrochimica Acta, 51 (2006) 3872–3883.
54. M. Bettge, Y. Li, B. Sankaran, N. Dietz Rago, T. Spila, R. T. Haasch, I. Petrov, and D. P. Abraham, J. Power Sources, 233 (2013) 346–357.
55. S. M. George, O. Sneh, A. C. Dillon, M. L. Wise, A. W. Ott, L. A. Okada, and J. D. Way, Appl. Surf. Sci., 82-3 (1994) 460.
56. Y. S. Jung, A. S. Cavanagh, A. C. Dillon, M. D. Groner, S. M. George, and S. H. Lee, J. Electrochem. Soc., 157 (2010) A75.
57. Y. S. Jung, A. S. Cavanagh, L. A. Riley, S. H. Kang, A. C. Dillon, M. D. Groner, S. M. George, and S. H. Lee, Adv. Mater., 22 (2010) 2172.
58. A. Rahtu and M. Ritala, Chemical Vapor Deposition, 8 (2002) 21.
59. M. Bettge, Y. Li, K. Gallagher, Y. Zhu, Q.Wu, W. Lu, I. Bloom, and D. P. Abraham, J. Electrochem. Soc., 160 (2013) A2046-A2055 .
60. K. G. Gallagher, J. R. Croy, M. Balasubramanian, M. Bettge, D. P. Abraham, A. K. Burrell, and M. M. Thackeray, Electrochem. Comm. 33 (2013) 96–98

V.D Materials Optimization

V.D.1 High Voltage Electrolytes for Li-ion Batteries (ARL)

Arthur von Wald Cresce, Kang Xu
Jan Allen, Oleg Borodin, Samuel Delp,
Joshua Allen, Richard Jow

Point of Contact:
T. Richard Jow / Kang Xu
U.S. Army Research Laboratory
2800 Powder Mill Road
Adelphi, MD 20783
Phone: (301) 394-0340 / (301) 394-0321
Fax: (301) 394-0273
E-mail: t.r.jow.civ@mail.mil / conrad.k.xu.civ@mail.mil

Start Date: March 2009
Projected End Date: September 2013

Objectives

- Develop high voltage electrolytes that enable the operation of 5 V Li-ion batteries.
  - Understand the surface chemistry at the high voltage cathode and electrolyte interface.
  - Understand the mechanism of interphase formation on high voltage cathode surfaces.
  - Evaluate the additives containing electrolytes using 4.7 V $LiNi_{0.5}Mn_{1.5}O_4$ (LNMO) and 4.8 V $LiCoPO_4$ (LCP) as testing vehicles.

Technical Barriers

This project addresses the following technical barriers of today's Li-ion batteries:

- SOA electrolytes do not support chemistries beyond 4.5 V.
- Although new electrolyte solvents, such as sulfones and nitriles, remain stable at high voltages on the cathode, they fail to simultaneously cater to the anode SEI formation.
- Replacing SOA carbonates with highly fluorinated solvents drives up the overall cost.
- Lack of reliable 5 V cathodes as testing vehicles for electrolyte development.

Technical Targets

- Design and synthesize new electrolyte additives that target the interphasial chemistry on high voltage cathode surfaces.

Accomplishments

- Designed, synthesized and scaled-up lithium perfluorinated butoxide (LiPFBO) additive. The effectiveness of LiPFBO has been demonstrated in LNMO/graphite cells.
- Identified additive A2 that is effective in enabling the cycling of LNMO/graphite cells at 55°C with high coulombic efficiency and capacity retention.
- Successfully improved capacity utilization, rate performance and coulombic efficiency of LFCP through new generation of substitution without relying high voltage electrolytes.
- Calculated how oxidative stability of electrolyte solvents changed with the presence of anion, other solvent molecules and their combinations using DFT.
- Studied SEI components and SEI-electrolyte interactions using MD simulations.

✧ ✧ ✧ ✧ ✧

Introduction

In order for 5 V class cathode chemistries such as LMNO and LCP to be used for HEV/PHEV/EV applications, electrolytes must maintain kinetic stability beyond 4.5 V. Despite the developments of new electrolyte solvents that were claimed to be able to support the above chemistries, the accompanying intrinsic weaknesses often make the effort impractical, such as the instability of sulfone and nitriles on graphitic anode, or the high cost of highly-fluorinated co-solvents FEC or FPC. We believe that by using properly-designed electrolyte additives the above intrinsic weaknesses could be circumvented, as our previous work on tris(hexafluoro-iso-propyl)phosphate (HFiP) demonstrated.

This year's work focused on further confirmation of HFiP on different cathode chemistries, surface analysis of these cathodes for understanding the HFiP

breakdown mechanism, as well as design and synthesis of new additives with perfected structures. Computational assistance was also employed to understand the thermodynamic oxidation of these new additives.

Approach

Design new additives and identify additives enabling the 5 V operations of Li-ion batteries using an understanding of the interfacial reactions at the cathode/electrolyte interfaces. – Electrochemical methods, surface analysis including XPS, and computational methods are used to understand the interfacial reactions and develop effective electrolyte additives.

Develop structurally stabilized with less reactive surfaces high voltage cathodes. – The approach of partially substituting the transition metal in high voltage cathodes with other elements is adopted. This development is in concert with the electrolyte additives development.

Results

Design, synthesis and evaluation of new additives (Arthur v. Cresce, Kang Xu).

The new additive, *lithium perfluoro-t-butoxide* (LiPFBO),whose structure is seen in Figure V - 118, was successfully scaled-up utilizing the Argonne National Laboratory's facilities. This was a key step in using the compound as an additive. Perfluoro-t-butoxide is an additive for high-voltage Li-ion electrolytes that effectively improves Coulombic cycling efficiency, as confirmed by Jeff Dahn at Dalhousie University, and shows promise as a low and high temperature additive as well. We are in the process of synthesizing several additives that contain the perfluoro-t-butyl and hexafluoroisopropyl moieties to expand upon work already performed on phosphate-based versions of these compounds. The goal is twofold: to react with the oxidizing cathode surface with the goal of stabilizing the electrolyte-cathode interface, and to improve SEI properties on the graphite anode by limiting the excess growth of SEI material. Current work is therefore focusing on the directed development of new additives that either can deliver fluorinated moieties to the electrode surfaces, or can perform similar functions.

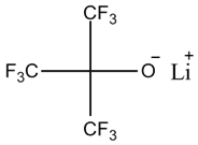

Figure V - 118: Lithium perfluoro-t-butoxide (LiPFBO) structure

The performance of the butoxide additive was noted by Jeff Dahn of Dalhousie University using high-precision coulometry, as seen in Figure V - 119, compared to other ARL additives and a control:

What the Dalhousie results indicate is that the butoxide (blue dots) effectively increases the retention of discharge capacity (although without a large number of cycles). Evolution of high CE is slow compared to a standard electrolyte control but ultimately exceeds the control. Low temperature tests have been performed but have not yet been disclosed.

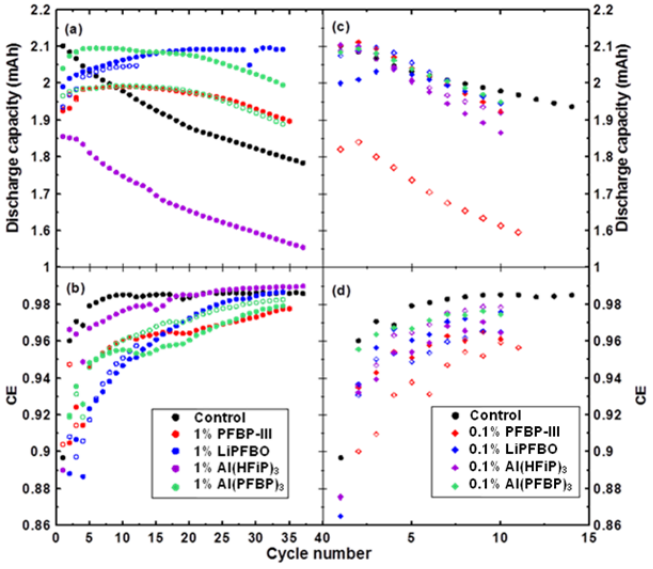

Figure V - 119: Discharge capacity and CE of LNMO / graphite cells cycled in control electrolyte (or Gen 2 electrolytes) with and without additives at 25°C

Impact of Additives on Cycling of LNMO/A12 at 55°C (Samuel Delp, Jan Allen, Richard Jow).

The cycling of LNMO at 55°C remains challenging. The LNMO/A12 full cells were tested at 25°C and 55°C to study the effectiveness of various additives including HFiP, VC and A2 on capacity retention. Both LNMO and A12 (graphite) were provided by ANL. The baseline electrolyte (or Gen 2 electrolyte) is 1.2 M $LiPF_6$ in EC:EMC (3:7).

As shown in Figure V - 120, the effectiveness of A2 additive has been demonstrated in capacity retention, CE, and capacity utilization for the LNMO/graphite full cells.

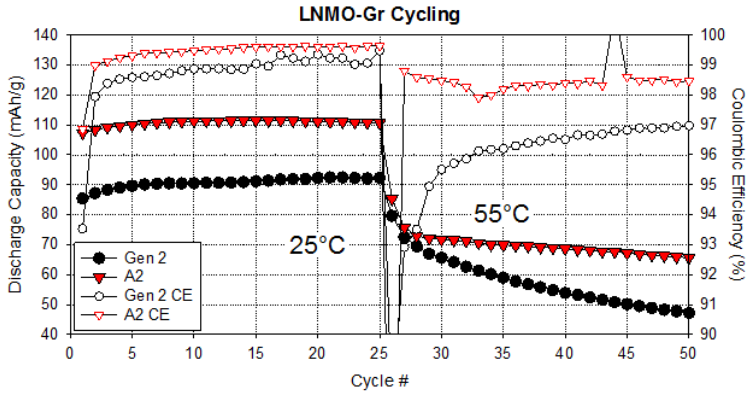

Figure V - 120: C/3 cycling data with capacity retention and CE for Gen 2 electrolyte without and with A2 additive. The first 25 cycles are at 25°C and the next 25 cycles are at 55°C

The effectiveness of A2 additive can also be demonstrated through the dQ/dV vs. V plots as shown in Figure V - 121. The plots were acquired using a C/3 cycling rate. The red line is for the 25th cycle at 25°C. The orange line is the next cycle (cycle 26) but the cells were moved to 55°C before this cycle. The yellow-green line is for the 25th cycle at 55°C (50th overall cycle). The electrolyte with A2 additive retains the overall peak shapes better than the baseline (Gen 2) electrolyte, specifically having a higher voltage on the discharge (bottom portion of curve) indicating faster kinetics/less resistance in the cells.

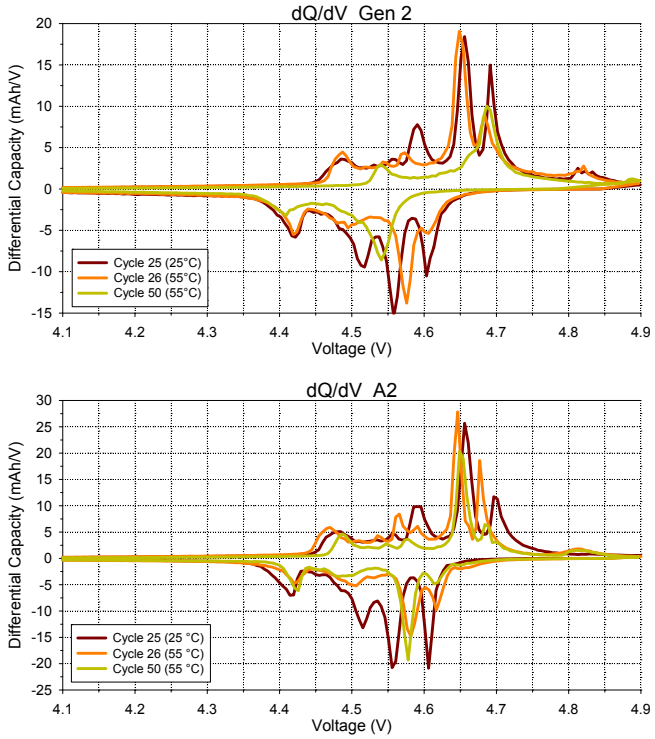

Figure V - 121: dQ/dV versus V plots for LNMO/graphite cells at 25°C and 55°C in Gen 2 electrolyte with and without A2 additive

Cycling of Modified LCP High Voltage Cathode (Jan Allen, Joshua Allen, Samuel Delp, Richard Jow).

Doping LCP has been demonstrated by our lab as a viable means for improving the cathode performance. Most notably, Fe-doping has been shown to greatly improve the cycle life of LCP and yielded half cells able to cycle in excess of 500 cycles when paired with a high voltage additive. Standard LFCP (mixed lithium iron and cobalt phosphate material), however, yields only ~110 mAh g^{-1} discharge capacity and a poor efficiency when cycled with the standard electrolyte (e.g., 1m $LiPF_6$ in EC:EMC, 3:7 w/w). Rather than modifying the electrolyte composition to stabilize the cathode surface, the cathode composition itself was modified to improve the overall cathode stability. By modifying the LCP-based cathode, a significant capacity increase was observed and an efficiency of >99.45% was observed after 100 cycles (see Figure V - 122 and Figure V - 123). This chemistry is being further tuned, as well as the electrolyte composition, to yield an optimized system.

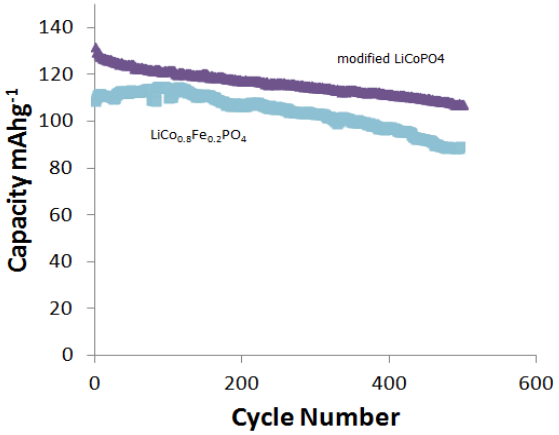

Figure V - 122: Capacity retention of standard LFCP and modified LCP cathodes cycled against Li in standard Gen 2 electrolyte at 25°C

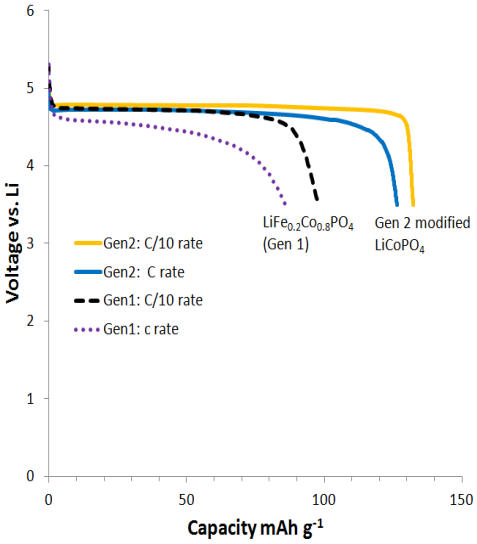

Figure V - 123: Comparisons of rate performance of Gen 1 LFCP cathode and Gen 2 modified LCP electrode in the standard electrolyte

Quantum Chemistry Studies of Electrolyte Oxidation Stability and Decomposition Reactions (Oleg Borodin, Richard Jow).

Oxidation stability and initial decomposition reactions were studied for a wide range of solvent/anion and solvent dimer complexes (carbonates, sulfones, phosphates). The quantum chemistry (QC) predictions [1] of the exothermic proton abstraction occurring in linear and cyclic carbonates such as DMC and EC were subsequently confirmed by radiolytic ionization experiments performed at ANL [2]. Our QC studies indicated that the cluster approach to understanding electrolyte oxidation stability yields a distribution of oxidation stabilities associated with the cluster composition [1, 3]. For example, the oxidation stability of model electrolyte complexes follows the order: $EC_4/BF_4^- < EC_n$ (n=2,3,4) < EC/ $BF_4^- < EC/PF_6^-$ < isolated EC [1]. The oxidation stability was found to be rate dependent. At low rates (high barriers) oxidation stability of theEC_n/ BF_4^- and EC_n/ PF_6^- complexes was predicted around 5 V vs. Li^+/Li, thus, indicating that the oxidation stability of dilute EC-$LiPF_6$ and EC-$LiBF_4$ electrolytes is predicted to be around 5 V even for non-active electrodes. The oxidation-induced electrolyte decomposition reactions were predicted using DFT calculations.[1] The predicted decomposition products were found in good agreement with experimental data.

The influence of salt concentration on the EC-LiTFSI electrolyte oxidation stability was investigated using DFT and compared with experimental data performed by collaborators from NCSU [4]. Only a slight (<0.4 V) increase of the electrolyte oxidation stability was observed when nearly all solvents/anions were complexed by a Li^+ cation at high salt

concentration. MD simulations combined with experiments (NCSU) also provided insight into the salt concentration dependence of the mechanism of Al current collector corrosion by EC/LiTFSI electrolyte [4].

Modeling the SEI and SEI-Electrolyte Interface (Oleg Borodin, Kang Xu).

Initial molecular dynamics (MD) simulations of dilithium ethylene carbonate (Li_2EDC) SEI component [5] were extended to the Li_2EDC-LiF melts and Li_2EDC – carbonate electrolyte interfaces. A snapshot of the simulated system is shown in Figure V - 124. The smectic-like ordered Li_2EDC was used in these simulations.

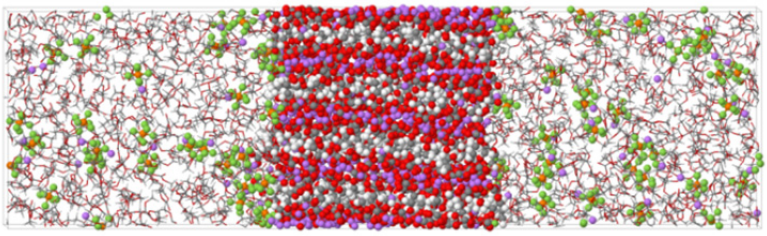

Figure V - 124: A simulation snapshot showing ordered Li_2EDC in contact with the electrolyte. Solvent molecules are shown as wireframe, while Li_2EDC and $LiPF_6$ are highlighted using a ball and stick model

Many-body polarizable force field APPLE&P was used in simulations. Examination of the SEI-electrolyte interface revealed an enrichment of EC and PF_6^- at the SEI surface and depletion of DMC compared to bulk electrolyte concentrations. The process of the Li^+ desolvation from electrolyte was examined with more than 80 of desolvation events occurring at the simulation timescale 300 ns for Li_2EDC-electrolyte at 393 K. During the initial desolvation step, a Li^+ cation showed a preference to shed DMC in a significantly faster rate than losing EC or PF_6^-. The rate of the Li^+ desolvation reaction was estimated from these preliminary simulations. The activation energy for the Li^+ desolvation process was predicted to be ~50 kJ/mol assuming the Arrhenius process. The activation energy for the desolvation reaction is lower than the activation energy for the Li^+ conduction in bulk Li_2EDC (64 kJ/mol) likely due to plasticizing effect of electrolyte on the dynamics of the interfacial SEI layer. The activation energy is, however, similar to the previously experimentally determined activation energy for the Li^+ desolvation from the EC:DMC-based electrolytes into lithiated spinel titanate ($Li_4Ti_5O_{12}$) of 50-52 kJ/mol, but lower than the previously reported activation energy for the desolvation into SEI covered graphite of 60-70 kJ/mol.

Conclusions and Future Directions

ARL has synthesized new additive LiPFBO that improves the capacity retention and coulombic efficiency (CE) of the LNMO high voltage cathode. ARL has also identified an additive A2 that is effective in enabling the cycling of LNMO/graphite cells at 55°C with high CE and capacity retention. With standard electrolyte, LCP based cathode can be cycled with improved capacity, rate and CE through new generation of modified LCP. This suggests that thedevelopment of high voltage Li-ion batteries will rely on improvements to both the electrolytes and the cathodes. Further understanding of the stability and reactivity between these components are critical for future development. Quantum chemistry methodologies will be utilized for high-throughput screening of oxidation stability and initial decomposition reactions occurring in electrolyte components assisting in the design of electrolytes.

References

1. Borodin, O.; Behl, W.; Jow, T. R., Oxidative Stability and Initial Decomposition Reactions of Carbonate, Sulfone, and Alkyl Phosphate-Based Electrolytes. *J. Phys. Chem. C*, 2013, 117, 8661-8682.
2. Shkrob, I. A.; Zhu, Y.; Marin, T. W.; Abraham, D. P., Reduction of Carbonate Electrolytes and the Formation of Solid-Electrolyte Interface (SEI) in Lithium Ion Batteries. 1. Spectroscopic Observations of Radical Intermediates Generated in One-Electron Reduction of Carbonates. *J. Phys. Chem. C*, 2013, 10.1021/jp406274e.
3. Borodin, O.; Jow, T. R., Quantum Chemistry Study of the Oxidation-Induced Decomposition of Tetramethylene Sulfone (TMS) Dimer and TMS/BF4–. *ECS Transactions*, 2013, 50, 391-398.
4. McOwen, D. W.; Seo, D. M.; Borodin, O.; Vatamanu, J.; Boyle, P. D.; Henderson, W. A., Concentrated Electrolytes: Decrypting Electrolyte Properties and Reassessing Al Corrosion Mechanisms. *Energy & Environmental Science* 2014, 7, 410-426.

5. Borodin, O.; Zhuang, G. V.; Ross, P. N.; Xu, K., Molecular Dynamics Simulations and Experimental Study of Lithium Ion Transport in Dilithium Ethylene Dicarbonate. *J. Phys. Chem. C* 2013, 117, 7433-7444.

FY 2013 Publications

1. Understanding Li+ - solvent interaction in nonaqueous carbonate electrolytes with 17O NMR. Xavier Bogle, Rafael Vazquez, Steven Greenbaum, Arthur Cresce, Kang Xu, *J. Phys. Chem. Lett*., 2013, 4, 1664-1668.
2. Analysis of the thickness and composition of the solid electrolyte interphase layer formed on lithium-ion battery graphite anodes. Arthur Cresce, Selena Russell, David Baker, Karen Gaskell, Kang Xu, *ACS Nano Letters*, submitted, December 2013.
3. Dual-graphite chemistry enabled by a high-voltage electrolyte. Jeffrey Read, Matthew Ervin, Kang Xu, Arthur Cresce. *Energy & Environmental Science*, accepted 19 November 2013.
4. Oxidative Stability and Initial Decomposition Reactions of Carbonate, Sulfone and Alkyl Phospate-Based Electrolytes, Borodin*, O.; Behl, W.; Jow. T. R. *J. Phys. Chem. C*. 2013, 117, 8661–8682.
5. Molecular Dynamics Simulations and Experimental Study of Lithium Transport in Dilithium Ethylene Dicarbonate, Borodin*, O.; Zhuang, V.; Ross, P. N.; Xu, K., *J. Phys. Chem. C* 2013, 117, 7433-7444.
6. Concentrated electrolytes: Decrypting electrolyte properties and reassessing Al corrosion mechanisms, McOwen, D. W.; Seo, D. M.; Borodin, O.; Vatamanu, J. ; Boyle, P. D.; Henderson, W. A., *Energy and Env. Sci.* 2014, 7, 410-426.
7. Quantum Chemistry Study of the Oxidation-Induced Stability and Decomposition of Propylene Carbonate-Containing Complexes, Wang, Y., Xing, L.; Borodin, O.; Huang, W.; Xu, M.; Li, X.; Li, W., *Phys. Chem. Chem. Phys*. (in press)
8. Lithium Battery Electrolyte Stability and Performance from Molecular Modeling and Simulations. Smith, G.; Borodin, O., in *Batteries for Sustainability*, Brodd, R. J., Ed. Springer New York: 2013; pp 195-23. ISBN 978-0-387-89469-0.
9. Quantum Chemistry Study of the Oxidation-Induced Decomposition of Tetramethylene Sulfone (TMS) Dimer and TMS/BF4-, Borodin, O.; Jow, T. R. (invited) , *ECS Transactions*, 2013, 50, 391-398.
10. Transport Properties of $LiCoPO_4$ and Fe-substituted $LiCoPO_4$, Jan L. Allen, Travis Thompson, Jeff Sakamoto, Collin R. Becker, T. Richard Jow and Jeff Wolfenstine*, J. Power Sources*, submitted.

FY 2013 Presentations

1. Interphases on Graphitic Anodes in Li-Ion Battery. Selena Russell, David Baker, Arthur Cresce, Kang Xu. Pacific Rim American Chemical Society Meeting, June 5, 2013.
2. Effect of anion-solvent interaction on the anodic stability of electrolytes in batteries. Selena Russell, Emily Wikner, Arthur Cresce, Kang Xu. The Electrochemical Society Fall 2013 meeting, Oct. 29, 2013.
3. *In situ* analyses on solid electrolyte interphases in Li-ion batteries. Selena Russell, Arthur Cresce, David Baker, Kang Xu. *The Electrochemical Society Fall 2013 meeting*, Oct. 29, 2013.
4. Effect of electrolyte additives on SEI properties in Li-ion batteries as analyzed by *in situ* AFM. *American Chemical Society Meeting*, 28 September 2013.
5. Investigation of Electrolyte Interaction with High Voltage Li-Ion Battery Cathodes, Samuel A Delp, Jan L Allen, T Richard Jow, *224th Meeting of the Electrochem. Soc.* San Francisco, California, October 27-31, 2013.
6. Substituted LiCoPO4 as Li-ion Cathode, Jan L Allen, Samuel A Delp, *224th Meeting of the Electrochem. Soc*. San Francisco, California, October 27-31, 2013.
7. Oxidation-Induced Decomposition of Electrolytes and Additives From Quantum Chemistry calculations, Oleg Borodin, Samuel A Delp, T Richard Jow , *224th Meeting of the Electrochem. Soc.* San Francisco, California, October 27-31, 2013.

FY 2013 Patent Applications

1. High Voltage Lithium Ion Positive Electrode Compositions, Jan L. Allen, Joshua L. Allen, Samuel A. Delp III, Jeff Wolfenstine, T. Richard Jow, *Provisional Patent 61911700* filed.

V.D.2 Development of Novel Electrolytes for Use in High Energy Li-ion Batteries with Wide Operating Temperature Range (JPL)

Marshall C. Smart

Electrochemical Technologies Group
Power and Sensor Systems Section
Jet Propulsion Laboratory
California Institute of Technology
4800 Oak Grove Drive, M/S 277-207
Pasadena, CA 91109-8099
Phone: (818) 354-9374; Fax: (818) 393-6951
E-mail: Marshall.C.Smart@jpl.nasa.gov

Start Date: October 1, 2009
Projected End Date: September 30, 2014

Objectives

- Develop a number of advanced Li-ion battery electrolytes with improved performance over a wide range of temperatures (-30° to +60°C) with projected long-life characteristics (5,000 cycles over 10-yr life span).
- Improve the high voltage stability of these candidate electrolyte systems to enable operation up to 5V with high specific energy cathode materials.
- Define the performance limitations at low and high temperature extremes, as well as life-limiting processes.
- Demonstrate the performance of advanced electrolytes in large capacity prototype cells.

Technical Barriers

This project addresses the following technical barriers associated with the development of PHEVs:

- 750 W/kg (10 mile) and 316 W/kg (40 mile).
- Cold cranking capability to -30°C.
- Cycle life: 5,000 cycles (10 and 40 mile PHEVs).
- Calendar life: 15 years (at 35°C).

Technical Targets

- Demonstrate improved performance of experimental and prototype cells with next generation electrolytes over a wide temperature range (-30° to +60°C) compared with baseline electrolytes.

Prepare and characterize experimental laboratory cells containing advanced electrolytes, which are designed to operate over a wide temperature range and in high-voltage systems (i.e., $LiNiMnCoO_2$), and identify performance-limiting characteristics.

Accomplishments

- Demonstrated good preservation of the low temperature performance (down to -50°C) of prototype 12 Ah cells (manufactured by Quallion) containing JPL-developed methyl propionate-based electrolytes that have been subjected to life testing. The use of mono-fluoroethylene carbonate (FEC) was observed to impede the capacity degradation.
- A methyl propionate-based electrolyte was observed to result in a five-fold improvement in the discharge capacity delivered with prototype NCA-based cells at very high discharge rates (20C) at low temperature (-20°C) compared with a baseline all carbonate-based electrolyte.
- Excellent cycle life performance has been demonstrated with methyl propionate-based wide operating temperature range electrolytes in NCA-based cells at 20°C, with an electrolyte consisting of 1.2M $LiPF_6$ in FEC+EMC+MP providing the best performance, outperforming the DOE baseline electrolyte.
- Demonstrated excellent cycle life performance (over 9,500 full depth-of-discharge cycles) with wide operating temperature electrolytes containing methyl butyrate in A123 $LiFePO_4$-based prototype (26650) cells. These cells have previously been demonstrated to have operational capability over a wide temperature range (-60° to +60°C), including the ability to support high rate discharge at low temperatures (i.e., >11C discharge rates at -30°C).
- Investigated the use of methyl butyrate-based electrolytes containing various additives in the graphite/high voltage NMC system in experimental and coin cells. An electrolyte consisting of $LiPF_6$ in EC+EMC+MB possessing LiDFOB as an electrolyte additive has been observed to provide the best low temperature performance of the electrolytes investigated.

✧ ✧ ✧ ✧ ✧

Introduction

JPL is working to develop electrolytes that enable the operation of Li-ion cells over a wide temperature range, while still providing the desired life characteristics and resilience to high temperature (and voltage). To meet the objectives, the electrolyte development includes the following general approaches: (1) optimization of carbonate solvent blends, (2) use of low viscosity, low melting ester-based co-solvents, (3) use of fluorinated esters and fluorinated carbonates as co-solvents, (4) use of "SEI promoting" and thermal stabilizing additives, and the (5) use of novel non-fluorine based salts. Many of these approaches will be used in conjunction in multi-component electrolyte formulations (i.e., such as the use of low viscosity solvents and novel additives and salts), which will be targeted at improved operating temperature ranges while still providing good life characteristics.

Approach

In the process of developing improved electrolyte formulations, they are characterized using a number of approaches, including performing ionic conductivity and cyclic voltammetry measurements, and evaluating their performance in coin cells as well as larger ~ 400 mAh three-electrode cells equipped with reference electrodes. Initial characterization is typically performed using state-of-art electrode couples, such as (a) MCMB /$LiNi_{0.8}Co_{0.2}O_2$ (a) MCMB /$LiNi_{0.8}Co_{0.15}Al_{0.05}O_2$, or (c) graphite/$LiNi_{1/3}Co_{1/3}Mn_{1/3}O_2$. More recent work has been extended to the high capacity, lithium excess mixed NMC-based cathode materials. In addition to performing charge/discharge characterization over a wide range of temperatures and rates on these cells, a number of electrochemical characterization techniques are employed, including: (1) Electrochemical Impedance Spectroscopy (EIS), (2) DC linear (micro) polarization, and (3) Tafel polarization measurements. The electrochemical evaluation in three-electrode test cells enables the electrochemical characterization of each electrode (and interface) and the identification of performance-limiting mechanisms. Electrodes are easily harvested from these test cells and samples are delivered to collaborators (i.e., URI and Hunter College). In addition to evaluating candidate electrolytes in spirally wound experimental cells, initial screening studies are also performed in coin cells, most notably in conjunction with high voltage cathode materials.

Results

Electrolytes Demonstrated in NCA-Based Systems. During the past year, we continued to evaluate the performance of large capacity prototype cells containing candidate wide operating temperature range electrolytes developed under this program. We continue to evaluate 12 Ah cells (MCMB Carbon/$LiNiCoAlO_2$) manufactured by Quallion, LCC that possess JPL methyl propionate (MP)-based wide operating temperature range electrolytes. We are currently evaluating their life characteristics and the degree to which the low-temperature capability degrades with time. These cells contain electrolytes previously shown to have excellent low temperature capabilities (supporting 2C rates even as low as -50°C), namely (i) 1.20M $LiPF_6$ in EC+EMC+MP (20:20:60 v/v %) and (ii) 1.20M $LiPF_6$ in EC+EMC+MP (20:20:60 v/v %) + 4% FEC. In addition to JPL-developed electrolytes, the group of cells contain a Quallion-developed wide operating temperature range electrolyte, as well as the DOE baseline electrolyte (i.e., 1.2M $LiPF_6$ in EC+EMC (30:70 v/v %)). The cycle life testing consists of partial DOD cycling (approximately 50% DOD), where one cycle is performed each day using variable load profile with low to moderate rates, as illustrated in Figure V - 125. After completing increments of 100 cycles (i.e., 100 days of testing), the cells are re-characterized to determine capacity, impedance, and low-temperature discharge rate capability. The cells recently completed 400 cycles, representing 400 days of life testing, and have been re-characterized at low temperature (down to -50°C). In total, the cells have been tested for ~2.5 years, including the initial rate characterization over the range of temperatures. In summary, of the wide operating temperature electrolytes, the best capacity retention, (as shown in Figure V - 126), was observed with the cell containing the MP-based electrolyte that contains FEC as an additive (4%), suggesting that the additive has produced a desirable, protective SEI layer. In addition, good retention of low temperature capability is observed at -40° and -50°C, at 2C and C/5 rates, after completing the cycling testing, with the MP-based cells delivering the highest capacity. For example, as illustrated in Figure V - 127, the cells containing the MP-based electrolytes were observed to deliver the highest capacity at -40°C using a C/2 discharge rate, with the cell containing the FEC as an electrolyte additive displaying the least amount of performance degradation as a result of life cycling. Excellent performance is also exhibited throughout the life of the cells at -50°C, as illustrated in Figure V - 128, with the best result being obtained with the cell containing the 1.20M $LiPF_6$ in EC+EMC+MP (20:20:60 v/v %) + 4% FEC, which displayed good preservation of the low temperature capability.

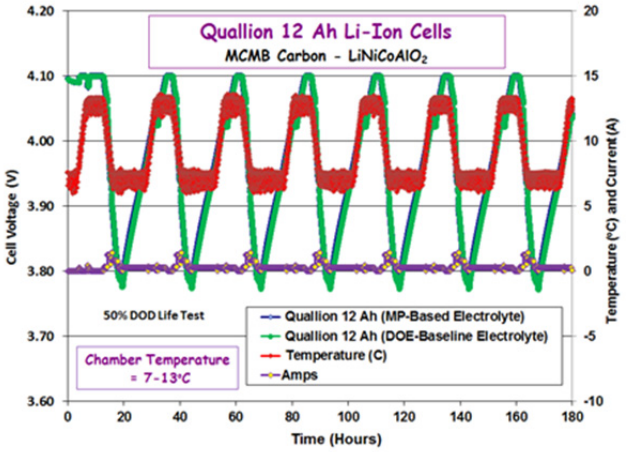

Figure V - 125: Profile of cycle life performance testing (50% DOD) being performing on Quallion 12 Ah cells containing various low temperature electrolytes

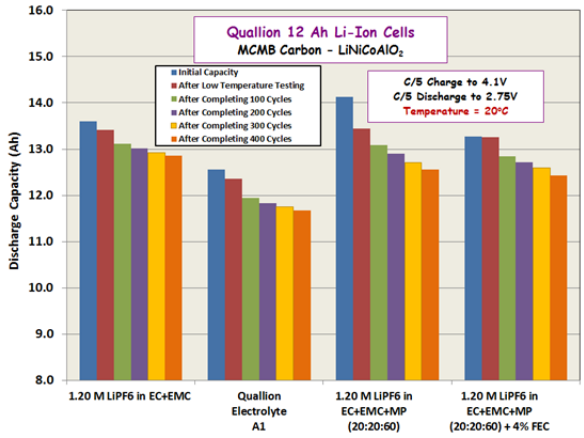

Figure V - 126: Discharge capacity (Ah) of Quallion 12 Ah cells containing various low temperature electrolytes at 20°C during the course of life testing

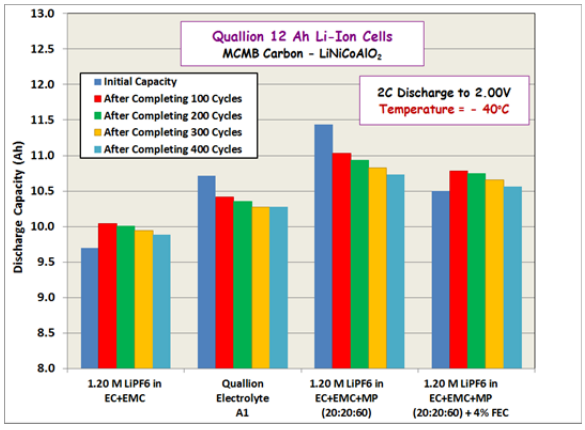

Figure V - 127: Discharge capacity (Ah) of Quallion 12 Ah cells containing various low temperature electrolytes at – 40°C with a 2C discharge rate during the course of life testing

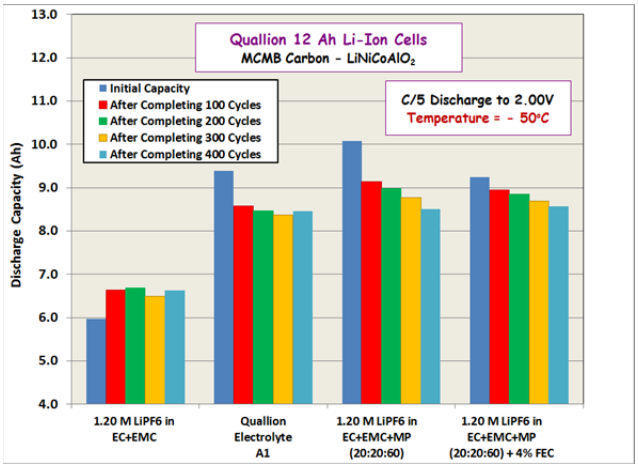

Figure V - 128: Discharge capacity (Ah) of Quallion 12 Ah cells containing various low temperature electrolytes at - 50°C with a C/5 discharge rate during the course of life testing

We also continue to investigate the performance characteristics of additional MP-based electrolytes in smaller hermetically sealed prototype 0.25Ah MCMB/$LiNiCoAlO_2$ cells (manufactured by Quallion, LCC). The electrolytes investigated are permutations of the previous approach described which consist of MP with varying amounts of FEC (4, 10, and 20%). In one case, we have entirely replaced the EC with FEC. Prior to evaluation in prototype cells, these electrolytes were investigated in experimental three-electrode cells, which enabled us to determine the impact of the additives upon the electrode kinetics as a function of temperature. Cells possessing 1.20M $LiPF_6$ in EC+EMC+MP (20:20:60 vol %) + 0.10M LiBOB were also fabricated, since the use of LiBOB as an additive has been previously identified to result in improved low temperature performance and improved cathode kinetics. These electrolytes were envisioned to have improved high temperature resilience compared to the baseline MP-containing electrolyte. A number of performance tests have been performed, including discharge rate characterization as a function of temperature, charge rate characterization, and cycle life performance under various conditions (including high temperatures). Recently, we have focused upon characterizing the cells with very high discharge rates at low temperature (i.e., 20C discharge rate at -20°C). As illustrated in Figure V - 129, the cells containing the 1.20M $LiPF_6$ in EC+EMC+MP (20:20:60 vol %) + 0.10M LiBOB electrolyte displayed the best performance (providing over 60 Wh/kg), delivering over 5 times the capacity obtained with the baseline formulations. This electrolyte was also previously reported to deliver the best performance at lower temperatures, being able to support 5C discharge rates at -40°C and 4C discharger rates at -50°C.

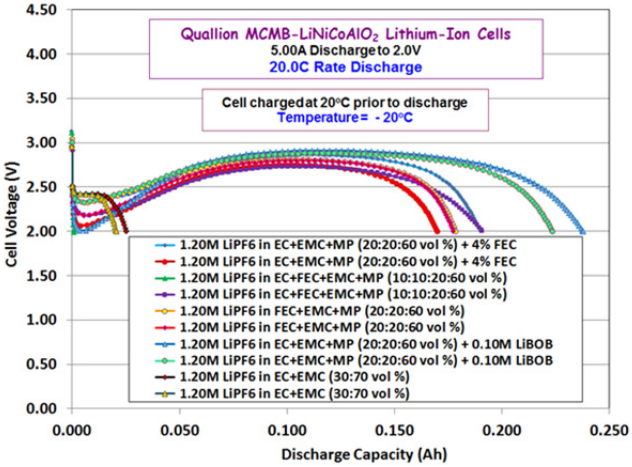

Figure V - 129: Discharge capacity (Ah) of Quallion 0.25 Ah cells containing various low temperature electrolytes at – 20°C with a 20.0 C discharge rate (5A)

We have also continued full DOD cycle life characterization on these prototype cells containing various MP-based electrolytes, including at 20°, 40°, and 50°C, as well under variable temperature conditions in a manner similar to that described previously. As illustrated in Figure V - 130, we continue to observe excellent performance with the cells when subjected to 100% DOD cycle life testing at 20°C, with over 2,600 cycles completed to-date on some of the cells. A trend of lower capacity fade is observed with increasing FEC content in the electrolyte, although high FEC content was observed to lead to somewhat lower initial capacity. As illustrated, the cell containing $LiPF_6$ in FEC+EMC+MP was observed to deliver > 88% of the initial capacity after completing 2,900 cycles, outperforming the baseline. In addition, excellent retention of the watt-hour efficiency was observed with the cell containing $LiPF_6$ in FEC+EMC+MP when subjected to cycling at +20°C, suggesting minimal impedance growth, as illustrated in Figure V - 131. In terms of the capacity fade observed, the cell containing the electrolyte with 10% FEC and 10% EC also outperforms the all carbonate baseline. Although the electrolyte with LiBOB resulted in cells with the best low temperature discharge rate capability, the cycle life performance was inferior to that of the baseline and the cells containing FEC in high proportion.

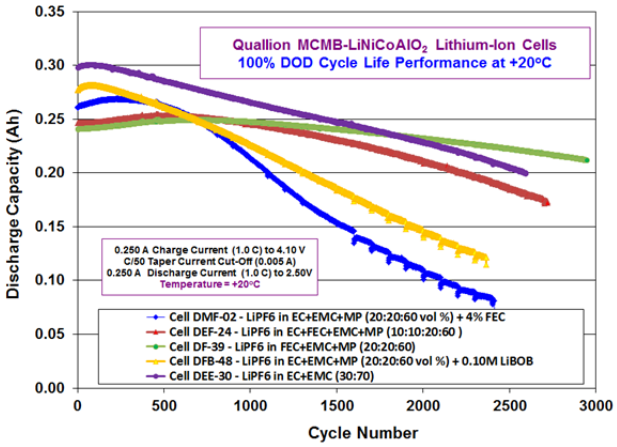

Figure V - 130: Cycle life (Ah) performance of 0.25Ah MCMB-LiNiCoAlO$_2$ cells (Quallion, LCC) containing various electrolytes at 20°C, using C rate charge and discharge over a voltage range of 2.50V to 4.10V

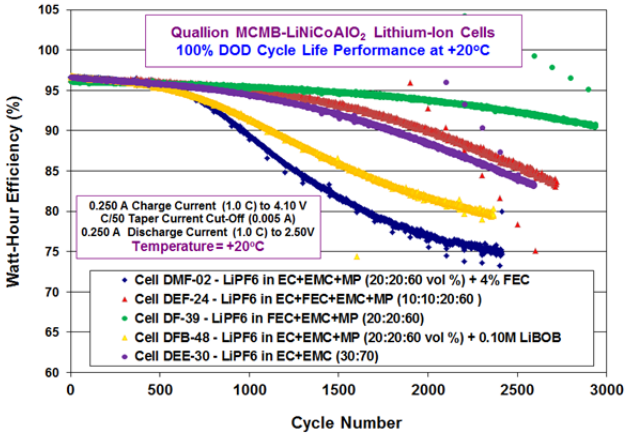

Figure V - 131: Cycle life (Wh) performance of 0.25Ah MCMB-LiNiCoAlO$_2$ cells (Quallion, LCC) containing various electrolytes at 20°C (using C rate charge and discharge)

Electrolytes Demonstrated in LFP-Based Systems. We also continued to evaluate the life characteristics of a number of lithium iron phosphate-based cells (i.e., A123 Systems cells) that possess methyl butyrate (MB)-based electrolytes developed under this program (i.e., specifically 1.20M $LiPF_6$ in EC+EMC+MB (20:20:60 vol %) + 4% FEC and 1.20M $LiPF_6$ in EC+EMC+MB (20:20:60 vol %) + 2% VC). As reported previously, these cells have been demonstrated to have excellent rate capability over a wide temperature range (-60 to +20°C), being able to support up to 10C rates at temperatures as low as -50°C

and C rates at -60°C. As illustrated in Figure V - 132, we continue to obtain excellent full DOD cycle life performance on these cells containing these MB-based electrolytes, exhibiting over 9,500 cycles to-date and displaying comparable performance to the baseline electrolyte (i.e., delivering over 81% of the initial capacity). As noted previously, these cells also have displayed good tolerance to high temperature cycling. These results are notable given the demonstrated low temperature performance capability of these systems.

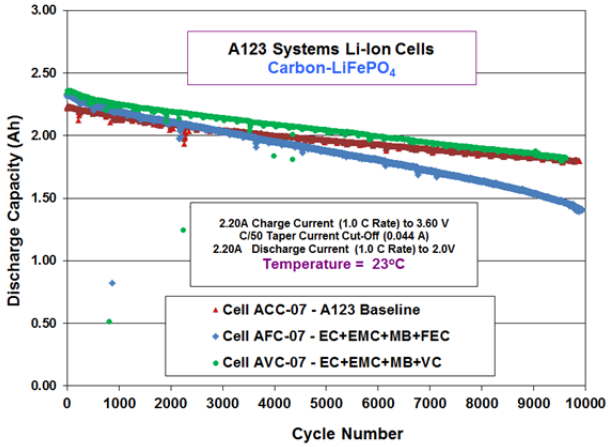

Figure V - 132: Cycle life performance of $LiFePO_4$-based A123 cells containing various electrolytes at +23°C

Electrolytes Developed for NMC-Based Systems. Recently, we have focused upon developing wide operating temperature range electrolytes for the graphite/high voltage NMC system (i.e., Conoco graphite anodes and Li_2MnO_3-$LiMO_2$ (M=Mn, Co, Ni) cathodes (Toda HE5050) supplied by ANL. To accomplish this goal, we have investigated MB-based formulations containing various additives, both coin cells as well as larger three-electrode cells equipped with lithium reference electrodes. The primary objective of utilizing electrolyte additives is to improve the high voltage stability, high temperature resilience, and in some cases improve the low temperature performance due to improved lithium kinetics at the interfaces. A number of electrolyte additives have been investigated, including (i) LiBOB, (ii) lithium difluoro(oxalato)borate (LiDFOB), (iii) lithium tetrafluoroborate ($LiBF_4$), (iv) lithium 4,5-dicyano-2-(trifluoromethyl) imidazole (LiTDI), (v) vinylene carbonate (VC), and (vi) lithium oxalate. The LiDFOB and LiTDI were synthesized and provided by Prof. Wesley Henderson's group at North Carolina State University (NCSU). Using three-electrode cells, we performed electrochemical measurements at a number of temperatures (23°, 0°, -20°, -30°, and -40°C), including EIS, Tafel polarization, and linear micro-polarization measure-ments. The most favorable kinetics at the anode was observed with the cells containing lithium oxalate and VC. Whereas, the most facile kinetics observed at the cathode was observed with the cell containing LiBOB as an additive, suggesting that it participates beneficially in the formation of the cathode electrolyte interface (CEI). Also, at -20°C, the kinetics of the cathode are much poorer than that of the anode for all of the samples (by nearly an order of magnitude), suggesting that the low temperature rate capability will be dictated by the cathode kinetics. We are currently evaluating the discharge performance of these systems as a function of temperature in both three-electrode cells and coin cells.

To complement the three-electrode cell study described above, a number of MB based electrolytes were also evaluated in coin cells consisting of the graphite anodes and Toda HE 5050 cathodes. The electrolytes investigated include: (1)1.20M $LiPF_6$ in EC+EMC +MB (20:20:60 v/v %) + 0.10M $LiBF_4$, (2) 1.20M $LiPF_6$ in EC+EMC+MB (20:20:60 v/v %) + 0.10M LiDFOB, (3) 1.20M $LiPF_6$ in EC+EMC+MB (20:20:60 v/v %) + 0.10M LiBOB, (4) 1.20M $LiPF_6$ in EC+EMC+MB (20:20:60 v/v %) + 0.10M LiTDI, and (5) 1.20M $LiPF_6$ in EC+EMC+MB (20:20:60 v/v %) + 2% DBPC (where DBPC= di-*t*-butyl pyrocarbonate). They were compared to the baseline electrolyte (i.e., 1.20M $LiPF_6$ in EC+EMC (30:70 v/v %).

After performing the formation cycling, a number of cells were subjected to systematic discharge rate characterization testing over a wide temperature range. In summary, the cell containing the MB-based electrolyte with LiDFOB delivered superior performance, approximately twice the capacity for the baseline electrolyte discharged at a C/10 rate at -20°C, and roughly four times the capacity at a C/2 rate at -20°C, as illustrated in Figure V - 133 and Figure V - 134. The beneficial attributes of LiDFOB appear to be associated with desirable film formation on both electrodes. In contrast, although LiBOB has been observed to have beneficial interactions at the cathode interface, it generally results in poorer kinetics at the anode, due to the formation of resistive films.

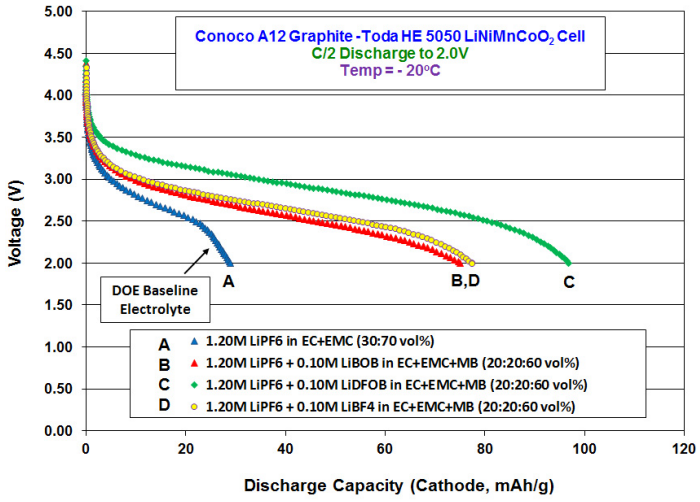

Figure V - 133: Discharge performance of graphite-NMC coin cells containing various electrolytes at -20°C (using a C/2 discharge rate). The cells were charged at room temperature prior to discharge

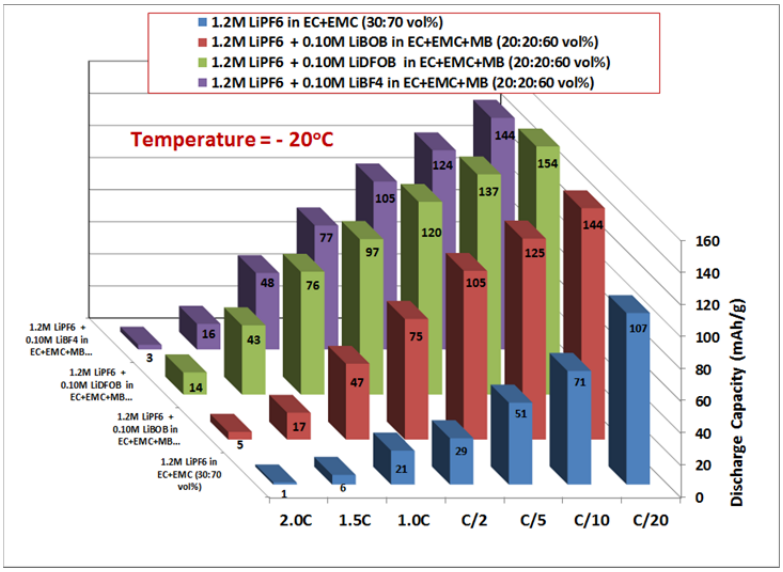

Figure V - 134: Discharge performance of graphite-NMC coin cells containing various electrolytes at -20°C using a range of discharge rates (C/20 to 2.0C). The cells were charged at room temperature prior to discharge

Future work will be focused upon further evaluating the low temperature performance characteristics of ester-containing electrolytes containing the various additives. This will consist of evaluating the discharge characteristics in various systems, as well as determine the electrode kinetics as a function of temperature with the benefit of three electrode cells. In addition, future work will also be focused upon characterizing the high temperature stability and cycle life performance of these electrolytes in the various systems.

Collaborations

During the course of this program, we have collaborated with a number of institutions, including: (a) Univ. Rhode Island (Brett Lucht: analysis of harvested electrodes, on-going collaborator), (b) Argonne Nat. Lab (Khalil Amine: source of electrodes, on-going collaborator), (c) LBNL (John Kerr) (evaluation of novel salt), (d) A123 Systems, Inc. (electrolyte development, on-going collaborator), (e) Quallion, LCC. (electrolyte development, on-going collaborator), (f) Yardney Technical Products (electrolyte development, on-going collaborator), (g) Saft America,

Inc. (industrial partner under NASA program), (h) NREL (Smith/Pesaran) (supporting NREL in model development by supplying data), (i) the Univ. of Southern California (Prof. Prakash, electrolyte salt development), (j) Sandia National Laboratory (Safety testing of low flammability electrolyte and supplier of electrode materials), (k) Hunter College (Prof. Greenbaum, *ex situ* NMR measurements), and (l) NCSU (Prof. Wesley Henderson, Evaluation of novel salts). Some of the work described here was carried out at the Jet Propulsion Laboratory, California Institute of Technology, under contract with the National Aeronautics and Space Administration.

FY 2013 Publications/Presentations

1. M. C. Smart, B. L. Lucht, S. Dalavi, F. C. Krause, and B. V. Ratnakumar, "The Effect of Additives upon the Performance of MCMB/$LiNi_xCo_{1-x}O_2$ Li-ion Cells Containing Methyl Butyrate-Based Wide Operating Temperature Range Electrolytes," *J. Electrochem. Soc*., **159 (6)**, A739-A751 (2012).
2. S. DeSilvan, V. Udinwe, P. Sideris, S. G. Greenbaum, M. C. Smart, F. C. Krause, K. A. Smith and C. Hwang, "Multinuclear NMR Studies of Electrolyte Breakdown Products in the SEI of Lithium-Ion Batteries," *ECS Trans. **41 (41),** 207 (2012).*
3. M. C. Smart, Ratnakumar V. Bugga, and L. D. Whitcanack, "Development of Low Temperature Electrolytes for Lithium-Ion Batteries," Advanced Automotive Batteries Conference, Pasadena, CA, February 5, 2013 (Invited Talk).
4. M. C. Smart, C. Hwang, F. C. Krause, J. Soler, W. C. West, B. V. Ratnakumar, and K. Amine, "Wide Operating Temperature Range Electrolytes for High Voltage and High Specific Energy Li-Ion Cells," ECS Transactions, submitted.
5. M. C. Smart, M. R. Tomcsi, L. D. Whitcanack, B. V. Ratnakumar, M. Nagata, and V. Visco, "The Use of Methyl Propionate-Based Electrolytes with Additives to Improve the Low Temperature Performance of $LiNiCoAlO_2$-Based Li-Ion Cells, 224th Meeting of the Electrochemical Society, San Francisco, October 2013.
6. F. C. Krause, C. Hwang, B. V. Ratnakumar, M. C. Smart, D. W. McOwen and W. A. Henderson, "The Use of Methyl Butyrate-Based Electrolytes with Additives to Enable the Operation of Li-Ion Cells with High Voltage Cathodes over a Wide Temperature Range," 224th Meeting of the Electrochemical Society, San Francisco, October 2013.

V.D.3 Novel Phosphazene-based Compounds to Enhance Safety and Stability of Cell Chemistries for High Voltage Applications (INL)

Kevin L. Gering, PhD

Idaho National Laboratory
2525 N. Fremont Avenue
Idaho Falls, ID 83415-2209
Phone: (208) 526-4173; Fax: (208) 526-0690
E-mail: kevin.gering@inl.gov

Collaborators (INL):
Eric J. Dufek, Mason K. Harrup, David K. Jamison, Harry W. Rollins, Sergiy V. Sazhin, Fred F. Stewart

(External to INL):
John Burba, Princess Energy Systems

Contract No. DE-AC07-05ID14517

Start Date: January, 2009
Projected End Date: Sept. 2013

Objectives

Our focus is producing electrolyte and electrode compounds resilient in both temperature and voltage regimes, while meeting a competitive baseline performance in transport properties and SEI characteristics. In meeting these goals we aim to reduce the presence of carbon in Li-ion cells to produce a more robust inorganic-based cell chemistry. We seek compounds that will:

- enable prolonged usage of advanced higher-voltage electrode couples,
- promote better safety performance under abusive thermal conditions,
- enhance cell life.

Another objective is to gain fundamental understanding of molecular-scale interactions between phosphazenes and other electrolyte species and cell components.

Technical Barriers

Safety and longevity of Li-ion batteries continues to be an issue for future vehicular applications. This is complicated by the drive toward higher voltage cells (5V+) and some usage patterns and conditions that would cause batteries to operate at higher temperatures. A viable alternative electrolyte for Li-ion batteries must simultaneously meet multiple criteria regarding transport properties, SEI film formation, voltage stability, flammability, aging mechanisms, chemical compatibility, performance at high and low temperatures, etc. A fundamental challenge remains to produce electrolyte components that will provide noteworthy levels of flame retardance while reducing viscosity to competitive levels to maintain attractive transport properties, and some success has been had at the INL toward that goal in 2013 within our overall ES materials program.

Technical Targets

Our targets are defined by primary categories:

- *Phosphazenes as primary solvents* (>40%) to greatly reduce electrolyte flammability. Our requirements for the pure phosphazene (with lithium salt) to be viable as a primary solvent: room temperature viscosity less than 5 cP, conductivity greater than 4 mS/cm, and lithium salt ($LiPF_6$) solubility at least 0.6 M.
- *Phosphazenes as cosolvents* (10-40%) to provide mixed benefits of reduced electrolyte flammability and prolonged cell life. Properties for the pure salted phosphazene to be defined as a cosolvent: room temperature viscosity within 5-40 cP, conductivity 0.2-4 mS/cm, and lithium salt solubility within 0.2-0.6 M.
- *Phosphazenes as additive solvents* (≤10%) to enhance chemical/thermal stability of the bulk electrolyte and improve SEI properties in terms of thermal runaway and stability over life. Viable additive candidates are defined as follows: room temperature viscosity exceeds 40 cP, conductivity ≤ 0.2 mS/cm, and lithium salt solubility < 0.2 M.
- Abuse testing at SNL of INL electrolytes looks squarely at how these compounds provide benefit to cell operation and safety at extreme conditions of temperature and voltage. Improvement over a baseline is sought.
- We have worked with ANL and DOE toward scale-up of the best INL phosphazene candidates. One of our compounds in now in the scale-up queue.
- Replace the typical carbon anode with a highly nonflammable polymer-based host that also adds benefit toward chemical compatibility across the cell.

Accomplishments

- Various forms of heterocyclic phosphazene solvent compounds have been synthesized, characterized, and tested in coin cells. More efficient and economical synthesis routes have been found for some classes of compounds to decrease manufacturing costs. Of note for 2013 are newer FM and PhIL (ionic liquid) series compounds.
- Cell testing completed for using INL electrolytes with the NCA (Toda)/Carbon couple, covering characterization of capacity and impedance attributes. Overall results show good compatibility of phosphazenes with the various cell environments, promoting stability at elevated temperatures.
- Completed prolonged thermolysis experiments at 60°C using FM and SM series additives with two markedly different baseline electrolytes.
- Investigation of Phase 3 polymeric alternative anode materials with improved electronic conductivity, porosity, crosslinking, and capacity.
- NMR evaluation of electrolyte fate at elevated temperatures (with Washington State Univ.)
- Further refined and expanded our methods for voltammetric electrolyte and interface characterization, which has the potential of being an important new tool for materials selection.
- Success of INL phosphazene-based electrolyte additives resulted in priority of scale-up of INL electrolyte compounds at ANL; one INL compound is in the scale-up queue.
- DFT modeling results published for trends between molecular configuration and phosphazene solvent-to-lithium binding energy.

✧ ✧ ✧ ✧ ✧

Introduction

Electrolytes play a central role in performance and aging in most electrochemical systems. As automotive and grid applications increasingly rely on electrochemical stored energy, it becomes more urgent to have electrolyte components that enable optimal battery performance while promoting battery safety and longevity. Safety remains a foremost concern for widespread utilization of Li-ion technology in electric-drive vehicles, especially as the focus turns to higher voltage systems (5V). This work capitalizes on the long established INL expertise regarding phosphazene chemistry, aimed at battery-viable compounds that are highly tolerant to abuse. Various references document/relate to the FY13 work [1-5].

Approach

The general heterocyclic phosphazene structure is shown in Figure V - 135.

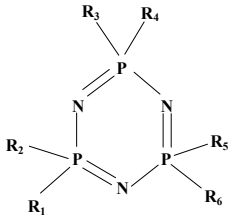

Heterocyclic Phosphazene Ring Structure

MWT: 400-600

Figure V - 135: General heterocyclic phosphazene structure

A change of chemical structure in the ring pendant arms has a strong influence on electrolyte properties, performance, and longevity in a higher-voltage system (5V+) and at higher temperatures. By customizing the pendant structures (R groups) we seek to improve transport properties while increasing flash point and having acceptable SEI characteristics and cell aging. Benefits include inherent stability and non-flammability, very low vapor pressure, good lithium salt dissolution. Challenges would include high viscosity and the need to attenuate N:Li+ attraction that occurs due to electron doublet transfer. To date our numerous compounds derive from the following four groups:

SM: ether groups attached to the phosphorus centers

AL: unsaturated analogues of the SM series

FM: fluorinated analogues of the SM series

PhIL: based on an ionic liquid structure.

The ionic liquid series helps to mitigate some of the limitations seen with traditional cyclic phosphazenic solvents, such as $N:Li^+$ association that can adversely affect conductivity. Non-cyclic phosphazene compounds are also being targeted through the INL internal R&D program (with success), and salts other than $LiPF_6$ are being considered.

We employ a number of diverse testing and characterization methods to determine viability of candidate compounds, including advanced voltammetry techniques, coupled viscosity and conductivity analysis, flash point, EIS, cell testing, as well as chemical physics and DFT modeling. Coin cells (type 2032) are used to test candidate electrolytes in an actual cell environment, covering crucial issues of formation, interfacial impedance, polarization testing, and aging.

Results

Summarized below are salient results from 2013 research. For brevity, only representative summaries are given. The baseline (BL) electrolyte is 1.2M $LiPF_6$ in EC-EMC (1:4, wt.), unless otherwise defined.

Figure V - 136 shows the result of prolonged thermolysis conditions at 60°C for electrolyte systems with and without (baseline) FM and SM phosphazene additives at 10% levels within each baseline. The baseline samples are the two left-most vials in each row. It is readily seen that the presence of the phosphazenes mitigates degradation of the baseline and have a preservation role at elevated temperatures. Benefits are longer cell life under higher-temperature conditions, and the opportunity to scale-back battery thermal management to balance with the resilient electrolyte.

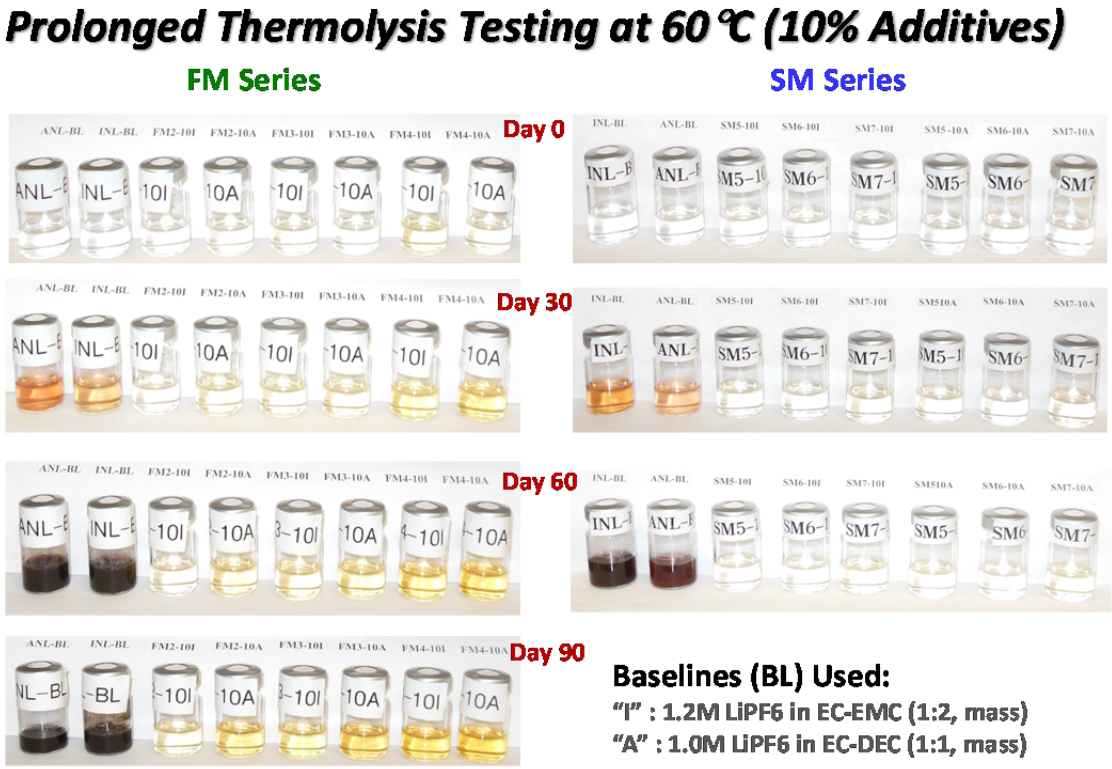

Figure V - 136: INL prolonged thermolysis testing results

Figure V - 137 attests that INL FM-series phosphazene additives extend the electrochemical window (EW) past what is achievable with the BL electrolyte. Presence of the phosphazene more than doubles the EW past the BL value. These additives act to moderate the oxidative processes at the positive electrode, and hence enhance stability at higher voltages. This attribute is also observed for other INL phosphazene compounds (SM, AL, etc.). Figure V - 138 shows the clear benefit of having 3% PhIL-2 in the baseline electrolyte, where the flame duration was dropped by an order of magnitude below the baseline. This adds greatly to the safety of the cell chemistry.

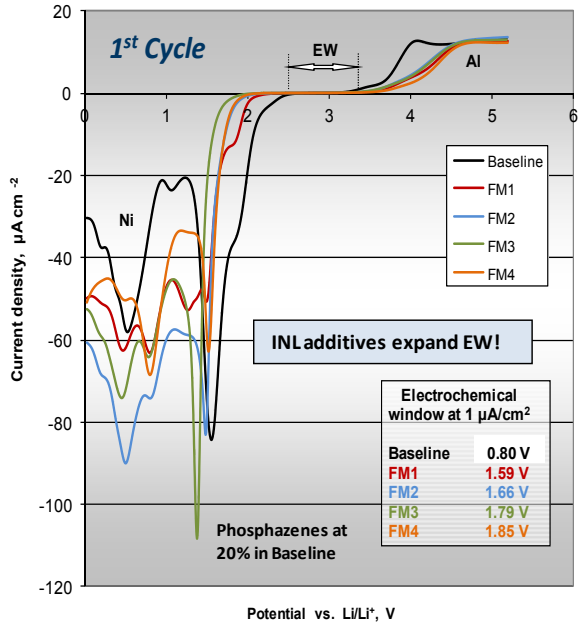

Figure V - 137: Electrochemical window enhancement with INL FTI-series phosphazene additives

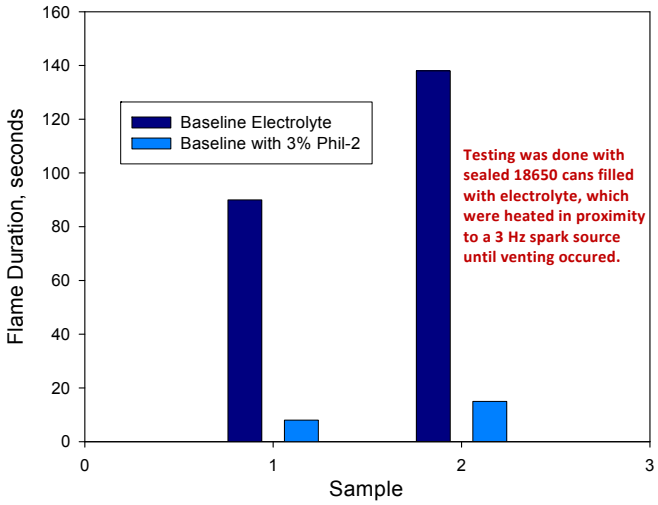

Figure V - 138: INL demonstration of reduced flame duration

Cell testing was performed using 2032-type coin cells to judge performance of the electrolytes with ABR electrode couples. Figure V - 139**(a,b)** summarize the early life capacity performance of coin cells using NCA/graphite, having FM series compounds at various amounts in the baseline. In Figure V - 139a improvement over baseline performance is seen in particular for FM-2 cases. In Figure V - 139b, systems with FM2 levels of at least 12.4 percent show good viability for rates up to C/1.

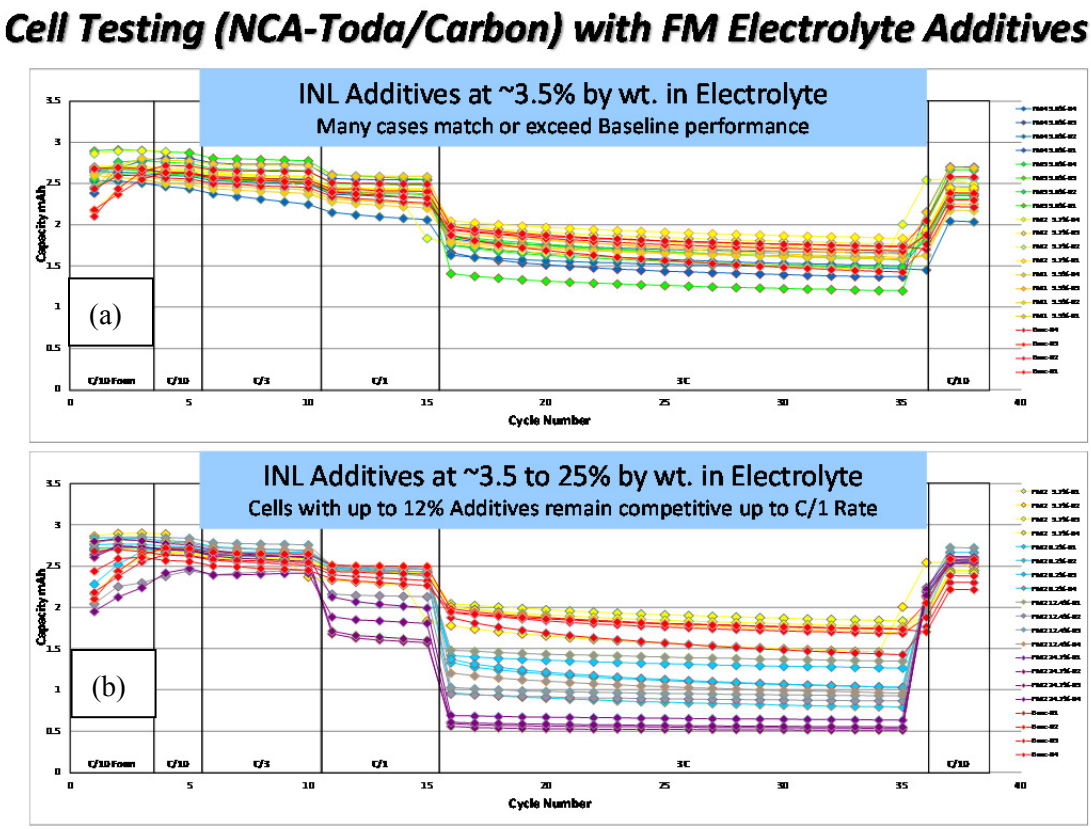

Figure V - 139: INL additive-included electrolyte performance with ABR electrode couples

From initial WSU findings, the BL sample formed a gel at the bottom of the sealed tube over time at 60˚C. This sample became much more viscous overall than Sample 1 (having the protective cyclic phosphazene additive). The evidence of phosphorus-proton coupling in the reaction products of the BL sample suggests that phosphorus is interacting with the solvent mixture. These NMR-observable product species may be intermediates in polymerization of the carbonates, leading to a polycarbonate formation (this might explain the apparent increase in viscosity).

Figure V - 140 contains post-formation capacities for representative cells containing phosphazene-based polymer anodes and thicker HE5050-type cathodes. The capacity range observed is competitive with that of graphitic anodes. Figure V - 141 demonstrates that cells with early-generation phosphazene anodes have reasonably low self-discharging behavior at elevated voltage; this behavior can be improved by modification of polymer attributes optimized over voltage. Better capacities were observed as we increased effective surface area within the polymer matrix (Figure V - 142). The mode of lithium insertion into the polymer host is facilitated in part by the by the electrostatic attributes of the phosphazene moiety, overall exhibiting a dual or hybrid mode of lithium residency surmised in Figure V - 143 (atomistic + micro-clustering) that is a function of voltage, and is highly reversible. The anode in Figure V - 143 was comprised mostly of INL polymer and A12-type graphitic carbon. These anode materials are a breakthrough – a highly “engineerable” option for anodes in Li-ion systems.

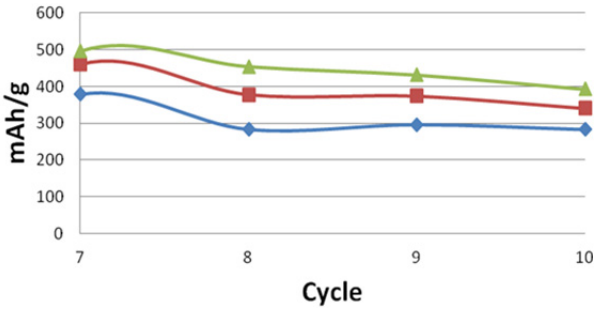

Figure V - 140: Post-formation capacities for representative cells containing phosphazene-based polymer anode and thicker HE5050-type cathodes

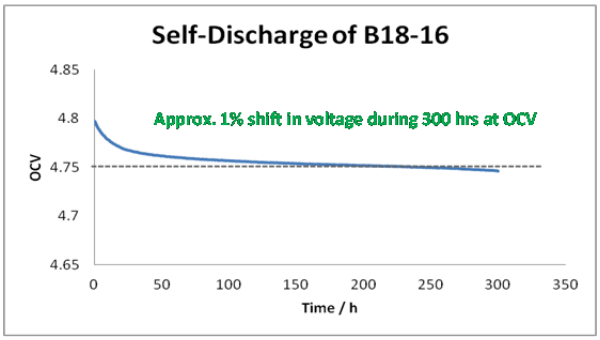

Figure V - 141: Demonstration of low self-discharging behavior at elevated voltage for cells with early generation phosphazene anodes

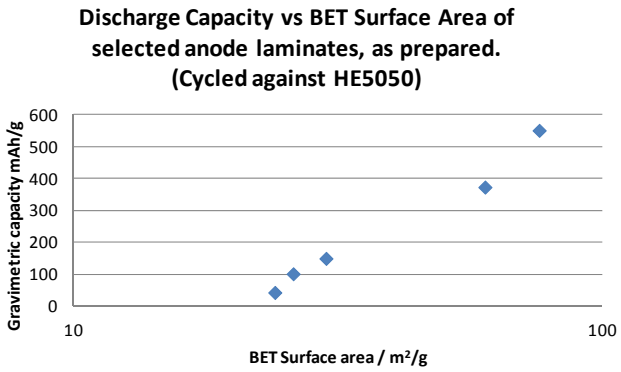

Figure V - 142: Capacity improvement with increased effective surface area within polymer matrix

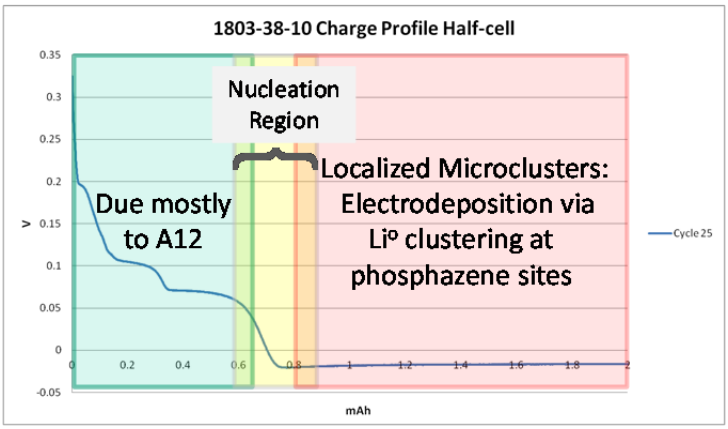

Figure V - 143: Dual/hybrid (atomistic and micro-clustering) mode of lithium residency

Conclusions and Future Directions

INL phosphazene materials improve electrolyte stability at higher voltage and elevated temperatures. The choice of the pendant R groups allows customization of the molecules to fine tune electrolyte properties tied to fate and performance in Li-ion cells. Ionic liquid phosphazenes drastically reduce the inherent association between nitrogen and Li^+, and have shown superior performance in abuse testing at SNL. In FY 13 we explored electrolytes having higher amounts of phosphazene solvents to exploit their low flammability, wherein amounts of at least 12.4% additives appear feasible for cells requiring modest rates. Newer compounds within the FM and PhIL series support optimization of these compound classes. NMR studies revealed mechanistic information regarding molecular fate and why/how our additives provide resilience to the baseline system.

Good progress was had on developing alternative anodes for Li-ion systems, wherein a phosphazene polymer basis was employed as the core host material, with modifications undertaken to modify crosslinking, porosity, and electronic conductivity. Cell capacities (vs HE5050-type thicker cathode) were often on the order of 300-500 mAh/g for these new materials.

FY 2013 Publications/Presentations (Selected)

1. M. T. Benson*, M. K. Harrup, K. L. Gering, "Lithium binding in fluorinated cyclic triphosphazenes," Computational and Theoretical Chemistry 1005 (2013) 25–34.
2. S. V. Sazhin*, K. L. Gering, M. K. Harrup, H. W. Rollins, "Highly Quantitative Electrochemical Characterization of Non-Aqueous Electrolytes & Solid Electrolyte Interphases," submitted to the Journal of the Electrochemical Society, manuscript tracking number JES-13-2932.
3. K. L. Gering* et al., "Advances Toward Inorganic Li-ion Cell Chemistries," Next Generation Batteries (April 30, 2013, Boston, MA).
4. K. L. Gering*, "The Influence of Molecular Interactions on Battery Electrolyte Properties and Processes," 222nd Meeting of the Electrochemical Society (October 11, 2012, Honolulu, HI).

** Lead author or presenter.*

V.D.4 Evaluate Impact of ALD Coating on Li/Mn-rich Cathodes (NREL)

Shriram Santhanagopalan and Ahmad Pesaran

National Renewable Energy Laboratory
15013 Denver West Parkway
Golden, CO 80401
Phone: (303) 275-3944
E-mail: Shriram.Santhanagopalan@nrel.gov

Collaborators:
Chunmei Ban, National Renewable Energy Laboratory
Mohamed Alamgir, LG Chem Power, Inc., Troy MI
David King, ALD Nanosolutions, Broomfield CO
Karen Buechler, ALD Nanosolutions, Broomfield CO

Start Date: June 2012
Projected End Date: Projected September 2013

Objectives

- To assess the technical viability of the Atomic Layer Deposition (ALD) technique on commercial battery active material such and Li/Mn-rich cathode materials.
- To mitigate durability and abuse tolerance issues associated with high capacity Li manganese-rich cathodes.

Technical Barriers

- Rapid fade in capacity of the high voltage Li - manganese rich cathode, particularly at high temperatures (45°C).
- Lack of uniformity in data from large batches of commercial active material treated with the ALD technique to overcome durability issues.
- Ineffectiveness in coating sheets of electrodes directly with ALD to achieve results similar to coating powders of active material.

Technical Targets

- Demonstrate capacity loss of less than 20% at C/2 rate over 500 cycles at 45°C for the high-voltage manganese-rich cathode.
- Demonstrate scalability of the ALD process by coating batches up to 500g, of the Mn-rich cathodes with alumina, to reproduce cell level performance observed at the lab-scale.
- Build capabilities to directly coat electrode sheets up to 6" x 6" in size.

Accomplishments

- In FY12, NREL initiated a collaborative work with LG Chem Power Inc. (LGCPI) and obtained commercial samples of Mn-rich cathode materials.
- These samples were coated with alumina using the ALD technique, in collaboration with ALD NanoSolutions, a leading company for coating ALD on battery materials.
- FY13 accomplishments include:
  - coating of large batches of cathod material powders (several tens of kg).
  - coating of sheet electrode samples in the modified reactor built in the previous year.
  - demonstration of cell performance using pouch cells.

Introduction

Extending the driving range of PHEVs requires the use of high-voltage cathodes that offer consistent performance over 5,000 cycles and 15 years of battery life without compromising safety. The Mn-rich cathode is an excellent material for these specifications and has been shown to have the potential to be stable over a wide voltage window between 4.5 and 2.7 V. Preliminary work at the lab-scale, between NREL and LGCPI indicated that while ALD coating of the cathode improved its cycling performance, no enhancements were observed on coating carbon-based anodes. This effort was initiated in June of 2012. In this report, we show findings from the preliminary study, using large format pouch cells.

Approach

Powders

- Coat 200-500g batches of Mn-rich cathode powders in pilot-scale reactors at a sub-contractor's facility.
- Optimize the coating conditions to minimize rate-capability losses, if any, by building cells using several batches of ALD-coated cathode material and testing them at NREL.
- Evaluate optimized coatings by building and testing pouch cells at LGCPI.

Electrodes

- Modify ALD-reactors to hold sheet-electrodes.

- Develop a processs to coat electrodes uniformly across the thickness of the sample.
- Characterize and test samples at NREL and LGCPI.
- Refine coating process based on initial evaluation results.

Results

In FY13, the focus was on evaluating the cycling performance of the cells fabricated using the ALD coated powders. The cathode powder samples were subjected to different ALD coating profiles to assess the uniformity of the coating and the resistance as a function of the number of cycles last year. Based on these results, the samples with the coating that best suited the requirements of cycling and resistance build-up were used to build pouch format cells and cycled at different temperatures. The coating procedure was the same as adopted last year.

ALD Coating.

The pre-processing step included drying at overnight. No unusual off-gassing or decomposition reactions were observed. The coating process involved the following steps:

i) loading the bed of powders into the fluidized bed reactor (shown in Figure V - 144),

ii) fluidizing the powders at the coating temperature and pressure, and

iii) introducing the ALD precursors sequentially. Each cycle comprised of the routine A-purge-B-purge – and the process was repeated for the desired number of cycles.

Figure V - 144: Fluidized Bed Reactor to coat powders with ALD cycles: the existing reactor at ALD Nanosolutions can process up to 8L of powder per batch

The coating was carried out at ALD Nanosolutions' facility in Broomfield, CO. ALD Nanosolutions has been doing ALD coating of battery materials and has the capability to process multiple batch sizes from tenss of grams to tens of kilograms. The samples were fluidized at 10 cm^3 per minute after the initial drying. The coating time per batch was about 2.5 hours. The initial trials focused on alumina coatings, since we had demonstrated the proof-of-concept with alumina on the Mn-rich cathode material.

Cell-Evaluation.

Sample results from cycling at 25 and 45°C are shown in Figure V - 145.

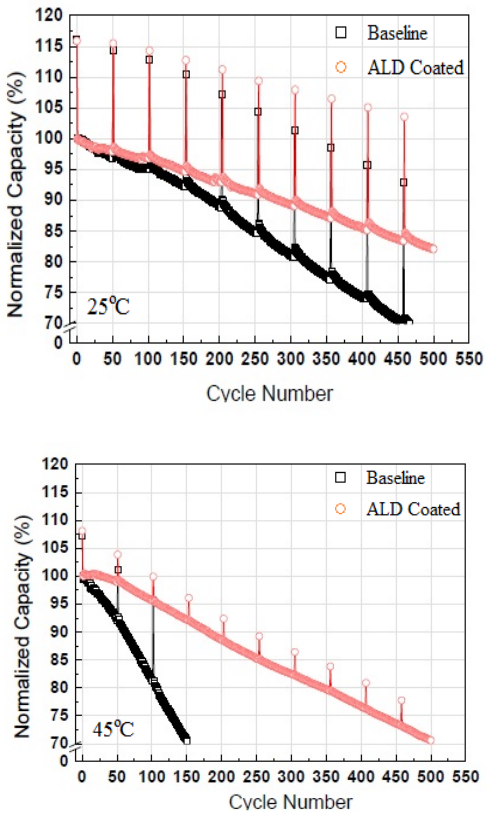

Figure V - 145: Cycling performance of ALD Coated Mn-rich Cathodes

The cell evaluation results indicate that the cycling performance at 25°C show a fade of less than 20%. At 45°C, the cycle life is considerably improved with the coating built under the present effort – however, the performance mark of less than 20% fade was reached around cycle 350.

Conclusions and Future Directions

The scalability of the ALD technique for coating battery materials is attractive – in fact, this technique has now become popular with several materials vendors, who are actively pursuing coating of cathodes to improve high-temperature performance. A roll-to-roll coating

option has also been explored separately, for large scale manufacturing. Future work will consider tailoring the composition of the coatings to improve functionality. For example, the coatings can be used to improve the processing ability of the cathode particles during the cell fabrication process by expanding the range of temperatures over which the performance of the mtaerial is stable.

FY 2013 Publications/Presentations

1. Shriram Santhanagopalan, Mohamed Alamgir, Karen Buechler, David King and Ahmad Pesaran, "Evaluate ALD Coatings of LGCPI Cathode Materials or Electrodes," Milestone Report # 55894, Submitted September 2012.
2. Shriram Santhanagopalan – AMR presentation.

V.D.5 Strategies to Enable the Use of High-Voltage Cathodes and Diagnostic Evaluation of ABR Program Lithium Battery Chemistries (LBNL)

Robert Kostecki

Lawrence Berkeley National Laboratory
Environmental Energy Technologies DIvision
1 Cyclotron Rd. MS 90-3026D
Berkeley, CA 94720
Phone: (510) 486-6002; Fax: (510) 486-5454
E-mail: r_kostecki@lbl.gov

Start Date: October 2012
Projected End Date: September 2013

Objectives

- Increase specific energy at the cell level by addressing the impact of elevated potentials on carbon black additives
  - Explore structural and chemical changes of carbon black additives associated with elevated potentials and investigate methods to reduce side reactions that occur.
  - Explore surface-modification methods to improve stability of carbon black additives in high-energy Li-ion systems.
- Study degradation mechanism(s) in the PHEV test cells and at the system and cell components level.
- Investigate the mechanism of chemical cross-talk between electrodes and its implication for electrochemical performance and lifetime of high-energy Li-ion systems.

Technical Barriers

This project addresses the following technical barriers related to the battery technology development effort of the DOE Office of Vehicle Technologies:

- Inadequate EV and PHEV battery energy, durability and safety, as well as the need for efficent cell-formation processes, are the major barriers addressed by LBNL diagnostic work.
- The primary LBNL role in the ABR Program is to carry out specific diagnostic evaluations to determine the changes in cell components that accompany Li-ion cell power fade, capacity fade and/or failure.
- LBNL also seeks to identify electrode and electrolyte processes that are significantly influenced by various cell-formation protocols.

Technical Targets

- Cycle life: 5,000 (deep) and 300,000 (shallow) cycles.
- Available energy: 200 Wh/kg.
- Calendar life: 15 years.

Accomplishments

- An improved carbon black additive was synthesized and tested in selected composite high-voltage positive electrodes. Enhanced lifetime and reversibility of modified electrodes have been demonstrated.
  - Invention disclosure/patent application filled by LBNL.
  - LBNL Technology Transfer grant obtained to commercialize the technology.
- The mechanism of chemical cross-talk in high-energy Li-ion cells has been determined and possible implications for cell electrochemical performance evaluated.

✧ ✧ ✧ ✧ ✧

Introduction

A primary aim of this project is to develop and use advanced diagnostic techniques to characterize basic physico-chemical properties of electrode active and passive components in ABR Program cells that are being developed for use in PHEV and EV applications. The focus of this task is to correlate fundamental processes that occur in Li-ion batteries with electrochemical performance. The diagnostic results are used to determine cell failure mechanisms, anticipate the system lifetime, and suggest new approaches to design more-stable materials, composites, and electrodes.

Approach

The goal of these studies is to unveil phenomena that determine battery performance and failure modes. A better understanding of the underlying principles that

govern these proesses is inextricably linked with successful implementation of high-energy-density materials such as Si and high-voltage cathodes in Li-ion cells for PHEVs and EVs. The proposed methodologies include:

- Strategies to minimize irreversible capacity losses
  - Determine the mechanism of carbon additive degradation and migration at high potentials and in high-voltage composite electrodes.
  - Improve carbon black stability at high potentials *via* surface treatment.
- Diagnostic evaluation of ABR Program lithium-ion cell chemistries
  - Carry out post-test diagnostic evaluation of components from ABR test cells and model cells (no test cells were sent to LBNL in FY2012 or FY2013.

Results

The focus of our work in FY13 included comprehensive analysis of the irreversible capacity losses (ICL) in high-energy composite positive electrodes, examination of the positive effect of the oxidative heat treatment of carbon black conductive additives, and fundamental investigations of the mechanism of chemical cross-talk in lithium-ion battery cells using fluorescence spectroscopy and imaging.

A new experimental approach has ben designed and created to quantify the extent of electrolyte oxidation at the Toda He5050/Super-P/PVdF positive Li-ion composite electrodes at potentials exceeding 4.2 V *vs*. Li/Li^+. The potential response of the 10^{th} galvanostatic charge-discharge cycle of the Toda He5050 electrode was used used to carry out voltage profile simulation (VPS) measurements on pure carbon black/PVdF electrodes with no active material present. These measurements provided direct quantitative information about the charge consumed by electrolyte decomposition at the carbon black additive alone during a typical charge-discharge process.

The electrolyte oxidation current at the pristine carbon black/PVdF electrode is substantially higher than for the CO_2 heat-treated carbon black/PVdF electrode for both the anodic and cathodic scans during the first cycle. The magnitude of the anodic current tends to decrease significantly in the following scans. However, the current density for untreated CB electrode still remains three time times higher at 4.7 V than that for the CO_2 heat-treated electrode. The calculated charge (mAh/g of carbon) consumed during the model "charge-discharge" cycles of the CB electrodes is shown in Figure V - 146.

This charge profile represents the faradaic component of the current. The significant charge consumed by the electrolyte oxidation processes at the unmodified carbon black electrode during the first anodic scan indicates that irreversible processes must have led to partial passivation of carbon black. The subsequent scans added to the total charge used in these irreversible processes to reach an equivalent of 163 mAh/g of carbon. This is ~5 time higher than the charge consumed during similar "charge-discharge" scans of the CO_2 heat-treated CB electrode. Interestingly, the electrochemical behavior of both samples becomes very similar after 8 cycles suggesting that an effective surface passive layer eventually forms at carbon black.

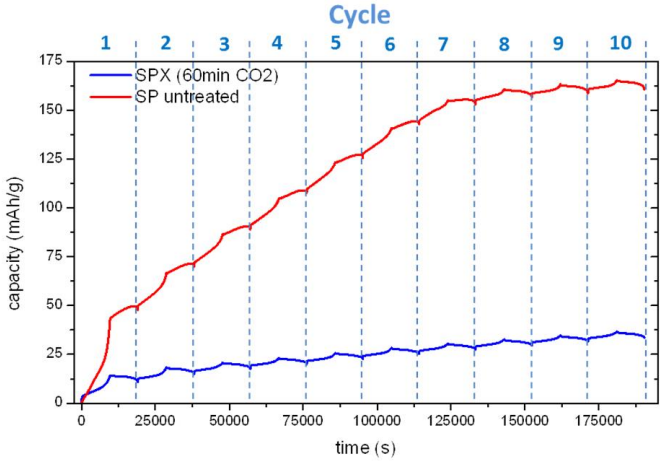

Figure V - 146: Charge consumed in the electrolyte oxidation side reactions during model "charge-discharge" scans of untreated (red), and CO_2 heat-treated Super-P/PVdF electrodes (blue) during the first ten cycles

A typical positive Li-ion composite electrode consists of ~7% carbon black conductive additive. Considering a reversible capacity of NMC-based positive electrode at 170 mAh/g, these results indicate that ~6.7% of the overall electrode charge capacity is consumed in the reversible processes on the carbon black during the first ten cycles. The use of CO_2 heat-treated carbon black additives can help reduce these irreversible losses to ~1.3%. These investigations provide more evidence of the importance of interfacial effects on passive electrode components for the overall performance and lifetime of Li-ion batteries.

In collaboration with the Battaglia group at LBNL, $LiNi_{0.33}Co_{0.33}Mn_{0.33}O_2$ composite electrodes (NMC, Umicore) with the baseline carbon black or the CO_2 heat-treated carbon black, have been manufactured and cycled between 2.5 and 4.6 V *vs* Li/Li^+ in coin cells with metallic lithium as counter and reference electrodes (Figure V - 147). The cells with baseline and modified cathodes perform similarly during the initial cycles. However, the cell with the modified CB cathode displays better capacity retention over the first 60 cycles, and the sudden decline in cell capacity occurs 30 cycles later than for the cell with the standard carbon black additive. This clearly indicates the beneficial effect the CO_2 heat-treatment on the interfacial stability of the carbon black and composite electrode, and on the lifetime of the full Li-ion cell.

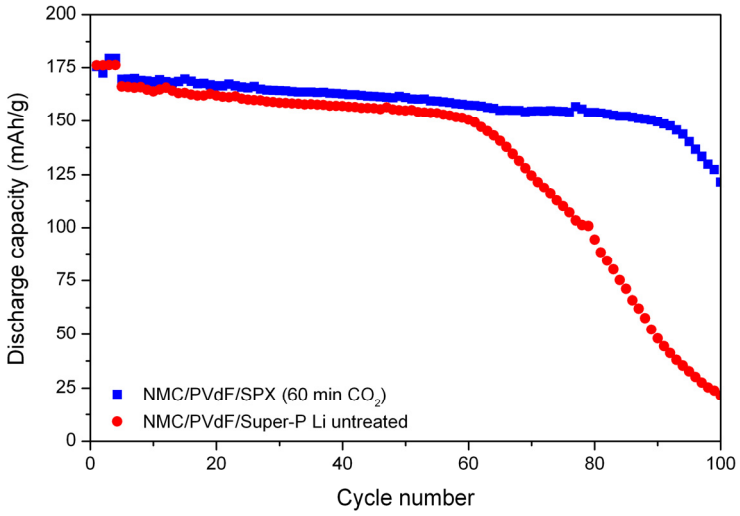

Figure V - 147: Discharge capacity *vs.* cycle number of coin cells utilizing $LiNi_{0.33}Co_{0.33}Mn_{0.33}O_2$ (NMC) and pristine (red) or heat treated (blue) carbon black in EC:DEC 1:2 1M $LiPF_6$

To investigate the mechanism of chemical cross talk in high-energy lithium-ion cells, a novel spectro-electrochemical cell was designed and constructed. The ABR baseline cell chemistry *i.e.*, Toda He5050 cathode, CPG A12 graphite anode and EC:DEC 1:2 1M $LIPF_6$ electrolyte was reproduced in a full cell setup. The composite electrodes provided by ANL were used, and the cell was cycled galvanostatically following ABR Program protocols. The charge cut-off voltage was set at 4.55 V, whereas the discharge cut-off cell voltage was 2.8 V. Figure V - 148 shows the voltage profile of the cell versus time (plotted in blue on the right side), and the corresponding fluorescence intensity across the electrolyte gap between the electrodes (middle image). The x-axis of the image represents the distance between cathode and anode whereas the y-axis shows time. The color of each pixel corresponds to the integrated intensity of the fluorescence spectra at this spot (1 micrometer diameter) at the particular time and cell state of charge (see legend on the left side).

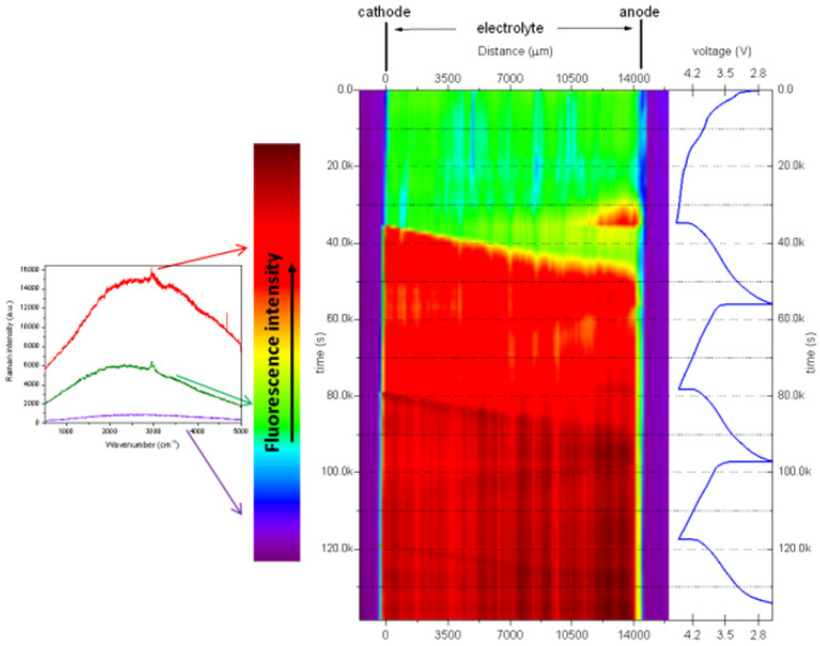

Figure V - 148: Cross-talk visualization by the means of fluorescence spectroscopy (distance between anode and cathode 14 mm, electrolyte EC:DEC 1:2 1M $LiPF_6$) and corresponding voltage profile for the A12-He5050 full cell cycled galvanostatically between 4.55 and 2.5 V vs. Li/Li^+).

At the end of the first charge, the graphitic anode releases fluorescent species into the electrolyte, which slowly migrate into the electrolyte toward the cathode. Interestingly, no photoluminescence active species were released from the He5050 cathode during the phase transformation. However, upon reversing the current from the beginning of the cell discharge, the composite cathode starts releasing fluorescent species into the electrolyte, which migrate across the electrolyte gap in the opposite direction of the lithium ions and reach the anode before the end of the first discharge. These species are most likely consumed by interfacial reactions at the anode because no accumulation effect is visible in the following cycles.

A similar process was observed on the $LiNi_{0.5}Mn_{1.5}O_4$ cathode, where some fluorescent species generated by oxidation of the electrolyte precipitated at the surface of the electrode and some dissolved and diffused away into the electrolyte. Further investigations are needed to determine the composition and origins of these soluble fluorescent species and assess their effect on the composition and stability of the SEI and Li^+ interacalation/deintercalation in graphite.

Conclusions and Future Directions

- Evaluated electrochemical behavior of carbon black additives in composite positive Li-ion electrode.
- The HT CO_2 activation of commercial carbon black additives process effectively suppresses unwanted side reactions in organic carbonate electrolytes.
- Carbon black as conductive additive in the cathode is responsible for 6.7% of the capacity loss in ABR baseline cells during the first 10 cycles
  - CO_2 heat treatment reduces such irreversible losses to 1.3%.
- Preliminary tests of CB-modified Toda He 5050 composite electrodes in full Li-ion cells demonstrated extended lifetime and a higher reversibility.
- Determined that inorganic and organic fluorescent electrolyte decomposition products form at the cathode and anode
  - Phase transformation in the lithium-rich NMC leads to formation of soluble fluorescent species, which diffuse toward the anode and interfere with the anode (SEI Mn poisoning?)
  - Mn and/or Ni dissolution is the root cause of fluorescence compound formation on positive electrode.
- Insoluble electrolyte decomposition products form electronic and ionic barriers in composite cathodes

    - These species contribute to the impedance rise in Li-ion cells.
    - Electrolyte additives and surface coatings could be effective strategies to reduce the surface reactivity of high-voltage cathodes.
- Work directly with Envia Systems and LBNL cell manufacturing/testing facilities on the development of high-energy Li-ion systems in the next phase of the ABR Program.
- Carry out post-test characterization of components from ABR model cells.
- Continue studies of degradation modes of high-voltage systems. Extend diagnostic studies to LMR-LMO.
- Continue search for remedies that decrease irreversible capacity losses and stabilize material during long-term cycling
    - Reduce irreversible charge losses from surface reactions.
    - Investigate pretreatment regimens to reduce side reactions.
    - Understand factors that can enhance the stability of SEI layers.
- Continue migration studies and assess the influence of this migration on cell internal resistance.
- Investigate the surface-treated carbon black in combination with different cathode materials, *e.g.*, NMC and LMNO (funded by received Technology Transfer grant from LBNL).

FY 2013 Publications/Presentations

1. Xiaobo Chen, Can Li, Michaël Grätzel, Robert Kostecki, Samuel S. Mao, "Nanomaterials for Renewable Energy Production and Storage," Chemical Reviews, accepted.
2. Chunjoong Kim, Nick S. Norberg, Caleb T. Alexander, Robert Kostecki, Jordi Cabana, "Mechanism of phase propagation during lithiation in carbon-free Li4Ti5O12 Battery Electrodes", Advanced Functional Materials, 23(9), pp 1214–1222, March 6, 2013.
3. S.F. Lux, I.T. Lucas, E. Pollak, S. Passerini, M. Winter and R. Kostecki, "The mechanism of HF formation in $LiPF_6$ based organic carbonate electrolytes," Electrochemistry Communications, 14, 47–50, 2012.
4. Robert Kostecki, Thomas Richardson, Ulrike Boesenberg, Elad Pollak, Simon Lux, "Modified carbon black materials for lithium-ion batteries," LBNL Invention Disclosure IB-3193 (patent filing planned May 2013).
5. N. Norberg, S. Lux, I. Lucas, J. Syzdek, and R. Kostecki, "*In situ* Fluorescence Spectroscopy of Interfacial Processes in High-Energy Li-ion Batteries," PRiME 2012 in Honolulu, Hawaii, October 7-12, 2012.
6. Kim, C. Alexander, N. Norberg, R. Kostecki, and J. Cabana, "Study of the Factors that Enable Carbon-Free Insulating Li-Ion Battery Electrodes," PRiME 2012 in Honolulu, Hawaii, October 7-12, 2012
7. R. Kostecki, I. Lucas, N. Norberg, and J. Syzdek, "Materials and Interfaces Degradation in High-Energy Cathodes for Li-ion Batteries," PRiME 2012 in Honolulu, Hawaii, October 7-12, 2012 (invited lecture).
8. Robert Kostecki, "Local Probe Studies of Interfacial Phenomena in Li-ion Batteries," Materials Research Society Spring 2012 Meeting, San Francisco, abstract ID: 1284582, (invited lecture).
9. Nick Norberg, Ivan T. Lucas, Robert Kostecki, "Interfacial Phenomena of Li-ion battery electrodes as probed by *in situ* spectroscopy and microscopy techniques," 1st Gordon Research Conference "Batteries, Advanced Characterization, Theory and Mechanisms of Processes in Rechargeable Batteries Across Length Scales, March 4-9, 2012, Four Points Sheraton / Holiday Inn Express, Ventura, CA.

V.D.6 Life and Abuse Tolerance Diagnostic Studies for High Energy Density PHEV Batteries (BNL)

Kyung-Wan Nam

Chemistry Department
Bldg. 555, Brookhaven National Laboratory
Upton, NY 11973
Phone: (631) 344-3202; Fax: (631) 344-5815
E-mail: knam@bnl.gov

Xiao-Qing Yang
Chemistry Department
Bldg. 555, Brookhaven National Laboratory
Upton, NY 11973
Phone: (631) 344-3663; Fax: (631) 344-5815
E-mail: xyang@bnl.gov

Start Date: October 2012
Projected End Date: September 2013

Objectives

- To establish and investigate the structural origin of thermal instability of various cathode materials.
- To search for new approaches on how to improve the thermal stability of cathode materials including surface modification and their effectiveness.
- To provide information on designing thermally stable cathode materials for HEV and PHEV applications.
- To develop new *in situ* diagnostic techniques with surface and bulk sensitivity for studying the thermal stability of various cathode materials.
- To develop *in situ* diagnostic techniques with surface and bulk sensitivity for studying the capacity, voltage, and power fading mechanisms of Li-ion battery.
- To establish and investigate the capacity, voltage and power fading mechanisms of various cathode materials, especially for the high energy density Li-rich Li_2MnO_3-$LiMO_2$ type cathode materials.

Technical Barriers

- Li-ion and Li-metal batteries with long calendar and cycle life.
- Li-ion and Li-metal batteries with superior abuse tolerance.
- To reduce the production cost of a PHEV batteries.

Technical Targets

- Complete the studies of thermal decomposition of charged $Li_{1.2}Ni_{0.15}Mn_{0.55}Co_{0.1}O_2$ (Toda HE5050) cathode materials during heating using combined Time-Resolved XRD (TR-XRD) and Mass Spectroscopy (MS).
- Complete the thermal stability studies of $Li_xNi_{1-2y}Mn_yCo_yO_2$ charged cathode materials with different values of "y" using *in situ* TR-XRD coupled with MS during heating.
- Complete the *in situ* hard XAS studies of Toda HE5050 cathode material for the voltage fading mechanism and limiting factors of their relatively poor rate capability.

Accomplishments

- Developed new *in situ* technique by combining the TR-XRD with MS and applied it to study the Toda HE5050 high energy density cathode material during heating. The co-relation between the structural changes and the oxygen release of this material was obtained.
- Through collaboration with Johnson Control, carried out the thermal stability studies of $Li_xNi_{1-2y}Mn_yCo_yO_2$ charged cathode materials using *in situ* TR-XRD coupled with MS during heating.
- Through collaboration with Argonne National Lab., R&D Center of GM, and other collaborators, carried out time resolved x-ray absorption spectroscopy (TR-XAS) diagnostic studies of Toda HE5050 cathode materials during constant voltage charge. The major limiting factor for the relatively poor rate capability of this type of materials was determined as the Li_2MnO_3 component in the composite material.

✧ ✧ ✧ ✧ ✧

Introduction

The high energy density composite cathode materials, or so called layered-layered

$xLi_2MnO_3 \cdot (1-x)LiMO_2$ (e.g., M=Mn, Ni, and Co) materials, are currently receiving worldwide attention because of their ability to deliver capacities of 250 mAh/g or more. One serious problem is, after the high voltage activation, these composite electrode materials show a continuous voltage fading during charge-discharge cycling. The integrated advanced *in situ* diagnostic studies are crucial in resolving these problems. We have developed a set of synchrotron based *in situ* diagnostic tools, such as TR-XRD and *in situ* XAS during heating. Recently we have further developed integrated simultaneous TR-XRD and MS at beamline X7B of the National Synchrotron Light Source (NSLS), and combined XAS and high-resolution transmission electron microscopy (HR-TEM) during heating. These *in situ* techniques were applied to study the same batch of samples with similar electrochemical histories and heating conditions. With the penetrating power and bulk averaging nature, the XRD results represent a road map of the average structural changes for the phase transitions. The MS is used to monitor the oxygen-releasing behavior during heating or high voltage charge. The XAS provides information about changes in local structure and oxidation states in an elemental selective way. The HRTEM results offer detailed pictures about where the nucleation of the new phases occurs and how the new phases propagate during phase transitions. The integration of these different *in situ* techniques provides a unique way to study the microscopic structural origin of the structural and thermal instability of the materials during cycling and heating. Another very important issue from the application point of view is how to improve the relatively poor rate capability of the Li-rich layered materials. In this regard, we have also developed *in situ* TR-XAS to investigate the dynamic local structure changes of Li-rich layered materials in an elemental selective way during high-rate charging. Therefore, the in-depth understanding with elemental selectivity for the delithiation kinetics distinguishing the $LiMO_2$ and Li_2MnO_3 components in bulk will provide valuable guidance for the optimization of Li-rich layered materials with improved rate capability.

Approach

A combination of TR-XRD and MS, together with *in situ* XAS, and *in situ* TEM techniques were used during heating to study the thermal stability of the electrode materials.

Using *in situ* XRD, soft and hard XAS to study the voltage and capacity fading mechanism of high energy density Li and Mn rich layer structured NCM (LMR-NCM) during charge-discharge cycling.

Results

Thermal stability studies of HE5050. Using combined TR-XRD and MS, the thermal decomposition of charged Toda HE5050 cathode materials during heating has been studied. The results of the $Li_{1.2}Ni_{0.15}Mn_{0.55}Co_{0.1}O_2$ cathode material charged to $Li_{0.3}Ni_{0.15}Mn_{0.55}Co_{0.1}O_2$ during heating from 25° to 550°C are plotted in Figure V - 149 (left and middle panel). The crystal structure evolution is illustrated in the right panel. It can be seen that the crystal structural changes of charged $Li_{0.3}Ni_{0.15}Mn_{0.55}Co_{0.1}O_2$ layered cathode material follow the similar path as the regular layered materials such as $Li_{0.33}Ni_{1/3}Mn_{1/3}Co_{1/3}O_2$ during heating: at about 220°C, the layered structure starts converting into disordered spinel structure. After completing this transition about 400°C, it starts the second phase transition at about 450°C from the disordered spinel to the rock-salt structure. Both of these two phase transitions are accompanied by the release of oxygen.

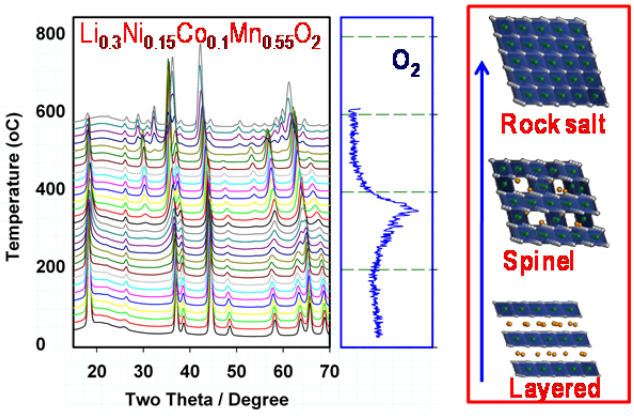

Figure V - 149: *In situ* TR-XRD patterns and simultaneously measured MS for O_2 released from $Li_{0.3}Ni_{0.15}Mn_{0.55}Co_{0.1}O_2$ during heating to 550°C. The right panel shows the models of ideal crystals with rhombohedral (layered), spinel, and rock-salt structures

Thermal stability studies of $Li_xNi_{1-2y}Mn_yCo_yO_2$ samples (y=0.3, 0.2, 0.1) from Johnson Control. Through collaboration with Johnson Control, the thermal stability of charged (4.3V) $Li_xNi_{1-2y}Mn_yCo_yO_2$ cathode materials (with y=0.3, 0.2 and 0.1) were studied using *in situ* technique by combining the TR-XRD with MS during heating. The results are shown in Figure V - 150 and Figure V - 151. It can be seen that the higher the Ni content, the poor the thermal stability, reflected by the lower temperatures of phase transitions and oxygen release. Comparison of phase transition temperatures for the series of charged $Li_xNi_{1-2y}Mn_yCo_yO_2$ samples (with y=0.3, 0.2 and 0.1) together with $Li_xNi_{1/3}Mn_{1/3}Co_{1/3}O_2$ and $Li_xNi_{0.5}Mn_{0.3}Co_{0.2}O_2$ (Figure V - 151, right panel) suggested that the $Li_xNi_{0.5}Mn_{0.3}Co_{0.2}O_2$ would be the ideal composition among the NMC chemistry to ensure the high capacity without compromising the thermal stability.

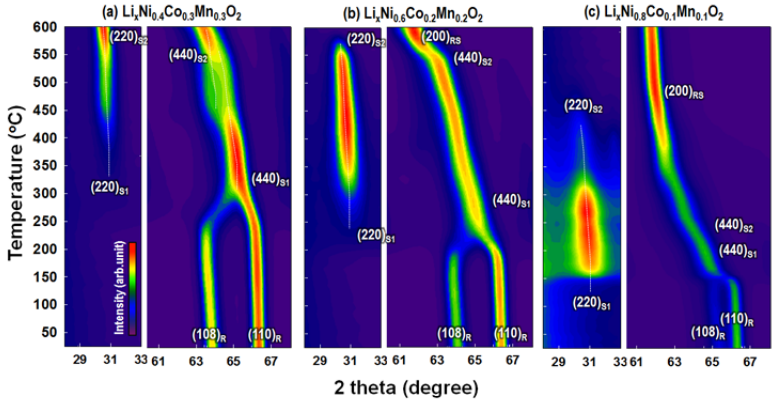

Figure V - 150: Time resolved XRD pattern combined with simultaneously measured mass spectroscopy (MS see the results in Figure V - 151) during heating up to 600°C for three charged (4.3V) $Li_xNi_{1-2y}Co_yMn_yO_2$ samples with y=0.3, y=0.2, and y=0.1

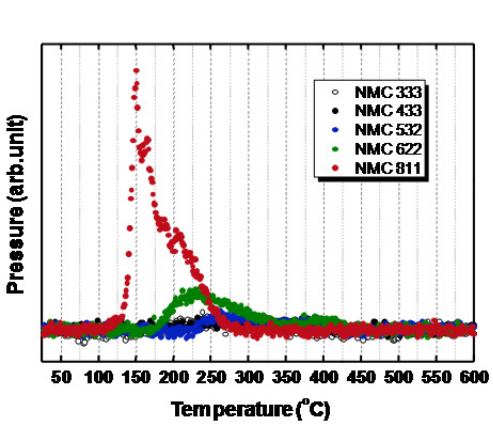

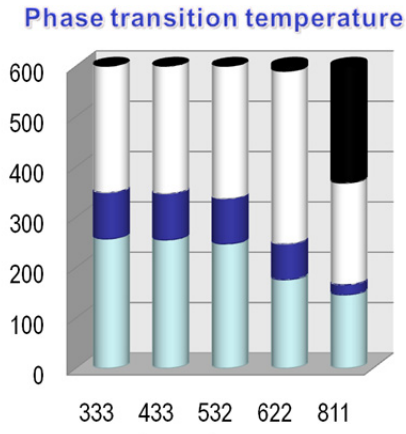

The capacity and thermal stability are strongly related to the percentage content of Ni, Co, and Mn. In general, the higher the content of Ni, the higher the capacity, but the poorer the thermal stability. This trade-off can be used to guide the development of the cathode materials with balanced properties.

Figure V - 151: Simultaneously measured MS data that trace oxygen gas release of charged (4.3V) $Li_xNi_{1-2y}Mn_yCo_yO_2$ samples (with y=0.3, 0.2, and 0.1) in comparison with charged(4.3V) $Li_xNi_{1/3}Mn_{1/3}Co_{1/3}O_2$ and $Li_xNi_{0.5}Mn_{0.3}Co_{0.2}O_2$ during heating up to 600°C

Rate capability studies of HE5050 using TR-XAS during constant voltage charge. The comparative Fourier transformed magnitude of the corresponding Ni, Co, Mn K-edge EXAFS spectra during constant voltage charge at 4.8V for a total time of 900 seconds are plotted in a two-dimensional view in Figure V - 152 by using color scale for the spectrum intensity. For Ni, the first coordination peaks (Ni-O) show dramatic changes in both position and intensity within the first 100 seconds, which represents the charge compensation occurring at the Ni sites. The EXAFS features remain unchanged after 160 seconds, indicating the oxidation of

Ni^{2+} to Ni^{4+} was almost completed within the first three minutes. Compared to Ni, the evolutions of the local structure around Co and Mn sites caused by Li^{+} extraction are more straightforward: the first coordination shell peak (Co-O and Mn-O) intensities show a continuous decrease. No obvious Co-O peak intensity changes can be observed after 200 seconds at 4.8V charge while Mn-O peak intensities continued to decrease in the whole observation time scale (900 second), indicating a much slower delithiation kinetics around Mn sites. The delithiation kinetic features revealed by this TR-XAS technique indicate a much poorer delithiation kinetic in Mn related process (mostly in Li_2MnO_3 component), comparing to the faster reaction kinetics for Ni and Co, which are not much negatively affected by the irreversible structure change of the Li_2MnO_3 component after initial delithiation process. New guidance for designing and improving Li-rich layered cathode materials with better reaction kinetics might be provided in term of tailoring the content of Li_2MnO_3 component as one of the approaches.

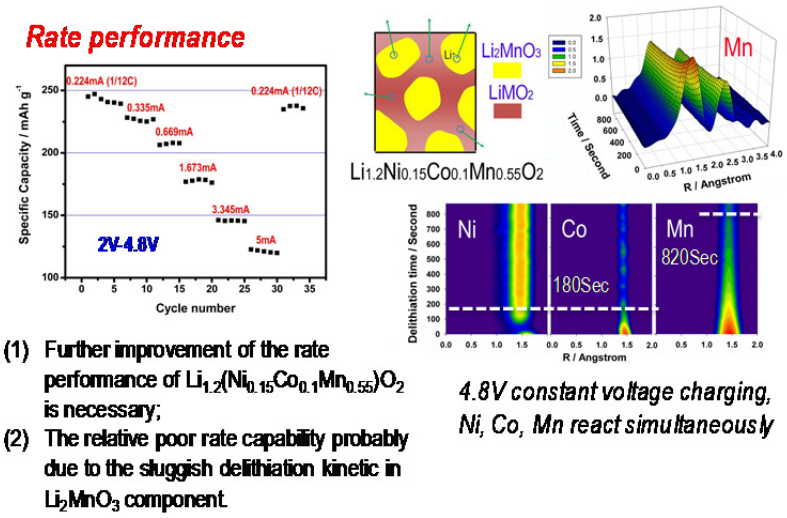

Figure V - 152: During constant voltage charge at 4.8V for a $Li_{1.2}Ni_{0.15}Mn_{0.55}Co_{0.1}O_2$ electrode, Ni, Co, Mn reacted simultaneously which was recorded by a time-resolved XAS technique. Magnitude of Fourier transformed Mn K-edge spectra of $Li_{1.2}Ni_{0.15}Mn_{0.55}Co_{0.1}O_2$ collected during 4.8V constant voltage charging and projection view of corresponding Ni-O, Co-O, Mn-O peak magnitudes of the Fourier transformed K-edge spectra as functions of charging time

Conclusions and Future Directions

The crystal structure evolution of charged high energy density layered cathode material $Li_{0.3}Ni_{0.15}Mn_{0.55}Co_{0.1}O_2$ follows a similar path to the regular layered materials such as $Li_{0.33}Ni_{1/3}Mn_{1/3}Co_{1/3}O_2$ during heating: at about 220°C, the layered structure starts converting into disordered spinel structure. After completing this transition about 400°C, it starts a second phase transition at about 450°C from the disordered spinel to the rock-salt structure. Both of these two phase transitions are accompanied with the release of oxygen.

For the series of $Li_xNi_{1-2y}Mn_yCo_yO_2$ samples with y= 0.3, 0.2, and 0.1, it was found that the thermal stability is poorer with higher Ni content, as the expense for the increased capacity. Comparison of phase transition temperatures for the series of charged $Li_xNi_{1-2y}Mn_yCo_yO_2$ samples together with $Li_xNi_{1/3}Mn_{1/3}Co_{1/3}O_2$ and $Li_xNi_{0.5}Mn_{0.3}Co_{0.2}O_2$ demonstrated that the $Li_xNi_{0.5}Mn_{0.3}Co_{0.2}O_2$ would be the ideal composition among the NMC chemistries for high capacity without compromising the thermal stability.

The TR-XAS studies of HE5050 during constant charge showed that the major source for slow reaction kinetics is the Li_2MnO_3 component. New guidance for designing and improving Li-rich layered cathode materials with better reaction kinetics might be provided by tailoring the Li_2MnO_3 component as one of the approaches. In addition, this novel TR-XAS diagnostic tool can also be applied to investigate the reaction kinetics of other lithium-ion battery materials as well as other battery systems.

In the future, new high energy density cathode materials such as layered NMC with Ni, Mn, and Co concentration gradient will be studied using time resolved XRD and XAS as well as other synchrotron based *in situ* x-ray techniques during heating and cycling.

FY 2013 Publications/Presentations

1. Seong-Min Bak, Kyung-Wan Nam, Won-Young Chang, Xiqian Yu, Enyuan Hu, Soo-Yeon Hwang, Eric A. Stach, Kwang Bum Kim, Kyung Yoon Chung and Xiao Qing Yang, “Correlating

Structural Changes and Gas Evolution during the Thermal Decomposition of Charged $Li_xNi_{0.8}Co_{0.15}Al_{0.05}O_2$ Cathode Materials," *Chemistry of Materials*, Vol. 25 (3), pp. 337–351, (2013).

2. Yong-Hun Cho, Donghyuk Jang, Jeongbae Yoon, Hyunchul Kim, Tae Kyu Ahn, Kyung-Wan Nam, Yung-Eun Sung, Woo-Seong Kim, Yun-Sung Lee, Xiao-Qing Yang, Won-Sub Yoon, "Thermal stability of charged $LiNi_{0.5}Co_{0.2}Mn_{0.3}O_2$ cathode for Li-ion batteries investigated by synchrotron based *in situ* X-ray diffraction," *Journal of Alloys and Compounds*, Vol. 562, pp 219 - 223 (2013).
3. K. Karthikeyan, S. Amaresh, V. Aravindan, W.S. Kim, K.W. Nam, X.Q. Yang, Y.S. Lee, "$Li(Mn_{1/3}Ni_{1/3}Fe_{1/3})O_2$-Polyaniline hybrids as cathode active material with ultra-fast charge-discharge capability for lithium batteries," *Journal of Power Sources*, Vol. 232, pp 240-245 (2013).
4. Jinping Dong, Xiqian Yu, Yang Sun, Lei Liu, Xiaoqing Yang, Xuejie Huang, "Triplite $LiFeSO_4F$ as cathode material for Li-ion batteries," Journal of Power Sources, Vol. 244, pp 716-720 (2013).
5. Xiqian Yu, Yingchun Lyu, Lin Gu, Huiming Wu, Seong-Min Bak, Yongning Zhou, Khalil Amine, Steven N. Ehrlich, Hong Li, Kyung-Wan Nam, Xiao-Qing Yang, "Understanding the rate capability of the high energy density Li-rich layered $Li_{1.2}Ni_{0.15}Co_{0.1}Mn_{0.55}O_2$ cathode material," *Advanced Energy Materials*, accepted.
6. Xiqian Yu, Kyung-Wan Nam, Enyuan Hu, Daniel Abraham, and Xiao-Qing Yang, "Structure Evolution and its relation to the Voltage Fading Behavior in Li-rich Layered $Li_{1.2}Ni_{0.15}Co_{0.1}Mn_{0.55}O_2$ Cathode Material during Cycling: X-ray diffraction and absorption spectroscopy study," presented at the "222th Meeting of the Electrochemical Society, October, 8-12, 2012, Honolulu, Hawaii, USA.
7. Seong-Min Bak, Kyung-Wan Nam, Enyuan Hu, Xiqian Yu, Kyung-Yoon Chung, Sung-Jin Cho, Frederic Bonhomme, Kwang-Bum Kim and Xiao-Qing Yang, "Insight into Thermal Instability of Charged Cathode Materials for Lithium-Ion Batteries: Combined *in situ* Synchrotron X-ray and Mass Spectroscopy Study," presented at the "222th Meeting of the Electrochemical Society, October, 8-12, 2012, Honolulu, Hawaii, USA.
8. Xiqian Yu, Xiao-Qing Yang, Qi Wang, Yongning Zhou, Kyung-Wan Nam, Huiming Wu, Khalil Amine, Yingchuan Lv, Hong Li and Xuejie Huang, Ying Shirley Meng, "The Studies On The Kinetic Behaviors Of Olivine Structured $LiFePO_4$ and Layer Structured $Li_{1.2}(Ni_{0.10}Co_{0.15}Mn_{0.55})O_2$ Cathode Materials Using Time Resolved X-ray Absorption Spectroscopy," presented at the International Battery Association IBA2013, March 11-15, 2013, Barcelona, Spain. **Invited.**
9. Xiqian Yu, Kyung-Wan Nam Xiao-Qing Yang, Yongning Zhou Enyuan Hu, Hung-sui Lee, Daniel Abraham, Huiming Wu, Khalil Amine, and Hong Li "Structure Evolution and its relation to the Voltage Fading Behavior in Li-rich Layered $Li_{1.2}Ni_{0.15}Co_{0.1}Mn_{0.55}O_2$ Cathode Material during Cycling: X-ray diffraction and absorption spectroscopy study," presented at the 2013 MRS Spring Meeting, April 1-5, 2013 San Francisco, USA, **Invited.**
10. Xiqian Yu, Xiao-Qing Yang, Yongning Zhou, Yingchuan Lv, Hong Li, Kyung-Wan Nam, Huiming Wu, and Khalil Amine, "Synchrotron based *in situ* XRD and XAS diagnostic studies on new electrode materials for advanced rechargeable batteries," presented at the 6th International Conference on Advanced Lithium Batteries for Automobile Applications (ABAA6), September 9-11, 2013, Argonne, Illinois, USA 60439, **Invited.**
11. Kyung-Wan Nam, Seong-Min Bak, Enyuan Hu, Xiqian Yu, Youngning Zhou, Lijun Wu, Yimei Zhu, Won-Young Chang, Eric A Stach, Kyung Yoon Chung, Xiao-Qing Yang, "Origin of thermal instability in charged cathode materials for Li-ion batteries: Combined *in situ* synchrotron X-rays and electron microscopy study," presented at the 245th National Meeting of the American-Chemical-Society (ACS) Location: New Orleans, LA Date: APR 07-11, 2013. **Invited.**

V.D.7 Overcharge Protection for PHEV Batteries (LBNL)

Guoying Chen, Principle Investigator

Environmental Energy Technologies Division
Lawrence Berkeley National laboratory
Berkeley, CA 94720
Phone: (510) 486-5843; Fax: (510) 486-5467
E-mail: gchen@lbl.gov

Start Date: October 2009
Projected End Date: September 2013

Objectives

- Develop and implement an inexpensive, long-lasting mechanism that provides self-actuated, reversible and high-rate overcharge protection for high-energy lithium-ion batteries for PHEV applications.

Technical Barriers

- Abuse tolerance.
- Safety.
- Poor cycle life.

Technical Targets

- PHEV40: 96 Wh/kg, 750 W/kg, 5,000 cycles.

Accomplishments

- Developed an inexpensive and scalable electrospinning technique to fabricate novel electroactive fiber separators suitable for overcharge protection in high-energy lithium cells.
- Demonstrated the most stable overcharge protection yet reported in several Li-ion cell chemistries.
- Obtained stable and high-rate overcharge protection in larger-sized pouch cells. Validated scale-up feasibility of the approach.
- Identified an electroactive polymer with good stability at low voltages and demonstrated the use of single-layer separator in providing stable overcharge protection.

✧ ✧ ✧ ✧ ✧

Introduction

Meeting the DOE targets for Li-ion batteries intended for vehicular applications requires the use of high energy density cells and large battery packs. This will no doubt lead to increased importance in addressing the safety hazards associated with cell overcharge and overdischarge. A variety of conditions may be responsible for overcharging in secondary lithium batteries, including charging at normal rates but beyond rated capacity, overvoltage excursions for varying periods, charging at a rate too high for one electrode without exceeding the maximum voltage, and other more complex scenarios. While overcharging is still a major safety issue for lithium batteries, it also has a major impact on battery life. Even slight overcharging reduces the discharge capacity of a cell, potentially causing overdischarging, increased impedance, and local heating.

Battery packs for consumer electronics are protected by electronic controls and by internal shutdown mechanisms like melting separators and pressure or temperature-activated disconnects. In a multicell stack capable of delivering several hundred volts, permanently shutting down a cell reduces the usable capacity of the stack and adds to the burden of the remaining cells in parallel circuit. The electroactive-polymer approach, developed at LBNL, protects cells by forming a reversible resistive shunt between the current collectors during overcharging. The process is self-activated by voltage, and it does not pose interference during normal cell charge and discharge. Unlike the commonly used redox shuttle method, it conducts overcharge current through an electronic rather than a diffusional path, and therefore is capable of high-rate and low-temperature protection. The polymer can be added to cells in a variety of configurations, opening the possibility for cell designs that best accommodate heat transfer during overcharging. Conversely, overheating in internal redox shuttle protected cells can only be avoided by restricting the cell to low cycling rates.

Approach

Electroactive polymers are used for self-actuating and reversible overcharge protection. The redox window and electronic conductivities of the polymers are fine-tuned to avoid interference with a given battery chemistry's normal operation. The morphology of polymer composite membranes and cell configuration of the protection are optimized to achieve the best rate capability and cycle life.

Results

Electroactive Polymer Fiber Separators. The team previously reported that non-woven electroactive-fiber-composite separators with high porosities and an open pore structures can be produced by electrospinning. The presence of the inert polymer phase reduces the concentration of the electroactive polymer in the composite fibers but does not compromise its electronic continuity. In order to expand the protection voltage window for high-energy cells, bilayer fiber membranes consisting of a high-voltage electroactive polymer, poly[(9,9-dioctylfluorenyl-2,7-diyl)] (PFO) on one side, and a low-voltage polymer, poly(3-butylthiophene) (P3BT) on the other were prepared. Chloroform solutions containing either PFO or P3BT were used for electrospinning, with a small amount of polyethylene oxide (PEO) added to adjust solution viscosity and to ensure the formation of polymer fibers during the process. After the initial deposition of PFO/PEO fibers on an aluminum collector, the P3BT/PEO polymer fibers were then directly electrospun onto the surface of the PFO/PEO film. The individual layer thickness is readily adjusted by controlling the amount of each polymer used during electrospinning. Optical images of the membranes show that smooth and uniform coverage were achieved for both layers (Figure V - 153a and Figure V - 153b). The prepared composite membrane was peeled from the Al substrate and the PEO component was removed by sonication in water. Figure V - 154 shows the top-view SEM images of a 50 μm-thick PFO/P3BT (weight ratio 3:1) fiber membrane obtained from the PFO (Figure V - 154a) and P3BT (Figure V - 154b) sides, respectively. It is clear that removal of the PEO had minimal impact on the fiber morphology, and both types of electroactive fibers were intact and well-connected in a highly porous structure.

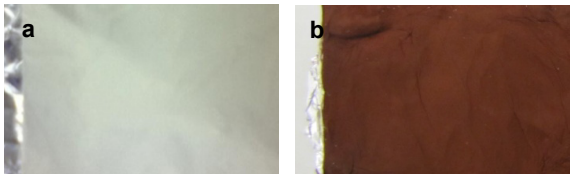

Figure V - 153: Digital images of electrospun-composite membranes on an Al substrate: a) after the deposition of PFO/PEO layer and b) after the deposition of both PFO/PEO and P3BT/PEO layers

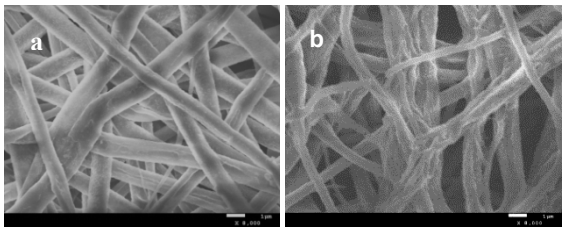

Figure V - 154: Top-view SEM images of an electrospun PFO/P3BT composite membrane: a) PFO side and b) P3BT side

Cells were assembled with the high-voltage PFO side facing the cathode and the low-voltage P3BT side facing the anode. The cycling performance of a spinel $Li_{1.05}Mn_{1.95}O_4$/Li cell protected by such a separator is shown in Figure V - 155a. When cycled at 2/3 C rate and 135% overcharge, the cell repeatedly reached and maintained a steady state potential of 4.2 V. The discharge capacity was retained under the severe overcharge conditions for well over 1,000 cycles in more than 5,000 h or one year of testing time with some rest periods (Figure V - 155b). This is the most stable overcharge protection reported in rechargeable lithium batteries so far, and the results demonstrate the ability of electroactive fiber separators in providing prolonged high-rate overcharge protection.

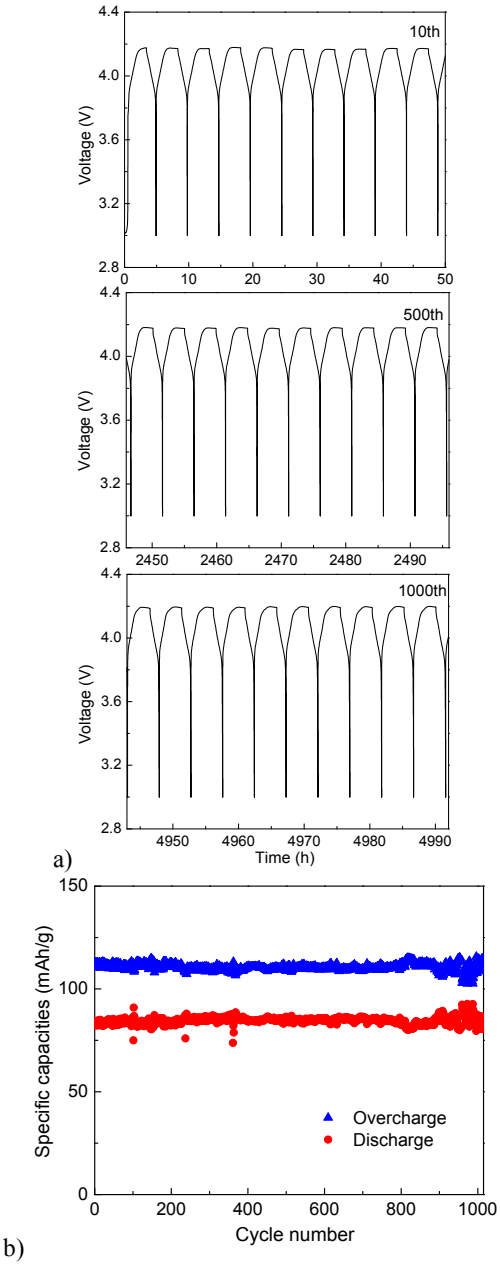

Figure V - 155: a) Charge-discharge cycling profiles and b) specific capacities as a function of the cycle number of a $Li_{1.05}Mn_{1.95}O_4$ half-cell overcharge protected by the electrospun PFO/P3BT composite separator

The performance of a protected $LiNi_{0.8}Co_{0.15}Al_{0.05}O_2$ /Li cell is shown in Figure V - 156. At C/4 rate and 50% overcharge, a constant voltage was reached at 4.2 V and the cell delivered steady performance for more than 160 cycles (Figure V - 156a). The upper limiting voltage is significantly lower compared to that of the previous cells protected by a similar PFO/P3BT composite prepared with either a microporous or glass-fiber membrane. This is likely due to improved polymer distribution and reduced internal resistance in the electrospun fiber separator. The discharge capacity of this cell gradually decayed during cycling (Figure V - 156b), a phenomenon previously observed in $LiNi_{0.8}Co_{0.15}Al_{0.05}O_2$ cells charged to 4.2 V. As a result, the extent of overcharge protection provided by the electroactive separator gradually increased, reaching nearly 100% at 160 cycles.

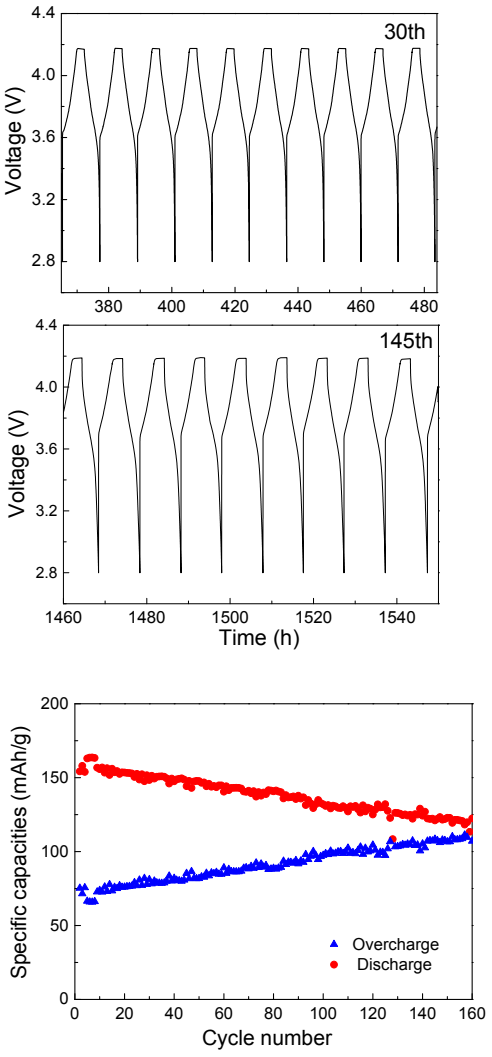

Figure V - 156: a) Charge-discharge cycling profiles and b) specific capacities as a function of the cycle number of a $LiNi_{0.8}Co_{0.15}Al_{0.05}O_2$ half-cell overcharge protected by the electrospun PFO/P3BT composite separator

The scalability of overcharge protection based on electroactive fiber composite separators was also evaluated. A $Li_{1.05}Mn_{1.95}O_4$-Li pouch cell with an electrode area of 3cm x 4cm, which is 15 times larger than that in a typical "Swagelok-type" cell, was equipped with the combination of the PFO/P3BT glass-fiber composites, a configuration previously used in the "Swagelok-type" cell tests. Figure V - 157 shows the

room-temperature voltage profiles of the cell at the various cycling rates. At C/8 rate and 125% overcharge, the cell was reversibly protected at 4.3 V during the first 50 cycles. The steady-state voltage increased with the current density, reaching 4.35 and 4.55 V at C/4 and C rates, respectively. Stable protection was achieved at all rates tested. Compared to the previous protection achieved on the pouch cells equipped with the PFO/P3BT Celgard composites, the upper cell limiting voltage was significantly reduced, further confirming lowered internal resistance and improved performance in the fiber composites.

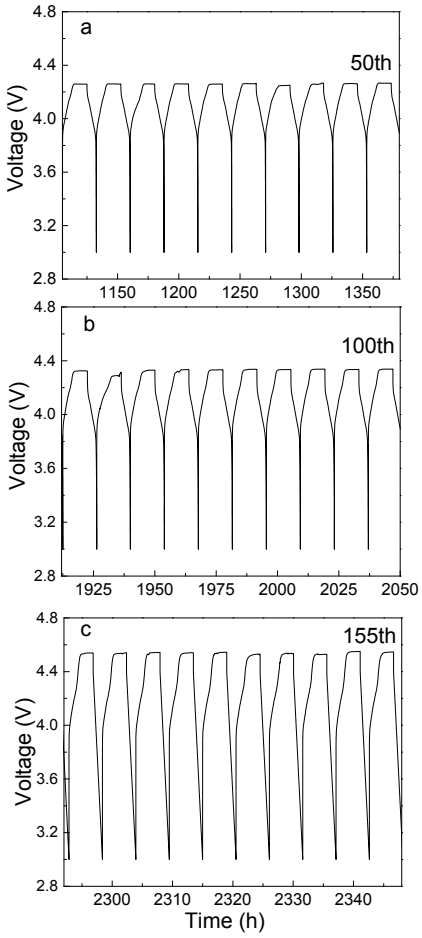

Figure V - 157: Varying-rate cycling profiles of a $Li_{1.05}Mn_{1.95}O_4$ /Li pouch cell overcharge-protected by the PFO/P3BT glass-fiber composites: a) C/8 rate and 125% overcharge, b) C/4 rate and 150% overcharge and c) C rate and 300% overcharge

Alternative electroactive polymers. Poly[(9,9-dioctylfluorenyl-2,7-diyl)-co-(1,4-phenylene)] (PFOP) was found to have an onset oxidation potential of 4.25 V, which is one of the highest values reported so far. When scanning the polymer between 0.1 and 4.5 V vs. Li/Li^+ at 5 mV/s, no obvious degradation was observed on the cyclic voltammogram (Figure V - 158a). This suggests improved low-voltage stability and the possibility of using single-layer polymer composite for overcharge.

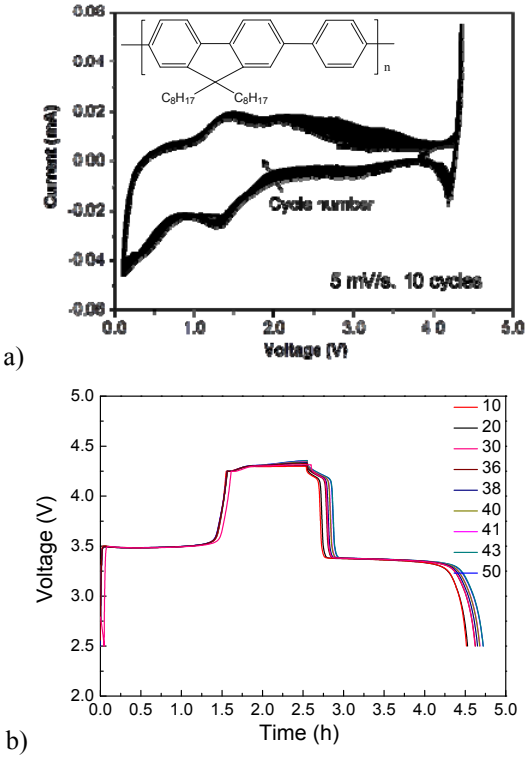

Figure V - 158: a) Cyclic voltammogram of PFOP in 1M $LiPF_6$ in EC: DEC electrolyte and b) cycling profiles of a $LiFePO_4$ half-cell overcharge-protected by the PFOP composite separator

To evaluate this possibility, a PFOP composite membrane was prepared by impregnating a concentrated chloroform solution of the polymer into a microporous Celgard membrane and then used as the separator in a "Swagelok-type" $LiFePO_4$ half-cell with 1M $LiPF_6$ in 1:1 (v/v) EC and DEC electrolyte. The cell was charged and discharged at 0.65 C rate and 80% overcharge. A steady-state potential was reached at 4.3 V which remained nearly constant during the test, suggesting reversible internal shorting established by PFOP (Figure V - 158b). Excellent capacity retention was also observed. The improved low-voltage stability of the polymer allows for stable single-polymer protection, which eliminates the need of the bilayer configuration that was previously adopted to protect the high-voltage polymer from degradation at the anode potential.

Conclusions and Future Directions

Novel electroactive-fiber-composite membranes with a uniform distribution of electroactive polymer were prepared by a simple electrospinning process. When used as battery separators, the membranes provided stable overcharge protection with a significant improvement in cycle life over that achieved with the previous composites prepared by solution impregnation. Electrospinning is a cost-effective and scalable way to produce lithium-ion battery separators with reliable voltage-regulated shunting. An electroactive polymer capable of providing single-layer overcharge protection was also identified and stable cycling performance in protected cells was achieved. Future work will further evaluate the rate capability of the fiber composites, as well as the performance of fiber-composite separators including a supporting polymer that is stable in the cell operating window, such as PVdF and PMMA.

FY 2013 Publications/Presentations

1. B. Wang, T. J. Richardson and G. Chen, "Stable High-Rate Overcharge Protection for Rechargeable Lithium Batteries," Physical Chemistry Chemical Physics, 15 (18), 6849 (2013).
2. G. Chen and T. J. Richardson, "High-Rate Overcharge-Protection Separators for Rechargeable Lithium-Ion Batteries and The Methods of Making The Same," PCT Application based on U.S. Provisional Application 61/647,389, May 2013.
3. G. Chen, "Overcharge Protection for Safer Li-ion Batteries," Energy Storage and Distributed Resources Department Seminar, Berkeley, CA, February 2013.
4. G. Chen, "Overcharge Protection for PHEV Batteries," DOE Hydrogen Program and Vehicle Technologies Program Annual Merit Review and Peer Evaluation Meeting, Washington, DC, May 2013.
5. "Overcharge Protection for Safer and Lasting Rechargeable Lithium Batteries," G. Chen, Berkeley Energy and Resources Collaborative Innovation Expo, Berkeley, CA, October 2013. The poster presentation won the 3rd place award.
6. "Reversible Overcharge Protection for Safer and Lasting Rechargeable Lithium Batteries," G. Chen, the 224th ECS Meeting, San Francisco, CA, October 2013.

V.D.8 Development of Abuse-Resistant Electrolyte Components (SNL)

Christopher J. Orendorff,
Ganesan Nagasubramanian,
Kyle R. Fenton, and Travis M. Anderson

Sandia National Laboratories
P. O. Box 5800, Mail Stop 0614
Albuquerque, NM 87185-0614
Phone: (505) 844-5879; Fax: (505) 844-6972
E-mail: corendo@sandia.gov

Collaborators:
Ram Nagubandi (Binrad Industries)

Start Date: October 2012
Projected End Date: September 2013

Objectives

- Develop and evaluate advanced material components that will lead to more abuse tolerant lithium-ion cell and battery systems.
- Study degradation mechanisms in lithium-ion cells that lead to poor abuse tolerance (runaway thermodynamics, gas evolution, electrolyte combustion).
- Evaluate materials in 18650 cells under abusive conditions to quantify safety performance improvements

Technical Barriers

There are several technical barriers to achieving the goals stated above including:

- Develop lithium-ion cells that are intrinsically abuse tolerant and do not lead to high order catastrophic failures.
- Mitigate the gas evolution and decomposition of the electrolyte.
- Passivation of cathode runaway reactions and interfacial reactions with electrolyte.
- Limited quantities of advanced materials (and numbers of cells with new materials) to evaluate abuse response.

Technical Targets

- Quantify the thermal runaway response of materials at the cell level (18650).
- Determine the effect of advanced material components on the abuse response of lithium-ion cells.
- Evaluate the thermal response of candidate active materials.
- Optimize electrochemical performance of new electrolyte components to meet DOE goals

Accomplishments

- Demonstration of an improvement in thermal runaway free energy for LiF/ABA electrolyte cells compared to $LiPF_6$-based electrolyte cells
- Purification and demonstration of improved performance of electrolyte salt LiF/ABA-1B.
- Synthesis and characterization of LiF/ABA-2 with greater electrochemical stability.

✧ ✧ ✧ ✧ ✧

Introduction

As lithium-ion battery technologies mature, the size and energy of these systems continues to increase (> 50 kWh for EVs); making safety and reliability of these high energy systems increasingly important. While most materials advances for lithium-ion chemistries are directed toward improving cell performance (capacity, energy, cycle life, etc.), there are a variety of materials advancements that can be made to improve lithium-ion battery safety. Specifically, issues related to conventional $LiPF_6$/carbonate electrolyte stability including PF_6^- reactivity, combustion enthalpy, and flammability continue to limit the safety performance of lithium-ion cells. This report highlights work to develop electrolyte components that inherently make lithium-ion cells more resistant to abuse conditions.

Approach

Our approach to developing advanced materials to improve abuse response focuses on redesigning lithium-ion cell electrolytes. This work starts with developing novel two-part electrolyte salts based on inherently stable lithium salts and anion binding agents (ABAs). The ABA components have two important design features: (1) improve the solubility of alternative lithium salts in carbonate solvents by coordinating the salt negative ion at the electron withdrawing coordination site of the ABA and (2) passivate chemical decomposition reactions at electrode interfaces or in the

bulk electrolyte to minimize the consequences and severity of thermal runaway and electrolyte combustion.

The effect of advanced electrolyte components on the thermal response of full cells is determined using several techniques. Full cells will be fabricated in the SNL cell protrotyping facility (2032 coin cells and 18650 cells). Calorimetry techniques will be used to quantifiy imrpovements in heat generation during decomposition reactions. These include accelerating rate calorimetry (ARC), isothermal battery calorimetry (IBC), and differential scanning calorimetry (DSC). Abuse tolerance improvements will be determined by abuse testing full cells which includes thermal, electrical and mechanical abuse conditions.

Results

The use of lithium fluoride (LiF) electrolyte salt has been considered as an alternative to $LiPF_6$ because of its chemical and thermal stability, but early generation anion binding agents (ABAs, used to improve LiF solubility) were large molecules that were inapplicable to lithium-ion cell systems (large molecular weights, low rate capability, low conductivity, voltage instability, etc.). In collaboration with Binrad Industries we have developed LiF/ABA salts for lithium-ion cells to show improved thermal stability and to eliminate some of the shortcomings of using $LiPF_6$ salts.

The primary driver for the development of LiF/ABA-based electrolytes is their ability to stabilize a cell runaway reaction. Figure V - 159 shows DSC on NMC cathodes with $LiPF_6$ and LiF/ABA electrolytes (top) and ARC profiles for 18650 NMC/graphite cells with the same electrolytes (bottom). These results show reduced heat generation not only on the cathode electrodes in DSC, but a significant reduction in the runaway enthalpy and reaction kinetics in 18650 cells. While the mechanism of this behavior is still under investigation, previous results suggest a passivation of the electrode/electrolyte interface by the ABA.

There are a few challenges with the electrochemical performance of the initial LiF/ABA-1A electrolytes. These include (1) 2x lower conductivity than $LiPF_6$ at ambient temperature (~7 mS/cm), (2) capacity fade at the anode electrode because of poor SEI formation, and (3) electrochemical stability (ABA molecule reduction near 0V vs. Li/Li+ and oxidation close to 4.5 V vs. Li/Li+). As prepared, the crystal structure of the initial LiF/ABA-1A shows a DMSO molecule bound to the coordination site of the ABA (Figure V - 160). In spite of its reasonable performance, the bound DMSO limits the ability of ABA to dissolve LiF. The systhesis was improved to prepare the LiF/ABA directly, leading to a replacement of the bound DMSO by afluoride anion (LiF/ABA-1B). The crystal structures for both modules are shown in Figure V - 160 (top). Removal of the DMSO impurity improved the LiF/ABA conductivity by a factor of 2 to 14 mS/cm giving the LiF/ABA comparable conductivity to $LiPF_6$ in EC:EMC shown in Figure V - 160 (bottom).

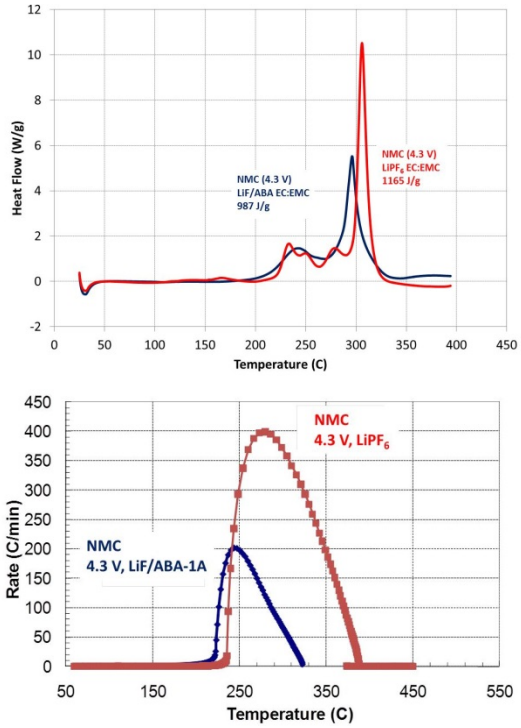

Figure V - 159: (top) DSC of NMC cathodes and (bottom) 18650 cells with in 1 M LiF/ABA-1A in EC:EMC (3:7) and in 1.2 M LiPF6 in EC:EMC (3:7) electrolyte

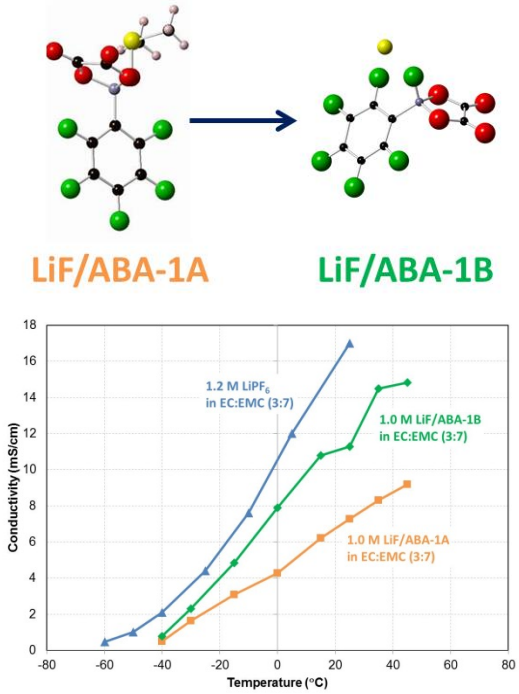

Figure V - 160: Crystal structures of LiF/ABA-1A and -1B and (bottom) conductivity of LiF/ABA-1A, -1B, and $LiPF_6$ in EC:EMC (3:7)

Work to optimize LiF/ABA electrolyte formulations includes improving the capacity fade at the negative electrode. Figure V - 161 shows discharge capacity as a function of cycle number for NMC/graphite cells in 1M LiF/ABA-1A in EC:EMC (3:7). Without any electrolyte additives, the cell shows almost a linear 4% fade/cycle because of poor SEI film formation at the negative electrode. The addition of 2% VC to the electrolyte helps to stabilize the anode interface and significantly reduces the capacity fade during formation. Further improvements to stabilizing the negative electrode interface are made with the addition of 10 mM $LiPF_6$ as an additive to initiate SEI formation. Figure V - 162 shows cyclic voltammetry (CV) data (current density vs. potential) for LiF/ABA cycled from 0-4.5 V (vs. Li/Li+) for 1 M LiF/ABA in EC:EMC and 1 M LiF/ABA + 10 mM $LiPF_6$ in EC:EMC. The addition of 10 mM $LiPF_6$ appears to stabilize the LiF/ABA at negative potentials because of good SEI formation with a current density of -200 $\mu A/cm^2$ at the first cycle (comparable to 1.2 M $LiPF_6$ in EC:EMC electrolyte).

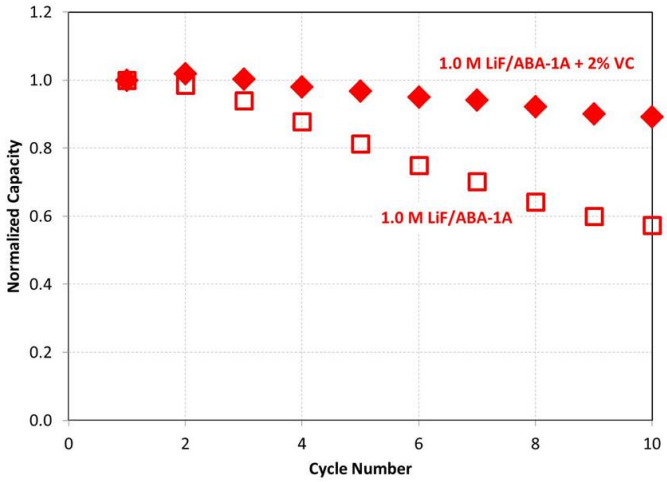

Figure V - 161: Normalized discharge capacity as a function of cycle number for NMC cells in LiF/ABA electrolyte with and without 2% VC (solid and open symbols)

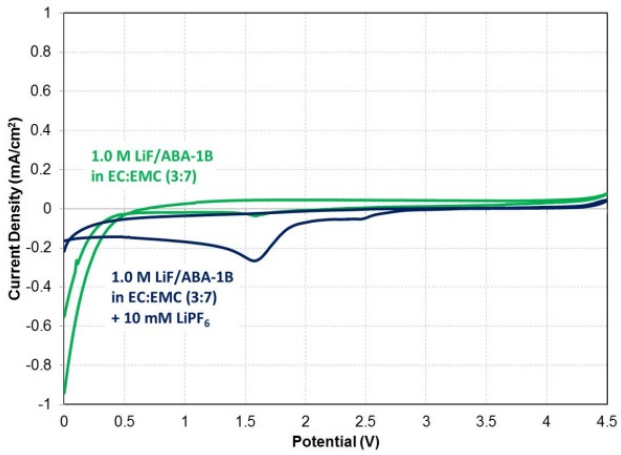

Figure V - 162: Cyclic voltammetry of LiF/ABA electrolyte with and without 10 mM $LiPF_6$ from 0-4.5 V (vs. Li/Li+)

Another task in optimizing the electrolyte performance is to improve the high voltage stability of LiF/ABA for use not only as a conventional cell chemistry but also for use with high voltage electrochemical couples. Figure V - 163 shows the cyclic voltammetry data of LiF/ABA and $LiPF_6$ electrolytes. In the absence of any other electrolyte additives, LiF/ABA-1B has a current density of ~80 µA at 4.5 V vs. Li/Li+, compared to ~20 µA at 4.5 V for $LiPF_6$. The structure of our ABA molecule was modified to improve the voltage stability. The CV of LiF/ABA-2 shows a reduction in the current density at 4.5 V and is comparable to $LiPF_6$ in EC:EMC. It is important to note that the LiF/ABA-2 suffers from the same DMSO impurity as described for LiF/ABA-1 and gives rise to the reduction peak at 2.2 V. This will be purified to improve performance in FY14.

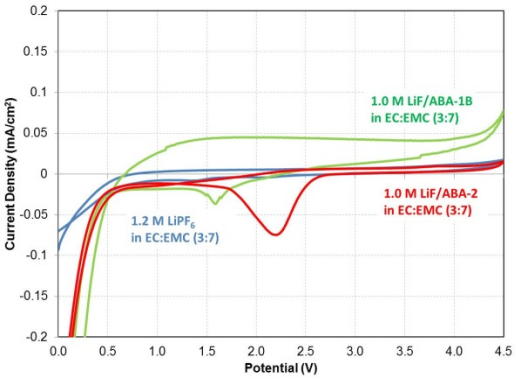

Figure V - 163: Cyclic voltammetry of 1.2 M $LiPF_6$ (blue trace), LiF/ABA-1B (green trace), and -2 (red trace) in EC:EMC (3:7)

Conclusions and Future Directions

LiF/ABA electrolytes are under development with promising results as potential lithium-ion cell components that can be designed to reduce the cell thermal runaway free energy. The challenges associated with electrochemical performance including SEI formation, capacity fade and voltage stability are addressed and improved through molecular design and synthesis of ABAs and optimization of electrolyte formulations. Future directions include demonstration of LiF/ABA electrochemical and safey performance in 18650 cells, continued improvements in observed capacity fade and voltage stability, and characterization of long term stability. We also airm to submit candidate LiF/ABA molecules to the Materials Energineering Research Facility (MERF) at Argonne for the synthesis to be scaled.

FY 2013 Publications/Presentations

1. C. J. Orendorff, J. Lamb, K. R. Fenton, and L. A. M. Steele, “Approaches to Evaluating and Improving Lithium-Ion Battery Safety” AABC February 2013.
2. J. Orendorff, “Approaches to Evaluating and Improving Lithium-Ion Battery Safety” CU-Boulder, February 2013.
3. 2013 DOE Annual Peer Review Meeting Presentation.

V.E Process Development

V.E.1 Manufacturability Study and Scale-Up (ORNL)

Claus Daniel, David Wood III, Jianlin Li, Debasish Mohanty
Oak Ridge National Laboratory
One Bethel Valley Road
P.O. Box 2008, MS-6472
Oak Ridge, TN 37831
Phone: (865) 241-9521; Fax: (865) 241-5531
E-mail: danielc@ornl.gov

Collaborators:
Ashfia Huq (ORNL), Athena Safa-Sefat (ORNL), Andrew Payzant (ORNL), Andy Jansen (ANL), Bryant Polzin (ANL), Chris Orendorff (SNL), Robert Tenent (NREL), Jerry Forbes (Frontier Industrial), John Arnold (Miltec UV), Derek Mainstone (Conquip), Jason Hamilton (Scientific Climate Systems), William Eggers (Bio-logic USA), Ben Schafer (Espec America), multitude of materials suppliers

Start Date: October 1, 2012
Projected End Date: September 30, 2015

Objectives

- Provide a processing and device level scale-up facility and corresponding expertise to the ABR program to scale technology to 1-7 Ah pouch cell demonstration.
- Allow benchmarking of new materials and systems in large scale pouch format.
- Process electrodes for round robin testing and integration in other systems.

Technical Barriers

- Lack of availability of materials processing, reliable cell assembly, and scaling facilities and benchmarking for devices greater than 0.5 Ah.
- Lack of availability for testing new processing and manufacturing routes.

Technical Targets

- Develop processing routes and standards to meet $290/kWh USABC storage goal for PHEVs and <$125/kWh for EVs.
- Lifetime of 10 years and 1,000 cycles at 80% DOD for EVs and 5,000 deep discharge cycles for PHEVs.

Accomplishments

- Successful installation and startup of facility and successful operation well above specified performance (dew point spec: <-30°C, achieved: <-56°C).
- Comparison of tape-cast and slot-die electrode coatings.
- Determined maximum electrode stack number and capacity in 12 mm thick pouch cell with ABR cathode reference NCM 532 and anode reference graphite A10/12 and demonstration of assembly issues with pouches beyond 10 mm thickness.
- Supplied over 100 ft of electrodes to ABR collaborators.

✧ ✧ ✧ ✧ ✧

Introduction

The ABR program's main objective is to solve issues for full electrochemical cells. While many problems can be solved with coin cells, scalability and manufacturability need to be addressed on a full pouch cell basis. Argonne National Laboratory's Cell Fab demonstrates electrochemistry in full pouch cells in devices up to 0.5 Ah. This effort collaborates with Argonne and other collaborators to scale devices beyond 0.5 Ah and further perform manufacturing science to evaluate new materials, develop new manufacturing routes, and enable a domestic supply chain.

Boundary conditions and edge effects need to be adequately addressed. Cell studies need to have a sufficient individual electrode area in order to allow large-scale testing at which further scaling to automotive battery sizes will be "engineering only." Electrode processing and cell assembly studies need to be performed at sufficient scale in order to allow for cost-saving analysis and low-cost processing development for establishing a domestic materials and battery supply chain.

Approach

DOE's open-access Battery Manufacturing R&D Facility (BMF) at the ORNL is specifically designed to take gram-to-kilogram quantities of new materials for performing R&D from slurry processing, through current collector treatment, electrode deposition and processing, and secondary drying studies to full battery pouch cell assembly and testing. Cell dimensions are 66 mm x 99 mm and can range in thickness from single electrode cells to 12 mm thick cells resulting in capacities of up to 6-7 Ah. This facility was set up to integrate new materials, optimize known electrochemical couples in pouch cells, analyze and optimize manufacturing steps individually, and benchmark all materials and processes versus the current state of the art.

The focus of the first year of the BMF was testing of commercially benchmarked electrodes and demonstration of cell performance with ORNL produced cells. Cells are being manufactured for integration into modules and packs for system-level testing. Electrode processing and secondary drying are also being optimized. New materials from our industrial supply chain partners (Vorbeck, Plextronics, FMC, etc.) are being integrated and benchmarked against commercially available technologies. New binder curing technologies are being demonstrated with new cell designs with Miltec UV.

Results

Installation and level of readiness. The 1,400 ft^2 dry room has been installed and is constantly running at 20°C with dew point and relative humidity below -56°C and 0.1%, respectively. A list of equipments (as shown in Table V - 12) have been installed at the BMF and they are currently up and running.

Table V - 12: ORNL BMF equipment list

Equipments	Description
Dry room	For maintaining low humidity environment for battery assembly
Fume hood	For handling chemicals
Balances	For weighing chemicals with various quantities
High shear and planetary mixers	For mixing slurry with various quantities, up to 2 liters and at different shear rates
Corona Treater	For modification of surface energy to improve wetting of wet coating on substrates
Tape caster	For small coating and proof-of-concept
Slot-die-coater	For high quality roll-to-roll electrode manufacturing
Karl-Fischer titration	For evaluation of residual moisture in samples
Vacuum oven	For drying electrodes before cell assembly
Pouch cell assembly line	For pouch cell assembly from forming pouches, punching electrodes, stacking jelly rolls, welding tabs, filling electrolyte to sealing pouch cells
Small assembly line for special pouch cells	For assembling special pouch cells with different dimensions and/or materials sensitive to air, moisture, etc.
Glove boxes	For coin cell and special pouch cell assembly and battery disassembly
Environmental chambers	For temperature control during battery aging and testing
Potentiostats	For testing battery performance
Optical microscope	For observation of electrode morphology and in-process microscopy

Figure V - 164 show a process of cathode coating via a slot-die coater at the BMF. Slurry is supplied by a progressive pump. Coatings are processed continuously and can be up to 10 inches wide. Drying capabilities include a drying furnace with 2 infrared heaters and 7 hot are blowers with independently controlled temperature in each zone. Additional drying capabilities are heating plates, convection heaters, infrared furnaces, and parallel and anti-parallel hot air roll to roll heaters. In the near future, an ultraviolet source will be added. This provides flexibility in studying drying protocols for electrode manufacturing. Figure V - 165 shows a roll of ABR standard A12 graphite anode and $LiNi_{0.5}Mn_{0.3}Co_{0.2}O_2$ cathode (NMC532).

Figure V - 166 shows intermediate products of each step during battery manufacturing: Dispersion/slurry, electrode coating, pouch, punched electrodes, electrode stack or "jelly roll," and finished pouch cell. The dimensions of cathode and anode are 8.44 cm×5.60 cm and 8.64 cm×5.80 cm, respectively. Pouch cell capacity ranges from 100 mAh to 7 Ah on single-side-coating electrodes.

Figure V - 164: Demonstration of electrode coating via slot-die coater

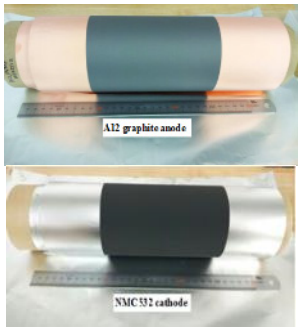

Figure V - 165: A roll of ABR standard A12 graphite anode and NMC532 cathode

Figure V - 166: Intermediate samples in battery manufacturing and finished pouch cell

Areal loading with pump speed and line speed. Coating thickness and areal loading of coating are determined by the pump speed and coating line speed. Figure V - 167 shows areal loading of NMC532 cathodes as a function of coating line speed and pump speed. The areal loading is in linear relation with line speed and pump speed.

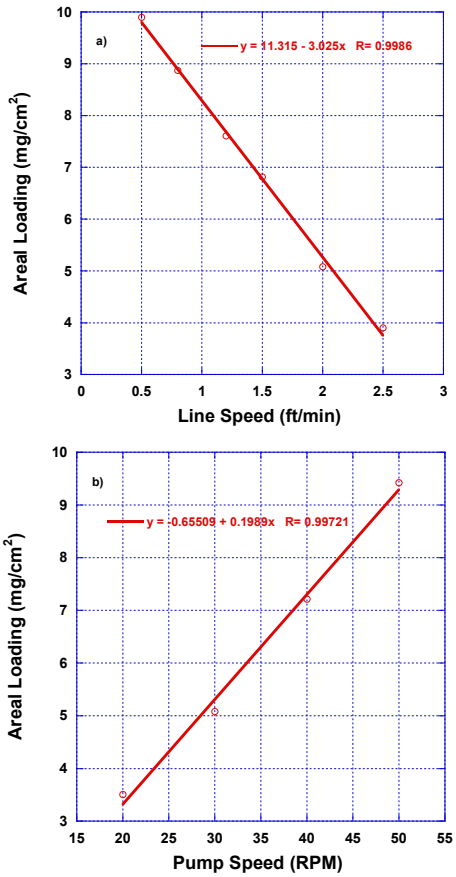

Figure V - 167: Calibration of areal loading of NMC532 cathode with line speed (a, pump speed=40 RPM) and pump speed (b, line speed=1 FPM)

Round robin testing. A roll of ABR standard A12 anode and NMC532 cathode fabricated at BMF was sent to ANL for round robin testing. Detailed information on the electrodes is listed in Table V - 13. The anode to cathode capacity ratio is 1.36. The cross-section of both A12 anode and NMC532 cathode is shown in Figure V - 168.

The electrode performance from full coin cells is plotted in Figure V - 169. The full cells went through four formation cycles at 0.1C between 3.0 and 4.3V before subsequent test. The rate performance shown in Figure V - 169a) was tested at charging and discharging rates of 0.2C, 0.5C, 1C and 2C, respectively, between 3.0 and 4.1 V. The capacity was reduced from 127 mAh/g of NMC532 to 102 mAh/g when the discharging rate increased from 0.2C to 2C. Capacity loss and RPT (reference performance test) capacity vs cycle number was tested between 3.0 and 4.1V, cycling the full cells at 0.2C for the first 19 cycles and 0.5C in subsequent cycles, HPPC (hybrid pulse power characterization) every 50 cycles and RPT (C/24) every 50 cycles. Two of the three cells tested went beyond 500 cycles before capacity dropped to 80% of original capacity. The three cells showed an RPT capacity of 80, 100 and 120 mAh/g after 400 cycles, respectively.

Table V - 13: Electrode information

Electrode	Composition	Areal loading (mg/cm^2)	Porosity (%)
A12	A12/Super P Li/9300 PVDF =92/2/6 wt	7.51	52.2
NMC532	NMC532/Denka carbon black/ 5130 PVDF =90/5/5 wt	12.57	49.0

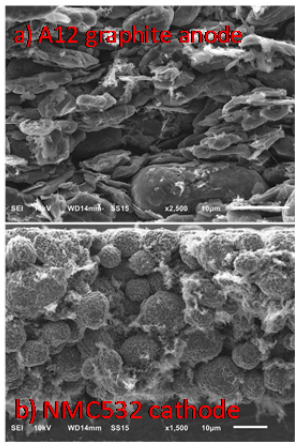

Figure V - 168: Cross-section morphology of A12 graphite anode (a) and NMC532 cathode (b)

Comparison in electrode performance from different coating techniques. NMC532 with TRD202A binder (JSR) was coated with slot-die coater and tape caster through aqueous processing and their performance was compared in Figure V - 170. Figure V - 170 shows the discharge capacity of both cathodes from half coin cells. The one from slot-die coating demonstrated not only much better rate performance, especially at high C-rates, but also cyclic life. There was dramatic capacity degradation after 80 cycles in the one from tape caster and the deviation from cell to cell was also much more substantial compared to that from slot-die coating. Thus, the NMC532 cathode from slot-die coating exhibited much superior electrode performance.

Pouch cell performance. ABR standard A12 anode and NMC532 cathode were assembled into pouch cells with various capacities. Figure V - 171a) shows cyclic performance of one pouch cell with 70 mAh at 0.1C. There was a substantial irreversible capacity loss at the 1st cycle due to formation of solid electrolyte interface (SEI).

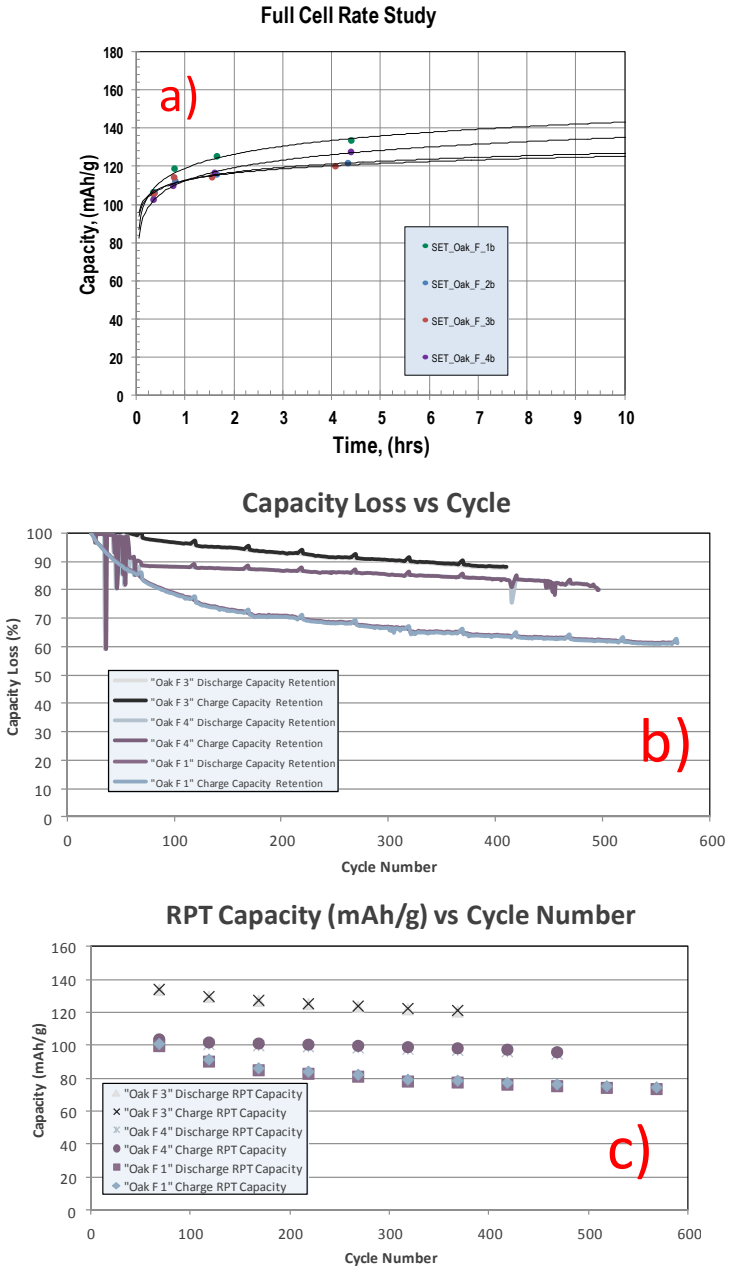

Figure V - 169: Full cell performance of ABR standard A12 anode and NMC532 cathode (a rate performance; b) capacity loss vs cycle number and c) RPT capacity vs cycle number. (Data from ANL)

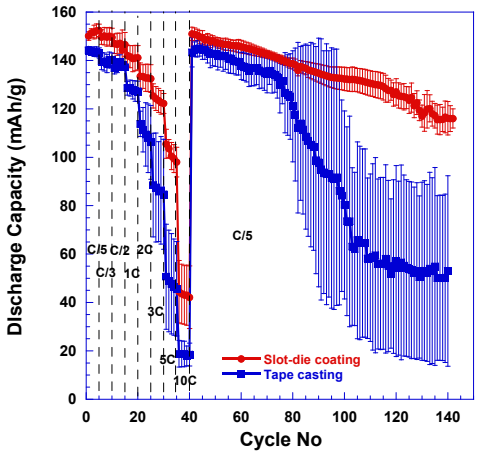

Figure V - 170: Comparison of NMC532 cathode performance through slot-die coating and tape casting

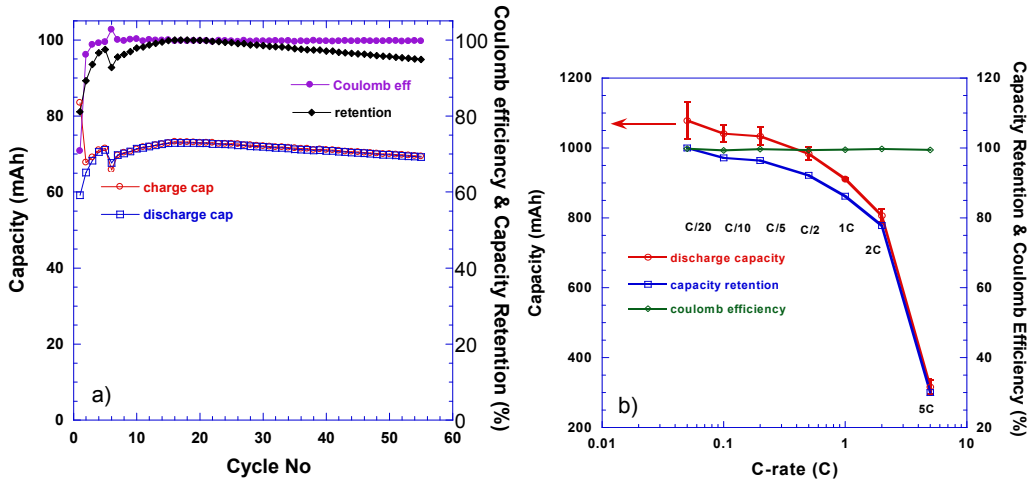

Figure V - 171: Pouch cell performance a) cyclic performance of a 70 mAh pouch cell and b) rate performance of 1Ah pouch cells

Coulombic efficiency increased dramatically and maintained above 99.5% in subsequent cycles. Capacity retention was above 95% after 55 cycles. Figure V - 171b) shows rate performance from nine pouch cells with 1-1.1 Ah. The cells demonstrated excellent repeatability and rate performance.

Construction of pouch cell with maximum capacity. A pouch cell was assembled to estimate maximum capacity with single-side-coated electrodes. The capacity depends on the layers of electrodes, which is limited by the maximum draw depth sustained by the pouch cell packaging material. As shown in Figure V - 172, when the depth exceeded 5.5 mm, mechanical damage to the polymer liner due to stretching started showing a color change along the two long edges. This indicated potential tearing or mechanical failure in the liner material of the packaging laminate. To accommodate more layers of electrodes, a double cup pouch was formed from two pouches with 5.5 mm depth. Also, the jelly roll for the cell with maximum capacity was divided into two separate jelly rolls with 30 layers of NMC532 and A12 in each jelly roll, respectively. This is to overcome misalignment issues in electrode stacking and ease of handling the stacks in the automatic stacker. Each jelly roll was welded with an aluminum and a nickel tab to the cathode and anode, respectively, before the two jelly rolls were welded together. The jelly roll was very thick and posed problems during welding tabs to the jelly roll, which eventually led to poor welding and low capacity as addressed later in this report. The pouch cell was filled with 28 g 1.2M $LiPF_6$ in EC/DEC (3/7 wt), a tab charge was applied, and then the cell was aged at 60°C for 48 h before formation cycle.

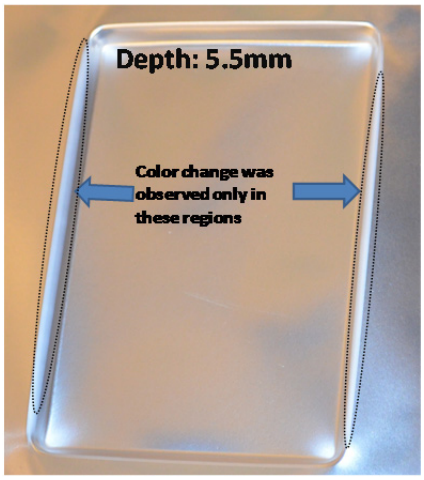

Figure V - 172: Pouch material with 5.5 mm depth showing sign of material tearing at the long edges

Figure V - 173: Pouch cell showing gas generation during aging process

There was substantial gas generation during the aging step as evidenced by the swelling in the pouch cell shown in Figure V - 173. The pouch cell was cut open and resealed in vacuum before testing. The pouch cell was estimated to be 6.5 Ah based on the electrode materials. However, it only delivered 1.52 Ah in capacity after formation cycles. The welding between one Al tab and one jelly roll was disconnected, which means that parts of the jelly roll could not participate in the cell test. This resulted in an immediate drop in capacity by 3.25 Ah. In addition, the strained seals allowed leakage of electrolyte around the tabs. The welding problem is due to short tabs (8 mm) in the BMF electrode design. The problem has been solved by welding the jelly roll at the middle instead of at one end. New cells will be assembled with the improved assembly procedure. It is expected that calendaring and double-side-coating will allow pouch cells to deliver up to 10 Ah.

Development of holders for pouch cell testing. It is critical to maintain stack pressure during testing. The amount of pressure has a significant effect on cell performance. Two types of holders have been developed, one with plastic material and the other with aluminum as shown in Figure V - 174. The plastic holder resulted in low or no significant stack pressure due to bending when tightening the wing screws. As a result, the performance was very poor as shown in Figure V - 175. When replacing the plastic holder with aluminum, the pouch cell performance was substantially improved, especially at high C-rates.

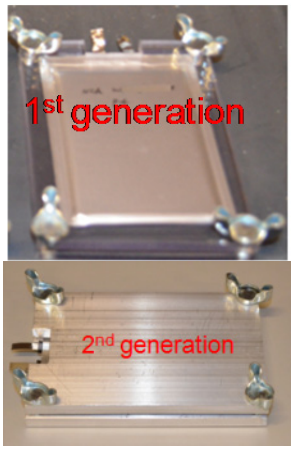

Figure V - 174: Pouch cells with two types of holders

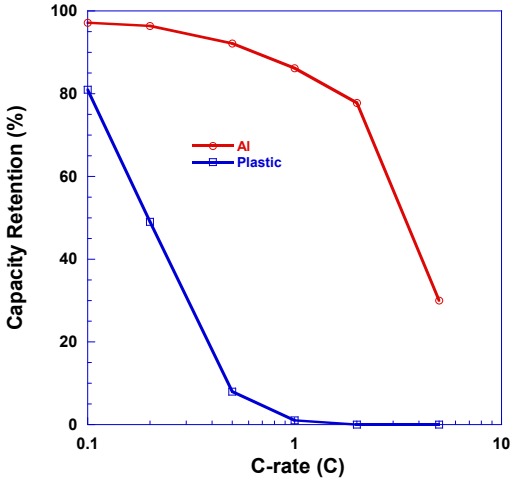

Figure V - 175: Comparison in pouch cell performance with two types of holders

Provide expertise for battery manufacturing and pouch cell assembly to collaborators. While the BMF efforts are funded for ABR activities only, the BMF expertise leverages many other activities funded through other industrial and federal sponsors. The BMF has successfully manufactured pouch cells and provided samples for many collaborators. This includes cells for other ABR work to characterize structure evolution of LMR-NMC cathode by neutron scattering and providing samples for other projects, including DOE's Manufacturing Demonstration Facility (MDF) for projects with FMC Lithium, industrial projects with Plextronics, and DOE's Clean Energy Research Center - Clean Vehicle Center, and others.

Conclusions and Future Directions

The BMF has installed a variety of instruments and has demonstrated successful pouch cell manufacturing. It has delivered pouch cells not only to internal projects but also several external projects, including promoting products for industry partners.

The BMF will continue to develop techniques in battery manufacturing to improve the reproducibility and production rates. Next year, a strong BMF focus will be on double-sided electrode fabrication. Special attention will be paid to edge alignment retrofitting for slot-die coater.

FY 2013 Publications/Presentations

1. D.L. Wood, III, J. Li, D. Mohanty, C. Daniel, B.L. Armstrong, R.B. Dinwiddie, H. Wang, R.M. Trejo, N.C. Gallego, C.I. Contescu, J.Y. Howe, R.A. Meisner, J. Kiggans, and B.D. Brown, "Advanced Materials Processing and Novel Characterization Methods for Low-Cost, High Energy-Density Lithium-Ion Batteries," *Proceedings of the Advanced Automotive Battery Conference* (2013).
2. Claus Daniel, David Wood, Jianlin Li, Debasish Mohanty, Beth Armstrong, and Jim Kiggans, "Cell Materials and Manufacturing," 2013 Cummings Energy Storage Systems Summit, Columbus, IN, October 29-30, 2013 (invited).
3. Claus Daniel, David, Wood, Jianlin Li, Beth Armstrong and Jim Kiggans, "Battery Production Technologies" Energy Storage Solution Industrial Symposium, Oak Ridge, TN, September 4, 2013 (invited).
4. Jianlin Li, Debasish Mohanty, Bradley Brown, David Wood, and Claus Daniel, "Status on electrode fabrication and battery manufacturing at ORNL's Battery Manufacturing R&D Facility," 2013 Clean Energy Research Center-Clean Vehicle Center-seminar Series, Ann Arbor, MI, July 17, 2013 (invited).
5. Claus Daniel, Debasish Mohanty, Jianlin Li, and David Wood, "Overview and progress in cathode materials for lithium ion batteries," 1st International Freiberg Conference on Electrochemical Storage Materials, Freiberg, Germany, June 3-4, 2013 (invited).
6. Claus Daniel, David Wood, Jianlin Li, Beth Armstrong, Jim Kiggans, Debasish Mohanty, and Sergiy Kalnaus, "Electrification of transportation-cost and opportunities," Bridging the Gap Conference 2013, Oak Ridge, TN, March 5-6, 2013 (invited).
7. David Wood, Jianlin Li, Debasish Mohanty, Claus Daniel, Beth Armstrong, Ralph Dinwiddie, Hsin Wang, Rosa Trejo, Nidia Gallego, Cristian Contescu, Jane Howe, Roberta Meisner, Jim Kiggans, and Bradley Brown, "Advanced materials processing and novel characterization methods for low-cost, higher energy-density lithium-ion batteries" Advanced Automotive Battery Conference 2013, Pasadena, CA, February 4-8, 2013 (invited).

V.E.2 Overcoming Processing Cost Barriers of High-Performance Lithium-Ion Battery Electrodes (ORNL)

David L. Wood, III, Jianlin Li, Claus Daniel, and Beth Armstrong
Oak Ridge National Laboratory
One Bethel Valley Road
P.O. Box 2008, MS-6065
Oak Ridge, TN 37831
Phone: (865) 574-1157; Fax: (865) 241-4034
E-mail: wooddl@ornl.gov

Collaborators:
Andy Jansen (ANL), Bryant Polzin (ANL), Chris Orendorff (SNL), David Telep (Dow Kokam), Erin O'Driscoll (Dow Kokam), Mike Wixom (A123 Systems now Navitas Systems), James Banas (JSR Micro), Gregg Lytle (Solvay Specialty Polymers), Mark Ewen (ConocoPhillips)

Start Date: October 1, 2011
Projected End Date: September 30, 2014

Objectives

- Transform lithium ion battery electrode manufacturing by eliminating the costly, toxic organic-solvents while increasing cell energy density through improved electrode architecture (active material utilization), increased electrode thickness, or both.

Technical Barriers

Elimination of Expensive Solvent and Recovery System. Electrode suspensions for lithium ion batteries are currently formulated using expensive polyvinylidine fluoride (PVDF) binder and expensive, toxic, and flammable n-methylpyrrolidone (NMP) solvent. It is desirable to replace these components with water and water-soluble binders, but methods of mass production of these suspensions are currently underdeveloped. The major problems with aqueous electrode dispersions are: 1) agglomeration of active phase particles and conductive carbon additive; 2) poor wetting of the dispersion to the current collector substrate; and 3) cracking of the electrode coating during drying resulting in poor device performance and short life. NMP based processing results in higher performance but has the inherent disadvantages of high solvent cost and the requirement for explosion proof processing equipment and solvent recovery. Initial projections of the minimum cost savings associated with changing to water and water-soluble binder are 70-75% of the electrode manufacturing step, or a reduction from \$0.210/Ah to \$0.055/Ah. That translates in 15-20% of cost reduction on the pack level. Improvements in this effort are projected to be chemistry-agnostic and with little additional effort adaptable to any electrode chemistry.

Technical Targets

- Low-cost, green manufacturing methodology for lithium ion battery anodes using aqueous suspensions (to meet \$290/kWh USABC storage goal for PHEVs).
- Correlation of properties of dispersions and electrode coatings to cell performance and advancement of energy storage manufacturing science.
- Lifetime of 10 years and 1,000 cycles at 80% DOD for EVs and 5,000 deep discharge cycles for PHEVs.

Accomplishments

- Completed half-cell and full coin cell round robin testing with ANL and SNL with CP A10/A12 and TODA NMC 532 electrochemical couple for NMP/PVDF based dispersion chemistry.
- Demonstrated that metal dissolution is of minimal concern for aqueous processing of $LiFePO_4$ and NMC 532 cathode active materials.
- Optimized vacuum drying temperature with dry air at 120°C for ensuring acceptable residual moisture after aqueous electrode processing.
- Matched full coin cell performance through 100 cycles (0.2C/-0.2C) of aqueous suspension and water-soluble binder to NMP/PVDF based suspensions for CP A10/A12 and $LiFePO_4$ electrochemical couple.
- Matched full coin cell performance through 100 cycles (0.2C/-0.2C) of aqueous suspension and water-soluble binder to NMP/PVDF based suspensions for CP A10/A12 and TODA NMC 532 electrochemical couple.

- Match pouch cell (≥3 Ah capacity) performance through 15 cycles (0.1C/-0.1C and 0.2C/-0.2C) of aqueous suspension and water-soluble binder to NMP/PVDF based suspensions for CP A10/A12 and TODA NMC 532 electrochemical couple.

✧ ✧ ✧ ✧ ✧

Introduction

There is growing evidence in the literature that the complex suspensions used during electrode processing, which contain solvent, active graphite, conductive carbon, polymer binder, and perhaps a dispersant (surfactant), must be optimized using colloidal dispersion science. These components have different surface interactions with the solvent and dispersant, and each dispersion must be tailored based on surface charges, rheology, material constituents, order of addition, mixing protocol, coating method, and drying protocol. Whether the suspension is organic or aqueous, there is still much development required to optimize these formulations for uniform coatings, reduce the cost associated with making the electrodes, and correlate suspension properties to electrode performance.

In conventional lithium ion batteries, PVDF is used as the electrode binder because of its electrochemical stability over a large potential window, and NMP is used as the solvent when preparing the suspension. The advantage of using this organic system is that extensive research has been carried out on the resulting electrode microstructure and cell performance. However, there are still areas related to this conventional suspension that are relatively unexplored such as performance effects of solids loading, order of component addition, coating parameters, and drying conditions when materials are varied. The PVDF/NMP system has some disadvantages that make researching replacements attractive, most notably its cost. PVDF also has low flexibility, which can lead to breaking of the physical bond between active graphite and conductive carbon during long-term cycling. It contains fluorine, which is a source of producing stable LiF as a degradation product. The LiF may adversely interact with the otherwise stable solid electrolyte interface (SEI) layers. The use of NMP requires a process of recovery and treatment of the organic vapors for disposal or recycling. Therefore, there is increasing interest in switching the fabrication of composite electrodes from an organic route to an aqueous route. Compared to the organic route, the aqueous route is significantly more economically and environmentally friendly. For example, the cost of NMP in bulk quantities is ~$2.25/L, whereas deionized water is only $0.015/L.

The calendering process, which is critical to balancing energy density and power density demands, is typically done just after electrode casting and drying steps with the goal of improving particle to particle contact and reducing the lithium-ion diffusion distance from the top to the bottom of the electrode. It is also assumed that pressing the electrode improves the adhesion of the active material to the current collector. However the beneficial effects of this step on the overall rate capability have not been studied systematically. Calendering of porous multi-phase materials with porosity gradient through the thickness of the electrode has not been investigated. Moreover, the degree of mechanical damage induced in the particles during the electrode pressing remains unknown.

Apparently, calendering increases the solid volume fraction (SVF) of the electrode material by reducing the thickness of the electrode. This could have a three-fold effect on the subsequent battery performance. Increase in SVF could change permeability of the compressed material. Tangential displacements may shift particles and cause agglomeration of different phases (this is especially relevant when the phases possess properties that differ by orders of magnitude). Finally, normal and shear stresses developed during this process may change the properties of the active material itself.

Approach

Subtask 1. **Aqueous Electrode Processing.** Fabrication of composite electrodes via organic (baseline) and aqueous suspensions will be completed. A focus will be placed on the effect of processing parameters and agglomerate size on the aqueous route cell performance and microstructure of the composite electrode. Several active anode graphite and cathode (NMC, $LiFePO_4$, etc.) materials will be selected with various water-soluble binders. An emphasis will be placed on the ABR baseline anode, ConocoPhillips A10/12, and cathode, Toda NCM 523. The conductive carbon additive will be held constant. Rheological (viscosity) and colloidal (zeta potential) properties of the suspensions with and without dispersant will be measured with a focus on minimization of agglomerate size. These measurements will show the effects of agglomerate size and mixing methodology on suspension rheology and help determine the stability (i.e., ion exchange processes across the surfaces of various crystal structures) of active materials in the presence of water. Composite electrodes will be made by tape casting and slot-die coating, and the drying kinetics of the electrodes will be measured by monitoring the weight loss as a function of time and temperature. Solvent transport during drying will also be monitored as a method to control electrode morphology, porosity, and tortuosity. Electrode microstructure and

surface chemistry will be characterized and correlated with cell performance. Electrochemical performance of electrode coatings made from the various suspensions will be supplied to ORNL's strategic industrial partners for external validation in large cell formats.

Subtask 2. **Electrodes with Tailored Electrode Architecture.** Graded electrode architectures can address the lithium ion mass-transport limitations and will be made by depositing different bilayer coatings using dual-slot die coating. The controlled settling approach (by optimizing dispersion solids loading and viscosity) will be used together with our novel coating method to achieve a two-to-three-layer structure. A detailed calendering study will be conducted to correlate finished electrode structural properties with performance. Different binder types (with a PVDF baseline) at higher loadings will be investigated to increase coating adherence to the current collector substrate and increase electrode pliability around coating line bends.

Subtask 3. **Cell Performance and Process Validation.** Improved cell performance with reduced processing and raw material cost will be demonstrated using pilot-scale coatings. Cells will be tested and evaluated for irreversible capacity loss, AC impedance, capacity vs. charge and discharge rates, and long-term behavior through 100-500 charge-discharge cycles. Half cells, coin cells, and pouch cells will be constructed and evaluated at the ORNL Battery Manufacturing Facility (BMF). The coin cells will be used for screening and coarse evaluation of different suspension chemistries and coating methodologies. A fine tuning of these research areas will be completed using ORNL pouch cells and large format cells with ORNL's industrial partners. Electrode coatings will be produced on the ORNL slot-die coater and supplied in roll form to the industrial partners for assembly into large format cells.

Subtask 4. **Electrode and Active Material Characterization.** Electrode morphology will be characterized by scanning electron microscopy (SEM) and TEM. The bulk microstructure and surface of the active materials will be characterized using XRD and XPS, respectively. In addition, *in situ* TEM will be performed to investigate real-time SEI layer formation as a function of the different suspension chemistries.

Results

Active material solubility in aqueous suspensions. A common question of aqueous lithium ion electrode processing is the solubility of the active-material elemental species in water. To address this issue, saturated $LiFePO_4$ (LFP) and $LiNi_{0.5}Mn_{0.3}Co_{0.2}O_2$ (NMC 532) aqueous suspensions were measured by inductively-coupled-plasma mass spectrometry (ICP-MS) for elemental solubility as a function of suspension age, and the results are shown in Figure V - 176. Lithium-ion solubility for NMC 532 was about 2-3× that of LFP after one hour of exposure to water, whereas the solubility of Ni, Mn and Co for NMC 532 (<0.001 µg/mL) was 1000× lower than that of Fe and P for LFP. In either case, the elemental solubility for all species was low, with no observed concentrations above 20 ppm after one day of aging. From these findings, it can be concluded that if dispersions are mixed, coated, and dried within a day, then exposure to water will not cause active-material solubility problems.

Electrode moisture evaluation and removal. Two additional frequently asked questions are how to remove enough residual moisture from the electrodes after aqueous processing and how any residual moisture would affect electrode performance. An aqueous-processed NMC 532 cathode was dried for two hours at four different temperatures of 80°C, 100°C, 110°C, and 120°C using the air from the ORNL BMF dry room with a dew point between -40°C and -53°C. Prior to drying, each cathode was exposed to the ambient atmosphere outside of the dry room for ~24 h to ensure saturated moisture content. The residual moisture in each cathode after drying was characterized by Karl Fischer titration, and the results are shown in Figure V - 177. The saturated moisture content in the NMC 532 cathode was 625 ppm with no drying, and the residual moisture level decreased with increasing drying temperature down to 45 ppm for 120°C.

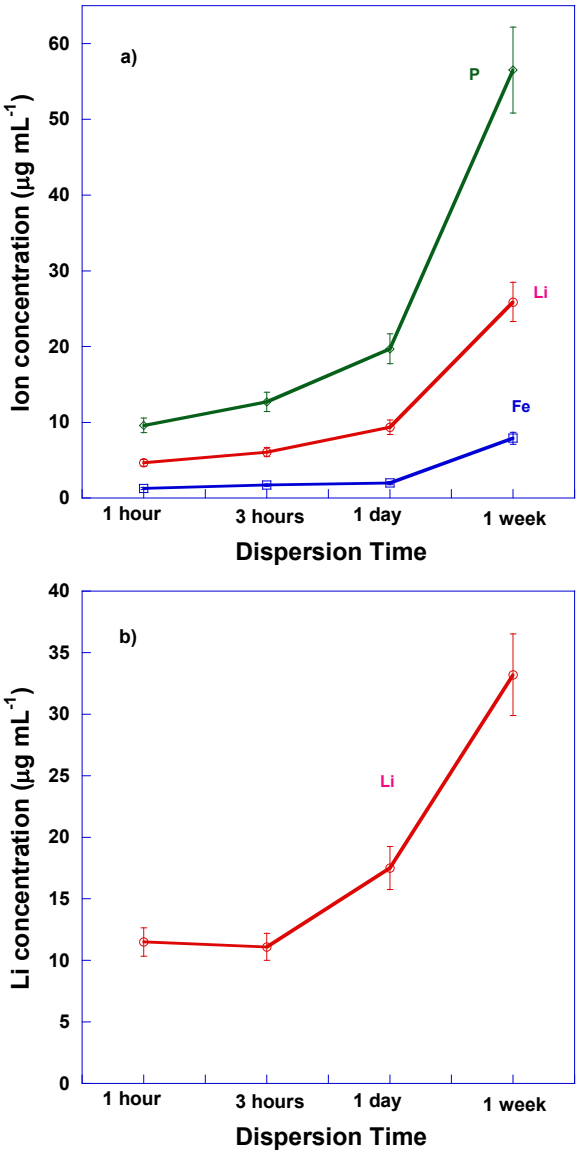

Figure V - 176: Ion solubility in a saturated aqueous suspension a) $LiFePO_4$ aqueous suspension and b) $LiNi_{0.5}Mn_{0.3}Co_{0.2}O_2$ (NMC 532) aqueous suspension

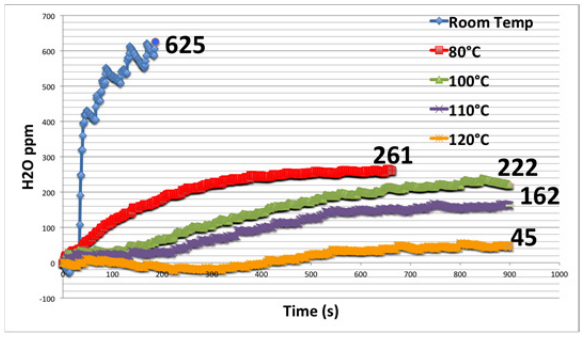

Figure V - 177: Residual moisture in NMC 532 cathodes using various drying temperatures

The effect of residual moisture content for the different drying temperatures on NMC 532 cathode performance was also investigated by evaluating half coin cells. All NMC 532 cathodes in this report had a composition of NMC 532/Denka carbon black/binder/carboxymethyl cellulose (CMC) at a 90/5/4/1 weight ratio. When the binder was PVDF, it was 5 wt% and contained no CMC. Three samples were tested for each condition, discharge capacity was normalized to the NMC 532 mass, and the C-rate was defined as 1C=160 mA/g. All the tests were conducted at 25°C with cutoff voltages between 2.5 V and 4.2 V. As shown in Figure V - 178, discharge capacity of the cathodes dried at 25°C, 80°C, 100°C and 110°C was similar and within 2σ. In contrast, the cathode dried at 120°C demonstrated superior capacity comparable to those processed with NMP (see Figure V - 179 for performance comparison). This finding shows that NMC cathodes made via aqueous processing need to be dried at 120°C or higher to effectively remove excess water and maintain required performance.

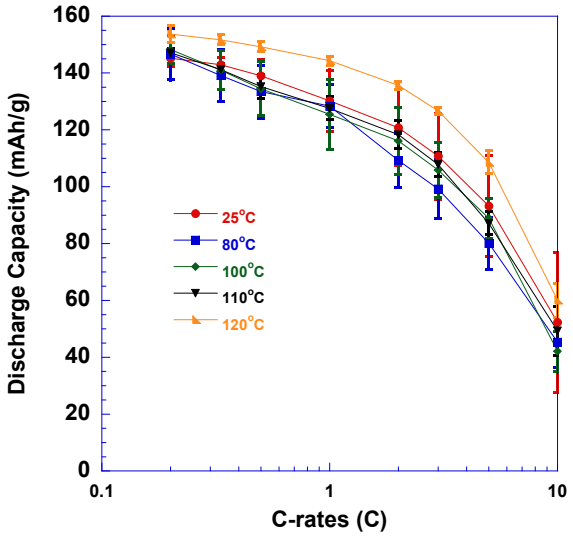

Figure V - 178: Discharge capacity of NMC 532 cathodes after various drying temperatures

Screening of novel water soluble binders for NMC 532 cathodes. Four significantly different water-soluble binders (descriptions are shown in Table V - 14) were investigated using NMC 532 cathodes, and the performance of each aqueous-processed electrode was compared to a PVDF/NMP baseline. At least three NMC 532 half coin cells were tested for each binder, and the average discharge capacity is shown in in Figure V - 179 with 2σ error bars. The tests were begun with rate capability evaluation using a constant charging rate of 0.2C and various discharging rates, followed by 40-100 cycles at 0.2C/-0.2C. All electrodes with water soluble binders demonstrated comparable or better rate performance compared to the one with 5130

PVDF binder and NMP. While the NMC 532 cathodes with water soluble binders exhibited similar capacity at low C-rates, the one with Solvay PVDF latex showed much higher performance at high C-rates. The electrode with PVDF latex also showed nearly identical long-term capacity fade to that with the PVDF/NMP baseline. Based on these findings, the Solvay PVDF latex was selected for full-scale pouch cell evaluation.

Table V - 14: Various binders screened in NMC 532 cathodes

Binder Names	Description	Manufacturer
TRD202A	Fluorine acrylic hybrid latex	JSR Corporation
PVDF Latex	Water soluble PVDF	Solvay Specialty Polymers
Nafion	Perfluorosulfonic acid	DuPont
SBR Latex	Styrene-butadiene copolymer	Targray
5130 PVDF	Polyvinylidene fluoride	Solvay Specialty Polymers

Based on the rate performance and initial 0.2C/-0.2C cycling data (see Figure V - 179), the JSR Micro TRD202A was also selected for full coin cell testing with the VTO ABR baseline ConocoPhillips (CP) A12 natural graphite anode. The A12 graphite was processed using NMP to limit the processing variables associated with the evaluation. Results, shown in Figure V - 180, were compared to the NMC 532/CP A12 full coin cells where both electrodes were processed using NMP. Each full coin cell went through 5 formation cycles at 0.1C/-0.1C. As shown in Figure V - 180 and Figure V - 181, the aqueous-processed cathode with TRD202A binder demonstrated either identical or slightly improved performance, depending on the C-rate, compared to that processed with NMP. Both electrodes also exhibited excellent capacity recovery after the rate capability test, and capacity fade was identical within 2σ error. These observations further confirm that NMC 532 cathodes made via aqueous processing can deliver identical performance to those made via conventional NMP-based processing. Therefore, this manufacturing improvement not only significantly reduces electrode processing cost, but also maintains electrode rate performance and preserves capacity over long-term cycling.

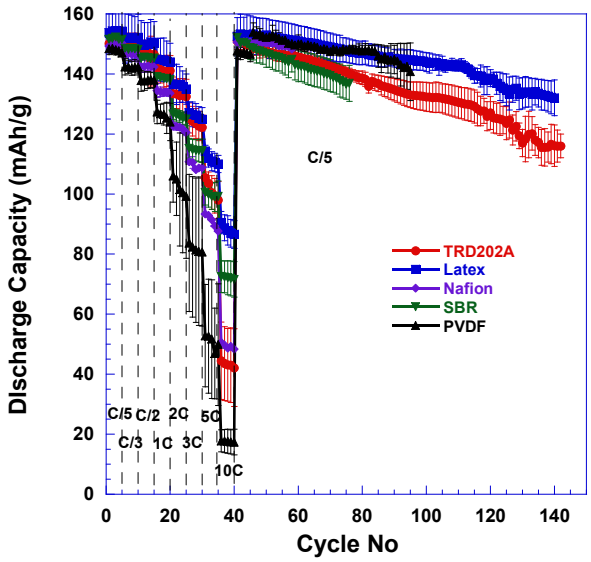

Figure V - 179: Comparison of performance with various water-soluble binders in NMC 532 half cells

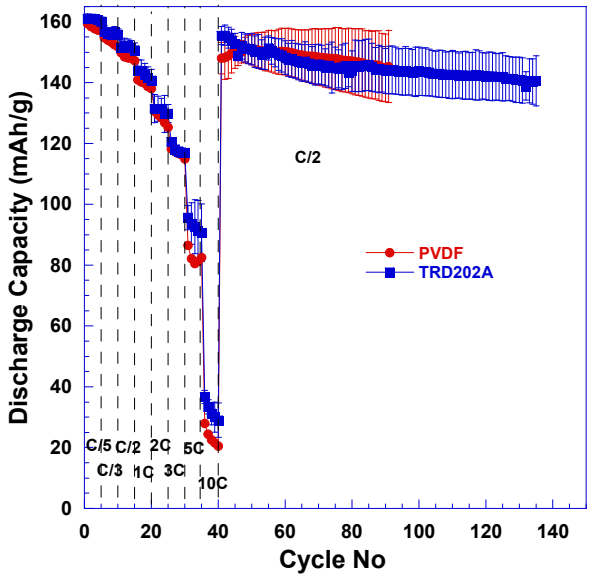

Figure V - 180: Cycling performance comparison of full cells with NMC 532 cathodes using JSR Micro TRD202A (aqueous processing) and baseline 5130 PVDF (NMP processing) binders

Demonstration of large-format pouch cells with NMC 532 cathodes through aqueous processing. Aqueous-processed NMC 532 cathodes with Solvay PVDF Latex as the binder were assembled into a 3-Ah pouch cell with CP A12 graphite anodes (via NMP-based processing). This pouch cell was aged at 60°C for 48 h followed by four formation cycles at 100 mA (0.033C/-0.033C) and exhibited 650 mAh irreversible capacity loss after the first formation cycle (Coulombic efficiency of 82%). As shown in Figure V - 182, the

Coulombic efficiency increased to 98% after the second formation cycle and continued to improve to >99% after subsequent cycles. This cell demonstrated a capacity of 3 Ah at 0.1C discharge rate and 2.8 Ah at 0.2C. The rate capability and long-term cycling (capacity fade) tests are still ongoing.

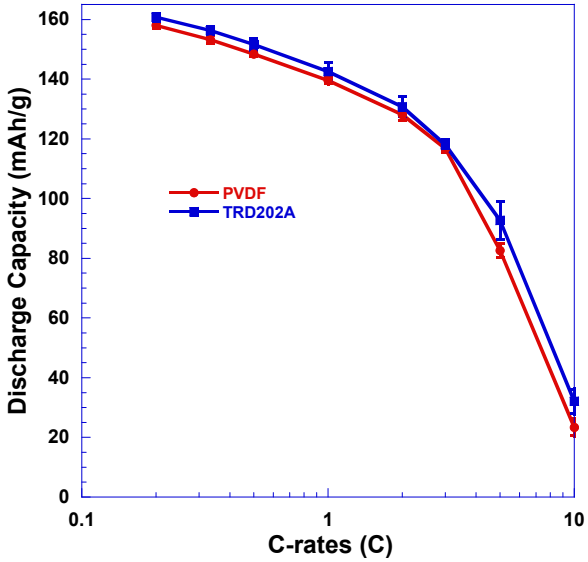

Figure V - 181: Rate performance comparison of full cells with NMC 532 cathodes using JSR Micro TRD202A (aqueous processing) and baseline 5130 PVDF (NMP processing) binders

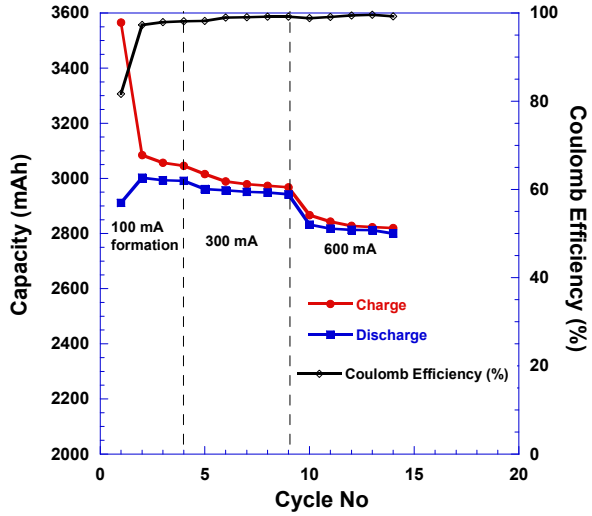

Figure V - 182: Successful scale-up and rate performance of a 3-Ah full pouch cell with a NMC 532 cathode and Solvay PVDF Latex binder via aqueous processing

Conclusions and Future Directions

It was demonstrated that if the exposure of the active material, such as NMC 532 or LFP, to water is less than ~1 day, solubility of the various elemental species is negligible. NMC 532 cathodes were successfully fabricated with four water soluble binders via aqueous processing. Residual moisture in these cathodes can be easily removed by oven drying with dehumidified air for 2 h. In addition, NMC 532 cathodes made through aqueous processing demonstrated comparable or better performance compared to those cathodes made with NMP, as demonstrated with half coin cells, full coin cells, and full-scale pouch cells.

ORNL will continue to optimize water-soluble binder content, particle size, molecular weight, and mechanical properties for NMC 532 cathodes, including applying a lithium-ion conductive binder, such as Li-exchanged Nafion®. Thick, high-energy electrodes will also be developed by incorporating novel design features such as a porosity gradient through dual-slot-die coating, calendering optimization, and inclusion of higher-conductivity additives such as multilayer graphene. Manufacturing of composite anodes and cathodes through aqueous processing will be further refined and commercialization partners will be sought.

FY 2013 Publications/Presentations/Patents

1. Aqueous Processing of Composite Lithium Ion Electrode Material, J. Li, B.L. Armstrong, C. Daniel, and D.L. Wood, III, U.S. Patent Application 13/651,270 (2013).
2. Jianlin Li, Beth Armstrong, Jim Kiggans, Claus Daniel, and David Wood, "Optimal polyethyleneimine concentration and mixing sequence for $LiFePO_4$ aqueous nanoparticle dispersions," *Journal of Colloid Interface Science*, **405** (1), 118-124 (2013).
3. Jianlin Li, Beth L. Armstrong, Jim Kiggans, Claus Daniel, David L. Wood, III, Lithium Ion Cell Performance Enhancement Using Aqueous LiFePO4 Cathode Dispersions and Polyethyleneimine Dispersant, *J Electrochem. Soc.*, **160** (2), A201-A206 (2013).
4. D.L. Wood, III, J. Li, D. Mohanty, C. Daniel, B.L. Armstrong, R.B. Dinwiddie, H. Wang, R.M. Trejo, N.C. Gallego, C.I. Contescu, J.Y. Howe, R.A. Meisner, J. Kiggans, and B.D. Brown, "Advanced Materials Processing and Novel Characterization Methods for Low-Cost, High Energy-Density Lithium-Ion Batteries," *Proceedings of the Advanced Automotive Battery Conference* (2013).
5. Claus Daniel, David Wood, Jianlin Li, Debasish Mohanty, Beth Armstrong, and Jim Kiggans, "Cell Materials and Manufacturing," 2013 Cummings Energy Storage Systems Summit, Columbus, IN, October 29-30, 2013 (invited).

6. Claus Daniel, David, Wood, Jianlin Li, Beth Armstrong and Jim Kiggans, “Battery Production Technologies” Energy Storage Solution Industrial Symposium, Oak Ridge, TN, September 4, 2013 (invited).
7. David L. Wood, III, Claus Daniel, Jianlin Li, Debasish Mohanty, and Bradley Brown, “Cutting Edge Lithium-Ion Cell Research at the Oak Ridge National Laboratory Battery Manufacturing Facility (BMF),” 2013 CERC-CVC Annual Technology Forum, Beijing, China, August 19-20, 2013.
8. Jianlin Li, Debasish Mohanty, Bradley Brown, David Wood, and Claus Daniel, “Status on electrode fabrication and battery manufacturing at ORNL’s Battery Manufacturing R&D Facility,” 2013 Clean Energy Research Center-Clean Vehicle Center-seminar Series, Ann Arbor, MI, July 17, 2013 (invited).
9. Claus Daniel, Debasish Mohanty, Jianlin Li, and David Wood, “Overview and progress in cathode materials for lithium ion batteries,” 1st International Freiberg Conference on Electrochemical Storage Materials, Freiberg, Germany, June 3-4, 2013 (invited).
10. Claus Daniel, David Wood, Jianlin Li, Beth Armstrong, Jim Kiggans, Debasish Mohanty, and Sergiy Kalnaus, “Electrification of transportation-cost and opportunities,” Bridging the Gap Conference 2013, Oak Ridge, TN, March 5-6, 2013 (invited).
11. David Wood, Jianlin Li, Debasish Mohanty, Claus Daniel, Beth Armstrong, Ralph Dinwiddie, Hsin Wang, Rosa Trejo, Nidia Gallego, Cristian Contescu, Jane Howe, Roberta Meisner, Jim Kiggans, and Bradley Brown, “Advanced materials processing and novel characterization methods for low-cost, higher energy-density lithium-ion batteries” Advanced Automotive Battery Conference 2013, Pasadena, CA, February 4-8, 2013 (invited).

V.E.3 Development of Industrially Viable Electrode Coatings (NREL)

Robert Tenent

National Renewable Energy Laboratory
16253 Denver West Parkway
Golden, CO 80401
Phone: (303) 384-6775
E-mail: Robert.tenent@nrel.gov

Subcontractor:
University of Colorado at Boulder

Start Date: January 2012
End Date: September 2013

Objectives

- The ABR program is focused on improving cycle life, abuse tolerance and reducing cost for PHEV battery technologies.
- Previous work conducted by NREL and the University of Colorado at Boulder has demonstrated that thin, conformal coatings of lithium ion battery electrodes formed by atomic layer deposition (ALD) can dramatically improve abuse tolerance and cycle life which in turn reduces ultimate cost.
- Current technology for performing ALD is not amenable to high throughput manufacturing methods and thus represents a high priced bottleneck in the implementation of ultrathin electrode coatings at a commercial scale.
- The objective of this current work is the development of a system for deposition of thin protective electrode coatings using a novel "in-line" atmospheric pressure ALD (AP-ALD) reactor design that can be integrated into manufacturing to address needs for improvement in rate capability, cycle life, and abuse tolerance in a cost effective manner.

Technical Barriers

- Limited calendar and cycle life.
- Abuse tolerance.
- High cost.

Technical Targets

- Design and construction of prototype in-line ALD coater for deposition on porous substrates

✧ ✧ ✧ ✧ ✧

Introduction

In previous work, NREL, in partnership with the University of Colorado, has shown that extremely thin, conformal coatings deposited with the ALD technique are capable of dramatically improving cycleability of lithium-ion cells. This project seeks to convert the common ALD processing format into a new reactor geometry that is compatible with battery electrode manufacturing.

As part of this effort for FY13, NREL and the CU-Boulder team has successfully completed design and construction of a new in-line ALD reactor. Work in this area has focused on modification of previous reactor designs to build a system capable of assessing the ability to obtain ALD-type coating processes in an in-line format and under acceptable battery manufacturing conditions. Earlier reactors were constructed to conduct initial feasibility testing of the ALD process when converted to an in-line format and with deposition occurring at atmospheric pressure; however, these early designs focused on planar substrates. More recent work has focused on creating a system that is capable of deposition onto moving coated battery electrode foils, as used in present manufacturing. Special emphasis was placed on designing a system to understand the impact of coating on porous substrates.

Approach

ALD coating methods are conducted by sequential and separate exposure of a sample substrate surface to gas phase precursors that react to form a film. Deposition is typically performed in a closed reactor system at mild vacuum as is shown in Figure V - 183. Precursor exposure steps are conducted in a single chamber and are separated in time. In a typical exposure "cycle", a sample is exposed to one precursor and the chamber is then purged with inert gas prior to exposure to the second precursor that completes the coating reaction. The "cycle" ends with another extensive inert

gas purging step before the process can be started again. Film growth takes place by repeating this cycling precursor exposure process multiple times. The sequential and separate exposures are key to achieving the excellent conformal film deposition on highly textured substrates for which the ALD technique is known.

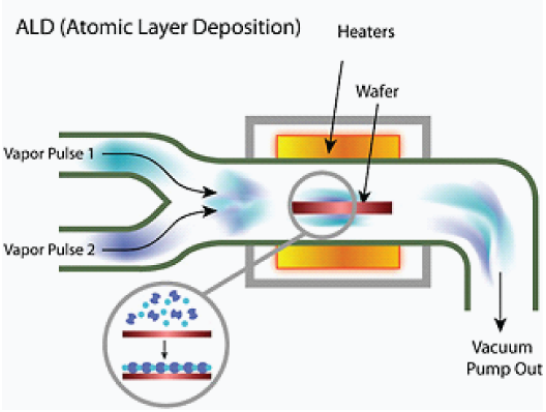

Figure V - 183: A typical ALD chamber with sequentially separated precursor exposures that draws out overall processing time

As an alternative to the temporal separation of precursor exposure in the same reaction chamber, our work proposes a ***spatial*** separation of precursor exposure steps that is more consistent with "in-line" processing techniques. Figure V - 184 shows a simplified conceptual schematic of our proposed apparatus.

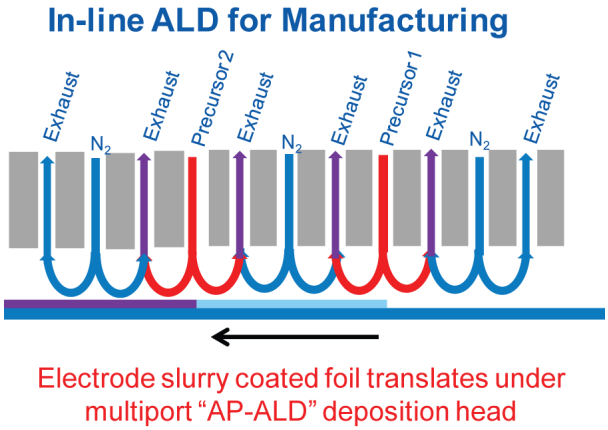

Figure V - 184: A simplified schematic demonstrating the in-line spatial ALD concept

Our "spatial" ALD approach employs a multichannel gas manifold deposition "head" that performs sequential exposure of precursor materials as an electrode foil transits beneath it. It is important to note that similarly designed deposition heads are currently employed by glass manufacturers for production of a variety of coated glass products using high-volume, in-line atmospheric pressure chemical vapor deposition (AP-CVD). Our approach leverages this existing knowledge base as well as our ALD expertise in order to enable in-line ALD coating that will allow the transfer of our previously demonstrated ALD-based performance improvements to larger format devices.

Results

Push-Pull Reactor Design. A crucial factor for successful coating of battery electrodes using in-line ALD technique is the ability to coat *porous* substrates. Coating of a porous substrate presents a specific technical challenge, as precursor materials must be able to fully penetrate as well as be removed from the porous film as rapidly as possible to enable high processing line speeds. This requires that the porous film be exposed to alternating high and low gas pressure regimes at different stages of the deposition process. At high local pressures (viscous flow conditions), a high number of gas phase collisions drive penetration of precursor gases into the film, while low local pressures (molecular flow conditions) allow rapid removal of unreacted precursor prior to the next precursor exposure step. We have termed the rapid progression through alternating high and low local pressure regimes the "push-pull" reactor design. A fundamental schematic of the "push-pull" reactor concept is shown in Figure V - 185. In addition to precursor introduction and exhaust channels, the system is also designed with a nitrogen gas window that is pressured higher than the dosing precursors in between the precursor ports. This nitrogen gas purge will ensure that there is no cross talk between the different reactants that would lead to bulk film deposition.

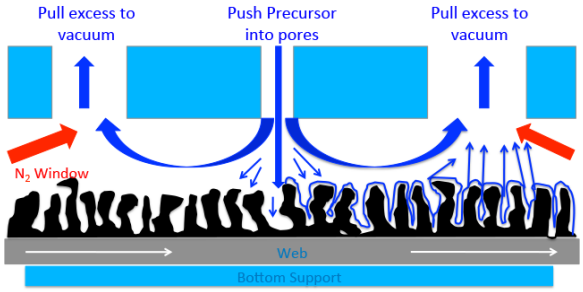

Figure V - 185: A simple schematic demonstrating the alternate high and low pressure regimes present in the "push-pull" reactor concept

Digital Modular Roll-to-Roll (R2R) System Design. As shown schematically earlier, a linear translational roll-to-roll design was initially considered for our "push-pull" deposition system. However, it was determined through earlier results and discussions with

additional R2R processing experts that a linear design would not be capable of maintaining adequate tension on the web substrate during the "push-pull" deposition process. An improved format is a rotating drum-in-drum design as shown in Figure V - 186. In the drum-in-drum system, a rotating inner drum on which substrates are mounted is set inside a fixed outer drum that contains all gas sources as well as purge and exhaust lines. The inner drum rotates the web radially while maintaining sufficient tension on the line to ensure accurate gas head to substrate spacing.

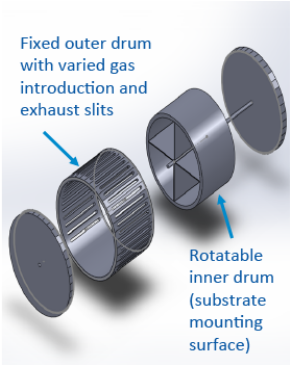

Figure V - 186: Diagram of drum-in-drum reactor format

In order to maximize reactor flexibility and enable extensive deposition condition optimization work, we have adopted what we term a "digital modular" system design. Figure V - 187 shows a more detailed schematic of the drum-in-drum reactor design and demonstrates the digital modular design. To implement the "digital modular" design, the fixed outer drum of the reactor is faceted and has slots drilled every 2.5 cm. Precursor introduction as well as reactant exhaust occurs through the attachment of specific "modules" to these slots. Precursor dosing and vacuum exhaust modules have been fabricated that are able to fit to any of the slots in the external drum. This design will allow the modules to be moved interchangeably on the external drum to allow the maximum amount of variability in dosing and vacuum modules spacing. This enables extensive experimentation across a broad range of deposition conditions in order to optimize performance.

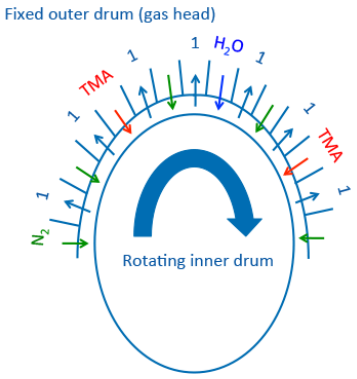

Figure V - 187: Schematic representation of the "digital modular" design concept

Module Design. Computational flow dynamics simulations were conducted to optimize the precursor introduction module design in order to ensure uniform precursor exposure to the moving substrate across the sample surface. As an example, Figure V - 188 shows output from CFD calculations as well as the final constructed precursor introduction module. Our simulations showed that under expected deposition conditions, a minimum height of 2" was required for the precursor concentration to become uniform across the entire width of the module. Modules were constructed at a height of 5" in order to allow sufficient time and space for the precursor concentration to become uniform.

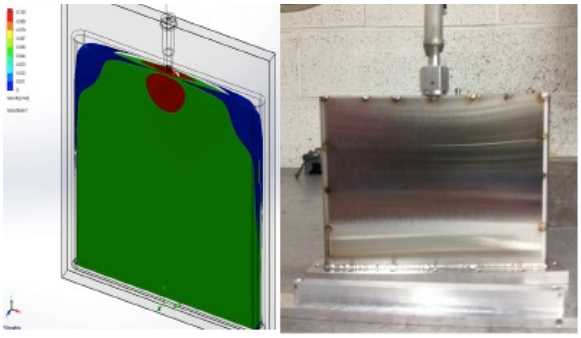

Figure V - 188: Fabricated and final assembly of the drum-in-drum in-line reactor

As discussed previously, another benefit of using the modular slot design is that blank modules can be added to modify channel spacing, furthermore, new modules can be added in the future without having to modify the main deposition head. As an example additional modules are being designed that will allow for the use of *in situ* diagnostics including pressure sensing and mass spectrometry as well as a module that will enable in-line plasma assisted deposition.

Reactor Construction and Assembly. Following the design phase, reactor parts were fabricated, assembled and are currently under test. Figure V - 189 shows the final fabricated internal and external drum units including the faceted slits for process module

interfacing as well as the full reactor at different stages of completion. Note that a portion of the external drum has been left intact. This was left unmodified to enable later integration of the unit within existing R2R processing units as will be briefly described below.

Figure V - 189: Compulational flow dynamic simulation of gas flow through the precursor introduction module and final construction

Conclusions and Future Directions

In FY13 the NREL/CU team designed and completed construction of a new in-line ALD based electrode coating reactor. Initital testing of the unit is currently underway. If additional funding can be obtained for a continuation of this effort into FY14, experiments will be conducted to determine optimal parameters for conformal coating on porous substrates. This work will entail detailed Design of Experiment methods used to determine optimal conditions to ensure conformal coating of a moving porous substrate. The output from this work will identify acceptable conditions for conformal coating of materials in an in-line format. Experiments will initially be conducted with model porous substrates with well-known geometries that will enable detailed measurements of coating quality. Following this initial optimization work, the NREL/CU team will partner with other ABR collaborators to coat larger format battery electrodes. Larger format electrodes will be fabricated into cells for testing at the NREL/CU laboratories within collaborating labs.

It is anticipated that in a later stage, the NREL/CU team will partner with battery manufacturers and other laboratories to integrate the new reactor design into a battery electrode coating process. Toward that end, the existing reactor was intentionally designed to enable integration with further R2R processing capabilities. Figure V - 190 shows an early stage schematic for integration of the digital modular reactor design into a R2R system. The unmodified sidewall of the outer drum of the reactor will be modified to include roller designs to bring an electrode foil into the reactor and into contact with the inner drum. The roller integration is shown on the left side of the Figure V - 190 schematic.

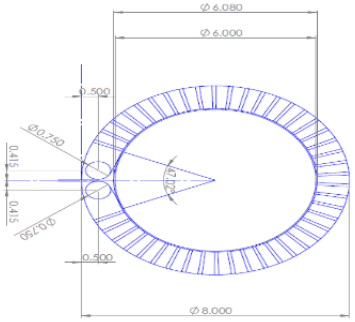

Figure V - 190: Initial schematic of roller integration within the drum-in-drum reactor design

FY 2013 Publications/Presentations

1. 2013 DOE Annual Peer Review Meeting Present.

V.E.4 Roll-to-Roll Electrode Processing NDE and Materials Characterization for Advanced Lithium Secondary Batteries (ORNL)

David Wood III, Debasish Mohanty, Jianlin Li, Curt Maxey, Ralph Dinwiddie, and Claus Daniel
Oak Ridge National Laboratory
One Bethel Valley Road
P.O. Box 2008, MS 6065
Oak Ridge, TN 37831
Phone : (865) 574-1157; Fax: (865) 241 4034
E-mail: wooddl@ornl.gov

Collaborators:
Daniel Abraham (ANL), Kevin Gallagher (ANL), Jason Croy (ANL), Guido Bender (NREL), Michael Ulsh (NREL), Mike Wixom (A123 Systems and Navitas Systems), Frank Reilly (Ceres Technologies), Mark Ewen (ConocoPhillips), Erin O'Driscoll (Dow Kokam), David Telep (Dow Kokam), Jerry Forbes (Frontier Industrial Technology)

Start Date: October 11, 2011
Projected End Date: September 30, 2014

Objectives

- Raise the production yield of lithium secondary battery electrodes from 80-90% and the associated cell acceptance rate by utilizing in-line measurement and *ex situ* diagnostic tools for electrode structural characterization to improve the performance.
- Reduce electrode and cell cost by investigating and implementing in-line X-ray fluorescence (XRF), laser scanning, infrared (IR) thermography, and thermal diffusivity as non-destructive evaluation (NDE) and quality control (QC) tools for coating areal weight, thickness, composition, and defect location:
  - Identify the nature of defects/flaws generated during electrode coating and their impact on battery performance.

Technical Barriers

- Material processing cost and electrode quality control.
- Cell acceptance rate, calendar life, and performance.

Technical Targets

- Low-cost manufacturing methodology with minimized scrap rate for lithium ion battery electrodes using both organic and aqueous suspensions (to meet $290/kWh USABC storage goal for PHEVs and <$125/kWh for EVs).
- Lifetime of 10 years and 1,000 cycles at 80% DOD for EVs and 5,000 deep discharge cycles for PHEVs.
- Correlation of electrode defects with performance to meet calendar life and long-term cycling needs.

Accomplishments

- In-line laser thickness measurement enabled data precision of less than ±2% for electrode wet thickness measurement. The high thickness precision was critical to evaluating thickness variation across electrodes at different regions.
- IR thermography was successfully implemented to identify pinholes, blisters, divots, and agglomerates in dried electrodes. Temperature variation in IR thermographs was critical for locating these different defects. An increase in the temperature profile suggested the presence of agglomerates, and a decrease in the temperature profile indicated divots, pinholes, and blisters.
- Off-line XRF was used to successfully measure the concentration of Cu contamination in electrodes. In addition, excellent off-line measurements of cathode transition-metal stoichiometry were obtained. However, this technique was de-selected as a viable in-line method due to the insufficient accuracy of areal weight measurement and low required line speed.

✧ ✧ ✧ ✧ ✧

Introduction

In-line XRF is a valuable, non-destructive QC tool that determines chemical composition uniformity and presence of contaminants in a variety of industries including geological analysis, plastics, textiles,

pharmaceuticals, fertilizers, foodstuffs, forensics, mining feeds and refineries, cement production, catalysts, glass, ceramics, heat resistant coatings, thin films, semiconductors, photovoltaics, multilayer films, etc. The measurement may be executed with an energy dispersive X-ray fluorescence detector (EDXRF) for high throughput and low cost or a wavelength dispersive detector (WDXRF) for high resolution and low detection levels. The technique is highly compatible with roll-to-roll manufacturing and film processing and is independent of coating technique. Other advantages are that a large sample area can be accommodated, 2-D (x-y) scanning over a coating surface can be implemented, and coating thicknesses can be measured. These many features make the technique highly compatible with lithium secondary battery electrode production. However, issues such as compatibility of XRF detection rate with desired coating line speeds (20-60 ft/min is the current state-of-the-art) and detection of trace, isolated metal contaminants (such as Fe, Al, and Cu) present considerable technical challenges. Compositional and thickness uniformity achieved via in-line XRF could be correlated with X-ray computed tomography (XCT) information regarding electrode morphological and microstructural changes during drying to provide additional insight.

Currently, the independent measurement of lithium secondary battery electrode loading via dual-side (slot-die) coating is achieved by pulling a sample from the master roll product, and removing the coated material from each side to measure the relative coating distribution. Total material loading is determined by Beta Gauge measurement of the total dried electrode mass. From this output, adjustments to the total loading are made by reducing or increasing the amount of electrode dispersion applied to both sides of the current collector. Output from a Beta Gauge does not capture the loading on each side of the electrode substrate; thus, potential imbalances may result in applying too much (or too little) coating to one side of the current collector. Extreme levels of imbalance may lead to localized lithium plating or excessive resistance growth in the operating cell due to relative over/under utilization of the electrode. Traditional thickness measurements of moving webs using laser displacement have been prone to inaccurate results due to vibration of the current collector substrate. Methods to directly monitor the applied coating for dual-side application would be beneficial for providing real time measurement to ensure the quality of production electrodes. The desired effect would be to provide feedback to the individual pumping device used to apply electrode dispersion to each side and meter the dispersion flow rate to either increase or decrease accordingly. This needed QC improvement would reduce the amount of total electrode dispersion required and finished electrode roll scrap discarded.

Recent advances in laser thickness measurement may provide a better opportunity to accurately measure the wet layer applied to each side of the current collector substrate. By positioning measuring devices after both the first and second slot dies (i.e., in a production setting) in discrete locations to measure across the entire width, the dispersion distribution across an individual lane could be monitored and feedback for adjustments to the applied wet layer on each side could be provided. Comparing the distribution profile of the wet coating layer to that achieved with the final dry layer (determined by inline EDXRF) could also provide insight into how the electrode coating settles during the drying process. The state-of-the-art is to operate the pump metering devices based on a relative pump speed, which dispenses a given amount of dispersion to either side of the current collector. Measurement of the applied wet layer for each side may better allow for adjustments needed as the dispersion properties change over the duration of a coating batch.

IR imaging, or thermography, will be used to determine the location and frequency of electrode coating defects such as pinholes, blisters, and particle agglomerates, as well as uniformity of coating thickness and quantification of areal weight. An IR camera will be installed on the dry coating end of our slot-die coater to obtain this data.

Approach

Determining defects in dried electrodes by IR thermography. An IR camera detects the IR energy emitted from an object and simultaneously displays the image as a function of temperature. Any defect or flaw in the object will appear as a temperature variation at that point. Therefore, IR thermography is essential to examine the dry electrode homogeneity exiting the slot-die coater oven and to detect any flaws, or defects (e.g., pinholes, divots, blisters, large agglomerates, or contaminants) present on the electrode surface. The IR imaging QC will be correlated with the battery performance data to determine any further systematic flaw formation mechanism and its impact on electrochemical performances.

Determining feasibility of in-line laser thickness measurement with equipment supplier. Recent advances in laser thickness measurement may provide a better opportunity to accurately measure the wet layer applied to each side of the current collector substrate. By positioning measuring devices after both the first and second slot dies (i.e., in a production setting) in discrete locations to measure across the entire width, the dispersion distribution across an individual lane could

be monitored and feedback for adjustments to the applied wet layer on each side could be provided. Comparing the distribution profile of the wet coating layer to that achieved with the final dry layer (determined by inline EDXRF) could also provide insight into how the electrode coating sets during the drying process. The state-of-the-art is to operate the pump metering devices based on a relative pump speed, which dispenses a given amount of dispersion to either side of the current collector. Measurement of the applied wet layer for each side may better allow for adjustments needed as the dispersion properties change over the duration of a coating batch. Keyence was selected as the partner for developing a laser thickness senor, or set of sensors, for lithium secondary battery electrode production. ORNL has a single-sided slot-die coating system, so only single-sided electrode coatings will be evaluated. ORNL will rent the sensors from Keyence and integrate them directly into ORNL's slot-die coating line for the proof-of-concept experiments.

Determining feasibility of in-line XRF with equipment supplier. In-line XRF is a valuable, non-destructive QC tool that determines chemical composition uniformity and presence of contaminants in a variety of industries. The measurement may be executed with an energy dispersive detector (EDXRF) for high throughput and low cost or a wavelength dispersive detector (WDXRF) for high resolution and low detection levels. The technique is highly compatible with roll-to-roll manufacturing and film processing and is independent of coating technique. Other advantages are that a large sample area can be accommodated, 2-D (x-y) scanning over a coating surface can be implemented, and coating thicknesses can be measured. These many features make the technique highly compatible with lithium secondary battery electrode production. However, issues such as compatibility of XRF detection rate with desired coating line speeds (20-60 ft/min is the current state-of-the-art) and detection of trace, isolated metal contaminants (such as Co, Al, and Cu) present considerable technical challenges. Compositional and thickness uniformity achieved via in-line XRF could be correlated with X-ray computed tomography (XCT) information regarding electrode morphological and microstructural changes during drying to provide additional insight. Ceres Technologies was selected as the equipment partner based on their commercial success with performing in-line XRF on PV panels.

Results

Successful alignment of two-laser-caliper system on ORNL slot-die coater and wet-electrode thickness data collection. The two-laser-caliper system (Keyence) was successfully mounted and aligned on the ORNL slot-die coater (Figure V - 191a). The schematic of the thickness measurement by this laser caliper system is shown in Figure V - 191b. The thickness of a sample "t" can be determined by adding the two output voltages from the lasers (Figure V - 191c) and then dividing by the slope, which is given as in the formula:

$$V_1 = m\left(\frac{t}{2}\right)$$

$$V_2 = m\left(\frac{t}{2}\right)$$

$$V_1 + V_2 = m(t)$$

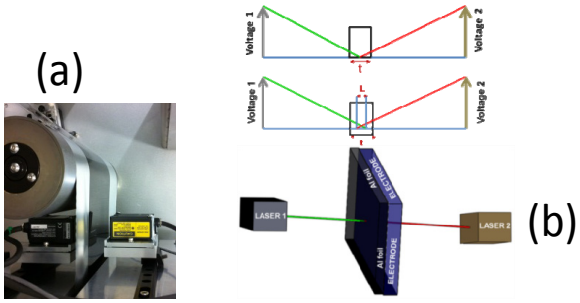

Figure V - 191: Mounted lasers (a); alignment of a two-laser-caliper system to measure the thickness of the electrode coating (b); determining sample thickness with a perfectly aligned system (c); determining sample thickness with calibration constant while measuring the thickness of the coating (d)

However, it is difficult to align two lasers perfectly and between the two lasers' focal points, an overlap of one thickness should be added to the equation above (Figure V - 191d) to represent the lack of coincidence of the two focal points. Rearranging the components, both "t" (sample thickness) and "l" (calibration constant) can be isolated, enabling the expression to be easily used for both calibrating the system with a known thickness and measuring thickness with a calibration constant. The equation can be rewritten as

$$V_1 + V_2 = m(t + l)$$

The various sources of errors such as physical and data acquisition errors were systematically studied particularly applicable to ORNL slot-die coater and summarized in the Table V - 15. The laser caliper system was utilized to measure the wet-thickness of TODA HE5050 cathode and ConocoPhillips graphite A12 anode. Before measuring the thickness of the TODA HE5050 the system was re calibrated with the current collector which is bare Al foil with a thickness of 15 µm and the thickness data was collected at a speed of 1ft/minute for 5 minutes. In Figure V - 192a, the Δd/d (Where d represents the thickness value and Δd is the difference between two adjacent data) vs. time with a confidence interval of 95% is presented. The data collected over the five minutes run were averaged to obtain the thickness of the Al foil. The average

thickness of the bare Al foil was calculated as 15.67 µm with a standard deviation of 0.23 µm (T=19°C). This value is in agreement with the expected thickness of a bare Al foil and shows the capability of our laser system to obtain an accurate thickness measurement. In the next step, the wet-thickness data of the TODA HE5050 coating was collected for a 20 minutes run at a speed of 1ft/minute. In Figure V - 192b, thickness data the Δd/d vs. time with a confidence interval of 95% is presented. The data obtained for 20 minutes were averaged and the thickness value was obtained as 118.51µm (T= 20°C) with a standard deviation of 2.75 µm. This indicates that the slurry coating is homogeneous across the measurement line, which was also confirmed from the Δd/d values that did not change over the time during coating is in agreement with this result.

The laser caliper system was also used to obtain the thickness of the ConocoPhillips A12 graphite anode. Before collecting the thickness of the anode coating, the system was recalibrated with the bare Cu foil (current collector) of thickness 20µm. The data was collected for 5 minutes at a speed of 1ft/min and the plotted as Δd/d vs. time (Figure V - 192c). The average thickness data was calculated as 19.97 µm (T =20°C) with a standard deviation of 0.76 µm. This value is in agreement with the expected thickness value for the bare Cu foil. After recalibration, the wet-thickness data for the A12 graphite coating was collected for 20 minutes at a speed of 1 ft/min and the data was plotted as Δd/d vs. time (Figure V - 192d). The average wet-thickness was calculated to be 89.96 µm with a standard deviation of 1.27 µm. Comparing the thickness variation of the cathode (Figure V - 192b) and anode (Figure V - 192d), Figure V - 192d shows a higher standard deviation than that in Figure V - 192b, which verifies that the laser sensors can effectively detect the thickness variation in an LIB electrode. Here the standard deviation can be taken as an indication of uniformity of the thickness.

Identification of nature of coating defects and flaws by IR thermography. The schematic of IR-setup for monitoring flaws in the dried electrodes coming out from the slot-die coater is given in Figure V - 193a. For experimental set-up, FLIR SC-8200 IR camera with a 25 mm lens (no filters or extender rings) and a 6,000 J Hensel flash system at ~60% flash power was used. The IR camera has 1,024 by 1,024 pixels and the wavelength range is 3 to 5 microns. The images were reordered during entire coating, and data were processed to detect any flaws in the electrode.

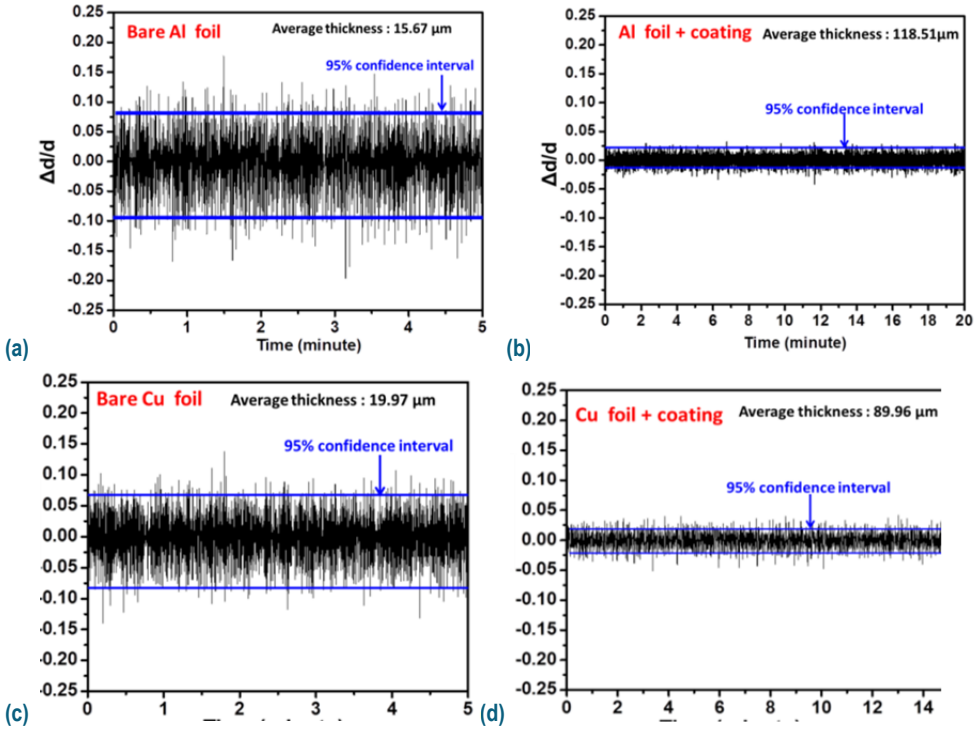

Figure V - 192: Thickness measurement data (Δd/d) from (a) bare Al foil, (b) TODA HE5050 cathode material, (c) bare Cu foil, and (d) ConocoPhillips A12 graphite anode with 95% confidence interval, where d represents the thickness value and Δd is the difference between two contiguous data

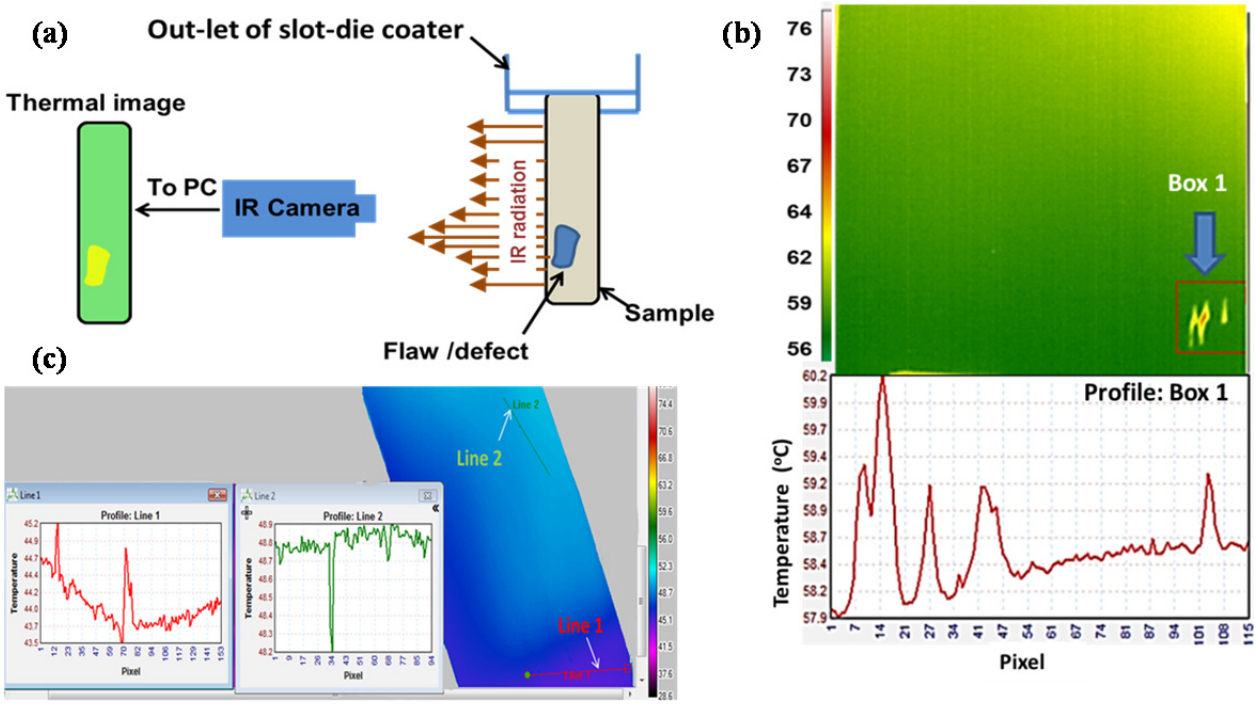

Figure V - 193: (a) Schematic of IR thermography experimental setup. The IR camera is set in front of the dried electrode exiting the slot-die coater, and the subsequent thermal image is digitally processed. (b) Scan along the TODA HE5050 cathode showing the temperature variation, which indicates the presence of defects in the electrode. (c) IR thermography from dried anode shows the increase (line 1) and decrease (line 2) in temperature profile indicating the blister and pinholes in the electrode which could not be visible optically

Table V - 15: Expected errors that may originate during thickness measurement by the laser caliper system mounted on the ORNL slot-die coater

Error Sources	Expected Error Range	Type	Remarks
Laser Alignment	0–10 µm	Lateral/ Thickness	Perfectly aligned laser triangulation sensors will result in perfect thickness measurements; misalignment will result in either lateral or cosine errors in thickness measurement.
Surface Reflectivity	Minimal	Reliability	Automatic gain control in sensors tends to negate these concerns. Sensors should be verified to be usable over the range of expected reflectivity.
Angle of Measured Surface	~1% thickness based on 8 degree tilt	Thickness	Any deviation from orthogonality results in a cosine error in the measurement.
Temperature	0–15 µm	Thickness	This error source is based on the thermomechanical properties of the mounting structure and the range of temperatures over which the system must operate.
Vibration	± 3 µm	Thickness	For a well-aligned caliper, this error range is the result of sampling error and the degree of vibration.
Dynamic Range	0.6 µm	Resolution	The laser displacement sensor controller output has less resolution than the computer's data acquisition system, and thus is the limiting factor in dynamic range.
Sampling Error	2 µm[b] With a speed of 5m/min	Lateral	This error source is greatly dependent on the speed at which a sample passes through the laser caliper.

A representative IR thermograph from a region of TODA HE5050 electrode with defect is shown in Figure V - 193b. The temperature scan from that area shows an increase in the temperature profile confirming the presence of defects in the electrode. This technique was also applied for the graphite A12 anode coating, and the results are given in Figure V - 193c. The observed increase in the temperature profile along the line-1 scan

and the decrease in the temperature profile along the line-2 scan may be due to (1) temperature increase across the defect region corresponding to a blister or agglomerate where heat cannot be released more quickly and (2) temperature decreases corresponding to pinholes and divots where heat is released from the coating surface more quickly.

XRF as a NDE technique to measure cathode transition-metal stoichiometry and electrode areal weight and to identify metal particle contaminants in the electrode. ORNL has contributed to designing an in-line XRF measurement system with Ceres Technologies specifically designed for lithium ion battery cathode coatings. The XRF desktop unit (Figure V - 194) was used to measure the cathode transition-metal stoichiometry and cathode areal weight and to identify deliberately introduced metal particle contamination in the electrode while coating. Only preliminary off-line data was obtained, as it was determined that this technique was not appropriate for production scaling due to insufficient areal-weight accuracy and incompatibility with coating line speeds.

The instrument was used to monitor the TM composition at different coating positions for two different cathode types: a traditional TODA NMC 532 coating and a TODA LMR-NMC HE5050 coating. The Mn to Co ratio and Ni to Co ratio for the NMC 532 cathode was found to be ~2.5 and 1.5 respectively. These results demonstrate excellent compositional uniformity across the electrode coating. The same compositional analysis was also completed on a LMR-NMC cathode (TODA HE5050), and the ratios between Mn to Co and Ni to Co in four different regions were found to be the nominal values of 1.5 and 5.5, respectively. However, the areal weight values measured by XRF were 20-25% too low as compared to the actual values measured with a balance. The actual areal weights of the NMC 532 and HE5050 were 11.9 mg/cm^2 and 10.2 mg/cm^2, respectively, as compared to 9.4 mg/cm^2 and 7.7 mg/cm^2, respectively, when analyzed by the desktop XRF unit.

Two different sample types were prepared for measuring metal particle contaminants:

Sample 1: Co and Cu metal powder were mixed into a TODA NMC 532 slurry, and then the electrode was prepared by tape casting (designated as NMC532-Co-Cu).

Sample 2a: Cu metal powder was sprinkled over the wet electrode after tape casting (NMC532-Cu).

Sample 2b: Co metal powder was sprinkled over the wet electrode after tape casting (NMC532-Co).

Figure V - 195 shows the relative TM ion composition collected from Sample 1 (NMC532-Co-Cu) in region R1 and R2. From the XRF data, it is evident that the Co concentration is higher because excess Co was added in the slurry before tape casting. It was also observed that the wt% of Cu in the region R1 is 5.378% and R2 is 7.213%, which demonstrates the ability of XRF technique for detecting metal-particle contamination of different concentration that might be present in the cathode slurry while mixing. Figure V - 195 shows the composition spectrum acquired from region R1, confirming the presence of Co and Cu impurities in the electrode.

Figure V - 194: Desktop Ceres Technologies XRF unit

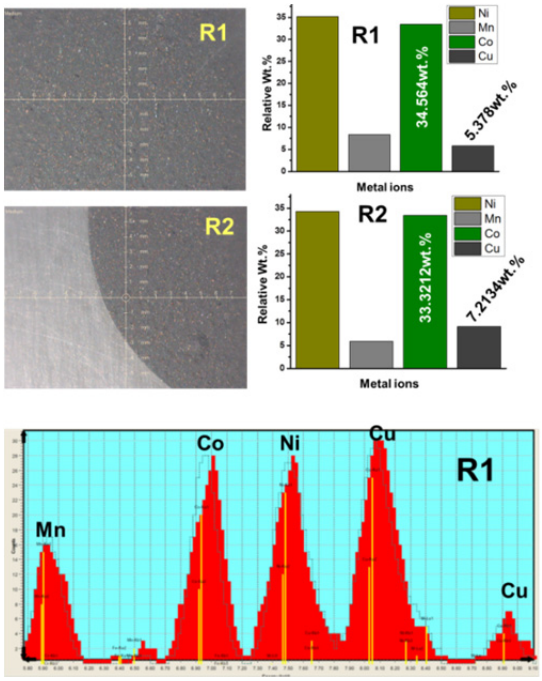

Figure V - 195: Optical images (top left), XRF data (top right), and composition spectrum (bottom) from two different regions of NMC 532 electrode contaminated with Co and Cu. The spectrum shows the presence of Cu in the electrode

Figure V - 196 shows the relative TM ion composition collected from Sample 2a (NMC532-Cu) in region R1 and R2. It was observed that the wt% of Cu in region R1 was 0.0071% and R2 was 0.0429%, showing that the XRF method can also trace very small amount of metal contamination from the Cu foil slitting process. The digital images also show a higher amount of Cu in

region R2 compared to R1. Figure V - 197 shows the relative transition metal ion composition collected from Sample 3 (NMC532-Co) in region R1 and R2. It was observed that the wt% of Co in region R1 was 22.77% and R2 was 29.45%, demonstrating that the R2 region had more Co contamination than R1 and that both regions had an excess of Co. In this electrode, a negligible amount of Cu (~0.003%) was detected).

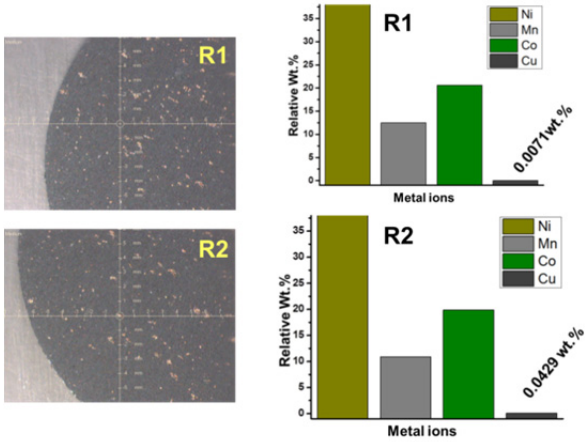

Figure V - 196: XRF data from sample 2a (NMC532-Cu). Optical image (left) and relative wt% of transition metal composition with Cu impurity from area R1 and R2 (right)

Figure V - 197 shows the relative transition metal ion composition collected from Sample 2b (NMC532-Co) in region R1 and R2. It was observed that the wt% of Co in region R1 was 22.77% and R2 was 29.45%, demonstrating that the R2 region had more Co contamination than R1 and that both regions had an excess of Co. In this electrode, a negligible amount of Cu (~0.003%) was detected.

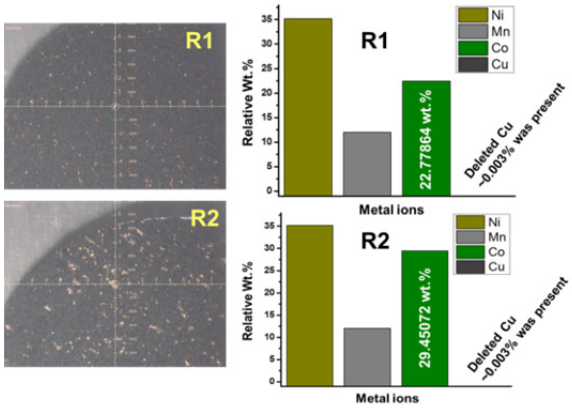

Figure V - 197: XRF data from Sample 2b (NMC532-Co). Optical image (left) and relative wt% of transition metal composition with Co impurity (right) from region R1 and R2 (right)

Conclusions and Future Directions

- The laser-caliper method was developed specifically for use as a LIB electrode NDE and QC tool on the ORNL slot-die coating line. Possible errors and uncertainties of the laser caliper system were provided. Thickness precision of less than ±2% for in-line laser thickness measurement was achieved. The thickness deviation of the cathodes was typically ± 2.0-2.3%, and for anodes, it was typically ± 2.2-2.6%. Differences in standard deviation values were taken as references for the thickness of the electrode at different regions. In the next step, the technique will be transferred to industry partner (TBD) pilot/production line.
- The XRF method yielded the concentration of deliberately added metal contaminants in the electrode; however, this technique could not provide the reliable areal weight accuracies (no-go decision).
- IR thermography successfully detected the defects in dried electrodes. An increase in the temperature profile suggests the presence of agglomerates, and a decrease in the temperature profile indicates divots, pinholes, and blisters that were not observed optically. In the next step:
  - Method(s) will be developed to generate different electrode coating defects such as pinholes, blisters, large agglomerates, divots, and metal particle contaminants for evaluation in full coin cell test matrix.
  - Comprehensive, statistically representative full coin cell data on different types of electrode coating defects will be obtained to determine which type of defects cause cell failures or substandard performance and correlate IR thermography electrode QC data with full coin cell statistical data quantifying capacity/voltage fade.
  - Pass/fail criteria will be developed for lithium-ion electrode coating defects such as metal particles, pinholes, blisters, divots, large agglomerates, etc.
  - Automatic flaw detection during the electrode coating will be developed.
- In-line electrode porosity measurement will be developed with NREL using thermal diffusivity.

FY 2013 Publications/Presentations

1. D. Mohanty, J. Li, L.C. Maxey, R.B. Dinwiddie, C. Daniel, and D.L. Wood, "Improved QC of Slot-Die Coated Lithium Ion Battery Electrodes by IR Thermography and Laser Thickness Techniques," *Analytical Methods*, Revised, 2013.
2. 2013 DOE Annual Peer Review Meeting Presentation.
3. Mohanty, J. Li, C. L. Maxey, R. B. Dinwiddie, C. Daniel and D. L. Wood, "In-Line Non-destructive testing of a lithium-ion Battery Electrode by Laser Caliper and Thermography" MRS Fall meeting Boston, Massachusetts, December 1-6, (2013) (accepted)
4. D.L. Wood, III, J. Li, D. Mohanty, C. Daniel, B.L. Armstrong, R.B. Dinwiddie, H. Wang, R.M. Trejo, N.C. Gallego, C.I. Contescu, J.Y. Howe, R.A. Meisner, J. Kiggans, and B.D. Brown, "Advanced Materials Processing and Novel Characterization Methods for Low-Cost, High Energy-Density Lithium-Ion Batteries," *Proceedings of the Advanced Automotive Battery Conference* (2013).
5. Claus Daniel, David Wood, Jianlin Li, Debasish Mohanty, Beth Armstrong, and Jim Kiggans, "Cell Materials and Manufacturing," 2013 Cummings Energy Storage Systems Summit, Columbus, IN, October 29-30, 2013 (invited).
6. Claus Daniel, David, Wood, Jianlin Li, Beth Armstrong and Jim Kiggans, "Battery Production Technologies" Energy Storage Solution Industrial Symposium, Oak Ridge, TN, September 4, 2013 (invited).
7. David L. Wood, III, Claus Daniel, Jianlin Li, Debasish Mohanty, and Bradley Brown, "Cutting Edge Lithium-Ion Cell Research at the Oak Ridge National Laboratory Battery Manufacturing Facility (BMF)," 2013 CERC-CVC Annual Technology Forum, Beijing, China, August 19-20, 2013.
8. Claus Daniel, Debasish Mohanty, Jianlin Li, and David Wood, "Overview and progress in cathode materials for lithium ion batteries," 1st International Freiberg Conference on Electrochemical Storage Materials, Freiberg, Germany, June 3-4, 2013 (invited).
9. Claus Daniel, David Wood, Jianlin Li, Beth Armstrong, Jim Kiggans, Debasish Mohanty, and Sergiy Kalnaus, "Electrification of transportation-cost and opportunities," Bridging the Gap Conference 2013, Oak Ridge, TN, March 5-6, 2013 (invited).
10. David Wood, Jianlin Li, Debasish Mohanty, Claus Daniel, Beth Armstrong, Ralph Dinwiddie, Hsin Wang, Rosa Trejo, Nidia Gallego, Cristian Contescu, Jane Howe, Roberta Meisner, Jim Kiggans, and Bradley Brown, "Advanced materials processing and novel characterization methods for low-cost, higher energy-density lithium-ion batteries" Advanced Automotive Battery Conference 2013, Pasadena, CA, February 4-8, 2013 (invited).

VI

Focused Fundamental Research

Introduction

Cathode Development

Anode Development

Electrolyte Development

Cell Analysis, Modeling, and Fabrication

Diagnostics

Beyond Lithium-Ion Battery Technologies

VI. Focused Fundamental Research

VI.A Introduction

The focused fundamental research program, also called the Batteries for Advanced Transportation Technologies (BATT) Program, is supported by the VTO to research and analyze new materials for high-performance, next generation, rechargeable batteries for use in HEVs, PHEVs, and EVs. The effort in FY 2013 continued the increased emphasis on high-energy materials for PHEV and EV batteries and expanded efforts into technologies for enabling the use of Li metal anodes.

Background and Program Context

The BATT Program addresses the fundamental problems of chemical and mechanical instabilities that have slowed the development of automotive batteries with acceptable cost, performance, life, and safety. The aim is to develop and test new materials and to use traditional and novel diagnostics and modeling methods to better understand cell and material performance and lifetime limitations before initiating battery scale-up and development. Emphasis is placed on the synthesis of components into cells with determination of failure modes, while continuing with materials synthesis and evaluation, advanced diagnostics, and improved model development. Battery chemistries are monitored continuously with timely substitution of more promising components. This is done with advice from within the BATT Program and from outside experts, including consultation with automotive companies and DOE. Also factored into the BATT Program direction is the monitoring of world-wide battery R&D activities. The Program not only supports research that leads to improvements to existing materials, but also into high-risk "leap-frog" technologies that might have a tremendous impact in the marketplace. An overview of the approach used in this program is shown in Figure VI - 1. BATT serves as a bridge between the basic science efforts in DOE and the applied offices, allowing translation of fundamental science into new battery chemistries.

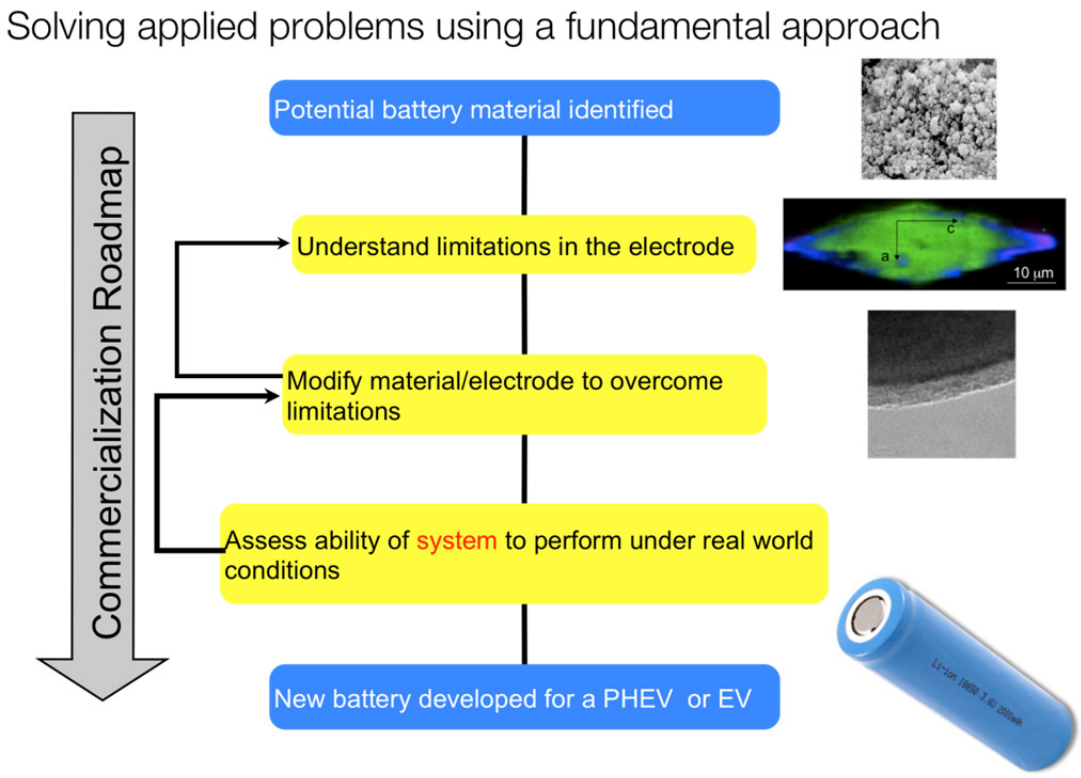

Figure VI - 1: BATT approach overview

The work is administered by the Lawrence Berkeley National Laboratory (LBNL), with principal researchers from LBNL, five additional national laboratories, fourteen universities, and two commercial companies. The program is organized into the following areas:

- Cathode Development..
- Anode Development.
- Electrolytes Development.
- Cell Analysis, Modeling, and Fabrication.
- Diagnostics.
- Beyond Lithium-ion Technologies.

The BATT Program has an enviable team of principal investigators, many of them world renowned, who push the battery field forward in each of these areas. The focus areas include advanced architectures that increase the energy and decrease the cost of batteries via "engineering" approaches and new materials that focus on advancing the state of the art in the short term (e.g., silcon anodes, high voltage electrolytes) and leapfrog chemistries for the long term (e..g, Lithium metal anode, sulfur and oxygen cathodes). This balanced materials effort is made more robust by coupling them with modeling at different length scale, microscopy and spectroscopy with *in situ* focus, and advanced electrochemical characterization. This is illustrated in Figure VI - 2.

The whole effort is undertaken in a coordinated fashion with focus groups formed to solve big challenges. Two such focus groups that bear mention is charged with solving the mechanical damage and surface instability of silicon anodes, and understanding the alleviating the problems at high voltages. Both teams bring together researchers with focus on material synthesis, advanced diagnostics and modeling to understand the issues and propose solutions.

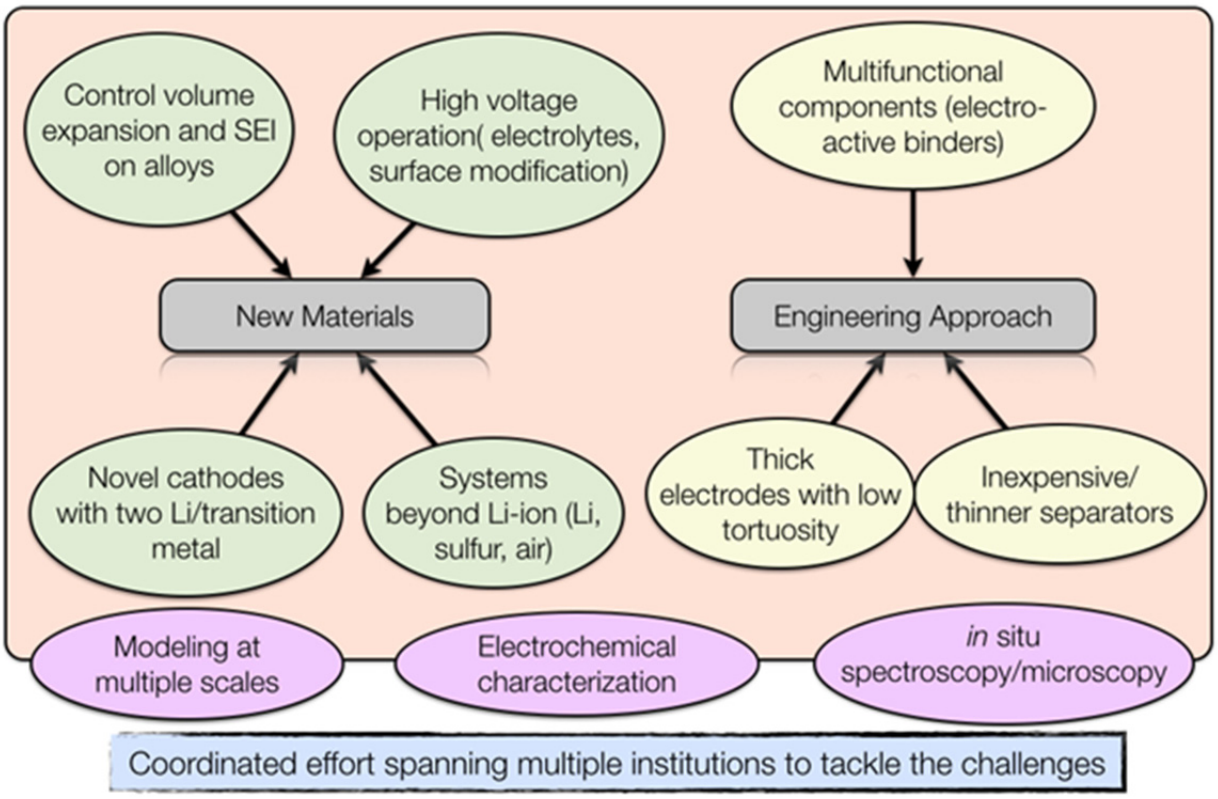

Figure VI - 2: BATT focus areas

This section summarizes the research activities of this program in FY 2013. The website for the BATT Program is found at http://batt.lbl.gov. Brief descriptions of each research area are as follows.

Cathode Development aims to find novel cathode materials and processing methods that offer significant improvements in volumetric and specific energy and/or power over current state of the art materials, like LiCoO2. Current projects include work on the high voltage, high-energy layered/layered or Li rich cathode materials, investigating Li bearing mixed polyanion glasses, investigating polyanions that may cycle more than one Li ion per transition metal ion (e.g., silicates), optimization of ion transport in high-energy composite cathodes, and developing *in situ* reactors designed to investigate solvothermal synthesis reactions in real-time using synchrotron-based tools.

Anode Development involves a significant focus on silicon, which offers ten times the capacity of currently used graphite anodes. Researchers are investigating several forms of Si, including nanowires, nanoparticles, clathrate structures, and others. They are also investigating methods for stabilizing Si and Sn composite negative electrodes, including the use of Cu foam current collectors, atomic layer deposition to stabilize alloy electrodes, and a number of Si/carbon nanocomposite materials. It also involves research on metal-based high capacity Li-ion anodes, layered nanolaminates for use in lithium battery anodes, nanoscale composite hetero-structures and thermoplastic resin binders.

Electrolyte Development includes research efforts focused on expanding the temperature range of cells, additives to stabilize the negative and positive interfaces, development of new overcharge shuttles to further stabilize Li-ion cells, new ionic liquids to enable higher voltage windows, sulfone liquids and sulfate/triflate solids for high voltage electrolytes, bifunctional electrolytes for lithium-ion batteries, interfacial and bulk properties and stability studies and first principles modeling to understand and construct a more stable SEI.

Cell Analysis, Modeling, and Fabrication involve several modeling approaches used to understand cell and fundamental material properties, including ab-initio calculations, macroscopic cell calculations, and finite element simulations. Standard cell making and testing techniques are developed and applied to provide a common evaluation process for new materials. Projects might involve predicting microstructure and performance for optimal cell fabrication, assembly of battery materials and electrodes, predicting and understanding novel electrode materials from first-principles, electrode fabrication and materials benchmarking, and the design and scalable assembly of high density low tortuosity electrodes.

Diagnostics involve the use of advanced diagnostics techniques, such as FTIR, X-ray absorption fine structure (XAFS), X-ray diffraction (XRD, nuclear magnetic resonance (NMR) and other techniques to investigate interfacial and other properties in Li-ion batteries. Sample projects include those using DOE's user facilities, advanced *in situ* diagnostic techniques, study of interfacial processes, *in situ* electron microscopy of electrical energy storage materials, microscopy investigation on the fading mechanism of electrode materials, and NMR and pulse field gradient studies of SEI and electrode structure.

Beyond Lithium-ion Technologies study issues critical to the realization of beyond Lithium-ion technologies. Two of the most promising (Lithium/Sulfur and Lithium/Air) require the use of a lithium metal anode. The main focus is to devise new methods to understand and stabilize lithium metal anodes (against mossy Li formation and dendrites) to bring about leaps in energy density without compromising durability and safety. LBNL, ANL and ORNL have partnered to design a series of projects that utilize recent advances in ceramic electrolyte materials, polymer science, and materials characterization to stabilize lithium metal anodes. Inorganic solid state lithium-ion conductors have been proposed as protective electrolyte layers in a lithium metal cell that contains a second, liquid electrolyte in contact with the cathode. The team is also studying various Li metal protective films and dopants that lead to a stable Li/electrolyte interface and permit long-term and stable cycling. Some projects focus on lithium selenium and selenium sulfur couple and composite electrolytes to stabilize metallic lithium anodes.

The BATT Program regularly solicits new proposals in each of the above-listed areas. BATT Program management regularly accepts unsolicited proposals on any advanced energy storage technology that can significantly advance the state-of-the-art and is appropriate for the R&D focus of the BATT Program. Unsolicited proposals are reviewed separately but by using a process similar to that for the solicited proposals.

VI.B Cathode Development

VI.B.1 Novel Cathode Materials and Processing Methods (ANL)

Michael Thackeray
Argonne National Laboratory

9700 South Cass Avenue
Argonne, IL 60439
Phone: (630) 252-9184; Fax: (630) 252-4176
E-mail: thackeray@anl.gov

Collaborators
ANL: J. R. Croy, D. Kim, R. Benedek, V. G. Pol, S. V. Pol, C. S. Johnson, J. T. Vaughey, K. G. Gallagher,
ANL's ABR 'Voltage Fade' team
APS: M. Balasubramanian, Y. Ren
Industry: Envia, BASF, Toda, LG Chem

Start Date: October 2011
Projected End Date: September 2015

Objectives

- Design high capacity, high-power and low cost cathodes for PHEVs and EVs.
- Improve the design, composition and performance of Mn-based cathodes.
- Explore novel processing routes for advanced electrodes with effective architectural designs.
- Use atomic-scale modeling as a guide to identify, design and understand the structural features and electrochemical properties of advanced cathode materials.

Technical Barriers

- Low energy density
- Poor low temperature operation
- Abuse tolerance limitations

Technical Targets

- 142 Wh/kg, 317 W/kg (PHEV 40 mile requirement)
- Cycle life: 5000 cycles
- Calendar life: 15 years

Accomplishments

- Identified promising electrode compositions and syntheses to achieve high capacity electrodes with stable surfaces and high rate capabilities.
- Identified changes to Li_2MnO_3-like environments as a possible trigger for continued voltage fade on high voltage cycling.
- Evaluated the effect of coatings on voltage fade.

✧ ✧ ✧ ✧ ✧

Introduction

Li_2MnO_3-stabilized composite electrode structures, such as 'layered-layered' $xLi_2MnO_3•(1-x)LiMO_2$ (M=Mn, Ni, Co), 'layered-spinel' $xLi_2MnO_3•(1-x)LiM_2O_4$ and even more complex 'layered-layered-spinel' $y\{xLi_2MnO_3•(1-x)LiMO_2\}•(1-y)LiM_2O_4$ systems are receiving international attention because they can provide rechargeable capacities between 200 and 250 mAh/g between 4.6 and 2.0 V vs. lithium. They offer, today, perhaps the best opportunity to make a significant improvement to the energy output and to improve the abuse tolerance of state-of-the-art, commercial lithium-ion cells in order to meet or exceed the 40-mile electric range targets of PHEVs. These manganese-rich composite cathode structures have to be electrochemically activated above 4.4 V in order to access the high capacity. Unfortunately, this process compromises the rate capability of these electrodes, which also suffer from voltage decay on cycling, thereby compromising the energy and power output of the cells and preventing their implementation in practical systems. This project directly addresses these limitations and challenges. A novel processing route using Li_2MnO_3 as a precursor to synthesize composite electrode structures is being explored. The technique is simple, versatile and seemingly low cost; it offers the possibility of opening the door to wide exploitation and, in particular, of synthesizing and tailoring composite electrode structures, including new systems, thereby enhancing the electrochemical properties of lithium-ion cells to meet the performance targets of PHEVs.

Approach

- Exploit the concept, and optimize the performance, of structurally-integrated, high-capacity electrodes, particularly 'layered-layered' $xLi_2MnO_3•(1-x)LiMO_2$ (M=Mn, Ni, Co) and 'layered-layered-spinel' $y\{xLi_2MnO_3•(1-x)LiMO_2\}•(1-y)LiM_2O_4$ electrodes.
- Explore new processing routes to prepare composite electrodes that provide acceptable capacity, power, and life.
- Design effective surface structures to protect the underlying metal oxide particles from the electrolyte and to improve their rate capability when charged at high potentials.
- Use first principles modeling to aid the design of bulk and surface cathode structures and to understand electrochemical phenomena.

Results

High Capacity $xLi_2MnO_3•(1-x)LiMO_2$ Cathodes. $xLi_2MnO_3•(1-x)LiMO_2$ (M = Mn, Ni, Co) high capacity cathode materials are currently viewed as the most viable options for achieving near-term performance goals for PHEVs. The Li_2MnO_3 component in these composite structures can serve as both a stabilizing agent and a source of 'excess' capacity relative to layered $LiMO_2$ (M = Mn, Ni, Co), materials. A detailed electrochemical study to explore the compositional space and to understand the important and complex role played by the Li_2MnO_3 component for $xLi_2MnO_3•(1-x)LiMn_{0.5}Ni_{0.5}O_2$ electrode materials (x = 0, 0.1, 0.3, and 0.5), was completed.

Figure VI - 3(a-d) show differential capacity plots of $Li/xLi_2MnO_3•(1-x)LiMn_{0.5}Ni_{0.5}O_2$ cells cycled at room temperature over three consecutive voltage windows after an initial activation to 4.7 V. Cycles were conducted at 5 mA/g in order to approach near equilibrium states during charge and discharge.

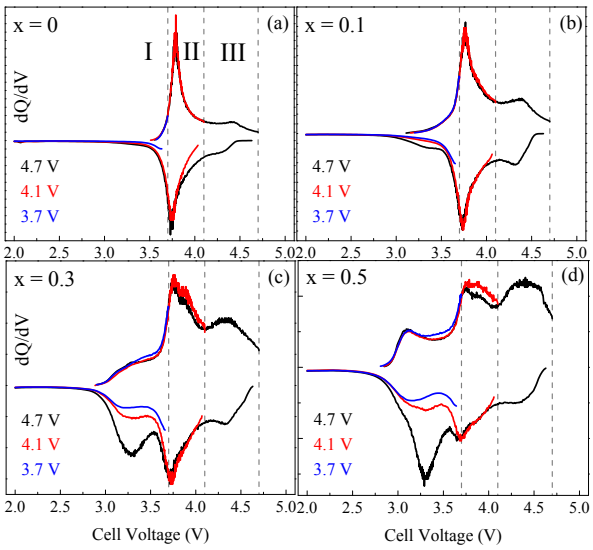

Figure VI - 3: dQ/dV data taken over consecutive voltage windows of 2.0-3.7, 2.0-4.1, and 2.0-4.7 V at 5 mA/g for $Li/xLi_2MnO_3•(1-x)LiNi_{0.5}Mn_{0.5}O_2$ cells with various values of x after activation to 4.7 V. x values are provided at the upper left of each panel; data from each window are color-coded for clarity

It was observed that with increasing Li_2MnO_3 content, x, significant capacity was generated in the low-voltage (2.0-3.7 V) and high-voltage (4.1-4.7 V) regions. Furthermore, a new process developed at ~3.8 V on charge as a consequence of the 'activation' process. From Figure VI - 3b-d, it is evident that some of the capacity extracted above ~4.0 V on charge was not delivered on discharge until ~3.2 V with substantial hysteresis occurring for x = 0.3, and 0.5.

Figure VI - 4a shows the difference in charge and discharge voltages at 50% state-of-charge for the 2.0-4.7 V windows shown in Figure VI - 3(black curves). The hysteresis clearly increases as a function of x. Extended cycling and monitoring of the capacity in each voltage window, as in Figure VI - 3, revealed that the high voltage charge capacity (>~4.0 V) decreased with cycling, concomitant with an increase in the low voltage (<~3.7 V) charge capacity. This low-voltage capacity is directly related to the continuously fading voltage profiles in composite materials and is a strong function of Li_2MnO_3 content (Figure VI - 4b). Furthermore, the data demonstrate that the hysteresis and voltage fade phenomena are correlated.

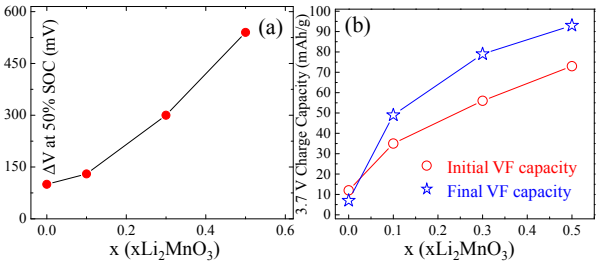

Figure VI - 4: (a) Hysteresis as a function of x measured as the difference between charge and discharge voltages (ΔV) at 50% SOC. (b) Growing capacity associated with the initial (cycle 2, circles) and final (cycle 30, stars) voltage fade of the material (2.0-3.7 V charge capacity) as a function of x

To better understand the structure of xLi_2MnO_3•(1-x)$LiMn_{0.5}Ni_{0.5}O_2$ materials as a function of Li_2MnO_3 content, x, X-ray absorption spectroscopy (XANES, EXAFS) studies were conducted on the as-prepared cathodes. Figure VI - 5a and b show the Mn and Ni K-edge XANES, respectively, of all samples (x = 0, 0.1, 0.2, 0.3) as well as Li_2MnO_3 and NiO references. It was observed that the average oxidation states of Mn and Ni were Mn^{4+} and Ni^{2+} for all values of x, in agreement with the respective references. This implies that substantial ordering occurs between Ni and Mn for all samples and reveals a strong tendency for charge ordering between Mn and Ni.

Figure VI - 6a and b show the corresponding Mn and Ni K-edge EXAFS data, respectively. Several interesting trends appeared in the Mn EXAFS data. Most apparent was the clear decrease in the first-shell Mn-metal correlations at ~2.5 Å (uncorrected for photoelectron wave shift). This trend reveals that the excess lithium in the transition metal layers preferentially orders with manganese on increasing x (Li_2MnO_3 content). The peaks between ~4-6 Å (arrowed) also show a strong shift towards the corresponding peaks of the Li_2MnO_3 reference at x ≥ 0.3, indicating a tendency of the local Mn environment towards that of pure Li_2MnO_3 with increasing x. The Ni K EXAFS data in Figure VI - 6b reveal that the Ni environment of the composite material has stronger $LiMO_2$ character (e.g., Ni-M coordination of ~6) that was relatively unchanged on increasing x with the exception of decreasing intensity at ~4 Å. This peak arises from the exchange of Li and Ni between the layers in these materials, indicating that increasing the Li_2MnO_3 content enhances the layering of the structure. In combination with the Mn EXAFS data of Figure VI - 6a, for which no intensity at 4 Å was observed for any x, it was concluded that Li/Ni exchange occurs predominantly within the $LiMn_{0.5}Ni_{0.5}O_2$ component.

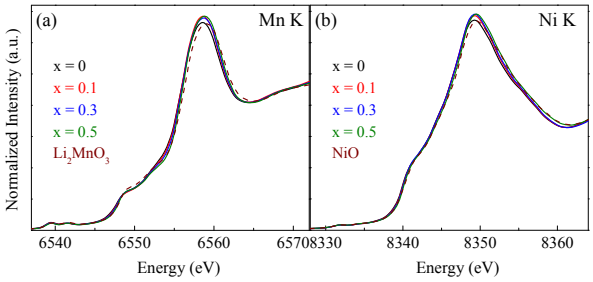

Figure VI - 5: (a) Mn and (b) Ni K-edge XANES data of the as-prepared xLi_2MnO_3•(1-x)$LiMn_{0.5}Ni_{0.5}O_2$ cathodes along with Li_2MnO_3 and NiO reference spectra

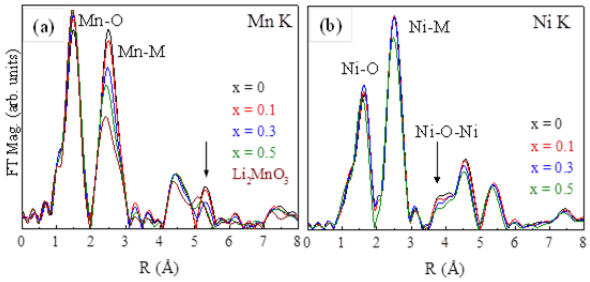

Figure VI - 6: (a) Mn and (b) Ni K-edge EXAFS of the as-prepared xLi_2MnO_3•(1-x)$LiMn_{0.5}Ni_{0.5}O_2$ cathodes for various values of x

Finally, in order to explore how synthesis conditions affect the formation of Li_2MnO_3 and $LiMO_2$ domains and the subsequent electrochemistry, a detailed synthesis study was combined with EXAFS to probe the structures of as-prepared cathodes. Figure VI - 7a and b show Mn and Co K-edge EXAFS, respectively, of $0.5Li_2MnO_3$•$0.5LiCoO_2$ cathode powders annealed via three different routes. All samples were annealed at 550°C in air followed by an annealing at 850°C, also in air. Subsequently, the samples were either 1) allowed to cool naturally in the furnace (uncontrolled), 2) slow-cooled by a programmed temperature profile (controlled), or 3) quenched (quenched). The EXAFS data in Figure VI - 7 reveal that that the local structure of all samples is essentially identical. It is known that voltage fade and hysteresis persist in similar samples prepared via different synthesis routes. Therefore, these data imply that the domain structure within these materials is largely insensitive to synthesis conditions, while charge ordering becomes a dominant driving factor in controlling their structural evolution.

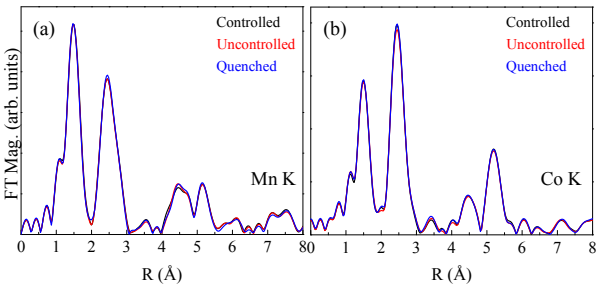

Figure VI - 7: (a) Mn and (b) Co K-edge EXAFS data of $0.5Li_2MnO_3$•$0.5LiCoO_2$ powders prepared under different annealing conditions

Conclusions and Future Directions

Conclusions

- A detailed electrochemical study of xLi_2MnO_3•$(1-x)LiNi_{0.5}Mn_{0.5}O_2$ cathodes has revealed that the voltage fade and hysteresis phenomena are correlated and may be related to the same mechanisms. Furthermore, both voltage fade and hysteresis are a strong function of the Li_2MnO_3 content, each increasing with increasing Li_2MnO_3.
- X-ray absorption data reveal a strong preferential ordering of lithium and manganese with increasing x in xLi_2MnO_3•$(1-x)LiMn_{0.5}Ni_{0.5}O_2$. While the local environment of manganese tends towards that of pure Li_2MnO_3, the local nickel environment remains similar to that of $LiMO_2$. Manganese and nickel EXAFS data combine to reveal that Li/Ni exchange occurs predominantly within the $LiMn_{0.5}Ni_{0.5}O_2$ component.
- EXAFS studies of $0.5Li_2MnO_3$•$0.5LiCoO_2$ synthesized under various conditions reveals that the local, electrochemically-relevant structure of layered-layered materials is largely insensitive to synthesis conditions. Furthermore, all samples showed distinctly different manganese and cobalt environments revealing the composite nature of the materials under all synthesis conditions.

Future Directions

- Continue to explore the complex, critical role played by Li_2MnO_3 and the stabilizing interactions of manganese and nickel in composite cathode structures to optimize structural stability during cycling and capacity/energy generation.
- Explore composite cathode structures with low ($x \leq 0.4$) and high ($x \geq 0.6$) Li_2MnO_3 content with the goal of tailoring the size and stabilization of Li_2MnO_3-like domains.
- Evaluate sonochemical coatings against wet-chemical and atomic layer deposition methods to identify optimum materials for protecting composite particle surfaces.
- Use theory to understand surface degradation in manganese-based cathode materials.

FY 2013 Publications/Patents/Presentations

1. D. Kim, G. Sandi, Jason R. Croy, K. Gallagher, S.-H. Kang, E. Lee, M. Slater, C. Johnson, and M. Thackeray, "Composite 'Layered-Layered-Spinel' Cathode Structures for Lithium-Ion Batteries," *JES* **160**, A31 (2013).
2. J. R. Croy, K. Gallagher, M. Balasubramanian, Z. Chen, Y. Ren, D. Kim, S.-H. Kang, D. Dees, and M. Thackeray, "Examining Hysteresis in Composite xLi_2MnO_3•$(1-x)LiMO_2$ Cathode Structures," *Phys. Chem. C* **117**, 6525 (2013).
3. K. Gallagher, J. R. Croy, M. Balasubramanian, M. Bettge, D. Abraham, A. Burrell, and M. Thackeray, "Correlating Hysteresis and Voltage Fade in Lithium- and Manganese-rich Layered Transition-Metal Oxide Electrodes," *Electrochem. Comm.* **33**, 96 (2013).
4. D. Kim, J. R. Croy, and M. Thackeray, *Comments on* "Stabilizing Layered Manganese Oxide Electrodes for Li Batteries," *Electrochem. Comm.* **36**, 103 (2013).
5. J. R. Croy, K. Gallagher, M. Balasubramanian, B. Long, and M. Thackeray, "Quantifying Hysteresis and Voltage Fade in xLi_2MnO_3•$(1-x)LiMn_{0.5}Ni_{0.5}O_2$ Electrodes as a Function of Li_2MnO_3 Content," (submitted).
6. M. M. Thackeray, D. Kim and J. Croy, "Electrode Structures and Surfaces for Li Batteries," USPTO, Filed November 19, 2012.
7. M. M. Thackeray, C. S. Johnson and S.-H. Kang, "Electrode Structures and Surfaces for Li Batteries," USPTO, Filed January 14, 2013.
8. M.M. Thackeray, "Development of High-Capacity Cathode Materials with Integrated Structures," *2013 DOE Annual Peer Review Meeting,* May 2013, Washington, DC.
9. J. R. Croy, K. Gallagher, M. Balasubramanian, B. Long, M. Thackeray, T. Burrell, D. Dees, Z. Chen, D. Abraham, M. Bettge, Y. Ren, "Structural and Electrochemical Insights on the Mechanisms of Voltage Fade and Hysteresis in Composite xLi_2MnO_3•$(1-x)LiMO_2$ Electrodes," *ABAA 6,* Argonne, IL, September 10, 2013 (Invited).
10. J. R. Croy, K. Gallagher, M. Balasubramanian, B. Long, M. Thackeray, "The Next Generation of Lithium-Ion Batteries: Challenges and

Opportunities," Ball State University, Muncie, Indiana, September 5, 2013 (Invited).

11. M. M. Thackeray, "Recent Developments in Lithium Battery Materials Research," Presentations to Samsung SDI, LG Chem (Korea); Nissan Research Center, Toda Kogyo (Japan), August 30 - September 2, 2013.
12. M. M. Thackeray, "Designing Energy Storage Materials: Intuition vs. Computation," *The Materials Genome Initiative Grand Challenges Summit,* Rockville, Maryland, June 25-26, 2013.
13. M. M. Thackeray, J. R. Croy, D. Kim, B. R. Long, V. G. Pol, S. V. Pol, M. Balasubramanian, Y. Ren and R. Benedek, "Design and Evaluation of High Capacity Cathodes," *DOE Annual Merit Review,* Vehicle Technologies Program, Arlington, Virginia, May 13-17, 2013.
14. J. R. Croy, K. Gallagher, M. Balasubramanian, B. Long, M. Thackeray, Challenges of Composite, High-Capacity, Li-Ion Cathodes," *Advanced Photon Source User's Meeting,* Argonne National Laboratory, IL, May 7, 2013 (Invited).
15. M. M. Thackeray, J. R. Croy, L. Trahey, V. G. Pol, M. Balasubramanian, K. G. Gallagher, J. Wen, M. Krumpelt, M. Chan, S. Kirklin, D. Miller, C. Wolverton, "Confronting the Challenges of High-Capacity Cathodes and Anodes for Lithium Batteries," *International Battery Association Meeting,* Barcelona, Spain, March 10-15, 2013.
16. J. R. Croy, D. Kim, K. Gallagher, M. Balasubramanian, Y. Ren, M. Thackeray, "Structural Stabilization of LMR-NMC Composite Cathodes," *U.S. DRIVE 2013,* Argonne National Laboratory, IL, 24 January, 2013.
17. J. R. Croy, S. Pol, M. Balasubramanian, D. Kim, S.-H. Kang, M. Thackeray, "High Capacity Lithium-Metal-Oxide Electrodes: Challenges and Opportunities," *John B. Goodenough Symposium,* Austin, TX, October 26, 2012.

VI.B.2 *In situ* Solvothermal Synthesis of Novel High Capacity Cathodes (BNL)

Feng Wang
Brookhaven National Laboratory (BNL)

Sustainable Energy Technologies Department
Upton, NY, 11973
Phone: (631) 344-4388; Fax: (631) 344-7905
E-mail: fwang@bnl.gov

Patrick Looney
Brookhaven National Laboratory (BNL)
Sustainable Energy Technologies Department
Upton, NY, 11973
Phone: (631) 344-3798; Fax: (631) 344-7905
E-mail: jlooney@bnl.gov

Start Date: October 2011
Projected End Date: November 2015

Objectives

- Develop low-cost cathode materials that offer high energy density (>660 Wh/kg) and electrochemical properties (cycle life, power density, safety) consistent with USABC goals.

Technical Barriers

Present day Li-ion batteries are incapable of meeting the 40-mile all-electric-range within the weight and volume constraints established for PHEVs by DOE and the USABC. Higher energy density cathodes are needed for Li-ion batteries to be widely commercialized for PHEV applications.

The development of new, safer lithium batteries requires new tools to better understand the physical and chemical processes that occur during cycling and the ability to predict and ultimately control the key electrochemical properties such as capacity, durability (calendar and cycle life), abuse tolerance (safety characteristics) and cost.

Technical Targets

- Higher energy density cathodes
- Lower cost

Accomplishments

- Developed *in situ* reactors and time resolved XRD techniques specialized for studying hydrothermal/solvothermal, ion-exchange, and solid-state synthesis reactions.
- Determined optimal procedures for synthesis of high-capacity Cu-V-O cathodes *via in situ* studies.
- Identified lithium electrochemical reaction and degradation mechanisms of Cu-V-O cathodes *via in situ* XAS, XRD and *ex situ* TEM.
- Developed procedures for synthesis of one new class of Cu-V-O compound, using both hydrothermal and solid-state reactions.
- Demonstrated feasibility of using hydrothermal-based ion exchange to prepare polyanion-type cathodes, and explored reaction pathways of ion exchange processes using a newly developed *in situ* reactor.

✧ ✧ ✧ ✧ ✧

Introduction

Despite considerable interest in the development of new cathodes for lithium ion batteries, only a small number of known materials show real promise for achieving significant improvement in capacity and/or a reduction in cost. The preparation of new compounds or materials with unique properties often relies on trial and error as there are a variety of synthesis parameters (precursor concentration, temperature, pressure, pH value, cation choice and reaction time) that can have a strong influence on the material properties (morphology, particle size, crystal structure) and electrochemical performance (e.g., capacity, rate capability, and durability). Most solution-based reactions are carried out in a sealed autoclave and therefore the reactor is a black box – the inputs and outputs are known, but little is known about intermediate phases and the overall reaction pathway. *In situ, real-time* probes of synthesis reactions can provide the details of reactions, elucidating intermediate phases and how temperature, pressure, time and the precursor concentrations affect the reaction pathways. The results of such studies enable strategies to optimize synthesis reactions, particularly the formation of materials of desired phases and properties. With a more fundamental understanding of

the correlation between synthesis conditions, crystallization processes, and material properties, a more rational design of advanced lithium electrode materials should emerge.

Approach

In this effort, specialized *in situ* reactors were developed to investigate solvothermal and other solution-based synthesis reactions in real-time using synchrotron X-ray diffraction (XRD) and absorption spectroscopy (XAS) techniques, with which crystal growth and changes in chemical bonds can be monitored while leaving the reaction undisturbed. This approach provides a real-time measurement of how reaction conditions affect nucleation and crystallization, bonding, particle size, morphology and defect concentration. In addition, *in situ* measurements reveal the formation of intermediate and short-lived phases formed during the reaction without the need for quenching. These new tools and insights are being used to prepare novel high-energy cathodes.

The structural and electrochemical properties of synthesized materials are evaluated *via* synchrotron XRD combined with Rietveld refinement, and various electrochemical measurements. The structural/chemical evolution of electrodes during cycling is systematically investigated using *in situ*, *in operando* synchrotron XRD and X-ray absorption near-edge (XANES) and extended fine structure (EXAFS) and advanced TEM techniques, which help to identify the mechanism(s) responsible for the capacity fade and provide guidance to further optimizing the synthesis.

Results

Synthesis of high-capacity Cu-V-O cathodes

Among the wide variety of Cu-based vanadium oxides, ε-$Cu_{0.95}V_2O_5$ (ε-CVO) is one of the few promising cathode materials with high capacities (~700 Wh/kg or above). Building on our previous work (in FY12) in which several hydrothermal approaches were identified for making ε-CVO compounds, the effort in FY13 focused on optimizing the synthesis procedures *via in situ* synthesis studies, by which the precursors, reducing agents and reaction conditions were systematically evaluated.

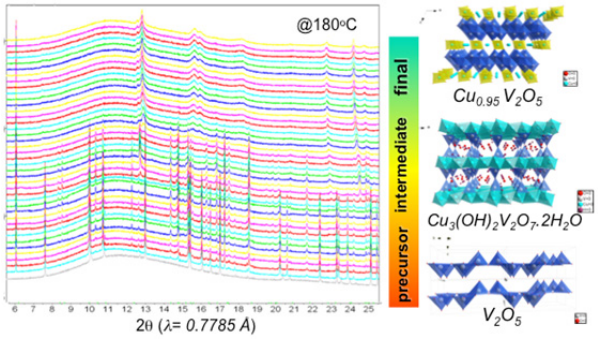

Figure VI - 8: *Time-resolved* XRD patterns acquired during *in situ* synthesis of ε-CVO

Figure VI - 8 shows one of the results on phase evolution during *in situ* synthesis of ε-CVO, using the procedure:

$$Cu(NO_3)_2 \cdot 3H_2O \text{ and } V_2O_5 + R.A \rightarrow Cu_xV_2O_5 \quad (1)$$

The pure ε-CVO phase in a capillary reactor was obtained by tuning the Cu/V ratio and concentration of the reducing agent (R.A.) at a temperature as low as 180°C. The intermediate phase, $Cu_3(OH)_2V_2O_7 \cdot 2H_2O$, was found to be a crucial step towards forming the desired final product. This phase was stable at low temperatures and, depending on the reaction conditions, either transformed into the pure ε-CVO phase, or a mixture with others (α-CuV_2O_6, Cu, …) at high temperatures. The exploration of all the possible reaction paths at real working conditions is critical for obtaining important information on optimizing synthesis and the ability to 'dial in' the desired phases.

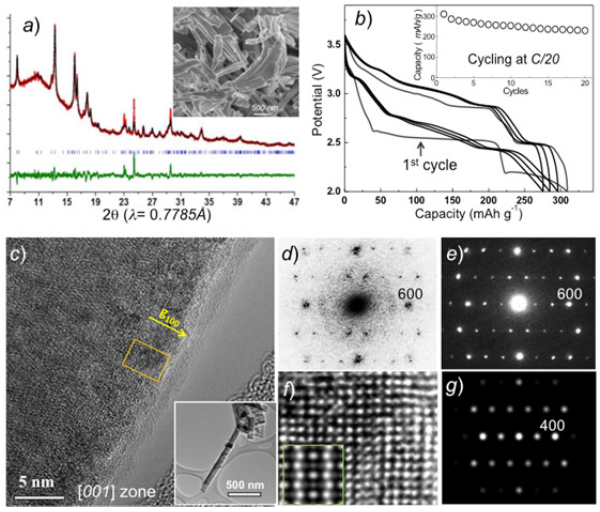

Figure VI - 9: Structural and electrochemical properties of ε-CVO powder. (a) XRD pattern (with refinement), and morphology (by SEM; inset), (b) galvanostatic cycling profiles and cyclability (inset), (c) HRTEM imaging, (d) FFT of (c), (e) e-diffraction pattern, (f, g) simulations

After determining the optimal reaction conditions and process, large amount of ε-CVO powder was

synthesized using an autoclave reactor, and then examined with synchrotron XRD (Figure VI - 9a). The as-synthesized material has a high degree of crystallinity and purity, and good electrochemical performance, as shown by its high capacity (~300 mAh/g) and reasonable cycling stability, (Figure VI - 9b). Detailed structural analysis of individual CVO nanorods, obtained using high-resolution TEM (HRTEM) imaging and electron diffraction (Figure VI - 9c-g), it was found that despite the good match of XRD pattern of the synthesized material to the monoclinic ε-$Cu_{0.95}V_2O_5$ phase (Figure VI - 9a), the local structural ordering is much different as a result of Cu-deficiency.

Li reaction mechanisms in Cu-V-O. Synchrotron XRD and TEM were used to examine the structural and morphological changes of ε-CVO as a result of lithium reaction (Figure VI - 10). With lithiation, long-range ordering in ε-CVO was lost due to the Cu extrusion, and not recovered with delithiation although the extruded Cu migrates back into the structure. This newly formed structure (after one cycle) appeared to be stabilized according to the similarity in the XRD patterns of electrodes subject to different cycles. This observation may explain the "multiple-plateau" profile in the 1st cycle, and repeatable, "slopy" curves in the following cycles (Figure VI - 9b).

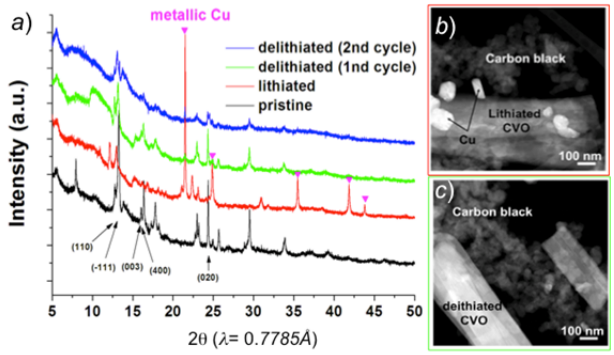

Figure VI - 10: Structural change of ε-CVO with lithium reactions, via (a) XRD, (b, c) dark field images

Due to the loss of long-range ordering with (de)lithiation, it is hard to determine the details of structural change in ε-CVO by XRD alone. To this end, detailed information on redox of Cu, V, and short-range ordering with Cu extrusion/insertion was obtained, *via* near-edge spectra (XANES) and extended fine structure (EXAFS); some of the results are given in Figure VI - 11. Cu and V were reduced at different lithiation stages, as illustrated in Figure VI - 11a. The $Cu^{2+/1+}$ reduction proceeds *via* solid solution, followed with displacement ($Cu^{1+/0}$), and concomitant $V^{5+/4+/3+}$ reduction. One set of V K-edge XANES spectra is given in Figure VI - 11b, in which the gradual edge shift to lower energies indicates the reduction of V with lithiation and correspondingly, the amplitude increase of V-O peak in the Fourier transform of EXAFS tells that initially distorted VO_6 octehedra become more symmetric due to Li insertion/Cu extrusion (Figure VI - 11c.)

The redox of Cu and V at different lithiated stages was illustrated in Figure VI - 11c started with $Cu^{2+/1+}$ reduction (*via* solid solution; state I'), followed with displacement ($Cu^{1+/0}$; II'), and $V^{5+/4+/3+}$ reduction (II, III). The VO_6 octahedra, initially distorted, become highly symmetric with Li insertion/Cu extrusion. Our studies also suggested the gradual Cu, V loss in ε-CVO electrodes should be the main cause of the capacity decay, which might be alleviated by surface coating.

Synthesis of new Cu-V-O compound. A new class Cu-V-O compound (α-CVO) was synthesized using hydrothermal (HT) reactions typically *via* the route:

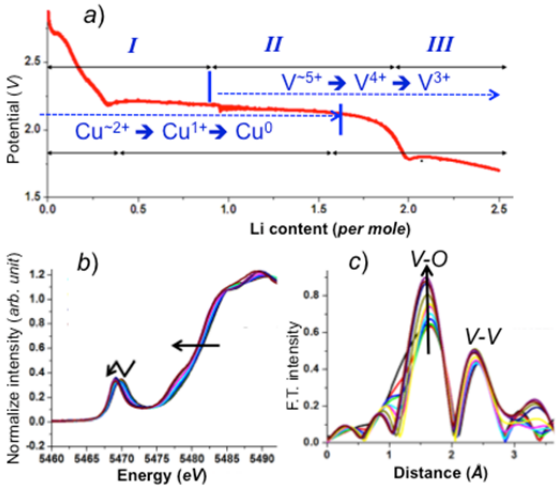

Figure VI - 11: Redox of V, Cu, and local structural re-ordering in ε-CVO by *in situ* XAS. (a) voltage profile, (b) V K-edge XANES spectra, and (c) Fourier transform (F.T.) of the V K-edge EXAFS

$$Cu(NO_3)_2+NH_4VO_3+R.A. \rightarrow \alpha\text{-}CuVO \quad (2)$$

The synthesis reaction at certain conditions, i.e., Cu/V ratio, pH value, and concentration of reducing agent, leads to the formation of an intermediate phase at low temperatures, and the final product of α-CVO phase at about 200°C. According to our structural analysis, this α-phase is promising for use as cathode due to its unique structure, with a 3D V-O framework and open channels for Cu-ion and Li-ion transport. The as-synthesized powder is composed of μm-sized particles, with uniform Cu, V elemental distribution across individual particles (Figure VI - 12a,b).

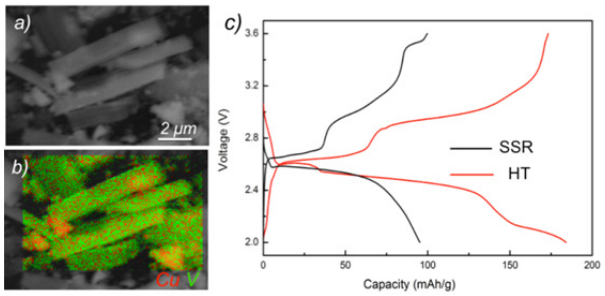

Figure VI - 12: Morphology and electrochemical properties of α-CVO. (a, b) SEM image and EDX mapping, (c) galvanostatic voltage profiles

Solid-state reaction (SSR) was also used to synthesize the α-phase; this material has similar crystal structure but larger particle size. Typical voltage profiles from electrochemical tests of the synthesized powders (by HT and SSR) at C/20 are provided in Figure VI - 12c. The long single plateau observed at about 2.5 V in the discharge curves suggests that the Cu displacement reaction should be dominant. But the reaction during charging appears to be asymmetric, as indicated by two plateaus. In this preliminary electrochemical test, a moderate capacity (of ~185 mAh/g) was obtained in α-CVO grown by HT, which, however, exhibits almost 2x higher capacity than that by SSR. Further performance improvement may be achieved *via* size reduction.

Synthesis of polyanion cathodes. Hydrothermal based methods for preparing polyanion-type cathodes were explored, either *via* direct chemical reaction or through ion exchange *via* lithium substitution in iso-structural Na-containing precursors in an aqueous solution. Synthesis of fluorophosphates $Li_xNa_{2-x}MnPO_4F$ and $Li_xNa_{1.5-x}VPO_5F_{0.5}$ *via* ion exchange was typically performed in a sealed autoclave at elevated temperatures, using Na_2MnPO_4F, $Na_{1.5}VPO_5F_{0.5}$ as precursors, LiBr as Li source and 1-hexanol as solvent. The extent of exchange was maximized *via* tuning reaction conditions, such as temperature and the concentration of Li sources.

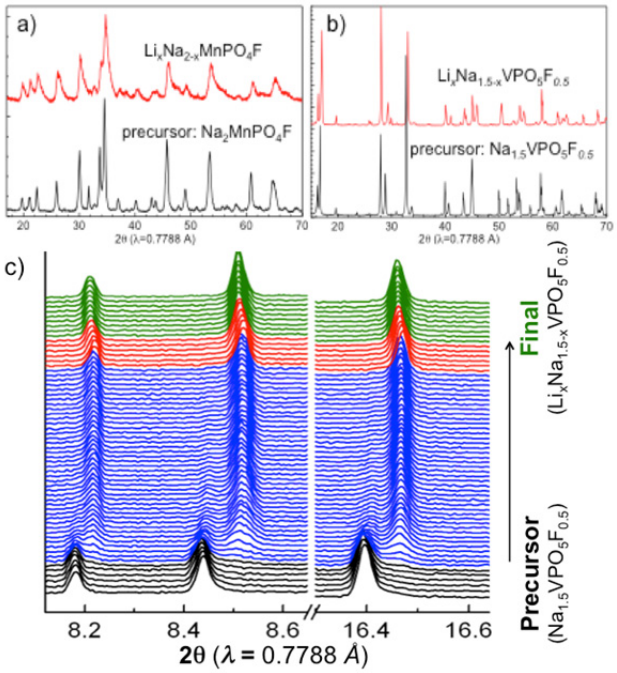

Figure VI - 13: Structural characterization of polyanion-type materials synthesized *via* hydrothermal ion exchange. (a,b) XRD patterns of precursors and Li-exchanged final products, (c) time-resolved XRD patterns from ion exchange process in $Na_{1.5}VPO_5F_{0.5}$

In Figure VI - 13a, the XRD patterns of synthesized $Li_xNa_{2-x}MnPO_4F$ and $Li_xNa_{1.5-x}VPO_5F_{0.5}$ exhibit similar structures as their precursors but smaller volumes. Subtle structural changes, and possibly a reduction in particle size, are suggested by the change in the relative intensity and broadening of diffraction peaks. The results demonstrate the feasibility of using ion exchange to prepare metastable phosphates which are mostly inaccessible by direct chemical reactions.

A new type of *in situ* reactor was developed for studying ion-exchange reactions and used for studies of the structural change in single-crystalline, μm-sized $Na_{1.5}VPO_5F_{0.5}$ particles throughout the entire Li exchange process. Time-resolved XRD patterns (Figure VI - 13c) show a gradual phase transformation (blue region) occurred in the early stage, followed by solid solution (red) and then stabilization of a final phase (green), which suggests a complicated reaction process with more than one phase involved. *In situ* measurements of the phase transformations and reaction kinetics during ion exchange of $Na_{1.5}VPO_5F_{0.5}$ have also been made.

Conclusions and Future Directions

In FY13, *in situ* reactors and time resolved XRD techniques were developed and utilized for studying materials made via hydrothermal, solvothermal, ion exchange, and solid-state reactions. It was shown that *in situ* studies are crtical for understanding synthesis reaction mechanisms and developing procedures for preparing compounds of desired phases and material properties. After optimization of reaction conditions, high-quality ε-$Cu_{0.95}V_2O_5$ materials were synthesized and the structural and electrochemical properties were evaluated. Li reaction process and possible mechanisms responsible for poor cycling stability of this material were also identified. In addition, a new class of Cu-V-O compounds was synthesized, and the feasibility of synthezing polyanion cathodes *via* ion exchange was also established.

In FY14, the work on ε- $Cu_{0.95}V_2O_5$ cathodes will be completed and efforts will be extended to the second Cu-V-O phase to improve the purity and yield, and to complete the evaluation of its structural and electrochemical properties. Hydrothermal based methods will be further explored, either *via* direct chemical reaction or through ion exchange, for preparing ternary and/or quaternary Li-V-PO_4(-*X)* type cathodes. Also opportunities for collaborating with theory efforts will be explored, wherein kinetic and dynamic parameters measured through *in situ* synthesis studies may be compared to calculations or direct input for design of new materials.

FY 2013 Publications/Presentations

1. "*In situ* Solvothermal Synthesis of Novel High Capacity Cathodes," *DOE Annual Peer Review Meeting*, May 13-17, 2013, Washington, DC.
2. F. Wang, Q. Wang, N.A Chernova, M.S. Whittingham, J. Graetz, "*In situ* Studies of Cathodes for Li-ion Batteries by Simultaneous Quick X-Ray Absorption/Diffraction Spectroscopy (QXAS/XRD)," *MRS Fall Meeting*, Nov. 26-30, 2012. Boston. (Oral).
3. F. Wang, X. Wang, S-W. Kim, J. Bai, J. Graetz, "Development of High-energy Cathodes *via in situ* Solvothermal Synthesis," *MRS Spring 2013 meeting*, April1-5, 2013, San Francisco. (Poster)
4. F. Wang, J. Bai, S-W. Kim, X. Wang, "Development of High-Energy Cathodes via *In situ* Solvothermal Synthesis," *ECS 223rd Meeting*, May 12 - 16, 2013, Toronto, Canada. (Oral)
5. F. Wang, S-W. Kim, J. Bai, X. Wang, L. Wu, Y. Zhu, and J. Graetz, "*In situ* studies of synthesis and lithium reaction of high-capacity electrodes for Li-ion batteries," *SPIE Meeting*, April 29 – May 3, 2013. Baltimore (Invited).

VI.B.3 Design of High Performance, High Energy Cathode Materials (LBNL)

Marca Doeff
Lawrence Berkeley National Laboratory

Environmental Energy Technologies Division
Berkeley, CA 94720
Phone: (510) 486-5821
E-mail: mmdoeff@lbl.gov

Start Date: October 2011
Projected End Date: September 2015

Objectives

- To develop high energy, high performance cathode materials based on Ti-substituted NMCs and composites of $LiNi_{0.5}Mn_{1.5}O_4$ and coated powders, using spray pyrolysis and other synthesis techniques.
- To understand surface and bulk structural properties of Ti-NMCs that lead to enhanced energy densities.

Technical Barriers

The cost of vehicular batteries is too high and the energy density needs to be improved. Cost on a $/kWh basis will be lowered if higher energy density can be obtained without adversely affecting cycle life. However, the performance of high-energy high voltage electrode materials like $LiNi_{0.5}Mn_{1.5}O_4$ needs to be improved by reducing its reactivity with the electrolyte. Alternatively, higher utilization of NMC cathode materials could lead to higher energy density, provided cycling issues can be successfully addressed.

Technical Targets

- Explore feasibility of increasing utilization of NMCs by partial Ti-substitution of Co and using higher voltage cutoffs during cycling.
- Understand origins of Ti-substitution effects in substituted NMCs.
- Use simple one-step synthesis procedures like spray pyrolysis to prepare cathode materials with uniform spherical particle morphologies.
- Prepare materials with protective layers on particle surfaces or composite materials consisting of a lower voltage material on surfaces of a higher voltage material, using spray pyrolysis and infiltration techniques.

Accomplishments

- Successfully synthesized high performance $LiNi_{0.5}Mn_{1.5}O_4$ cathode materials by spray pyrolysis
- Demonstrated successful coating of $LiNi_{0.5}Mn_{1.5}O_4$ with an Al_2O_3 target using atomic layer deposition (ALD)
- Observed and characterized surface reconstruction in baseline and Ti-substituted NMCs as a function of electrochemical history
- Successfully transferred Ti-NMC work to the new ABR program, with goal of characterizing materials in full cells.

✧ ✧ ✧ ✧ ✧

Introduction

Achieving DOE cost and energy goals for vehicle batteries based on Li-ion technologies requires improvement to existing cathode materials. Higher energy density can be achieved either by replacing conventional cathodes with high voltage materials such as $LiNi_{0.5}Mn_{1.5}O_4$, or by increasing the utilization of NMC ($LiNi_xMn_xCo_{1-2x}O_2$) cathodes. At present, either approach compromises the cycle life of the device, because of increased reactivity of the electrolytic solutions and/or the instability of the electrodes at high states-of-charge (particularly in the case of the NMCs). It was recently shown that partial Ti-substitution in NMCs improved the practical capacities as well as the cycling retention when cells containing the materials were repeatedly charged to 4.7V, in comparison to the baseline unsubstituted materials. The origins of this improvement are, as yet, unknown, although it was noted that Ti-substitution substantially reduced the first cycle irreversibility, resulting in improved capacity on the subsequent discharge. Work carried out this year was directed towards understanding surface and bulk structural changes occurring during high voltage cycling of NMCs using a variety of synchrotron radiation and electron microscopy techniques (in collaboration with A. Mehta, D. Nordlund and T.-C. Weng at SSRL and H. L. Xin at BNL). Experiments directed towards characterization of changes in the surface structures of baseline and Ti-substituted NMCs did not reveal substantial differences suggesting that the improvement is correlated to changes in bulk structural and electrochemical characteristics. To investigate this further, a collaboration with M. Asta (U.C. Berkeley)

was initiated this year to carry out first principles modeling on NMCs to understand these effects better.

$LiNi_{0.5}Mn_{1.5}O_4$ cycles stably in lithium half-cells, although coulombic efficiencies in the first few cycles are low. This arises from irreversible side reactions of the electrolyte and other cell components due to the high operating voltage (4.7V vs Li^+/Li). To ameliorate these effects, it is important to minimize the surface area of the spinel phase. Spray pyrolysis synthesis results in ideal morphologies of large, uniform spherical particles with low surface reactivity. Under some conditions, hollow particles are produced, which can be simultaneously filled and coated with a second, less reactive phase like $LiFePO_4$ by an infiltration process. Solid particles can also be coated with an ion-conducting, electronically insulating phase by a variety of techniques, including atomic layer deposition (ALD). Some effort this year was directed towards exploring the feasibility of using an Al_2O_3 target and an ALD process to deposit thin coatings on spray pyrolyzed $LiNi_{0.5}Mn_{1.5}O_4$ (collaboration with Chunmei Ban, NREL).

Approach

Coprecipitation methods are used to synthesize NMC materials and spray pyrolysis is used for $LiNi_{0.5}Mn_{1.5}O_4$. For the latter, a precursor solution is sprayed through an ultrasonic nozzle into a heated furnace tube. Particle characteristics such as size, size distribution, morphology, porosity, etc. can be controlled by varying experimental conditions including nozzle frequency, type and concentration of precursors in solution, the use of additives, temperature, and post-production thermal treatments. In some cases, hollow particles are produced, which can be filled and coated simultaneously by an infiltration process. Particles are also optionally coated postproduction by atomic layer deposition using an Al_2O_3 target.

Electrochemical characterization is carried out in lithium half-cell configurations. A variety of physical techniques are used to characterize materials before and after electrochemical cycling. Hard and soft x-ray absorption spectroscopy (XAS) experiments carried out at SSRL are used to probe oxidation states of transition metals at particle surfaces and in the bulk as a function of their electrochemical history and *in situ* and *ex situ* synchrotron XRD experiments are performed to follow bulk structural changes as a function of state-of-charge. High-resolution transmission electron microscopy (HR-TEM) and electron energy loss spectroscopy (EELS) at the National Center for Electron Microscopy (NCEM) at LBNL is used to characterize the structure and oxidation states of particle surfaces.

Results

$LiNi_{0.5}Mn_{1.5}O_4$. Either ordered (space group $P4_332$) or disordered (space group *Fd3-m*) spinels can be produced by spray pyrolysis or combustion synthesis techniques depending on details of the thermal treatments. Ordered $LiNi_{0.5}Mn_{1.5}O_4$ samples free of Mn^{3+} (judging by the lack of 4V capacity) were successfully synthesized, although the cycling behavior is inferior to that of the disordered spinel containing a few percent of Mn^{3+}. The reason for the poorer performance is not entirely clear, but *in situ* and *ex situ* synchrotron XRD experiments show differences in the phase behaviors as a function of state-of-charge, with a much larger solid solution region observed for the *Fd3-m* spinel (Figure VI - 14).

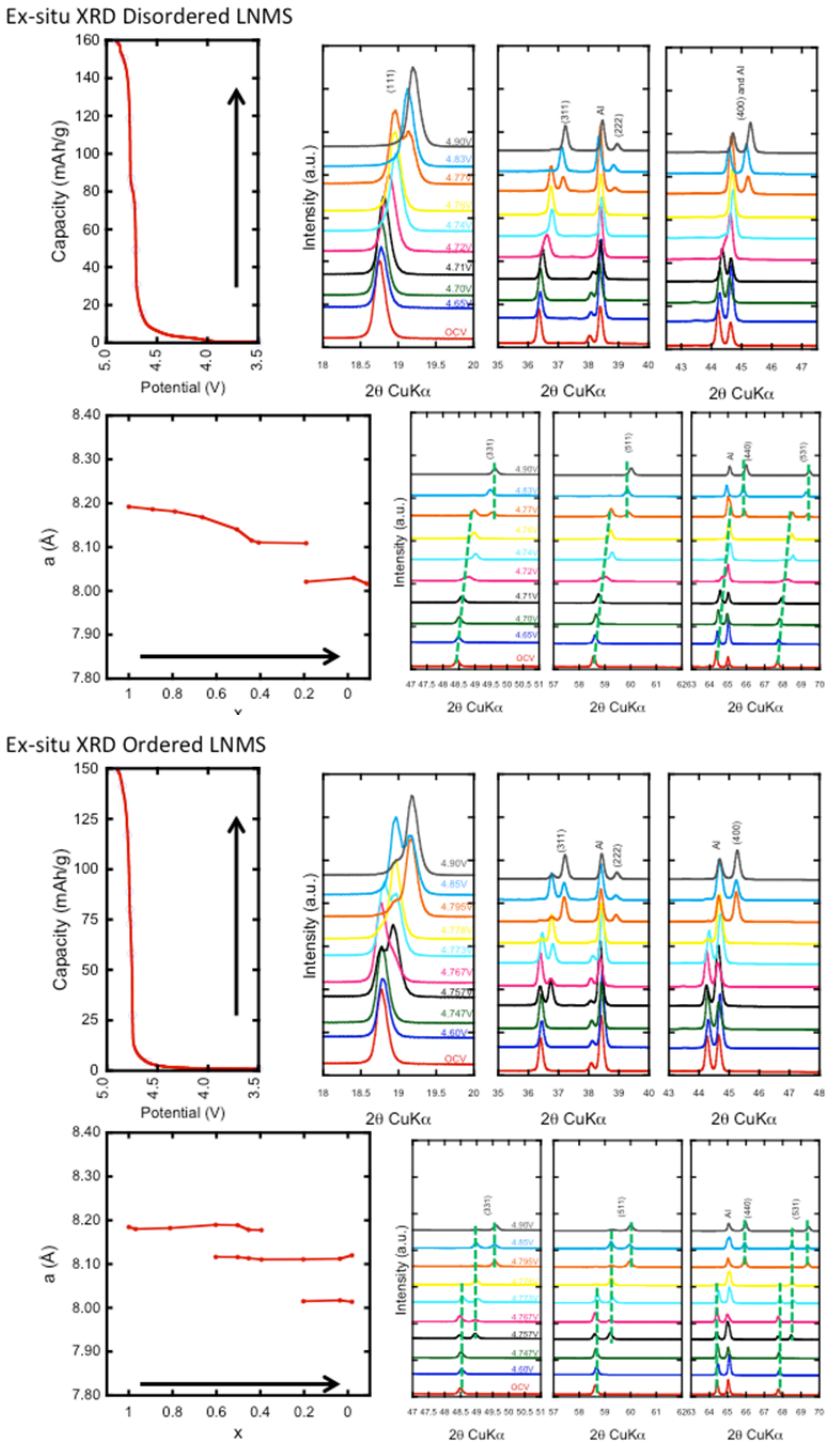

Figure VI - 14: Charge profiles, *ex situ* synchrotron XRD patterns and lattice parameters as a function of state-of-charge of disordered (top) and ordered (bottom) $LiNi_{0.5}Mn_{1.5}O_4$ cathodes

Figure VI - 15 shows initial results on an ALD-coated sample of $LiNi_{0.5}Mn_{1.5}O_4$ made by spray pyrolysis. An Al_2O_3 target was used for the deposition of the very thin (<1nm) layer on the particle surfaces. The coating does not adversely affect redox characteristics of the material although the Mn^{3+} content of this spray-pyrolyzed sample is higher than desirable. Once this procedure has been optimized, cycling will be carried out on the best samples to determine if coulombic efficiencies are improved.

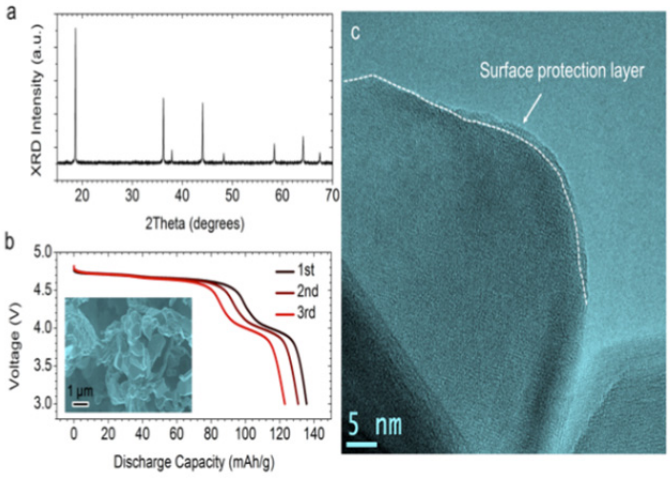

Figure VI - 15: XRD pattern (top left), discharge profiles and SEM image (bottom left) and HR-TEM image of a spray pyrolysed $LiNi_{0.5}Mn_{1.5}O_4$ cathode material coated by an ALD process

NMC characterization. Partial substitution of Ti for Co in NMCs appears to improve practical discharge capacity and cycling retention during cycling to high voltages (4.7 V) provided that the substitution level is kept below 4%, although capacity fading and impedance rise is still observed. Interestingly, impedance also increases upon extended electrolyte exposure without electrochemical cycling (Figure VI - 16).

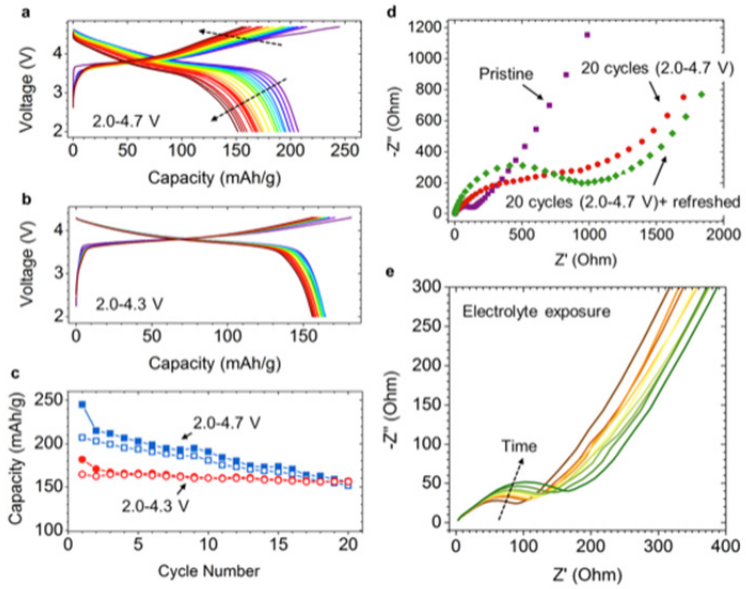

Figure VI - 16: Cycling profiles between 2.0-4.7V (top left), 2.0-4.3V (middle left) and capacity as a function of cycle number (bottom left) for Li half-cells containing an NMC cathode. Nyquist plots show increased cell impedance upon cycling to high voltages (top right) and upon extended exposure to electrolyte (bottom right)

Soft XAS and EELS investigations show unequivocally that a layer several nanometers thick containing reduced transition metal oxides forms on particle surfaces during high voltage cycling. Interestingly, this layer is also present on samples that have been exposed to electrolyte but have not been cycled, although it is thinner (Figure VI - 17).

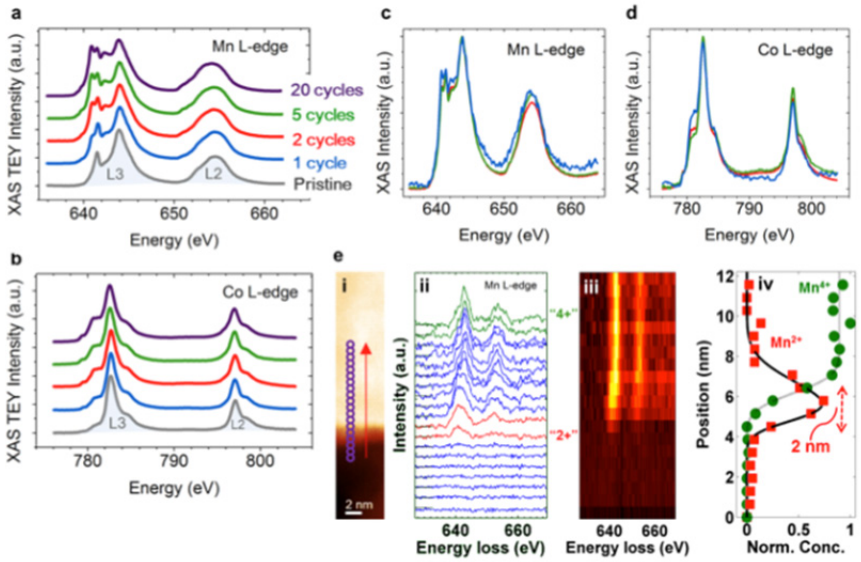

Figure VI - 17: Surface reconstruction and chemical evolution after charge-discharge cycles. (a) Mn L-edge XAS/TEY spectra. (b) Co L-edge XAS/TEY spectra. (c) Mn L-edge XAS after 5 charge-discharge cycles. (d) Co L-edge XAS after 5 charge-discharge cycles in the AEY (blue), TEY (red) and FY (green) modes. (e) EELS line scan profile for an NMC particle along the <001> direction

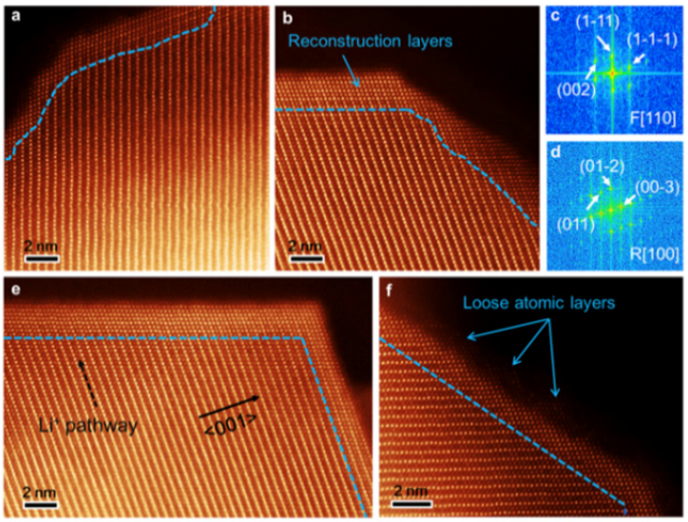

Figure VI - 18: Atomic resolution ADF-STEM images of NMC materials with electrolyte exposure and charge-discharge cycles. (a) NMC particle after electrolyte exposure. (b) NMC particle after 1 cycle. (c and d) correspond to the FFT results of the reconstruction shell and NMC layered structure in (b), respectively. (e) Orientation effects on the surface reconstruction shell. (f) NMC particle with loose atomic layers after 1 cycle

Atomic resolution annular dark film imaging (ADF)-STEM experiments show that the reconstructed layer on the particle surface has a rock salt structure, with a few atomic layers of spinel bridging between the surface and the bulk (Figure VI - 18). A loose atomic layer containing LiF in an organic matrix is also present on some surfaces as verified by STEM-EELS experiments (Figure VI - 19) and varies in thickness depending on the facet orientation. Surface reconstruction primarily occurs along lithium diffusion channels. This suggests that tailoring particle morphologies appropriately may minimize losses due to the surface reconstruction.

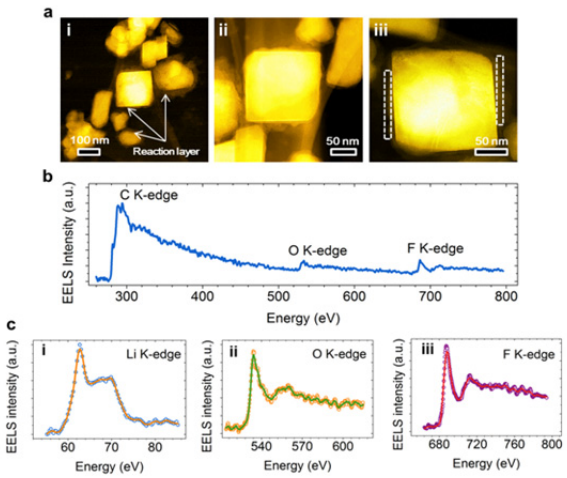

Figure VI - 19: STEM/EELS analysis of surface reaction layer (a) STEM image. (b) Broad EELS scan. (c) Li K-edge. (d) O K-edge. (e) F K-edge

Conclusions and Future Directions

Surface reconstruction due to electrolyte exposure is responsible for the first cycle inefficiencies observed in NMC cells. Upon cycling, the rock salt layer becomes thicker, resulting in increased impedance and capacity loss. Although both first cycle efficiencies and capacity retention are better in Ti-substituted NMCs than in baseline materials, there appear to be no significant differences in the surface reconstruction phenomena observed in these two types of materials. This strongly suggests that bulk effects are responsible for the improved performance of the Ti-NMCs. For example, Ti-substitution results in larger initial unit cell volumes, which change less upon delithiation than the analogous bulk materials. This may be partly responsible for the improved high voltage cycling. A collaborative effort with M. Asta at UC Berkeley, involving first principles modeling of the NMCs, was initiated this year to elucidate effects of Ti substitution on bulk properties of NMCs.

Most of the experimental portion of the Ti-NMC work has been transferred to the ABR program. For this project, synthesis of the Ti-NMCs will be optimized and scaled up, and an industrial partner (Farasis Energy, Inc.) will test the materials in full cells. A variety of diagnostic techniques (including ones first developed under BATT and described in this report) will be used to assess failure modes.

Spray pyrolysis synthesis of $LiNi_{0.5}Mn_{1.5}O_4$ cathode materials will continue under the BATT program. By varying the synthesis conditions, both hollow and solid spherical particles will be produced. Hollow particles will be filled and coated with a second electro-active phase in a single infiltration step. The coating of solid particles with a protective thin layer by ALD and other processes will be optimized. These materials will be evaluated in lithium half-cells to determine whether either or both of these approaches result in improved coulombic efficiencies.

FY 2013 Publications/Presentations

1. "Design of High Performance, High Energy Cathode Materials," *DOE Annual Peer Review Meeting*, May 13-17, 2013, Washington, DC.
2. A. Iturrondobeitia, A. Goñi, L. Lezama, C. Kim, M. M. Doeff, J. Cabana, and T. Rojo, "Effect of Si(IV) Substitution on Electrochemical, Magnetic, and Spectroscopic Performance of Nanosized $LiMn_{2-x}Si_xO_4$," *J. Mater. Chem. A,* **1**, 10857 (2013).
3. Marca M. Doeff, Guoying Chen, Jordi Cabana, Thomas J. Richardson, Apurva Mehta, Mona Shirpour, Hugues Duncan, Chunjoong Kim, Kinson Kam, and Thomas Conry, "Characterization of Electrode Materials for Lithium Ion and Sodium Ion Batteries using Synchrotron Radiation Techniques," *J. Vis. Exp.* doi:10.3791/50594 (2013).
4. Marca M. Doeff, "Batteries: Overview of Battery Cathodes" in *Springer Encyclopedia of Sustainability Science and Technology*, Springer Science + Business Media, LLC, New York, 709-739 (2012).
5. Kinson C. Kam and Marca M. Doeff, "Electrode Materials for Lithium Ion Batteries," *Materials Matters,* Aldrich Materials Science, **7**(4), 56 (2012).A. Iturrondobeitia, A. Goñi, L. Lezama, C. Kim, M. M. Doeff, J. Cabana and T. Rojo, *J. Mater. Chem. A*, **1**, 10857 (2013).

VI.B.4 Design and Synthesis of Advanced High-Energy Cathode Materials (LBNL)

Guoying Chen
Lawrence Berkeley National Laboratory

Environmental Energy Technologies Division
Berkeley, CA 94720
Phone: (510) 486-5843; Fax: (510) 486-5467
E-mail: gchen@lbl.gov

Start Date: October 2012
Projected End Date: September 2016

Objectives

- Obtain fundamental understanding on structural, chemical and morphological instabilities during Li extraction/insertion and extended cycling.
- Establish and control the interfacial chemistry between the cathode and the electrolyte at high operating potentials.
- Determine transport limitations at both material and electrode levels.
- Rationally design and develop next-generation electrode materials.

Technical Barriers

Low energy density, low power density, poor cycle life and poor safety.

Technical Targets

- PHEV40: 96 Wh/kg, 750 W/kg, 5,000 cycles.
- EV: 200 Wh/kg, 1,000 cycles.

Accomplishments

- Synthesized single-crystal samples of Li-excess layered composites and Ni/Mn spinels with a variety of physical characteristics for controlled studies.
- Isolated the effect of Mn^{3+} content from other variables and revealed its role in phase transformation behavior and rate capability of disordered Ni/Mn spinels.
- Utilized *in situ* XAS and scanning transmission X-ray microscopy (STXM) techniques to investigate cycling-induced structure changes at both bulk and single-particle levels.
- Illustrated the impact of particle size and morphology in the first cycle activation and the kinetic properties of Li-excess layered composite cathodes.
- Demonstrated that the side reactions between the high-voltage cathode particles and the electrolyte are surface-facet dependent.
- Developed and established the use of novel approaches to characterize the interfacial layer between the cathode and the electrolyte.

✧ ✧ ✧ ✧ ✧

Introduction

To meet the DOE targets for Li-ion batteries for vehicular applications, electrode materials with high-energy density and high stability are needed. Critical performance issues, such as structural and morphological instabilities, side reactions with the electrolyte, and transport limitations, are sensitive to materials' chemical compositions, crystal structures, surface facets, and particle sizes. Advances in materials development, therefore, require a better understanding of the relationships between their properties and functions. This project addresses these issues by synthesizing single-crystal versions of the commercially promising yet complex electrode materials, obtaining new insights into the materials by utilizing state-of-the-art analytical techniques that are mostly inapplicable on conventional, aggregated secondary particles, and subsequently establishing the relationships between structure and function. The goal is to use these findings to rationally design and synthesize advanced electrode materials with improved performance.

Approach

Prepare single crystals of Li-rich layered composites and high-voltage Ni/Mn spinels with well-defined physical attributes. Perform advanced diagnostic and mechanistic studies at both bulk and single crystal levels. Global properties and performance of the samples will be established from the bulk analyses, while the single-crystal-based studies will utilize time and spatial-resolved analytical techniques to probe solid-state chemistry and solid-electrolyte interfacial processes at the crystallite level.

Results

Synthesis of single-crystal samples. A collection of layered oxide crystals with compositions of $Li_{1+x}(Ni_{0.33}Mn_{0.33}Co_{0.33})_{1-x}O_2$ (x=0 and 0.14), $Li_{1.2}Ni_{0.13}Mn_{0.54}Co_{0.13}O_2$ and $Li_{1.2}Mn_{0.6}Ni_{0.2}O_2$ were prepared in plates, needles, and polyhedrons of different sizes. Progress was also made in synthesizing large $LiMn_{1.5}Ni_{0.5}O_4$ crystals intended for single-particle measurements. The molten-salt method was modified to include an additional flux top layer that promoted crystal growth into hundreds-of-micron size. Morphology was largely influenced by the choice of the flux and the ratio between the flux and precursors (denoted as R), as shown in Figure VI - 20. XRD characterization confirmed the formation of phase-pure spinels in all cases.

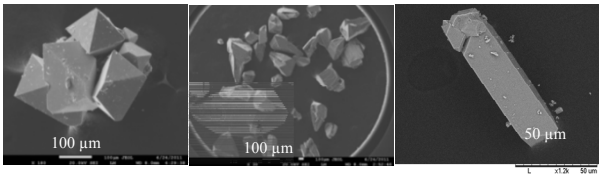

Figure VI - 20: SEM images of Ni/Mn spinel crystals synthesized with chloride precursors in: a) LiCl and R=100, b) LiCl and R=50, and c) eutectic LiCl-KCl flux

Structural evolution and phase transformations in the oxide cathodes. Previous reports have shown the importance of Ni/Mn ordering in influencing structural evolution during charge and discharge of the Ni/Mn spinels, but direct correlation was not established due to the lack of consistency in experimental results. This study intends to illustrate the importance of Mn^{3+} content which is likely the culprit of these inconsistencies found in the literature. To this end, controlled studies were performed on micron-sized $LiNi_xMn_{2-x}O_4$ (x=0.3 and 0.5) octahedron crystals with a disordered structure, confirmed by the signature disordered features on the FTIR spectra and the same peak separation of 60 mV on the dq/dV profiles in both samples. Area integration of the broad peaks at 4.1 V estimated 5.8 and 19.3% Mn^{3+} for x=0.3 and 0.5, respectively.

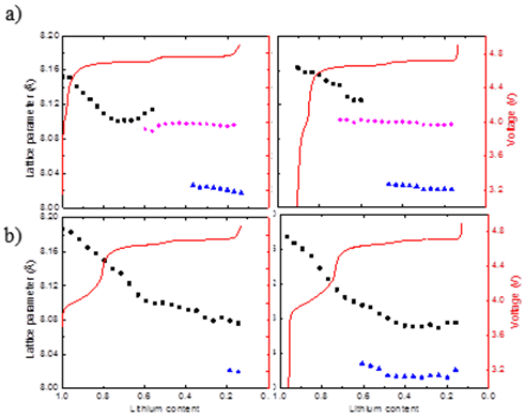

Figure VI - 21: Phase transformation in disordered $LiNi_xMn_{2-x}O_4$ crystals: a) x=0.5 and b) x=0.3. (left) charge and (right) discharge

Structural changes in the two crystal samples upon charge and discharge were then compared by synchrotron *in situ* XRD experiments performed at beamline 11-3 at SSRL. Figure VI - 21 shows the detailed phase composition at a given Li content obtained from structural refinement. While the crystal composite electrode with x=0.5 underwent two reversible two-phase transitions involving three cubic phases (Figure VI - 21a), an extensive solid-solution region with only two cubic phases were detected during the charge and discharge of x=0.3 (Figure VI - 21b). The latter sample also delivered enhanced rate capability. The results clearly demonstrate the intricacies in the relationships between spinel structure, phase transformation and rate capability, and the importance in optimizing physical properties in order to maximize the performance of the electrode materials.

The impact of particle size and morphology on structural evolution and the first cycle activation kinetics was demonstrated on layered $Li_{1.2}Ni_{0.13}Mn_{0.54}Co_{0.13}O_2$ crystals with four different shapes: plate, needle, large and small polyhedrons. The small polyhedron crystals prepared in a KCl flux had a particle size of 200 nm, while the other three samples had a similar size of 1-2 µm. *Ex situ* XRD experiments were performed on the samples during the first delithiation, and the results are shown in Figure VI - 22. The superlattice peaks between 20° and 34° (2θ), which are commonly used as an index for structural ordering in the transition metal layer, gradually weakened during Li extraction and eventually disappeared at a Li content of 0.5-0.3 in the plate-shaped crystals. This occurred faster in the small polyhedron sample but significantly slower in the large polyhedrons as high intensity remains even below Li=0.29. The results obtained in electrochemical cycling tests resonated this observation, where the highest and lowest rate capabilities were delivered by the small and large polyhedrons, respectively.

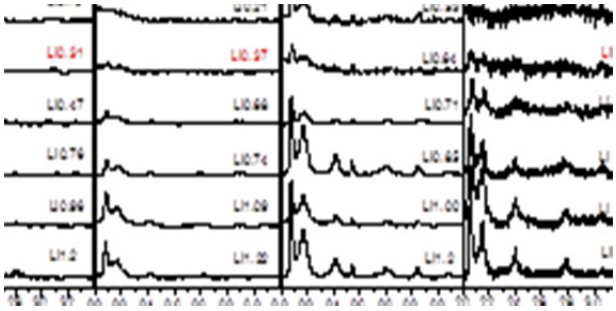

Figure VI - 22: Evolution of the XRD superlattice peaks during the first delithiation in $Li_{1.2}Ni_{0.13}Mn_{0.54}Co_{0.13}O_2$ crystals: a) plates, b) needles, c) large and d) small polyhedrons

Bulk structural changes in the layered oxides were further studied by soft X-ray absorption spectroscopy (XAS) at beamline 10-1 at SSRL on binder-and carbon-free electrodes containing the plate-shaped $Li_{1.2}Ni_{0.13}Mn_{0.54}Co_{0.13}O_2$ crystals. The electrodes were assembled into coin cells (with a Li metal anode) and then cycled to different states of charge in the first two cycles and then opened to recover the electrodes for analysis. Figure VI - 23 shows the Ni and Mn *L*-edge spectra in the total electron yield (TEY) mode that is surface sensitive. The Ni spectra show an increase in the oxidation state upon charge and then decreased upon discharge, consistent with the redox activity of Ni in the structure. Mn maintained at 4+ during the first charge, but a shoulder peak at 640.1 eV, which corresponds to Mn^{3+}, appeared upon discharge. The intensity of the shoulder peak further increased at the end of second discharge, suggesting structural irreversibility.

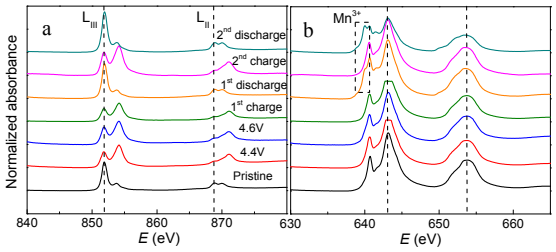

Figure VI - 23: XAS *L*-edge spectra of $Li_{1.2}Ni_{0.13}Mn_{0.54}Co_{0.13}O_2$ electrodes at the indicated stage of cycling: a) Ni and b) Mn

The investigation on these changes occurring at the particle-level was initiated by using scanning transmission X-ray microscopy (STXM) at beamline 11.0.2 at the Advanced Light Source (ALS), which has a high spatial resolution of 25 nm and an energy range of 95-2000 eV. In collaboration with Dr. Tolek Tyliszczak, layered $Li_{1+x}M_{1-x}O_2$ (M = Ni, Mn, Co) single crystals were chemically delithiated/relithiated or electrochemically cycled and then examined by STXM at the O *K*-edge as well as the Ni, Mn and Co *L*-edges. Figure VI - 24 shows the preliminary single-pixel (25nm x 25nm) Ni *L*-edge spectra collected on a plate-shaped $Li_{1.2}Ni_{0.13}Mn_{0.54}Co_{0.13}O_2$ crystal that was charged to 4.8 V in a binder- and carbon-free electrode. The variation of Ni oxidation state within the particle was evident as the dominate 4+ at the center of the crystal gradually lowered the oxidation state upon moving towards the edge, signaled by the increasing intensity of the peak at 853 eV (Figure VI - 24b). Since the large surfaces and the edges of the plates are composed of different surface facets, this variation may be evidence for the facet-dependent reactivity between the oxide particles and the electrolyte.

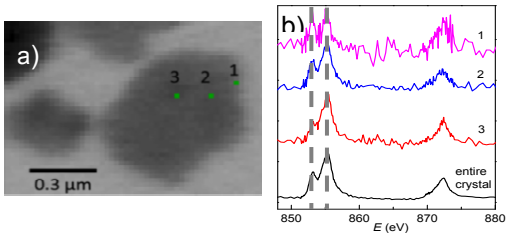

Figure VI - 24: a) STXM image of a $Li_{1.2}Ni_{0.13}Mn_{0.54}Co_{0.13}O_2$ crystal and b) Ni *L*-edge X-ray absorption spectra collected at the indicated single-pixel as well as the entire crystal

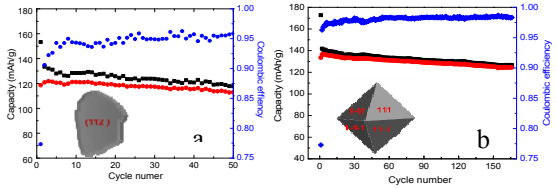

Figure VI - 25: Half-cell cycling performance of a) plate and (b) octahedral $LiMn_{1.5}Ni_{0.5}O_4$ crystal electrodes

Characterization of the cathode-electrolyte interfacial reactions. Understanding and controlling the oxidation of organic solvents, dissolution of transition metals from the cathodes, and the solid-liquid interface under high operating voltages is crucial in achieving stable cycling. To this end, the influence of crystalline orientation of particle surface on interfacial reactivity was evaluated on micron-sized spinel $LiMn_{1.5}Ni_{0.5}O_4$ single crystals with over 90% of (112) surface facets (plates) and 100% of (111) surface facets (octahedrons), respectively. Figure VI - 25 shows the extended half-cell cycling performance of the crystal composite electrodes. The octahedrons delivered a higher columbic efficiency of 99% for 170 cycles, as compared to 95% for 50 cycles in the plates. The per-cycle capacity loss was 0.05 and 0.14% for the octahedrons and plates, respectively, suggesting reduced parasitic reactions on (111) crystal facets. Selected *ac* impedance spectra at various state of charge, measured at the OCV conditions in the potential range of 4.0 to 4.85 V, are shown in Figure VI - 26a and b. Consistent with the previous reports, the spectra from both crystal electrodes are composed of a high-frequency semicircle from the surface-layer resistance (R_{sf}) and capacitance (C_{sf}), a medium-to-low-frequency semicircle from the charge transfer resistance (R_{ct}) and double layer capacitance (C_{dl}), and a low-frequency Warburg impedance (Z_w) due

to solid state diffusion of lithium ions within the active material. The surface-layer resistance as a function of Li content is compared in Figure VI - 26c. For both crystal samples, R_{sf} increased upon initial charge and then gradually decreased to reach a steady state at low Li contents, suggesting dynamic nature of the surface layer resulting from the reactions between the cathode and the electrolyte. The resistance on the octahedrons, however, is much lower compared to those on the plates. At any given Li content, the charge transfer resistance on the octahedrons is also much lower (Figure VI - 26d), with the difference most significant at low SOCs. The results clearly demonstrate that the side reactions between the high-voltage cathodes and the electrolyte are surface-facet dependent, and it is important to design particle morphology in order to minimize these unwanted reactions.

In collaboration with Drs. Phil Ross and Zhi Liu at beamline 9.3.1 at the ALS, tender X-ray photoelectron spectroscopy (TXPS) with excellent surface sensitivity as well as the depth-profiling capability was used to non-destructively probe the atomic and chemical compositions of the species at variable sampling depth. Initial studies were performed with incident photoelectron energy between 3 and 4 keV that probes particle surfaces at a depth of 10 and 15 nm, respectively. The results from a cycled, binder-and carbon-free $LiMn_{1.5}Ni_{0.5}O_4$ electrode showed significant attenuation to Li 1*s*, Mn 3*p* and O^{2-} intensities originated from $LiMn_{1.5}Ni_{0.5}O_4$, suggesting cycling leads to the deposition of solid products that suppress the detectable signals from the oxide underneath. A large amount of new carbon species with higher binding energies were revealed, and the presence of organic containing 'surface' species was further confirmed by the broadening of the higher binding energy O 1*s* peak. The chemical nature and thickness of this organic surface layer, as well as the role of particle surface features, are the topics of further investigation.

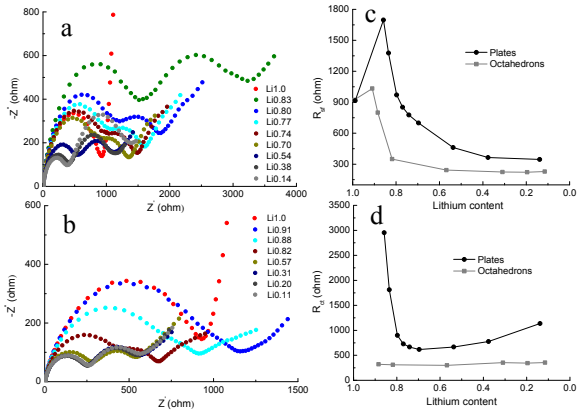

Figure VI - 26: Nyquist plots for the $LiMn_{1.5}Ni_{0.5}O_4$ crystal electrodes at the indicated Li content: a) plates and b) octahedrons; the relationships between lithium content and c) surface-layer resistance and d) charge-transfer resistance

Conclusions and Future Directions

In conclusion, single-crystal samples of Li-excess layered composites and Ni/Mn spinels with specific physical characteristics suitable for controlled studies were synthesized. Structural and chemical changes resulting from Li extraction/insertion were determined and their correlation to sample physical properties established. Mn^{3+} content influences the phase transformation process and the kinetic properties in Ni/Mn spinels, and particle size and morphology control is critical to the kinetics in layered oxides. Side reactions with the electrolyte were found to be dependent on the crystalline orientation of the cathode particle surfaces. Approaches were developed to obtain the details of the interfacial layer resulting from the side reactions between the cathode and the electrolyte.

Future work will focus on the examination of crystal-plane specific surface chemistries of the oxide cathodes and the stability of the interfacial layer. The chemical nature, thickness and properties of the interfacial layer, as well as the mechanism behind the role of particle surface features in side reactions will be investigated. Local structural and chemical changes as a function of lithium content and cycle number will be monitored at the single-particle level to explore the intrinsic failure mechanisms of the oxides. Synthesis conditions will be explored to produce electrode materials with properties optimized for both performance and safety.

FY 2013 Publications/Presentations

1. M. M. Doeff, G. Chen, J. Cabana, T. J. Richardson, A. Mehta, M. Shirpour, H. Duncan, C. Kim, K. C. Kam, and T. Conry, "Characterization of Electrode

Materials for Lithium Ion and Sodium Ion Batteries Using Synchrotron Radiation Techniques," *J. Vis. Exp.*, DOI:10.3791/50594 (2013).

2. U. Boesenberg, F. Meirer, Y. Liu, R. Dell'Anna, A. K. Shukla, T. Tyliszczak, G. Chen, J. C. Andrews, T. J. Richardson, R. Kostecki, and J. Cabana, "Mesoscale Phase Distribution in Single Particles of LiFePO4 Following Lithium Deintercalation," *Chemistry of Materials*, **25**, 1664 (2013).
3. B. Hai, A. K. Shukla, H. Duncan, and G. Chen, "Effect of Particle Surface Facets on the Kinetic Properties of $LiMn_{1.5}Ni_{0.5}O_4$ Cathode Material," *Journal of Material Chemistry A*, **1**, 759 (2013).
4. "Impact of Initial Li Content on Kinetics and Stabilitis of Layered $Li_{1+x}(Ni_{0.33}Mn_{0.33}Co_{0.33})_{1-x}O_2$," G. Chen, B. Hai, A. K. Shukla, and H. Duncan, *Journal of the Electrochemical Society*, **159**, A1543 (2012).
5. "Overcharge Protection for PHEV Batteries," *DOE Annual Peer Review Meeting*, May 13-17, 2013, Washington, DC.
6. "Synthesis and Performance of $Li_{1.2}Ni_{0.13}Mn_{0.54}Co_{0.13}O_2$ Crystals," H. Duncan and G. Chen, *Berkeley Energy and Resources Collaborative Innovation Expo*, October 2013, Berkeley, CA.
7. H. Duncan, B. Hai, A. K. Shukla, and G. Chen, "Influence of Particle Morphology on Structural Evolution and Electrochemical Performance of $Li_{1+x}M_{1-x}O_2$ Cathode Materials," *CalCharge Kickoff Event*, May 2013, Berkeley, CA,.
8. S. F. Lux, A. J. Jarry, H. Duncan, N. S. Norberg, G. Chen, R. Kostecki, *"In situ* Fluorescence Spectroscopy of Interfacial Processes in High-Voltages Cathodes," *CalCharge Kickoff Event*, May 2013, Berkeley, CA.
9. G. Chen, B. Hai, and A. K. Shukla, "Impact of Particle Surface Facets on the Performance of $LiMn_{1.5}Ni_{0.5}O_4$," *The 222nd ECS Meeting*, October 2012, Honolulu, HI.

VI.B.5 Novel and Optimized Phases for High Energy Density Batteries (LBNL)

Jordi Cabana
Lawrence Berkeley National Laboratory

Department of Chemistry[12]
University of Illinois at Chicago
845 W Taylor Street
Science and Engineering South (MC 111)
Chicago, IL 60607
Phone: (312) 355-4309
E-mail: jcabana@uic.edu

Start Date: October 2012
Projected End Date: July 2013

Objectives

- Enable higher density Li-ion batteries through an increase in operation voltage and capacity of the cathode.
- Design electrode structures that maximize active material utilization and charge density.
- Understand the structure-composition-properties relationship for bulk and surface properties of electrodes.
- Identify new compounds containing non-oxide or polyanions in their crystal structure that are electrochemically active.

Technical Barriers

Low energy-density, poor cycle life, safety.

Technical Targets

- PHEV: 96 Wh/kg, 5,000 cycles
- EV: 200 Wh/kg; 1,000 cycles.

Accomplishments

- The role of Mg modifications of the surface of $LiNi_{1/2}Mn_{3/2}O_4$ particles was elucidated by establishing the chemical changes during processing and cycling.
- The correlation between crystal-chemistry in $LiNi_{1/2}Mn_{3/2}O_4$, the phase transformation mechanism and electrochemical properties was fully ascertained.
- Established a low temperature synthetic method for the fluorination of lithium transition metal oxides.

✧ ✧ ✧ ✧ ✧

Introduction

Finding Li-ion battery electrode materials that can bring about increases in energy is a critical need if their use in electric vehicles is to meet expectations. In order to fulfill this goal, the following strategies can be envisaged: i) raising the voltage of operation of the battery by using anodes and cathodes that react at very high and very low potentials, respectively, and/or ii) improving the storage capacity by switching to alternative electrode materials that can exchange a larger amount of electrons/Li^+ ions. Yet these changes cannot come with a penalty in terms of safety and cycle life, which implies that the mechanisms of their reaction with lithium need to be well understood in order to locate possible sources of failure.

Spinel-type $LiNi_{0.5}Mn_{1.5}O_4$ was identified by the BATT program as model material for the study of the bottlenecks of positive electrode materials reacting at very high potential. Apart from being stable, $LiNi_{0.5}Mn_{1.5}O_4$ is seriously considered by industry as an alternative to currently used materials because lithium is extracted at around 4.7 V vs. Li^+/Li^0. While very high rate capability has been reported in several cases, it has not been fully ascertained what the role is of the crystal-chemistry of the compound, such as metal ordering and the existence of Mn^{3+} impurities in the spinel and segregated rocksalt particles. During FY2012, it was established that ordering and electrochemical proxies such as rate capability were strongly correlated, whereas Mn^{3+} contents were found to have a much more marginal role. In FY2013, our goal was to ascertain the origin of these correlations

[12] Current affiliation and mailing address.

The interface between an electrode and the electrolyte is critical to extended performance. It was previously shown that large micrometric particles showed more favorable performance than nanosized ones because they minimize the surface area. However, electrolyte decomposition is still generally found to be extensive. Thus, coatings appear to be a necessary way forward. However, the rules of design for these coatings have not fully been ascertained. Modifications based on the addition of basic oxides such as MgO in the form of coatings or simple additives were chosen as a case study and a combination of electrochemistry, elemental analysis and chemical characterization at different states was used to establish such rules.

Soft X-ray spectroscopy experiments conducted in FY2012 revealed that the Ni states at the surface of $LiNi_{0.5}Mn_{1.5}O_4$ particles were more reduced than the bulk of the crystals. This was interpreted as the consequence of the increased covalence of the Ni-O bond after lithium extraction. Ultimately, this covalence can lead to irreversible destabilization of the O^{2-} species toward oxygen evolution, a thermal event with negative safety consequences. Fluoride ions are less polarizable and, therefore, can provide chemical stability. In FY2013, synthetic methods for fluorinated compounds that contain redox active metals were explored, with the aim to discover new compounds that can have suitable properties.

Approach

Employ and develop a variety of synthetic methods to produce materials with controlled purity, crystal structure and particle morphology. Use spectroscopic and diffraction techniques to monitor the reactions involved in battery electrodes. Explore chemical spaces in a search for new phases that may provide performance improvements.

Results

All work on $LiNi_{0.5}Mn_{1.5}O_4$ was done in coordination within the Spinel Focus Group, which was concluded during FY2013.

Phase transformations determine performance in $LiNi_{0.5}Mn_{1.5}O_4$. The reader is referred to the FY2012 Annual Report for the study of correlations between crystal chemistry and electrochemistry, which provided motivation for this work. *Operando* X-ray diffraction experiments were conducted at beamline 11-3 at the Stanford Synchrotron Radiation Lightsource (SSRL) on $LiNi_{0.5}Mn_{1.5}O_4$ samples with different degrees of cationic ordering, as probed by nuclear magnetic resonance, neutron diffraction and electrochemical signatures. A series of reversible phase transitions were observed. The results are summarized in Figure VI - 27. The samples tested have decreasing degrees of crystallographic ordering, as follows: OO730 > OO700 > OO670 > A900. As it can be readily noticed, the difference in potential between the two faradaic electrochemical signatures smoothly traces ordering. The early stages of delithiation occur through a solid solution mechanism, followed by consecutive two-phase transitions. In contrast, the sample with the highest degree of ordering shows no discernible solid solution domains. The formation of a solid solution leads to a significant reduction in volume change between the phases involved in the first biphasic transition. It is hypothesized that such lower volume change results in smaller strain buildup in the active materials particles during this step, thereby increasing the rate of reaction that can be achieved.

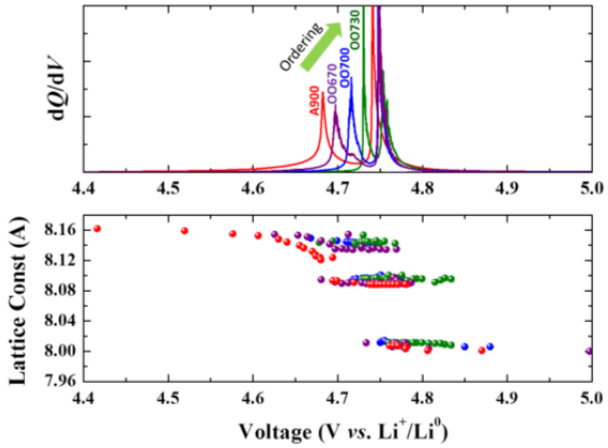

Figure VI - 27: Summary of *operando* XRD data collected upon Li deintercalation in a series of $LiNi_{0.5}Mn_{1.5}O_4$ samples showing varying degrees of cationic ordering

Role of surface Mg-modifications on the chemistry and electrochemistry of $LiNi_{0.5}Mn_{1.5}O_4$. A Mg precursor was coated on micrometric spinel particles, followed by annealing at 500 or 800°C. The results showed a rough coating with an inhomogeneous distribution of agglomerates, most likely MgO, across the surface of the material treated at 500°C. This coating was modified after treatment at 800°C, resulting in the incorporation of Mg^{2+} into the spinel sub-surface (Figure VI - 28).

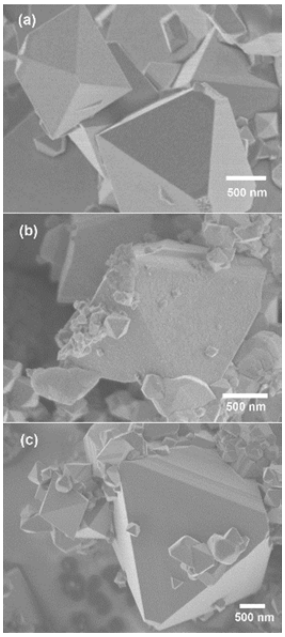

Figure VI - 28: Scanning electron micrographs of a) baseline $LiNi_{0.5}Mn_{1.5}O_4$, and after applying a Mg-based coating, treated at b) 500 and c) 800ºC

The electrochemical study revealed that the presence of Mg did not improve performance at room temperature, but was crucial at higher temperature. Among the two modified materials, the best results were obtained following annealing at 800°C, in terms of capacity, coulombic efficiency and rate capability at 50°C. The performance at room temperature was not severely compromised with respect to the baseline, although the presence of Mg^{2+} in the spinel lattice did result in slight specific capacity losses.

In order to shed light into the difference in properties between samples and testing conditions, X-ray absorption spectroscopy data were collected at the Ni $L_{II, III}$ and O K-edges at beamline 10-1 at SSRL for all samples after a full charge to 5 V, at both room temperature and 50ºC. Spectra were acquired using a total fluorescence and total electron yield (TFY and TEY) detector simultaneously. The TEY detector provides XPS-like, surface sensitive insight, whereas experimental conditions were designed to make TFY signals representative of the bulk of the material. A comparison between a baseline sample and the correspondingly coated materials treated at 500°C and 800°C was established. The existence of broad, low energy shoulders in the pre-edge peak at 531 eV was indicative of the formation of Ni^{4+}-O^{2-} species during Li deintercalation (Figure VI - 29). Their absence in the TEY data for the bare material is interpreted as evidence that the surface of the electrode is more reduced than the bulk. In contrast, the coated samples show pronounced shoulders, especially at 50ºC. It is hypothesized that Mg^{2+} ions pin the charges of the O^{2-} ions so that they cannot be polarized by the Ni^{4+} ions and turn electrophilic. The result is a more stable surface toward electrolyte oxidation in coated than in bare samples.

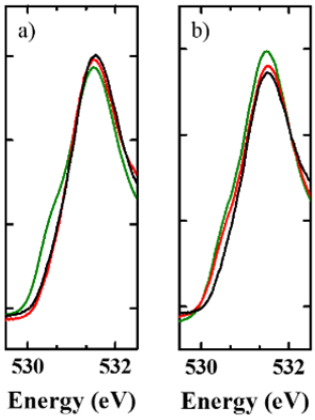

Figure VI - 29: Zoom of the region around 531 eV in the O K-edge XAS data, highlighting the differences in intensity of the 530.2 eV shoulder depending on the sample. The data correspond to the baseline material (black), as well as after applying a Mg-based coating, treated at 500 (red) and c) 800ºC (green), which were fully oxidized in Li metal cells at a) room temperature and b) 50ºC

The electrochemical data, together with analysis of spectra collected at the Ni $L_{II, III}$- and O K-edges, revealed two important lessons that could guide the rational design of stable high voltage materials. First, coatings that are semiconducting in nature and contain lithium are preferred to reduce charge (ion and electron) transfer losses. Second, small amounts of a redox inactive, strongly ionic species such as Mg^{2+} on the surface of an active material could have a significant stabilizing effect by changing the nature of chemical bonding vis-à-vis possible redox activity with the electrolyte.

Low temperature fluorination of oxides. Heating lithium transition metal oxides in the presence of transition metal fluorides at temperatures as low as 250°C is sufficient to incorporate significant amounts of fluorine into the oxide lattice; up to 40 mol% fluorination was observed in certain cases. A collection of compounds containing varying rations of Mn, Ni and Fe were thus synthesized. In collaboration with the Wang group at BNL, also in the BATT program, the fluorination reactions as well as the thermal stability of the resulting oxyfluorides was evaluated by collecting X-ray diffraction patterns during heating. It was found that these phases are metastable and decompose to binary phases above 500°C. Therefore, it appears that these kinds of phases cannot be obtained at high temperature. Electrochemical testing revealed that these oxyfluorides are redox active, creating avenues for future design of new materials with unprecedented properties.

Conclusions and Future Directions

During FY2013, work was finalized that provided new insight into the rules for the design of positive electrodes based on $LiNi_{0.5}Mn_{1.5}O_4$. It was determined that the excellent rate properties of materials with extensive Ni and Mn disorder was due to the direct dependence of the miscibility gap on such crystallographic parameter. The reduced miscibility gap is thought to lead to lower mechanical strain in the particles during cycling. At the surface, the formation of Ni^{4+}-O^{2-} covalent bonds was found to lead to electrolyte oxidation. Such electrophilic species could be partly stabilized by the presence of Mg^{2+}, which tends to favor ionic bonds. Fluorine could also be a stabilizing agent. Thus, a search for new lithium transition metal oxyfluorides was initiated. A low temperature fluorination method was demonstrated. These findings have general applicability to other materials beyond $LiNi_{0.5}Mn_{1.5}O_4$ and provide natural closure to the Spinel Focus Group.

This project was closed on July 2013 due to the relocation of the Principal Investigator to the University of Illinois at Chicago. Thus, there are no future directions to be discussed.

FY 2013 Publications/Presentations

1. "Novel and Optimized Materials Phases for High Energy Density Batteries," *DOE Annual Peer Review Meeting*, May 13-17, 2013, Washington, DC.
2. "Effect of the Crystal Chemistry of $LiNi_{0.5}Mn_{1.5}O_4$ Spinels on Electrochemical Properties," *Pacific Rim Meeting on Electrochemical and Solid State Science (PRiME) 2012*. October 7th-12th, 2012, Honolulu, HI (USA).
3. J. B. Cook, C. Kim, L. Xu and J. Cabana, J. *Electrochem. Soc.*, **160**, A46 (2013).
4. L. Xu, C. Kim, A. K. Shukla, A. Dong, T. M. Mattox, D. J. Milliron and J. Cabana, *Nano Lett.*, **13**, 1800 (2013).

VI.B.6 Studies on High Energy Density Lithium-ion Electrodes (ORNL)

Jagjit Nanda
Oak Ridge National Laboratory

Material Science and Technology Division
PO Box 2008, MS 6124
Oak Ridge, TN 37831-6124
Phone: (865) 241-8361
E-mail: nandaj@ornl.gov

Postdoctoral workers:
Surendra Martha, Hui Zhou

Collaborators:
Andy Drews (Ford); Joy Andrews and Yijin Liu (Stanford Synchrotron Radiation Lightsource); Kang Xu (Army Research Lab); Andrew Callendar (Tennessee Technical Univ.)

Start Date: October 2010
Projected End Date: Continuing

Objectives

- Investigate mechanisms behind capacity fade and voltage depression associated with high voltage Lithium-ion cathodes and provide mitigation methods.
- Improve C-rate performance and cycle life of high voltage cathodes in full cells.
- Perform *ex situ* and *in situ* micro-structural characterization to study electrodes at various states of charge (SOC) and subjected to stress cycles and correlate these to capacity fade and cycle life degradation.

Technical Barriers

This project addresses the following technical barriers as described in the USDRIVE & USABC goals [1, 2]:

- Performance at ambient temperatures: high DC-R especially at low SOC and C-rate capability
- Materials degradation leading to cycle life loss: transition metal dissolution and structural instability against high V cycling.

Technical Targets

- PHEV specific energy targets (pack): 3.4 (min) to 11.6 (max) kWh [1]
- EV specific energy targets (pack): 80 (min) to 200 (max) Wh/kg [2]

Accomplishments

- Applied transmission x-ray microscopy combined with x-ray near edge absorption spectroscopy (TXM-XANES) to lithium-manganese rich NMC (LMR-NMC) high voltage cathodes to measure the chemical state changes as well as morphology in 3D.
- Performed micro-Raman imaging of LMR-NMC cathodes.
- Investigated the role of high voltage electrolyte additives on the cycle life performance of LMR-NMC cathodes.

✧ ✧ ✧ ✧ ✧

Introduction

Current R&D efforts in lithium-ion batteries are directed towards increasing energy density with reduced cost and improved cycle-life and safety. Among other important factors, developing high energy density lithium-ion cathodes is a high priority area. Recently, there has been significant progress made on a number of high voltage cathode chemistries such as $LiMn_{1.5}Ni_{0.5}O_4$ [3] and LMR-NMC [4-5]. However, significant technical challenges still need to be addressed at the materials as well as the electrode level. These include (i) structural and phase stability under continuous high voltage cycling (>4.5 V) (ii) Mn dissolution leading to capacity fade (iii) electronic and ionic transport limitations intrinsic to the electrode material and (iv) higher first cycle irreversible capacity loss (ICL) due to interfacial issues and oxygen loss, etc. We report systematic studies on Lithium-rich NMC composite cathodes having nominal composition $Li_{1.2}Mn_{0.525}Ni_{0.175}Co_{0.1}O_2$ and address the various technical barriers mentioned above.

Approach

High voltage LMR-NMC cathode materials having nominal composition $Li_{1.2}Mn_{0.525}Ni_{0.175}Co_{0.1}O_2$ were obtained from a pilot scale facility of Toda-Kogyo Corporation, Japan. Cathode powders were fabricated into electrodes using the slurry coating method with PVdF binder (Sigma-Aldrich) and carbon diluents (super-P, Timcal). The electrodes were assembled in the form of half cells (Li-metal as counter electrode) or full cells using

modified graphite powders obtained from Conoco-Phillips (now Phillips 66). We performed life cycle studies in both coin cell and small pouch cell format to study capacity fade at room temperature as well as at 60°C. All cells were cycled between 2.5 V and 4.9 V (vs. Li^+/Li) at 10 mA/g for the first cycle, and then between 2 V and 4.9 V (vs. Li^+/Li) at 20 mA/g using the electrolyte of 1.2 M $LiPF_6$ salt dissolved in EC: DMC (1:2) solvent. Apart from standard charge-discharge cycling, we also carried out impedance spectroscopy (EIS), cyclic voltammetry (CV) and various structural and surface spectroscopy techniques to characterize the electrodes and correlate the observed electrochemical performance with the materials degradation. Material modifications such as nanoscale surface coating and electronic filler additives were also undertaken to improve the electrochemical performance. The surface spectroscopy and structural characterization techniques used include transmission x-ray microscopy combined with x-ray near edge spectroscopy (TXM-XANES), confocal Raman imaging, x-ray diffraction and electron microscopy.

Results

3D Chemical Imaging & X-ray Microscopy of LMR-NMC Cathodes. Using the TXM-XANES beam line at Stanford Synchrotron Radiation Lightsource (SSRL), we performed X-ray imaging combined with XANES [6-8] to map the chemical state and morphology of LMR-NMC electrodes at different SOC and cycle life. Changes in the Mn K-edge spectra as a function of cycle number are shown as false-color images of LMR-NMC cathode particles in Figure VI - 30.

The color maps in Figure VI - 30 are determined by fitting each of the observed spectra, ~106 per field of view (FOV) for the 200 & 50 times cycled electrode as well as the pristine electrode, which serves as the reference compound, and assigning red or green to the fraction of 200 cycle or pristine spectra, respectively. The changes observed in the Mn K edge spectra are consistent with the changes in the bulk electrochemical signature, shown by the differential capacity (dq/dv) versus voltage plot for the 1st, 50th and 200th cycle as presented recently [8]. Careful analysis of the XANES data by taking the 1st derivative spectra (not shown) shows the Mn K edge shifts from about 6553.5 eV (the pristine electrode) to 6552 eV (the 200-cycle sample), consistent with a clear change of Mn valence from 4+ to a lower valence state when the electrode material was cycled at a voltage greater than 4.5 V. The corresponding change in Ni and Co K edges under cycling are not significant.

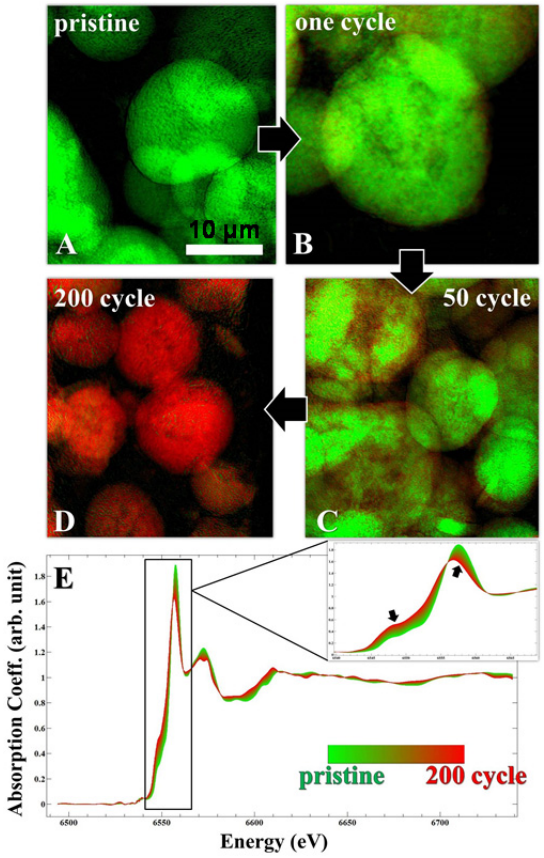

Figure VI - 30: Panels A to D: 2D XANES chemical maps of Mn within the LRM-NMC particles, as a function of cycling. Single pixel XANES (30 nm resolution; ~ 10^6 per FOV) are assigned to green or red based on least squares fitting to the Mn K-edge spectra of pristine, 50 and 200 times cycled electrodes, respectively. (E) Evolution of the Mn K edge with cycling

Although the 2D TXM-XANES analysis of LMR-NMC cathode materials presented above provides important information about the oxidation state evolution of Mn during repeated cycles, true 3D mapping is needed to distinguish particle heterogeneities and to quantify the transition metal (TM) cation concentration inside the bulk of the particle. Three-dimensional (3D) representations of the TM distributions within two typical particles are shown Figure VI - 31. As seen in the 3D renderings, the elemental concentrations of the particles show evidence for a difference in density near inner and outer surfaces.

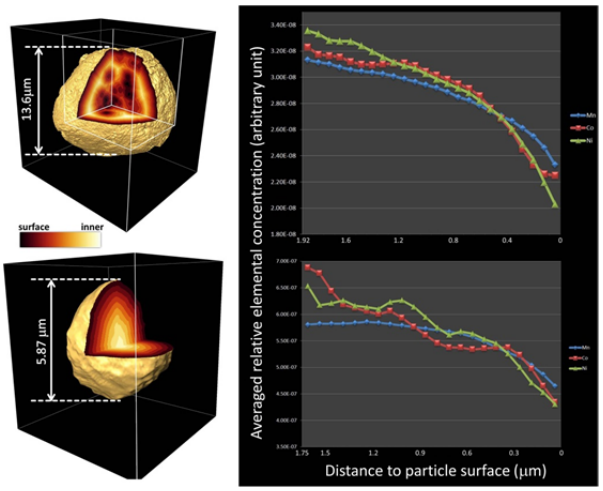

Figure VI - 31: (Left) Tomographic reconstruction of two selected LMR-NMC cathode particles after 1 full charge-discharge cycle

To put this observation on a firm footing, we have generated distribution plots (Figure VI - 31 right panel) to compare the shortest distance from each particle volume element, or voxel, to a particle surface (the outer surface of the particle and/or the surface of a macro pore inside the particle). In both cases there is a depletion of transition metals near the surface regions of the particles. The drop in relative concentrations of all three TMs indicates that the particles appear to be more porous at the surface even when the cathode particle undergoes only one full cycle of charge-discharge (2.5-4.9V). Specifically, we note that there is a significant drop of Co and Ni (comparing to Mn, which is the major TM in this electrode) at the layer(s) closest to the particle surface. 3D analysis of LMR-NMC cathode particles cycled for 50 and 200 cycles will reveal more information on the particle heterogeneities with cycling (analysis in progress).

Confocal Raman Imaging of LMR-NMC Electrodes. We carried out confocal-Raman imaging and spectral analysis of LMR-NMC electrodes at different SOC and cycle life stage. The Raman signature of LMR-NMC composition is sensitive to the lithium content in the lattice and, thus, is a good spectroscopic tool to map the variations in composition under different SOC or voltages. Further, Raman imaging provides a quantitative spectral tool for measuring spatial distribution of active materials and carbon on the electrode surface. Below we provide a summary of Raman imaging and analysis of LMR-NMC electrodes fabricated as per the procedure mentioned earlier.

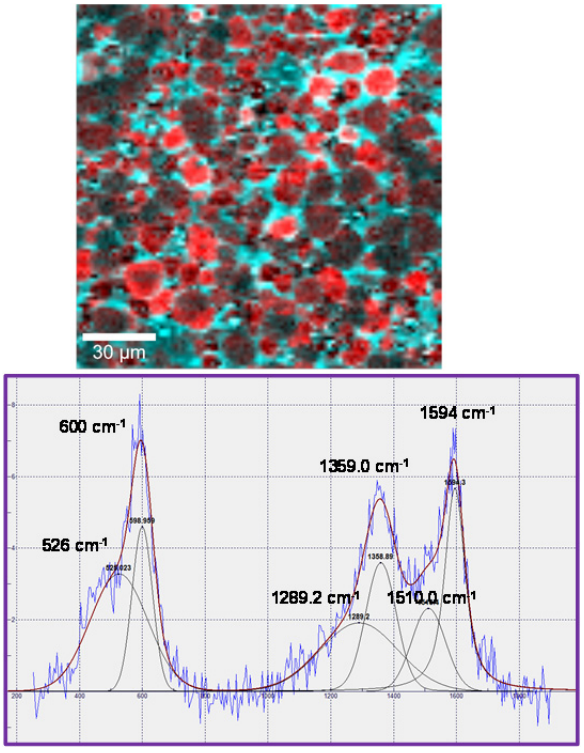

Figure VI - 32: Raman mapping (top) and spectral analysis (bottom) of pristine LMR-NMC composite electrodes. The false color maps show carbon rich regions (red) and metal oxide (cyan); mixed colors are both carbon-LMR NMC regions

Figure VI - 32 shows a typical Raman map of an LMR-NMC pristine electrode presenting LMR-NMC (cyan) and carbon (red) rich regions as well as a mixture of both. This map is based on the spectral component analysis as shown in the bottom figure. Typically, the fitted areal intensity is converted into a false color map as shown above. Briefly, the metal oxide Raman band is characterized by two Raman modes corresponding to Eg and A1g metal-oxide symmetric stretching modes [9] which for the given LMR-NMC particle are at around 526 and 600 cm^{-1}, respectively. The carbon region can be fitted with 4 components. Additionally we expect to see another Raman band at 420 cm^{-1} corresponding to Li_2MnO_3, [10] but this relatively weaker band was not representative across all the electrode regions for the pristine sample. The peak positions at 1359 and 1594 cm^{-1} correspond to D & G band of graphitic carbon while 1289 and 1510 cm^{-1} are representative of the amorphous/disordered carbon. The Raman maps and their spectral behavior change as the electrodes are charged (discharged). Both spectral position and full width at half maximum (FWHM) change with the voltage (SOC) and also under continuous cycling. To further quantify the inhomegneities of the LMR-NMC electrodes, we undertake Raman analysis for cathode particles selected from different regions of electrodes charged at 3.9, 4.2, 4.5 and 4.9V and compare to a pristine electrode. Analysis

was carried out on at least 5 cathode particles and results are summarized in terms of the ratio of their Eg to A1g band areal intensities and their respective Raman band positions (Figure VI - 33). There are some interesting trends from this analysis: (i) for a given bulk electrode SOC (or voltage), the cathode particles at different electrode locations vary widely in terms of the areal ratios and band positions; and (ii) the A1g band shifts consistently to red with increased SOC with exceptions for the 4.5 V electrode. We notice more inhomogeneity for cathode particles from the electrodes charged at 4.2 and 4.9 V. Detailed analysis showing variation of the local SOC of the cathode particles will be reported shortly in a journal article.

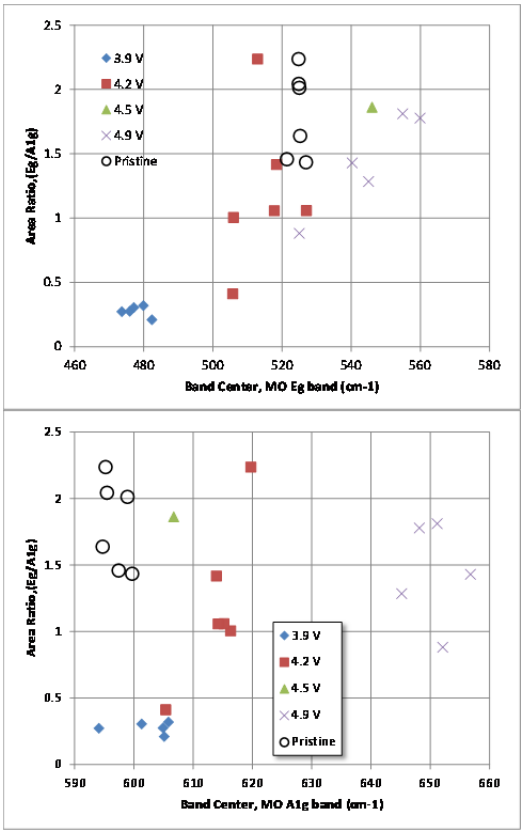

Figure VI - 33: Ratio of the areal intensities for the Eg and A1g band plotted with respect to the band center for various LMR-NMC cathode particles maintained at different SOC

Role of Electrolyte additives on the performance of LMR-NMC Electrodes. Collaborating with Dr. Kang Xu's group at Army Research Laboratory, we have tested the cycle life performance of LMR-NMC electrodes in the presence of 0.5 -1.5 wt% additives dissolved in the standard electrolyte (1.2 M $LiPF_6$ in EC-DMC 1:2 w/w). The additives are tris(hexafluoro-iso-propyl) phosphate (HFiP), aluminum substituted HFiP (AlHFiP), perfluorinated tert butoxide grafted phosphazene (PFBP), AlPFBP and PNF. HFiP has already demonstrated good cycle life benefits for high voltage spinel electrodes ($LiMn_{1.5}Ni_{0.5}O_4$) by forming a phosphate based passivation film on the cathode surface [11]. The hypothesis here is that HFiP and similar classes of compounds may also improve the cycle life performance, including 1st cycle irreversible capacity loss and columbic efficiency, for LMR-NMC high voltage cathodes. The additives were tested on several batches of electrodes (Figure VI - 34) using Argonne National Laboratory's voltage fade protocol [12].

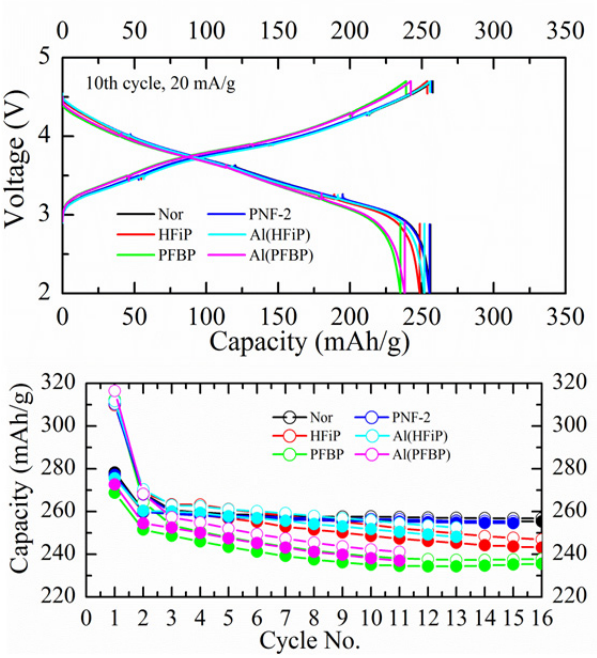

Figure VI - 34: Impact of various electrolyte additives on the cycle life performance of LMR-NMC electrodes. (Top) Charge-discharge capacity at the 10th cycle is shown for 5 different additives

We did not notice any improvement in the cycle life performance using any of the listed additives. Specifically, no appreciable improvement in 1st cycle irreversible capacity loss or columbic efficiency was observed as shown in Table VI - 1. In some case we even noticed a slight capacity fade when using additives such as PFBP. These data indicate that HFiP and their derivatives are most likely not forming a conductive passivation layer on the LMR-NMC cathode surface, but detailed studies are needed to investigate further. ARL will soon send purified versions of each these additives for further testing. It is likely that the presence of organic impurities in these additives can be detrimental to cycle life improvements. The overall goal of this study is to determine a suitable additive that forms a stable interphase on the LMR-NMC cathode surface to provide passivation during high voltage cycling (> 4.6 V).

Table VI - 1: Summary of the performance of various electrolyte additives on LMR-NMC electrodes

Electrolyte	1st (10 mA/g)			2nd (20 mA/g)			10th (20 mA/g)		
	Charge Capacity (mAg/h)	Discharge Capacity (mAh/g)	Irreversible capacity (mAh/g)	Charge Capacity (mAg/h)	Discharge Capacity (mAh/g)	Irreversible capacity (mAh/g)	Charge Capacity (mAg/h)	Discharge Capacity (mAh/g)	Irreversible capacity (mAh/g)
No Additive	311.98	278.23	33.75 (10.82%)	268.61	260.51	8.1 (3.01%)	257.61	255.93	1.68 (0.6%)
1%HFiP	309.82	276.08	33.74 (10.89%)	269.12	259.60	9.52 (3.54%)	253.74	248.59	5.15 (2.02%)
1%PFBP	312.5	268.76	43.74 (14%)	264.46	251.57	12.89 (4.87%)	239.00	235.15	3.85 (1.61%)
1%PNF-2	310.37	277.06	33.31 (10.73%)	267.96	259.79	8.17 (3.05%)	256.47	255.33	1.14 (0.4%)
1%Al(HFIP)	311.62	275.60	36.02 (11.56%)	270.34	260.31	10.03 (3.71%)	255.85	251.73	4.12 (1.61%)
1%Al(PFBP)	316.40	272.61	43.79 (13.84%)	268.20	254.41	13.79 (5.14%)	242.24	238.14	4.1 (1.69%)

Conclusions and Future Directions

Using the TXM-XANES technique, we could map the Mn, Ni and Co valence state in LMR-NMC cathodes in 2D as well as 3D with a large field of view (30 microns). Tomographic reconstruction of 2D XANES images of respective TM cations on individual cathode particles provides a quantitative estimation of various TMs in terms of 3D distance maps. The surface and bulk TM concentrations will change as the cathode material undergoes repeated cycling. Raman imaging and spectral analysis of LMR-NMC electrodes showed a wide variation of the SOC of individual particles even though the bulk electrode is maintained at a particular voltage or SOC. We also tested the high voltage electrolyte additives on LMR-NMC compositions. Future work will be focused on studying other high capacity cathode compositions that are not necessarily Mn-rich. Preliminary work is in progress to stabilize high capacity cathode materials with compositions $Li_2M^IM^{II}O_2$ and $Li_2M^IM^{II}O_3$ where M^I and M^{II} are TMs anionically coupled to oxygen. Examples include (but are not limited to) Cu, Ni, and Fe compositions.

FY 2013 Publications/Presentations

1. "Solid Electrolyte Coated High Voltage Layered-Layered Lithium-rich Composite Cathodes: $Li_{1.2}Mn_{0.525}Ni_{0.175}Co_{0.1}O_2$," S. K.Martha, J. Nanda, Y. Kim, R.R. Unocic, S. Pannala and N. J. Dudney, J. Mater. Chem. A 2013, 5587 (1).
2. "TXM-XANES Studies on High Voltage Lithium Rich Composite Cathodes: 3D Morphology and Phase at Nanoscale, Presented at MRS Fall Meeting," Boston, Nov 2012.
3. "Confocal Raman Imaging and Spectroscopy of High Voltage Composite Cathode for Lithium Batteries, J. Nanda, A. Callendar, H. Zhou and S. K. Martha," Confocal Raman Symposium, Ulm Germany, and September 2013 (invited presentation).
4. "Thermophysical Properties of $LiFePO_4$ Cathodes with Carbonized Pitch Coatings and Organic Binders: Experiments and First-Principles Modeling," J. Nanda et al., J. Power sources 2013 (accepted).
5. "Highly Robust Lithium-ion battery electrodes from Lignin: An Abundant Renewable and Low-cost Material," W. Tenhaeff et. al., Adv. Func. Mater., 2013.
6. Ira Bloom, Lynn Trahey, Ali Abouimrane, Ilias Belharouak, Xiaofeng Zhang, Qingliu Wu, Wenquan Lu, Daniel P. Abraham, Martin Bettge, Jeffrey W. Elam, Xiangbo Meng, Anthony K. Burrell, Chunmei Ban, Robert Tenet, Jagjit Nanda and Nancy Dudney, J. Power Sources, in press.
7. "Nanoscale X-Ray Microscopy of High Voltage Lithium-Rich MNC Composite Cathodes With 2D/3D Chemical/Elemental Sensitivity," Presented at 224th ECS Meeting, San Francisco, Oct 2013.

References

1. Battery Test Manual For Plug-In Hybrid Electric Vehicles, Rev. 1, June 2010, INL/EXT-07-12536.
2. USABC Electric Vehicle Battery Test Manual, 2011
3. R. Santhanam, and B. Rambabu, J. Power Sources, 195 (2010) 5442–5451.
4. M. M. Thackeray, C. Johnson, J. T. Vaughey, N. Li, and S. A. Hackney, J. Mater. Chem. 15 (2005) 2257–2267.
5. S. K. Martha, J. Nanda, G. M. Veith, and N. J. Dudney, J. Power Sources, 199 (2012) 220–226.
6. F. Meirer, J. Cabana, Y. J. Liu, A. Mehta, J. C. Andrews, and P. Pianetta, J. Synchrotron Rad. 18 (2011) 773–781.
7. W. C. Chen, Y. F. Song, C. C. Wang, Y. J. Liu, D. T. Morris, P. A. Pianetta, J. C. Andrews, H. C. Wu, and N. L. Wu, J. Mater. Chem. A, 1 (2013) 10847–10856.
8. Nanoscale X-Ray Microscopy of High Voltage Lithium-Rich MNC Composite Cathodes With 2D/3D Chemical/Elemental Sensitivity, Presented at 224th ECS Meeting, San Francisco, Oct 2013
9. J. Nanda, J. Remillard, A. O'Neill, D. Bernardi, T. Ro, K. E. Nietering, J. Y. Go, and T. J. Miller, Adv. Funct. Mater. 21 (2011) 3282–3290.
10. S. K. Martha, J. Nanda, G. M. Veith, and N. J. Dudney, J. Power Sources, 216 (2012) 179–186.
11. V. Cresce, and K. Xu, J. Electrochem. Soc. 158 (2011) A337–A342.
12. M. Bettge, Y. Li, K. Gallagher, Y. Zhu, Q.Wu, W. Lu, I. Bloom, and D. P. Abraham, J. Electrochem. Soc., 160 (2013) A2046-A2055.

VI.B.7 Lithium-bearing Mixed Polyanion (LBMP) Glasses as Cathode Materials (ORNL)

Jim Kiggans and Andrew Kercher
Oak Ridge National Laboratory

P.O. Box 2008; MS 6087
Oak Ridge, TN 37831-6087
Phone: (865) 574-8863; Fax: (865) 574-4357
E-mail: kiggansjojr@ornl.gov

Start Date: June 2012
Projected End Date: June 2016

Objectives

- Model and synthesize mixed polyanion (MP) glasses for use as active cathode materials in lithium ion batteries.
- Demonstrate enhanced material properties and electrochemical performance of glass cathode materials by varying the polyanion content.
- Produce MP glass cathode materials that undergo multivalent transitions in the transition metal cations during electrochemical testing.
- Through laboratory-scale battery testing, demonstrate novel glasses with excellent overall cathode performance that are viable replacements for current cathode materials in electric vehicle applications.

Technical Barriers

The development of MP glass cathode materials has the potential to address the key technical barriers of low energy density, poor high power performance, inadequate cycle life, safety, and high cost.

Technical Targets

- Produce an MP glass cathode with significantly greater capacity at high discharge rates than crystalline $LiFePO_4$.
- Develop an MP glass material with at least a 25% greater specific energy than $LiFePO_4$.
- Demonstrate multivalent MP glass cathodes with specific capacities exceeding 200 mAh/g.

Accomplishments

- Proof-of-principle of the MP glass cathode concept was demonstrated. Dramatic improvements in specific capacity and rate performance were observed with increased polyanion substitution into iron phosphate glass.
- A high-capacity 2nd electrochemical reaction mechanism was found to occur in polyanion glass cathodes. This 2nd mechanism has not been observed in polyanionic crystalline cathode materials.
- Good cycling performance has been demonstrated for an MP glass.
- Thermodynamic models of the electrochemical discharge of polyanion glass cathodes have been developed using the CALPHAD approach and have been refined by benchmarking with experimentally measured discharge curves.

✧ ✧ ✧ ✧ ✧

Introduction

Polyanionic crystalline materials, such as $LiFePO_4$, are promising cathode materials for lithium ion batteries for electric vehicle applications because they can have excellent safety and cycling performance due to their rigid covalently bonded structure. However, many polyanionic crystalline materials with theoretically excellent energy densities, such as $LiCoPO_4$, $LiFeBO_3$, and Li_2MnSiO_4, have not performed well as cathodes due to low electrical conductivity and/or crystal structure changes during cycling. Oak Ridge National Laboratory has proposed that mixed polyanion (MP) glasses can be excellent high capacity cathodes that can overcome the limitations of similar polyanionic crystalline materials.

Mixed polyanion glasses have three key advantages over similar polyanionic crystalline materials. First, with the proper choice of polyanion content, MP glasses can have higher electrical conductivities than similar polyanionic crystalline materials. For example, substitutions of molybdenum oxide, tellurium oxide, and vanadium oxide for phosphate in iron phosphate glasses have demonstrated increases in room temperature electrical conductivity by orders of magnitude. Second,

the disordered covalently bonded structure of MP glasses limits the ability of the structure to rearrange, which holds the promise to prevent undesirable microstructural arrangement during cycling. Third, the polyanion content of glasses can be tailored to produce a cathode with a maximized redox potential for a given electrolyte system. Changing the polyanion content of a polyanionic cathode material has been shown to change the redox potential due to the inductive effect of the polyanion (Isono, et al., J. Power Sources, 2010, 195: 593-598). Depending on the amount and electronegativity of the polyanion substituted in the glass, the voltage of a glass cathode could be increased or decreased to the desired optimal voltage.

Most polyanionic crystalline materials are phosphates, borates, or silicates. Phosphates, borates and silicates are renowned glass formers using conventional glass processing methods. Therefore, producing these novel glass cathode materials will not likely require exotic processing methods, but could be produced by low-cost conventional glass processing methods.

Approach

The research into MP glass cathode materials involves: (1) computational thermodynamic modeling, (2) glass processing, (3) glass structure and property characterization, and (4) electrochemical testing. Computational thermodynamic models of the electrochemical response of prospective MP glasses will be used to make decisions on the most promising glasses to pursue. Classical heat/quench glass processing has been the primary processing method. Characterization techniques are being used to confirm amorphous structure, to determine transition metal valences, and to measure fundamental glass properties. Electrochemical testing is being performed on coin cells with powdered glass cathodes produced by conventional slurry casting.

Results

Proof-of-principle for MP glass cathodes. A series of iron phosphate vanadate glasses (compositions based on $Fe_4([1\text{-}x]\ P_2O_7 \bullet [x]\ V_2O_7)_3$) were produced with the polyanion content containing 0%, 30%, and 50% vanadate. Micron-scale powders of these glasses were electrochemically tested in coin cells to demonstrate the effect of mixed polyanion content on electrochemical performance. As expected, the pure iron phosphate glass showed almost no capacity (0.36% theoretical) when discharged down to 2V. However, the capacity and rate performance improved dramatically with increasing vanadate substitution in the glass (Figure VI - 35). The demonstration of dramatically improved electrochemical behavior in a glass cathode by incorporating mixed polyanion content is a proof-of-principle for the MP glass cathode concept.

Complete discharge curves of the 50% vanadate substituted iron phosphate glass showed that the electrochemical intercalation reaction during discharge yielded full iron-based theoretical capacity (Fe^{3+} to Fe^{2+}) and some additional vanadium-based capacity (V^{5+} to V^{4+}). X-ray absorption spectroscopy (XANES) near the iron and vanadium edges performed at the National Synchrotron Light Source at Brookhaven National Laboratory (BNL) confirmed the iron and vanadium valence changes during the intercalation stage of battery discharge.

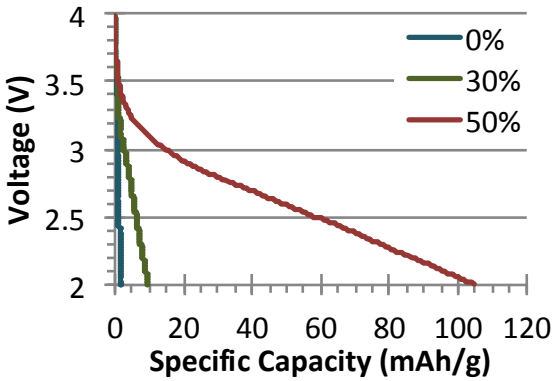

Figure VI - 35: Iron phosphate vanadate glasses with different amounts of vanadate substitution (0%, 30%, and 50%) were battery tested at ~C/30 from 4V to 2V. The specific capacity increased dramatically with increased vanadate substitution

High-capacity reaction mechanism. When discharged, cathodes of polyanionic crystalline materials undergo a lithium intercalation reaction. When MP glass cathodes were discharged down to 1V, the lithium intercalation reaction and a second lower-voltage, high-capacity reaction were observed (Figure VI - 36). Initial battery testing has suggested that both electrochemical reactions are reversible. The second electrochemical reaction has been observed in iron-bearing and manganese-bearing glasses.

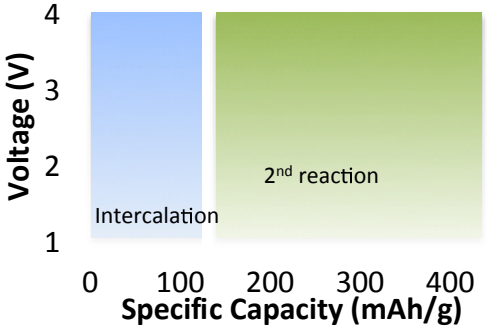

Figure VI - 36: A high capacity 2nd electrochemical reaction was discovered to occur in polyanion glasses. A discharge curve of $Fe_4(50\%\ P_2O_7 \bullet 50\%\ V_2O_7)_3$ glass (19 mA/g) is shown

MP glass cathodes at different electrochemical stages were analyzed by XANES at the National Synchrotron Light Source at BNL in order to study this second reaction mechanism. XANES analysis showed that, during discharge of iron phosphate vanadate glass cathodes, the iron changes from Fe^{3+} to Fe^{2+} during the intercalation reaction and from Fe^{2+} to Fe^{0} during the second reaction (Figure VI - 37). Vanadium valence was not observed to change during the second reaction. Using these insights into the second reaction mechanism, MP glasses could be designed that undergo this high-capacity reaction at higher voltages.

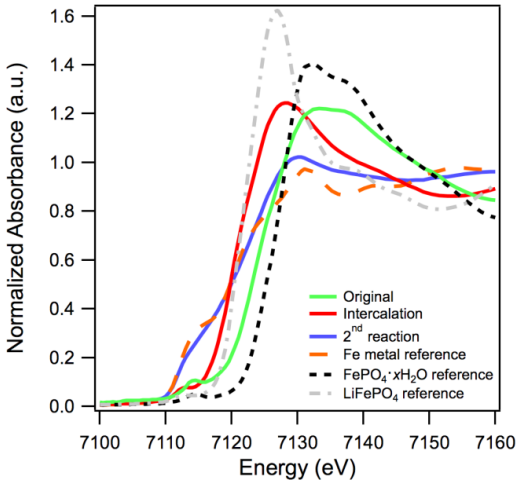

Figure VI - 37: XANES analysis showed how iron valence changed during the discharge of iron phosphate vanadate glass

Cycling performance of MP glass. Lithium iron phosphate is a polyanionic crystalline material that has excellent cycling performance. Cycle testing of MP glass cathodes was performed to determine how well polyanionic glass cathodes can cycle. Initial cycle tests have focused on the cyclability of $Fe_4(50\%\ P_2O_7 \bullet 50\%\ V_2O_7)_3$) in the intercalation reaction. The cathodes cycled well between 4V and 2V at C/10 for 100 cycles (every 20th cycle at C/50) (Figure VI - 38).

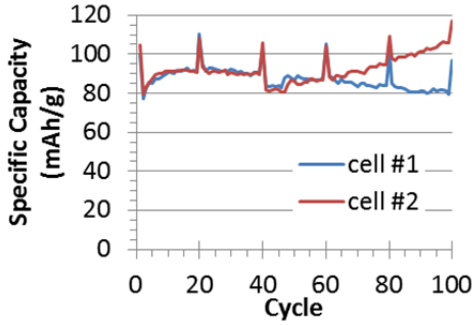

Figure VI - 38: Cycle testing of iron phosphate vanadate glass showed good cycleability. (C/10 cycling with every 20th cycle at C/50)

Computational model of MP glass. Unlike polyanionic crystalline materials, MP glasses have a large compositional flexibility and provide diverse options for prospective glass cathode compositions. Computational thermodynamic modeling using a CALPHAD (CALculation of PHAse Diagram) approach has been developed with the goal of predicting the discharge curves of MP glass concepts and guiding the project toward the most promising candidates.

Computational thermodynamic modeling has successfully reproduced the equilibrium discharge curve for crystalline lithium iron phosphate using the corresponding thermodynamic data for the constituent oxides. Since glass is inherently a non-equilibrium structure, different thermodynamic models have been developed to predict the electrochemical behavior of MP glass. The 1st generation model was based on the Gibbs free energy of the crystalline oxides of the desired composition mixed in different proportions with the Gibbs free energy of the glass melt extrapolated down to room temperature (dashed curves on Figure VI - 39). The sloped discharge curves observed in MP glasses could not be predicted based on 1st generation models. In the 2nd generation model, a symmetric sub-regular solution model was included to express non-ideality between the mixing of Li and vacancy in the dedicated sublattice. When benchmarked against experimental discharge curves for $Fe_4(50\%\ P_2O_7 \bullet 50\%\ V_2O_7)_3$), the 2nd generation model (90% solid / 10% liquid with aforementioned non-ideality) showed excellent agreement with experimental data (black solid curve on Figure VI - 39).

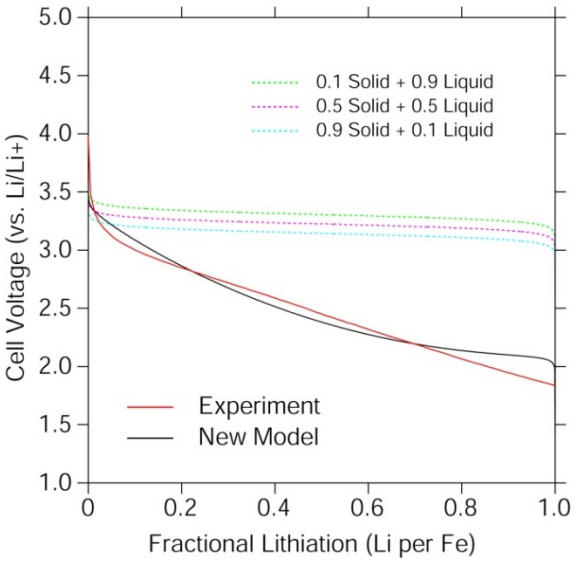

Figure VI - 39: 1st generation (dashed lines) and 2nd generation (black line) computational thermodynamic models of the equilibrium discharge curve for an iron phosphate vanadate glass benchmarked against an experimentally measured discharge curve (red line)

Conclusions and Future Directions

Battery testing of iron phosphate vanadate glass cathodes provided a solid proof-of-principle for the MP glass cathode concept, demonstrating both improved capacity and rate performance with mixed polyanion content. Cyclable intercalation of iron phosphate vanadate glass has been demonstrated. The unexpected discovery of a high capacity 2nd electrochemical reaction suggested the possibility of a new avenue for obtaining a high capacity cathode material. The second generation of computational thermodynamic models of glass electrochemical performance showed excellent agreement with experimental discharge curves. The second generation models will predict candidate glass performance and provide guidance toward the most promising glass candidates.

Now that proof-of-principle of MP glass cathodes has been demonstrated, the project focus has been placed on glass systems with theoretical specific energies that exceed lithium iron phosphate by at least 30%. Multivalent intercalation is one route to achieve high specific energies. Transition metals of interest for multivalent intercalation in a useful voltage window include manganese, copper, and molybdenum. The 2nd electrochemical reaction found in MP glasses could offer another potential route to achieve high specific energies. The 2nd reaction appears similar to the conversion reaction found in transition metal oxides and halides. Using the voltage trends observed in conversion cathodes, future glass candidates would be chosen to potentially have these 2nd reactions occur at higher voltages. Cycling performance of the 2nd reaction will also be studied to determine long-term reversibility of the reaction.

FY 2013 Publications/Presentations

N/A

VI.B.8 Development of High-Energy Cathode Materials (PNNL)

Ji-Guang Zhang
Pacific Northwest National Laboratory

902 Battelle Boulevard
Richland, WA 99352
Phone: (509) 372-6515, Fax: (509) 375-2186
E-mail: jiguang.zhang@pnnl.gov

Jie Xiao (co-PI)
Pacific Northwest National Laboratory
902 Battelle Boulevard
Richland, WA 99352
Phone: (509) 375-4598, Fax: (509) 375-2186
E-mail: jie.xiao@pnnl.gov

Start Date: October 2011
Projected End Date: September 2015

Objectives

- Develop high-energy cathode materials with improved safety.
- Develop low-cost synthesis routes for environmentally benign cathode materials with long cycle life.

Technical Barriers

This project addresses the following technical barriers:

- High cost of materials and synthesis methods
- Limited energy density and cyclability
- Safety

Technical Targets

- Understand the failure mechanism of Li-Mn-rich (LMR) active materials $xLi_2MnO_3 \cdot (1-x)LiMO_2$ (M = Mn, Ni, Co; $0 \leq x \leq 1$).
- Modify the synthesis methods to improve electrochemical performance of LMR cathode.
- Adjust interfacial properties between electrode and electrolyte to reduce parasitic reactions.

Accomplishments

- Revealed corrosion and fragmentation of LMR cathode after cycling that was detrimental to cell performances.
- Investigated the electrochemical kinetics of both layered $LiNi_{0.5}Mn_{0.5}O_2$ and Li_2MnO_3 components in LMR during the electrochemical processes.
- Identified electrolyte additive that alleviated the side reactions between oxygen species and electrolyte at high voltages.

✧ ✧ ✧ ✧ ✧

Introduction

LMR layered composites, for example, $Li[Li_{0.2}Ni_{0.2}Mn_{0.6}]O_2$, have attracted extensive interest because of highest energy density. The co-existence of two different components, i.e., layered $LiNi_{0.5}Mn_{0.5}O_2$ and Li_2MnO_3 in LMR improves the capacity of this type of layered composites. In the first few cycles, Li_2MnO_3 was activated and a discharge capacity of greater than 250 mAh g^{-1} can be achieved. However, this activation process always is accompanied by the layered-to-spinel phase transition that releases oxygen from the lattice due to cation migration. The released oxygen reacts with the carbonate-based electrolytes, generates insulating by-products and leads to low discharge rate and capacity fade. The structure change will also lead to voltage fading with cycling. Therefore, voltage fade and low discharge rate are the main barriers preventing large scale use of LMR cathode materials.

Approach

- Use advanced characterization technique to understand the effects caused by the oxygen release and phase transition.
- Apply knowledge gained in high voltage Li-ion battery system to study the degradation mechanism in LMR cathode.
- Explore novel electrolyte additives to control the interfacial reactions between LMR cathode and electrolyte at high voltages.

Results

1. LMR cathode morphology evolution during cycling. In order to identify key factors related with the layered-to-spinel transition for LMR cathode, aberration-corrected Scanning Transmission Electron Microscopy (S/TEM) combined with Electron Energy Loss Spectroscopy (EELS) were used to probe the structure evolutions of $Li[Li_{0.2}Ni_{0.2}M_{0.6}]O_2$ during long-term cycling (Figure VI - 40). Corrosion and

fragmentation of cathode particles were identified on the cycled layered composite. Additionally, Mn^{2+} species and reduced lithium content in the fragmented pieces were revealed by EELS, which were correlated with the capacity degradation mechanism.

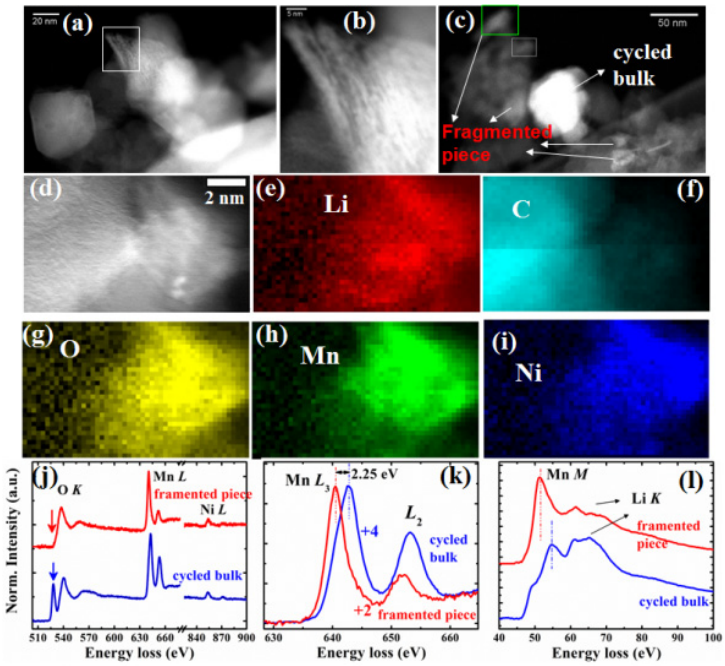

Figure VI - 40: (a) Overview image showing the cathode nanoparticles after cycling; (b) magnified image of the region labeled by the white rectangle shown in (a); (c) Overview image of another region with fragmented pieces of cathode; (d) magnified image of the region labeled by the rectangle in (c); (e) Li map (58.25-65.5eV); (f) C map (282.25-314.75 eV); (g) O map (527.75-564eV); (h) Mn map (634.25-659eV); (i) comparison of O K, Mn L, and Ni L edges; (k) Mn L edges normalized to Mn L_3 peak; (l) Mn M, and Li K edge comparison of cycled bulk region and fragmented piece region

Pristine $Li[Li_{0.2}Ni_{0.2}M_{0.6}]O_2$ was composed of crystallized particles (~200 nm) with well-defined layered structure. However, after 300 cycles, sponge-like etched surfaces were clearly observed (Figure VI - 40a-b) along with fragmented pieces (Figure VI - 40c-d). Li, C, O, Mn and Ni EELS maps (Figure VI - 40e-i) were collected from the selected region of fragmented pieces, which suggested that the fragmented pieces mixed with solid electrolyte interface (SEI) components, likely originated from the bulk particles after repeated cycling. In addition, consistent with the oxygen-deficient environment (Figure VI - 40j), Mn valence in the fragmented pieces was quantified to be 2^+ (Figure VI - 40k), much lower than in the bulk. In addition, Li K edge peak intensity in the fragmented particle was much lower than the cycled bulk region (Figure VI - 40l), suggesting that the fragmentation probably initiated during the lithium extraction/charge process. This was consistent with the large strain generated from extensive removal of Li^+ and oxygen release during charge. The etched surfaces, which may evolve into fragmented pieces after cycling, were detrimental to the electrochemical properties of LMR cathode due to the loss of intimate contact with the electrode, passivation of new surface, and related increase in cell impedance.

2. Electrochemical kinetics of LMR cathode. To understand the poor rate performances of LMR cathode materials, the electrochemical kinetics of LMR during cycling has been investigated. It was found that the diffusion rate of Li^+ in LMR was mainly determined by the Li_2MnO_3 and its derived phase. Li_2MnO_3-derived phase exhibited good charge rate capability but poor discharge rate capability, which became the limiting factor at high discharge rates.

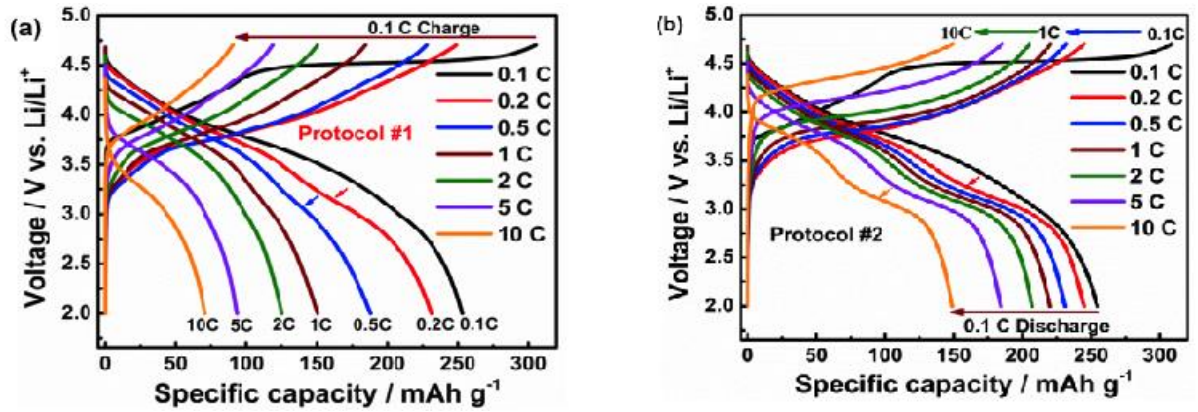

Figure VI - 41: Voltage profiles of $Li[Li_{0.2}Ni_{0.2}Mn_{0.6}]O_2$ (a) Constant charge at 0.1 C (1C=250 mA/g) and discharged at different rates for the subsequent cycles. (b) Charged at different rates and constant discharge at 0.1 C for the following cycles

Figure VI - 41(a) shows the voltage profiles of $Li[Li_{0.2}Ni_{0.2}M_{0.6}]O_2$ when a slow rate of 0.1C was used for all charges but different rates were applied during discharge. The voltage fading related to the spinel-phase transition (represented by a clear dent on the voltage curve at about 3.3V as shown in Figure VI - 41) was only observable at relatively slow discharge rates (≤ 2C) and completely disappeared at high rate above 2C. This result can be attributed to a poor rate capability of the Li_2MnO_3 component. In other words, discharge capacity delivered at 10C was dominated by the layered $LiNi_{0.5}Mn_{0.5}O_2$ component. When different charge rates were applied on the LMR cathode, followed by discharging at the same slow rates (Figure VI - 41b), the capacity retention is largely improved compared with Figure VI - 41a. In this case, the voltage fading is still seen during discharge even after charging at 10C, indicating that Li_2MnO_3-derived spinel phase has a good charge rate capability. It was suggested that slow discharge rate should be used to effectively capture and understand the voltage-fading phenomenon in LMR. The diffusion of Li^+ ions within lattice structure of Li_2MnO_3-derived phase had to be increased to improve the rate performances of LMR aided by the modifications of interfacial reactions, which is now under investigation.

3. Modification of interfacial reactions by using electrolyte additives. In order to modify the interfacial properties between the LMR cathode and electrolyte, boron-based anion receptor, tris(pentafluorophenyl) borane (TPFPB) was adopted as an electrolyte additive to limit the negative effects from oxygen species in the system. In previous works, TPFPB has been used to improve the performances of batteries containing graphite and $LiMn_2O_4$ by partially dissolving the byproducts such as LiF and Li_2O. Considering the strong anion coordination effect of TPFPB, the released oxygen species in the form of oxygen anions (O_2^{2-}/O_2^-) or radicals (O_2^{--}/O^-) may be trapped in the vicinity of TPFPB instead of attacking the electrolyte.

Figure VI - 42 summarizes the proposed working mechanism of TPFPB. During the activation of Li_2MnO_3, oxygen is extracted out of the structural lattice as highly active oxygen species, e.g., O_2^-/O_2^{2-}, or O^-, which are reactive Lewis base that could decompose the carbonate-based electrolyte. It is hypothesized that O_2^-/O_2^{2-} extracted out of LMR lattice can be partially captured by boron atom located in the center of TPFPB, eliminating direct exposure to the electrolyte which would initiate parasitic reactions. Even though O_2 still forms, it dissolves in the presence of TPFPB since the oxygen solubility in perfluorinated compound is much higher than in carbonate solvents. The byproducts derived from the interactions between electrolyte and O_2^-/O_2^{2-} were therefore substantially reduced. Other parasitic reactions such as electrolyte decomposition at high voltages also produced insulating salts such as LiF and Li_2O etc., which were again soluble in the presence of TPFPB. Therefore, the intensive interfacial reactions during the first cycle as well as the continuous accumulation of passivation film on cathode surface are significantly alleviated in the presence of TPFPB, which stabilizes the electrode/electrolyte interface.

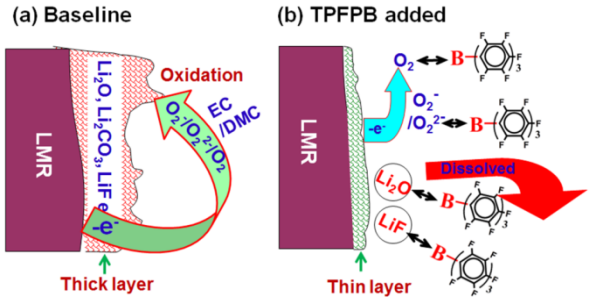

Figure VI - 42: Scheme of the functioning mechanism of TPFPB. (a) Thick passivation layer formation in baseline electrolyte; (b) significantly reduced passivation layer formation in TPFPB added electrolyte

Figure VI - 43a shows the initial charge/discharge curves between 2.0 and 4.7 V for $Li[Li_{0.2}Ni_{0.2}Mn_{0.6}]O_2$ cycled in electrolytes with different TPFPB concentrations. The charge/discharge profiles almost overlapped with each other for Li $[Li_{0.2}Ni_{0.2}Mn_{0.6}]O_2$ electrodes in baseline electrolyte and TPFPB containing electrolyte due to very low current density (0.1 C) used for the first three formation cycles. An irreversible voltage plateau at ca. 4.4 ~ 4.6 V was observed in all three cells caused by the irreversible loss of oxygen from the LMR electrode. After activation, the electrode materials delivered similar high discharge capacity of ca. 245 mAh g^{-1} in all electrolytes (Figure VI - 43a), indicating that TPFPB additive had good compatibility with both $Li[Li_{0.2}Ni_{0.2}Mn_{0.6}]O_2$ and the electrolyte during electrochemical processes. In the subsequent cycling at C/3 (Figure VI - 43b), an initial discharge capacity of ~200 mAh g^{-1} was still achieved in all cells. However, fast capacity fading was observed for $Li[Li_{0.2}Ni_{0.2}Mn_{0.6}]O_2$ in baseline electrolyte with cycling. In contrast, remarkably improved cycling stability was revealed with the addition of TPFPB. Even after 300 cycles, the discharge capacities were maintained at 157 and 161 mAh g^{-1} for cathodes tested in electrolytes with 0.1 M and 0.2 M TPFPB, respectively, correspond-ding to capacity retentions of 80.6% and 81.0%. For LMR cathode, one important reason for the continuous capacity fading was the deterioration of electrode/ electrolyte interface, associated with a thick passivation layer formation and the corrosion/fragmentation of LMR cathode bulk structure. If TPFPB in the electrolyte effectively accepted oxygen anions or radicals before O_2 was generated, the damages of active oxygen species (including O_2^-/O_2^{2-}, or O^-) to LMR electrode surface should be much less than that without TPFPB.

The above prediction is verified by the TEM analysis of the fresh and cycled electrodes in different electrolytes (Figure VI - 44). Before cycling, a relatively smooth particle surface is observed (Figure VI - 44a). After 300 cycles, clear difference in particle surfaces was identified for electrolyte without and with TPFPB. In baseline electrolyte (Figure VI - 44b), the image revealed a distinguishable passivation layer on the surface of cycled $Li[Li_{0.2}Ni_{0.2}Mn_{0.6}]O_2$ electrode, with a thickness of 10-15 nm. In comparison, electrode cycled in the presence of TPFPB (Figure VI - 44c and d) displayed well-maintained particle morphology with smooth particle surface covered by a much thinner passivation layer. These findings substantiated our hypothesis on the capability of TPFPB in modifying the interfacial reactions through the stabilization of anions/radicals as well as dissolution of oxygen species and insulating byproducts.

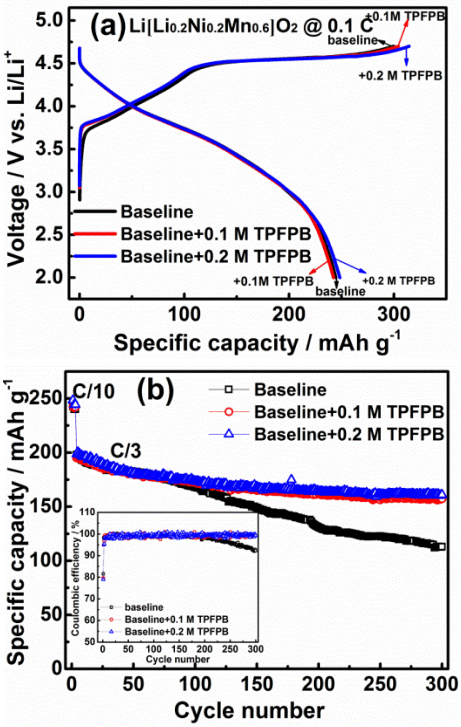

Figure VI - 43: (a) Initial charge/discharge profiles at 0.1 C (25 mA g^{-1}) and (b) long-term cycling performance of cathode material $Li[Li_{0.2}Ni_{0.2}Mn_{0.6}]O_2$ at C/3 after 3 formation cycles at 0.1 C. The inset of (b) is the corresponding Coulombic efficiency during cycling

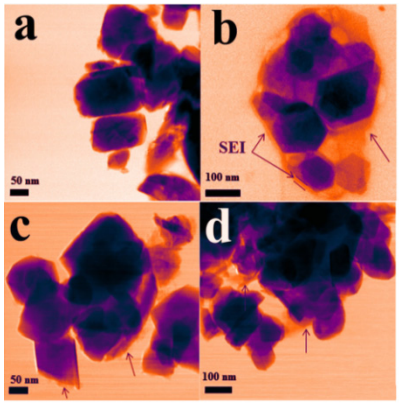

Figure VI - 44: TEM images of fresh electrode and electrodes cycled in electrolytes without and with additive after 300 cycles at C/3 rate. (a) fresh, (b) baseline, (c) 0.1 M TPFPB, (d) 0.2 M TPFPB

Conclusions and Future Directions

The adverse effects of oxygen release from LMR lattice during initial activation have been systematically investigated in terms of the electrode integrity after long term cycling and the interfacial side reactions, which were then correlated to the cell failure mechanism. The

electrochemical kinetics of LMR was studied to understand the poor rate capability of LMR. It was revealed that large strain was generated from oxygen release and cation migration during charge, etching LMR surfaces into fragmented pieces during cycling. The release of active oxygen species strongly interacted with carbonate-based electrolyte solvents and produced a large amount of insulating byproducts on LMR surface and largely increased cell impedance. All of the above key-chain reactions from oxygen release partially explained the fast capacity degradation, voltage fading and poor discharge rate capabilities of LMR. TPFPB as an anion acceptor effectively coordinated with oxygen species and reduced the parasitic reactions initiating on LMR surfaces, leading to improved cycling stability. Voltage fading was also alleviated in the presence of TPFPB additive, suggesting that voltage fading is a combined effect of phase transition and surface reactions.

Future efforts include the exploration of intrinsic layered-to-spinel transition at atomic level and understanding how to mitigate/prevent this lattice change by adjusting the synthesis route. Study on the interface reactions will also be continued with an emphasis on the electrolyte modification

FY 2013 Publications/Presentations

1. J. Zheng, M. Gu, J. Xiao, P. Zuo, C. Wang, J.-G. Zhang, "Corrosion/Fragmentation of Layered Composite Cathode and Related Capacity/Voltage Fading during Cycling Process," *Nano letters*, **13**, 3824-3830 (2013).
2. J. Xiao, X. Yu, J. Zheng, Y. Zhou, F.Gao, X. Chen, J. Bai, X.-Q. Yang, J.-G. Zhang, "Interplay between Two-Phase and Solid Solution Reactions in High Voltage Spinel Cathode Material for Lithium Ion Batteries," *J. Power Sources*, **242**,736-741 (2013).
3. J. Zheng, W. Shi, M. Gu, J. Xiao, P. Zuo, C. Wang, J.-G. Zhang, Electrochemical Kinetics and Performance of Layered Composite Cathode Material Li $[Li_{0.2}Ni_{0.2}Mn_{0.6}]O_2$, *J. Electro-chem. Soc.*, **160**, A2212-A2219 (2013).
4. J. Zheng, J. Xiao, Z. Nie, J.-G. Zhang, Lattice Mn^{3+} Behaviors in $Li_4Ti_5O_{12}/LiNi_{0.5}Mn_{1.5}O_4$ Full Cells, *J. Electrochem. Soc.*, **160**, A1264-A1268 (2013).
5. J. Zheng, J. Xiao, W.Xu, X. Chen, M.Gu, X. Li, J.-G. Zhang, "Surface and structural stabilities of carbon additives in high voltage lithium ion Batteries," *J. Power Sources,* **227**, 211-217 (2013).
6. M. Gu, I. Belharouak, J. Zheng, H. Wu, J. Xiao, A. Genc, K. Amine, S. Thevuthasan, D. R. Baer, J-G. Zhang, N.D. Browning, J. Liu, and C.M. Wang, "Formation Of The Spinel Phase In The Layered Composite Cathode Used In Li-Ion Batteries," *ACS Nano* **7**(1):760-767 (2013).
7. P.V. Sushko, K.M. Rosso, J-G. Zhang, J. Liu, and M.L. Sushko, "Oxygen vacancies and ordering of d-levels control voltage suppression in oxide cathodes: the case of spinel $LiNi_{0.5}Mn_{1.5}O_{4-\delta}$," Adv. *Funct. Mater,* DOI: 10.1002/adfm.201301205 (2013).
8. J.-G. Zhang and J.Xiao, *2013 DOE BATT Program Annual Peer Review Meeting*, March 2013, Washington, DC.
9. J. Xiao, J. Zheng, X. Li, Y. Shao, and J-G. Zhang, "Hierarchically Structured Materials for Lithium Batteries," *Nanotechnology*, 24, 424004, doi:10.1088/0957-4484/24/42/424004, 2013.
10. J. Xiao, J. Zheng, X. Chen, W. Xu and J. Zhang, "High Voltage Li-ion Batteries," *222th ECS Meeting, PRiME*, 2012, Honolulu, Hawaii.
11. J.-G. Zhang, J. Xiao, and C. Wang, "Factors Affecting the Structure and Performance of High Energy Cathodes," Presented in *2013 US Drive meeting* held at ANL, Jan. 24, 2013, Chicago, IL.

VI.B.9 Optimization of Ion Transport in High-Energy Composite Cathodes (UCSD)

Ying Shirley Meng
University of California San Diego

Department of Nanoengineering
9500 Gilman Dr. #0448
La Jolla, CA, 92093 – 0448
Phone: (858) 534-9553; Fax: (858) 534-9553
E-mail: shmeng@uced.edu

Start Date: October 2012
Projected End Date: September 2016

Objectives

- Investigate the factors that affect and control Li ion transportation, transition metal (TM) migration and oxygen activity in the high-energy Li rich composite cathodes.
- Explore the relationship between electrochemistry, particle morphology, bulk compositions, and surface characteristics.
- Design new compositions for Li excess layered cathode materials that have optimum rate capability, reversible capacity and voltage stability.

Technical Barriers

The low rate and poor voltage stability of high-energy Li rich composite cathodes.

Technical Targets

- PHEV: 96 Wh/kg, 5,000 cycles; EV: 200 Wh/kg; 1,000 cycles (80% DoD)

Accomplishments

- Identified dynamic structural changes and quantified voltage stability upon cycling.
- Identified at least two best Li rich layered candidate materials as focus samples.
- Demonstrated the chemical sensitivity and special resolution of the suite of surface characterization tools, including STEM/EELS, XPS and first principles computation modeling.

✧ ✧ ✧ ✧ ✧

Introduction

Advanced diagnostics are essential to investigate performance-limiting processes in batteries. Li transport is significantly more complex in composite structures that locally integrate different crystal structures at the nano-scales. At these scales, interfaces separating different local crystal structures can play a significant role on Li transport, but precisely how is not at all understood. Some composite arrangements and spacings may promote significantly higher Li mobilities than others while some may suppress Li transport. Insights about the role of nano-scale modulations in crystal structure and chemistry are lacking but essential for the directed design of composite electrodes with significantly improved rate capabilities. Careful engineering of the surface (coating) and bulk compositions (substitution) of these nanostructured materials may lead to significant improvement on ion transport. The aim of this project is to combine a suite of diagnostic tools, including scanning transmission electron microscopy and electron energy loss spectroscopy, as well as first principles computation, to characterize new generation high-energy density lithium transition metal oxides and high capacity silicon carbon composites.

Approach

The approach uniquely combines atomic resolution scanning transmission electron microscopy (a-STEM) & electron energy loss spectroscopy (EELS), X-ray photoelectron spectroscopy (XPS) and first principles computation to elucidate the dynamic changes in the bulk and surface of complex oxide materials during electrochemical cycling. A systematic study with powerful analytical tools is necessary to pin down surface coating mechanisms in order to determine the optimal surface characteristics of electrode materials for high rate and long life and to assist in the development of large scale synthesis methods for producing consistently high quality material.

Results

Materials. Li-excess materials with and without Co substitution have been successfully synthesized using a co-precipitation method. Sol-gel, double hydroxide and carbonate syntheses routes were explored and it was found that the different secondary particle morphologies

and surface characteristics subsequently resulted in different electrochemical performances. The trials led to the conclusions that the double hydroxide method would be most suitable to consistently synthesize high quality samples for diagnostic efforts.

The electrochemical performance (i.e., discharge capacity and rate performance) of these materials has been optimized by changing the weight ratios between lithium and transitional metals as represented by the chemical formula, $xLi_2MnO_3 \bullet (1-x)LiMO_2$ (M=Ni, Mn, and Co). A typical rate profile for the optimized $Li_{1.2}Ni_{0.2}Mn_{0.6}O_2$ composition is provided in Figure VI - 45. When the sample was discharged at 2.0 C (1C = 250 mAh/g) between 2.0 V and 4.8 V, it could still provide a capacity of 170 mAh/g.

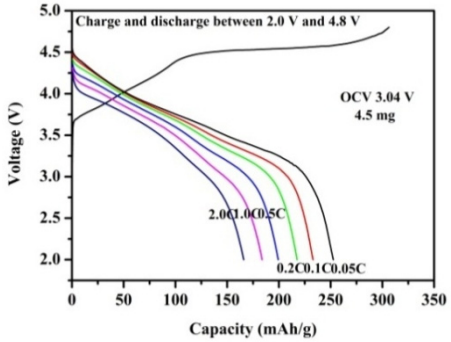

Figure VI - 45: typical rate performance of sample $Li_{1.2}Ni_{0.2}Mn_{0.6}O_2$

The effect that controlling $Li_{1.2}Ni_{0.2}Mn_{0.6}O_2$ sample morphology had on cyclic performance was studied. Figure VI - 46 compares the morphology of a pristine sample with no morphology control to that of a sample with morphology control. The morphologically controlled sample is composed of uniformly spherical particles with diameters in the range of 2–3µm. Although the spherical material initially exhibits a relatively smaller discharge capacity (Figure VI - 47) than the pristine sample, it cycles more stably. It was observed that morphology control improved capacity retention during cycling and partially prevented voltage fade.

XPS and STEM/EELS diagnosis. XPS and STEM/EELS were used to study the mechanism of voltage and capacity fade. The STEM for pristine and electrochemically cycled $Li_{1.2}Ni_{0.2}Mn_{0.6}O_2$ are shown in Figure VI - 48. After cycling, an amorphous 2–5 nm thick organic layer was observed on the surface of the material that might be related to the decomposition of electrolyte at high voltage. In addition, cation rearrangement at the surface of the particle formed a layer of the "defect spinel" phase and the amorphous outer layer was observed to increase in thickness upon further cycling.

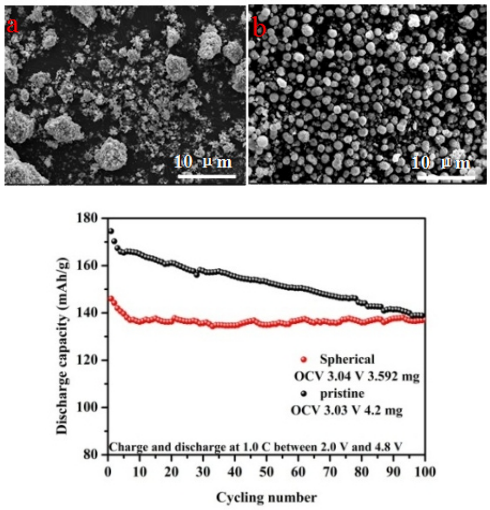

Figure VI - 46: SEM images of $Li_{1.2}Ni_{0.2}Mn_{0.6}O_2$: (a) non spherical pristine material, and (b) homogenous spherical material, both prepared by a co-precipitation method

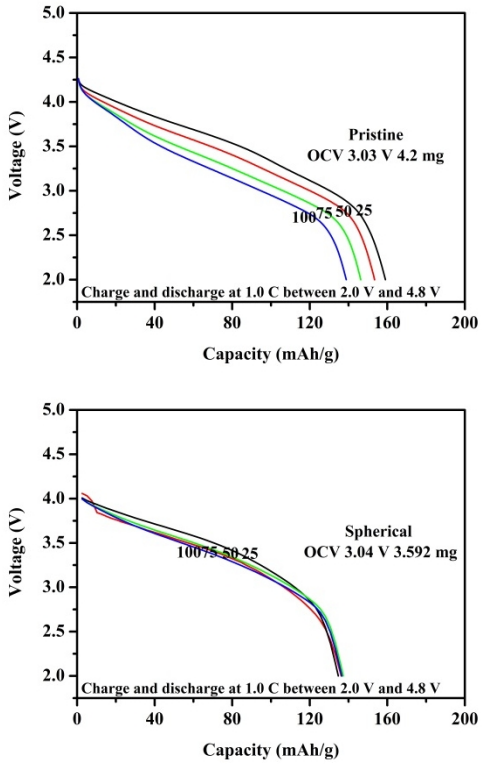

Figure VI - 47: Comparison of cycling performance between $Li_{1.2}Ni_{0.2}Mn_{0.6}O_2$ samples with different morphologies

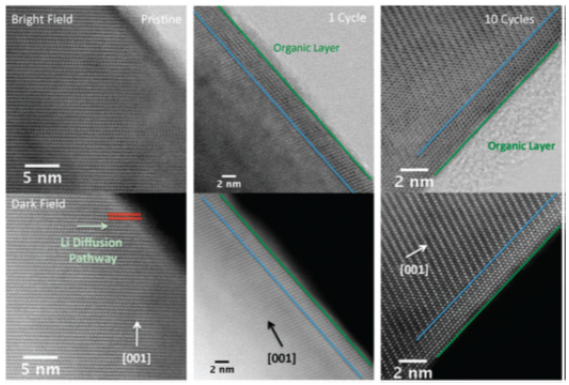

Figure VI - 48: a-STEM images for pristine, one and ten times electrochemically cycled electrode materials with their corresponding High-Angle Annular Dark-Field (HAADF) images showing surface rearrangement occurring after cycling

Ex situ surface XPS and EELS data is provided in Figure VI - 49, corresponding states of charge (SOC) are labeled A – H. In Figure VI - 49a, at SOC H, the oxygen signal did not fully recover to its original pristine state after one cycle (Figure VI - 49b). This indicated that the oxygen redox reaction was not fully reversible at the surface after the first electrochemical cycle. The XPS O1s region is provided in Figure VI - 49c. It was not until 4.45 V that the formation of a higher binding energy (535 eV) peak was observed. This peak may be associated with a superoxide species. The cause of the initial superoxide formation is believed to be the result of oxygen evolution and subsequent reaction with the electrolyte.

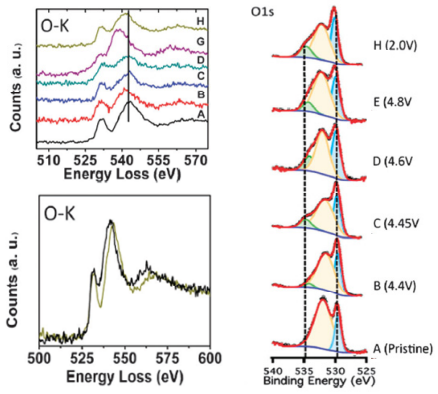

Figure VI - 49: Surface EELS data for the (a) O–K edge spectra, (b) comparison of the pristine and the fully discharged O–K edge, and (c) XPS data for the O1s region

The bulk EELS data are compared to the surface EELS results and are provided in Figure VI - 50. From SOC C to D, the ratio of the lower energy peak to the higher peak increased which may indicate the formation of oxygen vacancies. The ratio change may also be an indication of a local change to oxygen's local environment. After SOC C, the ratio of oxygen peaks remained constant. The ratio is larger than that for peaks in SOC A or B. A larger ratio may be a result of oxygen vacancy formation and a stronger bonding environment between oxygen and TM. The ratio shift was not reversible at the end of the first cycle.

In order to evaluate the effect of bulk substitution on the Li rich layered oxide, a series of samples with various substitutional elements were prepared. From XPS (Figure VI - 51a-b), the bonding energy shift of the Ni 3s peak identifies Ni^{2+}/Ni^{4+} as the redox couple during cycling. During the 4.5V plateau region, both the Co 2p satellite relative area and the Ni 3s bonding energy results show that the oxidation states of surface Co and Ni were reduced and that oxygen vacancies may have been formed. After cycling, a defect spinel phase was visualized by high resolution STEM. Chemical differences can be identified from the EELS spectra. While the bulk spectra (red) has an oxygen pre-peak and indicates that Mn was not reduced, the oxygen pre-peak is absent in the surface spectra (blue) and surface Mn was reduced.

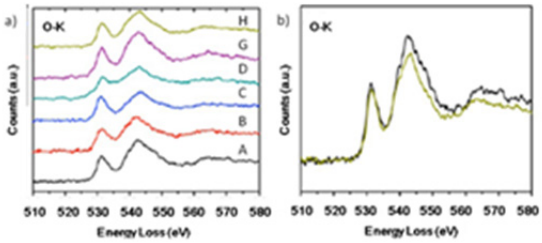

Figure VI - 50: Bulk EELS data for the (a) O–K edge spectra, and (b) comparison of the pristine and the fully discharged O–K edge

Based on the results above, the local environments of Ni^{4+}, Mn^{4+}, and O all simultaneously changed in the bulk and surface. Each may participate in charge compensation during the voltage plateau region, but some may not do so reversibly. Oxygen vacancies in the structure along with surface phase transformations are the two main hypotheses proposed to understand the voltage and capacity fading.

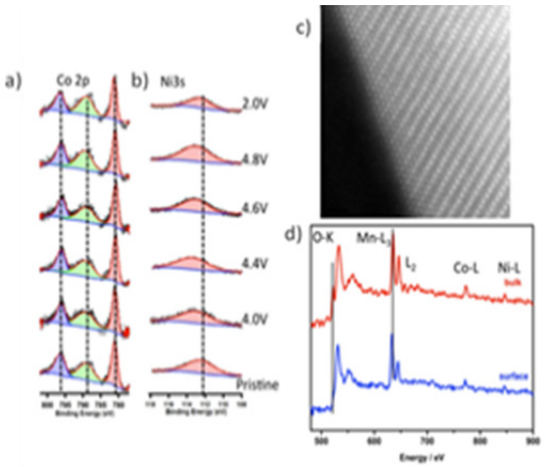

Figure VI - 51: (a, b) XPS of surface transition metal ions oxidation status changes; (c) HRSTEM images of surface phase transformation; (d) EELS spectrum from cycled samples

Computational results --- oxygen vacancy assisted surface phase transformation. From previous experimental results, it is understood that oxygen vacancies tend to form in the vicinity where phase transformation occurs. Thus, a computational study of oxygen evolution and transition metal migration barriers in Li-excess material were carried out using first principles with the Hubbard U correction on the generalized gradient approximation (GGA+U) to the density functional theory (DFT). A general trend of calculated oxygen vacancy formation energies (E_{fov}) versus lithium concentrations is shown in Figure VI - 52. The lithium concentration of these calculations ranges from 28/28 to 14/28. It is clear that E_{fov} decreases sharply from ~2.7eV at fully lithiated state to less than 1eV for Li concentration between 20/28 to 14/28. Note that at Li concentration 10/14, the tetrahedral Li-Li dumbbells begin to form, leading to the possible formation of defect spinel phases. All the calculations were bulk calculations. In reality, it is easier to form oxygen vacancies at material surfaces or sub-surfaces than in bulk due to slow oxygen diffusion.

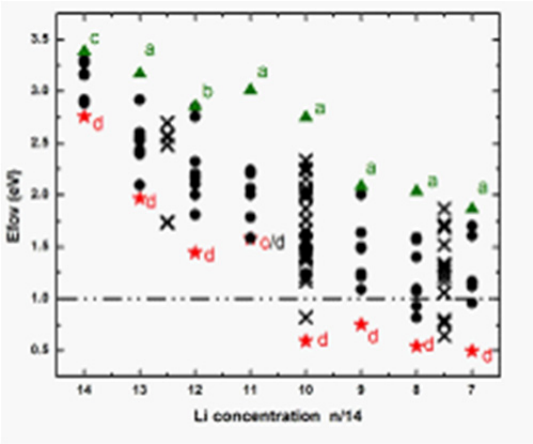

Figure VI - 52: Oxygen formation energy at different Li concentrations

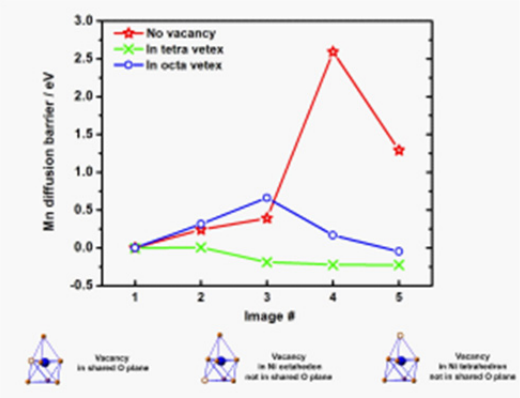

Figure VI - 53: Mn diffusion barrier at Li concentration 20/28

In order to investigate the migration mechanism of TM ions, the transition state theory is adopted in this work since it has been extensively utilized to describe the diffusion of cations in materials. Mn diffusion from an initial octahedral site in the TM layer to the nearest tetrahedral site in the Li layer was investigated at Li concentration $Li_{20/28}Ni_{1/4}Mn_{7/12}O_2$ where there is only one Li-Li tetrahedral dumbbell present in the cell. Oxygen vacancies, which are essential to the phase transformation process, start to form at a concentration of 20/28 in the presence of Li-Li dumbbells. Oxygen vacancies are located at three different positions in the Mn polyhedral site (shown in the footnote of Figure VI - 53): 1) in the shared oxygen plane between the octahedral site and tetrahedral site; 2) in the octahedral vertex but not in the shared oxygen plane; and 3) in the tetrahedral vertex but not in the shared oxygen plane. Although the exact values of Mn diffusion barriers are different for different configurations, the trend is consistent over all Li concentrations. Therefore results at lithium concentration 20/28 are discussed as the representative case. Figure VI - 53 shows the calculated Mn diffusion barriers at lithium concentration 20/28 with oxygen vacancies in two different locations. Generally speaking, the barrier to Mn diffusion can be reduced with the presence of an oxygen vacancy. Similarly, calculations were carried out to investigate the barrier to Ni diffusion, and it was found that the barrier can be lowered to 0.2-0.5eV by the presence of oxygen vacancies.

Conclusions and Future Directions

Both pristine and spherically shape Li-excess materials have been successfully prepared by a co-precipitation method. These materials, which exhibit excellent rate performance and cycling performance were used as samples for advanced characterization. Based upon XPS and STEM/EELS work, two main hypotheses were proposed to understand the voltage and capacity fade. (1) Beginning at the voltage plateau region, the redox of oxygen was not fully reversible, leaving oxygen vacancies in the structure. (2) At the same time oxygen vacancies in the structure facilitate structural transformation on the surface during cycling. Additionally, a novel oxygen vacancy assisted TM diffusion mechanism is proposed for the first time to explain the near-surface phase transformation in lithium excess transition metal layered oxides. Formation of (dilute) oxygen vacancies and their roles in assisting transition metal ion diffusion were investigated using first principles calculation. In the presence of oxygen vacancies, the activation barriers for TM diffusion were drastically and consistently reduced in reasonable range for room temperature diffusion.

Using advanced characterization methods, the mechanisms of structural transformation and oxygen vacancy formation will be revealed. Various modification methods including metal doping, substitution, and surface coatings will be adopted to further improve the electrochemical performance of the $Li_{1.2}Ni_{0.2}Mn_{0.6}O_2$ Li-excess material.

FY 2013 Publications/Presentations

1. K. J. Carroll, D. Qian, C. R. Fell, S. Calvin, G. M. Veith, M. Chi, L. Baggetto, Y. S. Meng, "Probing the electrode/electrolyte interface in the Li-excess material $Li_{1.2}Ni_{0.2}Mn_{0.6}O_2$," *Physical Chemistry Chemical Physics*, **15**, p11128-11138 (2013).
2. C. R. Fell, D. Qian, K. J. Carroll, M. Chi, J. L. Jones, Y. S. Meng, "Correlation between oxygen vacancy, microstrain, and cation distribution in Lithium-excess layered oxides during the first electrochemical cycle," *Chemistry of Materials*, **25**(9), p1621-1629 (2013).
3. D. Qian, B. Xu, M. F. Chi, and Y. S. Meng, "Uncovering the roles of oxygen vacancy on cation migration in lithium excess layered oxides," submitted and under review, 2013.

VI.B.10 Novel Cathode Materials for High-Energy Lithium Batteries (UTA)

Arumugam Manthiram
University of Texas at Austin

Materials Science and Engineering Program
204 E. Dean Keeton Street, Mail Stop C2200
Austin, TX 78712
Phone: (512) 471-1791; Fax: (512) 475-8482
E-mail: manth@austin.utexas.edu

Start Date: October 2011
Projected End Date: September 2015

Objectives

- Development of high-performance cathodes for lithium-ion batteries and a fundamental understanding of their structure-composition-performance relationships.
- Develop novel synthesis approaches for polyanion-containing cathodes such as phosphates and silicates that can offer high energy and good thermal stability.
  - Assess the factors controlling the voltages.
- Develop a fundamental understanding of the factors that control the electrochemical performances of the high-voltage spinel oxide cathodes and utilize the understanding to develop high-performance spinel compositions.
  - Assess the relative roles of morphology, cation ordering, and Mn^{3+} content.

Technical Barriers

Focusing on the cathode materials, this project addresses the following technical barriers in order for lithium-ion batteries to be employed for vehicle applications: cost, safety, cycle life, energy, and power.

Technical Targets

- Realize high capacity through the reversible insertion/extraction of more than one lithium per transition-metal ™ ion in polyanion cathodes.
- Achieve long life and high rate with high-voltage spinel cathodes.
- Develop a fundamental understanding of the factors controlling the voltages of polyanion cathodes and the electrochemical performances of high-voltage spinel cathodes.

Accomplishments

- Synthesis of three polymorphs of $LiVOPO_4$ by a novel microwave-assisted approach in various solvent mixtures of water and alcohols/glycols.
- Reversible extraction/insertion of more than one lithium per vanadium from/into $LiVOPO_4$.
- Optimization of the particle size of $LiVOPO_4$ by controlling the reaction time and reactant concentrations or by adding a surfactant.
- Synthesis of Li_2MnSiO_4 and $Li_2MnP_2O_7$ by novel template-assisted and microwave-assisted approaches.
- Accurate prediction of the voltages of polyanion cathodes based on coordination geometry and covalence of metal-oxygen bond.
- Understanding the relative roles of morphology and surface crystal planes on the electrochemical properties of high-voltage spinel cathodes in comparison to other factors.

✧ ✧ ✧ ✧ ✧

Introduction

Cost, safety, energy, and power are the major issues that hamper the adoption of lithium-ion technology for vehicle applications. Accordingly, this project focuses on developing (i) polyanion cathodes that offer high energy while keeping the cost low and exhibiting good safety characteristics and (ii) high-voltage spinel cathodes that offer high energy and power. With polyanion cathodes, the project is specifically focused on phosphate and silicate cathodes that can facilitate the reversible extraction/insertion of more than one lithium ion per TM ion. On the other hand, the major issue in employing the high-voltage spinel is the capacity fade during cycling. Accordingly, this project is focused on understanding the relative roles of the various factors that control the electrochemical performances of $LiMn_{1.5}Ni_{0.5}O_4$ spinel cathodes: morphology, surface planes, cation ordering, Mn^{3+} content, and surface reaction with electrolyte.

Approach

Polyanion cathodes such as $LiVOPO_4$ and Li_2MSiO_4 (M = Mn, Fe, Co, and Ni) have the potential to cycle more than one lithium per TM ion. However, their practical capacities are limited due to the poor electronic and ionic conductivities. Synthesis and processing conditions play a critical role in realizing the full capacities of these polyanion cathodes. Accordingly, novel solution-based synthesis approaches such as microwave-assisted solvothermal and template-assisted methods that offer controlled morphologies and particle size are pursued to maximize the electrochemical performances. With the high-voltage spinel, a continuously stirred tank reactor and cation doping are utilized to obtain samples with different morphologies and surface compositions to achieve a better interface with the electrolyte. The synthesized samples are characterized by a variety of techniques including X-ray diffraction, electron microscopy (SEM, TEM, and STEM), X-ray photoelectron spectroscopy, time of flight – secondary ion mass spectroscopy, and in-depth electrochemical measurements. Based on the characterization data gathered, a fundamental understanding of the structure-composition-property-performance relationships is developed, which is then utilized to design better-performing cathodes.

Results

Phosphate cathodes. Three polymorphs of $LiVOPO_4$ (α – triclinic, β – orthorhombic, and-α_1– tetragonal) were synthesized by the microwave-assisted solvothermal process. In order to reduce the particle size, the α phase was synthesized in various solvent mixtures of water and alcohols/glycols (Figure VI - 54). The ratio of water to alcohols/glycols (3:1) was crucial to eliminate impurities at a 230°C synthesis temperature. Various solvent mixtures formed micro-flower morphology as seen in Figure VI - 54, with the smallest particle size achieved with the water/glycol mixtures.

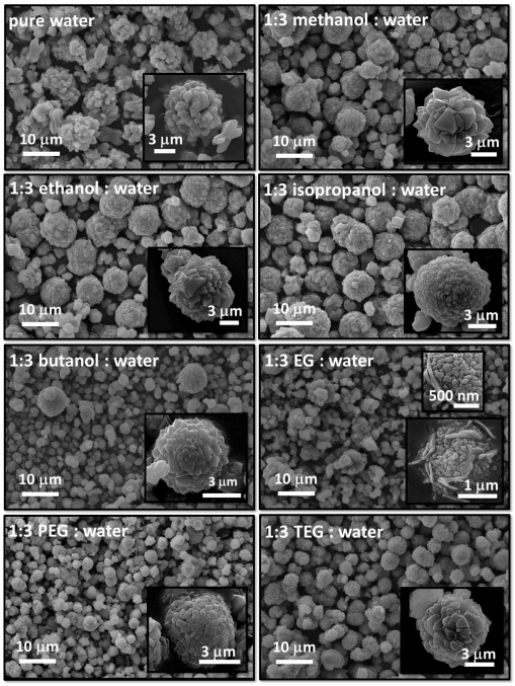

Figure VI - 54: SEM of α-LiVOPO4 prepared in various mixed solvents at 230°C except that in water, which was held at 240°C

Figure VI - 55 shows the electrochemical performance of each of the samples formed with the various solvent mixtures. The influence of the particle size can be seen as the highest capacities in the potential window of 3.0 – 4.5 V (indicated by dashed line in Figure VI - 55) were achieved with water/glycol mixtures, which had the smallest particle size. In addition, the importance of the solvent is apparent when comparing the electrochemical performances (Figure VI - 55) of samples with similar particle sizes. For example, the water/glycol and butanol/water samples have similar particle sizes, but the former exhibits better performance in the 3.0 – 4.5 V range. Likewise, the pure water and alcohol/water samples have similar particle sizes, but the latter exhibits a higher capacity.

The typical voltage range to cycle $LiVOPO_4$ is 3.0 and 4.5 V. Figure VI - 55 shows that by cycling to 2.0 V instead of 3.0 V, more than one lithium can be inserted/extracted by accessing the $V^{3+/4+}$ redox couple between 2.0 and 2.5 V. By increasing the voltage window, a discharge capacity of ~ 200 mAh/g was achieved.

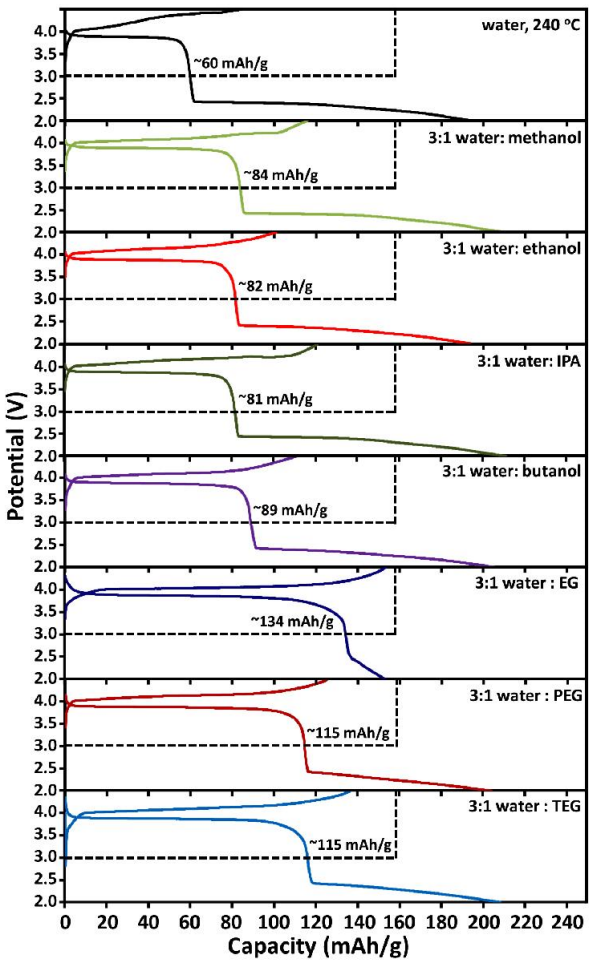

Figure VI - 55: First charge−discharge profiles at a C/20 rate of α-LiVOPO4 prepared in various mixed solvents at 230°C except that in water, which was held at 240°C

With a water to alcohol/glycol ratio of 3:1, we focused on optimizing the particle size further by controlling the reaction time and reactant concentrations as well as by adding cetyl trimethylammonium bromide (CTAB) to the precursor solution as shown in Figure VI - 56. Higher initial capacities were generally realized with smaller particle size when the cells were cycled in the potential window (3.0 – 4.5 V, shown by dashed box), as seen in Figure VI - 57 for the samples shown in Figure VI - 56. For instance, the initial capacity for the material with a 10 min. hold time (0.067 M in V, 0 mL CTAB) was ~ 115 mAh/g, while that for the material with a 45 min. hold time was ~ 72 mAh/g. The addition of CTAB helped to prevent particle growth and agglomeration and reduced particle size as seen in Figure VI - 56. The electrochemical performance was improved with the addition of an optimum amount of CTAB. For example, the first discharge capacity increased from ~ 82 mAh/g to ~ 124 mAh/g on going from 0 to 0.5 mL of CTAB, but decreased to ~ 90 mAh/g with further addition of CTAB (1 mL). The cycling performance was also improved by coating the particles with the conductive PEDOT:PSS.

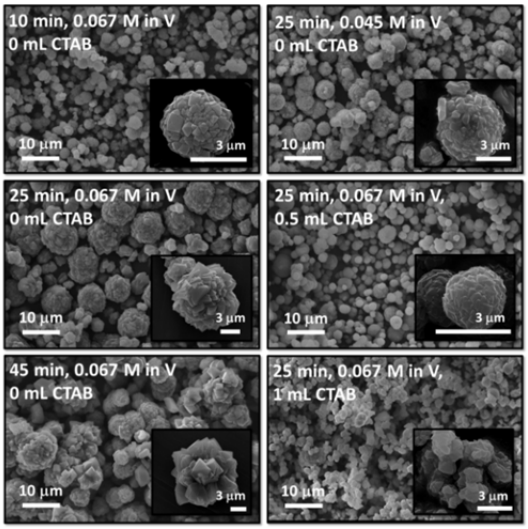

Figure VI - 56: SEM of α-LiVOPO4 prepared with a water:ethanol ratio of 3:1 for the various indicated reaction hold times at 230°C (not including ~ 25 min ramp time to 230°C), V concentrations, and amounts of CTAB solution substituted for water

$Li_2MnP_2O_7$ and $Li_2CoP_2O_7$ were also synthesized by the microwave-assisted solvothermal process, but their capacities were 90 – 100 mAh/g with the extraction of only 0.8 – 0.9 lithium due to a larger particle size (3 – 5 µm). Further work is needed on reducing the particle size.

Silicate Cathodes. Li_2MnSiO_4/C nanocomposite cathodes were synthesized with unique morphologies, employing poly(methyl methacrylate) (PMMA) crystals as a hard-template and the phenolic-resin polymer as the carbon source. The PMMA template decomposes to gaseous products at elevated temperatures during the synthesis without requiring any extra step to remove the template, unlike other hard-templates such as silica.

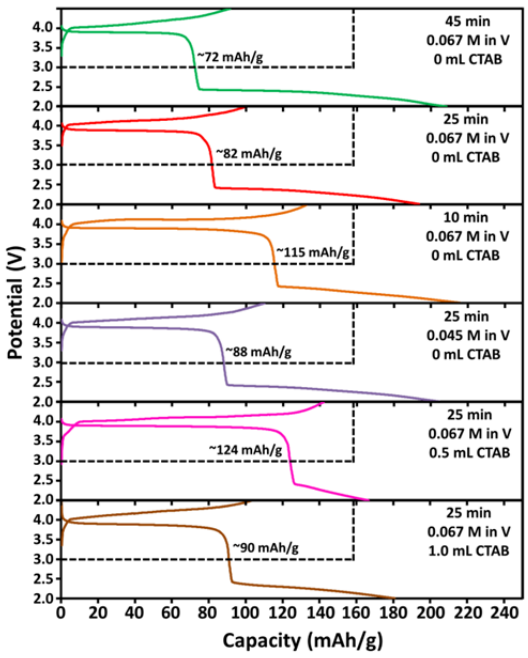

Figure VI - 57: First charge-discharge curves at C/20 rate of α-LiVOPO$_4$ prepared with water:ethanol = 3:1 for various reaction hold times at 230°C, V concentrations, and amounts of CTAB solution substituted for water

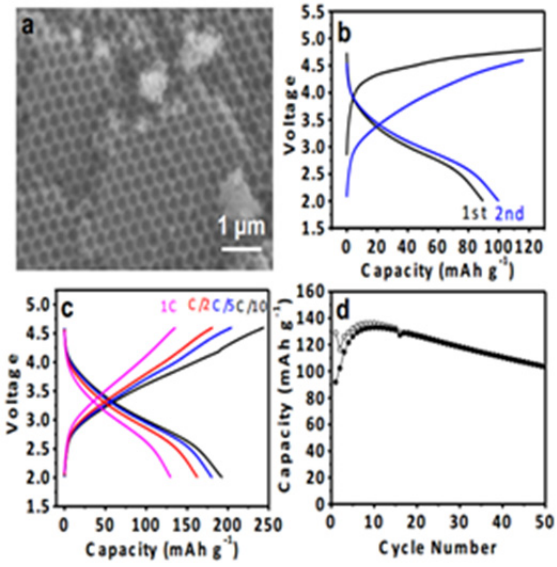

Figure VI - 58: (a) SEM image, (b) first two charge-discharge profiles, (c) the highest capacity obtained at various rates, and (d) cycling performance at 1C rate of the Li2MnSiO4/C nanocomposite cathode material

A long-range ordered macroporous structure resulted as seen in Figure VI - 58a due to the close-packed PMMA template. The first two charge-discharge profiles of Li_2MnSiO_4/C shown in Figure VI - 58b suggest a possible structural rearrangement during the first cycle. The sample exhibited a reversible capacity of ~ 200 mAh g^{-1} (Figure VI - 58c) at 55°C corresponding to the extraction of 1.2 lithium per Mn. However, the cathode exhibited some capacity fade as seen in Figure VI - 58d (at a rate of 1C at 55°C) after an intial increase in capacity during the first 10 cycles. Also, $Li_2Fe_{0.9}Mn_{0.1}SiO_4$ was synthesized by a hydrothermal process at 200°C, followed by heating at 650°C, but the particle size was larger (~ 1 μm).

Understanding the voltage variations in polyanion cathodes. The voltage variations in polyanion cathodes have largely been explained in the past for isostructural materials. With an aim to develop a broader understanding, a crystal-chemical guide was provided for understanding how factors such as the crystal structure and covalency of the polyanion affect the M2+/3+ redox energies in polyanion cathodes having different structures. An accurate prediction of the voltage could be made based on how the coordination of the TM ion affects the covalency of the M-O bond. Additionally, a new method for assessing the covalency of the polyanion (beyond the electronegativity of the counter-cation) was presented and used to explain why the voltage delivered by Li2MP2O7 cathodes is higher than that of LiMPO4 for a given M. A comparison of the silicate and phosphate structures revealed that edge sharing between transition-metal polyhedra and other cation polyhedra has an opposite effect on the voltage delivered by these materials. It was also shown that crystal-field theory alone is not sufficient to explain the voltages of polyanion cathodes, demonstrating the necessity of considering the structural effects to fully understand the voltage trends.

High-voltage spinel cathodes. In order to achieve consistent performance with the high-voltage spinel cathode $LiMn_{1.5}Ni_{0.5}O_4$, a deeper understanding of the relationship among cation ordering, impurities, and particle morphology was developed. Careful chemical, structural, and electrochemical characterizations of $LiMn_{1.5}Ni_{0.5}O_4$ cathodes prepared by different methods with varying morphologies and degrees of cation ordering revealed that although an increase in the degree of cation ordering decreases the rate capability, the crystallographic planes in contact with the electrolyte have a dominant effect on the electrochemical properties. For instance, samples with octahedral morphology and {111} surface planes exhibit superior cyclability and high rate capability compared to samples with truncated {100} planes. Furthermore, doping with small amounts of certain cations was found to stabilize {111} surface planes as they segregate to the surface.

Conclusions and Future Directions

Reversible extraction of more than one lithium per TM ion has been demonstrated with α-LiVOPO$_4$

(triclinic) and Li_2MnSiO_4 by employing novel synthesis approaches to control the particle size and morphology. With these polyanion cathodes, synthesis medium, reaction time, reactant concentration, and addition of surfactant were all found to play a role in controlling the morphology and particle size. Also, an accurate prediction of the voltages of the polyanion cathodes could be made based on how the coordination of the TM ion affects the covalency of the M-O bond. With the high-voltage spinel, investigation revealed that morphology and surface planes play a dominant role in controlling the performance compared to other parameters.

Future work is focused on (i) improving the performance of $LiVOPO_4$ through further tuning of the synthesis, (ii) whether or not $LiMnPO_4$ and $LiCoPO_4$ can be aliovalently doped with V^{3+} and determining the doping effect on electrochemical performance, and (iii) microwave-assisted synthesis of carbonophosphates.

FY 2013 Publications/Presentations

1. "Stabilized Spinel and Polyanion Cathodes," *DOE Annual Peer Review Meeting*, May 13-17, 2013, Washington, DC.
2. K. Chemelewski, D.W. Shin, W. Li, and A. Manthiram, "Octahedral and Truncated High-voltage Spinel Cathodes: Role of Morphology and Surface Planes on Electrochemical Properties," *Journal of Materials Chemistry,* **1**, 3347-3354 (2013).
3. K.L. Harrison and A. Manthiram, "Microwave-assisted Solvothermal Synthesis and Characterization of Various Polymorphs of $LiVOPO_4$," *Chemistry of Materials,* **25**, 1751–1760 (2013).
4. B. Pei, Z. Jiang, W. Zhang, Z. Yang, and A. Manthiram, "Nanostructured $Li_3V_2(PO_4)_3$ Cathode Supported on Reduced Graphene Oxide for Lithium-ion Batteries," *Journal of Power Sources,* **239**, 475 - 482 (2013).
5. Gutierrez and A. Manthiram, "Understanding the Effects of Cationic and Anionic Substitutions in Spinel Cathodes of Lithium-ion Batteries," *Journal of the Electrochemical Society,* **160**, A901 - A905 (2013).
6. K.R. Chemelewski and A. Manthiram, "Origin of Site Disorder and Oxygen Non-stoichiometry in $LiMn_{1.5}Ni_{0.5-x}M_xO_4$ (M = Cu and Zn) Cathodes with Divalent Dopant Ions," *Journal of Physical Chemistry C*, **117**, 12465 – 12471 (2013).
7. K.R. Chemelewski, E.-S. Lee, W. Li, and A. Manthiram, "Factors Influencing the Electrochemical Properties of High-voltage Spinel Cathodes: Relative Impact of Morphology and Cation Ordering," *Chemistry of Materials,* **25**, 2890 – 2897 (2013).

VI.C Anode Development

VI.C.1 Novel Anode Materials (ANL)

Jack Vaughey
Argonne National Laboratory

Chemical Sciences and Engineering
Building 205
9700 S Cass Avenue
Lemont, IL, 60439
Phone: (630) 252-8885; Fax: (630) 252-4176
E-mail: vaughey@anl.gov

Start Date: October 2010
Projected End Date: September 2014

Objectives

- Design electrode architectures containing main group metal, metalloid or intermetallic components that can tolerate the volumetric expansion of the materials and provide an acceptable cycle life.
- Exploit electrochemical deposition reactions to improve the design and performance of silicon-based electrodes
- Develop methods to assess the internal changes within the electrode on cycling as a tool to improve performance.

Technical Barriers

There are several technical barriers to the utilization of silicon as an electrode material for lithium-ion batteries – notably its high volume expansion on lithiation, reactivity with its environment, and a large kinetic resistance to lithiation are all obstacles that must be addressed before silicon can be considered as a replacement electrode material for graphitic carbons. These barriers include:

- Low energy
- Poor low temperature operation
- Abuse tolerance limitations

Technical Targets

- 142 Wh/kg, 317 W/kg (PHEV 40 mile requirement)
- Cycle life: 5,000 cycles
- Calendar life: 15 years

Accomplishments

- Utilized a combined synthesis, impedance spectroscopy, and MAS-NMR study to determine the types of functional groups that are at the silicon-electrolyte interface and how they can be changed as a function of synthesis.
- Discovered a new synthetic variable in the electrodeposition of electrochemically active silicon that allows some control over the crystallinity and functionality of the materials deposited.
- With Advanced Photon Source (APS) beamline scientists, micro-CT X-Ray tomography was utilized on a complex multicomponent silicon electrode to assess the role of cycling on the free space and the silicon particle size. Utilizing an element sensitive analysis technique, it was possible to differentiate the elements involved and 'see' the SEI layer grow to fill the electrode void space on cycling.
- Interactions with the EFRC – Center for Electrical Energy Storage - *Tailored Interfaces* (Argonne-Northwestern University-University of Illinois, Urbana-Champaign, were continued around the micro CT tomography effort.

✧ ✧ ✧ ✧ ✧

Introduction

Elemental silicon has been considered the heir apparent for graphitic carbon as the negative electrode in lithium-ion batteries for many years. Among the possible main group elements with high theoretical capacities, silicon has the highest gravimetric capacity and, when combined with its high availability and low cost, it is a very desirable electrode material. Because it does not work by intercalation, it can store significantly higher energy than graphite (372 mAh/g, 818 mAh/ml), and insert lithium only a few hundred millivolts above the potential of metallic lithium. However, the limited internal void volume translates to a significant expansion on reaction and insertion of lithium as the constituent Si atoms complete their p-orbitals and become much larger anions. Although this expansion among other kinetic issues presently limits its utility, the

high potential payoff associated has made silicon a focus for the BATT-Anode program.

A major objective of our research is to understand how a silicon electrode interacts with its cell environment and how these interactions can be controlled to increase cycle life and limit capacity fade. Initial work focused on designing microporous copper host architectures that could be used to 1) simplify the lithium-ion battery electrode by combining requirements for a binder, and conductive additive and extending the current collector into the active phase, and 2) provide a sufficiently large void volume to accommodate the volumetric expansion that occurs during charging. Utilizing these electrode designs, it is possible to create a combined synthetic -diagnostic effort to understand and adapt the excellent cycling performance seen for deposited silicon electrodes to the commercially utilized laminated electrodes. Specifically, the role of synthesis on the active surface of silicon, the interfacial region with the electrolyte, and role of electrode porosity has been studied to improve the electrochemical performance of silicon-based electrodes.

Approach

Utilizing silicon electrodeposition as a synthetic tool, the amount of silicon, its morphology, and crystallinity can be controlled to create samples that are amenable to spectroscopic studies. These electrode materials can then be evaluated to determine how their composition and surfaces interact with the electrolyte on cycling leading to capacity fade via degradation reactions. In addition, element specific microtomography techniques have been developed at the APS, to study how the electrodes are changing internally as a function of cycling.

Results

Tomography. One of the biggest issues for silicon based electrodes when incorporated into lithium-ion batteries is the effect the volume expansion of the silicon has on the surrounding electrode structure. This expansion has dramatic effects on both the ability of the binder to maintain good contact with the particles and the ability to maintain good electrical contact throughout the electrode. Previous efforts (e.g., Liu, et al., *ACS Nano*, **2012**, 6(2) 1522–1531) have shown that there exists a critical particle size for silicon particles. Above approximately 150 nm, the particles are unable to withstand the stress of lithiation and degrade. Below this number they are stable.

X-Ray tomographic studies of silicon electrodes to evaluate the role of cycling on silicon particles greater than 150 nm have continued. Because most binders require the secondary particles to be on the micron scale, a standard 70% active Si/PVdF/acetylene black (AB) electrode was evaluated to establish how the particle breakdown is absorbed. The electrode was evaluated before cycling and again after 20 cycles (vs Li and with Gen2 electrolyte, [1.2 M $LiPF_6$ in EC/EMC 3:7 weight ratio]). In Figure VI - 59, the element sensitive X-Ray tomography data is shown. In Figure VI - 59a, the silicon within the electrode is shown before cycling with a typical particle size (primary) of ~20 µm. In Figure VI - 59b, the pulverization due to repeated cycling is evident with the largest particle size now in the 300-500 nm range. Additionally, another electrode level event evident in this series of experiments was the overall expansion of the entire electrode from 60 µm to 160 µm. In Figure VI - 60a, the initial pre-cycled electrode is shown, with the void volume highlighted. In Figure VI - 60b, the compactness and even distribution of pores has been altered, in part to take into account the formation (and continuous growth) of SEI within the sample. In these electrodes it can be seen that the volume expansion of the silicon has multiple effects on its surroundings, including pulverization leading to poor connectivity to the current collector, and gross changes in volume from SEI formation and inclusion within the voids of the electrodes. The effect of the void filling on performance over time is under investigation as it is probably tied to electrolyte starvation effects and capacity fade.

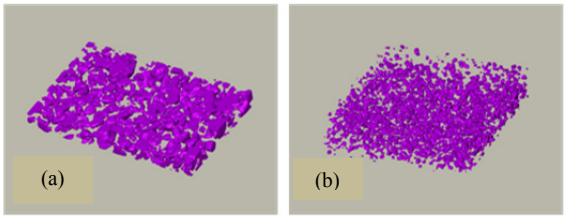

Figure VI - 59: (a) a Si electrode of average particle size of 20 µm before cycling, (b) the same electrode after 20 cycles (vs Li)

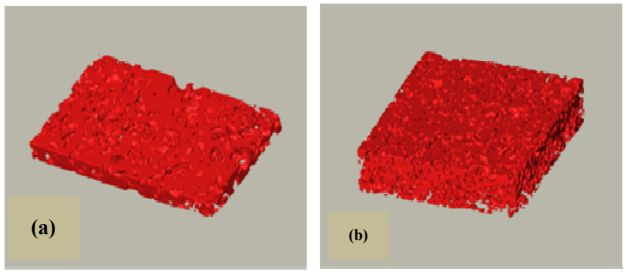

Figure VI - 60: (a) the void volume within a Si electrode of average particle size of 20 µm before cycling, (b) the same electrode after 20 cycles (vs Li)

Synthesis. In support of the goal of understanding how elemental silicon interacts with its electrochemical

cell environment, the deposition of electrochemically active elements (elemental Si or Sn) into a three-dimensional metallic foam structures was explored. This design allows us to control the amount of active material precisely while maintaining some electrode porosity. Utilizing two different porosity foam structures, the role of deposition method on morphology and cycling for a Sn on Cu three dimensional electrode was investigated. Tin was chosen as an active material initially because its air stability allows for electrode optimization outside a controlled atmosphere drybox. Previous electrodeposition work had focused on the effect of synthesis and film morphology on cycling. Testing concluded that the smoother films had more stable cycling performance. This was attributed to a variety of factors including lower surface area and possibly less of the high reactivity crystal facets being exposed to the electrolyte (Kostecki, et al., *Electrochem Comm*, 2011).

Initially an electro-less deposition process was used, optimized industrially for Sn deposition, as it has rapid turnaround and does not have 'line-of-sight' requirements.

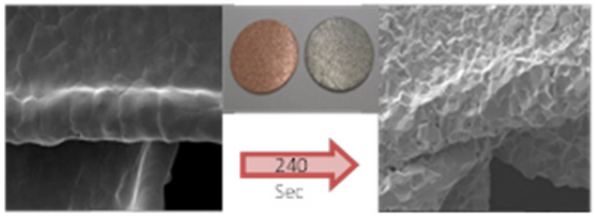

Figure VI - 61: SEM images from the electro-less deposition of metallic Sn from a commercial plating bath on a copper-foam. Total deposition time was 240 seconds

In Figure VI - 61, utilizing a commercial plating process, a copper substrate with tin was even coated. XRD analysis of the annealed samples at temperatures above 100°C indicated alloying to form Cu_xSn phases. Of particular note is the conformal nature of the deposition throughout the substrate, a trait identified earlier as beneficial to extended cycle life. Cycling of the films showed typical capacities and plateaus expected for a tin-based anode.

Once the deposition properties of the metal foams had been established, the effort to silicon films was extended. Electrodeposition was reverted to when no electroless deposition process equivalent was reported. For silicon, silicon tetrachloride was utilized as our Si source and a supporting electrolyte of tetra-alkyl ammonium salts in propylene carbonate (PC) was used. Because a synthetic process based on electrochemical deposition is an inherently complex method, several variables were changed and we assessed the products formed and their electrochemical properties. Interestingly, it was observed that the counter-cation in the supporting electrolyte salt played a significant role on the surface chemistry and crystallinity of the silicon product. Specifically, significant changes in first cycle irreversible capacity and overall half-cell capacity were noted when supporting salts were changed.

The cycling data are shown in Figure VI - 62a and highlights the performance when using tetraethyl ammonium chloride (TEACl) as the supporting salt. The cell showed > 2000 cycles. Although both samples were synthesized and tested under the same conditions it is evident from the electrochemical curves and powder X-Ray diffraction, the measured mAh/g and >99.7% cycling efficiency over the first 125 studies, are all consistent with the deposited Si film (on Cu foam) being amorphous. Figure VI - 62b shows a similar film in terms of quantity of silicon deposited using the larger tetrabutyl ammonium chloride (TBACl) as the supporting electrolyte salt, but immediate differences, including fade rate and overall capacity are noticeable. In addition, the electrochemical curves and powder X-Ray diffraction studies are consistent with the deposited Si film (on Cu foam) being semi-crystalline.

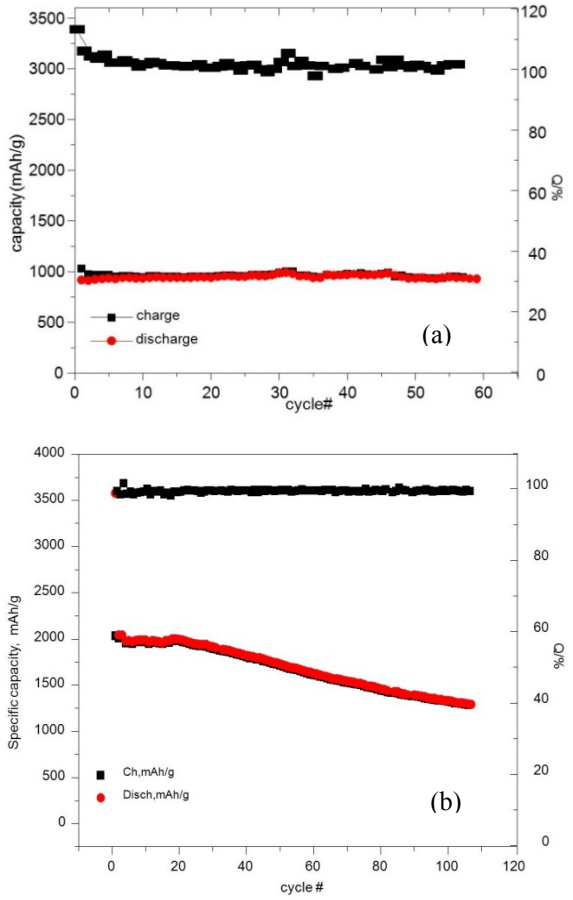

Figure VI - 62: Cycling performance of a Si film on Cu using (a) TEACl as supporting electrolyte salt and (b) using TBACl as the supporting electrolyte salt

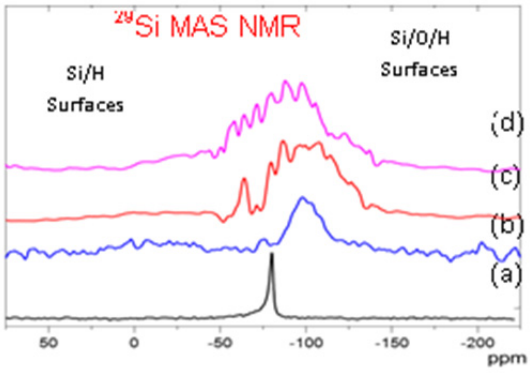

Figure VI - 63: ^{29}Si NMR data collected from four different types of samples is shown. Specifically, the samples are (a) uncycled bulk silicon, (b) an oxidized sample (SiO_2), (c) TBACl supporting electrolyte, (d) TEACl supporting electrolyte

Utilizing spectroscopic techniques that are more surface sensitive, several differences between the samples have been identified. While XRD analysis of the bulk samples showed some particle size and crystallinity differences, the surfaces were very different. In Figure VI - 63, ^{29}Si NMR data collected from four different types of samples is shown. Specifically, the samples are (a) uncycled bulk silicon, (b) an oxidized sample (SiO_2), and the two samples from the different deposition baths. From these *ex situ* experiments, the more crystalline TBACl sample electrodeposited with more oxygen as its passivation layer while the amorphous TEACl-derived sample had a passivation layer more consistent with a hydride/protonated surface. Although the exact reason why such similar cations yield such different results has yet to be determined, it has been pointed out in the electrolyte literature that the coordination requirements of the larger cations significantly reduce the availability of free solvent molecules. Such behavior has been associated with increases in ion-pairing and viscosity which may affect the deposition process.

These types of differences have implications on how the material interacts with electrolyte solvents and how the silicon attaches to binders. Since many binders are designed to work with a specific surface functionality, the ability to vary that functionality may extend electrode lifetimes.

Conclusions and Future Directions

During these studies, the role of interfaces in silicon electrodes has been examined and the results have been extrapolated to identify underlying mechanisms that cause capacity fade and poor coulombic efficiency. Building on our initial work to design high capacity carbon-free electrodes to allow clearer interpretation of spectroscopic data, and electrodeposition as a synthetic tool to control the amount of active silicon and its surface functionality, spectroscopic tools were developed that helped identify the relationship between functionality and synthesis and how the interfaces of these electrodes with the electrolyte controls cycling performance, e.g., SEI growth and electrode side reactions. This effort has been done in tandem with an effort to develop elemental specific micro-CT as a diagnostic tool to evaluate SEI growth and electrode porosity. Future work will focus on:

- Devising model systems in conjunction with the BATT-Anode teams that better describe the surfaces and materials present in a working electrode.
- Utilizing tools, such as MAS-NMR, to understand the underlying surface-electrolyte reactions and propose strategies that decrease the losses associated with various side reactions.
- Tomography experiments on BATT-Anode baseline electrodes will be completed to compare the results to other standard electrodes and identify differences in performance related to their cycling history.

FY 2013 Publications/Presentations

1. J.T. Vaughey, L. Trahey, F. Dogan "Novel Anode Materials: Three Dimensional Architectures," *DOE Hydrogen Program and Vehicle Technologies Program Annual Merit Review*, May 2013, Washington, DC.
2. Joyce, L. Trahey, S. Bauer, F. Dogan, J. T. Vaughey "Copper Metal Binders: the Copper-Silicon System," *J. Electrochem. Soc*., **159**, A909 (2012).
3. Fulya Dogan, Christopher Joyce, John T. Vaughey "Formation of New Silicon Local Environments upon Annealing for Silicon Anodes: A ^{29}Si Solid State NMR Study," *J. Electrochem. Soc*, **160**, A312 (2013).
4. Lynn Trahey, Fikile R. Brushett, Zhenzhen Yang, Xianghui Xiao, Michael M. Thackeray, John T. Vaughey "Microbalance and Microtomographic Analysis of Rechargeable Battery Electrodes," *SEM 2013 Annual Conference & Exposition on Experimental and Applied Mechanics*, June 2013, Lombard, IL.
5. Dogan, D. Sanjeewa, L. Trahey, J. Vaughey "Three-Dimensional Silicon Anode Architectures via Electrodeposition on Copper Foam Current Collectors," *224th Meeting of the Electrochemical Society*, October 2013, San Francisco, CA.

VI.C.2 Metal-Based High Capacity Li-Ion Anodes (Binghamton U.)

M. Stanley Whittingham
Binghamton University

Department of Chemistry and Materials
Vestal Parway East
Binghamton, NY 13902-6000
Phone: (607) 777-4623; Fax: (607) 777-4623
E-mail: stanwhit@binghamton.edu

Start Date: October 2010
Projected End Date: September 2014

Objectives

- Replace the presently used carbon anodes:
  - With safer materials that will be compatible with lower-cost layered oxide and phosphate cathodes and the associated electrolyte.
  - With materials having higher volumetric energy densities, twice that of carbon.

Technical Barriers

This project addresses the following technical barriers facing the use of lithium-ion batteries in PHEV and all-electric vehicles:

- Materials and manufacturing cost of lithium-ion batteries
- Safety of lithium-ion batteries
- Volumetric capacity limitations of lithium-ion batteries

Technical Targets

- Determine the reaction mechanism of the nano-Sn-Fe-C system.
- Identify the cause of the first cycle excess lithium capacity and propose approaches to mitigate it.
- Identify an anode candidate having an energy density of 2 Ah/cm^3 for at least 100 cycles.
- Determine the electrochemistry of the leached nano-silicon material, and compare to the standard silicon.

Accomplishments

- Several key steps in the reaction mechanism of the nano-Sn-Fe-C system have been identified. Carbon plays several key roles, including a protective covering for the active tin components and is electrochemically active contributing to the reversible capacity.
- Several causes for the excess capacity have been identified. These include reaction of the titanium oxides giving lithium titanium oxides, which are not delithiated in the charging regime used. In addition, irreversible reactions with the carbon also contribute. Some of the reaction may also be associated with SEI formation.
- The nano-Sn-Fe-C system has been identified as having the potential to double the volumetric capacity of carbon, to date for at least 50 cycles. The nano Sn_5Fe phase was not found to be a suitable candidate.
- The electrochemistry of the leached nano-silicon has been determined, and compared with two samples from commercial companies. Its behavior falls between the two standard materials.

✧ ✧ ✧ ✧ ✧

Introduction

Achieving the DOE cost and energy/power density targets will require improved anode materials that have higher volumetric energy densities than carbon, and have lower cost production methods. At the same time the material must have higher lithium diffusion rates than carbon and preferably be at a slightly higher potential to improve the safety. Replacing the present carbon anode with a Si or Sn based composite will increase the overall cell capacity.

Approach

The anode approach is to synthesize, characterize and develop inexpensive materials that have higher volumetric energy densities than carbon. Emphasis is being placed on simple metal alloys/composites at the nano-size. The initial focus is being placed on tin, building on what we learnt from our studies of the tin-cobalt anode, the only commercial anode besides carbon. All materials will be evaluated electrochemically in a variety of cell configurations, and for thermal, kinetic and structural stability to gain an understanding of their behavior. Ideally these will have a potential slightly higher than that of carbon and above

that of pure lithium, so as to minimize risk of Li plating and thus enhance safety, whilst allowing for rapid charging.

Results

Reaction Mechanism of the Nano-Sn-Fe-C System. The reaction mechanism of nano-sized Sn-Fe-C anode materials has been studied by X-ray absorption spectroscopy (XAS), which reveals it is a conversion reaction that converts tin and Sn_2Fe to Li-Sn alloys. *Ex situ* samples prepared at different lithiation and delithiation states were tested. As shown in Figure VI - 64 (top) and (bottom), an obvious absorption edge energy shift can be found in the Sn K-edge X-ray absorption near edge structures (XANES), which means the oxidation state of Sn undergoes a substantial change during the lithiation/delithiation process. The XAS study of pure Sn during lithiation/delithiation is underway in order to compare and get further information of this structure evolution.

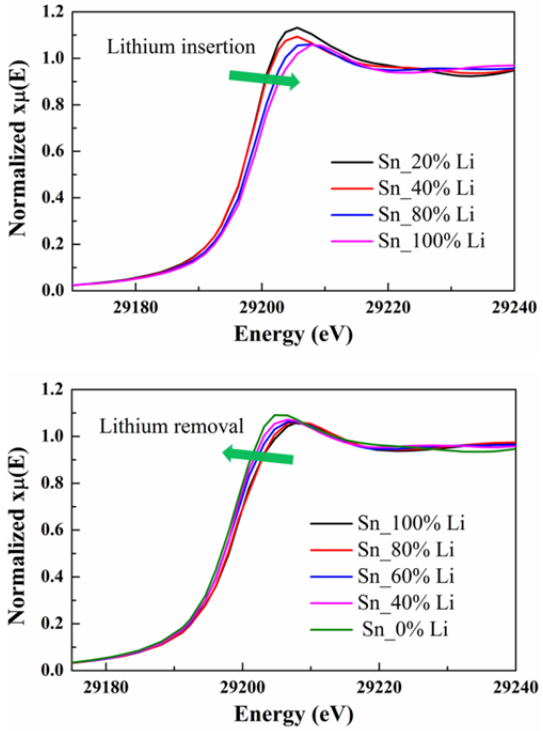

Figure VI - 64: Sn K-edge XANES for different (top) lithiation states and (bottom) delithiation states of nano-sized Sn-Fe-C

First Cycle Excess Li Capacity. The first cycle excess capacity of this material is mainly due to the formation of LiC_2 from the carbon; this carbon contributes significantly to the overall capacity. In addition, the existence of titanium oxides may also contribute to the first cycle excess capacity, since the lithium titanium oxide formed in the first discharge is not reversible at the charging potentials used. Further investigation is in progress to mitigate this excess capacity, including decreasing the amount of carbon and titanium used. There is close collaboration between these studies on tin and those of the BATT team on silicon, which has very similar issues.

Identification of Anode Candidate. The nano-Sn-Fe-C composite has been synthesized by two different techniques: mechanochemical and solvothermal. These are showing some quite different characteristics. For the mechanochemically synthesized nano-sized Sn-Fe-C anode materials it was found that Ti serves better than Al as the reducing agent for the SnO, and hard iron balls work better than soft ones. The mechanochemical reaction time is another key parameter. The XRD patterns, in Figure VI - 65 (top), show that as the reaction time increases, all the tin is converted to Sn_2Fe; further grinding leads to Fe metal impurities. Optimum electrochemical behavior, as shown in Figure VI - 65 (bottom), is found for 10 h reaction time, where there is still residual tin metal. Capacity retention is very good after the first few cycles.

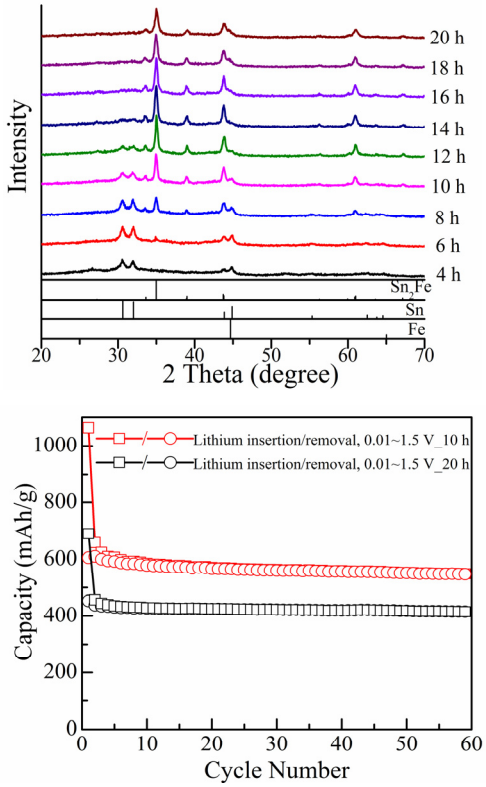

Figure VI - 65: (Top) XRD patterns and (bottom) cycling performance of nanosized Sn-Fe-C materials

A study of the electrochemical performances of nano-Sn_5Fe material provided by our collaborators at Brookhaven National Laboratory showed that an increase in the Sn content, from Sn_2Fe to Sn_5Fe, reduces both cyclability and rate capability (Figure VI - 66).

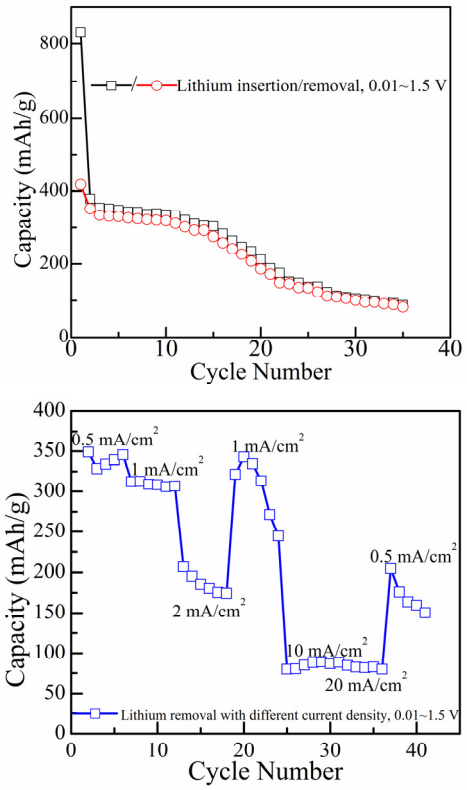

Figure VI - 66: (Top) Electrochemical cycling and (bottom) rate capability of nano-Sn_5Fe

Sn_2Fe materials were also synthesized by the solvothermal method. When the initial molar ratio of Sn: Fe is increased (e.g., from 2:1 to 10:1), the product is a mixture of Sn/Sn_2Fe instead of pure Sn_2Fe as shown in Figure VI - 67. The capacity retention was found to fall dramatically on cycling when excess tin was present. Even for the pure Sn_2Fe material the capacity faded much more rapidly than the mechanochemical Sn_2Fe composite.

Leached Nano-Silicon. Nano-silicon anode materials have been synthesized through a novel etching approach with low-cost eutectic Al-Si alloy as the precursor. An in-depth study of the structure using Rietveld refinement of the XRD data yields a lattice parameter of a = 5.45(3) Å, V = 162.06 (6) $Å^3$ for this nano-silicon, which is larger than the standard silicon (a = 5.43Å, V = 160.15 $Å^3$), suggesting possibly a minor dissolution of other atoms in this nano-silicon material. This observation is consistent with Energy Dispersive X-ray spectroscopy (EDS) mapping, which shows that there is around 5 wt. % Al uniformly distributed in the nano-silicon particles.

The electrochemistry of leached nano-silicon has been determined, Figure VI - 68; the initial results are promising and have now been published (#3). A comparative study has been carried out on the leached nano-silicon, standard silicon and another company's silicon sample. The testing protocol is: 0.12 mA (~C/40) for the first cycle, followed by 0.5 mA (~C/10) for the remaining cycles over the potential range 0.01 V to 2 V. Among these silicon materials, the leached nano-silicon possesses a good capacity stability, which attains 1350 mAh/g after 18 cycles and is still growing. The standard silicon has a high capacity up to 2,300 mAh/g but it fades gradually. The company provided silicon behaves similarly with a capacity of 1,250 mAh/g after 17 cycles.

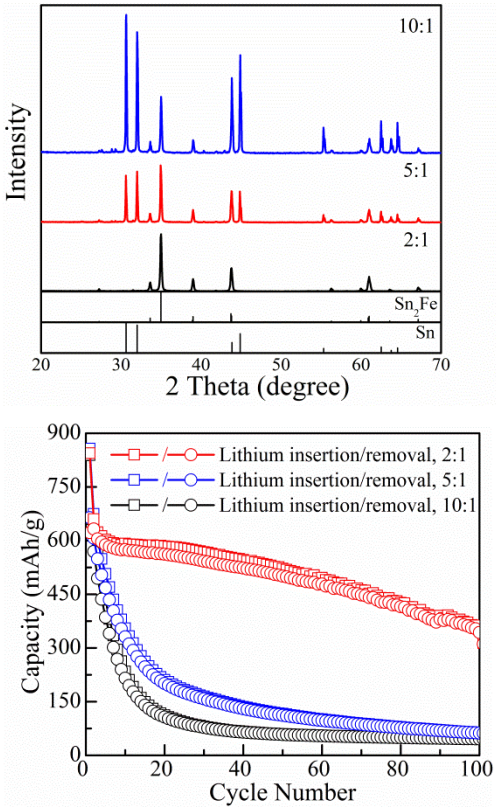

Figure VI - 67: (top) XRD patterns and (bottom) electrochemical performance of Sn_2Fe materials synthesized by the solvothermal method with different initial molar ratios of Sn:Fe

Conclusions and Future Directions

Nano-Tin. The excellent electrochemical behavior of nano-Sn_2Fe has been determined, and this anode is equal to the SONY Sn-Co-C anode in capacity and rate capability. It is in a position to double the volumetric capacity of carbon. Two synthesis methods are being explored with the mechanochemical approach giving the better material, but the solvothermal approach being more amenable to scale-up. The synthesis methods will be optimized. For the mechanochemical approach, a viable source of iron for scale-up that maintains the nano-size needs to be found. In addition, the optimum

carbon and titanium content needs to be determined. For the solvothermal method, the tin metal and oxide impurity need to be eliminated and the electrochemical capacity needs increasing. A GO/NOGO decision will be made on the solvothermal approach in mid-2014. In both cases the first cycle excess capacity needs reducing. To do this a better understanding of the reaction mechanism will be achieved.

Nano-Silicon. Nano-silicon has been formed by two different methods - leaching an Al-Si alloy has a unique morphology and the preliminary results look promising. It was found that this contains about 5 at% Al in the Si. Nano-silicon was also formed from SiO by magnesium reduction; it had a lower capacity than the Si-Al alloy, so most effort will be placed on the former. The future effort on the nano-Si will emphasize reducing the first cycle loss and improving the cycling performance.

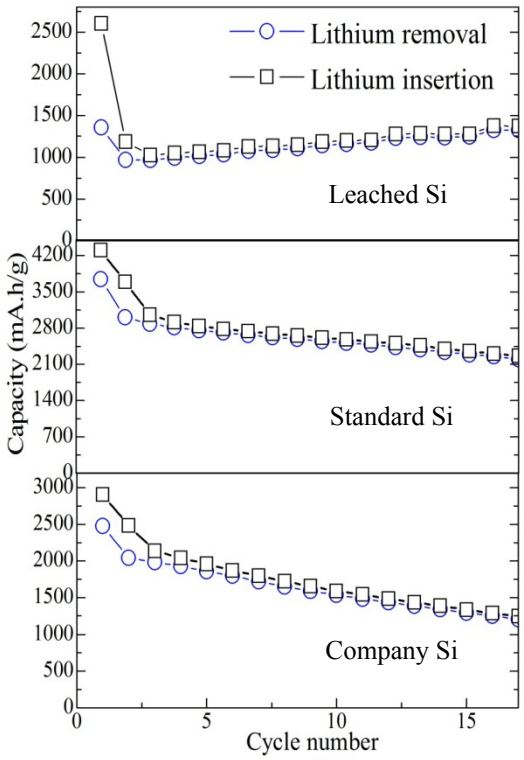

Figure VI - 68: Electrochemical Performance of (top) leached nano-silicon, (middle) standard silicon, and (bottom) another company's silicon

FY 2013 Publications/Presentations

1. "Metal-Based, High-Capacity Lithium-Ion Anodes," *DOE Annual Peer Review Meeting*, May 13-17, 2013, Washington, DC.
2. 2013 DOE-BATT Anode focused Meeting presentation, May 16, 2013, Washington, DC.
3. Wenchao Zhou, Tianchan Jiang, Hui Zhou, Yuxuan Wang, Jiye Fang and M. Stanley Whittingham, "The nanostructure of the Si-Al eutectic and its use in lithium batteries," *MRS Communications*, **3**, 119-121 (2013).
4. M. Stanley Whittingham, "What are the Materials Limitations to Intercalation Batteries," *2013 KAUST,* September 25, 2013, Thuwal, Saudi Arabia.
5. W. Zhou, Z. Dong, H. Yang, F. Omenya, R. Zhang, N. A. Chernova and M. S. Whittingham, "Enhancing the Electrochemical Cycling of Si-carbon Anode with Electrolyte Additives for Lithium-ion Batteries," *Materials Research Society*, November 2012, Boston.
6. R. Zhang, W. Zhou, J., H. Zhou, Z. Dong, X. Hong and M. S. Whittingham, "Sn-Fe-C Composites as Anode Materials for Rechargeable Lithium-ion Batteries," *Materials Research Society*, November 2012, Boston.

VI.C.3 New Layered Nanolaminates for Use in Lithium Battery Anodes (Drexel U.)

Yury Gogotsi
Drexel University

Department of Materials Science and Engineering
3141 Chestnut Street
Philadelphia, PA 19104
Phone: (215) 895-6446; Fax: (215) 895-1934
E-mail: gogotsi@drexel.edu

Michel W. Barsoum (Co-PI)
Drexel University
Department of Materials Science and Engineering
3141 Chestnut Street
Philadelphia, PA 19104
Phone: (215) 895-2338; Fax: (215) 895-6760
E-mail: barsoumw@drexel.edu

Start Date: October 2010
Projected End Date: September 2014

Objectives

- Replace graphite with a new material selected from a group of layered (two-dimensional) binary carbides and nitrides known as MXenes, which may offer combined advantages of graphite and Si anodes with a higher capacity than the former, less expansion, longer cycle life and a lower cost than the latter.

Technical Barriers

This project aims to address the following technical barriers facing modern lithium-ion battery (LIB) technology:

(A) short life-span of modern batteries,

(B) low charge density, and

(C) compromised safety.

Technical Targets

- Perform the a*b initio* simulation of Li incorporation into MAX phase carbides.
- Screen electrochemical experiments on a variety of MAX phases to select the most promising ones for more detailed study.
- Study the effect of particle size on the capacity of the three best materials.
- Improve capacity by selective extraction of A atoms, to add space for the Li.
- Investigate solid electrolyte interface (SEI) formation on selected carbides.
- Optimize the material. Testing the rate capability of the anode.
- *In situ* study of charge/discharge processes and better understanding of the mechanisms of Li insertion.
- Compare powder *vs.* solids with 10-20% porosity.

Accomplishments

- Discovered and synthesized four new materials showing potential for battery anode applications.
- Achieved reversible volumetric capacities of 820 mAh/cm^3 at a 1C cycling rate and 220 mAh.cm^{-3} at 36C for additive-free delaminated Ti_3C_2 that cannot be achieved with commercial graphite electrodes.
- Conducted electrochemical testing of three new MXenes with different compositions (Nb_2C, V_2C, and Mo_2C) in LIBs.
- Completed a study of the effect of different binders on the performance of MXenes in Li-ion batteries.
- Achieved reversible areal capacities for additive-free Nb_2C that are higher than what was reported for Si, the baseline electrode under the same conditions.

✧ ✧ ✧ ✧ ✧

Introduction

In FY 2011 a new family of two-dimensional materials was discovered, and labeled MXenes. In FY 2012 several MXenes (such as Ti_3C_2, Ti_2C, $Ti_3(C_{0.5}N_{0.5})_2$, and Ta_4C_3) were successfully produced by selectively etching Al from corresponding MAX phases. As a result, it was shown that MXenes are, in fact, a family of 2-D transition metal carbides and carbonitrides with excellent potential as anode material in LIBs. In FY 2013 the main focus was on selection of the most promising MXenes for LIBs and their

optimization to maximize Li^+ uptake. In particular, the effect of binder additive on MXene anode performance was investigated. *In situ* study of charge/discharge processes was carried out for better understanding of the mechanism of Li insertion in order to improve the material further. The focus also shifted to lighter MXenes of M_2X formulae and *additive-free* anodes.

Approach

Since at this time the relationship between capacity and MXene phase chemistry is unknown, a rapid screening of as many MXene phases as possible is being carried out to determine the most promising chemistry, by testing their performance in LIBs. This work will also be guided by *ab initio* calculations.

Results

Exfoliated Ti_3C_2-Based anodes for LIBs. To increase Li uptake and life-time of the anodes, the effect of different binders (polyvinylidene fluoride, poly(ethylene oxide), and alginate) on the performance of anodes was studied. Ti_3C_2 was used as the active material and representative for all MXenes. The carbon additive-free Ti_3C_2 anode with 10 wt. % of various binders delivered > 150 $mAh.g^{-1}$ at a C/3 rate after more than 50 cycles (Figure VI - 69). The increase in specific capacity was attributed to the increase in conductivity, confirmed by EIS results; the lowest charge transfer resistance (R_{CT}) (not shown) was obtained for a Ti_3C_2 with 10 wt. % alginate electrode. Combining both alginate and previously reported onion-like carbon (OLC) as the best binder and carbon additive, respectively, should result in the best performance, but it is challenging, since hydrophobic OLC does not disperse easily in alginate.

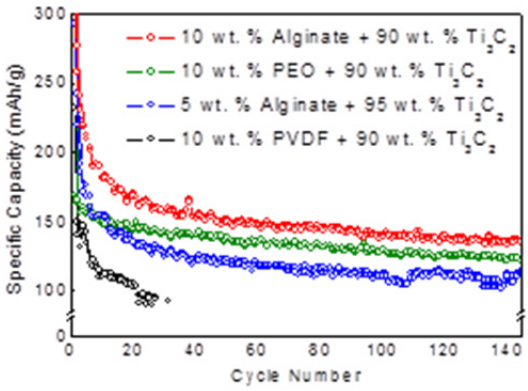

Figure VI - 69: Effect of different binders on the capacity of exfoliated Ti_3C_2.

To understand the physical changes that occur in the anodes during charging and discharging, an *in situ* dilatometric study was carried out. Ti_3C_2 with 10 wt.% PVDF and 10% carbon black was used as an anode. As shown in Figure VI - 70, during the first lithiation cycle, the expansion in electrode thickness, $\Delta H_{Li}/H_o$, where H_o was the initial height of the electrode, was around 7%. After around 20 cycles, $\Delta H_{Li}/H_o$ was < 1%. The change in $\Delta H_{\text{delithiation}}/\Delta H_{lithiatio}$ was in a good agreement with the coulombic efficiency results (not shown). *Ex situ* XRD, however, after lithiation, showed a 21.5% increase in *c* lattice parameter during the first cycle (*c*-LP), $\Delta c_{Li}/c_o$ where c_o is the *c*-LP prior to lithiation. The difference between the latter and the 7% expansion electrodes thickness can be attributed to the fact that the electrode was porous and accommodated expansion of the particles. Expansion of the MXenes upon lithiation presumably only occurs along [0001].

Furthermore, when the irreversibility of the first cycle, as measured by $\Delta H_{\text{delithiation}}/\Delta H_{lithiation}$, was compared to that estimated by comparing $\Delta c_{delithiation}/\Delta c_{Li}$, excellent agreement was found. In other words, most of the 1st cycle irreversibility is due to Li trapped between the MXene layers. More work is ongoing to further understand the lithiation and delithiation mechanisms and to minimize the 1st cycle irreversibility, e.g., by prelithiation.

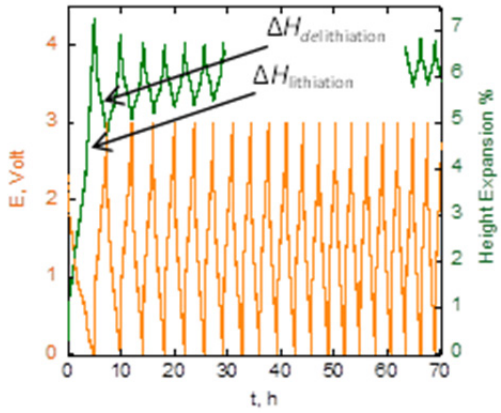

Figure VI - 70: *In situ* dilatometry results for exfoliated Ti_3C_2: electrode expansion %, and voltage during lithiation and delithiation

Delaminated Ti_3C_2-Based anodes for LIBs. In order to achieve the highest accessibility for Li and to make additives-free MXene electrodes, the possibility of layers separation by chemical intercalation and delamination was investigated. It was found that some organic compounds, such as hydrazine monohydrate, dimethylformamide, urea, dimethylsulfoxide (DMSO), can be inserted between the Ti_3C_2 sheets resulting in expansion along [0001]. This was confirmed by the shift of the major (0002) XRD peak to lower 2θ values. The intercalant molecules could also be de-intercalated by drying at higher temperatures, signifying that the intercalation process is reversible.

Intercalation of DMSO in Ti_3C_2 resulted in the largest downshift of the (0002) peak position among all intercalated composites. Further sonication of aqueous solution of DMSO intercalated material led to the delamination of Ti_3C_2 single flakes. By filtering the sonicated colloidal solution though a membrane, the flakes formed binder-free films or "paper" (see inset in Figure VI - 71). The volumetric capacity of the paper was 820 mAh/cm^3 at 1C and 220 mAh/cm^3 at 36C (Figure VI - 71). Such values cannot be achieved with commercial graphite electrodes. Overall, the capacity of the delaminated material was a factor of 4 higher than that of as-synthesized MXene.

The lightest MXenes (M_2X) as anodes for LIBs. In principle, M_2X MXenes should have 50% higher Li^+ capacities as compared to their M_3X_2 counterpart. For this reason Nb_2C and V_2C were synthesized by etching Al from Nb_2AlC and V_2AlC, respectively, and tested as electrodes for LIBs.

Cycling of Nb_2C anode at 1 C yields a first cycle capacity of ~ 422 mAh/g. After 100 cycles, a reversible capacity of 170 mAh/g was obtained. Reasons for the first cycle irreversibility include SEI formation or irreversible reactions of Li with the surface groups and water molecules in the as-synthesized MXenes. The irreversibility could be minimized by controlling the surface MXene chemistry or by prelithiating the electrode material. Similarly, the first cycle capacity for V_2C at 1 C was found to be ~380 mAh/g; the reversible capacity was ~ 210 mAh/g.

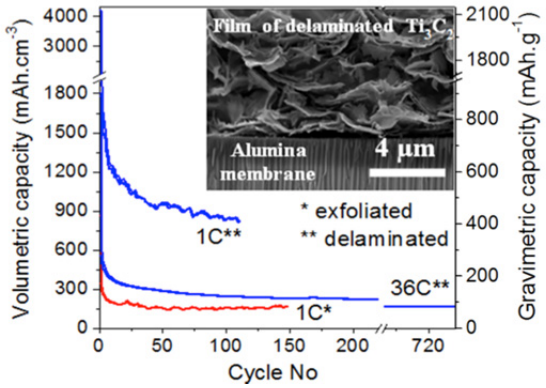

Figure VI - 71: Volumetric and gravimetric capacities of exfoliated and delaminated Ti_3C_2. Inset shows SEM image of an additive-free film of delaminated Ti_3C_2 filtered through the membrane

Intriguingly, the V_2C, produced from etching attrition milled V_2AlC powders, showed > 30 % enhancement in Li uptake (Figure VI - 72) compared to V_2C produced from un-milled V_2AlC. This can be explained by the decreased particle size, facilitating Li diffusion between the layers. A reversible capacity of 280 mAh/g was obtained instead of 210 mAh/g at the same cycling rate of 1 C.

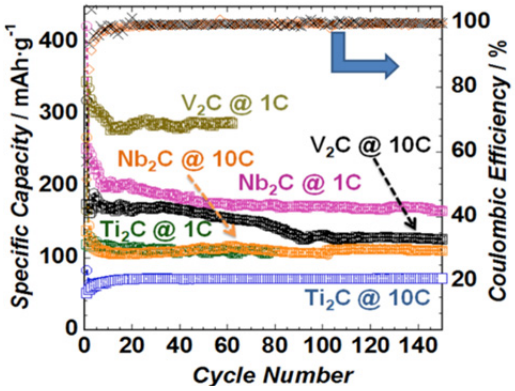

Figure VI - 72: Electrochemical performance of Nb_2C and V_2C (produced by HF treatment of attrition milled V_2AlC) compared to what was reported previously for Ti_2C

It was also observed that > 2/3 of the reversible lithiation capacity for Nb_2C was below 1 V. Conversely, in the case of V_2C, less than 1/2 of the reversible lithiation capacity was < 1 V and more than 2/3 of the delithiation capacity of V_2C was at voltages > 1.5 V. This was an important finding since it showed that each MXene had its own active voltage window. With the variety of possible MXene chemistries, selection of an optimum MXene for a required voltage window can in principle be achieved. Said otherwise, some MXenes could function better as anodes, while others could, in principle, be used as cathodes allowing for the construction in principle of an all MXene-Li-ion battery.

Figure VI - 72 further shows that capacities of 110 mAh/g for Nb_2C and 125 mAh/g for V_2C were obtained after 150 cycles at 10 C. These values were ≈ 50 % higher than what was reported previously for Ti_2C, at the same rate, and closer to the capacities obtained at 1 C. The coulombic efficiency was about 99.6% for Nb_2C at 10 C. For V_2C it varied between 98% and 100%.

To increase the areal capacity, Nb_2C MXene powders were cold pressed into 300 µm free-standing discs without any additives under 1 GPa at room temperature (Figure VI - 73a) and tested as an anode material using the testing conditions suggested by the BATT Anode team leaders: viz. cycling between 5 mV and 1.0 V, using a lithiation current of 0.5 mA/cm^2 and delithiation current of 0.75 mA/cm^2. The areal capacity *vs.* cycle number obtained using the aforementioned conditions is shown in Figure VI - 73b for two different cells with different loadings (cell I loading was 94 mg.cm^{-2}; cell II loading was 136 mg.cm^{-2}). A reversible capacity of 3.3 mAh.cm^{-2} was obtained after 60 cycles for cell I, this value is more than double that reported for the Si baseline electrode after 20 cycles tested using the same conditions. By increasing the loading to 136 mg.cm^{-2}, a reversible areal capacity of 7 mAh.cm^{-2} was obtained after 11 cycles (cycling is still ongoing for cell II). The latter value is 5 times higher than what was reported for the Si baseline electrode after 11 cycles.

The ratio of the areal capacity for the two cells after the same number of cycles was 7:4.6 which is close to the loading ratio for the two cells: 136:94. This suggests that even higher loadings can be achieved to further increase the areal capacity without deteriorating electrode performance, a crucial consideration for practical applications. More recently a new MXene, Mo_2C, was synthesized from a Mo-containing MAX phase. To date the conversion process is incomplete. Etching resulted in a sample that contained only ~ 17 wt. % Mo_2C. Despite this low conversion, this sample exhibited a reversible capacity of 70 mAh/g after more than 500 cycles at 1C. Since in this case the unreacted MAX phase is electro-chemically inactive, the 70 mAh/g achieved was the contribution of only 17% of the electrode mass. It follows that the specific capacity of Mo_2C exceeds 400 mAh/g at 1C even before delamination. Work is ongoing to make pure Mo_2C and delaminate it.

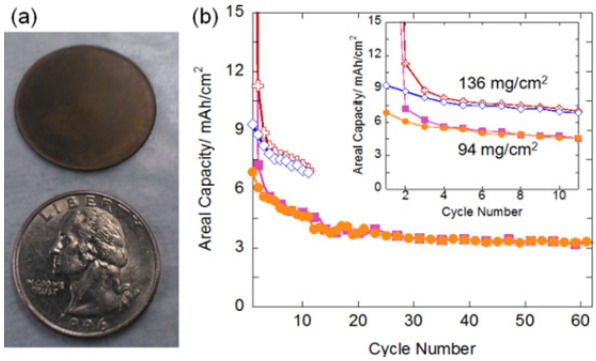

Figure VI - 73: a) Free-standing additive-free Nb_2C MXene disc. b) Areal capacity vs. cycle number for pressed additives-free Nb_2C. Inset zooms in on the first 11 cycles for cells with two different loadings squares and crosses are for lithiation capacities, while the circles and diamonds are for delithiation capacities for two discs with loadings of 94 and 136 mg/cm², respectively

Conclusions and Future Directions

During FY 2013, all our milestones were reached. The effect of binder on the performance of exfoliated Ti_3C_2 in LIBs was studied. The alginate was found to be the best binder showing specific capacity higher than 150 mAh/g at a C/3 rate after more than 50 cycles.

A number of chemical compounds were shown to be able to intercalate into MXene structures leading to its expansion and delamination. Totally *additive free* anodes made with delaminated Ti_3C_2 showed good reversible specific capacities at high rates (820 mAh/cm³ at 1C, and 220 mAh/cm³ at 36C) that cannot be achieved with graphite electrodes.

Three new MXene members (Nb_2C, V_2C and Mo_2C) were synthesized by HF treatment of MAX phases at room temperature. Nb_2C and V_2C showed specific capacities of 110 mAh/g and 125 mAh/g, respectively, obtained at a 10 C cycling rate after 150 cycles. Reversible areal capacities of 3.3 mAh/cm² and 7 mAh/cm² were obtained after 60 and 11 cycles for cells of 94 and 136 mg/cm² loading, respectively. These values are 4 times higher than what was reported for the Si baseline electrode after the same number of cycles or less using the same conditions. Mo_2C exhibited a reversible capacity of 70 mAh/g after more than 500 cycles at 1C.

It was also confirmed that the first cycle irreversibility is due to Li trapped between the MXene layers. More work is needed for complete understanding of the mechanisms involved in order to minimize it.

Future research will focus on reducing the first cycle irreversibility, doubling the areal capacity, further increasing gravimetric and volumetric capacities, and reducing the production cost of the MAX phases (the material from which MXenes are made). First, all *in situ* and *ex situ* studies of the lithiation and delithiation of MXenes will be finished in order to determine the most promising materials. To solve the first cycle irreversibility problem, chemical modification (purification) and chemical pre-lithiation will be used. Further investigation will focus on optimization and modification of the material manufacturing process to enable large-volume, low-cost production followed by optimization of the MXene electrodes to achieve a reversible areal capacity of larger than 5 mAh.cm^{-2} at higher current densities.

FY 2013 Publications/Invited Presentations

1. Naguib, M. *et al.*, "New Two-Dimensional Niobium and Vanadium Carbides as Promising Materials for Li-ion Batteries," *Journal of the American Chemical Society* (2013). DOI: 10.1021/ja405735d.
2. Naguib, M. *et al.*, "*MXenes*: A New Family of Two-Dimensional Materials," *Advanced Materials* (2013). DOI: 10.1002/adma.201304138. **Invited Paper.**
3. Lukatskaya, M.R. *et al.*, "Cation Intercalation and High Volumetric Capacitance of Two-dimensional Titanium Carbide," *Science,* **341** (6153), 1502 (2013).
4. Mashtalir, O. *et al.*, "Intercalation and Delamination of Layered Carbides and Carbonitrides," *Nature Communications,* **4**, 1716-1722 (2013).
5. Ruvinskiy, P. *et al.*, "Nano-Silicon Containing Composite Graphitic Anodes with Improved Cycling Stability for Application in High Energy

Lithium-Ion Batteries," *ECS Journal of Solid State Science and Technology*, **2** (10), M3028-M3033 (2013).

6. Mashtalir, O. *et al.*, "Kinetics of Aluminum Extraction from Ti_3AlC_2 in Hydrofluoric Acid," *Materials Chemistry and Physics,* **139** (1), 147-152 (2013)1.
7. N. Lane, *et al*. "Correlation Effects and Spin-orbit Interactions in Two-dimensional Hexagonal 5d Transition Metal Carbides, $Ta_{n+1}C_n$ (n = 1; 2; 3)," *European Physics Letters*, 57004 (2013).
8. "New Layered Nanolaminates for Use in Lithium Battery Anodes," *DOE Annual Peer Review Meeting*, May 13-17, 2013, Washington, DC.
9. Plenary (luncheon) presentation, International Materials Research Congress (IMRS 2013), Mexico.
10. Plenary lecture, International Conference on Advanced Capacitors (ICAC 2013), Osaka, Japan.
11. Invited talk, "Flatlands beyond Graphene," Bremen, Germany.
12. Invited talk, *37th International Conf. & Expo on Advanced Ceramics and Composites*, Daytona, FL
13. Invited talk, *Workshop at the Argonne National Lab*, Argonne, IL.
14. Invited talk, *1st International Workshop on Energy Storage at KAUST*, Saudi Arabia.
15. Invited talk, *The Minerals, Metals & Materials Society (TMS 2013)*.
16. Invited talk, *MRS* Spring Meeting 2013, Boston.
17. Invited talk, "NOVAMaking Stuff: Faster Innovation Café," *World Café Live*, Philadelphia.
18. Invited talk, *Materials Science & Technology (MS&T 2013)*, Montreal, Canada.
19. Invited talk, *Royal Swedish Academy of Engineering Sciences*, October 2013, Stockholm, Sweden.

VI.C.4 A Combined Experimental and Modeling Approach for the Design of High Current Efficiency Si Electrodes (GM)

Dr. Xingcheng Xiao
General Motors LLC

Research and Development
Warren, MI 48090
Phone: (586) 947-0187
E-mail: Xingcheng.xiao@gm.com

Dr. Yue Qi
Michigan State University
Department of Chem. Eng. and Mat. Sci.
Engineering Building
428 S. Shaw Lane
East Lansing, MI 48824
Phone: (517) 432-1243
E-mail: yueqi@egr.msu.edu

Start Date: October 2012
Projected End Date: September 2016

Objectives

- Combine modeling and experimental approaches to understand, design, and fabricate stabilized nano-structured Si anode with high capacity and high coulombic efficiency.

Technical Barriers

The real challenges to developing a model that allows us to design high current efficiency Si electrodes with electrochemically and mechanically stable artificial SEI layer are: a) poor understanding of SEI failure mechanisms; b) lack of accurate mechanical properties of the SEI; and c) difficulty in validation of the model. All of these are due to the extreme challenges associated with characterizing the properties of nm thin SEI layer on lithiated Si in real battery systems. Therefore, we will first address these questions based on simpler thin film electrodes.

Technical Targets

- Fundamentally understand the mechanical degradation of SEI (including artificial coatings) on Si electrode.
- Establish a correlation between the capacity loss (or current efficiency) and mechanical degradation of SEI on Si.
- Develop a multi-scale model to predict the stress/strain in the SEI layer on Si.
- Predict and measure the basic material properties required in the mechanics model.
- Use the model to guide the design of nanostructured Si electrode.
- Ultimately assist USABC to achieve its goal on EV energy storage: 200 Wh/kg (EV requirement); 96 Wh/kg, 316 W/kg, 5,000 cycles (PHEV 40 mile requirement). Calendar life: 15 years and improved abuse tolerance.

Accomplishments

- Correlated the Young's modulus (E) of amorphous Al_2O_3 coatings with its density (which can be controlled by ALD deposition conditions and cycles), using molecular dynamics (MD) and ReaxFF.
- Successfully applied Laser Acoustic Wave system (LAWS) to characterize the mechanical properties of artificial SEI coating layers (ALD- Al_2O_3). The modulus of ALD- Al_2O_3 coating is around 150 GPa, consistent with the value reported in literature and MD simulations.
- Correlated the interfacial charge-transfer kinetics and coating thickness.
- Derived models showing that Li consumption varies with different SEI failure mechanism. This insight is being used to design new experiments to test SEI failure modes.

✧ ✧ ✧ ✧ ✧

Introduction

Volume changes of up to ~300 vol% for Si during lithiation and delithiation lead to fracture of Si and/or loss of electrical contact with the conductive phase or the current collectors. Nano-structured Si effectively mitigates Si cracking/fracture. Unfortunately, the high surface to volume ratio in nanostructures leads to unacceptable amounts of solid-electrolyte interphase (SEI) formation, thereby lowering current efficiencies. Artificial SEI coated Si nanostructures will resolve this

issue, if the coating can be stable. Based on mechanics models we demonstrate that the SEI coating can be mechanically stable despite the volume change in Si, if the material properties, thickness of the SEI and the size/shape of Si are optimized. Engineering such a system is extremely difficult due to the large number of variables involved, especially as many are unknown.

In order to develop a validated model, it is critical to fundamentally understand the mechanical and chemical stability of SEI (hereafter, SEI refers to both naturally formed native SEI and artificial SEI coatings) in electrochemical environments, the correlation between the coulombic efficiency and the dynamic process of SEI evolution, and the structural optimization of both the SEI and the Si electrode. However, it is extremely difficult to characterize the structure and to measure the mechanical properties of SEI layers that are tens of nm thick on complicated geometries. In this project, we will take advantage of a thin-film geometry that simplifies the investigations while providing fundamental parameter values. Many measurements (e.g., AFM, indentation, XPS and TOF-SIMS depth profile) can be readily conducted with thin films, whereas similar measurements on particles or nanofibers are difficult. These thin-film electrodes can be appropriately modeled using continuum-based models, thus allowing the direct comparison of measurements with models to support model validation.

Approach

In this project, four coherent steps will be taken: a) Develop a multi-scale model to predict the stress/strain in the SEI layer (including artificial SEI) on thin-film Si and establish a correlation between the capacity loss (or current efficiency) and mechanical degradation of SEI on Si. b) Use atomic simulations combined with experiments performed on Si-thin-films to provide critical material properties used in the continuum modeling. c) Investigate the impact of the SEI formation on the stress/strain evolution, combined with modeling to quantify the current efficiency related to a variety artificial SEI layers using *in situ* electrochemical experiments. d) Use the validated model to guide surface coating design and Si size/geometry optimizations that mitigate mechanical degradation to both SEI and Si.

Results

1) Determined the Mechanical property of ALD-Al_2O_3 coating on Si. Using MD and ReaxFF, it has been found that the Young's modulus (E) of amorphous Al_2O_3 coatings decreases with its density, which can be controlled by ALD deposition conditions and cycles. To capture the main characteristics of the ALD-Al_2O_3 coating, the atomic structures were designed to be disordered within the film in-plane directions but to have an average layer distance of 1.1Å along the film growth direction. The predicted Young's modulus compared well with experimental measurements (listed in Table VI - 2).

Experimentally, Laser Acoustic Wave system (LAWS) has been successfully applied to characterize the mechanical properties of artificial SEI coating layer (ALD-Al_2O_3). The modulus of ALD-Al_2O_3 coating is around 150 GPa, consistent with the value reported in literature and MD simulations.

Thus, it is confirmed the LAWS is a reliable approach to measure the modulus of ultrathin coating and our ALD- Al_2O_3 model is accurate.

Table VI - 2: Density and Young's modulus of various Al_2O_3

	ρ (g/cm^3)	E (GPa) Simulation	E (GPa) Experiment
a-Al_2O_3	2.2 ~3.3		95~110
ALD a-Al_2O_3	2.4±0.7	110	150
a-Al_2O_3	2.8	135.4	
a-Al_2O_3	4.0	268.3	
Crystal Al_2O_3	3.95	401	366~410

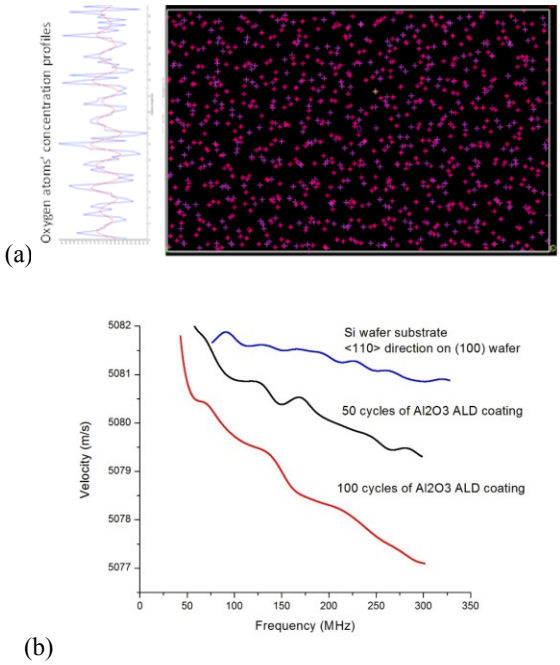

Figure VI - 74: (a) The atomic structure of amorphous ALD-Al_2O_3, the concentration profile of O atoms shows 1.1Å periodicity, (c) LAWS characterization of the mechanical properties of ALD coatings

2) Correlated the interfacial charge-transfer kinetics and coating thickness. The kinetics of Si thin film electrodes coated with Al_2O_3 by ALD was studied using a model thin film system, which provides the intrinsic properties of electrodes. Using a modified PITT measurement, the overall interfacial resistance of ALD-Al_2O_3 coated Si electrodes was quantified by means of a fit exchange current density. Three physicochemical parameters were extracted, including the lithium diffusion coefficient within silicon, the interfacial exchange current density, and the reaction rate constant.

The light blue curve in Figure VI - 75 portrays the trend of B vs. film thickness. The data shows the optimum surface coating thickness was identified as ~0.7nm. Thus, with five to ten atomic layers of an alumina ALD coating, the silicon electrode can deliver 2600 mAh g^{-1} capacity within 3 seconds.

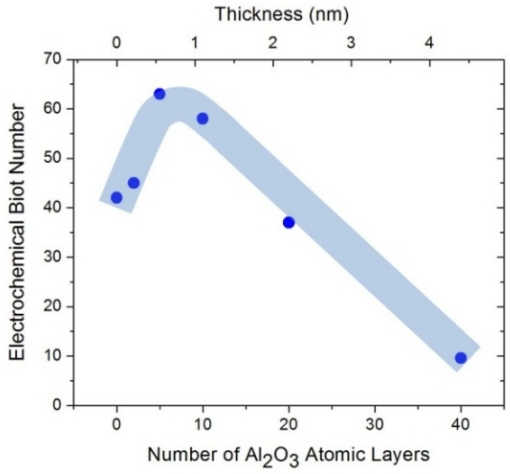

Figure VI - 75: Electrochemical Biot number B obtained from PITT measurement

3) Measured and computed the chemical composition of the initial SEI formed on uncoated Si thin film electrodes at different voltages. An uncoated Si electrode is naturally terminated by a thin layer of SiO_2, and the coated Si electrode considered in the 2nd quarter of the project is ALD-Al_2O_3 coated. Based on DFT calculations, both SiO_2 and Al_2O_3 will be lithiated at the voltage above EC decomposition (~0.8V), contributing to the initial irreversible capacity loss. Experimentally, the composition of SEI layer formed on uncoated Si at different voltages was characterized by XPS. More organic compound formed at voltage >0.4 V and more inorganic compounds formed at voltage range of 0.2V<HV<0.4V. Consequently, preliminary LAWS measurement shows the modulus of SEI layer formed at lower potential is relatively higher.

4) Confirmed the design of patterned Si thin film. The patterned Si thin film has been designed to evaluate the evolution of stress of the Si electrode during SEI formation and growth in *in situ* cells to inform the continuum stress model. If the Si/Cu interface is fixed, the deformation of Si will be along the film thickness direction, so only minimum strain will be applied to the SEI layer. In contrast, if the Si/Cu interface can slide and allow Si islands to expand laterally, the SEI layer will be stretched and compressed. In fact, this interface can be controlled. Using combined DFT calculations and TOF-SIM measurements, it was revealed that Li will segregate to the Si/Cu interface and cause almost frictionless interface sliding. The sliding interface will in turn change the stress developed in the Si islands.

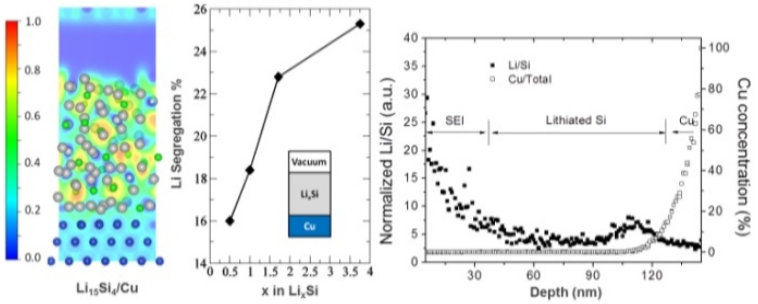

(a) (b) (c)

Figure VI - 76: DFT results show the (a) charge transfer from Li to Cu substrate leads to (b) higher Li/Si ratio at the LixSi/Cu interface. The Li segregation behavior has also been observed in (c) SIMS depth profile

5) Derived that Li consumption will be different with different SEI failure mechanism. For example if the SEI fractures, the current efficiency is lost during lithiation. If the SEI wrinkles and peels off, the current efficiency loss occurs during delithiation. This insight is used to design new experiments to test SEI failure modes.

Conclusions and Future Directions

This project is progressing with closely integrated modeling and experiments. The experimental mechanical and electrochemical data obtained on ALD-Al_2O_3 coated Si show good agreement with modeling and results. This initial work validates the methods being used and demonstrates that the results are accurate. Other ALD coating samples will be sent to GM for mechanical property measurements.

The understanding of the Li_xSi/Cu interface allows us to design patterned Si on Cu substrate with different interface properties in order to control the deformation of Si and the mechanical strain imposed on the SEI film. The next step is to measure the stress evolution in the SEI while Si is lithiated and deliathiated. This will reveal the failure mechanism of SEI on Si and provide fundamental knowledge for constructing the mechanics models.

This team started the project in April 2013. It has already initiated collaborations with other BATT research groups. More collaboration is expected as the project continues along its path.

FY 2013 Publications/Presentations

1. Maria E. Stournara, Xingcheng Xiao, Yue Qi*, Priya Johari, Peng Lu, Brian Sheldon, Huajian Gao*, Vivek B. Shenoy, "Lithium segregation induced structure and strength change at amorphous-Si/Cu interface," *Nano Letters*, **13** (10), 4759-4768 (2013).
2. Juchuan Li, Xingcheng Xiao*, Yang-Tse Cheng, and Mark W. Verbrugge, "Atomic Layered Coating Enabling Fast Surface Kinetics at Silicon Electrodes in Lithium Ion Batteries," *Journal of Physical Chemistry Letter*, **4**, 3387-3391 (2013).
3. Hamed Haftbaradaran, Xingcheng Xiao and Huajian Gao*, "Critical film thickness for fracture in thin film electrodes on substrate," *Modeling and Simulation in Materials Science and Engineering*, **21**, 074008 (2013).
4. Xin Su, Qingliu Wu, Juchuan Li, Xingcheng Xiao, Amber Lott, Wenquan Lu, Brian W. Sheldon, Ji Wu, "Silicon-based Nanomaterials for Lithium Ion Batteries - A Review," *Advanced Energy Materials*, DOI: 10.1002/aenm.201300882 (2013).
5. Mingyan Wu, Xingcheng Xiao, Shidi Xun, Prodip Das, Xiangyun Song, Paul Olalde-Velasco, Dongdong Wang, Adam Z. Weber, Vince Battaglia, Wanli Yang and Gao Liu, "An Ideal Polymer Binder for High-Capacity Battery Anodes," *Journal of American Chemical Society*, **135 (32)**, 12048-12056 (2013).
6. X. Xiao, "Ultrathin surface coating as artificial solid electrolyte interphase for lithium ion batteries," *246th ACS National Meeting*, Sept. 12, 2013, Indianapolis, IN (Invited).
7. X. Xiao, "High Capacity Electrode Materials for Lithium Ion Batteries: Challenges and Opportunities," *Department Seminar*, Chemical Engineering and Materials Sciences, Oct. 7, 2013, Michigan State University (Invited).
8. Y. Qi, "Predicting the transport and mechanical properties of the solid electrolyte interphase in Li-ion batteries," *Society of Engineering Science 50th Annual Meeting*, July 29, 2013, Providence, RI (Invited).
9. Y. Qi, "*Ab initio* Interface Design for Si-based electrodes," *ACS National Meeting*, April 10, 2013, New Orleans, LA (Invited).
10. B.W. Sheldon, "Chemically Induced Stresses in Li-ion Battery Electrodes," *ACS National Meeting*, April 10, 2013, New Orleans, LA (Invited).
11. B.W. Sheldon, "Lithiation Induced Stresses and Interfacial Phenomena in Li-ion Battery Electrodes," *Society of Engineering Science Annual Meeting*, July 29, 2013, Providence, RI (Invited).
12. B.W. Sheldon, "Electrochemically Induced Stresses in Energy Storage Materials," October 17, 2013, University of Wisconsin, Madison, WI (Invited).
13. Y. Cheng, "Understanding diffusion-induced-stresses and fracture, including effects of the Solid-Electrolyte-Interphase (SEI), in lithium ion battery electrodes," *Gordon Research Conference on Nano-Mechanical Interfaces*, August 4-9, 2013, Hong Kong, China (Invited).

VI.C.5 Hierarchical Assembly of Inorganic/Organic Hybrid Si Negative Electrodes (LBNL)

Gao Liu
Lawrence Berkeley National Laboratory

Environmental Energy Technologies Division
1 Cyclotron Road, MS 70R108B
Berkeley, CA 94720
Phone: (510) 486-7207; Fax: (510) 486-7303
E-mail: Gliu@lbl.gov

Start Date: October 2012
Projected End Date: September 2016

Objectives

- Develop new conductive polymer binder materials to enable large volume change lithium storage materials to be used in lithium-ion electrode.
- Explore additives to increase coulomb efficiency (CE) and stabilize capacities of Si electrode by forming a stable SEI during cycling.

Technical Barriers

This project addresses the following technical barriers from the Energy Storage section of the Vehicle Technologies Program Multi-year Research, Development and Demonstration Plan:

- Calendar and cycle life
- Energy density

Technical Targets

Relevant USABC goals

- EV:
  - $150/kWh.
  - 230 Wh/dm^3.
  - 1000, 80% capacity, discharge cycles.
  - 10-year system life.
- PHEV 40-mile:
  - $220/kWh.
  - 193 Wh/dm3.
  - 5,000 discharge cycles.
  - 15-year system life.

Accomplishments

- Successfully developed PEFM conductive polymer binder for Si nanoparticles in lithium-ion negative electrode applications. As a modification of PFM binder, PEFM enables the Si electrode to cycle at almost full capacity.
- Successfully adapted the PFM conductive polymer binder to Sn nanoparticles for lithium-ion negative electrode applications. Optimized the composition of the Sn/PFM electrode composition. Demonstrated extended cycling of pure Sn nanoparticles with PFM binder composite electrode at 500 mAh/g-Sn capacity.
- Developed a propylene carbonate (PC) co-solvent system for lithium-ion battery, which improves the cycle life performance of lithium ion batteries.

✧ ✧ ✧ ✧ ✧

Introduction

Achieving the DOE energy, cycle life and cost targets will require materials of higher capacity and improved coulombic efficiency or cells with higher voltage. High capacity Si or Sn alloy based anode material has the potential to fulfill the energy density requirements for EV/PHEV applications. However, full capacity cycling of the materials results in significant capacity fade due to a large volume change during Li insertion and removal. Decreasing the particle size to nanometer scale can be an effective means of accommodating the volume change. However, it is very challenging to make electric connections to all the alloy nanoparticles in the electrode by using similar size acetylene black conductive additive. The repeated volume change of the alloy nanoparticles during cycling can lead to repositioning of the particles in the electrode matrix and result in particle dislocation from the conductive matrix. This dislocation of particles causes the rapid fade of the electrode capacity during cycling. In order to address this issue, Si/conductive polymer composite electrodes were developed in this work. This new electrode can be fabricated with the current lithium-ion manufacturing processes. A new class of electric conductive binder materials was developed, which the

Lowest Unoccupied Molecular Obital (LUMO) energy is controlled to match the reduction potential of the alloy materials. The electrodes made with these binders have significantly improved cycling capability.

Approach

Use functional polymer design and synthesis to develop new conductive polymers with proper electronic properties, strong adhesion and improved flexibility to provide electric pathways in the electrode, and to accommodate large volume change of the Si or Sn alloy active material during lithium insertion and removal. The rational design of binder is assisted with advanced diagnostic techniques such as XAS at Advance Light Sources and with advanced molecular computation at National Energy Research Scientific Computing Center – both are DOE national user facilities.

Results

Conductive Polymer Binder with an Ideal Structural Design for Si Alloy Materials. Li-ion transportation in the binder system is critical for achieving the full capacity of the active materials in battery electrodes, because the binder coats the surface of the active material and may impede the Li-ion diffusion. Although ion mobility in the doped conductive polymer system has been demonstrated, strategies to further improve the ion mobility are still necessary. In our polymer system, this issue is tackled by improving the electrolyte uptake through the incorporation of the polar ethyleneoxide side chains.

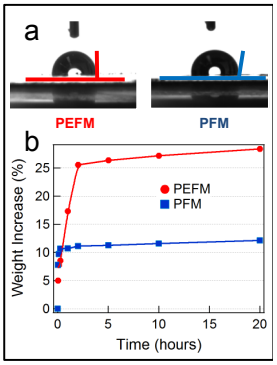

Figure VI - 77: (a) Water contact angles on the surfaces of PEFM and PFM films. The E side chains in PEFM increase the polarity, and thus improve the swelling of the polymer. Therefore the PEFM has a lower contact angle with water. (b) The swelling tests of PEFM and PFM polymer film in the 1M LiPF6 EC/DEC (1:1) electrolyte. The electrolyte uptake in PEFM is three times higher than that in PFM, and is at the same level as that for conventional non-conductive PVDF binder

The enhanced polarity of the PEFM polymer results in a three-fold electrolyte uptake (Figure VI - 77). The better swelling is due to the increased polarity of the polymer, which is indicated by the water contact angle measurements (Figure VI - 77a). The static contact angle is 90.9° for PEFM with the E group, versus 101.0° for PFM. The ether side chains tend to distribute uniformly in the polymer because they are chemically attached to the backbone. The uniform distribution of the ether moieties in the binder helps to improve the overall electrolyte uptake. Although PFM also swells in the electrolyte solution, the total electrolyte uptake is about 10 percent of its final weight. In swelled PEFM films, the electrolyte uptake is tripled, accounting for 30 percent of the final swelling weight (Figure VI - 77b). This number is similar to the non-conductive PVDF swelling in the electrolyte. As explained above, the enhanced electrolyte uptake is important for allowing facile Li-ion transportation through the polymer binder to the active materials.

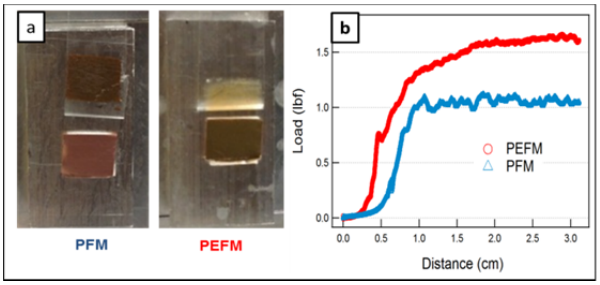

Figure VI - 78: Peel tests comparison of the electrode laminate made with PFM and FEFM binder. (a) Peel testing photos of the two electrodes during the tests. The photo shows the PFM based electrode was peeled off (left), but PEFM based electrode remains attached to the Cu current collector with only small amount of surface materials peeled off by the tape (right). This shows that the adhesion force of the developed PEFM is too strong to be measured by such conventional method. (b) Force measured during the peel tests of PFM and PEFM based electrodes. Note again that the adhesion force of PEFM based electrode is beyond the measurement range of such method, and actually even higher than the value (1.7 lbf) showed by the red curve

Another important benefit associated with the increased polarity of the polymer is the significantly improved adhesion force of the binder to the Si particles, and with the current collector. The photo of the peel result (Figure VI - 78) shows that almost the whole PEFM laminate persists on the current collector, while for the PFM delamination takes place between the electrode laminate and the current collector. This shows that the large adhesion force of the PEFM binder is beyond the testing range of such conventional peeling test, which is a standard technique used in the battery industry. Although the force to delaminate the PEFM-based laminate electrode is too strong to be measured,

the great improvement on adhesion among the laminate, current collector, and particles is obvious.

Figure VI - 79 shows that the cycling capacity of Si particles in the initial cycle reaches theoretical capacity (3750 mAh/g) in the PEFM/Si electrodes, indicating 100% utilization of Si material embedded in the PEFM binder. This is corresponding to 2500 mAh/g capacity of the entire laminate weight when the weight of conductive binder is included and a 1200 mAh/cm3 volumetric energy density of the electrode. In both the PF/Si and PFM/Si electrodes, the delithiation capacity of Si in the first cycle is much lower. The specific delithiation is stable and higher in PEFM/Si than that in PFM/Si electrodes over extended cycles.

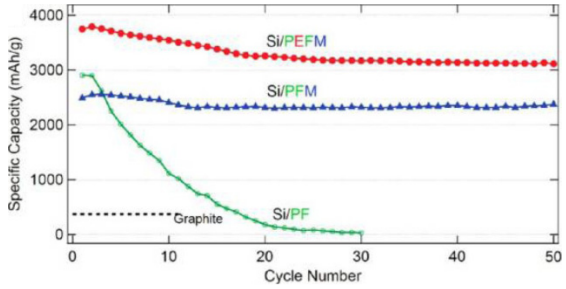

Figure VI - 79: Cycling performance of polymer/Si composite electrodes. (The current density at C-rate is 0.92 mAh/cm^2)

Performance of Sn/Conductive Polymer Composite Electrode Both Si and Sn work at the same potential range between 10 mV to 1 V as anode materials in the lithium-ion chemistry. A comprehensive evaluation of the conductive polymer binder with a Sn compound was performed. It is demonstrated that pure Sn nanoparticles can be stably cycled at high capacity (> 500 mAh/g) with a polyfluorene-type conductive polymer binder in composite electrodes. Crystalline Sn nanoparticles (< 150 nm) were used as anode materials in this study. The average diameter of Sn secondary particles is 270 nm, calculated based on BET surface area. The composite electrodes contain a conductive polymer binder that constitutes 2% to 10% of the material, without any conductive additives. The electrode containing 5% conductive binder showed the best cycling performance, with a reversible capacity of 510 mAh/g (Figure VI - 80a) Crystallinity of Sn particles gradually degrades during cycling, and pulverization of particles was observed after long-term cycling, leading to capacity fade. The conductive polymer binder shows advantages over other binders, such as poly(vinylidene fluoride) (PVDF) and carboxymethylcellulose (CMC) binders, because it can provide electrical conductivity and strong adhesion during Sn volume expansion (Figure VI - 80b).

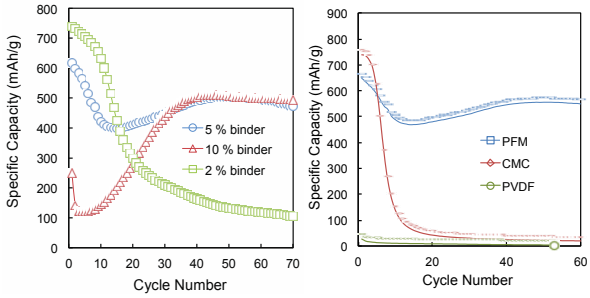

Figure VI - 80: Pure Sn nanoparticle composite electrodes. (a) Different amount of PFM. (b) Different binders

New Propylene Carbonate (PC)-Based Electrolytes with High Coulombic Efficiency for Lithium-ion Batteries Ethylene carbonate (EC) forms a stable SEI at ~0.8 V before lithium intercalation. Li+ permeable and electronically non-conductive, SEI prevents further electrolyte decomposition and allows reversible lithiation and delithiation of the graphite or Si anode. The major disadvantage of EC is its high melting point at around 34°C, which limits the use of lithium-ion batteries at low temperatures. Propylene carbonate (PC) has a wide liquid temperature range (-48.8 ~ 242.0°C) and very good low-temperature performance compared to EC. However, with only a negligible structural difference from EC, PC undergoes a detrimental solvent decomposition on the surface of graphite. This causes disintegration of the graphite electrode, usually accompanied by delamination of the active material from the current collector, and finally, cell failure.

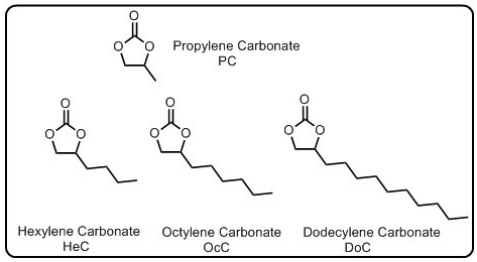

Figure VI - 81: The structure of hexylene carbonate (HeC), octylene carbonate (OcC) and dodecylene carbonate (DoC)

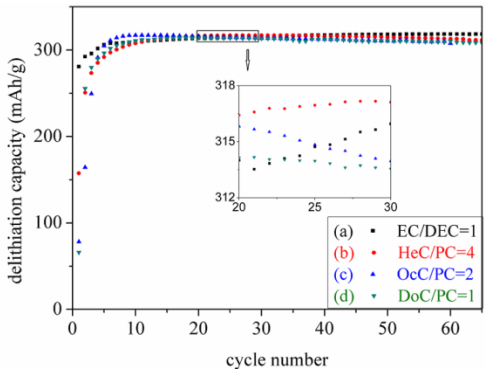

Figure VI - 82: Cycling performances of a graphite half cell in a 1 M $LiPF_6$ solution of (a) EC/DEC=1, (b) HeC/PC=4, (c) OcC/PC=2, and (d) DoC/PC=1 (v/v) at a C/10 rate

A homologous series of PC analogue solvents (Figure VI - 81) with increasing length of linear alkyl substitutes were synthesized and used as co-solvents with PC for graphite-based lithium-ion half cells. A graphite anode reaches a capacity of around 310 mAh/g in PC and its analogue co-solvents, with 99.95% Coulombic efficiency, similar to the values obtained with EC-based electrolytes. Figure VI - 82 shows cycling performances of graphite half cells using co-solvents of hexylene carbonate (HeC)/PC=4, octylene carbonate (OcC)/PC=2, and dodecylene carbonate (DoC)/PC=1 with 1 M $LiPF_6$. Cell capacities reach ~ 310 mAh/g in the first 10 cycles in all the electrolytes. This indicates the formation of a stable SEI on graphite surface that prevents PC exfoliation and allows reversible cycling in graphite anode. The PC co-solvents from different batches of HeC, OcC, and DoC gave the same cell performance, which indicates the consistency of the data shown in Figure VI - 82.

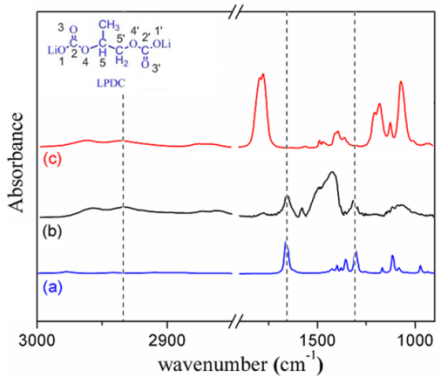

Figure VI - 83: FTIR spectra of (a) a standard LPDC, (b) a graphite electrode cycled in a 1 M $LiPF_6$ solution of HeC/PC=4 for around 10 cycles at C/10, and (c) the electrolyte used in the cell, 1 M $LiPF_6$ in HeC/PC=4

Figure VI - 83 shows the FTIR spectra of a graphite electrode after being cycled in HeC/PC=4 electrolyte. Besides the leftover electrolyte, the major component of SEI is lithium propylene dicarbonate (LPDC), which is the single-electron reduction product of PC. The bulky cyclic carbonate solvents compete with PC for Li solvation, which delayed the PC co-intercalation into graphene layers. PC then went through single-electron decomposition on graphite surface and formed a stable SEI.

Conclusions and Future Directions

A modified conductive polymer, PEFM, was synthesized and characterized. Electronic, mechanical, and electrolyte-uptake properties are optimized individually without detrimental effect to each other. Full-capacity cycling of Si was accessed in this conductive polymer binder with excellent rate performance. The performance characteristics of this Sn/PFM electrode were studied and stable cycling performance was demonstrated. A homologous series of propylene carbonate (PC) analogue solvents with increasing length of linear alkyl substitutes were synthesized and used as co-solvents with PC for graphite-based lithium-ion half cells. A graphite anode reaches a capacity of 310 mAh/g in PC and its analogue co-solvents, with 99.95 percent Coulombic efficiency

[1] PFM stands for Poly(9,9-dioctylfluorene-co-fluorenone-co-methylbenzoic ester); PEFM stands for Poly(2,7-9,9-dioctylfluorene-co-2,7-9,9-(di(oxy-2,5,8-trioxadecane)) fluorine-co-2,7-fluorenone-co-2,5-1-methylbenzoic ester).

FY 2013 Patents/Publications/Presentations

1. Gao Liu and Hui Zhao, New *in situ* elastic coating to stabilization of Si anode surface for lithium-ion rechargeable battery applications, IB-2974 disclosure filed in 2013.
2. Liu, X.; Wang, D.; Liu, G.; Srinivasan, V.; Liu, Z.; Hussain, Z.; Yang, W., "Distinct charge dynamics in battery electrodes revealed by *in situ* and *operando* soft X-ray spectroscopy," *Nature Comm.* 2013, Accepted.
3. Wu, M.; Sabisch, J. E. C.; Xun, S.; Minor, A.; Battaglia, V. S.; Liu, G., "*In situ* Formed Si Nanoparticle Network with Micronsized Si Particles for Lithium-ion Battery Anodes." *Nano Letters,* Article ASAP (2013).
4. Xun, S.; Xiang, B.; Minor, A.; Battaglia, V. S.; Liu, G., "Conductive Polymer and Silicon Composite Secondary Particles for a High Area-Loading Negative Electrode," *J. Electrochem. Soc.,* **160(6)**, A1380-A1383 (2013).
5. Xun, S.; Song, X.; Battaglia, V. S.; Liu, G., "Conductive Polymer Binder-Enabled Cycling of Pure Tin Nanoparticle Composite Anode

Electrodes for a Lithium-Ion Battery," *J. Electrochem. Soc.* **160(6)**, A849-A855 (2013).

6. Wu, M.; Xiao, X.; Vukmirovic, N.; Xun, S.; Das, P. K.; Song, X.; Olade-Velasco, P.; Wang, D.; Weber, A. Z.; Wang, L.-W.; Battaglia, V. S.; Yang, W.; Liu, G.; "Toward an Ideal Polymer Binder Design for High-Capacity Battery Anodes," *Journal of the American Chemical Society,* **132**, 12048–12056 (2013).
7. "Development of Conductive Binders for Silicon Anodes," *Advanced Automotive Battery Conference,* Feb 2013, Pasadena, CA.
8. "Development of Conductive Binders for Silicon and Tin Anodes," *10th Pacific Rim Conference on Ceramic and Glass Technology*, June 2013, San Diego, CA.
9. "Advanced Binder and Si Anode Design for High Energy Batteries," *Beyond Lithium Ion Conference,* June 2013, Boulder, CA.
10. "The Advancements of Conductive Polymer Binder for High Capacity Alloy Anode Materials," *U.S.-China Meeting*, Sept., 2013, Chengdu, China.

VI.C.6 Electro-Deposition of Silicon and Other Metals for Li-Ion Battery Anodes (NETL)

Dr. Manivannan Ayyakkannu
Contractor: NETL/DOE

Dr. Prashant N Kumta
Subcontractor: University of Pittsburgh, Pittsburgh

Project Start Date: October 2010
Project End Date: September 2013

Objectives

- This research is aimed at exploring electrodeposition as a low cost and scalable approach to replace graphite with metal alloy systems such as Li, Sn, Sb, etc as a high energy density anode system. The main objectives of this research are
  - Develop thin films of Si and other electroactive metal alloy systems as high capacity Li-ion anodes
  - Obtain similar or lower irreversible loss compared to graphite
  - Attain high specific capacities (>1000 mAh/g)
  - Achieve similar or better cyclability and calendar life of the developed anode systems
  - Obtain columbic efficiency close to 100%
  - Attain good rate characteristics for high load applications

Technical Barriers

One of the major challenges of silicon based anodes is the loss of mechanical integrity and poor cyclability due to the colossal stress related problems associated with the huge volumetric changes in Si (>300%) during lithium alloying and delloying.

Technical Targets

- Synthesize amorphous Si films for Li-ion system by cost effective electrodeposition process.
- Improve the cyclability of Si anode based system for Li-ion cell.
- Lower the first cycle irreversible loss of Si anodes.
- Application of pulse plating electrodeposition technique to control the morphology of the Si anode.

Accomplishments

- Synthesized binder-free amorphous silicon films on copper substrate by electroreduction of Si salts from an inorganic solvent bath.
- The amorphous Si films exhibited a stable and reversible capacity of 1300 mAh/g with a columbic efficiency of 99.5% upto 100 cycles.
- Modified the morphology of the electrodeposited Si thin films using pulse plating techniques.

✧ ✧ ✧ ✧ ✧

Introduction

Silicon, with a theoretical capacity of 4212 mAh/g, corresponding to the maximum lithiated phase of $Li_{22}Si_5$, was identified as an alternative anode which can store more than 10 times more charge than graphite. However, during alloying and dealloying of lithium, there is a very large volumetric change leading to mechanical stresses in the electrode causing cracking and consequently loss of inter – particle contact. Hence, there is delamination of the electrode layer leading to rapid capacity fade.

Nanostructured and amorphous Si synthesized by physical and chemical vapor deposition show improved performance but are not economically viable for secondary batteries. Electrodeposition is a very inexpensive process which has been widely studied and used in many industrial applications for plating metals and alloys. Electrodeposition of silicon from organic solvents and ionic liquids on metallic and graphite substrates has previously been reported in the literature. Additionally, the electrodeposition technique offers to provide the deposited films with different morphologies and functional properties by controlling the parameters such as electrolyte composition, applied voltage/current density and time of deposition.

Approach

Silicon thin films were electrodeposited on copper substrate using galvanostatic conditions and pulse current conditions from an electrolyte of 0.5M silicon

tetrachloride ($SiCl_4$) and 0.1M tetrabutylammonium chloride (TBACL) in propylene carbonate (PC) solution in an argon environment (<0.1 ppm oxygen and <0.1 ppm water). The current density of the deposition done at constant current (galvanostatic condition) was -1mA/cm^2. The frequencies of negative cycle at the same deposition current density for pulse conditions were 0Hz (galvanostatic), 500Hz, 1000Hz, 2000Hz, 3000Hz, 4000Hz and 5000Hz. The current cycle had a duty cycle (active deposition time/total time) of 50%.

Electrochemical investigations were performed on the electrodeposited Si thin films on copper foil which served as the working electrode. A 2016/2025 coin cell assembly in a half cell configuration was used by employing lithium (Li) foil as counter electrode and 1 M LiPF6 in (EC:DEC = 1:2, by volume) as the electrolyte. The assembled cells were tested by cycling between 0.02 and 1.2 V employing a constant current density of 400 mA/g.

Results

Material Characterization. The glancing angle X-Ray diffraction did not show any peaks corresponding to crystalline silicon. Raman spectra showed the presence of broad peak at 480 cm-1 which is indicative of the transverse optical phonon mode of amorphous silicon.

SEM analysis (Figure VI - 84) of galvanostatically deposited amorphous Si film showed islands ranging from 10–20µm with a film thickness of approximately 0.3–1µm. The EDAX indicated the presence of Si, C, O and Cu; the oxygen present was due to the surface oxidation and carbon from the residual PC and acetone.

Electrochemical Characterization. A first discharge and charge capacity (Figure VI - 85) of ~3400 mAh/g and ~1150 mAh/g respectively, were obtained with a first cycle irreversible loss of ~65%. This huge first cycle irreversible loss may be due to the presence of oxide layer over the Si thin film, formation of large solid electrolyte interface (SEI) layer or impurities from the electrolyte. The major alloying in the first cycle occurs near the 0.2V which is indicative of lithiation process of amorphous silicon and consistent with other literature reports.

The columbic efficiency shown in Figure VI - 85 was very close to 100%. A fade rate of ~0.016% per cycle and a capacity of ~1260 mAhg−1 were observed at the end of the 100th cycle which is an almost four fold increase over the capacities observed for graphite anode. There was no extension, modification or growth of the crack width or length in comparison to what was already prevalent in the as deposited films prior to cycling as shown in Figure VI - 84.

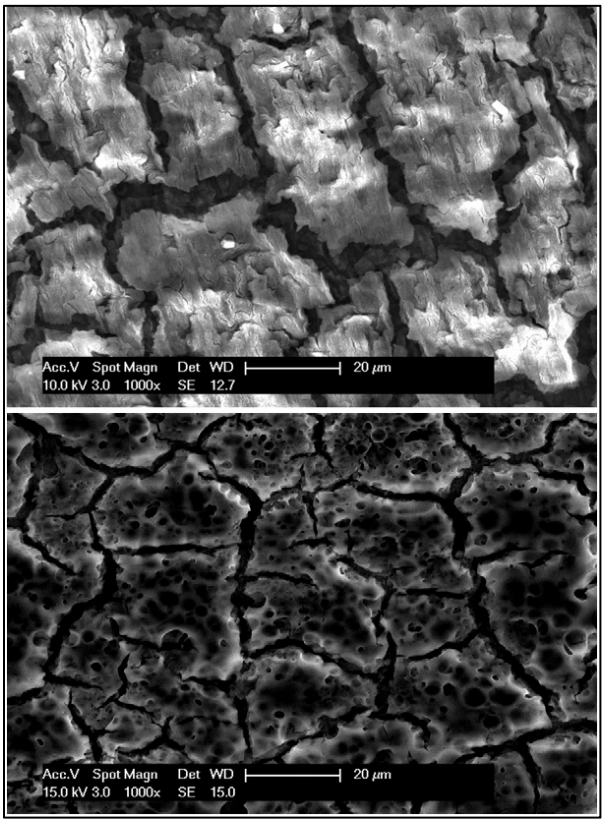

Figure VI - 84: SEM images of electrodeposited Si before cycling (top) and after 100 cycles of testing for Li/Li$^+$ battery (below)

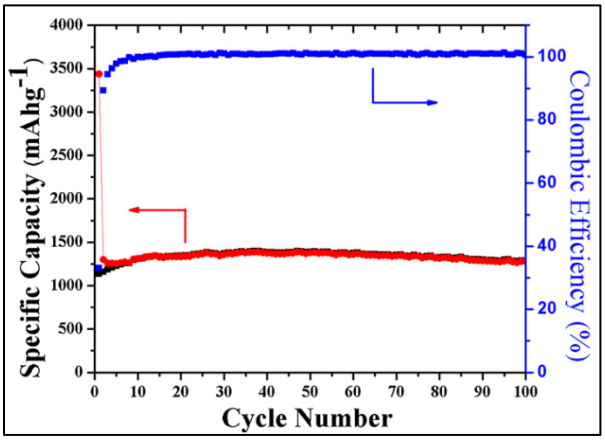

Figure VI - 85: Capacity and columbic efficiency plots cycled at 400 mA/g between 0.02 and 1.2 V for 100 cycles

Pulse Electrodeposition Condition. A major change in the morphology of the electrodeposited Si was observed with the change in the frequency of deposition as can be observed in Figure VI - 86. The morphology of thin films for 0Hz (galvanostatic) showed islands of Si, 500Hz showed islands of Si formed from Si particles and 1000Hz resulted in continuous thin films of Si. The formation of continuous films at high frequency

deposition can be attributed to the increased diffusion of Si4+ ions in the depletion layer close to the electrode-electrolyte interface during the relaxation time (zero current) of the deposition cycle.

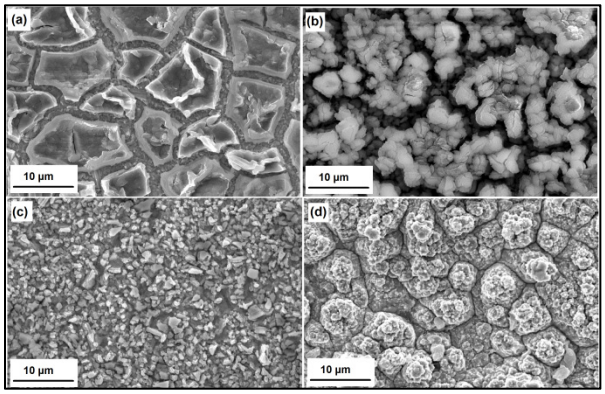

Figure VI - 86: SEM images of electrodeposited Si films at (a) 0Hz, (b) 500Hz, (c) 1000Hz and (d) 5000Hz pulse frequency

The electrochemical testing of these films as Li-ion anode system showed stable cycling with an improvement in the stability of the films. These films showed a decrease in the percentage loss per cycle with the increase in the frequency of the deposition cycle. The SEM analysis of the films showed that the films were stable even after 100 cycles of testing.

Conclusions and Future Directions

Electro-reduction of $SiCl_4$ to silicon has been achieved at a cathodic potential ~−1.6 V vs. Pt.QRE on copper substrates using a PC based solvent. The electrodeposited Si films which were predominantly amorphous in nature, showed a reversible capacity of ~1300 mAh/g when cycled at a current density of 400 mA/g between 1.2 V and 0.02 V. Columbic efficiencies exceeding 99.5% and a fade rate of less than 0.016% per cycle were obtained for up to 100 cycles.

The change in frequency of electrodeposition cycle under pulse plating conditions exhibited a major change in the morphology of the Si thin films. The testing of these Si films showed stable capacity for 100 cycles and the percentage loss per cycle decreased with increase in the deposition frequency. Development of electrodeposited Si anode systems can be further carried out to decrease the first cycle irreversible loss by changing the electrolyte, post deposition heat treatment and by developing carbon/metal coatings on the Si thin films. Further multi-layer Si – (metal/carbon) system can be developed to increase the loading capacity of the active Si material on the electrode.

FY 2013 Publications/Presentations

1. Rigved Epur, Madhumati Ramanathan, Faith R. Beck, Ayyakkannu Manivannan & Prashant N. Kumta, "*Electrodeposition of amorphous silicon anode for lithium ion batteries*"- Materials Science and Engineering: B, 2012, 177, pg:1151-1156
2. Rigved Epur, Faith Beck, Moni Kanchan Datta, Ayyakkannu Manivannan and Prashant N. Kumta, 2012 AIChE Annual Meeting, Pittsburgh, PA, USA
3. Rigved Epur, Faith R. Beck, Ayyakkannu Manivannan and Prashant N. Kumta, 221st ECS meeting at Seattle, WA – Oral presentation

FY 2013 Patent

Silicon-Containing Compositions, Methods of Their Preparation, and Methods of Electrolytically Depositing Silicon on a Current Carrier for Use in Lithium Ion Battery Applications, U.S. Patent AppNo: 13/733992, Filed: January 4, 2013.

VI.C.7 Atomic Layer Deposition for Stabilization of Amorphous Silicon Anodes (NREL)

Chunmei Ban
National Renewable Energy Laboratory

15013 Denver West Pkwy
Golden, CO, 80401
Phone: (303) 384-6504; Fax: (303) 384-6432
E-mail: Chunmei.ban@nrel.gov

Steve M. George and Se-Hee Lee
University of Colorado, Boulder
Department of Chemistry and Mechanical Engineering
University of Colorado Boulder
914 Broadway, Boulder, CO 80309
Phone: (303) 492-7471; Fax: (303) 492-7889
E-mail: steve.george@colorado.edu;
sehee.lee@colorado.edu

Start Date: October 2010
Projected End Date: September 2014

Objectives

- Develop a low-cost, thick and high-capacity silicon anode with sustainable cycling performance, by advanced surface modification.
- Synthesize novel stable and elastic coatings for Si anodes using Atomic Layer Deposition (ALD) & Molecular Layer Deposition (MLD).
- Demonstrate durable cycling performance of thick Si anodes by using new ALD/MLD coatings and electrode designs.
- Investigate coating mechanism on electrochemical cycling performance via
  - Study of the mechanical properties of MLD coating materials.
  - Research on the morphology and structural evolution during lithiation/delithiation
- Explore the importance and mechanism of various coatings via the BATT Coating Group.
- Collaborate within the BATT program with the aim of developing high-rate plug-in hybrid electric (PHEV) compatible electrodes (both anodes and cathodes).

Technical Barriers

Major barriers addressed include:

(A) Cost: Inexpensive processing techniques are employed to fabricate conventional thick electrodes.

(B) High Capacity: Silicon is predominantly being explored as a high capacity anode material. There is also a collaborative emphasis to enable high capacity cathode materials.

(C) High Rate: Both ALD coatings and nanostructured materials are being developed such that high-rate capability is demonstrated for emerging materials.

(D) Safety: The ALD coatings are targeted to improve safety for a variety of electrode materials.

Technical Targets

- Stabilize the high-capacity silicon anodes by employing the advanced surface coating techniques, ALD and MLD
- Demonstrate the stable high-range cycling performance of Si anodes
- Relevant to USABC goals: 200Wh/kg (EV requirement); 96Wh/kg, 316W/kg, 5,000 cycles (PHEV 40 miles requirement). Calendar life: 15 years. Improved abuse tolerance

Accomplishments

- Growth of an aluminum alkoxide polymer (alucone) film using the sequential reactions of trimethylaluminum (TMA) and ethylene glycol (EG);
- Achieved durable cycling (>100 cycles) of the MLD-engineered thick Si anodes (>15μm) using optimized MLD coating reactions and conditions;
- Demonstrated a specific capacity of ~ 900 mAh/g at the 150th cycle for the aulcone coated Si anodes, whereas the uncoated Si electrode undergoes the rapid degradation;
- Characterized the effect of MLD alucone coatings on the morphology and structure of silicon anodes during cycling.
- Investigated the cyclization of polyacrylonitrile (PAN) coating for Si

composite anode to address Si expansion and enable greatly improved cycling performance.

Introduction

Significant advances in both energy density and rate capability for Li-ion batteries will be critical for their implementation in next generation EVs. Due to the high theoretical capacity of Si, 3579 mAh/g for $Li_{15}Si_4$, and its natural abundance, it has attracted much attention as a promising Li-ion anode material. However, progress towards a commercially viable Si anode has been impeded by Si's rapid capacity fade caused by the large volumetric expansion. Such a massive volumetric change can result in cracking and pulverization of the Si particles, which then leads to the interruption of electronic transport pathways and the electrochemical isolation of pulverized particles. In this project, new conformal nanoscale coatings with desirable elastic properties and good conductivity are being developed via ALD and MLD, to accommodate the volumetric expansion, protect the surface from the reactive electrolytes, as well as ensure the electronic paths through the composite electrodes.

Greatly improved performance has been achieved for both ALD coated nano-MoO_3 anodes and cathodes. The effect of Al_2O_3 ALD coatings on the structure and SEI composition have been studied last year by using *in situ* synchrotron XRD and *ex situ* XPS and TOF-SIMS. It shows that ALD coatings have mitigated the side reaction on the surface of electrodes and preserved the structure during severe cycling. These past results suggest that new ALD coatings with improved mechanical properties and conductivity can help accommodate the volumetric expansion in electrodes, as well as ensure the electronic paths through the electrodes.

Both high rate and durable cycling of Si will be achieved by employing the ALD coating and new elastic (polymer-like) coatings with low elastic moduli (MLD coating). Successful completion of this project will enable the coated Si anodes to have significantly improved cycling stability and high coulombic efficiency. In the end, the development of new flexible and conductive MLD films will enable both anodes and cathodes within the BATT program achieving durable high rate capability.

Approach

Metal-organic hybrid films have been developed and grown on the Si electrodes by using MLD, with the aim to accommodate the volumetric changes in Si particles The growth of an aluminum alkoxide polymer (alucone) has been demonstrated using the sequential exposures of trimethylaluminum (TMA) and ethylene glycol (EG). Besides an aluminum-based precursor, other metal precursors are being used to enhance the conductivity in the MLD flexible coatings.

Chemical vapor deposition via silane decomposition on a hot filament was used to synthesize the silicon thin films with different degree of crystallinity. Recently, a Nanocrystal RF Plasma Reactor has been utilized to synthesize silicon/alloy nanocrystals with uniform size and shape. Size may be tuned from <10 to ~100 nm by varying the plasma conditions that will allow the study of how Si nanocrystal size affects the electrochemical performance. Additionally, commercial silicon particles have been used to identify the coating effects. Conventional electrodes containing active material, conductive additive and binder have been fabricated to evaluate the cycling properties.

Results

Develop elastic coatings by using MLD. The new metal-organic hybrid coating, aluminum alkoxide coating (alucone), was grown based on reactions of inorganic trimethylalumium ($Al(CH_3)_3$) and organic glycerol polyols ($HOCH_2CH(OH)CH_2OH$) precursors. The sequential exposure of $Al(CH_3)_3$ and HOCH2CH(OH)CH2OH in AB cycles produces the evolution of alucone coatings with growth rates of about 3-5 Å per AB cycle at a substrate temperatures of 100-140°C.

Figure VI - 87 shows a schematic of the controlled layered chemistry structure of the aluminum alkoxide alucone polymer used in this work.

The growth of the alucone MLD coating occurs by reaction of hydroxyl groups on the alcohol with AlCH3. With more than two hydroxyl groups on the alcohol, there is greater probability that unreacted hydroxyl groups will remain after polyol reactions with AlCH3* surface species. These unreacted hydroxyl groups can produce additional crosslinking between growing polymer chains that can strengthen the alucone films and lead to higher fracture toughness.

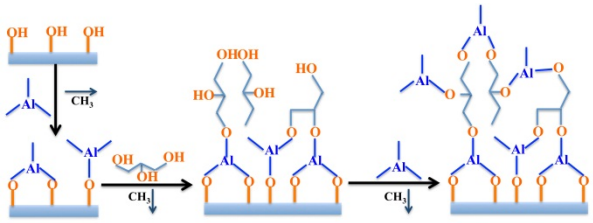

Figure VI - 87: Schematic depicting alucone MLD reaction

Challenges are encountered during the MLD on high-surface-area nano-Si electrodes with a tortuous

architecture. Two different reaction modes, static reactants exposure and viscous flow, were used during MLD to address the challenges in fabricating conformal coating. The static reactants exposure allows the precursor gas to reach more surfaces of the electrode, and then enhance the completion of the self-limited reaction on the surface. High angle annular dark field (HAADF) scanning transmission electron microscopy (STEM), which is highly sensitive to atomic number contrast (Z-contrast imaging), was used to further clarify the conformity of the MLD coating. HAADF-STEM image (Figure VI - 88a) shows that the alucone layer is a thin (~5 nm), dense, and conformal coating adhered to the Si particles. Electron energy loss spectroscopy (EELS) was also utilized to characterize the microstructure of the MLD coated electrodes. The conformal thin coating of the metal-alkoxide films MLD (red mapping) on the nano-Si particles (cyan mapping), as displayed in Figure VI - 88b. Note that the alucone MLD was coated on the laminated electrodes, rather than the powdery Silicon. However, the static reactants exposure facilitates the surface reactions through the entire electrode, thereby provides an intimately linked conductive network.

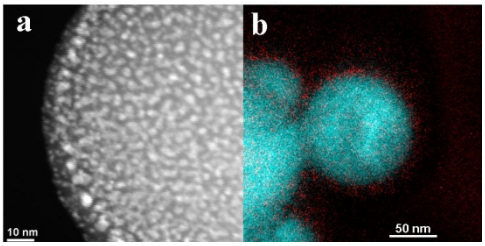

Figure VI - 88: (a) HAADF-STEM of the alucone MLD coated particle; (b) EELS elemental mapping (Si highlighted in cyan, Al highlighted in red) confirming the conformal alucone MLD coating on the Si composite electrode

Improving electrochemical performance by alucone MLD coating. Electrochemical cycling performance of the alucone coated Si electrodes has been investigated in the coin-cell configuration, with Li-metal as a counter electrode. The Si electrodes were prepared with 60% Si nanoparticles (purchased from Alfa without further treatment), 20% acetylene black and 20% PVDF binder. All of the cells were first cycled at 175 mA/g (C/20), and then cycled at 350 mA/g (C/10) in the voltage window between 0.05-1V.

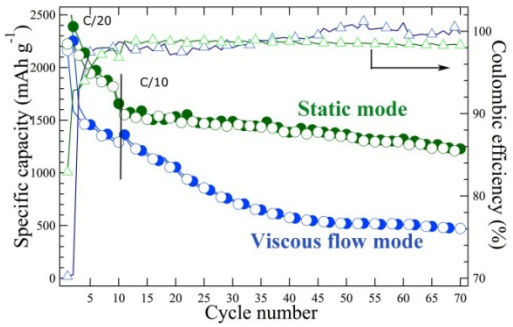

Figure VI - 89: Cycling performance of alucone coated Si anodes by using static and viscous flow modes

Figure VI - 89 shows the significantly improved cycling stability for the alucone MLD coated Si electrodes. The capacity obtained at a cycling rate of 0.1C has been stabilized for the static-coated Si electrode, while the slow fade in capacity is observed for the viscous-flow coated Si electrode. Besides, the static-coated Si electrode has the higher coulombic efficiency for the first cycle, which further confirms the static-coat enhancing the conformality on the tortuous electrode structure. In contrast, the bare silicon anode capacity decays to nearly zero after 28 charge-discharge cycles.

Figure VI - 90 displays the impact of different coating thicknesses on the cycling performance. The highest capacity was obtained for both thicker MLD-coated Si anodes. We expect that the better conductivity in the conformal alucone coatings may lead to the higher capacity and better cycling performance than bare electrodes.

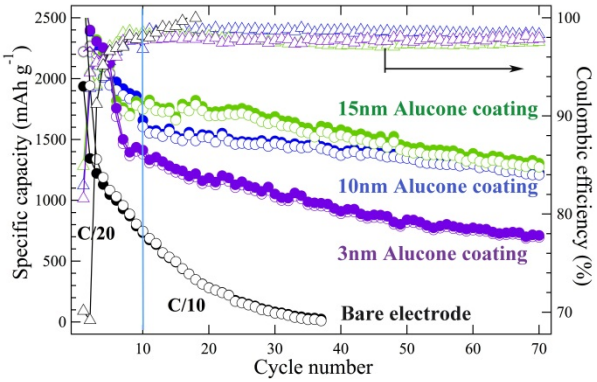

Figure VI - 90: Cycling performance as a function of coating thickness

Cycling stability has been demonstrated for the alucone coated Si anodes, as indicated in Figure VI - 91. Fast capacity decay was observed in the bare Si electrode. But the alucone coated Si anodes exhibit sustainable cycling over hundreds of cycles with CE in excess of 99%. The specific charge capacity of 900 mAh /g at the 150th cycle corresponds to a volumetric capacity of 569 mAh/cm^3 considering an initial

electrode thickness of 12.7 µm. Such good cycle life and CE for the thick electrodes is evidence that the alucone MLD coating provides favorable mechanical properties, accommodating the volumetric changes of the Si electrode and preserving the structural integrity of the electrode network throughout deep cycling.

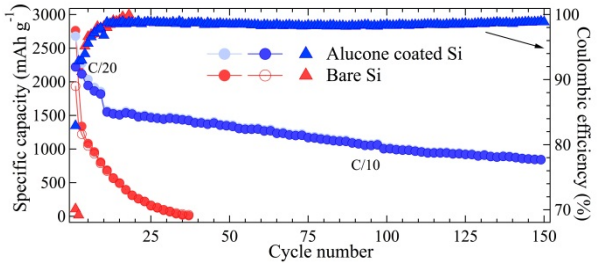

Figure VI - 91: Greatly enhanced cycling stability in alucone MLD coating Si anodes

SEM characterizing the resilience of the alucone MLD coating: The cross-section SEM images at different stages of cycling are shown in Figure VI - 92. The fresh bare and alucone coated electrodes have initial thicknesses of 12.2 µm and 12.7 µm, respectively, in Figure VI - 92b and Figure VI - 92e correspond to the first lithiation of the bare and coated electrode with the thickness of 20.3 µm and 23.0 µm. The volume expansion at the thickness direction was observed for both bare and coated electrodes. Similar volume expansion on the coated electrodes indicates that the alucone coating allows volume expansion in the coated electrodes to complete fully lithiation. The cross-sections after the 20th delithiated electrodes, as listed in Figure VI - 92c and 2f, show that the uncoated and coated electrodes have the thickness of 18.1 µm and 15.0 µm, respectively. A nearly full recovery from the massive volumetric expansion was observed for the alucone coated electrodes. On the contrary, the bare electrode remains almost fully expanded after the 20th delithiation. It indicates that bare electrode may lose the original electrical contact and structural integrity. The findings imply that the good resilience of the alucone coatings provides sufficient mechanical support to accommodate the major volumetric changes experienced by Si anodes, as well as to aid in the recovery and preservation of the whole composite network upon delithiation.

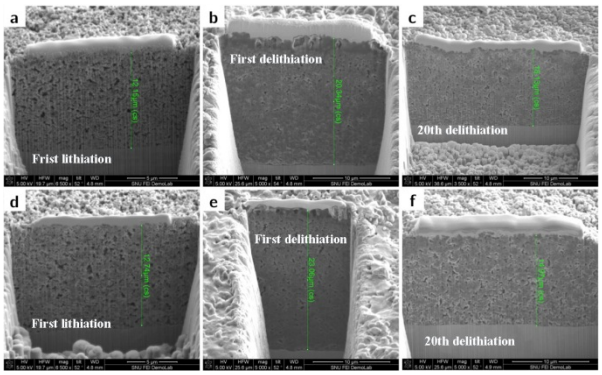

Figure VI - 92: SEM images showing the cross-sections of the bare electrodes (a, b, c) and alucone coated electrodes (d, e, f)

Conclusions and Future Directions

Growth of the flexible metal-organic coatings on Si electrodes has been accomplished by using the MLD technique. Using sequential reactions of the TMA and EG precursors has coated Si electrode with the aluminum alkoxide films. To enhance the coating conformality for the tortuos electrodes, optimized static reactants exposure has been used in MLD.

The significantly-improved performance has been demonstrated for the alucone coated nano-Si electrodes. The alucone coated Si anodes exhibits sustainable cycling over hundreds of cycles with coulombic efficiency in excess of 99%. The specific charge capacity of 900 mAh/g at the 150th cycle corresponds to an electrode volumetric capacity of 569 mAh/cm^3. The thin and conformal coating, observed by advanced microscopy, accommodates the complete volume expansion during lithiation, but also helps preserve the structure integrity during delithiation.

Given the observed electrochemical and spectroscopic data, it is concluded that an alucone MLD coating provides a mechanically robust, resilient and conductive network for Si composite electrodes, allowing for a long cycle life and remarkable stability. Employment of the alucone coating on conventional nano-Si composite electrodes provides significant improvement in cycling stability, rate, and coulombic efficiency.

In FY2014, the research efforts will focus on developing the conformal elastic coatings with enhanced ionic and electronic conductivity. In order to better understand the coating effects, one of the FY2014 objectives will be to *in situ* characterize the impact of coatings on the structure and morphology evolution during cycling, and explore the importance and mechanism of various coatings via the BATT coating group.

FY 2013 Publications/Presentations

1. M. Piper, T. A. Yersak, S-B. Son, S. C. Kim, C. S. Kang, K. H. Oh, C. Ban, A. C. Dillon, and S.H. Lee, "Conformal Coatings of Cyclized-PAN for Mechanically Resilient Si nano-Composite Anodes," *Adv. Energy Mater.* doi: 10.1002/aenm.201200850 (2013).
2. M. Piper, J. J. Travis, M. Young, S-B Son, S. C. Kim, K. H. Oh, S. M. George, C. Ban, S-H Lee, "Reversible High Capacity Si Nanocomposite Anodes enabled by Molecular Layer Deposition," *Adv. Mater.* Under review.
3. C. Ban, M. Xie, X. Sun, J. J Travis, G. Wang, H. Sun, A. C Dillon, J. Lian and S. M George, "Atomic layer deposition of amorphous TiO2 on graphene as an anode for Li-ion batteries," *Nanotechnology*, **24**, 424002, 2013, doi:10.1088/0957-4484/24/42/424002
4. I. Abdulagatov, K. E. Terauds, J. J. Travis, A. S. Cavanagh, R. Raj, and S. M. George, "Pyrolysis of titanicone molecular layer deposition films as precursors for conducting TiO2/Carbon composite films," *J. Phys. Chem. C*, **117** (34), pp 17442–17450 DOI: 10.1021/jp4051947 (2013).
5. "Atomic Layer Deposition of Al2O3 for Highly Improved Performance in Li-ion Battery Electrodes," *2012 Fall MRS*, Boston, MA, USA (Invited).
6. "Nanoscale Interface Engineering for Improved Li-ion Batteries," *2013 Spring MRS*, San Francisco, CA, USA (Invited).
7. "Atomic Layer Deposition for Stabilization of Silicon Anodes," DOE Annual Peer Review Meeting, May 13-17, 2013, Washington, DC.

VI.C.8 Synthesis and Characterization of Si/SiOx-Graphene Nanocomposite Anodes and Polymer Binders (PSU)

Donghai Wang
Pennsylvania State University

Department of Mechanical and Nuclear Engineering
328 Reber Building
University Park, PA 16802
Phone: (814) 863-1287; Fax: (814) 863-4848
E-mail: dwang@psu.edu

Michael A. Hickner
Pennsylvania State University
Department of Materials Science and Engineering
310 Steidle Building
University Park, PA 16802
Phone: (814) 867-1847; Fax: (814) 865-2917
E-mail: hickner@matse.psu.edu

Start Date: October 2010
Projected End Date: September 2014

Objectives

- Design, synthesize and test novel polymer binders with varying mechanical properties and surface linker groups for Si anodes
- Synthesize and characterize Si/SiOx-graphene nanocomposites,
- Identify and evaluate the electrochemical performance of the Si/SiOx-graphene nanocomposites and the polymer binder.
- Improve management of volume change characteristics of Si-based anodes, impede the capacity fading with enhanced capacity reliability, decrease initial irreversible capacity loss, and improve the specific capacity and coulombic efficiency (CE) of Si/SiOx-based anodes.

Technical Barriers

There are several technical barriers to developing Si/SiOx-based anodes for lithium-ion batteries including:

- Poor capacity cycling.
- Large initial irreversible capacity and corresponding low CE.
- Need to add a high percentage of conductive carbon to obtain good rate (C/3) performance.

Technical Targets

- Prepare Si nanoparticles with controlled particle size, and demonstrate Si-graphene nanocomposite anodes.
- Synthesize and evaluate novel polymer binders with controlled SiOx binding groups and Li-conducting blocks.
- Determine electrochemical properties of Si/SiOx nanoparticle, Si/SiOx-graphene nanocomposites and the polymer binders in lithium half cell.
- Achieve stable reversible capacity in excess of ~1,000 mAh/g.
- Obtain above 40% first cycle coulombic efficiency as well as 90% CE cycle to cycle.

Accomplishments

- Synthesized SiO/Fe_2O_3 composite from commercially available SiO with improved capacity retention than that of SiO (capacity retention >75% after 50 cycles) and better high rate performance.
- Developed a novel type of micron-sized Si-C composites which exhibit a reversible capacity of 1459 mAh/g after 200 cycles at 1 A/g with capacity retention of 97.8%.
- Carried out fundamental studies on the influence of Si building block size, surface modification and heteroatom doping on the performance of the micron-sized Si-C composites and the results were demonstrated
- Synthesized and demonstrated crosslinking binder that achieved equivalent cycling performance to NaCMC.
- Measured binder-Si nano particle (NP) interactions and investigated factors contributing to high binder performance with commercial Si NPs.

✧ ✧ ✧ ✧ ✧

Introduction

An increase in energy and power densities of Li-ion cells clearly depends on improvements in electrode

materials. As the commercial anode, graphite has the theoretical capacity of 372 mAh/g, which is low relative to the requirement of high-energy applications. Thus, the search for an alternative anode to replace graphite in Li-ion batteries has been underway for many years. So far, silicon has the highest theoretical capacity ($Li_{4.4}Si$ ~ 4200 mAh/g) of all known materials, and is abundant, inexpensive, and safer than graphite (it shows a slightly higher voltage plateau than that of graphite, and lithiated silicon is more stable in typical electrolytes than lithiated graphite). Unfortunately, the practical use of Si powders as anodes in Li-ion batteries is still hindered by several problems. One of the problems is severe volume changes during Li insertion/extraction, leading to loss of electric contact and poor cycling performance.

One approach to obtain a high-performance Si anode is to use silicon/carbon composites. In this project, the aim is to develop novel Si/SiO_x-carbon nanocomposites to improve cycling performance of Si anodes. On the other hand, many important battery characteristics, including stability and irreversible capacity losses, are critically dependent on the polymer binder's properties. High capacity electrochemically active Si particles that exhibit significant volume changes during insertion and extraction of Li require improved binder characteristics to ensure electrode integrity during use.

Inspired by these features this project seeks to mitigate the electrochemical limitations of Si-based anodes during charge/discharge by designing novel Si/SiO_x-carbon nanocomposite and polymer binders to tolerate volume change, improve electrode kinetics, and decrease initial irreversible capacity loss.

Approach

Our approach is 1) to synthesize different Si-based nanocomposites and identify novel commercially available binders to tolerate volume change upon lithiation/delithiation so as to improve cycling performance; and 2) to develop novel polymer binder with controlled elastic properties, ion-conductive moieties, and SiOx surface binding functionality, in order to stabilize and bridge SiOx particles to improve cycling performance of Si-based anodes.

Results

Si-based anode materials. A SiO/Fe_2O_3 composite, composed of SiO coated with Fe_2O_3 nanoparticles, was synthesized by mechanical milling and characterized by XRD, SEM, TEM, and EDS. The TEM image and corresponding EDS maps showed that the SiO particles in the composite are coated uniformly with crystalline Fe_2O_3 nanoparticles (Figure VI - 93A). As shown in Figure VI - 93B, both SiO and milled SiO show very poor capacity retention. The SiO/Fe_2O_3 composite shows considerably better cyclability than either SiO sample, with 71% charge capacity retention (1335 mAh/g) with respect to the first charge capacity after 50 cycles. The rate capability of the SiO/Fe_2O_3 composite is also superior to that of SiO and milled SiO. The composite still has a capacity of ~600 mAh/g at a high current density of 4.8 A/g, while the SiO can only achieve a low capacity of ~200 mAh/g at this current density. We propose that metallic Fe forms during lithiation of SiO/Fe_2O_3, increasing the conductivity of the composite and thereby significantly improving its performance.

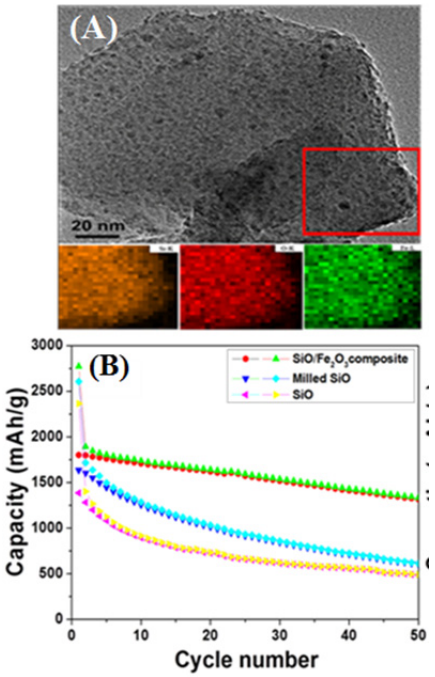

Figure VI - 93: (A) TEM images and corresponding EDS elemental mappings of the SiO/Fe_2O_3 composite. (B) Cycling performance of SiO, milled SiO, and SiO/Fe_2O_3 composite in 50 cycles between 0.01-1.5V

A novel micron-sized Si-C composite, which is composed of interconnected nano-scale building blocks of Si and carbon, was synthesized via a scalable and low-cost method. The composite was thoroughly characterized by a variety of methods including XRD, XPS, FT-IR, Raman, TEM and SEM. The TEM image showed that the average particle size of the composite was around 20 μm (Figure VI - 94A). The Si-C composite exhibits a reversible capacity of 1459 mAh/g after 200 cycles at 1 A/g with capacity retention of 97.8% (Figure VI - 94B) and has a high tap density of 0.78 g/cm^3. The first cycle CE is 77%. Capacities of 1100 and 700 mAh/g can be obtained at high current densities of 6.4 A/g and 12.8 A/g, respectively. The excellent performance is attributed to the nanoscale size of primary particles and interconnected carbon and Si

networks which can maintain internal electrical contact and sustain cycling stability.

The influence of Si nanoscale building block size and carbon coating on the electrochemical performance of the microsized Si–C composites was then further investigated. Four primary Si building sizes (10nm, 15nm, 30nm, and 50nm) were obtained by adjusting the heat treatment temperature. It was found that the critical Si building block size was 15 nm, which enables a high capacity without compromising the cycling stability (Figure VI - 95A).

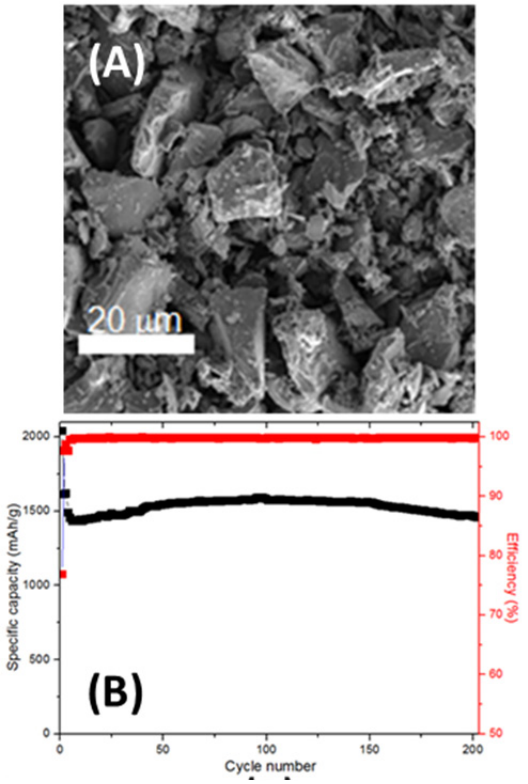

Figure VI - 94: (A) SEM image of the micro-sized Si-C composite. (B) Cycling performance of the Si-C composite in 200 cycles between 0.01-1.5V

It is also confirmed that carbon coating at higher temperature improves the first cycle CE and the rate capability. At elevated temperature, the carbon source gas help reduce the surface oxides, which was examined by Raman and XPS spectroscopy. A better graphitic carbon layer was also achieved at higher temperature. An optimized coating temperature of 800°C was confirmed according to experimental results (Figure VI - 95B).

The influence of further boron doping on the electrochemical performance of the micro-sized Si–C composites was also investigated. Boron doping was achieved by simply introducing dopant precursors (B_2O_3) during thermal disproportionation of SiO. Compared to undoped Si-C, the XRD peaks of B-doped Si-C shift to higher angles due to the replacement of Si atoms by smaller B atoms, which leads to a smaller lattice constant. This result, combined with the absence of Si-B alloy peaks, indicates the successful doping of B into Si. The Si Raman peak shifts from 510 cm^{-1} for undoped Si to 494 cm^{-1} for B-doped Si due to disorder in the Si structure caused by the stress developed in the surrounding Si atomic network after B doping, which is consistent with the XRD results (Figure VI - 96A). B in carbon was not detected as shifting of C peaks is not observed, which is due to the moderate carbon coating temperature, thus. Only Si was doped with B in the composite. The B-doped Si-C composite shows much improved rate capability, delivering a capacity of 575 mAh/g at 6.4 A/g without any external carbon additive, 80% higher than that of undoped composite (Figure VI - 96B).

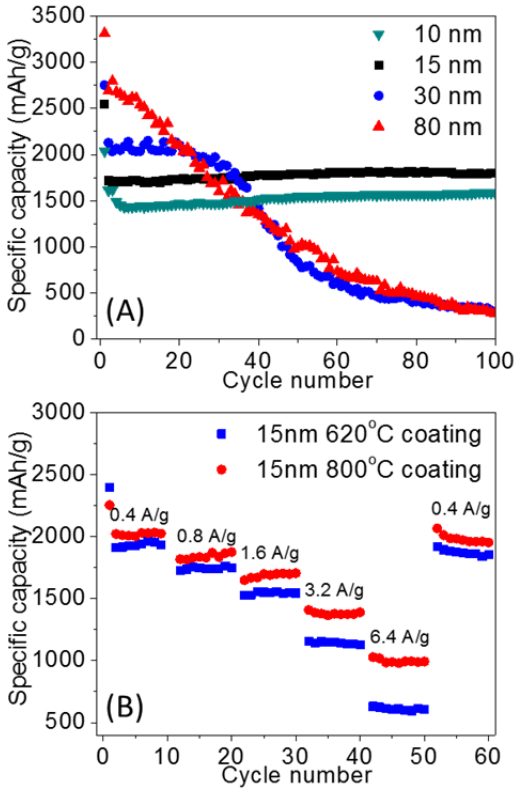

Figure VI - 95: (A) Cycling performances of micro-sized Si-C composites with different building block sizes. (B) Rate performance of Si-C composite Si-15nm with different C coating temperatures

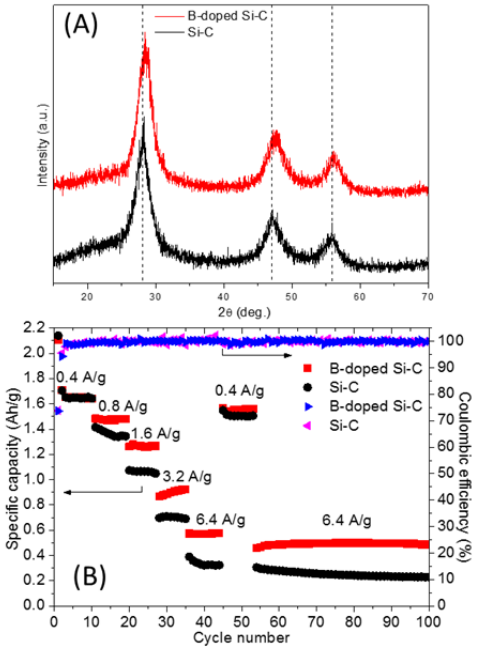

Figure VI - 96: (A) XRD patterns of B-doped Si-C and Si-C composites. (B) Rate performance comparison of B-doped Si-C and Si-C composites

The B-doped Si-C composite also exhibits better cycling stability at high rates. In contrast to the obvious capacity fading of Si-C, the capacity of B-doped Si-C was stable for about 50 cycles at 6.4 A/g. The improved rate capability and cycling stability are attributed to lower charge transfer resistance of B-doped Si-C.

Synthesis and Evaluation of Polymer Binders. A number of ionic polymer binders based on stiff backbones have been synthesized. Figure VI - 97 shows the capacity retiontion of anodes based on commercial Si NPs with NaCMC and experimental binders.

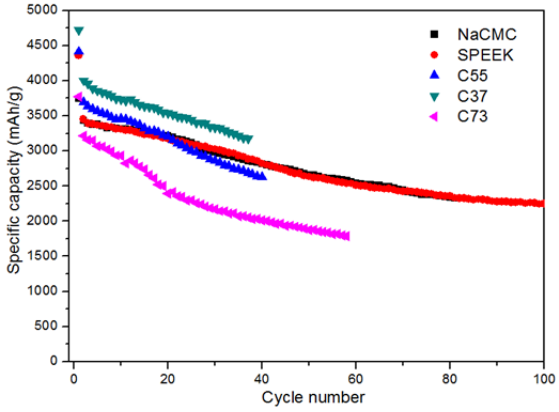

Figure VI - 97: Cycling performance of commercial Si NP anodes with a range of ion-containing polymer binders

By examining a range of binder compositions and looking at ionic forms of the binders in Na, H, and Li forms, the capacity fade performance was correlated to the interaction of the bonder with the Si-NP surface. Swelling of the binder in electrolyte was combatted with crosslinking of the binder by poly(acrylic acid). Optimized crosslinking showed binder performance that matched or exceeded the commercial NaCMC standard material. Higher cycling rates at equivalent capacity fade were observed with the experimental binders due to their electrolyte uptake and ionic conductivity.

Conclusions and Future Directions

A novel SiO/Fe_2O_3 composite from commercially available SiO has been developed, synthesized and characterized. The composite showed improved capacity retention than that of SiO (capacity retention >75% after 50 cycles) and better high rate performance (~600 mAh/g at 4.8 A/g). A proposed mechanism that metallic Fe forms during lithiation of SiO/Fe_2O_3, increasing the conductivity of the composite and thereby significantly improving its performance has been made according to the experiment result and literature. A series of micro-sized Si-C composites has been synthesized and characterized. The overall particle size is micrometer range with a primary building block size of ~10 nm crystalline Si. The Si-C composite exhibits a reversible capacity of 1459 mAh/g after 200 cycles at 1 A/g with capacity retention of 97.8%. A further study on the influence of building block size and C-coating condition showed an optimized primary particle size of 15nm and a C-coating temperature of 800°C, which provide the best electrochemical performance as well as long cycling ability. In addition, boron doping was found to help increase the conductivity of the Si-C composite. The B-doped Si-C composite shows much improved rate capability, delivering a capacity of 575 mAh/g at 6.4 A/g without any external carbon additive, 80% higher than that of undoped composite.

Binder properties were shown to influence the performance of commercial Si-NP based anodes. The capacity fade was controlled by the interaction between the binder and the NPs and could be modulated based on the chemistry of the binder and crosslinking.

During the remainder of the project period, future work will focus on: 1) Introducing Si alloy with different forms (e.g., surface coating, alloy) to further improve the performance of previous reported Si-based materials. 2) Electrochemical characterization of the modified Si-based anode materials with improved mass loading. 3) Synthesis and optimization of semiconducting polymer binders with strong surface-bonding groups.

FY 2013 Publications/Presentations

1. "Development of High Energy Density Lithium-Sulfur Cells," *DOE Annual Peer Review Meeting*, May 13-17, 2013, Washington, DC.
2. Wang, D. H., "In Symposium of Nanostructured Materials for Lithium Ion Batteries and for Supercapacitors," *TMS Annual Meeting & Exhibition*, San Antonio, TX, March 2013.
3. Yi, R., Dai, F., Gordin, M. L., Chen, S., Wang, D., *Advanced Energy Materials* **3**, 295-300 (2013).
4. Yi, R., Dai, F., Gordin, M. L., Sohn, H., Wang, D., *Advanced Energy Materials,* DOI:10.1002/aenm.201300496 (2013).
5. Yi, R., Zai, J., Dai, F., Gordin, M. L., Wang, D. *Electrochem. Communications,* **36**, 29-32 (2013).
6. Zhou, M., Gordin, M. L., Chen, S., Xu, T., Song, J., Lv, D., Wang, D. *Electrochem. Communication*s, **28**, 79-82 (2013).

VI.C.9 Development of Silicon-based High Capacity Anodes (PNNL)

Ji-Guang Zhang
Pacific Northwest National Laboratory

902 Battelle Boulevard, Mail Stop K2-44
Richland, WA, 99352
Phone: (509) 372-6515; Fax: (509) 375-2186
E-mail: Jiguang.Zhang@pnnl.gov

Jun Liu
Pacific Northwest National Laboratory
902 Battelle Boulevard, Mail Stop K2-01
Richland, WA, 99352
Phone: (509) 375-4443; Fax: (509) 351-6242
E-mail: Jun.Liu@pnnl.gov

Start Date: October 2010
Projected End Date: September 2014

Objectives

- Develop Si-based anodes with high capacities, high cycle stabilities and high rate capabilities.
- Develop low-cost synthesis routes for Si-based anodes.
- Advance the fundamental understanding on the electrolyte additive effect, stress and volume expansion effect, and degradation mechanism of Si-based anodes.

Technical Barriers

Low energy density, limited cycle life, and high cost.

Technical Targets

- Identify the main failure mechanisms of Si-based anodes.
- Develop low-cost and scalable approaches to synthesize Si-based nanocomposite materials with improved performance (a capacity retention of >700 mAh/g over 250 cycles).
- Demonstrate good cyclability of thick electrodes.

Accomplishments

- Developed high-capacity stable Si anodes using a scalable anodization method. Porous Si synthesized by the electrochemical etching process has demonstrated excellent cycling performance with a high capacity of up to ~750 mAh/g (based on the full electrode including the carbon additive and binder) and >80% capacity retention over 1000 cycles.
- Developed pre-lithiation treatment of anode and reduced the first cycle irreversible capacity loss of the porous Si anode to <10%.
- Demonstrated good cycling stability of thick porous Si anodes with a high areal specific capacity of ~1.5 mAh/cm^2 and a capacity retention of >95% over 200 cycles.
- Identified the fundamental mechanism on how FEC additive affects the formation of solid electrolyte interphase (SEI) film on Si anode: 1) FEC is reduced through the opening of the five-member ring leading to the formation of lithium poly(vinyl carbonate), LiF and some dimers; 2) The FEC-derived lithium poly(vinyl carbonate), which has good mechanical flexibility, leads to enhanced the stability of the SEI film.

✧ ✧ ✧ ✧ ✧

Introduction

Si has very high theoretical capacity of ~4200 mAh/g and has a good potential to be used as an anode for next generation Li-ion batteries. However, large volume expansion during the lithiation process usually leads to a fast capacity fade hindering its practical applications. Several nanostructured Si materials have demonstrated good performance, but most of them work best only in low loading conditions and their performance degrade quickly with increasing capacity loading required by practical applications. Another barrier in this field is that most of high capacity Si based electrodes have to be prepared by high cost processes that are difficult to scale up. Therefore, to pave the road for practical applications, a cost effective and scalable approach needs to be developed to prepare Si based anodes which can retain good performance at high loading conditions.

Approach

Two approaches have been developed for a highly stable, high-capacity anode based on silicon composite. First, the meso-porous sponge-like Si particles (MSS) with nano size pores and high porosity are synthesized

by a scalable anodization method. The etched material was then coated with a thin layer of carbon using chemical vapor deposition to improve its electronic conductivity. Although the etched samples exhibit a size of >20 μm, they were not pulverized even after thousands of charge/discharge cycles. This is a significant improvement as compared to those of the conventional large silicon particles. The large volume expansion of MSS during lithiation/de-lithiation was mainly accommodated by the inner pores so only ~30% expansion of the whole particle was observed. The large irreversible capacity loss in the as prepared anode was minimized by pre-lithiation of Si anodes using a controlled amount of stabilized Li metal powder (SLMP™, FMC Lithium) on the electrode.

In another effort, the cost-effective and scalable ball-milling method was further optimized to improve the cycling stability and rate performance of the core-shell structured Si/B_4C/graphite composite with high area specific capacity. In this composite, conductive B_4C with high Mohs hardness serves not only as micro-/nano-millers in a high energy ball-milling process to break down micron-sized Si, it also improves the electronic conductivity of the composite. A low energy ball milling process was then used to coat a thin layer of conductive carbon to further enhance the conductivity of the composite.

The volume expansion effect and the electrolyte additive effect on the formation of the SEI film was investigated using advanced characterization techniques such as *in situ* TEM, ^{6}Li nuclear magnetic resonance (NMR), and x-ray photoelectron spectroscopy.

Results

1. Mesoporous Silicon Sponge (MSS): An anti-pulverization structure for high-performance Lithium-ion anodes. Porous Si with large pore sizes of ~50 nm has most of the volume change accommodated by the inner channels. Therefore, large Si particles (>20 μm) with such large pore sizes exhibit only ~30% volume expansion in their outside dimension and can be charged/discharged more than 1000 cycles without pulverization. Figure VI - 98 shows the *in situ* TEM result of the lithiation process of a porous Si particle. The dimension and crystallinity change at different lithiation states are monitored. Porous Si became amorphous during lithiation and the expansion along <01 1> is only 7.8%. The overall volume expansion of the whole particle is ~30%, much less than 300% observed in the fully lithiated conventional Si particles.

Porous Si anode showed excellent cycling stability with a high initial capacity (based on the whole electrode weight including binder and conductive carbon) of up to ~750 mAh/g. By tuning the weight ratio of the MSS in electrodes, the capacity and the cycling stability of the anode can be fine-tuned for different applications. Figure VI - 99a shows the representative results of an electrode with ~46 wt% MSS. It exhibits a specific capacity of ~640 mAh/g and ~81% capacity retention over 1000 cycles. Figure VI - 99b is the long term cycling data of a battery with ~40 wt% MSS in the electrode. A capacity of ~570 mAh/g and ~87% capacity retention over 1000 cycles were obtained.

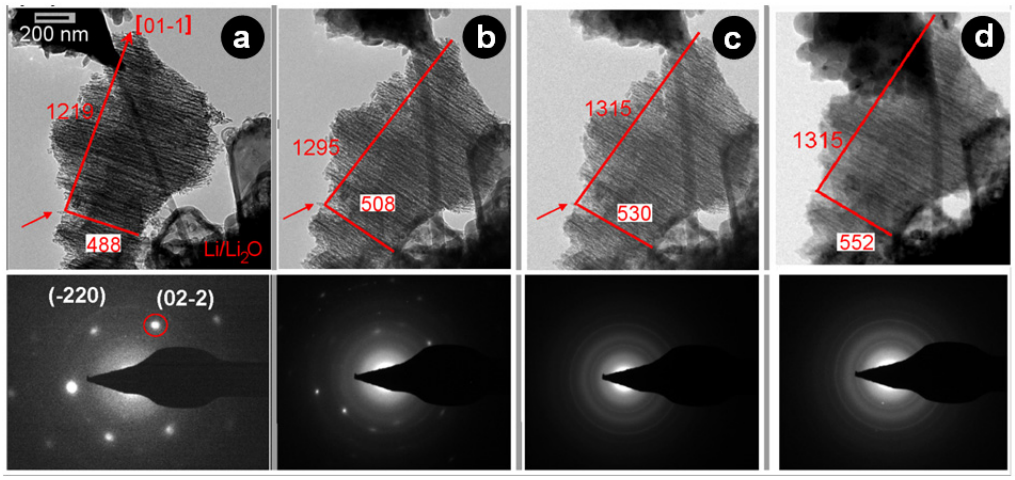

Figure VI - 98: *In situ* TEM observation of the lithiation process of an MSS particle. a) -d) TEM images and selected area electron diffraction patterns of the MSS particle at different lithiation states: a) before lithiation; b) 22 min of lithiation; c) 40 min of lithiation; d) 160 min of lithiation. Note that the scale bar in b) applies to b-d)

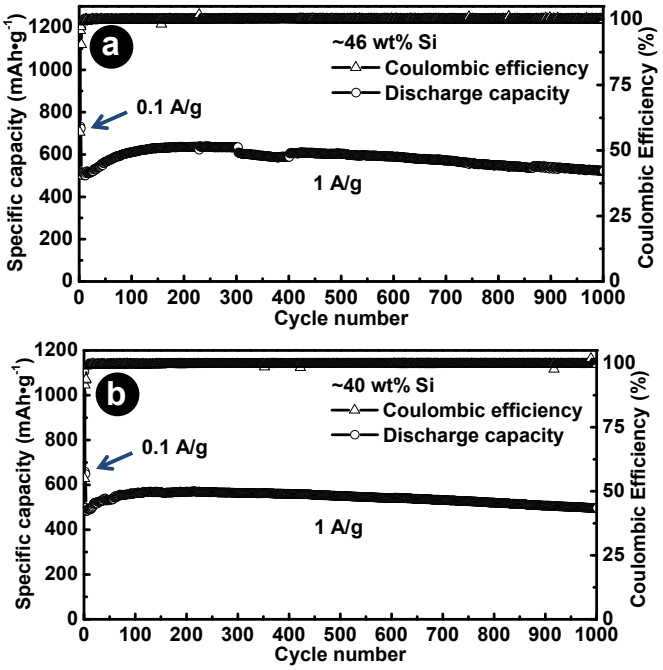

Figure VI - 99: Long-term cycling of the MSS electrode with a) 46 wt% and b) 40 wt% Si loading

With the pulverization eliminated and particle volume expansion limited to ~30%, MSS allows good cycling stability for electrodes with high Si loading per unit area. A high area specific discharge capacity of ~1.5 mAh/cm^2 at 0.5 mA/cm^2 discharge and 0.75 mA/cm^2 charge current density has been demonstrated (Figure VI - 100). The sample has demonstrated excellent cycling stability with ~95% capacity retention over 200 cycles.

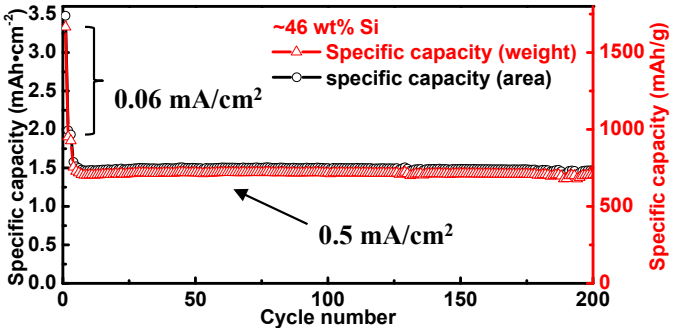

Figure VI - 100: Cycling stability of the porous Si anode with a high areal discharge capacity of ~1.5 mAh/cm^2

2. Improved Si/B_4C/graphite (SBG) composites. The SBG composite shows improved cycling stability after further modification. Figure VI - 101 shows the modified SBG material with a high areal specific capacity of ~1.25 mAh/cm^2 with >95% capacity retention over 100 cycles. The area specific capacity of the electrodes can be tuned by adjusting the ratio of the electrode and electrolyte additives.

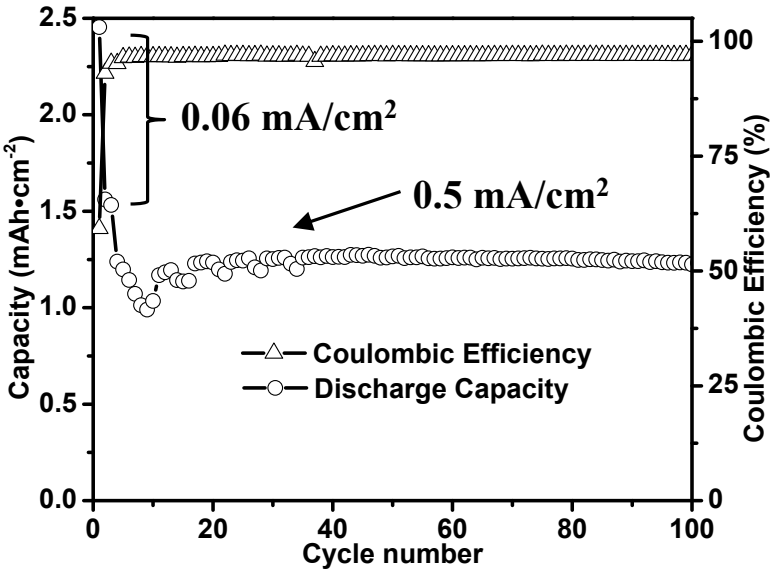

Figure VI - 101: Cycling performance of the modified SBG composite with ~12.8 wt% additive

3. Pre-lithiation treatment of Si anodes. The pre-lithiation of Si anodes was done by adding an appropriate amount of SLMP™, from FMC Lithium, on the electrodes. The irreversible capacity loss of Si based anode in the first cycle was greatly reduced after pre-lithiation treatment. Figure VI - 102a shows the cycling performance of a modified SBG electrode after pre-lithiation. It has a high areal specific capacity of ~1.5 mAh/cm^2 and ~88% capacity retention after 50 cycles. Figure VI - 102b and c are the cycling performance of pre-lithiated MSS electrodes of different thickness. For thin electrodes, it has a capacity of ~740 mAh/g and the capacity retention is ~96% over 300 cycles (Figure VI - 102b). For thick electrodes, it has ~95% capacity retention over 200 cycles even with a high area specific capacity of ~1.5 mAh/cm^2 (Figure VI - 102c).

4. The fundamental mechanism on FEC effects. The fundamental mechanism on how FEC additive affects the formation of the SEI film on Si anode has been investigated. Based on the SEM morphology and ^{6}Li NMR investigations, it was found that the SEI film formed in the FEC-free electrolyte grows much faster than in the electrolyte with FEC. The results of x-ray photoelectron spectroscopy study (Table VI - 3) indicates that Li/F ratio in SEI film formed in FEC containing electrolyte is much larger than that which is predicted by the previous SEI formation mechanisms. Based on these results, a molecular-level mechanism (Figure VI - 103) was proposed on how FEC affects the formation of the SEI film: 1) FEC is reduced through the opening of the five-member ring leading to the formation of lithium poly(vinyl carbonate), LiF and some dimers; 2) The FEC-derived lithium poly(vinyl carbonate) would enhance the stability of the SEI film. The proposed reduction mechanism opens a new path to explore new electrolyte additives that can improve the cycling stability of silicon-based electrodes.

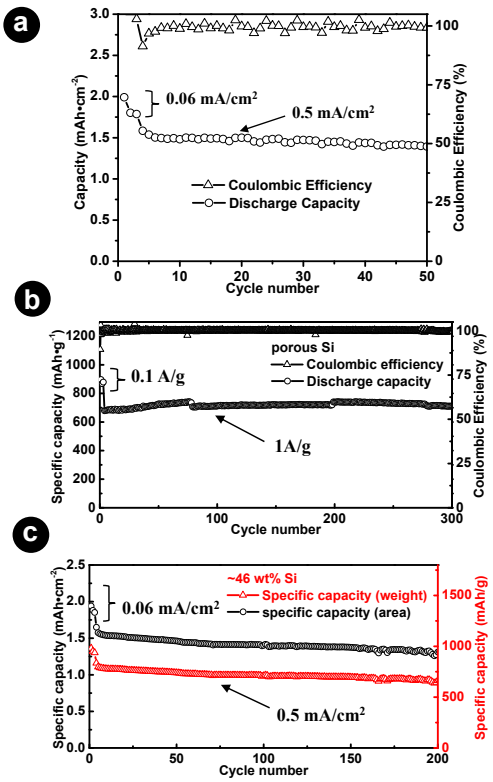

Figure VI - 102: Cycling stability of pre-lithiated Si anodes. a) Modified SBG composite electrode with a high area specific capacity of ~1.5 mAh/cm^2. b) Thin MSS electrode. c) Thick MSS anode with a high area specific capacity of ~1.5 mAh/cm^2

Table VI - 3: The percentage of Li, C, O and F in the SEI films in electrolytes. a) 1M $LiPF_6$ in EC/DMC (1:2 in vol.); b) 1M $LiPF_6$ in EC/DMC (1:2 in vol.) with 10 wt% FEC; c) 1M $LiClO_4$ in pure FEC

Table 1. The ratio of Li, C, O and F in the SEI films in electrolytes (a) 1M $LiPF_6$ in EC/DMC (1:2 in vol.), (b) 1M $LiPF_6$ in EC/DMC (1:2 in vol.) with 10% FEC and (c) 1M $LiClO_4$ in pure FEC					
Samples \ Elements	Li	C	O	F	Li/F ratio
Electrolyte (a), 2 cycles	27.7	23.3	24.1	24.9	1.11
Electrolyte (a), 35 cycles	22.7	31.3	37.6	8.4	2.70
Electrolyte (b), 2 cycles	22.9	32.5	32.1	12.5	1.83
Electrolyte (b), 100 cycles	21	33.8	31.9	13.3	1.58
Electrolyte (c), 2 cycles	21.1	34.7	32.2	12	1.76

5. Optimization of binder. Several different binders including PVDF, CMC, sodium alginate, PEO, and CMC-SBR have been investigated to further improve the cyclability and Coulombic efficiency of the SBG composite electrode. A mixture of CMC-SBR (10 wt%-10 wt%) binder is found to be the best choice for electrodes with high area specific capacity. Figure VI - 104 shows the typical cycling performance of a thick SBG electrode with the capacity of ~1.4 mAh/g. The capacity retention is 78% after 95 cycles.

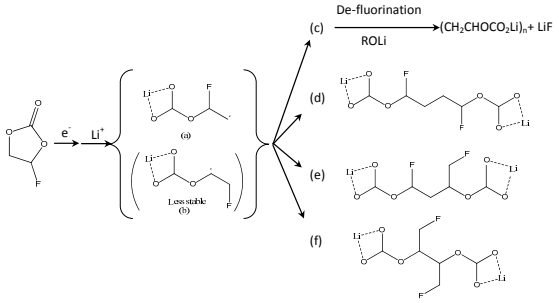

Figure VI - 103: A proposed decomposition mechanism of FEC

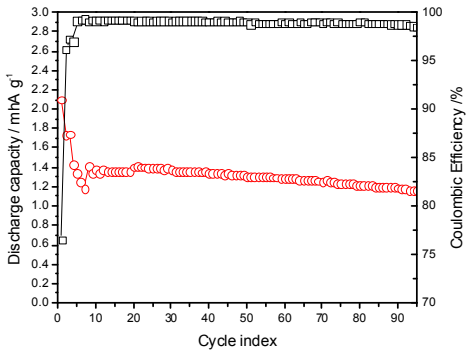

Figure VI - 104: Cycling stability of the SBG electrode with CMC-SBR binder

Conclusions and Future Directions

Micron sized Mesoporous silicon sponge was synthesized by the electrochemical etching process. It exhibits only ~30% overall volume expansion during full charge process so a large MSS particles (>20 μm) can be cycled without pulvurization. The thin electrode prepared with MSS demonstrated excellent cycling performance with a high capacity of ~750 mAh/g (based on the full electrode including the carbon additive and binder) and >80% capacity retention over 1000 cycles. The thick electrodes with a high area specific capacity of ~1.5 mAh/cm^2 also demonstrated a capacity retention of >95% over 200 cycles. The SBG composite was further optimized to improve their cycling stability especially for thick electrodes. The modified SBG material demonstrated good cycling stability with > 95% capacity retention over 100 cycles even at a high area specific capacity of ~ 1.25 mAh/cm^2. Pre-lithiation treatment was developed to reduce the first cycle irreversible capacity loss. By adding Li powder to Si electrodes, the first cycle irreversible loss can be reduced to <10% while the capacity and cycling stability almost remain the same. At last, the fundamental mechanism on how FEC additive affects the formation of the SEI film on Si anode has been identified. This will open a new path to explore electrolyte additives that can improve the cycling stability of silicon anodes.

Future work will focus on the following areas:

- Develop new approaches and electrode structures to enable electrodes with high Si mass loading without compromising the long-term cycling stability.
- Optimize porosity of porous Si and the architecture of rigid skeleton supported Si composites to further investigate the stress and volume effect to the capacity fading.
- Develop new electrolyte additives and binders to improve stability of the SEI layer and stability of the thick Si-based anode.
- Develop a more cost-effective method to synthesize porous Si.

FY 2013 Publications/Presentations

1. Xilin Chen, Xiaolin Li, Donghai Mei, Ju Feng, Mary Y Hu, Jianzhi Hu, Mark Engelhard, Jianming Zheng, Wu Xu, Jie Xiao, Jun Liu, Ji-Guang Zhang, "Reduction and polymerization of fluoroethylene carbonate for stable SEI via alternative ring opening mechanism," *Chem Sus Chem.* In press.
2. Cong-Min Wang, Xiaolin Li, Zhiguo Wang,Wu Xu, Jun Liu, Fei Gao, Libor Kovarik, Ji-Guang Zhang, Jane Howe, David J. Burton, Zhongyi Liu, Xingcheng Xiao, Suntharampillai Thevuthasan, and

Donald R. Baer, "*In situ* TEM Investigation of Congruent Phase Transition and Structural Evolution of Nanostructured Silicon/Carbon Anode for Lithium Ion Batteries," *Nano Letters,* **12**(3):1624–1632.

3. Meng Gu, Ying Li, Xiaolin Li, Shenyang Hu, Xiangwu Zhang, Wu Xu, Suntharampillai Thevuthasan, Donald R. Baer, Ji-Guang Zhang, Jun Liu, and Chongmin Wang, "*In situ* TEM Study Of Lithiation Behavior Of Silicon Nanoparticles Attached to and Embedded in a Carbon Matrix," *ACS Nan,* **6**(9):84398447.
4. "Development of Si-based High Capacity Anodes," *DOE Annual Peer Review Meeting*, May 13-17, 2013, Washington, DC.
5. Xiaolin Li, et al., "Porous structured silicon-based nanocomposites as high performance Li-ion battery anodes," *2013 MRS Spring Meeting*, San Francisco, CA.
6. Xiaolin Li, et al., "Porous Si as high performance Li-ion battery anodes," *246th ACS Meeting*, 2013, Indianapolis, IN (Invited).
7. Ji-Guang Zhang et al., "Meso-Porous Silicon Sponge as High Performance Li-ion Battery Anodes," *8th China-U.S. EV and Battery Technology Workshop*, Sep. 21, 2013, Chengdu, China.
8. Ji-Guang Zhang, "Next Generation of energy storage systems," Naval Postgraduate School-Defense Energy Seminar, August 7, 2013, Monterey, CA.

VI.C.10 Wiring up Silicon Nanoparticles for High Performance Lithium Ion Battery Anodes (Stanford U.)

Yi Cui
Stanford University.

Department of Material Science and Engineering
476 Lomita Mall, McCullough 343
Stanford, CA 94305
Phone: (650) 723-4613; Fax: (650) 725-4034
E-mail: yicui@stanford.edu

Start Date: October 2010
Projected End Date: September 2014

Objectives

- Go beyond the charge capacity limitation of conventional carbon anodes by designing nano-architectured silicon electrodes.
- Design, synthesize and characterize Si nanostructure-based anodes to overcome the volume change-induced materials challenges and to realize high performance.
- Understand the fundamental structure-property relationship on electrode materials with large structure and volume changes.
- Develop low-cost materials processing methods.

Technical Barriers

The large structure and volume changes of Si during cycling causes multiple materials challenges: 1) mechanical breaking; 2) unstable solid electrolyte interface (SEI); 3) difficulties in maintaining good electrical connections. These fundamental challenges result in the following technical barriers to good battery performance:

- Large first cycle irreversible capacity loss
- Poor cycle life
- Inadequate coulombic efficiencies

Technical Targets

- Develop fundamental materials guidelines through structure and property correlations and nanostructured Si anodes with these features to address the material challenges outlined above.
- Develop synthesis techniques to produce the designed nanostructured Si anodes.
- Develop low-cost materials processing methods.

Accomplishments

- Used *in situ* transmission electron microscopy (TEM) to examine critical size and rate for fracture of crystalline, polycrystalline and amorphous Si nanostructures
- Developed a synthesis strategy to make Si nanoparticles from rice husks, an abundant and cheap source
- Developed an *in situ* polymerization method to incorporate conducting hydrogel into Si nanoparticle anodes
- Developed a variety of carbon templates from crab shells to make Si-C nanocomposites with controllable morphology

✧ ✧ ✧ ✧ ✧

Introduction

Next generation high capacity electrode materials are needed in order to generate high energy battery technology to meet the demands of the transportation sector. Silicon is an exciting and promising anode material for replacing carbon in Li-ion batteries due to: 1) a high gravimetric capacity of ~4200 mAh/g, ten times higher than graphite (~370 mAh/g); 2) a high volume capacity; 3) its relatively low working potential (~0.5 V Vs Li/Li^+), which makes it suitable as an anode; 4) the abundance and environmentally friendly nature of Si; and 5) the ability to leverage the fundamental and manufacturing knowledge that has been established in the Si semiconductor and solar industries. However, there exist several scientific and technical challenges for silicon anodes: 1) Mechanical fracture caused by large volume changes. The electrochemical alloying reaction of Li with Si involves volume expansion of up to 300% and significant contraction during lithium extraction. The stress induced by the large volume changes causes cracking and pulverization of silicon, which leads to loss of electrical contact and eventual capacity fading. 2) Unstable SEI. The repetitive volume expansion/contraction causes the continuous movement of the interface between Si and organic electrolyte, which makes it challenging to form a stable SEI layer, resulting in low coulombic efficiency and capacity loss during cycling. 3) It is challenging to maintain good

electrical contact between Si materials and the current collector. Even though mechanical fracture does not take place in Si nanostructures below critical sizes, large volume changes can still cause the movement of Si nanostructures and their detachment from the conducting framework during long-term battery cycling. 4) Challenges associated with generating Si materials to address the above three challenges with low-cost and scalable processing.

The goal of this project is to study the fundamental principles related to alloy anodes, to design nanostructured Si anodes to solve the three fundamental challenges and to develop low-cost and scalable processing for these materials.

Approach

This project takes a two-pronged approach to solving these problems. First, *ex situ* and *in situ* observation techniques are developed and used to uncover the fundamental nature of the Li-Si reaction and volume changes. Insight gained from this fundamental study is used as the framework for designing new nanostructured anodes that feature minimal structural damages and dimensionally stable surface/electrolyte interface regions. A focal point of the project is to also develop low-cost and scalable methods to synthesize these designed nanostructured Si anodes.

Results

Unexpected two-phase lithiation in amorphous Si. Amorphous hydrogenated Si spheres were fabricated via decomposition of trisilane in supercritical n-hexane at high temperature. The *in situ* TEM set-up is shown in Figure VI - 105a. When a negative bias was applied to the amorphous Si electrode, Li diffused into the Si and it became lithiated, as shown in Figure VI - 105b-e.

The sharp contrast between the core and shell regions in Figure VI - 105c, d during lithiation is unexpected, because this indicates that there is a reaction front that sweeps through the particle. The lithiation mechanism is important to understand because it affects fracture behavior and reaction kinetics. Analysis of the TEM images showed that this contrast difference could not be caused by conventional diffusion. Previously, it was thought that amorphous Si is lithiated via a single-phase reaction because of its sloping potential profile in electrochemical experiments, but these TEM experiments show that it is a two-phase reaction. Further experiments showed that this two-phase behavior was limited to the first lithiation – later lithiation cycles did not show a reaction front. The two-phase reaction is attributed to the activation energy required to break up the Si-Si bonds in the amorphous Si phase, which is actually similar to crystalline Si lithiation. The single-phase reaction on later cycles may occur because of lingering damage (dangling bonds) in the amorphous Si or perhaps even trapped Li in the structure. This study shows that the first lithiation of amorphous and crystalline Si is more similar than previously thought. However, there are some important differences: 1) amorphous Si particles up to 800 nm in diameter did not fracture upon lithiation, whereas crystalline Si particles >~200 nm did fracture, and 2) the amorphous Si particles show better kinetics (there is not reaction front slowing, as in crystalline Si). These features suggest that amorphous Si may be more advantageous in real Si electrodes.

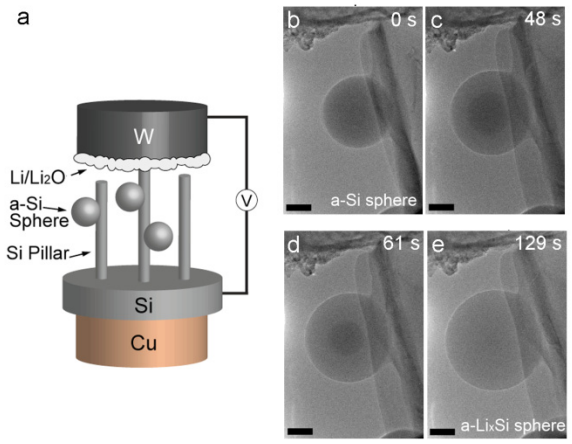

Figure VI - 105: (a) Schematic of *in situ* device. (b-e) Time series of amorphous Si sphere during lithiation

Si nanoparticles from abundant and cheap sources for Li battery anodes. Si is an abundant element in nature, but the electronic-grade Si that is commonly used to synthesize nanomaterials is quite expensive. Cheap methods to easily synthesize large quantities of lower-purity Si are needed. We have developed a method to synthesize Si nanoparticles for Si batteries directly from agricultural waste products. Specifically, we use rice husks, which are extremely cheap (~$18 per ton) and naturally contain up to 20 wt% SiO_2. We first convert the rice husks to pure silica by burning in air and then we reduce the silica to silicon. This results in an interconnected network of nanoparticles, as shown by the SEM images in Figure VI - 106a. The particles are agglomerated and are physically interconnected, but the void space between the particles should allow for accommodation of volume expansion during lithiation. The synthesis process results in a 5 wt% yield of Si when considering the weight of the initial rice husks. The Si nanoparticles were made into slurry-type electrodes and tested in half cells vs. Li metal. Galvanostatic curves are shown in Figure VI - 106b. The initial discharge capacity is ~4,100 mAh/g at C/50. After this, the rate is increased to

C/2, and a stable capacity of about 1,750 mAh/g is exhibited over 300 cycles.

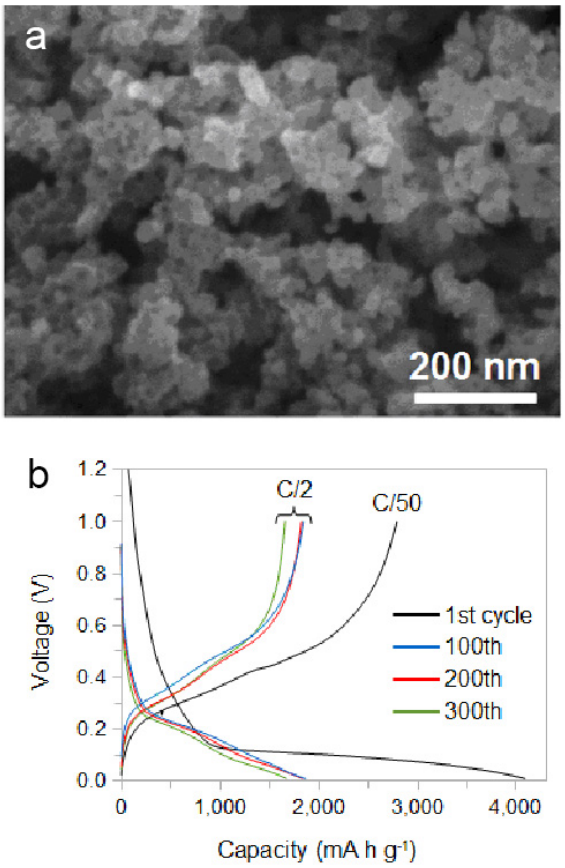

Figure VI - 106: (a) SEM images of the Si nanoparticles. (b) Galvanostatic cycling of the Si nanoparticle electrode

Incorporation of conducting hydrogel into Si nanoparticle anodes. A high-performance Li-ion battery anode has been fabricated by encapsulating Si nanoparticles in a 3D porous conductive polymer hydrogel framework. Typically, Si nanoparticles are mixed with monomer and crosslinker in the solution first, and then initiator was added to start the polymerization. This unique *in situ* polymerization fabrication technique results in a well-connected 3D network structure consisting of Si nanoparticles conformally coated by the conducting polymer (Figure VI - 107a). Such hierarchical hydrogel framework combines multiple advantageous features. First, the continuous electrically conductive PANi network provides fast electronic and ionic transfer channels. Second, strong interactions were introduced between Si nanoparticles and PANi hydrogel to make the framework more stable. Third, the porous hydrogel network provides enough free space for Si volume change during lithiation/delithiation process. With this anode, we successfully achieved high capacity and extremely stable electrochemical cycling. The electrode demonstrates a cycle life of 5,000 cycles with over 90% capacity retention at current density of 6.0A/g (Figure VI - 107b). The solution synthesis and electrode fabrication process are highly scalable and compatible with existing slurry coating battery manufacturing technology. This will potentially allow for the high-performance composite electrode to be scaled up for manufacturing the next generation of high-energy Li-ion batteries.

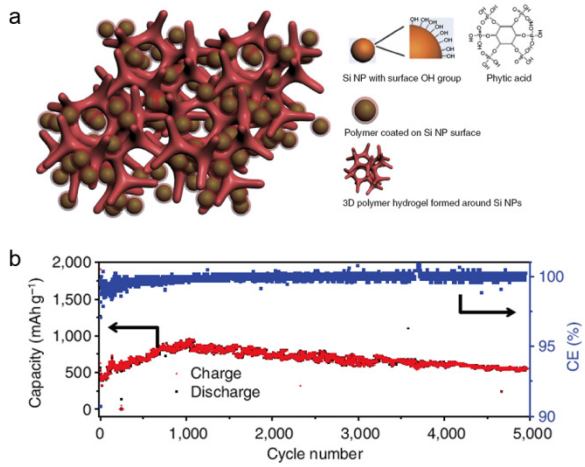

Figure VI - 107: (a) Schematic illustration of 3D porous SiNP/conductive hydrogel composite electrodes. (b) Lithiation/delithiation capacity and CE of Si-PANi electrode cycled at current density of 6.0 A/g for 5000 cycles

Crab shells as sustainable templates from nature for Li-ion battery anodes. Crab shells with the unique Bouligand structure consisting of highly mineralized chitin-protein fibers can be used as biotemplates to fabricate hollow carbon nanofibers. Typically, crab shell was calcined in the air to remove the chitin-protein organic to form pure $CaCO_3$ frameworks containing twisted hollow channels with ~60 nm inner diameter. As illustrated in Figure VI - 108b, a carbon thin layer was then coated on the whole surface of the frameworks, followed by silicon deposition into the carbon channels. Final Si encapsulated carbon fibers was obtained after removing $CaCO_3$ with HCl solution. The resulting nanostructured Si/C electrodes show high specific capacities (3060 mAh/g) and excellent cycling performance (up to 200 cycles with 95% capacity retention). The coulombic efficiencies of the cells over 200 cycles are ~98.6% at C/2 and ~98.9% at 1C (Figure VI - 108c). All these results indicate the high stability of crab shell-templated Si/C anode materials. Since crab shells are readily available due to the 0.5 million tons produced annually as a by-product of crab consumption, this waste-recycling preparation process is cheap and scalable for advanced rechargeable lithium ion batteries.

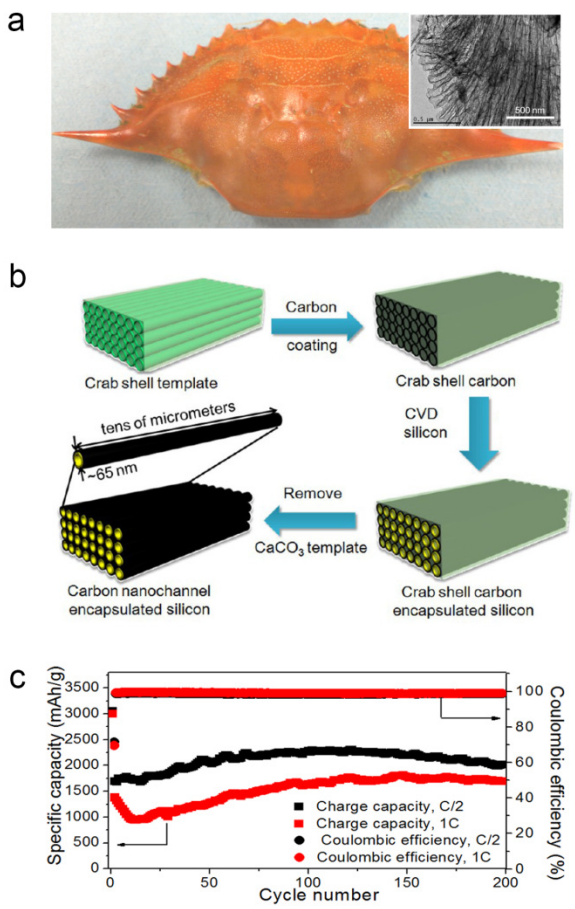

Figure VI - 108: (a) Photo of a crab shell. The inset is TEM image of final carbon nano-channel arrays from crab shell. (b) Schematic illustration of the fabrication procedure for hollow carbon nanofiber arrays encapsulating silicon. Lithiation/delithiation capacity and CE of Si encapsulated crab shell-templated carbon channel

Conclusions and Future Directions

Much progress has been made on these projects this year. A variety of *in situ* and *ex situ* microscopy techniques have been used to determine the effect of nanostructure size, shape, and crystallinity on volume expansion/contraction and structural changes. Based on these fundamental studies, tailored nanostructured anodes were designed and fabricated that showed high capacity, high coulombic efficiency, and good cycle life. *In situ* polymerization of conducting hydrogel on Si nanoparticles makes a 3D porous Li-ion anode. By taking advantage of the conducting polymer matrix, as well as free space for Si volume changes, we successfully achieved high capacity and extremely stable electrochemical cycling. In addition, we developed various strategies to obtain Si nanostructures from sustainable sources, such as rice husks and crab shells. This green, cost-effective, and scalable synthesis will open a new avenue for producing nanostructured electrode materials from low-cost sustainable sources.

Future directions include: 1) further developing and exploring conducting polymer additives, coatings, and binder to improve the connectedness of the Si electrode framework during cycling. This includes the use of viscous polymers for a self-healing effect. In addition, the use of micron-scale Si particles will be explored in conjunction with polymer coatings. 2) *In situ* TEM and *ex situ* SEM study of two or multiple Si nanostructures during lithiation/delithiation will be started to understand how neighboring particles affect each other as volume changes. 3) Other conducting coating materials will be evaluated to increase the coulombic efficiency and cycling stability. 4) Finally, prelithiation of Si structures will be used to increase the first cycle coulombic efficiency.

FY 2013 Publications/Presentations

1. N. Liu, K. Huo, M.T. McDowell, J. Zhao, Y. Cui, "Rice husks as a sustainable source of nanostructured silicon for high performance Li-ion battery anodes." *Scientific Reports*, **3**, May 2013.
2. M.T. McDowell, S.W. Lee, J.T. Harris, B.A. Korgel, C. Wang, W.D. Nix, Y. Cui, (2013). "*In situ* TEM of Two-Phase Lithiation of Amorphous Silicon Nanospheres." *Nano Letters*, **13**, 2, 758-764 January 2013.
3. M.T. McDowell, S.W. Lee, W.D. Nix, Y. Cui, "25th Anniversary Article: Understanding the Lithiation of Silicon and Other Alloying Anodes for Lithium-Ion Batteries." *Advanced Materials*, **25**, 36, 4966-4985 August 2013.
4. H. Wu, G. Yu, L. Pan, N. Liu, M.T. McDowell, Z. Bao, Y. Cui, "Stable Li-ion battery anodes by *in situ* polymerization of conducting hydrogel to conformally coat silicon nanoparticles." *Nature Communications*, **4**, June 2013.
5. H. Yao, G. Zheng, W. Li, M.T. McDowell, Z. Seh, N. Liu, Z. Lu, Y. Cui, "Crab Shells as Sustainable Templates from Nature for Nanostructured Battery Electrodes." *Nano Letters*, **13**, 7, 3385-3390, June 2013.

VI.C.11 Synthesis and Characterization of Silicon Clathrates for Anode Applications in Lithium-ion Batteries (SwRI)

Kwai S. Chan
Southwest Research Institute

Department of Materials Engineering
Mechanical Engineering Division
6220 Culebra Road
San Antonio, TX 78238
Phone: (210) 522-2053; Fax: (210) 522-6965
E-mail: kchan@swri.org

Michael A. Miller
Southwest Research Institute
Department of Materials Engineering
Mechanical Engineering Division
6220 Culebra Road
San Antonio, TX 78238
Phone: (210) 522-2189; Fax: (210) 522-6220
E-mail: mmiller@swri.org

Start Date: October 2010
Projected End Date: September 2014

Objectives

- Develop scalable synthesis methods for producing empty and substituted silicon clathrates
- Design, synthesize, and characterize silicon clathrate compounds for anode applications in Li-ion batteries
- Fabricate and characterize prototype silicon clathrate anodes designed to exhibit small volume expansion during lithiation, high specific energy density, while avoiding capacity fading and improving battery life and abuse tolerance

Technical Barriers

This project addresses the following technical barriers of the lithium-ion battery technology, especially focusing on the development of silicon clathrate compositions as anode materials:

- Low energy density
- Low power density
- Short calendar and cycle lives

Technical Targets

Develop silicon clathrate anodes to meet PHEV and EV goals by exceeding current benchmarks (Conoco Phillips CPG-8 Graphite/1 M $LiPF_6$+EC:DEC (1:2)/ Toda High-energy layered (NMC) in the following metrics:

- Energy density
- Power density
- Calendar and cycle lives

Accomplishments

- Synthesized 20 mg of empty silicon clathrate (Si_{46}) via a Hofmann-type elimination-oxidation reaction scheme done in solution
- Constructed and evaluated several electrochemical half-cells using $Ba_8Al_8Si_{38}$ synthesized as anodes combined with best-case additives and electrolyte formulations
- Characterized electrochemical properties of silicon clathrate anodes and achieved an initial capacity of 300 mAh/g (active material basis) on the 4^{th} cycle which decayed gradually to 54 mAh/g at near steady-state conditions after 200 cycles with a coulombic efficiency of 98.79±0.14%. at C/2 for $Ba_8Al_8Si_{38}$
- Identified structural and mechanical states of silicon clathrate anodes during lithiation and delithiation processes and validated against theoretical calculations

✧ ✧ ✧ ✧ ✧

Introduction

Low-cost advanced anode materials with high-energy density, high-power density, and longer calendar and cycle lives are needed to achieve DOE's performance targets for PHEV and EV applications. In an effort to address these needs, this project explores the viability of silicon clathrates (Type I) as an anode material for potential applications in PHEV and EV Li-ion batteries, and focuses efforts on the development of scalable synthetic methods, complete characterization of electrochemical performance, and the design and fabrication of prototype anodes for evaluation.

Silicon clathrate, a polymorph of silicon, is an emerging anode material that is composed of sp^3 bonded

silicon atoms arranged in cage-structures. It consists of crystalline Si with a regular arrangement of 20- and 24-atom cages fused together through five atom pentagonal rings (Type I clathrate) (see Figure VI - 109). It has a simple cubic structure with a lattice parameter of 10.335 Å and 46 Si atoms per unit cell (Si_{46}). The crystal structure (Space Group $Pm\bar{3}n$) of the Si_{46} clathrate is different from the common form of crystalline Si (c-Si), which is diamond cubic (Space Group $Fd\bar{3}m$) with a lattice parameter of about 5.456 Å.

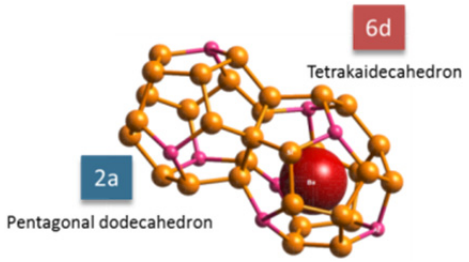

Figure VI - 109: Silicon calthrate crystal structure

First-principles computations performed at SwRI® have revealed that significant amounts of Li ions can be inserted into and extracted from the cage structure of silicon clathrates without substantial volume changes or pulverization of the cage structure. Theoretical predictions of the total, occupyable, and accessible volumes within Type I silicon clathrate structures indicate that the empty spaces within the cage structures are accessible to Li and amenable to Li intercalation through electrochemical means, while overcoming the usual problems of irreversible volume expansion encountered in *d*-Si-based anodes. On this basis, silicon clathrates are attractive as anode materials for Li-ion battery applications.

Approach

SwRI is working with LBNL to develop silicon clathrate anodes for PHEV and EV applications. The approach is to synthesize guest-free Type I silicon clathrate (Si_{46}) using a number of high-temperature processing methods, while concurrently exploring an investigational low-temperature route for direct synthesis of guest-free clathrate. *Ab initio* and classical molecular dynamics (MD) computations are being carried-out to predict the lattice energies of pure-silicon and intermetallic (substitutional) clathrate structures, and to identify the lithiation pathways involved as these structures are intercalated with lithium atoms. Silicon clathrates will be utilized in combination with the appropriate or best-case additive to fabricate prototype anodes. Electrochemical characterization will be performed to evaluate and improve, if necessary, anode performance including cyclic stability. The final year of the program will be directed at the design, assembly, and characterization of a complete small-scale, prototype battery suitable for concept demonstration.

Results

Batch Synthesis via Soft Oxidation of Na_4Si_4. The conditions for the phase transformation of fuel-grade sodium silicide ($NaSi_2$) were optimized to yield the highest purity of the Zintl phase Na_4Si_4 possible by varying excess additions of NaH combined with the silicide. XRD analyses of the thermal transformation products (Figure VI - 110) showed that new reflections emerge at or near the positions theoretically computed for the Zintl phase, and with similar relative intensities, when 10% excess NaH was combined with the silicide during thermal processing. Higher additions of NaH did not manifest the required XRD reflections for the Zintl phase. Using these process conditions, about 10 g of Na_4Si_4 was synthesized for subsequent use in the batch synthesis of Si_{46}.

After successful scale-up of Na_4Si_4, this Zintl compound was employed in combination with a previously-synthesized alkylammonium-$AlCl_3$ ionic liquid (IL) to synthesize empty silicon clathrate (Si_{46}) in batch quantity via a Hofmann-type elimination-oxidation reaction scheme done in solution. The XRD analysis (Figure VI - 111) of the reaction product indicated that the desired Type I clathrate was formed along with unreacted Zintl compound and the reaction by-products. The product will be further purified for subsequent electrochemical measurements as an anode material.

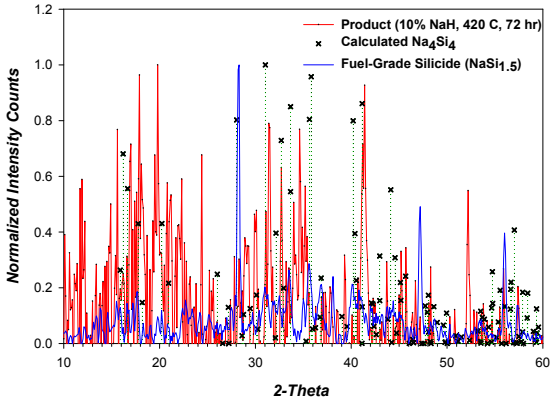

Figure VI - 110: Overlay of powder XRD patterns for the fuel-grade silicide and transformation product, compared with the calculated reflections for the Zintl phase (Na4Si4)

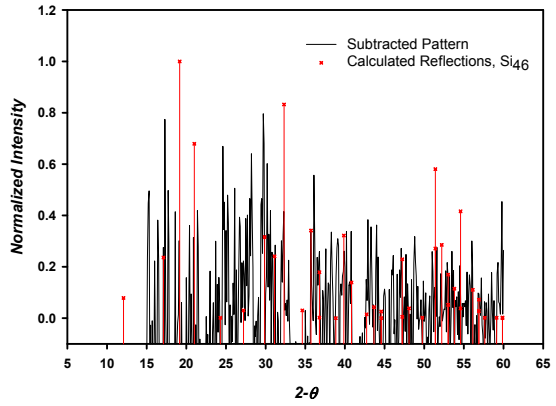

Figure VI - 111: Overlay of powder XRD patterns for the synthesis product and the calculated reflections of empty clathrate (Si46), after subtraction of impurity phases

Molecular Modeling of Silicon Clathrates. The lithiation pathways for Na-stabilized Si_{46} were identifying by first-principles computations and the results are evaluated against those of Ba-stabilized and empty Si_{46} clathrates by comparing the lattice constant and energy change as a function of the number of Li atom in Figure VI - 112. For all cases, insertion of Li causes expansion of the cage structure when the number of Li atoms inserted exceeds about 20 to 24 (Figure VI - 112a), depending on the number of Na or Ba guest atoms residing within the cage structure but not on the number of Al substituted atoms on the framework. The energy charge associated with Na- and Ba-stabilized silicon clathrates is comparable to those for lithiated silicides (Figure VI - 112b).

Prototype Silicon Clathrate Anode Fabrication. **Several** different additive and binder combinations were attempted in the fabrication of silicon clathrate anodes. The framework-substituted Type I clathrate, $Ba_8Al_8Si_{38}$, synthesized in bulk (200g) in the previous year, was processed via ball milling and sequential particle sizing to produce sub-micron particles (Figure VI - 113). The milled product was combined with a conductive additive to make a slurry. The conductive additive used included (1) 0.2 to 4 wt. % Graphenol®, (2) 10 wt.% Super P carbon, and (3) 20 wt.% Super P carbon. The resulting slurries were then used to cast thin-film anodes for electrochemical half-cell evaluation.

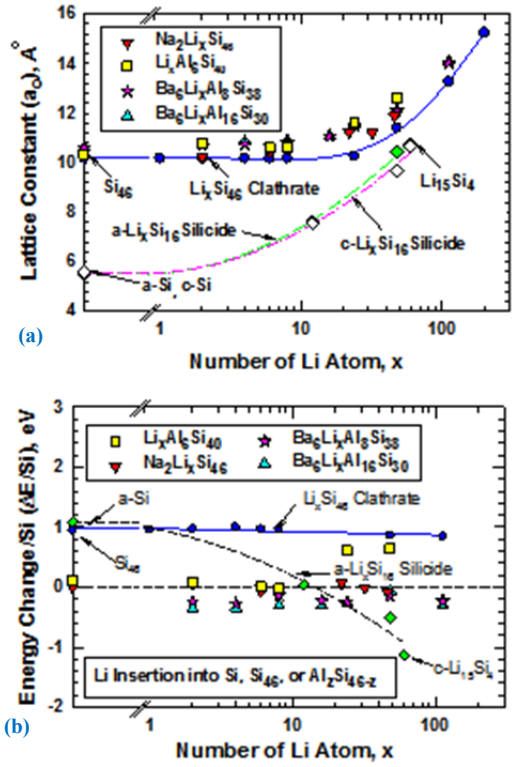

Figure VI - 112: Lattice constant expansion and energy change associated with lithium insertion in Na- and Ba-stabilized clathrates against those for empty silicon clathrates: (a) lattice constant expansion, (b) energy change

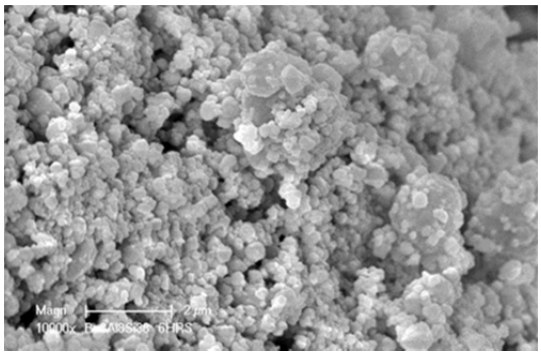

Figure VI - 113: Particle morphology of processed $Ba_8Al_8Si_{38}$ milled powder for prototype anode

Half-Cell Electrochemical Characterization. Half-cell charge/discharge cyclic tests were performed on an anode composed of the intermetallic clathrate, $Ba_8Al_8Si_{38}$, combined with Super-P carbon (10 wt.%) and EC/DEC/FEC electrolyte. The specific capacity and coulombic efficiency were recorded out to 200 cycles at C/2, allowing the half-cell to rest at OCP for ~ 8 hrs at the end of the 50th and 100th cycle (Figure VI - 114). These results showed an initial capacity of 300 mAh/g (active material basis) on the 4th cycle which decays to 54 mAh/g at near steady-state conditions upon reaching the 200th cycle. The average steady-state coulombic efficiency was 98.79±0.14%. Peak capacities much greater than the theoretical value (259 mAh/g for invariant lattice constant), along with marked improvements in the capacity fade, are expected from the use of higher than present carbon loadings.

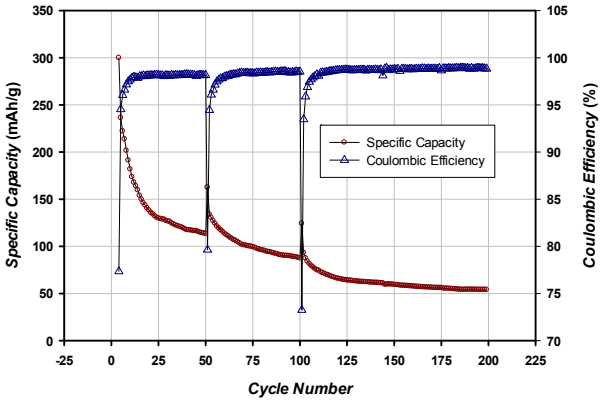

Figure VI - 114: Long-term cyclic capacity and coulombic efficiency profiles measured for Ba8Al8Si38 anode (10 wt.% Super P + 10 wt.% PVDF) using ED/DEC/FEC (45:45:10). Cell was allowed to rest at OCP for ~8 hrs at end of 50th and 100th cycles before resuming test

A suite of *ex situ* techniques was employed to map the structural and mechanical state of the clathrate anodes as a function of lithiation/delithiation cycles. Structural and compositional analysis of $Ba_8Al_8Si_{38}$ was done using high-resolution magic angle spinning nuclear magnetic resonance (MAS-NMR), and neutron diffraction measurements (facilitated through ORNL).

In the case of NMR, the chemical shift environments of ^{29}Si and ^{27}Al along with that of the ^{7}Li were probed to study the effects of lithium intercalation on structural parameters and local interactions. Notably, the ^{27}Al-NMR spectra acquired for the unlithiated and lithiated clathrate (Figure VI - 115) show three distinct magnetic environments, most likely associated with the three known framework substitution sites in the dodecahedron and tetrakaidecahedron cages of the Type I clathrate structure. Upon lithiation, only the 16i framework sites near 80 ppm appear to be affected by the presence of Li^+, but only with respect to relative amplitude when comparing the integration ratios for the three lines. No significant change in chemical shift was observed, suggesting that Li^+ interactions with Al framework atoms are weak and the structural order of the framework remains intact. Only the spin-lattice (T_1) relaxation times are influenced by the local structuring of Li^+ near the 16i framework sites giving rise to a change in relative amplitude after lithiation. Additionally, the near-baseline resolution of the NMR lines corresponding to the three framework sites is remarkable from the viewpoint of substitutional order. This result indicates that Al substitution of framework atoms during synthesis does not occur randomly, but rather prefers ordered substitution for the bulk material. By contrast, random substitution would otherwise result in one broad peak due to the superposition of all site-substitution combinations.

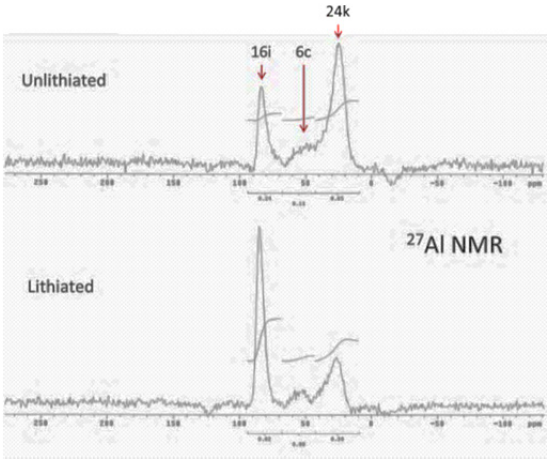

Figure VI - 115: Solid-state ^{27}Al NMR spectra acquired for unlithiated ($Ba_8Al_8Si_{38}$) and lithiated ($Li_xBa_8Al_8Si_{38}$) clathrate anode material. The results show near-baseline resolution of the three known and magnetically-distinct framework substitution sites for a Type I structure: 6c, 16i, and 24k

Neutron diffraction measurements (Figure VI - 116) were used to verify against first principles computations that the lattice constants for the clathrate alloy ($Ba_8Al_ySi_{46-y}$) do not change as a function of lithium intercalation up to the theoretical capacity (259 mAh/g for invariant lattice constant). Figure VI - 116 shows that the neutron diffraction patterns for the unlithiated (blue) and lithiated $Ba_8Al_8Si_{38}$ anodes exhibit the same intact structure and lattice constant. Additional diffraction measurements are needed to determine the extent to which the clathrate framework can be lithiated reversibly beyond its theoretical capacity.

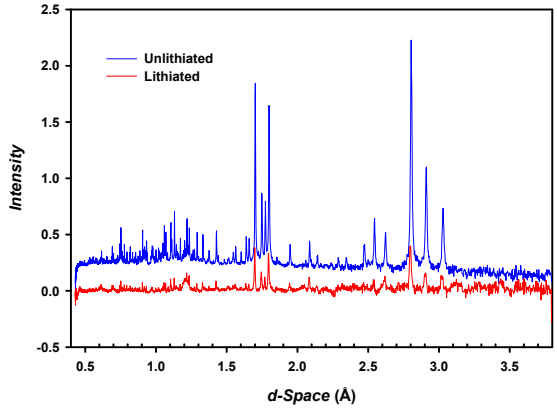

Figure VI - 116: Neutron diffraction patterns obtained for Ba8Al8Si38 before (blue) and after lithiation (red), providing evidence that the clathrate framework remains structurally intact up to its theoretical capacity

Conclusions and Future Directions

A solution synthesis method based on the Hofmann-elimination oxidation reaction scheme was successful in producing empty Si_{46}. Future work will be to prepare half-cells with Si_{46} anodes and demonstrate a cyclability of 50 cycles at C/2 and a capacity of 750 mAh/g.

Half-cells with a $Ba_8Al_8Si_{38}$ anode were successfully cycled for 200 cycles at C/2 with an initial capacity of 300 mAh/g and an average steady-state coulombic efficiency of 98.79±0.14%. Future work will be to prepare half-cells of $Ba_8Al_8Si_{38}$ with higher conductor contents and demonstrate a cyclability of 50 cycles at C/2 and a capacity of 1500 mAh/g.

A suite of *ex situ* techniques will be employed to map the structural and mechanical state of the clathrate anodes as a function of lithiation/delithiation cycles for both Si_{46} and $Ba_8Al_8Si_{38}$ anodes. The experimental data will be evaluated against theoretical predictions based on first-principle computations.

FY 2013 Publications/Presentations

1. "Synthesis and Characterization of Silicon Clathrates for Anode Applications in Lithium-Ion Batteries," *DOE Annual Peer Review Meeting*, May 13-17, 2013, Washington, DC.
2. M.A Miller, K.S. Chan, W. Liang, and C.K. Chan, "Clathrate Allotropes for Rechargeable Batteries," U.S. 2012/0295160 A1, Nov. 22, 2012.
3. C. K. Chan, M. A. Miller, and K. S. Chan, "Alloys of Clathrate Allotropes for Rechargeable Batteries," U.S. Patent Application No. 13/452,403 (pending).

VI.C.12 First Principles Modeling of SEI Formation on Bare and Surface/Additive Modified Silicon Anode (TAMU)

Perla Balbuena
Texas A&M University

Department of Chemical Engineering
3122 TAMU
College Station, TX 77843
Phone: (979) 845-3375; Fax: (979) 845-6446
E-mail: balbuena@tamu.edu

Jorge Seminario (co-PI)
Department of Chemical Engineering
3122 TAMU
College Station, TX 77843
Phone: (979) 845-3301; Fax: (979) 845-3301
E-mail: seminario@tamu.edu

Start Date: October 2012
Projected End Date: September 2016

Objectives

- Develop fundamental understanding of the molecular processes that lead to the formation of a solid electrolyte interphase (SEI) layer due to electrolyte decomposition on Si anodes.
- Develop a rational selection of additives and/or coatings.

Technical Barriers

Description of the electrode surface chemistry; characterization of the electron transfer rate through the SEI layer; description of the SEI layer structure and its evolution as well as that of the electrode during cycling.

Technical Targets

- Elucidate solvent and additive reduction mechanisms on Si surfaces as a function of degree of lithiation and nature of the exposed facet.
- Develop a method for evaluating electron transfer through solid surfaces and apply it to model SEI layers of various thicknesses on Si surfaces.
- Understand solvent and additive reduction mechanisms on surfaces covered with oxides.

Accomplishments

- Effects of degree of lithiation and nature of the exposed surface on EC and FEC reductions were fully characterized and the most probable reduction mechanisms identified.
- Reactivity of oxide surfaces Li_4SiO_4 and $Li_2Si_2O_5$ were evaluated.
- Electron transfer through simple models of SEI layers on model electrodes (LiF and Li_2O between EC and Li_xSi_y) was assessed.

✧ ✧ ✧ ✧ ✧

Introduction

Investigation of the formation/growth mechanisms of the SEI layer on bare surfaces requires incorporation of effects from surface structure and chemical states: the presence of functional groups, surface oxidation, nature of exposed facets, and electrolyte composition including additive species. Finding the correspondence between additive molecular properties and SEI formation mechanism, structure, and properties will allow identification of new/improved additives. Including the state of lithiation of the surface is also a key factor to determine possible changes in the electrolyte reduction mechanism and/or nature of the products. Finally, it is crucial to understand how the electron transfer from the electrode to the electrolyte is modified by deposition of the initial SEI intermediates or products of the SEI formation reaction.

Approach

A comprehensive first-principles computational approach employed in this work includes density functional theory (DFT), *ab initio* molecular dynamics (MD), and *ab initio*-Green's function theory. Static DFT is utilized within two approaches: cluster models are used to investigate electrolyte reduction on model Si surfaces with ultra-low state of lithiation, whereas periodic surfaces represent both quasi-amorphous low lithiated surfaces and well-characterized crystalline Si_xLi_y alloys. Adsorption of solvent (EC) and additives (FEC and VC) on the surface and the potential energy surfaces including activation barriers for their decomposition are studied with these methods. Models of periodic surfaces in contact with liquid electrolyte

mixtures are also utilized to investigate mechanisms of electrolyte reduction using *ab initio* MD (AIMD). Electron transport through the composite material (electrode/ SEI layer/electrolyte molecule) is determined using *ab initio* Green's functions calculations.

The procedure consists of separate DFT optimizations of the electrode (bare or coated), electrolyte, and "extended molecule" including all the components present in the interfacial region. These optimizations yield the Hamiltonian and overlap matrices needed to create the transition matrix used to evaluate the rate of electron transfer.

Results

Mechanisms of EC and FEC reductions on ultra-low lithiated surfaces. EC and FEC reactions on $LiSi_{15}H_{16}$ clusters representing Si (001) surfaces were employed to model reduction on surfaces with an ultra-low degree of lithiation using DFT. For adsorbed EC, the barrier for ring opening via one e^- transfer (1.08 eV) was found higher than that in gas phase or solution. A 2nd e^- transfer to the adsorbed opened molecule yielded adsorbed CO_3 and C_2H_4. Two oxygen atoms bound on the Si(001) surface, leading to significant charge transfer from the Si cluster to CO_3. Alternatively, a 2nd electron may be transferred instead to the intact adsorbed molecule which then dissociates with a comparable barrier of 1.18 eV yielding adsorbed CO_3 and C_2H_4. Reaction energies were calculated for the subsequent association and reaction steps to form 5 different products. In general, the surface reactions have more favorable reaction energy compared to those taking place in the gas phase. In the presence of another EC molecule, both pathways (single and double e^- transfer) are possible. However, a much lower energy barrier (0.24 eV) for the single electron transfer pathway suggested that this may be the favorable mechanism in very low lithiation stages at high EC concentrations.

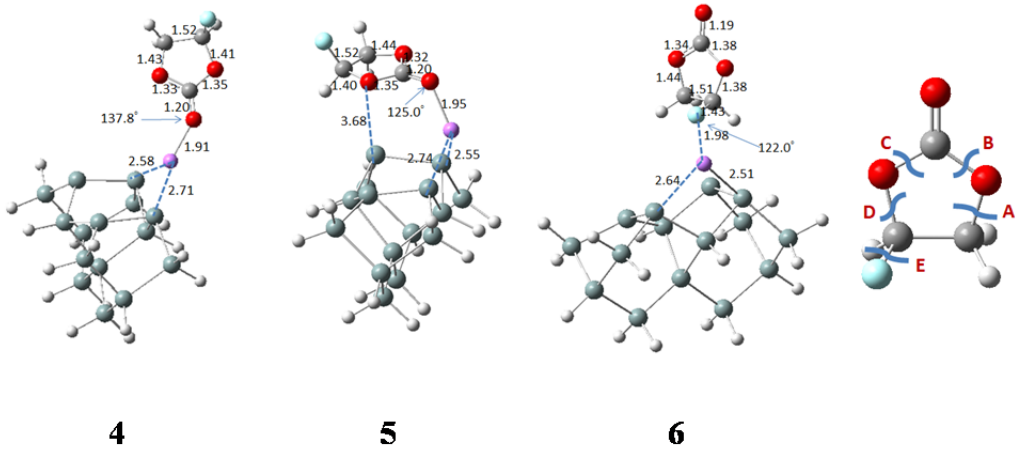

Figure VI - 117: Calculated geometries of adsorbed FEC configurations on a low-lithiated Si (001) surface after 1 or 2 e^- transfer processes. Image of FEC illustrates bond breaking pathways

The FEC adsorbed system (FEC-Li^+-$Si_{15}H_{16}$) may receive one or two e^- before the decomposition reactions take place. Figure VI - 117 illustrates the most stable configurations found. The most stable obtained via 1e^- transfer is **4**, and **5** is the most stable after transfer of 2e^-. To understand the bond-breaking in FEC on the ultra-low lithiated Si surface, the first step of bond dissociation was examined for both mechanisms. Bond dissociation via 1 and 2 e^- transfers was found plausible via C-O bond breaking (carbonyl C_C or ethereal C_E may be involved) and in some cases simultaneous breaking of two C-O bonds was found. The bond-breaking positions, A, B, C, D and E, are denoted in Figure VI - 117. For the 1 e^- mechanism, bond cleavage occurs at A, B, C, D, and B/D. Bond-breaking at E was not found. It is deduced that the C-F breaking may not be viable for the 1 e^- mechanism. The corresponding reaction energies and energy barriers are listed in Table VI - 4. C_E-O bond-breakings were thermodynamically favorable for the 1 e^- mechanism, but kinetically unfavorable due to a high energy barrier (1.14-1.57 eV). The lowest energy barrier (0.43 eV) was found for the C_e-O cleavage. The intermediates had more binding site(s) on the Si surface, via O and C_E atoms.

Table VI - 4: First step for the reduction of FEC on Li-$Si_{15}H_{16}$ cluster. (Structure 4, Figure VI - 117). Reaction energies (E_{reac}) and energy barriers (E*) are in eV. Route refers to Figure VI - 117

Reactant	Product	Route	E_{reac}	E^*
4	•CH_2-CHF-CO_3-Li($Si_{cluster}$)	A	-0.48	1.14
4	•OCH_2-CHF-OCO-Li($Si_{cluster}$)	B	0.68	1.24
4	•OCHF-CH_2-OCO-Li($Si_{cluster}$)	C	0.35	0.43
4	•FCH-CH_2-OCO_2 -Li($Si_{cluster}$)	D	-0.36	1.57
4	•CHF-CH_2-O-Li($Si_{cluster}$)-CO_2	B, D	-0.15	1.24

C_C-O bond breakings via the 2 e^- mechanism were found both thermodynamically and kinetically favorable in agreement with AIMD simulations (Table VI - 5).

Table VI - 5: First step for reaction of FEC-Li-$Si_{15}H_{16}^-$. Reaction energies (E_{reac}) and energy barriers (E*) are in eV. Route refers to Figure VI - 117

Reactant	Product	Route	E_{reac}	E^*
5	$^{\bullet}OCO_2$ -($Si_{cluster}$)$^-$ + CH_2=CHF	A, D	-2.85	1.24
5	$^{\bullet}$O-CH_2-CHF-OCO-Li($Si_{cluster}$)$^-$	B	-2.38	0.11
5	$^{\bullet}$O-CHF-CH_2-OCO-Li($Si_{cluster}$)$^-$	C	-1.86	0.28
6	$^{\bullet}$EC-($Si_{cluster}$)-LiF	E	-2.06	0.72

Effects of degree of lithiation and nature of exposed surfaces on EC and FEC reduction mechanisms. Low, intermediate, and high stages of lithiation were represented by quasi-amorphous $LiSi_4$ and $LiSi_2$, and crystalline LiSi, and $Li_{13}Si_4$ respectively. The (100) surface was predicted to be the most stable low-index surface of the LiSi phase, with a surface energy of 0.039 eV/Å^2. For $Li_{13}Si_4$, the two most stable low-index surfaces were (100) and (010), with surface energies of 0.356 and 0.371 eV/Å^2, respectively. Reactivities of the minimum energy surfaces were investigated with O, OH, and H functionalizations. Results from AIMD simulations showed two different 2 e^- EC reduction mechanisms (simultaneous vs. sequential) at intermediate lithiation (LiSi) surfaces independently of surface functionalization or nature of exposed facets. The surface is able to start reducing EC molecules once they are located at a critical distance where they form a C-Si bond (Figure VI - 118) and the carbonyl O interacts strongly with Li, inducing ring opening via C_c-O cleavage. This simultaneous 2 e^- mechanism yields a radical anion $O(C_2H_4)OCO^{2-}$ adsorbed species. On the other hand, a sequential 2 e^- reduction was also observed, where initially a single electron is transferred from the surface to a lithium-coordinated EC molecule, causing a C_E-O bond breaking. Subsequently, a second electron is transferred to the EC^- anion, breaking a second C_E-O bond and generating C_2H_4 + CO_3^{2-}.

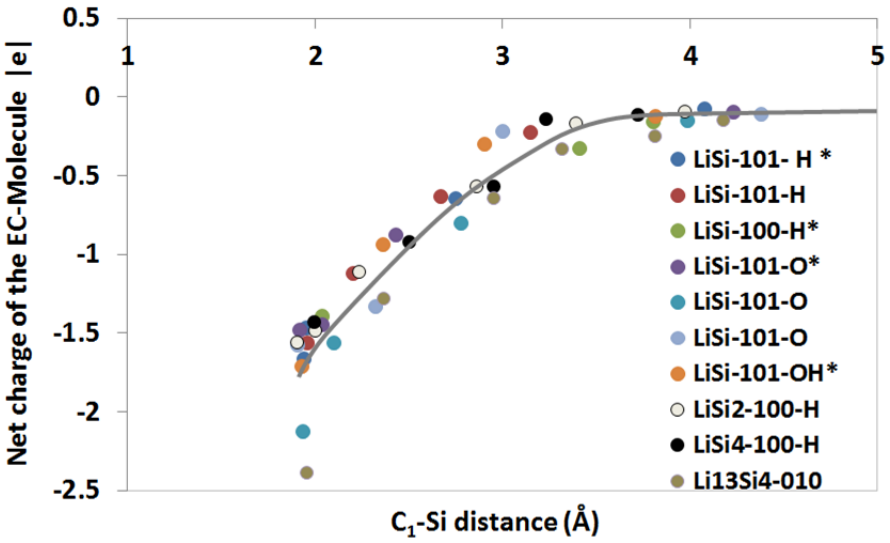

Figure VI - 118: Evolution of the EC charge (in e$^-$) as a function of the C-Si distance for various surface facets and terminations

On less lithiated surfaces (quasi-amorphous $LiSi_4$ and $LiSi_2$) the simultaneous 2 e$^-$ reduction was more frequently found. Strongly lithiated $Li_{13}Si_4$ surfaces were found to be highly reactive. Reduction of adsorbed EC molecules occurred via a 4 e$^-$ mechanism (Figure VI - 119) yielding as reduction products adsorbed CO^{2-} and $O(C_2H_4)O^{2-}$ usually in the liquid phase. Direct transfer of 2 e$^-$ to EC molecules in liquid phase was also found, resulting in $O(C_2H_4)OCO^{2-}$ anions that remained in the liquid phase possibly ready for further reaction.

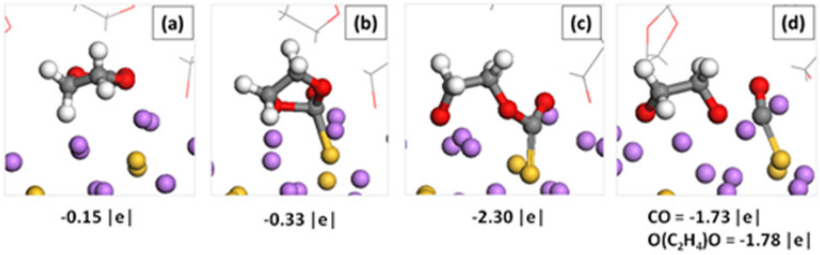

Figure VI - 119: EC decomposition on the $Li_{13}Si_4$-(010) surface. The sequence shows charge transfer to EC and reaction products

FEC was much more reactive and very fast processes involving sequential 4 or 5 e$^-$ were found independently of surface functionalization or degree of lithiation. Bonds were broken in the order CO/CF/CH/CO (Figure VI - 120) yielding CO^{2-} and $C_2O_2H_2^{2-}$, or CO_2^{2-} and $C_2OH_3^{2-}$, with F and H adsorbed. In the first case, the sequence of events includes (see Figure VI - 120 for atom nomenclature): 1) C_{33}-O_{41} breaking during its adsorption on the surface corresponding to the reaction FEC + 2e$^-$ → $(C_3O_3H_3F)^{2-}$(ads); 2) C_{32}-F_1 bond breaks and F adsorbs: $(C_3O_3H_3F)^{2-}$(ads) → $(C_3O_3H_3)^-$(ads) + F^-(ads); 3) C_{31}-H_{42} bond breaks and H may adsorb: $(C_3O_3H_3)^-$(ads) + 1 e$^-$ → $(C_3O_3H_2)^{2-}$(ads) + H(ads); 4) C_{33}-O_{40} bond breaks resulting in the final products: $(C_3O_3H_2)^{2-}$ (ads)+ 2 e$^-$ → $(CO)^{2-}$(ads) + $(C_2O_2H_2)^{2-}$

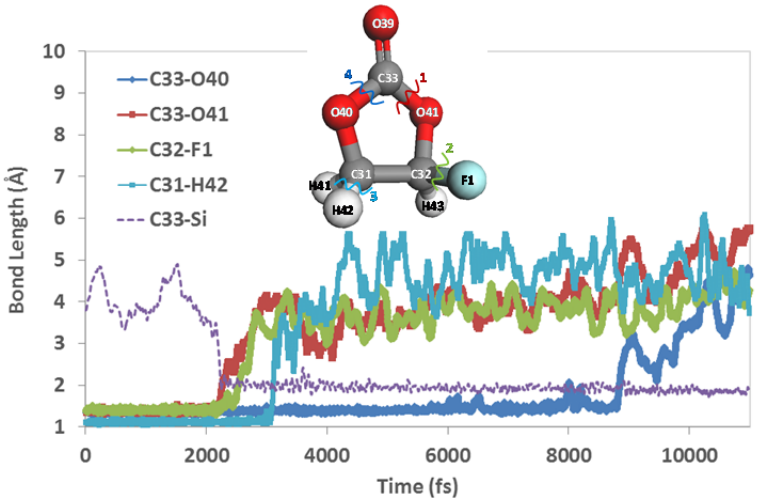

Figure VI - 120: FEC decomposition on the $Li_{13}Si_4$-(010) surface. As the molecule gets adsorbed on the surface (C-Si bond forms), there is a sequential bond breaking illustrated by the time evolution of the respective bond distances

An alternative FEC reduction mechanism takes place with the same initial steps yielding adsorbed $(C_3O_3H_3F)^{2-}$ that decomposes into $(C_3O_3H_3)^-$(ads) + F^- (ads). However, the last step is different, where the C_{31}-O_{40} bond breaks, resulting in the final products according to the reaction $(C_3O_3H_3)^-$ (ads) + 2 e^- → $(CO_2)^{2-}$(ads) + $(C_2OH_3)^-$.

VC reduction mechanisms were found similar to those of EC (although yielding double-bonded products).

Electron transfer through model electrode/SEI/EC interfaces. Electron transfer was calculated through electrode/SEI/EC interfaces.

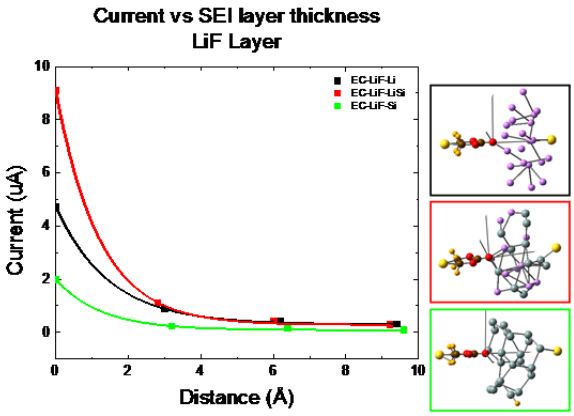

Figure VI - 121: Decay of electron transfer from the electrode to an EC molecule through a model SEI layer as a function of SEI thickness. Three model electrodes represent degrees of lithiation of the Si anode

SEI layers were represented by a composite cluster model of one component (Li_2O or LiF) and the electrode modeled by Si, LiSi, and Li clusters respectively (Figure VI - 121). Calculations were done for variable thicknesses and configurations of the SEI layer. Gold tips were attached at each end of the interfacial system and a bias voltage was applied to evaluate electron transfer using a DFT/Green's function method. It was found that the rate of electron transfer followed the expected trend depending on the type of electrode (Li > LiSi > Si) and both model SEI layers showed similar degrees of electron transfer resistance. At constant applied voltage (2V), the electron current was found to decay exponentially by ~94% at SEI thicknesses of ~10 Å (Figure VI - 121). However, both for Li and LiSi electrodes, a non-zero constant current was still detected (although very low) suggesting that the system may be able to sustain a low-rate growth at even larger thicknesses.

Reactivity of oxide surfaces. A preliminary attempt was made at modeling 1 e^- attacks on FEC in the presence of a $Li_{13}Si_4$ electrode, with each surface coated with a 7 Å thick Li_4SiO_4 layer so that FEC liquid is no longer in contact with $Li_{13}Si_4$ surfaces. FEC is found to decompose in picosecond time scales. Despite the expectation that the oxide should slow down electron transfer and enhance 1-e^- attack on FEC over 2 e^- reduction, Bader charge decomposition analysis showed that the products are still consistent with 2 e^--induced reactions. However, EC and FEC reductions tested on slabs of pure Li_4SiO_4 and $Li_2Si_2O_5$ were found not possible. These results suggested a critical role of the oxide thickness on surface reactivity.

Conclusions and Future Directions

At very early stages of lithiation (Li/Si ratio 1:15), the presence of adsorbed Li on the Si surface is able to generate EC reduction via a single electron transfer to the adsorbed molecule. When EC is surrounded by other EC molecules this single e^- transfer is more favorable than the 2 e^- transfer. At slightly higher Li/Si ratios (1:4, 1:2 and 1:1) the 2 e^- mechanism is favored by the large proportion of Li on the surface able to interact with EC molecules. The reaction starts by formation of a C-Si bond and a strong O-Li interaction sustained by charge transfer from the surface which favors ring opening. Two types of 2 e^- mechanisms were found: simultaneous and sequential, yielding different charged or neutral fragments either adsorbed or in the liquid phase. Strongly lithiated surfaces are very reactive and 4 e^- transfer reactions were detected.

FEC was found much more reactive than EC and its reaction mechanisms were found to be independent of the degree of lithiation, type of exposed surface and/or details of surface functionalization. DFT calculated barriers at the lowest Li/Si ratio (1:15) indicated that the 2 e^- transfer via C_c-O cleavage is the most favorable, in agreement with the AIMD results which illustrate the complete sequence of bond breakings involving 4 or 5 e^- mechanisms. The products include adsorbed F and sometimes H, as well as charged CO or CO_2 and other radical anions.

VC reduction mechanisms were found similar to those of EC (although yielding double-bonded products).

Initial studies of electron transfer done in model systems including electrode/SEI layer/EC showed how the resistance of the film increases with its thickness. The SEI layer was represented by LiF or LiO_2. For the case of LiF the current from Li or LiSi electrodes was found to decrease exponentially and decay to very low constant values (but not completely zero) at about 1 nm thickness, suggesting that a low-rate SEI growth may subsist at larger SEI thicknesses.

Preliminary studies were conducted to investigate the role of surface oxides. AIMD simulations resulted on 2 e^- transfers from a composite surface ($Li_{13}Si_4$ coated with Li_4SiO_4) to FEC and EC molecules similar to those found in bare Li_xSi_y electrodes. However, AIMD simulations in slabs of Li_4SiO_4 and $Li_2Si_2O_5$ showed no FEC reductions. Thus, it is not clear if the results are a consequence of DFT inaccuracies to treat the oxide systems or if indeed a very thin film of the oxide may allow e^- transfer.

Future work will address: 1) Comparisons of reduction behavior between additives (FEC vs. VC) and their consequences on the SEI layer composition; 2) Product aggregation and SEI layer growth from the initial fragments; 3) Further characterization of the role of surface oxides; 4) Growth on SEI layers deposited on the Li_xSi_y or Li_xSi_y coated with oxides; 4) Further clarification on the electron transfer mechanisms, identification of electron channels and electron-blocking regions, tests of additional SEI products and "mosaic" model films.

FY 2013 Publications/Presentations

1. J. M. Martinez de la Hoz, Y. Ma, and P. B. Balbuena, "Solvent reduction on Si anodes of Li-ion batteries," *2013 ACS Fall National Meeting*, Sept. 2013, Indianapolis, IN.
2. P. B. Balbuena, J. M. Martinez de la Hoz, Y. Ma, L. Espinoza, and J. M. Seminario, "SEI layer formation on Si anodes of Li-ion batteries," *64th Annual ISE Meeting*, Sept. 2013, Queretaro, Mexico.
3. P. B. Balbuena, J. M. Martinez de la Hoz, Y. Ma, L. Espinoza, and J. M. Seminario, "SEI layer formation on Si anodes," *2013 ECS Fall Meeting*, Oct. 2013, San Francisco, CA.
4. K. Leung, S. B. Rempe, M. E. Foster, Y. Ma, J. M. Martinez de la Hoz, N. Sai, and P. B. Balbuena, "Modeling Electrochemical Decomposition of FluoroEthylene Carbonate on Silicon Anode Surfaces in Lithium Ion Batteries," submitted.
5. J. M. Martinez de la Hoz, K. Leung, and P. B. Balbuena, "Reduction Mechanisms of Ethylene Carbonate on Si Anodes of Lithium-Ion Batteries: Effects of Degree of Lithiation and Nature of Exposed Surface," submitted.

VI.C.13 Analysis of Film Formation Chemistry on Silicon Anodes by Advanced *In situ* and *Operando* Vibrational Spectroscopy (UCB)

Gabor Somorjai
University of California, Berkeley

Department of Chemistry
Berkeley CA 94720
Phone: (510) 642-4053; Fax: (510) 643-9668
E-mail: somorjai@berkeley.edu

Philip Ross
Lawrence Berkeley National Laboratory
Materials Sciences Division
Berkeley CA 94720
Phone: (510) 486-5821
E-mail: pnross@lbl.gov

Start Date: October 2012
Projected End Date: September 2015

Objectives

- Understand the composition, structure, and formation/degradation mechanisms of the solid electrolyte interface (SEI) on the surfaces of Si anodes during charge/discharge cycles by applying advanced *in situ* vibrational spectroscopies.
- Determine how the properties of the SEI contribute to failure of Si anodes in Li-ion batteries in vehicular applications. Use this understanding to develop electrolyte additives and/or surface modification methods to improve Si anode capacity loss and cycling behavior.

Technical Barriers

High energy density Si anodes have large irreversible capacity and are not able to cycle. These failures are due in part to loss of electrolyte by reduction and a SEI that is not stable on the surface with repeated cycling.

Technical Targets

- EV: > 200 wh/kg with > 1,000 cycles to 80 % depth of discharge.

Accomplishments

- A novel *in situ* ATR-FTIR spectroelectrochemical cell was developed that provided unprecedented tuning of the depth of probing the vibrational spectra of molecules near the electrode surface.
- Two alternative anode materials were studied, Si and Sn, with Au used as a contrasting "inert" metallic electrode.
- It was determined that with Si and Sn reduction of electrolyte solvent, mostly the alkyl carbonate co-solvent formed soluble products via alkyl and alkoxide radicals, the main products observed (in EC:DEC) being lithium propionate and diethyl 2,5 dioxohexane dicarboxylate (DEDOHC).
- In contrast, electrolyte reduction on Au produces different products, more like those observed with graphite anodes, insoluble compounds such as lithium ethylene dicarbonate (LiEDC) and lithium oxalate. The precipitation of these compounds on the gold surface passivates the surface to further electrolyte reduction.
- Since soluble lithium propionate is the primary reduction product observed in lithiated Si, passivation does not occur, electrolyte reduction is continuous.

Introduction

Major efforts are under way to develop novel materials that provide higher battery capacity for increased driving distances of electric vehicles. A high capacity alternative to graphitic carbon anodes is Si, which stores 3.75 Li per Si versus 1 Li per 6 C yielding a theoretical capacity of 4008 mAh/g vs. 372 mAh/g for C. Unfortunately, this high capacity comes at a cost: the Si anodes exhibit excessive irreversible capacity loss and short cycling lifetime. The irreversible capacity loss is believed to be caused by lattice expansion accompanying lithiation that is followed by particle cracking, continued reduction of electrolyte and formation of SEI on freshly exposed surface. Detachment of the SEI from the Si surface occurs even when the potential region of cycling is restricted to

produce a degree of expansion similar to that of graphite. These observations suggest that the SEI on Si is not intrinsically passivating and that the chemistry of the SEI on the Si surface is different from that of the SEI on graphite. Nonetheless, there are no studies to date suggesting that the SEI on Si is significantly different than that on graphite.

Studies of the electrolyte reduction products (i.e., SEI) have been performed on both inert (Au, Ni, or Cu) and electroactive (Li or graphite) materials where many properties of the SEI including its chemical composition, electrical resistance, and Li+ ion conductivity have been determined. The SEI is considered to contain organic and inorganic components that are comprised of lithium carbonates (e.g., $(CH_2OCO_2Li)_2$, $ROCO_2Li$, Li_2CO_3, polycarbonates), oxalate and alkoxides (e.g., $Li_2C_2O_4$, ROLi, HCOLi) and inorganic materials (e.g., LiF, Li_2O, LiOH). The formation mechanism of the interphase on anodes is still under debate, yet there are some properties that are generally agreed upon. Formation is suggested to occur in two voltage stages: at 1.5-0.8 V vs. Li/Li+ a porous, resistive, and dimensionally unstable phase is formed by electrochemical reduction of electrolyte components; a second stage of reduction occurs concomitantly with intercalation or lithium deposition forming a compact phase that prevents further electrolyte reduction, i.e., passivation, yet allows Li ion conduction, i.e., the solid electrolyte interphase. While lithium diethylcarbonate (LEDC) is considered to be a primary product from the one electron reduction of EC in the first stage, the overall composition of the inhomogeneous compact passivating SEI layer remains unclear. It is not known whether the SEI on graphite is unique to that electrode material, or that the cyclability of graphite is due entirely to the relatively small lattice change accompanying lithiation/delithiation.

The uncertainty regarding composition, structure, and formation and degradation mechanisms of the SEI is in general due to the poor interfacial sensitivity obtained using conventional spectroscopies. These issues will be addressed with a development of advanced *in situ* vibrational spectroscopies, sum frequency generation (SFG) and a new type of attenuated total reflection (ATR) Fourier transform infrared spectroscopy. Using these new tools, the focus will be on determining the failure modes of an operating Si/Li electrochemical system for vehicular applications. These results will lead to an improved an understanding of the:

- chemical composition and structure of the SEI at the Si/electrolyte interface, including
  - which electrolyte components are involved,
  - how lithium ion solvation is involved;
- formation mechanisms as a function of potential, time, and number of cycles;
- degree of SEI inhomogeneity across Si electrodes;
- stability of the SEI with respect to
  - the physical changes of Si that incur with lithiation and delithiation,
  - the crystal size, structure, and orientation of Si
  - doped or undoped Si,
  - electrolyte composition.

This knowledge will be used to develop and tailor SEI films for Si anodes that reduce irreversible capacity loss, improve long-term stability and cyclability for vehicular applications.

Approach

Model Si anode materials including single crystals, e-beam deposited polycrystalline films, and nanostructures are studied using baseline electrolyte and promising electrolyte variations. A combination of *in situ* and *operando* Fourier Transform Infrared (FTIR), Sum Frequency Generation (SFG), and UV-Raman vibrational spectroscopies are used to directly monitor the composition and structure of electrolyte reduction compounds formed on the Si anodes. Pre-natal and post-mortem chemical composition is identified using X-ray photoelectron spectroscopy. The Si films and nanostructures are imaged using scanning and transmission electron microscopies.

Results

A new design for an *in situ* ATR-FTIR cell to analyze the chemistry of the electrolyte reduction at the surface of a p-type Si(100) single crystal (doped) *in operando* was developed. This design is shown in Figure VI - 122, which made it possible to vary the penetration depth of the IR radiation and analyze both near-surface (< 1 μm) and boundary layer (> 10 μm) regions, thus analyzing for both dissolved and precipitated products. This cell was used to compare the chemistry of reduction on Si versus Au and Sn surfaces obtained earlier by conventional *in situ* reflection absorption infrared spectroscopy (RAIRS) and *ex situ* ATR-FTIR.

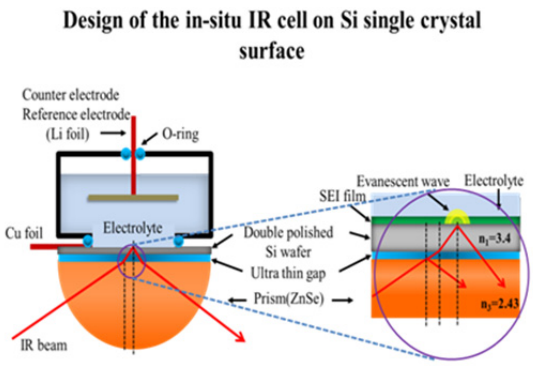

Figure VI - 122: The use of an index matching dielectric liquid in the thin gap between the Si crystal and the ZnSe optic enables tuning of the position of the evanescent wave from the surface of the Si into the bulk

The *in situ* spectra from the near surface region changed when the potential was applied to the electrode. Two strong peaks appeared above the electrolyte features which could be attributed to diethyl 2,5 dioxohexane dicarboxylate (DEDOHC) by comparison to the spectrum of the pure compound synthesized in this work. The spectrum of DEDOHC is very similar to that of the co-solvent DEC, diethylcarbonate, but the effect of solvation with the Li ion (or ion-pair) shifts the frequency of DEC enough for resolution of the two. The relative intensities of the vibrations are also significantly different to resolve the two molecules. The amount of DEDOHC was time-potential-depth dependent. Briefly summarizing numerous measurements, it was concluded that the DEDOHC appears over a large potential window beginning at around 1.5 V vs. Li/Li+, but not increased by stepping to lower potentials. The DEDOHC diffuses away from the surface quickly and the concentration in the bulk is very low. The reaction appeared to be self-limiting, possibly due to a parallel reaction forming an insoluble product, i.e., passivation. The passivating product appeared to be lithium propionate, seen only *ex situ*. There were also experiments that indicated that the reaction to form DEDOHC is a surface reaction with oxide on the surface of the Si. Similar results were observed with Sn.

By varying the penetration depth of the IR radiation, analysis of both near-surface (<1 µm) and boundary layer (>10 µm) regions of the Si electrode was possible. The wide wave number range (4000-800 cm^{-1}) allows us to correlate the stretching vibration of PF_6^- anion near 840 cm^{-1} with new features appearing near 1600-1700 cm^{-1} that indicate a change in the Li ion solvation state commensurate with solvent reduction. It was discovered that with different depth into the electrolyte, the PF_6^- vibration peak shifts without correlation to solvent reduction. Interpretation of these shifts in terms of solvation states will require quantum chemical modeling.

The electrochemical properties of Si (100), Si (110), Si (111), both doped and undoped wafers (450 microns thickness), were characterized during the charging-discharging cycles, using primarily cyclic voltammetry (at 0.1 mV/s equivalent to ca. 4 hr. constant current cycling). The kinetics of Li diffusion was observed to be dependent on crystal orientation and more importantly changes in depth of lithiation with number of cycles was also orientation dependent. Typically, the charge for delithiation increased progressively in the first few cycles, and achieved a quasi-equilibrium value (after about 30 cycles) as a result of the competition between Li diffusion rate and potential scanning rate. The level and type of dopant (n or p) strongly affected the bulk electrical conductivity and also the Li capacity of the Si wafers - increasing n-type dopant concentration decreased capacity, while p-type dopant density demonstrated the opposite trend. These results are consistent with some reports in the literature, e.g., *J. Phys. Chem. C*, 2011, **115**, 18916–18921. The correlation between the electrochemical properties of model Si wafers and real world Si may therefore be problematic, as the nature of the bulk impurities is typically unknown and/or uncontrolled. Perhaps a better model electrode of Si would be thin films fabricated from commercial bulk Si material vs. the doped Si single crystals often employed in spectroelectrochemistry.

At the recommendation of the Anode Focus Group in September 2013, fluoroethylene carbonate (FEC) has been chosen, the monofluorinated version of ethylene carbonate, as the additive for future study by SFG and ATR-FTIR.

Conclusions and Future Directions

- Here it was determined that on Si electrodes reduction of electrolyte solvent, mostly the alkyl carbonate co-solvent, formed soluble products via alkyl and alkoxide radicals, the main products observed (in EC:DEC) being lithium propionate and diethyl 2,5 dioxohexane dicarboxylate (DEDOHC).
- In contrast, electrolyte reduction on gold produces different products, more like those observed with graphite anodes, insoluble compounds such as lithium ethylene dicarbonate (LiEDC) and lithium oxalate. The precipitation of these compounds on the gold surface passivates the surface to further electrolyte reduction.
- Since soluble lithium propionate is the primary reduction product observed in lithiated Si,

passivation does not occur, electrolyte reduction is continuous. This appears to be the primary problem with cycle life of Si anodes. A change in electrolyte composition from the conventional Li-ion electrolyte is therefore needed.

- It is recommended that co-solvents other than DMC or DEC be employed with EC.
- Fluorinated ethylene carbonate (FEC) was selected as an additive for future studies by SFG and ATR-FTIR.
- Selectively directing the solvent reduction reactions pathways by surface modification of the Si will also be a future direction of study.

FY 2013 Publications/Presentations

1. Feifei Shi and Kyriakos Komvopoulos (Mechanical Engineering Department, U.C. Berkeley, Berkeley, CA, United States), Philip N Ross (Materials Sciences Division, LBNL, Berkeley, CA, United States), and Gabor Somorjai (Chemistry Department, U.C. Berkeley, Berkeley, CA, United States), "Li-Ion Battery Solid Electrolyte Interface (SEI) Investigation With *In situ* Attenuated Total Reflection-Infrared (ATR-IR) Spectroscopy," *224th Electrochemical Society Meeting*, October 27 – November 1, 2013, San Francisco CA.

VI.C.14 Nanoscale Composite Hetero-structures and Thermoplastic Resin Binders: Novel Li-ion Anode Systems (U. Pittsburgh)

Prashant N. Kumta
University of Pittsburgh

Department of Bioengineering, Chemical and Petroleum Engineering, Mechanical Engineering and Materials Science
Pittsburgh, PA 15261
Phone: (412) 648-0223; Fax: (412) 624-8069
E-mail: pkumta@pitt.edu

Start Date: October 2010
Projected End Date: September 2014

Objectives

- Identify new alternative nanostructured anodes to replace synthetic graphite providing higher gravimetric and volumetric energy densities.
- Similar or lower irreversible loss (≤15%) in comparison to synthetic graphite.
- Similar or better coulombic efficiency (>99.9%) in comparison to synthetic graphite.
- Similar or better cyclability and calendar life in comparison to synthetic graphite.
- Improve the coulombic efficiency, available energy density, rate capability and cycle life of high specific capacity Si based electrodes.
- Investigate nano-structured (*nc*-Si) and amorphous Si (*a*-Si) based composite or hybrid heterostructured anode.

Technical Barriers

The important technical barriers of alternative anodes for lithium ion batteries (LIBs) to be used in electrical vehicles or plug in hybrid electrical vehicles are following:

(A) Low energy density
(B) Large first cycle irreversible loss (>25-40%)
(C) Inadequate coulombic efficiencies
(D) Poor cycle life
(D) Poor rate capability
(E) Low charge/discharge rates

Technical Targets

- Synthesize nano-structured (*nc*-Si) and amorphous Si (*a*-Si) based composite or hybrid structured anodes using cost effective processing techniques.
- Achieve reversible capacity of ≥ 1200 mAh/g.
- Reduce first cycle irreversible loss to less than ~15%.
- Improve coulombic efficiencies higher than 99.7%.
- Improve the rate capability.
- Characterize the nano-scale hetero-structures for structure and composition using electron microscopy techniques such as SEM, TEM and HREM.

Accomplishments

- Developed a scalable approach to generate hollow silicon nanotubes (SiNTs) using a low cost and high throughput sacrificial inorganic nanowire (INW) template.
- Binder-free and slurry based SiNTs were fabricated with capacities >2500 mAh/g.
- Specific capacities >1000 mAh/g were obtained for SiNTs after 400 cycles with a fade rate 0.067 % loss per cycle and a high coloumbic efficiency ~99.9%.
- Reversible capacities around ~1000 mAh/g were achieved on the SiNTs using DOE-BATT test conditions for over 100 cycles.
- Novel high strength and elastomeric natural and modified polymer binders, GG and MAB were identified and developed which exhibited comparable first cycle irreversible loss and better capacity retention (0.08% loss per cycle) compared to the commercial PVDF and CMC based binder (0.37% loss per cycle).

✧ ✧ ✧ ✧ ✧

Introduction

In the earlier quarterly and annual reports, several novel approaches have been explored to achieve DOE-BATT technical targets for Si based anodes: high specific capacity (>1200 mAh/g), lower first cycle irreversible loss (<15%), high coloumbic efficiency (>99.9%), good cyclability and rate capability. These approaches involved the development of nano-scale heterostructures of vertically aligned carbon nanotube (VACNT) forests coated with nanocrystalline/

amorphous silicon films/droplets, thin films of interface control agent (ICA), thin films of electrodeposited amorphous silicon and high strength thermoplastic binders. The VACNT-Si composites exhibited capacities >2800 mAh/g with a very low irreversible loss (~12%) with moderate cyclability. Addition of a thin layer of ICA between the VACNT and Si improved the adhesion of Si film resulting in better cyclability and capacity retention. Electrodeposition of amorphous silicon films also showed excellent cyclability with a capacity of 1300 mAh/g over 100 cycles.

Hollow silicon nanostructures such as silicon nanotubes (*h*SiNTs) have been shown to offer mechanical strain relaxation during the colossal volume expansion of silicon occurring in the lithiation process, thus preventing mechanical failure (decrepitation of electrode) and hence improving the cyclability of the electrode for hundreds of cycles. The current known methods for synthesizing SiNTs involve a sacrificial template (anodized alumina and electrospun carbon fibers) made by expensive precursors onto which silicon was deposited by decomposing silane (SiH_4) and then removing the underlying template either by etching or by heat treatment resulting in a low yield of SiNTs. In the current work, scalable quantities of smooth and long nanowire templates were generated using inexpensive precursors and equipment. Reaction parameters including pH of the precursor solution and heat treatment conditions were further optimized to produce uniform and smooth inorganic nanowires (INWs) with high aspect ratio.

Currently, PVDF is the accepted commerical binder for anodes and cathodes. However, the large volume expansion of Si results in a significant stress field in the PVDF binder matrix leading to mechanical failure of the electrode. A high fracture strength binder is hence necessary to accommodate the volume strain that arises due to the large related Si volume expansion. In this report, results obtained on the electrochemical properties of Si/C composite with our newly developed modified natural polymer binders, named GG and MAB are discussed.

Approach

For the hollow silicon nanotube (*h*SiNTs) synthesis, a sacrificial one dimensional inorganic nanowire template (INW) was first synthesized in an autoclave reactor under hydrothermal conditions (Figure VI - 123). Surfactants comprising long chain ampiphilic molecules were added to improve the dispersibility of the nanowires. The effect of other parameters such as pH of the precursor solution and heat treatment were studied and optimized to generate smooth and long sacrificial nanowire templates with very high aspect ratio. A thin layer of amorphous silicon was then deposited on the surface of these nanowires either by RF magnetron sputtering at 50W or by thermal cracking of silane gas (SiH_4) in a low pressure CVD reactor resulting in a core-shell (INW/Si) structure. This composite structure was dispersed in a mineral acid to dissolve the nanowire template to generate the hollow silicon nanotubes (*h*SiNTs).

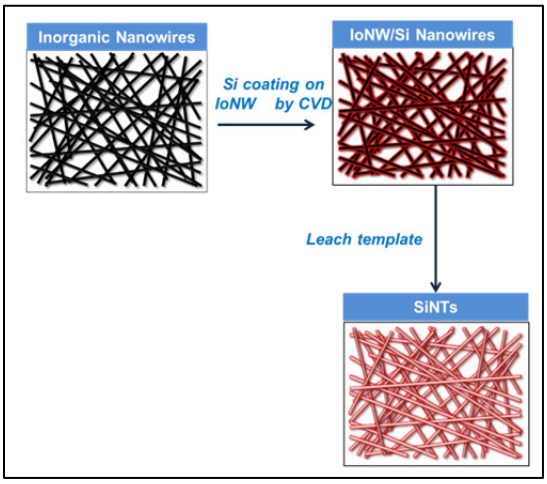

Figure VI - 123: Schematic of *h*SiNT synthesis using inorganic nanowire (INW) template

The newly identified water soluble natural and modified elastomeric binders (GG & MAB) were tested against a high energy mechanical milling (HEMM) derived high specific capacity Si/C system. The modified binders were synthesized using alkylation method of natural polymer AB. In this method, sodium monochloroacetate has been used as a crosslinking agent to AB polymer in order to improve the mechanical properties such as fracture strength.

Results

Hollow Silicon Nanotubes (*h*SiNTs): The morphology of the hollow silicon nanotubes is largely dependent on the morphology of the INW template since the silicon deposited via sputtering or CVD assumes the nanowire morphology and hence a smooth, un-agglomerated and high aspect ratio nanowire of the inorganic template is desired. The inorganic nanowire (INW) template synthesis was optimized by controlling several parameters such as use of surfactants, pH and heat treatment conditions. The use of long chain amphiphilic molecules greatly enhanced the dispersibility of the nanowires that also proved essential for obtaining a uniform coating of silicon in the next step. Increasing the pH of the initial precursor solution further improved the surface smoothness of the INWs. In the first approach, the INWs drop casted onto the copper foils were used as the substrate onto which silicon was deposited by RF sputtering at 50W for one

hour. Hollow silicon nanotubes were generated after the Si coated INWs were dispersed in mineral acid to dissolve the INW template. The binder-less *h*SiNT electrode exhibited a very high first discharge capacity (~ 4100 mAh/g) close to the theoretical capacity of silicon when cycled with a current density of 100 mA/g in a voltage range 0.02V to 1.2 V vs. Li^+/Li. These smooth *h*SiNTs also exhibit good cyclability with a capacity retention of 89% at the end of 50 cycles.

In order to make slurry derived electrodes, scalable quantities of *h*SiNTs are required and hence a low pressure CVD technique was employed wherein large quantities of the INWs were used as the template onto which silicon was deposited by thermal cracking of silane gas (SiH_4) at 500°C. Similar to the earlier approach, the INW/Si core-shell structure was dispersed in mineral acid to remove the INW template thus generating scalable quantities of *h*SiNTs which were used to make slurry along with binder and conductive additives.

SEM, HRTEM and EDAX spectra of the resultant *h*SiNTs are shown in Figure VI - 124. The length of the INWs varied from 5µm to 100µm while the diameters were in the range 0.6µm to 1µm. The wall thickness of the *h*SiNTs was estimated to be in the 60 nm to 100 nm range. Both the SEM and HRTEM images (Figure VI - 124b and c) show the open eneded hollow structures of SiNTs. The EDAX spectra shows that the final product obtained contained only Si with some amount of surface oxidation. Raman spectra of the SiNTs showed a broad peak around 480 cm^{-1} clearly validating that the Si formed is amorphous.

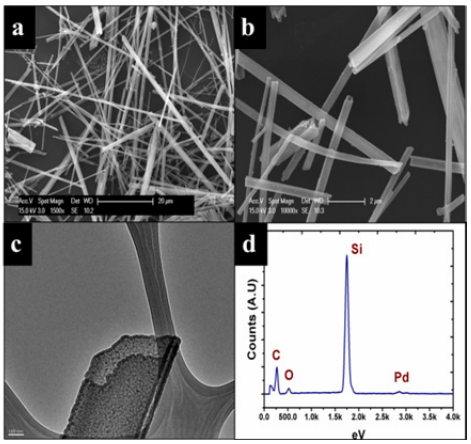

Figure VI - 124: SEM images of (a) INW template, (b) *h*SiNTs after acid leaching, (c) HRTEM image of an open ended *h*SiNT & (d) EDAX spectra of *h*SiNTs

A medium current density of 300 mA/g was employed between the voltage range 0.01 and 1 V vs. Li^+/Li for the first cycle and a high current of 2A/g was applied for subsequent cycles to determine the cycling and long term stability. The charge-discharge characteristics of *h*SiNTs are shown in Figure VI - 125. A specific capacity of 2615 mAh/g and 1960 mAh/g were obtained for the first cycle discharge and charge capacity, respectively. A first cycle irreversible loss of ~25% was observed for these *h*SiNTs which may be due to the SEI layer formation on the surface of the SiNTs. At 2A/g, the SiNTs show excellent cycling stability over hundreds of cycles. Specific capacities in excess of 1000 mAh/g were obtained after 400 cycles corresponding to a fade rate of 0.067% loss/cycle (for 400 cycles) and a coulombic efficiency in the range of 99.9% was achieved.

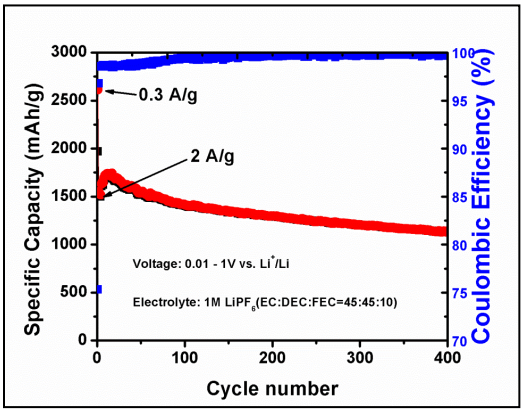

Figure VI - 125: Long term cycling of *h*SiNTs performed at 2A/g (1st cycle at 0.3 A/g)

The *h*SiNTs were also cycled using the DOE-BATT recommended protocol at a current density of 0.02 mA/cm^2 between the voltage range 0.005 to 1 V vs. Li^+/Li for the first 3 cycles (to form a stable SEI layer). A first discharge and charge capacity of 2810 mAh/g and 2035 mAh/g were oberved resulting in a first cycle irreversible loss of 27%. Current densities of 0.5 mA/cm^2 and 0.75 mA/cm^2 were applied for the lithiation and de-lithiation processes, respectively as shown in Figure VI - 126. A stable and reversible capacity around ~1500 mAh/g was obtained for 100 cycles and the coloumbic efficiency close to 99.5% was achieved when cycled with current densities of 0.5 mA/cm^2 and 0.75 mA/cm^2 for lithiation and de-lithiation processes, respectively. This translates to a capacity retention of 93.2% and a fade rate of 0.07% loss per cycle (for 100 cycles). The *h*SiNTs also showed good rate capability when cycled from a curent density of 0.5 A/g to 4 A/g. Capacities close to 1200 to 1500 mAh/g were obtained at high current densities of 4 A/g.

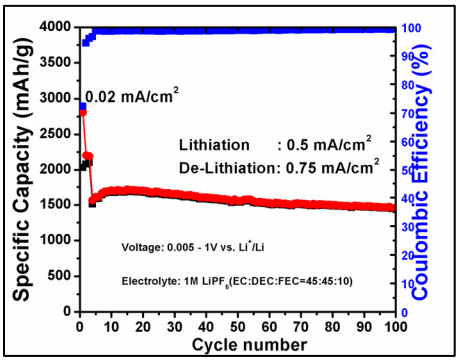

Figure VI - 126: Electrochemical cycling of *h*SiNTs using DOE recommended test conditions

High strength and elastomeric binders: As shown in Figure VI - 127, the Si/C nanocomposite with GG binder (3mg/cm^2) loading shows a 1st cycle discharge (~1179mAh/g) and charge capacity (~960mAh/g) with an irreversible loss ~18%, while the Si/C composite with PVDF binder (3mg/cm^2 laoding) exhibited an irreversible loss (IR) of ~17%, indicating that the newly developed GG binder has no negative effect on the 1st cycle IR loss. The long term cycling of Si/C composite cycled at 160mA/g (C/6) shows that the GG binder exhibits better cycling stability (0.08% loss per cycle) in contrast to the commercial PVDF (0.37% loss per cycle). However, significant chemical modification of the GG binder reflecting improvements in the mechanical strength is necessary for achieving excellent cycling stability (0.01% loss per cycle).

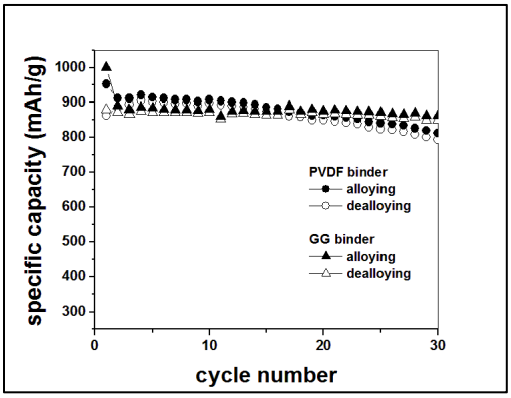

Figure VI - 127: Variation of specific capacity vs. cycle number of Si/C composite with PVDF and GG binder

Recently, a modified water soluble amine based binder (MAB) has been identified which shows excellent cyclability even when tested with high specific capacity Si/C based anode (~1000mAh/g) synthesized by high energy mechanical milling (Figure VI - 128). Si/C composite with MAB shows 21% 1st cycle irrversible loss and excellent capacity retention of specific capacity ~800mAh/g when cycled at a rate of 300mA/g and 3mg/cm^2 total loading.

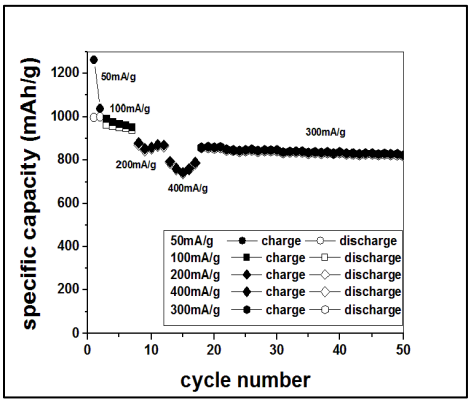

Figure VI - 128: Charge-discharge characteristics of Si/C composite with MAB binder

Conclusions and Future Directions

A cost effective and scalable approach has been developed to generate *h*SiNTs using a sacrificial inorganic nanowire template. The silicon obtained was identified to be amorphous (from Raman spectra) and the SEM and HRTEM images showed the hollow tubular structure of *h*SiNTs. These *h*SiNTs were used in both binder-free and slurry based electrode systems delivering capacities >2600 mAh/g. Slurry based *h*SiNTs exhibited excellent cycle life and capacities >1000 were obtained after 400 cycles. This corresponds to a fade rate of 0.067% loss/ cycle. High strength water soluble elastomeric polymers, GG and amine based MAB binder were identified and chemically modified to achieve excellent capacity retention (fade rate of <0.08% loss/cycle) compared to the commercially available PVDF (~0.35% loss/cycle).

Future work will be directed to study the SEI layer formed on the surface of *h*SiNTs, perform rate capability studies and use HRSEM tools to investigate the morphological changes that may occur at the end of extended cycling (>500 cycles). Impedance studies will also be performed on the *h*SiNTs to study the interface and charge transfer characteristics. To further lower the cost of synthesizing *h*SiNTs, regeneration of the nanowire template will be explored where the dissolved INW templates to produce *h*SiNTs will be recovered again by a cost effective solution based chemical approach. The aforementioned efforts will enable us to comprehensively investigate and understand the chemical, materials and electrochemical characteristics of *h*SiNTs and further advocate their commercial viability as a replacement for graphite anodes in the next generation lithium ion batteries (LIBs).

FY 2013 Publications/Presentations

1. R. Epur, M. K. Datta & P. N. Kumta, *Electrochim. Acta*, **85**, (2012) 680-684.
2. R. Epur, M. Ramanathan, F. R. Beck, A. Manivannan and P. N. Kumta, *MSEB*, 177, **14**, (2012) 1157-1162.
3. R. Epur, M. K. Datta & P. N. Kumta, J. *Solid State Chem.* (2013) http://dx.doi.org/10.1016/j.jssc.2013.09.002.
4. M. K. Datta, R. Epur, P. Saha, K. Kadakia, S. K. Park & P. N. Kumta, *J. Power Sources*, 225, **1**, (2013) 316-322.
5. S. Pal, S. S. Damle, P. N. Kumta & S. Maiti, *Computational Materials Science*, **79**, (2013) 877-887.
6. S. Pal, S. S. Damle, S. H. Patel, M. K. Datta, P. N. Kumta & S. Maiti, *J. Power Sources*, **246**, 149-159 (2013).
7. L. Minardi, R.Epur & P. N. Kumta, *2012 AIChE Annual Meeting*, Pittsburgh, PA USA.

.

VI.D Electrolyte Development

VI.D.1 Advanced Electrolytes and Electrolyte Additives (ANL)

Khalil Amine
Argonne National Laboratory

Chemical Sciences and Engineering Division
Argonne, IL 60439
Phone: (630) 252-3838; Fax: (630) 252-4672
E-mail: amine@anl.gov

Larry Curtiss
Argonne National Laboratory
Material Science Division
Argonne, IL 60439
Phone: (630) 252-7380; Fax: (630) 252-5999
E-mail: curtiss@anl.gov

Start Date: October 2009
Projected End Date: September 2013

Objectives

- Use advanced quantum chemical (QC) models to predict electrolyte additives that can (1) act as redox shuttles for overcharge protection and (2) form stable Solid Electrolyte Interphases (SEI) on electrode interfaces
- Use the model to predict how additives interact with the surface of the anode and cathode to form good protective films.
- Synthesize suitable additives predicted by the modeling, characterize them, and carry out extensive cycle and calendar life tests.

Technical Barriers

This project addresses the following technical barriers in lithium-ion battery technology (a) Cycle/calendar life (b) Abuse tolerance

Technical Targets

- New additives that exhibit stable film formation on anodes and cathodes
- Increased cycle life
- Improved safety

Accomplishments

- The database of potential additives for SEI formation and overcharge protection has been added to by using QC models for screening of reduction and oxidation potentials. The database now has over 500 additive molecules.
- Density functional methods were used to examine the oxidation potential and other properties of a potential redox shuttle F3-DDB. This molecule has less symmetry compared to previously studied shuttles DDB and F6-DDB. The F3-DDB compound was synthesized and tested as a redox shuttle and found to perform well.
- Density functional methods were used to examine the oxidation potential and decomposition reactions of a new fused ring shuttle OFDDB. Ortho methoxy groups make the shuttle more polar. Two decomposition pathways also were examined using density functional theory (DFT) and found to be stable. Experimentally, the fused ring structure and increased dipole moment significantly improves the solubility and provides a promising new platform for a variety of new shuttles.
- The stability of a potential redox shuttle, quaterphenyl, was investigated using DFT, which indicates that it should have high oxidative stability and is potentially a viable redox shuttle candidate. Substituted quaterphenyls are also predicted to be stable and possible redox shuttle candidates.
- DFTs were used to examine one and two electron reduction reactions of maleic, citraconic and dimethylmaleic anhydrides. They have good reduction potentials and have reaction pathways that are likely to lead to anionic polymerization following one electron reduction. Experimentally, the performance of citraconic anhydride has been examined, and it exhibits excellent performance.

✧ ✧ ✧ ✧ ✧

Introduction

The development of advanced electrolytes with functional additives that provide for stabilization of the interfaces of lithium-ion batteries to prevent detrimental degradation is important for enhancing their cycle life and safety. In addition, electrolyte additives can provide protection against overcharge at the cathode. This project involves the use of high level QC methods for accurate energy assessments to screen for electrolyte additives that can be added to the electrolyte and form a protective SEI during the initial charging to prevent the conventional passivation film from forming first. Similar QC methods are being used to screen for new additives for redox shuttles to provide for overcharge protection in Li-ion batteries.

Approach

This is a joint theoretical/experimental approach for the design and discovery of new electrolyte additives that act during cell operation to prevent detrimental decomposition of cell components. QC screening based on DFT and wave-function based methods are used to predict accurate oxidation and reduction potentials. In addition, these methods are used to investigate decomposition pathways of the additives that will result in a protective layer on the anode as well as to find stable additives for overcharge protection. Synthesis and testing of the new additives is done to determine the cycle life of the batteries followed by characterization.

Results

Electrolyte additives for SEI formation. Calculations are being used to screen for additives for protective film formation on anodes with some being studied experimentally. Following are results for some of the additives that have been investigated.

Anhydrides. DFT were used to examine one and two electron reduction reactions of maleic, citraconic and dimethylmaleic anhydrides shown in Figure VI - 129. The calculated reduction potentials are all greater than 2 V vs. Li/Li+ due to conjugation but decrease as more electron releasing methyl groups are attached. There are various reaction pathways for decomposition after reduction including anionic polymerization following one electron reduction, formation of Li_2CO_3 after two electron reduction, and reaction with EC after one electron reduction. The first pathway (polymerization) has been examined in detail and was found to be favorable.

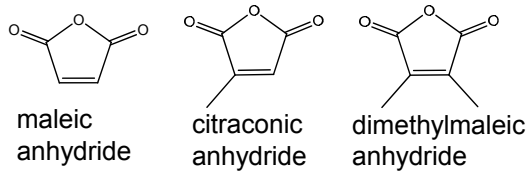

Figure VI - 129: Structures of the three anhydrides

Experimentally, the performance of citraconic anhydride has been examined, and it exhibits excellent performance. The citraconic anhydride additive (1%) was added to the electrolyte of a cell having the following components: $LiNi_{1/3}Co_{1/3}Mn_{1/3}O_2$ //1.2M $LiPF_6$ EC/EMC//MCMB. It is found that the citraconic anhydride can be easily reduced consistent with the theoretical predictions. It also results in improved cycling performance compared to the electrolyte without the additive as shown in Figure VI - 130.

Redox shuttle screening. Calculations are being used to screen for redox shuttles for overcharge protection with promising ones being studied experimentally. Following are results for some of the shuttles that have been investigated.

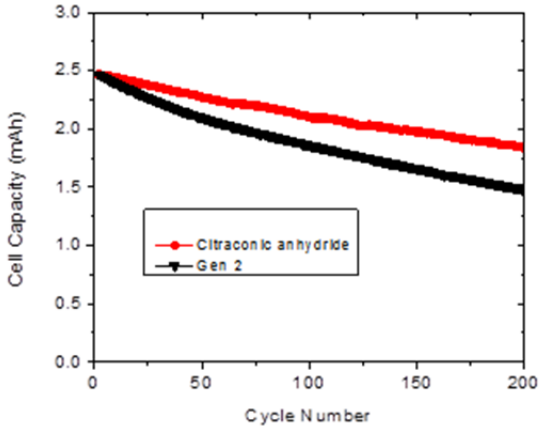

Figure VI - 130: Cell performance for citraconic acid showing improved cycling

Ortho-6,7-dimethoxy-1,1,4,4-tetramethyl-1,2,3,4-tetrahydronaphthalene. DFT methods were used to examine the oxidation potential and decomposition reactions of a new fused ring shuttle ortho-6,7-dimethoxy-1,1,4,4-tetramethyl-1,2,3,4-tetrahydronaphthalene (OFDDB). Ortho methoxy groups make the shuttle more polar. Steric repulsion between methoxy groups causes a higher oxidation potential than DDB because one methoxy group is rotated out of the plane of the ring and cannot contribute electrons to the ring via resonance, whereas both methoxy groups are coplanar in DDB. The methoxy groups of both shuttles are coplanar with the ring in the cation radical.

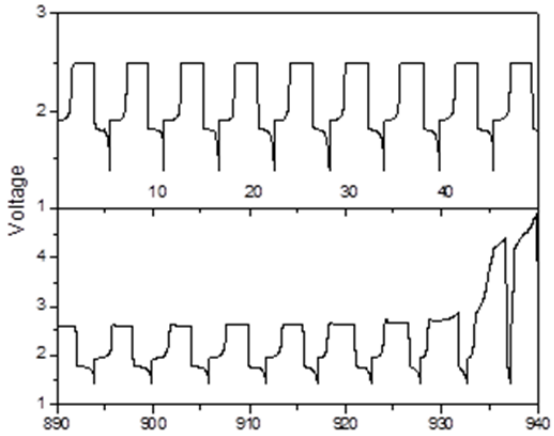

Figure VI - 131: Voltage profile as a function of time (in hours) of LiFePo4/LTO cell at 100% overcharge condition (electrolyte containing 0.4 M OFDDB in the Gen2 electrolyte)

Experimentally, the redox potential of OFDDB is in agreement with theory. The negative voltage sweep does not show any significant peaks indicating good stability of the redox shuttle on the low voltage range. The fused ring structure and increased dipole moment significantly improve the solubility of the shuttle compound. The OFDDB can survive over 150 overcharge cycles (100% overcharge; more than 900 hours) as shown in Figure VI - 131 at a relatively high charge rate for a $LiFePO_4$ based cathode materials. The OFDDB shuttle provides a promising new platform for a variety of new shuttles by simple molecular engineering. Replacement of the electron-rich methoxy groups with other electron-poor functional groups can tune the oxidation potential to create new shuttles for overcharge protection of high voltage cathode materials.

1-(2,2,2-trifluoroethoxy)-4-methoxy-2,5-di-tert-butylbenzene. DFT methods were used to examine the oxidation potential and other properties of a potential redox shuttle 1-(2,2,2-trifluoroethoxy)-4-methoxy-2,5-di-tert-butylbenzene (F3-DDB). This molecule has less symmetry compared to the previously studied shuttles DDB (1,4-di-t-butyl-2,5-dimethoxybenzene) and F6-DDB (bis-(2,2,2-trifluoroethoxy)-2,5-di-tert-butylbenzene). The structures are illustrated in Figure VI - 132. The calculated oxidation potential of F3-DDB is 4.02 V in good agreement with the experimental value of 4.09 V measured as part of this study. Calculated spin densities suggest that the less symmetric F3-DDB is slightly more prone to radical attack than the symmetric DDB and F6-DDB. Decomposition pathways were also examined. F3-DDB has three exergonic side arm reactions, F6-DDB has two and parent DDB has one. All investigated have large activation barriers so they are unlikely to decompose. However, decomposition could be catalyzed by transition metal sites on the electrode surface.

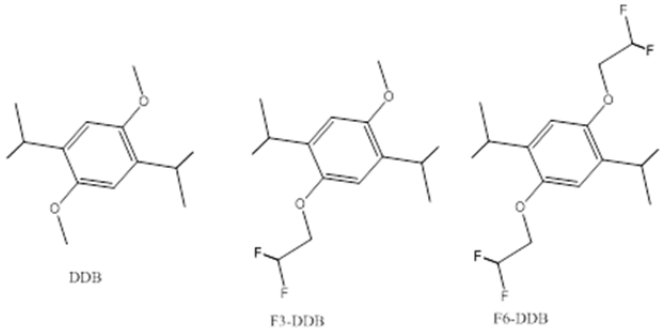

Figure VI - 132: DDB and fluorine modified DDB redox shuttles

The F3-DDB compound was synthesized using a commercially available precursor for testing as a redox shuttle. The introduction of –OCH2CF3 group increase the oxidation potential compared to DDB. The compound was characterized using NMR. F3-DDB also showed improved solubility in carbonate-based electrolytes due to the introduction of the fluorinated alkoxy group.

Quaterphenyl: The stability of another candidate. Quaterphenyl was investigated using DFT. Quaterphenyl can undergo anodic polymerization in which two cation radicals bond to form a "sigma" dication dimer followed by slow loss of two H+ ions to form octaphenyl. From theory the free energy change for 2 quaterphenyl cation radicals to form a dication dimer is uphill by 1.3 eV. The oxidation potential of octaphenyl is slightly lower than that of quaterphenyl which means that octaphenyl can oxidize more easily and attack another cation radical and continue the polymerization process. However, octaphenyl cation radical has decreased spin on external carbons making it less reactive. From theory, if H radicals are available, it is thermodynamically favorable for quaterphenyl to break down into biphenyl and benzene. The quaterphenyl cation radical can also form an adduct with EC, but the free energy change is uphill by about 2.4 eV. The dication dimer can also form an adduct with EC, but this leads to fragmentation into two quaterphenyl species, one of which is bonded to EC. Quaterphenyl cation radicals can break down into cation and radical fragments or cation radical and benzyne fragments. In the absence of additional radicals, quaterphenyl is expected to have high oxidative stability and could potentially be a viable redox shuttle candidate.

Conclusions and Future Directions

The results obtained during the past year have shown how advanced QC methods can be used to successfully screen molecules as candidates for additives for advanced electrolytes in Li-ion batteries. Some of these candidate molecules that have been identified in these studies have been explored experimentally for their performance in Li-ion batteries. The calculations have been used to calculate the reduction and oxidation potentials of potential additives and to calculate decomposition pathways. This information has been used to help screen the new additives for optimal reduction/oxidation potentials and for needed stability or favorable protective SEI film formation. The development of electrolyte additives for SEI formation and overcharge protective is important for improving the safety and lifetime of Li-ion batteries.

FY 2013 Publications/Presentations

1. "Electrolytes - Advanced Electrolyte and Electrolyte Additives," *DOE Annual Peer Review Meeting*, May 13-17, 2013, Washington, DC.
2. W. Weng, Y. T. Tao, Z. Zhengcheng, Paul C. Redfern, L. A. Curtiss, K. Amine, "Asymmetric Form of Redox Shuttle Based on 1,4-Di-tert-butyl-2,5-dimethoxybenzene," *J. Electrochem. Soc.,* **160**, A1711-A1715 (2013).
3. Z. C. Zhang, L. B. Hu, H. M. Wu, W. Weng, M. Koh, P. C. Redfern, L. A. Curtiss, K. Amine, "Fluorinated electrolytes for 5 V lithium-ion battery chemistry," *Energy and Environmental Science,* **6**, 1806-1810 (2013).
4. Z. C. Zhang, L. B. Hu, H. M. Wu, W. Weng, M. Koh, P. C. Redfern, L. A. Curtiss, K. Amine, "Fluorinated electrolytes for 5 V lithium-ion battery chemistry," *Energy and Environmental Science*, **6**, 1806-1810 (2013).

VI.D.2 Sulfone Liquids and Sulfate/Triflate Solids for High Voltage Electrolytes (ASU)

C. Austen Angell
Arizona State University

Department of Chemistry and Biochemistry
Tempe, AZ 85287
Phone: (480) 965-7217; Fax: (480) 965-2747
E-mail: caa@asu.edu

Start Date: May 2010
Projected End Date: December 2013

Objectives

- To complete study of sulfone and sulfone-carbonate based electrolytes for high voltage cathode cells.
- To demonstrate the possibility of alternative electrolytes that are less likely to have capacity- limiting side reactions
- Complete the development of amorphous metal organic frameworks (MOF) nanoporous membrancs as electrolyte supports.

Technical Barriers

Technical barriers to development of sulfone electrolytes stable to high voltage cathodes lie in the unexpected inability of all-sulfone solutions to withstand high voltage cathodes, indicated by preliminary cyclic voltammetry (CV) studies on in-house fabricated LNMO cathodes. It appeared to be due to an inability to establish a suitable SEI between cathode material and the solution. Intrinsic oxidative stability, which seemed so high at the manganate cathode, and platinum cathode, had not been found at LNMO spinel cathode. For success, it seemed SEI-forming additives need to be developed.

Concerning the alternative solvent-free electrolytes that were to be investigated, the barriers were mainly those of synthesis of new concept inorganic plastic crystals with high alkali cation mobility. The preliminary indications were that these might have high enough conductivities to replace the liquid electrolytes. However, problems of purity and validation of conductance mechanism, remain to be solved.

For amorphous and glassy MOF studies, there are technical barriers to be overcome in measuring accurately the available internal surface areas, and in changing the compositions so as to generate high conductivities and, in particular, to obtain single alkali ion conductivities of favorable magnitudes.

Technical Targets

- Finding suitable co-solvents and additives for sulfone based liquid electrolytes, and executing half-cell tests to evaluate their performances.
- Finding novel physical systems for electrolytes in which mobile species are the alkali cations, targeting inorganic ionic liquid and plastic crystal systems.
- For glassy MOFs, finding the conditions for reducing the mechanical fragility of the monolithic glassy films, and finding the conditions for optimizing the alkali ion conductivity.

Accomplishments

- With new battery cycler equipment, half-cell tests have been made on cathodes using BATT Program- supplied LNMO cathode sheets. Excellent cycle life (2.9 mAh/g loss over 100 cycles) with 99% coulombic efficiencies have been obtained using a mixed sulfone (EMS)-carbonate (DMC) solvent with $LiPF_6$ electrolyte. Furthermore, similar or better performance has been demonstrated at the high power LTO cathode. However, *all*-sulfone solvents have been eliminated as candidates.
- For plastic crystals alkali ion conductors, where problems with completeness of reactions have been encountered, completely revamped synthetic procedures have been developed.
- For glassy MOFs, compositions that are analogs of sodium ion conducting minerals have been developed, but conductivities have been disappointing. High conductivities of tetrahedrally linked small chain polyethers containing LiTFSI have been recorded.

✧ ✧ ✧ ✧ ✧

Introduction

Electrolytes for high voltage cells. The original objectives of this project emphasized a search for

electrolytes that might be able to avoid the side reactions that afflict the current generations of lithium batteries that incorporate high voltage cathodes, such as the high rate-capable LNMO spinel cathode. Electrolytes based on molecular solvents that were believed to be the most resistant to oxidation of all, were being investigated. These were the sulfones, the known high oxidative stability of which was attributed to the character of the dipolar group of the molecule (the sulfone group). However, after finding an all-sulfone solvent electrolyte that seemed to behave very well at the graphite anode, apparently intractable problems with stability at the cathode were encountered. The cathode half-cells could not be charged beyond the first stage, and evidence of gaseous products was found. This implied that the alkyl groups comprising the remainder of the molecules were being attacked, and so implied that a favorable SEI (that must be invoked to explain the success of the intrinsically more oxidizable carbonate solvent based electrolytes) was not being formed. Success in improving cycle life of high voltage cathodes by incorporation of phosphite additives, had been reported from by Xu at ARL, indicating that the only route to success for sulfones would be through the use of additives. This was deemed contrary to the research group strengths, and a new approach, seeking a quite different solution based on removing all oxidizable elements and focusing on single ion conductors, such as those bringing limited success (at expense of high current) to glassy electrolyte technologies, was substituted, perhaps prematurely.

This lead to the development of a quite new class of solid electrolytes that, in principle, could provide the answer to many of the problems that are currently afflicting the field of high voltage cathode electrochemistry. These were reported on in some detail in the 2012 annual report, and remain in focus.

However, the perceived failure of the original aims of the proposal (to develop high voltage sulfone solvent-based electrolytes) was not fully accepted, and new equipment for cell testing, purchased for new system evaluation, was available in this third year for their further investigation, using cathode material supplied under the BATT program. The favorable outcome of these further studies is reported on in detail in the present report.

Approach

Electrolytes. (i) sulfone-based electrolytes. Sulfone electrolytes both of all-sulfone and sulfone-carbonate hybrid varieties, which had seemed to have failing behavior from the initial CV studies, have been resurrected after the performance of half-cell studies using a new battery tester purchased early in the current year. Half-cell charge/discharge cycles are performed using both types (all sulfone, and sulfone- carbonate [EMS-DMC]) of electrolytes, over 100 cycles. These compare well with the same tests using the ($LiPF_6$ in EC:DMC 1:1) electrolyte, over 100 cycles (see below).

In view of new, favorable, results with the ASU hybrid electrolyte, in half-cells with the newly-provided LNMO cathode sheets (from Hydro-Quebec under arrangement with the BATT Program), further tests of half-cells using graphite electrodes, also supplied by Hydro-Quebec, were suggested. Finally, half-cell 100 cycle tests need to be extended to the 1.5 V "safe" LTO anodes.

Then tests of 100 cycle performance at LMNO cathode need to be made for the EMS-DMC -based electrolyte containing molecular and ionic additives, in part provided by collaborating laboratory personnel (Kang Xu at ARL).

(ii) New generation solid state alkali cation conducting electrolytes. As an alternative to using liquid electrolytes with oxidizable carbon-containing groups, all-inorganic materials in which alkali cations are the least strongly bound elements, have been sought. Alternative to alkali-metal conducting glasses, systems with low melting inorganic salts, or systems in which there is rapid ion rotation within a crystal lattice (rather than alkali cation migration alone), have been sought.

(iii) Nanoporous electrolyte supports. A successful approach to synthesizing nanoporous network glasses, developed in the 2012 period, is further developed by varying choice of strut and linker, including compositions to mimic ceramic alkali ion conductors. Evaluation of reliable conductivities has been problematic because of the poor mechanical strength of the glasses. Much effort is invested in improving mechanical properties.

Results

Results for each of the three components of the Technical Targets section are reported but most attention is devoted to results from the successful electrolytes for high voltage cathode and high power anode findings.

Electrolytes. (i) sulfone-based electrolytes. The electrochemical window for the sulfone-carbonate with $LiPF_6$ (1M) solute is shown in Figure VI - 133, where it is seen to be a clean 6.0 V wide when allowance is made for the scan rate.

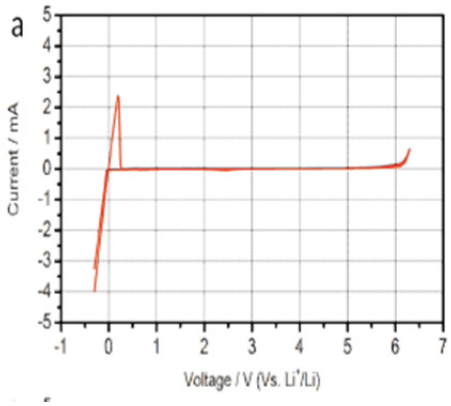

Figure VI - 133: Electrochemical window for EMS:DMC ($LiPF_6$ 1M)

The derivative dQ/dV for the half-cell with the LNMO cathode with reference Li+/Li is shown in Figure VI - 134. The two stages of the oxidation, and reduction on the negative sweep are clearly differentiated. The coulombic efficiency is shown in the lower panel of Figure VI - 134, and is seen to reach ~100% after about 20 cycles.

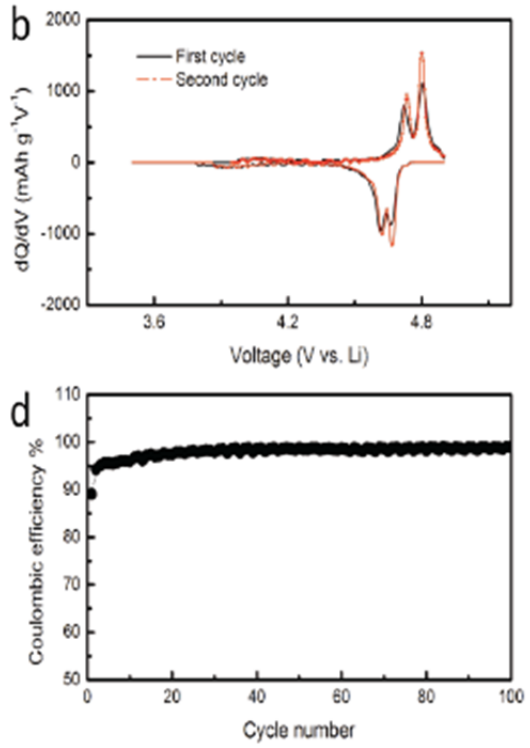

Figure VI - 134: (Upper) dQ/dV for LNMO high voltage cathode vs. Li+/Li, (Lower) Coulombic efficiency vs. cycle number showing ideal behavior after 20 cycles

Capacity retention in the half-cell with EMS-DMC/1M $LiPF_6$ as an electrolyte, is almost the equal of the half-cell with the standard electrolyte, while offering greater protection against thermal runaway in event of battery failure. The oscillatory behavior of the charge/discharge capacity in four cycle repeats is shown in the blow-ups to Figure VI - 135. The excursions appear to be increasing with increasing cycle number.

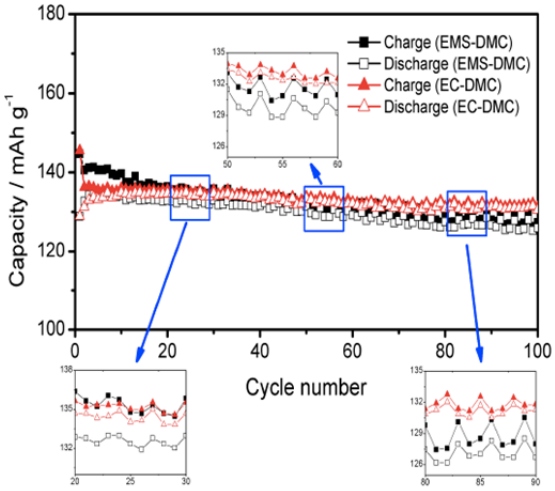

Figure VI - 135: Superposition (on expanded scale) of capacity retention plots for LNMO half cell with EMS:DMC($LiPF_6$ 1M) electrolyte and with standard EC:DMC($LiPF_6$ 1M) electrolyte

Studies at the anode. For successful cells, the cathode quality needs to be matched with anode quality. Figure VI - 136 shows the almost ideal behavior of the highly conducting LTO anode with the present electrolyte which would enable 3.5 V cells. To realize a full 4.7 V battery, the success with the LNMO and LTO electrodes has to be matched by success at the Graphite (or equivalent) anode.

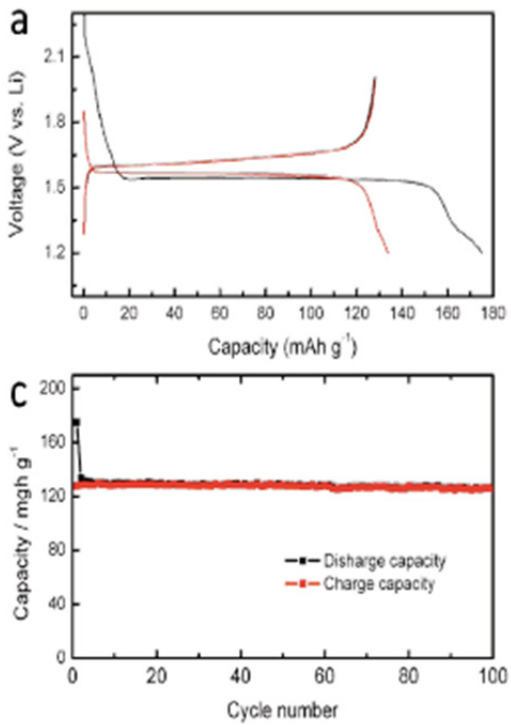

Figure VI - 136: Half-cell tests at LTO anode: (Upper) Half-cell voltage profiles for charge and discharge vs state of charge for LTO high power anodes Li+/Li, (Upper) Charge and discharge capacities in relation to cycle number, showing almost ideal behavior

Unlike the standard EC-DMC electrolyte, the sulfone-carbonate does not form a stable SEI at the graphite electrode, without additives. A vinyl carbonate (VC) additive was found, in earlier work with sulfones, to provide a stable SEI but, to date, VC has not been tested with the present electrolyte.

(ii) New generation solid state alkali cation conducting electrolytes. In order to reduce the risk of errors due to traces of unreacted acid (detected by NMR) in plastic crystal formulations of novel lithium ion conductors (2012 annual report), a complete revision of the preparative procedures has been undertaken. New findings will be reported in future publications.

(iii) Nanoporous electrolyte supports. Some new results on alkali metal salt conductivities in tetrahedral nets containing flexible struts and showing ionic conductivities comparable with the best linear "salt in polymer" solid electrolytes of Armand and co-workers, (red dashed line for 100ºC) are shown in Figure VI - 137.

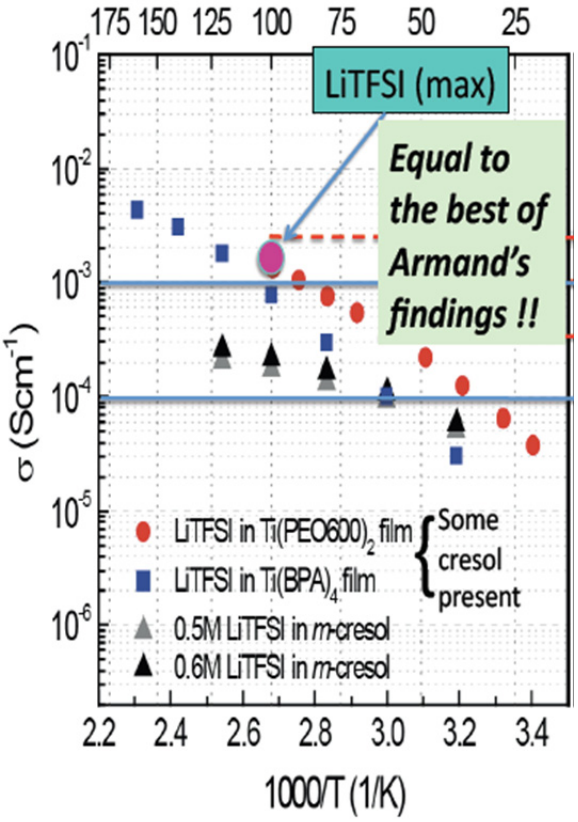

Figure VI - 137: Conductivity of new semi-flexible tetrahedral net, using PEO 600 struts and containing LiTFSi in the interstices. Comparison is made with findings of Armand and co-workers on LiTFSI in high MW linear PEO polymers

Conclusions and Future Direction

It is evident, from Figure VI - 134, Figure VI - 135 and Figure VI - 136, that with the high quality of LNMO cathode material presently available to the BATT Program investigators, the 3.5 V high safety battery can be implemented with both standard carbonate and the new sulfone-carbonate electrolytes, with anticipation of less than 5% capacity loss over 100 cycles, and (in view of recent 500 cycle studies by Batelle NW lab), probably less than 20% capacity loss over 1000 cycles. Both sulfone-carbonate and all-carbonate-based cells have substantial conductivity and cost advantages over the recently reported fluorinated carbonate type electrolyte cells from the Amine group at Argonne. The sulfone-based system has a safety advantage due to diminished thermal runaway propensity.

In future work, this group will explore half-cells with variants of the present sulfone-based electrolyte incorporating 15 mol% of the smaller but higher-melting dimethyl sulfone DMS; earlier work showed

that it forms a low-melting eutectic with EMS. This should lead to increased protection against low temperature crystallization, coupled with some increase in conductivity at the same weight fraction of co-solvent carbonate.

Explorations of crystallization resistance and effect of increased co-solvent content and changes of carbonate co-solvent formula from DMC to the asymmetric ethylmethyl carbonate will also be investigated. Finally to be included will be studies with additional SEI-forming co-solvents that are not to be disclosed here.

FY 2013 Publications/Presentations

1. C. Austen Angell, "Electrolytes and separators for high voltage Li-ion cells," *2012 DOE Annual Peer Review Meeting*, May 13-17. 2013, Washington, DC.
2. Seung-Yul Lee, Kazuhide Ueno, and C. Austen Angell, "Lithium salt solutions in mixed sulfone, and sulfone-carbonate, solvents: a Walden plot analysis of the maximally conductive compositions," *J. Phys. Chem. C*, **116**, 23915-23920 (2012).
3. Leigang Xue, Kazuhide Ueno, S.-Y. Lee and C. Austen Angell, "Performance of sulfone, and sulfone-containing, solvents at lithium ion battery electrodes, including the LiNiMnO high voltage cathode," *J. Electrochem. Soc.* (submitted).

VI.D.3 Bifunctional Electrolytes for Lithium-ion Batteries (CWRU)

Daniel Scherson
Case Western Reserve Univ ersity

Department of Chemistry
10900 Euclid Avenue
Cleveland, OH 44106
Phone: (216) 368-5186
E-mail: dxs16@case.edu

John Protasiewicz
Case Western Reserve University
Department of Chemistry
10900 Euclid Avenue
Cleveland, OH 44106
Phone: (216) 368-5060
E-mail: jdp5@case.edu

Start Date: October 2009
Projected End Date: September 2013

Objectives

- Design, synthesize, and characterize physical, electrochemical, and interfacial characteristics of functionalized Li-salt anions containing phosphorus moieties known to impart materials with flame retardant properties (Flame Retardant Ions or FRIONs) and additional functional redox active groups capable of providing overcharge protection (FROPs).
- Develop and implement ATR-FTIR spectroscopic methods for monitoring *in situ* the nature of products generated at Li-ion battery anodes under highly controlled conditions

Technical Barriers

This project addresses the abuse tolerance barriers from the BATT program.

Technical Targets

- Demonstrate superior abuse characteristics compared to a baseline cell: Conoco Philips CPG-8 Graphite/1 M LiPF6+EC:DEC (1:2)/Toda High energy layered (NMC)

Accomplishments

- Several new FRION salts of two different classes were prepared and characterized
- A select number of these FRIONs were analyzed by TGA showing excellent thermal stability and minimal mass loss.
- Precursors to other potential FRIONs were also prepared.
- The electrochemical properties of new FRIONs were examined by cyclic voltammetry (CV) over a wide potential range using Ni working electrodes and differences were noted in their behavior.
- A new approach was developed to gain insight into the structure and composition of the solid electrolyte interphase (SEI) in electrolytes of relevance to lithium ion batteries

✧ ✧ ✧ ✧ ✧

Introduction

The main objectives of this project are to develop rational guidelines for the design and synthesis of new classes of Li-based salts endowed with flame retardant properties. In addition, such bifunctional electrolytes should be weakly coordinating and of low molecular weight, exhibit low toxicity, promote formation of low impedance SEIs and from an economic viewpoint be relatively inexpensive.

Approach

The strategy being implemented involves the chemical functionalization of anions of Li salts known to improve the performance of Li-ion batteries with covalently linked groups displaying flame retardant and/or overcharge protection attributes. The ultimate goal is to establish guidelines for the rational design and synthesis of optimized FRIONs and FROPs based on the analysis of results of testing in actual Li-ion batteries. Spectroscopic characterization of the products generated at Li-ion battery anodes and of the SEIs formed therein is pursued using *in situ* ATR-FTIR.

Results

Synthesis. Two categories of precursors have been synthesized during this year, namely: diphosphinato

catechol (DPC) and 2,3-dihydroxy-1,4-diphosphinato napthalene (DPN). These two classes of compounds are based upon the use of an organo-phosphorus containing di-anionic bidentate ligand which chelates to either a boron or phosphorus atom center. Scale up of the previously reported FRION Li[B(DPC)(oxalato)] (Figure VI - 138, middle) has been completed by Argonne National Laboratory based on this procedure.

New DPC based FRIONs synthesized and characterized include $Li[B(DPC)F_2]$ (Figure VI - 138, top) and $Li[P(DPC)_3]$ (Figure VI - 138, bottom). $Li[B(DPC)F_2]$ contains two units of organophosphorus per anion. It is prepared using one molar equivalent of DPC and $LiBF_4$. The FRION $Li[P(DPC)_3]$ was synthesized by reacting three molar equivalents of DPC with PCl_5 in the presence of a lithium source. The $Li[P(DPC)_3]$ possesses a negatively charged phosphorus atom center, which is analogous to the atom center of $LiPF_6$. $Li[P(DPC)_3]$ contains six units of organophosphorus per anion. The DPN based FRION $Li[B(DPN)_2]$ was synthesized from DPN and boric acid in the presence of a lithium source (Figure VI - 140). The $Li[B(DPN)_2]$ contains four units of organophosphorus per anion.

The structure of $Li[P(DPC)_3]$ was determined using single crystal X-ray diffraction (XRD) methods and is shown in Figure VI - 139. As expected, the phosphorus atom center is octahedral. The DPC ligands bind to the phosphorus atom center in a bidentate fashion. The lithium atom center is tetrahedral and coordinates to four phosphoryl (P=O) oxygen atoms. The negative charge formally located on the phosphorus atom should be delocalized via resonance on the aromatic ring. This effect should be enhanced due to the electron withdrawing nature of the phosphoryl group attached to the benzene ring.

Thermogravimetric Analysis (TGA) was performed on $Li[B(DPC)F_2]$ and $Li[P(DPC)_3]$ and the results are shown in Figure VI - 141. Both salts are stable at the normal operating temperatures of Li-ion batteries. The $Li[P(DPC)_3]$ is thermally stable at temperatures below 150°C. When exposed to higher temperatures, the salt maintains approximately 60% of its original mass after decomposition. The $Li[B(DPC)F_2]$ is stable at temperatures below 270°C, and maintains 67% of its original mass.

Although attempts to prepare other types of FRIONs were unsuccessful, new precursors were obtained in the process. These include phosphonic acid incorporating both H and isopropyl groups to reduce symmetry and thus impart the resulting FRIONs increased solubility and also novel phosphorus containing biphenol precursors.

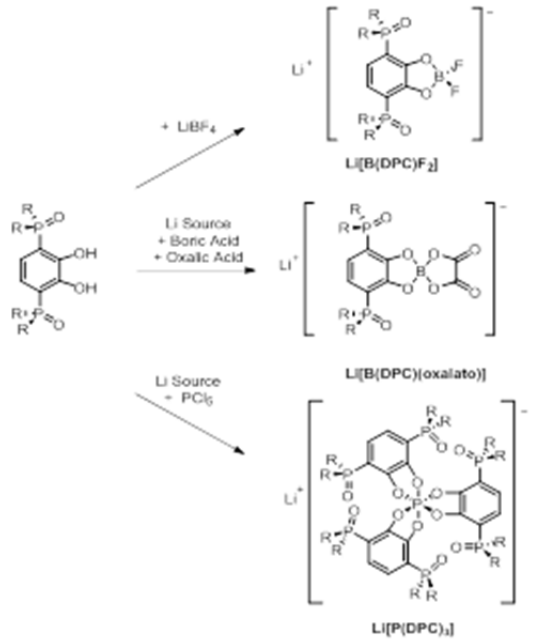

Figure VI - 138: Synthesis of $Li[B(DPC)F_2$, $Li[B(DPC)(oxalato)]$ and $Li[P(DPC)_3]$

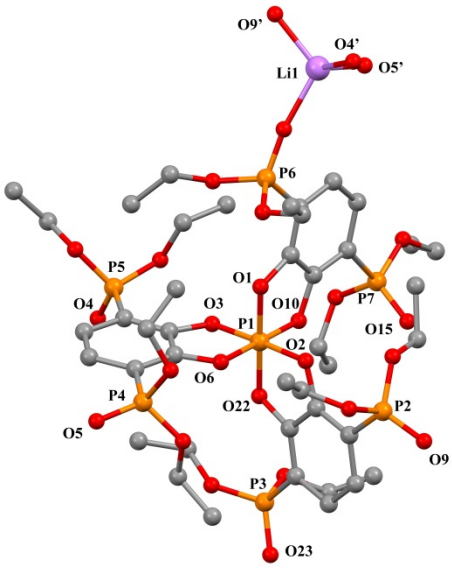

Figure VI - 139: Single Crystal X-Ray Structure of $Li[P(DPC)_3]$

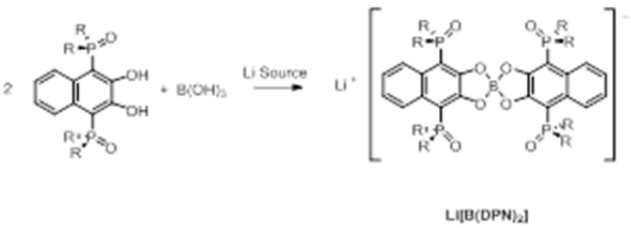

Figure VI - 140: Synthesis of Li[(DPN)2]

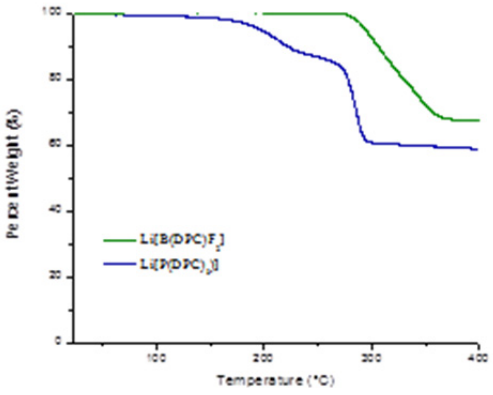

Figure VI - 141: TGA of FRION Salts

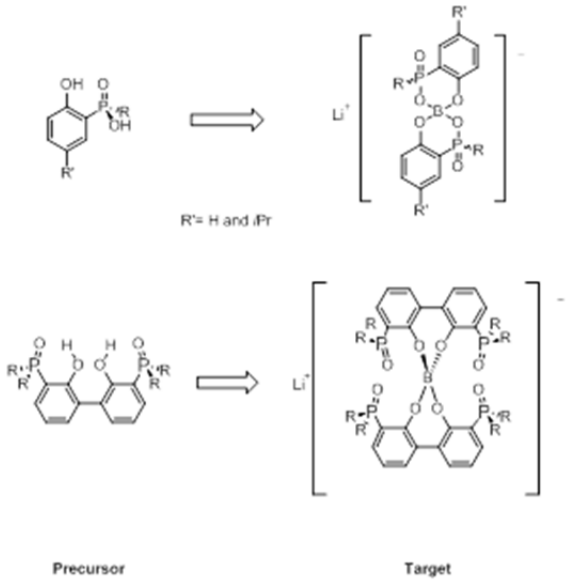

Figure VI - 142: Synthesized Novel Precursors with Target Frions

Electrochemistry. At present there exists no rational guidelines for correlating the properties of the SEI formed at the anode-solution interface during the initial charge discharge cycles of Li-ion batteries with those of both the solvent and the anion of the Li salt dissolved therein. The strategy that has been implemented toward unveiling such correlations involves systematic studies of structurally related materials using CV as a diagnostic tool. To this end, measurements were performed with some of the newly synthesized materials in deareated EC/EMC(50/50 by volume) using a Ni wire as the working electrode and a piece of metallic Li as the counter-reference electrode. In all cases, the materials were dissolved to saturation. The voltammetric curves shown in Figure VI - 143, recorded as a scan rate of 10 mV/s, illustrate some of the changes induced by the structure of the material. In particular, the B-containing materials (see panels B and C, Figure VI - 143) display features reminiscent of those obtained in the standard 1M $LiPF_6$ in the same solvent mixture (see Panel A in this figure). In stark contrast, the response of the phosphorous analogue yielded a resistive type behavior (see panel D, Figure VI - 143) over a wide potential range, which is indicative of the formation of a different film on the Ni electrode derived from the reduction of the anion.

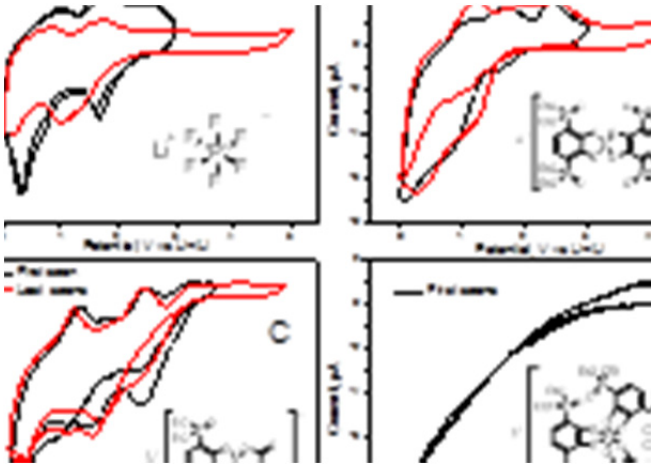

Figure VI - 143: Cyclic voltammetric curves recorded with a Ni wire electrode in EC/EMC(50/50 by volume) solutions at a scan rate of 10 mV/s, for solutions containing the materials shown in the insets

***In situ* spectroscopy**. Analyses of numerous experiments aimed at acquiring *in situ* FTIR data of the film formed upon electrodeposition and stripping of Li on an inert substrate surface both in the attenuated total reflection (ATR) and internal reflection absorption (IRAS) modes, failed to reveal the presence of spectral features attributable to species other than those of the solvent mixture employed. It may be concluded on this basis that: i. the products of the reaction are not IR active and/or ii. the sensitivity of the techniques are not sufficient to detect otherwise IR active products due to their very small cross sections. A new approach is being currently pursued involving deposition of a very thin boron doped diamond layer on top of the diamond window of the ATR-FTIR cell designed under this program which will serve as the electrode onto which metallic Li will be deposited. As evidenced by the CV data collected for B doped diamond films supported on glass, shown in Figure VI - 144, this inert surface can promote the reversible deposition and stripping of Li metal.

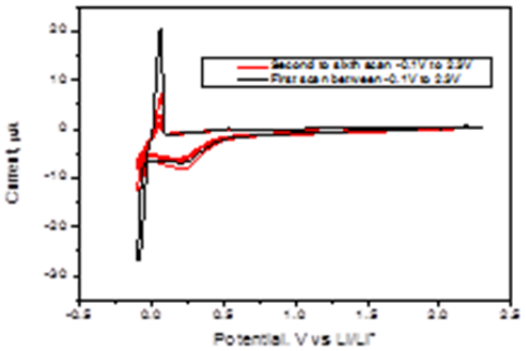

Figure VI - 144: Series of cyclic voltammetric curves of a boron-doped diamond film supported on glass in 1 M LiPF6 in EC/EMC(50/50 by volume) using Li metal as counter reference electrode, recorded at a scan rate of 10mV/s

Conclusions and Future Directions

Novel DPC and DPN FRIONs containing multiple units of organophosphorus per anion have been synthesized and characterized. This expanded library of compounds features FRION salts that incorporate either a negatively charged boron or phosphorus atom as the anion center. The structure of $Li[P(DPC)_3]$ was determined using single crystal XRD. $Li[B(DPC)F_2]$ and $Li[P(DPC)_3]$ were analyzed by TGA and found to be stable at normal operating temperatures of lithium-ion battery and to maintain a high percentage of their original weight after being exposed to high temperatures. Details regarding the synthesis of the most promising FRION prepared to date were made available to scientists at Argonne National Laboratories who scaled up the procedure to hundreds of grams to be made the material available to other agencies for testing.

Future directions include optimizing electrochemical and flame retardant performance of FRION salts, as well as maximizing the solubility of FRIONs. Arrangements will be made with ANL and LBNL for these new compounds to be thoroughly evaluated in coin cells or other formats. The electrochemical and thermal properties of possible FRION decomposition products will be analyzed to better understand the fate of FRIONs in a battery system. As always attention will be paid to structure-function relationships.

Vendors have been contacted for the design and construction of a novel ATR-FTIR optical attachment compatible with the *in situ* spectroscopic cell now available in our laboratories to conduct measurements of a boron-doped diamond electrode. This configuration may be regarded as ideal to detect the elusive spectral properties of the passive film formed on nascent Li metal in contact with electrolytes of relevance to Li-ion batteries.

FY 2013 Publications/Presentations

1. "Bifunctional Electrolytes for Lithium-ion Batteries," *DOE Annual Peer Review Meeting*, May 13-17, 2013, Washington, DC.
2. Rectenwald, M.F.; D. Scherson; and J. Protasiewicz, "Bifunctional Electrolytes for Lithium-Ion Batteries," *Research ShowCASE*, April 13, 2013, Cleveland, OH.
3. Rectenwald, M.F.; Shaffer, A. R.; and J. Protasiewicz, "Bifunctional Electrolytes for Lithium-Ion Batteries," *American Chemical Society Meeting in Miniature*, March 13, 2013, Cleveland, OH.
4. Michael Rectenwald, Andrew R. Shaffer, Joshua Gaffen, Nihal Deligonul, Daniel A. Scherson, and John D. Protasiewicz "FRIONs: Flame Retardant Ions for Safer Lithium Ion Batteries," *National ACS Meeting*, Sept. 11, 2013, Indianapolis, IN.

VI.D.4 Interfacial and Bulk Properties and Stability (LBNL)

John B. Kerr
Lawrence Berkeley National Laboratory

Environmental Energy Technologies Division
1 Cyclotron Road, MS 62R0203
Berkeley, CA 94720
Phone: (510) 486-6279; Fax: (510) 486-4995
E-mail: jbkerr@lbl.gov

Start Date: October 2009
Projected End Date: September 2013

Objectives

- Determine the role of electrolyte structure upon bulk transport and intrinsic electro-chemical kinetics and how it contributes to cell impedance (Energy/power density).
- Determine chemical and electrochemical stability of electrolyte materials to allow elucidation of the structure of and the design of passivating layers, e.g., solid polymer electrolyte (SEI).

Technical Barriers

This project addresses the following technical barriers:

- Low power and energy densities, including fast charge capability.
- Poor cycle and calendar life.
- High manufacturing cost.
- Safety

Technical Targets

- Determine the contribution to the interfacial impedance of the salt structure in terms of reactivity versus intrinsic electrode kinetics.
- Determine the contribution to the interfacial impedance of the solvent or polymer structure in terms of reactivity versus intrinsic electrode kinetics.
- Determine the contribution to the interfacial impedance of the physical properties of the electrolyte – liquid vs. gel. vs. SEI.

Accomplishments

- Scaled up polysulfone single ion conductor (SIC) synthesis to 20g scale.
- Improved degree of functionalization of polysulfone synthesis to allow wider variation of ion exchange capacity in SICs.
- Scaled up polyether synthesis procedures to 20g scale.
- Scaled up functionalization of carbon to 20g levels.
- Prepared and tested TiO_2 nanocable anode materials as test of surface functionalization methods.
- Material preparation methods improved to a level of reproducibility that allows optimization of electrode fabrication to proceed.

✧ ✧ ✧ ✧ ✧

Introduction

The choice of electrolyte used in lithium ion batteries presents significant challenges from the point of view of charge transport as well as electrochemical and chemical stability. The impedances introduced by the electrolyte are frequently the major source of failure of the battery and consist of the bulk ohmic resistance (conductivity), concentration polarization (transport properties) and interfacial impedance (intrinsic electrochemical kinetics of charge transfer at the electrodes). Most of the attention of electrolyte researchers over the years has focused upon the ohmic resistance (conductivity) of the bulk electrolyte yet this impedance is usually smaller than that due to concentration polarization (especially in composite electrodes) and much smaller than that of the interface. Both interfacial and concentration polarization impedances are critical barriers to the deployment of lithium ion batteries in traction vehicles. In fact, without a solution to the concentration polarization issue, a rapid charge of a high energy battery with a composite electrode will be impossible.

Single-ion polyelectrolyte lithium conductors possess the solution for many of the problems with present electrolytes. They can be used with no liquid solvent thereby reducing the safety problem. They can be prepared and deployed in ways that avoid many of the reactivity issues both in the bulk of the electrolytes

and at the interfaces and hence offer a solution to the lifetime problem. Because they possess a unity transference number, there is no concentration polarization through the composite electrodes. Thus, provided the conductivity is in excess of 10^{-4} S/cm, the SICs can facilitate the use of thicker composite electrodes thereby leading to higher energy and power densities. Without such a capability, rapid charging is not possible for high energy batteries suitable for vehicular use. They further appear to have application to the operation of large volume expansion electrodes where concentration gradients have a considerable negative effect on cycling.

In past years this group has demonstrated that SIC materials, both dry and as gels, possess the transport properties required both in the bulk separator and in the composite electrodes. However, the interfacial impedance has presented a particular challenge which has been at least partially overcome in the last two years of the project. The progress has been sufficiently encouraging to warrant scale up of the polymer synthesis and composite electrode fabrication to more practical levels that allow for synthesis of sufficient materials to conduct optimization studies of the composite electrodes. This is a necessary requirement for practical application of the materials to practical systems.

Approach

The work involves use of model compounds as well as synthesis of new materials to test hypotheses which may explain battery behavior. Examples include:

- SIC polyelectrolytes (dry polymers and gels) as separators and binders in composite electrodes.
  - Measure transport, chemical and mechanical properties of polyelectrolytes as bulk separators.
  - Measure transport, chemical and mechanical properties of electrode coating inks and coated electrodes
- Different solvents and single ion salts, including polymer gels and solid polymer electrolytes.
- Functionalized surfaces for electrode components to control interfacial impedances
- Use electrode materials with different reaction potentials to determine electrochemical stability.
- Measure thermal and inherent chemical stability of electrolytes.
- Develop chemical analysis methods to assist in improvements in stability and lifetime.

Figure VI - 145 illustrates the types of polymers and functionalized materials that are under study and how they are deployed in practical batty systems. The goal is to provide electrolytes that allow the electrodes to be made as thick as possible in order to maximize the energy density of the cell while also allowing the rates to be maximized.

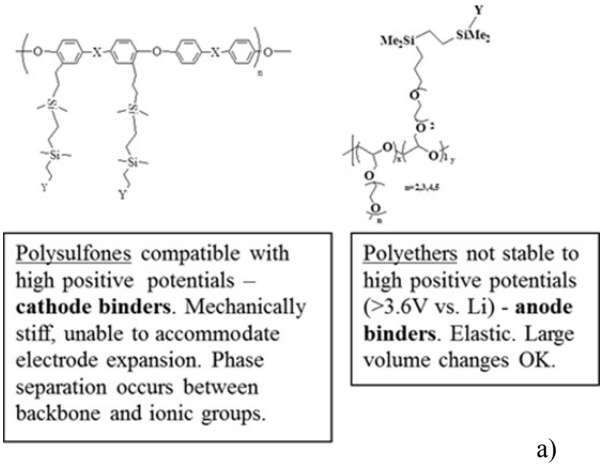

Figure VI - 145: Methods of immobilizing electrolyte anions in lithium ion batteries. (a) Polyelectrolyte ionomers for use as separators and binders; (b) surface modified carbons for incorporation into composite electrodes to control lithium ion concentration

Results

Preparation of Polymer Backbones. Commercially available polysulfone (Udel) material is chemically modified to provide the backbone for gel SICs. The reaction is shown in Figure VI - 146 and the optimization processes are shown in Table VI - 6.

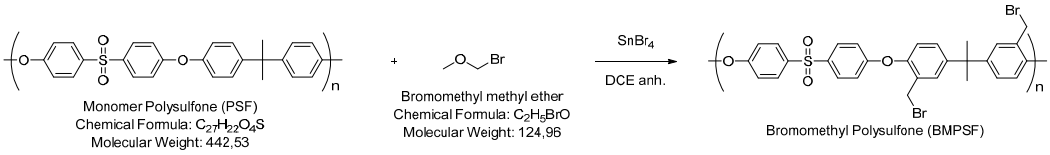

PSF	Bromomethyl methyl ether	Tin(IV) Bromide	1,2-Dichloroethane anhydrous
20 g	20.0 ml	6.0 ml	250 ml
45.19 mmol	220.5 mmol	45.19 mmol	50°C
	(4.9 eq)	(1 eq)	24h

Figure VI - 146: Functionalization of Polysulfone polymer backbone

Table VI - 6: Optimization of polymer functionalization conditions

Ref	CH_3O-CH_2Br	Tin (IV)	Temp.	time	Subs. Rate	Mn[1]	Comment
SG5	5 eq	1 eq	40°C	21h	~168%	~55 kDa	
SG7#1	5 eq	1 eq	Reflux[2]	24h	~199%	~86 kDa	Cross linking
SG7#2	5 eq	1 eq	Reflux[2]	48h	~208%	~94 kDa	Cross linking & burned
SG10	5 eq	1 eq	80°C	24h	~179%		Cross linking
SG12	10 eq	2 eq	60°C	66h	~188%		
SG13	5 eq	1 eq	60°C	6h	~129%		Mixed[3]
SG14	5 eq	1 eq	60°C	14h	~172%		Trace of monomer
SG19	5 eq	1 eq	60°C	24h	~193%		Part of insoluble or cross linking
SG22	5 eq	1 eq	40°C	24h	~161%		
SG27	5 eq	1 eq	50°C	24h	~189%	~75 kDa	

[1] Calculated with kaleïdagraph; Mn_{PSF} ~152 kDa. [2] oil bath at 100°C. [3] large mix of substituted and non-substituted monomer

Table VI - 6 illustrates the issue with polymer synthesis involving cross-linking and overreaction that leads to unusable product. Such problems tend to increase as the process is scaled up and hence considerable effort has been expended on optimizing the reaction as is illustrated by Table VI - 6. The resulting bromomethyl substituted polymer is converted to the SIC by the reactions shown in Figure VI - 147, which shows to synthesis of a fluorosulfonate. The resulting material has good film-forming properties and Figure VI - 148 shows the results of small angle x-ray scattering (SAXS) for such a membrane compared with the SAXS for Nafion®. The SAXS data for PSF-Li shows only small activity as the material has much less fluorine content.

The purpose of the SAXS experiments is to detect signs of phase separation which might account for the better conductivity and interfacial performance observed before when the SIC polymer was prepared as a gel with carbonate solvents. However, it was noted that the polymer dissolved in the usual EC/EMC solvents and hence cross-linking of the polymer is required. This creates a complication in preparation of composite electrodes that will require extensive further study. However, the availability of large amounts of reproducible polymer makes such as study possible where it was not practical before.

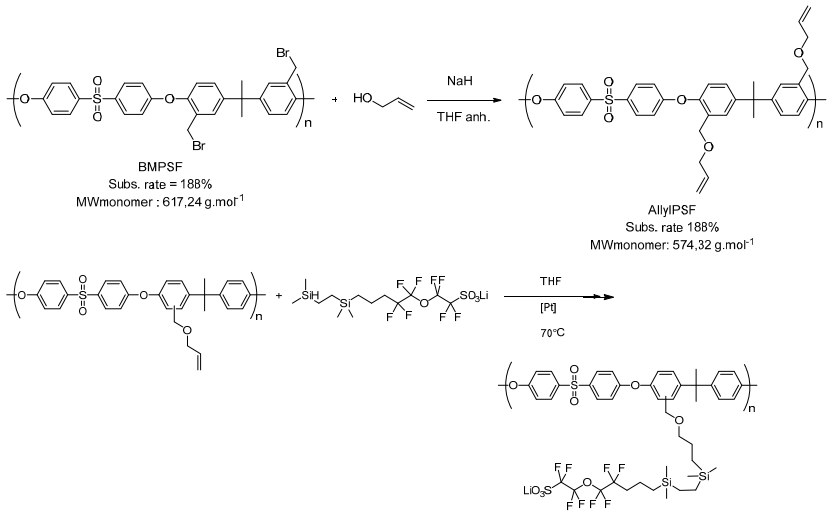

Figure VI - 147: Preparation of Polysulfone substituted with fluorosulfonate groups

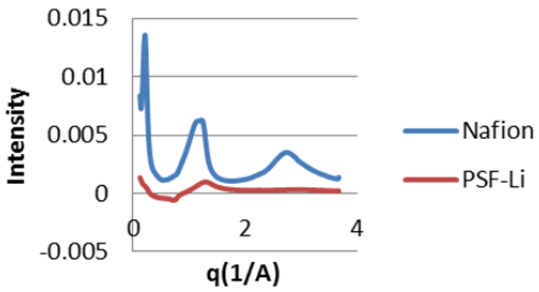

Figure VI - 148: Background subtracted SAXS data for Nafion® and fluoroalkylsulfonate-substituted polysulfone

Similar progress on preparation of the polyether backbones shown in Figure VI - 145 has also uncovered issues. The molecular weight that is achievable with long chain combs is quite low and this is inherent to the polymerization of such materials due to chain transfer in the reaction. This again will require considerable optimization of crosslinking conditions to achieve the mechanical properties desired in both the separator and the composite electrodes.

Surface Modification of Conducting Carbon Components in Composite Electrodes. In an effort to increase the local concentration of ions at the electrode surface, carbon conducting elements have been functionalized by a number of methods. Figure VI - 149 illustrates the concept of functional carbon which is substituted with allyl groups. This can be carried out on a variety of carbon substrates but the best results have been obtained with multiwalled carbon nanotubes (MWCNT). The functionalization step has been scaled up to 30g batches which is more than adequate to allow detailed optimization studies. This process has been monitored closely by means of TGA and FTIR. Figure VI - 149 shows how the allyl groups are used to attach fluorocarbonsufonylimide groups which have been shown to provide the best interfacial behavior. The fluorosulfonate groups can be similarly attached for use in fuel cell electrodes.

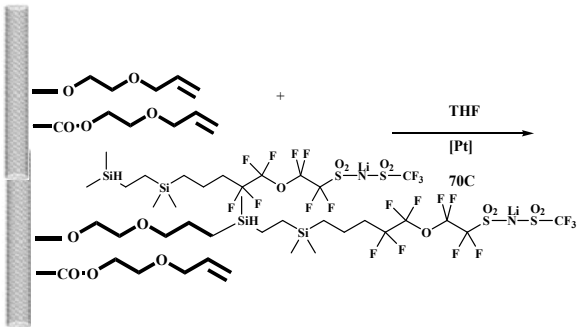

Figure VI - 149: Preparation of carbon modified with fluorosulfonylimide groups

The procedures for preparation of the carbons have been used to prepare new composite electrodes that overcome some of the conductivity limitations of some electrode materials.

Figure VI - 150 shows the synthesis of MWCNT nanocables with TiO_2 and some of the electrochemical properties of these composite electrodes are shown on Figure VI - 151.

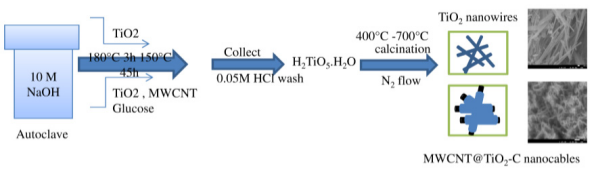

Figure VI - 150: Synthesis of MWCNT@TiO_2 nanocables

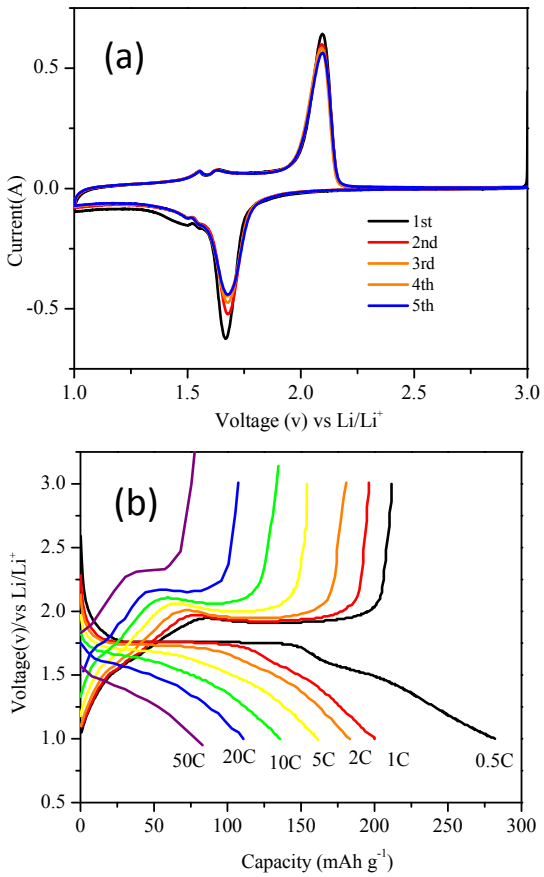

Figure VI - 151: (a) Voltammograms of the CNT@TiO_2-C nanocable electrode at a scan rate of 0.1 mV s-1; (b) The first charge-discharge voltage profiles at different current rates

Conclusions and Future Directions

Generation of electrochemical performance data has been delayed in order to produce sufficient materials of reproducible quality to allow a meaningful optimization study to be carried out. The activities described in this report detail the achievement of this objective. The final year of the project will now involve optimization of composite electrodes with single ion conductor electrolytes to fully demonstrate the advantages of this approach.

FY 2013 Publications/Presentations

1. John B. Kerr, Li Yang, Jianli Cheng and Peter Driscoll, “Electrolytes - R&D for Advanced Lithium Batteries. Interfacial and Bulk Properties,” 2012 *DOE Annual Peer Review Meeting*, May 17, 2013, Washington, DC.

VI.D.5 Development of Electrolytes for Lithium-Ion Batteries (URI)

Brett Lucht
University of Rhode Island

Department of Chemistry
51 Lower College ROAD, Pastore
Kingston, RI 02881
Phone: (401) 874-5071; Fax: (401) 874-5072
E-mail: blucht@chm.uri.edu

Start Date: April 2009
Projected End Date: December 2014

Objectives

- Develop novel electrolytes with superior performance to state of the art (SOA) ($LiPF_6$ in carbonates).
- Develop an understanding of the source of performance fade in graphite/$LiNi_{0.5}Mn_{1.5}O_4$ cells cycled to high voltage (4.8 V vs Li).
- Develop an electrolyte formulation that allows for superior performance of graphite/$LiNi_{0.5}Mn_{1.5}O_4$ cells.
- Synthesize and characterize novel non-fluorinated lithium salts for lithium battery electrolytes.

Technical Barriers

This project addresses the following technical barriers from the Batteries for Advanced Transportation Technologies Research, Development Plan regarding electrolytes: Improving the cell performance, cell life, and cost; Improving the calendar life of lithium ion batteries; Expanding the survival temperature range.

Technical Targets

- Cell performance, life, cost: Calendar life: 40°C, 15 years.
- Survival Temperature Range: -46 to +66°C
- Unassisted Operating & Charging Temperature Range, -30 to + 52°C.

Accomplishments

- Developed an understanding of the role of electrolyte in capacity fade for graphite/ $LiNi_{0.5}Mn_{1.5}O_4$ full cells cycled at moderately elevated temperature (55 °C).
- Designed electrolyte formulations to decrease cell inefficiency (50 % of SOA) and decrease capacity fade (50 % of SOA) for graphite/$LiNi_{0.5}Mn_{1.5}O_4$ full cells.
- Attemmpted to synthesize and characterize novel non-fluorinated lithium salts and test novel electrolytes in graphite/$LiNi_xCo_{1-2x}Mn_xO_2$ cells.
- Completed electrochemical cycling of Si nano-particle electrodes with electrolytes containing added VC or FEC.

✧ ✧ ✧ ✧ ✧

Introduction

While commercial lithium-ion batteries (LIBs) perform well for most home electronic applications, currently available LIB technology does not satisfy some of the performance goals for Plug-in Hybrid Electric Vehicles (PHEV). In particular, currently available LIB technology struggles to meet the 15 year calendar life requirement and suffers rapid fade at elevated voltage (>4.5V) and temperature.

The most extensively used LIB electrolytes are composed of $LiPF_6$ dissolved in organic carbonates. However, $LiPF_6$ based electrolytes have poor thermal stability and performance when cycled to high voltage. Significant energy fading occurs after several years at room temperature and over only a few months at the moderately elevated survival temperature of 66°C. While there are several different factors that limit the thermal stability, calendar life and voltage window of LIBs, the reactions of the electrolyte with the surface of the electrode materials are frequently reported to be the most important.

Approach

Investigate the surface of cathodes and anodes cycled with novel electrolytes, with or without additives, to develop a mechanistic understanding of interface formation and degradation. Develop additives for high voltage (~4.8 V) cathode materials which inhibit performance fade via reduction of Mn dissolution or cathode surface passivation. Use novel synthetic methods to prepare non-fluorinated lithium salts for lithium ion battery electrolytes. Conduct electrochemical cycling of Si-nanoparticle cells with electrolytes containing various quantities of commonly used additives, such as vinylene carbonate (VC) and/or

fluoroethylene carbonate (FEC), to determine optimal electrolyte formulation for silicon anodes.

Results

Capacity fade of graphite/$LiNi_{0.5}Mn_{1.5}O_4$ cells. Due to significant differences in the observed capacity retention and efficiency of Li/$LiNi_{0.5}Mn_{1.5}O_4$ cells compared to graphite/$LiNi_{0.5}Mn_{1.5}O_4$ cells, a detailed analysis of the capacity retention and cycling efficiency of graphite/$LiNi_{0.5}Mn_{1.5}O_4$ cells cycled to high voltage at moderately elevated temperature has been conducted. The cycling performance of graphite/$LiNi_{0.5}Mn_{1.5}O_4$ cells at 25°C is good, but capacity decreases dramatically upon cycling at 55°C, see Figure VI - 152. Independent electrochemical analysis of anodes and cathodes extracted from cells cycled at 55°C suggest that both electrodes have significant capacity loss, although the cathode capacity can be recovered with longer charging times consistent with a significant increase of impedance on the cathode.

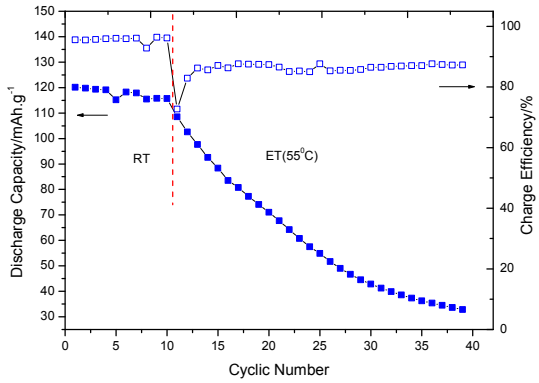

Figure VI - 152: Cycling performance of graphite /$LiNi_{0.5}Mn_{1.5}O_4$ cell at 25°C (RT) and 55°C (ET)

Capacity loss on the graphite anode is typically reported to be due to continuous dissolution/reformation of SEI film during cycling at 55°C. Surface analysis of the graphite anodes after cycling suggests that the anode SEI is changing and becoming thicker, but the changes to the graphite SEI do not explain the significantly poorer performance of graphite/ $LiNi_{0.5}Mn_{1.5}O_4$ cells cycled to 55°C than graphite/$LiCoO_2$ cells. Anodes extracted from graphite/$LiNi_{0.5}Mn_{1.5}O_4$ cells cycled at 55°C and analyzed by ICP-MS, contain 0.06 mg Mn which is approximately 1% of the available Mn from cathode, while fresh anodes and anodes cycled at 25°C contain two orders of magnitude lower concentrations of Mn. The deposited Mn may result in damage to the graphite SEI contributing to the capacity fade of the cell.

Analysis of the cathodes by XPS after cycling at 55°C reveal that the intensity of the Mn 2p peaks are decreased, consistent with Mn dissolution, but C 1s, O 1s, F 1s, and P 2p spectra are very similar (Figure VI - 153), consistent with small changes to the thin cathode surface film composed of electrolyte decomposition products including lithium alkyl carbonates, polyethylene carbonate, and lithium flouride. Changes to the XPS spectra of the PVDF binder are also observed. The C1s peak at 290.4 eV is diminished and the F1s peak is shifted from 687.6 eV to slightly lower binding energy (~ 687 eV), suggesting that the PVDF may be decomposing.

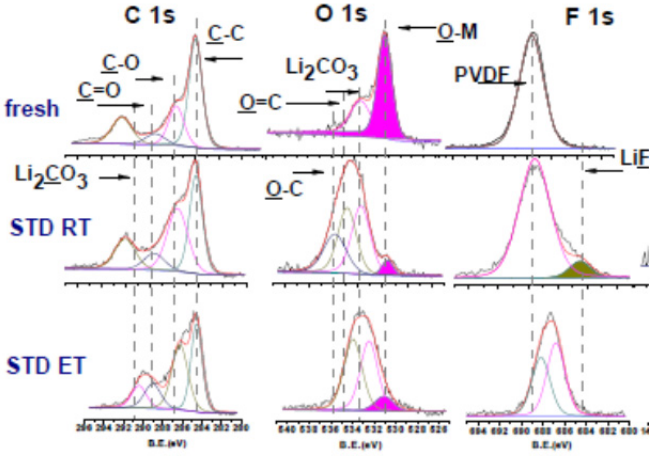

Figure VI - 153: XPS spectra of LiNi0.5Mn1.5O4, fresh and after cycling at 25°C and 55°C

Ex situ surface analysis of the cathode with SEM reveals that the bulk cathode particles and the cathode laminate are retained. Cross-sectional SEM images clearly indicate that the graphite electrode is delaminating from the Cu current collector. The increased performance loss of the graphite anode is likely related to Mn dissolution and reduction on the anode which may be damaging the anode SEI and contributing to anode delamination. The results suggest that both the anode and the cathode contribute to performance loss in graphite/$LiNi_{0.5}Mn_{1.5}O_4$ cells.

Additives which improve the performance of graphite/$LiNi_{0.5}Mn_{1.5}O_4$ cells. Novel additives have been prepared which improve the performance of graphite/ $LiNi_{0.5}Mn_{1.5}O_4$ cells cycled to 4.8 V (vs Li) with $LiPF_6$ in EC/EMC at 55°C. Figure VI - 154 shows the cycling performance of the graphite/$LiNi_{0.5}Mn_{1.5}O_4$ cells with baseline electrolyte and electrolyte containing the additive at RT, ET (55°C) and RT. The initial discharge capacity of the cells with 1.5% and 2.5% (lithium bis(oxalato) borate, LiBOB) are slightly lower than the cells with baseline electrolyte at RT. This difference is ascribed to the irreversible decomposition of the additive on the electrode surface. However, after 30 cycles at 55°C, the cell with baseline electrolyte suffered significant capacity loss, only delivering 24 % of the original capacity. The cells with 1.5% and 2.5%

additive showed improved cycling stability upon cycling at 55°C, 63 and 69 % capacity retention, respectively. After cycling at 55°C the cells were cycled at RT. The cell with baseline electrolyte had continued capacity fade; while the cells with additive exhibited much better cycling stability. In addition to the improved capacity retention, the cells containing the additive have better columbic efficiency while cycling at 55°C.

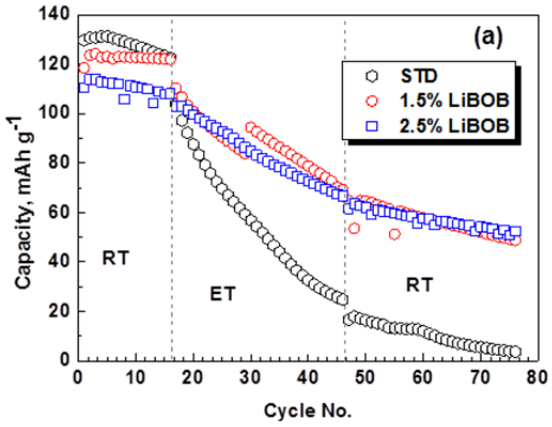

Figure VI - 154: Cycling performance of graphite/ LiNi0.5Mn1.5O4 cells with STD and LiBOB containing electrolyte at RT, ET (55°C), and RT

Ex situ surface analysis of both the anode and the cathode extracted from graphite/$LiNi_{0.5}Mn_{1.5}O_4$ cells was conducted via a combination of XPS, SEM, TEM with EDX, and ICP-MS to develop a better understanding of the role of the additive in capacity retention upon cycling at elevated temperature. Incorporation of the additive results in the generation of a thin cathode surface film. The cathode surface film inhibits the deposition of poly(ethylene carbonate) and dissolution of Mn and Ni at the cathode surface during cycling at 55°C. The additive also inhibits damage to the anode surface. The presence of the additive results in less Mn and Ni deposition on the anode surface and less damage to the anode SEI. Incorporation of the novel additives to graphite/ $LiNi_{0.5}Mn_{1.5}O_4$ cells cycled to 4.8 V (vs Li) results in improved capacity retention and efficiency. The improved cycling performance can be attributed the inhibition of electrolyte decomposition at the electrode surfaces and inhibition of Mn and Ni dissolution from the cathode and deposition on the anode. Second generation additives which further improve the performance of graphite-$LiNi_{0.5}Mn_{1.5}O_4$ cells have been developed. A patent is being filed and the results will be published in the future.

Preparation and investigation of novel non-flourinated salts. Synthetic methods to prepare novel salts were attempted. Two different novel salts were targeted, however, significant difficulties were experienced during the development of the synthetic methods. The project goals were realligned to support the new Silicon Focus Group within the BATT program.

Investigation of electrolyte additives on the performance of silicon anodes. Developing an understanding of the role of common additives, such as VC and FEC, on the capacity retention of silicon nano-particle electrodes is being conducted. Li/silicon nano-particle cells were prepared with seven different electrolyte formulations. The baseline electrolyte was 1.2 M $LiPF_6$ in EC/DEC (1:1). The other electrolyte formulations included 3 and 6 % VC and 5, 10, 15, and 25 % FEC (wt %). The cycling performance of the different electrolytes is provided in Figure VI - 155. The best capacity retention was observed for cells containing 10 and 15 % of FEC. Interestingly, the electrolytes with a lower concentration (5 %) and a higher concentration (25 %) of FEC have inferior capacity retention. In addition, the cells with 3 and 6 % VC had comparable cycling performance to the baseline electrolyte. *Ex situ* analysis of the silicon-nano-particle electrodes with XPS, SEM, and FT-IR is currently being conducted and will be presented in FY 14 reports.

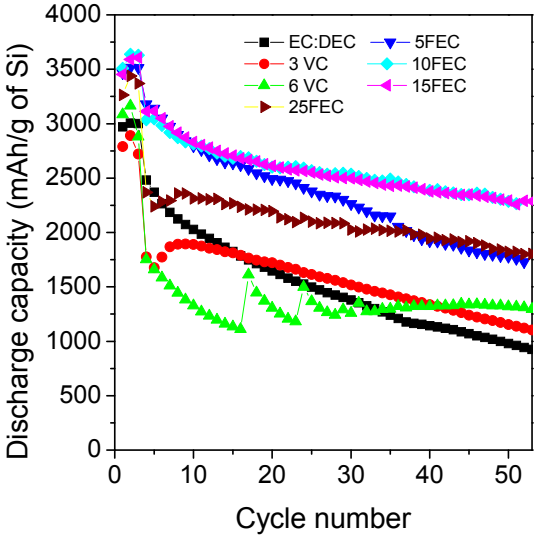

Figure VI - 155: Capacity retention of Li/silicon nano-particle cells cycled with different electrolytes

Conclusions and Future Directions

The failure mechanism of graphite/$LiNi_{0.5}Mn_{1.5}O_4$ cells cycled at 25°C and 55°C have been analyzed by electrochemical methods and *ex situ* surface analysis of the electrodes. Graphite / $LiNi_{0.5}Mn_{1.5}O_4$ cells cycle well at 25°C, but have rapid capacity fade upon cycling at 55°C. Independent electrochemical analysis of anodes and cathodes extracted from cells cycled at 55°C suggest that both electrodes have significant capacity loss, although the cathode capacity can be recovered

with longer charging times. *Ex situ* surface analysis of the cathode with SEM reveals that the bulk cathode particles and the cathode laminate are retained while XPS confirms the presence of a cathode electrolyte interface composed of the decomposition products of the electrolyte. *Ex situ* analysis of the anode reveals a thick anode SEI, anode delamination, and the presence of Mn. The results suggest that both the anode and the cathode contribute to performance loss in graphite/ LiNi0.5Mn1.5O4 cells.

The performance of the graphite/ $LiNi_{0.5}Mn_{1.5}O_4$ cells cycled to 4.8 V (vs Li/Li+) with 1.0 M $LiPF_6$ in EC/EMC (3/7, v/v) with and without added LiBOB (1.5 and 2.5 % (wt)) at 25 and 55°C has been investigated. The initial discharge capacity of the cells with added LiBOB is slightly lower than the cells without added LiBOB. However, after 30 cycles at 55°C, the cells with standard electrolyte suffer poor capacity retention (20 %). The cells with 1.5% or 2.5% LiBOB have improved cycling stability at 55°C with 63 and 69 % capacity retention, respectively, after 30 cycles. The cells containing added LiBOB also have better coulombic efficiency and lower impedance after cycling at 55°C. *Ex situ* surface analysis of both the anode and the cathode extracted from graphite/ $LiNi_{0.5}Mn_{1.5}O_4$ cells was conducted via a combination of XPS, SEM, TEM with EDX, and ICP-MS. The improved cycling performance with added LiBOB can be attributed to the inhibition of electrolyte decomposition at the electrode surfaces and inhibition of Mn and Ni dissolution from the cathode and deposition on the anode upon cycling at high voltage and elevated temperature. Additional novel additives which provide superior performance of graphite/$LiNi_{0.5}Mn_{1.5}O_4$ cells are currently being developed.

The future direction of the project is to develop an understanding of the mechanism of improved capacity retention for Si nano-particle electrodes in the presence of electrolyte additives FEC and/or VC. A direct comparison of the cycling performance of electrolytes with different concentrations of added FEC and/or VC will be conducted and the results will allow the determination of an optimized electrolyte for use with Si nano-particle electrodes. This formulation will be suggested as a standard formulation for BATT researchers to allow for better cross comparison of electrochemical cycling data for different novel Si anode materials. After cycling Si-nanoparticle electrodes with different electrolyte formulations, the electrodes will be extracted and *ex situ* surface analysis will be conducted. The surface analysis and cycling data will be used to develop a mechanism for capacity retention enhancement via addition of FEC or VC.

FY 2013 Publications/Presentations

1. "Development of Electrolytes for Lithium Batteries," *DOE Annual Peer Review Meeting*, May 13-17, 2013, Washington, DC.
2. "Effect of electrolyte and additives on performance of $LiNi_{0.5}Mn_{1.5}O_4$," *Pacific Rim Meeting on Electrochemistry and Solid State Sciences*, Honolulu, HI, October 2012.
3. "Effect of electrolyte and additives on performance of $LiNi_{0.5}Mn_{1.5}O_4$," *NAAT Batt Annual Meeting and Symposium*, Austin, TX, January 2013.
4. "Role of Electrolyte in interface formation and cycling performance in Lithium Ion Batteries," *IBA Meeting*, Barcelona, Spain, March 2013.
5. 2010 DOE Annual Peer Review Meeting Presentation, May 2013.
6. "Improved performance of graphite/ Li $Ni_{0.5}Mn_{1.5}O_4$ cells with electrolyte additives," *6th International Conference on Advanced Lithium Batteries for Automotive Applications*, Argonne IL, September 2013.
7. L. Zhou, M. Xu, B. L. Lucht, "Performance of lithium tetrafluorooxalatophosphate in methyl butyrate electrolytes," *J. Appl. Electrochem.* 43, 497-505, 2013.
8. M. Nie, D. Chalasani, D. P. Abraham, Y. Chen, A. Bose, B. L. Lucht, "Failure Mechanism of Graphite/$LiNi_{0.5}Mn_{1.5}O_4$ Cells at High Voltage and Elevated Temperature," *J. Electrochem. Soc.* 160, A3138-A3143, 2013.
9. M. Xu, L. Zhou, Y. Dong, Y. Chen, A. Garsuch, B. L. Lucht, "Improving the Performance of Graphite/ $LiNi_{0.5}Mn_{1.5}O_4$ Cells at High Voltage and Elevated Temperature with added Lithium bis(oxalato) borate (LiBOB)," *J. Electrochem. Soc*. **2013**, *160*, A2005-A2013.

VI.E Cell Analysis, Modeling, and Fabrication

VI.E.1 Predicting Microstructure and Performance for Optimal Cell Fabrication (BYU)

Dean Wheeler
Brigham Young University

Department of Chemical Engineering
350 Clyde Building
Provo, UT 84602
Phone: (801) 422-4126
E-mail: dean_wheeler@byu.edu

Brian Mazzeo
Brigham Young University
Department of Electrical and Computer Engineering
459 Clyde Building
Provo, UT 84602
Phone: (801) 422-1240; Fax: (801) 422-0201
E-mail: bmazzeo@ee.byu.edu

Start Date: October 2012
Projected End Date: September 2016

Objectives

- Develop rapid, reliable, and standardized methods for measuring electronic and ionic conductivities in porous electrodes.
- Determine and predict microstructures for porous electrodes.
- Understand tradeoffs and relationships between fabrication parameters and electrode performance.

Technical Barriers

One main technical barrier to improved battery performance is to understand electrode conductivity and spatial variability. Within a cell there are inhomogeneities on multiple length scales, from sub-particle size up to hundreds of microns and across the width of full rolls of commercially-prepared electrode films. New approaches must be devised to quantify and better understand these variations. Additionally, while, x-ray tomography (nano-CT) and SEM/FIB can be used to determine a few Li-ion electrode microstructures at very fine resolution, a 3D microstructure prediction model needs to be developed to routinely generate structures for new materials and fabrication conditions, especially over much larger length scales. Because electronic and ionic transport take place in different phases that cannot occupy the same volume, new experimental and modeling techniques are needed to bring greater clarity to the relationships between electrode composition and morphology.

Technical Targets

- Fabricate micro-four-line probes to determine bulk electronic conductivity in non-delaminated battery films.
- Develop mathematical-model inversion technique to determine current collector contact resistance from film measurements.

Accomplishments

- Cleanroom procedure established to fabricate the first generation micro-four-line probe.
- Utility of the micro-four-line measurement technique was demonstrated on laboratory-prepared and commercial films.
- Mathematical inversion technique was used to provide first-order estimates of bulk conductivity.

✧ ✧ ✧ ✧ ✧

Introduction

A great deal of effort is expended by battery researchers and battery manufacturers worldwide to develop improved materials for Li-ion storage batteries; yet a greater understanding of how best to turn those materials into composite porous electrodes with optimized and uniform performance is needed. A lack of fundamental understanding about the relationships between fabrication parameters, microstructure, and performance prevents appropriate feedback and hurts the development of next-generation battery materials and process improvement in battery manufacturing.

Either experimental measurements or predictive models can be used to make the processing-structure-property connection for battery electrodes. In this project, both are used. The effort on this project is

intended to be general and system agnostic, but must of necessity focus on a few key materials in a validation and test environment. For this reason, synergistic collaborations with other researchers, for example, at Argonne National Laboratory (ANL) and A123 Systems, is an important part of this work.

Approach

The general approach of this project is to use particle-based microstructural modeling, coupled with extensive experimental validation and diagnostics, to understand relationships between fabrication processes, microstructure, and corresponding electron and ion transport in composite electrodes. The fabricated probes will be used to assess electronic and ionic conductivities of porous electrodes attached to current collectors, including local heterogeneities and anisotropic effects, through the use of newly designed instrumentation. The measurements will be used to validate and parameterize the particle model using experimental microstructural and macroscopic properties. Then, these modeling and diagnostic tools will be used to suggest processing conditions that will improve cell performance.

Results

Materials. BYU has received three batches of electrode materials for testing, one from ANL, and two from A123, including commercial $LiFePO_4$ and NCM films from production runs. Additionally, a graphite anode sample from A123 was obtained, as was a batch of $LiCoO_2$ electrode films from Saft America that were calendared to different porosities. Not all of these materials were tested in FY2013, and more complete testing is part of FY2014 milestones.

Fabrication of four-line-probe. Planar probes allow the surface of the probe to be placed directly upon electrode materials and thus allow an even pressure to be applied to the films while remaining mechanically robust. As shown in Figure VI - 156, a micro-four-line probe was fabricated in the BYU Cleanroom with inner conducting lines spaced 10 microns apart. The base material is nickel and gold was electrodeposited onto this nickel layer to provide good electrical contact to the electrode films. Because the spacing of the contacts is on the order of the cathode material thickness, a significant amount of the current passing through the battery electrode sample bypasses the current collector. This allows the probe to sample the bulk cathode conductivity without being unduly influenced by the stray current passing through the current collector metal film.

Construction of automated measurement apparatus. To be able to consistently make measurements with the fabricated four-line-probe, an apparatus was constructed to make automated measurements. As shown in Figure VI - 157, the electrode material was mounted on an X-Y stage with a force gauge under the target position. Then, the wafer probe was clamped in an inverted configuration to a Z-axis stage that descended on the electrode material. The entire measurement procedure with current source and multimeters was controlled using a computer control and data logging interface.

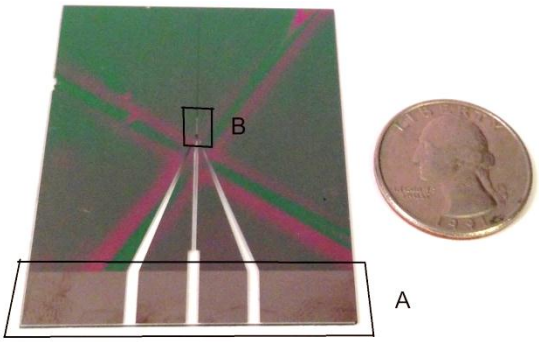

Figure VI - 156: Completed micro-four-line-probe wafer showing: (A) exposed connection pads, and (B) window for exposing the four contact lines

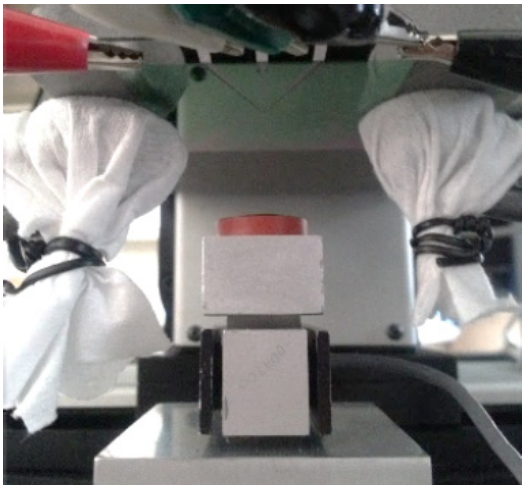

Figure VI - 157: Measurement apparatus for electronic conductivity measurements. The probe wafer is gently clamped in an inverted orientation to an aluminum block that descends upon the electrode target. Electrical connections are made to the exposed connection pads. The electrode film target is mounted on a disc that is attached to a force gauge to measure and allow the control of the applied pressure

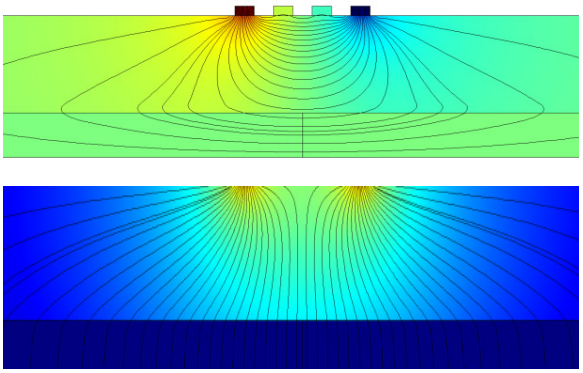

Figure VI - 158: Simulations of current and potential distributions for two orthogonal electrical measurements of an intact electrode using the four-line probe procedure

Numerical inversion procedure. To be able to properly interpret the micro-four-line probe measurements, a numerical inversion procedure was developed using simulations of the electrode conductivity as well as the current collector-cathode interface resistance. Examples of the COMSOL simulations of these properties are shown in Figure VI - 158. The simulations show different measurement configurations for determining bulk conductivity of the composite electrode and bulk-to-current-collector interface resistance.

Demonstration on commercial film. As shown in Figure VI - 159, conductivity variations were assessed for an NCM cathode film of thickness 70 μm. The repeatability of measurements at single locations was very high. On other hand, there was significant condsuctivity variability at different locations on the film (each separated by a few mm). A more complete study of such spatial variations is planned in FY2014.

In another test, the two experiments illustrated in Figure VI - 158 were carried out on a single location of an NCM electrode. The bulk conductivity at this location was determined to be 58.7 mS/cm. The contact resistance to the current collector was determined to be 9.8 mΩ cm^2. This preliminary measurement satisfies our "proof of concept" technical target or milestone; further validation of these measurements is planned in FY2014.

A

B

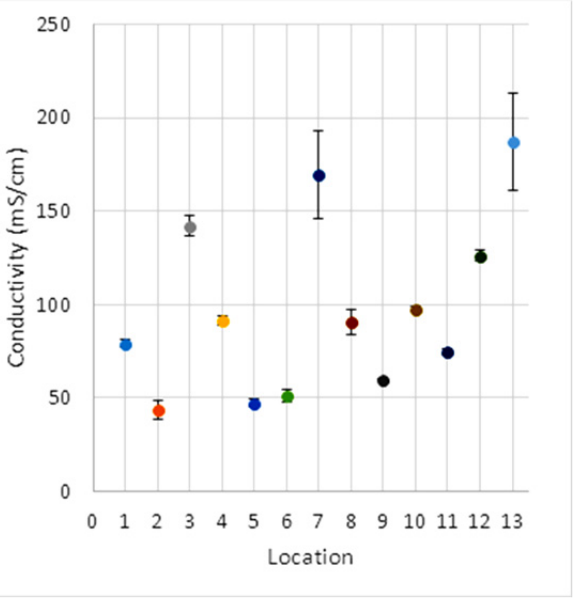

Figure VI - 159: (A) Relative locations of repeated electrical sampling on 17-mm-diameter circular electrode. (B) Location mean conductivities with 95% confidence intervals, showing significant spatial variability of the sample electrode compared to probe variability

Conclusions and Future Directions

This was the first (partial) year of a new contract and so the above results constitute completion of the expected technical targets or milestones for FY2013. Micro-four-line probes were successfully fabricated and the utility of the measurement technique was demonstrated on laboratory-prepared and commercial films, including those obtained from ANL and A123. Multiple iterations of the probe device and associated computer model took place during the year. Each iteration led to improvement in the robustness and utility of the design.

Significant improvements are expected over the coming contract year that will increase the reliability as well as the durability of the probes that are used to measure these important conductivity properties of the

electrode films. This will feed into the modeling efforts to understand the relationship between the electrode processing conditions and the electronic film conductivity.

This year did not include any milestones explicitly dealing with the particle-based microstructure model. Activities to build the model were carried out and will be reported in FY2014 as part of model-associated milestones.

FY 2013 Publications/Presentations

1. B. Lanterman, J. Flygare, A. Cutler, B. A. Mazzeo, D. R. Wheeler. "Development of a micro four-line probe for the measurement of thin-film battery electrode conductivity," *224th ECS meeting*, The Electrochemical Society, Oct. 2013, San Francisco, CA.
2. B. A. Mazzeo, B. Lanterman, J. Flygare, A. Cutler, N. Gates, D. R. Wheeler. "Conductivity measurements of thin-film battery films," *3rd SHPE Engineering Research Symposium*, Nov. 2013, Indianapolis, IN.
3. L. Zielke,T. Hutzenlaub, D. R. Wheeler, I. Manke, A. Tobias, N. Paust, R. Zengerle, S. Thiele, "A Synthesis of X-ray Tomography and Carbon Binder Modeling - Reconstructing the Three Phases of $LiCoO_2$ Li-ion Battery Cathodes," *Advanced Energy Materials*, submitted, 2013.

VI.E.2 Assembly of Battery Materials and Electrodes (HydroQuebec - IREQ)

Karim Zaghib
Hydro-Québec (IREQ).

IREQ, Hydro-Quebec
1800 Lionel Boulet
Varennes, QC J3X 1S1, Canada
Phone: (450) 652-8019; Fax: (450) 652-8204
E-mail: Zaghib.Karim@ireq.ca

Start Date: October 2012
Projected End Date: September 2016

Objectives

- Develop high-capacity, low-cost electrodes with good cycle stability and rate capability to replace graphite anodes in Li-ion batteries.
  - Identify an optimized silicon-carbon-binder electrode composition
  - Use *in situ* SEM methods to determine the failure mode of Si-based anodes.

Technical Barriers

The challenge is to overcome the electrochemical capacity limitations (both gravimetric and volumetric) of conventional carbon anodes by developing low-cost electrode architectures based on silicon. One of the biggest challenges of this anode material is related to its volume expansion and structural changes which lead to capacity fade and shorten the cycle life.

Technical Targets

- Identify Si-based anode materials that can achieve a capacity of 1200 mAh/g.
- Produce Si nano powder and supply a 1 kg batch as a baseline material for BATT PIs.
- Supply laminate Si-based electrodes to BATT PIs.

Accomplishments

- Identified an optimized silicon-carbon-binder electrode composition with an appropriate mixing method.
- Demonstrated a Si-anode composition with 1600 mAh/g and more than 100 cycles with 100% capacity retention.
- Successfully synthesized a new Si material as an alternative source for BATT PIs.

✧ ✧ ✧ ✧ ✧

Introduction

The BATT Program is looking for the next-generation systems for high-energy batteries. Thus, identifying new anode and cathode materials is necessary. One of the BATT recommendations was the spinel $LiMn_{1.5}Ni_{0.5}O_4$ as cathode and Si-based alloy as anode materials. Thus, the Hydro-Quebec (HQ) project was directly affected with these changes, which were made to better integrate with the other DOE programs. This modification has oriented HQ to work on Si-anode materials.

HQ proposed a strategy to design the architecture of the Si-anode material that can tolerate the volumetric expansion and provide acceptable cycle life with low capacity fade. The particle size, binder type and the electrode composition are the main parameters to define the formulation of the Si-anode. The porosity of the electrode has a direct impact on the performance, and therefore should be optimized by investigating various mixing methods.

To further improve the comprehension of the failure mode of the Si-based anode material, *in situ* SEM was used to monitor the anode during cycling. In this case, a dry polymer was used as the binder to avoid electrolyte evaporation inside the SEM.

Approach

To address and overcome the electrochemical capacity limitations (both gravimetric and volumetric) of conventional carbon anodes, low-cost electrode architectures based on silicon that can tolerate volumetric expansion and provide an acceptable cycle life with low capacity fade were proposed. Volume expansion, which is a common problem with Si-based electrode materials, will be addressed by: i) tortuosity/porosity optimization and ii) improved current collector technology.

Results

Electrode Preparation. To prepare useful Si-based electrodes, optimizing the process formulation is

necessary. The Si (Umicore) material recommended as a reference anode material by the BATT Program was used. This Si material consists of 25-100 µm agglomerates composed of primary spherical particles of 20-150 nm diameter. In order to minimize the stress on these anode materials, it is important to redesign the anode architecture.

The first step is to develop an appropriate method for mixing the Si composite. Different mixing methods were explored such as jar mill, ball mill (Spex), planetary mixer (Thinky) and their combinations. The initial study utilized acetylene black and alginate binder in the electrode composition, which was compared at low and high loadings of Si and carbon contents. Two composition ratios (Si: binder: carbon black) were identified; (83:15:2) and (50:25:25), one with high Si content and the second with high carbon content. The difference in electrode composition and mixing method will help to better understand the electrode behavior and also identify the appropriate conditions to make a preformed anode. The cells were formed at C/24 with a cut-off voltage at 5 mV and 1 V. The reversible capacity (Figure VI - 160) was 3500, 3810 and 4380 mAh/g, respectively, for the mixing methods; Jar mill (JM), Jar mill + thinky (JMT) and Jar mill + Spex (JMS). The 1st and 2nd cycle coulombic efficiencies of these cells were; (88, 97), (85, 97) and (88, 98), respectively. AC impedance spectroscopy was used to compare the electrodes prepared by different mixing methods. Figure VI - 160 shows the interface resistance (Ri) before and after formation cycles; higher Ri was found with (JMS) followed by (JMT) then JM. But, this trend cannot explain the capacity fade during cycling (Figure VI - 161).

The highest capacity, at C/6, was obtained with JMS (4280 mAh/g), followed by JMT (3710 mAh/g) then JM (3300m Ah/g). The capacity fade after 70 cycles was 48%, 34% and 65%, respectively. These results indicate that JM alone is not effective as a mixing method.

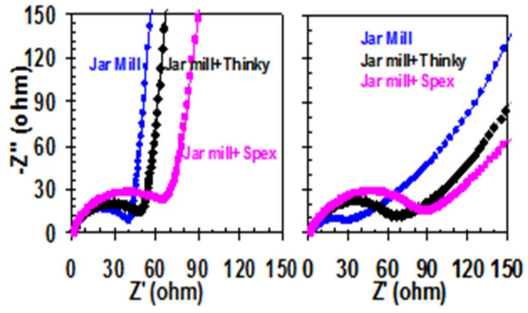

Figure VI - 160: AC impedance before and after formation cycles of Li/EC-DEC-LiPF$_6$/Si cells

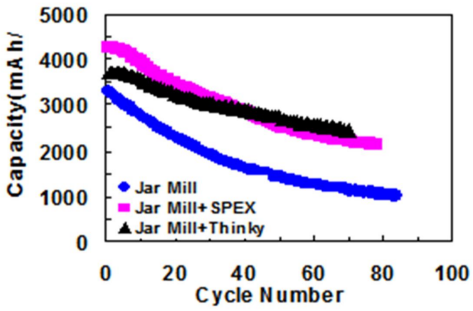

Figure VI - 161: Cycling life of Li/EC-DEC-LiPF$_6$/Si cells at C/6

Loading Effect. HQ focused on optimizing the Si-anode formulation and electrode architecture using the reference material provided by Umicore. The studies identified the best anode composition and the appropriate method for mixing the Si composite. By using the appropriate mixing method of jar-mill followed by planetary mixing, two Si loadings were evaluated 50% and 83%. As expected, Ri in Figure VI - 162.a is low in electrodes with more carbon and low Si. The high carbon content played an important role in producing an appropriate anode structure and higher cycle life. The carbon facilitated improved electric contact between particles, hence high capacity was obtained and cycle life with 48% fading after 80 cycles compared to 72% for the low loading anode (Figure VI - 162).

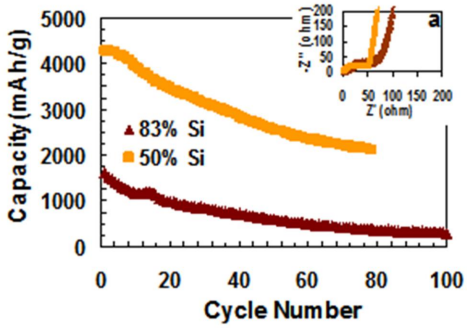

Figure VI - 162: AC Impedance before cycling and cycling life of Li/EC-DEC-LiPF$_6$/Si cells with different loading

The porosity of the electrode, which is strongly influenced by the electrode composition, is a major parameter affecting the electrode performance. A high carbon content and low Si ratio in the anode composition yielded significantly better performance.

The studies identified that the optimal range of the anode composition (Si:binder:carbon) is between (50:25:25) and (60:20:20). By increasing the Si content to 70%, the specific capacity fades faster than when the Si content is lower. The porosity and tortuosity of the electrode, which are strongly influenced by the electrode composition, are major parameters affecting electrode performance. The porosity varied from 0.5 to

0.4, respectively, in anodes with 50% and 70% Si content, and the influence on capacity is shown in Figure VI - 163. The capacity fade is more pronounced when the Si content is higher and porosity is lower. This implies that with the current mixing technique, the composition should be limited to 60% Si material in the electrode. In another study, a Cu current collector with rougher surface showed lower impedance compared to a standard one; but it does not appear to improve the cycling stability.

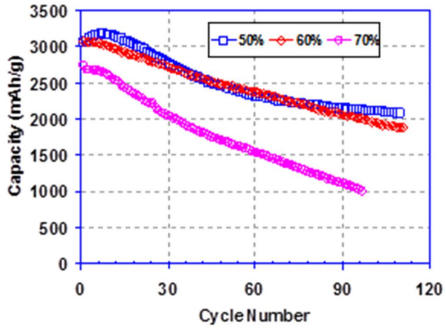

Figure VI - 163: Cycle life of Li/EC-DEC-LiPF$_6$/Si cells at C/6 with anodes having different loading

Cycling Conditions. An electrode with the composition (50%:25%:25%) was selected for investigations of different cycling conditions.

Cells were cycled at C/6 and 1C rates to determine the effect of stress on the particles after prolonged cycling, Figure VI - 164 shows that the capacity fade is more pronounced when the rate is higher. The Si particles suffers more stress at high rate (1C), which induces a fade of 85% of the initial capacity compared to 56% at C/6.

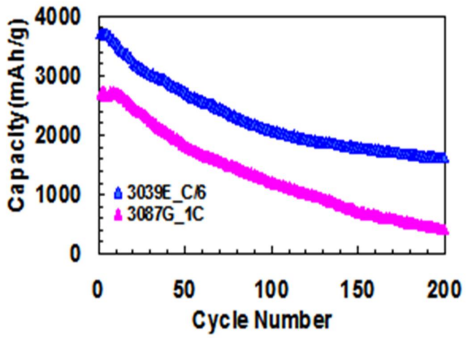

Figure VI - 164: Cycle life of Li/EC-DEC-LiPF$_6$/Si cells at 1C and C/6 rates

Studies at various depth of discharge (DoD) were used to monitor the stress on Si particles and its effect on the cycling performance. The stress level was controlled by varying DoD. At low DoD, the Si particles in the anode will experience minimum stress. Figure VI - 165 shows clearly the effect of DoD on the cycling stability at C/6. Capacity fade is severe when Si is cycled at high DoD, and the particles suffer from high stress that induces cracks. At DoD higher than 50% (2000 mA/g capacity), the cells show capacity fade that ultimately degrade in the same trend. At 40% DoD, an acceptable reversible capacity of 1670 mAh/g with good stability after 100 cycles is obtained.

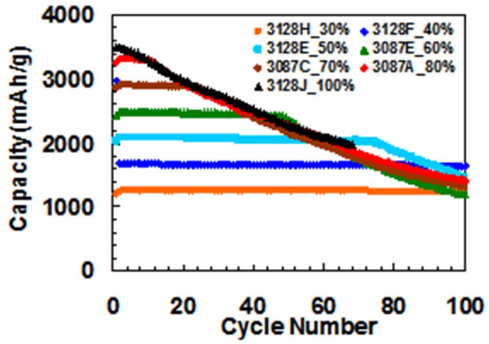

Figure VI - 165: Cycle life at C/6 of of Li/EC-DEC-LiPF$_6$/Si cells at different DoD

***In situ* Analysis.** The stress on the Si particles during charge and discharge will spread throughout the electrode, and thus destroy the integrity of the anode, as observed by *in situ* SEM. The *in situ* study (Figure VI - 166) was performed on the electrode using Umicore Si with composition 50%:25%:25%.

The results of the *in situ* analysis revealed an increase in the electrode thickness during discharge to 5 mV, resulting from lithium insertion in the host structure of the Si particles.

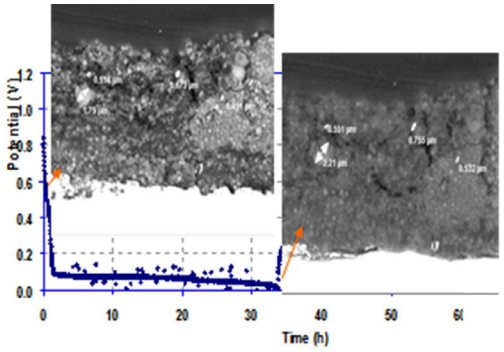

Figure VI - 166: *In situ* analysis of Li/polymer_LiTFSI/Si cell in polymer matrix

The average electrode expansion was about 58%. The volume expansion also depends on the electrode composition; a different value was obtained with different electrode compositions. An increase in the primary particle size was noted, with an important morphology change in the electrode (Figure VI - 166). Less cracks in the particles were observed with this material and only few larger particles break down during lithium de-insertion and insertion. Several

fractures in the electrode were observed during the 1st charge. These fractures could be a consequence of electrode densification.

Conclusions and Future Directions

The *in situ* analysis and cycling studies on the Si anode materials indicate that controlling the rated capacity by limiting %DoD is beneficial to reduce stress and to maintain the mechanical integrity of the particles. Thus, sacrificing some capacity could be an acceptable compromise to obtain a useful Li-ion cell with longer cycle life.

HQ proposes to continue development of the Si-nano material as an improved anode for the BATT PIs, and to continue using *in situ* methods to better understand the failure mechanism of this material.

FY 2013 Publications/Presentations

1. K. Zaghib, A. Guerfi, P. Hovington, A. Vijh, M. Trudeau, A. Mauger, J.B. Goodenough, C.M. Julien "Review and analysis of nanostructured olivine-based lithium rechargeable batteries: Status and trends," *Journal of Power Sources*, **232**, 357-369 (15 June 2013).
2. "Facile dry synthesis of sulfur core-shell composite for the scalable fabrication of lithium/sulfur batteries," Chi-Su Kim,*6th International Conference on Advanced Lithium Batteries for Automobile Applications*, September 9-11, 2013, Argonne Advanced Photon Source Conference Center Argonne, IL.

VI.E.3 Model-Experimental Studies on Next-generation Li-ion Battery Materials (LBNL)

Venkat Srinivasan
Lawrence Berkeley National Laboratory

Environmental Energy Technologies Division
1 Cyclotron Road, MS 70R0108B
Berkeley, CA 94720
Phone: (510) 495-2679; Fax: (510) 486-4260
E-mail: vsrinivasan@lbl.gov

Start Date: October 2012
Projected End Date: September 2016

Objectives

- Quantify the usefulness of alloy anodes for use in PHEVs.
- Understand the mechanical degradation in electrodes used in EVs and PHEVs.
- Model reaction distribution in battery electrodes.

Technical Barriers

Low energy efficiency; low calendar/cycle life; high cost.

Technical Targets

- Available energy: 56 Wh/kg (10 mile) and 96 Wh/kg (40 mile).
- 10-s discharge power: 750 W/kg (10 mile) and 316 W/kg (40 mile).

Accomplishments

- Modeled NMC electrode behavior with a systematic approach of finding parameters used in the model. Final model has no fitting parameters.
- Created general-purpose software package capable of solving systems of nonlinear discretized equations on two-dimensional grids.
- Simulated lithium insertion and extraction for model particle-binder systems. Model reveals conditions under which binder, silicon, or interface fails and is how failure is related to mechanical properties.
- Experimentally determined concentration dependent transport properties for $LiPF_6$ in EC:DEC (1:1)

✧ ✧ ✧ ✧ ✧

Introduction

Modeling porous electrodes with layered $LiNi_{1/3}Co_{1/3}Mn_{1/3}O_2$ (NMC) active material. High energy density and long cycle life are critical for reducing the cost of rechargeable Li-ion batteries. Thick porous electrodes result in large energy densities; however, transport limitations can decrease power capability. The primary goal of this project is to develop mathematical models for candidate Li-ion chemistries with little to no adjustable parameters. The layered $LiNi_{1/3}Co_{1/3}Mn_{1/3}O_2$ (NMC) cathode material has been selected as the baseline system to study rate performance associated with the transport limitations in solid and electrolyte phases.

Over the past year, work has been focused on developing mathematical models for porous electrodes with the aim of predicting electrode behavior. When charging/discharging at high rates, electrode performance is limited in solution phase of the porous electrode. Therefore, it is important to understand mass transport in tortuous pores of the electrode. The effective transport properties are associated with electrode structure, i.e., porosity and tortuosity, and bulk properties of the electrolyte. While porosity is a measureable parameter, tortuosity is non-measurable and is usually estimated from porosity through the Bruggeman relation. Literature studies have measured electrode tortuosity and bulk electrolyte properties.

An accurate model prediction requires correct estimate of effective transport properties. In the present model, both electrode tortuosity and electrolyte properties are taken from literature to show a preliminary prediction of experimental data and understand limitations in the NMC electrode. Separate experiments were performed to measure the electrolyte properties for use in the model in future work.

Estimating electrolyte transport properties. In order to predict the cell performance under a variety of cycling conditions, reasonable estimates of the concentration dependent transport properties in the electrolyte becomes imperative. The electrolyte used in this project is $LiPF_6$ in EC:DEC (1:1 by weight) which is also the baseline electrolyte for the BATT program.

According to Onsager reciprocal relations, there are *n(n-1)/2* independent transport properties, where *n* is the number of species in the electrolyte. If the solvent mixture (EC and DEC) is treated as a single species, the number of transport properties become three: (a) conductivity; (b) salt diffusion coefficient; (c) transference number. In addition to these three properties, the salt activity coefficient (which is a thermodynamic property) also needs to be measured.

Stress and strain in silicon electrodes. The high capacity of silicon for inserted lithium is associated with large volume changes and large stresses. In a porous electrode, the material surrounding silicon particles is also subjected to stress. Stresses can cause material damage and reduce battery capacity. In order to understand the conditions under which binders must operate, and to determine the qualities that binders should possess in order to better tolerate these conditions, a mathematical model was developed.

Approach

Rate limitations in NMC electrode. A systematic approach has been applied to find the kinetic parameters needed for the model for studying limitations in NMC cathode. The rate constant associated with Li anode in 1M $LiPF_6$ in EC:DEC (1:1) was obtained from the rate experiment data of Li-Li symmetric cells in coin-cell configuration. At each applied current, the corresponding potential was measured and plotted as a function of current. The I-V curve was fitted using the Butler-Volmer equation and the exchange current density was obtained from the Tafel slope.

The rate constant associated with NMC electrode was obtained from a NMC-Li coin cell. The electrode was made thin, so the mass transport in the electrolyte phase was minimized. An open circuit relaxation experiment was used with a model to extract diffusion coefficient as a function of the state of charge (SOC) for this cathode. In addition, the experimental potentials can be fitted to the model. The discharge potential at each rate was calculated with a correction for the potential drop at Li anode. The exchange current density of NMC cathode was then obtained by fitting the model with experimental data.

Transport properties. The diffusion coefficient as a function of concentration was measured using the restricted diffusion method. In this technique free standing $LiPF_6$ in EC:DEC (1:1 by weight) was placed between Li-Li electrodes. Constant current was passed for a certain time to build up a concentration gradient. The current was then stopped and the cell potential monitored during this open-circuit relaxation period. Chapman and Newman (1980) have shown that at long relaxation times the slope of ln V vs. time curve is a straight line, which is proportional to the salt diffusion coefficient at that particular electrolyte concentration. The procedure was repeated for different electrolyte concentrations and at different polarization times to check for reproducibility. The functionality of the salt activity coefficient and transference number as a function of concentration was obtained using a concentration cell. The cell consisted of two separate chambers that were separated by a glass frit to prevent rapid mixing of the electrolyte. The concentration in one of the chambers was kept constant at 2M whereas in the other chamber it was varied in between 0.2M to 2M. The open circuit voltage was measured for each concentration and lithium metal was used as the electrode in the experiments. The conductivity of the electrolyte as a function of concentration was measured using a conductivity meter.

Stress and strain in silicon electrodes. In order to capture important mechanical behavior in a relatively simple model, the finite-deformation graphite model of Christensen and Newman (2006) was adopted, modified, and cast into set of two-dimensional equations on an axisymmetric cylinder. Binder regions were attached to the active material region and coupled through stress and displacement.

Working in two spatial dimensions introduces significant complications relative to a one-dimensional model, but supplies a wealth of additional information. The resulting model equations proved to be difficult to solve with available software packages, so a new general-purpose package was written in order to provide the necessary flexibility.

The model equations were solved over lithium insertion/extraction cycles and stresses were computed throughout the model systems. Calculated stress values and strain energies are comparable to published yield stresses and adhesion energies.

Results

Rate limitations in NMC electrode. The model-experiment comparison of NMC electrode at different rates is shown in Figure VI - 167 using kinetic parameters obtained from experiments and electrode tortuosity and transport properties taken from literature studies of $LiPF_6$ in EC:DEC or similar electrolyte. The electrode behavior is well predicted at rates smaller than 1C. For rates larger than 1C, the model is able to predict the electrode potential at the beginning of discharge, but not the capacity loss near the end of discharge. This is because electrolyte concentration increases at the Li anode and extrapolating the literature values might not reflect the real electrolyte properties towards the end of discharge.

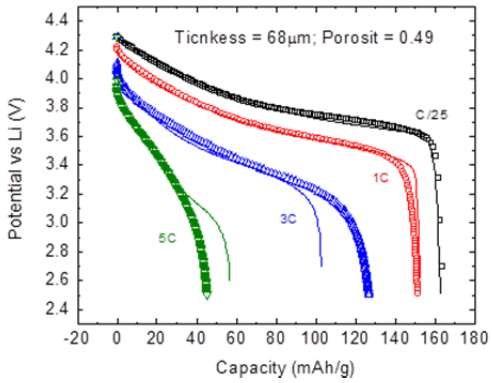

Figure VI - 167: Model-experiment comparison of NMC electrode discharge at different rates

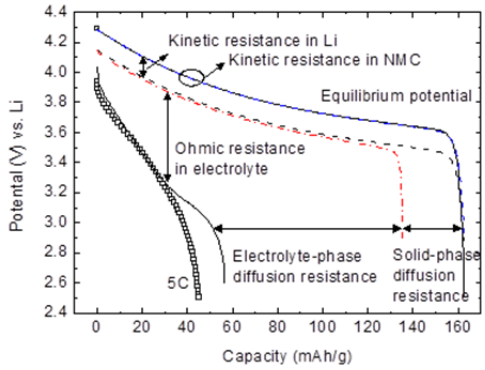

Figure VI - 168: Potential drop estimation of NMC electrode at 5C

Figure VI - 168 shows the estimate of potential drops in NMC electrode at 5C. While some potential drops are due to kinetic resistances at Li anode and NMC cathode and some capacity loss is due to solid-phase diffusion resistance, most of the potential drops and capacity loss come from ohmic resistance and diffusion resistance in the electrolyte. This is evidence that the electrode performance is limited in the electrolyte phase of the porous electrode. Therefore, understanding the effective transport properties is important to improve battery design and model predictions, especially at high rates.

Transport properties – diffusion coefficient. The diffusion coefficient at different salt concentrations was measured using the restricted diffusion method. Figure VI - 169 shows the experimental data points and model fit for the diffusion coefficient at different salt concentrations for $LiPF_6$ in EC:DEC (1:1).

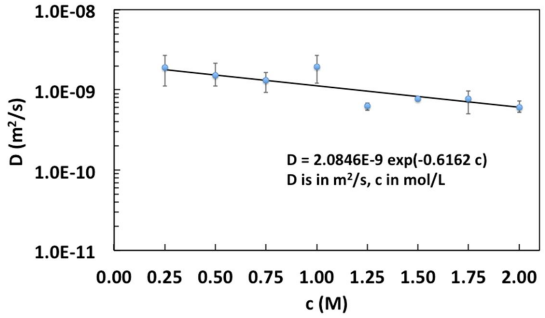

Figure VI - 169: Diffusion Coeffcient as a function of concentration for LiPF6 in EC:DEC (1:1) measured using Restricted Diffusion method

Transference number and salt activity coefficient. Concentrated solution theory suggests that the open – circuit voltage (U) measured from a concentration cell at different salt concentrations (c) is related to transference number (t_+) and thermodynamic factor $\left(1+\frac{dlnf}{dlnc}\right)$ by the relationship: $\frac{dU}{dlnc}=\frac{2RT}{F}(1-t_+)\left(1+\frac{dlnf}{dlnc}\right)$, where R is ideal gas constant, T is temperature and F is Faraday's constant. The variation of $(1-t_+)\left(1+\frac{dlnf}{dlnc}\right)$ with concentration is shown in Figure VI - 170. At infinite dilution, the curve approaches $(1-t_+)$ as $\left(1+\frac{dlnf}{dlnc}\right)$ approaches unity. The value of transference number at infinite dilution was found to be 0.38.

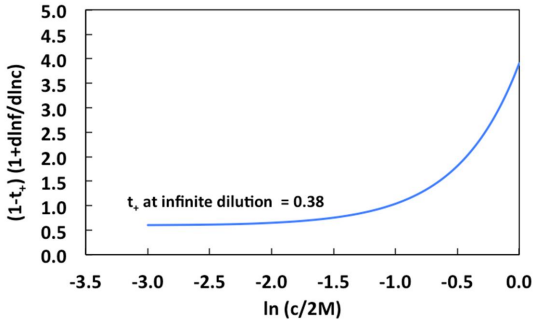

Figure VI - 170: Variation of $(1-t_+)\left(1+\frac{dlnf}{dlnc}\right)$ with concentration for LiPF6 in EC: DEC (1:1)

Conductivity. Figure VI - 171 shows the experimental data and model fit for the conductivity of the electrolyte as a function of concentration.

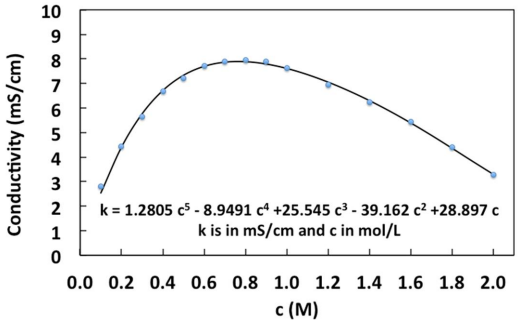

Figure VI - 171: Conductivity as a function of concentration for $LiPF_6$ in EC:DEC (1:1)

Stress and strain in silicon electrodes: Solutions to the model equations were calculated as spatial distributions of inserted lithium and material displacement throughout the active material domain, as well as displacement in the binder region. From this information, stresses are calculated throughout the entire system, and available strain energy is calculated from auxiliary relaxation simulations.

Figure VI - 172 shows visualization from a typical simulation, near the end of lithium insertion. The vertical axis is the cylinder's axis of symmetry, and the horizontal axis is a plane of symmetry. Colors reflect the mole fraction of lithium-occupied sites, and the binder region is drawn as a wireframe. All material is shown in its "present" deformed location. The binder has been given the material properties of PVdF.

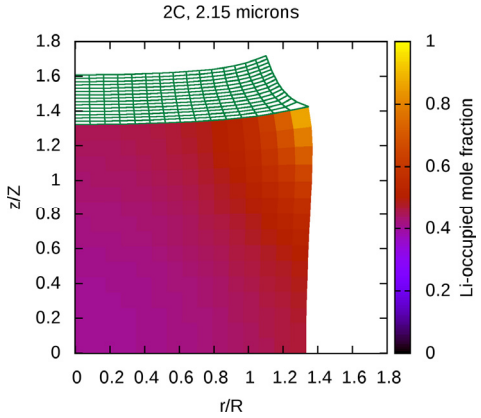

Figure VI - 172: Lithium-occupied mole fraction near end of lithium insertion for active material cylinder sandwiched between binder layers

The von Mises yield criterion and definition for equivalent tensile stress has been adopted because it is simple and common and provides a qualitative understanding of the stress distribution. This is shown in Figure VI - 173 for the same situation shown in Figure VI - 172. Unfortunately, a quantitatively-correct theory of yielding does not seem to exist for lithiated silicon or typical binder materials.

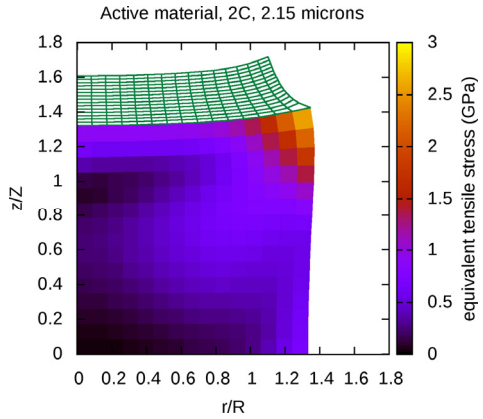

Figure VI - 173: von Mises equivalent stress throughout the active material region

Figure VI - 174 shows the maximum equivalent stress in the active material domain for different particle sizes. The particle size relative to the diffusion length scale determines the degree of uniformity in lithium distribution and material displacement for a given system. The maximum stress increases with particle size, which is qualitatively consistent with reports from many other researchers. A reported yield stress for the lithium-silicon system is shown on the plot in order to demonstrate that computed results are in reasonable and physically-significant range.

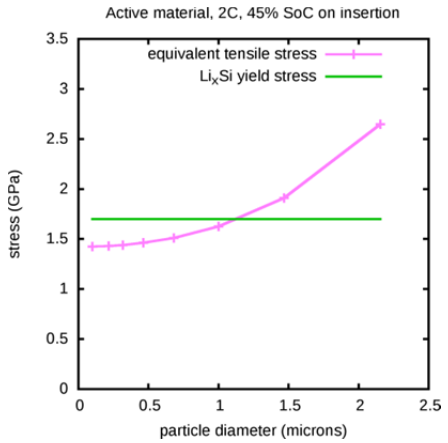

Figure VI - 174: Maximum equivalent stress in active material as a function of particle size, compared with reported yield stress

Conclusions and Future Directions

The analysis of potential drops of NMC electrode showed that most of the potential drops and capacity loss come from resistances in the electrolyte phase. Accurate model predictions require correct estimate of effective transport properties in the porous electrode. Therefore, future studies will focus on investigating electrode structure and electrolyte transport properties to improve electrode performance.

Simulations of lithium insertion and removal in model systems produced qualitative trends that are generally in agreement with the findings of other researchers. However, in order for the simulations to have predictive power, they require the input of much more comprehensive experimental data, as well as additional, quantitatively-correct theories of material behavior.

In order to address, in part, this lack of experimental data, fabrication of material samples and measurements of mechanical properties are now being trialed. Once reliable parameter values are obtained, they will be incorporated into the simulations in order to improve predictive power.

FY 2013 Publications/Presentations

1. Shao-Ling Wu, Venkat Srinivasan, "Understanding Limitations in $LiNi_{1/3}Mn_{1/3}Co_{1/3}O2$ Electrode," *224th ECS Meeting of The Electrochemical Society*, Oct. 27- Nov. 1, 2013, San Francisco, CA.
2. Amal Mehrotra, Sunil Mair, Venkat Srinivasan, "Transport Property Measurements for $LiPF_6$ in EC:DEC (1:1)," *224th ECS Meeting of The Electrochemical Society*, Oct. 27- Nov. 1, 2013, San Francisco, CA.
3. Kenneth Higa, Venkat Srinivasan, "Stress and Strain in Silicon Electrode Models," *224th ECS Meeting of The Electrochemical Society*, Oct. 27- Nov. 1, 2013, San Francisco, CA.

VI.E.4 Predicting and Understanding Novel Electrode Materials from First-Principles (LBNL)

Kristin Persson
Lawrence Berkeley National Laboratoty.

Energy and Environmental Technologies Division
1 Cyclotron Road
Berkeley, CA 94563
Phone: (510) 486-7218
E-mail: kapersson@lbl.gov

Start Date: October 2012
Projected End Date: September 2016

Objectives

- Model and predict the behavior of electrode materials from first-principles.
- Understand the atomistic interactions underlying the behavior and performance of the high-capacity lithium excess and related composite cathode materials.
- Predict new materials using the recently developed Materials Project high-throughput computational capabilities at LBNL.

Technical Barriers

Investigating electrode materials with atomistic modeling require rigorous bench marking as well as insight into the materials chemistry and its effect on electrode performance. In the case of the Li-excess materials, it is challenging, as there are an increased number of variables associated with the unknowns regarding possible composite or solid solution structure of the material, the amounts of each phase, synthesis procedure, etc.

Technical Targets

- Elucidate the phase space of the layered Li_2MnO_3, and associated defect spinel phases that can form as a function of different Mn and Li sites and migration patterns.
- Understand the charging mechanism in Li_2MnO_3.
- Chart out and elucidate the transformation paths in Li_2MnO_3 as a function of charge.
- Increase the number of predicted battery compounds available on the Materials Project.

✧ ✧ ✧ ✧ ✧

Introduction

There is increasing evidence that many of the performance limiting processes present in electrode materials are highly complex reactions occurring on the atomic level. The Persson BATT effort at LBNL is studying these processes using first-principles density-functional theory modeling tools. By understanding the underlying reasons for the electrode materials working performance, improvements or design schemes can be directed at the root cause of the process.

The composite cathode materials show great promise for high voltage and high capacity, however, they also present voltage fade, structural degradation and safety concerns. The voltage and capacity fade of the composite cathode materials are due to possible 1) dissolution of the transition metal ions and 2) structural transformation reactions as a function of rate and cycling. There are safety concerns relating to oxygen loss and electrolyte breakdown. All these aspects will in turn be addressed in this project and during the first year the main focus was to understand the structural and chemical changes in the layered Li_2MnO_3 structure which is a key material to explain the high capacity in layer-layer or layer-spinel composite electrode materials. Layered Li_2MnO_3 has been assumed to be largely electrochemically inactive due to the high oxidation state of Mn (4+ in the discharged state). Additions of Li_2MnO_3 to other spinel and/or layered materials have been used to increase the structural stability of the composite materials and allow more Li extraction than for the layered or spinel materials alone. However, many recent experimental studies have shown that the Li_2MnO_3 component is actually electrochemically active, which demands a re-examination of the conventional belief on the structural and chemical behavior of Li_2MnO_3 and the existing explanation of the origin of high capacity in the composite materials.

Furthermore, the last results for the $LiNi_{0.5}Mn_{1.5}O_4$ (LNMO) project are reported. For many systems, nano-scaling of electrode materials is frequently used in battery applications to enhance performance, particularly concerning rate capability. However, for the high-voltage spinel, LNMO, conflicting results have been reported on the effectiveness of nano-scaling to enhance its rate performance.

Approach

The Persson group uses atomistic modeling to study the relevant thermodynamic and kinetic processes. The calculations are performed at NERSC and on the Lawrencium cluster at LBNL. To elucidate the atomistic interactions, first-principles zero-temperature calculations are employed and coupled with the cluster expansion technique to examine the structural and chemical space, establish ground states, and resulting electrochemical signature of the materials. To examine temperature-induced properties, statistical mechanics and kinetic Monte Carlo methodologies are utilized.

Results

Transformation mechanisms of Li_2MnO_3. Layered-layered composites containing Li_2MnO_3 show a large 'activation' capacity (about 350 mAh/g) for the first charge, but then for the 1st discharge and later charge/discharge cycles it exhibits lower capacity. This is believed to be due to partial phase transformation to the spinel structure. A cluster expansion model of the ionic interactions in Li_xMnO_3 (0<=x<=2) was employed to predict the ground states as a function of Li. Hundreds of Li/Mn arrangements within the Li_2MnO_3 structure (see Figure VI - 175) were computed within GGA+U and used to fit the cluster expansion to arrive at a converged model of the coupled ionic interactions.

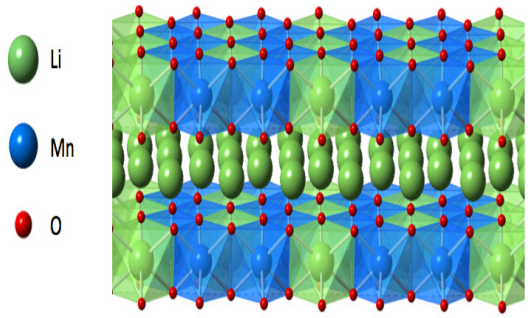

Figure VI - 175: The crystal structure of Li2MnO3 where the Li layer is shown without local coordination spheres but the combined Li/Mn layers shows the octahedrally coordinated Mn (blue) and Li (green) ions

In combination with the cluster expansion, possible phase transformations in the Li_2MnO_3 structure and their driving mechanisms are investigated. In Figure VI - 176, the formation energies ('stability') of a large number of Li_xMnO_3 structures are presented, including a large number of Mn/Li defect phases. The blue points signify compounds which retain the overall Li_2MnO_3 structure and the red points correspond to compounds which exhibit large structural deformations from the parent Li_2MnO_3 compound. As can be seen in Figure VI - 176, the structural deviations significantly increase with the amount of Li extracted from the compound, especially at $x_{Li} < 1$. Furthermore, in cases of large deformation, there exist a significant driving force for Mn ions to migrate from the Mn-layer into the Li-layer. The Mn migration results in spinel-like structures, as the major difference between the layered structure and the spinel is the existence of Mn tetrahedrons formation spanning the Mn-layer and Li-layer. The degree of Mn migration is determined by thermodynamic as well as kinetic factors, which means that the migration could be slow enough for material to retain its original structure during fast Li-extraction even if the structure is thermodynamically unstable.

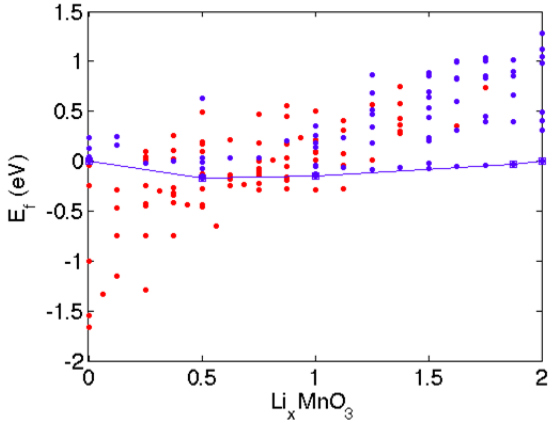

Figure VI - 176: Calculated formation energies of LixMnO3 structures with Li/vacancy defects spanning both the Li and the Mn layer. The blue points signify structures that retain the overall Li2MnO3 structure but the red points correspond to structures with a large deformation and defect formations compared to the parent structure

Analyzing the chemical and structural arrangements of the defect structures (red points) provides evidence of the thermodynamic stable states and driving force towards structural transformations in the Li_2MnO_3 compound. Hence, further calculations of the energy barriers of Mn migration were performed. The elastic band method was employed for several different hypothesized Mn migration paths at three different Li content, x = 0, 0.5, and 1. For low Li content, a favorable Mn migration path was found which implies a correlation between high charge, and increased spinel transformation.

Surface morphology effects in high-voltage spinel $LiMn_{1.5}Ni_{0.5}O_2$ (LNMO). To investigate the effect of nano-scaling on LNMO, specifically focusing on the role of surface stability and cation ordering, the surface energy for the low index facets (100), (110), and (111) was calculated. It was found that the most stable facet is dependent on the cation ordering at the surface layer. For a uniformly disordered structure (the most highly occurring local ordering in the disordered spinel with random cation arrangements), the (111) facet has the

lowest surface energy among the investigated facets, which agrees with several existing experimental observations.

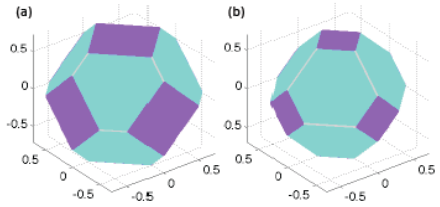

Figure VI - 177: The equilibrium shape of (a) the ordered spinel structure with a local inverse spinel surface structure and (b) the disordered spinel structure. The (100), (110) and (111) facets are colored violet, grey and turquoise, respectively

For the ordered structure, however, using only the atomic rearrangement required to remove the dipole moment and routine cell relaxations, the (100) facet with the Li/Mn/Ni/O-termination is predicted to be most stable, which contrasts with experimental observations. The surface reconstruction previously found successful for the $LiMnO_2$ spinel [4] was applied, where the (111) facet can be drastically lowered if a targeted surface reconstruction is employed where the Mn ions on the surface are locally swapped with the Li ions in the next available layer leading to an inverse spinel structure near the surface. This reconstruction successfully rendered the (111) facet the most stable for the LMNO ordered system, as expected for the spinel structure.

Conclusions and Future Directions

Through extensive calculations and analyses of the layered-spinel Li_xMnO_3 phase space, it has been found that the original structure of Li_2MnO_3 is thermodynamically unstable towards transformation and deformation to spinel-like domains, especially at low Li content. For low Li content, a favorable Mn migration path is found which implies a correlation between high charge, and increased spinel transformation. Future studies involve analysis of the charge and positions of the oxygen around each path which will provide further understanding on the phase transformation mechanism. Further studies also include oxygen migration.

For the LMNO surface project, the calculations predict that the (111) facet is the most stable surface facet (followed by the (100) and the (110) facets) for both the ordered as well as the disordered LMNO materials, resulting in the equilibrium cubo-octahedral particle morphology. The surface reconstruction in the ordered material results in a deviation from the ideal ordered surface cation arrangement, which will likely result in an enhanced accessibility to the Li-vacancy solid-solution region close to the surface.

FY 2013 Publications/Presentations

1. Anubhav Jain, Shyue Ping Ong, Geoffroy Hautier, Wei Chen, William Davidson Richards, Stephen Dacek, Shreyas Cholia, Dan Gunter, David Skinner, Gerbrand Ceder, Kristin A Persson, "Commentary: The Materials Project: A materials genome approach to accelerating materials innovation," *APL Mater.,* **1**, 011002 (2013).
2. Nadeem Tahir, Altaf Karim, Kristin A. Persson, Syed Tajammul Hussain, Alejandro Gabriel Cruz Gonzalez, Muhammad Usman, Muhammad Naeem, Ruimin Qiao, Wanli Yang, Yi-De Chuang, Zahid Hussain, "Surface Defects: Possible Source of Room Temperature Ferromagnetism in Co Doped ZnO Nanorods," *J. Phys. Chem. C*, **117** (17), pp 8968–8973 (2013).
3. Eunseok Lee and Kristin A Persson, "First-principles study of the nano-scaling effect on the electrochemical behavior in LiNi0.5Mn1.5O4," *Nanotechnology*, **24**, 424007, 2013 doi:10.1088/0957-4484/24/42/424007.
4. Altaf Karim, Sonia Fosse and Kristin A. Persson, "Surface structure and equilibrium particle shape of the LiMn2O4 spinel from first-principles calculations," *Phys Rev. B*, **87** (7), 075322 (2013) DOI: 10.1103/PhysRevB.87.075322.
5. Dan Gunter, Shreyas Cholia, Anubhav Jain, Michael Kocher, Kristin Persson, Lavanya Ramakrishnan, Shyue Ping Ong, Gerbrand Ceder, *5th Workshop on Many-Task Computing on Grids and Supercomputers (MTAGS) 2012*, Conference proceedings.
6. Shyue Ping Ong, William Davidson Richard, Gerbrand Ceder, Anubhav Jain, Michael Kocher, Shreyas Cholia, Daniel Gunter, Kristin A. Persson, Geoffroy Hautier, and Vincent L. Chevrier, "Python Materials Genomics (pymatgen): A Robust, Open-Source Python Library for Materials Analysis," *Computational Materials Science*, **68**. 314–319 (2013).

VI.E.5 Electrode Fabrication and Materials Benchmarking (LBNL)

Vincent Battaglia
Lawrence Berkeley National Laboratory

Environmental Energy Technologies Division
1 Cyclotron Road
Berkeley, CA 94960
Phone: (510) 486-7172; Fax: (510) 486-4260
E-mail: vsbattaglia@lbl.gov

Start Date: October 2012
Projected End Date: September 2016

Objectives

- Make good cells for testing experimental chemistries
- Optimize the electrode fabrication processes
- Bring fundamental understanding to the processes
- Test materials developed in the BATT Program
- Test for initial performace.
- Test for cycling performance
- Identify limitations and failure modes

Technical Barriers

Energy density and cycle life are critical to the realization of electric vehicles.

Technical Targets

- Energy Density: 200 Wh/kg
- Cycle Life: 1000 full discharge cycles

Accomplishments

- High speed shearing and long mixing times lead to electrodes with more uniform carbon distribution and higher electronic conductivities.
- When mixing components, there is a peak in the viscosity of the slurry.
- The viscosity after peaking the viscosity drops to a steady level at *ca*. 80 minutes of mixing.
- A new FRION from Scherson's Group shows a drop in reversible capacity but no negative impact on cyclability.

✧ ✧ ✧ ✧ ✧

Introduction

The BATT Program positions itself as a fundamental research program focused on applied problems. As such, 50% of the program is dedicated to finding new materials. The talented investigators that make up this portion of the program train their efforts on materials synthesis and pay less attention to the application. A good material does not a good electrode make. Our responsibility in the program is to develop the ability to make good electrodes with a limited amount of material. For this reason, electrode preparation procedures are constantly being investigated in order to gain greater insight into the steps used to fabricate a good electrode and cell.

This year the group is focused on mixing. Specifically, investigating the time and speed of mixing to help us understand what mixing step is most critical and what is not so critical and to determine whether there is an optimum condition for mixing that may be overshot as a result of over mixing.

The group is also responsible for providing facilities for other LBNL investigators to make electrodes and cells, to provide baseline laminates to investigators with expertise in diagnostics, to support Focus Groups with baseline performance data, and to provide a venue for other BATT PIs to send materials for testing in well made electrode and cells. This report discusses some of those efforts.

Approach

All BATT PIs are made aware of the facilities here at LBNL for providing laminates and testing of materials. Once a year, a call is issued to investigators who are either half-way through their funding or just about finished their funding to send us materials for evaluation. Once materials arrive, they go through a series of physical characterization tests, including BET measurement, particle size analysis, and SEM. This data is used by the electrode fabrication team to decide how much conductive additive and binder is needed in the electrode. The Group has been successful at making quality electrodes of cathode materials with a secondary particle size greater than 1 micron. The present effort is focused on optimizing some of the levers available for making electrodes such that the electrodes are as good as possible and that any deterioration that one may see during testing can be attributed to the material being tested and not the electrode formulation.

Results

Priority of mixing steps. Mixing of materials is a critical step in the making of a quality electrode. The fractional composition and order of mixing of the components that make up an electrode was investigated. Part of this year's effort is the investigation of mixing time. In making an electrode, the active material and conductive carbon are interspersed in N-methylpyrrolidone (NMP) with a high speed mixer. Once combined, the binder is added and the components are sheared together for a second mixing time. The initial research of this process involves the investigation of the length of the first mixing time, the shear rate during the first mixing time, and the length of the second mixing time. The table below was followed in the development of nine laminates.

Table VI - 7: Mixing Conditions

1st mixing(NMC 94%wt+AB 2%wt)(min)	Speed I (krpm)	2nd mixing (PVDF 4%) (min)
4	2.5	10
30	2.5	10
30	10	10
4	10	10
4	2.5	120
30	2.5	120
30	10	120
4	10	120
17	5.5	65

The results of conductivity measurements of cast laminates are provided in the Table VI - 8. The numbers in the first column correspond with the order of experiments listed in Table VI - 7.

These results indicate that the longest total mixing time combined with the highest shear rate results in a laminate with the highest conductivity. The data also indicate that the length of time of the second mixing step is the most important of the three parameters.

Table VI - 8: Electronic conductivity of laminates prepared by mixing conditions (in Table VI - 7)

Laminate	Average conductivity (S cm^{-1})
1	0.0107
2	0.0120
3	0.0154
4	0.0170
5	0.0209
6	0.0224
7	0.0310
8	0.0234
9	0.0185

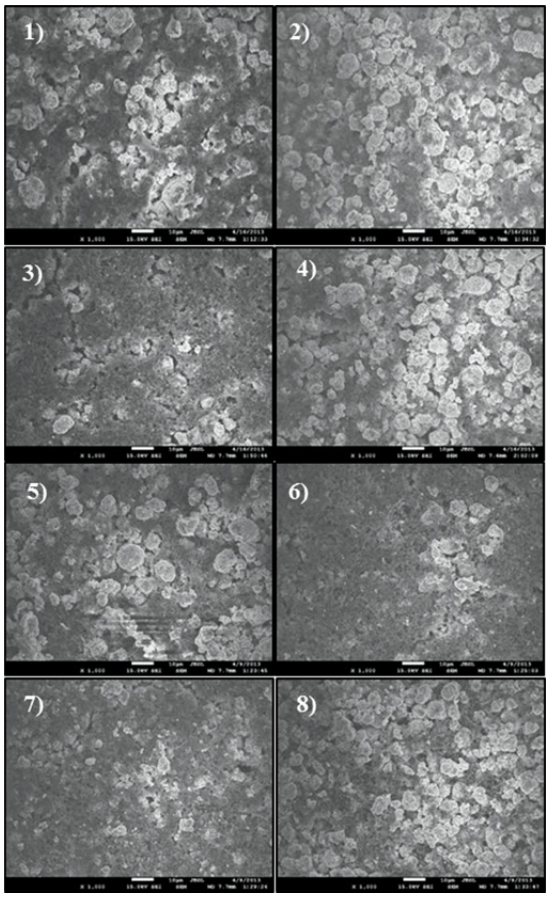

Figure VI - 178: SEMs provided in order of first 8 mixing conditions as listed in the tables above

The SEMs of the laminates that resulted from the first eight mixing conditions are provided in Figure VI - 178.

Careful inspection of these SEMs reveals that the laminate with the highest conductivity, #7, is also the laminate with the most uniform distribution of carbon black.

Viscosity*versus* mixing time. An investigation of mixing time on slurry properties was also conducted. The objective of this study was to understand the effects of the mixing process on cell performance, where performance includes reversible capacity, rate capability, and long-term cyclability. Thus, a more refined analysis was undertaken to investigate the effect of the second mixing step on slurry properties, specifically, viscosity.

A more in-depth analysis of the second mixing step was conducted. In this experiment, NCM (Micro MX6) and carbon black (Super P) were combined at a ratio of 94:2 in NMP at a ratio of 5:4 solids to liquids. The materials were mixed with a homogenizer at 10,000 rpm for twenty minutes. This was followed by the addition of PVDF 1100 at twice the concentration as that of the carbon additive for nearly two hours with the same homogenizer at 2500 rpm. The viscosity was measured every 10 minutes at different shear rates. The results are presented in Figure VI - 179. As expected, the slurry is shear thinning, thus, at higher shear rates, the proportionality constant between shear rate and shear force, i.e., the viscosity, is lower. It is also evident from the figure that there is a maximum in the viscosity at around 50 minutes into the mixing. It is believed that the first 50 minutes is a reflection of the macro mixing of the solids mix with the polymer. Once the two materials are uniformly distributed in the jar, the mixture of solids, and in particular, the high-surface area carbon additive which begins highly agglomerated starts to breakdown and the solution shows a lower viscosity. After 80 minutes, the viscosity of the solution begins to level off with time.

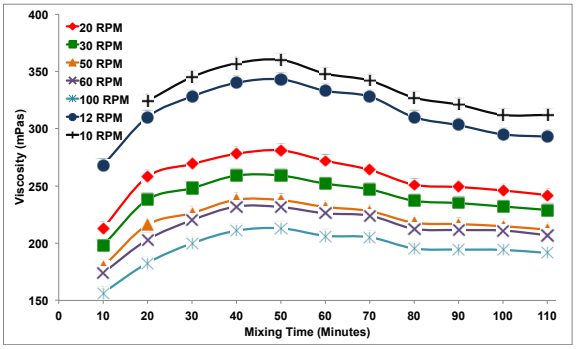

Figure VI - 179: Viscosity *versus* mixing time at different shear rates

Testing BATT materials. Two LNMO materials were received from Prof. Manthiram. These materials were based on findings in half-cells by the High-voltage Focus Group. However, as shown in previous reports, the biggest problems identified for this class of materials is the high first-cycle-irreversible-capacity loss in a full cell, additional capacity loss as a result of impedance rise in the cell, and rapid capacity fade at 55°C. These problems are believed to be a result of interactions with the graphite anode, which were not considered by the Focus Group. As might be expected, the materials from Manthiram did not improve upon these limitations in cells cycled against graphite.

Prof. Scherson sent a second FRION for testing. The results of full-cell testing are provided in the Figure VI - 180. In Figure VI - 180a, the cycling of a Graphite/NCM cell with baseline electrolyte 1M $LiPF_6$ in EC:DEC 1:2, and in Figure VI - 180b is the same chemistry plus 1 wt% FRION. These graphs demonstrate that the cyclability of the cell is not adversely affected by the presence of the salt and actually shows less capacity fade than the cell without the FRION. Rate performance, not shown, was not affected to a C-rate of 1C. However, there are some differences between the two cells. For one, the first cycle loss is worse for the cell with the FRION; second, the cell with the FRION shows less coulombic efficiency. In fact, the coulombic inefficiency is 15 times worse with the FRION than without it, yet shows better cyclability. At this stage it is not evident that this coulombic inefficiency will lead to a faster loss of electrolyte and therefore fewer overall cycles before catastrophic cell failure. If the FRION does not adversely affect long-term cycle life, it is possible that addition of more FRION may lead to a protective shuttle.

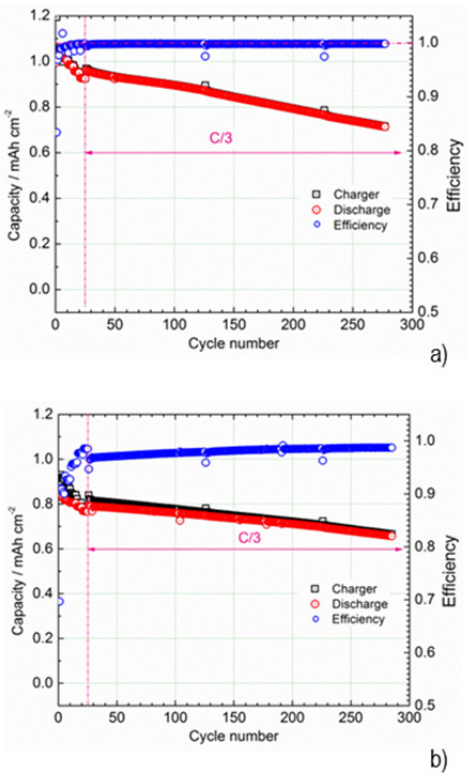

Figure VI - 180: Cycling and coulombic efficiency data for a Graphite/NCM cell, a), without FRION and b), with FRION

Conclusions and Future Directions

The degree of mixing clearly has an effect on the dispersion of the materials and the conductivity of the laminates, however, the effect on cycle life and all the other factors that dictate electrode performance is not clear. Cells need to be prepared from these laminates and tested for rate capability, adhesion to the current collector, and cyclability. This work will occur in 2014.

As the SEM images only the surface of an electrode, cross sections of electrodes will be made to determine if the distribution is the same through the electrode as it is across the electrode surface. Results will be reported in the next fiscal year.

From the viscosity measurements it appears that the mixing is nearly complete after 80 minutes. In the next stage of this experiment, electrodes and cells will be fabricated from the 80th minute and the two hour limit to determine if the time after 80 minutes shows any performance improvements. Also, extended mixing will be performed to see how long this constant viscosity interval lasts. There is a presumption in the electrode fabrication community that a slurry can be over mixed. The goal is to try to reach such a point and to understand what occurs in the slurry beyond this point.

The latest FRION from Scherson was tested. Unlike the first material sent, this did not require the addition of vinyl carbonate. Since testing of the first FRION, ANL has scaled it up and just sent us some material to re-test. Hopefully some of this material will make its way to SNL and they will be able to put it into 18650s to see if the FRION improves the response to abuse.

FY 2013 Publications/Presentations

1. "Scale-up and Testing of Advanced Materials from the BATT Program," *DOE Annual Peer Review Meeting*, May 13-17, 2013, Washington, DC.

VI.E.6 Cell Failure: Electrochemical Diagnostics (LBNL)

Vincent Battaglia
Lawrence Berkeley National Laboratory

Environmental Energy Technologies Division
1 Cyclotron Road
Berkeley, CA 94960
Phone: (510) 486-7172; Fax: (510) 486-4260
E-mail: vsbattaglia@lbl.gov

Start Date: October 2012
Projected End Date: September 2016

Objectives

- Develop tools to assess performance limitations
- Develop a means of measuring the gas composition in a Li-ion cell
- Interpret 3-electrode impedance data.
- Assess failure of cells and electrodes

Technical Barriers

Energy density and cycle life are critical to the realization of electric vehicles.

Technical Targets

- Energy Density: 200 Wh/kg
- Cycle Life: 1,000 full discharge cycles

Accomplishments

- Established the abilty to sample gas from a coin cell.
- Able to interpret impedance data of an electrode *versus* a reference electrode in a 3-electrode coin cell.
- Benchmark a $LiFePO_4$ electrode.
- Estalish that the electrode suffers from a side reaction and impedance rise.

✧ ✧ ✧ ✧ ✧

Introduction

The BATT Program consists of six major groupings: Cathode, Anode, Electrolyte, Diagnostics, Modeling, and Electrode Architecture. This project falls under the last category. The goal of this project is to test materials developed under the cathode, anode, and electrolyte projects. To perform this task appropriately, requires the ability to fabricate quality electrodes of active materials and to build quality cells. These capabilities have been developed over the past years. With this established, the next step is to develop better tools to assess performance. This year the ability to assess the gas formed in a coin cell was developed and the understanding of 3-electrode impedance data was acquired.

This group also contributes to Focus Groups when it can. This year the BATT Program is focused on understanding the issues that limit the use of Si-based materials as the anode in high energy cells. Several investigators have started to report coulombic efficiencies of Si greater than 99% in half-cells. Our group will investigate the performance of Si in a full cell. $LiFePO_4$ was selected as the cathode against which a Si-baseline electrode will be tested. The immediate focus is the development of this nanomaterial based cathode.

✧ ✧ ✧ ✧ ✧

Approach

The approach is to identify the most likely problem facing a technology of interest and then develop a tool that will bring greater insight and isolate that problem. Last year the main technology of interest was the high-voltage $LiNi_{1/2}Mn_{3/2}O_4$ material. Electrochemical evaluation suggested that a gas was formed in the cell that delayed the first charge *via* a shuttle. It was also clear that there was quite a bit of capacity fade in the cell as a result of side reactions and impedance rise. What was not known was the quantity or composition of the gas and the electrode where most of the impedance rise was occurring. For this reason, the focus was on developing the capability of analyzing gas in a coin cell and analyzing impedance data in a three electrode coin cell.

It is well known that many of the transition metal based oxide cathodes considered for Li-ion batteries lose metal into the electrolyte during operation and the metal then interferes with the performance of the anode. In testing Si in a full cell, the goal is to avoid issues unrelated to the Si itself. For this reason, the iron phosphate material was chosen for the cathode.

Results

An apparatus was designed to sample gas from a coin cell. Modifications were made to an apparatus designed to sample gas from a coin cell, specifically, hardware was selected with minimal void volume. A half-cell of high-voltage Ni-spinel and Li metal was assembled. The cell was connected to the mass spec through a thin tube and a valve that entered the cell behind the cathode.

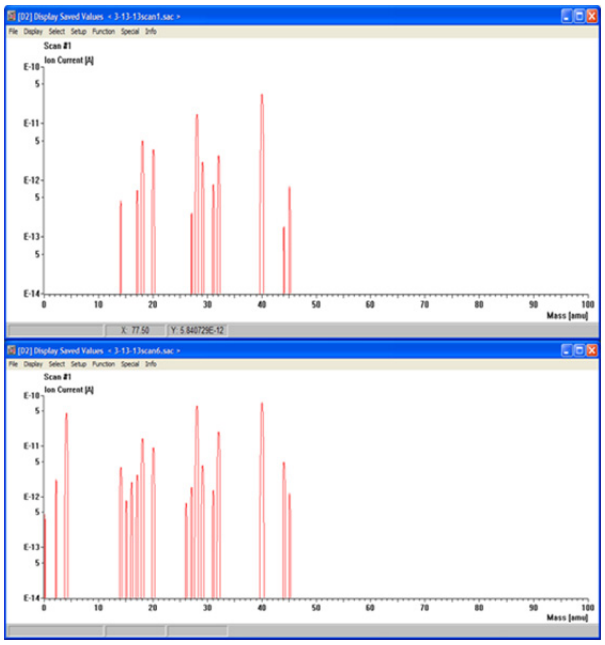

Figure VI - 181: Mass spectrograph of the vapor in a coin cell 2 hours into a 10 hour charge (top) and 4 hours into the first charge (bottom). The spikes to the far left on the bottom graph suggest the pressure of hydrogen

The cell was charged at a 10-hour rate and after 2 hours of testing the valve was opened briefly and the mass spec pulled a small vacuum on the cell. Only a background gas was detected which was indicative of the vapor pressure of the carbonate electrolyte. Two hours later the valve was opened for a second time and this time hydrogen was detected, as indicated by the differences in the graphs shown in Figure VI - 181. This was somewhat unexpected and still needs to be confirmed.

Three electrode cell. A visiting researcher in Srinivasan's Group used Comsol to see if he could duplicate the "inductance" loops seen experimentally by researchers that use three-electrode cells. To be clear, instead of the 2-D geometry in cylindrical coordinates, he solved the 2-D problem in Cartesian coordinates. However, we are certain that the results cross over these two geometries. He solved Laplace's equation for the potential distribution with linear kinetics as boundary conditions and ignored mass transfer effects (secondary current distribution). In so doing, he could reproduce the inductance loops. The impedance data for a full cell looks like what most others find when they perform ac-impedance on 2-electrode cells. In addition, one can show that the impedance data from one electrode *versus* the reference can be added to the data of the other electrode *versus* the reference electrode to give the 2-electrode cell data. However, the 3-electrode cell data typically contains "inductance" loops. It appears that the source of the loops in the individual cell data comes from geometries where the reference electrode is placed close to a region where the anode and cathode are not perfectly aligned. Simulations of different electrode alignments and reference electrode placements indicates that anything short of perfectly aligned electrodes leads to loops in one set of the reference electrode data. However, the simulations suggest that one should still be able to use the reference electrode impedance data to distinguish the contributions from the anode and the cathode in the 2-electrode cell data. In the figure below is an example of two electrode data, upper left; three electrode data of ref/cathode and ref./anode, middle right; and the sum of the ref/anode and ref./cathode, on the lower left. [In this example, the reference electrode is under the cathode and a small hole has been punched through the cathode.] One can see that the two electrode data is indistinguishable from the sum of the data from each electrode *versus* the reference. According to the modeling, impedance associated with the cathode is being captured by the impedance data measured on the ref./anode couple.

This would clearly lead to a false interpretation of what is happening in the cell.

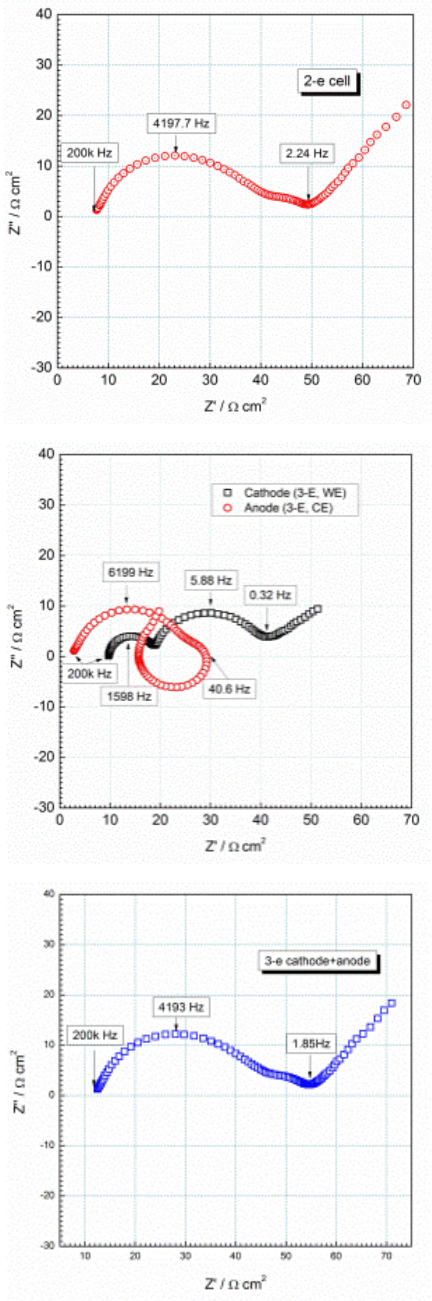

Figure VI - 182. Upper, Nyquist plot of two-electrode impedance; middle, Nyquist plot of each electrode versus a Li ref. electrode; lower, sum of the reference electrode data

Cathode for Si Focus Group. As part of the BATT Program, this group contributes to Focus Groups, in particular this group will investigate the performance of a Si-based anode in a full cell. The Liu Group will supply the Si anode, our group will develop the cathode. Since many of the oxide cathodes are known to lose transition metals during cell cycling, this group decided to use $LiFePO_4$ for the cathode. This material is considered to perform well with regard to cycling, although our group has little experience in making a cycleable electrode from this material. An SEM of the material is provided in Figure VI - 183. The sample is a distribution of particles from 100 nm to 700 nm. 7.5 wt% PVDF and an equal amount of Super-P. Li was added to the active material and mixed in NMP. Half-cells of the electrodes were tested at different discharge

rates and for cyclability. The results of the cyclability are provided in Figure VI - 184.

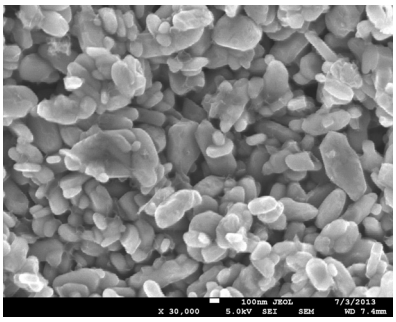

Figure VI - 183: SEM of LFP powder

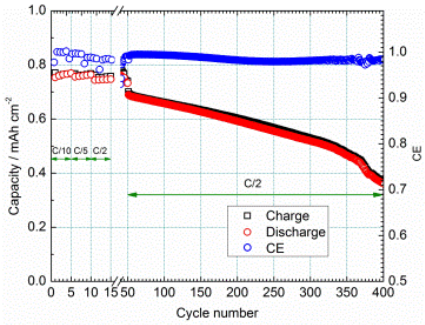

Figure VI - 184: Capacity versus cycle number for an LFP electrode

The cycling results are not acceptable at this point. A more in-depth analysis shows that there is a side reaction and an impedance rise with cycling. There are several possible reasons for the sub-optimum performance. First, this is our initial experience with this material and our typical electrode formulation was applied.

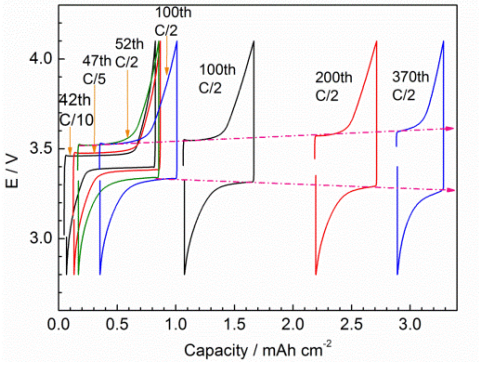

Figure VI - 185: Voltage versus capacity plotted sequentially. Certain cycles are displayed to high light motion due to side reactions and impedance rise in the cell with time

Conclusions and Future Directions

Although the electrochemical data suggested that gas in a Li/NMO cell was responsible for a delay in charging the cell, it was difficult to measure it in a coin cell. For this reason, pouch cells with this chemistry will be fabricated in an attempt to measure the quantity of gas produced. The gas collection apparatus will also be modified such that a pouch cell can be sampled instead of just coin cells. This work will be expanded to a full cell of graphite and Ni-spinel and to a pouch cell. If the result turns out to be significant, the chemistry responsible for the gas will be sought.

With regard to the impedance data, it appears one can *a priori* determine which contribution of impedance is due to which electrode. In the next year, the experiment will be repeated but with several electrode geometries to demonstrate that the impedance data for each electrode can be unequivocally identified and the rate of growth appropriately measured.

With regard to the LFP electrode, since this is a sub-micron material, it is possible that the standard formulation does not contain enough carbon conductive additive to ensure particle-to-particle connectivity from cycle to cycle. It is also possible, given the large number of particles per gram for this material, that the time of mixing as recommended in the standard formulation protocol is not long enough to lead to complete dispersion of the materials. Also, the cells with these electrodes were cycled between 2.8 and 4.1 V. Shifting the cycling regime to 2.1 to 3.8 V may reduce the side reactions. Together with Hydro-Quebec, the hope is to get to low capacity loss electrodes early in the next fiscal year.

FY 2013 Publications/Presentations

1. "Scale-up and Testing of Advanced Materials from the BATT Program," *DOE Annual Peer Review Meeting*, May 13-17, 2013, Washington, DC.

VI.E.7 First Principles Calculations of Existing and Novel Electrode Materials (MIT)

Gerbrand Ceder
Massachusetts Institute of Technology

Department of Materials Science and Engineering
77 Massachusetts Avenue
Cambridge, MA 02139
Phone: (617) 253-1581
E-mail: gceder@mit.edu

Start Date: May 2013
Projected End Date: Dec 2016

Objectives

- Develop more stable high capacity Li-excess layered cathodes.
  - Identify the structure of layered cathodes that leads to high capacity.
  - Clarify the role of the initial structure as well as structural changes upon first charge and discharge.
- Give insight into the factors that control the capacity and rate of Na-intercalation electrodes, and make suggestions for novel Na-intercalation cathode materials.
- Generate insight into the behavior of alkali-intercalating electrode materials.

Technical Barriers

- Low rate capabilities
- High cost
- Poor stability
- Low energy-density

Accomplishments

- Investigated the relation between voltage and thermal stability of materials.
- Indicated that most poly-anion cathodes are unlikely to be competitive with layered oxides
- Identified diffusion mechanism of Na in P2 layered oxides.
- Obtained high capacity $LiMn(BO_3)$

✧ ✧ ✧ ✧ ✧

Introduction

Improving cathode performance is an important component towards higher energy density batteries. Currently, the BATT Program has multiple new cathode materials under investigation, including several high voltage materials, as well as the high capacity layered materials. First principles modeling can provide insight into how these materials function and what their limitations are. There are now many cathode properties which can be modeled fairly accurately using first principles methods. This includes voltage, ion mobility, electron mobility, cation ordering and phase diagrams, and aspects of thermal stability. In addition to using these methods on individual materials, some of these computational techniques can also be scaled to scan through hundreds of materials.

This BATT Program project is a systematic approach towards higher energy density. To achieve high energy density one needs either high voltage or high capacity. High *voltage* tends to correlate with strong oxidation strength of the charged cathode, and hence degradation and lack of safety. As part of this BATT project, the relation between voltage and safety of the cathode material is being investigated. This is done through the computational screening of hundreds of compounds in order to obtain good statistics on this relation. Specific focus is on the oxidation chemical potential and decomposition reaction pathways of some high voltage materials that are being studied in this BATT project: $LiCoPO_4$, $Li_2MnP_2O_7$, $Li_2FeP_2O_7$, and $Li(Ni_{0.5}Mn_{1.5})O_4$.

To achieve large specific and volumetric *capacity* requires a large amount of Li to be cycled in and out of a compact and light crystal structure. The relation between theoretical and practical capacity and chemistry is being investigated in this program. Previous findings under the BATT Program indicate that there are very few useful two-electron couples in polyanion systems, as many redox couples are moved to very high voltage due to the inductive effect of the polyanion, which is why this program is focused on understanding better the high-capacity layered oxides (Li-excess materials) (together with Persson and others in the BATT Program).

In addition, a limited exploration of layered Na-intercalation materials is performed to understand better if high energy density Na-intercalation battery systems are possible.

Approach

First principles computations are being used to evaluate existing and novel materials. Voltages and intercalation curves are calculated with GGA+U, and if highly accurate results are required HSE methods are used. Phase diagrams are calculated with the Materials Project infrastructure. Configurational disorder for elevated temperature and off-stoichiometry is modeled with either point defect models (when off-stoichiometry is small) or with the cluster expansion for larger disorder. Ion mobility is evaluated with the Nudged Elastic Band Method or with direct Molecular Dynamics Simulations. Thermal stability is investigated with the approach developed previously under this program. Some of the computational work is performed in collaboration with Persson and with the Materials Project. Work on Li-excess layered materials is done in coordination with Persson (computational) and with the experimental efforts in the BATT Program (e.g., Thackeray, Grey).

Results

General Analysis: Figure VI - 186 shows the best specific capacity that can be obtained with a single electron reaction for a 3d transition metal and a specific anion chemistry. The results indicate that most polyanion chemistries are not competitive with today's layered oxides. Only borates, fluorides, and oxy-fluorides can achieve competitive specific capacities.

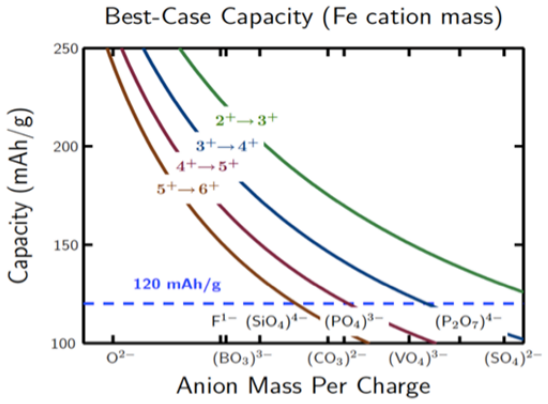

Figure VI - 186: Best case capacity for single electron redox couples for each anion chemistry

Borates. As borates are the only polyanion systems that combine good safety with competitive specific capacity, the $LiMnBO_3$ system was investigated extensively. Previous work indicated potential transport limitations. For this reason, the particle size dependence of the Li transport in this system was investigated. The monoclinic $LiMnBO_3$ is another example of a one-dimensional Li-ion conductor. In such a case, Li transport can be impeded by antisite defects which block the migration path (Mn in Li sites). In addition, assuming homogeneous distribution of the defects, this clogging of the channel becomes more serious in large particles than in small ones since Li will have a higher probability to encounter the defect as the particle becomes larger.

The experimentally achieved capacity (100 mAh/g) of $LiMnBO_3$ so far has been limited to 50% of its theoretical value (222 mAh/g). Considering both Mn and Li sites are trigonal-bipyramidal with similar ionic radii in $LiMnBO_3$, a fair amount of antisites are expected. Indeed, a refined XRD pattern of the as-synthesized $LiMnBO_3$ revealed that more than 4% Mn occupy the Li sites (Figure VI - 187). After firing at 500°C, the average particle size of $LiMnBO_3$ was 100 nm with a wide distribution ranging from 20 to 230 nm.

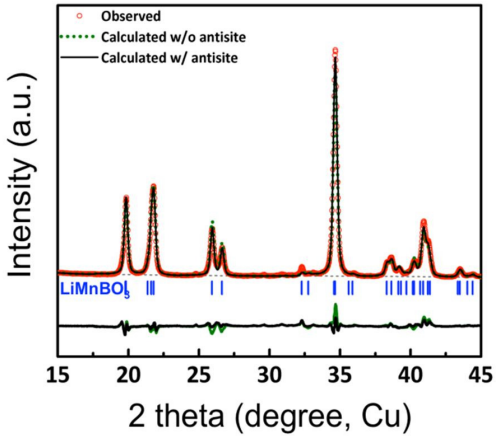

Figure VI - 187: Profile matching of XRD pattern of monoclinic $LiMnBO_3$ with and without considering antisite defects in the unit cell

Small particles (less than 50 nm) are not likely to be affected by the channel blockage, but its portion to the overall volume is insignificant. On the other hand, particles larger than 150 nm may not contribute to the Li intercalation reaction at all because almost all of the diffusion channels will be effectively shut off by the antisite defects. In the particles with intermediate sizes, Li migration can occur even if the migration path is blocked since there is a chance for Li to detour the blockage via neighboring channels. Although possible, however, this rate is estimated to be very low. All in all, the limited capacity of monoclinic $LiMnBO_3$ results from the size dependency of Li transport rooted in the channel blockage in large particles due to the antisite defects.

Work is continuing to gauge the actual diffusivity values of $LiMnBO_3$ by using standard diffusion analysis (Figure VI - 188).

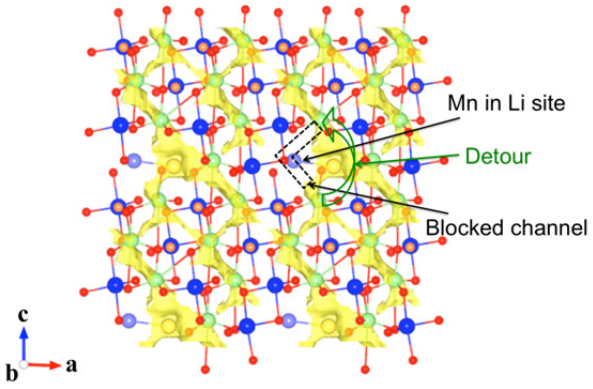

Figure VI - 188: Li trajectory as calculated by ab initio computation

Li-excess layered oxides. This is a newly initiated program. Progress is currently mainly on the algorithm side, with limited technical results to report. Algorithms have been constructed to enumerate possible atomic arrangements for layered and spinel structures in the Li-Co-Mn-O system. These structures will be queued up and computed in order to give us information on the phase diagram of this system. Once a reliable set of ground states is obtained, the phase diagram construction will be initiated.

Work on the Li transport in Li-excess materials has been initiated to understand the effect of Li-excess on Li diffusion. Exciting initial results have been obtained and will be further refined in the coming year.

Na layered oxides. Work on Na-ion intercalating layered oxides has begun with aims to design high energy density Na-ion battery cathodes and understand the effects of structure (P2 or O3) on their functional properties. First principles work has included the calculation of voltage curves for both structure types and the determination of the Na-ion diffusion mechanisms for the O3 and P2 versions of these structures. *Ab initio* molecular dynamics work has been initiated to calculate the diffusion mechanisms in both the O3 and P2 type structures to examine how they differ (Figure VI - 189).

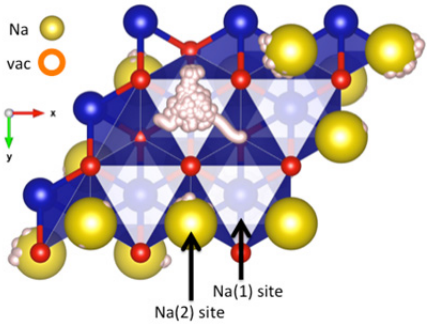

Figure VI - 189: Sodium trajectory as calculated by AIMD simulation

These calculations have so far determined that the di-vacancy diffusion mechanism present in O3 type structures is absent in P2 type structures. Work is continuing on how these contribute to Na-ion mobility and diffusion rates.

Conclusions and Future Directions

An initial conclusion is that very few poly-anion compounds can be competitive with layered oxides in terms of specific capacity. Only borates can combine reasonable theoretical capacities with high voltage and good safety.

As this new program was only started a few months ago, there are no clear conclusions on the Li-excess layered materials and Na-intercalation compounds.

Future work will focus on the phase diagram of Li-excess materials, diffusion of transition metals and lithium in these materials, and the role of the overcharge. In Na materials, the focus will be on the role of crystal structure on Na diffusion.

FY 2013 Publications/Presentations

1. H. Chen, Q. Hao, O. Zivkovic, G. Hautier, L-S Du, Y. Tang, Y-Y Hu, X. Ma, C.P. Grey, G. Ceder, "Sidorenkite ($Na_3MnPO_4CO_3$): A New Intercalation Cathode Material for Na-Ion Batteries," *Chem. Mater.*, **25**(14), 2777-2786 (2013).
2. G. Hautier, A. Jain, T. Mueller, C. Moore, S.P. Ong, G. Ceder, "Designing Multielectron Lithium-Ion Phosphate Cathodes by Mixing Transition Metals," *Chemistry of Materials*, **25**(10), 2064-2074 (2013).
3. S.P. Ong, Y. Mo, W. D. Richards, L. Miara, H.S. Lee, G. Ceder, "Phase Stability, Electrochemical Stability and Ionic Conductivity of the Li10 +/-1MP2X12 (M = Ge, Si, Sn, Al or P, and X = O, S or Se) Family of Superionic Conductors," *Energy & Environmental Science,* (**6**), 1, 148-156 (2013).
4. H. Chen, G. Hautier, G. Ceder, "Synthesis, Computed Stability, and Crystal Structure of a New Family of Inorganic Compounds: Carbonophosphates," *Journal of the American Chemical Society*, **134**(48), 19619–19627 (2012).

VI.E.8 Design and Scalable Assembly of High Density Low Tortuosity Electrodes (MIT)

Yet-Ming Chiang
Massachusetts Institute of Technology

Department of Materials Science and Engineering
77 Massachusetts Avenue
Cambridge, MA 02139
Phone: (617)-253-6471, Fax: (617)-253-6201
E-mail: ychiang@mit.edu

Antoni P. Tomsia, Collaborator
Lawrence Berkeley National Laboratory
Materials Science Division
1 Cyclotron Road
Berkeley, CA 94720
Phone: (510) 486-4918; Fax: (510) 486-4761
E-mail: APTomsia@lbl.gov

Start Date: October 2012
Projected End Date: September 2016

Objectives

- Develop scalable high density binder-free low-tortuosity electrode designs and fabrication processes to enable increased cell-level energy density compared to conventional Li-ion technology.
- Characterize electronic and ionic transport as a function of state-of-charge (SOC) in relevant systems including Li(Ni,Co,Al)O_2 (NCA), Li_2MnO_3-LiMO_2 and high-voltage spinels $LiM_xMn_{2-x}O_4$ and iron doped $LiMn_{1.5}Ni_{0.5-x}Fe_xO_4$.

Technical Barriers

Achieving sufficient electronic conductivity, avoiding mechanical failure upon cycling, meeting automotive duty cycles, lowering cost.

Technical Targets

- Identify high energy density cathode compositions with electronic transference number >0.5 across the SOC range for use in directional freeze-casting processing.
- Fabricate conductive additive free sintered cathodes with controlled pore volume fraction and topology yielding tortuosity values less than 2.
- Increase cell-level specific energy and energy density, and lower inactive materials cost, by achieving area capacity of 10 mAh/cm^2 at C-rates or current densities commensurate with operating conditions for PHEV and EV.

Accomplishments

- Measured electronic and ionic conductivity and diffusivity of NCA as a function of temperature and lithium content.
- Measured electronic conductivity of sintered Fe-doped $LiMn_{1.5}Ni_{0.5-x}Fe_xO_4$ (x = 0.00, 0.08, 0.10, 0.50) as a function of lithium content *x*.
- Fabricated NCA cathodes by directional freeze casting and sintering.

✧ ✧ ✧ ✧ ✧

Introduction

This project aims to develop alternative electrode architectures and scalable fabrication methods that result in thick, high density electrodes with low tortuosity porosity oriented normal to the electrode plane, using electrode actives of interest for future EV battery systems. Previously, it was shown that sintered $LiCoO_2$ cathodes with aligned, low tortuosity porosity fabricated by co-extrusion or directional freeze-casting could reach area capacities of 7.5-9.5 mAh/cm^2 at 1C rate and 6.5-7.5 mAh/cm^2 at 2C rate (Figure VI - 190). Here, a key technical performance target is to achieve at least triple the capacity per unit area at 1C-2C rate (e.g., >10 mAh/cm^2) that the same active materials can deliver in a conventional calendared electrode, and in cathodes of interest for next-generation lithium ion batteries. The electrode density and thickness at which the discharge energy and discharge power are optimized for PHEV and EV applications critically depends on the pore topology of the sintered electrodes. Data on capacity per unit area and tortuosity of conventional calendared electrodes is available from literature and prior work under BATT. The baseline approach for the current project is pressureless sintering of cathode compounds. The open porosity of sintered electrodes allows for electrolyte infusion and ion transport with a low tortuosity compared to that in conventional calendared electrode technology. However, in order to maximize the density and thickness of electrodes at which the desired utilization can be achieved, it is desirable to

introduce lower tortuosity porosity into the dense sintered electrodes.

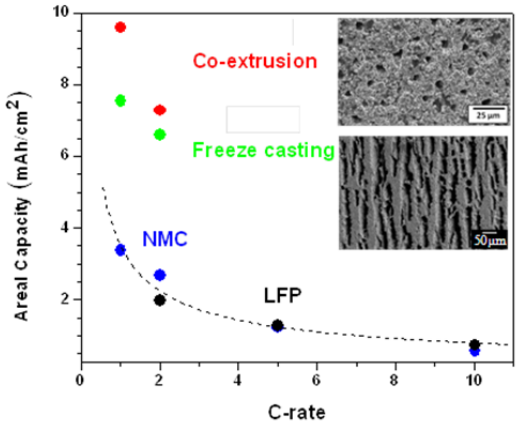

Figure VI - 190: Area capacity vs C-rate of sintered $LiCoO_2$ with oriented mesocale porosity prepared by two methods, compared to conventional calendared Li-ion electrodes (H. Zheng, J. Li, X. Song, G. Liu, V.S. Battaglia, *Electrochimica Acta* 2012, *71*, 258)

Approach

Since the current program began in May 2013, efforts have been, firstly, focused towards identifying cathode compositions with sufficiently high electronic conductivity that conductive additives need not be incorporated. Secondly, the bulk lithium transport of candidate cathodes has been characterized in order to define the microstructural scale that is necessary to achieve the target performance without solid-state transport being rate-limiting. Thirdly, NCA electrodes have been fabricated by directional freeze-casting and sintering, and electrochemical characterization to identify rate-limiting mechanisms has been conducted.

Results

Electronic and ionic conductivity and diffusivity of $Li_{1-x}Ni_{0.8}Co_{0.15}Al_{0.05}O_2$. Despite its widespread use in current Li-ion technology, there is a paucity of transport data for NCA. Here, electronic conductivity was measured in sintered dense $Li_{1-x}Ni_{0.8}Co_{0.15}Al_{0.05}O_2$ (NCA) plate as a function of temperatures and lithium content. Measurements were performed on additive-free, sintered NCA, and therefore reflect pure phase conductivity. Samples were fired at 850°C for 12h and cooled at 5°/min, resulting in samples of 96% sintered density. Electrochemical delithiation was conducted to obtain a range of *x* values. Ag paste electrodes were used as ion-blocking electrodes for the measurement of electronic conductivity (Ag/NCA/Ag). DC polarization technique as well as AC impedance measurement was performed to obtain the electronic conductivity. Representative results are shown Figure VI - 191. The electronic conductivity of the fully lithiated phase increases monotonically with increasing *x*, with a sudden enhancement of conductivity occurring at 60% delithiation. NCA is semiconducting over the range of lithium concentrations measured. The values of activation energy calculated using the Arrhenius law varies from 0.22 eV to 0.14 eV as shown in Figure VI - 191a, similar to literature values for $Li_xNi_{0.8}Co_{0.2}O_2$ and typical for the small polaron migration process generally observed in mixed-valence systems. The electronic configuration for Ni^{3+}, Co^{3+} and Ni^{4+} has the (t_2) orbitals filled, with electron delocalization being less probable. The increase in electronic conductivity with delithiation is attributed to hole formation in the narrow (Ni^{4+}/Ni^{3+}) band. The sudden increase in conductivity at ~60% delithiation (Figure VI - 191b) may be due to the onset of Co^{3+} oxidization.

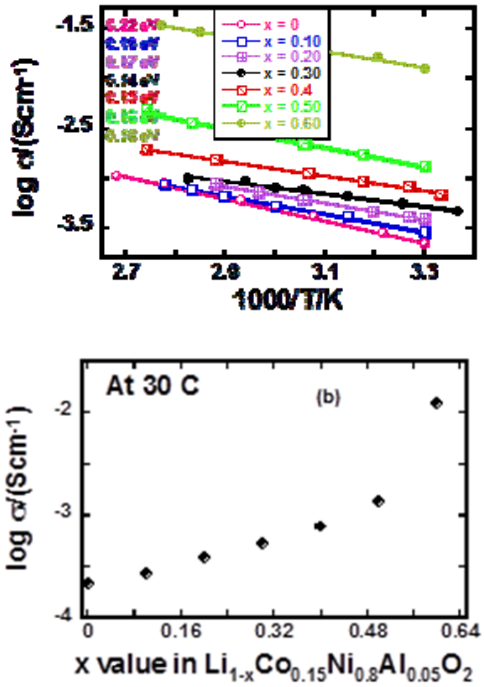

Figure VI - 191: (a) Electronic conductivity of NCA as a function of temperature and (b) lithium content

To measure ionic conductivity, ion conducting/electron blocking electrodes of polyethylene oxide (PEO) with 1% lithium iodide salt were used in the configuration: Li/PEO/NCA/PEO/Li. The DC polarization technique as well as AC impedance measurements were performed to obtain the ionic conductivity and diffusivity (Figure VI - 192), with good agreement between the two methods. Activation

energies are almost the same for ionic conductivity (1.15 eV) and diffusivity (1.20 eV) (within±0.20 *eV* error) as shown in Figure VI - 192b. Despite the extensive commercial use of NCA and its long research history, this is, to our knowledge, the first report of such data.

The lithium ion diffusivity as a function of lithium concentration *x* was also measured using GITT and depolarization techniques. The diffusivity was found to vary strongly with x, being nearly 10^2 lower for x<0.5 than for *x*>0.5. While the lithium concentration dependence is complex, the absolute value of diffusivity is high enough that it can be concluded that for micron-scale particles and at practical C-rates, solid-state transport in NCA is not rate-limiting in lithium ion cells.

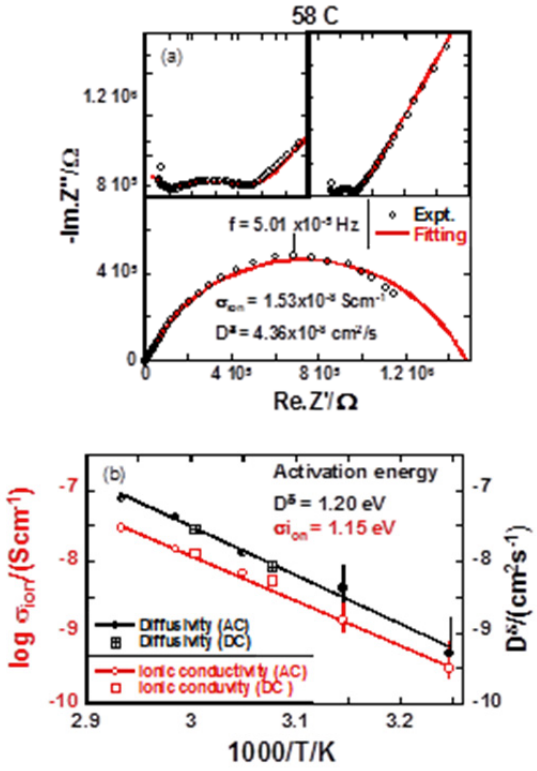

Figure VI - 192: (a) AC impedance spectra obtained from electron-blocking cell at 58°C and fitted with equivalent circuit, (b) lithium ionic conductivity and diffusivity as a function of temperature

Electronic conductivity of $LiMn_{1.5}Ni_{0.5-x}Fe_xO_4$. $LiMn_{1.5}Ni_{0.5-x}Fe_xO_4$ (x = 0.00, 0.08, 0.10, 0.50) powder was synthesized by solid state reaction, producing an octahedral crystallite morphology (Figure VI - 193), and sintered for electronic conductivity measurements. The ordered phase was obtained by heating the pellet at 950°C for 24h followed by annealing at 650°C for 48h and cooling to room temperature (1°C/min). The disordered phase was obtained by heating the pellet at 950°C for 24h and cooling to room temperature at 10°C/min.

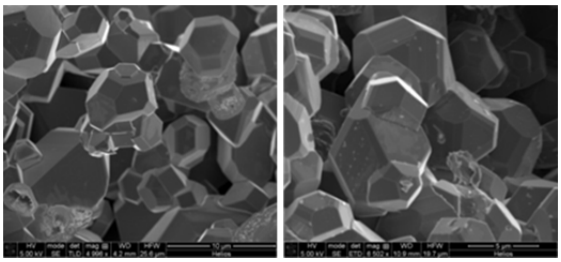

Figure VI - 193: Microstructure of ordered (a) $LiMn_{1.5}Ni_{0.5}O_4$, (b) $LiMn_{1.5}Ni_{0.42}Fe_{0.08}O_4$

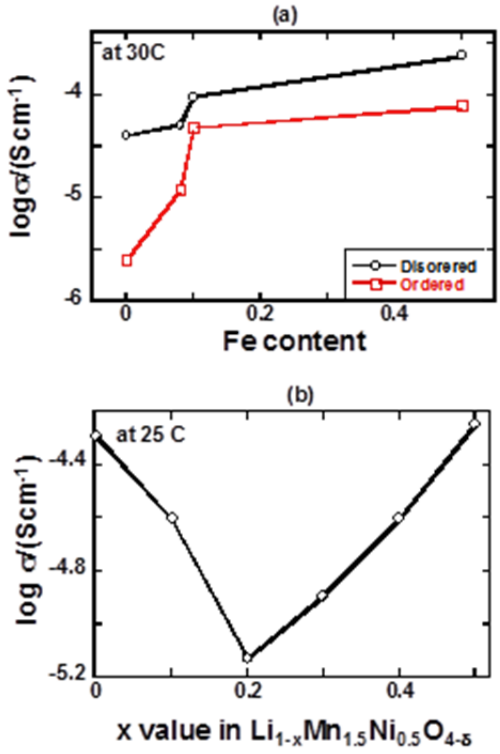

Figure VI - 194: The electronic conductivity of ordered and disordered $LiMn_{1.5}Ni_{0.5-x}Fe_xO_4$ (x = 0.00, 0.08, 0.10, 0.50) as a function of Fe content at 30°C (a) and the electronic conductivity of disordered $LiMn_{1.5}Ni_{0.42}Fe_{0.08}O_4$ as a function of lithium content at 25°C (b)

The electronic conductivity was measured by AC and DC techniques as a function of temperature using the symmetrical cell configuration (Ag/LMNO/Ag). Figure VI - 194 (a) shows the electronic conductivity at 30°C for both ordered and disordered phases increases as a function of Fe content. The electronic conductivity of partially electrochemically delithiated disordered $LiMn_{1.5}Ni_{0.42}Fe_{0.08}O_4$ as a function of lithium content is shown in Figure VI - 194 (b). This behavior is similar to that seen previously for undoped LMNO: the electronic conductivity decreases until the end of the 4V

intercalation plateau (complete oxidation of Mn^{3+} to Mn^{4+}) and inceases thereafter.

Conclusions and Future Directions

- Both NCA and Fe-doped LMNO have sufficient electronic conductivity for use as additive free sintered cathodes.
- The measured lithium transport coefficients allow a maximum microstructural length scale to be defined in fabricated microstructures such that solid state transport is not rate-limiting.
- In the coming year, directionally-freeze cast NCA electrodes (already fabricated) will be characterized, and Fe-doped LMNO electrodes will be fabricated.
- At very high area capacity, pulse power performance may differ substantially from conventional electrodes. This behavior will be characterized using PHEV- and EV-specific "drive cycles."

FY 2013 Publications/Presentations

1. **"**Studies on the transport properties of ordered and disordered high voltage cathode," *International Conference on Energy Harvesting, and Storage: Materials, Device and Application*, 29-30th April, 2013, Baltimore, USA.
2. "Transport properties of high voltage spinel cathode lithium ion battery," *ECS 223th Meeting,* 12-16th May, 2013, Toronto, Canada.
3. "Investigation of transport properties of $LiNi_{0.8}Co_{0.15}Al_{0.05}O_2$ (NCA)," *ECS 224th Meeting,* 27th Oct-1st Nov, 2013, San Francisco, California.

VI.F Diagnostics

VI.F.1 Energy Storage Materials Research using DOE's User Facilities (ANL)

Michael Thackeray
Argonne National Laboratory

9700 South Cass Avenue
Argonne, IL 60439
Phone: (630) 252-9184; Fax: (630) 252-4176
E-mail: thackeray@anl.gov

Collaborators
ANL: Jason Croy, Brandon Long, Paul Fenter, Tim Fister
Advanced Photon Source, ANL: Mali Balasubramanian, Matthew Suchomel
Electron Microscopy Center, ANL: Dean Miller
Northwestern University: Michael Bedzyk, Xiao Chen
Rutherford Appleton Laboratory, UK: Bill David

Start Date: October 2012
Projected End Date: September 2015

Objectives

- The primary objective of this project is to broaden the scope of studies of electrode materials relevant to the BATT program, using DOE and international user facilities through collaborative efforts.
- More specifically, the goal is to use a range of x-ray spectroscopic techniques, including *in situ* methods, such as X-ray diffraction (XRD), X-ray absorption (XAS), and X-ray reflectivity (XR) at the Advanced Photon Source (APS); high-resolution transmission electron microscopy (HRTEM) at Argonne's Electron Microscopy Center (EMC); and neutron scattering at the ISIS facility, Rutherford Appleton Laboratory (RAL), UK and/or ORNL's Spallation Neutron Source (SNS).

Technical Barriers

- Low energy density
- Poor low temperature operation
- Abuse tolerance limitations

Technical Targets

- 142 Wh/kg, 317 W/kg (PHEV 40 mile requirement)
- Cycle life: 5,000 cycles
- Calendar life: 15 years

Accomplishments

- High resolution XRD and XAS data were collected at the APS to examine and unravel the complex structural features of high capacity, composite electrode structures.
- HRTEM data of composite electrode structures were collected to monitor differences in the domain structures of quenched and slow cooled samples.
- XRD analyses of $LiMn_2O_4$ (LMO) spinel and Ge anode thin films were undertaken as an exploratory study to probe electrochemical reactions at lithium-metal oxide (cathode) and lithium-alloy (anode) surfaces.
- A proposal to conduct neutron diffraction studies of high capacity composite electrode structures at ISIS in the UK was submitted.
- Two papers in preparation. One presentation.

✧ ✧ ✧ ✧ ✧

Introduction

Bulk and interfacial electrochemical processes are of fundamental scientific interest as well as of technological importance. The performance of energy storage and power supply systems is largely dependent on these processes, which can occur at an electrode-electrolyte interface or in the bulk of the electrode. In this project, the structural features, ionic transport phenomena and charge-transfer reactions at the electrode/electrolyte interface of lithium battery electrode materials, notably high potential metal oxide cathodes, are studied.

This project is relevant to Argonne's BATT research on electrodes with integrated 'composite' structures, which has highlighted the possibility of designing new, high-potential and high capacity electrodes with

Li_2MnO_3 as a stabilizing component; in particular, the project complements and supports the BATT project *'Novel Cathode Materials and Processing Methods (VI.B.1)'*. It has been demonstrated that it is possible to integrate Li_2MnO_3 with layered $LiMO_2$- or spinel LiM_2O_4 components (e.g., M=Mn, Ni, Co) at the atomic level, and that these composite materials can provide a very high capacity (250 mAh/g), which is significantly higher than the capacity offered by conventional layered $LiCoO_2$, spinel $LiMn_2O_4$ and olivine $LiFePO_4$ electrodes. These lithium- and manganese-rich composite materials have extremely complex structures which are surprisingly stable when delithiated at high potentials (~5 V). Despite the enhanced stability of these electrode materials, it is still necessary to passivate the electrode surface to prevent electrode/electrolyte reactions, and to improve lithium-ion transport at the surface, thereby enhancing the power capability. In this respect, several coating techniques and passivating agents, such as metal oxides (Al_2O_3, ZrO_2), fluorides (AlF_3) and phosphates ($AlPO_4$) have been shown to improve the surface stability and rate capability of electrodes, but little is known about surface structures, or the mechanisms by which lithium-ion transport occurs at the electrode surface.

Approach

Important analytical techniques for probing the structure-electrochemical property relationships of lithium battery electrode materials, notably at electrode surfaces, include neutron scattering, XAS, photoelectron spectroscopy, nuclear magnetic resonance, Raman spectroscopy, Fourier transform infrared spectroscopy, and electron microscopy. Over the past year, analytical efforts have focused predominantly on x-ray techniques, including "*in situ"* experiments, and high-resolution electron microscopy. Major facilities are available at Argonne to conduct these experiments, notably at the APS and the EMC. In addition, new initiatives using X-ray reflectivity and neutron scattering techniques were initiated.

Surface-protected 'coated' cathode materials to be studied include those with integrated 'composite' structures in which the coating contains specific 3d/4d transition metals that are not present in the core structure. Coatings are applied by various techniques, for example, from solution by standard sol-gel methods or by atomic layer deposition (ALD). *"In situ"* synchrotron hard x-ray spectroscopic techniques including XAS, resonant and non-resonant x-ray emission spectroscopy (XES) and x-ray Raman scattering (XRS) are useful techniques for monitoring reactions at the electrode-electrolyte interface. A comparison of the electrochemical properties of uncoated and coated electrodes will be made. It is envisioned that these studies will provide important information about the structure of coatings at the molecular level, the mechanism of lithium-transport at the electrode-electrolyte interface and an insight into degradation mechanisms. Another aspect to be investigated is the effect of the coating on the bulk structure of the composite material itself, particularly on deintercalation at high voltages, for example 4.6 V, during the initial charge. Recent XAS studies of uncoated composite materials have shown convincing evidence of oxygen loss during the first charge. The exact mechanism for oxygen loss and the accompanying reactions are not yet known. Detailed studies of the local structure within the bulk are likely to provide key insights on structure-property relationships of coated materials. In addition to the studies of composite cathode structures, investigations of well defined electrode surfaces will be undertaken using spectroscopic and microbeam methods. Such studies will utilize the property of total external reflection of x-rays at small incident angles, which minimizes the contribution from the bulk of the material, thereby providing interface sensitivity without sacrificing the "*in situ*" capability of hard x-rays.

Results

A novel technique to synthesize composite electrode structures was recently devised at Argonne. Specifically, layered Li_2MnO_3 is used as a precursor template. The precursor is treated in an acidic solution in the presence of soluble transition metal cations of interest, for example, Ni^{2+}. In the process, lithium and oxygen can be leached from the Li_2MnO_3 precursor with concomitant ion-exchange of lithium with the desired cations. On subsequent annealing, the exchanged cations are driven into the manganese layers to form the composite structure. The technique is extremely versatile and can produce a wide range of integrated, composite structures including 'layered-layered', 'layered-layered-spinel', and 'layered-layered-rocksalt' configurations. Furthermore, it was discovered that elements and compounds of interest for surface stabilization (e.g. fluorides, phosphates, Al, etc.) can be added to the initial acidic solution to yield products with modified surfaces and bulk structures.

Figure VI - 195 shows cycling data from a $Li/0.5Li_2MnO_3 \bullet 0.5LiMn_{0.5}Ni_{0.5}O_2$ electrode synthesized from a Li_2MnO_3 precursor with the addition of 2.5% F. Cells were cycled at room temperature at 15 mA/g. The first 20 cycles were between 4.6 – 2.0 V where the electrodes delivered a stable 250 mAh/g. Starting with cycle 21 the upper voltage cut-off was increased to 5.0 V. The electrode delivered a steady capacity of 275 mAh/g for the remaining 30 cycles on test. The inset of Figure VI - 195 shows that these electrodes

achieve ~200 mAh/g discharge capacity at close to C rates.

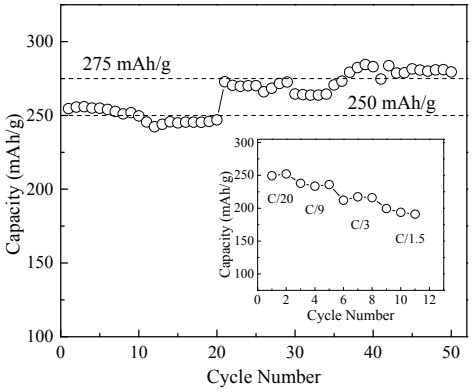

Figure VI - 195. Li/0.5Li_2MnO_3•0.5$LiMn_{0.5}Ni_{0.5}O_2$ electrodes cycled between 4.6-2.0 V (cycles 1-20) and 5.0-2.0 V (cycles 30-50) at 15 mA/g. The inset shows rate data

XAS (APS)

In order to probe the structures of these fluorinated electrodes XANES and EXAFS were carried out on fresh (MnNiF_fresh) and cycled (MnNiF_cycled) as well as un-fluorinated (MnNi_fresh) electrodes at the APS. Figure VI - 196a shows Mn K-edge XANES data of all samples along with Li_2MnO_3, a Mn^{4+} standard reference. It was observed that all uncycled, fresh samples had an average Mn oxidation state of 4+, in agreement with Li_2MnO_3. Figure VI - 196b shows Mn K-edge EXAFS data of the samples in Figure VI - 196a. Again, all of the fresh materials are similar and reveal that fluorination has not altered the bulk, local structure and, therefore, likely resides predominantly at the surface. For the cycled materials, Figure VI - 196a and Figure VI - 196b reveal clear changes that are associated with the local manganese environment including significant disorder, which is evident from the increased intensity of the pre-edge peaks in Figure VI - 196a. Figure VI - 196b also reveals a significant reduction of the first shell Mn-O correlations at ~1.5 Å (not corrected for photoelectron wave shift) as well as longer range correlations between ~4-6 Å. These changes to the local manganese environment are similar to those observed in the Mn K-edge data of all lithium-rich xLi_2MnO_3•0(1-x)$LiMO_2$ (M=Mn, Ni, Co) electrodes after activation and high-voltage cycling. These changes are directly linked to the voltage fade phenomenon triggered by processes (e.g. oxygen loss) occurring along the first cycle, activation plateau.

These data reiterate the importance of surface modifications to produce desirable electrochemical performance in high-voltage systems; they also highlight the inherent, bulk nature of performance degradation (e.g., voltage fade) with cycling.

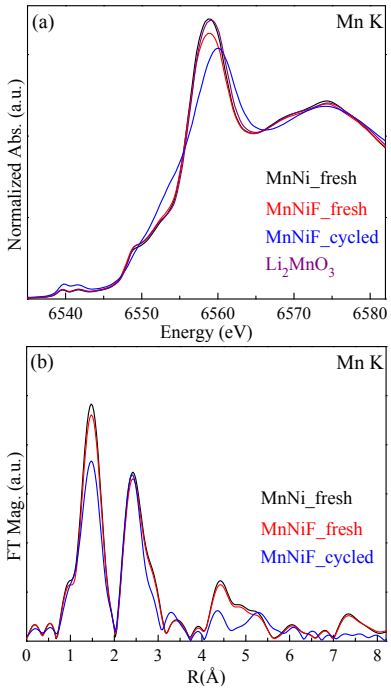

Figure VI - 196: Mn K-edge XANES (a) and EXAFS (b) of fresh and cycled 0.5Li_2MnO_3•0.5$LiMn_{0.5}Ni_{0.5}O_2$ electrodes. (a) Includes a Li_2MnO_3, Mn^{4+} reference

XRD (APS) and HRTEM (ECM)

High resolution XRD data of 0.5Li_2MnO_3•0.5$LiCoO_2$ electrode samples that had been annealed at 850°C followed by slow cooling, quenching and intermediate (programmed) protocols were collected at the APS (Beamline 11). The XRD patterns of all the samples (not shown here to save space) were virtually identical – irrespective of the cooling protocol. The HRTEM images of the 0.5Li_2MnO_3•0.5$LiCoO_2$ samples that had been slow cooled and quenched are shown in Figure VI - 197a and Figure VI - 197b, respectively. In this case, it is clear that slow cooling increases the Li_2MnO_3 and $LiCoO_2$ domain size and the degree of order, as illustrated in Figure VI - 197 by the 213 domains of Li_2MnO_3 (blue) and 112 domains of $LiCoO_2$ (red). These structural differences impact the electrochemical behavior of the electrodes, thereby highlighting the critical need to control synthesis parameters and procedures in order to fabricate optimized compositions and structures in a reproducible manner.

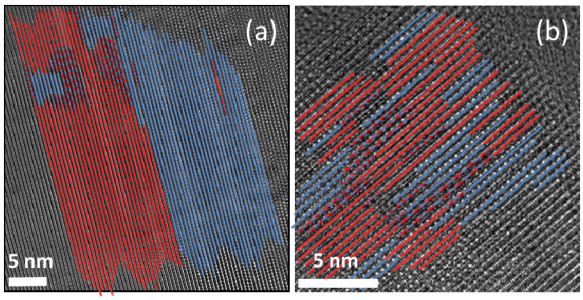

Figure VI - 197: Transmission electron microscopy images of $0.5Li_2MnO_3 \cdot 0.5LiCoO_2$ annealed at 850°C followed by (a) slow cooling and (b) quenching

XR (APS)

A project to prepare and characterize model thin-film electrode structures for high resolution *in situ* studies of charge/discharge processes was initiated in FY2013. This project is a collaborative effort between staff at the APS from Argonne (Paul Fenter and Tim Fister) and Northwestern University (Michael Bedzyk and Xiao Chen). The goal is to obtain a mechanistic understanding of the changes to electrode and electrode-electrolyte structures as a function of applied potential, through direct, *in situ* and real-time observations. Efforts have focused on developing and studying two model thin film electrode systems: a germanium (Ge) film as a model anode, and lithium manganese oxide (LMO) spinel thin film as a model cathode. The films were grown by sputter deposition. The film structures were characterized and studied by X-ray reflectivity (XR) at the APS. Ge films were found to have a controlled morphology with a uniform thickness of a few nanometers. Preliminary *in situ* XR studies have shown that these films can be reversibly lithiated with associated changes to film thickness and density. The growth of laterally uniform LMO films has been a greater challenge. It was found that LMO films grow in a complex 3d morphology when deposited on Al_2O_3 or MgO substrates, which is not ideal for XR studies. The use of an interfacial coating (e.g., TiN films) on the substrate prior to the growth of the electrode to control the LMO film morphology and to provide an electronic collector layer is being explored (see Figure VI - 198.)

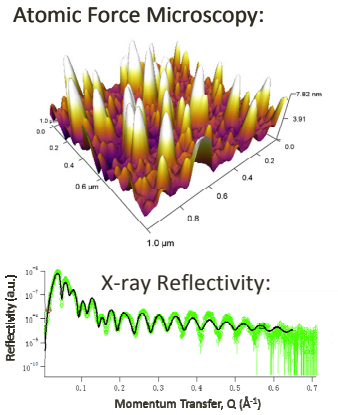

Figure VI - 198: (Top) AFM image and (bottom) X-ray reflectivity data of $LiMn_2O_4$/TiN/MgO(001) films grown by RF-sputtering. The LMO film is crystallographically aligned with the substrate, but is rougher than optimal

NS – ISIS, UK

A proposal was submitted to ISIS, UK for beamtime on POLARIS to undertake a preliminary neutron study of the structure and nanostructure of 'layered-layered' cathode materials that contain both Mn and Ni as active redox sites using PDF and Rietveld analyses. In combination with electron microcopy and electrochemical measurements undertaken at ANL, these measurements will enable an assessment of the efficacy of neutron powder diffraction to gather an understanding of complex structure-electrochemical property relationships in Mn and Ni-containing electrode materials. A longer range goal is to undertake *in situ* studies of cycled electrodes and use isotopically labeled (e.g. ^{62}Ni) materials. The main objectives of this task are to:

- Gather detailed information about the structures of 'layered-layered' and 'layered-layered-spinel' composite electrode materials, structure-electrochemical property relationships, electrochemical activation processes, and degradation mechanisms.
- Identify structural configurations associated with voltage fade and hysteresis phenomena.

Conclusions and Future Directions

Conclusions

This project is a work in progress. An approach has been adopted to use a wide variety of analytical methods, notably with DOE's user facilities, to probe electrode materials of interest to the BATT program. A novel synthesis method is being exploited to tailor and optimize the composition and the surface and bulk structures of lithium- and manganese-rich composite electrodes. Electrochemical and XAS data have revealed

that surface modifications with fluorine result in enhanced electrochemical stability, delivering 275 mAh/g when cycled over a wide voltage window, 5.0-2.0 V. HRTEM images have highlighted that the domain structure of composite electrodes depends on processing conditions, impacting electrochemical performance. Efforts to conduct neutron diffraction experiments to determine structure-property relationships have been initiated to broaden the scope of research on these complex materials. X-ray reflectivity techniques at the APS have been introduced to probe surface structures of lithium transition metal oxide and lithium-alloy anodes.

Future Work

This work reiterates the importance of engineering and controlling surface reactivity of high-voltage systems, and combating inherent degradation mechanisms. At the core of both surface and bulk phenomena in lithium- and manganese-rich composite electrode materials is the incorporation and utilization of the Li_2MnO_3 component. Significant advances are only likely to be made with a full understanding of structure-electrochemical property relationships using a full suite of characterization techniques. Studies will focus on understanding the Li_2MnO_3 activation process and the influence of domain size on electrochemical performance. Optimization of composite electrodes will be investigated by studying cation-substituted materials of interest (e.g., Mg, Zn), before and after cycling. The analytical studies will be extended to include high-voltage spinels.

FY 2013 Publications/Patents/Presentations

Publications

1. J. R. Croy, B. Long, M. Balasubramanian and M. M. Thackeray, *An Electrochemical and Structural Study of Substituted $xLi_2MnO_3 \bullet (1-x)LiMO_2$ Composite Electrodes Prepared from an Li_2MnO_3 Precursor* (2013). In preparation.
2. J. R. Croy, B. Long, M. Suchomel, D. Miller and M. Balasubramanian, *Cooling Effects on the Domain Structure of $xLi_2MnO_3 \bullet (1-x)LiCoO_2$ Electrode Materials* (2013). In preparation.

Presentations

1. 2013 DOE Annual Peer Review Meeting Presentation, Arlington, VA.

VI.F.2 Advanced *in situ* Diagnostic Techniques for Battery Materials (BNL)

Xiao-Qing Yang
Brookhaven National Laboratory

Chemistry Department
Building 555, Brookhaven National Laboratory
Upton, NY 11973
Phone: (631) 344-3663; Fax: (631) 344-5815
E-mail: xyang@bnl.gov

Kyung-Wan Nam
Brookhaven National Laboratory
Chemistry Department
Building 555, Brookhaven National Laboratory
Upton, NY 11973
Phone: (631) 344-3202; Fax: (631) 344-5815
E-mail: knam@bnl.gov

Start Date: October 2012
Projected End Date: September 2016

Objectives

- To determine the contributions of electrode material changes, interfacial phenomena, and electrolyte decomposition on cell capacity and power decline.
- To develop and apply synchrotron based *in situ* X-ray techniques such as X-ray diffraction (XRD) and X-ray absorption spectroscopy (XAS) to study materials in an environment that is close to the real operating conditions.
- To perform diagnostic studies of the potentially low cost and high energy density cathode materials such as spinel structured $LiNi_xMn_{2-x}O_4$.
- To perform diagnostic studies of the Si-based high energy density anode materials.
- To develop new diagnostic tools for battery studies.
- To alleviate the chemical interaction between superoxide ($O_2^{\cdot-}$) and electrolyte.
- To enhance the rechargability of lithium-air batteries.

Technical Barriers

- Li-ion and Li-metal batteries with long calendar and cycle life
- Li-ion and Li-metal batteries with superior abuse tolerance
- To reduce the production cost of a PHEV batteries

Technical Targets

- Complete the *in situ* time resolved XRD studies of $LiMn_{2-x}Ni_xO_4$ cathode material with ordered ($P4_332$) spinel structure during heating.
- Complete the XAS studies of $LiMn_{2-x}Ni_xO_4$ cathode material with ordered ($P4_332$) spinel structure during heating.
- Complete the *in situ* time resolved XRD studies of $LiMn_{2-x}Ni_xO_4$ cathode material with disordered (Fd-3m) spinel structure during heating.
- Complete the XAS studies of $LiMn_{2-x}Ni_xO_4$ cathode material with disordered (Fd-3m) spinel structure during heating.
- Complete the *ex situ* Si K-edge XAS studies of Si-based high energy density anode materials after cycling.

Accomplishments

- Developed new "quick XAS" technique to do kinetic studies on cathode materials for Li-ion batteries during electrochemical delithiation at constant voltage.
- Carried out thermal stability studies of high voltage cathode material $LiMn_{1.5}Ni_{0.5}O_4$ with spinel structure (both ordered $P4_332$ and disordered Fd-3m structures) using time resolved XRD combined with mass spectroscopy during heating.
- Carried out thermal stability studies of high voltage cathode material $LiMn_{1.5}Ni_{0.5}O_4$ with spinel structure (both ordered $P4_332$ and disordered Fd-3m structures) using XAS during heating.
- Carried out studies on electronic structure changes of high energy density Si anode using Si K-edge X-ray absorption near edge structure (XANES) spectroscopy during lithiation-delithiation cycling.
- Developed a boron containing Lewis acid which could catalyze rapid disproportionation of the superoxide ions to prevent their reaction with electrolytes.

- Li_2O_2 can be dissolved and soluble complex O_2^{2-} can be electrochemically oxidized on carbon electrode.

✧ ✧ ✧ ✧ ✧

Introduction

4V-spinel $LiMn_2O_4$ is one of the important cathode materials for lithium-ion batteries (LIBs) as the power sources of electric vehicles due to high ionic- and electronic- conductivity, excellent thermal stability, and low cost. Recently, one of its derivatives, $LiNi_xMn_{2-x}O_4$, denoted as LNMO, (where x is around 0.5) has attracted research attention as a promising high-energy density cathode material with higher operating voltage at ~4.7V. On the other hand, the poor cycle and calendar life of LNMO, especially at elevated temperatures, still needs to be improved. Heat treatment procedure is very important since LNMO is formed in two different kinds of structures, depending on the annealing procedure adopted after the 900°C solid-state reaction. Reportedly, spinel-structured LNMO, formed through the solid-state reaction, loses oxygen between 700°C and 900°C, causing the partial transformation of a spinel phase to a rock-salt phase. The majority of the rock-salt structure can be transformed back to a spinel structure during cooling by regaining oxygen below 700°C. However, if the cooling is not slow enough, the amount of oxygen regained is low and a significant amount of the rock-salt impurity phase will be retained. Under such conditions, the disordered phase is formed, in which Mn^{4+} and Ni^{2+} cations are randomly distributed in the transition metal layer, with the space group *Fd*-3*m* (to be referred as *d*-LNMO). On the other hand, if the cooling of the material is slow enough (in some cases, a constant temperature-annealing duration below 700°C is used), the re-incorporation of oxygen is almost complete, and the rock-salt impurity residues will be negligible. Under the latter conditions, the ordered phase is formed in which Mn^{4+} and Ni^{2+} cations are located at certain different sites in the crystal lattice with the space group $P4_332$ (to be referred as *o*-LNMO). Although most researchers presently believe that the cycling performance of the disordered *d*-LNMO is better than that of the ordered *o*-LNMO, there are more and more reports demonstrating that the *o*-LNMO can display a satisfactory cycling performance, while preserving other properties like higher average operating voltage and larger capacity than those of the *d*-LNMO. The thermal stability of LNMO, which could greatly impact the safety of LIBs, has received little attention. This lack of interest probably could be attributed to the assumption that the excellent thermal stability of the delithiated LNMO can be naturally inherited from its parent material $LiMn_2O_4$, for which only a subtle structural rearrangement takes place without the oxygen release up to 500°C in the fully delithiated state. Therefore, $Li_xMn_2O_4$ has been regarded as a thermally safer cathode material than layered materials. However, for LNMO, what was overlooked at is that when a quarter of the Mn is replaced by Ni, the thermodynamics of the material inevitably changes yielding a very different thermal stability than its parent $LiMn_2O_4$. Unfortunately, little research has been published on the thermal stability of LNMO materials and their doped derivatives. There are very few studies correlating thermal stability either with structural differences (ordered or disordered) or with oxygen-releasing structure changes during heating for LNMO. The systematic studies reported here are aimed to explore these correlations.

Electrochemical reduction of molecular O_2 is known to form superoxide ions (O_2^-), which can react with organic solvents and specifically carbonate solvents. The decomposition of the solvents induced by O_2^- consumes the electrolyte as well as forming undesired side-products (e.g. Li_2CO_3), which are difficult to re-oxidize during the recharge process. We hypothesize that the chemical interaction between the superoxide ions and the electrolyte is one of a few competing parallel reactions that O_2^- may undergo. Other reactions may also include the disproportionation and further reduction of O_2^-. To alleviate the problems associated with the O_2^-/electrolyte reactions, we have attempted to facilitate the disproportionation and further reduction of O_2^-, while hindering its chemical interaction with the electrolyte.

One of the major problems for Li-air battery is the precipitation of Li_2O_2 on the surface of the porous electrode as when the pores in the GDE are filled up, the electrode will cease functioning. In order to unlock the potential of Li-air chemistry, it is crucial to increase the solubility dramatically for these reaction products formed in charge-discharge cycling for Li-air batteries.

Approach

Use both time resolved XRD and mass spectroscopy to study the structural changes of high voltage cathode material $LiMn_{2-x}Ni_xO_4$ with spinel structure (both ordered $P4_332$ and disordered *Fd-3m* structures) during heating.

Use *in situ* XAS, both XANES and EXAFS to study the structural changes of high voltage cathode material $LiMn_{2-x}Ni_xO_4$ with spinel structure (both ordered $P4_332$ and disordered *Fd-3m* structures) during heating.

Investing a Lewis acid compound to dissolve solid Li_2O_2 and catalyze superoxide disproportionation.

Results

In situ TR-XRD combined with mass spectroscopy TR-XRD/MS were used to study both charged *d*- and *o*-LNMO during heating up to 375°C as shown in Figure VI - 199 and Figure VI - 200. The phase transitions and accompanying oxygen release can be tracked

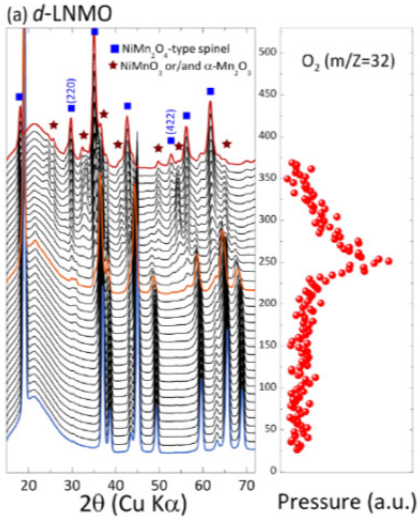

Figure VI - 199: *In situ* XRD pattern combined with simultaneously measured mass spectroscopy (MS) data that trace oxygen gas release of fully charged disordered LNMO during heating up to 370°C

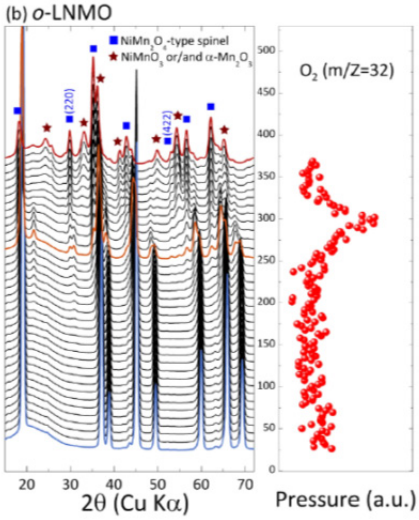

Figure VI - 200: *In situ* XRD pattern combined with simultaneously measured mass spectroscopy (MS) data that trace oxygen gas release of fully charged ordered LNMO during heating up to 370°C

closely during heating. There was clear evidence of thermal-decomposition-related phase transitions accompanied with noticeable oxygen release below 250°C for both *d*-LNMO and *o*-LNMO. These results are in sharp contrast to the conventional spinel $Li_xMn_2O_4$ at the fully charged (x = ~0.0) state, where no oxygen-release peak was observed below 375°C. This tells us that when 25% of the Mn in conventional spinel $LiMn_2O_4$ is replaced by Ni, the thermal stability of this high voltage LNMO is greatly changed for both *d*-LNMO and *o*-LNMO. Also it was found that the thermal stability *o*-LNMO is better than *d*-LNMO.

***In situ* X-ray Absorption Spectroscopy (XAS).** XAS can provide information about the changes in local- and electronic-structure surrounding the absorbing atoms in an elemental-selective way. This is very helpful in identifying which element is mainly responsible for thermal instability. Ni K-edge XANES data for delithiated *d*- and *o*-LNMO during heating up to 370°C are shown in Figure VI - 201. The most notable change in Ni K-edge XANES spectra is the inhomogeneous edge-shifting to lower energy (i.e., the decrease in average oxidation state of Ni); this sudden jump of edge shift divides the series of spectra into two parts. It occurs at some temperature between 220°C and 270°C for the charged *d*-LNMO, and between 270°C and 320°C in the charged *o*-LNMO. This feature is clearly shown in the Figure VI - 201 where the changes in edge position are plotted as a function of temperature.

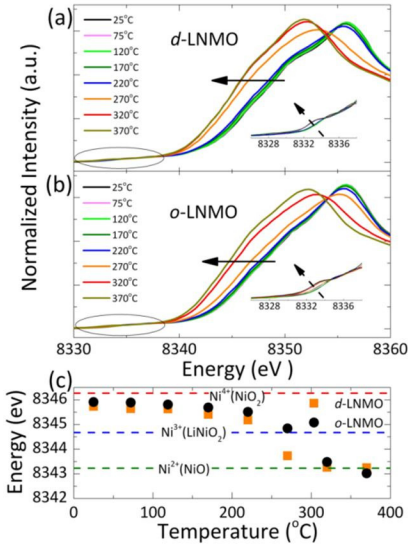

Figure VI - 201: *In situ* Ni K-edge XANES spectra of fully charged a) *d*-LNMO and b) *o*-LNMO during heating up to 370°C. Insets show the detailed feature of pre-edge region. c) Variations of the Ni-K edge positions (defined as the energy at half height of the energy step at main edge)

The Mn K-edge XANES results depicted in Figure VI - 202 showed only a moderated edge shift to lower energy for both samples, even during oxygen release, compared with the Ni K-edge results. The Mn reduction commenced at higher temperatures and ended with

lesser change than did the Ni reduction, demonstrating the structural-stabilizing role of Mn. At 370°C, after major oxygen release, the average oxidation state of Mn in both charged *d*- and *o*-LNMO only fell to somewhere between Mn^{3+} and Mn^{4+}, while that for Ni was reduced to close to Ni^{2+}. This finding suggests that the release of oxygen was initiated by the Ni^{4+} to Ni^{2+} reduction for LNMO upon heating resulting in highly disordered and defective structures and decomposition compounds, which, in turn, triggered the reduction of Mn^{4+} ions. Figure VI - 202 shows that the charged *o*-LNMO has higher average oxidation state of Mn than the charged *d*-LNMO at 370°C confirming the better thermal stability of the former than the latter in the charged state.

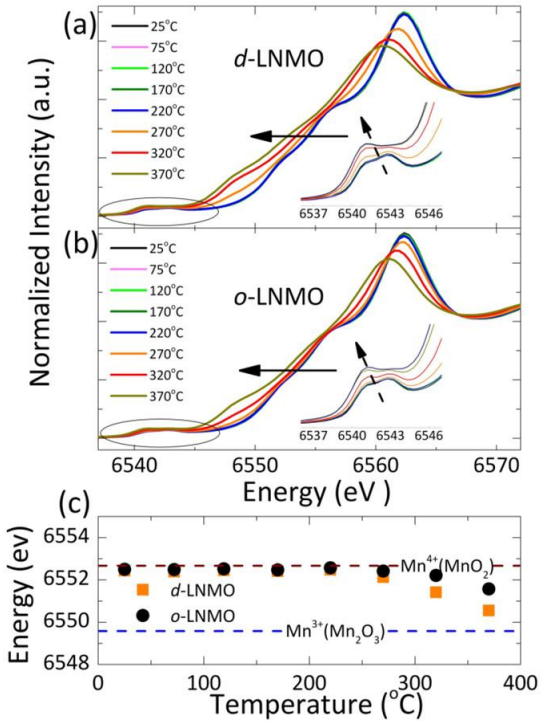

Figure VI - 202: *In situ* Mn K-edge XANES spectra of fully charged a) d-LNMO and b) o-LNMO during heating up to 370°C. Insets show the detailed feature of pre-edge region. c) Variations of the Mn-K edge positions (defined as the energy at half height of the energy step at main edge)

Si K-edge XANES study. The electronic structure changes of Si anode were studied during the first cycle as shown in Figure VI - 203. During lithiation, the spectra showed continuous edge shift to lower energy side probably due to the expansion of Si-Si bonds. The intensity of the 1s → 2p transition peak (A) also decreased during lithiation, revealing increased local structural disordering around Si. The evolution of peak B was found to originate from the formation Li_xSi alloy using DFT calculation. After the 1st cycle, the XANES feature changed back to nearly its pristine spectrum but not completely, showing the irreversible lithiation/delithiation behavior of the Si anode studied in this work.

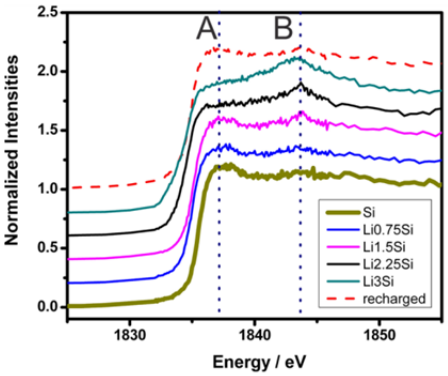

Figure VI - 203: Si K-edge XANES spectra of Si anode at different states of lithiation and delithiation

Li-air batteries. A boron containing Lewis acid compound can increase the solubility of Li_2O_2 and the complexed peroxide ion can be re-oxided electrochemically (see Figure VI - 204).

The negative impact of the reaction between the electrolyte and O_2^- produced by the O_2 reduction is minimized by a rapidly catalyzed superoxide disproportionation. The pseudo 2-electron O_2 reduction reaction due to the replenishment of O_2 at the electrode surface. This discovery could lead to a new avenue for the development of high capacity, high rate, rechargeable Li-Air batteries (see Figure VI - 205).

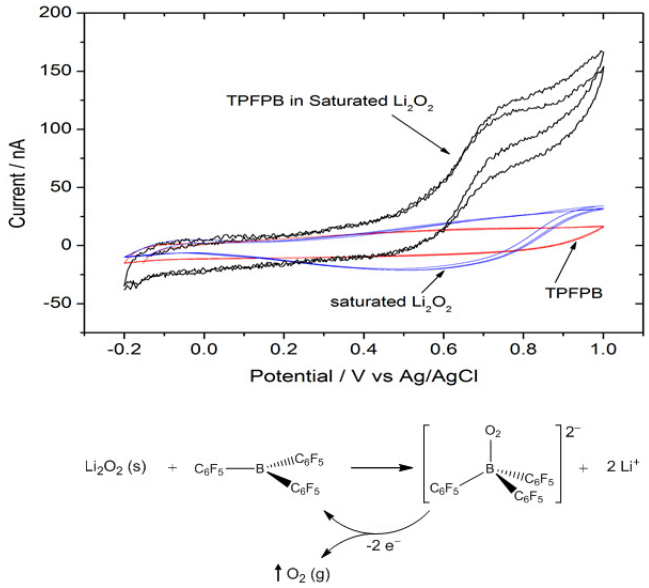

Figure VI - 204: Comparison of the cyclic voltammetry for the powder microelectrode of the same carbon material in Li_2O_2 saturated PC/ACN electrolyte and supporting electrolyte (0.5 M $LiPF_6$), PC/ACN electrolyte containing only TPFPB and supporting electrolyte (0.5 M $LiPF_6$) and Li_2O_2 saturated PC/ACN solution with 0.5 wt% TPFPB. Scan rate: 1mV/sec

Conclusions and Future Directions

New findings on the thermal-stability are discovered for the high-voltage spinel LNMO with ordered (*o*-) and disordered (*d*-) structures at fully delithiated state were obtained using a combination of *in situ* TR-XRD coupled with mass spectroscopy (MS) and XAS during heating: Both *o*- and *d*-LNMO at their fully charged states start oxygen-releasing structural changes at temperatures below 300°C, which is in sharp contrast to the good thermal stability of the 4V-spinel $Li_xMn_2O_4$. In addition, charged *o*-LNMO shows better thermal stability than the *d*-LNMO counterpart.

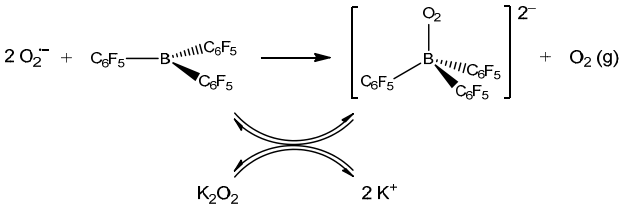

Figure VI - 205: Mechanism for the catalyzed superoxide disproportionation

The solubility of solid Li_2O_2 can be dramatically increased through the Lewis acid-base interaction between boron and peroxide. The solube O_2^{2-} ion can be re-oxided electrochemically. Rapid superoxide disproportionation can be catalyzed by tris(penftafluorophenyl) borane additive.

In the future more *in situ* XRD and XAS studies of Fe substituted high voltage spinel cathodes during charge-discharge cycling will be performed.

In the future study, more Lewis acid compounds will be syntheized and tested. A unique flow lithium air cell design is being tested

FY 2013 Publications/Presentations

1. Jianming Zheng, Jie Xiao, Xiqian Yu, Libor Kovarik, Meng Gu, Frederick Omenya, Xilin Chen, Xiao-Qing Yang, Jun Liu, Gordon L. Graff, Stanley M. Whittingham, Ji-Guang Zhang, "Enhanced Li^+ ion transport in $LiNi_{0.5}Mn_{1.5}O_4$ through control of site disorder," *Physical Chemistry Chemical Physics*, **14**, 13515-13521 (2012).
2. Jie Xiao, Xiqian Yu, Jianming Zheng, Yungang Zhou, Fei Gao, Xilin Chen, Jianming Bai, Xiao-Qing Yang, Ji-Guang Zhang, "Interplay between two-phase and solid solution reaction in high voltage spinel cathode material for lithium ion batteries," *Journal of Power Sources*, **242,** 736-741 (2013).
3. Huilin Pan, Xia Lu, Xiqian Yu, Yong-Sheng Hu, Hong Li, Xiao-Qing Yang, Liquan Chen, "Sodium storage and transport properties in layered $Na_2Ti_3O_7$ for room-temperature sodium-ion batteries," *Advanced Energy Materials*, **3**, 1186-1194 (2013).
4. Yuesheng Wang, Xiqian Yu, Shuyin Xu, Jianming Bai, Ruijuan Xiao, Yong-Sheng Hu, Hong Li, Xiao-

Qing Yang, Liquan Chen, Xuejie Huang, "A zero-strain layered metal oxide as the negative electrode for long-life sodium-ion batteries," *Nature Communications*, **4,** 2365 (2013).

5. J.J. Ding, Y.N. Zhou, Q. Sun, X.Q. Yu, X.Q. Yang, Z.W. Fu, "Electrochemical properties of P_2-phase $Na_{0.74}CoO_2$ compounds as cathode material for rechargeable sodium-ion batteries," *Electrochimica Acta,* **87**, 388-393 (2013).
6. Yong-Ning Zhou, Jing-Jing Ding, Kyung-Wan Nam, Xiqian Yu, Seong-Min Bak, Enyuan Hu, Jue Liu, Jianming Bai, Hong Li, Zheng-Wen Fu* and Xiao-Qing Yang*, "Phase transition behavior of $NaCrO_2$ during sodium extraction studied by synchrotron-based X-ray diffraction and absorption spectroscopy," *A Journal of Materials Chemistry*, **1**, 11130 (2013).
7. Zheng, H-S Lee, X.Q. Yang, D.Y. Qu, "Electrochemical Oxidation of Solid Li_2O_2 in Non-aqueous Electrolyte Using Peroxide Complexing Additives for Lithium-Air Batteries," *Electrochemistry Communications*, **28**, 17-19 (2013).
8. "Diagnostic Studies to Improve Abuse Tolerance and Life of Li-ion Batteries," *DOE Annual Peer Review Meeting*, May 13-17, 2013, Washington, DC.
9. Xiqian Yu, Hung-Sui Lee, Xiao-Qing Yang, Kyung-Wan Nam, and Yongning. Zhou, Hong Li, Xuejie Huang, Liquan Chen, Kan Xu and Arthur von Cresce, "Studies on the formation and stability of solid electrolyte interphase on the surface of anode and cathode of lithium-ion batteries," *222nd Meeting of the Electrochemical Society*, October, 8-12, 2012, Honolulu, Hawaii, USA, **Invited.**
10. Xiqian Yu, Kyung-Wan Nam, Chao Ma, Hong Li, and Xiao-Qing Yang, "Investigation on Si anode materials for Lithium-ion batteries using X-ray absorption spectroscopy," *222nd Meeting of the Electrochemical Society*, October, 8-12, 2012, Honolulu, Hawaii, USA.
11. Xiqian Yu, Kyung-Wan Nam, Xiao-Qing Yang, Yongning Zhou, Enyuan Hu, Yingchuan Lv Hong Li, Daniel Abraham, Huiming Wu, and Khalil Amine "Structure Evolution and Its Relation to the Voltage Fading Behavior In Li-Rich Layered $Li_{1.2}Ni_{0.15}Co_{0.1}Mn_{0.55}O_2$ Cathode Material During Cycling: X-Ray Diffraction And Absorption Spectroscopy Study," *Advanced Electrochemical Energy Symposium and Shanghai Jiao Tong University-Sinopoly Battery Technology Forum (2012 AEES)*, December 22, 2012, Shanghai, China. **Invited.**

VI.F.3 Interfacial Processes (LBNL)

Robert Kostecki
Lawrence Berkeley National Laboratory

Environmental Energy Technologies Division
1 Cyclotron Road, MS 90-3026D
Berkeley, CA 94720
Phone: (510) 486-6002; Fax: (510) 486-5454
E-mail: r_kostecki@lbl.gov

Start Date: October 2012
Projected End Date: September 2016

Objectives

- Establish direct correlations between electrochemical performance of high-energy Li-ion composite cathodes, and surface chemistry, morphology, topology and interfacial phenomena
- Improve the capacity and cycle life limitations of Li_xSi anodes
  - Determine physico-chemical properties of the SEI, i.e., chemical composition, reaction kinetics, morphology, ionic/electronic conductivity etc.
  - Investigate electrocatalytic behavior of intermetallic anodes in organic electrolytes
  - Provide remedies to interface instability e.g., new alloys and/or structures, electrolyte additives, codeposition of other metals etc.
  - Characterize degradation modes, improve SEI long-term stability in high-energy Li-ion systems
  - Evaluate the effect of surface composition and architecture on electrochemical behavior of the electrode

Technical Barriers

This project addresses the following technical barriers related to the battery technology development effort of the DOE Office of Vehicle Technologies:

- Inadequate Li-ion battery energy (related to cost)
- Poor lithium battery calendar/cycle lifetime for PHEVand EV applications
- High electrode impedance that limits power density
- Need for new advanced battery materials and composite electrodes with acceptable specific energy, durability, cost, and safety characteristics.

Technical Targets

- Cycle life: 5,000 (deep) and 300,000 (shallow) cycles
- Available energy: 200 Wh/kg ·
- Calendar life: 15 years

Accomplishments

- Determined the mechanism of interfacial processes on $LiNi_{0.5}Mn_{1.5}O_4$
  - Inorganic and organic fluorescent electrolyte decomposition products form at the cathode and anode
  - Mn and/or Ni dissolution leads to formation of soluble fluorescent species, which diffuse toward the anode and interfere with the anode (SEI Mn/Ni poisoning?)
  - Insoluble electrolyte decomposition products form electronic and ionic barriers in composite cathodes and contribute to the impedance rise in Li-ion cells
- Pioneered the use of near-field IR spectroscopy and microscopy to study electrochemical interfaces in Li-ion systems
  - New technique and experimental methodology was developed under the BES-funded NECCES (Energy Frontier Research Center)
  - Preliminary measurements carried out on a model Sn-foil anode revealed non-uniform distribution of electrolyte decomposition products at nanometer scale

✧ ✧ ✧ ✧ ✧

Introduction

A primary aim of this project is to develop and use advanced diagnostic techniques and experimental methodologies to characterize basic physico-chemical properties and function of Li-ion electrode active and passive components that are being developed for use in PHEV and EV applications. The main objective of this task is to apply novel far- and near-field optical multifunctional probes to obtain detailed insight into the

dynamic behavior of molecules, atoms, and electrons at electrode/electrolyte interfaces of intermetallic anodes (Si) and high voltage Ni/Mn-based materials at a spatial resolution that corresponds to the size of basic chemical or structural building blocks. The goal of these studies is to unveil the structure and reactivity at hidden or buried interfaces and interphases that determine battery performance and failure modes. A better understanding of the underlying principles that govern these phenomena is inextricably linked with successful implementation of high energy density materials such as Si and high voltage cathodes in Li-ion cells for PHEVs and EVs.

Approach

Design and employ novel and sophisticated *in situ* analytical methods to address the key problems of the BATT baseline chemistries. The proposed experimental strategies combine imaging with spectroscopy aimed at probing electrodes at an atomic, molecular, or nanoparticulate level to unveil structure and reactivity at hidden or buried interfaces and determine electrode performance and failure modes in baseline Li_xSi-anodes and high-voltage LMNO cathodes. The proposed methodologies include *in situ* and *ex situ* Raman, FTIR and laser induced breakdown spectroscopy (LIBS) far- and near-field spectroscopy/microscopy, scanning probe microscopy (SPM), spectroscopic ellipsometry, electron microscopy (SEM, HRTEM), and standard electrochemical techniques and model single particle and/or monocrystal model electrodes to probe and characterize bulk and surface processes in Si anodes, and high-energy cathodes.

Results

Fluorescence spectroscopy/imaging investigations of interfacial phenomena that occur at different crystal facets/orientations of $LiNi_{0.5}Mn_{1.5}O_4$ single microcrystals, namely <112> and <111> in EC:DEC 1:2, 1M $LiPF_6$ electrolyte between 3.5 and 5.0 V vs. Li/Li^+ revealed that the fluorescence intensity at the electrode interface always rises at the beginning of the nickel oxidation and then slowly vanishes upon relithiation. In fact, the fluorescence response of the model $LiNi_{0.5}Mn_{1.5}O_4$ single crystal electrodes was somewhat similar to the signal observed for a regular polycrystalline material. Insoluble products of the electrolyte oxidation tend to accumulate at the surface of the electrode contributing to a gradual increase of the fluorescence background signal whereas soluble compounds diffuse away into the electrolyte (Figure VI - 206).

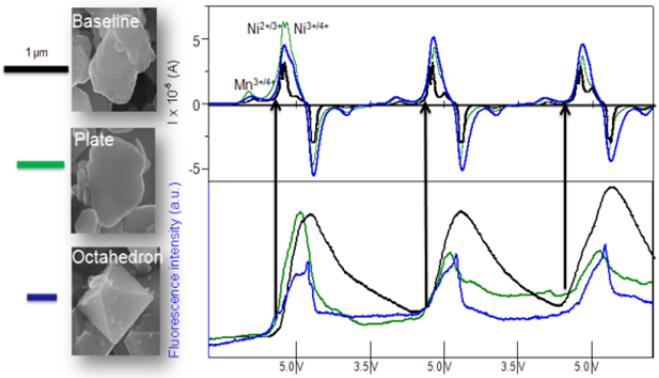

Figure VI - 206: SEM images (left) (courtesy of Guoying Chen, LBNL), Electrochemical data (right-top), corresponding integrated fluorescence intensity (right-bottom) of $LiNi_{0.5}Mn_{1.5}O_4$ baseline (black), <112> platelet (green) and <111> octahedron (blue) particles in EC:DEC 1:2 1M $LiPF_6$

Both model electrodes showed a steady increase of the fluorescence background with cycling. However, for the octahedrons the intensity of the fluorescence background remains unchanged after the first cycle whereas fluorescence on the platelets seem to keep growing after every cycle. These compounds that formed on $LiNi_{0.5}Mn_{1.5}O_4$ octahedrons tend to passivate the material better during the initial charge/discharge cycles. This may indicate quite radical differences in surface activity of $LiNi_{0.5}Mn_{1.5}O_4$ depending on material surface orientation. In other words, the steady fluorescence signal from the octahedrons can be associated with the formation of a more stable surface layer on this crystal facet. Further investigations will focus on identification of the fluorescence compounds, their formation mechanism and possible implications for Li-ion battery systems.

Interfacial phenomena occurring on Si (100), (110) and (111) single crystal electrodes in organic electrolytes showed that electrochemical response upon polarization depends on surface crystal orientation of silicon. The (111) crystal facet displays higher current

density and lower decomposition potential. Chemical composition of the SEI layer varied strongly on the different crystal orientations of Si and included $LiPF_6$ salt and EC and DEC solvents decomposition products. On (100) facets, the SEI contains more carbonate and salt decomposition products and appears to be less stable. At potentials below 0.5 V, the SEI undergoes reformation due to Si cracking and structural transition from crystalline to amorphous Si upon alloying with lithium. This results in similar SEI chemical composition for the three different crystal orientations. A lower potential induces an increase in decomposition products, e.g., LiF, P-O-C and P-F.

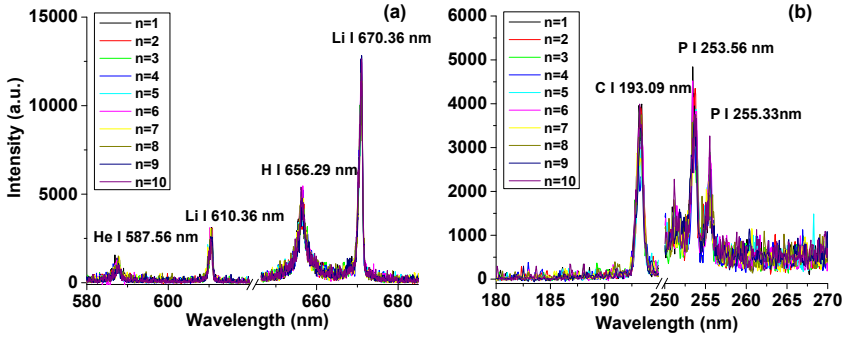

Figure VI - 207: Ultrafast LIBS emission intensity from the Si electrode/organic electrolyte system as a function of wavelength in the (a) 580-685nm and (b) 180-270 nm spectral region

Figure VI - 207 depicts the ultrafast LIBS spectral emission originating from a 1M $LiPF_6$ EC:DEC [1:1] electrolyte in contact with a Si wafer with (100) crystal orientation. All major elements of interest (C, P, Li, H) were successfully detected from the electrolyte for the first 10 laser pulses. Subsequent experiments involved optimization of laser parameters including laser energy/pulse and laser repetition rate as well as organic electrolyte thickness above the working electrode to control the contribution of the electrolyte in the emission signal. It was found that higher repetition rates can contribute significantly towards improvement of the Si signal-to-noise ratio, a phenomenon associated with cavitation in the electrolyte due to the laser material interaction in the examined laser energy regime.

Clear correlation between surface activity, SEI composition and stability and crystal facets has been highlighted. Those results point out the critical role of Si crystal orientation in achieving longer Li battery lifetime and its impact on electrochemical performance.

Preliminary *ex situ* near-field IR (NF-IR) imaging of an SEI layer on Sn-foil model electrode was successfully carried out. NF-IR images of the Sn electrode (Figure VI - 208) wavelengths display local spectral variance, which indicates non-uniform distribution of SEI layer basic building blocks at the nanometer level. These new results are consistent with earlier far-field spectroscopy observations.

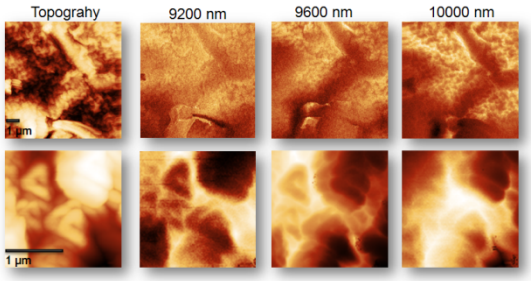

Figure VI - 208: *Ex situ* near-field IR and topography images of the SEI layer on Sn at 0.8V (top) and Li_xSn at 0.1V (bottom)

Conclusions and Future Directions

- Inorganic and organic fluorescent electrolyte decomposition products form at the LNMO cathode and dissolve in the electrolyte
  - Fluorescence rise correlates with the beginning of the Ni^{2+} oxidation.
  - Ni and possibly Mn ions constitute flourophore centers in fluorescence compounds formed on LMNO positive electrodes.
  - Solvent oxidation at LMNO leads to formation of soluble fluorescent species, which diffuse toward the anode and interfere with the SEI (Mn/Ni poisoning?).
  - Well-designed particle morphology is critical in achieving optimal rate capability and stability of the high-voltage LMNO spinel.

- Insoluble electrolyte decomposition products form electronic and ionic barriers in composite cathodes and contribute to the impedance rise in Li-ion cells.
- Electrolyte additives and surface coatings could be effective strategies to reduce surface reactivity of high-voltage cathodes.
- Preliminary *ex situ* near-field IR imaging of an SEI layer on Sn-foil model electrode was successfully carried out.
- Near-Field IR images reveal chemical complexity of the SEI layer and its functionality at nanometer level.
- These new experimental results are in concert with earlier far-field spectroscopy observations and provide new insight into the mechanism of interfacial processes on intermetallic anodes.
- Need to work with model samples of similar dimensions of functional electrode materials.

Near-field optical techniques constitute a class of emerging analytical tools with unprecedented analytical capabilities toward electrical energy materials and systems. With this underpinning knowledge, wholly new concepts in materials design can be developed for producing materials that are capable of storing higher energy densities and have long cycle lifetimes.

- Develop and apply novel innovative experimental methodologies to study and understand the basic function and mechanism of operation of materials, composite electrodes, and Li-ion battery systems for PHEV and EV applications.
- Apply novel far- and near-field optical multifunctional probes to obtain detailed insight into the dynamic behavior of molecules, atoms, and electrons at electrode/electrolyte interfaces of intermetallic anodes (Si) and high voltage Ni/Mn-based materials at a spatial resolution that corresponds to the size of basic chemical or structural building blocks.
- Unveil the structure and reactivity at hidden or buried interfaces and interphases that determine battery performance and failure modes.
- Understanding of the underlying principles that govern these phenomena is inextricably linked with successful implementation of high energy density materials such as Si and high voltage cathodes in Li-ion cells for PHEVs and EVs.
- Cooperate with the BATT Task Groups "SEI on Alloys," "High-Voltage Cathodes" and industrial partners (3M, Dow Chemical) to investigate the effect of material structure, morphology on formation of the SEI layer

FY 2013 Publications/Presentations

1. Boesenberg, Ulrike; Meirer, Floria; Liu, Yijin; Shukla, Alpesh; Dell'Anna, Rossana; Tyliszczak, Tolek; Chen, Guoying; Andrews, Joy; Richardson, Thomas; Kostecki, Robert; Cabana, Jordi, "Mesoscale phase distribution in single particles of $LiFePO_4$ following lithium deintercalation," *Chemistry of Materials,* in press. DOI: 10.1021/cm400106k.
2. Addy, S. E. A.; Gadgil, A.; Srinivasan, V.; Kowolik, K.; Muller, M.; Huang, J.; Kostecki, R., "Arsenic removal from groundwater using iron electrocoagulation: Effect of charge dosage rate," *Journal of Environmental Science and Health***,** in press.
3. Chunjoong Kim, Nick S. Norberg, Caleb T. Alexander, Robert Kostecki, Jordi Cabana, "Mechanism of phase propagation during lithiation in carbon-free $Li_4Ti_5O_{12}$ battery electrode," *Adv. Funct. Mater.* 2013, **23**, 1214–1222 (DOI:10.1002/adfm.201201684) (2013).
4. Nick S. Norberg, Robert Kostecki, "The Degradation Mechanism of a Composite $LiMnPO_4$ Cathode," *J. Electrochem. Soc.* **159(9)**: A1431-A1434; doi:10.1149/2.018209jes (2012).
5. Vassilia Zorba, Jaroslaw Syzdek, Xianglei Mao, Richard E. Russo and Robert Kostecki, "Ultrafast laser induced breakdown spectroscopy (LIBS) of electrode/electrolyte interfaces," *Applied Physics Letters*, **100**, 234101 (2012).
6. Nick S. Norberg and Robert Kostecki, "Interfacial Phenomena at a Composite $LiMnPO_4$ Cathode," *J. Electrochem. Soc.* **159(7)**: A1091-A1094; doi:10.1149/2.076207jes (2012).
7. S.F. Lux, I.T. Lucas, E. Pollak, S. Passerini, M. Winter and R. Kostecki, "The mechanism of HF formation in $LiPF_6$ based organic carbonate electrolytes," *Electrochemistry Communications*, **14**, 47–50, (2012).
8. "Interfacial Processes in EES Systems Advanced Diagnostics," *DOE Annual Peer Review Meeting*, May 13-17, 2013, Washington, DC.
9. Kostecki, Nick Norberg, "*In situ* Studies of Interfacial Phenomena at a $LiMn_{0.5}Ni_{0.5}O_2$ cathode in organic carbonate Electrolyte," *International Battery Association 2013 Meeting*, March 11-15, 2013, Barcelona, Spain. (invited lecture)
10. Robert Kostecki, Jaroslaw Syzdek, Ivan Lucas, "Near Field Optical Imaging of Interfaces and Interphases in Battery Materials," *Special*

Symposium to honor Michael Thackeray, March 10th 2013, Casa de Convalescència, Barcelona. (invited lecture)

11. Robert Kostecki, “Characterization of Interfaces and Interphases in Li-ion Systems with Far- and Near-Field Optical Probes,” *FIRST International Symposium Innovation of Energy Storage Device by Interdisciplinary Synergy*, January 17-18, 2013 Tokyo, Japan. (invited lecture)
12. Syzdek, V. Zorba, X. Mao, R. Russo, and R. Kostecki, "Ultrafast Laser Spectroscopy of Electrode/Electrolyte Interfaces," *PRiME 2012*, October 7-12, 2012, Honolulu, Hawaii.
13. Norberg, S. Lux, I. Lucas, J. Syzdek, and R. Kostecki, "*In situ* Fluorescence Spectroscopy of Interfacial Processes in High-Energy Li-ion Batteries," *PRiME 2012,* October 7-12, 2012, Honolulu, Hawaii.
14. Kim, C. Alexander, N. Norberg, R. Kostecki, and J. Cabana, “Study of the Factors that Enable Carbon-Free Insulating Li-Ion Battery Electrodes,” *PRiME 2012,* October 7-12, 2012, Honolulu, Hawaii.
15. Kostecki, I. Lucas, N. Norberg, and J. Syzdek, “Materials and Interfaces Degradation in High-Energy Cathodes for Li-ion Batteries,” *PRiME 2012,* October 7-12, 2012, Honolulu, Hawaii. (invited lecture)
16. S. Lux, I. Lucas, J. Chevalier, T. Richardson, and R. Kostecki, “Time-Dependent Determination of HF Formation in $LiPF_6$-Containing Electrolytes by Spectroscopic Ellipsometry,” *PRiME 2012,* October 7-12, 2012, Honolulu, Hawaii.
17. I. Lucas, J. Syzdek, S. Lux, N. Norberg, A. McLeod, Z. Fei, D. Basov, and R. Kostecki, “Scanning Near-Field Infrared Microscopy of a Li_xFePO_4 Single Particle,” *PRiME 2012,* October 7-12, 2012, Honolulu, Hawaii.

VI.F.4 *In situ* Electron Microscopy of Electrical Energy Storage Materials (ORNL)

Raymond R. Unocic
Oak Ridge National Laboratory

Center for Nanophase Materials Sciences
One Bethel Valley Road
PO Box 2008, MS-6064
Oak Ridge, TN 37831
Phone: (865) 574-0096; Fax: (865) 576-5413
E-mail: unocicrr@ornl.gov

Start Date: January 2010
Projected End Date: September 2013

Objectives

- The primary objective of this research is to develop the tools and methodology to conduct *in situ* electron microscopy studies of electrical energy storage materials using a microfluidic electrochemical cell and the transmission electron microscope (TEM) as the experimental platform.
- The key benefits of this characterization method include the ability to: 1) wholly contain and image through volatile organic liquid electrolytes; 2) perform controlled nanoscale electrochemistry experiments within the high vacuum environment of the TEM column; and 3) image electrochemical processes at high spatial and temporal resolution.

Technical Barriers

- The technical barrier is the present lack of advanced electron microscopy based materials characterization methods that allow for the direct visualization of electrochemical processes during electrochemical charge-discharge cycling.

Technical Targets

- Develop *in situ* characterization technique and methodology to investigate dynamically evolving electrochemical reaction mechanisms. Use this method to perform detailed *in situ* TEM experiments on the following subjects:
  - Investigate the dynamics of solid electrolyte interphase (SEI) formation mechanisms in relevant electrode/electrolyte systems.
  - Investigate dendrite nucleation and growth mechanisms.
  - Fabricate thin film electrodes of relevant electrode materials and perform electrochemical cycling feasibility studies.

Accomplishments

With the development of a microfluidic electrochemical liquid cell for *in situ* TEM, we have gained insight into:

- The dynamics of SEI formation mechanisms, including tracking the growth of the SEI at the natural graphite anodes and organic liquid electrolyte interfaces during cell discharge.
- The nucleation and growth mechanisms of lithium dendrites during electrodeposition conditions.
- The electrochemical cycling behavior of thin film electodes deposited on small-scale electrochemical microchip devices.

✧ ✧ ✧ ✧ ✧

Introduction

The direct visualization of electrochemical reactions that occur in Li-ion batteries necessitates the development of alternative *in situ* characterization methodologies and is absolutely critical if we are to further our fundamental understanding into a range of transport phenomena that occur within batteries. TEM, combined with diffraction and spectroscopic capabilities is a characterization technique that enables the unmatched ability to image and analyze the structure and chemistry of materials at multiple length scales. Recently, *in situ* TEM methods have been developed and used for Li-ion battery research to study the structural evolution in nanowire electrodes during Li intercalation. These experiments were facilitated by the use of TEM vacuum-compatible, ionic liquid-based electrolytes as a medium for Li-ion transport in an open cell configuration. Most commercial Li-ion battery electrolytes have a high vapor pressure and would rapidly evaporate when placed into the high vacuum environment of the TEM column if used in the same experimental setup; therefore, the main experimental

challenge for simultaneously conducting quantitative electrochemical measurements and imaging the resultant reactions depends upon the ability to image through highly volatile Li-ion battery liquid electrolyte while testing under realistic electrochemical conditions. This is the ultimate goal of this project.

Approach

In this program, we have developed an electrochemical liquid cell for *in situ* TEM studies of electrochemical reactions that take place in electrical energy storage systems. The core challenge of preventing the evaporation of volatile organic liquid electrolytes is overcome by sealing the liquid electrolyte between thin electron transparent viewing membranes. The general concept for conducting *in situ* TEM characterization is as follows: MEMS based silicon microchip devices containing a central thin electron transparent silicon nitride (SiN_x) viewing membrane are stacked upon one another and placed withing the tip of a precision-machined TEM holder. Liquid electrolyte is delivered through the TEM holder with a microfluidic delivery system to fill the gap between the SiN_x membranes. Gold or platinum biasing contacts that are deposited onto the lower chip/window of the cell serve as a platform for attaching battery electrodes and for interfacing with an external potentiostat for electrochemical testing. A 500nm thick spacer material patterned on the upper chip controls the thickness of the liquid electrolyte layer in the cell.

Results

***In situ* environmental cell (ec)-TEM Characterization of the SEI.** The *in situ* electrochemical cell was used to visualize the dynamics of SEI formation. Natural graphite was used as the anode and lithium metal as the counter electrode. Figure VI - 209A shows an image of the natural graphite within the electrochemical cell, imaged without any electrolyte. Figure VI - 209B shows the same region of the graphite electrode when 1M $LiPF_6$ EC:DEC is present in the cell during discharge to 1.75V. Here we observe the dynamics of SEI formation and growth.

***In situ* ec-TEM Characterization of Dendrite Nucleation and Growth Mechanisms.** Understanding the mechanisms of dendrite formation in lithium ion batteries is critical. We utilize the *in situ* electrochemical cell to image dendrite nucleation and growth and quantitatively measure dendrite growth kinetics. Figure VI - 210A – Figure VI - 210B are false-colored bright-field TEM micrographs depicting dendrite growth from a gold working electrode. The dendrites were grown by electrodeposition using cyclic voltammetry in a 1.2M $LiPF_6$ EC:DMC electrolyte.

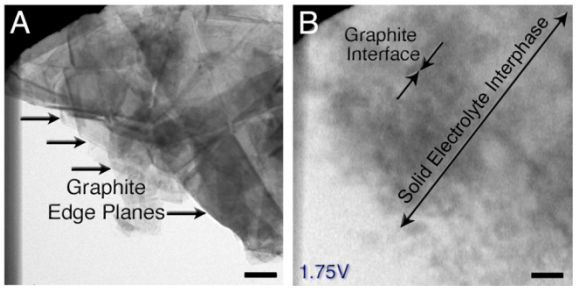

Figure VI - 209: A) Bright-field TEM image of natural graphite anode between two electron transparent SiN membranes within the electrochemical cell. B) Extracted frame-shot of the same region showing SEI growth

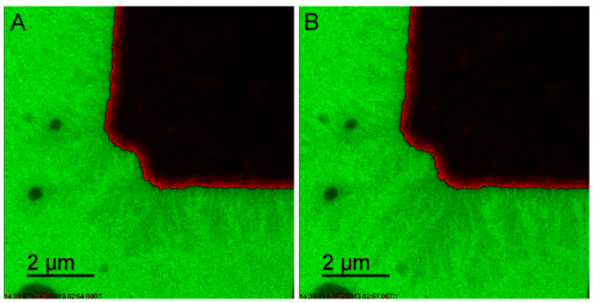

Figure VI - 210: *In situ* observations of dendrite nucleation and growth from a gold working electrode in a 1M $LiPF_6$ EC:DMC electrolyte

Thin Film Device Fabrication and Electrochemical Cycling. RF Magnetron sputtering techniques have been used to deposit thin film electrode materials directly on the microfabricated electrochemical microchip devices. Figure VI - 211A shows the size scale of the electrochemical microchip with the top portion covered with a thin layer Cu-Sb anode material. Figure VI - 211C – Figure VI - 211D shows bright-field TEM image and selected area electron diffraction pattern from the SiN_x viewing region of the cell and shows that the sputtered thin films are nanocrystalline in nature. Figure VI - 211E is the electrochemical discharge-charge profile of the "on-chip" microbattery. Continued research in this direction has demonstrated the feasibility to deposit thin film electrode materials for a wide range of anode and cathode chemistries ($Li_4Ti_5O_{12}$, $LiMn_2O_4$, $LiMn_{1.5}Ni_{0.5}O_4$, etc) directly on the microchip device for *in situ* experimentation.

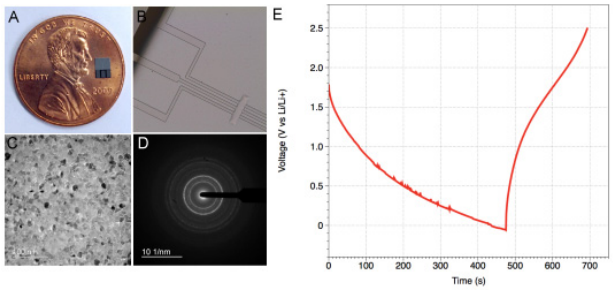

Figure VI - 211: *In situ* observations of dendrite nucleation and growth from a gold working electrode in a 1M $LiPF_6$ EC:DMC electrolyte

Conclusions and Future Directions

The *in situ* electrochemical liquid cell microscopy technique is a versatile characterization method that is useful for characterizing dynamically evolving electrochemical processes in battery grade liquid electrolytes. With this method, it is possible to visualize the dynamics of electrochemical proceses such as SEI formation, dendrite nucleation and growth and degradation mechanisms in electrode materials. In future work, this system will be used to study the influence of electrolyte additives on SEI formation and dendrites and the lithiation/delithiation behavior of relevant electrode materials.

FY 2013 Publications/Presentations

1. Unocic RR, Baggetto L, Sacci RL, Veith GM, Dudney NJ, More KL, "*In situ* Electron Micrscopy of Electrical Energy Storage Materials," DOE VTO Annual Merit Review and Peer Evaluation Meeting, Arlington, VA, May 2013.
2. Unocic RR, Sacci RL, Dudney NJ, More KL, "Quantitative *In situ* Electrochemical Liquid Cell Characterization of SEI Formation in Lithium Ion Batteries." Microscopy and Microanalysis Annual Meeting, Indianapolis, IN, August 2013.
3. Unocic RR, "Development and Application of *In situ* Electrochemical Cell TEM Methods for Electrical Energy Storage Research," Electron Microscopy Laboratory and the Hitachi Electron Microscopy (HEMIC) Product Development Centre at the National Institute for Nanotechnology, Edmonton, Canada, June 2013.

Submitted Publications:

1. Unocic RR, Sun XG, Adamczyk LA, Alsem DH, Salmon NJ, Dai S, Dudney NJ, More KL, "Visualizing SEI Formation in Li-ion Batteries with *In situ* ec-TEM," (2013).
2. Sacci RL, Dudney NJ, Veith GM, More KL, Browning ND, Unocic RR, "Direct Visualization of Dendrite Nucleation and Growth Kinetics with *in situ* ec-TEM," (2013).
3. Unocic RR, Baggetto L, Unocic KA, Veith GM, Dudney NJ, More KL, " Probing Materials Chemistry in Liquid Enviornments with *In situ* Liquid Electron Energy Loss Spectroscopy," (2013).

VI.F.5 Microscopy Investigation on the Fading Mechanism of Electrode Materials (PNNL)

Chong-Min Wang
Pacific Northwest National Laboratory

Environmental Molecular Sciences Laboratory
902 Battelle Boulevard, Mail Stop K8-93
Richland, WA 99352
Phone: (509) 371-6268; Fax: (509) 371-7866
E-mail: Chongmin.wang@pnnl.gov

Start Date: July 1, 2013
Projected End Date: September 30, 2016

Objectives

- Develop *ex situ*, *in situ*, and *operando* high-resolution transmission electron microscopy (TEM) and spectroscopy to probe the fading mechanism of electrode materials
- Probe the structural and chemical evolution of interfaces between the electrode and electrolyte
- Directly correlate structural and chemical evolution with battery performance to guide the design of new materials.

Technical Barriers

- Capacity and voltage fading of Li-ion batteries
- Materials with a theoretical high capacity that cannot be fully extracted in practical use.

Technical Targets

- Develop new *ex situ*, *in situ, and operando* TEM diagnostic techniques for directly probing the structural evolution of electrode and interfaces
- Identify the quantitative correlation of the structural and chemical change with the fading and failure of Li-ion batteries

Accomplishments

- Use *in situ* TEM to study mesoscale structure change of silicon nanoparticles wrapped by conductive polymer
- Discovered that capacity/voltage fading of $Li_{1.2}Ni_{0.2}Mn_{0.6}O_2$ cathode is closely related to the corrosion and fragmentation of material
- Discovered that Ni segregation in the $Li_{1.2}Ni_{0.2}Mn_{0.6}O_2$ is directly related to the capacity and voltage fading.

Introduction

Most previous microscopic investigations on the structural/chemical evolution of electrode materials and the solid-electrolyte interphase (SEI) layer formation have been either *ex situ* studies or used low-vapor-pressure/solid electrolytes for *in situ* TEM studies. Therefore, these results do not reveal fully detailed dynamic information under practical conditions. It is necessary to develop new *operando* characterization tools to characterize the structural/chemical evolution of electrode and SEI formation and electrode/electrolyte interaction using a practical electrolyte. This will be critical for making new breakthroughs in this field. The success of this work will increase the energy density of Li-ion batteries and accelerate market acceptance of electrical vehicles (EV) and plug-in hybrid electrical vehicles (PHEV) as described by the *EV Everywhere* Grand Challenge proposed by DOE/EERE.

Approach

Extend and enhance the unique *ex situ* and *in situ* TEM methods for probing the structure of Li-ion batteries, especially for developing a biasing liquid electrochemical cell that uses a real electrolyte in a nano-battery configuration. Use various microscopic techniques, including *ex situ*, *in situ*, and especially the *operando* TEM system, to study the fading mechanism of electrode materials in batteries. This project will be closely integrated with other research and development efforts on high-capacity cathode and anode projects in the BATT Program to 1) discover the origins of voltage and capacity fading in high-capacity layered cathodes and 2) provide guidance for overcoming barriers to long cycle stability of silicon (Si)-based anode materials.

Results

1. Mesoscale *in situ* TEM study of Si nanoparticles wrapped in a conductive polymer. In this study, we studied the lithiation characteristics of two types of Si-nanoparticle (Si-NP)-based electrodes at the mesoscale using *in situ* TEM. The functional composite unit well represents structural changes of the whole electrode

during cycling as shown in Figure VI - 212. The Si-NP conductive polymer composite anode exhibits excellent electrochemical cycling stability and high energy density, which are attributed to a good and sustained electrical contact between the Si-NP and the surrounding conductive polymer because of the resilient bonding between the two. On the other hand, a conventional Si-NP based anode is obviously not good at establishing and maintaining good electrical contact between the Si-NPs and the additives. Typically, Si-NPs that are not in contact with the acetylene black additive carbon cannot be lithiated during cycling. *In situ* TEM observations directly pinpoint the failure mechanism of the conventional Si composite as compared with Si-NP conductive polymer composite anode, which agrees well with available electrochemical performance data. The present results serve as an excellent example for linking mesoscale phenomenon with the properties of the real device.

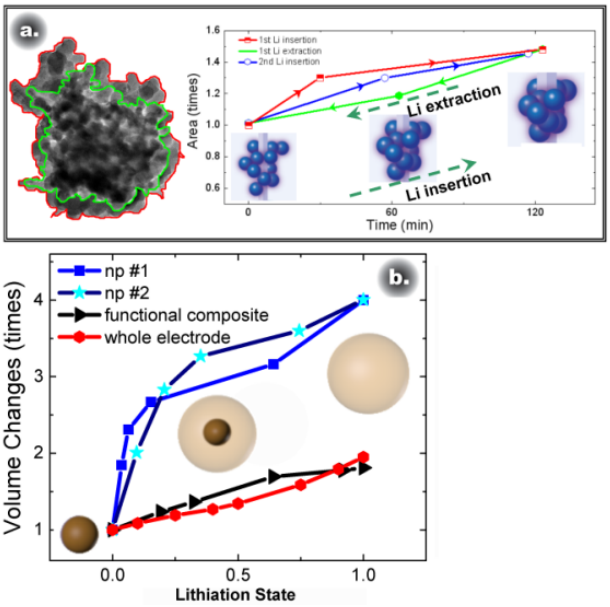

Figure VI - 212: (a) Comparison of the starting fresh state and lithiated state of the SCP anode and plot of the measured areas of the anode in the TEM image acquired at different times (b) Comparison of the volume expansion of the whole electrode, functional composite, and single NP. The inset drawing in panel (b) shows structure changes of the single Si-NP during the lithiation process

2. Capacity/voltage fading of $Li_{1.2}Ni_{0.2}Mn_{0.6}O_2$ cathode is closely related to the corrosion and fragmentation of material. The Li- and Mn-rich (LMR) layered cathode materials exhibit very high discharge capacities that exceed 250 mAh/g and are very promising cathodes. However, significant barriers, such as voltage fade and low rate capability, still need to be overcome before these materials can be used in practical applications. A detailed study of the mechanisms of voltage/capacity fading will be beneficial for further tailoring the electrode structure and, thus, improving the electrochemical performance of these layered cathodes. Detailed studies of structural changes of the LMR layered cathode $Li[Li_{1.2}Ni_{0.2}Mn_{0.6}O_2]O_2$ after long-term cycling were undertaken using aberration-corrected scanning transmission electron microscopy (STEM) and electron energy loss spectroscopy (EELS). The results are shown in Figure VI - 213. The fundamental findings provide new insights into the mechanisms of capacity/voltage fading of Li[Li0.2Ni0.2Mn0.6]O2. A sponge-like structure and fragmented pieces were found on the surface of the cathode after extended cycling. Formation of Mn^{2+} species and reduced Li content in the fragments leads to the significant capacity loss during cycling. These results also imply the functional mechanism of surface coatings; for example, AlF_3, which can protect the electrode from etching by acidic species in the electrolyte, suppress cathode corrosion/fragmentation, and thus improve long-term cycling stability

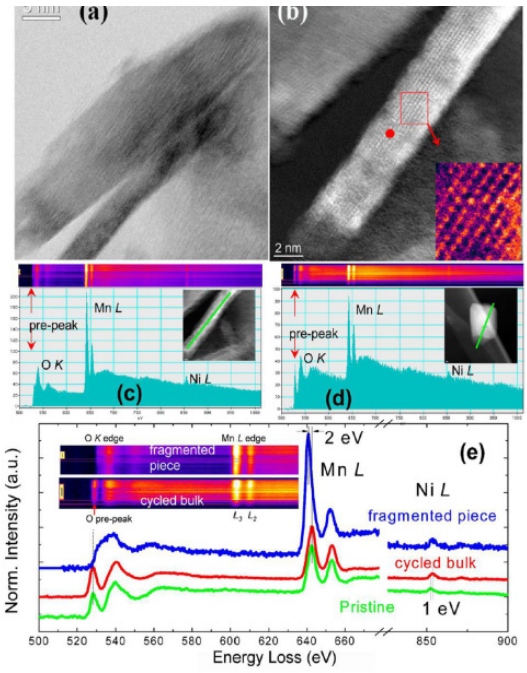

Figure VI - 213: (a) Bright-field image showing lattice fringes in this region. (b) Z-contrast image showing the destroyed electrode structure (the inset shows a magnified view of the region within the red rectangle. 2D map and EELS spectra of the core edges of O K, Mn L, and Ni L by EELS line scan from (c) fragmented piece and (d) cycled bulk. (e) Comparison of the O-K, Mn-L, and Ni-L edges of the fragmented piece, and the cycled bulk and pristine materials

3. Direct correlation of Ni segregation in $Li_{1.2}Ni_{0.2}Mn_{0.6}O_2$ to the capacity and voltage fading. State-of-the-art energy dispersive x-ray spectroscopy (EDS) in aberration corrected STEM was used to map the spatial distribution of chemical species in the $Li[Li_{0.2}Ni_{0.2}M_{0.6}]O_2$ cathode. A direct correlation of Ni segregation with the capacity fading characteristics of the battery has been established as illustrated in Figure VI - 214. Collective experimental evidence has indicated that, for the LMR layered composite cathode materials, local cation ordering and distribution play key roles in the battery performance. However a direct demonstration of the correlation of cation distribution with the electrochemical performance has not been established. In this task, a newly developed x-ray energy dispersive spectroscopy (XEDS) system, aberration-corrected STEM), and EELS were used to investigate the effects of cation distribution and local crystal structure on the performance of a typical LMR cathode (i.e., $Li[Li_{0.2}Ni_{0.2}M_{0.6}]O_2$) prepared by different approaches. The uniqueness of the new EDS system is high collection efficiency (~10 times more efficient than the traditional one), which enables direct observation of trace elemental segregation. The results reveal that materials prepared by co-precipitation and sol-gel approaches exhibit obvious Ni segregation at certain crystallographic surface and grain boundaries of the particles. Materials with Ni segregated show poor rate capability and fast capacity degradation, which is attributed to the bulk structural instability and deteriorated electrode/electrolyte interface that result from side reactions between highly active Ni^{4+} at the particle surface and the electrolyte at high voltage. On the other hand, the material prepared by the hydrothermal assisted approach shows significantly improved Ni/Mn cation uniformity and reduced Ni segregation, which could explain its excellent cycling performance and enhanced rate capability.

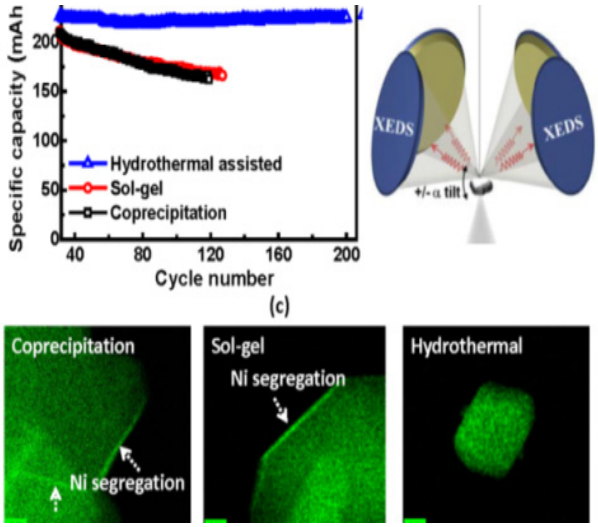

Figure VI - 214. Direct correlation of capacity fading of the $Li[Li_{0.2}Ni_{0.2}M_{0.6}]O_2$ cathode with the Ni distribution. (a) Specific capacity as a function of cycle numbers for $Li[Li_{0.2}Ni_{0.2}M_{0.6}]O_2$ prepared by three different methods. (b) Schematic drawing showing the newly developed 4-detector system in a TEM, which enables efficient collection of the EDS signal. (c) EDS mapping showing Ni segregation in $Li[Li_{0.2}Ni_{0.2}M_{0.6}]O_2$ prepared by different methods. The work is done in collaboration with FEI Company in Hillsboro, Oregon

Conclusions and Future Directions

A combination of *ex situ* and *in situ* TEM and STEM techniques were used to study the structural and chemical evolution of both anode and cathode materials for Li-ion batteries, such as Si nanoparticle wrapped in a conductive polymers for the anode and $Li(Ni_{0.2}Mn_{0.6}Li_{0.2})O_2$ for the cathode.

Lithium insertion into Si is an interface-controlled process. Transformation of a-Li_xSi to c-$Li_{15}Si_4$ is a congruent process that is solely controlled by Li concentration and is not accompanied by large-scale atomic migration and phase separation. Formation of c-$Li_{15}Si_4$ is favored because the electronic structures of c-$Li_{15}Si_4$ and a-$Li_{3.75}Si$ are similar. The conductive polymer deforms consonantly to accommodate the volume change of the Si-NPs, resulting in the excellent cycling capability of the material. We discovered that dopant may selectively segregate in $Li(Ni_{0.2}Mn_{0.6}Li_{0.2})O_2$, which will affect the Li-ion transport; and, therefore, the charge/discharge rate of battery. The layer to spinel phase transformation, corrosion, and segmentation are the main factors that contribute to the capacity and voltage fading of the cathode. Furthermore, the capacity/voltage fading of the cathode also is closely related to the distribution of Ni, typically Ni surface segregation leads to fast capacity/voltage fading.

Future work will focus on: (1) Investigate the fundamental characteristics of the SEI layer on a Si anode and its correlation with the chemistry of electrolyte as well as the battery fading mechanism. Different types of Si-based materials will be studied. (2) Investigate the cathode electrolyte interface structure and phase stability of $Li(Ni_{0.2}Mn_{0.6}Li_{0.2})O_2$). *In situ* TEM will be used to directly observe the characteristics of $Li(Ni_{0.2}Mn_{0.6}Li_{0.2})O_2$-electrolyte interface structures with respect to different electrolyte additives and surface coatings. The future work will intend to answer questions such as: What is the structure between the cathode particle and the electrolyte, and how does this structure evolve during Li-ion transport? How does the phase transformation happen? How does electrolyte additive affect the phase stability and the interface structure and their correlation with the voltage and capacity stability?

FY 2013 Publications/Presentations

1. Jianming Zheng, Meng Gu, Jie Xiao, Pengjian Zuo, Chong-Min Wang, and Ji-Guang Zhang, "Corrosion/Fragmentation of Layered Composite Cathode and Related Capacity/Voltage Fading during Cycling Process," Nano Lett. 13, 3824−3830 (2013).
2. Meng Gu, Xing-Cheng Xiao, Gao Liu, Suntharampillai Thevuthasan, Donald R. Baer, Ji-Guang Zhang, Jun Liu, Nigel D. Browning, and Chong-Min Wang, "Mesoscale Origin of the Enhanced Cycling-Stability of the Si-Conductive Polymer Anode for Li-ion Batteries," Sci. Rep., 2013, in press.
3. M Gu, B Li, W Wang, V Sprenkle, CM Wang, "*In situ* Analytical Electron Microscopy Study of the Lithiation of TiO2 Nanowires Used in Li-Ion Batteries Microscopy and Microanalysis 19 (S2), 1102-1103 (2013).

4. CM Wang, M Gu, Z Wang, F Gao, JG Zhang, DR Baer, S Thevuthasan, N Browning, J Liu, "*In situ* TEM Study of Lithiation of Si and Phase Transformation," Microscopy and Microanalysis 19 (S2), 1468-1469 (2013)

VI.F.6 NMR and Pulse Field Gradient Studies of SEI and Electrode Structure (Cambridge U.)

Clare Grey
Cambridge University

Department of Chemistry
Lensfield Road
Cambridge, CB2 8BJ
Phone: +44(1223)336509; Fax: +44(1223)336362
E-mail: cpg27@cam.ac.uk

Start Date: October 2012
Projected End Date: September 2016

Objectives

- Identify major solid electrolyte interphase (SEI) components, and their spatial proximity, and how this changes with cycling.
- Contrast SEI formation on Si vs. graphite and high voltage cathodes.
- Correlate Li^+ diffusivity in particles and composite electrodes with rate.
- Investigate local structural changes of high voltage/high capacity electrodes on cycling.

Technical Barriers

Capacity fade due to significant SEI formation (focusing on Si); Reduced rate performance due to SEI formation; High energy density; High power

Technical Targets

- Specific power 300 W/kg,
- 10 year life,
- < 20% capacity fade

Accomplishments

- Used solid state nuclear magnetic resonance (NMR) spectroscopy to determine the extent of ordering in high voltage $Li(Ni_{0.5}Mn_{1.5})O_4$ spinels and correlated this with performance
- Used NMR and diffraction based methods to investigate layered oxides within the $Na_xNi_{x/2}Mn_{1-x/2}O_2$ ($2/3 \leq x \leq 1$) system to determine cation ordering and the nature of stacking.
- *In situ* ^7Li and ^6Li NMR studies of working batteries have been performed to investigate paramagnetic cathode materials. Initial studies have focused on $Li_{1.08}Mn_{1.92}O_4$ and have shown that the method can be used to detect changes of lithium transport within the electrode, *in situ.* Variable temperature *in situ* NMR studies have been used to examine the effect of temperature on Li dynamics and Mn dissolution.
- Established protocol for investigating SEI in Si with multinuclear NMR spectroscopy

✧ ✧ ✧ ✧ ✧

Introduction

The formation of a stable SEI is critical to the long-term performance of a battery, since the continued growth of the SEI on cycling/aging results in capacity fade (due to Li consumption) and reduced rate performance due to increased interfacial resistance. Although arguably a (largely) solved problem with graphitic anodes/lower voltage cathodes, this is not the case for newer, much higher capacity anodes such as silicon, which suffer from large volume expansions on lithiation, and for cathodes operating above 4.3 V. Thus it is essential to identify how to design a stable SEI. The SEI study will be complemented by investigations of local structural changes of high voltage/high capacity electrodes on cycling focusing on new *in situ* NMR methodologies and methods developed to study paramagnetic materials.

Approach

- Multinuclear NMR of local structure.
- *In situ* and *ex situ* NMR studies of Li^+ transport and structural changes
- Pulse Field Gradient (PFG) measurements of electrolyte diffusivity and tortuosity
- SIMS and XPS of SEI composition

Results

1. Ordering in layered $Na_xNi_{x/2}Mn_{1-x/2}O_2$ ($2/3 \leq x \leq 1$): A series of layered cathode materials within the $Na_xNi_{x/2}Mn_{1-x/2}O_2$ ($2/3 \leq x \leq 1$) system were synthesized by solid-state methods and their long and short-range structure was investigated by combining X-ray diffraction (XRD) and NMR spectroscopy.[1] A transition

from P2 to O3 stacking was observed at x>0.8 when samples were made at 900°C, which was accompanied by disordering of ions in the transition metal layer. This cation order/disorder could be clearly observed via the ^{23}Na NMR spectra of these materials (Figure VI - 215), a very broad ^{23}Na signal being observed for the O3 materials.

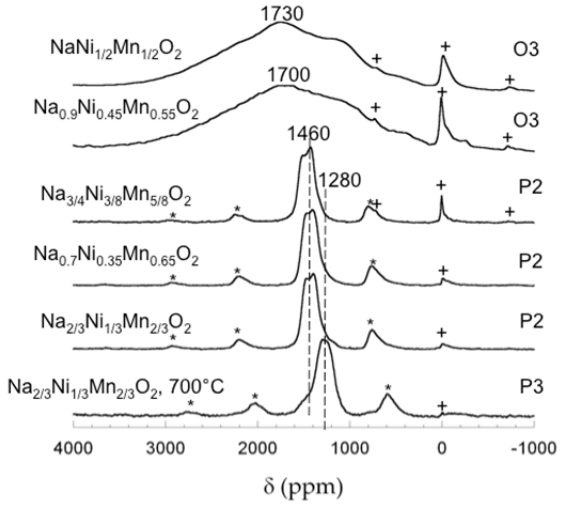

Figure VI - 215: 23Na MAS NMR spectra of the NaxNix/2Mn1-x/2O2 series. All the samples were prepared at 900°C unless noted

At x=2/3, both the P2 and a P3 structures were observed, depending on the synthesis temperature. Na/Li exchange led to structures with octahedral or tetrahedral coordination of the alkali metal. The transition from alkali metal prismatic coordination to octahedral/tetrahedral involves $[TMO_6]_\infty$ layer shearing that induces structural disorder through the formation of stacking faults. These results help the understanding of how these materials operate as Na and Li-ion batteries. This project was performed in collaboration with BATT PI's J. Cabana and M. S. Whittingham. Studies are currently being performed on related materials with BATT PI Y. S. Meng. ^{23}Na NMR studies on the new battery material sidorenkite were performed in collaboration with BATT PI G. Ceder.[2]

2. Application of *In situ* NMR studies to study lithium-ion mobility in paramagnetic cathode materials – application to Li. A new NMR methodology has been applied to study the cathode, $Li_{1+x}Mn_{2-x}O_4$ (chosen as a model cathode material to develop the technique).[3] This is challenging primarily due to three factors: (1) The resonance lines are broadened severely; (2) spectral analysis is made more complicated by bulk magnetic susceptibility (BMS) effects, which depend on the orientation and shape of the object under investigation; (3) the difficulty in untangling the BMS effects induced by the paramagnetic and metallic components on other (often diamagnetic) components in the system. In an important finding, the BMS induced shift was minimized by orienting the cell at an angle of 54.7°, facilitating the interpretation of the *in situ* NMR spectra of a working battery containing paramagnetic electrodes. Importantly, the NMR spectra (Figure VI - 216) were shown to be highly sensitive to changes of Li dynamics and cation ordering as the battery was cycled, and two-phase reactions vs. solid solutions could be separated in this system. The method is now being used to examine how dynamics varies as a function of temperature.

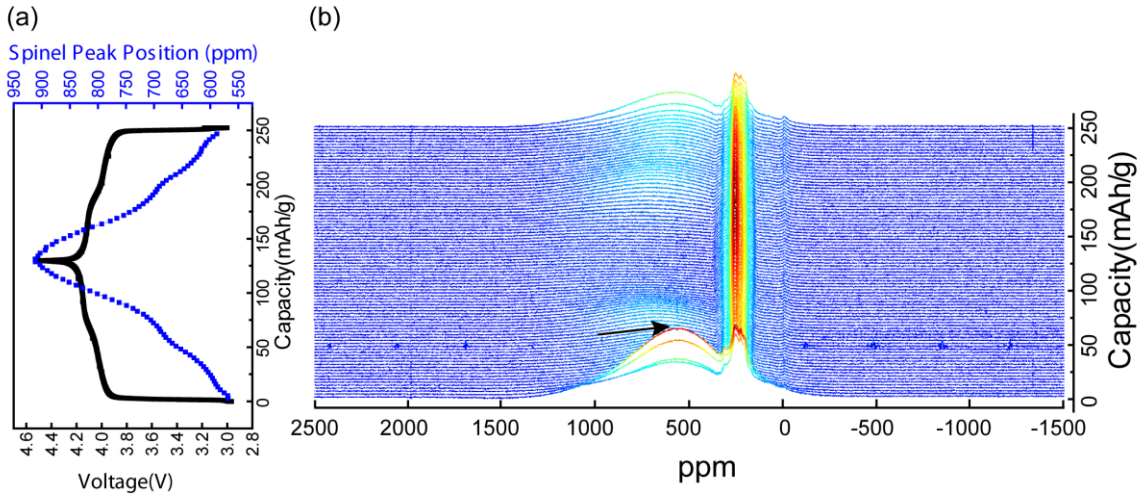

Figure VI - 216: *In situ* 7Li static NMR spectra for the first cycle of an Li1.08Mn1.92O4 vs. Li/Li+ bag cell. (a) Voltage profiles and Li1.08Mn1.92O4 isotropic shifts vs. capacity plots. (b) Stacked plot of the 7Li spectra. The *in situ* cell was cycled galvanostatically with a C/50 rate between 3.0 and 4.5 V during the spectral acquisition. Note the increase of intensity following 50% Li extraction (at the end of the 1st process) consistent with cation ordering

3. Silicon and its SEI Work has focused on the development of a new approach to allow *in situ* NMR spectroscopy of Si nanomaterials to be performed. The method allowed multiple cycles to be performed, which had not been possible in previous work, allowing the processes that occur in the 2nd cycle involving the amorphous phase to be explored.

A second focus was to develop a robust NMR methodology with which to monitor SEI formation. To this end ^{13}C experiments have been performed with ^{13}C enriched electrodes DMC and EC. Finally, PFG methods have been performed during diffusion through the electrodes, with a long-term goal to extract tortuosity as a function of cycle number.

The ^{13}C NMR studies of the enriched carbonate electrodes have been initiated. Since the focus has been on establishing a protocol and identifying key SEI components, studies with FEC and VC have not yet been initiated. These will be commenced in the next quarter. The work to determine the voltage at which key breakdown products are formed will continue, along with comparison studies with FEC and VC additives. The effect of cycle number on reversible capacity will continue to be explored. New Si coatings have been explored electrochemically and with NMR studies.

Conclusions and Future Directions

The work described here has established and applied new NMR methodologies that are sensitive to cation dynamics (Li and Na) of a battery while cycling. Cation arrangements and their implications for the electrochemical cycling of layered materials have been investigated.

Major products in the Si SEI have been identified and the focus is now on identifying all the different components, when they are formed and whether they are stable on cycling. Future work will include an investigation of additives and Si coatings.

FY 2013 Publications/Presentations

1. J. Cabana, N. A. Chernova, K. A. Aldi, J. Xiao, M. Roppolo, M. S. Whittingham and C. P. Grey, "Study of the Transition Metal Ordering in Layered $Na_xNi_{x/2}Mn_{1-x/2}O_2$ (2/3 <= x <= 1) and Consequences of Na/Li Exchange," *Inorganic Chem.istry*, **15**, 8540 – 8550 (2013).
2. H. -L. Chen, Q. Hao, O. Zivkovic, G. Hautier, L. -S. Du, Y.-Z. Tang, Y. –Y. Hu, X. –H. Ma, C. P. Grey, G. Ceder, "Sidorenkite ($Na_3MnPO_4CO_3$): A New Intercalation Cathode Material for Na-Ion Batteries," *Chem. Mater*., **25**, 2777-2786 (2013).
3. L. Zhou, M. Leskes, A. J. llott, N. M. Trease, and C. P. Grey, "Paramagnetic electrodes and bulk magnetic susceptibility effects in the *in situ* NMR studies of batteries: Application to $Li_{1.08}Mn_{1.92}O_4$ spinels," *J. Magn. Reson.,* **234**, 44 – 57 (2013).

VI.F.7 Chemical and Structural Gradients in Composite Electrodes (LBNL)

Jordi Cabana
Lawrence Berkeley National Laboratory.

Department of Chemistry[13]
University of Illinois at Chicago
845 W Taylor Street
Science and Engineering South (MC 111)
Chicago, IL 60607
Phone: (312) 355-4309
E-mail: jcabana@uic.edu

Start Date: September 2011
Projected End Date: July 2013

Objectives

- Enable higher energy density Li-ion batteries by informing the design of optimized electrode architectures that maximize active material utilization and charge density.
- Establish correlations between inhomogeneities in local states of charge (SOC), pore structure and inactive component distribution in commercially relevant electrodes.
- Understand the role of phase transformations within active materials vis-à-vis utilization and durability.

Technical Barriers

Low energy-density, poor cycle life, safety.

Technical Targets

- PHEV: 96 Wh/kg, 5,000 cycles
- EV: 200 Wh/kg; 1,000 cycles.

Accomplishments

- Establish the validity of using *operando* bulk X-ray diffraction (XRD) to study the formation of chemical gradients in thick NMC composite electrodes.
- The first maps of local SOCs in commercially relevant materials were produced.
- Determined changes during delithiation of new fluoride phases using *operando* bulk XRD.

✧ ✧ ✧ ✧ ✧

Introduction

The quest for gains in energy density that fulfill cost and safety requirements constitutes a major thrust in Li-ion battery research. These gains can be brought about through a reduction of the dead weight in the battery by optimizing the architecture of the system. This approach is attractive from the technological perspective because it involves engineering changes within the current material space. Thus, in principle, it is also free of the time constraints that occur from materials discovery to implementation.

In Li-ion batteries, the dual transport of electrons and ions required to complete an electrochemical reaction is achieved with a 50-100 μm thick, porous composite of the redox active material, a conductive additive and a polymeric binder. The energy density of the device can be raised by increasing the mass loading of active material per unit area in the electrode, either by reducing the ratio of support components or by reducing electrode porosity through calendaring methodologies (or both). Thick, additive-free electrodes in the form of sintered pellets have reportedly been cycled successfully, albeit at low to moderate rates. However, what appear to be trivial changes actually constitute a significant challenge. Reducing the amount of carbon and binder can lead to structures that have lower mechanical stability against the continued particle volume changes that occur during cycling. In turn, thick electrodes and/or low porosity result in depletion of ionic carriers within the composite structure. The reason is that the paths for electrolyte wetting become longer due to the effect of pore tortuosity. As a result, the gains in energy density are offset by significant losses in the power capability of the electrode. Indeed, a few studies have demonstrated that the active materials currently considered have inherently higher rate capabilities than

[13] Current affiliation and mailing address.

when employed in "real life" electrodes, clearly pointing at a bottleneck that goes beyond individual components.

While the limitations observed in current electrode designs are macroscopically well described, their origin needs to be clearly defined at multiple length scales (from nano to macro) if they are to be overcome. Differences in behavior between electrodes of different thickness must be related to disparate utilization with respect to the distance from the supply of ions (electrolyte) and electrons (current collector). Likewise, failure could be defined as the extent of disconnected regions and component shuffling. Both these effects lead to electrode inhomogeneity. Mathematical models of porous composite electrodes have been employed in order to explain macroscopic observations and predict long term behavior. These models are based on the simulation of the reaction distribution, i.e., the location of the electrode fractions that have undergone a redox transformation, for which little experimental observation exists. Therefore, experimental validation of this aspect in the models is not yet possible. This gap is particularly important when considering that currently available models fail to account precisely for the poor behavior of thick electrodes. Apart from the impossibility of visualizing local SOCs in an electrode, another factor in this discrepancy is the difficulty of experimentally quantifying pore size, distribution and tortuosity in order to provide input parameters for the models. In their absence, these parameters are fit during the simulations, or a semi-empirical value is introduced. However, this approach can lead to serious deviations between predictions and macroscopic observations. As 3D models of porous composite electrodes are being developed, the need for experimental data will be accentuated.

This project aims to provide input for models that accurately predict battery degradation, as well as inform electrochemical engineers in their optimization of designs that increase energy storage while preserving power performance. Changes in porosity, component distribution and utilization with manufacturing procedures (e.g., calendaring, mixing protocols) will be revealed. Further, our work will identify modes of failure associated with processes that occur in buried regions, such as the creation of internal isolated portions.

Approach

Use spectroscopic and diffraction techniques to monitor the reactions involved in battery electrodes. Use synchrotron-based spectromicroscopy tools to probe porous composite electrodes at high chemical and spatial resolution, in 2D and 3D. Develop methodologies that rely on less sophisticated techniques to probe inhomogeneities in battery electrodes. Correlate chemical and morphological information.

Results

Validation of *operando* XRD as a tool to probe in-depth gradient formation in NMC electrodes. In collaboration with the Battaglia and Srinivasan groups in BATT at LBNL, a baseline cathode material of relevance to battery engineering was identified as the system of study for this project. The choice was $LiNi_{1/3}Co_{1/3}Mn_{1/3}O_2$ (NCM333, hereafter); electrodes of different thickness were provided by the Battaglia group. The electrochemical properties of these electrodes are being evaluated both experimentally and computationally by the Battaglia and Srinivasan groups.

Operando XRD was performed on a series of NCM333 electrodes of different thickness (from 50 to 150 μm). The experiments were performed at beamline 11-3 at the Stanford Synchrotron Radiation Lightsource (SSRL), at SLAC National Accelerator Laboratory. Data were acquired after the X-ray beam was transmitted through the electrochemical cell, which consists of a standard coin cell with a very small window (~1 mm diameter) that is covered with conductive tape. The small size of the window minimizes concerns over pressure gradients. Consequently, to a first approximation, the collected patterns represent an average of the composition of the composite cathode in depth. These data are, thus, amenable to comparison and fit using continuum models pioneered by the Srinivasan group. In the case of a material undergoing a second-order phase transformation (i.e., solid solution mechanism) such as NCM, a continuous shift of the XRD peaks, with no new reflections appearing, is expected.

Figure VI - 217 shows the electrochemical profile of the *operando* cell using a 150 μm NCM333 electrode, together with selected XRD patterns at relevant points of the reaction. After an initial charge to 4.3 V at 1C rate, the cell was relaxed for 100 min. XRD patterns were collected every 2 minutes during these processes. As expected, a smooth shift of the peaks, indicative of a solid solution mechanism of Li deintercalation, was observed during charge. However, such shift was accompanied by a significant increase in peak width, indicative of the formation of compositional in-homogeneities in the electrode. This observation appears to be in contradiction with the fact that a homogeneous electrochemical potential is expected throughout the electrode when the reaction follows such mechanism. More importantly, an evolution of the peak width and position was observed during cell rest, indicating that compositional relaxation was occurring in the electrodes.

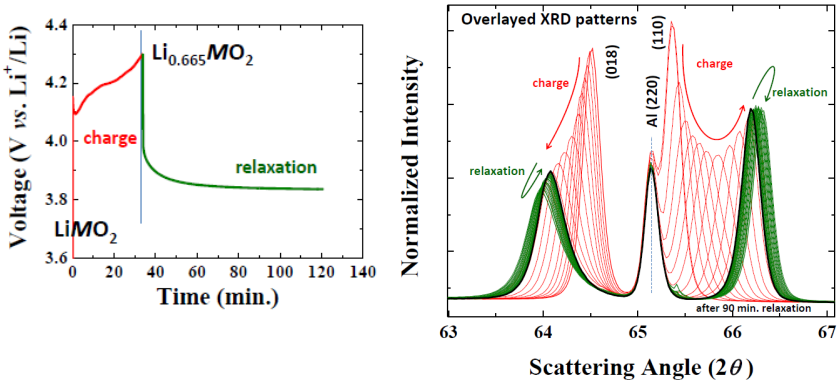

Figure VI - 217: (Left) Voltage vs. time trace of an operando XRD cell with Li metal and NCM333 electrodes. (Right) Selected patterns taken during operation of the cell

The study of 150 µm thick NCM333 electrodes was complemented by comparing the data in Figure VI - 217 with a different set collected at C/10, instead. While a continuous evolution of the XRD peaks was observed during relaxation after the 1C charge, the peaks remained unchanged during relaxation after a charge at C/10. This observation provides further support to the conclusion that a fast charge in such thick composite electrodes results in the buildup of in depth chemical gradients due to kinetic limitations imposed by inhomogeneous carrier transport. When thinner (50 µm) electrodes with very low porosity were used instead, the gradients became so significant that peak splitting, mimicking what would occur in a first order transition, were observed. They are indicative of areas that are not supplied with a sufficiently high concentration of ions to let the reaction proceed.

Detection of reaction homogeneities in NCM333 using microprobe spectroscopy. The electrode SOC based on transition metals can be obtained by measuring the oxidation state of these metals using X-ray absorption spectroscopy (XAS). Through the use of a beamline like 2-3 at SSRL, the X-ray probe can be focused down to 2 µm, so that spectra can be collected at many points within a composite electrode. This methodology can thus be used to build chemical maps of local SOCs. Figure VI - 218, top, shows an *ex situ* chemical map of the cross section of a 150 µm thick NCM333 electrode harvested after a charge to 4.3 V at 3C. The current collector was located at the bottom in the image. This map was produced by collecting µ-XAS at the Ni K edge. The energy of the beam was set at a discrete number of energies in the vicinity of the edge, at values where the spectroscopic difference between pristine and oxidized material is largest. The intensity at these points was normalized by collecting maps above and below the edge. Separately, full spectra were collected at selected points (Figure VI - 218, bottom right) to confirm the trends in the map. The results indicated the existence of areas in the electrode that did not charge (oxidize, red) as effectively as the rest. Contrary to what would be expected based on porous electrode theory of materials reacting through solid solutions, such as NCM333, there is no homogenization of the composition when the electrochemical potential is removed. This effect could be an indication of poor electrical connection of the domain, an early sign of a possible source of failure upon extended cycling.

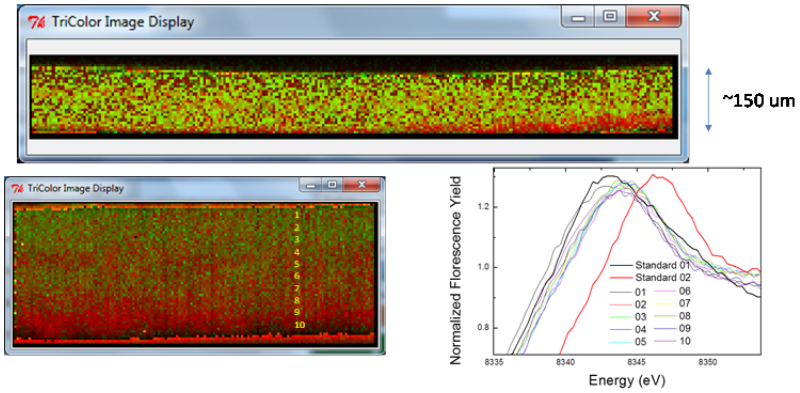

Figure VI - 218: (Top) Ni K edge µ-XAS of the cross-section of a NMC333 electrode charged to 4.3 V at 3C. (Bottom) Zoom-in of the top image, indicating the points where individual full spectra were collected (right)

***Operando* XRD study of new fluoride phases synthesized in the Cathode effort.** The goal in this sub-task was to provide characterization insights into new compounds identified under a separate Cathode task by the same PI. Following the general theme of the task, the role of the phase transformations occurring upon delithiation will be tied to the properties of the materials and their durability in composite electrodes.

During FY2013, electrodes based on of alkali metal iron fluorides such as $KFeF_3$ (Figure VI - 219) were evaluated. Despite the low crystallinity of the material due to the need to aggressively mill with carbon to achieve electrochemical activity, it was possible to observe a shift to lower angles of the peaks during charging. This shift was indicative of removal of K^+ through a solid solution mechanism. This removal was found to be reversible.

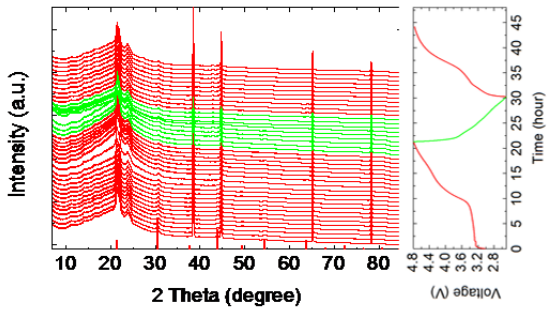

Figure VI - 219: Operando XRD data of a Li metal cell with a KFeF3 working electrode

Conclusions and Future Directions

During FY2013, proof of concept was established of the value of simple *operando* XRD experiments to detect the generation of gradients in SOC of commercially relevant NCM333 electrodes. These gradients were found to aggravate with cycling rate. Using μ-XAS, their localization could be ascertained. It was found that they form in close proximity of the current collector and do not always homogenize when the circuit is open, indicative of poor ionic connectivities. In parallel to this tool development effort, characterization of the phase transformations of alkali metal transition metal fluorides synthesized by the same group under a Cathode project was undertaken. Electroactivity was confirmed for a variety of phases, such as $KFeF_3$.

This project was closed on July 2013 due to the relocation of the Principle Investigator to the University of Illinois at Chicago. Thus, there are no future directions to be discussed.

FY 2013 Publications/Presentations

1. "High resolution chemical imaging of phase transformations during intercalation reactions," *Pacific Rim Meeting on Electrochemical and Solid State Science (PRiME) 2012,* October 7th-12th, 2012, Honolulu, HI (USA).
2. "Multiscale phase transformations in battery electrodes: visualization and consequences," *ALS-CXRO Seminar,* Lawrence Berkeley National Laboratory, February 27th, 2013, Berkeley, CA (USA).
3. "Study of the factors that enable carbon-free insulating Li-ion battery electrodes," *International Battery Association Meeting: IBA2013*, March 10th-15th, 2013, Barcelona (Spain).
4. "High resolution chemical imaging of phase transformations during electrochemical reactions," *2013 MRS Spring Meeting*, April 1st-5th, 2013, San Francisco, CA (USA).
5. Kim, N. S. Norberg, C. T. Alexander, R. Kostecki and J. Cabana, *Adv. Funct. Mater.*, **23**, 1214 (2013).
6. C. Kim, R. Buonsanti, R. Yaylian, D. J. Milliron and J. Cabana, *Adv. Energy Mater.*, **3**, 1286, (2013).
7. P. F. Teh, S. S. Pramana, C. Kim, C.-M. Chen, C. H. Chuang, Y. Sharma, J. Cabana and M. Srinivasan, *J. Phys. Chem. C*, 2013, Just Accepted, DOI: 10.1021/jp408762v.

VI.G Beyond Lithium-Ion Battery Technologies

VI.G.1 Novel Chemistry: Lithium Selenium and Selenium Sulfur Couple (ANL)

Khalil Amine and Ali Abouimrane
Argonne National Laboratory

Chemical Sciences and Engineering Division
9700 S. Cass Avenue, Building 205
Argonne, IL 60439-4837
Phone: (630) 252-3838; Fax: (630) 972-4440
E-mail: amine@anl.gov; Abouimrane@anl.gov

Start Date: October 2010
Projected End Date: September 2013

Objectives

The proposed work has the following objectives:

- Solve the problems facing the new Li/Se battery system, such as low efficiency, high polarization, and poor cyclability through component optimization.
- Develop new battery design based on an improved mechanistic understanding and use of
  - enriched Se phases such as alpha-, beta-, or gamma-monoclinic or gamma trigonal phase and
  - Se_xS_y compounds that decrease the battery cost and increase the capacity.
- Design an effective electrode structure to allow for full capacity utilization:
  - Prepare different carbon-Se_xS_y composites to optimize the electrochemical performance
  - Develop a method for morphology control of Se-containing cathode material, for example, nanotube or nanowire
- Optimize Na battery analogue.

Technical Barriers

This project addresses the following technical barriers from the Energy Storage section of the Vehicle Technologies Program Multi-year Research, Development and Demonstration Plan:

- Cycle and calendar life performance: good cyclability with high coulombic efficiency is needed to meet the automotive requirement.
- Cost: High energy can significantly reduce cost.

Technical Targets

USABC goals for electric vehicle: \$150/kWh, 230 Wh/dm^3, 1000 cycles with 80% capacity retention, and 10-year system life.

USABC goals for 40-mile plug-in hybrid vehicle: \$220/kWh, 193 Wh/dm^3, 5,000 discharge cycles with 75% capacity retention, and 15-year system life.

Accomplishments

- Gained mechanistic understanding through advanced materials characterization techniques: *in situ* synchrotron high-energy X-ray diffraction (XRD) that monitors the crystalline phase changes during the electrochemical process.
- Adopted new electrolytes, such as ether-based electrolyte, instead of carbonate-based electrolyte to enable this new system.
- Tested different carbons (nanotubes, graphene, etc.) and different binders, such as PVDF, polytetrafluoroethylene (PTFE), or conductive polymer binders to improve cycle life.

✧ ✧ ✧ ✧ ✧

Introduction

A new class of cathode materials based on selenium has been discovered for both lithium and sodium batteries Notably, unlike the existing Na/S batteries that only operate at high temperatures, these new Se-based electrodes are capable of cycling against Na at room temperature. The choice of selenium, which is a *d*-electron-containing member of Group 16 in the periodic table, is due to its higher electrical conductivity compared to sulfur, as well as its high theoretical capacity (678 mAh/g) and volumetric capacity (3268 mAh/cm^3). However, as a new battery system, some fundamental issues still need to be clarified. For example, the charge and discharge voltages evolve in

the Li/Se system during the initial cycles. Significant polarization occurs once the charge and dicharge voltages are stabilized after 5 cycles, which leads to a low roundtrip efficiency. In addition, the coulombic efficiency is quite low during the first 20 cycles. The mechanisms or underlying reasons for this unsatisfactory performance are still not well understood due to inadequate characterization on the battery materials during electrochemical cycling. In particular, the effects of organic electrolytes on both lithiation and delithiation of the Li/SeS_x cells, if any, are still not clear, nor are the effects of the sulfur content in SeS_x. As the selenium-sulfur system has a rich phase diagram, we have found in the literature many selenium-sulfur composites, such as Se_5S, Se_5S_2, Se_5S_4, SeS, Se_3S_5, SeS_2 (commercially available), SeS_7, and $Se_{1.5}S_{10.5}$. These materials offer a capacity between 675 and 1550 mAh g^{-1}. Not only does the Se electrode show promising electrochemical performance with Li anodes, but the additional potential for mixed Se_xS_y systems allows for tunable electrodes, combining the high capacities of S-rich systems with the high electrical conductivity of the d-electron-containing Se. Unlike the widely studied Li/S system, both Se and Se_xS_y can be cycled to high voltages (up to 4.6 V) without failure in the GEN 2 electrolyte (1.2 M $LiPF_6$ dissolved in EC/EMC in 3:7 weight ratio). Their high densities and voltage output offer greater volumetric energy densities than S-based batteries, opening possibilities for new energy storage systems that can enable EVs and smart grids.

Results

In this work we show that Se and Se-S represent an attractive new class of cathode materials capable of reacting with lithium ions with promising electrochemical performance. Furthermore and unlike existing Na-S batteries that operate only at high temperature, these new electrodes can cycle well in a Na battery system at room temperature. This is the first report of room temperature rechargeable lithium or sodium coupled with Se and Se-S systems. Not only does Se provide opportunities for developing new high performance batteries, including mixed chalcogenide-systems, but has the potential to enhance our fundamental understanding of batteries. The Se-C composite was used as the cathode material for cycling against lithium and Na. Elemental Se and multiwalled carbon nanotubes were combined (mass ratio 7 to 3) and mixed for one hour using high-energy ball miller. The mixture was pressed into a pellet and heated at 260ºC for 12 hours under an oxygen atmosphere. The weight loss was below 1% due to the low pressure vapor of selenium above its melting point (~10-2 torr at 260ºC). The Se-C composite had an electronic conductivity of 6.2 S•cm^{-1}.

The Li/Se-C cell was cycled between 0.8 V and 4.2 V at 50 mA/g, and its electrochemical behavior was found to differ from that of the Li/S system. If the latter system is charged to only 3.9 V, the voltage drops to 2 V, and the cell cannot cycle again. Figure VI - 220 and Figure VI - 221 show the capacity retention over 100 cycles and the voltage profiles for the 25th of the Li/Se-C system. A capacity of more than 300 $mAhg^{-1}$ was sustained for one-hundred cycles, with charge discharge efficiency higher than 99% (see Figure VI - 220). Inductively coupled plasma spectroscopy showed no variation in the amount of Se in the cathode with cycling from the 20th cycle.

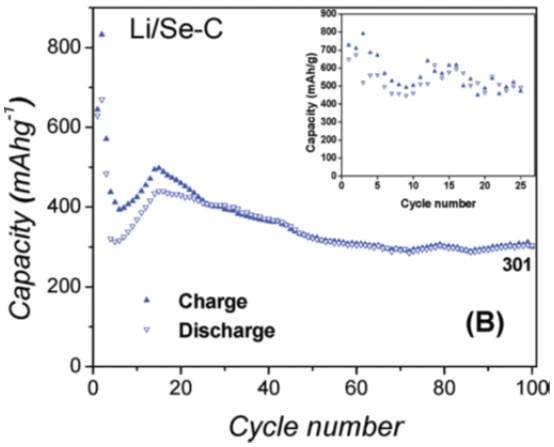

Figure VI - 220: Cyclability of Li/Se−C system showing more than 300 $mAhg^{-1}$ as capacity

These results can be explained by the fact that no further polyselenide dissolution in the electrolyte has happened. Furthermore, with regard to the reversibility of Li/Se-C system, we noticed, from the 50th cycle, essentially no variation in the charge/discharge capacities (Figure VI - 220) or in the cell voltage profile (Figure VI - 221). Even though the theoretical capacity of the Li /Se system based on the formation of Li_2Se is only 675 mAh/g, much lower than that of the Li/S system (1675 mAh/g). However, the high density of Se (4.82 g/cm^3) versus S (2.07 g/cm^3) makes the volumetric capacity of these materials very close (~3,253 Ah/l for Se and ~3,467 Ah/l for S). Furthermore, we found that the Li/Se system delivers an output voltage at least 0.5 V higher than Li/S (Figure VI - 221) and thus could surpass the Li/S system in terms of volumetric energy density.

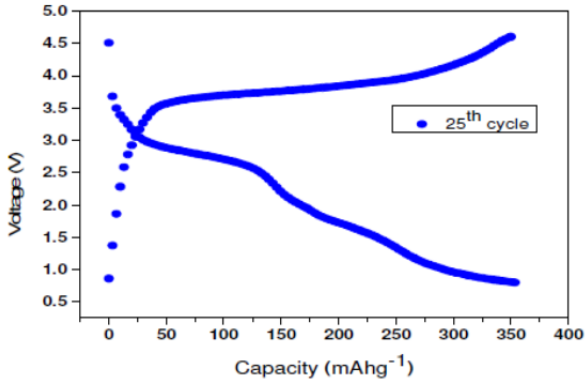

Figure VI - 221: Voltage profile of Li/Se–C system

To understand what happens during the lithium insertion and de-insertion in selenium, we performed pair density function (PDF) and *ex situ* x-ray diffraction (XRD) measurements for various states of discharge and charge at a low current rate of 10 mAh/g. During the Se reduction, one voltage plateau appears at 1.9 V. At 0.8 V, the capacity was about 650 mAh/g, which corresponds to 90% of the theoretical capacity based on the formation of Li_2Se and traces of selenium being present, as observed by XRD and PDF measurement (Figure VI - 222).

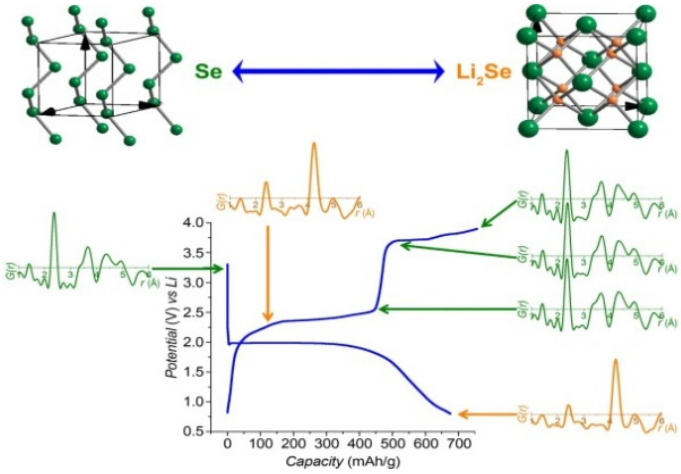

Figure VI - 222: PDFs for the pristine Se–C electrode and upon recovery from various states of discharge/charge. Structural representations of the Se and Li_2Se (antifluorite) phases are shown at top

The PDF provides local and long-range structural information as a histogram of all atom-atom distances within a system, independent of crystallinity. Unlike conventional diffraction methods, it allows phases to be identified regardless of any changes in particle size (including nanoscale), particle morphology or structural order. PDFs for the pristine and recovered Li/Se materials are shown in Figure VI - 222. Refinement of a structure against the data obtained for pristine Se confirmed the tetragonal structure, with chains of Se atoms linked by Se-Se bonds of 2.36Å. For the Li/Se system, PDF results reveal that during the discharge (1.99V~240 mAh/g), Li_2Se and Se are present.

Organic electrolytes are known to be important in Li/O_2 and Li/S batteries. We tested an ether-based electrolyte with our Li/Se system, as it has proven to be superior to the carbonate-based electrolyte. The results demonstrated that cell performance is significantly improved in terms of voltage profile and coulombic efficiency. The voltage profiles of these cells indicate that complete lithiation of Se to Li_2Se is occurring through the formation of intermediate phases, i.e., Li_2Se_n (Figure VI - 223). This behavior differs from the single-phase transition in the carbonate-based electrolyte, as reported earlier. This result clearly suggests that cell performance highly depends on the nature of the electrolyte. To better understand the relationship between the formation of the intermediate phases and voltage profile of the cells with the ether-based electrolyte, we performed an in-depth study by different characterization techniques, including high-energy X-ray diffraction (HEXRD) and X-ray absorption spectroscopy (XAS). The powerful capability of *in situ* HEXRD and XAS, available at the Advanced Photon Source (APS) at ANL, allowed us to monitor instantly the phase transition, the intermediate phases, and their oxidation states during cycling. We have proposed a mechanism behind the (de)lithiation processes for Li/SeS_x cells, based on the results obtained from *in situ* X-ray absorption near edge structure (XANES) probes (Figure VI - 224). This work has helped us to better understand and correlate the formation of intermediate phases with the electrochemical performance of Li/SeS_x cells, and shines new light on how to improve the cell

performance by tuning the electrolyte composition. Detailed analysis demonstrated that lithium polyselenides are formed during the charge and discharge process, and the formation and existence of the polyselenides in the electrolyte were further proved by end-product solubility tests.

During lithiation, the critical points (at 2.04 and 1.67 V) of the electrochemical process are well-correlated with the evolution of the XANES spectra. For example, the inflection point at 2.04V in the voltage profile coincides with the shift of the XANES spectrum to lower energy. The precipitous voltage drop at around 6-hour of discharging corresponds to the sudden appearance of the Se K-edge of Li_2Se. Generally, the energy position of the edge is determined as the maximum at the lowest energy of the first derivative of the XANES spectra. To determine the edge positions, we show the first derivatives of the XANES spectra in Figure VI - 224c. This plot shows that the Se edges are shifted significantly with (de)lithiation. When the cell is first discharged through the inflection point at 2.04 V, the edge shifts from 12,657.9 eV to 12,656.7 eV. In the following 3 hr (more than 300 mAh/g capacity), the edge positions do not change much and are accompanied by the voltage plateau around 2 V. When the cell is discharged to 1.67 V, the Se K-edge jumps to 12,660 eV, suggesting the formation of Li_2Se. During charge, the Se edges slowly shift back to lower energy. These observations indicate that polyselenides might have formed during the cycling, but in a non-crystalline state; hence, they are not detected by XRD.

In addition, excellent performance was demonstrated with the ether-based electrolyte in cell tests for 50 cycles (Figure VI - 225).

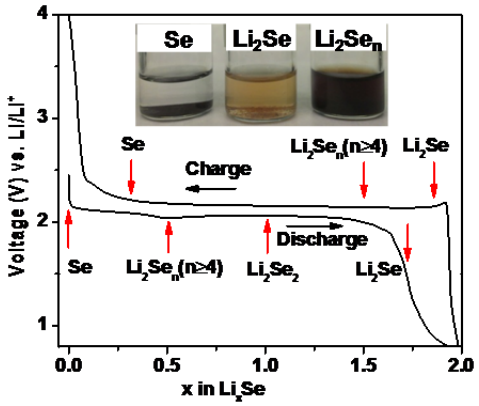

Figure VI - 223: Representation of cathode phase evolution during charge and discharge of a Li/Se cell with an ether-based electrolyte

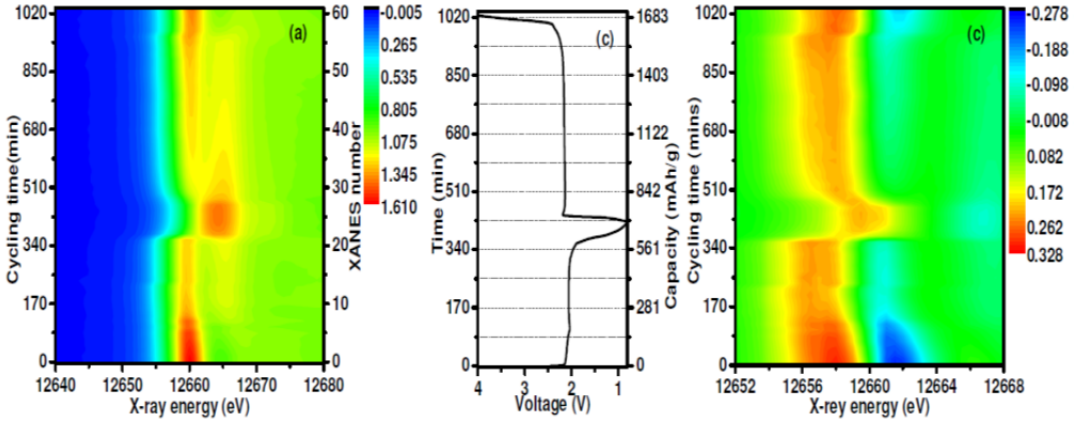

Figure VI - 224: (a) Normalized XANES spectra of Li/Se cell during cycling, (b) battery voltage profile, and (c) derivative of normalized XANES spectra of Li/Se cell during cycling

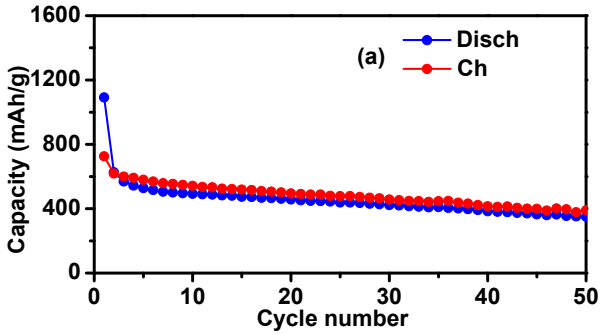

Figure VI - 225: Cycle performance of Li/Se cell in ether-based electrolyte

Conclusions and Future Directions

In this project we demonstrated that Se-containing materials are promising cathode materials for high-energy-density battery applications, while system optimization is still needed. *In situ* XANES provided valuable information on the oxidation states of crystalline and amorphous phases, including intermediate species dissolved in the electrolyte. A mechanism for lithiation/(de)lithiation was obtained on the basis of a combination of *in situ* synchrotron X-ray techniques and electrochemical methods. We intend to adopt several strategies to prove that the Se-S/Li or Na system can exhibit long cycle life and be cost competitive with sulfur batteries. Our first strategy is to design a SeS_2 /carbon composite where carbon conductive matrix is closely linked to the SeS_2 particle to ensure continuous good electronic conductivity. We will also develop an electrode processing technology that allow for maximizing the SeS_2 active material in the electrode. Unlike S where over 65% of electrode is made of high surface area carbon and binder which are inactive, SeS_2 has high conductivity and therefore the inactive element in the electrode will be reduced and the energy at the electrode level will increase significantly.

FY 2013 Publications/Presentations

1. Y. Cui, A. Abouimrane, J. Lu, T. Bolin, Y. Ren, W. Weng, C. Sun, V. A. Maroni, S. M. Heald, and K. Amine, J. Am. Chem. Soc. 2013, 135 (21), 8047.
2. Abouimrane, D. Dambournet, K.W. Chapman, P.J. Chupas, W. Weng, and K. Amine, J. Am. Chem. Soc. 2012, 134, 4505.
3. Y. Cui, A. Abouimrane, J. Lu, T. Bolin, Y. Ren, W. Weng, C. Sun, V. A. Maroni, S. M. Heald, and K. Amine, "(De)Lithiation Mechanism of Se-based Lithium Batteries Determined by *In situ* Synchrotron X-ray Probe," Extended Abstract #520, 224th Meeting of Electrochemical Society, San Francisco, CA, U.S., Oct. 27- Nov. 01, (2013).
4. Abouimrane, Y. Cui, and K. Amine, "Electrochemical Mechanism Study of Selenium-Based Rechargeable Lithium Battery," 6th International Conference on Advanced Lithium Batteries for Automobile Applications, Argonne, IL, September 9-11, (2013).
5. Abouimrane, D. Dambournet, K. W. Chapman, P. J. Chupas, W. Weng, Y. Cui, H. El Tayeb, and K. Amine, "Selenium and Selenium Sulfide − A New Class of Positive Electrode Material for Room Temperature Lithium and Sodium Rechargeable Batteries," Extended Abstract #335, 222nd Meeting of Electrochemical Society, Honolulu, Hawaii, U.S., October 7-12, (2012).

VI.G.2 Development of Novel Electrolyte for Lithium Air (ANL)

Khalil Amine and Jun Lu
Argonne National Laboratory
Chemical Sciences and Engineering Division

9700 S. Cass Avenue, Building 205
Argonne, IL 60439-4837
Phone: (630) 252-3838; Fax: (630) 972-4440
E-mail: amine@anl.gov and junlu@anl.gov

Larry Curtiss
Argonne National Laboratory
Material Science Division
9700 S. Cass Avenue, Building 200
Argonne, IL 60439-4837
Phone: (630) 252-7380
E-mail: curtiss@anl.gov

Start Date: October 2010
Projected End Date: September 2013

Objectives

- Develop stable electrolytes and new cathode architectures in lithium air batteries to lower the charge overpotential, improve the cell efficiency and cycle life.
- Understand the oxygen crossover effect at the anode on the electrochemical performance of Li-air battery.

Technical Barriers

This project addresses the following technical barriers from the Energy Storage section of the Vehicle Technologies Program Multi-year Research, Development and Deomnstration Plan.

- **Unstable electrolytes**: electrolyte decomposition (in particular the carbonate-based electrolyte) in the presence of the reduced oxygen species, especially superoxide anion (O_2^-).
- **Inefficient cathode structure and catalysis**: Commonly used carbons and cathode catalysts do not access the full capacity of the oxygen electrode and cause significant charge overpotentials. This lowers power capability.
- **Lithium electrode poisoning** due to oxygen crossover and reaction with the electrolyte. This degrades cycle life.

Technical Targets

The goal of this project is to enable Li-air battery for automotive applications. The targets are to achieve 300 cycles and an energy density of 600~700 Wh/kg. This will provide the necessary breakthroughs and a firm basis for follow-on optimization and incremental improvements.

Accomplishments

- Enabled a new stable silicon-containing oligo(ethylene oxide) solvent 1NM3 for Li-air battery
- Developed a new nanostructured cathode architecture utilizing atomic layer deposition (ALD) technique to lower the charge overpotential and improve the efficiency of the Li-air cell.
- Investigated oxygen crossover effect at the anode of a Li-air battery from density functional studies and *in situ*/*ex situ* measurements.

✧ ✧ ✧ ✧ ✧

Introduction

Li-air batteries can be considered the 'holy grail' of lithium batteries because they offer, in principle, at least ten times the energy density of conventional lithium-ion systems. The lithium-ion cell chemistry, the best to date, would provide a theoretical specific energy of ~900 Wh/kg if the calculation is based on the masses of the anode and cathode materials alone; in practice, 150-200 Wh/kg has been accomplished at the cell level. In contrast, a lithium-air cell, when discharged to Li_2O_2 at an average 3.1 V would provide a theoretical specific energy of 3623 Wh/kg, or when discharged to Li_2O at the same voltage, 5204 Wh/kg. Note that gasoline (octane) offers a theoretical energy of ~13,000 Wh/kg if the mass of the injected oxygen is not considered in the calculation because it is supplied externally and combusted within, and exhausted from, the engine. By the same token, a lithium-air cell would offer a specific energy of ~11,000 Wh/kg if the 'free' oxygen supplied during discharge and released during charge is ignored in the calculation.

While the inherent energy potential of Li-air approaches that of gasoline, today's battery manufacturers have not yet been able to unlock this

potential. While today's lithium-ion batteries may provide acceptable power for hybrid electric vehicles (HEVs) and all-electric vehicles (EVs), they do not provide sufficient energy for an acceptable driving distance. This range limitation and the absence of a battery charging infrastructure have limited public interest in EVs. A breakthrough in Li-air battery technology would significantly increase the possibility of extending the electric range of these vehicles with the added advantages of reducing battery cost and weight.

This Li-air battery technology is still in its infancy and, no doubt, will require significant research efforts in a variety of fields to unlock its full potential. The successful implementation of non-aqueous Li-air cells has been hampered because of severe materials problems that have limited electrochemical performance: (1) the non-aqueous electrolytes are unstable at high potentials and are easily oxidized by the oxygen released during charge, thereby seriously limiting cycle life; (2) during discharge, the solid and insoluble Li_2O_2 and/or Li_2O products are deposited on the surface or within the pores of the carbon cathode, thereby clogging the pores and restricting oxygen flow; (3) poisoning of the lithium electrode due to oxygen crossover destroys the integrity and functioning of the cell; and (4) commonly used cathode catalysts, such as MnO_2 or Mn metal, do not access the full capacity of the oxygen electrode or enable sufficiently high rates.

This team is working on problems that limit the electrochemical performance of the Li-air battery, including the stability of the organic electrolyte, cathode catalysts and structures, and stability of the lithium anode under oxygen-crossover conditions. This effort will lead to the development of a reversible lithium air battery that provides 10 times the energy density of the state-of-the-art lithium ion battery for powering EVs. The technology, if successful, can also benefit many military applications that require very high energy density such as satellite, military vehicles for silent watch and operation.

Approach

This project addresses the current limitations of Li-air batteries through: (a) New electrolytes, based on siloxanes and ethers, that will be more stable than incumbent carbonates, (b) Catalytic activated carbons with an optimal pore size distribution that will create the maximum volumetric density of triple-phase boundaries, (c) Metal/metal oxide cluster catalysts, incorporated onto carbon support, that will promote formation of electronically-conductive superoxide species, and (d) Protected lithium, through a coated lithium powder anode and/or ceramic protection layer for a lithium foil anode that will reduce dendrite formation.

The experimental designs to create advanced electrolytes, carbons, catalysts, cathodes, and anodes was guided by theory and modeling and the experimental results were thoroughly analyzed with very sophisticated analytical techniques that were used to fine-tune the computational studies.

Results

Stable electrolytes for Li-air cells: There is a wealth of experimental and theoretical evidence that the organic carbonates, e.g., propylene carbonate (PC), ethylene carbonate, and dimethyl carbonate, commonly used in Li-ion batteries are not stable toward the oxygen reduction products formed during Li-air discharge. It has been reported that, during discharge, in addition to formation of the desired lithium peroxide, propylene carbonate is decomposed, resulting in the formation of lithium carbonate and other organic species. Another challenge beside the decomposition of the electrolyte is the large overpotential observed in lithium air cell which affects both power and cycle life.

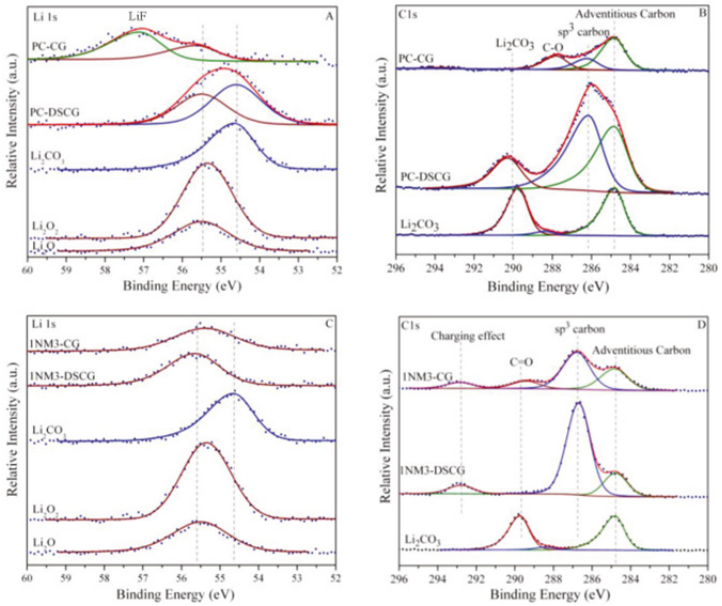

Figure VI - 226: XPS spectra of Li 1s and C 1s core peaks of the cathode carbon electrodes after discharge and charge when using PC or 1NM3 as solvent in the electrolyte

In order to understand the source of the large polarization observed in Li-air cell, we carried out a detailed investigation of the charge and discharge products formed in systems employing the PC based electrolyte. In this work we employed XPS as a primary tool to characterize the charge and discharge products, as shown in Figure VI - 226. The results indicated that Li_2CO_3 was the major product formed during discharge with only minor amounts of lithium oxides being formed. During the first charge cycle the Li_2CO_3 was decomposed based on the XPS data and is believed to be the primary cause of the large charge overpotential required for charging. This is due to the need to oxidize the carbonate or other materials rather than the formation of desired Li_2O_2. Density functional (DFT) calculations confirmed that PC is unstable to oxygen reduction species. As it stands, the cells based upon PC cannot be considered viable as the overall reaction appears to be oxidation of PC to CO_2.

In contrast, the silicon-containing oligo(ethylene oxide) compound 1NM3 was shown by DFT calculations to be more stable to the highly active oxygen reduction species when compared to PC. When 1NM3 is used in place of PC, the XPS data collected after single discharge (see Figure VI - 226c and Figure VI - 226d) show that only lithium oxides are formed and moreover they are partially decomposed upon charging. The increased stability of the 1NM3 solvent results in a significantly lower overpotential for the Li-air cell as shown in Figure VI - 227. We have to confirm that the product from charging in the 1NM3 is oxygen, but the lower overpotential could be due to the fact that oxidation of lithium oxides is easier that the oxidation of carbonate which is formed in the PC cells. Clearly, the electrolyte solvent stability plays a key role in the performance of Li-air batteries and will be a key factor in improving their efficiencies.

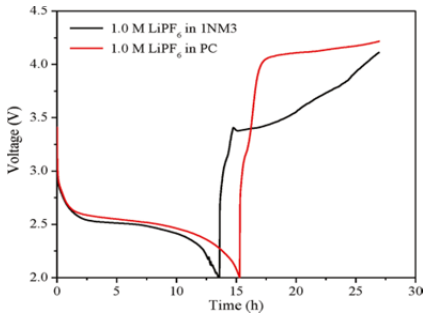

Figure VI - 227: First charge and discharge cycles or a Li-air cell with propylene carbonate (PC) as and polylethylene oxide siloxane (1NM3) showing the reduced charge overpotential due to the stability of 1NM3 to oxygen reduction products

While the stability during discharge found for the 1NM3 electrolyte is a key result, electrolytes that provide stability during charge as well as discharge are needed as well as ones that aid in reversibility of the reactions. Further work is underway to improve the reversibility of the system in the presence of this new electrolyte. However, one should comsider other factors that affect cycleability and charge overpotential before optimizing the full cell system. For instance we have found that the oxygen cross over can significantly degrade the lithium anode and affect the cycle life. We also found that the cathode structure can impact the efficiency of the cell.

Nanostructured Cathode Architecture for Low Charge Overpotential in Li-O_2 Batteries: There may be a number of other contributing factors for the large charge overpotentials other than the lack of an effective electrocatalyst. Poor electronic conductivity of Li_2O_2 may limit the charge process. Contaminants in the Li_2O_2 discharge product from electrolyte decomposition such as Li_2CO_3 may also cause a higher charge potential. The electrolyte decomposition may result from reaction of the electrolyte with defects on the carbon surface. Therefore, it may be possible to significantly lower the charge potential if solutions to the above problems can be discovered. We are able to demonstrate a conceptually new approach as illustrated in Figure VI - 228 based on a new cathode architecture for the Li-O_2 cells that shows promising results for solving the charge overpotential problem. The cathode architecture addresses the electrolyte decomposition problem with a porous carbon passivated by a protective Al_2O_3 coating applied by ALD. Very small Pd nanoparticles attached to the surface by ALD act as effective electrocatalysts (Figure VI - 229) and seem to promote formation of a nanocrystalline form of Li_2O_2 that provides good electronic transport.

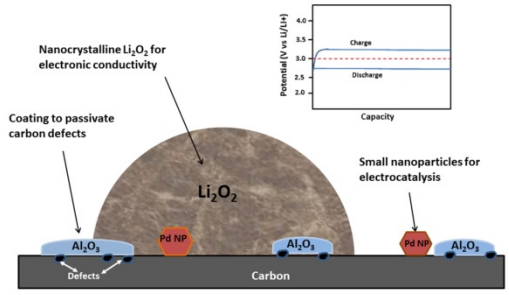

Figure VI - 228: Schematic of the nanostructured cathode architecture shows the Al_2O_3 coating, the palladium nanoparticles and the nanocrystalline lithium peroxide, all of which contribute to lowering the overpotential. The inset shows a hypothetical charge/discharge voltage profile vs. capacity

The resulting low charge overpotential is about 0.2 V, as shown in Figure VI - 230. The formation of lithium peroxide was confirmed by XRD and SEM as well as High Resolution Transmission Electron Microscopy (HRTEM) techniques. Computational modeling was used to provide insight into the role of the Al_2O_3 protective coating and the Pd nanoparticles for preventing electrolyte decomposition and catalyzing the lithium peroxide decomposition, respectively.

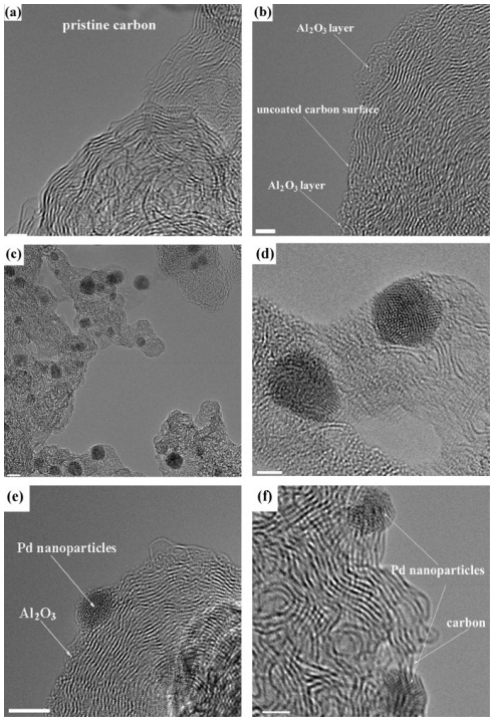

Figure VI - 229: HRTEM of the cathode structure: (a) pristine Super P carbon (scale bar, 2nm); (b) carbon surface coated with 3 ALD cycles of Al_2O_3, (scale bar, 2nm); (c)-(f) carbon + 3 ALD cycles Al_2O_3 + 3 ALD cycles Pd nanoparticles, (scale bar for (c)-(f), 5nm, 2nm, 4nm, and 2nm respectively)

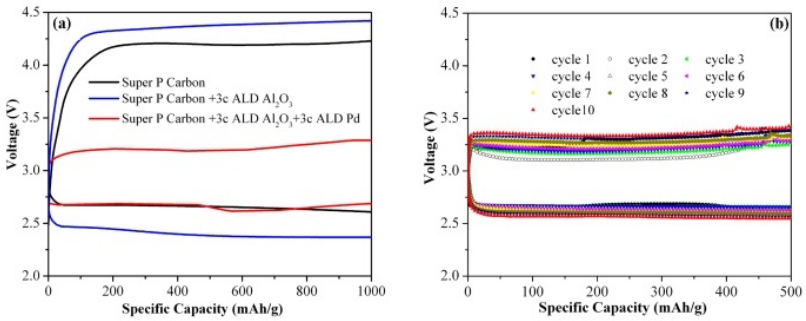

Figure VI - 230: (a) Voltage profile during discharge-charge of cells (to 1000 mAh/g) based on super P carbon; super P carbon coated with Al_2O_3; and Al_2O_3 coated super P carbon further coated with Pd nanoparticles. (b) Voltage profile during discharge-charge of cells (to 500 mAh/g) based on Al_2O_3 coated super P carbon further coated with Pd nanoparticles. The electrolyte used is TEGDME-$LiCF_3SO_3$

Investigation of oxygen crossover effect at the anode: The electrolyte chemistry occurring at the Li-anode in the presence of an oxygen crossover may play an important role in the cyclability and capacity of the Li-O_2 cells. It is of interest to investigate possible electrolyte decomposition mechanisms at the lithium anode especially in the presence of O_2 crossing over from the cathode and the possible effects on the performance of the Li-O_2 cell. In this work, the reductive stability of an ether-based electrolyte (tetraglyme) and subsequent reactions in an O_2 environment is addressed using *in situ*/*ex situ* high-energy X-ray diffraction (HE-XRD), and *ex situ* FT-IR techniques.

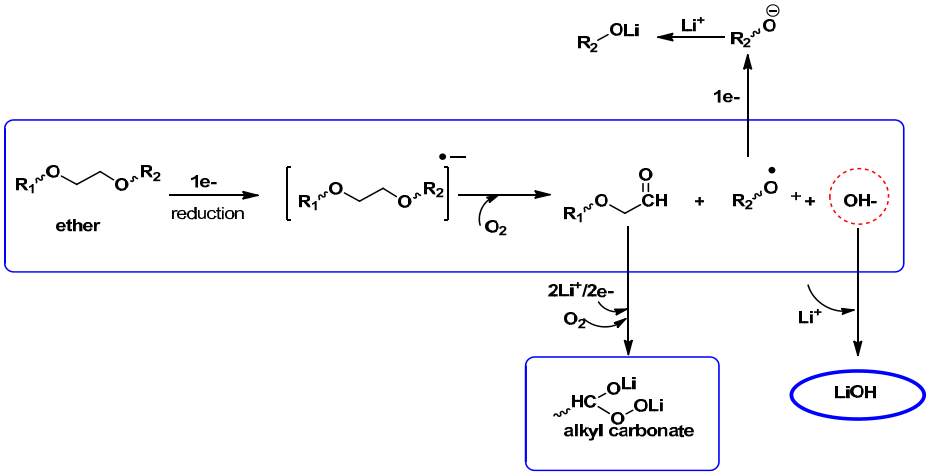

Figure VI - 231: Scheme 1 Possible reaction mechanisms of decomposition of ethers to form LiOH and alkyl carbonates at the anode surface upon electron attachment and oxygen crossover

In order to investigate potential products that are formed at the anode in a Li-air battery such as proposed in Scheme I (see Figure VI - 231), we have carried out a detailed characterization study of the anode in a Li-air cell during various stages of discharge and charge using a TEGDME-$LiCF_3SO_3$ electrolyte. Figure VI - 232b shows the charge and discharge profile for the cell for 4 cycles. The *in situ* XRD data is shown in Figure VI - 232a for the Li anode during the first four charge and discharge cycles. The peaks in the XRD spectra clearly show the formation of LiOH and a decrease in the Li (peak 110) metal on cycling. This suggests that an electrolyte decomposition reaction is occurring during charge at the electrolyte/Li surface with the hydrogen coming from the ether-based electrolyte and Li from the anode (which results in depletion of the Li metal). The *ex situ* XRD patterns in Figure VI - 233b for the anode after the first and tenth cycles provide clear evidence that the accumulation of LiOH is occurring on the anode and also the severe consumption of Li anode was taking place (evidenced by the absence of the (110) peak at the 10th cycle). This was further confirmed by FT-IR results from the anode after 10 cycles in Figure VI - 233a, which show an OH peak.

It is necessary to consider other possible sources of the species found on the anode. Another potential source of electrolyte decomposition could be the carbon cathode defect sites or by lithium peroxide surface. This could lead to the formation of LiOH or Li_2CO_3 on the

cathode. However, these solid species would not move across the membrane to the anode. Therefore the formation of LiOH at the anode is probably predominantly due to the oxygen crossover effect (a small percentage of LiOH may be from small amounts of water contaminants from the TEGDME or $LiCF_3SO_3$ salt). It is also noted that the TEGDME decomposition may lead to soluble products that could react further on the cathode or anode involving other reaction mechanisms.

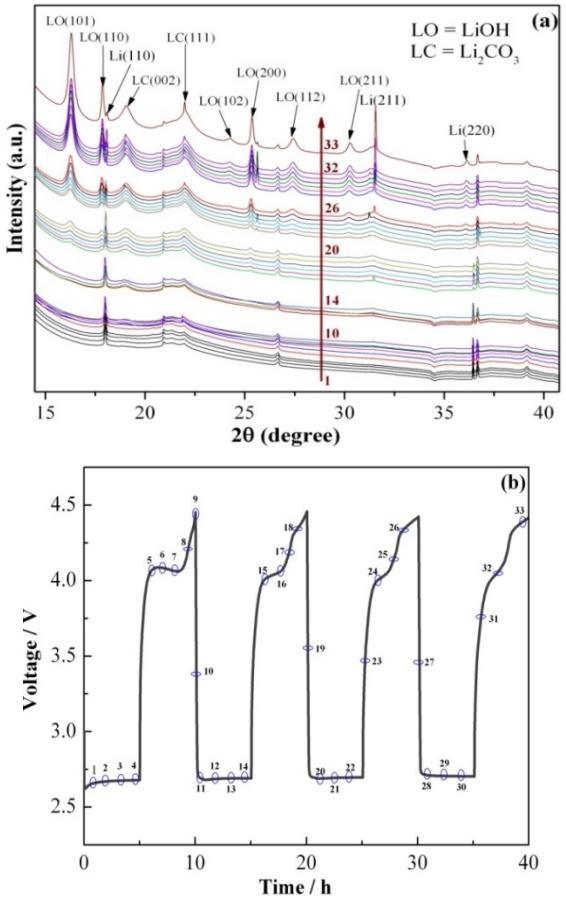

Figure VI - 232: a) *In situ* XRD patterns of Li anode and LiOH formation during the operations conditions, and (b) corresponding voltage vs time profile. Numbers on XRD data correspond to those on voltage profile

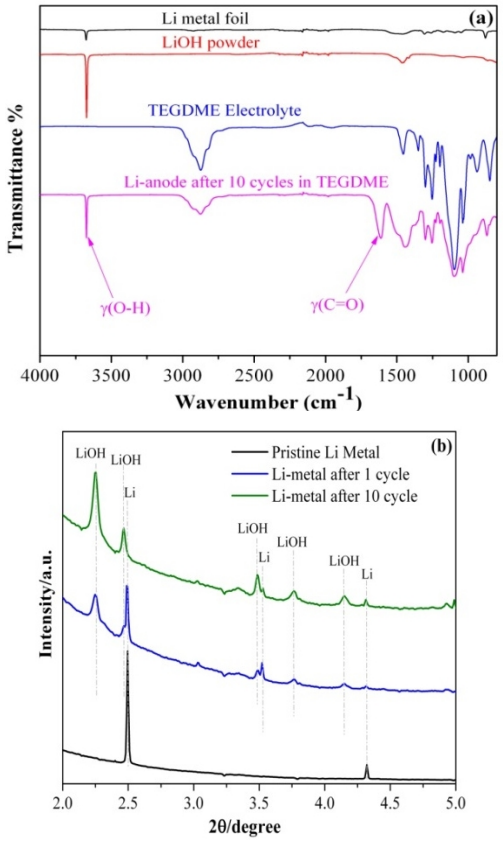

Figure VI - 233: *Ex situ* FT-IR spectra of Li anode after 10 cycles and (b) HE-XRD patterns of the Li-anode after being cycled for 1 and 10 cycles. For the FT-IR spectra, we have included the standard Li metal, LiOH powder and TEGDME electrolyte for comparison

Conclusions and Future Directions

In this project, several approaches were developed to address the technical barriers for non-aqueous Li-air battery.

- New silicon-containing oligo(ethylene oxide) solvent 1NM3 was developed to lower the charge overpotential of the Li-air cell.
- New cathode utilizing palladium nanoparticles on a carbon surface with an alumina ALD coating for passivation of carbon defect sites was developed to lower the charge overpotential and improve the efficiency of the Li-air cell.
- Demonstrate that the crossover of O_2 from the cathode to the anode in Li-air cells will result in different decomposition reactions occurring at the Li-anode than occur in at a lithium anode in a Li batteries. The evidence indicates formation of LiOH as well as carbonates at the anode in a Li-O_2 battery with a tetraglyme-

based electrolyte. Thus, controlling reactions of ethers at the lithium anode through suitable membranes or passivation films will be essential for achieving good performance of Li-O_2 cells based on ether electrolytes

Future research will focus on further developing new electrolytes and novel catalysts to lower the charge overpotential and increasing the cycle life of the Li-air battery. We will also develop model systems to understand the mechanism of formation and dissociation of lithium peroxide using size-selective metal cluster catalyst.

FY 2013 Publications/Presentations

1. Jun Lu, Yu Lei, Kah Chun Lau, Xiangyi Luo, Peng Du, Jianguo Wen, Rajeev S. Assary, Ujjal Das, Dean Miller, Jeffrey W. Elam, Hassan M. Albishri, D. Abd El-Hady, Yang-Kook Sun, Larry A. Curtiss, Khalil Amine, "A Novel Nanoscale Cathode Architecture for Low Charge Overpotentials in Li-O_2 Batteries," *Nature Commun. 4*, 2383, **2013**.
2. Jun Lu, Yan Qin, Peng Du, Zonghai Chen, Yang Ren, Tianpin Wu, Jeffery T. Miller, Jianguo Wen, Dean J. Miller, Zhengcheng Zhang and Khalil Amine, "*In situ* fabrication of porous-carbon-supported α-MnO_2 nanorods at room temperature: application for rechargeable Li–O2 batteries" *Energy and Environmental Science*, 6, 519-531**,** **2013**.
3. Jun Lu, Rajeev S. Assary, Peng Du, Xiangyi Luo, Xiaoyi Zhang, Yang Ren, Larry A. Curtiss and Khalil Amine, "The Effect of Oxygen Crossover on the Anode of a Li–O_2 Battery using an Ether-Based Solvent: Insights from Experimental and Computational Studies" *ChemSusChem*, *6(1)*, 51-55, **2013**.
4. Jun Lu, Peng Du, Kah Chun Lau, Xiangyi Luo, Javier Bareño, Xiaoyi Zhang, Yang Ren, Zhengcheng Zhang, Larry A. Curtiss, Yang-Kook Sun and Khalil Amine "Compatibility of lithium salts with solvent of the non-aqueous electrolyte in Li–O_2 batteries" *Phys. Chem. Chem. Phys., 15*, 5572-5581, **2013**.
5. Jun Lu, Hun-Ji Jung, Kah Chun Lau, Zhengcheng Zhang, John A. Schlueter, Peng, Du, Rajeev S. Assary, Jeffrey Greeley, Glen A. Ferguson, Hsien-Hau Wang, Jusef Hassoun, Hakim Iddir, Jigang Zhang, Lucia Zuin, Yongfeng Hu, Yang-Kook Sun, Bruno Scrosati, Larry A. Curtiss, and Khalil Amine, Evidence for Magnetism in Lithium–O_2 Discharge Product. *ChemSusChem.*, *6(7)*, 1196-1202, **2013**.
6. Jun Lu, Yan Qin, Peng Du, Xiangyi Luo, Tianpin Wu, Yang Ren, Jianguo Wen, Dean J. Miller, Jeffrey Miller and Khalil Amine, "Synthesis and Characterization of Uniformly Dispersed Fe_3O_4/Fe Nanocomposite on Porous Carbon: Application for Rechargeable Li-O_2 Batteries" *RCS Adv.*, 3, 8276-8285, **2013**, (DOI: 10.1039/C3RA40451J)
7. Jun Lu, Yu Lei, Xiangyi Luo, Tianpin Wu, Yang Ren, Jeffery T. Miller, Jeffery Elam and Khalil Amine, "Synthesis of Porous Carbon Supported Pd/PdO Nanoparticles by Atomic Layer Deposition: Application for Rechargeable Li-air Battery" *Nano Letter*, 13 (9), 4182-4189, **2013**.
8. Jun Lu, "*In situ* Fabrication of Porous-carbon-supported α-MnO_2 Nanorods at Room Temperature: Application for Rechargeable Li-O2 Battery," 2013 APS/CNM/EMC Users Meeting, Argonne National Laboratory, IL, May 6-9, 2013. (Invited Talk)
9. Jun Lu, "Metal Oxide Prepared by a Wet-Chemistry Approach: Application for Rechargeable Li-O_2 Battery," 7th U.S.-China Electric Vehicle and Battery Technology Workshop, Lawrence Berkeley National Laboratory, Berkeley, California, April 4-5, 2013. (Invited Talk)

VI.G.3 Integrated Lab-Industry Research Project. (LBNL, ANL)

Marca Doeff[1], Jordi Cabana[1], John T. Vaughey[2]
Lawrence Berkeley National Laboratory

[1]Environmental Energy Technologies Division
1 Cyclotron Road, MS62R0203
Berkeley, CA 94720-8168
E-mail: mmdoeff@lbl.gov

[2]Chemical Sciences and Engineering Division
9700 S Cass Avenue
Argonne National Laboratory
Lemont, IL 60439
E-mail: vaughey@anl.gov

Participants:
Guoying Chen, Tom Richardson, Robert Kostecki, Marca Doeff, Gao Liu, John Kerr, Vince Battaglia, Nitash Balsara, Robert Kostecki, Vassilia Zorba, Brian Ingram, Aude Hubaud, D. Schroeder (NIU)

Start Date: August 2010
Projected End Date: September 2013

Objectives

- Design, synthesize and characterize solid lithium ion conductors that enhance the cycle life of lithium metal based anodes.
- Search for phases with high Li-ion conductivity that are stable against lithium.
- Improve the mechanical properties of the prospective layers using ceramic composites.

Technical Barriers

Energy density, poor cycle life (incompatibility with electrolyte, dendrite formation) and safety.

Technical Targets

- PHEV: 96 Wh/kg, 5,000 cycles.
- EV: 200 Wh/kg; 1,000 cycles.

Accomplishments

- Sintered cubic LLZO ($Li_7La_3Zr_2O_{12}$) to a relative density of 94% at a considerably lower temperature than previously reported.
- Established that the processing conditions strongly affect the morphology and impurity formation in the sintered pellets. These properties, in turn, have a significant impact on the electrochemical properties.
- Determined the mechanism of Al(III) doping of LLZ via a combination of ^{27}Al MAS-NMR and high resolution XRD.
- Isolated and determined the ionic conductivity of the low temperature cubic polymorph of LLZ.
- Determined processing conditions for $Li_{1.3}Ti_{1.7}Al_{0.3}(PO_4)_3$ that alter the grain boundary phases and increase the conductivity by an order of magnitude.

✧ ✧ ✧ ✧ ✧

Introduction

One important challenge to the development of rechargeable batteries for large format applications such as electric vehicles is to increase their practical energy density. Successful use of lithium metal as the negative electrode would enable a very high energy density device, especially when coupled with a high capacity positive electrode such as air or sulfur. There are, however, serious safety concerns due to the extreme reactivity of metallic lithium with most liquid electrolytes. The use of a solid electrolyte is considered one way to enable a metallic lithium electrode, provided that the criteria of high conductivity and chemical stability are met. Among the ceramic electrolytes that have been studied, the garnet $Li_7La_3Zr_2O_{12}$ (LLZO) is promising due to its fast ion transport and purported good chemical stability against metallic lithium. Two polymorphs of this material have been described. The high temperature cubic phase is reported to have an ionic conductivity two orders of magnitude higher than that of the tetragonal phase, but high temperature synthesis (above about 1000ºC) and the presence of small amounts of Al are generally required to form it.

A key factor for any application is controlling the microstructure of the solid conductor because it defines the overall mechanical integrity. Sintered densities below 90% can result in a lower total conductivity and risk the penetration of lithium dendrites through the pores during cycling, which may lead to an electrical short or fracturing of the pellet. In polycrystalline ceramics, large grains are desirable because they also minimize the grain-boundary resistance. But long sintering times and high sintering temperature often result in impurity phases due to lithium migration and loss. The stringent processing requirements, together

with reported difficulties controlling the chemistry of the Al-substituted compounds provided motivation for the work in this program. During FY2013, the effects of processing conditions on formation, grain size and impurity formation during sintering of an Al-substituted cubic LLZO were systematically studied.

Approach

Explore the existence of conductive crystalline and glassy phases in phase diagrams of candidate lithium-ion conducting ceramic systems. Deposite complex ionic conductors using physical methods. Measure the ionic conductivity of ceramic layers. Evaluate the compatibility of the ceramic layers with lithium metal.

Results

Sintering of LLZO pellets and the influence of processing on impurity formation and interfacial chemistry. A powder mixture of precursors containing the right stoichiometry to form Al-substituted LLZO was fired at 1000°C. The resulting oxide showed the cubic structure, as expected. Part of this fresh LLZO powder was milled and used for compacting pellets, while the rest was used to cover the pellets during sintering. The influence of the history of the powder bed was explored by comparing fresh powders with those employed after having been annealed at 1100°C for either 6 h or 12 h during pellet processing.

Differences in the morphologies of pellets sintered with different powder covers were observed (Figure VI - 234). The pellets under fresh powder cover were successfully densified to 94% at only 1100°C, more than 100°C lower than previously reported for conventional methods. A thin pellet that was only a single grain (~150 μm) thick was also prepared by these means. The pellet prepared using the powder annealed for 6h was also well sintered. However, there appeared to be a phase preferentially segregated at grain boundaries on the surface, which show a darker contrast than that the bulk of the grains. SEM-EDS spectral imaging revealed that the grain boundaries were rich in Al but low in La and Zr, pointing at a $LiAlO_2$ impurity. Finally, the pellet sintered in the powder annealed for 12h was porous, with a particle size of only 1-2 μm. The electrochemical properties of this pellet were not studied. Thus, the powder cover can dramatically affect the morphology of sintered pellets, depending on its thermal history. Given that all three powder covers consisted of cubic LLZO (with slight lattice parameter variations) and had similar particle sizes (10 μm), this phenomenon must be attributable to the differences in the chemical compositions, in particular, Li and Al contents.

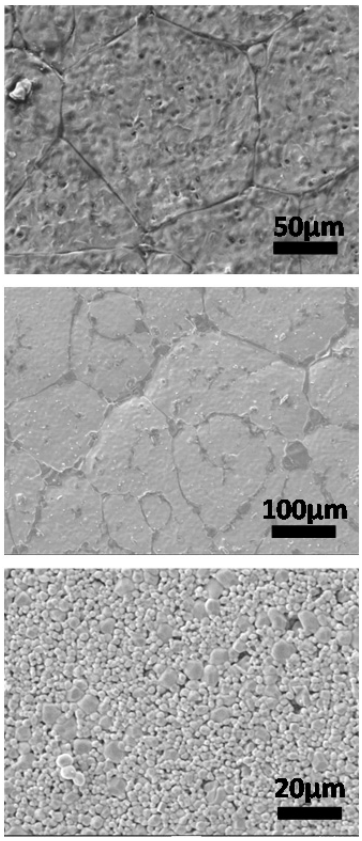

Figure VI - 234: SEM images of pellets sintered in fresh (top), 6h annealed (middle) 12h annealed (bottom) LLZO powder covers

Elemental atomic ratio maps of major (Li, La, Zr) and minor element (Al) distribution were obtained using femtosecond laser induced breakdown spectroscopy (LIBS, Figure VI - 235), a tool that is highly depth sensitive and, thus, can lead to insight into the variation of chemistry in the pellet. In the case of the pellet sintered in the fresh powder, a constant Al/La atomic ratio of 0.1 was measured from near the surface to 35 μm deep. In contrast, Al enrichment appeared to occur at greater depths for the pellet sintered with the powder cover annealed for 6h. The Al/La atomic ratio was highest at the surface and gradually decreased with pellet depth, and only at a depth of 20 μm did the ratio approach the expected value of 0.1. In contrast, the two pellets both had a consistent Zr/La ratio throughout the material. The atomic ratios of Li/La, Zr/La and Al/La were plotted in the form of 2D cross-sections (Figure VI - 235). Plots of total ionic conductivities vs. temperature revealed the LLZO film that is a single grain thick (Figure VI - 236) had the highest total ionic conductivity of 5.2×10^{-4}S/cm at 25°C, and the activation energy was 0.29 eV.

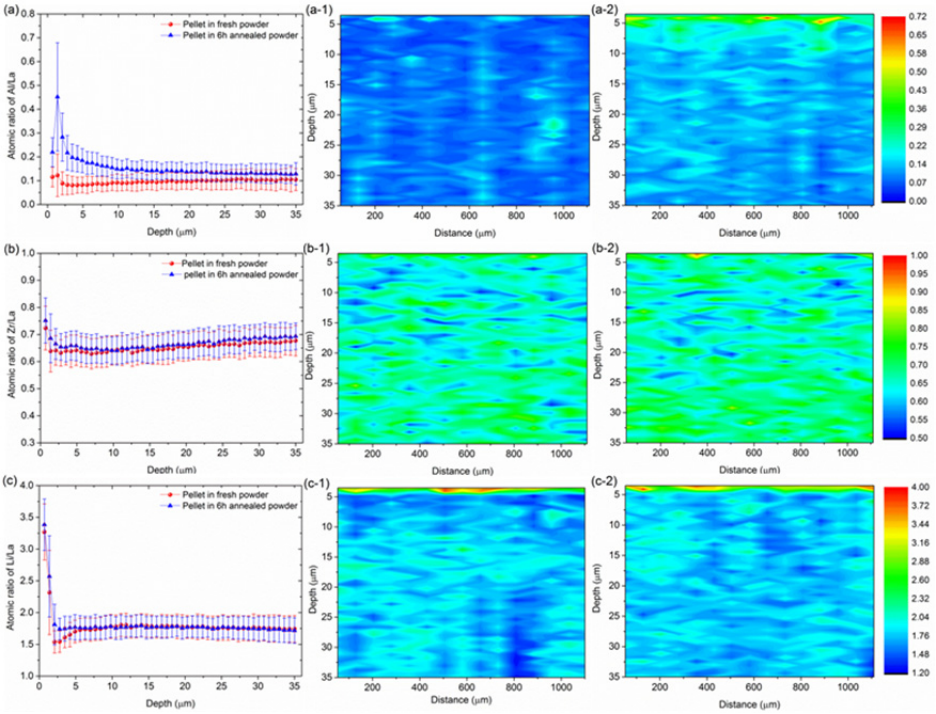

Figure VI - 235: LIBS depth profiles (a, b, c) and cross-section imaging (a-1, a-2, b-1, b-2, c-1, and c-2) of Al/La (a, a-1, and a-2), Zr/La (b, b-1, and b-2) and Li/La atomic ratios (c, c-1, and c-2) of pellets made in fresh powder (middle column) and the powder annealed for 6h (right column)

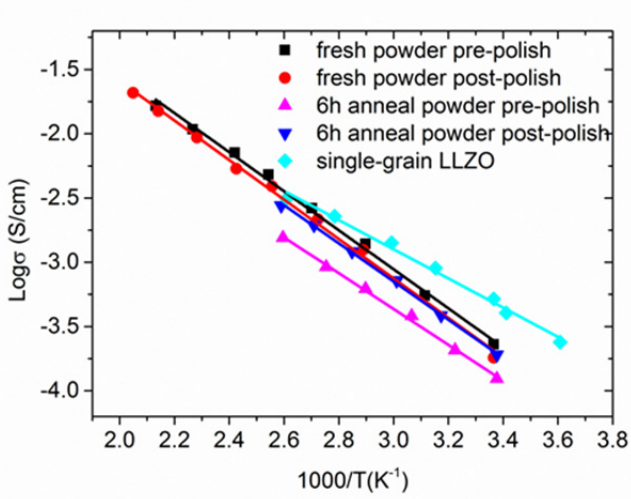

Figure VI - 236: Total ionic conductivities of pellets prepared in fresh powders or those annealed for 6 h

At the same temperature, the total ionic conductivity and the activation energy of the thick pellet sintered in fresh powder prior to polishing were 2.3×10^{-4}S/cm and 0.37 eV, respectively. This strongly implies that the room temperature ionic conductivity and activation energy of the bulk is higher than it is in the grain-boundaries, because the concentration of grain boundaries is much lower in the thin sample than in the thick pellet. The room temperature conductivities varied somewhat with the conditions used to process the pellets. The room temperature total ionic conductivity of the pellet processed in the annealed powder was only half the value of that of the pellet processed in fresh powder but it increased to 1.9×10^{-4} S/cm after the surface impurity layer was polished away, indicating that this layer has some influence on the total ionic conductivity depending on its chemical composition.

Symmetrical Li/LLZO/Li cells were assembled and subjected to galvanostatic charge and discharge, using a thick pellet processed in fresh powder without polishing. No increase in voltage or other significant change in the response was seen over 10 cycles, indicating that LLZO is reasonably stable against lithium metal under these conditions.

Deposition of LLZO thin films and interfacial chemistry. The LLZO sintered pellets were used as the targets for pulsed laser deposition (PLD) of the thin films. A Lambda Physik 248nm KrF excimer laser with 350mJ at the source was used for ablating the target in 0.3mtorr background oxygen gas environments in the deposition chamber. The films were found to be dense and ~200 nm thick. In order to assess the stability of these films to lithium metal, X-ray photoelectron spectroscopy (XPS) experiments were carried out on LLZO films in contact with lithium foil for 15 hours at 90ºC. For comparison, an Ohara LATP glass-ceramic plate was treated the same way. As expected, the glass-ceramic darkened in contact with the lithium, and the XPS results showed clearly that some of the Ti^{4+} was reduced to Ti^{3+}, as is known to occur for this material. In contrast, the LLZO film did not appear to change (Figure VI - 237).

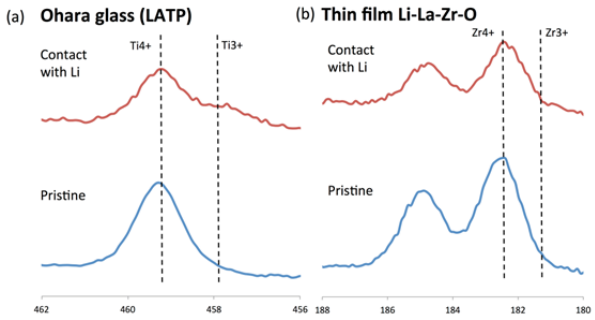

Figure VI - 237: XPS spectra of (a) Ti in Ohara glass-ceramic and (b) Zr in thin film amorphous LLZO, before and after contact with lithium metal at 90°C

Low Temperature Cubic LLZO. There are two known stable polymorphs of LLZ as noted previously. However, it has been reported that a lower temperature cubic phase can exist in a small temperature window as long as aluminum cations are present. Seeing it as a secondary phase in several samples, the synthetic conditions under which it forms were investigated. Specifically, we sought to determine the mechanism of the Al cation incorporation into the LLZO structure and the eventual formation of the cubic LLZO phase. The movement of Al(III) cations at 850°C was tracked by a combined powder X-ray diffraction (XRD), ^{27}Al and ^{7}Li MAS NMR, seen in Figure VI - 238, and high-resolution XRD (HRXRD) effort. Analysis shows that initially, the Al cations are mainly in the phase Li_5AlO_4, a phase that forms quickly in this Li_2O rich environment. This phase then acts as the highly mobile source of Al(III) cations and gets incorporated into the garnet via reaction with tetragonal LLZO, where it migrates to the Li(1) site and gradually transforms the overall garnet to a cubic LLZO.

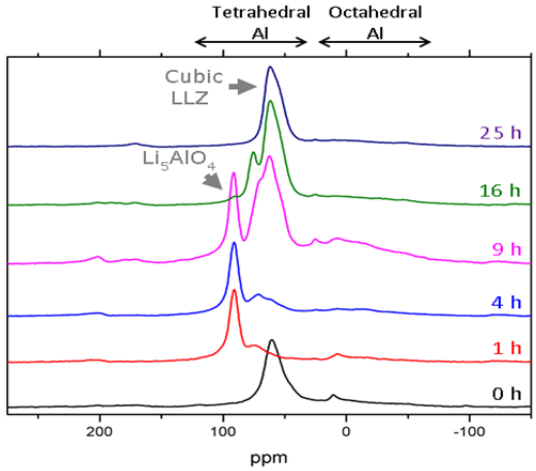

Figure VI - 238: 27Al MAS NMR spectra of LLZO powders annealed at 850°C over time

This transformation, driven by both aluminum and lithium cation movement, was tracked using ^{27}Al MAS-NMR and using high resolution XRD at the APS. Under the conditions which were used, the Al(III) continues to equilibrate forming a series of phases differentiated by small differences in Al content and cell parameters. After 24h at temperature (850°C) Al(III) incorporation has not reached equilibrium positions (*24d* site). The low temperature cubic phase, stable from 750-850°C, appears to result from the disorder created on the garnets tetrahedral site as Al displaces lithium from the structure. In order to compare how the structure affects conductivity, the ionic conductivity of the low temperature cubic phase (estimated from ^{7}Li MAS-NMR) was compared to the other two LLZO phases. The low temperature cubic phase was found to have a conductivity of 10^{-5} S/cm, approximately in between the values reported for the tetragonal and high temperature cubic phases.

Conclusions and Future Directions

Pellets of cubic Al-substituted LLZO were successfully sintered to a relative density of 94% at 1100 ºC, the lowest temperature reported using conventional ceramic processing techniques. The microstructure, composition, and distribution of minor impurities in the pellets were strongly influenced by the thermal history of the powder cover used for processing. These factors, in turn, impacted the total conductivity and interfacial behavior of the pellets in contact with lithium electrodes. The best results were obtained on samples which were heated for 12 hours in a fresh

LLZO powder bed. Using the same processing conditions, it was also possible to fabricate a freestanding thin film only a single grain thick (~150 μm). This sample exhibited the highest total conductivity (5.2×10^{-4}S/cm at 25°C) because fewer grain boundaries were present than in the thicker pellets. AC and DC experiments are consistent with the interpretation that LLZO is a single ion conductor and that it has negligible electronic conductivity. Symmetrical cells with lithium electrodes and a thick LLZO pellet as electrolyte could be cycled without noticeable deterioration in performance over 10 cycles for 20 hours, suggesting good stability of LLZO against lithium. This project was finalized on September 2013. Thus, there are no future directions to be discussed.

FY 2013 Publications/Presentations

1. "Protective layers for the lithium electrode based on ceramic phases." *Pacific Rim Meeting on Electrochemical and Solid State Science (PRiME) 2012.* October 7th-12th, 2012, Honolulu, HI (USA).
2. "Thin film lithium ion conducting electrolyte for Li metal cells." *Pacific Rim Meeting on Electrochemical and Solid State Science (PRiME) 2012.* October 7th-12th, 2012, Honolulu, HI (USA).
3. "Study of the sintering of $Li_7La_2Zr_3O_{12}$ as an electrolyte for Li metal cells." *Pacific Rim Meeting on Electrochemical and Solid State Science (PRiME) 2012.* October 7th-12th, 2012, Honolulu, HI (USA).
4. "Aluminum Migration During Deposition of $Li_7La_2Zr_3O_{12}$ Thin Films on Aluminum Oxide Substrates." *223rd Electrochemical Society Meeting,* May 12th-16th, 2013, Toronto (Canada).
5. J. H. Park, W.-S. Hong, J. S. Park, L. Cheng, J. Cabana, G. Chen, M. M. Doeff, Y. Li, T. J. Richardson and J.-W. Son, *ECS Trans.*, **53**, 1 (2013).
6. I. Gurevitch, R. Buonsanti, A. A. Teran, B. Gludovatz, R. O. Ritchie, J. Cabana and N. P. Balsara, *J. Electrochem. Soc.*, **160**, A1611 (2013).
7. L. Cheng, J. S. Park, H. Hou, V. Zorba, G. Chen, T. J. Richardson, J. Cabana, R. Russo and M. M. Doeff, *J. Mater. Chem. A*, In press.
8. A. Hubaud, B, Ingram, B. Key, D. Schroeder, J. Vaughey, "Role of Al Substitution in Stabilizing the Structure of the Solid Lithium-Ion Conductor $Li_{7-x}Al_xLa_3Zr_2O_{12}$," *J. Mat Chem. A*, **1**, 8813 (2013).
9. D. J. Schroeder, A. A. Hubaud, J. T. Vaughey, "Stability of the Solid Electrolyte Li_3OBr in Non-Aqueous Solvents," *Mat. Res. Bulletin,* in press.
10. "Understanding the Formation of Solid Lithium-Ion Conductors," *Beyond Lithium VI*, June 2013, Boulder, Colorado.
11. "Protection of a Lithium Metal Anode with a Conductive Solid Ceramic Electrolyte," *Beyond Lithium VI*, June 2013, Boulder, Colorado.
12. "Protection of a Lithium Metal Anode with a Conductive Solid Ceramic Electrolyte*," 6th International Conference on Advanced Lithium Batteries for Automobile Applications*, September 2013, Argonne, IL.

VI.G.4 Integrated Lab-Industry Research Project (LBNL, ANL, FMC, Saft)

Gao Liu, Vince Battaglia and Venkat Srinivasan
Lawrence Berkeley National Laboratory

Environmental Energy Technologies Division
1 Cyclotron Road, MS 70R108B
Berkeley, CA 94720
Phone: (510) 486-7207; Fax: (510) 486-7303
E-mail: gliu@lbl.gov; vsbattaglia@lbl.gov; vsrinivasan@lbl.gov

Zhengcheng Zhang and Khalil Amine
Argonne National Laboratory
Chemical Sciences and Engineering Division
9700 S. Cass Avenue, Building 205
Argonne, IL 60439-4837
Phone: (630) 252-7868; Fax: (630) 972-4440
E-mail: zzhang@anl.gov,amine@anl.gov

Marina Yakovleva
FMC Corporation
Lithium Division
2801 Yorkmont Road, Suite 300
Charlotte, NC 28208
Phone: (704) 426-5391; Fax: (704) 426-5387
E-mail: marina.yakovleva@fmc.com

Bridget Deveney
Saft America, Inc.
Space and Defense Division – U.S.
107 Beaver Court
Cockeysville, MD 21030
Phone (410) 568-6415; Fax (410) 771-0234
E-mail: bridget.deveney@saftbatteries.com

Start Date: October 2010
Projected End Date: September 2013

Objectives

- Apply Stabilized Lithium Metal Powder (SLMP) in lithium ion batteries to achieve lower cost and high energy density.
  - Reduce the high cost associated with formation process.
  - Improve the cycle life of the high energy density lithium ion battery for electrify vehicles (EVs).

Technical Barriers

This project addresses the following technical barriers from the Energy Storage section of the Vehicle Technologies Program Multi-year Research, Development and Demonstration Plan:

- Performance: High first-cycle irreversible capacity loss (ICL), low coulombic efficiency, and poor cycle life.
- Life: Poor calendar life.
- Cost: High manufacture cost.

Technical Targets

- DOE/USABC goals (EV): \$150/KWh, 230 Wh/dm^3, 1,000 cycles with 80% capacity retention, and 10-year system life.
- DOE/USABC goals (PHEV, 40-miles): \$220/KWh, 193 Wh/dm^3, 5,000 discharge cycles, and 15-year system life.

Accomplishments

- Enabled the application of SLMP to lithium ion battery electrode during the slurry making process by developing SLMP-compatible solvents and polymer binders.
- Developed new process to activate the SLMP particles in the negative electrodes.
- Investigated the impact of the SEI layer formed by the incorporated SLMP and the cell cycling performance with the new SLMP incorporation and activation process.

✧ ✧ ✧ ✧ ✧

Introduction

To meet the requirement for applications in EVs and plug-in hybrid electric vehicles (PHEV), it is desirable to develop high energy density and low cost materials. With current Li-ion technology, the lithium source in the cell is limited to that from the cathode material, e.g., $LiCoO_2$, and electrolyte. Solid-Electrolyte Interphase (SEI) formation on the surface of the anode during the initial cycles consumes lithium and results in partial capacity loss irreversibly. The incorporation of Stabilized Lithium Metal Powder (SLMP), developed by FMC Corporation, into graphite has been suggested to help overcome the ICL, and increase the capacity by 5~10% in lithium-ion cells. A recent study on

prelithiation of silicone-carbon nanotube (Si-CNT) anodes in lithium-ion batteries by using SLMP showed that the 20-40% first cycle ICL could be eliminated. This implies that anode materials inside commercial lithium ion cells can be chosen from other promising anode materials such as Si and Sn, which have very high capacity but large first cycle ICL and thus cannot be used in current lithium-ion batteries. Moreover, some non-lithiated materials with high specific capacities such as Reduced Graphene Oxide/Fe_2O_3 composite and V_6O_{13} can be used as cathode materials if coupled with pre-lithiated anodes. Using this prelithiation strategy, the full cell energy density can be significantly improved and meet requirements for EV batteries in the future.

There is a trend in the battery and ultracapacitor industry of experimenting with SLMP® to address ICL and other issues. However, these efforts are not coordinated and lack a focus on fundamental understanding of the SLMP material properties, and their impact on long-term performance. ILIRP is aimed to solve the fundamental issues in order to apply SLMP in the lithium-ion battery. The success of this material will have a broad impact to the lithium-ion industry.

SLMP is an air stable surface-coated lithium metal powder material manufactured by FMC-Lithium (Figure VI - 239). The product consists of spheres of lithium metal with an average particle diameter of 40-50 µm with a coating consisting primarily of a 100 nm layer of Li_2CO_3. The lithium metal content is over 98% by weight. Initially developed as an easy-to-handle reducing agent for synthetic organic chemists, FMC-Lithium has also explored potential applications of SLMP as a lithium source in primary and secondary lithium-ion batteries. Initial work has demonstrated its utility as an additive in the battery manufacturing process.

LBNL and ANL are teaming with FMC-Lithium and lithium battery manufacturer Saft America to work on problems that impede or prevent the SLMP from being used as a performance enhancing additive in the negative electrode in commercial lithium ion batteries. This effort will lead to commercialization of batteries with lower ICL (leading to higher energy densities) and allow for a wider range of cathode materials to be utilized for transportation applications.

Approach

Three issues have been identified that limit SLMP's widespread acceptance with battery manufacturers: (1) chemical incompatibility between the SLMP and common solvents used to formulate electrode slurries; (2) lack of practical activation of SLMP; and (3) unknown long-term stability of the direct SEI formation by SLMP. With these identified limitations, SLMP has achieved only limited marketplace penetration.

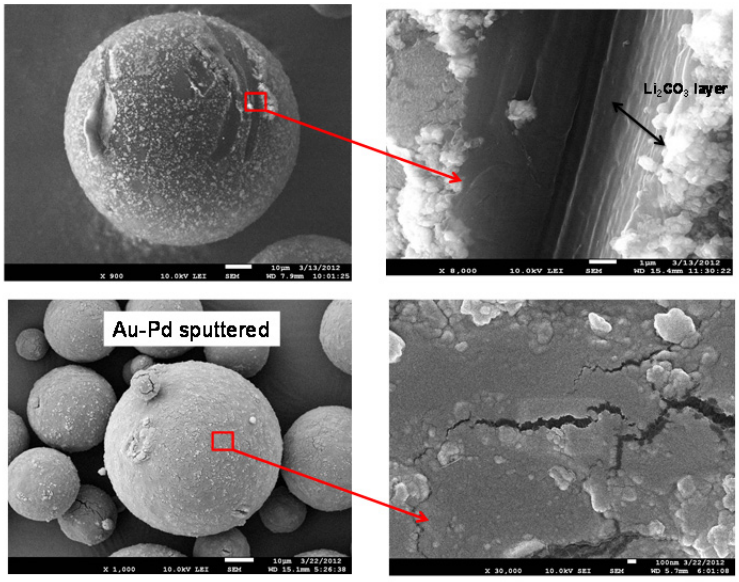

Surface scratches and cracks were observed on the pristine and the sputtered SLMP-Li_2CO_3 particles with 20nm Au/Pd coating: intrinsic surface morphology or due to Au/Pd surface tension.

Figure VI - 239: Particle morphology of pristine SLMP (top) and Au-Pd surface sputtered SLMP (bottom) analyzed by SEM

In this project, corresponding approaches were developed jointly at LBNL and ANL. The first issue is the chemical incompatibility between the SLMP and conventional slurry-making solvent NMP. To increase acceptance, new solvents, new polymer binders and new solvent/binder compositions that are chemically stable towards SLMP have been synthesized and evaluated. The second issue is related to the activation of SLMP in

the electrode. The Li_2CO_3 coating on SLMP is very robust and the activation to expose the active lithium metal is typically done using compression to physically break the coating. The coating chemistry and the effect of compression on the SLMP particles have been investigated. New activation processes are being developed and investigated. The third issue is that SLMP can be used as an additive in the negative electrode to accelerate the formation of the SEI. The long-term stability of the direct SEI formation by SLMP is not well understood and is therefore investigated here.

Results

New solvent/binder combinations for SLMP. A large number of solvent/polymer combinations and their reactivity with SLMP were investigated. A variety of organic solvents were selected and their chemical reactivity with SLMP was evaluated by the amount of the remaining active lithium after long term mixing. The stable solvents were chosen for the polymer solubility test. The first feasible combination is toluene/SBR and the process of incorporation and activation of SLMP is illustrated in Figure VI - 240.

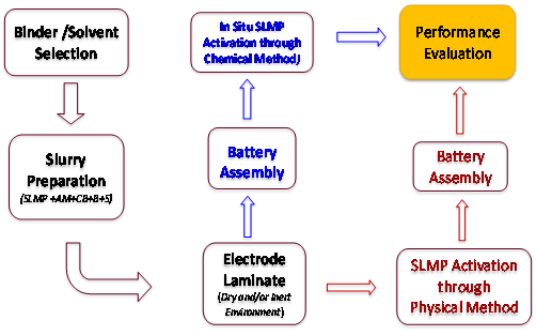

Figure VI - 240: Flow chart of application of SLMP to electrode including incorporation and activation of SLMP particle through electrode slurry-making process

SBR/toluene as a binder solution mixed with SLMP and graphite powder can form a uniform slurry, and can be coated into uniform electrode laminate. However, SBR covered graphite particles tend to have degraded rate performance compared to the PVDF based electrode. To solve the lithium-ion transport issue at the binder particle interface, a thin layer of PVDF or cross-linked PEO (1-2% by weigh) is coated on the surface of graphite to improve the electrolyte transport. This has led to significantly enhanced rate and cycling performance of the SBR/toluene processed SBR/graphite electrode, as shown in Figure VI - 241.

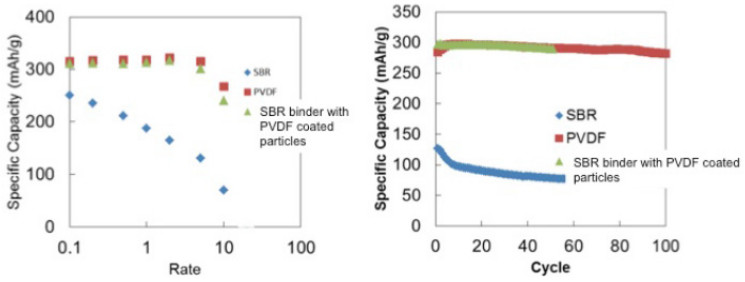

Figure VI - 241: C-rate (left) and cycling performance (right) for the Li/graphite cell using SBR/toluene combination when the graphite is coated with 2% of PVDF

Another new polymer binder poly(phenylene oxide) (PPO) suitable with SLMP and a solvent (dichlorobenzene) (DCB), compatible with both SLMP and the binder have been developed. A graphite anode was fabricated using the solvent of dichlorobenzene and with the binder poly(phenylene oxide). In the screening test, DCB showed the highest chemical stability towards SLMP among all the selected solvents (cyclohexylbenzene, anisole, DCB, chlorobenzene, DMSO). A mixture of MCMB (84 wt%), carbon black (4 wt%), PPO (5-10 wt%) dissolved in DCB and SLMP (2 wt%) were added to a container inside an argon-filled glovebox, an appropriate amount of dichlorobenezene was added to adjust the viscosity of the slurry. The slurry was coated onto a copper foil using a Dr. Blade coater, and dried in the oven at 75°C for 0.5 hour to 3 hours, then further dried in vacuum oven under dynamic vacuum for overnight. The electrode was activated by conventional compression method and high first cycle coulombic efficiency (99.1%) and cycling stability was achieved as shown in Figure VI - 242.

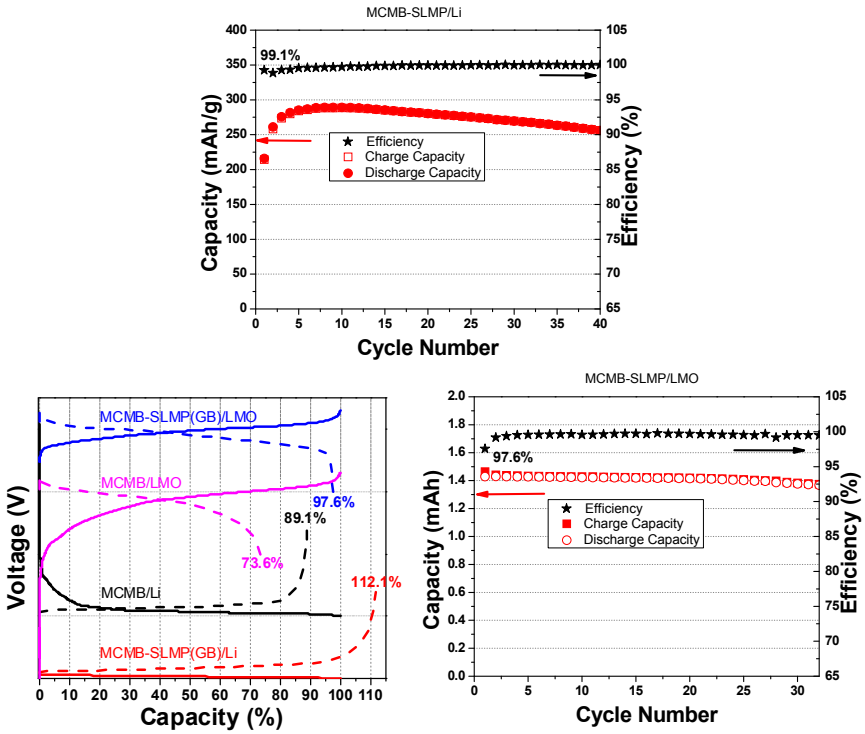

Figure VI - 242: Li/MCMB-SLMP half-cell cycling data (top) and $LiMn_2O_4$/MCMB-SLMP full cell voltage profiles (left, bottom) and capacity retention and coulombic efficiency (right, bottom)

Demonstration of the activation of SLMP in the electrode laminate. A compression method to activate the SLMP has been demonstrated in previous research. When the electrode went through a compression/calendaring process, the SLMP particles were broken to expose lithium metal, which made intimate contact with the graphite particles. In the past year, a new activation method was developed by thermal treatment and its activation mechanism is illustrated in Figure VI - 243. The aforementioned activated laminates were cut into certain size suitable as anode. The anode electrodes were then placed in an appropriate heating source to heat at 180-200°C for 10-30 minutes to activate the lithium inside the SLMP.

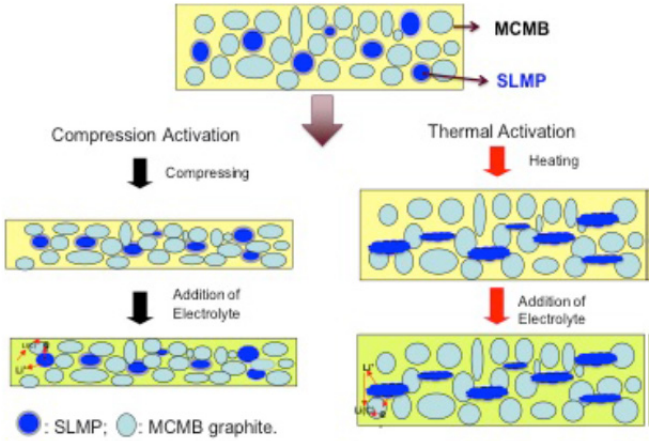

Figure VI - 243: MCMB-SLMP electrode activated by compression method and new thermal treatment method

After the SLMP was activated through the thermal treatment method, the anode electrodes were used to assemble the half-cell and the full cell. Upon addition of Gen 2 electrolyte (1.2 M $LiPF_6$ in EC/EMC (3/7), the graphite anodes will be lithiated *in situ* by the activated SLMP. An illustration of the mechanism of lithiation

process is shown in Figure VI - 243. An MCMB-SLMP electrode was thermally treated and assembled into a coin cell battery with LMO cathode and Gen 2 electrolyte. The charge discharge profiles of these batteries indicated that first cycle ICL could be greatly reduced as shown in Figure VI - 244. When heated to 180-190°C, the surface coatings were broken and the active lithium was released. When the electrolyte was added, the prelithiation occurred without electrically charging the electrode. The cycle performance of MCMB-SLMP/LMO cell is shown in Figure VI - 244, indicating that the thermal-activation is as effective as the conventional compression activation method.

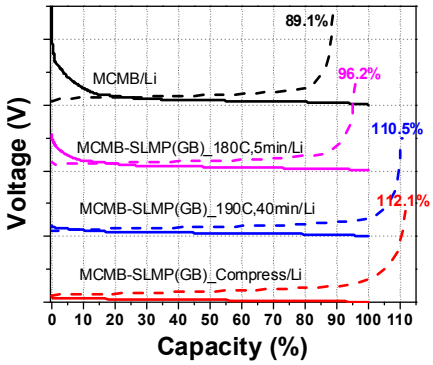

Figure VI - 244: The first voltage profiles of half-cells using MCMB-SLMP (2%) electrodes activated by thermal treatment at 180°C and 190°C

Electrode performance improvement. The first cycle voltage profiles of the two graphite-SLMP/Li cells starting with C/3 cycle rate are shown in Figure VI - 245A. First, the plateau at 0.6-0.7V is absent; suggesting development of SEI is already completed by the SLMP during the rest period. The first cycle coulombic efficiency of this cell is about 100%, showing that 1.2% of SLMP is enough to provide a full compensation to the capacity loss in this system, and therefore its charge capacity was not sacrificed. For the first regular cell without SLMP (no formation), its first discharge and charge capacities at C/3 current rate only reach 297 and 276 mAh/g, respectively (Figure VI - 245A), but the coloumbic efficiency does not vary much (about 93%). Cycle performance and Coulombic efficiency of these two cells as well as one graphite/Li cell after formation are compared and results are shown in Figure VI - 245B. Specific capacity of the cell without SLMP and without formation reaches only around 280 mAh/g, while both the cell with SLMP and the one without SLMP but with formation process reach capacity of around 320 mAh/g when the cells cycling capacities are stabilized (Figure VI - 245B). The cell with SLMP has an even better cycle performance than the cell without SLMP but with formation (Figure VI - 245B), indicating SEI formed in the cell with SLMP is as effective as, or better than that formed in the regular cell during low current (e.g., C/25 or C/10) formation process. The coulombic efficiencies of all three cells are comparable. These results confirm the effective prelithiation of anode by SLMP, and SLMP induced SEI formation on graphite electrode surface.

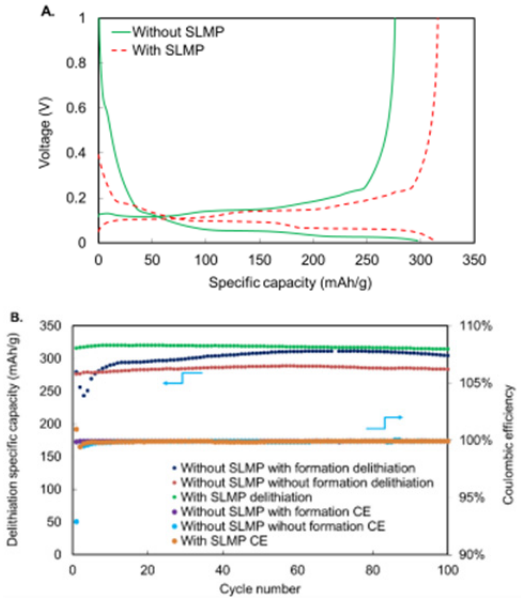

Figure VI - 245: (A) The first cycle voltage profiles for graphite half-cells with 1.2% wt SLMP (red line) and without SLMP (green line) at C/3 rate. The cell with SLMP was rested under open circuit for four days before cycling and the cell without SLMP was cycled at C/3 after assembling; (B) The cycle performance and coulombic efficiency for graphite half-cells with (green symbols) and without SLMP (blue and red symbols) at C/3 rate. The cell without SLMP with formation (blue symbols) was cycled at C/25 for two cycles, followed by C/10 for five cycles, then cycled at C/3 rate. The cell without SLMP without formation (red symbols) was cycled at C/3

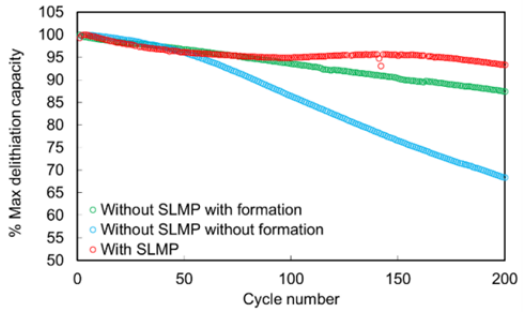

Figure VI - 246: Cycle performance for graphite/NMC full cells with (red symbols) and without SLMP (green and blue symbols) at C/3 rate. The cell with SLMP was rested at open circuit for four days before cycling. The cell without SLMP with formation (green symbols) was cycled at C/25 for five cycles, followed by C/10 for ten cycles, then cycled at C/3 rate. The cell without SLMP without formation (blue symbols) was cycled at C/3 after assembling

Cycle performance for the first 200 cycles of the graphite/NMC cells are shown in Figure VI - 246. As expected, the cell without SLMP and without formation decays the fastest, most likely due to the poor quality of formed SEI. After 200 cycles, the capacity decays to only 68.2% of its initial value. Meanwhile, capacity retention of the cell with SLMP and the one without SLMP but with formation was 93.2% and 87.3%, respectively. Among these three cells, SLMP-contained cell displays the highest capacity retention upon cycling. These results indicate that SEI formation in the SLMP prelithiated cell occurred during its resting time and the quality of the developed SEI is the same or even better than that developed in the regular cell upon low current formation.

This study, therefore, has provided direct evidence that SLMP can effectively help SEI formation. Particularly, after the cell with SLMP prelithiated anode is assembled, it could be rested at open circuit and the SEI formation occurred spontaneously. It is possible to skip the external current driven formation process to reduce lithium battery manufacturing cost by applying this strategy.

Conclusions and Future Directions

In this project, corresponding approaches were developed jointly at LBNL and ANL to address the technical barriers of application of SLMP to the battery industry. New polymer binders and new compatible solvents were developed to enable the incorporation of SLMP through the slurry-making process. A new activation method has developed and the long-term effect of the SEI formed by the SLMP was thoroughly studied. Future research will focus on the validation of new materials in the large format lithium ion battery.

FY 2013 Publications/Presentations

1. Jung-Je Woo, Zhengcheng Zhang, and Khalil Amine, "Separator/Electrode Assembly for Safe Lithium-ion Battery," *Adv. Energ. Mater.*, (2013), in press.
2. Jung-Je Woo, Zhengcheng Zhang, Nancy L. Dietz Rago, Wenquan Lu and Khalil Amine, "A high performance separator with improved thermal stability for Li-ion batteries," *J. Mater. Chem. A*, **1**, 8538-8540, (2013).
3. Z. Xue, Z. Zhang, L. Hu, K. Amine, "Polysiloxane-epoxide as cross-linkable binders for lithium-ion Batteries," *J. Electrochem. Soc*., **160**(10), A1819-A1823, **(2013)**.
4. Z. Xue, Z. Zhang, K. Amine, "Cross-linkable urethane acrylate oligomers as binders for lithium-ion battery," *Electrochem. Commun.,* **34**, 86-89, (2013).
5. Xiang, B.; Wang, L.; Liu, G.; Minor, A. M., "Electromechanical Probing of Li/Li2CO3 Core/Shell Particles in a TEM," *J. Electrochem. Soc.,* **160** (3), A415-A419, (2013).
6. Wu, M.; Xiao, X.; Vukmirovic, N.; Xun, S.; Das, P. K.; Song, X.; Olalde-Velasco, P.; Wang, D.; Weber, A. Z.; Wang, L.-W.; Battaglia, V. S.; Yang, W.; Liu, G., "Toward an Ideal Polymer Binder Design for High-Capacity Battery Anodes," *J. Am. Chem. Soc.*, **135** (32), 12048-12056, (2013).
7. Wang, L.; Fu, Y.; Battaglia, V. S.; Liu, G., "SBR-PVDF based binder for the application of SLMP in graphite anodes," *Rsc Advances*, **3** (35), 15022-15027, (2013).
8. Chong, J.; Xun, S.; Song, X.; Liu, G.; Battaglia, V. S., "Surface stabilized $LiNi_{0.5}Mn_{1.5}O_4$ cathode materials with high-rate capability and long cycle life for lithium ion batteries," *Nano Energy,* **2** (2), 283-293, (2013).
9. Jung-Je Woo, Zhengcheng Zhang, Nancy L. Dietz Rago, Wenquan Lu and Khalil Amine, "A thermally stable separator for improved safety and cycle life of lithium ion batteries," *6th International Conference on Advanced Lithium Batteries for Automobile Applications*, Sep. 9-11, 2013, Argonne National Laboratory, Lemont, IL.
10. Z. Xue, Z. Zhang,* L. Hu, K. Amine, "Cross-linkable urethane acrylate oligomers as binders for lithium-ion battery," *6th International Conference on Advanced Lithium Batteries for Automobile Applications*, Sept. 9-11, 2013, Argonne National Laboratory, Lemont, IL.
11. Shengwen Yuan, Zhengcheng Zhang, Khalil Amine, "Application of SLMP in Lithium ion battery," *DOE Integrated Laboratory and Industry Research Program Review Meeting*, July 16, 2013, Berkeley, CA.
12. Shengwen Yuan, Zhengcheng Zhang, Khalil Amine, "Application of SLMP in Lithium ion battery," Meeting with FMC, Sep. 10, 2013, Argonne National Laboratory, Lemont, IL.
13. Lei Wang, Vincent S. Battaglia, and Gao Liu, "Prelithiated Graphite Anode SEI Formation by Stabilized Lithium Metal Powder in Li-Ion Batteries," Abstract 1010*, 222nd meeting of The Electrochemical Society, PRiME*, Oct 7-11, 2012, Honolulu HI.
14. Zhihui Wang, Lei Wang, Vince Battaglia, Gao Liu, "Applications of Stabilized Lithium Metal Powder (SLMP) in Lithium-ion Batteries," *2013 MRS Spring Meeting*, Apr. 3, 2013, San Francisco, CA.

15. Zhihui Wang, Vince Battaglia1, Gao Liu, Marina Yakovleva, "Applications of Stabilized Lithium Metal Powder (SLMP®) in Lithium-ion Batteries," *2013 The 6th International Conference on Advanced Lithium Batteries for Automobile Applications (ABAA6)*, Sep 9-11, 2013, Argonne National Laboratory, Lemont, IL.
16. Gao Liu, Vince Battaglia, and Lei Wang, Lithium Metal Doped Electrodes for Lithium-ion Rechargeable Chemistry, WO/2013/052916, International applications No. PCT/US2012/059127.
17. Zhengcheng Zhang, Shengwen Yuan, Khalil Amine, Electroactive compositions with poly(arylene oxide) and stabilized lithium metal particles, ANL-IN-12-027.

VI.G.5 Developing Materials for Lithium-Sulfur Batteries (ORNL)

Chengdu Liang
Oak Ridge National Laboratory

Center for Nanophase Materials Sciences
Building 8610 MS 6493
Oak Ridge, TN 37831-6493
Phone: (865) 456-9185; Fax: (865) 574-1753
E-mail: liangcn@ornl.gov

Collaborators:
Nancy J. Dudney (ORNL)

Start Date: June 2010
Projected End Date: September 2014

Objectives

- Overcome the technical hurdles for the longevity of lithium-sulfur (Li-S) batteries through innovative design of solid-state battery configuration.
- Identify key problems for cycling solid state Li-S batteries.
- Develop enabling materials for solid-state Li-S batteries.

Technical Barriers

Among known battery chemistries, lithium-sulfur (Li-S) holds the greatest promise for high-energy batteries. However, the development of Li-S batteries has been impeded by the intrinsically low electronic and ionic conductivities of the sulfur cathode and the poor cyclability of the metallic lithium anode. To enable the cycling of the sulfur cathode in a conventional Li-S battery, a liquid electrolyte that has a high solubility of polysulfides is required in order to overcome the poor ionic conductivities of the solid sulfur species. As a result of the dissolution of polysulfides in the liquid electrolyte, the diffusion of polysulfides from the cathode to the anode during battery cycling leads to intrinsically short cycle-life. In addition to the problems with the sulfur cathode, the dendritic growth of lithium metal in liquid electrolytes and the ever growing solid electrolyte interphase on the anode surface shorten the cycle life of Li-S batteries and also cause safety concerns.

Technical Targets

- Derive the relationship of ionic conductivity of Li-S cathode materials with their electrochemical cyclability.
- Achieve long-term cyclability of Li-S batteries without polysulfide shuttle.

Accomplishments

- Developed solid-state Li-S batteries through a simple cold pressing procedure.
- Unraveled the relationship of ionic conductivity of cathode material with their cycling conditions
- Developed composite electrolytes for achieving high conductivity.
- Explored the possibility of using air-stable sulfide-based solid electrolytes for Li-S batteries.

✧ ✧ ✧ ✧ ✧

Introduction

The electrification of vehicle transportation requires electrical energy storage technologies that have high energy density, low cost, and enhanced safety. The Li-S battery, which uses elemental sulfur as the cathode material, is expected to meet the needs for electric vehicles (EV). However, conventional Li-S batteries have a short cycle-life because of the intrinsic polysulfide shuttle phenomenon. The use of a liquid electrolyte inside the electrochemical cell enables the polysulfide shuttle. ORNL proposed to develop solid-state Li-S batteries that completely eliminate the polysulfide shuttle phenomenon. The solid electrolytes do not dissolve the polysulfide formed during discharge of Li-S batteries. Therefore, solid-state Li-S batteries exclude the migration of sulfur species that is caused by the polysulfide shuttle mechanism. In addition to the prevention of polysulfide migration, the solid electrolyte addresses the challenges of cycling the metallic lithium anode. Solid-state Li-S batteries are expected to have long cycle-life.

Although solid-state Li-S batteries are an enticing solution to the growing demand for inherently safe and higher capacity energy storage devices, there are still hurdles for the deployment of solid-state Li-S batteries. Selecting a suitable solid state electrolyte is critical to

the success of solid-state batteries. Few solid electrolyte materials are available for battery applications, and none of them satisfies all desirable characteristics. While some electrolytes have high Li-ion conductivity at room temperature, they lack the chemical and electrochemical stability to be practical in real-world devices. Where stability is present, conductivity is not as high, or material processing is difficult. Besides the challenges of solid electrolytes, the extremely low ionic conductivity of sulfur and its discharge products precludes the direct cycling of solid-state sulfur. Facilitation of ionic transport at the electrode and across the solid electrolyte is of paramount importance to enabling the function of solid-state Li-S batteries.

Approach

ORNL is working on the development of solid-state Li-S batteries to completely eliminate the polysulfide shuttle. A sulfide-based solid electrolyte has been used to achieve compatibility with the cathode and anode. Stoichiometric lithium thiophosphate (Li_3PS_4) is known for its excellent stability with metallic lithium among all sulfide-based solid electrolytes. The high conductivity beta phase has been stabilized through nanostructures. Using β-Li_3PS_4 as the platform, ORNL developed a series of solid-state Li-S batteries. In FY13, a core-shell nanostructure of $Li_2S@Li_3PS_4$ was developed as a cathode material. A comparison of this new material with the lithium polysulfidophosphate (LPSP) developed during FY12 illustrated the positive correlation of ionic conductivity of the cathode materials with their electrochemical cyclability. The research validated that these solid-state Li-S batteries completely blocked the polysulfide shuttle. Long term cyclability has been achieved. To enable the solid-state Li-S battery for EVs, further research efforts have been focused on the following directions: (1) improve the ionic conductivity of the solid electrolyte to achieve high power; (2) enhance the mechanical strength and flexibility of the solid electrolyte membrane by forming polymer-ceramic composites through addition of a polymer mesh in the membrane; and (3) explore cost reductions through use of air-stable solid electrolytes.

Results

Relationship of ionic conductivity of the cathode materials and their electrochemical performance. In the previous fiscal year, the lithium polysulfidophosphate (LPSP) was developed as an excellent cathode material for solid-state Li-S batteries. A salient characteristic of LPSP is its high conduction of lithium ions. A basic question regarding this new material is how the ionic conductivity affects the electrochemical cycling performance of the cathode material. To this end, two additional new materials were developed to investigate the effect of ionic conductivity of the sulfur cathode on cycling performance: nanoparticles of Li_2S and core-shell structured $Li_2S@Li_3PS_4$. Among these three samples, the LPSP showed the best cycling performance with a stable capacity over 100 cycles and showed no sign of degradation after 100 cycles. Both the Li_2S nanoparticles and the core-shell structured $Li_2S@Li_3PS_4$ samples had significant capacity decay after 100 cycles. The $Li_2S@Li_3PS_4$ cathode retained a capacity of 581 mAh/g while the Li_2S nanoparticles retained a capacity of 381 mAh/g. The room temperature ionic conductivity of these materials followed the same trend as their cyclability: LPSP (8.2×10^{-5} S/cm) > $Li_2S@Li_3PS_4$ (4.5×10^{-6} S/cm) > Li_2S nanoparticles (2.1×10^{-11} S/cm). It is obvious that the ionic conductivity has a positive correlation with the electrochemical cycling performance of the cathode. The charge capacities of all samples are equal to or less than the discharge capacity. Therefore, the solid-state batteries do not have problem associated with the polysulfide shuttle, which causes the charge capacity to be much higher than the discharge capacity.

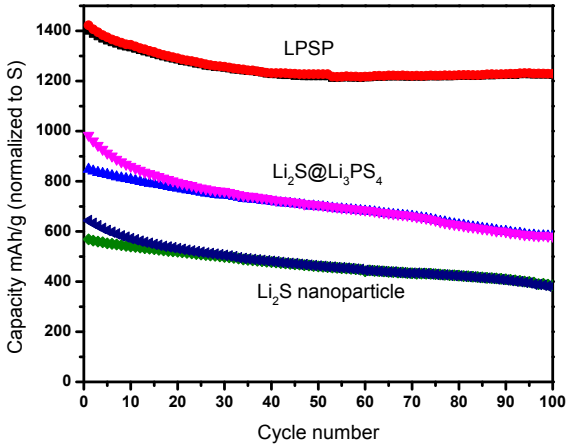

Figure VI - 247: Comparison of cycling performance of LPSP, $Li_2S@Li_3PS_4$ and Li_2S nanoparticles

Composite of oxide and sulfide electrolytes for high conduction of lithium ions. Lithium thiophosphate (Li_3PS_4) was used in our previous development because it meets the basic requirements of good compatibility with both the metallic lithium anode and the sulfur cathode. However, the ionic conductivity of Li_3PS_4 is only 2.0×10^{-4} S/cm at room temperature. To improve the ionic conductivity of solid electrolytes for Li-S batteries, lithium lanthanum zirconium oxide $Li_7La_3Zr_2O_{12}$ (LLZO), a garnet structure, has been used as a filler with Li_3PS_4 to enhance the ionic conductivity and mechanical and chemical properties of the solid electrolyte. It is known that LLZO has good ionic conductivity (>10^{-4} S/ cm) with excellent

electrochemical stability and mechanical properties. However, it has a high interfacial resistance with metallic lithium. LLZO is difficult to press at room temperature. Compression at 1100°C is needed to get a solid electrolyte membrane. In stark contrast to LLZO, Li_3PS_4 is a much softer material that can be cold pressed. In addition, Li_3PS_4 has a very low interfacial resistance with metallic lithium. From the aforementioned properties, it can be observed that the LLZO and Li_3PS_4 are complementary to each other, making them interesting candidates for a composite electrolyte material.

Mechanical mixing of LLZO and Li_3PS_4 was done under mild ball-milling conditions. Shown in Figure VI - 248 are the trends of ionic conductivity and activation energy as a function of weight fraction of LLZO in the composites. The maximum Li-ion conductivity for the nanocrystalline Li_3PS_4 composites was observed at the 30:70 (LLZO:Li_3PS_4) composition as 9.12 $\times 10^{-4}$ S/cm, which is greater than the parent Li_3PS_4 electrolyte. There were no chemical reactions between LLZO and Li_3PS_4. Therefore the enhanced conductivity is attributed to the interfacial conduction.

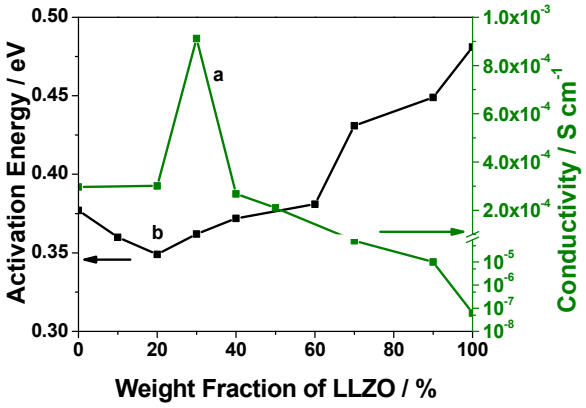

Figure VI - 248: Ionic conductivity (right y-axis) and activation energy (left y-axis) as a function of the weight fraction of LLZO

Polymer mesh enhanced solid-electrolyte membranes. One of the key impediments for the use of a fragile ceramic membrane in a mobile battery is its poor mechanical strength. To overcome this problem, a polypropylene (PP) mesh has been used to enhance the mechanical strength and impart flexibility to the solid electrolyte membrane. The PP is 100 microns thick with 90% open porosity. Taking advantage of the ductility of the β-Li_3PS_4, a composite of PP mesh and solid electrolyte membrane was prepared by dry-pressing the powder and the mesh together at room temperature. Figure VI - 249 shows photos of the PP mesh (left) and the mesh enhanced membrane (right). The composite membrane is intact and flexible.

Figure VI - 249: Photos of polymer mesh (left) and mesh enhanced β-Li_3PS_4 membrane (right). The thickness of the membrane is 100 µm

Development of high-conductivity air-stable sulfide-based solid electrolytes for Li-S batteries. Although lithium thiophosphate (Li_3PS_4) meets the basic requirements of all-solid-state Li-S batteries, the hypersensitivity of Li_3PS_4 to air and moisture requires sophisticated handling under a dry inert gas atmosphere, which increases the processing cost. A new series of arsenic-doped lithium tin sulfide solid electrolytes have been developed to replace Li_3PS_4. Figure VI - 250 shows the effect of arsenic doping on the ionic conductivity. The highest conductivity achieved is 1.39×10^{-3} Scm^{-1} at 25°C with the composition $Li_{3.833}Sn_{0.833}As_{0.166}S_4$. Considering Li^+ as the only mobile species in the solid electrolyte, the conduction of Li^+ in the solide electrolyte is comparable to that of current carbonate-based liquid electrolytes. It is worth noting that the activation energy versus the concentration of As substitution shows an inverse relationship to the conductivity (Figure VI - 251). The lowest activation energy (0.21 eV) was observed in the composition that had the highest ionic conductivity ($Li_{3.833}Sn_{0.833}As_{0.166}S_4$). Such low activation energy ensures a flat conductivity curve in a broad temperature range.

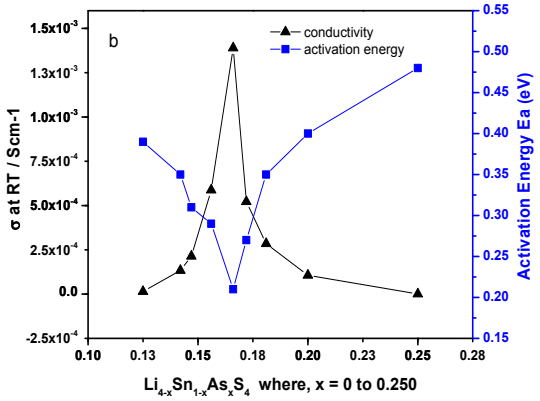

Figure VI - 250: Ionic conductivity (right y-axis) and activation energy (left y-axis) as a function of As concentration doped in Li_4SnS_4

An important goal of this research is to achieve air stability of sulfide-based solid electrolytes. To test the air stability, a representative sample of $Li_{3.833}Sn_{0.833}As_{0.166}S_4$ was shaken in ambient air for over

48 h. For comparison purposes, a sample of β-Li_3PS_4 was synthesized and shaken in ambient air at identical conditions. The ionic conductivities of the pristine and air-exposed samples were measured by ac impedance. Figure VI - 251 presents the temperature dependencies of the conductivity of $Li_{3.833}Sn_{0.833}As_{0.166}S_4$ and β-Li_3PS_4 before and after exposure to air. The room-temperature ionic conductivities of $Li_{3.833}Sn_{0.833}As_{0.166}S_4$ before and after air exposure were 1.39×10^{-3} Scm^{-1} and 9.95×10^{-4} Scm^{-1}, respectively. There was only a very minor change in conductivity, which may be due to a very small amount of moisture uptake or to variance in sample preparation. In stark contrast to the stable $Li_{3.833}Sn_{0.833}As_{0.166}S_4$ phase, the β-Li_3PS_4 showed more than an order of magnitude drop in ionic conductivity after air exposure.

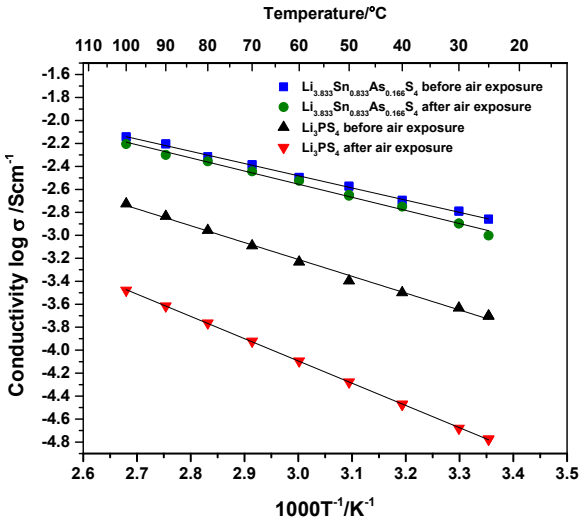

Figure VI - 251: Comparative Arrhenius plots for $Li_{3.833}Sn_{0.833}As_{0.166}S_4$ and β-Li_3PS_4 before and after air exposure

Conclusions and Future Directions

Solid-state Li-S batteries overcome the problems caused by the polysulfide shuttle. The ionic conductivity is crucial for the cycling performance of the cathode. In order to use ceramic membranes for mobile batteries, two problems must be overcome: the relatively low ionic conductivity and the fragility of the membrane. Sulfide-based solid electrolytes hold great promise for high conduction at room temperature. When LLZO is used as the filler for Li3PS4, the ionic conductivity is significantly improved. The mechanical properties of sulfide-based solid electrolytes can be improved using a polymer mesh as a scaffold. Air-stable high conduction sulfide-based electrolytes provide an avenue for processing the Li-S batteries in a dry-room. Air-stable battery components would significantly reduce the cost of material handling and battery assembly.

Future efforts will focus on the use of these newly developed solid electrolytes in the assembly of Li-S batteries and the complete evaluation of solid-state Li-S batteries.

FY 2013 Publications/Presentations

1. Z. Lin, Z. Liu, N. Dudney, and C. Liang "A Lithium Superionic Sulfide Cathode for All-Solid Lithium-Sulfur Batteries," ACS Nano, 2013 7, 2829-2833.
2. "High-Energy All-Solid Li-S Batteries," DOE-VTO Annual Merit Review and Peer Evaluation Meeting, Arlington, VA, May 2013.
3. "New Materials for All-Solid-State Lithium-Sulfur Batteries," Beyond Lithium-ion Symposium VI, Boulder, CO, June 6, 2013.
4. "Material Challenges for All-Solid Lithium-Sulfur Batteries," The 10th Pacific Rim Conference on Ceramic and Glass Technology including GOMD 2013, San Diego, CA, June 4, 2013.
5. "New Directions for Li-S Batteries," DOE BATT program Li-S focus group symposium, July 17, 2013
6. "Li-S cathode Materials," Energy Storage Solutions Industrial Symposium, Oak Ridge, TN, Sept. 4, 2013
7. "Li-ion Conducting Sulfur-Rich Compounds for All-Solid Lithium-Sulfur Batteries," 2013 Fall ECS meeting, San Francisco, CA, Oct 27, 2013
8. "Aliovalent Doping of Tetra Lithium Ortho-sulfidostannate Li4SnS4 as Air Stable Solid Electrolyte with High Ionic Conductivity," C. Liang, G. Sahu, and N. Dudney; (2013 invention disclosure)
9. "A High Conducting Oxide – Sulfide Composite Lithium Superionic Conductor," C. Liang, E. Rangasamy, J. K. Keum, A. J. Rondinone, N. J. Dudney; (2013 invention disclosure)

VI.G.6 Composite Electrolyte to Stabilize Metallic Lithium Anodes (ORNL)

Nancy Dudney
Oak Ridge National Laboratory

Material Science and Technology Division
PO Box 2008, MS 6124
Oak Ridge, TN 37831-6124
Phone: (865) 576-4874
E-mail: dudneynj@ornl.gov

Start Date: October 2011
Projected End Date: September 2016

Objectives

- Understand Li^+ transport at the interface between two dissimilar solid electrolytes, e.g. ceramic/polymer.
- Develop composites of electrolyte materials with the requisite electrochemical and mechanical properties as guided by simulation.
- Fabricate thin membranes and demonstrate stability upon cycling of a thin metallic lithium anode with good power performance and long cycle life.
- Identify design rules that can be generally applied to composites of other solid electrolyte materials.

Technical Barriers

Advanced lithium batteries, including Li-air and Li-S, require robust protection of the metallic lithium anode to maintain a mechanically and chemically stable lithium anode. Any reaction or roughening of the lithium will result in loss of capacity, degradation of performance and may also compromise safety. A robust solid electrolyte to protect the lithium while ensuring rapid cycling is the clear solution, yet fabricating such an electrolyte with the required ionic transport, electrochemical stability, and mechanical strength is a technical challenge. The electrolyte must be very thin and light, and cost effective for manufacturing. To provide a lithium anode with significantly higher energy density than current Li-ion anodes, all components of the anode including the packaging, current collector, protective electrolyte, and indeed the lithium itself, must be minimized.

Technical Targets

- Develop a solid electrolyte membrane that stabilizes the long-term, safe, and efficient cycling of lithium metal anodes to enable high energy density batteries.
- Provide an electrolyte protected anode to promote the equivalent electric range of 40 miles (PHEV) and 200-300 miles (EV).
- Enable battery anodes for very high energy Li-S Battery (500 Wh/kg) by 2020 and Li-Air Battery (700 Wh/kg) by 2030.

Accomplishments

- Results show that many polymer-ceramic interfaces have similar behavior, possibly related to PEO conformation. Even a small interface resistance will alter Li^+ path through a composite.
- Vapor deposited lithium contacts are generally less resistive than pressure contacts to lithium foil, but may cause premature failure of ceramic electrolytes.
- Simulation shows that formation of sintered necks between ceramic particles greatly enhances both conduction and stiffness of the dispersed particle electrolyte composites.
- Grain boundaries contribute only a small increase in resistance for dense sintered garnet electrolytes.
- When equilibrated, composites with ~50vol.% submicron ceramic powder demonstrate that Li^+ ion path accesses both ceramic and polymer phases. The thin 100-200μm membranes are pliable and robust.

✧ ✧ ✧ ✧ ✧

Introduction

This program is based on the observation that no single solid electrolyte, either polymer, ceramic, or glass, can currently meet all of the requirements for a stable interface with the active lithium anode. Many inorganic materials are not stable in contact with lithium metal and also suffer from being too brittle when thinned to a light weight membrane. Polymer electrolytes, even those with rigid block co-polymer structures, gradually roughen with lithium cycling and

are too resistive for room temperature operation. Formation of a composite polymer-ceramic structure offers a pragmatic approach to optimizing the electrolyte properties. Using the wealth of known solid electrolyte materials, this program is addressing the fabrication and testing of such composites, both experimentally and through simulation. A critical aspect of such a composite is the properties of the interface formed between two different electrolytes, which must offer mechanical integrity while not impeding the transport of lithium ions. Characterizing and modifying these interfaces is a primary focus of this program.

Approach

Material selection. Although new solid electrolytes are being reported, only well understood and relatively stable electrolytes are chosen from different classes of electrolyte materials for this study. The intent is to identify design rules that can later by applied to composites of alternative and perhaps more conductive electrolyte materials. Representative materials from different classes of electrolytes include: sputter deposited Lipon glass film; dry PEO polymer-based electrolytes having either LiTFSI or $LiCF_3SO_3$ salts; powders and sintered ceramic plates of Al-doped $Li_7La_3ZrO_{12}$ garnet (LLZO) from Prof. Sakamoto (Michigan State Univ.) and of phosphate electrolytes from Ohara and nGimat Corps.; and block co-polymer electrolytes from Prof. Balsara (UC Berkeley).

Preparation and electrochemical characterization of bi-layer interfaces. Following earlier work, bi-layer structures create a simple planar interface with which to characterize the resistance for lithium ion transport from one material to another. Bilayers include pairs of dissimilar solid electrolytes, principally ceramic and polymer couples, and also the interface formed with vapor deposited lithium films onto various solid electrolytes. Care is taken to prepare clean and adherent interfaces for these studies. A high-vacuum chamber is used for thermal evaporation of the lithium thin films directly onto clean electrolyte surfaces. Ceramic electrolyte pellets are carefully polished and dried. Only dry processing of the polymer electrolytes is used to eliminate all solvent effects. Electrochemical impedance spectroscopy (EIS) and DC transport are used to extract the impedance of the interface from the series summation of the individual components. An interfacial impedance that is significant in magnitude relative to the bulk resistance can be readily resolved. Results from these investigations provide the interface resistance used in simulations of the composite properties.

Simulation of ion transport and mechanical stability of composite structures. Codes were developed in our earlier work to predict both ion transport and also elastic modulus of various composite electrolyte structures including dispersed particle composites and ordered laminar structures. Comsol tools were developed to evaluate how variation in the interfacial resistivity alters the overall ionic conduction path and the uniformity of current through the composite electrolyte. In the current year, a new approach was developed for high volume loading of dispersed particles with varying extents of the contact area (necks) assumed between ceramic particles.

Fabrication and characterization of electrolyte composites for conduction and mechanical properties. Based on results of bilayer and simulation studies, selected materials are prepared as dispersed composites. Using EIS, ion transport measurements are compared against the simulations to evaluate the influence of the interfaces to block or direct the ionic current. Promising composite electrolytes are also prepared with metallic lithium contacts to evaluate the dc transport, transference number and electrochemical stability with Li. As work progresses, alternative fabrication methods and materials will be investigated to improve performance. This may require highly aligned or partially sintered network structures with high volume fractions of the hard ceramic phase.

Results

Studies of bi-layer electrolyte laminates and polycrystalline electrolytes. Results for interface impedance between a variety of polymer and ceramic electrolytes were compared. Many follow the Arrhenius temperature dependence; it is noteworthy that the activation energies are quite similar (see Table VI - 9), although the specific area resistance varies by orders of magnitude. This may reflect the conformation of the polymer at the interface.

Table VI - 9: Bilayer and activation energy of the interface resistance

Lipon\PMMA-EO_{10}:$LiClO_4$	106 kJ/mol
Lipon\PS-EO_{10}:$LiClO_4$	104 kJ/mol
LLZO\PEO_{10}:LiTFSI (laminated film)	95 kJ/mol
LLT\PEO_{20}:$LiCF_3SO_3$ (Abe,et.al, *J. Electrochem. S.* (2005)	96 kJ/mol

For the relatively conductive interfaces, it is harder to accurately extract the small resistance and its temperature dependence using EIS of the bilayer. More sensitive characterization methods will be developed as needed. Examples of these results, where the area specific resistance is only a few ohms, both positive and negative, are shown in Figure VI - 252.

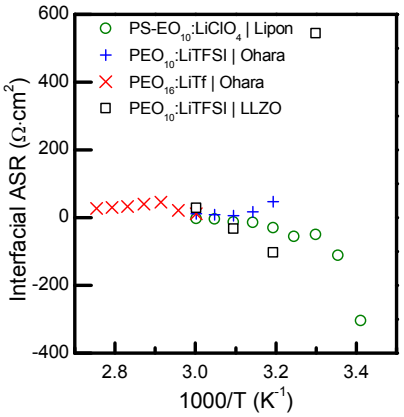

Figure VI - 252: Area specific resistance for the interface between polymer and inorganic electrolytes. Values were determined from impedance of the bilayer compared to individual components as a function of the temperature

Similarly, EIS approaches are used to characterize the interface resistance of vapor deposited Li onto various solid electrolytes. In general, this interface is less resistive than those formed by hot-pressing lithium foil against the solid electrolyte.

Simulation of dispersed particle composites. Our prior work demonstrated that a very high volume fraction (~60%) of dispersed ceramic particles is needed for mechanical stability and good ionic conduction, assuming a well adhered and conductive interface is formed between the phases. To accurately address the complex contacts between dispersed particles, we developed software and methods to simulate microstructures with varying extents of neck formation between the ceramic particles. The contact area (necks) is assumed to be perfectly adhered and conductive. Calculations were conducted with material properties typical for PEO-based electrolytes and a garnet ceramic electrolyte. Figure VI - 253 shows that a reasonably effective Li ion conductivity can be achieved even for a poorly conductive polymer electrolyte. The size of the necks between particles is a key variable. Similarly, the mechanical stability of a composite improves with necks at the particle contacts and the ceramic loading needed for a high bulk modulus is somewhat reduced. Because of these predictions, efforts are underway to develop a fabrication method that allows for partial sintering and percolation of the ceramic phase as a 3D network.

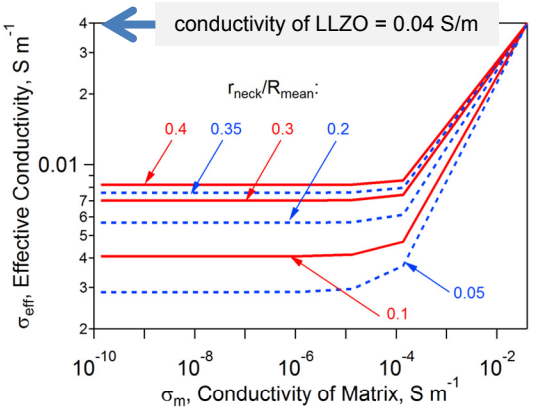

Figure VI - 253: Effective conductivity for 50 vol.% loading of randomly dispersed LLZO particles in a polymer matrix. Conductive necks are assumed to form at contacts between the ceramic particles

Grain boundary conductivity. The effect of grain boundaries on the ionic conductivity of garnet ceramic electrolytes was unknown, with conflicting reports appearing in the literature. This is important to resolve as grain boundaries likely form at sintered necks. Using very dense hot-pressed pellets from Prof. Sakamoto (Michigan State University), impedance analysis over an extended temperature and frequency window was used to carefully extract the grain boundary contribution, such as shown in Figure VI - 254. From this work, grain boundaries are expected to add only a small resistance at ambient temperatures to the composites if the boundary is pure and dense.

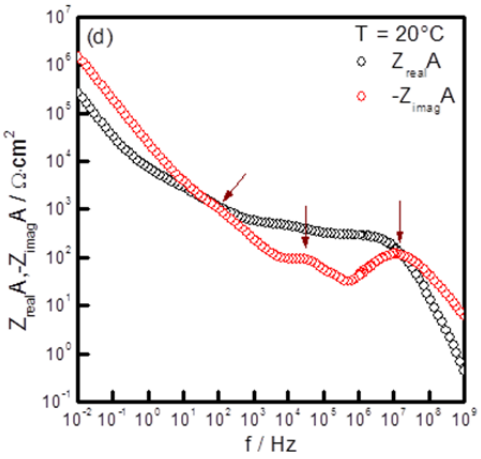

Figure VI - 254: Example of extended impedance scan showing dispersion attributed to the grain boundary resistance

Dispersed particle composites. Composites with promising mechanical and ion transport properties have been prepared using submicron ceramic powder in several different polymer-salt matrices. The fabrication approach is critical to ensure good adhesion and contact

between the phases, as earlier attempts resulted in a highly resistive ceramic-polymer interface and hence a suppression of the conductivity of the composite relative to the pure polymer phase. An example is shown in Figure VI - 255 where the conductivity of the composite falls between that of the pure sintered ceramic (Ohara Corp.) and the pure polymer, a melt cast sheet of PEO with lithium triflate salt. Interestingly, initial measures of the conductivity with blocking electrodes gave values that were quite resistive, less than or equal to that of the polymer matrix, but the conductivity equilibrated to values within an order of magnitude of the dense ceramic. This is consistent with the simulation shown in Figure VI - 253 for a minimal neck radius. Ongoing studies will probe the equilibration process and form composites containing the garnet ceramic. The garnet is proving to be chemically stable with lithium metal, and the larger micron-size particles of the garnet ceramic will minimize the number of interfaces across the membrane that add resistance.

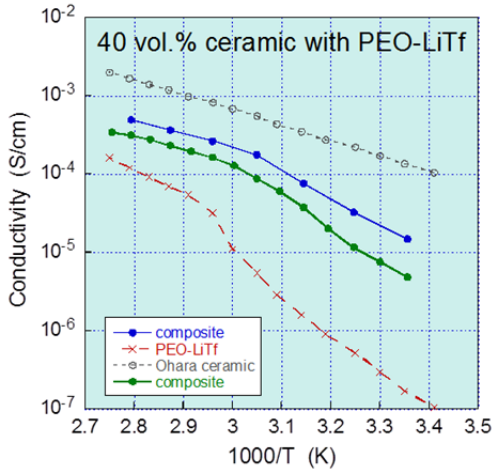

Figure VI - 255: Conductivity of dispersed ceramic polymer composite electrolyte compared to those of the pure and dense phases

Conclusions and Future Directions

Bilayer results demonstrate that, with optimized fabrication, the interface resistances of grain boundaries, lithium metal contacts, and polymer electrolyte to ceramic electrolyte boundaries can be minimized. Simulation results indicate that composites where the hard ceramic phase forms an interconnected skeleton, preferably with sizeable necks, will compensate for a polymer electrolyte that has a low bulk modulus and high resistivity. Successful composites that are conductive and mechanically robust have been prepared using submicron powders of the Ohara phosphate electrolyte in several polymer electrolyte matrices. Future work will seek similarly promising composites with the stable garnet electrolyte.

FY 2013 Publications/Presentations

1. N.J. Dudney, W.E. Tenhaeff, S. Kalnaus, K.A. Perry, “Composite Electrolyte to Stabilize Metallic Lithium Anodes,” DOE-VTO Annual Merit Review and Peer Evaluation Meeting, Arlington, VA, May 2013.
2. W. E. Tenhaeff, K. A. Perry, S. Kalnaus, N. J. Dudney, “Tough Solid Composite Electrolytes to Enable Lithium Metal Anodes,” Prime Pacific Rim Meeting on Electrochemical and Solid-State Science. Honolulu, HI, Oct. 2012.
3. Wyatt E. Tenhaeff, Nancy J. Dudney*, Sergiy Kalnaus, Kelly Perry, Erik G. Herbert, Ezhiylmurugan Rangasamy, Jeff Sakamoto, “Transport and Mechanical Properties of Bilayer and Composite Electrolytes for Li-metal Batteries,” Fall MRS, Boston, MA Nov. 29, 2012 (invited).
4. W.E. Tenhaeff, K.A. Perry, N.J. Dudney, “Impedance characterization of Li ion transport at the interface between laminated ceramic and polymeric electrolytes,” J. Electrochem. Soc, 159 [12] (2012) A2118-2123.
5. Sergiy Kalnaus, Wyatt E. Tenhaeff, Jeffrey Sakamoto, Adrian S. Sabau, Claus Daniel, Nancy J. Dudney, “Analysis of composite electrolytes with sintered reinforcement structure for energy storage applications,” J Power Sources 241 (2013) 178-185.
6. Wyatt E. Tenhaeff, Ezhiyl Rangasamy, Yangyang Wang, Alexei P. Sokolov, Jeff Wolfenstine, Jeffrey Sakamoto, Nancy J. Dudney, “Resolving the grain boundary and lattice impedance of hot pressed $Li_7La_3Zr_2O_{12}$ garnet electrolytes,” in press, ChemElectroChem.

VI.G.7 Lithium Dendrite Prevention for Lithium-Ion Batteries (PNNL)

Wu Xu
Pacific Northwest National Laboratory

Energy and Environment Directorate
902 Battelle Boulevard
Richland, WA 99354
Phone: (509) 375-6934; Fax: (509) 375-2186
E-mail: wu.xu@pnnl.gov

Ji-Guang Zhang (Co-PI)
Energy and Environment Directorate
902 Battelle Boulevard
Richland, WA 99354
Phone: (509) 372-6515; Fax: (509) 375-2186
E-mail: jiguang.zhang@pnnl.gov

Start Date: October 1, 2011
Projected End Date: September 30, 2015

Objectives

- Prevent Li dendrite growth and improve the safety of Li-ion batteries during overcharging and low-temperature operating conditions
- Enable Li metal as an anode material for rechargeable Li-battery applications.

Technical Barriers

Li dendrite growth and low Li Coulombic efficiency are the two major problems hindering the application of Li metal as an anode material in rechargeable Li batteries. Li dendrite growth on carbonaceous anodes in Li-ion batteries also has been a serious safety issue during abusive charging conditions, such as overcharging, charging at high rates, and charging at low temperatures. All of these barriers have hindered commercialization of rechargeable Li-metal batteries as well as state-of-the-art Li-ion batteries for use in plug-in hybrid electric vehicles and pure electric vehicles.

Technical Targets

- Optimize electrolyte compositions to effectively prevent Li dendrite growth on Li-metal anode.
- Identify appropriate electrolyte formulations to minimize the formation of Li dendrite growth on carbonaceous anodes.
- Identify optimal electrolyte formulations to extend the cycle life of Li-metal batteries without internal shorting.

Accomplishments

- Significantly improved Li Coulombic efficiency by using appropriate EC-based electrolytes and adding SEI film formation additives.
- Demonstrated dendrite-free Li morphologies on Li and carbon anodes by adding small amount of a cesium (Cs) additive.
- Successfully prevented Li plating or dendrite formation on a hard carbon anode during the overcharging process.
- Successfully demonstrated that the addition of a Cs additive does not affect the rate capability and long-term cycling stability of a Li-metal anode, a hard-carbon anode, and cathode materials.

✧ ✧ ✧ ✧ ✧

Introduction

Li-metal batteries have been called the “holy grail” of energy storage systems because the Li metal anode has an ultra-high theoretical specific capacity, low density, and the lowest negative electrochemical potential. They have been extensively investigated over the last 40 years but two major problems—Li dendrite growth and low Li Coulombic efficiency—hinder its commercial applications. For a Li-ion battery, Li plating and Li dendrite formation during overcharging or fast charging, or charging at low temperatures also is a serious problem to be solved. It has been found that Li dendrite formation is related to the non-uniformity of the passivation layer at the electrode/electrolyte interface, which results in fluctuation of the current density across the anode surface and in turn causes different Li deposition rates at different sites, resulting in the formation of dendrites. A rough or dendritic Li film generated at the anode surface is an intrinsic characteristic and a self-accelerated process. The formation of Li dendrites may lead to internal short circuiting of the battery and result in a shortened battery cycle life or even more serious safety problems such as thermal runaway, fire, and explosion. A general solution to the dendrite growth problem will not only enable a series of Li-metal based energy storage systems, but also significantly improve the safety of Li-ion batteries.

Approach

The PNNL approach is to develop appropriate electrolyte solvents and additives to prevent Li dendrite growth on the Li-metal and the carbon anode surface during repeated charging/discharging cycles and overcharging processes of Li-metal and Li-ion batteries by the self-healing electrostatic shield (SHES) mechanism recently developed at PNNL. Electrolyte solvents, Li salts, and self-healing additives will be investigated to minimize or even eliminate Li dendrite formation that is detrimental to the safety of Li-ion batteries. The surface smoothing electrolytes proposed in this work are expected to significantly improve the safety of Li-ion batteries and ultimately enable application of Li metal batteries.

Results

1. Effects of solvents and salts on Li Coulombic efficiency. The average Columbic efficiency of Li deposition and the morphologies of deposited Li film in the electrolytes of different organic solvents and Li salts were studied by using the Li|Cu cell configuration and modified Aurbach's method. The Li Coulombic efficiency in electrolytes containing EC-PC mixtures (EC:PC = 0 to 100) shown in Figure VI - 256 indicates that Li Columbic efficiency is significantly improved by adding EC into the PC electrolyte, and the efficiency increases with EC content in the EC-PC mixtures. For example, Li Columbic efficiency is increased from 76% to 93% when the EC:PC ratio is increased from 0 to 80%. Without the $CsPF_6$ additive, significant dendrites were observed on the Li film deposited in an electrolyte of 1-M $LiPF_6$/EC-PC mixture, which is similar to that using 1-M $LiPF_6$/PC electrolyte. When 0.05-M $CsPF_6$ is added to the electrolytes, Li films exhibit a metallic shining surface without dendrite growth. However, no significant difference in the Columbic efficiency of Li deposition was found among the electrolytes either with or without Cs additives (represented by the red dots in Figure VI - 256).

In addition to $CsPF_6$, another two Cs-based additives, CsTFSI and $CsClO_4$, also were studied in PC-based electrolytes to investigate the effect of anions on Li deposition morphology and Columbic efficiency. Both Cs additives can significantly improve the Li deposition morphology, but they significantly affect the Columbic efficiency of Li deposition. For CsTFSI, the efficiency slightly increased from 70.4% to 72.3% with addition of 0.01- to 0.1-M CsTFSI. For $CsClO_4$, the efficiency slightly decreased from 72.1% to 70.7% (67.4%) with addition of 0.01-M (0.05-M) $CsClO_4$.

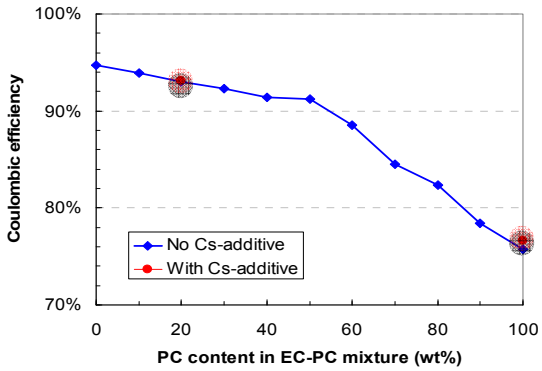

Figure VI - 256: Li Columbic efficiency of $LiPF_6$/EC-PC electrolytes

The average Coulombic efficiency of Li deposition in electrolytes containing different carbonate and ether solvents is summarized in Table VI - 10 and Table VI - 11. It is seen from both tables that the cyclic carbonate and ether solvents give much higher Columbic efficiency than the linear solvents. FEC, VEC, and VC (these are the carbonate solvents often used as SEI formation additives in Li-ion battery electrolytes) give even higher Li Coulombic efficiencies (above 97%) than EC. Therefore, these chemicals can be added as co-solvents or additives to protect Li-metal anodes and to further increase the Coulombic efficiency of the anode. As for ether-based solvents, DOL gives the highest Coulombic efficiency among other tested solvents. The average Coulombic efficiency is over 90% depending on the Li salt used. With the combination of $LiAsF_6$ in DOL, the Li Coulombic efficiency is greater than 99%. However, addition of $CsPF_6$ in the DOL solvent leads to gelation, and the dendrite still appear when Li deposits in $LiAsF_6$ in the DOL.

Table VI - 10: Summary of average Li Coulombic efficiency in 1-M $LiPF_6$-based electrolytes

Carbonate solvent	Average Li Coulombic efficiency	
	Without $CsPF_6$	0.05M $CsPF_6$
PC	75.7%	76.6%
EC	94.8%	
EC-PC (8:2 wt)	93.1%	93.1%
DMC	23.6%	
EMC	7.3%	
VC	97.1%	
FEC	97.6%	
VEC	98.2%	

It is also seen from the results in the two tables that the addition of Cs-additives into the electrolytes has negligible effects on the Coulombic efficiency of Li deposition. In ether-based electrolytes, the salt significantly affects the Li deposition morphology. LiTFSI and $LiClO_4$ lead to very poor Li deposition with low coverage on copper (Cu). Even with the addition of CsTFSI into LiTFSI electrolytes, the morphology is not improved. On the other hand, $LiAsF_6$ gives good coverage and morphology of Li film deposited on Cu. It can be concluded that the nature of the organic solvent has a significant effect on the Coulombic efficiency and morphology of lithium deposition. The selection of lithium salts also plays an important role.

Table VI - 11: Summary of average Li Coulombic efficiency in 1-M ether-based electrolytes

Solvent	Salt	Ave. Li Coulombic efficiency		
		No CsTFSI	0.01M CsTFSI	0.05M CsTFSI
DME	LiTFSI	61.1%		
Diglyme	LiTFSI	36.8%		
Triglyme	LiTFSI	54.1%		
Tetraglyme	LiTFSI	42.0%		
THF	LiTFSI	78.8%	80.2%	79.2%
DOL	LiTFSI	94.0%	93.0%	93.7%
DOL	LiTFSI	94.0%		
DOL	$LiClO_4$	90.6%		
DOL	$LiAsF_6$	99.1%		

2. Effect of additives on Li Coulombic efficiency. The average Li Coulombic efficiency of control electrolytes can be improved by adding SEI formation additives, even at 2% addition by weight (see Table VI - 12). The high Coulombic efficiency of 97% and good morphology for Li deposition is obtained for an electrolyte of 1-M $LiPF_6$ in EC/PC (8:2 by wt.) with 0.05-M $CsPF_6$ and 2% VC.

Table VI - 12: Summary of average Li Coulombic efficiency in carbonate-based electrolytes with different additives

	No	VC	FEC	$LiAsF_6$	LiBOB	LiDFOB
1	73.2%	93.3%	93.7%	77.4%	80.0%	80.3%
2	74.7%	91.7%		80.9%		
3	94.4%			98.2%		
4		96.6%				

Notes:
1 = 1M $LiPF_6$ in PC
2 = 1M $LiPF_6$ in PC + 0.05M $CsPF_6$
3 = 1M $LiPF_6$ in EC/PC (8:2 wt)
4 = 1M $LiPF_6$ in EC/PC (8:2 wt) + 0.05M $CsPF_6$

3. Effect of Cs-additive on hard carbon electrodes. First, the effect of the Cs additive on the Li deposition morphology on a carbonaceous surface during overcharge was studied. The carbon electrode was prepared using hard carbon/SP/PVDF at 8:1:1 by weight. The overcharging test was conducted inside an argon-filled glove box in a beaker cell, where the carbon electrode was used as the working electrode, a Li plate as the counter electrode, and 1.0-M $LiPF_6$ in PC with 0.05-M $CsPF_6$ as the electrolyte. The theoretical capacity of the hard carbon was selected as 500 mAh/g. After two formation cycles between 0.01 V and 1.5 V at a C/4 rate, the carbon electrode was charged to a capacity three times its theoretical capacity (i.e., 200% charged over the theoretical capacity). The scanning electron microscopy images in Figure VI - 257 shows that Li dendrites formed during overcharging in the control electrolyte that did not contain an additive (Figure VI - 257a), while only small spherical Li particles were formed in the Cs-containing electrolyte (Figure VI - 257b). When overcharging was 100%, a large amount of silver colored Li dendrites were formed on the carbon electrode surface in the control electrolyte that did not contain $CsPF_6$ (Figure VI - 258a), while no Li dendrites are found on the carbon surface from the Cs-containing electrolyte (Figure VI - 258b). This demonstrated that the $CsPF_6$ additive can prevent Li dendrite formation on a carbon surface during overcharging, which should improve the safety of Li-ion batteries during abuse conditions.

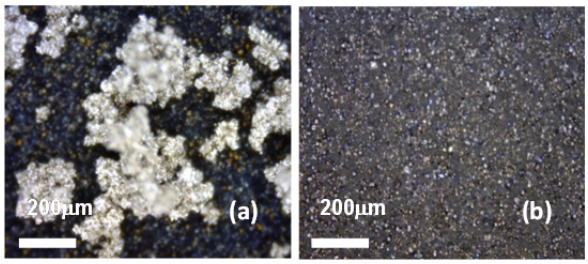

Figure VI - 257: Scanning electron microscopy images of surface morphologies of hard carbon electrodes after 200% overcharging in the control electrolyte (a) and the electrolyte with 0.05 M $CsPF_6$ as additive (b)

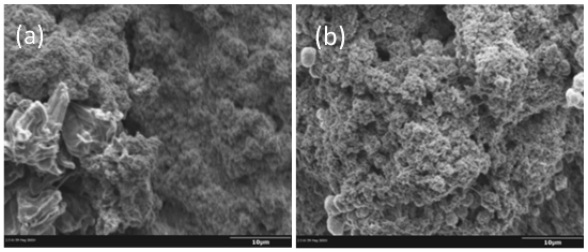

Figure VI - 258: Optical images of surface morphologies of hard carbon electrodes after 100% overcharging in (a) control electrolyte of 1.0-M $LiPF_6$ in PC and (b) the electrolyte with 0.05-M $CsPF_6$

The effect of the Cs-additive on the rate capability and long-term cycling stability of the hard carbon electrodes was examined. Figure VI - 259a and Figure VI - 259b show that the addition of $CsPF_6$ into the electrolyte does not affect the rate capability (up to 10 C rate) and the cycling stability of the hard carbon electrode, respectively, in more than 250 cycles. The hard carbon shows a slightly higher capacity in Cs-containing electrolyte than in the control electrolyte.

4. Effect of Cs-additive on cathode cycling stability. The long-term cycling stability of several electrolytes both with and without $CsPF_6$ additive in Li half cells containing three cathodes $LiFePO_4$ (LFP) $LiNi_{0.80}Co_{0.15}Al_{0.05}O_2$ (NCA) from ANL and $LiNi_{1/3}Mn_{1/3}Co_{1/3}O_2$ (NMC) from an industry partner have been investigated. The NCA and NMC cells show fast capacity fading with cycling, even in conventional Li-ion battery electrolytes, indicating the poor quality of these two electrodes (figures not shown here). However, both of them show slightly better cycling performance for the electrolytes with $CsPF_6$ additive. As for the LFP electrode that was homemade, no significant difference was observed for about 1600 cycles (Figure VI - 260), and it seems no short circuit occurs even for the control electrolytes that did not contain $CsPF_6$. The main reason is probably the excellent stability of LFP at low LFP loading condition (1.7 mg/cm^2 or 0.29 mAh/cm^2). High loading LFP electrodes and high quality NCA and NMC electrodes are under development and will be used to test Cs-containing electrolytes.

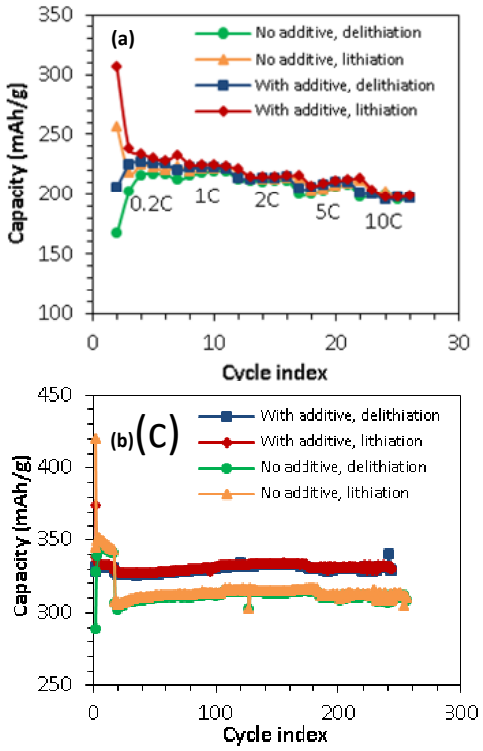

Figure VI - 259: Rate capability (a) and long-term cycling stability (b) of electrolyte (1.0-M $LiPF_6$ in EC/PC/EMC) with and without 0.05-M $CsPF_6$ on hard carbon electrodes

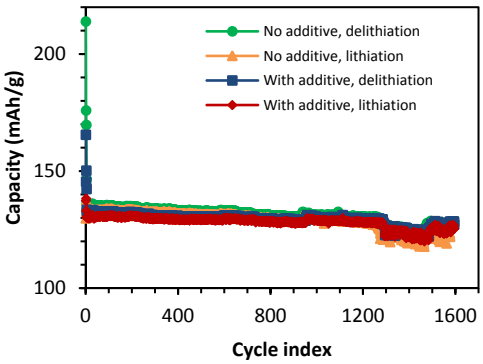

Figure VI - 260: Long-term cycling stability of Li|LFP cells with electrolytes of 1.0-M $LiPF_6$ in PC both with and without 0.05-M $CsPF_6$

Conclusions and Future Directions

Dendrite-free Li films with high Coulombic efficiency of Li deposition/stripping have been demonstrated. Coulombic efficiency can be significantly improved by using appropriate EC-based electrolytes and by adding SEI film formation additives. The deposited Li

morphologies on Li and carbon anodes can be dendrite-free by adding small amount of a Cs additive. Such an additive also can prevent Li plating or dendrite formation on hard carbon anode during overcharging process. The addition of a Cs additive does not affect the rate capability and long-term cycling stability of a Li-metal anode, a hard carbon anode, and cathode materials. We will further investigate new electrolyte formulations to prevent Li dendrite formation on Li-metal and carbon anodes during overcharging and/or low temperature conditions as well as to improve the battery performance.

FY 2013 Publications/Presentations

1. F. Ding, W. Xu*, G. L. Graff, J. Zhang, M. Sushko, X. Chen, Y. Shao, M. H. Engelhard, Z. Nie, J. Xiao, X. Liu, P. V. Sushko, J. Liu, J.-G. Zhang*, "Dendrite-Free Lithium Deposition via Self-Healing Electrostatic Shield Mechanism", *J. Am. Chem. Soc.*, 2013, **135**, 4450-4456.
2. F. Ding, W. Xu*, X. Chen, J. Zhang, M. H. Engelhard, Y. Zhang, B. R. Johnson, J. V. Crum, T. A. Blake, X. Liu, J.-G. Zhang*, "Effects of Carbonate Solvents and Lithium Salts on Morphology and Coulombic Efficiency of Lithium Electrode", *J. Electrochem. Soc*., 2013, 160, A1894-A1901.
3. W. Xu, F Ding, J. Zhang, X. Chen,M. H. Engelhard, M. Sushku, E. Nasybulin, J. Xiao, G. L. Graff, and J.-G. Zhang. "Enhanced Morphology and Cycling Efficiency of Li Metal Anode by Electrolyte Additives for Rechargeable Li Batteries," Presented in 222nd ECS Meeting, Oct. 7, 2012, Honolulu, Hawaii.
4. J.-G. Zhang, W. Xu, F. Ding, G. L. Graff, X. Chen, Y. Zhang, M. Sushku, "Self-Healing of Dendrite Growth in Li-Metal Batteries," Invitaed talk at 2013 International Battery Association Meeting, March 13, 2013, Barcelona, Spain.
5. J.-G. Zhang, W. Xu, F. Ding, X. Chen, Y. Zhang, E. Nasybulin, G. L. Graff, "Revival of Rechargeable Li Metal Batteries," Invited talk at Beyond Lithium-Ion VI, June 4-6, 2013, Boulder, Colorado.
6. W. Xu, M. H. Engelhard, E. Nasybulin, Y. Zhang, X. Chen, J.-G. Zhang, "XPS—A powerful technique for battery electrode surface analysis", Invited talk at 2013 Symposium of the Pacific Northwest Chapter of the AVS, September 19-20, 2013, Troutdale, Oregon.

VI.G.8 Development of High Energy Lithium Sulfur Batteries (PNNL)

Jie Xiao
Pacific Northwest National Laboratory

Energy and Environment Directorate
902 Battelle Boulevard
Richland, WA 99352
Phone: (509) 375-4598; Fax: (509) 375-2186
E-mail: jie.xiao@pnnl.gov

Jun Liu (Co-PI)
Pacific Northwest National Laboratory
Energy and Environment Directorate
902 Battelle Boulevard
Richland, WA 99352
Phone: (509)375-4443;Fax: (509)371-6242
E-mail: jun.liu@pnnl.gov

Start Date: October 1, 2011
Projected End Date: September 30, 2015

Objectives

- Develop high energy lithium-sulfur (Li-S) batteries
  - Investigate the fundamental chemistry and failure mechanism in the Li-S system
  - Apply fundamental research to help address the challenges in practical applications.

Technical Barriers

- High cost of materials and synthesis routes
- Limited energy density and cycling ability.

Technical Targets

- Systematic investigation of the sulfur/carbon (S/C) composite cathode in terms of carbon properties and electrochemical redistribution process of polysulfides
- Understand the interfacial reactions between the electrode and the electrolyte
- Explore novel strategies to mitigate the parasitic reactions that irreversibly consume polysulfides throughout cycling.

Accomplishments

- Constructed a baseline S/C cathode with 80% S in the composite
- Identified key factors for obtaining reproducible results for Li-S batteries.
- Modified Li metal surface by using co-solvent to alleviate polysulfide contamination
- Developed a novel approach for fabricating a pinhole-free thick sulfur electrode with a sulfur loading of 2 to 8 mg/cm^2 over a large area.

✧ ✧ ✧ ✧ ✧

Introduction

Li-S batteries have attracted increasing attention because of their high theoretical capacity, natural abundance of materials, low cost, and environmental friendliness. Assuming Li_2S as the end-product, the maximum specific capacity and energy of Li-S batteries are 1675 Ah/kg and 2650 Wh/kg, respectively, which are significantly higher than those of state-of-the-art Li-ion batteries. However, the low electrical conductivity (5×10^{-30} S/cm) of sulfur and the "shuttle reaction" caused by the soluble polysulfides are detrimental to Li-S battery performances, leading to low utilization of sulfur, poor Coulombic efficiency, fast capacity fading and self-discharge.

Approach

Although there are many approaches reported in literature for addressing the challenges in Li-S systems, the sulfur content in the S/C composite, the electrode thickness, and testing conditions vary largely in different groups, making direct comparison or evaluation of various methods difficult. The approaches we took included:

- Side-by-side comparison of different carbons by controlling 80% sulfur content in the composite
- Electrochemical understanding by using the baseline S/C cathode
- Evaluation of novel strategies in Li-S batteries by using baseline cathodes
- Application of the knowledge gained from the baseline cathode to a thick sulfur electrode for practical application.

Results

1. Baseline S/C composite cathode. Four different carbons (e.g., Ketjenblack [KB], graphene, acetylene black [AB], and hollow carbon nanoSphere [HCNS]), were chosen to construct C/S composites. To eliminate other factors (e.g., sulfur content in the electrode) that may influence the accurate evaluation of carbon effects, sulfur in all C/S composites was controlled at ca. 80 wt%, and the sulfur loading on each electrode was approximately 1 mg/cm^2.

Figure VI - 261 compares the morphologies of different S (80%)/C composites. KB (1400 m^2/g) and graphene (840 m^2/g) both had high surface areas. KB manifested a highly porous structure (Figure VI - 261a3), while graphene only formed two-dimensional sheets (Figure VI - 261b3). On the other hand, AB and HCNS both had low surface areas of 124 m^2/g and 76 m^2/g, respectively, while the latter was hollow (Figure VI - 261d3) for the individual carbon particle. Incorporation of high sulfur content led to the complete coverage of sulfur on the outside surfaces of all different carbons (Figure VI - 261a2-Figure VI - 261d2) and the pore filling in most KB and HCNS (Figure VI - 261a3 and Figure VI - 261d3).

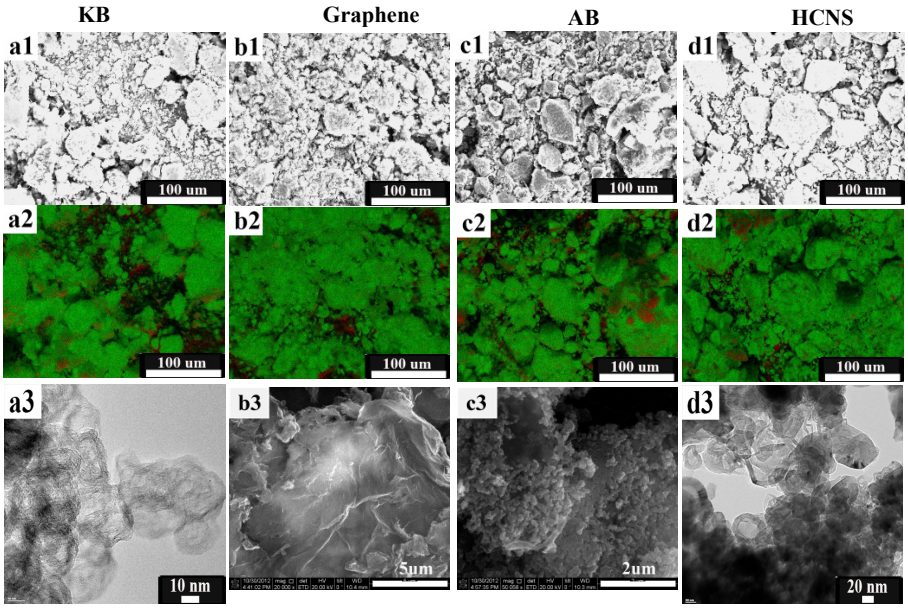

Figure VI - 261: Morphology comparison of original S /C composites. a1-d1: Scanning electron microscope; a2-d2: Elemental mapping for sulfur in different carbon hosts; a3-d3: Transmission electron microscope (TEM) of these S/C composites

Figure VI - 262a further reveals that, as the carbon surface area increases, the discharge capacity also increases. This can be explained by the increased utilization rate of sulfur in KB and graphene scaffolds. For carbons that contained similar surface areas, the capacity degradation rates followed exactly the same trend (Figure VI - 262a). At a relatively high rate of 0.5 C (Figure VI - 262a), the cycling data for KB and graphene overlap significantly, although KB has a porous structure while graphene does not. Similar phenomena were observed for AB and HCNS with the close low surface areas shown in Figure VI - 262a. The additional benefits from the pore volumes of KB and HCNS were seen only when the rate decreased to 0.2C (Figure VI - 262b). The lower rate (0.2C) provided sufficient time for soluble polysulfides to move from the cathode side during each cycle. The existence of porous structures on carbon slightly slowed down this “leaking” process for polysulfides by increasing the diffusion length within the carbon through the pores. Based on these results, KB with its high surface area and large pore volume was therefore chosen for the construction of the baseline sulfur electrode.

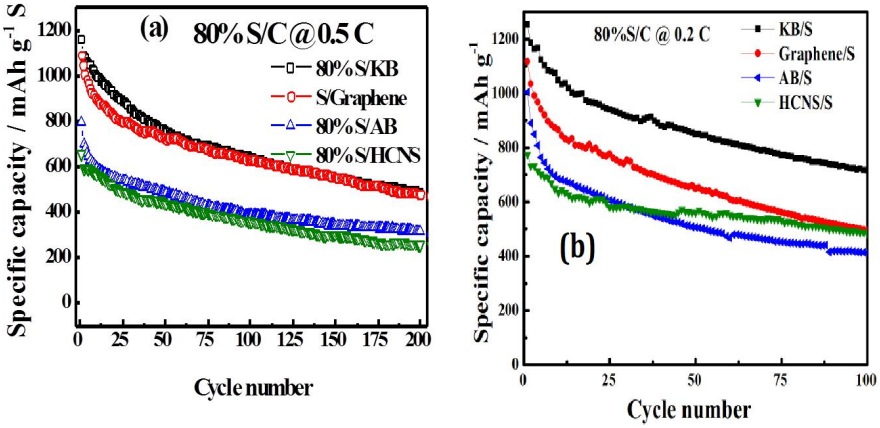

Figure VI - 262: Comparison of the cycling stability of different S/C composites at (a) 0.5 C and (b) 0.2 C rates

2. Key parameters to obtain reproducible Li-S battery results. For Li-ion batteries tested in the laboratory, excessive amount of electrolyte was always used to maximize the performance of active materials. Although it is not the case for practical applications, electrolyte-rich cells almost have become the default approach in the laboratory studies reported in the literature. However, for Li-S cells, the intermediate product is soluble, which allows the electrolyte content to directly influence the concentration of dissolved polysulfides and their subsequent nucleation and re-deposition. It was found that the relative S/electrolyte ratio significantly affected the cycling stability of Li-S cells and needed to be carefully controlled in each cell to generate reproducible/reliable results. Figure VI - 263a compares the cycling stability of Li-S cells in different amounts of electrolyte. The greater the amount of electrolyte (i.e., a lower S/L ratio), the higher the initial discharge capacity because of the increased utilization rate of sulfur caused by wetting. However, capacity decayed much faster in the presence of an excessive amount of electrolyte (i.e., S/L = 14 shown in Figure VI - 263a). The highest capacity retention rate is optimized at S/L = 50. It was found that the fast capacity degradation in the initial few cycles (circled area in Figure VI - 263a), which is commonly reported in the literature, was largely alleviated by reducing the relative amount of electrolyte in the cell.

Figure VI - 263b further compares electrode morphologies harvested from different cells. When the relative content of solid sulfur was low (S/L = 14 or 20 in Figure VI - 263b), more cracks and aggregates were found. The loss of cathode structure integration was probably related to the easy dissolution of polysulfide in the flooded cell. When the S/L ratio was increased to 75, the cathode exhibited a much smoother surface due to the much higher rate of polysulfide nucleation than growth in the concentrated electrolyte (S/L = 75), thus improving the Coulombic efficiency (data not shown here). Different morphology evolutions also were identified on the Li anode side. When electrolyte is excessively high (i.e., a low S/L ratio), more sulfur-containing electrolyte contacted with the Li anode and penetrated into the bulk lithium during cycling, which resulted in a rapid increase in cell impedance. When the electrolyte content was controlled (S/L >20) in the cell, Li corrosion was largely alleviated, which is consistent with the cycling stability results shown in Figure VI - 263a.

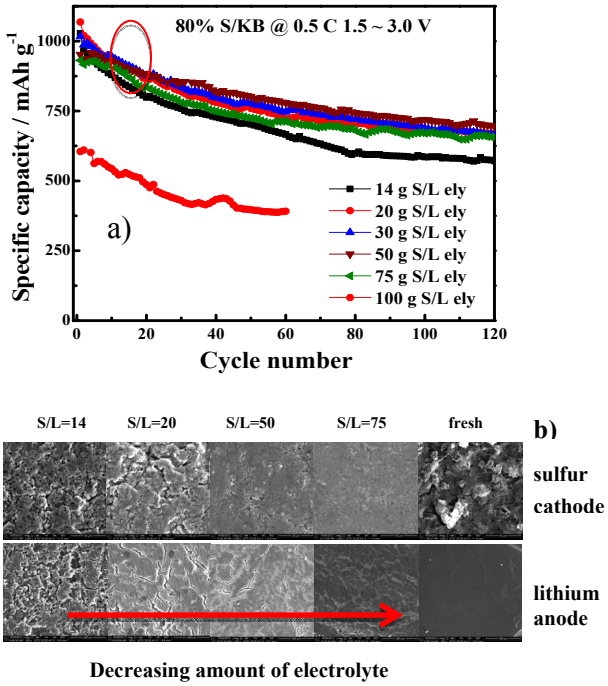

Figure VI - 263: a) Cycling stability of baseline S/KB cathodes in different amounts of electrolyte. Numbers in the figure represent the solid-to-liquid ratio calculated from sulfur weight (in grams)/electrolyte volume (in liters). The higher ratio in a) corresponds to a smaller amount of electrolyte added in the cell. b) SEM images of cycled sulfur cathodes and Li anodes harvested from different cells in a)

3. Enhanced solid state electrolyte interface. Parallel efforts also were pursued for the Li side focusing on the improvement of solid electrolyte interface (SEI) stability in the presence of corrosive polysulfides. Ionic liquid (IL) N-methyl-Nbutylpyrrolidinium bis(trifluoromethylsulfonyl)imide (Py14TFSI) was employed to modify the SEI layer shown in Figure VI - 264. When the 75% IL containing electrolyte was used in the Li–S battery, the electrochemical performance improved significantly, exhibiting high Coulombic efficiency and very stable cycling with high capacity retention of 94.3% for 120 cycles (Figure VI - 264). Integrated studies from SEM (insets of Figure VI - 264), EIS, and XPS (data not shown here) revealed that the ionic liquid facilitated formation of a more stable SEI layer and improved the quality of the Li metal surface (insets of Figure VI - 264). These improvements effectively prevent continuous penetration of soluble polysulfides into the bulk Li and slow down the otherwise rapid corrosion of Li and the rapid increase of the cell impedance.

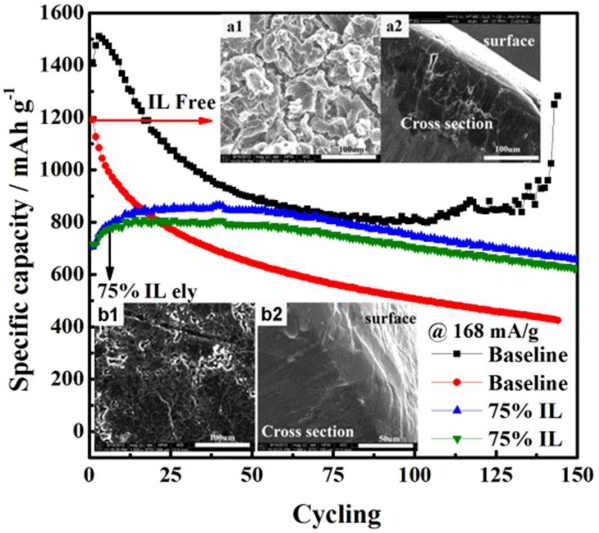

Figure VI - 264. Comparison of cycling stability with and without ionic liquid (IL) as the co-solvent. The insets compare the surface and cross sectional images of Li metal cycled in (a1, a2) the baseline electrolyte and (b1, b2) in the presence of IL-co-solvent

4. Fabrication of thick sulfur electrode (S: 2 to 8 mg/cm^2). Uniform coating of nanoparticles including S/C composite into thick electrode is always challenging but urgently needed for real applications of Li-S batteries. A novel and cost-effective method (for which a patent application has been submitted) has been developed at PNNL to prepare a practically usable sulfur cathode. Figure VI - 265a compares the coated sulfur electrode before and after modification. By using a newly developed method, the pinhole-free thick sulfur electrode displayed a large area of pinhole-free film, adaptable for mass production. The sulfur loading on the as-prepared electrode is also adjustable from 2 to 8 mg/cm^2 depending on the specific requirement.

Figure VI - 265b shows the cycling performance of as-prepared sulfur electrode with sulfur loading of 3.8 mg/cm^2. The areal specific capacity achieved was 4.5 mAh/cm^2 at 0.1 C, which is compatible with that of state-of-art electrodes for Li-ion batteries. Further increasing the rate to 0.2 C, a high area capacity of 3 mAh/cm^2 was still obtained. Of note, 1 C used in Figure VI - 265b was 1000 mA/g, translating to a current density of 3.8 mA/cm^2, which is much higher than that in traditional Li-ion batteries. By using the knowledge gained from our baseline S/C cathode, good cycling ability was observed in this thick electrode without complicated treatment on the electrodes (still under testing). This confirms the importance of the baseline cathode in assuring that the understanding is transferrable to electrodes with increased thickness and sulfur loadings. More work is underway to identify the balance between sulfur loading and electrochemical performance.

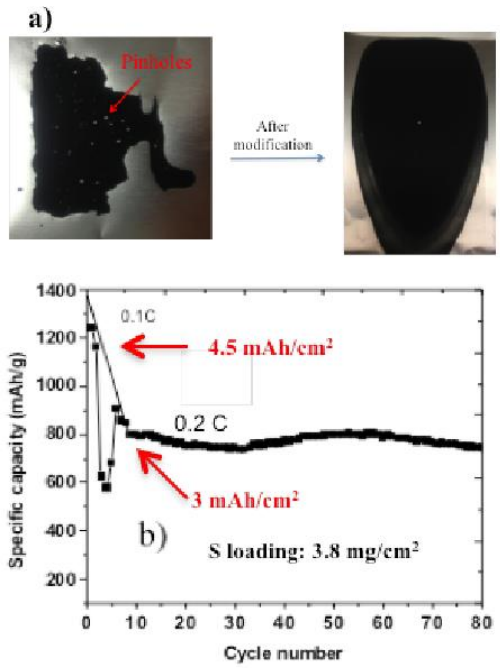

Figure VI - 265: a) Comparison of as-coated thick sulfur electrodes before and after modification. b) Cycling performance of thick sulfur cathode. 0.1 C was used for the first two cycles, followed by 0.2 C in subsequent cycling (1 C = 1000 mA/g)

Conclusions and Future Directions

Beginning with construction of the sulfur baseline cathode, the Li-S battery system has been systematically

investigated during FY13. After correlating the carbon properties to electrochemical behavior of the S/C composite, high-surface-area KB with a porous structure was selected as the carbon host with a sulfur content of 80% in the composite. Based on the baseline electrode, the ratio between solid sulfur and liquid electrolyte was identified to significantly influence the reproducibility of Li-S battery results and optimized to be around 50 g/L for S/KB-type electrode. Ionic liquid was introduced as a co-solvent in the ether-based electrolyte to improve the quality of SEI film on the Li-metal anode side, which effectively improved the cycling stability of Li-S batteries. In addition, a cost-effective approach was invented to homogeneously coat S/C nanoparticles onto large-area pinhole-free cathode films. The sulfur loading is adjustable from 2 to 8 mg/cm^2 and the process is readily adaptable for mass production. Knowledge obtained from the baseline S/C cathode was successfully applied in the thick sulfur cathode, which led to considerably improved cycling stability with high areal specific capacity of 3 to 4 mAh/cm^2.

Future work will continue to investigate the electrochemical and chemical processes in Li-S batteries, with a focus on thick sulfur cathodes. Appropriate modifications of the anode side will be explored to further improve system performance. Advanced characterization techniques will be coupled with electrochemical measurements to develop fundamental understanding towards the practical application of lithium sulfur batteries for vehicle electrification.

FY 2013 Publications/Presentations

1. J.Zheng, D. Lu, M.Gu, C.Wang, J.-G. Zhang, J. Liu and J. Xiao, "How to Obtain Reproducible Results for Lithium Sulfur Batteries?" *J. Electrochem. Soc*., **2013**, 160, A2288-2292.
2. J. Zheng, M.Gu, H. Chen, P. Meduri, M.H. Engelhard, J.-G. Zhang, J. Liu and J. Xiao, "Ionic liquid-enhanced solid state electrolyte interface (SEI) for lithium-sulfur batteries", *J. Mater. Chem. A*, **2013**, 1, 8464-8470.
3. J. Zheng, Me. Gu, C. Wang, P.Zuo, P.K. Koech, J.-G. Zhang, J. Liu and J. Xiao, "Controlled Nucleation and Growth Process of Li_2S_2/Li_2S in Lithium-Sulfur Batteries", *J. Electrochem. Soc*., **2013**,160, A1992-A1996.
4. J. Zheng, M. Gu, M. J. Wagner, K. A. Hays, X. Li, P. Zuo, C. Wang, J.-G. Zhang, J. Liu, and J. Xiao, "Revisit Carbon/Sulfur Composite for Li-S Batteries", *J. Electrochem. Soc*., **2013**, 160, A1624-A1628.
5. J.Zheng, J. Xiao, H. Chen, M. Gu, P. Meduri, M.H. Engelhard, J.-G. Zhang, "Ionic Liquid Enhanced Solid Electrolyte Interface (SEI) for Lithium Sulfur Batteries", Materials Research Society (MRS) Spring Meeting, San Francisco, April, 2013.
6. J. Liu, "Recent Progress of Li-S and Na Batteries at Pacific Northwest National Laboratories", 7th U.S.-China Electric Vehicle and Battery Technology Workshop, Lawrence Berkeley National Laboratory, Berkeley, California, April, 2013.

VI.G.9 Rechargeable Lithium-Air Batteries (PNNL)

Ji-Guang Zhang
Pacific Northwest National Laboratory

Energy & Environment Directorate
902 Battelle Boulevard, Mail Stop K2-44
Richland, WA 99352
Phone: (509) 372-6515; Fax: (509) 375-2186
E-mail: Jiguang.Zhang@pnnl.gov

Wu Xu (Co-PI)
Pacific Northwest National Laboratory
Energy & Environment Directorate
902 Battelle Boulevard
Richland, WA 99352
Phone: (509) 375-6934; Fax: (509) 375-2186
E-mail : wu.xu@pnnl.gov

Start Date: October 1, 2012
Projected End Date: September 30, 2015

Objectives

- Identify stable components that can enable long-term, rechargeable operation of Li-air batteries for potential application in long-range EV.

Technical Barriers

Reduced oxygen species ($O_2^{-\bullet}$, LiO_2, O_2^{2-}, LiO_2^-, and Li_2O_2) generated on the air electrode surface during the discharge of a Li-O_2 battery are strongly reactive. These reduced oxygen species attack all components in a Li-O_2 battery that are in contact with the liquid electrolyte and significantly limit the reversibility of rechargeable Li-O_2 batteries. In addition, the overvoltage that occurs during the charging process of a Li-O_2 battery also is high (i.e., normally over 1 V) and can lead to low Coulombic efficiency of the batteries.

Technical Targets

- Identify appropriate substrates that will be stable with the reduced species of oxygen (i.e., superoxide radical anion, and Li_2O_2) and at high voltages in an oxygen atmosphere.
- Identify appropriate catalysts for the oxygen evolution reaction to lower the charging overvoltage of Li-air batteries.

Accomplishments

- Identified polyethylene (PE) as the most stable polymer that can be used against superoxide radical and peroxide anions. PE can be used as the polymer binder for air-electrode construction.
- Developed poly(3,4-ethylenedioxythiophene) (PEDOT) as an organic catalyst to reduce overvoltage during charging process of Li-O_2 batteries.
- Developed a carbon nanotube/ruthenium (CNT/Ru) nanocomposite as an electrocatalytic substrate for improving cycling performance of Li-O_2 batteries.

✧ ✧ ✧ ✧ ✧

Introduction

Li-air or Li-O_2 batteries have an ultra-high theoretical specific energy (~5200 Wh/kg when the weights of Li and O_2 are included), and are expected to have a practical specific energy of around 800 Wh/kg that is about four times of those of the state-of-the-art Li-ion batteries (ca. 200 Wh/kg). However, the development of rechargeable Li-O_2 batteries faces significant challenges including the decomposition of electrolyte, the large over-voltage that occurs during charge process, design of cathode materials with high capacity and stability, and protection of the Li anode. More importantly, highly reactive oxygen species ($O_2^{-\bullet}$, LiO_2, O_2^{2-}, LiO_2^-, and Li_2O_2) are generated on the air electrode surface during the discharge of a Li-O_2 battery, and these species attack every component in Li-O_2 batteries that are in contact with the liquid electrode and significantly limit the reversibility of the rechargeable Li-O_2 batteries. Therefore, the chemical and electrochemical stability of all Li-O_2 battery components, including the electrolyte solvent, electrolyte salt, cathode material (typically carbon-based), and binder, needs to be reevaluated in an O_2-rich environment. Also, good catalysts need to be developed to reduce the overvoltage during oxygen reduction and evolution reactions so the cycling stability of Li-O_2 batteries can be improved.

Approach

The PNNL approach is to develop new non-carbon based air electrodes and oxygen evolution reaction

(OER) catalysts to avoid carbon oxidation, reduce the charging overvoltage, and improve the cycling stability of rechargeable Li-air batteries. The air electrode study also includes the investigation of the stability of polymer binders against superoxide radical anion and peroxide anion. Catalysts and non-carbon electronic-conductive substrates will be prepared, characterized, and investigated. Relatively stable electrolytes, CF_3SO_3Li (i.e., LiTf) and tetraglyme (i.e., 4G) will be used in these investigations based on our previous investigations. The optimized components and compositions will improve the Coulombic efficiencies and cycle lives of rechargeable Li-O_2 batteries.

Results

1. Stability of polymer binders. The effects of 11 polymers on the discharge performance of Li-O_2 batteries were evaluated using Ketjenblack-based air electrodes. The nature of the binder significantly affects discharge capacity. In general, a strong binder decreases the capacity by forming a strong bond among the carbon particles, thus reducing the active surface area and pore size/pore volume of the prepared air electrode.

The stability of the polymer binders with KO_2 was investigated using x-ray diffraction (XRD) patterns of ball milled powders (Figure VI - 266). The curves in the figure show that PVDF decomposes and forms KHF_2; PS decomposes and forms Li_2CO_3; PEO decomposes and forms amorphous products; PAN decomposes and forms KCN; PVC decomposes and forms KCl; PVP, PMMA and CMC decompose and form K_2CO_3, LiH, and presumably alkylcarbonates; PTFE, PE and PP are relatively stable against KO_2.

The stability of PE, PP, and PTFE along with PVDF was further investigated by x-ray photoelectron spectroscopy (XPS) to analyze corresponding powders after ball milling with KO_2 and Li_2O_2. The XPS results shown in Figure VI - 267 indicates signs of PTFE and PP decomposition when they are in contact with Li_2O_2 and KO_2. PE was found to be the only stable polymer under the applied experimental conditions. PE is completely stable even in the aggressive ball milling environment and, therefore, will certainly be beneficial to long-term operation of Li-O_2 batteries when stable electrolytes are developed.

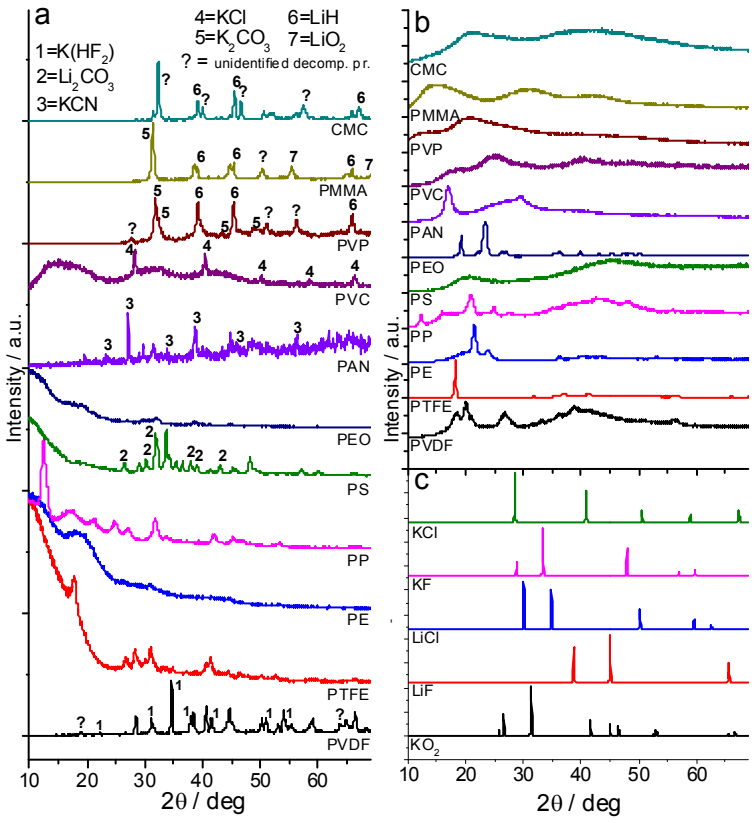

Figure VI - 266. XRD of reaction products of polymer with KO_2

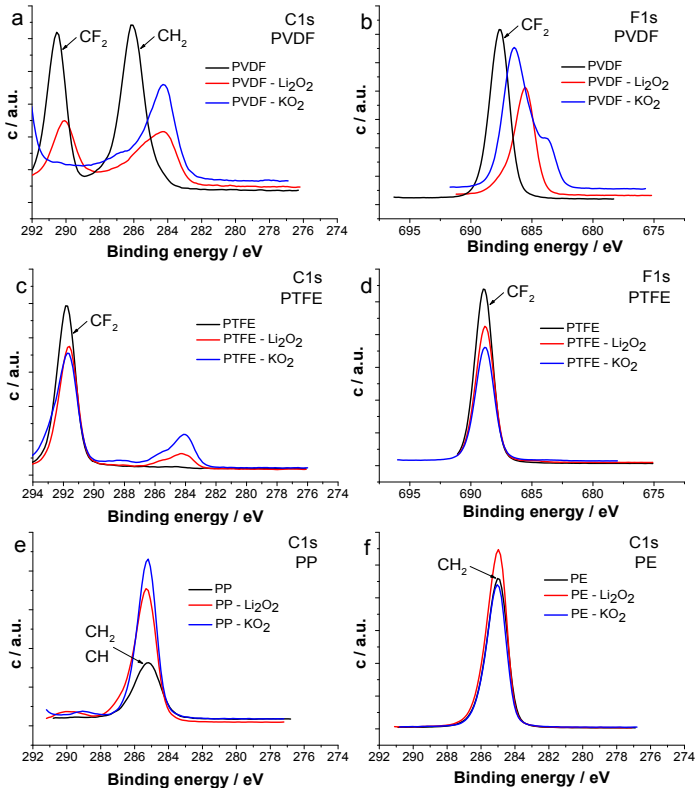

Figure VI - 267: XPS spectra of the reaction products and pure polymers after ball milling with KO_2 and Li_2O_2

2. Electrocatalytic effect of PEDOT

PEDOT was successfully polymerized inside Super P carbon (SP) using the chemical oxidative method. The composite of PEDOT-SP was confirmed by Fourier transform infrared spectroscopy (FTIR) and scanning electron microscopy (SEM) with energy dispersive x-ray spectroscopy mapping. The Li-O_2 batteries with the SP and PEDOT-SP air electrodes were compared. As shown in Figure VI - 268a, use of PEDOT significantly decreases the charging voltage (potential for oxygen evolution reaction [OER]) by 0.7 to 0.8 V and slightly increases discharge voltage (potential for oxygen reduction reaction) for the first cycle although the cycling performance is not significantly improved due to electrolyte decomposition and relatively high carbon loading. The electrocatalytic activity of PEDOT can be explained by its electrochemical activity in the applied potential range (Figure VI - 268b). PEDOT acts as a mediator in electron transfer between the discharge products and the carbon electrode, decreasing overpotential of the reactions. The electrocatalytic effect of PEDOT is reduced with cycling because of the irreversible decomposition of electrolyte and passivation of PEDOT by side reaction products.

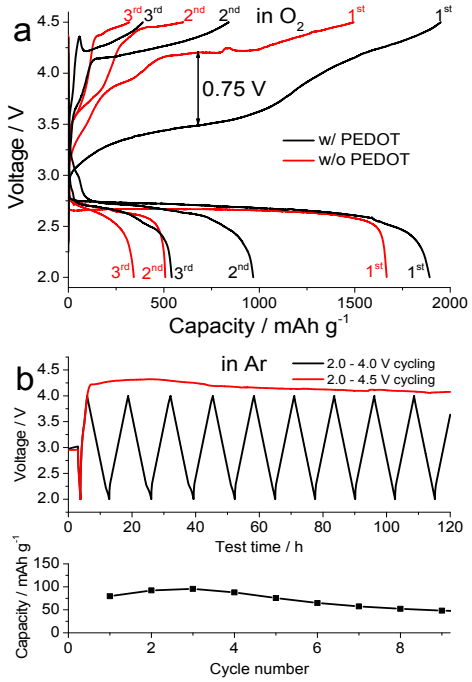

Figure VI - 268: Voltage profiles for the PEDOT-containing battery and the control battery without PEDOT

Formation/decomposition of discharge products as well as stability of PEDOT was analyzed by XPS (Figure VI - 269). Li_2O_2 was identified as a major discharge product with a contribution from a carbonate-based side product generated during electrode/electrolyte decomposition. After charging, Li_2O_2 disappeared while carbonate-based side products stay on the surface, greatly limiting cycling performance. Based on the XPS data, PEDOT with incorporated TFSI counter ions seems to be stable.

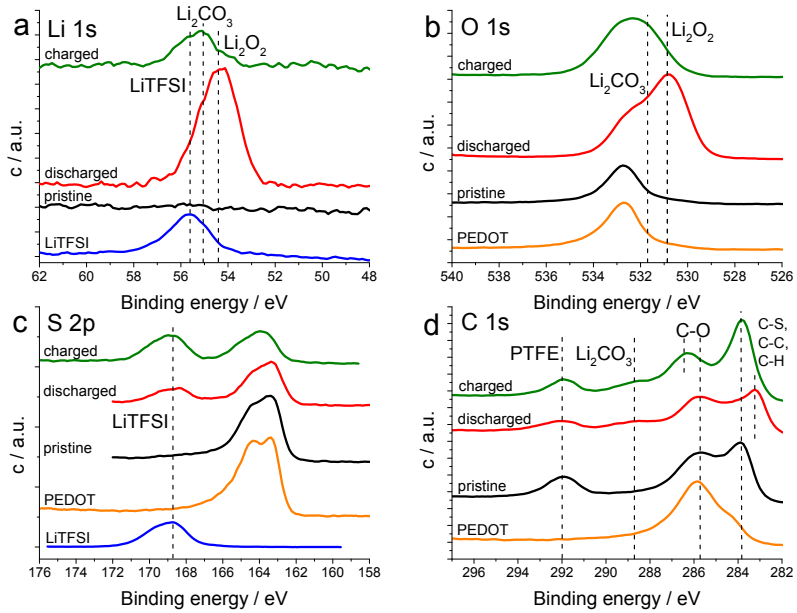

Figure VI - 269: XPS results for the pristine, discharged, and charged PEDOT/SP/PTFE electrodes in O_2

3. Ru nanoparticle catalyst. Ru-decorated CNTs were prepared by thermal reduction of $RuCl_3$ solution in water/glycerol mixture. SEM anlaysis showed an even distribution of Ru particles in the CNT matrix (Figure VI - 270a), while EDS elemental analysis demonstrated 46 wt% Ru in the composite (Figure VI - 270b). TEM analysis revealed that the Ru nanoparticles observed in SEM images represent aggregates of <2 to 4-nm Ru nanoparticles (Figure VI - 270c,d). The high-resolution TEM image (Figure VI - 270d, insert) shows single Ru nanoparticles with a characteristic 0.27-nm lattice space. XRD results (Figure VI - 271a) confirmed the characteristic Ru peaks at 44°, 38.2°, and 69° and a shoulder at 59° in the CNT/Ru nanocomposite. The cycling performance of CNTs/Ru nanocomposite was tested in Li-O_2 batteries with the LiTf-tetraglyme electrolyte at 0.1 mA/cm^2 current density.

Charge/discharge voltage profiles taken during the selected cycles of the batteries are shown in Figure VI - 271. Long cycle life was observed with a discharge capacity above 1000 mAh/g for nearly 50 cycles. The first cycle of the battery had a discharge capacity of 2500 mAh/g with a discharge plateau at 2.6 V. It is seen that Ru possesses electrocatalytic properties towards OER and decreases charge voltage by 0.3 to 0.5 V depending on loading. Ru also improves the cycle life of the Li-O_2 battery, although formation of side products (carbonates) takes over after 5 to 10 discharge cycles, similar to that occurring in non-catalyzed batteries.

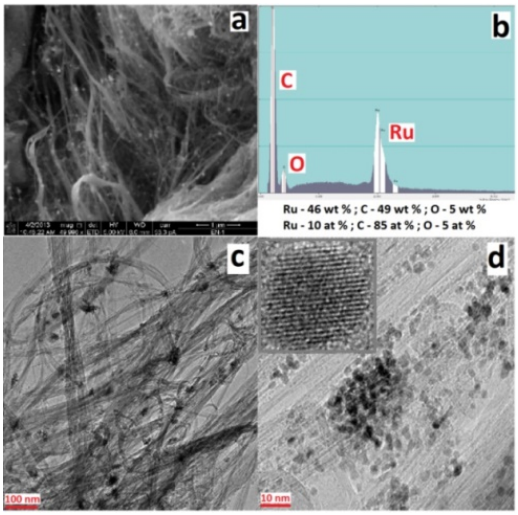

Figure VI - 270: a) SEM image and b) EDS analysis of the prepared CNTs/Ru composite; c) and d) TEM images of the prepared CNTs/Ru composite

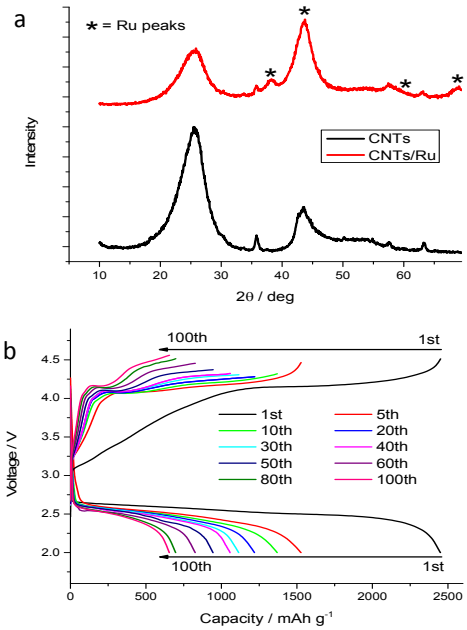

Figure VI - 271: a) XRD spectra of CNTs and CNTs/Ru composite; b) cycling performance of CNTs/Ru electrode in Li-O_2 battery

Conclusions and Future Directions

Polyethylene has been identified as the most stable polymer binder for air electrodes. PEDOT proved to be a good organic catalyst for reducing overvoltage during the charging process of Li-O_2 batteries, and the CNT/Ru nanocomposite demonstrated good electrocatalytic effect on improving the cycling performance of Li-O_2 batteries.

Future work will focus on the investigation of the new electrolytes that are stable against the reactive reduced-oxygen species. Polymer encapsulated air electrodes will be prepared to improve the stability of carbon-based electrodes. The OER catalysts will be further studied to reduce charging overvoltage and improve the cycling stability of the Li-O_2 batteries.

FY 2013 Publications/Presentations

1. Nasybulin, W. Xu,* M. H. Engelhard, Z. Nie, S. D. Burton, L. Cosimbescu, M. E. Gross, J.-G. Zhang,* "Effects of electrolyte salts on the performance of Li-O_2 batteries", *J. Phys. Chem. C*, 2013, **117**, 2635-2645.
2. Nasybulin, W. Xu,* M. H. Engelhard, S. X. Li, M. Gu, D. Hu, J.-G. Zhang,* "Electrocatalytic properties of poly(3,4-ethylenedioxythiophene) (PEDOT) in Li-O_2 battery", *Electrochem. Commun.*, 2013, **29**, 63-66.
3. Nasybulin, W. Xu,* M. H. Engelhard, Z. Nie, X. S. Li, J.-G. Zhang,* "Stability of polymer binders in Li-O_2 batteries", *J. Power Sources*, 2013, **243**, 899-907.
4. J.-G. Zhang, W. Xu, J. Xiao, E. Nasybulin Y. Shao, D. Mei, and J. Zhang, "Critical Components of Rechargeable Li-Air Batteries", Presented at the 222nd ECS Meeting, Oct. 7-11, 2012, Honolulu, HI.
5. E. Nasybulin, W. Xu, J.-G. Zhang, "The effects of electrolyte salts on the performance of Li-air batteries", Presented at the 222nd ECS Meeting, Oct. 7-11, 2012, Honolulu, HI.
6. W. Xu, E. Nasybulin, J.-G. Zhang, "Stability of Electrolyte Solvents, Salts and Electrode Binders in in Li-O_2 batteries", Invited talk at Beyond Lithium Ion VI, June 4-6, 2013, Boulder, CO.
7. W. Xu, M. H. Engelhard, E. Nasybulin, Y. Zhang, X. Chen, J.-G. Zhang, "XPS—A powerful technique for battery electrode surface analysis", Invited talk at 2013 Symposium of the Pacific Northwest Chapter of the AVS, September 19-20, 2013, Troutdale, OR.

VI.G.10 Simulations and X-ray Spectroscopy of Li-S Chemistry (UCB)

Nitash Balsara
University of California, Berkeley

Dept. of Chemical and Biomolecular Engineering
201 C Gilman Hall
Berkeley, CA 94720
Phone: (510) 642-8973; Fax: (510) 642-5033
E-mail: nbalsara@berkeley.edu

David Prendergast
Lawrence Berkeley National Laboratory
1 Cyclotron Road
Berkeley, CA 94720
Phone: (510) 486-4948; Fax: (510) 486-7424
E-mail: dgprendergast@lbl.gov

Start Date: October 2013
Projected End Date: September 2016

Objectives

- Develop a unique diagnostic tool to study Li-S battery reaction intermediates that employs X-ray spectroscopy and molecular modeling.
- Elucidate Li-S battery charge/discharge reaction mechanisms.
- Examine physical and chemical nature of Li-S battery reaction intermediates in electrolyte environment.

Technical Barriers

As lithium-sulfur batteries are charged and discharged, Li_2S_x reaction intermediates formed can leave the cathode, causing capacity fade and battery failure. Redox reaction mechanisms that form Li_2S_x intermediates are still unclear. Elucidation of reaction pathways requires an experimental tool that can differentiate Li_2S_x intermediates in their native environment. Little is known about the physical and chemical nature of Li_2S_x intermediates dissolved in electrolytes.

Technical Targets

- Obtain X-ray absorption spectroscopy (XAS) signatures for Li_2S_x intermediates dissolved in electrolytes of poly(ethylene oxide) (PEO) and a diblock copolymer of polystyrene-poly(ethylene oxide) (SEO) by experiment and by simulations.
- Develop Li-S cell that facilitates use of soft and hard X-ray spectroscopy during charge-discharge cycles
- Perform detailed (first-principles or empirical force-field) molecular dynamics (MD) simulations to interpret associated X-ray spectra and reveal molecular nature of Li_2S_x intermediates in electrolyte.

Accomplishments

- Experimental XAS were obtained for Li_2S_x (x = 2, 4, 6, 8) intermediates dissolved in PEO and a diblock copolymer of SEO.
- MD simulations of Li_2S_x molecules dissolved in tetraglyme were performed. eXcited Core Hole (XCH) simulations were used to obtain theoretical Li_2S_x X-ray signatures for representative *ab initio* molecular dynamic motifs.
- Li-S cells appropriate for *in situ* soft X-ray measurements were developed.

✧ ✧ ✧ ✧ ✧

Introduction

The objectives of this work are to: (a) elucidate mechanisms by which redox reactions in the sulfur cathode proceed, and (b) study the physical and chemical nature of Li_2S_x intermediates. Past studies of Li-S battery reaction mechanisms have been inconclusive due to the difficulty of Li_2S_x molecule speciation. Li_2S_x species cannot be isolated, and tend to undergo reversible disproportionation reactions in solution. The equilibrium constants and reaction kinetics governing disproportionation are system-dependent. A combination of XAS and simulations provides us with an unprecedented ability to detect Li_2S_x molecules in solution and study their local chemical environments. Experimental XAS signatures were obtained for Li_2S_x molecules dissolved in PEO and SEO. MD simulation of Li_2S_x solvation revealed that lithium polysulfide molecules elect to form nano-agglomerates in solution. Theoretical XAS signatures for Li_2S_x/tetraglyme configurations were obtained and used to interpret signatures of experimental Li_2S_x/polymer electrolyte systems.

Approach

- Obtain simulation results of S_8, Li_2S_x, and Li_2S in tetraglyme (an oligomer analog of PEO).
- Obtain theoretical XAS signatures of Li_2S_x molecules in tetraglyme using XCH methods at the sulfur K-edge.
- Obtain experimental sulfur K-edge XAS signatures for Li_2S_x dissolved in thin films of solid-state PEO and SEO.
- Design a Li-S cell appropriate for measurement of X-ray spectra as a function of state of charge in cathode.

Results

MD simulations of Li_2S_x molecules. MD simulations of Li_2S_x molecules dissolved in tetraglyme have shown that lithium polysulfide molecules elect to form nano-agglomerates in solution, and are not poly-dispersed as is commonly assumed. These nano-agglomerates are exemplified in Figure VI - 272a for Li_2S_8. The thermodynamics of agglomeration have been investigated by calculating the free energy of agglomeration for two Li_2S_8 molecules in tetraglyme (inset of Figure VI - 272b) using *ab initio* MD simulations. These studies show that the agglomerates are the thermodynamically stable state. A 0.4 kcal/mol (0.5 eV) barrier was calculated, which is accessible at room temperature. These simulations are the most extensive ever performed on this system and provide the first molecular level insights into the mechanism of lithium sulfide dissolution into the electrolyte and concurrently, the failure mechanism in Li/S batteries.

Spectroscopic signatures obtained using XCH methods for both single polysulfide molecules in tetraglyme and polysulfide molecules that have formed nano-crystals in simulation have been obtained. Due to computational limitations, the nano-agglomerates were modeled as solid phase structures. Then, the sulfur K-edge X-ray absorption spectra was calculated. As shown in Figure VI - 273, the nano-agglomerate of Li_2S_8 is in closer agreement with experiment than the isolated Li_2S_8 molecule. In particular, the separation between the pre-edge and main-edge peaks (labeled 'a' and 'b') is significant in the isolated molecule but absent in the Li_2S_8 solid and experiment. This result connects the experimental and computational spectra. Ongoing work involves understanding the physical basis of the observed differences in the isolated molecule and nano-agglomerates and quantifying this effect in other Li_2S_x species.

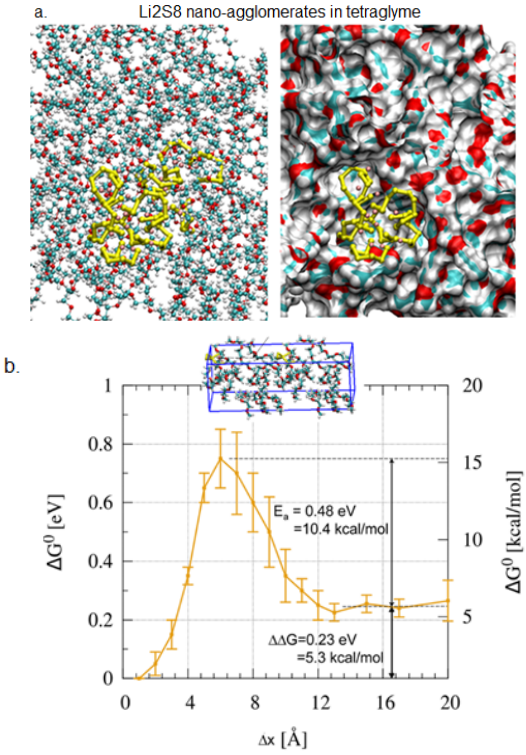

Figure VI - 272: (a) Example of equilibrium structure of Li_2S_8 dissolved in tetraglyme from classical molecular dynamics simulations showing nano-aggregation. (b) Free energy *ab initio* molecular dynamics simulations of the association of 2 Li_2S_8 molecules in tetraglyme. This study reveals a 10.4 kcal/mol barrier for nano-agglomeration of Li_2S_8

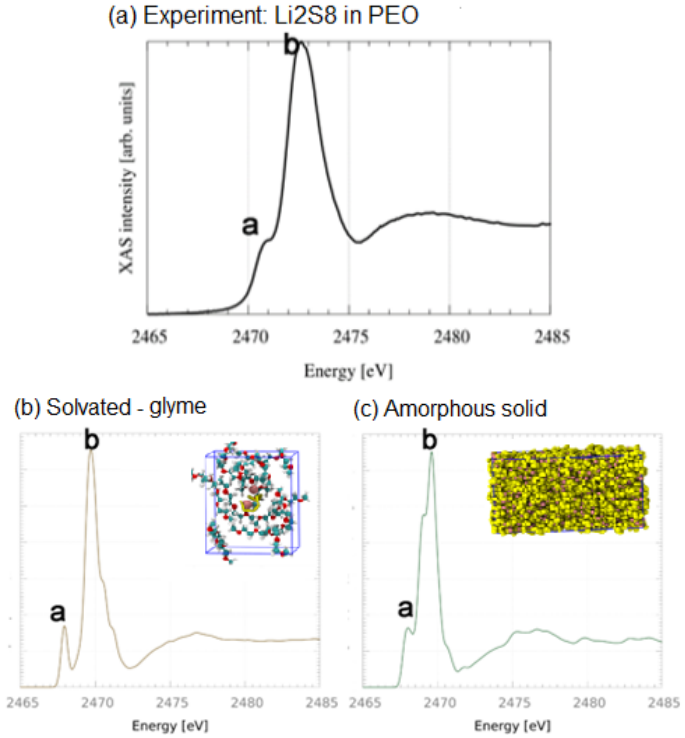

Figure VI - 273: Li_2S_8 XAS Sulfur K-edge spectra from (a) experimental measurements (b) theoretical calculations of the isolated molecule in tetraglyme (c) theoretical calculations of the amorphous solid as a model of the nano-agglomerates. The pre-edge 'a' and main edge 'b' peak are labeled

XAS spectroscopy of Li_2S_x intermediates. Experimental X-ray signatures were obtained for Li_2S_x (x = 2, 4, 6, 8) dissolved in PEO and SEO. Samples were spin-cast solid-state thin films having a sulfur concentration of 30 wt%. XAS measurements were taken at the sulfur K-edge. Resulting spectra are shown in Figure VI - 274.

The set of Li_2S_x spectra displayed three spectral features: a pre-edge peak at 2471.0 eV (attributable to anionic sulfur chain ends), a main-edge peak at 2472.7 eV (as typically found in S—S covalent bonds), and a broad peak from 2475-2485 eV (related to S—S bond length). The main-edge peak grows in intensity as polysulfide chain length increases, while the pre-edge peak decreases. This agrees with what would be expected, qualitatively, given the increasing ratio of S—S covalent bonds to anionic sulfur chain ends as polysulfide chain length increases. This trend was also seen in theoretical Li_2S_x X-ray spectra, as shown in Figure VI - 275.

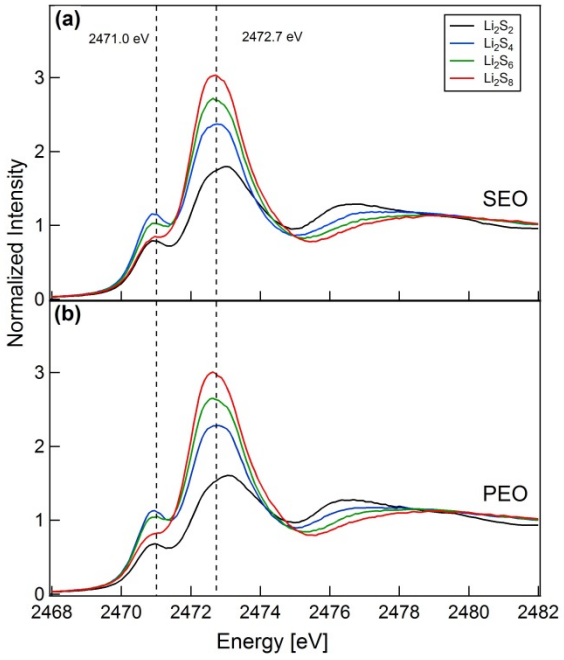

Figure VI - 274: XAS sulfur K-edge spectra of Li_2S_x dissolved in: (a) SEO, and (b) PEO

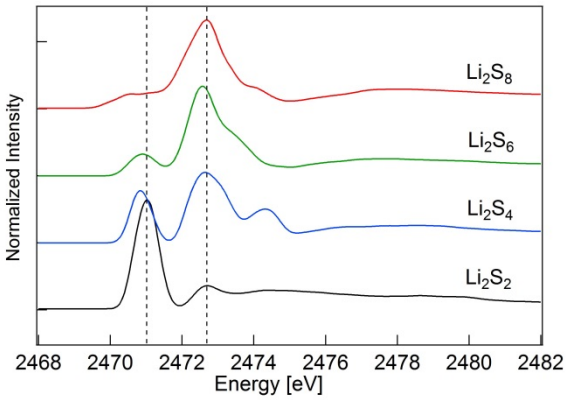

Figure VI - 275: Theoretical Li_2S_x spectra of Li_2S_x amorphous solids.

Li_2S_x speciation is complicated by the fact that Li_2S_x molecules may disproportionate in solution. While above, spectra were labeled with a given Li_2S_x 'x' value, 'x' is an average value, and a distribution of Li_2S_x species may be present in each system. For this reason, a principal component analysis (PCA) was performed on the system of Li_2S_x spectra in attempt to deconvolute the spectra into spectra of individual mixture components. The PCA analysis revealed that the system of spectra could be represented by three unique components.

An iterative target factor analysis (ITFA) was then performed to convert abstract components generated by the PCA into spectra. Through linear combination, these components were then used to recreate experimental X-ray spectra. Component weightings needed to recreate each experimental spectrum were determined and are plotted in the ternary diagram in Figure VI - 276.

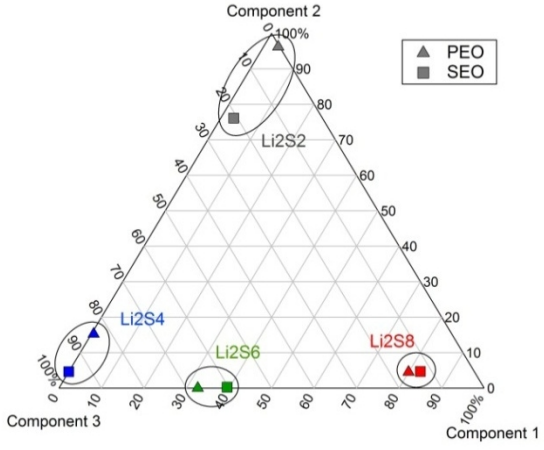

Figure VI - 276: Ternary diagram of individual PCA/ITFA generated spectra weightings needed to recreate experimental Li_2S_x spectra

An important note regarding PCA/ITFA is that it cannot identify spectra/components as being unique if they truly are, in reality, a linear combination of other spectra/components.

Li-S battery development for *in situ* XAS experiments. Li-S cells for *in situ* X-ray experiments have been designed. As a first step, Li-S cells with a more traditional design have been assembled to study both the cathode and electrolyte composition effect on performance, the polysulfide shuttle process, and interfaces. The addition of $LiNO_3$ to the electrolyte has led to improved performance; discharge capacity of 600 mAh/g sulfur has been observed after 15 cycles with an initial discharge at C/50 and subsequent charging/discharging at C/20, as shown in Figure VI - 277.

Conclusions and Future Directions

MD simulations of Li_2S_x molecules have been used in conjunction with experimental XAS of Li_2S_x species for: (a) elucidating Li-S battery chemistry, and (b) examining the fundamental nature of Li_2S_x/electrolyte systems. Simulations of Li_2S_x molecules in tetraglyme revealed that Li_2S_x molecules elect to form nano-agglomerates. Theoretical XAS spectra were obtained using XCH methods. When compared to experimental Li_2S_x spectra, theoretical spectra suggest that Li_2S_x molecules form nano-agglomerates in experimental Li_2S_x/PEO systems as well. Experimental XAS sulfur K-edge spectra were obtained for Li_2S_x (x = 2, 4, 6, 8) in PEO an SEO. PCA/ITFA was used to determine that the Li_2S_x systems may be comprised of three unique components. Weightings of each component needed to recreate experimental Li_2S_x/polymer system were determined. Cells for *in situ* XAS studies of Li-S battery cathodes during charging/discharging were assembled. Preliminary analysis has revealed that $LiNO_3$ increases specific capacity and efficiency of Li-S cells.

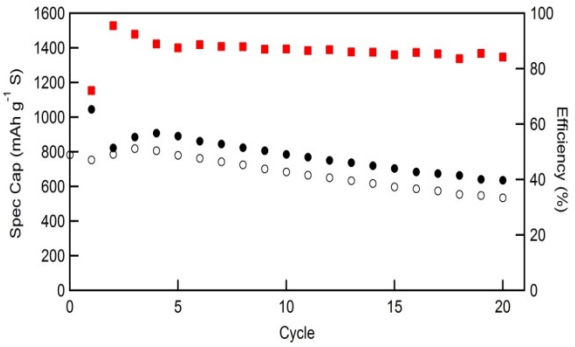

Figure VI - 277: Li-S battery specific charge (full symbol) and discharge (open symbol) capacities at 90°C as a function of the cycle number. The efficiency for each cycle is indicated on the right Y-axis. The electrolyte and the cathode are made of SEO/LiTFSI(r=0.05)/$LiNO_3$(r=0.025) and Li_2S_8/SEO-LITFSI/Carbone (70/25/15$_{wt}$%), respectively

Simulation work is now focused on: accessing the free energy of association barriers for all other Li_2S_x species, accessing the role of solid lithium sulfide interfaces on the agglomeration barrier, and the development of a semi-classical forcefield to investigate Li_2S_x inter-conversion and speciation. Experimental spectroscopy will focus on elucidating the Li-S battery reaction mechanisms by performing *in situ* XAS experiments during charge/discharge. Already obtained Li_2S_x spectra will be used to interpret *in situ* spectra.

FY 2013 Publications/Presentations

1. N.P. Balsara, "Polymer Electrolytes for Advanced Lithium Batteries," *2013 DOE Annual Merit Review*, May 2013, Washington, DC.

VI.G.11 Lithium Batteries of Higher Capacity and Voltage (UT Austin)

John B. Goodenough
The University of Texas at Austin

Department of Mechanical Engineering
204 East Dean Keeton
C2201, ETC 9.184
Austin, TX 78712
Phone: (512) 471-1646; Fax: (512) 471-7681
E-mail: jgoodenough@mail.utexas.edu

Start Date: January 2013
Projected End Date: December 2016

Objectives

- To increase cell voltage by:
  - enabling use of a lithium anode and,
  - allowing use of a liquid catholyte compatible with higher-voltage cathodes.
- To increase capacity by:
  - the elimination of the irreversible loss of Li from the cathode on first charge and,
  - the introduction of cathode strategies other than insertion-compound hosts.

Technical Barriers

Technical problems in developing a hybrid redox flow battery with an aqueous catholyte and a thin garnet membrane as a separator turned out to be high interfacial Li^+-transfer impedance and chemical stability of the garnet pellet in water. Moreover, the ceramic membrane is brittle and not scalable to be used in a large-scale energy storage system. Therefore, a new type of Li^+-ion conducting membrane is required to overcome the problems of the ceramic electrolyte membrane. A polymer/ceramic composite membrane has been developed in UT Austin. New sets of problems have been identified in the new approach, and novel solutions were required to use the membrane for an electrochemical cell.

Technical Targets

- Identify solid Li^+ electrolytes stable on contact with Lithium and having $\sigma_{Li} > 10^{-4}$ S cm^{-1},
- Test their stability in various liquids: aqueous of different pH, organic, oxidative,
- Fabricate as a thin, durable membrane or coating, and,
- Test performance of single cells.

Accomplishments

- Obtained $\sigma_{Li} > 5 \times 10^{-4}$ S/cm with an oxide garnet framework stable versus Li^0, but with a high Li^+-transfer impedance across its interface.
- Prepared robust Al_2O_3/PEO composite membrane with $\sigma_{Li} \approx 10^{-3}$ S/cm.
- Shown little crossover of Al_2O_3/PEO by 6-bromohexyl ferrocene redox molecule.
- Stabilized osmosis of liquid electrolyte across Al_2O_3/PEO membrane.
- Reduced absorption of anolyte into membrane by introducing gel PVdF-HFP (hexa fluoropropene) polymer electrolyte between Li^0 and membrane.

✧ ✧ ✧ ✧ ✧

Introduction

UT Austin proposed to develop a solid Li^+-electrolyte separator that could block dendrites from a metallic lithium or sodium anode and allow the development of alternative cathode strategies. Two strategies were pursued: (a) development of the garnet $Li_{7-x}Zr_{2-x}Ta_xLa_3O_{12}$ as a solid that would allow a dual-electrolyte cell and (b) development of a flexible, mechanically robust Al_2O_3/PEO-polymer composite membrane that would block dendrites from an anode and allow a flow-through liquid cathode of high voltage for a high capacity battery. Although a Li-ion conductivity $\sigma_{Li} \geq 5 \times 10^{-4}$ S/cm was obtained for a bulk garnet, the oxide ions of the garnet structure proved to be too weakly bound by the garnet cations; the surface oxygen were attacked by Na from the furnace and Li was leached out on exposure to air to form Li_2CO_3 and Li_2O, on the surface, thus blocking Li transport across the garnet/liquid-electrolyte interface. Therefore, effort was concentrated on the porous Al_2O_3/PEO-polymer electrolyte which restricts the battery to a single liquid electrolyte. With this membrane, three of the four objectives of the proposal were realized.

Approach

UT Austin has experience developing solid state Li^+-ion conducting materials, especially the garnet-

structured ceramics. The thin garnet pellets have been tested to be used in various electrochemical cells.

In parallel, a polymer composite membrane has been studied to make a thin, flexible, and mechanically robust Li^+-ion conducting separator. A PEO/Al_2O_3 composite membrane has been developed to block metal (lithium and sodium) dendrite penetration through the membrane. A PEDOT:PSS (polystyrene sulfonate)-coated polypropylene (PP) separator has been developed to block the redox molecule crossover.

Results

Garnet-type solid electrolytes for electrochemical cells. A garnet-structured solid electrolyte, $Li_{7-x}La_3Zr_{2-x}Ta_xO_{12}$ (x=0.6) was synthesized via a solid-state reaction method. It showed a Li^+-ion conductivity of ~ 5 × 10^{-4} S/cm. A garnet pellet with a thickness of ~ 300 μm was used as a solid electrolyte and combined with a lithium metal electrode to check its electrochemical properties. The Li/garnet interface showed a very high electrochemical impedance (> 10,000 Ω), which hindered Li^+-ion transport through the interface. Since the origin of the high impedance is not clear, the surface chemistry of the garnet electrolyte and interface barriers should be responsible for that problem and will be further investigated.

PEO/Al_2O_3 composite membrane. A flexible PEO/Al_2O_3 (2/1 in weight) composite membrane has been developed as a solid electrolyte layer for a dual-electrolyte cell (see Figure VI - 278). The Al_2O_3 particles in the membrane are used to enhance the mechanical stability and to block lithium dendrite.

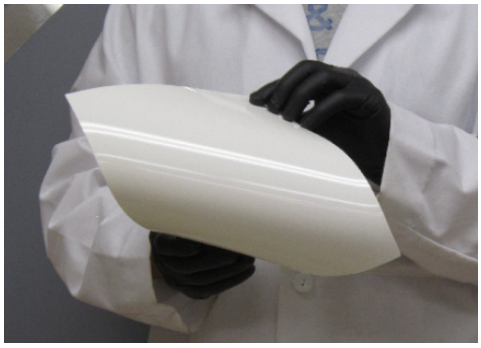

Figure VI - 278: A 68-72 membrane

The membrane was soaked with 1M LiTFSI in EC/DEC (1/1) electrolyte prior to electrochemical tests. Charging a Li|PEO/Al_2O_3(2/1)|Li symmetric cell has demonstrated that the lithium dendrite cannot penetrate the membrane. Cycling performance of Li|PEO/Al_2O_3(2/1)|Catholyte dual-electrolyte cell depends on the catholyte crossover and the osmotic pressure across the membrane. A redox molecule, 6-Bromohexyl ferrocene was used in the catholyte. After cycling, the crossover of the redox molecule has been identified by color change of the membrane. Controlling polymer structure was not successful enough to block the crossover, which initiated an extra activity to develop an electronic/ionic mixed conducting membrane. Another issue after cycling is the presence of the osmotic pressure across the membrane because it is semi-permeable to the Li^+-ion electrolyte, not to the big redox molecule. Higher concentration of the catholyte induced electrolyte transfer from the anode side, so the anode side was dried up at the end of cycles. It also affected the cell performance: a continuous increase in the cell polarization and drop in capacity were observed (see Figure VI - 279).

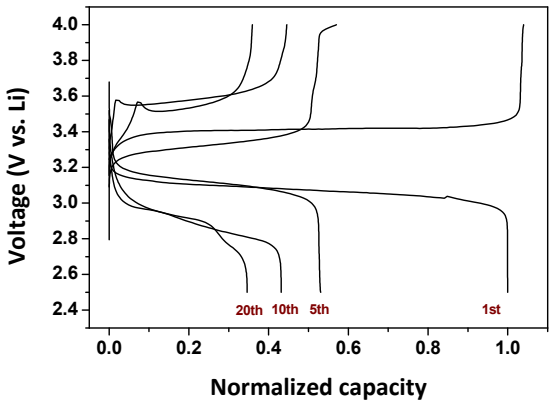

Figure VI - 279: Charge/discharge voltage curves of Li|PEO/Al_2O_3| 6-Bromohexyl ferrocene catholyte cell. Base electrolyte is 1M LiTFSI in EC/DEC (1/1)

The first approach to solve the issue was to balance the concentrations of anolyte and catholyte. A high molecular weight ionic liquid or soluble polymer could stabilize the cyclability and the polarization notably by inducing a dynamic equilibrium between catholyte and anolyte.

PEDOT:PSS-coated PP separator. An electronic/ionic mixed conducting membrane was tested as an additional layer to the PEO/Al_2O_3 membrane to block crossover while ensuring Li^+-ion transfer between cathode and anode.

First, amorphous vanadium oxide (VO_x) was coated on a commercial battery separator (Celgard 2500) by a drop casting method. However, a thin VO_x film was immediately detached from the separator after wetting with catholyte. When the film got thicker, cell impedance greatly increased. It was suggested that to form a thin Li^+-ion-conductive film with good adhesion to the separator was necessary.

Second, a conducting polymer, PEDOT:PSS, was spin-coated on the PP separator. Concentration of the polymer solution and spinning speed were controlled to form a thin and uniform film without any macro-/micro-holes. A defect-free film was introduced between

electrodes to block the crossover of 6-bromohexyl ferrocene molecule from the catholyte. With this approach, stable charge/discharge cycle performance was achieved without a capacity fade over 50 cycles (see Figure VI - 280).

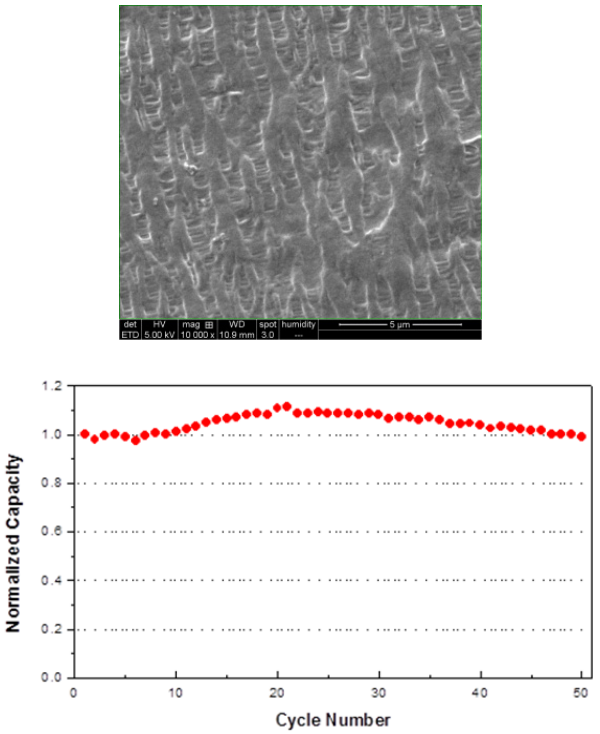

Figure VI - 280: SEM image of a PEDOT:PSS-coated polypropylene separator and its electrochemical cycle performance of a Li/PVDF-HFP|PEO/Al_2O_3(2/1)|PEDOT:PSS/PP|6-bromohexyl ferrocene cell. Base electrolyte is 1M LiTFSI in EC/DEC (1/1) and the spectator molecule in anolyte is PEGDME (M.W. 500)

Conclusions and Future Directions

The development of a flexible, thin Al_2O_3/PEO-polymer membrane that allows penetration of a liquid electrolyte has been shown to block dendrites from a metallic lithium and also a sodium anode. This development allows safe use of a metallic anode and assembly of a charged cell rather than a discharged cell. As a result, a greater cell voltage and a greater capacity can be achieved for a given insertion-compound cathode since it eliminates loss of anode voltage and the loss of cathode capacity by formation of a Li-permeable SEI layer on the anode on the initial charge.

In order to develop the possibility of a redox flow-through liquid cathode, two problems were overcome: first, the problem of osmosis driving the liquid electrolyte from the anode to the cathode side of the membrane and, second, the development of a surface layer on the cathode side of the membrane that blocks crossover of the cathode redox molecule to the anode. Both of these problems were successfully solved.

Future work involves optimizing the composition, pore size, and thickness of an oxide/polymer composite membrane and development of alternative solid coatings on the surface of the Al_2O_3/polymer membrane that will allow realization of a dual liquid-electrolyte cell. In particular, the development of a solid that will block the small Li_2S_2 soluble molecules from the sulfur cathode of a Li-S cell and will also enable an aqueous catholyte for realization of a Li-air cell. Meanwhile, tests will continue for the membrane in a Na/cyano-perovskite cell that has a voltage of about 3.4 V to give a commercially viable Na-S cell.

FY 2013 Publications/Presentations

1. Park, K.-S., Cho, J.H., Kadhiravan, S., Ellison, C.J., and Goodenough, J.B., "Chemical and ElectroChemical Properties of a Dual Electrolyte Cell Employing a Solid Electrolyte Membrane for Large Scale Energy Storage," *2013 ECS Fall Meeting* Presentation.
2. Lu, Y., Wang, L., Song, J., Zhang, D.W., Xu, M., and Goodenough, J.B., "Aluminium-Stabilized NASICON-Structured $Li_3V_2(PO_4)_3$," *J. Mater. Chem.*, **1,** 68-72 (2013).

Appendix A: List of Contributors and Collaborators

Contributor/ Collaborator	Affiliation	FY 2013 Annual Progress Report Section(s)
Abouimrane, Ali	Argonne National Laboratory	V.C.1, V.C.6, V.C.3, VI.G.1
Abraham, Daniel P.	Argonne National Laboratory	V.B.2, V.B.3, V.C.1, V.C.2, V.C.5, V.C.6, V.E.4
Ahmed, Shabbir	Argonne National Laboratory	IV.A.1
Alamgir, Mohamed	LG Chem Power, Inc.	III.A.5, V.D.4
Allen, Jan	U.S. Army Research Laboratory	V.D.1
Allen, Joshua	U.S. Army Research Laboratory	V.D.1
Allu, S.	Oak Ridge National Laboratory	IV.C.2
Amine, Khalil	Argonne National Laboratory	V.C.1, V.C.3, VI.D.1, VI.G.1, VI.G.2, VI.G.4
Anderson, Travis M.	Sandia National Laboratories	V.D.8
Andrews, Joy	Stanford Synchrotron Radiation Lightsource	VI.B.6
Angell, C. Austen	Arizona State University	VI.D.2
Armstrong, Beth	Oak Ridge National Laboratory	V.E.2
Arnold, John	Miltec UV International, LLC	III.C.2, V.E.1
Arsenault, Renata	USABC Program Manager	III.A.4
Ashton, Clair K.	Idaho National Laboratory	IV.B.3
Averill, William A.	Sandia National Laboratories	IV.B.4
Bae, Chulheung	USABC Program Manager	III.A.3, III.A.8, IV.A.7
Balasubramanian, Mahalingam	Argonne National Laboratory	V.C.1, V.C.4, V.C.5, VI.B.1, VI.F.1
Balbuena, Perla	Texas A&M University	VI.C.12
Balsara, Nitash	University of California, Berkeley	VI.G.10, VI.G.3
Ban, Chunmei	National Renewable Energy Laboratory	V.C.6, V.D.4, VI.C.7
Banas, James	JSR Micro	V.E.2
Bareño, Javier	Argonne National Laboratory	V.B.6
Barsoum, Michel W.	Drexel University	VI.C.3
Basco, John	Argonne National Laboratory	IV.B.1
Battaglia, Vincent	Lawrence Berkeley National Laboratory	V.B.4, VI.E.5, VI.E.6, VI.G.3, VI.G.4
Bedzyk, Michael	Northwestern University	VI.F.1
Belharouak, Ilias	Argonne National Laboratory	V.C.1, V.C.6, V.C.3

Contributor/ Collaborator	Affiliation	FY 2013 Annual Progress Report Section(s)
Bender, Guido	National Renewable Energy Laboratory	V.E.4
Benedek, Roy	Argonne National Laboratory	V.C.1, VI.B.1
Bennett, Taylor L.	Idaho National Laboratory	IV.B.3
Bettge, Martin	Argonne National Laboratory	V.B.3, V.C.2, V.C.5, V.C.6
Bewley, Randy L.	Idaho National Laboratory	IV.B.3
Billings, J.	Oak Ridge National Laboratory	IV.C.2
Bloom, Ira D.	Argonne National Laboratory	IV.A.1, IV.B.1, IV.B.2, IV.B.4, V.B.6, V.C.1, V.C.2, V.C.6, V.C.3
Borodin, Oleg	U.S. Army Research Laboratory	V.D.1
Brodie, Brad	DENSO International America, Inc.	III.B.7
Brooker, Aaron	National Renewable Energy Laboratory	IV.A.2, IV.A.7
Buechler, Karen	ALD Nanosolutions	V.D.4
Bugga, Kumar	Jet Propulsion Laboratory	V.B.1
Burba, John	Princess Energy Systems	V.D.3
Burke, Andy	University of California, Davis	IV.A.3
Burrell, Anthony K.	Argonne National Laboratory	V.C.1, V.C.6
Cabana, Jordi	University of Illinois at Chicago	VI.B.5, VI.F.7, VI.G.3
Callendar, Andrew	Tennessee Technical University	VI.B.6
Carlson, Steven A.	Optodot Corporation	III.C.4
Ceder, Gerbrand	Massachusetts Institute of Technology	VI.E.7
Chan, Kwai S.	Southwest Research Institute	VI.C.11
Chen, Guoying	Lawrence Berkeley National Laboratory	V.D.7, VI.B.4, VI.G.3
Chen, Xiao	Northwestern University	VI.F.1
Chen, Zonghai	Argonne National Laboratory	V.C.1, V.C.3
Chiang, Yet-Ming	Massachusetts Institute of Technology	VI.E.8
Christophersen, Jon P.	Idaho National Laboratory	IV.B.2, IV.B.3, IV.B.4
Cresce, Arthur von_Wald	U.S. Army Research Laboratory	V.D.1
Croy, Jason R.	Argonne National Laboratory	V.C.4, V.C.5, V.E.4, V.C.3, VI.B.1, VI.F.1
Cui, Yi	Stanford University.	VI.C.10
Cunningham, Brian	U.S. Department of Energy	III.E, IV
Curtiss, Larry	Argonne National Laboratory	VI.D.1, VI.G.2
Daniel, Claus	Oak Ridge National Laboratory	V.C.1, V.C.4, V.E.1, V.E.2, V.E.4
David, Bill	Rutherford Appleton Laboratory	VI.F.1

Contributor/ Collaborator	Affiliation	FY 2013 Annual Progress Report Section(s)
Dees, Dennis W.	Argonne National Laboratory	IV.A.1, V.B.3, V.C.1, V.C.2, V.C.5
Delp, Samuel	U.S. Army Research Laboratory	V.D.1
Deppe, John B.	Deppe Consulting	I, II, III, IV, V, VI
Deveney, Bridget	Saft America, Inc.	VI.G.4
Dietz-Rago, Nancy	Argonne National Laboratory	V.B.6
Dinwiddie, Ralph	Oak Ridge National Laboratory	V.E.4
Doeff, Marca	Lawrence Berkeley National Laboratory	VI.B.3, VI.G.3
Dogan, Fulya	Argonne National Laboratory	V.C.4
Drews, Andy	Ford	VI.B.6
Dudney, Nancy	Oak Ridge National Laboratory	V.C.6, VI.G.6
Dufek, Eric J.	Idaho National Laboratory	V.D.3
Duffield, Michael	Saft	III.A.7
Dunn, Jennifer	Argonne National Laboratory	IV.A.5, IV.A.6
Duong, Tien Q.	U.S. Department of Energy	VI
Dzwiniel, Trevor	Argonne National Laboratory	V.B.2
Eggers, William	Bio-logic USA	V.E.1
Eitouni, Hany	Seeo, Inc.	III.B.5
Elam, Jeffrey W.	Argonne National Laboratory	V.C.6
Elder, R.	Chrysler	IV.A.7
Elwasif, W.	Oak Ridge National Laboratory	IV.C.2
Evans, Michael C.	Idaho National Laboratory	IV.B.3
Ewen, Mark	ConocoPhillips	V.E.2, V.E.4
Faguy, Peter W.	U.S. Department of Energy	V
Fenter, Paul	Argonne National Laboratory	VI.F.1
Fenton, Kyle R.	Sandia National Laboratories	V.B.5, V.D.8
Feridun, Ozgenur K.	Argonne National Laboratory	V.B.1
Ferry, Mike	California Center for Sustainable Energy	IV.A.3
Fister, Tim	Argonne National Laboratory	VI.F.1
Forbes, Jerry	Frontier Industrial Technology	V.E.1, V.E.4
Gaines, Linda	Argonne National Laboratory	IV.A.6
Gallagher, Kevin G.	Argonne National Laboratory	IV.A.1, V.B.3, V.C.1, V.C.2, V.C.5, V.E.4, VI.B.1
Garcia-Ontiveros, Javier Bareno	Argonne National Laboratory	V.C.1

Contributor/ Collaborator	Affiliation	FY 2013 Annual Progress Report Section(s)
George, Steve M.	University of Colorado, Boulder	V.B.5, VI.C.7
Gering, Kevin L.	Idaho National Laboratory	V.B.5, V.D.3
Gogotsi, Yury	Drexel University	VI.C.3
Goodenough, John B.	University of Texas at Austin	VI.G.11
Grey, Clare	Cambridge University	VI.F.6
Groshek, Paul	USABC Program Manager	III.A.5
Halalay, Ion	USABC Program Manager	III.A.9
Hamilton, Jason	Scientific Climate Systems	V.E.1
Han, Taeyoung	General Motors LLC	IV.C.3
Harrup, Mason K.	Idaho National Laboratory	V.D.3
Hartridge, Steve	CD-adapco, New York	IV.C.4
Henderson, Wesley	North Carolina State University	V.B.2
Hendricks, Christopher E.	University of Maryland, College Park	IV.B.2
Hickner, Michael A.	Pennsylvania State University	VI.C.8
Ho, Chinh D.	Idaho National Laboratory	IV.B.2, IV.B.3
Holmes, John	San Diego Gas & Electric	IV.A.3
Howell, David	U.S. Department of Energy	I, II, III
Hubaud, Aude	Argonne National Laboratory	VI.G.3
Huq, Ashfia	Oak Ridge National Laboratory	V.C.4, V.E.1
Iddir, Hakim	Argonne National Laboratory	V.C.1
Ingram, Brian	Argonne National Laboratory	V.C.1, VI.G.3
Jamison, David K.	Idaho National Laboratory	V.D.3
Jansen, Andrew N.	Argonne National Laboratory	V.B.3, V.E.1, V.E.2
Jeka, Gerald	Argonne National Laboratory	V.B.1
Johnson, Christopher	NETL Program Manager	III.B.6, III.B.7, III.C.1, III.D.3
Johnson, Christopher	Argonne National Laboratory	VI.B.1, V.C.1, V.C.3
Jorgensen, Scott	USABC Program Manager	III.A.6
Jow, Richard	U.S. Army Research Laboratory	V.D.1
Judes, Avie	Johnson Controls Inc.	III.A.4
Juzkow, Marc	Leyden Energy, Inc.	III.A.8
Kalhammer, Fritz	Electric Power Research Institute	IV.A.1
Kalnaus, S.	Oak Ridge National Laboratory	IV.C.2
Kepler, Keith	Farasis Energy, Inc.	III.A.2

Contributor/ Collaborator	Affiliation	FY 2013 Annual Progress Report Section(s)
Kercher, Andrew	Oak Ridge National Laboratory	VI.B.7
Kerr, John B.	Lawrence Berkeley National Laboratory	VI.D.4, VI.G.3
Key, Baris	Argonne National Laboratory	V.C.4
Keyser, Matt	National Renewable Energy Laboratory	IV.B.5, IV.B.6
Kiggans, Jim	Oak Ridge National Laboratory	VI.B.7
Kim, D.	Argonne National Laboratory	VI.B.1
Kim, Gi-Heon	National Renewable Energy Laboratory	IV.C.1, IV.C.3, IV.C.6, IV.C.7
King, David	ALD Nanosolutions	V.D.4
Kostecki, Robert	Lawrence Berkeley National Laboratory	V.D.5, VI.F.3, VI.G.3
Kras, Mike	Argonne National Laboratory	V.B.1
Krumdick, Gregory K.	Argonne National Laboratory	V.B.1, V.B.2
Kubal, Joseph J.	Argonne National Laboratory	V.B.3
Kumar, Bijayemdra	Energetics, Inc.	I, II, III,IV, V, VI
Kumta, Prashant N.	University of Pittsburgh	VI.C.14, VI.C.6
Lamb, Josh	Sandia National Laboratories	IV.B.4, V.B.5
Lee, Eungje	Argonne National Laboratory	V.C.3
Lee, Se-Hee	University of Colorado, Boulder	VI.C.7
Li, Jianlin	Oak Ridge National Laboratory	V.C.1, V.C.4, V.E.1, V.E.2, V.E.4
Li, Yan	Argonne National Laboratory	V.B.3, V.C.2, V.C.3
Liang, Chengdu	Oak Ridge National Laboratory	VI.G.5
Lin, Chi-Kai	Argonne National Laboratory	V.C.3
Liu, Gao	Lawrence Berkeley National Laboratory	V.B.2, VI.C.5, VI.G.3, VI.G.4
Liu, Jun	Pacific Northwest National Laboratory	VI.C.9, VI.G.8
Liu, Yijin	Stanford Synchrotron Radiation Lightsource	VI.B.6
Long, Brandon R.	Argonne National Laboratory	V.C.3, VI.F.1
Looney, Patrick	Brookhaven National Laboratory	VI.B.2
Lopatin, Sergey	Applied Materials, Inc.	III.C.3
Lopez, Herman A.	Envia Systems	III.A.1
Lu, Jun	Argonne National Laboratory	VI.G.2
Lu, Wenquan	Argonne National Laboratory	IV.A.1, V.B.1, V.B.2, V.B.3, V.C.1, V.C.2, V.C.5, V.C.6
Lucht, Brett	University of Rhode Island	VI.D.5
Lytle, Gregg	Solvay Specialty Polymers	V.E.2

Contributor/ Collaborator	Affiliation	FY 2013 Annual Progress Report Section(s)
Mainstone, Derek	Conquip	V.E.1
Manivannan, Ayyakkannu	National Energy Technology Laboratory	VI.C.6
Manthiram, Arumugam	University of Texas at Austin	VI.B.10
Martha, Surendra	Oak Ridge National Laboratory	VI.B.6
Maxey, Curt	Oak Ridge National Laboratory	V.E.4
Mazzeo, Brian	Brigham Young University	VI.E.1
McDonald, Joe	U.S. Environmental Protection Agency	IV.A.1
Meng, Xiangbo	Argonne National Laboratory	V.C.6
Meng, Ying Shirley	University of California San Diego	VI.B.9
Michelbacher, Christopher J.	Idaho National Laboratory	IV.B.3
Mikhaylik, Yuriy	Sion Power Corporation	III.D.1
Miller, Dean	Argonne National Laboratory	V.C.1, VI.F.1
Miller, Michael A.	Southwest Research Institute	VI.C.11
Mixer, Bruce	NETL Program Manager	III.B.1, III.B.5, III.D.2
Mohanty, Debasish	Oak Ridge National Laboratory	V.C.1, V.C.4, V.E.1, V.E.4
Morrison, John L.	Montana Tech	IV.B.2
Morrison, William H.	Montana Tech	IV.B.2
Nagasubramanian, Ganesan	Sandia National Laboratories	V.B.5, V.D.8
Nagubandi, Ram	Binrad Industries	V.D.8
Nam, Kyung-Wan	Brookhaven National Laboratory	V.D.6, VI.F.2
Nanda, Jagjit	Oak Ridge National Laboratory	V.C.6, VI.B.6
Nelson, Paul A.	Argonne National Laboratory	IV.A.1
Neubauer, Jeremy	National Renewable Energy Laboratory	IV.A.2, IV.A.3, IV.A.7
Nine, Ralph	NETL Program Manager	III.B.2
O'Driscoll, Erin	Dow Kokam, LLC	III.B.2, V.E.2, V.E.4
Orendorff, Christopher J.	Sandia National Laboratories	IV.B.4, V.B.5, V.D.8, V.E.1, V.E.2
Pannala, S.	Oak Ridge National Laboratory	IV.C.1, IV.C.2
Park, Kyungjin	SK Innovation	III.A.3
Payzant, Andrew	Oak Ridge National Laboratory	V.C.4, V.E.1
Pekala, Richard W.	ENTEK Membranes LLC	III.A.9
Persson, Kristin	Lawrence Berkeley National Laboratoty.	VI.E.4
Pesaran, Ahmad	National Renewable Energy Laboratory	IV.A.2, IV.A.7, IV.B.4, IV.C.1, V.D.4
Pol, S. V.	Argonne National Laboratory	VI.B.1

Contributor/ Collaborator	Affiliation	FY 2013 Annual Progress Report Section(s)
Pol, V. G.	Argonne National Laboratory	VI.B.1
Polzin, Bryant J.	Argonne National Laboratory	V.E.2, V.B.1, V.B.3, V.E.1
Prendergast, David	Lawrence Berkeley National Laboratory	VI.G.10
Prezas, Panos	Argonne National Laboratory	IV.B.1
Privette, Rob	XG Sciences	V.B.5
Protasiewicz, John	Case Western Reserve University	VI.D.3
Pupek, Krzysztof (Kris)	Argonne National Laboratory	V.B.2
Qi, Yue	Michigan State University	VI.C.4
Rajagopalan, Satish	Electric Power Research Institute	IV.A.1
Reilly, Frank	Ceres Technologies	V.E.4
Ren, Yang	Argonne National Laboratory	V.C.1, VI.B.1
Richardson, Tom	Lawrence Berkeley National Laboratory	VI.G.3
Robertson, David	Argonne National Laboratory	IV.B.1
Rollins, Harry W.	Idaho National Laboratory	V.D.3
Ross, Philip	Lawrence Berkeley National Laboratory	VI.C.13
Rousseau, Aymeric	Argonne National Laboratory	IV.A.1, IV.A.5
Safa-Sefat, Athena	Oak Ridge National Laboratory	V.E.1
Santhanagopalan, Shriram	National Renewable Energy Laboratory	IV.B.5, IV.C.1, IV.C.5, IV.C.7, V.D.4
Santini, Danilo J.	Argonne National Laboratory	IV.A.1, IV.A.5
Sazhin, Sergiy V.	Idaho National Laboratory	IV.B.2, V.D.3
Schafer, Ben	Espec America	V.E.1
Scherson, Daniel	Case Western Reserve University	V.B.2, VI.D.3
Schroeder, D.	Northern Illinois University	VI.G.3
Sefa-Safat, Athena	Oak Ridge National Laboratory	V.C.4
Seminario, Jorge	Texas A&M University	VI.C.12
Shaffer, Chrisitan E.	EC Power	IV.C.5
Shin, YoungHo	Argonne National Laboratory	V.B.1
Shirk, Matthew G.	Idaho National Laboratory	IV.B.3
Simunovic, S.	Oak Ridge National Laboratory	IV.C.2
Singh, Jagat D.	3M Company	III.B.4
Slater, Michael D.	Argonne National Laboratory	V.C.3
Smart, Marshall C.	Jet Propulsion Laboratory	V.D.2
Smith, Kandler	National Renewable Energy Laboratory	IV.A.2, IV.A.4, IV.C.1, IV.C.4

Contributor/ Collaborator	Affiliation	FY 2013 Annual Progress Report Section(s)
Somorjai, Gabor	University of California, Berkeley	VI.C.13
Son, YK	Johnson Controls	III.C.1
Spotnitz, Robert	Battery Design, LLC	IV.C.4
Srinivasan, Venkat	Lawrence Berkeley National Laboratory	VI.E.3, VI.G.4
Sriramulu, Suresh	TIAX LLC	III.D.3
Steele, Leigh_Anna M.	Sandia National Laboratories	IV.B.4
Stefan, Ionel	Amprius	III.B.1
Stewart, Fred F.	Idaho National Laboratory	V.D.3
Stoneberg, Allen	Maxwell Technologies, Inc.	III.A.6
Stringfellow, Richard	TIAX LLC	III.D.3
Suchomel, Matthew	Argonne National Laboratory	VI.F.1
Tabacchi, John	NETL Program Manager	III.B.3, III.B.4, III.C.2, III.C.3, III.C.4, III.D.1
Tataria, Harshad	USABC Program Manager	III.A.2, IV.A.7, III.A.1, III.A.7
Telep, David	Dow Kokam	V.E.2, V.E.4
Tenent, Robert	National Renewable Energy Laboratory	V.B.5, V.C.6, V.E.1, V.E.3
Thackeray, Michael M.	Argonne National Laboratory	V.C.1, V.C.5, VI.B.1, V.C.3, VI.F.1
Thomas, Ed	Sandia National Laboratories	IV.B.2
Tomsia, Antoni P.	Lawrence Berkeley National Laboratory	VI.E.8
Trahey, Lynn	Argonne National Laboratory	V.C.1, V.C.6
Trask, Stephen E.	Argonne National Laboratory	V.B.3
Turner, John A.	Oak Ridge National Laboratory	IV.C.1, IV.C.2
Ulsh, Michael	National Renewable Energy Laboratory	V.E.4
Unocic, Raymond R.	Oak Ridge National Laboratory	VI.F.4
Vaughey, John T.	Argonne National Laboratory	V.C.1, V.C.4, VI.B.1, VI.C.1, VI.G.3
Velev, Omo	Aerovironment	IV.A.3
Vijayagopal, Ram	Argonne National Laboratory	IV.A.1
Voelker, Gary E.	Miltec UV International, LLC	III.C.2
Vu, Anh D.	Argonne National Laboratory	V.C.3
Walker, Lee	Argonne National Laboratory	IV.B.1
Wang, Chong-Min	Pacific Northwest National Laboratory	VI.F.5
Wang, Donghai	Pennsylvania State University	III.B.6, VI.C.8
Wang, Feng	Brookhaven National Laboratory	VI.B.2

Contributor/ Collaborator	Affiliation	FY 2013 Annual Progress Report Section(s)
Washom, Byron	University of California, San Diego	IV.A.3
Wheeler, Dean	Brigham Young University	VI.E.1
Whittingham, M. Stanley	State University of New York at Binghamton	VI.C.2
Williams, Brett	University of California, Berkeley	IV.A.3
Wixom, Mike	A123 Systems (now Navitas Systems)	V.E.2, V.E.4
Wood, E.	National Renewable Energy Laboratory	IV.A.7
Wood, Eric	National Renewable Energy Laboratory	IV.A.2
Wood III, David L.	Oak Ridge National Laboratory	V.C.1, V.C.4, V.E.1, V.E.2, V.E.4
Wu, Qingliu	Argonne National Laboratory	V.B.3, V.C.2, V.C.6
Xiao, Jie	Pacific Northwest National Laboratory	VI.B.8, VI.G.8
Xiao, Xingcheng	General Motors LLC	VI.C.4
Xu, Kang	Army Research Laboratory	V.B.2, V.D.1, VI.B.6
Xu, Wu	Pacific Northwest National Laboratory	VI.G.7, VI.G.9
Yakovleva, Marina	FMC Corporation	VI.G.4
Yang, Xiao-Qing	Brookhaven National Laboratory	V.D.6, VI.F.2
Zaghib, Karim	HydroQuebec - IREQ	VI.E.2
Zhang, Ji-Guang	Pacific Northwest National Laboratory	VI.B.8, VI.C.9, VI.G.7, VI.G.9
Zhang, Xiangwu	North Carolina State University	III.D.2
Zhang, Xiaofeng	Argonne National Laboratory	V.C.6
Zhang, Zhengcheng (John)	Argonne National Laboratory	V.B.2, VI.G.4
Zhou, Hui	Oak Ridge National Laboratory	VI.B.6
Zhu, Ye	Argonne National Laboratory	V.B.3, V.C.2
Zhu, Yimin	Nanosys, Inc.	III.B.3
Zorba, Vassilia	Lawrence Berkeley National Laboratory	VI.G.3

Appendix B: Acronyms

3M	Minnesota Mining and Manufacturing Company
AABC	Advanced Automotive Batteries Conference
AAO	Anodized aluminum oxide
AB	Acetylene black
ABA	Anion Binding Agent
ABAA	Advanced Lithium Batteries for Automotive Applications (Conference)
ABDT	ANSYS Battery Design Tool
ABR/ABRT	Applied Battery Research for Transportation
AC	Alternating Current
ACS	American Chemical Society
ADF-STEM	Annular dark film imaging - scanning transmission electron microscopy
ADP	Ammonium dihydrogen phosphate
AE	Available energy
AEES	Advanced Electrochemical Energy Symposium
AEM	Analytical electron microscopy
AER	All electric range
AEV	All-electric vehicle
AE-XRD	Acoustic emission (AE) and X-ray diffraction
AF	Antiferromagnetic
AFM	Atomic force microscopy
AGM	Absorbed Glass Mat
AIMD	Ab initio molecular dynamics
ALABC	Advanced Lead Acid Battery Consortium
ALD	Atomic layer deposition
ALS	Advance light source
AMO	Advanced Manufacturing Office
AMPED	Advanced management and protection of energy storage devices
AMR	Annual Merit Review
ANL	Argonne National Laboratory
AP-ALD	Atmospheric pressure atomic layer deposition
AP-CVD	Atmospheric pressure chemical vapor deposition
APQP	Advanced Product Quality Planning
APS	Advanced Photon Source
APXPS	Ambient-pressure XPS
ARC	Accelerated rate calorimetry
ARL	Army Research Laboratory
ARPA-E	Advanced Research Projects Agency - Energy
ARRA	American Recovery & Reinvestment Act
ARXS	Angle resolved X-ray spectroscopy
ASCS	Automotive Simulation Centre Stuttgart
ASI	Area-specific impedance

ASR	Area specific resistance
ASU	Arizona State University
ASWC	Automotive Simulatiuon World Congress
ATC	Aluminum tetrachloride
ATD	Advanced Technology Development
ATR	Attenuated total reflection
BAJ	Battery Institute of Japan
BATT	Batteries for Advanced Transportation Technologies
BCF	Binder and carbon free
BCLE	Battery Calendar Life Estimator
BCU	Battery control unit
BDOD	1,4-benzodiozane-6,7-diol
BDS	Battery Design Studio
BDU	Battery disconnect unit
BE	Band Excitation
BEC	Bussed Electrical Center
BECM	Battery Energy Control Module
BES	Basic Energy Sciences (DOE Office)
BET	Brunauer, Emmett, and Teller surface area
BEV	Battery electric vehicle
BL	Base-Line
BLE	Baseline electrolyte
BLM	Bureau of Land Management
BMF	Battery manufacturing facility
BMS	Battery management system
BMU	Battery management unit
BNL	Brookhaven National Laboratory
BOL	Beginning of life
BOM	Battery ownership model
BPSM	Battery Pack Sensor Module
BSF	Battery scaling factor
BTC	Battery Technology Center
BTFMSI	Bis(trifluoromethylsulfonyl)imide
BTM	Battery Thermal Management
BYU	Brigham Young university
CAD	Computer-aided Design
CAE	Computer-aided engineering
CAEBAT	Computer-aided engineering of batteries
CAFE	Corporate Average Fuel Economy (Standards)
CALPHAD	CALculation of PHAse Diagram
CAMP	Cell analysis, modeling, and prototyping facility
CATARC	China Automotive Technology and Research Center
CB	Carbon black
CCSE	California Center for Sustainable Energy
CD	Charge depleting

CE	Coulombic efficiency
CED	(U.S.-Canada) Clean Energy Dialogue
CEES	Center for Electrical Energy Storage
CEF	Cathode Energy Factor
CEI	Cathode electrolyte interphase
CEO	Chief Executive Officer
CERC	Clean Energy Research Center
CFC	Chemetall Foote Corp.
CFD	Computational Fluid Dynamics
CFF	Cell Fabrication Facility
CI	Continuous improvement
CID	Current interrupt device
CMC	Sodium Carboxy Methyl Cellulose
CN/CNF	Carbon nanofibers
CN-SC	Carbon Nanofiber Impregnated Soft Carbon
CNT	Carbon nano-tubes
CO	Certificate of Occupancy
COGS	Cost of goods sold
COP	ConocoPhillips
COTS	Commercial-Off-The-Shelf
CPE	Constant phase element
CPI	Compact Power Inc.
CPMD	Carr-Parrinello molecular dynamics theory
CPU	Central Processing Unit
CRADA	Cooperative Research and Development Agreement
CS	Charge-sustaining
CSC	Cell Supervisory Circuit
CSIRO	Commonwealth Scientific and Industrial Research Organization
CSTR	Continuous-stirred tank reactor
CT	(X-ray) Computed tomography
CTAB	Hexadecyltrimethylammonium bromide
CTB	Cyclic triol borates
CV	Cyclic voltammogram
CVD	Chemical vapor deposition
CVO	Cu-V-O (compound)
CWRU	Case Western Reserve University
CWU-FRION	Lithium [(2,5-bis(diethylphosphoryl) catecholato) oxalatoborate]
CY	Calendar year
DADT	Developmental and applied diagnostic testing
DAQ	Data Acquisition
DBPC	Di-t-butyl pyrocarbonate
DC	Direct current
DCB	Dichlorobenzene
DCR	Direct current resistance
DCS	Distributed control system

DCTA	Dicyanotriazolate
DDB	1,4-di-t-butyl-2,5-dimethoxybenzene
DDQ	2,3-Dichloro-5,6-dicyano-1,4-benzoquinon
DEC	Diethyl carbonate
DEDOHC	Diethyl 2,5 dioxohexane dicarboxylate
DEMS	Differential electrochemical mass spectroscopy
DFOB	Difluoro(oxalate)borate
DFT	Density function theory
DK	Dow Kokam
DMA	Dimethyl acetamide
DMC	Dimethyl carbonate
DME	Dimethyl ether
DMF	Dimethylformamide
DMMP	Diethyl Methyl Phosphonate
DMMSA	Dimethylmethanesulfonamide
DMS	Dimethyl sulfone
DMSO	Dimethylsulfoxide
DNS	Direct numerical simulation
DOD	Depth-of-discharge
DOE	Department of Energy
DOL	1,3-dioxolane
DOT/NHTSA	Department of Transportation/National Highway Traffic Safety Administration
DPA	Destructive physical analysis
DPC	Diphosphinato catecholate
DPDM	Discrete Particle Diffusion Model
DPN	2,3-dihydroxy-1,4-diphosphinato napthalene
DSC	Differential scanning calorimetry
DST	Dynamic stress test
DTA	Differential thermal analysis
DTAB	Dodecyltrimethyl-ammonium bromide
DTC	Daily thermal cycle
DTF	Density functional theory
DU	Degree of unsaturation
DV	Daily vehicle
DVMT	Daily vehicle miles traveled
DX	(ANSYS) DesignXplorer
EA	Environmental assessment
EADL	Electrochemical Analysis and Diagnostic Laboratory (ANL)
EB	Electron beam
EBSD	Electron backscatter diffraction
EC	Ethylene carbonate
ECM	Equivalent Circuit Model
ECS	Electrochemical Society
EDLC	Electrochemical double layer capacitor
EDS	Energy dispersive spectroscopy

EDV	Electric Drive Vehicle
EDX	Energy-dispersive x-ray (spectroscopy)
EDXRF	Energy dispersive X-ray fluorescence detector
EDXS	Energy dispersive X-ray spectroscopy
EELS	Electron energy loss spectroscopy
EERE	Energy Efficiency and Renewable Energy (DOE Office)
EES	Electrochemical energy storage
EESTT	Electrical Energy Storage Tech Team
EFRC	Energy Frontier Research Center
EFTEM	Energy-filtered transmission electron microscopy
EG/W	Ethylene glycol/water
EIS	Electrochemical Impedance Spectroscopy
EL	Electrode Library
EM	Electrochemical materials
EMC	Electron Microscopy Center
EMS	Ethyl methyl sulfone
EOC	End-of-charge
EOL	End of life
EOP	End of period
EPA	Environmental Protection agency
EPMA	Electron probe micro-analysis
EPRI	Electric Power Research Institute
EREV	Extended range electric vehicle
ES	Ethylene sulfite
ESM	Electrochemical strain microscopy
ESMS	Energy Storage Monitoring System
ESS	Energy storage system
EUCAR	European Council for Automotive Research and Development
EV	Electric vehicle
EVI	Electric Vehicle Initiative
EVMS	Earned value management system
EVPC	EV power characterization
EVS	Electric Vehicle Symposium
EW	Electrochemical window
EXAFS	Extended X-ray absorption fine structure
FA	Fluorinated acrylic (hybrid latex binder)
FC	Field cooling
FCG	Full concentration gradient
FE	Finite element
FEA	Finite element analysis
FEC	Fluoro ethylene carbonate
FESEM	Field-emission scanning electron microscope
FFCC	FutureFuel Chemical Company
FFT	Fast Fourier Transforms
FIB	Focused Ion Beam

FMS	Fluoromethyl sulfone
FOA	Federal Opportunity Anouncement
FOV	Field of view
FPM	Feet per minute
FRION	Flame Retardant Ions
FS	Fault signal
FTBA	Perfluorotributylamine
FTIR	Fourier Transform InfraRed spectroscopy
FUDS	Federal Urban Driving Schedule
FVLSM	Finite Volume Linear Superposition Methods
FWHM	Full width at half maximum
FY	Fiscal year
G&A	General and administrative (costs)
GB	Glove box
GC	Gas chromatography
GCMC	Carbonate derivative of GC
GC-MS	Gas chromatography - mass spectroscopy
GDE	Gas-diffusion-electrodes
GHG	Green house gases
GITT	Galvanostatic intermittent titration technique
GM	General Motors
GREET	Greenhouse gases, Regulated Emissions, and Energy use in Transportation (model)
GUI	Graphic user interface
HAADF	High Angle Annular Dark Field
HC	High capacity
HCA	High capacity anode
HCC	High capacity cathode
HCMRTM	High capacity manganese rich cathode materials
HCNS	Hollow carbon nanoSphere
HCSD	Harmonic Compensated Synchronous Detection
HE	High energy
HEBM	High energy ball milling
HEM	High energy material
HEMIC	Hitachi Electron Microscopy
HEMM	High energy mechanical milling
HEV	Hybrid electric vehicle
HEXRD	High energy X-ray diffraction
HF	Hydrofluoric acid
HFP	Hexafluorophosphate
HIL	Hardware-in-the-loop
HIP	Hot isostatically pressing
HNEI	Hawaii Natural Energy Institute
HOMO	Highest occupied molecular orbital
HOPG	Highly-oriented pyrolytic graphite
HP	High power

HPLC	High performance liquid chromatograph
HPPC	Hybrid pulse power characterization
HQ	Hydro-Québec
HREM	High resolution electron micrograph
HRL	Heat resistant layer
HR-SEM	High-resolution scanning electron microscopy
HRSTEM	High resolution scanning transmission electron microscopy
HR-SXRD	High resolution Silicon X-tal Reflective Display,
HRTEM	High resolution transmission Electron Microscopy
HR-TEM	High resolution transmission electron microscopy
HR-XPS	High resolution X-ray photoelectron spectroscopy
HRXRD	High resolution XRD
HS	High speed
HS-CAN	High Speed Controller Area Network
HSE	Heyd-Scuseria-Ernzerhof (exchange-correlation functional)
HT	Hydrothermal
HTMI	High temperature melt integrity
HV	High voltage
HVAC	Heating, Ventilation and Air-conditioning
HVBS	High voltage battery system
HVC	High voltage cathode
HVM	High volume manufacturing
HVTB	High Voltage Traction Battery
HW	Hot wire
HWCVD	Hot wire chemical vaporization deposition
IA	(IEA) Implementing Agreement
IA-HEV	Implementing Agreement - hybrid electric vehicles
IAPG	Interagency Advanced Power Group
IBA	International Battery Materials Association
IBC	Isothermal battery calorimeter
IBM	International Business Machines
IC	Inner composition
ICA	Incremental capacity analysis
ICACC	Internationational Conference on Advanced Ceramics and Composites
ICE	Internal combustion engine
ICL	Irreversible capacity loss
ICP	Inductively coupled plasma
ICP-AES	Inductively coupled plasma atomic emission spectroscopy
ID	Intensity of the carbon D-band
ID/IG	Ratio of integrated intensities of the D and G peaks
IEA	International Energy Agency
IEA-HEV	International Energy agency - hybrid electric vehicle
IEA-HEV-IA	International energy Agency - Hybrid Electric Vehicles - Implementing Agreement
IEEE	Institute of Electrical and Electronics Engineers
IEP	Isoelectric point

ILEET	Ionic Liquids & Electrolytes for Energy Technologies
ILIRP	Integrated Lab-Industry Research Program
IMB	Impedance Measurement Box
IMLB	International Meeting on lithium Batteries
IMRS	International Materials Research Society
IMTP	Injection-molded thermoplastic polymer
INL	Idaho National Laboratory
INW	Inorganic nanowire
IP	In-plane (signal)
IPS	Integrated Plasma Simulation
IR	Infra-red
IRAS	*In situ* external reflection-FTIR
IRCL	Irreversible Capacity Loss
ISC	Internal short circuit
ITFA	Iterative target factor analysis
JCI	Johnson Controls, Incorporated
JCS	Johnson Controls - Saft
JES	Journal of the Electrochemical Society
JPL	Jet Propulsion Laboratory
JV	Joint venture
KB	Ketjenblack
KIST	Korea Institute of science and Technology
LAHM	Loss of active host material
LAM	Loss of active material
LATP	14 Li_2O•9Al_2O_3•38TiO_2•39P_2O_5 (lithiated glass ceramic)
LAWS	Laser Acoustic Wave system
LBMP	Lithium-bearing mixed polyanion
LBNL	Lawrence Berkeley National Laboratory
LCA	Life cycle analysis
LCC	Linear cyclic carbonate
LCFP	Lithium cobalt iron phosphate
LCMO	Lithium cobalt manganese oxide
LCO	Lithium cobalt oxide
LCP	Lithium cobalt phosphate
LCPM	Levelized cost per mile
LE	Leyden Energy
LEDC	Lithium diethylcarbonate
LEED	Leadership in Energy and Environmental Design
LEES	Lower-energy energy storage (systems)
LEESS	Lower-energy energy storage systems
LFO	Li_5FeO_4
LFP	Li iron phosphate
LGCMI	LG Chem, Michigan
LGCP	LG Chem Power
LGCPI	LG Chem Power Inc.

L-HPPC	Low-current Hybrid Pulse Power Characterization
LIB	Lithium-ion battery
LIBS	Laser induced breakdown spectroscopy
LIC	Lithium ion capacitor
LLI	Loss of lithium inventory
LLNL	Lawrence Livermore National Laboratory
LLTO	$(Li,La)TiO_3$
LMCT	Ligand to metal charge transfer
LMNO	Lithium manganese nickel oxide
LMO	Lithium manganese oxide
LMR	Lithium Manganese-rich (layered cathode material)
LMR-NCM	Lithium manganese rich nickel cobalt manganese oxide
LNCA	$LiNiCoAlO_2$
LNCM	$LiNiCoMnO_2$
LNMO	$LiNi_{0.5}Mn_{0.5}O_2$
LNP	Lithium-nickel-phosphate
LPDC	Lithium propylene dicarbonate
LPSP	Lithium polysulfidophosphate
LPV	Linear Parameter Variable
LS	Low spin
LSV	Linear sweep voltammetry
LTFOP	Lithium tetrafluoro(oxalate) phosphate
LTI	Linear Time Invariant
LTO	Lithium titanate, $Li_4Ti_5O_{12}$
LTOP	Lithium tris(oxalato) phosphate
LUMO	Lowest unoccupied molecular orbital
LVO	Lithium vanadium oxide (LiV_3O_8)
MAB	Modified water soluble amine based (binder)
MAS	Magic angle spinning
MB	Methyl butyrate
MCC	Motor control center
MCMB	Mesocarbon micro beads
MD	Molecular dynamics
MDF	Manufacturing demonstration facility
MEF	Materials Engineering Facility
MERF	Materials Engineering Research Facility
MIN	Methyl isonicotinate
MIT	Massachusetts Institute of Technology
ML	Markup language
MLD	Molecular layer deposition
MNC	Metal-nitrogen- carbon
MNO	Manganese nickel oxide
MOF	Metal organic frameworks
MP	Methyl propionate
MPPC	Multiple Potential-Pair Continuum

MRS	Materials Research Society
MS	Mass spectroscopy
MS&T	Materials Science and Technology (conference)
MSI	Mass specific impedance
MSMD	Multi-scale, multi-dimensional
MSR	Mass specific resistance
MSS	Meso-porous sponge-like Si (particles)
MT	Metric ton
MTAGS	Many-Task Computing on Grids and Supercomputers (Workshop)
MW/MWCNT	Multi-wall carbon nanotubes
MWCNT	Multi-wall carbon nanotube
MW-HT	Microwave-assisted hydrothermal
MWNT	Multi-wall carbon nanotubes
MWST	Microwave-solvothermal
MW-ST	Microwave-assisted solvothermal
MYPP	Multi-year program plan
NASA	National Aeronautics and Space Administration
NASA-JSC	NASA, Johnson Space Center
NCA	$LiNi_{0.8}Co_{0.15}Al_{0.05}O_2$
NCEM	National Center for Electron Microscopy
NCM	$Li_{1+w}[Ni_xCo_yMn_z]_{1-w}O_2$
NCSU	North Carolina State University
NDA	Non-Disclosure Agreement
NDE	Non-destructive evaluation
NEDO	New Energy and Industrial Technology Development Organization (Japan)
NEI	Natural Energy Institute (Hawaii)
NERSC	National Energy Research scientific Computing Center
NETL	National Energy Technology Laboratory
NF-IR	Near field - infrared
NG	Natural graphite
NGP/CNF	Nano-graphene platelets/carbon nanofibers
NHTSA	National Highway Transportation Safety Administration
NIST	National Institute of Standards and Technology
NIU	Northern Illinois University
NMC	$LiNi_{1/3}Co_{1/3}Mn_{1/3}O_2$
NMP	N-methylpyrrolidone
NMP/PVDF	N-Methyl Pyrrolidinone/PVDF
NMR	Nuclear magnetic resonance
NP	Nanoparticle
NRC	National Research Council
NREL	National Renewable Energy Laboratory
NSLS	National Synchrotron Light Source
NSWC	Naval Surface Warfare Center
NSWCCD	Naval Surface Warfare Center, Carderock Division
NTGK	Newman-Tiedemann-Gu-Kim (model)

OAS	Open architecture software
OBD	3-Oxabicyclo[3.1.0]hexane-2,4-dione
OC	Outer composition
OCP	Open-circuit potential
OCV	Open circuit voltage
OECD	Organization for Economic Cooperation and Development
OEE	Overall equipment effectivenss
OEM	Original equipment manufacturer
OER	Oxygen evolution reaction
OES	Optical emission spectrometry
OFDDB	Ortho-6,7-dimethoxy-1,1,4,4-tetramethyl-1,2,3,4-tetrahydronaphthalen
OHD	3-Oxabicyclo[3.1.0]hexane-2,4-dione
OLC	Onion-like carbon
OP	Out-of plane (signal)
ORNL	Oak Ridge National Laboratory
ORR	Oxygen reduction reaction
OS	Output split
OSA	Open Software Architecture
OVT	(DOE) Office of Vehicle Technologies
PAA	Polyacrylic acid
PAHEV	Power-assist hybrid electric vehicle
PA-HEV	Power assist - hybrid electric vehicle
PAHEV, PA-HEV	Power assist - hybrid electric vehicle
PAN	Polyacrylonitrile
PAQS	Poly(anthraquinonyl sulfide)
PBE	Perdew Burke Ernzerhof (correlation)
PBM	Planetary ball milling
PC	Propylene carbonate
PCA	Principal component analysis
PCB	Printed circuit board
PCFC	Pyrolysis combustion flow calorimetry
PCM	Polarized continuum model
PD	Path dependence
PDF	Pair density function
PE	Polyethylene
PEAA	Polyethylene-co-acrylic acid
PEC	Polyethylene carbonate
PEDOT	Poly(3,4-ethylenedioxythiophene)
PEDOT-SP	PEDOT - Super P carbon
PEFM	Poly(2,7-9,9-dioctylfluorene-co-2,7-9,9-(di(oxy-2,5,8-trioxadecane)) fluorine-co-2,7-fluorenone-co-2,5-1-methylbenzoic ester)
PEI	Polyethyleneimine
PEMS	Plasma-enhanced magnetron sputtering
PEO	Polyethyleneoxide
PEV	Plug-in electric vehicle

PF	Polyfluorene
PFA	Polyfluoroalkyl
PFBP	Perfluorinated tert butoxide grafted phosphazene
PFG	Pulse field gradient
PFM	Poly(9,9-dioctylfluorene-co-fluorenone-co-methylbenzoic ester)
PFO	Poly(9,9-dioctylfluorene)
PFOP	Poly[(9,9-dioctylfluorenyl-2,7-diyl)-co-(1,4-phenylene)]
PHEV	Plug-in hybrid electric vehicle
PHEV10	PHEV with 10-mile range
PHEV40	PHEV with 40-mile range
PI	Principal Investigator
PLA	Protected lithium anode
PLD	Pulsed laser deposition
PMMA	Poly-methyl methacrylate
PMP	Project Management Plan
PNF	Functionalized phosphazene
PNNL	Pacific Northwest National Laboratory
PPAP	Production Part Approval Process
PPO	Poly(phenylene oxide) (binder)
PPSS	Pacific Power Sources Symposium
PQ	Project Quarter
PS	Polystyrene
PSP	Particle Stability Parameter
PS-PE-PS	Polystyrene-b-polyethylene-b-polystyrene
PSU	Pennsylvania State University
PTC	Positive temperature coefficient (device)
PTF	Post-Test Facility
PTFE	Poly(tetrafluoroethylene)
PV	Photovoltaic
PVDF	Poly(vinylidenefluoride)
PXRD	Powder X-ray diffractometry
R&D	Research and Development
R2R	Roll-to-roll
RAIRS	Reflection absorption infrared spectroscopy
RAL	Rutherford Appleton Laboratory
RC	Resistance-Capacitor
RDE	Rotating-disk electrode
RF	Radio frequency
RFP	Request for proposals
RFPI	Request for proposal information
RMS	Root mean square
ROM	Reduced Order Modeling
RPM	Revolutions per minute
RPT	Reference performance test
RSOXS	Resonant soft X-ray scattering

RT	Room temperature
RTO	Regenerative Thermal Oxidizer
RUL	Remaining useful life
SAD	Selected area diffraction
SAE	Society of Automotive Engineers
SAED	Selected area electrode diffraction
SAEDP	Selected area electron diffraction pattern
SAXS	Small Angle X-ray Scattering
SBG	Si/B4C/graphite
SBIR	Small Business Innovation Research
SBIR/STTR	Small Business Innovation Research/Small Business Technology Transfer
SBR	Styrene-Butadiene Rubber
SCFM	Standard cubic feet per minute.
SCP	Spherical carbon particles
SDG&E	San Diego Gas & Electric Co.
SED	Stacked electrode design
SEI	Solid electrolyte interphase
SEM	Scanning electron microscopy
SEM/FIB	Scanning electron microscopy/focused ion beem
SEM-EDS	Scanning electron microscopy/Energy Dispersive X-ray spectroscopy
SENB	Single Edged Notched Bend
SEO	Poly(styrene)-b-poly(ethylene oxide)
SES	Poly(styrene-block-ethylene-block-polystyrene)
SET	Source Evaluation Team
SFG	Sum Frequency Generation
SHES	Self-healing electrostatic shield
SIC	Single ion conducting
SIMS	Secondary ion mass spectrometry
SLAC	Stanford acceleration laboratory
SLI	Starting-Lighting-Ignition
SLMP	Stabilized lithium metal powder
SLP	Single layer pouch (cells)
SLPB	Superior Lithium Polymer Batteries
SNL	Sandia National Laboratories
SNS	Spallation Neutron Source
SOA	State of the art
SOC	State of charge
SOH	State of health
SOP	Start of production
SORP	Start of Regular Production
SOW	Statement of Work
SP	Super-P (carbon)
SPI	Schedule performance index
SPM	Scanning Probe Microscopy
SPPC	Single Potential-Pair Continuum

SQUID	Superconducting Quantum Interference Device
SRP	Solvent Recovery Process
SRS	Safety Reinforcing Separator
SSR	Solid-state reaction
SSRL	Stanford Synchroton Radiation Lightsource
STEM	Scanning transmission electron microscopy
STEM/EELS	Scanning transmission electron microscopy/electron energy loss spectroscopy
STTR	Small Business Technology Transfer Program
STXM	Scanning transmission X-ray microscopy
SUNY	State University of New York
SUV	Sport utility vehicle
SVF	Solid volume fraction
SWIM	Simulation of RF Wave Interactions with Magnetohydrodynamics
TAC	Technical Advisory Committee
TAMU	Texas A&M University
TAP	Technology Assessment Program
TARDEC	(United States) Army Tank Automotive Research, Development and Engineering Center
TBACL	Tetrabutylammonium chloride
TCNQ	Benzoquinone, Tetracyanoquinodimethane
TCO	Total cost of ownership
TCS	Traffic Choices Study
TDI	4,5-dicyano-2-(trifluoromethyl)imidazolide
TEGDME	Tetraethyleneglycoldimethyl
TEM	Transmission electron microscopy
TEY	Total electron yield
TFSI	Bis(trifluoromethanesulfonyl)imide
TFY	Total fluorescence yield
TGA	Thermal gravimetric analysis
TLVT	Technology Life Verification Testing
TM	Transition metal
TMA	Tri-methyl aluminum
TMS	Tetramethylene sulfone
TOF-SIM	Time-of-flight – secondary ion mass spectroscopy
TOF-SIMS	Time-of-flight – secondary ion mass spectroscopy
TOS	3,9-divinyl-2,4,8,10-tetraoxaspiro[5,5] undecane
TPB	Thermal protective barrier
TPFPB	Tris(pentafluorophenyl) borane
TPP	Tri(2-furyl)phosphine
TPYT	2,4,6-Tris(2-propen-1-yloxy)-1,3,5-triazene
TRB	Transportation Research Board
TR-XAS	Time resolved x-ray absorption spectroscopy
TR-XRD	Time-resolved X-ray diffraction
TR-XRD/MS	Time-Resolved XRD/Mass Spectroscopy
TSE	Twin-screw extruder
TT	Technical Team

TTF	Thermal Test Facility
TTT	1,3,5-triallyl-[1,3,5]triazinane-2,4,6-trione
TXM	Transmission X-ray Microscopy
TXM-XANES	Transmission X-ray microscopy with X-ray near edge absorption spectroscopy
TXPS	Tender X-ray photoelectron spectroscopy
UC	University of California
UCB	University of California, Berkeley
UCSD	University of California, San Diego
UCV	Upper cut-off voltage
UDDS	Urban Dynamometer Driving Schedule
UHMWPE	Ultra High Molecular Weight Polyethylene
UL	Underwriters Laboratory
URI	University of Rhode Island
USABC	United States Advanced Battery Consortium
USBAC	United States Advanced Battery Consortium
USCAR	United States Council for Automotive Research
USDRIVE	Driving Research and Innovation for Vehicle efficiency and Energy sustainability
USGS	United States Geological Survey
USPTO	United States Patent and Trademark Office
UTA	University of Texas, Austin
UV	Ultraviolet
VACNT	Vertically aligned carbon nanotube
VASCNT	Vertically aligned silicon carbon nanotube
VASP	Vienna Ab-initio Simulation Package
VC	Vinylene carbonate
VCU	Virginia Commonwealth University
VEC	Vinyl ethylene carbonate
VF	Voltage fade
VIBE	Virtual Integrated Battery Environment
VMS	Variational multi-scale simulation
VMT	Vehicle miles traveled
VPS	Voltage profile simulation
VRLA	Valve Regulated Lead-Acid
VSATT	Vehicle Systems Analysis Technical Team
VT, VTO	Vehicle Technologies Office
WB	Workbench
WC	Wu-Cohen (correlation)
WDT	Wildcat Discovery Technologies
WDXRF	Wavelength dispersive dispersive X-ray fluorescence detector
WECC	Western Electrical Coordinating Council
WPPC	Wound Potential-Pair Continuum
WSU	Washington State University
WTW	Well-to-wheels
XAFS	X-ray absorption fine structure
XANE	X-ray absorption near-edge structure (spectra)

XANES	X-ray absorption near edge structure
XAS	X-ray absorption spectroscopy
XCH	eXcited Core Hole
XCT	X-ray Computed Tomography
XEDS	X-ray energy dispersive spectroscopy
XES	X-ray emission spectroscopy
XPS	X-ray photoelectron spectroscopy
XR	X-ray reflectivity
XRD	X-ray diffraction
XRF	X-ray fluorescence spectroscopy
XRS	X-ray Raman scattering
ZFC	Zero field cooling

DOE/EE-1038 February 2014
Printed with a renewable-source ink on paper containing
at least 50% wastepaper, including 10% post consumer waste.

U.S. DEPARTMENT OF ENERGY | Energy Efficiency & Renewable Energy

For more information
eere.energy.gov